



The Commission of the European Communities and the European Committee for the Study and Application of Analytical Work in the Steel Industry (CETAS) are pleased to announce the

8th International Workshop on

Progress in Analytical Chemistry & Materials Characterisation in the Steel and Metal Industries.



Luxembourg - May 17-19, 2011

D'Coque, the "National Athletic and Cultural Center"

co-organised by the Centre for Research in Metallurgy (CRM) and the Public Research Centre (CRP) Henri Tudor,

Full papers

Symposium Secretariat

LD Organisation
Scientific Conference Producers
Rue Michel de Ghelderode 33/2
1348 Louvain-la-Neuve - Belgium
Tel: +32 10 45 47 77, Fax: +32 10 45 97 19
Secretariat@ldorganisation.com

www.cetas2011.org



LIST OF FULL PAPERS

OC01	OPTIMIZATION OF NITROGEN ANALYSIS BY SPARK OPTICAL EMISSION SPECTROMETRY AT ARCELORMITTAL TUBARÃO <i>Mr Alex Matilha, ARCELORMITTAL TUBARÃO, Brazil</i>	1
OC02	CHEMICAL ANALYSIS OF HIGH-ALLOYED STEEL BY XRF SPECTROSCOPY AS BORATE FUSED BEAD <i>Dr Simona Rollet, COGNE ACCIAI SPECIALI, Italy</i>	9
OC03	On-site Direct Microscopy and Composition Analysis in Metal Industry <i>Mr Olivier Lemaire, CRM, Belgium</i>	14
OC04	MICROWAVE ASSISTED HIGH-PRESSURE DIGESTION SYSTEMS – TECHNIQUES AND APPLICATIONS <i>Dr Eckhard Pappert, THYSSENKRUPP STEEL EUROPE AG, Germany</i>	26
OC05	MICROWAVE DIGESTION - IMPROVED SAMPLE PREPARATION FOR ICP-OES ANALYSIS OF METAL POWDER IN THE QUALITY CONTROL LAB <i>Dr Alexander Henrich, HÖGANÄS SWEDEN AB, Sweden</i>	33
OC06	THE TRIBOLOGICAL PROPERTIES OF ROLLING OIL EMULSIONS WITH AND WITHOUT NANOPARTICLES <i>Dr Karin Persson, YKI; INSTITUTE FOR SURFACE CHEMISTRY, Sweden</i>	40
OC07	THE USE OF FIB IN METAL RESEARCH <i>Dr Chris Xhoffer, OCAS, Belgium</i>	48
OC08	ELEMENTAL MONITORING OF STEEL SCRAP LOADING AN ELECTRICAL ARC FURNACE <i>Dr Volker Sturm, FRAUNHOFER ILT, Germany</i>	55
OC09	LIBS – A PROMISING TOOL FOR FAST STEEL CHARACTERISATION <i>Dr Fabienne Boue-Bigne, TATA STEEL EUROPE R&D, United Kingdom</i>	62
OC10	MATRIX SEPARATION WITH NONIONIC SURFACTANTS AND IONIC LIQUIDS FOR THE DETERMINATION OF TRACE ELEMENTS IN HIGH-PURITY IRON METALELEMENTS IN HIGH-PURITY IRON METAL <i>Prof Masataka Hiraide, NAGOYA UNIVERSITY, Japan</i>	69
OC11	EFFECT OF THE DUTY RATIO OF PULSED BIAS CURRENT ON THE ANALYTICAL PERFORMANCE IN RADIO-FREQUENCY GLOW DISCHARGE PLASMA OPTICAL EMISSION SPECTROMETRY ASSOCIATED WITH BIAS-CURRENT MODULATION TECHNIQUE <i>Dr Kazuaki Wagatsuma, IMR, TOHOKU UNIVERSITY, Japan</i>	76
OC12	INSIGHT INTO THE ROLL GAP - REVEALING HIDDEN PROCESSES BY ANALYTICAL MEANS <i>Dr Martin Raulf, THYSSENKRUPP STEEL EUROPE, Germany</i>	82
OC13	COMBINED APPLICATION OF MICRO CLEANLINESS MEASUREMENT DEVICES FOR SUCCESS IN MAGNESIA INCLUSION DETECTION IN SLABS <i>Dr Andreas Pissenberger, VOESTALPINE STAHL, Austria</i>	89
OC14	RAPID INCLUSION MAPPING TECHNOLOGY FOR SLAB SAMPLE <i>Dr YongTae Shin, POSCO, South Korea</i>	95
OC15	ADVANCES IN THE ULTRA-FAST INCLUSION ANALYSIS IN STEEL BY SPARK OES - PHENOMENOLOGY, IMPROVEMENTS AND CALCULATION OF INCLUSIONS' COMPOSITION AND SIZE <i>Dr Jean-Marc Böhlen, THERMO FISHER SCIENTIFIC, Switzerland</i>	101



LIST OF FULL PAPERS

OC16	STEEL CLEANNES AND REFERENCE MATERIALS <i>Dr Gunilla Runnsjö, OUTOKUMPU STAINLESS, Sweden</i>	109
OC17	THREE DIMENSIONAL ESTIMATION OF MULTI-COMPONENT INCLUSION <i>Prof Ryo Inoue, TOHOKU UNIVERSITY, Japan</i>	118
OC18	USE OF ON-LINE EVALUATION OF PDA-DATA AT SSAB AT OXELÖSUND AND OUTOKUMPU STAINLESS AB AT AVESTA <i>Ing Torbjörn Engkvist, OUTOKUMPU STAINLESS, Sweden</i>	126
OC19	LASER-BASED METHODS FOR CHEMICAL COMPOSITION ANALYSIS OF PARTICULATE EMISSIONS FROM STEELMAKING PROCESSES <i>Dr Cord Fricke-Begemann, FRAUNHOFER ILT, Germany</i>	131
OC20	NATURALLY OCCURRING RADIOISOTOPES (POLONIUM-210 / LEAD-210) IN STEELMAKING MATERIALS AND THE IRON ORE SINTERING PROCESS <i>Mr Franck DAL-MOLIN, TATA STEEL UK LTD, United Kingdom</i>	139
OC21	SPECIATION OF FE, NI AND CO FOR RECYCLING PURPOSES <i>Mr Xavier Vanden Eynde, CRM GROUP, Belgium</i>	147
OC22	DEVELOPMENT OF A NEW METHOD FOR THE DETERMINATION OF PARTICLE- BOUND PAHS BASED ON DIRECT THERMAL EXTRACTION - GAS CHROMATOGRAPHY - MASS SPECTROMETRY <i>Ms Diane Ciaparra, TATA STEEL RD&T, United Kingdom</i>	156
OC23	RESISTANCE SPOT WELDING FUMES OF COATED STEEL <i>Dr Veerle Van Lierde, OCAS, Belgium</i>	163
OC24	THE MEASUREMENT OF GAS PHASE REACTIONS AT STEEL SURFACES USING A MASS SPECTROMETER PROBE <i>Prof Heinz Falk, SCIENTIFIC CONSULTANCY PROF. FALK, Germany</i>	168
OC25	DETERMINATION OF ARGON BY INERT GAS FUSION - TIME-OF-FLIGHT MASS SPECTROGRAPH METHOD <i>Dr Peng Wang, BEIJING NCS ANALYTICAL INSTRUMENTS CO., China</i>	175
OC26	CORRECTION METHOD OF MASS SPECTRAL INTERFERENCE BETWEEN CO⁺⁺ AND N₂⁺ AND ITS APPLICATION IN SIMULTANEOUS ANALYSIS OF CO AND N₂ <i>Dr Peng Wang, BEIJING NCS ANALYTICAL INSTRUMENTS CO., China</i>	182
OC27	ORIGINAL STATISTIC DISTRIBUTION ANALYSIS BY LASER INDUCED - BREAKDOWN SPECTROMETRY <i>Mr Lei Zhao, BEIJING NCS ANALYTICAL INSTRUMENTS CO., China</i>	190
OC28	ToF-SIMS ANALYSIS OF ANTICORROSION ADDITIVES ON TECHNICAL SURFACES <i>Mr David Poerschke, THYSSENKRUPP STEEL EUROPE, Germany</i>	196
OC29	EXPERT SYSTEMS FOR PREDICTION OF CORROSION PROPERTIES OF ZN- BASED COATINGS FROM THE CHEMICAL ANALYSIS <i>Dr Arne Bengtson, SWEREA KIMAB AB, Sweden</i>	201
OC30	EXPLORATION AND VALIDATION ON THE CHARACTERISATION OF THIN COATING ON STEEL SURFACE IN INDUSTRY APPLICATION <i>Mrs Li Lei, SHANGHAI BAOSTEEL INDUSTRY INSPECTION CORP., China</i>	208



LIST OF FULL PAPERS

OC31	ANTI-CORROSION PROPERTIES OF ORGANOSILICON PLASMA POLYMER COATINGS FILLED WITH CERIUM NANOPARTICLES DEPOSITED FOR PROTECTION OF GALVANIZED STEEL <i>Mr Julien Bardon, CENTRE DE RECHERCHE PUBLIC HENRI TUDOR, Luxembourg</i>	213
OC32	XRF VERSUS GDOES IN STEEL INDUSTRY APPLICATIONS <i>Dr Myriam Madani, ARCELOR MITTAL, Belgium</i>	219
OC33	IN SITU XPS FOR SURFACE SPECIATION DURING ANNEALING OF STEELS <i>Mr Xavier Vanden Eynde, CRM GROUP, Belgium</i>	224
OC34	HYDROGEN DETERMINATION IN STEEL AT VOESTALPINE <i>Dr Hubert Duchaczek, VOESTALPINE STAHL, Austria</i>	236
OC35	DETERMINATION OF HYDROGEN IN STEEL BY THERMAL DESORPTION MASS SPECTROMETRY <i>Mrs Karin Bergers, THYSSENKRUPP STEEL EUROPE, Germany</i>	240
OC36	DESTRUCTIVE AND NON-DESTRUCTIVE DETERMINATION OF HYDROGEN IN METALS WITH SPECIAL EMPHASIS ON STEELS <i>Prof Reiner Kirchheim, UNIVERSITY OF GOETTINGEN, Germany</i>	250
OC37	APPLICATION AND INNOVATIONS FOR CS AND ONH ANALYZERS ~ SURFACE CARBON SEPARATION WITH HIGH FREQUENCY HOT EXTRACTION AND CARRIER GAS ANALYSIS <i>Mr Alain SALAVILLE, HORIBA SCIENTIFIC, France</i>	256
OC38	TATA STEEL IJMUIDEN LAB MADE FIT FOR THE FUTURE <i>Mr Robert Heemskerk, TATA STEEL, The Netherlands</i>	261
OC39	INTEGRATION OF THE ROBOTIZED BORATE FUSION TECHNIQUE FOR THE XRF ANALYSIS IN THE FERROALLOY INDUSTRY <i>Mr Sebastien Rivard, CORPORATION SCIENTIFIQUE CLAISSE, France</i>	263
OC40	THE IMPORTANCE OF SAMPLE PREPARATION AS PART OF LABORATORY WORKFLOW AUTOMATION SOLUTIONS <i>Mr Marc Bassin, THERMO FISHER SCIENTIFIC, Switzerland</i>	271
OC41	A NEW GENERATION IN SPARK EMISSION SPECTROMETRY <i>Dr Joerg Niederstrasser, OBLF, Germany</i>	278
OC42	SAMPLING METHODS AND SAMPLE PREPARATION (76) <i>Mrs Maria PELE, CTIF, France</i>	286
OC43	IMPROVEMENT OF THE SAMPLING FOR CLEANNES MEASUREMENT AT LIQUID STEEL STAGE <i>Mrs Fabienne RUBY-MEYER, ASCOMETAL CREAS, France</i>	294
OC44	INVESTIGATION OF THE POSSIBILITIES TO CHANGE SAMPLE PREPARATION FROM GRINDING TO MILLING FOR FE- AND NI-BASE ALLOYS <i>Mr Peter Henningsson, AB SANDVIK MATERIALS TECHNOLOGY, Sweden</i>	302
OC45	EFFECT OF SAMPLING CONDITIONS ON INCLUSION CHARACTERISTICS IN SAMPLES FROM LIQUID STEEL <i>Dr Ola Ericsson, SUZUKI GARPHYTTAN, Sweden</i>	303
OC46	DETERMINATION OF BORIC ANHYDRIDE IN THE ASCHARITE ORES BY INDUCTIVELY COUPLED PLASMA ATOMIC EMISSION SPECTROMETRY <i>Ms wen xiangdong, WISCO, China</i>	311



LIST OF FULL PAPERS

OC47	PROGRESS ON ANALYTICAL METHODS FOR COMPOSITION OF NICKEL-BASE ALLOYS IN CHINA <i>Mr Xiaodong Shao, CNPC TUBULAR GOODS RESEARCH INSTITUTE, China</i>	317
OC48	METALLURGICAL AND MECHANICAL CHARACTERIZATION OF CU ELECTROLYTIC COATING ON ALUMINIUM ALLOYS <i>Mrs Irene Calliari, UNIVERSITY OF PADOVA, Italy</i>	326
OC49	MICRO-STRUCTURAL AND CHEMICAL CHARACTERIZATION OF ELECTRIC ARC FURNACE SLAG <i>Ing Davide Mombelli, POLITECNICO DI MILANO, Italy</i>	331
OC50	COMPREHENSIVE ANALYSIS OF PRECIPITATES IN RICH CR STEELS BY ELECTRON ENERGY LOSS SPECTROMETRY SPECTRUM IMAGING <i>Dr Mhaela Albu, ZENTRUM FÜR ELEKTRONENMIKROSKOPIE GRAZ, Austria</i>	339
OC51	MAGNETIC AND METALLOGRAPHIC INVESTIGATION OF PHASE TRANSFORMATIONS IN DUPLEX STAINLESS STEELS <i>Mrs Irene Calliari, UNIVERSITY OF PADOVA, Italy</i>	347
OC52	IMPROVED ANALYSIS OF CARBON IN CAST IRON <i>Dr Heinz-Gerd Joosten, SPECTRO ANALYTICAL INSTRUMENTS, Germany</i>	353
OC53	TRACEABLE ANALYSIS OF IMPURITIES IN METALLIC REFERENCE MATERIALS USING GD-MS <i>Dr Sebastian Recknagel, BAM, Germany</i>	361
OC54	THE EVOLUTION OF MINIMUM SAMPLE MASS OF RMS BY HOMOGENEITY STUDY <i>Mr JIANPING XU, WUHAN UNIVERSITY OF SCIENCE AND TECHNOLOGY, China</i>	366
OC55	STANDARDISATION OF ICP-OES ROUTINE METHOD(S) FOR LOW ALLOY STEEL ANALYSIS (77) <i>Mrs Maria PELE, CTIF, France</i>	370
OC56	CHARPY IMPACT PROFICIENCY TESTING IN MECHANICAL TESTING LABORATORIES <i>Ms Yifei Gao Yifei, BEIJING NCS ANALYTICAL INSTRUMENTS CO. LTD, China</i>	378
OC57	ANALYTICAL TREATMENT OF UNCERTAINTIES FOR A MACROSCOPIC TRIBOLOGY INSTRUMENTATION <i>Ing Valentina Mazzanti, UNIVERSITY OF FERRERA, Italy</i>	383
OC58	EXPRESSING MEASUREMENT UNCERTAINTY IN SPARK-OES ANALYSIS WITH APPLICATION FOR THE MATERIAL CONFORMITY PROBABILITY CALCULATION <i>Mr Edmund Halasz, THERMO FISHER SCIENTIFIC, Switzerland</i>	391
OC59	ORIGINAL POSITION STATISTIC DISTRIBUTION ANALYSIS OF TRACE ELEMENT SEGREGATION IN NICKEL-BASE SUPER ALLOY BY LA-ICP-MS <i>Mr Lei Zhao, BEIJING NCS ANALYTICAL INSTRUMENTS CO., China</i>	398
OC60	SUPERMAGNAG : A NEW MAGNETIC SENSOR FOR AN ON-LINE MONITORING OF THE SINTERING PROCESS <i>Mrs Cécile Mathy, CRM, Belgium</i>	407
OC61	DEVELOPMENT OF AN ON-LINE LIBS-BASED SENSOR FOR MONITORING THE HOT METAL COMPOSITION IN THE BLAST FURNACE RUNNERS <i>Mr Guy MONFORT, CRM GROUP, Belgium</i>	415
OC62	ELEMENT ANALYSIS OF OXIDE MATERIALS IN STEEL INDUSTRY BY LASER-INDUCED BREAKDOWN SPECTROSCOPY <i>Mr Johannes D. Pedarnig, JOHANNES KEPLER UNIVERSITY LINZ, Austria</i>	423



LIST OF FULL PAPERS

OC63	SRM: AN INDUSTRIAL ON-LINE TOPOGRAPHY MEASUREMENT <i>Dr Wolfgang Bilstein, AMEPA, Germany</i>	427
OC64	WAVIMETER: ON LINE MEASUREMENT OF WAVINESS <i>Mrs Genevieve Moreas, CRM GROUP, Belgium</i>	435
OC65	ON-LINE DETERMINATION OF MG COATING THICKNESS ON ELECTROLYTICALLY GALVANIZED STEEL IN MOTION USING A LIBS DEMONSTRATOR <i>Mr Javier LASERNA, UNIVERSITY OF MALAGA, Spain</i>	444
OC67	ORIGINAL POSITION STATISTIC DISTRIBUTION ANALYSIS FOR THE SULFIDES IN GEAR STEELS <i>Mrs Dongling Li, BEIJING NCS ANALYTICAL INSTRUMENTS CO., China</i>	452
OC68	BRIEF OF THE QUALITY CONTROL OF THE AUTOMATIC ANALYSIS SYSTEM IN STEEL-MAKING INDUSTRY <i>Mr Yang Le, BAOSHAN IRON & STEEL CO., LTD., China</i>	460
OC69	QUALITATIVE AND QUANTITATIVE ANALYSIS OF PRECIPITATE PHASES IN 2205 DUPLEX STAINLESS STEEL WITH DIFFERENT ISOTHERMAL TREATMENT SITUATION <i>Mr Miao Lede, BAOSHAN IRON AND STEEL CO., China</i>	466
OC70	PRECIPITATION STUDY ON TI-NB-MO CONTAINED HIGH STRENGTH STEELS <i>Dr Ning Cai, SHOUGANG TECHNIC RESEARCH INSTITUTE, China</i>	474
OC71	MONITORING OF HEAT TREATMENT PROCESSES WITH HIGH ENERGY X-RAY <i>Mr Thomas Rieger, RWTH AACHEN UNIVERSITY, Germany</i>	479
OC73	APPLICATION OF LASER ABLATION ICP MASS SPECTROMETRY FOR RAPID ANALYSIS OF OXIDE PARTICLES IN METAL SAMPLES <i>Mr Andrey KARASEV, ROYAL INSTITUTE OF TECHNOLOGY (KTH), Sweden</i>	487
OC74	DETERMINING INCLUSION SIZE DISTRIBUTIONS FROM OES/PDA DATA <i>Dr Rolf Wester, FRAUNHOFER INSTITUT FÜR LASERTECHNIK, Germany</i>	495
OC76	TRUE SIMULTANEOUS ELEMENTAL ANALYSIS FOR RAPID PROCESS CONTROL BY XRF <i>Dr Kai Behrens, BRUKER AXS, Germany</i>	502
OC77	ONLINE MONITORING OF HOT DIP GALVANIZING BATH BY LIBS TECHNIQUE <i>Mrs Sophie Jacques, ARCELORMITTAL, France</i>	503
OC78	DIRECT DETERMINATION OF TRACE ELEMENTS IN STEEL BY LASER ABLATION/ICP-MS <i>Mr Tomoharu Ishida, JFE STEEL CORPORATION, Japan</i>	511
OC79	CHARACTERIZATION OF THIN FILMS ON ROUGH STEEL SUBSTRATES: WHICH METHOD FITS BEST? <i>Dr Ann De Vyt, OCAS, Belgium</i>	517
OC80	MECHANICAL RESISTANCE OF ALUMINIUM-EPOXY ASSEMBLIES AS A FUNCTION OF ALUMINIUM SURFACE TREATMENT WITH ATMOSPHERIC PLASMA <i>Mr Joao Bomfim, CRP HENRI TUDOR, Luxembourg</i>	525
OC81	USE OF GLOW DISCHARGE SPECTROMETRY FOR BULK AND COATING <i>Mr Thomas Brixius, THYSSENKRUPP STEEL EUROPE, Germany</i>	533



LIST OF FULL PAPERS

OC82	ESTABLISHMENT AND APPLICATION OF ANALYSIS MODEL FOR AL INCLUSION SIZE ON THE BASIS OF ABNORMAL SPARK FREQUENCY DISTRIBUTION <i>Mrs Meiling Li, CHINA IRON & STEEL RESEARCH INSTITUTE GROUP, China</i>	540
OC83	APPLICATION OF EXTRACTION METHODS FOR INVESTIGATION OF NON-METALLIC INCLUSIONS AND CLUSTERS IN STEEL AND ALLOYS <i>Ms Diana Vasiljevic, ROYAL INSTITUTE OF TECHNOLOGY, Sweden</i>	547

OPTIMIZATION OF NITROGEN ANALYSIS BY SPARK OPTICAL EMISSION SPECTROMETRY AT ARCELORMITTAL TUBARÃO

Laura Paes Sales Fagundes, Marina Theresa Antunes Garcia Mendes, Ana Carolina de Oliveira Dieguez, Alex Matilha

ArcelorMittal Brasil S/A – Av. Brigadeiro Eduardo Gomes, 930 – Jardim Limoeiro – Serra – Brasil

1) Summary

In the latest years, as steel industry becomes more demanding and competitive, steel shop process has an increasing need to control the production specifications on time with reliable results. In this context, accurate nitrogen results are essential to control process sealing and to guarantee desired product characteristics (especially tenacity and machinability).

Clearly, classical combustion techniques (CC) have been widely used in past years for determining carbon, sulfur and nitrogen in steel. However, spark emission has also been used and has been gaining popularity as a result of improved performances, reduction in consumables costs (associated with CC) and time gains.

This work aimed to optimize nitrogen analysis by optical emission spectrometry (OES) in the Steel Chemical Analysis Laboratory of ArcelorMittal Tubarão located in Serra, Brazil and was performed according to DMAIC methodology (specific tool to improve the quality of processes). The potential influence variables were analyzed (shift, sample and period), the basic causes related to nitrogen precision were identified and prioritized. After that the action plan was implemented and the results were evaluated focusing in precision (evaluated based on an internal reference material standard deviation) and accuracy (evaluated comparing with OE certified reference material and LECO cross checks).

Before this project development, nitrogen standard deviation by optical emission reached 0.0040%. The trials made after the implementation of all planned actions in one of ArcelorMittal Tubarão's spectrometers showed the potential of this technique, since a standard deviation of 0.0005% was achieved. This result was monitored weekly during 3 months, floating from 0.0003 to 0.0005% what demonstrate its stability. Therefore optical emission technique appears as a promising method to perform nitrogen analysis, attending process requests besides other mentioned secondary gains.

2) Introduction

ArcelorMittal Tubarão is among the largest Brazilian exporters of flat steel. Its products serve the automobile, auto parts, electro-electronic, tubes, civil construction, naval and other industries. It was the first steelmaking company in the world to obtain the Certified Emission Reduction (CER) from the UN and to negotiate carbon credits in the market. Responsible for almost 20% of the national production of hot coils and plates, ArcelorMittal Tubarão operates one integrated steel plant with a capacity of 7.5 million tons/year of steel. Its advantageous location in the Great Vitoria Region in the State of Espírito Santo, favors trade with customers from all corners of the world.

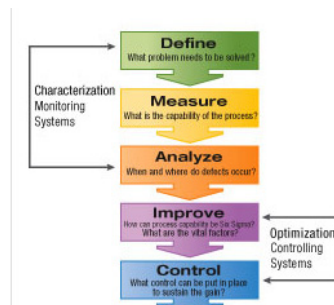
In this context, the Chemical Lab performs analysis to different production areas of ArcelorMittal Tubarão, being steel shop its main client (slag and steel analysis). To attend this demand the Lab has the following resource:

- Slag analysis: 2 X-Ray Fluorescence Spectrometers
- Steel analysis: 3 Automatized Steel Analysis Systems (3 Optical Emission Spectrometer, 1 grinding machine, 2 milling machines and 3 Robots)
- 2 Nitrogen & Oxygen Analyzer: Nitrogen and oxygen in steel

The Optical Emission Spectrometer (supplied by Thermo ARL) is an instrument used to measure concentrations of chemical elements. The measure object is a metallic sample of the material. The atomic spectra emitted by the sample are used to determine its quantitative elemental composition (light emission from different elements can be distinguished by differing wavelengths).

The Nitrogen Analyzer (supplied by LECO) is based on the sample melting in electrode oven in helium constant flow, releasing nitrogen in N₂ form. The nitrogen is detected on a thermal conductivity cell. This technique is world wide known as classical combustion, and is the most common method used for carbon, sulfur and nitrogen analysis in steel.

Because of ArcelorMittal Tubarão Unit recent production capacity expansion from 5.0 to 7.5 million tons / year (finished in 2007) and steel shop increasing needs of accurate nitrogen results for process and product monitoring, it was identified the necessity to reduce nitrogen analysis response time. In order to develop this project with the guaranty to achieve faster and consistent results, the DMAIC methodology (Picture 1) was applied.

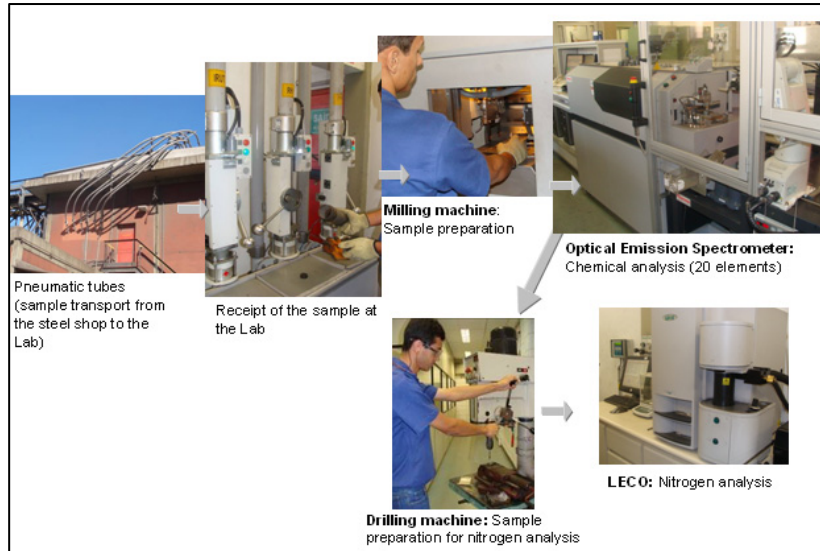


Picture 1 – DMAIC methodology.

3) Define

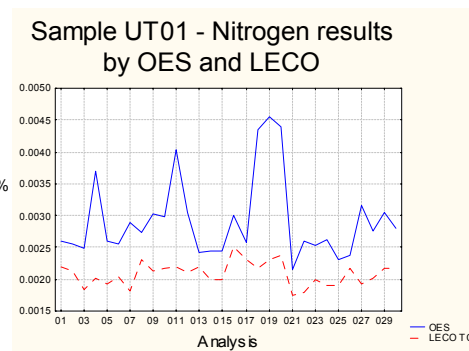
The main objective of this first step is to well establish the scope of the project.

The Lab analyze an average of 9 samples per heat, consisting of 1 pig iron sample, 3 steel samples from Converter, 3 steel samples from Secondary Refining and 2 steel samples from Continuous Casting. The steel analysis flow at the Lab is shown at Picture 2. The OES analysis takes 4 minutes and the LECO analysis, 8 minutes in average. Therefore, nitrogen analysis response time is in average 12 minutes.



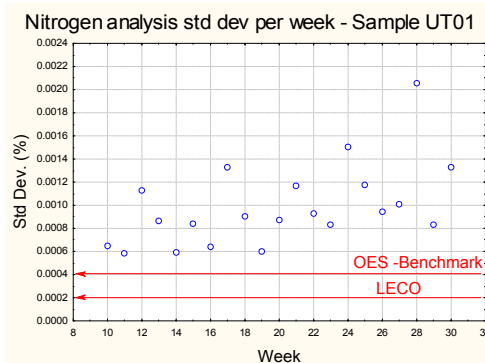
Picture 2 – Steel analysis flow at the Lab.

The two OES purchased because of the unit expansion are equipped with CNOPS technology, which means the ability to perform carbon, nitrogen, oxygen, phosphorus and sulphur analysis in low concentrations (10-30 ppm). But at this time it was noticed that nitrogen results were too scattering and not accurate comparing to LECO results. Picture 3 shows results of the same sample, an internal standard analyzed by OES and LECO before the project implementation.



Picture 3 – Comparison between OES and LECO nitrogen analysis

The performance indicator chose for this project is the standard deviation of an internal standard with approximately 0.0020% of nitrogen content and the goal is to reach the standard deviation of 0.0004%, which is the benchmarking value (other ArcelorMittal Unit) in OES. The OES results before the project implementation, the LECO results and the benchmark value are shown at the Picture 4 below.



Picture 4 – OES, LECO and benchmark standard deviation

Especially because of the development of new steel grades and the increasing demand for IF (interstitial free) steel, the nitrogen result became an important data to control process and guarantee product quality. The present

response time (LECO time) performance does not meet with these requirements, as well as nitrogen precision by OES, showing the real interest on the development of this project.

Besides the gains expounded above, there are notable costs involved with CC analysis, related with its consumables, valued in approximately US\$ 90,000 per year.

4) Measure

The main objective of this step is to identify the focus of the problem and establish prime targets.

In order to do that some potential influence variables on nitrogen scattering were identified and analyzed, which are: shift, sample and period of the day.

Because none of the variables analyzed demonstrated impact on nitrogen results, no specific goal was established.

The standard deviation in control samples with different nitrogen concentrations was evaluated. Two internal standards were chose with the following nitrogen contents: UT01 = 0,0020% and MX01 = 0,0085%. No significant difference was identified.

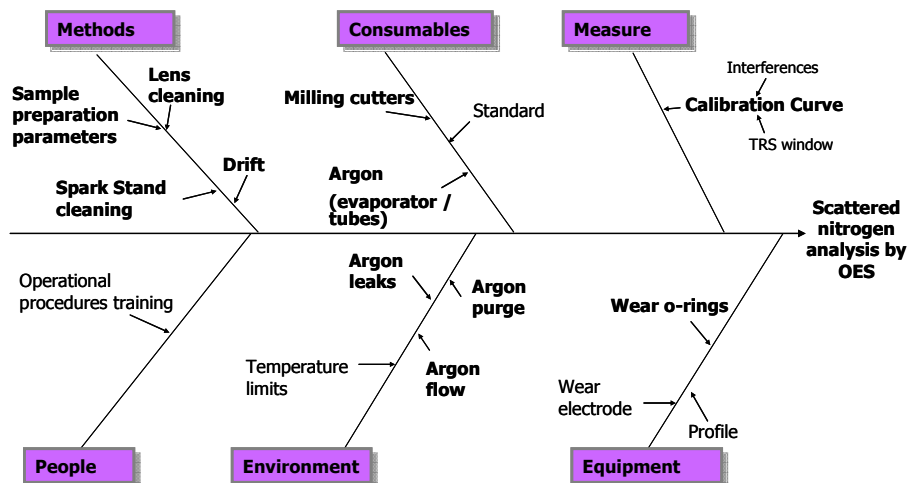
The shifts results standard deviation were evaluated too in order to better identify differences in procedures, maintenance, etc between the working shifts which could affect nitrogen precision. No difference was identified either.

Finally, the lost through the time after the drift correction (performed at the beginning of the shift at 6 AM) was evaluated using the same parameter and no correlation was found.

5) Analyze

The objective of this step is to study the process, identifying key relationships among various variables, and the possible causes providing additional insight into process behavior.

At this stage of the project we counted with a consultancy of other ArcelorMittal unit (benchmark in nitrogen analysis by OES) and ArcelorMittal R&D Europe, which were essential to the development of the project. With this support it was built a cause-and-effect diagram (Ishikawa) to identify potential factors causing scattered nitrogen results at OES.

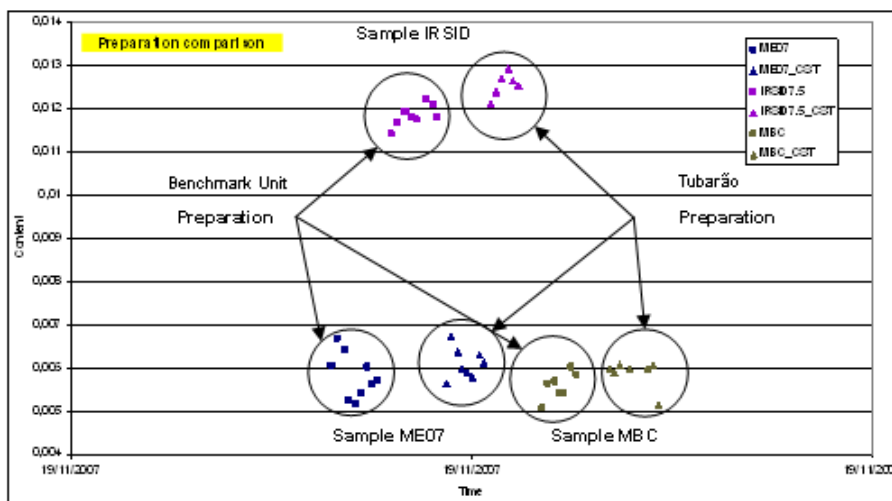


Picture 5 – Cause-and-effect diagram for scattered nitrogen analysis by OES.

The causes brought at the diagram above were prioritized in order to guide the action plan. There were possible optimizations for all items in bold.

Comparison of sample preparations

The results obtained with different sample preparation parameters (advance and rotation speed) from benchmark Unit and ArcelorMittal Tubarão showed no significant differences between the two types of preparation. Nevertheless, it was identified the necessity to validate the point to change the milling cutters considering the particular analytical application.



Picture 6 – Preparation comparison

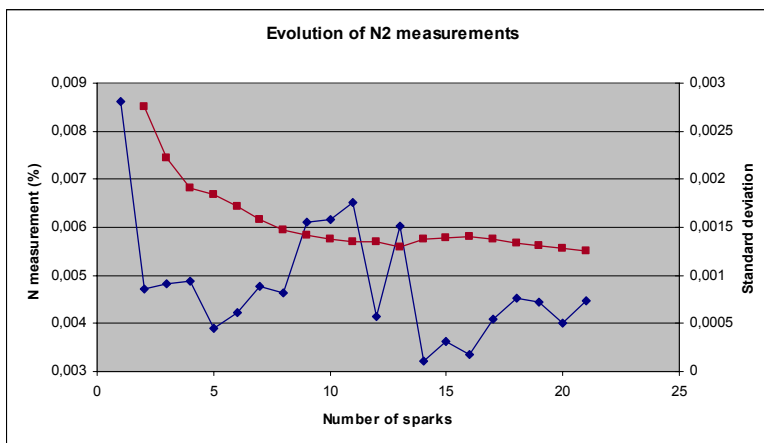
OES analysis practices

Argon: Argon was supplied by tubes system at ArcelorMittal Tubarão. To prevent all risk it was installed a double alimentation of three tubes that make operators can by-pass argon alimentation with a minimum of pollution risks. However, it was verified that Argon alimentation by tubes is not the best and involves a notable instability at the beginning and the end of the tube besides the risk of pollution. All laboratories known working to perform traces and nitrogen measurements by OES have replaced Ar tubes by Ar evaporator, which was done at Tubarão.

It was identified either the importance of maintaining a non contaminated environment while the instrument is in stand-by, in order to avoid nitrogen peaks at the first burn. With this purpose, the stand-by argon flow of the instrument and the argon purge at the beginning of the analysis were adjusted. In order to maintain the quality of the results, a leak test frequency was established.

Calibration: Two sample were selected to perform the standardization of nitrogen, a very low alloyed steel (like an iron) which is used as a low nitrogen point and a high point sample in which nitrogen content is at the level of 0,02% which is well adapted for the usual steel production. Add to that the calibration curve was corrected taking into account three interferences: Si, P and Mn (nitrogen channel wavelength used is 149.26 nm).

Spark Stand: To perform Nitrogen analysis, it was identified to be important to limit actions inside the spark stand in order not to contaminate it or generate small leaks. Because of that, the spark stand cleaning frequency was reviewed for each 24 hours (approximately 200 analyses). Still concerning spark stand stabilization, it was performed a test in order to evaluate the necessary burning analysis after spark stand cleaning, which are important to reach stable nitrogen results (Picture 7). In Tubarão it was reviewed from 6 to 18 burns.



Picture 7 - Nitrogen response after spark stand cleaning

According to the manufacturer, 1 ppm N in the spark discharge will cause a 30 ppm enhancement in background on the instrument. Therefore, the flatness of samples is also very important to maintain a good seal on the stand and prevent air contamination in the chamber. It is necessary too to pass a lint-free cloth from time to time (before the controls for example) to avoid that black depots accumulate on the table.

Data treatment: After a certain time (around half an hour) without analyses, the first nitrogen results are unstable mainly on the first sparking sequence. Therefore it's crucial to put on a limit of acceptance value on N₂, to reject bad measurements. That permits to improve accuracy and standard deviation measurements for nitrogen.

Other maintenance issues: As suggested in the benchmarking report, the operational procedures were reviewed establishing a frequency to change the door-filter with pyrophoric iron (before that it was only cleaned and reused until get to really bad condition). This action is important because the back pressure it creates in the spark stand will change as the filter gets dirtier. Even small changes in the back pressure will lead to "large" variations in the results. The results after this action were notably more stable.

Based on the benchmarking support, it was confirmed that the lens cleaning will affect the accuracy of the results especially for the elements with little sensitivity such as N. The more the lens is appropriate (clean), the more the incomes (results) are stable. In Tubarão a Fe control was established in order to identify sensitivity loss.

6) Improve

Considering all the actions figured out on the *Measure* step, an action plan was developed as shown below:

Table 1 – Project Action Plan

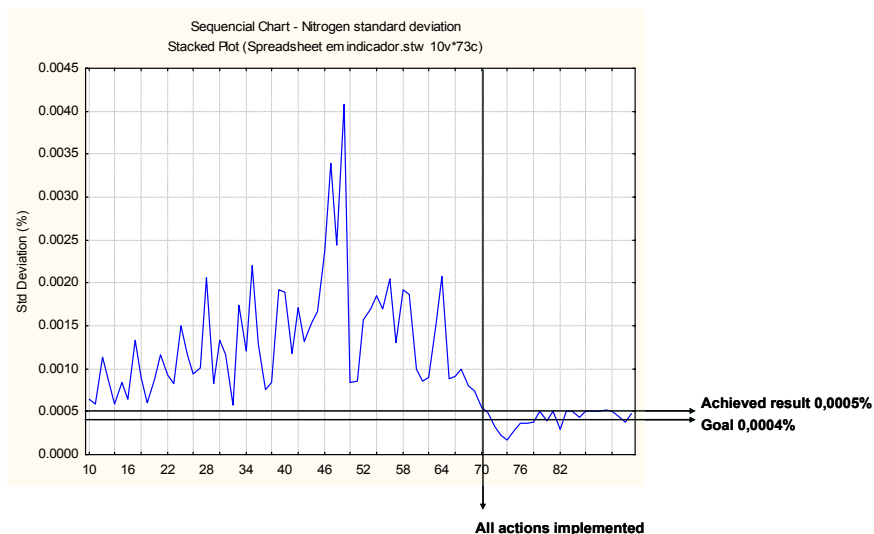
What	Who	When	Status
INCREASE OF ARGON PURGE AT THE BEGINNING OF THE ANALYSIS	LAB TEAM	APRIL/2009	FINISHED
INCREASE OF BURNING ANALYSIS NUMBER AFTER SPARK STAND CLEANING	LAB TEAM	APRIL/2009	FINISHED
INSTALLATION OF A LIQUID ARGON TANK (REPLACING ARGON CILINDERS) WITH 99,999% OF PURITY	LAB TEAM	DEC/2009	FINISHED
ADJUSTMENT OF ARGON FLOW IN STAND-BY	LAB TEAM	JAN/2010	FINISHED
NEW CALIBRATION CONSIDERING P, SI E MN AS INTERFERING ELEMENTS	LAB TEAM	MAR/2010	FINISHED
ESTABLISHED LENS CLEANING AND LEAK TEST FREQUENCY	LAB TEAM	APR/2010	FINISHED

DEFINED ACCEPTANCE VALUE TO REJECT BAD SPARKS	LAB TEAM	APR/2010	FINISHED
IMPROVE SAMPLE PREPARATION (PARAMETERS AND CONSUMABLES)	LAB TEAM	JUL/2010	FINISHED
MAINTENANCE CONDITIONS OPTIMIZATION (STAND CLEANING, FILTERS, ANALYSIS FLOW)	LAB TEAM	JUL/2010	FINISHED

7) Control

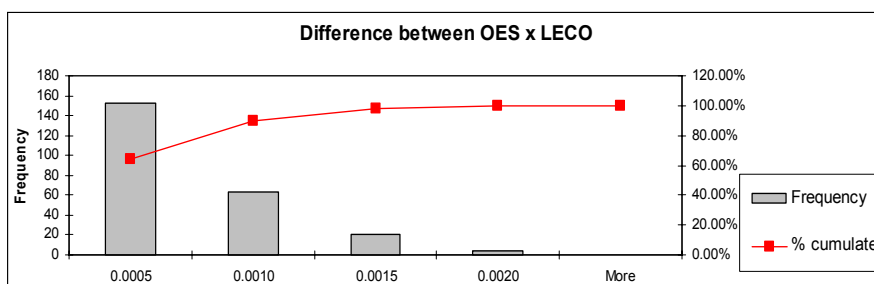
After the implementation of all the actions, achieved results were evaluated focusing on accuracy and precision.

The standard deviation of an internal control sample with nitrogen content of 0.0020% was monitored weekly. The result of 5 ppm was achieved (attending most of the present process requests), maintaining its stability.



Picture 8 – Nitrogen standard deviation

Aiming at evaluate the accuracy, a comparison between OES and LECO was performed for a period of a month on routine samples (about 1350 analysis). The results obtained (Picture 9) confirmed the standard deviation achieved – approximately 68% of the results comprehended in 1 sigma, 95% comprehended in 2 sigma and 100% in 3 sigma).



Picture 9 – OES x LECO comparison

8) Conclusion

Finally, spark optical emission showed up as a really interesting technique for nitrogen analysis once reliable and precise results are achievable. Nevertheless it's mandatory to implement some routine maintenance procedures because reproducibility of this element becomes sensibly degraded if this is not done very regularly. Therefore the

main objective of this project, which was response time gains of approximately 8 minutes, were accomplished added to other steelmaking processes benefits.

It's important to remember that because of the various influences on nitrogen analysis and its disastrous consequences on precision, it's essential to establish routine controls and to have a critical eye in the emitted results, to faster identify and act in order to correct anomalies.

References

- 1) OSMONT, Philippe; MEILLAND Raymond; NICCO Olivier. "Chemical Laboratory Benchmark in the frame of share of competencies in the ArcelorMittal Group", ArcelorMittal R&D Industrial Operations, France, 2007.
- 2) Manual ARL 4460, N° AA 83478-04, Thermo Fisher Scientific, 1999.
- 3) Manual ARL 4460, N° AA83644-01, Thermo Fisher Scientific, 2004.
- 4) http://www.baldrige.com/criteria_processmanagement/process-management-dmaic-for-everyone/ in 21/03/2011.
- 5) AGUIAR, Silvio. "Integração das ferramentas da qualidade ao PDCA e ao programa seis sigma", Volume 1, Editora DG, Minas Gerais, 2002.
- 6) WERKEMA, Cristina. "Criando a cultura seis sigma", Volume 1, 3ª Edição, Werkema Editora, Minas Gerais, 2004.
- 7) Manual de Referência. "Análise dos sistemas de medição", 3ª Edição, AIAG, São Paulo, 2002.
- 8) SKOOG, D. A.; HOLLER, F.J.; NIEMAN, T.A. "Princípios de análise instrumental", 5ª Edição, Bookman, Porto Alegre, 2002.

CHEMICAL ANALYSIS OF HIGH-ALLOYED STEEL BY XRF SPECTROSCOPY AS BORATE FUSED BEAD

Simona Rollet, Andrea Franciscono

*Chemical and Corrosion Laboratory
Cogne Acciai Speciali S.p.a., Aosta - Italy*

ABSTRACT

Chemical analysis of high-alloyed steel is often a critical step when high concentration (>10%w/w) of valuable metals like nickel and chromium are involved. In order to prevent an over or underestimation, both the producer and the customer aim to assess the best performance of precision and accuracy.

Among all the instrumental methodologies, OES-Spark, XRF spectroscopy and ICP-OES are the most widespread techniques. However, when elements in high concentration are involved, absorption enhancements, grain size effects, differences in metallurgical phases composition, inter-elemental interferences (OES-Spark and XRF) and poor precision (ICP-OES) affect the accuracy of the response.

The preparation of samples as borate beads would lead to many advantages, i.e. elimination of phase composition and metallurgical grain-size effects, high homogeneity and dissolution of inclusions (oxides, nitrides, carbides) and treatment of any shape and amount of sample. Unfortunately there has been no way up to now to apply this method of dissolution to stainless steel.

In this work a new method of preparation has been developed.

The experimental trials on international certified materials lead to excellent results in term of precision and accuracy.

INTRODUCTION

The state of the art in the field of metallurgical chemical analysis is mostly related to XRF and Spark-OE spectrometries, which represent very fast and reliable routine techniques. However the sample, analyzed in the bulk form, needs to satisfy shape and dimensional requirements. The instrumental response is affected by strong interferences too: differences in metallurgical phases and in grain size cannot be neglected for the assessment of the final result and inter-elemental interferences require strong mathematical corrections. Moreover the calibration of those instruments is made with CRM secondary standards and matrix-matched reference materials are not always available.

On the other hand, ICP-OES, a technique in which matrix effects can be overcome with matrix-matched synthetic standards, is characterized by poorer precision and accuracy in the high concentration range, if compared with XRF. Although there have been a lot of improvements for this spectrometric technique, thanks to the efforts of manufacturers and operators (stabilisation with internal standards, "bracketing" techniques, improvement of plasma and instrument stability, etc...), we still do not get the precision obtained with other techniques, above all the XRF one. What is more, inclusions and inter-metallic phases often hinder a complete dissolution of the sample.

In the fifties Fernand Claisse described for the first time a revolutionary preparation technique, in which a sample is fused with a borate salt as a bead and analyzed by mean of XRF spectrometry [1].

The main advantages lie in the excellent repeatability and reproducibility of both the borate fusion technique and the XRF spectrometry. The complete fusion of the matrix and the dilution of the sample in the borate lattice makes this method almost completely matrix-independent and no or lighter mathematical corrections are required. Then, the calibration can be carried out with pure salts and pure oxides and the results can thus be related to primary reference materials.

Very good results have been obtained in the mineralogical field with oxidized samples, such as minerals, oxides, slag and cements, that are directly soluble in the borate salt.

With metallic samples a previous oxidation step is necessary. According to the literature, there is more than one way to adapt the method to this kind of samples.

For example iron can be oxidized by adding a solid oxidant like lithium carbonate in the crucible [2], low-alloyed steel can be previously oxidized with HNO_3 [3] and dry corrosion has proven to be the ideal solution for the oxidation of a copper-tin alloy [4]. During our experiments we realized that stainless steel cannot be oxidized with any of these methods.

EXPERIMENTAL

Stainless steel is not suitable for the borate fusion technique. Firstly there is no way to obtain a fine powder of a stainless steel sample and so the use of a solid oxidant during the fusion is not considered, because the fine mixing of the reagent and the sample would be scarcely effective. Various mixtures of acids - phosphoric, sulphuric and perchloric - are strongly effective on steel oxidation, but the residues of the dissolution are detrimental for the fusion. Moreover, hydrochloric acid, that would represent the best choice for stainless steel dissolution, must be avoided because of the corrosive action of chlorine on the platinum ware. The hypothesis of the halide removal has been quickly discarded. Unlike bromide or iodide, in fact, chloride requires a significant amount of energy and very strong oxidizing conditions to be removed as chlorine.

SAMPLE PREPARATION

An oxidation strategy we realized to be very efficient is the bromine/methanol attack.

This is a very old and powerful dissolution technique, that has been widely used since the IXth century, but only to isolate inclusions in steel and as an etchant in metallography. The mechanism of the reaction is still not fully understood and very little information is available in the literature. The main findings have been described on GaP semiconductors [5].

In our case, instead of discarding the dissolved part of the sample, we needed to keep it, together with the inclusions, in order to maintain the sample in its integrity.

A small amount (0.1 – 0.3 g) of steel chips or small fragments was weighed in a flask. Methanol and half a millilitre of bromine were added. The reaction was slightly exothermic at first, but then proceeded at room temperature with no need of supervising and the dissolution was completed in 5 to 8 hours.

Then the solvent and the reagent had to be removed and replaced with water. By heating the solution at a temperature lower than 100°C , the methanol and the residues of bromine were volatilized. A small addition of water and some drops of nitric acid allowed the oxidation of the bromide, formed during the reaction, to volatile bromine. The final result was an aqueous solution of metals nitrates and undissolved non-metallic inclusions, that could be transferred in a platinum crucible and dried on a hot plate. In Fig.1 a picture of how the oxidized steel appeared can be seen.



Fig.1 – Oxidized stainless steel in the crucible

Then the fusion technique could proceed as with mineral samples.

The flux was a 50:50 mix of lithium tetraborate and lithium metaborate. A solid oxidant, BaNO_3 , was added to improve the dissolution of carbide, sulphide and nitride inclusions. The fusion was performed in an automated bead preparation machine (Philips Perl'X 3).

INSTRUMENT CALIBRATION

The calibration of the instrument (PANalytical Axios PW4400) was carried out with beads obtained from pure substances: stable and anhydrous oxides (Venctron 99.999% purity) or aqueous solution of weighed pure compounds, mixed together to match any stainless steel composition.

The aqueous sample was represented, for example, by low carbon nickel (Venctron 99.999% purity) dissolved in HNO_3 , electrolytically reduced on a platinum grid and dissolved again in HNO_3 , resulting in a pure solution of known concentration (in g/kg) that could be weighed on a high precision analytical balance.

Checking the calibration as well as the reliability of the method were possible with beads obtained from certified international standards, namely BCS, NBS, etc.... standards.

RESULTS and DISCUSSION

The beads obtained from the fusion were transparent and perfectly vitrified, indicating that the sample was completely oxidized. The XRF analysis confirmed that no residues of bromine could be found in it.

Then we checked whether the sample preparation was suitable for the setting up of an analytical method with XRF spectrometry by making a calibration curve with synthetic standards.

The linearity of the calibration was confirmed by a very good correlation of the data (Fig. 2).

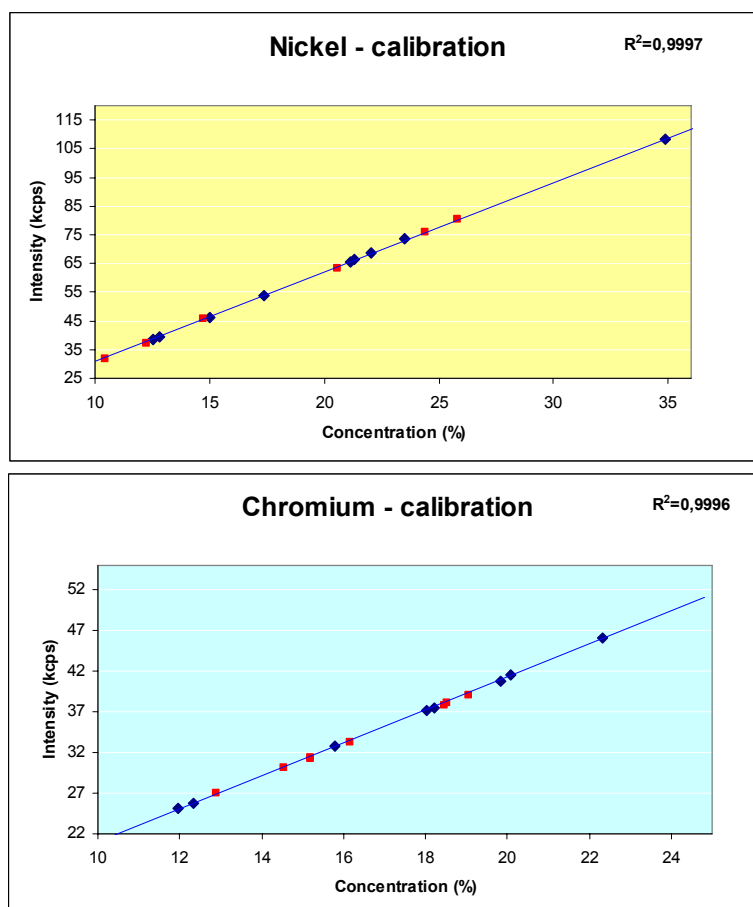


Fig.2 – Nickel and Chromium calibration curves. Blue dots: synthetic standards – Red dots: CRM certified standards.

Finally we applied the bromine/methanol preparation method to the CRM samples listed in table 1, in order to evaluate how well they fitted in the calibration curve and we observed that the measured values matched the certified ones with high accuracy (Fig. 2-3 and Tab.1).

It's worth noting that no inter-elemental corrections was applied.

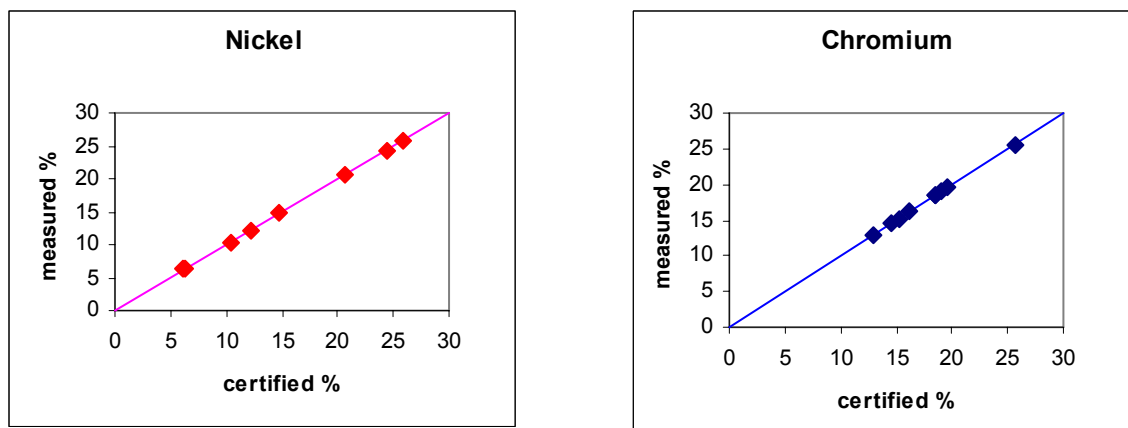


Fig.3 – Comparison between certified and measured values for 7 CRM standards

International Certified Material		
	Cr %	Ni %
CRM 295-1	Certified	19,51 24,40
	Measured	19,52±0.03 24,39±0.03
BS 348	Certified	14,54 25,80
	Obtained	14,51±0.03 25,82±0.04
BCS 334	Certified	25,60 20,60
	Obtained	25,65±0.05 20,56±0.04
BCS 474	Certified	19,06 14,74
	Obtained	19,03±0.04 14,74±0.03
NBS 160/b	Certified	18.45 12.26
	Obtained	18,47±0.05 12,24±0.03
BCS 461	Certified	15.20 6.16
	Obtained	15,22±0.02 6,17±0.01
BAM 231/1	Certified	18.53 10.47
	Obtained	18,49±0.05 10,45±0.03

Tab.1 – Comparison between certified and measured values for 7 CRM certified standards

The precision of the method was evaluated by applying it to three aliquots for each CRM sample. The result was a mean relative standard deviation lower than 0.3%.

CONCLUSIONS

Thanks to the preparation method described in this work we succeeded in applying the borate fusion technique to stainless steel samples.

The most innovative aspect is that high-alloyed steel analysis can now best exploit the precision and accuracy typical of XRF on beads, together with the possibility to relate the results to primary standards and without mathematical corrections.

Any amount and any shape of stainless steel sample can be easily oxidized and fused as a bead.

Whereas a CRM is not available, for example for a new kind of steel, experimental heats or fusion intermediates, a synthetic standard with the same composition can be prepared in about half an hour.

A possible evolution of the method can be envisaged in the metal matrix composite field. In this case the metallic and the ceramic part can be fused and analyzed separately or all together with one single method.

REFERENCES

- [1] Claisse, F. Department of Mines, Quebec, Canada, P.R 327 (1956) - The Norelco Reporter 4 (3), 95 (1957)
- [2] Claisse F., Blanchette J. – “Physics and Chemistry of Borate Fusion”, Fernand Claisse INC. (2004)
- [3] Sieber J., Yu L., Marlow A., Butler T. – “Uncertainty and Traceability in Alloy Analysis by Borate Fusion and XRF”, X-Ray Spectrom. 2005; 34: 153-159
- [4] Gagnon J.P (Claisse Inc.) – “Preparing Borate Disks Using Metal Fragments and Filings” - Colloque Rayons X et Matières (2001)
- [5] K. Strubbe, W. P. Gomes - “Bromine-Methanol as an Etchant for Semiconductors: A Fundamental Study on GaP” - J. Electrochem. Soc., 1993, Volume 140; 11: 3294-3300

ON-SITE DIRECT MICROSCOPY AND COMPOSITION ANALYSIS IN METAL INDUSTRY

O.Lemaire, Xavier Vanden Eynde, S Flament, V.Tusset

C.R.M Group, Liège, Belgium

ABSTRACT

The combination of on-site microscopy and on-site OES spectrometry for fast quality control of various metal substrates has been already investigated by CRM.

More and more frequently, customers require the determination of metal composition but also its microstructure. As a matter of fact, the steel chemical composition is important but the final properties are complementary defined by the material microstructure.

As concern metal composition, a large number of samples (low and ultra low carbon steels, stainless steels, aluminium, nickel and copper based alloys) have been analysed with portable spectrometers. Results have been evaluated by using chemical reference methods available in the laboratories such as ICP-OES, XRF, C and S combustion, ...

As concern microstructure analysis, CRM on-site microscope has been used to perform direct analysis of HSM rolls as well as on other metallic materials for characterization requested by, for instance, Small and Medium Enterprises.

This paper illustrates various interesting cases in these fields: direct microscopy and metal analysis without sampling.

1 INTRODUCTION

Since 1948, CRM is involved in metallography and optical emission spectroscopy development devoted to metal analysis. During this large period, all the equipments used at CRM are stationary microscopes or stationary spectrometers; the OES were equipped with multiwavelengths dispersion using photomultipliers as detection device; the XRF were also generally multiwavelengths instrument.

During industrial processes or during industrial modification, it can be necessary to sort different metals very quickly, without sampling, taking into account their composition and their microstructure.

To sort different metals and especially to respond to the requirement of small and medium industries, CRM has decided to use portable microscope and portable spectrometer for a lot of specific applications.

This paper is devoted to the description of the day per day CRM experiences with portable microscope and portable spectrometer and to the possibility of using such type of equipment for process control application or for quality control.

Various suppliers are producing such type of equipment. CRM has started his experience in portable spectrometer by using PMI-Master developed by WAS company (for OES), Nyton and Bruker for XRF and by using Olympus for the portable microscope.

In the OES PMI Master, a handle-sparking pistol is connected, by the use of optic fibre, with the multi CCD spectrometer (ranging from 220 nm to 460 nm).

As concern the portable optical microscope, an Olympus BXFM trinotubus has been acquired. It is equipped with a Colorview II camera and a Z axis motor which allows depth measurements.

At CRM, specific supports were designed and built in order to assess the availability of the microscope to examine different equipment like, for example, rolls. The different configurations allow the examination of rolls in vertical or horizontal position.

As the portable XRF is concerned, CRM experiences will not be described in this paper.



Figure 1 First portable OES equipment used at CRM

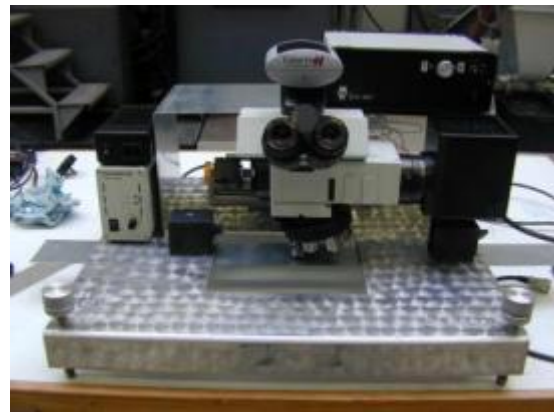


Figure 2 Portable microscope with support

2 ON-SITE METALLOGRAPHY

CRM started to investigate the use of “on site metallography” in order to follow the rolls degradation during HSM rolling.

Roll degradation during hot-rolling is a complex process involving many interplaying mechanisms. Indeed synergy effect between several phenomena can enhance or inhibit the degradation of the roll substrate. Therefore, it is not only important to study at the laboratory scale the complete fatigue/wear/corrosion/oxidation process but also to follow, in real time, the rolls evolution inside the rolling mill (Fig. 3).

Because sampling on industrial roll is most often impossible, surface analyses with a portable optical microscope allow to understand the degradation mechanisms. Figure 4 illustrates one configuration of rolls examination.

By using the sample surfaces view coming from this equipment, specialist characterised the oxide microstructure and composition by a comparison with complete set of techniques available at CRM (Optical analysis, Auger microscopy, Glow Discharge depth profiling, Secondary ion imaging, X-Ray photoelectron spectroscopy...).

Cross-sections have been analysed in order to determine the extent of the corrosion/oxidation and the physical phenomena governing these processes.

Finally, a comparison between results provided by replica in one hand, and by direct optical observation in the other hand, is illustrated at Figures 5 and 6. The results are very close.



Figure 3 Hot strip mill



Figure 4 Use of portable microscope on rolls

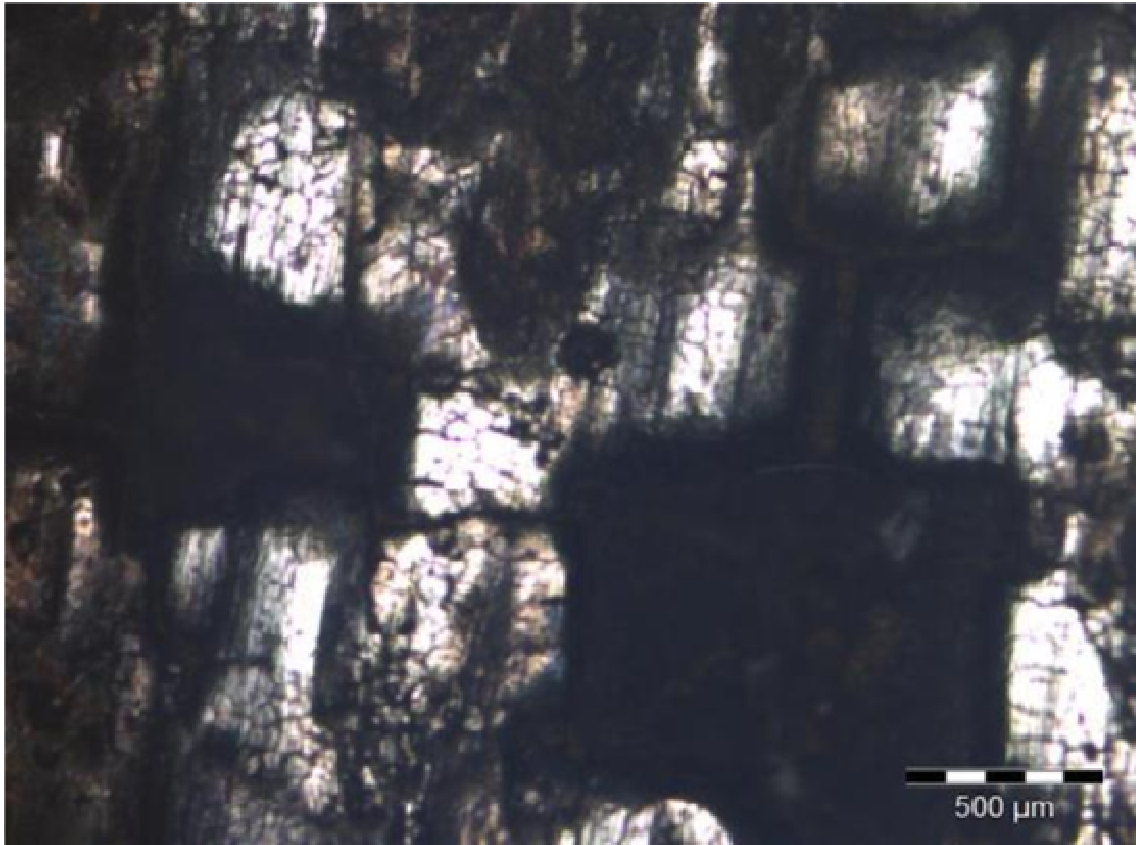


Figure 5 View of the degradation (optical view)

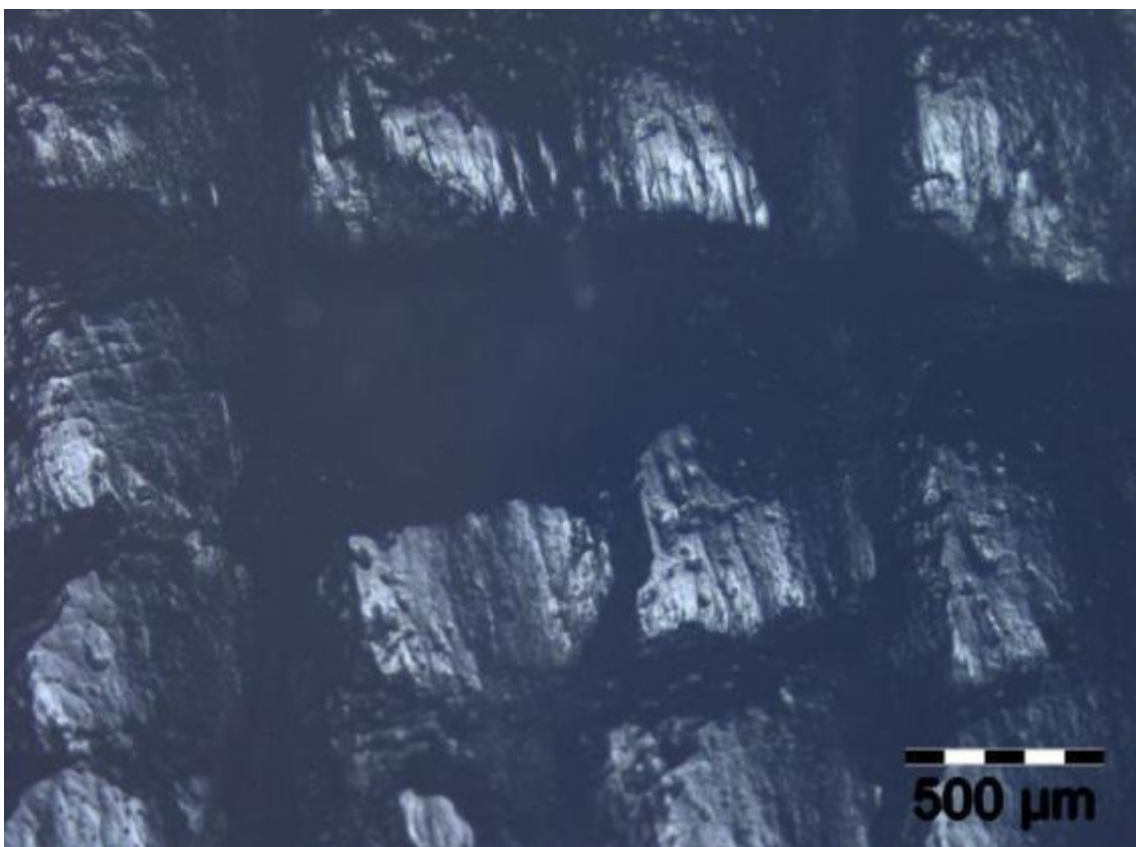


Figure 6 View of the degradation (replica view)

Taking into account the experience acquired, CRM decided to open this possibility to other applications. CRM has decided to extend its expertise in the fields of characterisation of the structure of various metals. The field of large metallic pieces, which have undergone heat treatment, is particularly interested in this type of characterisation.

3. COMPARISON BETWEEN RESULTS OBTAINED BY CHEMICAL REFERENCE METHODS AND BY PORTABLE SPECTROMETER

Large numbers of analysis have been carried out by CRM in the fields of :

- Plain carbon steels
- Low alloys steels
- Stainless steels
- Copper alloys
- Nickel alloys
- Aluminium alloys

Table 1

316L	XRF	ICP-OES /combustion	Portable OES
Mn	1.42	1.34	1.35
Cr	17.81	17.24	17.08
Ni	9.47	10.11	9.88
Cu	0.23	0.250	0.26
Mo	1.98	2.000	2.16
Si	0.26	0.263	0.36
Ti	-	<0.001	0.01
V	0.06	0.065	0.07
As	< 0.01	0.012	-
Co	0.13	0.103	0.10
Sn	< 0.01	0.007	-
Al	-	0.002	0.01
Fe	68.5	-	68.65
C	-	0.029	-
S	-	0.009	-
N	-	0.023	-

Table 2

904L	XRF	ICP-OES - /Combustion	Portable OES
Mn	1.66	1.610	1.48
Cr	21.01	20.08	21.04
Ni	23.35	24.06	23.77
Cu	1.25	1.340	0.95
Mo	4.22	4.870	4.90
Si	0.28	0.307	0.34
Ti	-	0.001	0.02
V	0.05	0.060	0.07
As	< 0.01	0.010	-
Co	0.19	0.165	0.21
Sn	< 0.01	0.004	-
Al	-	0.016	0.02
Fe	47.9	-	47.05
C	-	0.013	-
S	-	0.001	-
N	-	0.047	-

Table 3

3127 HMO	XRF	ICP-OES /combustion	Portable OES
Mn	1.57	1.610	1.17
Cr	27.74	26.58	28.69
Ni	30.51	31.92	30.27
Cu	1.15	1.180	0.70
Mo	6.31	7.070	5.12
Si	0.06	0.249	0.08
Ti	-	0.001	0.02
V	0.04	0.056	0.07
As	< 0.01	0.014	-
Co	0.07	0.074	0.14
Sn	-	0.002	-
Al	0.08	0.098	0.06
Fe	32.3	-	33.47
C	-	0.008	-
S	-	0.003	-
N	-	0.181	-

Table 4

Alloy 59	XRF	ICP-OES /combustion	Portable OES
Mn	0.13		0.07
Cr	22.80		22.60
Ni	60.78		62
Cu	0.04		0.00
Mo	15.03		13.96
Si	0.03		0.07
Ti	-		<0.00
V	0.13		0.14
As	< 0.01		-
Co	0.02		0.05
Sn	-		-
Al	0.25		0.25
Fe	0.49		0.85
C	-	0.004	-
S	-	0.002	-
N	-	0.022	-

A lot of comparisons have been established between the results obtained by the portable spectrometer and by conventional methods (ICPOES-C S by coulometry method-XRF- ...).

In the tables (1 to 4) and in the figures 7 to 9 hereafter, for the elements like Mn, Si, Ni, Cr and Mo, the concentrations obtained by the PMI Master system, are close to the values obtained with reference methods

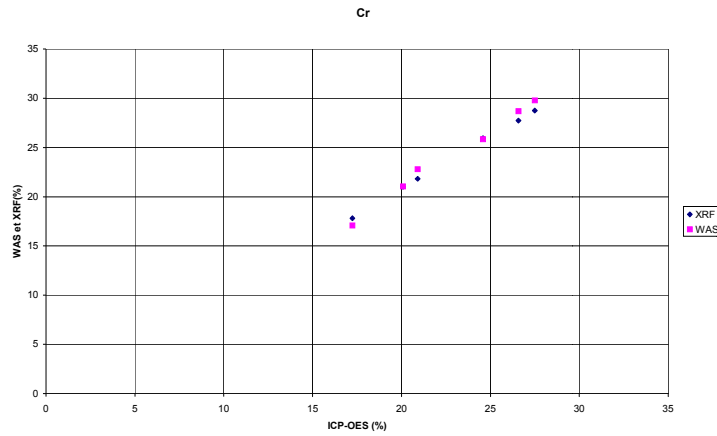


Figure 7

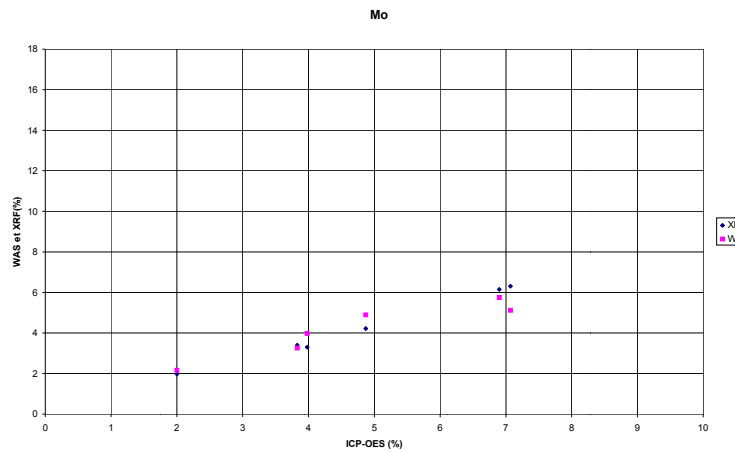


Figure 8

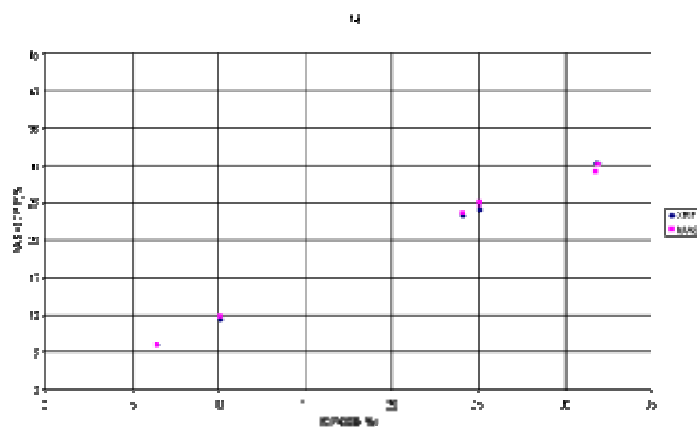


Figure 9

Table 1 to 4 and Figure 7 to 9: Comparison between analysis obtained by portable OES and by XRF/ICPOES/combustion methods

The determination of carbon content by PMI Master system does not allow to determine carbon in a precise way but on the other hand it makes it possible to classify the various types of carbon steels.

Within sight of the results obtained, CRM has sought how to obtain more reliable results for assessing the carbon content.

Use of portable spectrometer for determining carbon, sulphur and phosphorus in Carbon steel and ultra low carbon Steel analysis

After three years of measurements with the PMI Master, CRM was searching for the delivery of an OES equipment ranging from 170 to 460 nm. The development of the PMI Master + opens the way to the analysis of elements like C, S and P at low concentration. This new device combined multi CCD spectrometer with a mini optic UV spectrometer. A specific sparking stand has been required by CRM for research.

Figure 10 presents the PMI Master + and figure 11 focuses on the mini optic **UV-PRO** that enables to analyse elements like C, S and P, generally determined under UV and vacuum conditions.



Figure 10 PMI Master +



Figure 11 UV PRO

By using PMI Master +, calibration curves and reproducibility tests have been established; the following diagrams summarise the results obtained.

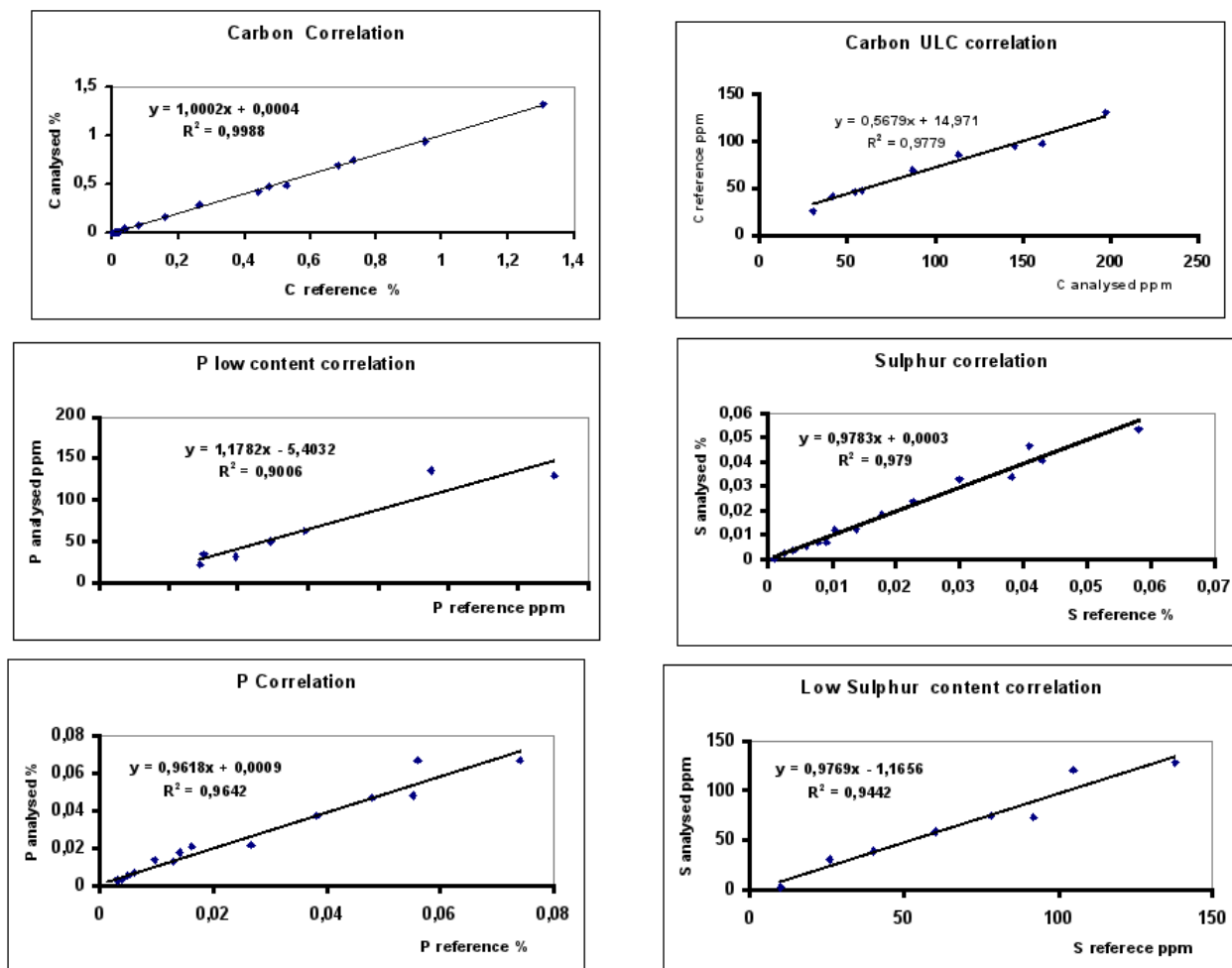


Figure 12 C, S and P, portable spectrometer performance

From the works of CRM, it arises that by using the specific methods of calibration and well defined protocols of analysis, the performances of portable spectrometers, provided with detectors CCD, become close to those of the more traditional spectrometers and in any case often sufficient to ensure a follow-up of various step of steel production.

By using portable spectrometer, a production control of metals carried out at each stage of the process directly by the operators can now be considered. For the steel-works, which are not yet equipped with pneumatic transfers, it must be recommended to use such equipment installed near the process.



Figure 13 direct analysis without sampling

Hereafter an overview of industrial problems solved by CRM by using the portable equipment (Fig. 13):

- In the first example, it was necessary to determine the composition of the whole of materials present on the site of railways station in the course of revamping.
- In the second case, a control of the composition of materials present in cisterns devoted to the transport of chemical products was required to face specific requirements.

4 Example of a coupled OES-Metallography case

We present now an example of examining a metal shaft that has undergone treatment for a welding build-up.

The presence of a zone of a different kind of metal obliges to determine:

- the chemical composition by using OES
- its structure: metallography
- its origin (melted or not-melted)
- its hardness

In a first step, analyses with the portable spectrometer were carried out on the unknown area. It revealed that this area was composed by a stainless steel:

	Base Metal	Unknown Area
Fe	~95.57	~68.93
Cr	0.32	18.77
Ni	2.21	10.04

The second step consisted to identify the microstructure by taking replicas (Figure 14, 15, 16, 17, 18).

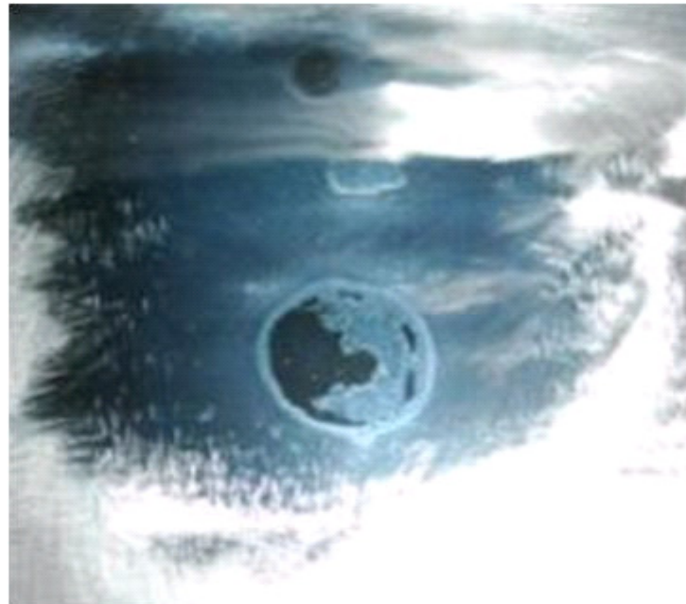


Figure 14 Sample with welding build-up.



Figure 15 Polishing



Figure 16 Metallurgical etching



Figure 17 Taking of replicas

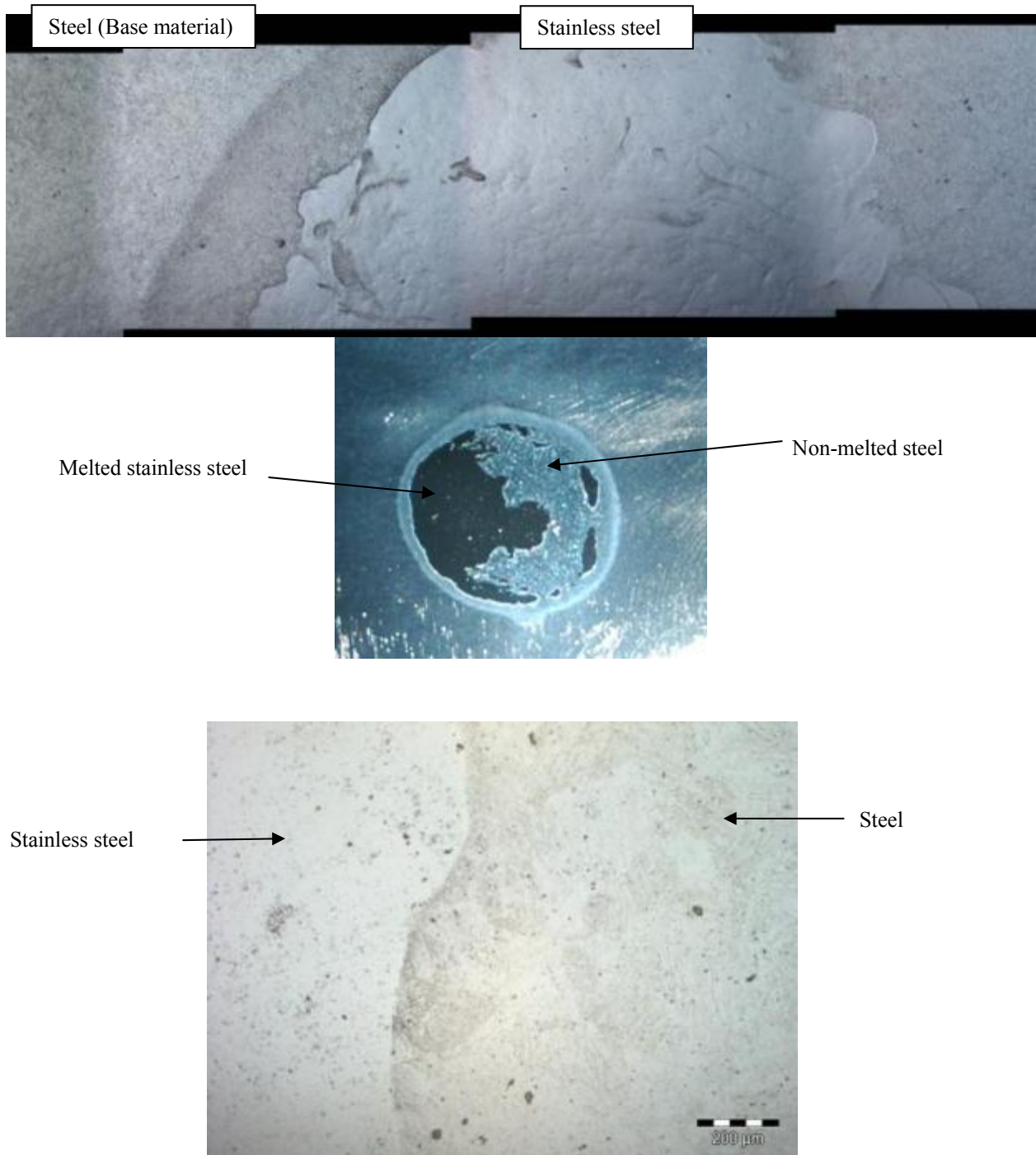


Figure 18 Micrographs done with a microscope

The micrographies taken on replicas allow to determine that the unknown area was in fact composed by a stainless steel coming from the weld, and by a piece of metal used for the repairing.

These conclusions were confirmed by the hardness measurements:

Unknown Area	Vickers (HV)
Stainless Steel	149
Steel	379

All these results open the way to use the portable spectrometer and portable microscope as equipment of analysis and not only like a tool to sort metals.

5 CONCLUSION

For solving industrial problems, it is often necessary to quickly determine the composition and the structure of various metals. To join this goal, there are methods consisting in cutting a piece of the metal and sending them to be analysed in a traditional laboratory but it is often impossible to implement because the sampling operation is not always convenient.

Portable spectrometers and portable microscope open the way to solve such types of problems.

6 ACKNOWLEDGEMENT

The authors would like to thank Ph. Fourneaux, Team Leader at CRM, G. Walmag, Program Leader at CRM Group for her helpful comments and A. Dupont and D. Dominguez, from the CRM Group Laboratories department, for all the tests.

7 BIBLIOGRAPHY

- [1] PDA TECHNIQUES FOR STEEL CLEANNESS EVALUATION, V. MULLER, V.TUSSET, CRM(B), B.D. SUMMERHILL, R.JOWITT, British Steel plc (UK), G. Willay, F. Meyer, IRSID (F); p. 444, *Progress in analytical chemistry in the steel and metals industry, Ed. R. NAUCHE, 1992*
- [2] COCKERILL SAMBRE'S AUTOMATED LABORATORIES, A. Daniels, J-C HOET (S.A. Cockerill Sambre, Couillet, Belgium), p 327; *Progress in analytical chemistry in the steel and metals industry, Ed. R. NAUCHE, 1996*
- [3] PRODUCTION CONTROL BY CABIN LABORATORY, B.D. SUMMERHILL(British Steel Technical, Teesside Laboratories Middlesbrough, Cleveland), T.D. MURDOCH (British Steel General Steels, Scunthorpe Works, South Humberside,UK), p. 333, *Progress in analytical chemistry in the steel and metals industry, Ed. R. NAUCHE, 1996*

MICROWAVE ASSISTED HIGH-PRESSURE DIGESTION SYSTEMS – TECHNIQUES AND APPLICATIONS

Pappert E., Flock J.

Thyssen Krupp Steel Europe AG, Duisburg, Germany

Abstract

At the beginning of the nineties the microwave-assisted high-pressure digestion systems found its way into the routine work of steel laboratories. The first commercial systems suffered from insufficient control of temperature and pressure but rapidly worked out to be fully computer controlled. The basic advantage of this technique, in closed and chemical inert vessels, is the high digestion temperature and thus efficient and quick dissolution of a wide variety of samples. Any kind of acid and acid mixture can be used and due to the high reproducibility and sample capacity microwave based applications are perfectly suited for multi-element spectrometers like the ICP-OES and ICP-MS.

During the last 10 years many normative-procedures e.g. the aqua-regia extraction, the (waste-)water preparation and the digestion of oil and lubricants describe supplementary microwave procedures.

Continuous improvements and new concepts of the microwave digestion technology offer higher sample capacity, extreme specifications for temperatures and pressure (max. 300 °C, 200 bar), easier handling and far more precise and reproducible digestion results.

Thus even more applications of the steel laboratories could economically and easily be performed.

In the chemical laboratories of the Thyssen Krupp Steel Europe AG currently a variety of specialized microwave digestion system are in operation. Analytical and economical aspects of the systems available are discussed and their performance for new and classical applications is shown.

Introduction

The most important and essential step to achieve accurate and precise analytical results in elemental analytics is the sample preparation. Due to a variety of physical and chemical effects it is also the most time-consuming part and rate-limiting step for multi-element techniques like the ICP-OES and ICP-MS [1]. Thus in routine laboratories which are faced with small as well as huge series of samples which have to analysed in little time the economical aspect and the reliability of the sample preparation procedures play the decisive role.

Looking back to the seventies and eighties the first ICP-OES and ICP-MS spectrometers were used in the elemental analysis and their high sample and multi element capacity shortened the times for analysis. In the following decades the performance of the ICP-spectrometers was steadily increased and still is. The development of sample preparation techniques on the other hand lagged behind and classical digestions techniques were applied to a great extent. The disadvantages of these were apart from labour and time intensive steps, the use of difficult to handle chemicals, incomplete digestion and that they had to be performed by very experienced staff.

In 1985, 10 years after the already in the sixties introduced microwave ovens in the kitchen were used in analytical chemistry as rapid heating source for wet open-vessel digestions, the first multimode cavity microwave was introduced [2]. Its primary improvements over the home or domestic units were some additional safety features like an isolated and ventilated cavity to prevent acid fumes from attacking the electronics. Finally the microwave systems of the 1st generation could perform digestions in closed vessel with 600 W microwave energy, a maximum temperature of 200 °C and an inner pressure of 7 bar.

The advantages of the microwave-assisted digestion were quickly recognized to be superior to classical digestion techniques. A great potential as a tool in analytical laboratories was predicted in 1988 [1]. Nevertheless it was pointed out that many weaknesses of the current digestion systems had to be overcome.

The following aspects had to be taken into account:

- precise reproducibility of the decomposition conditions
- homogeneity of the microwave field
- real time monitoring of the temperature and pressure
- temperature and pressure stable vessels systems
- security options (ventilation systems, sensors)

In 1994 a review and discussion on the advantages of the microwave assisted digestion systems compared to conventional sample preparation methods pointed out that the microwave will replace the conventional preparation in many fields [3]. Several matrices are even impossible to digest with traditional procedures like e.g. ceramics, heavy oils, coal and ores [4].

At this time the first microwave assisted digestion system was introduced into the routine of the analytical laboratories of the ThyssenKrupp Steel Europe AG (TKSE). After a short time many applications were exclusively performed by microwave assisted dissolution. To increase the sample capacity many other systems followed within the next years. Presently 75 % of all sample preparation methods for the ICP-OES and ICP-MS are based on the three conceptual different microwave assisted digestion systems.

Microwave systems at TKSE

Basic microwave system with single closed vessels

The closed single vessel based systems with a sample capacity of 10 to 24 samples and a approx. maximum pressure of 35 bar were the first systems in use. With one temperature controlled reference beaker, an IR sensor for the outer shell temperature control and a turntable, many of the above necessary improvements were implemented in this system. Standard 100 mL TFM vessels jacketed with a PEEK casing are used in a 10 position rotor in combination with 1000 W microwave power systems. A special reversible ventilation system in the lid, which works in combination with single segments placed in the rotor and a highly sensitive so-called Q/P sensor, which detects reaction products like NO_x, Cl₂, takes care that losses of the sample will be detected as well as kept to a minimum. In the case of gas-alert the microwave power will immediately be switched off [5]. For bigger series there are taller inliner vessels with thinner walls (Fig. 1). The casing-lid system is easily screwed by hand and placed into the rotor. Because of the in this case much higher sample volume, the rotor it is preferably used with microwave systems of 1500 W to speed up the time for heating. Both systems are operated with compressed air blown through the rotor during the run to keep the temperature of the cover down.

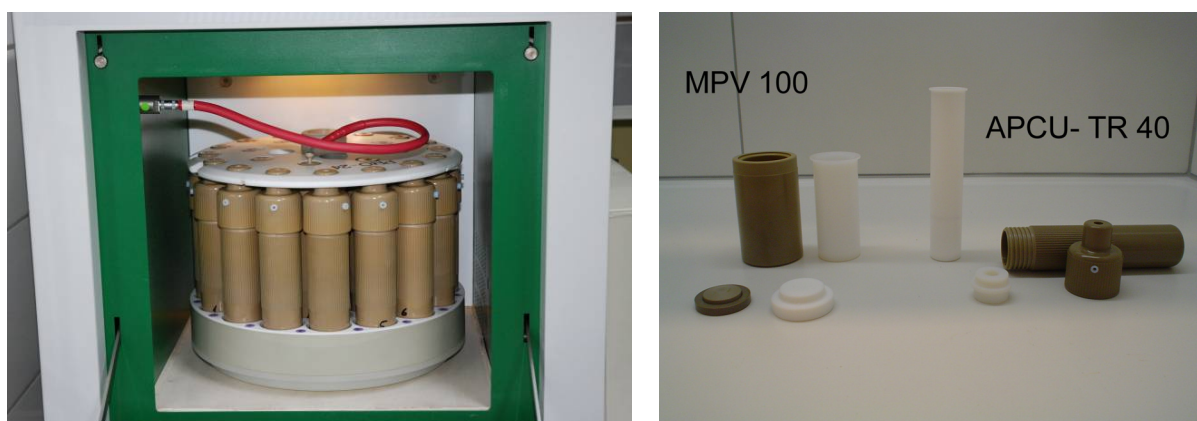


Fig. 1: Closed single vessel systems for high-pressure microwave digestions

Due to the single pressurized vessels after digestion and in view of volatile compounds the vessels must be cooled down to at least lower than 80 °C before they are opened. This is in practice done in a cooling bath containing cold water of 2 °C.

Advanced microwave system with one high pressure cavity

A microwave-heated autoclave, developed by the Milestone Corporation in 1995, was a new and completely unique approach to microwave dissolution. The “ultraCLAVE” uses a high pressure (200 bar) cavity of 4,5 L volume and maximum temperatures of 300 °C. Usually 6 (100 mL) to 40 (25 mL) TFM or Quartz vessels, which are simply closed with a lid smoothly sliding on the vessel and having a little hole in it, are placed into one common cavity [Fig.2]. Using a loading pressure of pure nitrogen gas at the start of the program, the inside cavity pressure is always during the run at a level that the reaction solution never reaches its boiling point and is not able to leave the vessels. The microwave energy couples into an absorption solution in which the vessels are dipped and takes care for constant heating of all reaction mixtures [Fig 2].

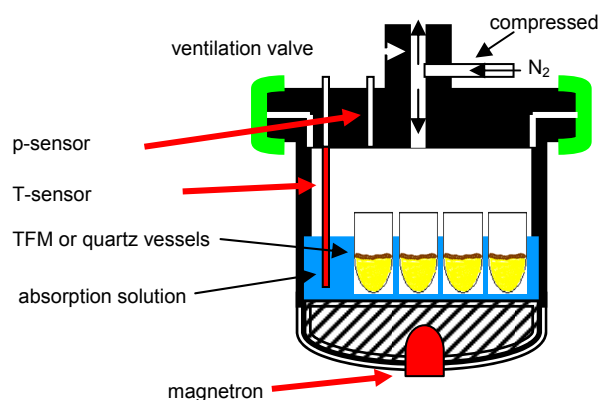


Fig. 2: The ultraCLAVE system of MLS and its basic principle

A quite similar system, the so-called “turboWAVE” was developed in 2010 and is based on the same principle as the “ultraCLAVE” but its cavity as a main difference is reduced to only 1 L. The standard number of samples of the biggest available vessels of 18 mL is 15. Figure 3 shows the “turboWAVE” system with a 40 position sample rack of the “ultraCLAVE” in comparison.



Fig. 3: The turboWAVE system and a 40 position ultraCLAVE rack for comparison reasons

A comparison of the technical specifications is shown in table 1.

Table 1: Comparison of technical specification of the available microwave-assisted digestion system at TKSE

Specification	Single vessel system (Ethos 1600)	ultraCLAVE	turboWAVE
Samples	10 - 24	6 - 40	15
Max. sample volume / mL	45	10 - 35	6
Magnetron power / W	1000 -1500	1000	1200
Vessel (cavity) volume / mL	100	3500	1000
Approx. max. pressure / bar	35 (each)	200 (sum)	200 (sum)
Max. temperature / °C	230	300	300
Use of HCl	yes	no	yes

The technical specifications have to be interpreted for application purposes very carefully. Especially for the single vessel systems, not all of the max specifications can be reached at one time. Extreme pressures and temperatures with 24 samples will not work at the same time in practice. Neither it is sensible to use single vessel systems for the digestion of great amounts of organic sample matrices. Figure 4 illustrates clearly the great advantage of the ultraCLAVE system for decomposition of oils as opposed to the Ethos 1600.

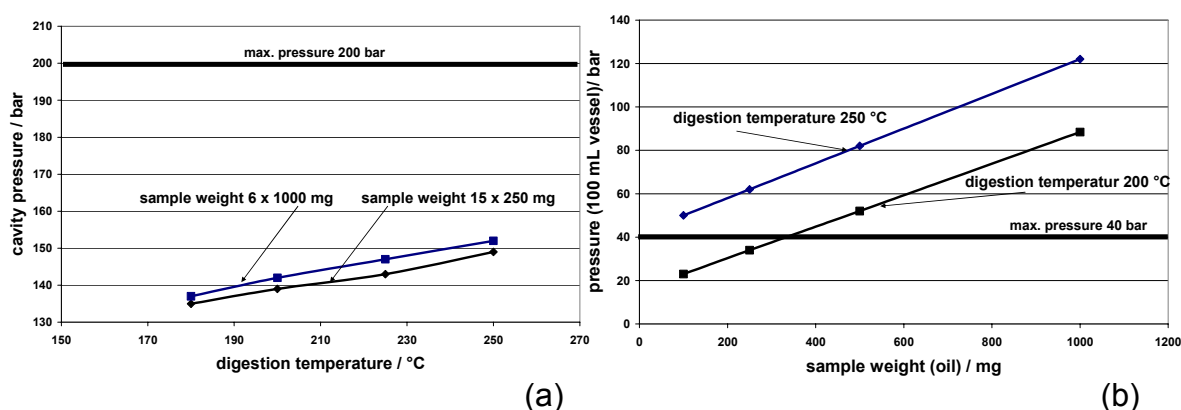


Fig. 4: Pressure-temperature relation for the digestion of oil a) ultraCLAVE b) Ethos 1600

The wear on sample vessel will become extremely high due to diffusion of gases (NO_x , Cl_2 , NOCl , HF). Even quartz will be attacked simply by water at temperature above 230 ° [6]. Unfortunately many producers are very generous in promoting their specification and sometimes compare the microwave assisted digestion in the laboratory with the procedure of cooking coffee.

Like shown in figure 4, only the ultraCLAVE and the turboWAVE systems are suited for high-temperatures at high-pressures, respectively for high organic sample weights.

From the view of cost efficiency, wear on vessels, manpower and investment costs play the most important role. In table 2 some relevant economical aspects are compared.

Table 2: Comparison of relevant economical aspects (average data / ranges)

Aspect / Step	Single vessel system (Ethos 1600)	ultraCLAVE	turboWAVE
Investment / T€	30	75	45
Vessel system / €	200	35	35
Change of vessel system / runs	After approx. 200 runs	> 500	> 500
Time for one run incl. cooling / min	60 - 90	90 - 150	45 - 60
Regular maintenance and service / T€	-	3 (per year)	3 (per year)
Handling (open/close/cleaning)	Time-consuming	Quick and easy	Quick and easy

Finally the requirements for the application itself and the number of samples will decide on the right choice of the microwave system.

Applications

In the laboratories of TKSE a huge variety of sample matrices are handled each day:

- wastewaters, processwaters, emulsions
- pickling acids
- coal, coke, oil, polymers
- ores, sinter, dusts
- soil, sludges
- ferro-alloys, high-alloyed steel, low-alloyed steel
- ceramics

Of the more than 100 applied methods at TKSE for microwave dissolution procedures, there are only very few normative analytical procedures in which microwave assisted procedures are described.

In the DIN EN ISO 15587-1/2, the DIN EN ISO 11885 and the DIN EN ISO 17294-2 the application of the microwave assisted digestion can be found for the analysis of waters using ICP-OES and ICP-MS [7-10]. Furthermore the VDI 2267 Part 15 describes the use of microwave system for the analysis of dust precipitation [11] and the DIN EN 13346 the extraction using aqua regia solutions [12]. The newest normative procedure was released in 2007 for the preparation of products of the mineral oil industry [13]. No normative procedure has been so far published for the iron and steel industry.

Thus microwave procedures are individually developed and validated, which in most cases could take a few weeks especially with regard to trace analysis. A deep knowledge of "microwave chemistry" is a basic requirement to avoid systematic errors.

One application which is run with great success is the digestion of organic products especially oil and emulsions. The difficulties the analytical chemist is faced with single vessel systems are well described [14]. Users of the ultraCLAVE system in contrast underline the good performance for organic matter in comparison to other digestion techniques [15]. A typical time, temperature, pressure diagram of the digestion in the ultraCLAVE is shown in figure 4.

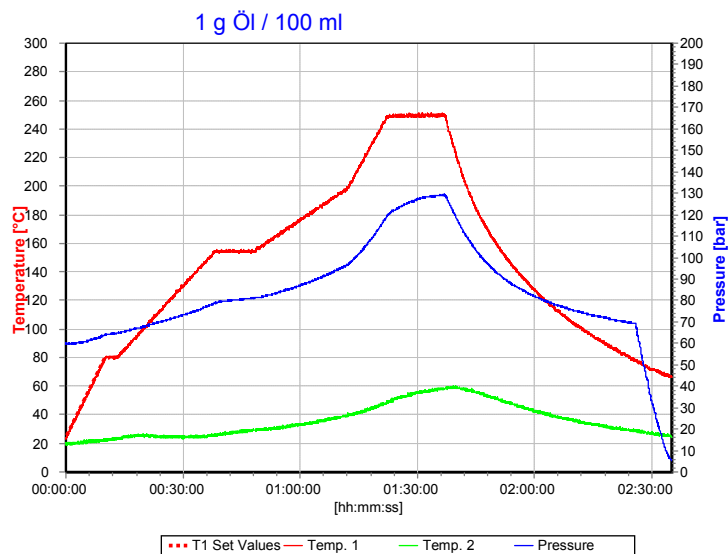


Fig. 4: Typical run for the digestion of oil using the ultraCLAVE

Apart from high-pressure and temperature applications, the ultraCALVE can due to its unique principle, also be used for material, with a high reactivity and volatile reaction products at room-temperature. For these applications it is easy to freeze reactants and the sample by liquid nitrogen before the sample vessels will be put into the microwave system [Fig. 5].



Fig. 5: Preparation of FeB for the ultraCLAVE

Due to several specific advantages, disadvantages and for economical reasons, the turboWAVE as well as the basic one vessel based systems have their fixed place in the laboratory at TKSE.

Conclusion

The different microwave-assisted digestion systems in the laboratory of the TKSE can cover all applications of an iron and steel laboratory and even beyond. The right choice of application for each system depends on several factors.

Since there are not many normative procedures and if there are not updated for the new generation of microwave systems it is still up to the analytical chemist to develop his own methods. The analytical chemist is not freed from working out his method in detail and to look at precipitates and elements/compounds which could be volatile during the digestion step as well as contamination from vessel materials.

Also it should be obeyed that, although the systems have a lot of security on board, spontaneous reactions in some unlucky cases can lead to little explosions [Fig. 6]. Due to the high standard of passive security of the systems only little material damage was produced in this case.



Fig. 6: Explosion of a vessel due to mishandling

References:

- 1) Kingston, H.M., Jassie, L.B.: Microwave Acid Sample Decomposition for Elemental Analysis, J. Res. Natl. Bur. Stand. (U.S.), **93**, 269-274(1988)
- 2) Kingston H.M., Haswell, S.J.: Microwave-Enhanced Chemistry, American Chemical Society, Washington, DC, (1997)
- 3) Bitsch, R., Merck, E.: Probenvorbereitung per Mikrowelle, Labor Praxis **18**, 76-81 (1994)
- 4) Lautenschläger, W.: Microwave digestion in a closed-vessel high-pressure system, Spectroscopy (Eugene, Oreg.), **4**, 16-21(1989)
- 5) Lautenschläger, W.: Optimum control of microwave processes, Labor Praxis **23**, 24-28 (1999)
- 6) Lautenschläger, W., Kopp, G.: Mikrowellen-Aufschlusstechnik für Fortgeschrittene, Labor Praxis **4**, 76-78 (2000)
- 7) DIN EN ISO 15587-1, Aufschluss für die Bestimmung ausgewählter Elemente in Wasser Teil1: Königswasser-Aufschluss (Juli 2002)
- 8) DIN EN ISO 15587-2, Aufschluss für die Bestimmung ausgewählter Elemente in Wasser Teil2: Salpetersäure-Aufschluss (Juli 2002)
- 9) DIN EN ISO 11885, Bestimmung von ausgewählten Elementen durch induktiv gekoppelte Plasma-Atom-Emissionsspektrometrie (ICP-OES) (September 2009)
- 10) DIN EN ISO 17294-2, Anwendung der induktiv gekoppelten Plasma-Massenspektrometrie (ICP-MS) – Teil 2: Bestimmung von 62 Elementen (2004)
- 11) VDI 2267 Part 15, "Determination of suspended matter in ambient air Measurement of the mass concentration of Al, As, Ca, Cd, Co, Cr, Cu, K, Mn, Ni, Pb, Sb, V and Zn as part of dust precipitation by mass spectrometry (ICP-MS) November 2005
- 12) DIN EN 13346, Bestimmung von Spurenelementen und Phosphor, Extraktionsverfahren mit Königswasser (April 2001)
- 13) DIN 51460-1, Prüfung von Mineralölerzeugnissen – Verfahren zur Probenvorbereitung – Teil 1: Mikrowellenunterstützter Druckaufschluss (November 2007)
- 14) Wondimu, T., Gössler, W., Irgolic, K.J., Microwave digestion of „residual fuel oil“ (NIST SRM 1634b) for the determination of trace elements by inductively coupled plasma-mass spectrometry, Fres. J. Anal. Chem. **367**, 35-42 (2000)
- 15) Krachler, M., Mohl, C., Emons, H., Shotyk, W.: Analytical procedures for the determination of selected trace elements in peat and plant samples by inductively coupled plasma mass spectrometry, Spectrochim. Acta Part B **57**, 1277-1289 (2002)

MICROWAVE DIGESTION – AN IMPROVED SAMPLE PREPARATION METHOD FOR ICP-OES ANALYSIS OF METAL POWDER IN THE QUALITY CONTROL LAB

Alexander Henrich

Höganäs Sweden AB, SE – 263 83 Höganäs, Sweden

Abstract

The majority of trace and alloying element determinations in iron and metal powder mixes are carried out by well established quality control methods like XRF in order to meet internal and external customer requirements and specifications in the powder metallurgy business area of Höganäs AB. The powder samples are remelt to a compact steel sample in an induction furnace, preparing them for XRF analysis. Some elements, e.g. Ca, Cr, Mg, Mn, Si, and V, cannot be determined by XRF accurately due to their high affinity to oxygen. They may form slag products during the remelting step. These elements have to be determined by ICP-OES. Sample preparation for this analysis is based on dissolving of the powder sample by acids and digestion of the residue by fusion melting. This is time consuming compared with sample preparation for XRF. Microwave digestion was established as sample preparation method which saves time and consumption of chemicals. This digestion method is used for all incoming trace and alloying element analyses carried out by ICP-OES. The set-up of the microwave digestion unit and ICP-OES, the results according to recovery of the elements, precision, working time, consumption of chemicals, and experienced issues will be evaluated and discussed. Microwave digestion was established.

Introduction

Höganäs Sweden AB produces metal powder and manufactures metal powder mixes after customers need. Final analyses are performed in the quality control section to meet customer requirements regarding trace and alloying elements.

The majority of the trace and alloying elements is analyzed by X-ray fluorescence analysis (XRF) after remelting the powder samples to a compact steel sample in an induction furnace. Some elements have a high affinity to oxygen ¹⁾. They form slag products which migrate to the remelt sample surface. XRF analysis would lead to a wrong determination due to uneven contribution of slag forming elements in the sample.

Those oxygen sensitive elements are determined by inductively coupled plasma optical emission spectroscopy (ICP-OES) after transferring the solid sample to a solution by digestion in the Chemical Analysis Services section. This section mainly serves the production with trace and alloying element analyses which cannot be determined by XRF. Furthermore, the section helps R&D and production with special analytical requests.

Situation and motivation

Roughly 1700 trace and alloying element determinations for the production and roughly 1500 determinations for R&D, Sales and complaints were carried out in the Chemical Analysis Services section during 2008. A percental distribution of different sample preparation methods and applied analytical instruments during 2008 is shown in figure 1.

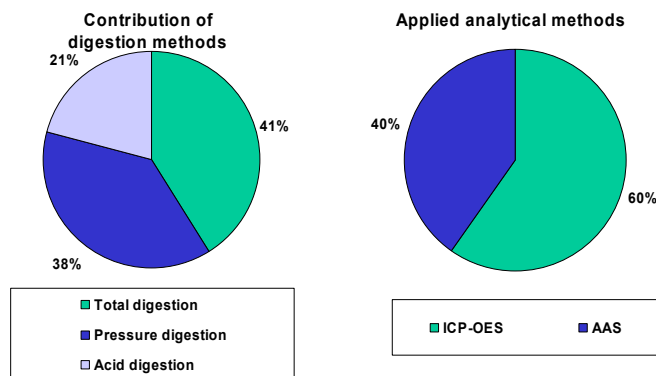


Figure 1: Contribution of the different sample preparation methods and applied analytical instruments based on 2008 statistics.

Three different digestion methods are applied in total 2). These are “total digestion”, “acid digestion”, and “pressure digestion”. The total digestion is based on an acid digestion followed by fusion decomposition of the residue. The elements of interest in the obtained solutions are analyzed by atomic absorption spectroscopy (AAS) and ICP-OES. Si, Na, and K determinations were carried out by AAS after pressure digestion. Ca and P determinations were among others carried out by ICP-OES after acid digestion. B, Cr, Mg, Mn, and V determinations were among others carried out by ICP-OES after total digestion.

“Can the number of digestion methods be reduced by applying another digestion method?” was defined as a first requirement from the discussion above.

Different chemicals are used for different digestion methods which are shown in figure 2. The majority of digestion methods are total digestions which has highest consumptions of chemicals.

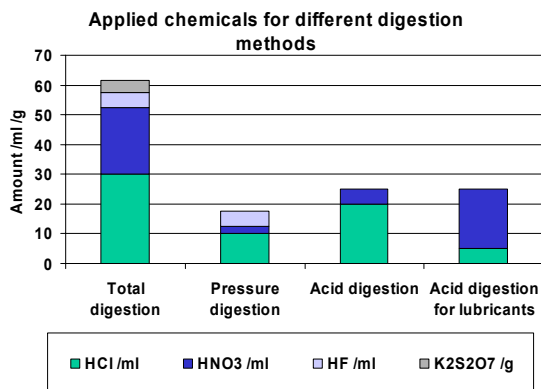


Figure 2: Consumption of chemicals for the four digestion methods.

“Can the amount of chemicals be reduced by applying another digestion method?” was defined as a second requirement from the discussion above.

Implementation

The new set-up for sample preparation and analysis of trace and alloying elements consists of a microwave digestion unit 3) and a new ICP-OES equipped with an autoloader as well as a HF-resistant sample introduction system.

Table 1 shows the applied microwave digestion programs in detail for all incoming samples for metal analyses.

Table 1: Applied microwave digestion programs in detail which cover all incoming samples for metal analyses.

Type of sample and amount /g	Ramp time /min	Reaction temperature /°C	Hold time /min	Chemicals
Iron and metal powder, 0,5 g	20	200 Alternatively 220	20 alternatively 40	1 ml H ₂ O 8 ml HNO ₃ 4 ml HCl 2 ml HF, alternatively 4 ml HF
Lubricant, 0,2 g	15	190	15	12 ml HNO ₃ 2 ml HF
HF-complexation (if necessary as a 2nd step)	15	190	15	20 ml H ₃ BO ₃ (8% w/v)

A higher temperature and a higher amount of HF is necessary for a complete digestion of material which contains Chromium and Manganese oxides. Lubricants are digested only with HNO₃ 4). HF is added if Si has to be determined. Some elements form insoluble fluorides (e.g. Al, Y) or slightly soluble fluorides (e.g. Ca) 5). A HF complexation with boric acid should be performed as a second step to redissolve the precipitated fluorides 6).

The different working steps for the total digestion and the microwave digestion are compared in a flow chart in figure 3. Needed time from weighing the sample until receiving the analytical result from ICP-OES takes about five hours for the total digestion compared to about two hours for the microwave digestion. Time estimation is the sum of handling and waiting time.

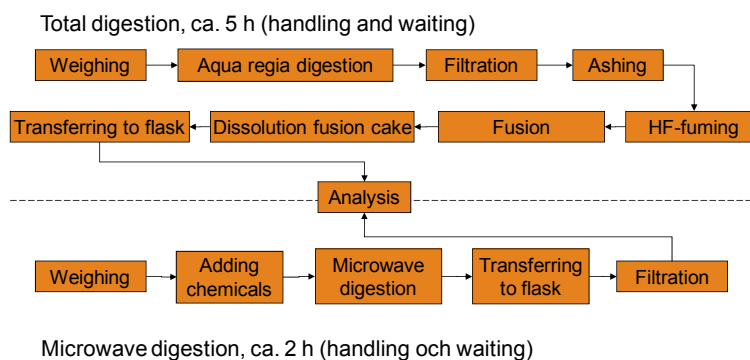


Figure 3: Comparison of the different working steps for total digestion and microwave digestion.

Results and discussion

Reducing the number of digestion methods was fulfilled as the first requirement. Microwave digestion is applied to all incoming samples for metal analysis. Only one digestion is necessary to analyse different elements in the same solution.

Reducing the amount of chemicals was fulfilled as the second requirement. Figure 4 shows the comparison between the amount of used chemicals for the different microwave digestion programs and the different previous digestion methods. The total amount of chemicals was reduced to a total volume of 14 ml acids for the digestion or 2 g H₃BO₃ for the HF complexation.

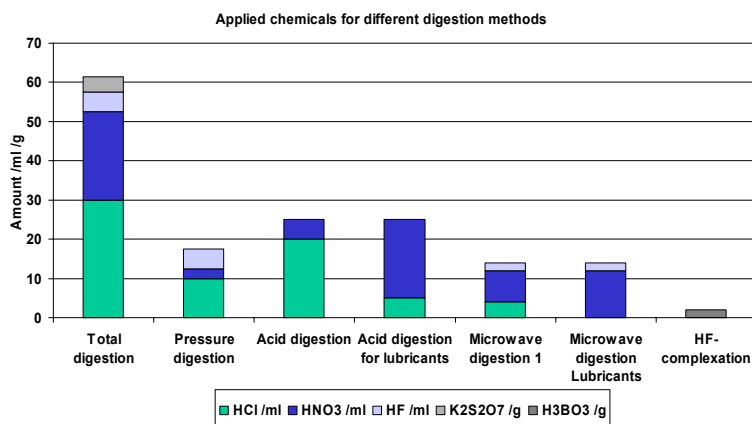


Figure 4: Comparison between the amounts of used chemicals for the different previous digestion methods and the different microwave digestion programs.

In the following, two examples for successful validation and implementation of microwave digestion are presented.

For validation and implementation, microwave digestion followed by ICP-OES for Si analysis was compared with the former method of pressure digestion followed by AAS, see figure 5. This transfer shows no significant differences between the two digestion and analytical methods.

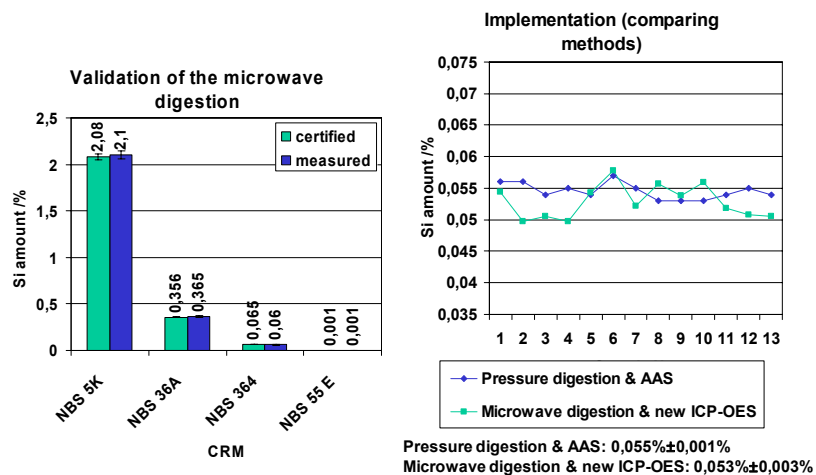


Figure 5: Validation and implementation of Si analysis.

For validation and implementation, microwave digestion followed by ICP-OES for V analysis was compared with the former method of total digestion followed by ICP-OES, see figure 6. This transfer shows no significant differences between the two digestion and analytical methods.

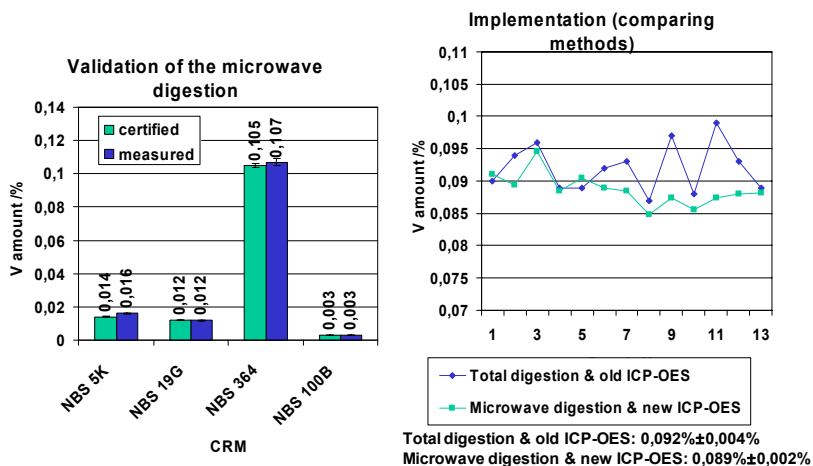


Figure 6: Validation and implementation of V analysis.

The need of different microwave digestion parameters for a complete microwave digestion of Chromium and Manganese oxides are shown in figure 7. The adjustment of acid composition, reaction temperature, and hold time are necessary for a complete digestion of samples containing Cr and Mn oxides.

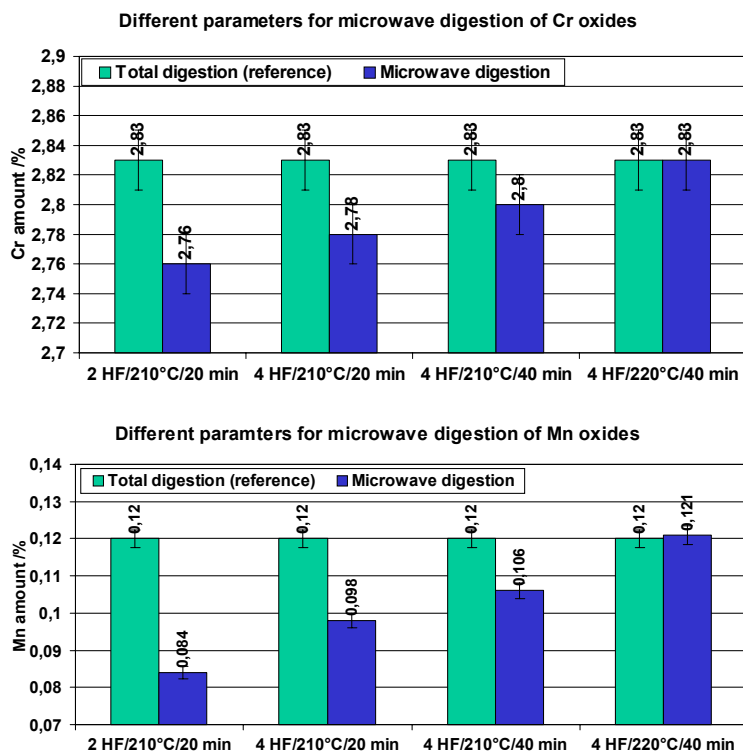


Figure 7: Impact of different microwave digestion parameters (acid composition, reaction temperature, and hold time) on a complete microwave digestion of samples containing Cr and Mn oxides.

Some elements form insoluble or slightly soluble fluorides. A HF-complexation with H3BO3 is a necessary second step after microwave digestion to redissolve insoluble fluorides and to achieve a complete digestion for Al and Y as it is shown in figure 8.

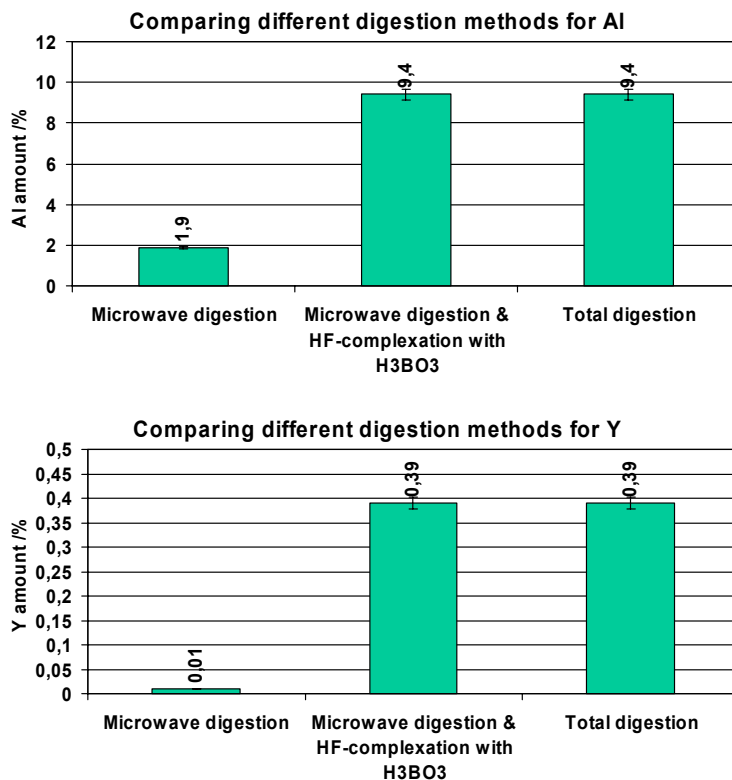


Figure 8: HF-complexation with H3BO3 as a necessary second step for a complete digestion of Al and Y.

The yield of Al and Y is similar to the analytical results obtained by a total digestion which is used as a reference digestion in this case. All samples are analyzed against matrix matched calibration standards.

Conclusion

Microwave digestion as a sample preparation method was established for the determination of trace and alloying elements with ICP-OES. Reducing the number of digestions and the amount of chemicals as defined requirements were fulfilled. Even the number of chemicals was reduced.

The implementation of microwave digestion as sample preparation method was successful as discussed for some examples. Today all incoming samples for trace and alloying metal analysis from production, R&D, sales and complaints can be digested by microwave digestion.

The handling time for sample preparation was reduced. This leads to a shorter response time from incoming samples until obtaining analytical results.

Increasing of temperature and reaction time as well as variation of chemicals are necessary to gain complete digestion of samples containing compositions which are difficult to digest like Cr and Mn oxides.

A HF-complexation with H3BO3 shall be applied as a second step after microwave digestion in order to redissolve insoluble fluorides as discussed for Al and Y.

One drawback of using microwave digestion as sample preparation method is the use of HF in order to digest Si. Working with HF demands particular precautions, HF resistant laboratory ware and a HF resistant sample introduction system for the ICP-OES.

The need of a reduced sample weight to minimize the risk of a vessel failure during microwave digestion is another drawback of this method. Investigations have to be carried out to evaluate if the precision and trueness for the analytical method are still fitting the demands with reduced sample weight.

The capacity of one microwave digestion run can be the bottle neck in the analytical method if a lot of samples have to be digested and analyzed.

Unknown samples should be treated in a different way. The selection of acid composition, reaction temperature, and hold time should be considered carefully in order to minimize the risk of vessel failures during microwave digestion.

References:

- 1) http://web.mit.edu/2.813/www/readings/Ellingham_diagrams.pdf
- 2) Bock, R., Handbook of Decomposition Methods in Analytical Chemistry, International Textbook Co. London, 1979
- 3) Introduction to Microwave Sample Preparation: Theory and Practice, eds. Kingston, H.M., Jassie, L.B., American Chemical Society, Washington DC., 1988
- 4) CEM application notes for acid digestion reports "Petroleum Based Wax", CEM Corporation
- 5) Handbook of chemistry and physics, 1961, 43rd edition
- 6) CEM application note for acid digestion reports "Boric HF neutralization", CEM Corporation

THE TRIBOLOGICAL PROPERTIES OF ROLLING OIL EMULSIONS WITH AND WITHOUT NANOPARTICLES.

**Karin Persson¹, Sajid Ali Alvi¹, Johan Andersson¹, Irena Blute¹
Fernando Alonso², Achim Losch², Rolf Luther², Albert Mascaró², Juergen Rausch²**

¹ YKI, Box 5607, SE-116 87 Stockholm, Sweden

² Fuchs Europe, Freisenheimer Straße 15, 68169 Mannheim, Germany

Abstract

There is an interest in understanding the possibilities that nano-particles can provide to lubricants for metal forming. In this paper we have investigated multi-walled carbon nano-tubes (CNT) and IF-WS₂ (Inorganic Fullerene-like WS₂) added to emulsion concentrates (EC) at a concentration of 0.1%. The properties of the 2% oil-in-water rolling oil emulsions were studied with Mini Traction Machine (MTM), particle sizing, surface characterization of the tribosurfaces with HR-SEM/EDS and profilometry and dynamic wetting with three-phase contact angle measurements.

The MTM measurements showed that at high speeds the friction coefficient was similar with and without added particles. At low speeds the nanoparticles frequently provided time dependent friction coefficients. With CNT in the EC the friction coefficient initially decreased but after 5 minutes increased again. 0.1% IF-WS₂ provided a more stable friction coefficient after the initial running in. It was observed that for CNT, there is a tendency of formation of amorphous carbon, and formation of carpet like debris on the surface due to the high pressure exerted in the contact.

The stability of the emulsions against coalescence was not impaired by the addition of nano-particles. However, the dynamic wetting was significantly altered by the addition of the nano-particles, which can affect the film forming properties and thus the friction coefficient at medium speeds. When Stribeck curves are measured, it is observed that it is important to measure the effect of both increasing and decreasing the speed, especially for emulsions, which can show considerable differences at medium speeds, but also for nano-particle containing ECs. In summary, the lubrication of emulsions and the effect of addition of nano-particles do markedly depend on how the lubricant is tested and used.

Background

The lubrication enhancement of nano-particles suspended in oils have been reported to be due to different mechanisms involved such as the ball bearing effect [1], protective film [2], mending effect [3] and polishing effect [4]. Such mechanisms are mainly classified into two groups [5]. The first group is classified as direct effect which involves the mechanism of rolling effect and protective film formation. The nano-particles then tend to act as ball bearing balls in between the friction surfaces provided that the shape of nano-particles is preserved. This is a less likely mechanism for four rough surfaces and high pressures. Some types of nano-particles can also generate a protective film by coating rough surfaces through exfoliation of external sheets at high contact loads [6]. The second group is classified as the secondary effects of nano-particles for surface enhancement consisting of mending effect and polishing effect. The mending effect is defined as deposition of nano-particles on the friction surface to compensate for the loss of mass and the polishing effect is defined as the reduction of roughness of lubricating surfaces by nano-particle assisted abrasion. The shape of IF-WS₂ under higher loads gets damaged, however most of the damaged IF will still serve as a solid lubricant, as the exfoliated layers of the IF-WS₂ will serve as a transfer film. The performance of IF-WS₂ in a lubricant also depends on the film thickness between the contact surfaces. When the thickness of the film becomes smaller than the size of, for example IF-WS₂, particles

under high loads, it is expected that IF-WS₂ nano-particles are deformed and destruction of the nano-particles lead to the formation of transferred IF film on the surface. The asperity contact can be limited by IF nano-particles, which are delaminated by forming transferred films at the asperity, crests and partially preserved in the valleys of roughened surfaces [7].

Carbon nanotubes (CNTs) can be classified as single-walled nanotubes (SWNTs) or multi-walled nanotubes (MWNTs). The MWCNTs, first observed in 1991, can be described as rolled up graphene sheets in a nested form which can slip one inside the other. Single walled nanotubes discovered in 1993 [8], can be described as a rolled up single sheet of graphene. Carbon nanotubes have a length of several micrometers, often gathered in bundles. MWCNTs have an interlayer spacing of 0.34-0.36nm, which is close to the atomic spacing of graphite. The nanotubes have C-C bond lengths of 0.14 nm which is shorter than the bond lengths in diamonds, suggesting that nanotubes are much stronger than diamond [9]. The CNTs have been found very effective in the tribological application in areas such as solid films for dry lubrication, additives for liquid lubricants and greases and composites for wear parts. However, their lubrication mechanism has not yet been completely elucidated. Friction reducing and anti-wear properties of carbon nanotubes can be categorized based on the type of CNTs in question. For SWNTs it has been found that for Ni/Y-based SWNTs dispersed in synthetic polyalphaolefin base oil (PAO), an optimal concentration of 1 wt% SWNTs gives high friction reduction reaching a value of 0.08 and wear of the sliding surfaces is strongly reduced, as compared to PAO oil without CNTs which gives a high friction coefficient of ≈ 0.25 . The coefficient of friction also decreased with increasing contact pressure for SWNTs dispersed in PAO oil. The low friction coefficient and anti-wear properties obtained has been suggested to be due to flake-like wear debris which is made of amorphous carbon containing catalytic particles and wear particles [9]. Furthermore, the formation of flake-like wear debris can be observed in simulation work performed by Ni and Sinnott [10], which suggests that under high loads the CNTs end up breaking during shear and change into amorphous carbon to give flake-like debris. In the case of MWCNTs, a very small concentration of 0.1% CNTs dispersed in oil can be enough for good tribological properties and the friction coefficient is reduced even more with increasing contact pressure compared to SWNTs. The difference in friction coefficient with respect to contact pressure between SWNTs and MWNTs can be explained by the fact that multi-walled nanotubes are flattened at higher loads than single walled ones [11].

Experimental

Dispersion of the additives

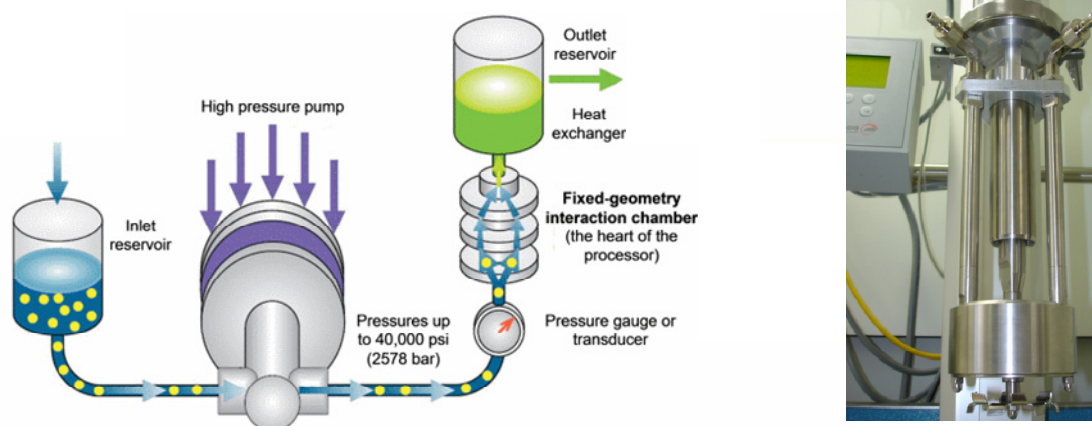
FUCHS was mainly involved in the incorporation of different nano-particles into ECs for rolling oil emulsions. In particular, the dispersion of nano-particles was done in the EC (prior to emulsification in water), using different types of oil-soluble synthetic dispersants as stabilizer for the dispersion. The aim of the work was the evaluation and reduced sedimentation and agglomeration. From other experiences FUCHS did know two promising methods to disperse the nano-particles and to break up the agglomerates, the roller bearing four-ball tester for small volumes and the Dispermat CN F2 for larger volumes. To determine the quality of the dispersion, the dispersed fluid has been poured completely into another beaker. This procedure leaves the undispersed nano-particles on the bottom or the walls of the original beaker, so that an evaluation of different dispersant additive combinations was possible. For the comparison the amount of precipitation and its location on the bottom or the walls was important. The larger volumes prepared in this project (up to 2 liters) were prepared on the Dispermat, at 6000 RPM, at 60 °C for 4 hours, with cooling. The concentration of nano-particles in the results presented below were 0.1% and no other dispersants than the additives and emulsifiers used in a typical rolling oil emulsion concentrate were added.

The M-110Y Microfluidizer processor (Microfluidics, USA) is a lab machine that provides the high shear rates of fluids by maximizing the energy-per-unit fluid volume to produce uniform submicron particle and droplet size. The

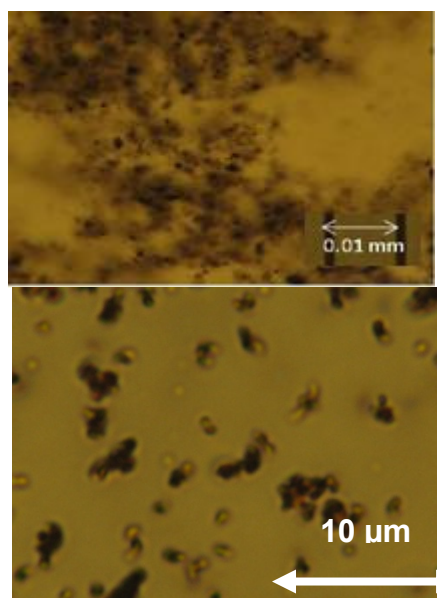
Microfluidizer processor can be used for emulsification, dispersions, de-agglomeration, encapsulation and cell rupture.

The operating principle of the microfluidizer is based on an air powered intensifier pump operated at a pressure range of 206-1586 bar which is designed to supply the desired operating pressure at a constant rate through fixed-geometry micro channels within the interaction chamber. Very high shear rates are created due to the product stream acceleration to high velocities. During the passage of product through the channels, the entire product experiences uniform processing conditions.

This technique was used to investigate if the level of dispersion of nano-particles could be improved over that achieved with the Dispermat. The processing parameters were set to temperatures of 60 ± 5 °C and 50 ± 5 °C with inlet pressure around 4 ± 0.5 bar in different runs. The number of passes was varied in each experiment to see its effect on the final dispersion. In all of the microfluidizer runs the system was cleaned with 2-propanol prior to running the experiment and then filled with emulsion concentrate as a base. We performed microfluidization with one pass, two passes and undefined number of passes for the time period of one hour.

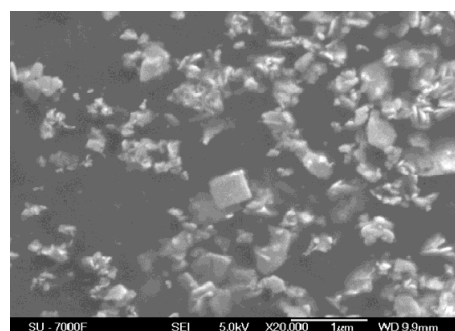


The schematic construction and photo of the microfluidizer and the Dispermat CN F2.



Optical micrograph of emulsion concentrate with 0.1% IF-WS₂, after 1 pass in the microfluidizer.

To the left, an optical micrograph of microfluidized CNT emulsion concentrate with one pass at 1300X. From the manufacturers info the outer mean diameter of CNTs are 13-16 nm. It is clear that the CNTs are agglomerated.



HRSEM micrographs of IF-WS₂ emulsion concentrate after one pass in the microfluidizer at X20,000. The scale is 1 μm.

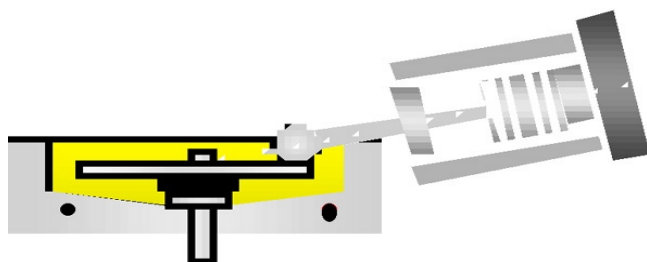
Tribological instrumentation

A mini traction machine (MTM2, PCS Instruments, London, UK) has been used to measure the friction coefficient of lubricants under a wide range of rolling and sliding conditions. The various parameters which can be changed include temperature, load, sliding/rolling ratio (SRR) and the mean speed. Sliding/rolling ratio (SRR) is defined in terms of percentage between the sliding and mean speed. SRR can be varied within a range from 0% to 200%, 0% being pure rolling whereas 200% being pure sliding.

$$SRR = \frac{(V_{disc} - V_{ball})}{(V_{ball} + V_{disc})/2} * 100$$

The basic setup of the instrument involves steel/steel contact at varying loads. The load is applied on a steel disc (4.5 mm thick; 46 mm diameter) through a steel ball (19.05 mm diameter) and frictional force is measured through a force transducer as the ball is in contact with the steel disc. Both the steel ball and the steel disc were of AISI 52100 steel and had a smooth finish with roughness less than 0.01 μm (Ra).

All measurements were performed at 50% SRR which is suitable for studying of rolling [12] and a mean speed in the range of 3000 mm/s to 2 mm/s. The steel disc was submerged in a temperature controlled pot maintained at 50°C. The amount of lubricant used was enough to cover the contact between steel disc and ball and 35 ml of lubricant is usually needed per measurement. Different profiles were generated with varying load and mean speed to understand the variation of friction coefficient with measurement conditions. A new disc was used for each test.



Specifications

- Slide/roll ratio 0 - 100%
- Speeds 0 - 5 m/s
- Loads 1 - 75N
- Contact pressures up to 3 GPa
- Temperature range from 5 - 150°C

Results

The stability of the 2% emulsions were determined with droplet size determination using light diffraction/scattering. The emulsions made of concentrates with 0.1% CNT of IF-WS₂ has similar droplet size as emulsions without nano-particles. The CNT emulsions and emulsion without nano-particles were stable for at least two weeks against coalescence of the emulsion droplets.

Results from a typical MTM measurement on an emulsion concentrate is shown in Figure 2. Increasing the contact pressure at higher speeds, above 100 mm/s, in the elastohydrodynamic regime, the friction is caused by the viscosity of the lubricant. Normalizing the data with the friction at the speed where the friction reaches its minimum yields a master curve, valid for the friction at different contact pressures in the mixed and elastohydrodynamic regime (not shown).

Measuring the Stribeck curve for concentrates with 0.1% CNT the friction was dependent on if the speed was increased or decreased, see Figure 3. Starting at low speed the friction coefficient in the boundary range was

0.1, whereas after the speed had been increased to 1000 mm/s and then reduced it was 0.14. Other phenomena such as ageing of the concentrate for a few months after the initial dispersion also increased the friction coefficient with 0.02 in the boundary regime. In the EHD regime the friction is independent of history as expected since the friction in this case is dependent of the viscosity of the lubricant.

The Stribeck curve of the concentrate with 0.1 % IF-WS₂ did not show any hysteresis effects. At all speeds the friction was higher than for the concentrate without particles. Adding the same amount of WS₂ platelets did not increase the friction to the same extent as the nanoparticles, see Figure 3.

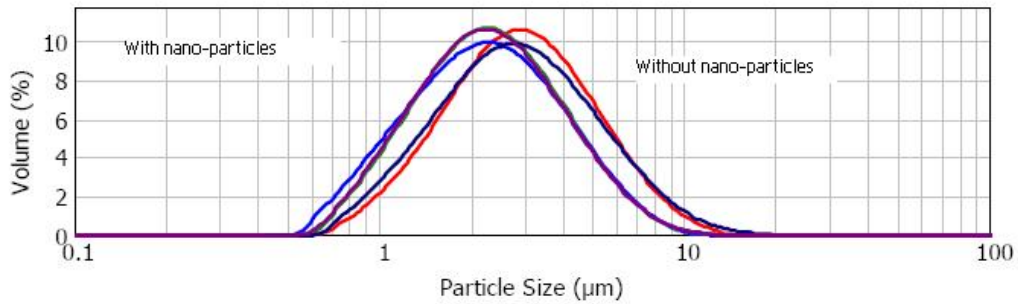


Figure 1 Droplet size of 2% oil in water emulsions.

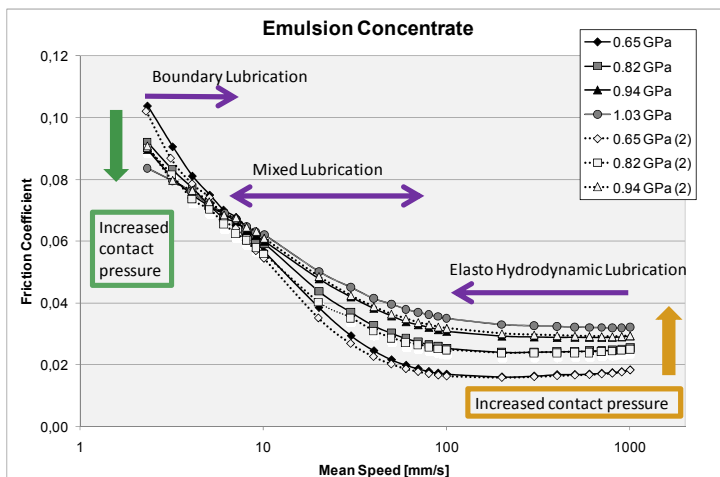


Figure 2 MTM Stribeck curves of emulsion concentrate performed at four different contact pressures at 50 °C. The measurements were performed from high to low speeds. Consecutively measurements were made on the same surface, from low to high pressures, and a repeat from low to high pressures labelled as (2).

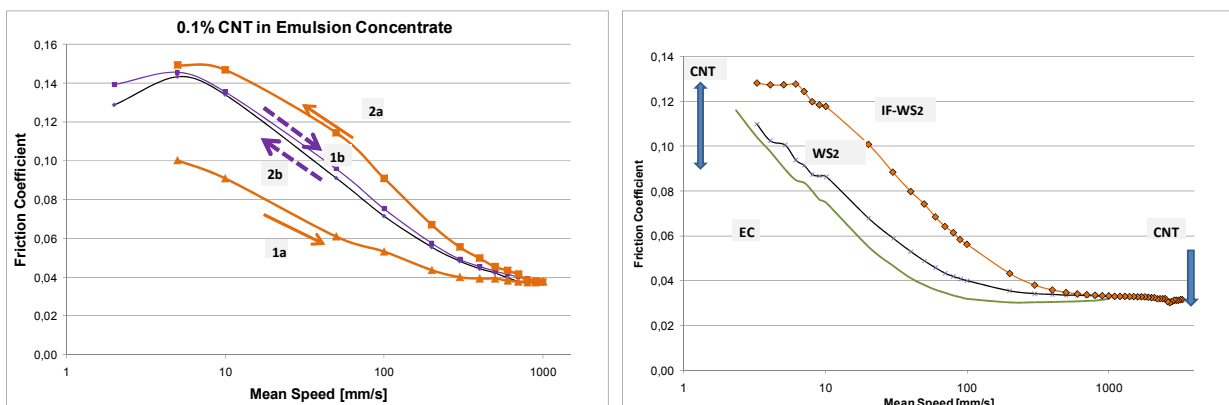


Figure 3 The Stribeck curve for emulsion concentrates, with and without particles. Only the concentrate with CNTs showed any effect on if the measurement was run from high to low, or low to high speeds. The measurement a was performed on one disc and measurement b on another.

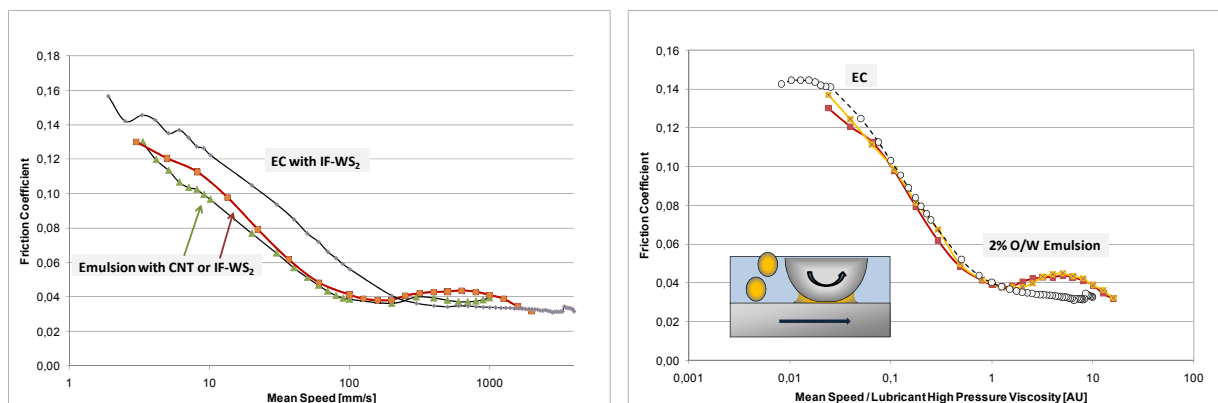


Figure 4a Stribeck curves at 0.82 GPa for 2% IF-WS₂ emulsion compared to the emulsion concentrate (EC). Increased friction in EHD regime for emulsion due to starvation.

Figure 4b Stribeck curves at 0.82 GPa for the EC. with 0.1% IF-WS₂ and the corresponding 2% emulsions measured from high to low and reversed speed.

The Stribeck showed the typical form shown in Figure 4a, where they in addition to the typically observations also has an increased friction at higher speeds. For IF-WS₂, the Stribeck curve is similar for both increasing and decreasing speeds, however, this is not the case neither for the emulsion with and nor without CNT above 50 mm/s. In this region the friction depends on the level of starvation, i.e. to which extent and under which conditions the emulsion droplets are able to form a lubricating film, as will be discussed below. Below this speed the Stribeck curves can form a mastercurve if the mean speed is normalized with the viscosity of the lubricant, here taken as the friction coefficient at the start of the EHD region, see Figure 4b.

In the boundary and mixed lubrication the two nano-particle containing emulsions show similar friction, see Figure 4a. At low speeds the nano-particles frequently provided time dependent friction coefficients. With CNT in the oil concentrate the friction coefficient initially decreased but after 5 minutes increased again. 0.1% IF-WS₂ provided a more stable friction coefficient after the initial running in, see Figure 5. In the mixed regime there is running in for 1.5 minutes after which the friction is stable. The running in at 50 mm/s is quite similar for all three emulsions. SEM analysis showed that there were presence of holes and surface wear in the mixed regime. Large amounts of black spots with high carbon content were also observed at the onset of starvation. For CNT emulsions, SEM analysis showed the presence of CNTs in the wear track, see Figure 6, were they may coat wear particles. There is also a tendency of formation of amorphous carbon, Figure 7 and carpet like debris on the surface due to the high pressure exerted in the contact. Furthermore, there was also several black spots with high carbon content.

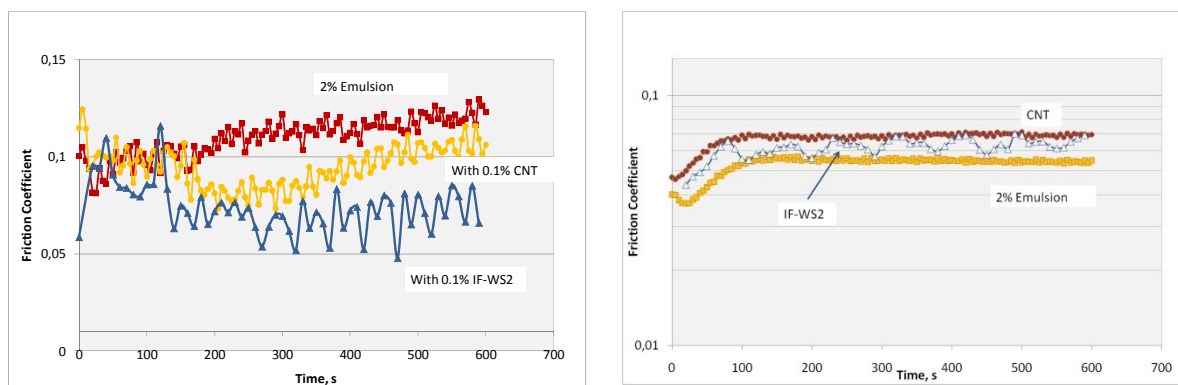


Figure 5 Friction coefficient at 0.82 GPa as a function of time in the boundary regime (5 mm/s) (left) and mixed regime at the onset of starvation (50 mm/s) (right) for 2% emulsions with and without nano-particles in the concentrate.

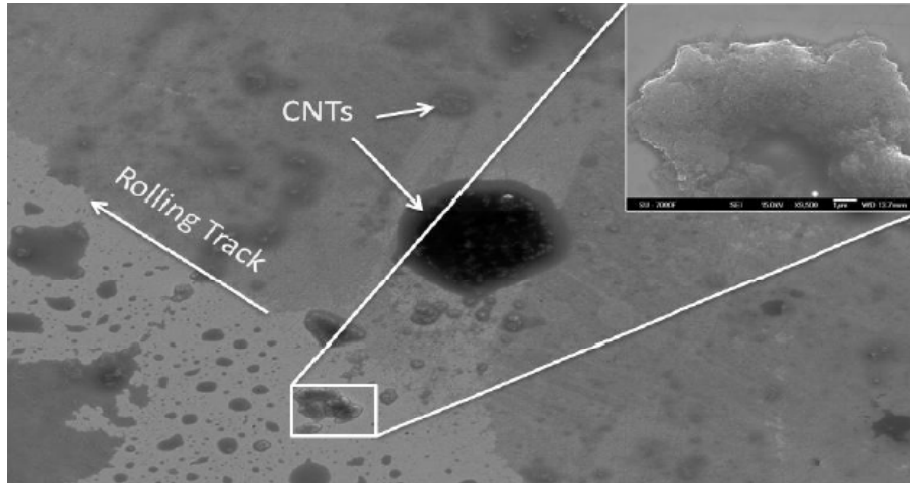


Figure 6 High resolution SEM micrograph of CNTs in the rolling track.

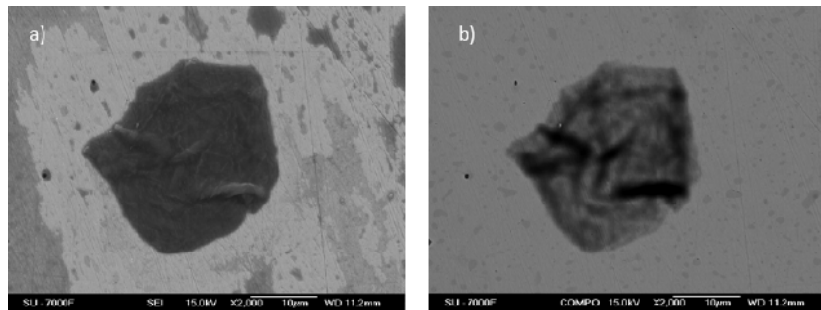
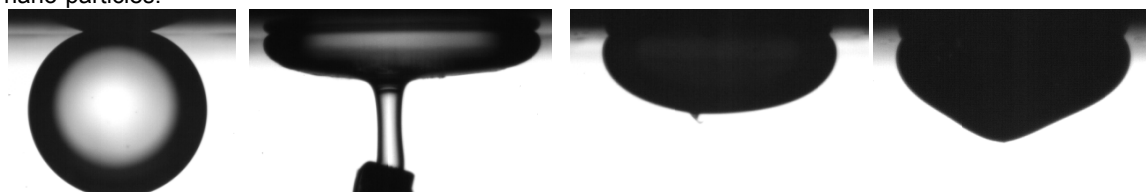


Figure 7 High resolution SEM micrograph of amorphous carbon from CNT observed in the rolling track a) secondary mode and b) back scattering mode.

It is well known that starvation of emulsion depend on the effectiveness of the capturing of emulsion droplets and form a lubricating film. For this reason the ability of the emulsion concentrate to displace the water phase from the surface was investigated. As seen below, Figure 8, the dynamic wetting was significantly altered by the addition of the nano-particles, possibly due to viscosity and possibly due to interfacial tension. Nevertheless, it was observed that the film forming properties and thus the friction coefficient at medium speeds was altered by the presence of nano-particles.



- a) Base oil, 25 °C
- b) Emulsion Concentrate (EC), low interfacial tension of oil. 25 °C.
- c) EC with IF-WS₂, after dispensing, 50 °C. Higher viscosity and/or interfacial tension affects the form of the sessile drop.
- d) EC with CNT, after dispensing, 50 °C. Viscosity or possibly sedimentation of particles inside the drop affects the form of the sessile drop.

Figure 8 Images taken during contact angle on steel measurements in water. Measurements in the presents of the water phase of the emulsion showed similar results, but then also air bubbles were present on the surface demonstrating that the additives rendered the surface more hydrophobic.

Conclusions

The stability of the emulsions against coalescence was not impaired by the addition of nano-particles. The lubrication of nano-particle lubricants does markedly depend on the tribosystem, i.e. how the lubricant enters the contact, the contact pressure etc. The same is observed for emulsions and thus the effect of addition of nano-particles does depend on how the lubricant is tested. Nevertheless, although nano-particles show high friction when tested in emulsion concentrates, in an emulsion they can provide reduced friction at constant speed both in the mixed and boundary regime. Hopefully rolling trials can be conducted with these systems in the near future.

References:

- 1 Rapaport, L. et al., Mechanism of friction of fullerenes. *Industrial Lubrication and Tribology*, 2002, 54(4); p 171-176.
- 2 Ginzburg, B.M., et al., *Antiwear effect of fullerene C-60 additives to lubricating oils*. *Russian Journal of Applied Chemistry*, 2002. 75(8): p. 1330-1335.
- 3 Liu, G., et al., *Investigation of the mending effect and mechanism of copper nano-particles on a tribologically stressed surface*. *Tribology Letters*, 2004. 17(4): p. 961-966.
- 4 Xu, T., J.Z. Zhao, and K. Xu, *The ball-bearing effect of diamond nanoparticles as an oil additive*. *Journal of Physics D-Applied Physics*, 1996. 29(11): p. 2932-2937.
- 5 Lee, K., et al., *Understanding the Role of Nanoparticles in Nano-oil Lubrication*. *Tribology Letters*, 2009. 35(2): p. 127-131.
- 6 Cizaire, L., et al., *Mechanisms of ultra-low friction by hollow inorganic fullerene-like MoS₂ nanoparticles*. *SURFACE & COATINGS TECHNOLOGY*;160 (2-3): 282-287 OCT 22 2002, 2002. 160.
- 7 L. Rapoport Tribological properties of WS₂ nanoparticles under mixed lubrication
- 8 Lijima, S. and T. Ichihashi, *SINGLE-SHELL CARBON NANOTUBES OF 1-NM DIAMETER*. *Nature*, 1993. 363(6430): p. 603-605.
- 9 Bonard, J.M., et al., *Field emission from carbon nanotubes: the first five years*. *Solid-State Electronics*, 2001. 45(6): p. 893-914.
- 10 Ni, B. and S.B. Sinnott, *Tribological properties of carbon nanotube bundles predicted from atomistic simulations*. *SURFACE SCIENCE*;487 (1-3): 87-96 JUL 20 2001, 2001. 487.
- 11 Joly-Pottuz, L., et al., *Ultralow friction and wear behaviour of Ni/Y-based single wall carbon nanotubes (SWNTs)*. *TRIBOLOGY INTERNATIONAL*;37 (11-12): 1013-1018 NOV-DEC 2004, 2004. 37.
- 12 Jolly-Pottuz, L.; Martin, J. M. Nanolubricants, *Tribology Series* 2008, 133-143
- 13 Helmetag, K., Predictive testing of steel rolling oils using the elastohydrodynamic lubrication rig. *Tribology Transactions*, 2005. 48(1): p. 119-126.

Acknowledgements

The work was carried out with a financial grant from the Research Fund for Coal and Steel of the European Union under the contract number: RFSR-CT-2008-00011.

FIB TO STEEL

Chris Xhoffer, Annick Dhont and Annick Willems

ArcelorMittal Research Industry Gent, J. Kennedylaan 3, B9060 Zelzate, Belgium

Abstract

The recent use of the Focused Ion Beam (FIB) microscopes has allowed fast developments in materials science. The interest from the steel industry for the FIB technique is not only related to the ever decreasing thickness of coatings and passivation layers. Indeed, the FIB technique is particularly adapted for the preparation of TEM lamellae of multiphase or very heterogeneous and/or porous materials.

Four years ago, a triple beam FIB instrument was installed at ArcelorMittal Gent and since then, a wide variety of materials have been screened and/or processed for further TEM analysis. FIB was successfully applied in the field of coating, substrate and interface studies e.g.:

Coating applications	Substrate analysis	Interface analyses
thickness - homogeneity	crack propagation	intermetallic phases
defectology	grain boundaries	diffusion - segregation
corrosion studies	grain orientations	epitaxial studies

The high cost of a FIB instrument and the dedicated operator skills are certainly drawbacks for its routine applications in steel research. Nevertheless, a lot of economical benefit can be gained from its unique way of sample preparation such as the shorter sample preparation time, the choice or selectivity of the sampling area, and of course, the extremely limited effect of artefacts. Very often, FIB sample preparation is the only way to produce TEM lamellae that cannot be obtained by other preparation techniques.

FIB in combination with TEM analysis opens a new world of chemical, microstructural and crystallographic information as will be highlighted in the following topics.

- (1) Eutectic phase characterization of Zn-Al-Mg coatings
- (2) Defectology studies of Cr-rich passivation layers
- (3) Structural composition of weathering steels
- (4) Microstructure of Zn-free coatings : Aluminium/Magnesium showing nano crystalline Al-Mg rich phases.

1. Introduction

The Focused ion beam (acronym is FIB) technique was originally used as a micro-fabrication method for analysis of defects in semiconductor devices, but subsequently, applications have been expanded out to a variety of research domains as e.g.: materials science, biology, medicine, pharmacy...

Nowadays, FIB is a micro analytical tool that is well suited for the preparation of very thin samples of surfaces, interfaces and cross sections especially when used in combination with TEM and SEM applications.

FIB systems operate in a similar way as a scanning electron microscope (SEM) except, rather than a beam of electrons, they use a finely focused ion beam (in most cases Ga^+) that can be operated at various beam currents.

At high beam currents, the irradiated areas of the material will be removed by sputtering, allowing precision milling of the specimen down to a sub micron scale.

At lower beam currents, FIB imaging resolution begins to rival the more familiar scanning electron microscope (SEM) in terms of imaging topography, however the FIB's two imaging modes, using electron induced secondary electrons and ion induced secondary ions, both produced by the primary ion beam, offer many advantages over SEM.

Ions are larger than electrons and have therefore a lower penetration depth. The mass of ions is much higher than that of electrons and so, for the same energy, ions have about a few hundred times higher momentum and consequently induce atom and ion sputtering (milling).

The choice to use Ga^+ ions has several reasons:

- Ga is metallic with a low melting point.
- High brightness due to the surface potential.
- Positioned in the middle of the periodic table and therefore widely applicable.
- Might be analyzed as a dopant in the milled matrix but has low interference in EDX analysis.

Some years ago, a triple beam FIB from Seiko/Jeol (SMI3050SE) was installed at OCAS. This triple beam FIB system is unique since it offers a soft finishing by Ar-etching rather than Ga-milling and thus reducing sputter damage to a minimum. An overview of a typical triple beam FIB instrument is shown in figure 1.

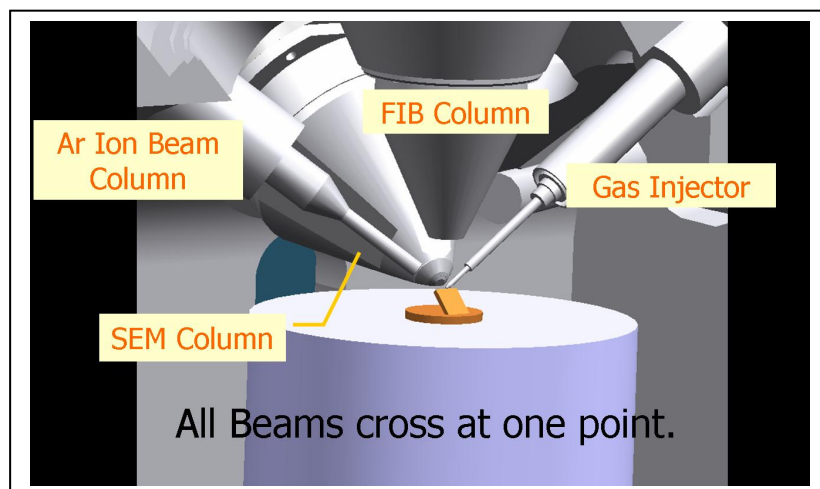


Figure 1: Layout of a triple beam FIB system

The interest from the steel industry for the FIB technique is related to the innovative characteristics of new products. Because of its strength and recyclability, steel is more and more used in combination with other materials as e.g. organics, ceramics, composites, glasses... It is just this use of soft-hard, fragile, porous and brittle combinations of materials that makes FIB an attractive tool for the current steel research programs.

The use of FIB to steel samples can be classified into 3 main domains namely coatings, substrates and interfaces, each having a diversity of specific applications:

Coating applications

- thickness determination
- homogeneity – continuity
- defectology
- adhesion/delamination
- pitting initiation
- corrosion studies
- polymer distributions

Substrate analysis

- precipitates
- grain boundaries
- grain orientations
- welding
- crack propagation

Interface analysis

- intermetallics
- diffusion
- segregation
- contamination

2. Examples of FIB applications to steel research

2.1. Coating applications

The evolution on steel coating research has evolved from sub-millimeter thick coatings towards nano layer systems as demonstrated in the figure below.

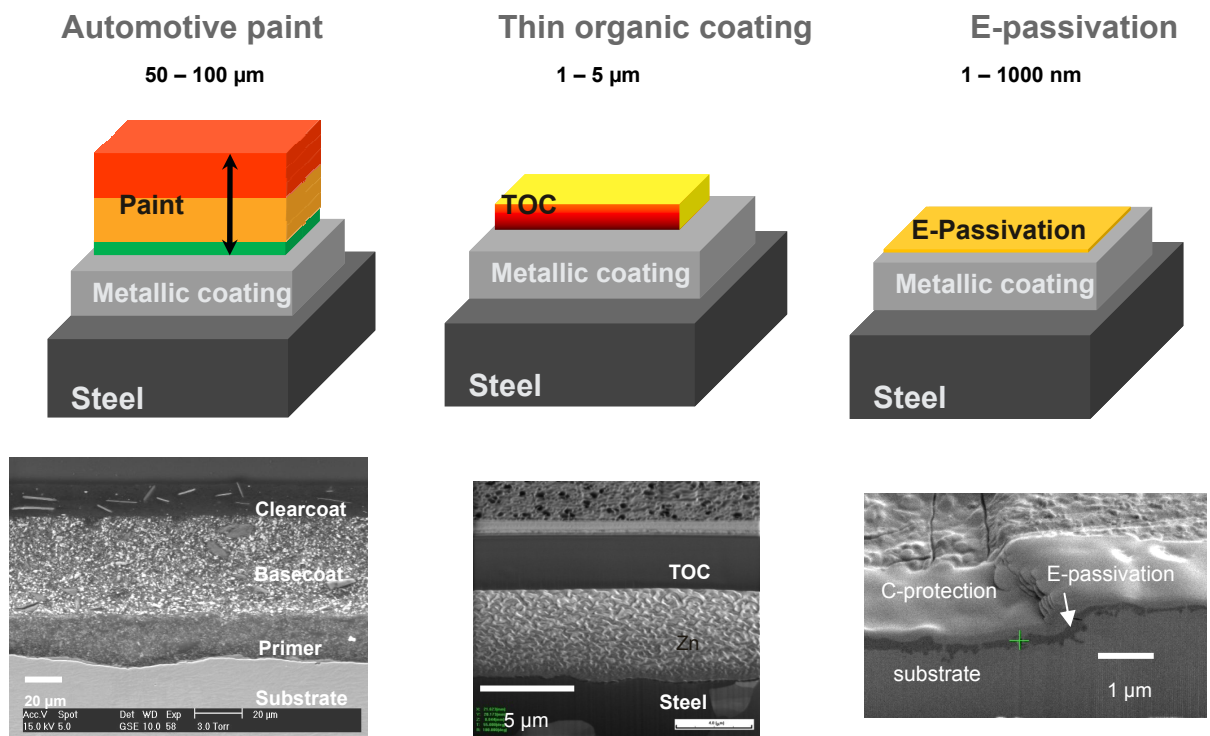


Figure 2: Various types of coating systems that differ in thickness by several orders of magnitude.

Typical passivation system (e.g. Cr(VI) free systems) used nowadays on galvanized steel have a thickness in the range of 100 to 500nm and are very critical towards homogeneity and continuity of the layer. Some failure or defect areas of such a Cr(VI)-free application is shown in figure 3.

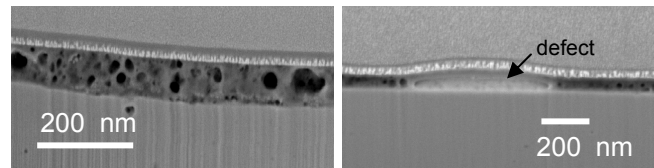


Figure 3: Cross section of a Cr(VI)-free passivation layer showing a porous structure and a small bubble (delamination) defect.

To study the interface and various intermetallic layers of Zn-Al-Mg coatings on steel, thin foils of the entire coating system can be uniquely prepared by FIB. Figure 4 shows a transversal FIB cross section through such a metallic coating. Various crystalline phases and eutectic phases can be recognized using TEM-EDX analysis.

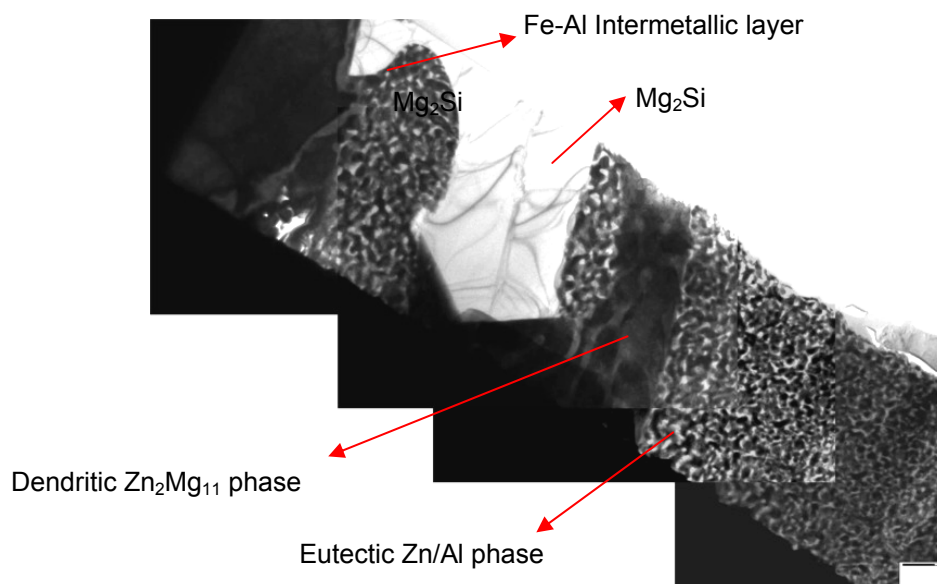


Figure 4: FIB prepared lamellae of a 40 μm thick Zn-Al-Mg coating on steel showing some typical intermetallic phases.

2.2. Substrate related applications

During reheating of alloyed steels in an austenitic annealing cycle, a selective oxidation of the surface can be seen. After horizontal milling of a few nanometers, heavier oxidized equiaxed grain boundaries are seen as whiter contours in figure 5. These surface grains are believed to belong to the recrystallized microstructure (oxidized during the heating in the ferritic region) whereas for deeper lying microstructures still correspond to the parent grain structures.

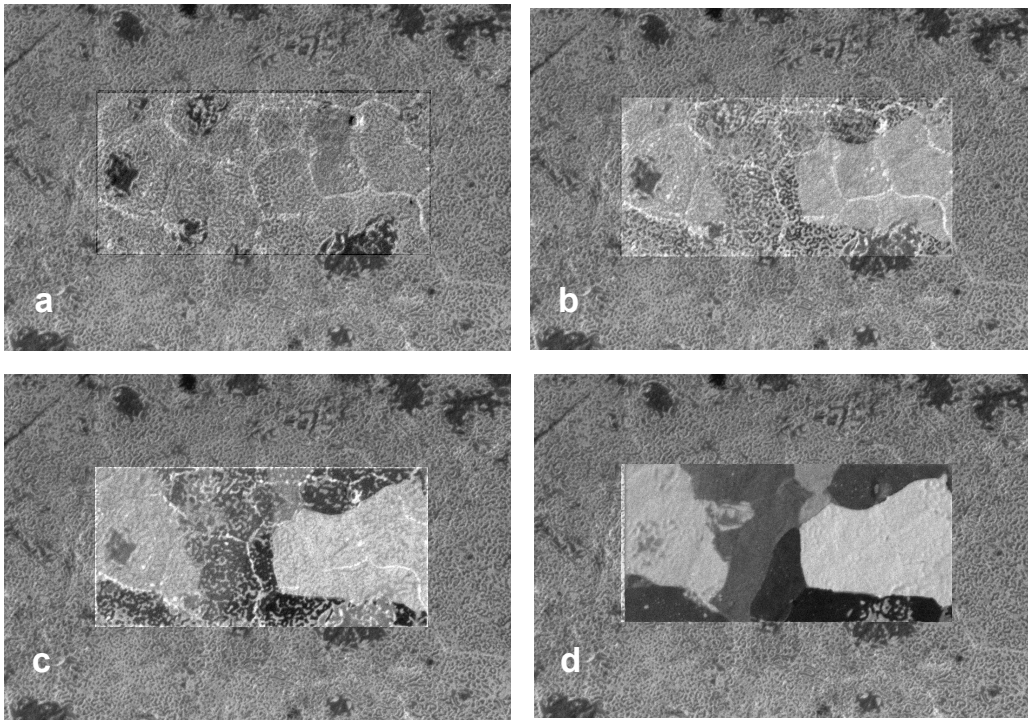


Figure 5: Horizontally milled steel sample showing heavier oxidized equiaxed grain boundaries (white lines) that do not correspond to the parent grain boundaries. Images a, b, c and d are taken at increasing depth below the surface.

Another example is showing surface defects occurring during electro-deposition of metallic coatings on steel substrates. The origin of this local surface defect is in this example related to a steel micro-flap (figure 6).

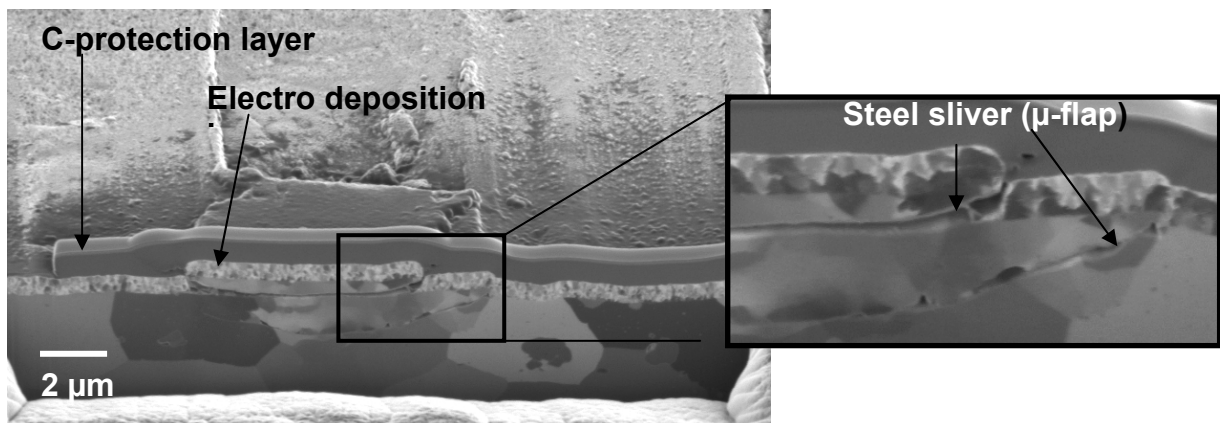


Figure 6: Cross section of a defect area showing a steel micro sliver underneath a metallic electrodeposited coating.

2.3. Interface analysis

Thin foil analysis by TEM of an interface between an enamel and a hot dip galvanized steel substrate. Coloured element maps obtained by TEM-EELS (transmission electron microscopy – electron energy loss spectroscopy) of Fe, Zn, K and Si are also shown. There exists a very sharp interface between the Fe-Zn eutectic and the Si-matrix of the enamel while for potassium, a diffusion area is observed.

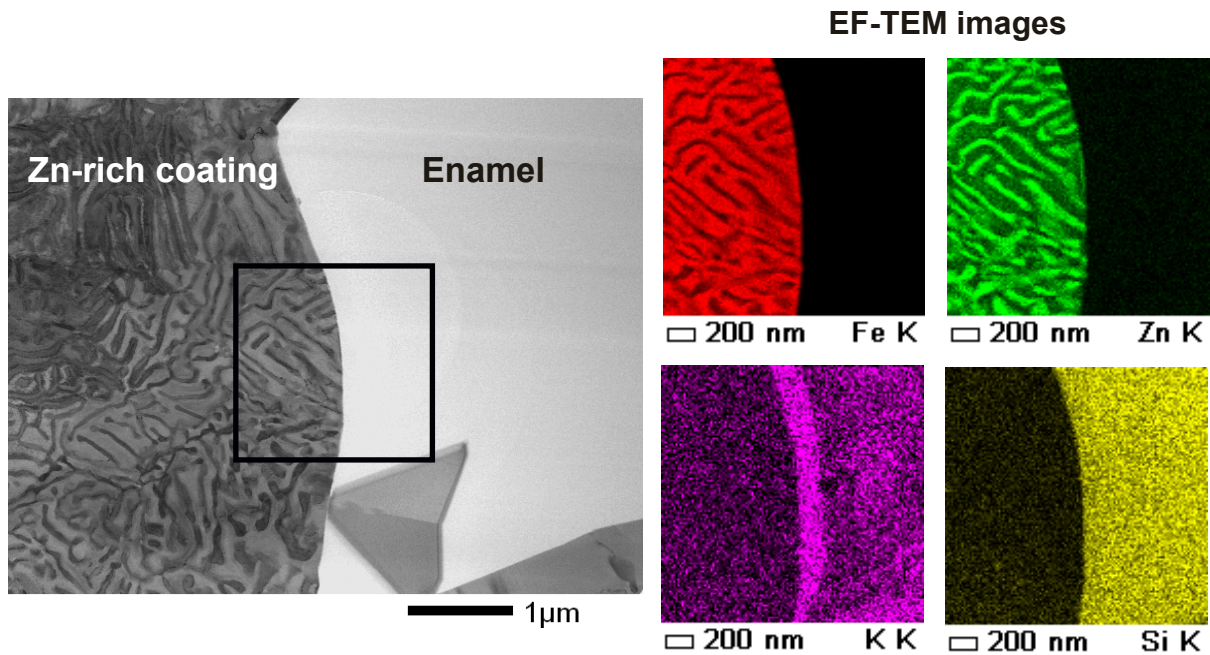


Figure 7: FIB cross section of an enamelled galvanized substrate showing a diffusion of K at the interface as determined by EELS and EF-TEM (Energy Filtered TEM)

Another example of a FIB application related to interface analysis is demonstrated in the occurrence of bare spot in hot dip galvanized steel sheets. In this particular case, the bare spot is the result of the absence of the intermetallic Fe_2Al_5 layer (inhibition layer) caused by selective surface oxidation of the substrate (figure 8).

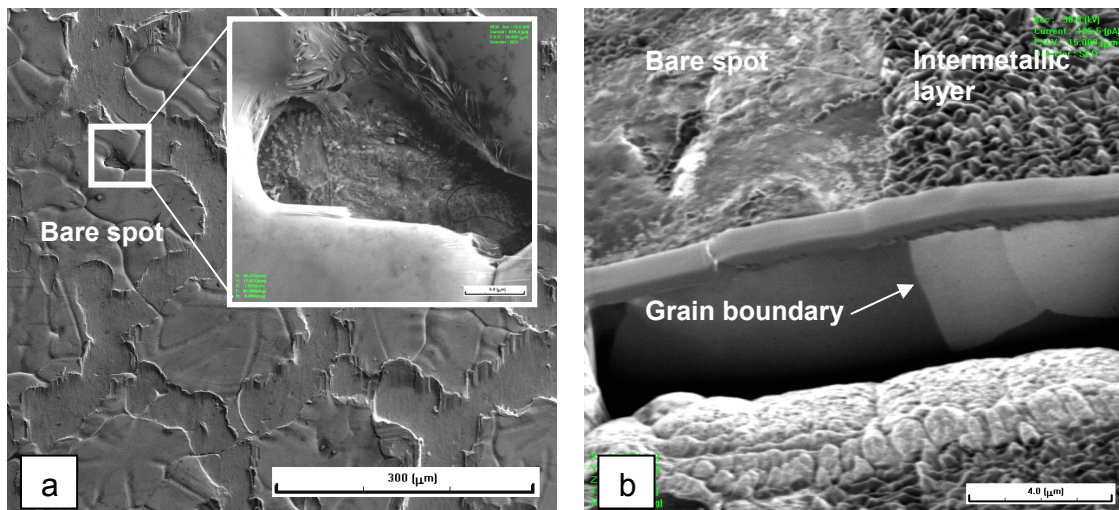


Figure 8: (a) Bare spot visible at the surface of the hot dip galvanized steel and (b) FIB cross section across the edge of a bare spot (after removal of the Zn-coating) and showing the relation with a steel grain boundary.

3. Conclusions

A Focused Ion Beam (FIB) system is a micro analytical tool that combines high resolution imaging (electron and ion images) with specific sample preparation techniques. It is therefore situated in the field of nanotechnology and has many possibilities and applications in metal industry such as:

- In situ characterization of surface defects and interface related problems.
- cross sectioning for direct observations of coating thickness, coating adherence, paint delamination, corrosion studies at interfaces, particle distributions in organic or metallic coatings etc., especially when combined with in situ EDX
- a sample preparation technique for the thinning of samples that can be directly used for (S)TEM studies.

ELEMENTAL MONITORING OF STEEL SCRAP LOADING AN ELECTRICAL ARC FURNACE

V. Sturm¹, D. Eilers¹, P. Werheit¹, R. Noll¹, U. Chiarotti², V. Volponi², V. Moroli², U. DeMiranda³, M. Zanforlin³, M. Zani³, J. Makowe⁴, F. Vestin⁵, A. Bengtson⁵

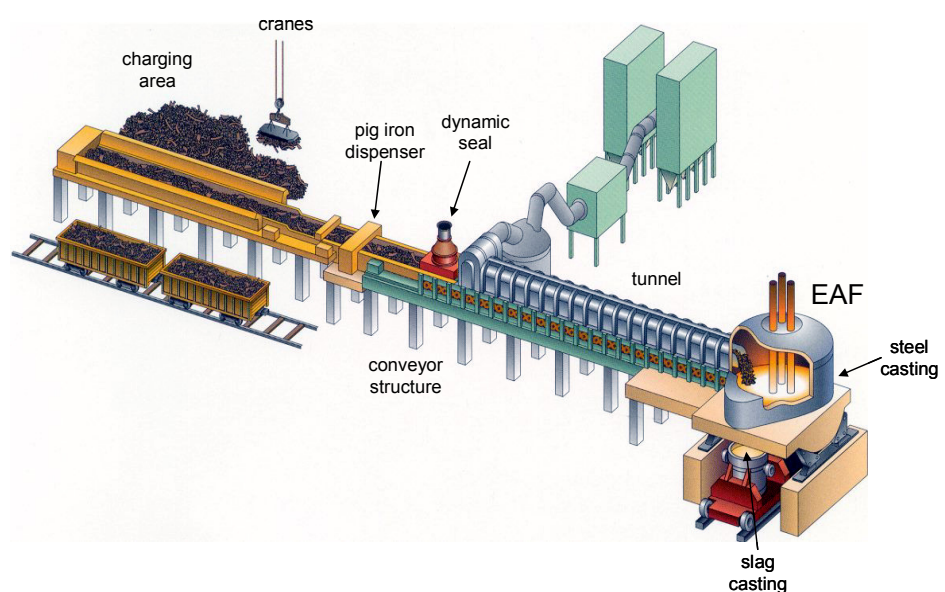
¹ Fraunhofer ILT, Aachen (DE), ² Centro Sviluppo Materiali CSM, Rome (IT), ³ O.R.I. Martin, Brescia (IT), ⁴ LSA Systems, Aachen (DE), ⁵ Swerea KIMAB AB, Stockholm (SE)

The use of laser-induced breakdown spectroscopy (LIBS) for scrap analysis has been evaluated for elemental monitoring of steel scrap loading an electrical arc furnace (EAF). A LIBS prototype was developed and installed during a field test above a pendulum conveying trough between the scrap charging area and the EAF, approx. 25 m from the EAF. The width and depth of the conveying trough filled with the scrap are approx. 2 m and 1 m, respectively. The average scrap velocity is adjusted to the EAF loading requirements within a range of 0.3 to 5.5 m/min, resulting in a scrap throughput of 100 tons per hour, typically. At the installation site, primarily, the detection of a high content of silicon in the low-alloy steel scrap is of interest for an improved control of the EAF. The on-line LIBS measurement showed the capability of detecting high silicon scrap in an industrial environment, although the developed prototype detected only a fraction of the scrap load surface due to the restricted measuring volume of 600 x 600 x 180 mm³. Increasing the measuring volume should further improve the performance in order to exploit it for charging/process control and management.

Steel scrap recycling and EAF data

The recycling of steel scrap as raw material for steel making is a contribution for a sustainable production. ORI Martin produces carbon steel for drawing applications, reinforcement bars, springs, wires, etc. The steel production is based on a mixture of 90%-95% of recycled steel and 5%-10% of pig iron. The EAF is charged continuously with scrap from a pendulum conveyor (Consteel[®] plant). A general layout of the ORI Martin plant is shown in Fig. 1. The tapping weight is about 80 tons of liquid steel and the liquid heel is 30-40 tons. After charging and melting, the conveyor is halted for about 10 minutes for steel refining. The speed of the scrap on the conveyor is in the range 0.3-5.5 m/min and depends upon the density of the scrap. Heavy scrap reduces the belt speed and with low density scrap, e.g. machining chips, the belt speed is higher. The density of the scrap is typically 600 kg/m³. The width of the belt (conveying trough) is about 2 m and the depth about 1 m.

Fig. 1 General layout of the plant. Scrap is charged on the conveyor by means of electro-magnetic cranes. The scrap moves towards the EAF through a tunnel and during the heat the EAF is continuously fed. The off gas is collected in the same tunnel in counter current with the charging scrap. At the end of the heat the furnace is stopped and tilted, leaving in the furnace an adequate liquid heel to start the next heat.



The EAF is fed by scrap mixtures subdivided in classes. Each class of scrap mixture is named from A to F and composed by a mix of “primary scrap selection” itself, chosen among 8 different selected rough scrap selection (Fig. 2). Table 1 shows several characteristics of each primary scrap selection. The first column gives a reference code, the second column correspond approximately to European Steel Scrap Specifications E2, E3, E5, E8, column three shows a rough scrap description and the other columns the percentage of the most important elements for each primary scrap selection. Generally speaking, the scrap mix is mostly composed of tubes, metal forming residuals, etc., which has typically 0.5 m in maximum size. Predominantly, there are no surface coatings at the scrap pieces.

Fig. 2 Scrap handling and selection at ORI Martin by means of an electro-magnetic crane.



Table 1 Scrap main characteristics, mass fractions are given in m.-%. (*) EU code is the closest corresponding European Steel Scrap Specifications code. Steriles are non-ferrous metals and non-metallic materials, earth, insulation, excessive iron oxide, according to this specifications [1].

Scrap reference code	EU code (*)	Scrap Description	Max. Cu	Max. Sn	Max. S	Max. P	Steriles
1	E8	Small size sheet	0.10	0.01	0.02	0.02	
2	E8	Deep drawing sheet swarf	0.10	0.01	0.02	0.02	< 0.3%
3	E8	Sheet	0.20	0.01	0.02	0.02	< 0.3%
4	E2	Mechanical workshop swarf	0.40	0.02	0.03	0.03	< 0.3%
5	E3	Cut structural and plate scrap from industrial dismantle	0.40	0.02	0.05	0.05	< 0.3%
6	E3	Cut heavy scrap	0.50	0.02	0.05	0.05	< 1%
7	E5H, E5M	Rough turnings	0.40	0.02	0.06	0.06	< 1%
8	E5H, E5M	Turnings	0.40	0.02	0.06	0.06	-

Requirements for scrap monitoring at ORI Martin

The ORI Martin EAF plant is different from a conventional EAF. The most important characteristic is the charging system with a special conveyor able to feed the furnace continuously. The EAF produces special carbon steel and a typical scrap mix is prepared to fill the conveyor depending on the steel type to be produced. The mix composition is controlled before charging by means of occasional chemical analysis of scrap samples. This methodology, generally, assure satisfactory scrap mix composition control. However, in some situations the mix composition can be very different from the programmed one. When this occurs, real time corrections are attempted although a preventive knowledge of the correct chemical scrap composition would lead to a better management both for process and steel quality.

For a conventional EAF batch furnace which is feeded by baskets with scrap, the analysis of the average composition of the scrap can be done only during the filling of the baskets. The reason is that for a filled basket only a small part of its volume is visible and thereby measurable from its surface. On the contrary, in a Consteel® plant the scrap is transferred into the furnace on a conveyor, and a large part of the scrap is at that time directly

observable and consequently measurable from the surface. Hence, this fact facilitates any surface measuring technique including LIBS for the on-line scrap chemical characterisation in a Consteel® plant.

From the point of view of optimum process behaviour, detection of undesired elements or unexpected high content of highly reactive elements, primarily Si, in the scrap is the main target. The normal process operation can be impaired by producing a reactive slag in the furnace and consequently wear of the furnace lining. Furthermore, additional energy into the furnace due to the Si oxidation may produce unbalanced energy input and changes furnace control operations. In fact Si is generally added by scrapped transformer steel that contains 3-4 m.-% Si (as well as pig iron). Furthermore, also other reactive elements like carbon and chromium may be important if precisely and quickly identified and quantified in the charge but the first need for ORI Martin plant was to detect undesired and unexpected high Si content scrap on-line within a range of 0.01-4 m.-%. The challenge is to receive a representative value for the scrap flow volume from the surface while time requirements are moderate due to the slow conveyor belt velocity within a range of 0.3 to 5.5 m/min.

Set-up for LIBS measurements

The Si content of the scrap is detected by a LIBS set-up installed in the EAF plant at ORI Martin during a two weeks measurement campaign. For LIBS, a laser pulse is directed to the scrap surface in order to ablate a small fraction of scrap material and to excite that material to light-emission for spectrochemical analysis, e.g. [2]. A small crater of about a few 100 µm remains after the laser irradiation at the scrap pieces.

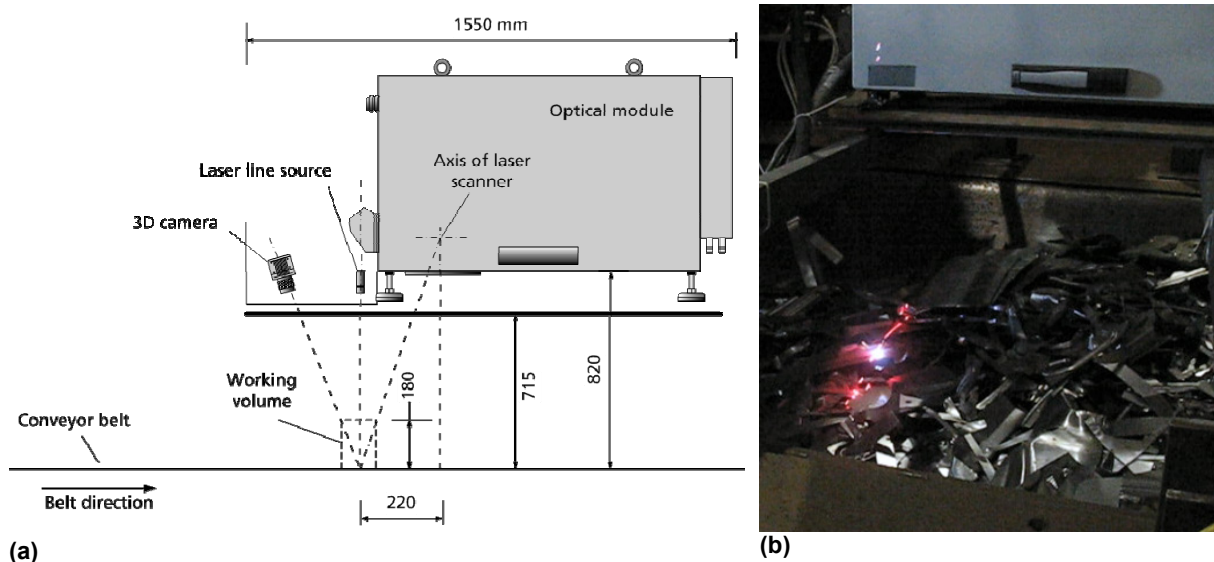


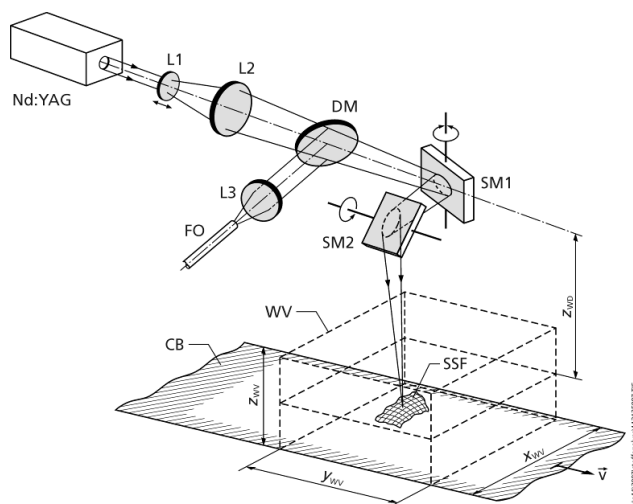
Fig. 3 Schematics (a) and photograph (b) of the optical module of the LIBS set-up mounted above the pendulum conveyor trough filled with scrap. In (b) the light-emitting laser-induced plasma at a scrap piece below the optical module can be seen together with the surface topology of the scrap flow.

The LIBS set-up consists of the optical module mounted above the pendulum conveying trough (Fig. 3), the spectrometer (Paschen-Runge type with photomultipliers PMT) and the control unit. The layout of the optical module - as shown in Fig. 4 - contains the head of the Nd:YAG laser (Q-switched, pulse duration approx. 10 ns, wavelength 1064 nm, repetition rate 15-50 Hz, depending on the multiple pulse mode used, here 15 Hz were used during the field tests), a motorised focusing telescope (L1, L2), a dichroic mirror that is transparent to the laser irradiation but reflects the plasma light (DM) and mirrors for scanning in the x- and y-directions (SM1 and SM2). The lens L3 images the emitted plasma light from the sample to be analysed (SSF) onto an optical fiber (FO, fused silica fibre, length 10 m, core diameter 600 µm) that guides the light to the spectrometer. Furthermore, safety appliances are installed and the housing shields the inside laser radiation and it protects against the dust in the EAF environment. The laser, scan head and focusing telescope are operated by the process control. The

laser beam focus can be positioned by the scanning mirrors SM1 and SM2 and the focusing unit inside a working volume of $600 \times 600 \times 180 \text{ mm}^3$ (x_{wv} , y_{wv} , z_{wv} , see Fig. 4). Due to the restricted variation in z direction, the working volume was set into the middle height of the conveying trough. In order to improve the rate of laser pulses hitting a scrap piece at the irregular surface of the scrap flow, the surface topology of the scrap is analysed by an image analysis system (3D camera and laser line source in Fig. 3) in order to find good positions for the LIBS measurement. The image analysis system gives the target values for beam positioning and focusing to the scanning mirrors and the motorised focusing unit.

Fig. 4 Schematics of the beam guiding optics of the LIBS set-up above the conveyor belt.

Nd:YAG laser head;
L1, L2, L3 lenses;
DM dichroic mirror;
FO fibre optic cable;
SM1, SM2 scanning mirrors; CB conveyor belt; v velocity; SSF scrap sample surface; Z_{wD} working distance; WV working volume; x_{wD} , y_{wD} , z_{wD} working volume coordinates



The spectrometer is equipped with 40 spectral lines for different elements. Due to the sensitivity and time characteristics of PMT's and a multichannel electronics the LIBS signals can be integrated in an exactly determined integration time that gives the possibility to use the ratio method (dividing each elemental signal with a reference signal) for every single laser pulse. For Si, the spectral line at a wavelength of 390.55 nm is used with the reference line of Fe at 371.99 nm or the zeroth order of the spectrometer (= reflected beam of the spectrometer grating). The LIBS set-up has been calibrated with a set of certified reference samples.

Results of the onsite measurements

During the two-weeks onsite measurements, different scrap fractions were charged onto the conveyor during different heats. The LIBS measurements were carried out after the pig iron dispenser (see Fig. 1) about 25 m before the conveyor belt trough ends at the EAF furnace. A heat requires about 45 to 60 min. The following fractions were charged during the LIBS measurements:

- Normal fraction "C": Scrap which is similar to the European steel scrap code E2, E3 and E5, i.e. it is mainly composed by mechanical workshop scrap, cut structural and plate scrap from industrial dismantle, cut heavy scrap, rough turnings and turnings with a maximum content of Si of 0.5 m.-%.
- Low Si fraction "A": Low Si content scrap similar to European steel scrap code E8 and it consists mostly of small size sheet and deep drawing sheet.

These basic scrap fractions are measured in their original compositions in heats 1451, 1454, 1464, 1466 and 1467, see Table 2. During charging of the EAF for heat 1452, 1453 and 1465, high Si scrap ($> 3.5 \text{ m.-%}$) was added in defined time intervals according to the schedule listed in Table 2.

Figs. 5(a) and (b) gives the corresponding measured Si mass fractions for these two measuring days. The horizontal levels of the solid line show the measured average Si mass fractions of the charged scrap. In addition, some values for defined time points are averaged over 2 minutes for comparison with reference values obtained through slag and steel analysis. These data are marked by the symbols in Fig. 5.

Table 2 Time intervals of the heats and basic scrap fractions used during the measurements in May 2009. The last column gives the time intervals of the high Si scrap addition.

Day	Time	Heat number	Basic scrap fraction	Additional high Si scrap charging
26	20.15-21.08	1451	C	none
26	21.20-22.10	1452	C	21.23-21.25; 21.26-21.27; 21.27-21.29; 21.40-21.46
26	22.10-22.58	1453	C	22.20-22.25
26	22.58-23.45	1454	A	none
27	20.04-21.14	1464	C	none
27	21.14-22.05	1465	C	21.18-21.20, 21.25-21.26, 21.32-21.42
27	22.05-22.54	1466	C	none
27	22.54-23.40	1467	A	none

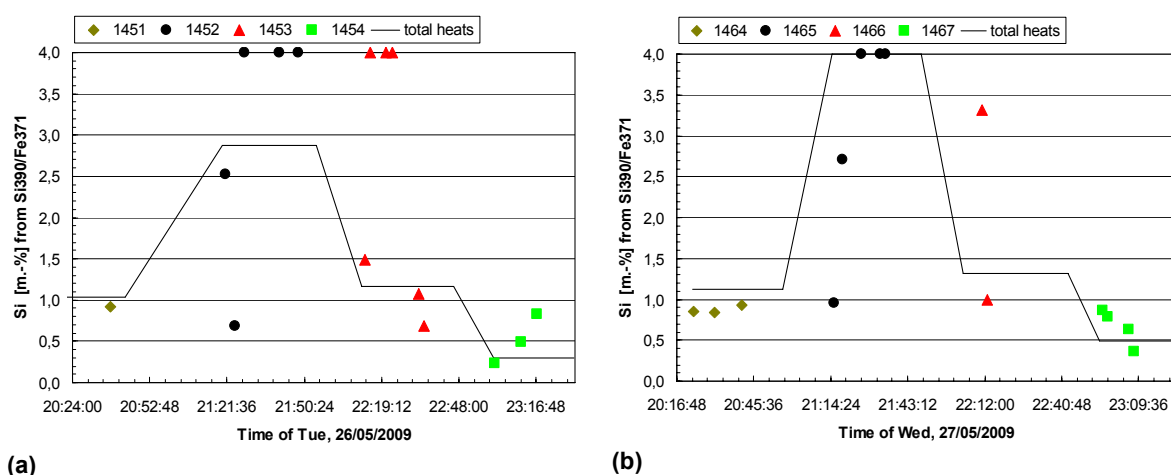


Fig. 5 Si mass fraction vs. time during the onsite LIBS measurements for the two days listed in Table 2. The horizontal levels of the solid curve give the total average of the charged scrap fraction of a heat while the symbols represent selected mean values for intervals of 2 minutes according to special process time points. Therefore the total average values are not the mean of the values marked by symbols.

The average values in Fig. 5 correspond very well with the expected values from Table 2:

- the highest Si value is monitored for the heats 1452 and 1465 with a “C” fraction and largest addition of high Si scrap
- the lowest Si content is detected for the low Si fraction “A” of the heats 1454 and 1467
- the added high Si scrap during heat 1453 is detected while the average value is risen only slightly due to the small average amount of added scrap

A comparison between the slag and steel analysis at the end of the heat and the LIBS results during those 2 minutes average values are shown in Fig. 6. Only one slag and steel analysis was performed for each heat and therefore the same value is plotted for all points during the heat. However, in these graphs the total Si calculated from slag analysis is assumed to have a fixed value of 3.5 m.-% in periods when additional high Si scrap was added to the charging scrap bed. The Si detection by LIBS using the two-minutes sets of data is roughly in agreement with the estimated value calculated from final slag composition at the end of the heats and the foreseen Si percentage during high Si scrap addition periods, except for slight temporal disagreement due to time shifts in data logging.

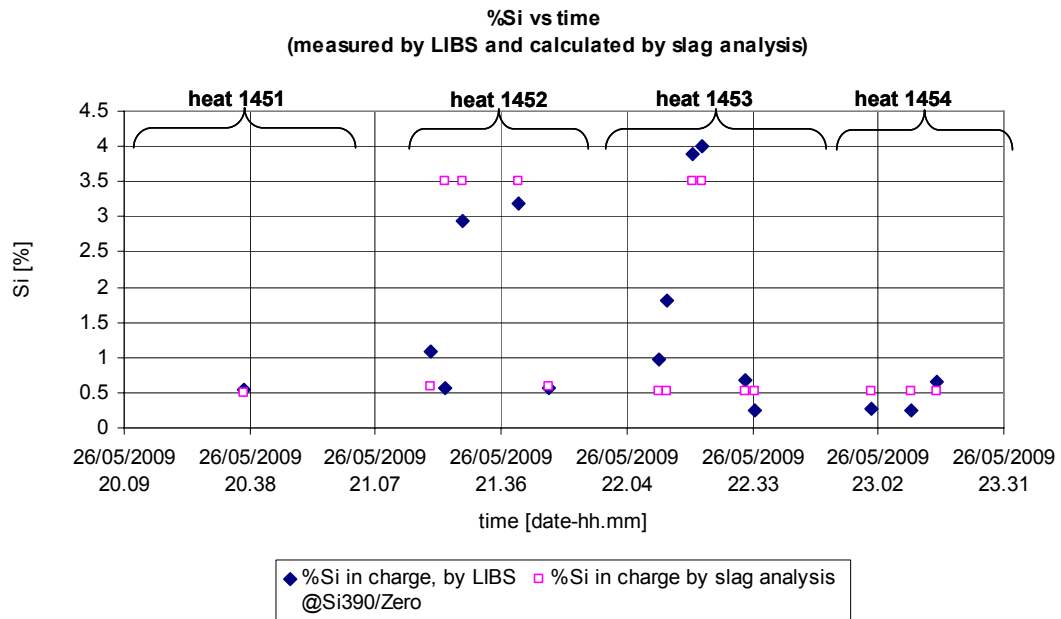


Fig. 6 Measurement of Si (in m.-%) vs. time by LIBS in comparison with Si calculated from slag analysis for the 26/05/2009 during the measuring campaign. A fixed value of 3.5 m.-% is assumed in the periods when additional high Si scrap was added to the charging scrap bed. Only one slag analysis was performed during each heat and therefore the same value is plotted multiple times during one heat.

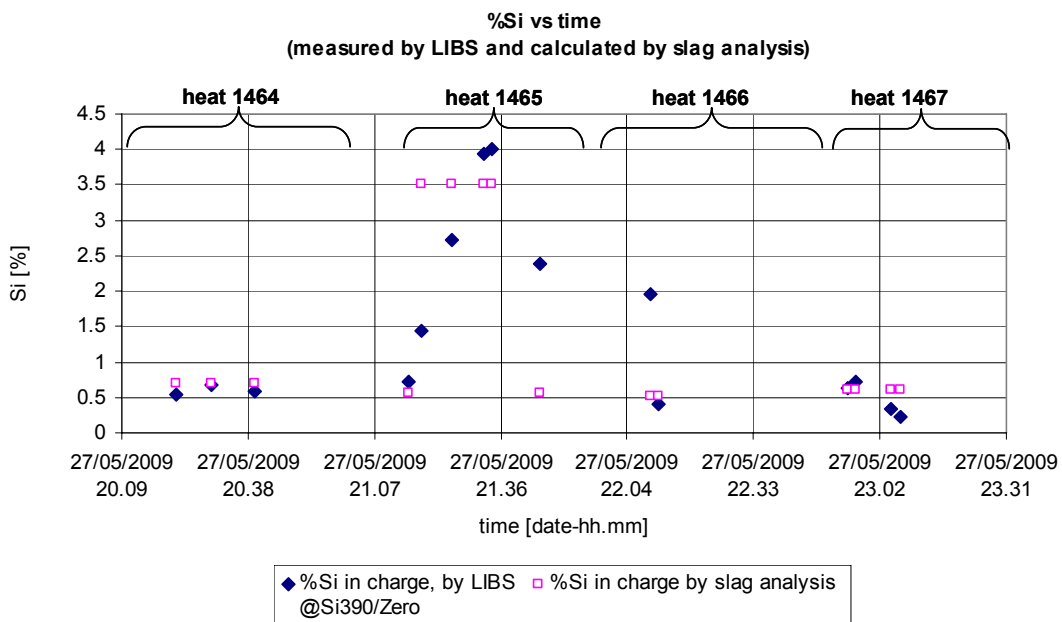


Fig. 7 Same as previous Fig. 6 for the measurements on 27/05/2009.

Conclusions

The LIBS device is able to detect onsite high Si scrap in the harsh environment of an industrial EAF conveyor. After installation, the LIBS demonstrator was in stable operation during the two-weeks campaign. The accuracy of the device is sufficient to discriminate well between standard and high Si scrap charges. Temporarily occurring high Si additions were detected during the onsite measurements. The technique can be introduced without too much adaption in an existing infrastructure.

Nevertheless, improvements should be achievable by increasing the number of sampled points which can be done in general by increasing the working volume and the laser repetition rate. A better imaging of the surface topology could also lead to a higher measuring rate by reducing the number of laser pulses with incorrect laser positioning and focusing. Another improvement for increased accuracy would be to alter the handling of the scrap on the conveyor belt, allowing in this way a larger portion of the scrap to be sampled with the LIBS device. Stacking and piling of scrap affects the measurements which was recognized when scrap with high Si content was added on top of the bulk scrap material, resulting in a LIBS value too high compared to the mean of the bulk scrap.

Outlook

Considering the practical view of future LIBS prototype developments, the optical and spectrometer modules can be built smaller in order to access further industrial applications. The working volume of the optical module should be enlarged to recognize more scrap. The practical use of the on-line scrap analysis by LIBS on a EAF conveyor is both as warning for incoming undesired high Si scrap as well as improving EAF charging and process control strategies.

Acknowledgements

Work carried out with a financial grant from the European Coal and Steel Community.

References

- 1 L. Muchova, P. Eder, End-of-waste criteria for iron and steel scrap: Technical Proposals, JRC Scientific and technical reports, EUR 24397 EN – 2010, Luxembourg: Publications office of the European Union, 2010
- 2 A.W. Miziolek, V. Palleschi, I. Schechter (Eds.), Laser-induced breakdown spectroscopy (LIBS), Cambridge University Press, Cambridge, 2006.

LIBS – A PROMISING TOOL FOR FAST STEEL CHARACTERISATION

Fabienne Boué-Bigne^a

^aTata Steel Europe - Research, Development and Technology, Swinden Technology Centre, Moorgate Road, Rotherham, S60 3AR, South Yorkshire, UK

Corresponding author:

E-Mail: fabienne.boue-bigne@tatasteel.com

Tel: +44 (0)1709 825 225

Abstract

Fast LIBS mapping is a major breakthrough in steel characterisation. The development of LIBS applications is providing the user with quantitative characterisations of its steel products in comparison to some of the qualitative characterisation tests used conventionally. The current characterisation tests require skilled personnel to make interpretations of metallographic features such as segregation, or decarburisation, which are open to subjective interpretation. Other drawbacks of some conventional techniques for cleanness assessment are their time-consumption (for scanning electron microscopy – energy dispersive analysis) or their lack of chemical information (as in optical microscopy – image analysis).

The potential for LIBS is to provide a fast and quantitative assessment for segregation and cleanness, and so prevent potential unnecessary downgrade, or release of potentially defective material. It can also provide accurate product quality tracking and trending, to highlight deterioration of the steel quality.

1. Introduction

Increasingly, steel is becoming a commodity material. Consequently, production is being switched to low cost economies, which are generally outside Europe. In order to retain jobs within the European steel sector, products with higher added value must be produced with consistently high quality standards.

The characterisation of finished steel products, for internal quality monitoring or for customer specifications compliance, involves a range of diverse techniques. Some of these techniques involve etching agents to reveal aspects of the crystal structure that allow determination of the extent of defects such as segregation and decarburisation. Such techniques suffer from subjectivity, as the rating of severity is ultimately down to the analyst's judgement. They rely heavily on the availability of skilled staff with many years of experience and judgement to ensure reproducibility and consistency of assessment. Other techniques used for the characterisation of steel cleanness are optical microscopy and scanning electron microscopy, with the former not providing full chemical identification of the inclusions detected, and the latter being limited to the characterisation of small sample areas. From the point of view of logistics and speed of information acquisition, all these techniques contribute to our understanding of product integrity, but none answer all the questions simultaneously, nor very rapidly.

Laser Induced Breakdown Spectroscopy (LIBS) can be applied to both metallic and inclusion species¹⁻⁶, and has the potential for mapping their distribution with good spatial resolution. The high speed of data acquisition, coupled with the simultaneous availability of data for a large range of elements, gives the potential for acquiring information on segregation, decarburisation and cleanness simultaneously. The availability of a quantitative approach to assess the properties of steel would ensure the characterisations are valid and supported by quantitative data instead of subjective personal judgement.

In this paper, the development and applications of fast scanning LIBS analysis for the characterisation of segregation and cleanness is described. At this stage, the different applications are considered separately. The development of appropriate software that can handle the large amount of data generated will also be discussed.

2. Experimental

2.1 Instruments

For all the analysis described, a LIBS instrument offering high spectral resolution is required in order to resolve the lines of interest from the multitude of interfering Fe lines. High spatial resolution from the motorised stages is also necessary to generate elemental maps at the micro-scale. The instrument used was manufactured by the Fraunhofer Institute of Laser Technology. It is designed to generate very fast scans with a laser pulsing at 1 kHz, with associated fast electronics on the detection system. Full description of the instrument is available elsewhere⁶. The instrument was operated in an Ar atmosphere.

The Electron Probe Micro Analyser (EPMA) used for qualitative mapping and quantification of segregation was a CAMECA SX50. The data were measured with a defocused electron beam at 20 μ m diameter. A set of seven Carbon standards were used for the quantification of the element at 44.7 Å.

A FEI Quanta 600 Scanning Electron Microscope (SEM) coupled to an EDAX Energy Dispersive Analyser (EDA) was used for the characterisation of the inclusion populations. Inclusions were considered down to 0.8 μ m diameter, at a magnification of 1000.

2.2 Samples and standards

The samples used in this study were from high carbon steel products. Rod samples were used to illustrate the segregation and cleanliness measurements. The response of the instrument being known as linear in the concentration range considered, a set of four Certified Reference Materials (CRM) were used to calibrate the emission signals for the segregation analysis: CRM 059-2, 401-2, 402-2 and 434-1. Calibration curves were measured every five samples, to follow and correct the potential drift of the instrument's sensitivity.

All standards and samples were polished to a finish of 1 μ m for all applications, as the same sample surface was previously analyzed by either chemical etching method, or Electron Probe Microscopy (EPMA), or Scanning Electron Microscopy, according to the aspect of characterisation investigated, for validation data.

2.3 Measurement conditions

All scanning was performed with single-shot measurements on the standards and on the samples, with a laser energy of 1.7 mJ, in an Ar environment. Standards and samples were placed in a sample holder so that their position coincided with the focus point of the laser beam, yielding the smallest possible ablation craters. The diameters of the resulting craters were approximately 13 μ m. Depending on the step size chosen, the consecutive ablation craters were adjacent or spaced. The step size was selected as a compromise between three parameters: the amount of spatial resolution required (related to how fine the features monitored were), the size of the total area measured (enabling generation of more representative data if the features were heterogeneously distributed), and the duration of the overall measurement. The emissions of the elements were measured at the wavelengths listed in Table 1, and without background correction.

Table 1: List of emission wavelengths used during LIBS measurements.

Element	C	Mg	Al	Si	Ti	Mn	Fe
Wavelength (nm)	193.09	285.21	396.15	212.41	337.28	293.31	187.75

3. Results and Discussion

3.1. Segregation characterisation

A conventional segregation assessment method consists of an optical etch, where the sample is dipped in an etching solution for a few seconds, and the revealed crystal structure is observed visually to judge of the severity of the segregation. Various factors can influence the outcome of the etching technique, such as the source and angle of the lighting, and the use of binocular or direct viewing when assessing the mark on the etch sample. The subjectivity of the assessment is also an additional and not the least of the factors that will make it possible that a given segregation in a given sample will be perceived differently by different operators. It has become clear in recent years that this method suffers from inconsistency and subjectivity that may lead to misleading segregation results. Although such approach is still the accepted method for segregation evaluation in small samples, the use of Electro-Probe Microscope Analysis (EPMA) to obtain quantitative concentration data to characterise the casts is becoming more popular. However, only a limited number of samples and sample areas can be measured by EPMA, due to the time-consuming nature of the analysis.

To obtain segregation information from LIBS measurement, elemental maps were generated on cross-section rod samples, with a step size of 15 μm . A 4 x 4 mm² sample area was measured in six minutes. An automated procedure is then used to generate calibration curves, calculate the concentration maps from the intensity maps for all elements of interest, identify the pixels with concentration at a certain level above bulk concentration and extract the pixels that are in the segregated area with systematic cut-off threshold levels. This way, a quantitative characterisation of the segregation is obtained on each sample measured, with respect to concentration and size.

In order to validate the LIBS segregation results, a number of EPMA measurements were also performed on a selection of samples displaying a wide range of segregation. In a first stage, the qualitative distribution of the segregation on three rod samples displaying a range of segregation severity was compared when measured by EPMA and by LIBS. A 3 x 3 mm² map was measured by EPMA on each of the three samples.

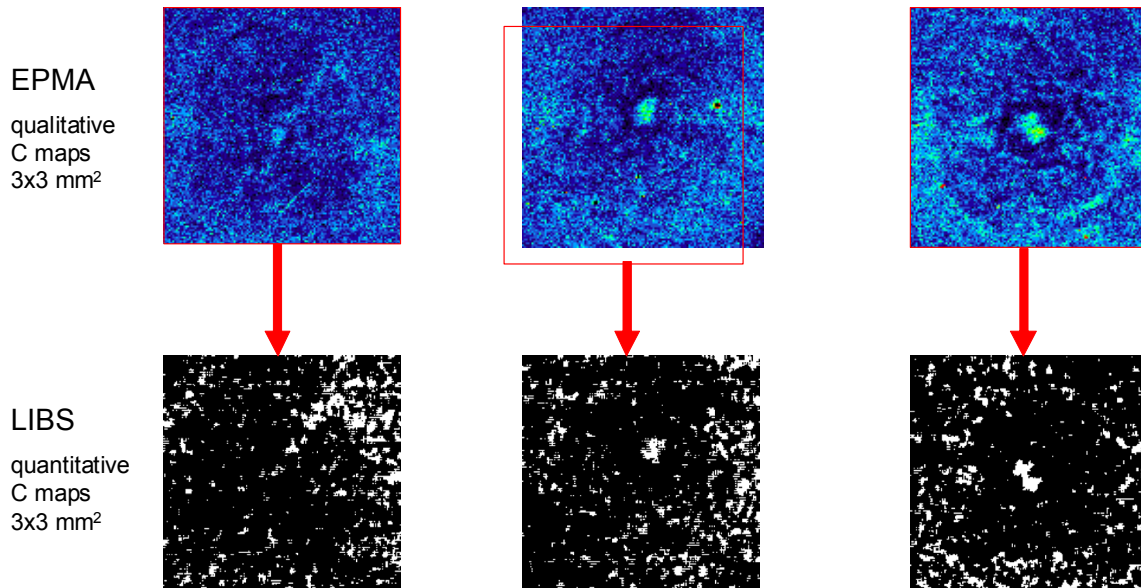


Fig.1: EPMA and LIBS Carbon maps comparison, displaying various degrees of segregation.

The three examples show that EPMA and LIBS detected the different degrees of segregation very similarly from a qualitative point of view (Fig.1). Not only the obvious central segregation in the two samples displaying segregation, but also the finer features of Carbon concentration distributions in the mid-radial zone of the most homogenous sample.

In order to conduct a quantitative comparison, up to seven lines were scanned across the rod cross-section, at the vicinity of the central segregation by EPMA. The maximum concentration value was extracted for each sample and the associated C_{\max}/C_0 calculated, with C_{\max} being the maximum concentration measured on each sample and C_0 the measured bulk concentration. The same samples surfaces were subsequently measured by LIBS and the quantitative results from both techniques were compared (Fig.2).

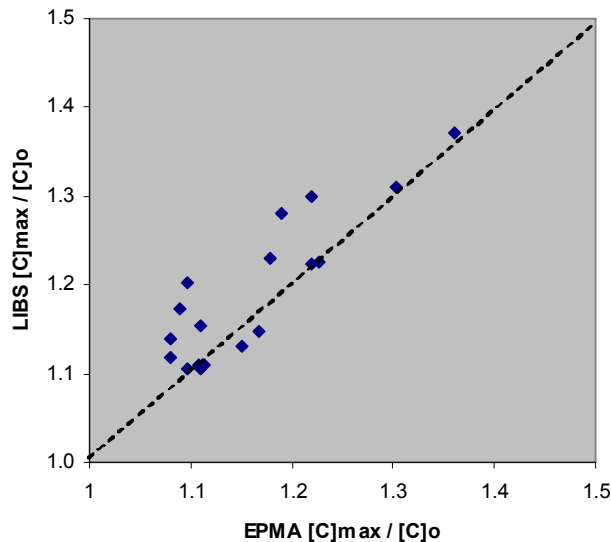


Fig.2: EPMA – vs – LIBS maximum carbon concentration ratios extracted from central segregation.

The dotted line across the graph indicates the point locations for the results from both analytical techniques agreeing. The techniques correlated very well in over 50% of the cases, and higher concentration ratios were obtained by LIBS compared to EPMA for the rest of the dataset.

The discrepancy observed could be possibly due to two intrinsic differences in the measurement of the maximum concentration value from a sample surface by EPMA and LIBS: the difference in measurement coverage of the sample cross section and the difference in signal emission depth. Sixteen times more data points are acquired by LIBS, providing a complete concentration map, against a limited number of scan-lines at selected positions for EPMA. This implies that there is a possibility that the maximum concentration point might be missed during EPMA quantitative measurement. Additionally, the spectral signals emitted by both techniques come from very different depths in both techniques, with EPMA being a very surface-sensitive technique with a signal emitted from less than 0.5 μm below the surface, whereas the LIBS signal is generated from the ablation of 4 to 5- μm deep craters. Variation in segregation along the central line, which can be drastic, might influence the outcome of its measurement by both techniques.

The quantitative characterisation of segregation of over 1000 samples by LIBS analysis has enabled determination of threshold values of relevant parameters above which the segregation is found to have a negative impact on future performance. The consistent comparison carried out between the optical etch method and LIBS results has also highlighted cases where conventional assessment can lead to misleading conclusions.

3.2. Cleanness characterisation

Studies have been carried out by various research groups to characterise inclusion populations from LIBS measurements, from both qualitative and from a quantitative aspects, from relatively simple inclusion types³ to more complex ones⁶. Attempts to quantify the chemical make-up of inclusions commonly found in any type of steel grade comes up against the hurdle of the lack of standards readily available for inclusions elemental

calibration. A novel approach was investigated in this current work, where artificial neural networks (ANN) were used for the recognition of inclusions chemistry from the LIBS raw data. Benefits from the ANN use are to counter-act the non-linear response of the LIBS intensities for the different elements as a function of the instrument spectral response, the inclusions types and the inclusions sizes.

In order to train the ANN system, a representative population of the inclusions of interest needed to be characterised. This being done, the trained system can be used for the recognition of inclusions for a period of time, as long as the LIBS instrument sensitivity is relatively stable, with the trained ANN system still allowing for a degree of variation in the sensitivity.

The training, testing, validation and application of the ANN system was carried out on rod samples with an inclusion population of an average size of 1.5 μm and maximum size of 4 μm -diameter. The steel grade studied being Si-killed, the majority of inclusions were high-silica, manganese silicate and Pseudo-Wollastonite. The samples were characterised by SEM-EDA, prior to LIBS measurement, to provide a training set for the ANN, as well as for validation purposes.

An in-house built automated procedure was used to extract the inclusion data sets from both SEM-EDA and LIBS, using the basic extraction rule of mean + n x standard deviation. This provided a training and validation data set with EDA elemental concentrations and the corresponding LIBS intensities for a variety of inclusions chemistries and sizes. A Back Propagation method was used to train the neural network system that could be subsequently used to predict the chemistry of the inclusion populations of unknown samples. Its application to a set of LIBS data from a sample of the same grade provided a very satisfactory recognition of the chemical compositions of the various inclusions, as displayed in the ternary diagram in Fig.3. The same ANN system was then applied to two sets of LIBS inclusion data measured at different points in time without re-training the system: one data set measured 25 days before the measurement used for the ANN system training, and one data set 23 days later. Again, the prediction of the chemical make-up of the inclusion populations was satisfactory from the two sets of LIBS data measured a month and a half apart. This illustrates the overall stability of the LIBS/ANN system, where variation in instrument sensitivity was found to be between 4 and 6% depending on elements, over the period of time that separates the two LIBS measurements furthest apart.

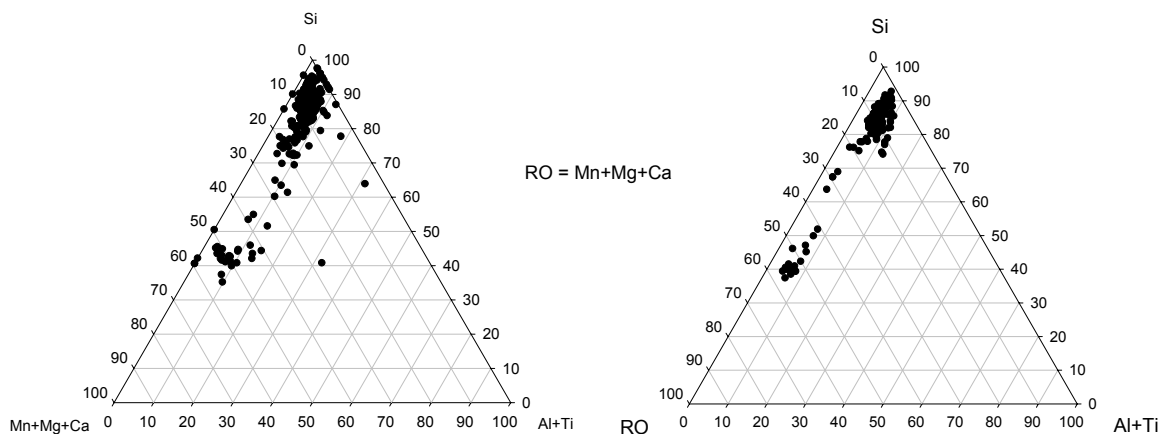


Fig.3: Ternary diagram displaying the chemical composition of inclusion population in one steel grade as measured by SEM-EDA (left) and by LIBS combined with ANN prediction (right).

A recurrent problem in the examples of chemical prediction given above was the lack of identification of the few Al-rich inclusions present, as seen on the SEM-EDA ternary diagram with approximately 40% Al. Given the very low occurrence of such inclusions in Si-rich grades, very few of them were included in the SEM/LIBS data sets used for the training, testing and validation of the ANN, and as a consequence, making the ANN system unable to identify them. This re-highlights the importance and the potential down-fall of using ANNs, where it is vital to

thoroughly train the neural network for all the chemical regions which inclusions are likely to be present, without which, the ANN will only perform a partial identification of the inclusions types measured by LIBS.

4. Development of software for data extraction and results presentation

The fast measurements performed during LIBS analyses, on square centimetre areas, with a micro-scale spatial resolution, generate very large data files that require automated procedures to handle the raw data efficiently on a routine basis. Software was developed with automated routines that enabled carrying out, in a user-friendly manner, a variety of functions such as the concentration quantification using data files from the measured standards, area cropping, extraction of line profile, statistical and arithmetic functions to extract elemental features of interest, etc. In particular, an automated routine was written for segregation data where the quantification (Fig.4) and the extraction of segregation features (Fig.5) were integrated under the same command.

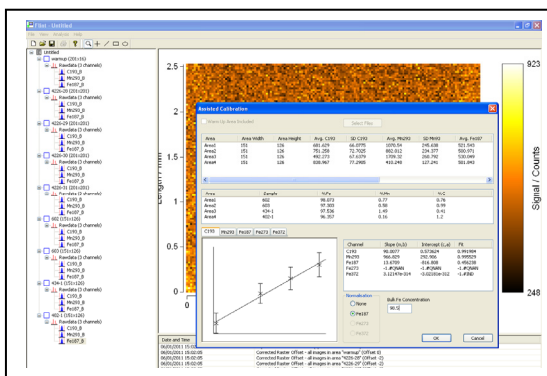


Fig.4: Automated quantification of the elemental maps generated from LIBS measurement.

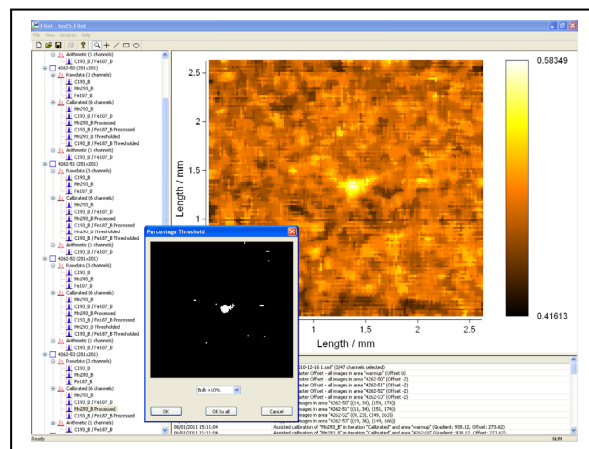
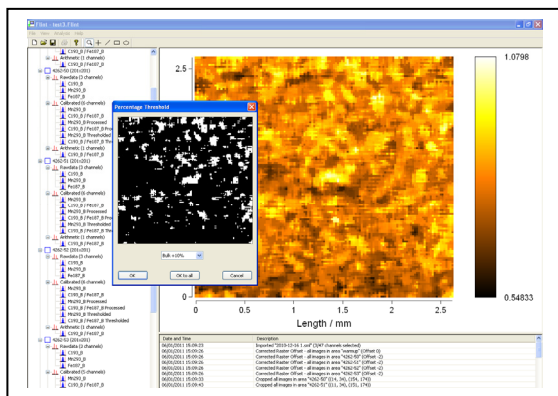


Fig.5: Automated extraction of segregation features on Carbon (left) and Manganese (right).

Similarly, functions dedicated to cleanliness data extraction were gathered under a same function where pixels related to inclusions could be extracted. For the purpose of generating SEM-EDA/LIBS inclusion data sets for the training, testing and validation of the ANN, a function enables the comparison of the inclusion maps to identify coinciding inclusions detected by both techniques and so generate data files that can be used directly by the ANN.

5. Conclusions

Although the optical etch method is widely used to characterise segregation in rods, it lacks sensitivity and appears unsuited to today's requirements, as the steel quality is higher these days. The availability of quantitative concentration data to characterise the segregation in steel products has proved to be an advantage over the sole qualitative data from optical etch. The quantitative characterisation of segregation in rod samples by LIBS has been developed and the LIBS concentration results were found to compare well with EPMA results. The comparison of optical etch and LIBS results over a large number of samples have identified cases where the visual assessment has led to the wrong conclusions.

For the determination of cleanness, the combination of LIBS measurement with Artificial Neural Network proved worth considering. The difficulty to calibrate, or train the ANN in this case, is still a noticeable hurdle. However, depending on the stability of the LIBS instrument, it was found that a trained ANN system can be used over a relatively long period of time.

LIBS is still a technique not yet well-established in industry, with its developments needing to be translated into industrial applications. However, this technique has to date found relatively little industrial interest; mainly, and contradictorily, due to its huge versatility, and as a consequence, the lack of instruments fully developed and commercially available for specific tasks. This means that the acquisition of such an instrument requires a certain degree of in-house development to get useful information out.

We have used the ability that LIBS can offer to perform fast multi-elemental mapping of steel samples to obtain quantitative characterisation of segregation and cleanness in steel. The information on the two parameters can be obtained from one single LIBS measurement, as they are obtained under exactly the same conditions.

6. Acknowledgements

I would like to thank Martyn Whitwood for providing EPMA data and colleagues from the Tata Steel Long Products Division for supporting this work.

7. References

1. M. Aimoto, H. Kondo, H. Yamamura, T. Toh, Tetsu to Hagane Journal of the Iron and Steel Institute of Japan, **2007**, 93 (7), p.483-488.
2. F. Boué-Bigne, Spectrochimica Acta Part B: Atom. Spectrosc., **2008**, 63 (10), p.1122-1129.
3. M. Kuss, H. Mittelstädt, G. Müller, and C. Nazikkol, Anal. Lett. **2003**, 36, 3, p. 659-665.
4. Bette, R. Noll, G. Müller, H. W. Jansen, C. Nazikkol, and H. Mittelstädt, J. Laser Appl., **2005**, 17 (3), p.183-190.
5. Müller, F. Stahnke, D. Bleiner, Talanta, **2006**, 70, p. 991-995.
6. F. Boué-Bigne, Appl. Spectrosc., **2007**, 61 (3), p.333-337.

MATRIX SEPARATION WITH NONIONIC SURFACTANTS AND IONIC LIQUIDS FOR THE DETERMINATION OF TRACE ELEMENTS IN HIGH-PURITY IRON METAL

Masataka Hiraide and Hiroaki Matsumiya

Graduate School of Engineering, Nagoya University, Nagoya 464-8603, Japan

ABSTRACT

Novel matrix separation techniques were developed for the reliable determination of trace impurities in high-purity iron metal. In the emulsion method, nonionic surfactant (Span-80) molecules were oriented to the aqueous and oil interface to form water in oil type emulsion droplets. They allowed the separation of trace metal ions from the iron matrix (preliminarily converted to colloidal hydroxide particles). In the admicellar method, polyoxyethylene-type nonionic surfactant (PONPE-20) molecules were anchored to the styrene-divinylbenzene copolymer XAD-4 resin by hydrophobic interactions. The resulting admicelles trapped the iron matrix effectively from 8 M hydrochloric acid solutions. The same surfactant was also used for the salting-out method, where the iron-rich surfactant phase was segregated by the addition of lithium chloride. Trace elements were determined by inductively-coupled plasma mass spectrometry and graphite-furnace atomic absorption spectrometry. The detectability approached the ng/g level in high-purity iron samples. For the determination of P, As and Si, these elements were adsorbed on the admicellar column as heteropoly molybdic acids from 0.03 M hydrochloric acid solutions. They were desorbed and analyzed by high-performance liquid chromatography. Because P and As were not separated chromatographically each other, molybdoarsenic acid was preliminarily decomposed with citric acid. Serious contamination for Si was successfully overcome by using ionic liquids instead of admicelles.

INTRODUCTION

The analysis of high-purity iron is essential for the study of synergistic effect of impurities, the assessment of the purification process and the quality control of products. Although modern analytical instruments are highly sensitive and selective, the direct determination is often difficult or impossible because of serious interferences due to the large amount of iron matrix. Therefore, chemical treatments of the sample are indispensable prior to the determination to obtain the sufficient precision and accuracy of the analytical results [1-3]. Among separation techniques reported to date, the most typical and famous procedure is liquid-liquid extraction, where the iron matrix is extracted into the organic phase (*e.g.*, diethyl ether or diisopropyl ether), leaving many trace elements in the aqueous solution [4]. Problems of this method include the use of volatile, flammable, and ill-smelling organic solvents as well as a narrow range of the optimal extraction acidity.

Recently, we developed the novel separation techniques based on nonionic surfactants, where surfactant aggregates are formed on liquid-liquid interface (*i.e.*, emulsion method) [5-7] or on the liquid-solid interface (*i.e.*, admicellar method) [8, 9]. The phenomenon of salting-out of the nonionic surfactant was also useful for the separation of the iron matrix [10, 11]. The present paper describes the fundamentals and applications of the surfactant-based separation techniques developed in our laboratory. Useful findings of the ionic liquid method and its potential and applicability will also be mentioned.

EXPERIMENTAL

Apparatus

A Seiko SPQ-6500 ICP-mass spectrometer (plasma conditions: RF power 1.2 kW; sampling depth 12 mm;

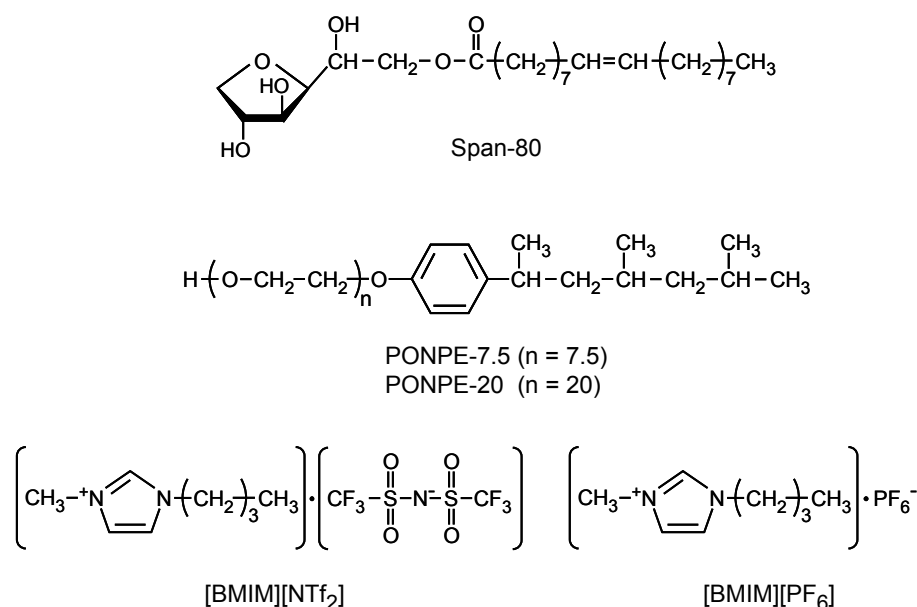


Fig. 1 Nonionic surfactants and ionic liquids

argon flow rate 18 L/min for outer, 0.8 L/min for intermediate and 1.0 L/min for carrier) and a Perkin-Elmer AAnalyst 600 graphite-furnace atomic absorption spectrometer were used for the determination of trace metals. A Jasco liquid chromatograph with a Merck Chromolith RP-18 column and a Jasco UV-2070 detector were employed for the determination of heteropoly molybdic acids. Separation procedures were carried out in a Hitachi ECDV-843 BY clean bench.

Reagents

Typical surfactants and ionic liquids used in the present work include sorbitan monooleate (Span-80), polyoxyethylene-4-isononylphenoxy ether (PONPE), polyoxyethylene-4-*tert*-octylphenoxy ether (Triton X), 1-butyl-3-methylimidazolium bis(trifluoromethanesulfonyl) imide ([BMIM][NTf₂]), and 1-butyl-3-methylimidazolium hexafluorophosphate ([BMIM][PF₆]). The chemical structures of some reagents are shown in Fig. 1. The w/o emulsion was prepared by dissolving 50 mg of Span-80 and 10 mg of Kelex-100 in 1.5 mL of organic solvent (toluene : *n*-heptane = 1 : 2) and mixing with 0.5 mL of 1 M hydrochloric acid with the ultrasonic irradiation. A styrene-divinylbenzene copolymer Amberlite XAD-4 resin (pulverized to 0.1-0.2 mm) was washed with ethanol and water and employed as core particles of admicelles. Lithium chloride was purified with an iminodiacetic acid Amberlite IRC-748 resin column and used for the salting-out separation. An Empore disk cartridge (hydrophobic polystyrene resins embedded in a PTFE fiber disk, 10 mm in diam.) was used for the preconcentration of trace metals. Certified reference iron metals include NIST 2168 (chips, National Institute of Standards & Technology) and CMSI 1010b (powder, China Metallurgical Standardization Research Institute). Water was purified by a Millipore Milli-Q Gradient A-10 system.

Emulsion method

To a sample solution (Fe 20 mg, 25 mL, pH 1-2) was added 0.1-5 M sodium hydroxide solution in small portions to adjust the pH to 3.5. While stirring the solution with a magnetic stirrer, the w/o emulsion was gradually injected into the sample solution to produce numerous tiny globules. After collecting and demulsifying the emulsion, the segregated aqueous phase was analyzed by inductively-coupled plasma mass spectrometry (ICP-MS).

Admicellar method

A sample solution (Fe 25 mg, 5 mL, 8 M HCl) was introduced onto the admicellar column (consisting of 150 mg of PONPE-20 and 1.0 g of XAD-4) to adsorb the iron matrix. The column effluent was evaporated to near dryness and the residue was dissolved in 2 mL of 0.1 M nitric acid for the determination of trace elements by ICP-MS or graphite-furnace atomic absorption spectrometry (GFAAS). For the determination of P and As, the sample solution (adjusted to 0.03 M acidity) was mixed with 0.3 mL of sodium molybdate solution (8 mg Mo/mL) and equimolar EDTA (to mask the iron matrix). The resulting heteropoly molybdic acids were adsorbed on the admicellar column (consisting of 15 mg of PONPE-20 and 0.1 g of XAD-4) and then desorbed with 1 mL of 0.3 M tetramethylammonium hydroxide solution for the analysis by high-performance liquid chromatography (HPLC).

Salting-out method

A sample solution (Fe 50 mg, 3 mL, 0.03-1.5 M HCl) was mixed with 1.1 g of PONPE-7.5 and 7 mL of 10 M lithium chloride solution to cause the aggregation of surfactant. The segregated iron-containing surfactant phase was removed by centrifugation and the pH of the supernatant was adjusted to 7-8. After adding 0.1 mL of ammonium pyrrolidinedithiocarbamate (APDC) solution (30 mg/mL), the resulting hydrophobic APDC chelates were collected on an Empore disk cartridge. The desired trace metals were desorbed with 0.5 mL of 5 M nitric acid with the ultrasonic irradiation and the disk cartridge was washed with 0.5 mL of 5 M nitric acid and water. The combined solution (10 mL) was analyzed by ICP-MS or GFAAS.

RESULTS AND DISCUSSION

Separation with emulsion globules

Previously, we found the unique property of emulsion globules, in which trace metal ions and suspended particles were well discriminated through the water-oil interfaces [12]. This property was used for the separation of trace impurities from the iron matrix. Fig. 2 illustrates the structure of an emulsion globule and how trace metal ions are transported to the inner acidic regions. Traces of Ti(IV), Cu(II), Ga(III), In(III), and Bi(III) were quantitatively recovered at pH 3.5-4 with Kelex-100 as shown in Fig. 3. At around pH 3.5, the permeation of the iron matrix (existing as hydroxide particles) was blocked nearly completely. Table 1 shows that the trace metals can be collected with the recovery of better than 90 % in the presence of 0.5-20 mg of iron. The detection limits (ng/mg) were 0.05 for Ti, 0.08 for Cu, 0.02 for Ga, 0.01 for In, and 0.02 for Bi. The proposed emulsion method was successfully applied to the analysis of high-purity iron metal (NIST 2168 and CMSI 1010b).

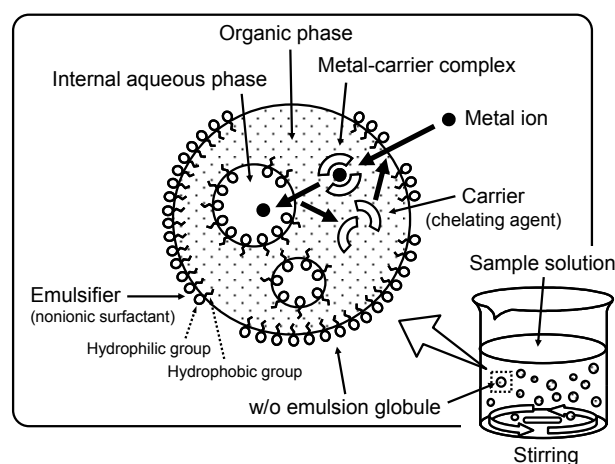


Fig. 2 Collection of trace metals in water with w/o emulsion globules

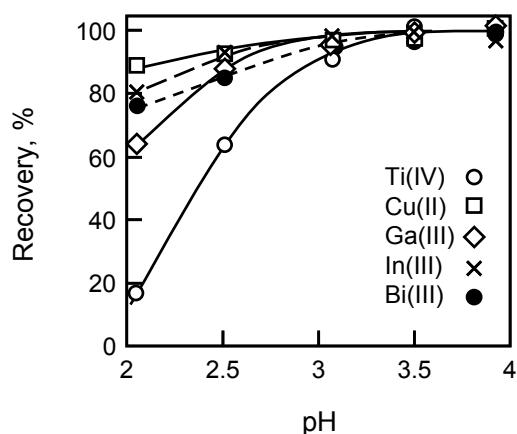


Fig. 3 Effect of pH on the recovery of 100 ng each of Ti, Cu, Ga, In and Bi

Table 1 Effect of the amount of Fe(III) on the recovery of trace metals

Fe(III) taken / mg	Recovery, %				
	Ti(IV)	Cu(II)	Ga(III)	In(III)	Bi(III)
0.5	96 (0.014)	99 (0.013)	98 (0.014)	96 (0.014)	99 (0.013)
10	98 (0.009)	99 (0.010)	93 (0.010)	91 (0.010)	95 (0.010)
20	95 (0.012)	97 (0.012)	92 (0.012)	95 (0.012)	97 (0.012)
30	78 (0.015)	86 (0.014)	80 (0.015)	73 (0.011)	82 (0.014)

Trace metals: 50 ng each. Separation factors in parentheses.

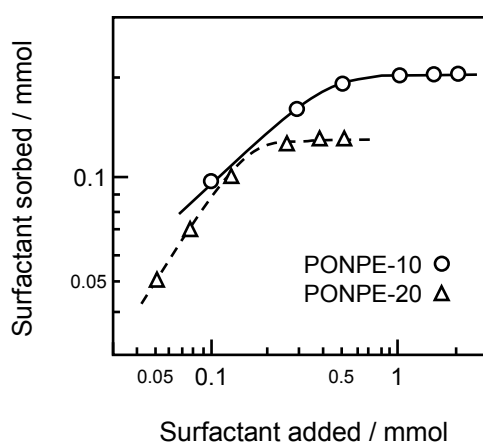


Fig. 4 Adsorption of surfactants on 1.0 g of XAD-4

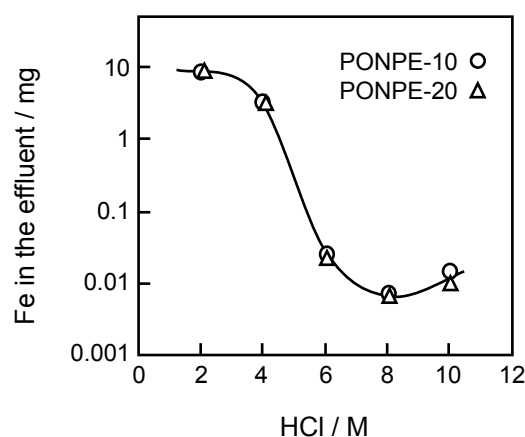


Fig. 5 Effect of the acidity on the adsorption of 10 mg of Fe

Separation with admicelles

Previously, admicelles were prepared electrostatically between ionic surfactants and oppositely charged core particles [13-15]. In the present method, however, admicelles were prepared based on the hydrophobic interactions between the polyoxyethylene type nonionic surfactant and the XAD resin. Figure 4 shows the adsorption behavior of PONPE on the XAD-4 resin. The maximum amount of PONPE adsorbed on 1.0 g of XAD-4 was 0.20 or 0.14 mmol for PONPE-10 or PONPE-20, respectively. The surfactant molecules are expected to be in a monolayer form, with the apolar lipid groups on the XAD resin and the hydrophilic moieties in the outer aqueous solutions. These hydrophilic ethylene oxide chains may interact with the iron matrix.

As shown in Fig. 5, the recovery of iron(III) increased with increasing the acid concentration up to 8 M but slightly decreased around 10 M acidity. The adsorption capacity of the admicellar column was measured by using synthetic sample solutions containing different amounts of iron(III). The PONPE-20 admicellar column provided higher adsorption capacity: the maximum adsorption of iron was 30 mg (see Fig. 6).

The multielement separation was carried out using the PONPE-20 column from 8 M hydrochloric acid solutions. Many trace elements (*e.g.*, Ti, Cr, Mn, Co, Ni, Cu, Zn, Ag, Cd, Pb and Bi) were successfully separated from the iron matrix with the nearly complete recoveries. The analytical results obtained for the certified reference high-purity

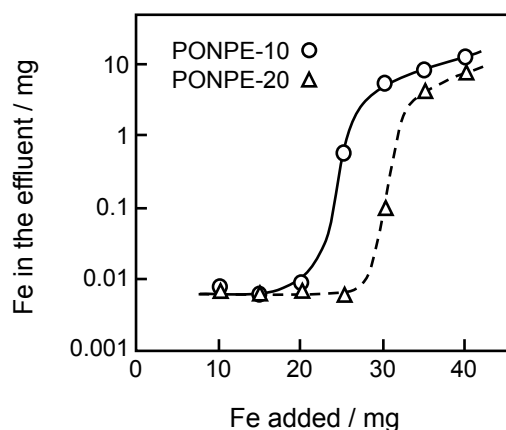


Fig. 6 Adsorption capacity of the PONPE admicelles

Table 2 Analysis of high-purity iron metals by the admicellar method

Element	Concentration / $\mu\text{g g}^{-1}$			
	NIST 2168		CMSI 1010b	
	Determined	Certified	Determined	Certified
Ti	< 0.03	(<3)	0.55 ± 0.05	(<1)
Cr	3.0 ± 0.1	3	2.1 ± 0.1	2.1
Mn	5.8 ± 0.2	6	1.3 ± 0.1	1.3
Co	5.8 ± 0.2	6	0.93 ± 0.03	(1)
Ni	11 ± 1	12	15 ± 1	15
Cu	4.9 ± 0.2	5	1.4 ± 0.1	1.4
Zn	4.7 ± 1.6	(<5)	1.5 ± 0.6	(1)
Ag	0.045 ± 0.005	—	0.072 ± 0.003	—
Cd	0.23 ± 0.03	(<1)	0.35 ± 0.01	(<1)
Pb	0.63 ± 0.07	(<1)	1.0 ± 0.1	(1)
Bi	0.12 ± 0.02	(<3)	0.21 ± 0.01	(<1)

Indicative values in parentheses.

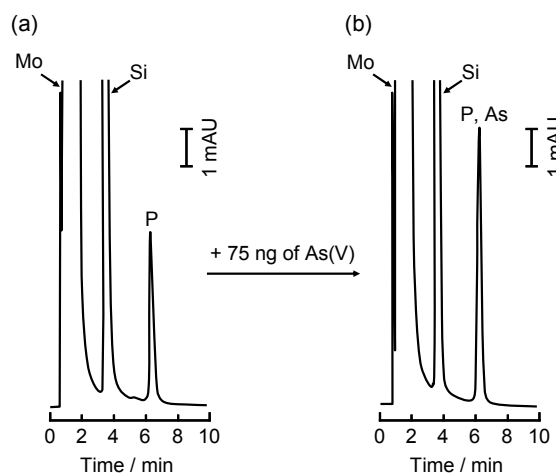


Fig. 7 Typical chromatograms for NIST2168 (Fe 5 mg)

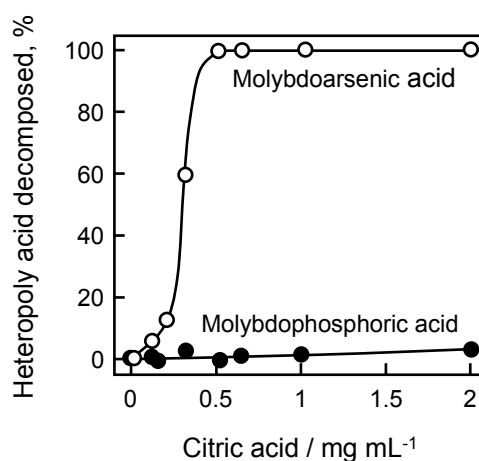


Fig. 8 Decomposition of heteropoly molybdic acids

materials (NIST 2168 and CMSI 1010b) well agreed with the certified or indicative values (see Table 2). The detection limits (ng/g) were 200 for Zn, 60 for Pb, 40 for Cr, 30 for Ti, Ni and Cu, 4 for Mn, 3 for Ag, 2 for Co and Cd, and 1 for Bi.

For the determination of traces of Si, P and As, the sample acidity was decreased to 0.03 M HCl, where the iron matrix became passable through the admicellar column. On the other hand, these trace elements were quantitatively retained on the column as heteropoly molybdic acids. After desorption with tetramethylammonium hydroxide, they were determined by HPLC. As shown in Fig. 7, P and As were well separated from large absorbances of molybdosilicic acid (probably due to contamination) and the excess of molybdate. However, they were not separated from each other, although many experimental parameters (*e.g.*, packing material, column size, composition of mobile phase, flow rate, etc.) were studied in detail. Therefore, molybdoarsenic acid was decomposed selectively by citric acid (see Fig. 8). The proposed method was successfully applied to the determination of P and As at low- to fractional ppm levels in iron metal.

Separation by salting-out effect

Nonionic surfactant molecules aggregate to form the condensed surfactant phase when the solution was mixed with a large amount of chloride. This salting-out effect was employed for the removal of the iron matrix because

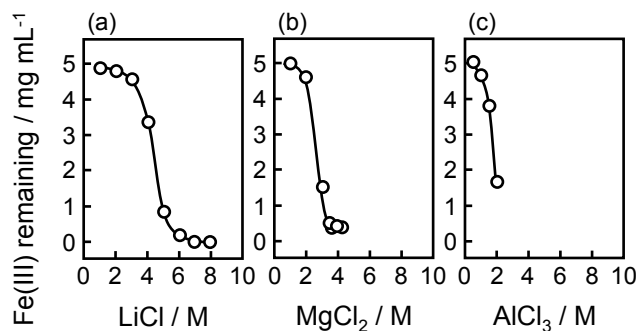


Fig. 9 Effect of different chlorides on the removal of iron (5 mg/mL)

Table 3 Removal of different amounts of Fe(III)

Fe(III) taken / mg mL ⁻¹	Acidity / M	Fe(III) remaining / µg mL ⁻¹
4	0.1	2, 2
5	0.1	1, 2, 2, 2
	0.2	2, 2
	0.5	4, 5
	1.0	6, 6
	2.0	7, 7
6	0.2	22, 23
8	0.2	910, 940
10	0.2	3400, 3500

some interactions were expected between iron(III) species and polyoxyethylene-type nonionic surfactants. Under optimal conditions, the iron matrix quantitatively migrated into the surfactant-rich phase, leaving many trace elements in the solution. As shown in Fig. 9, lithium chloride was most effective and convenient; more than 99.9 % of iron was removed at higher concentrations than 7 M lithium chloride. Table 3 summarizes the removal efficiency of the iron with 0.2 M PONPE-7.5 and 7 M lithium chloride. The satisfactory removal was obtained for up to 5 mg/mL of iron. The trace elements were further concentrated with APDC and the Empore disk cartridge. The proposed salting-out method allows the detection of various metals (e.g., Ti, Cr, Mn, Co, Ni, Cu, Zn, Cd, Pb and Bi) down to the fractional ppm level in iron samples.

Separation with ionic liquids

Recently, ionic liquids have attracted considerable attention in the different scientific fields. We tried to use ionic liquids for the separation of trace elements from the iron matrix. For example, heteropoly molybdic acids of Si, P and As were simultaneously extracted into a small amount of 1-butyl-3-methylimidazolium bis(trifluoromethanesulfonyl) imide ([BMIM][NTf₂]), leaving the iron matrix in the aqueous solution. The contamination for Si through the whole procedure was negligibly small, which allowed the HPLC determination of Si at low ppm levels in high-purity iron metal. Traces of sulfur in water were also extracted into 1-butyl-3-methylimidazolium hexafluorophosphate ([BMIM][PF₆]) as Methylene Blue compound and determined by spectrophotometry. The ionic liquid method seems to be very promising from the viewpoints of potentiality and applicability. Optimization of detailed experimental conditions is now in progress in our laboratory.

CONCLUSION

The novel separation techniques based on nonionic surfactants and ionic liquids were developed to effectively separate trace elements from the iron matrix. These separation procedures were essential for obtaining the accurate and reproducible analytical results. Coupled with ICP-MS, GFAAS and HPLC, the detectability of many trace elements approached ng/g levels in iron samples. Among several separation techniques developed in our laboratory, admicellar and ionic liquid methods are particularly exciting and promising. They are expected to open new vistas and play important roles in the purification and assessment process for the production of high-purity materials.

References:

- [1] A. Mizuike: *Enrichment Techniques for Inorganic Trace Analysis*, Springer, Berlin, 1983.
- [2] Yu. A. Zolotov and N. M. Kuz'min: *Preconcentration of Trace Elements*, Elsevier, Amsterdam, 1990.
- [3] M. Hiraide: *Feramu* (Bulletin of the Iron and Steel Institute of Japan, in Japanese), 2002, Vol.7, p.436.
- [4] O. G. Koch and G. A. Koch-Dedic: *Handbuch der Spurenanalyse, Teil 1*, Springer, Berlin, 1974, p.259.
- [5] T. Kageyama and M. Hiraide: *Bunseki Kagaku* (Journal of the Japan Society for Analytical Chemistry, in Japanese), 2002, Vol.51, p.741.

- [6] T. Kageyama, H. Matsumiya and M. Hiraide: *Anal. Bioanal. Chem.*, 2004, Vol.379, p.1083.
- [7] H. Matsumiya and M. Hiraide: *Tetsu-to-Hagane* (Journal of the Iron and Steel Institute of Japan, in Japanese), 2007, Vol.93, p.85.
- [8] H. Matsumiya, S. Furuzawa and M. Hiraide: *Anal. Chem.*, 2005, Vol.77, p.5344.
- [9] H. Matsumiya, T. Kikai and M. Hiraide: *Anal. Sci.*, 2009, Vol.25, p.207.
- [10] H. Matsumiya, Y. Sakane and M. Hiraide: *Anal. Chim. Acta*, 2009, Vol.653, p.86.
- [11] H. Matsumiya, M. Kuromiya and M. Hiraide: *Tetsu-to-Hagane* (Journal of the Iron and Steel Institute of Japan, in Japanese), 2011, Vol.97, p.61.
- [12] M. Hiraide, M. Ogoh, S. Itoh and T. Kageyama: *Talanta*, 2002, Vol.57, p.653.
- [13] M. Hiraide, M. H. Sorouradin and H. Kawaguchi: *Anal. Sci.*, 1994, Vol.10, p.125.
- [14] M. Hiraide, J. Iwasawa and H. Kawaguchi: *Talanta*, 1997, Vol.44, p.231.
- [15] T. Saitoh, T. Kondo and M. Hiraide: *J. Chromatogr. A*, 2007, Vol.1164, p.40.

EFFECT OF THE DUTY RATIO OF PULSED BIAS CURRENT ON THE ANALYTICAL PERFORMANCE IN RADIO-FREQUENCY GLOW DISCHARGE PLASMA OPTICAL EMISSION SPECTROMETRY ASSOCIATED WITH BIAS-CURRENT MODULATION TECHNIQUE

Satomi Urushibata and Kazuaki Wagatsuma*

Institute for Materials Research, Tohoku University, Katahira 2-1-1, Sendai 980-8577, Japan

** wagatuma@imr.tohoku.ac.jp*

ABSTRACT/SUMMARY: A spectrometric method based on frequency separation using a fast Fourier transform (FFT) analyser, where a pulsated bias-current was introduced to a radio-frequency glow discharge (RF-GD) plasma, was developed to improve the detection sensitivity for the atomic emission analysis. An FFT analyser has an ability to disperse signal components by frequency, and it was thus employed to select the component of a particular frequency. A dc bias current introduced into the GD plasma can enhance the emission intensities of analyte species greatly, and furthermore, it can be easily pulsated to modulate the emission intensities from the plasma. The modulated emission signal was selectively detected with the FFT analyser, with removing any noise components from the overall signal. This method greatly reduced the fluctuation of the detected emission signal as well as the background level and eventually improved the analytical performance. The duty ratio of the pulsed bias current largely affected the amplitude of frequency components detected with the FFT analyser, because the pulse waveform comprised sine-function components having different coefficients. This paper reported how the duty ratio was optimized for the experimental condition.

1. Introduction

In metallurgical industry, it is required to quantify constituent elements in a manufactured material as rapidly and precisely as possible, because their analytical values should be on-site monitored for the production control. Especially in steel materials, several properties of the steel products are principally determined by impurity elements as well as alloyed elements in the iron matrix. For instance, carbon is the most important alloyed element for steel making, whereas other nonmetallic elements such as P and S are harmful impurities because they may cause cracking in the hot rolling process; therefore, their contents are strictly controlled within each allowed value. On the other hand, several metallic elements, such as Ni, Cr, Mo, V, Nb, Ta, and W, are alloyed in the iron matrix at various concentrations, to improve various properties of the steel products, such as strength, toughness, heat resistance, and corrosion resistance. The contents of these elements have to be also controlled strictly.

Glow discharge optical emission spectrometry (GD-OES) is an analytical method in which a glow discharge plasma works as both the atomization and the excitation source for solid samples. The sampling process through cathode sputtering enables it to be widely employed for the quality control of various manufactured materials [1,2]. However, the detection sensitivity in conventional GD-OES is not high for impurity elements in a steel material enough to be determined with good precision. Therefore, further studies on GD-OES have been conducted to improve the analytical performance. This paper describes a new detection method in a radio-frequency (RF) GD-OES, based on a modulation technique of the RF plasma.

An RF-GD plasma induces a negative dc voltage, called self-bias voltage, between the powered electrode and the grounded electrode due to a large difference in the mobility between positive particles and electrons [3]. When a low-pass filter circuit is connected with the plasma source, the self-bias voltage is separated and monitored, and then a dc current can be introduced into the plasma through an external load resistor. We have reported that the dc current largely elevates the intensities of particular emission lines from the resulting plasma [4,5]. We called this current a dc bias current. The dc bias current could enhance the emission intensities by a factor of 10-20 when atomic emission lines having relatively low excitation energies (3-5 eV) were employed as the analytical line [6]. Furthermore, the dc bias current can be easily pulsated so that the resultant emission signal can be varied periodically and then the component can be detected selectively by using a modulation

spectrometric method. We have reported a measuring system for detecting the modulated emission signal using a fast Fourier transform (FFT) analyser in the pulsed RF-GD-OES [7, 8]. The duty ratio of the pulse waveform would be an important parameter for determining the amplitudes of frequency components separated with the FFT analyser. In this paper, the effect of the duty ratio is investigated for the optimum operating conditions.

2. Apparatus and Experimental Conditions

We have reported on the bias-current introduction to an RF glow discharge plasma, which enables the emission signal in RF-GD-OES to be much elevated [4,5]. We have also suggested a modulation detection method for the pulsed bias current by using an FFT analyser [8], where the bias current is pulsed with a square waveform and then the synchronously-pulsated component of the emission signal is selectively detected, in order to further improve the analytical performance in RF-GD-OES. The apparatus and the measurements for the modulation method are described briefly.

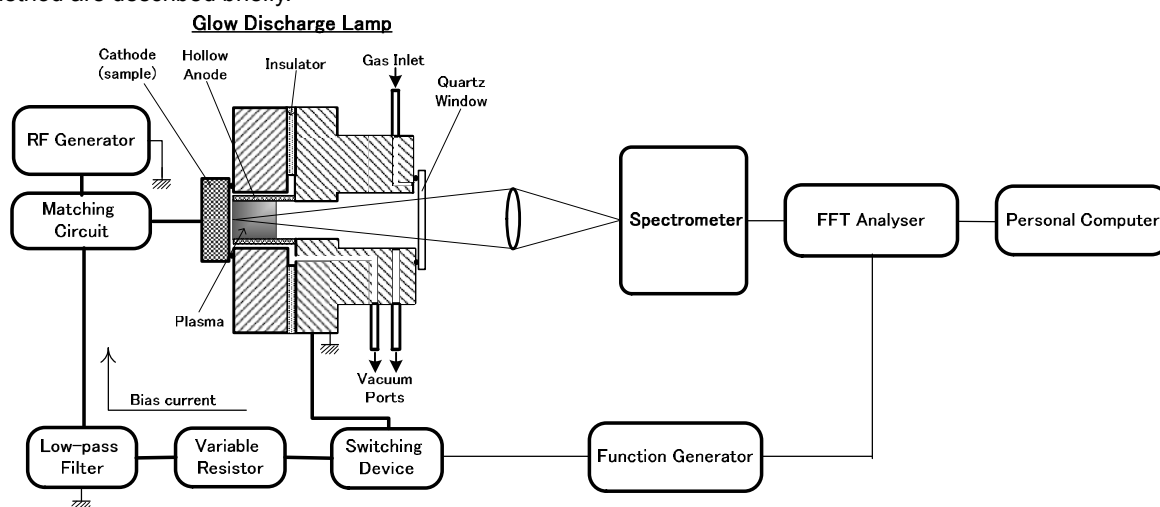


Fig. 1 Block diagram of the measuring system.

Figure 1 is a block diagram of the measuring system employed. A GD plasma source, comprising a hollow anode having 8.0 mm in diameter and a planer cathode (sample), was made in our laboratory. The electrode gap was adjusted to be 0.2-0.4 mm. An RF generator (SRF-02A, Shindengen Electric Mfg. Corp., Japan) was connected with the plasma source through a matching circuit (SMB-02, Shindengen Electric Mfg. Corp., Japan), by using a co-axial cable. This power supply had a maximum power of 200 W at a frequency of 13.56 MHz. A dc self-bias voltage [3] was separated from the RF component by connecting with a low-pass filter, which was made in our laboratory using a high-voltage capacitor and a coil [4]. The RF filter worked at a cut-off frequency of ca. 300 kHz, and thus the RF component of 13.56 MHz was fully removed. A dc bias current can be conducted through the overall circuit including the plasma body, when a variable load resistor is inserted between the RF filter and the GD plasma source. The bias current could be adjusted by varying the resistance value. The flow of the bias current leads to a large number of electrons introduced into the plasma [4,5]. The electrons from

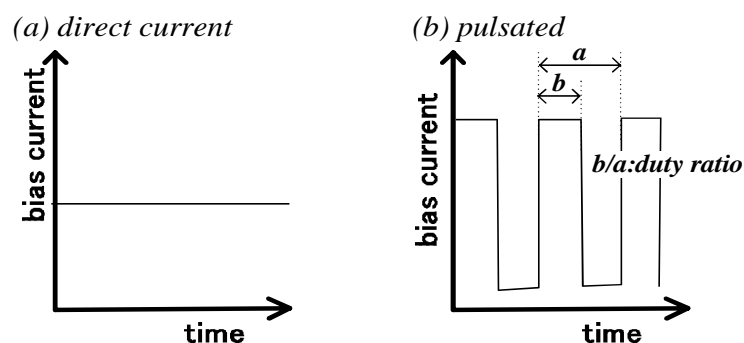


Fig. 2 Waveform of bias current

the hollow anode could take part in various collision processes, and thus the excitation of analyte atoms would occur more actively, so that the emission intensity from the GD plasma is elevated. As schematically shown in Fig. 2, the current value is kept constant at a fixed resistance value. However, the bias current can be on/off controlled when a switching circuit is added to this electric circuit, which also produces a modulated component of the

emission signal because the emission intensity is periodically varied by switching the bias current at a certain frequency. The switching circuit was in-laboratory made using a photoMOS-relay device (AQY210EH, Panasonic Corp., Japan). Parameters for the switching such as the waveform, the frequency, and the duty ratio, were controlled with a digital function generator (DF-1906, NF Electronics Instruments, Japan).

The emission signal was dispersed and detected on a scanning spectrometer (P-5200, Hitachi Corp., Japan), comprising a modified Czerny-Turner mounting monochromator and a photomultiplier tube (R955, Hamamatsu Photonics Corp., Japan). The focal length is 0.75 m and the grating has 3600 grooves/mm at a blaze wavelength of 200 nm. A fast Fourier transform (FFT) analyser (SR-760, Stanford Research Systems, USA) was employed to detect the signal component which was modulated at the switching frequency for the bias current and to remove noise components having any other frequencies. Based on an algorithm of the fast Fourier transform, the FFT analyzer computes a power spectrum, where the intensity components are separated by frequency from the overall emission signal. Therefore, only the modulated component in the power spectrum can be recorded on a personal computer. Because the FFT calculation is very fast, the calculator can use a part of the previous data for estimating the next spectrum in the data accumulation [9]. Such overlapping of the data enables a power spectrum to be averaged many times for a short measuring time, and thus averaging of the power spectrum can contribute to an accurate estimation of the intensity data in addition to the removal of noise components having any other frequencies [8].

High-purity argon (>99.999%) was introduced as the plasma gas after evacuating the chamber to below 10 Pa. The plasma gas continued to flow during a measurement while maintaining a chamber pressure of 2.7×10^2 Pa. Three standard reference materials (iron-based alloys containing 0.18, 0.46, and 0.83 mass % Al), which were provided by the Iron and Steel Institute of Japan, were prepared as test samples. A pure iron sample was also prepared as a reference sample. Their surfaces plates were polished with water-proof abrasive papers and then fixed at the sample port of the chamber. Our previous study has indicated that atomic emission lines having lower excitation energies are predominantly enhanced through the introduction of the bias current [4,6]. Therefore, an atomic resonance line of Al [10], Al I 396.154 nm (3.14 eV), was selected as the analytical line.

3. Introduction of Bias-Current

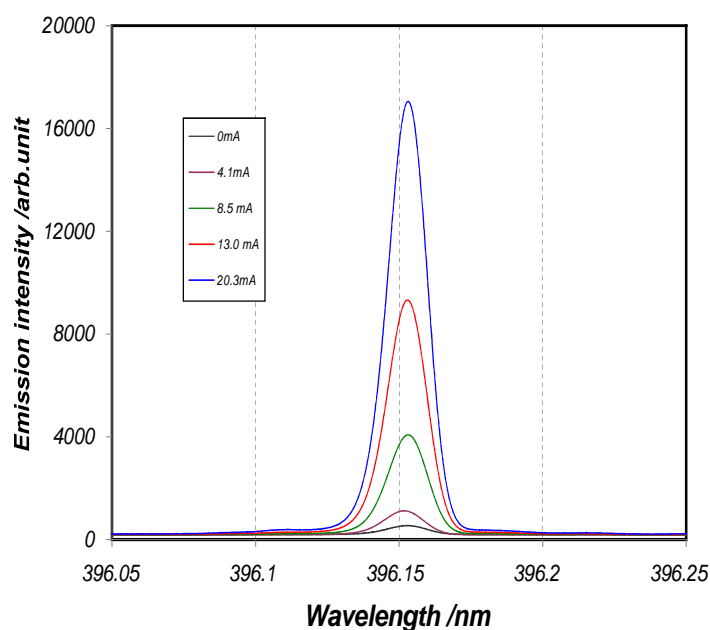


Fig. 3 Spectral scans of Al I 396.153 nm with increasing the pulsed bias current.

Figure 3 shows variations in an emission spectrum in the neighborhood of the Al I 396.153-nm line in an Fe-0.83 mass % Al alloy sample, when the pulsed bias current increases from 0 to 20.3 mA at an rf forward power of 120 W. The pulsed bias current was recorded as an effective value on a digital ammeter. In this case, the pulse waveform was a symmetric square at a frequency of 77 Hz. The spectral scans were recorded through a conventional filter/amplifier on a personal computer. The emission intensity of the Al I line is greatly raised with increasing dc bias current: the Al I intensity becomes 27 times larger than that excited by the normal RF plasma, while the background intensity becomes only 1.8 times greater. This result implies that the emission intensity of the Al I line could be modulated by varying the dc bias current, and that a detection method with an FFT analyser could be applied to detect the modulated

component while removing any noise components.

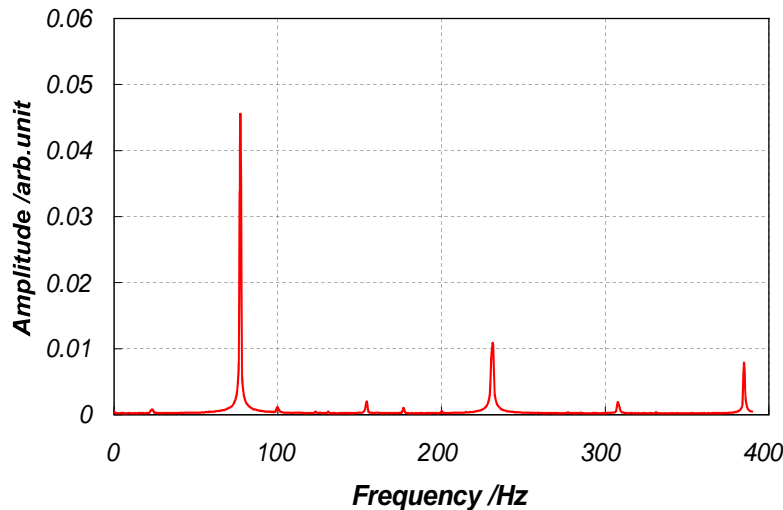


Fig. 4 FFT power spectrum for Al I 396.153 nm at a duty ratio of 50 %.

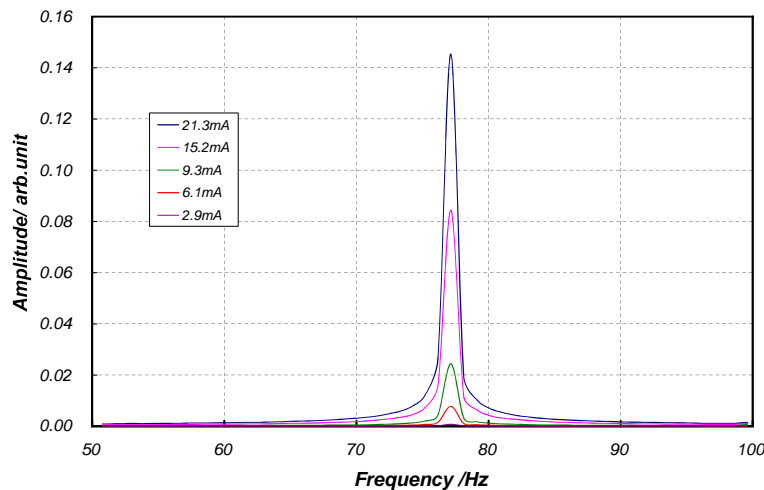


Fig. 5 FFT spectra of the fundamental component for Al I 396.153 nm when varying the pulsated bias current at a duty ratio of 50 %.

follows:

$$F(t) = A \sin(\omega t) + B \sin(2\omega t) + C \sin(3\omega t) + D \sin(4\omega t) + E \sin(5\omega t) + \dots, \quad \omega = 2\pi f \quad (1)$$

A symmetric square waveform (duty ratio of 50 %) comprises a series of sine waves having only the odd-number-

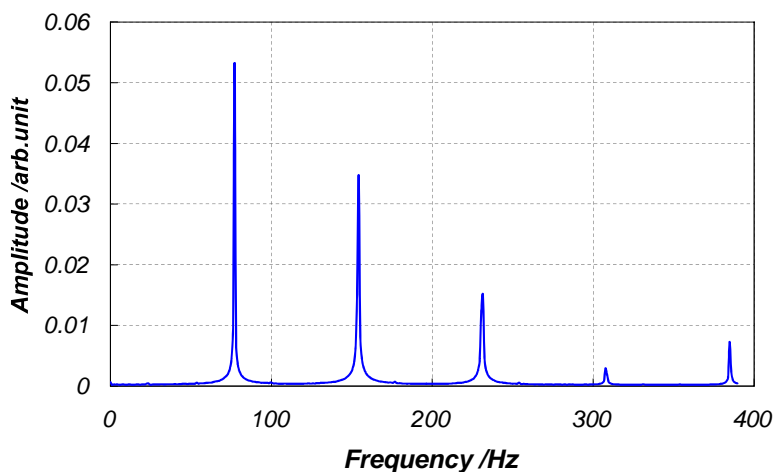


Fig. 6 FFT power spectrum for Al I 396.153 nm at a duty ratio of 25 %.

4. Detection Using FFT analyser

Figure 4 shows an FFT power spectrum in an Fe-0.46 mass % Al alloy sample, when the emission intensity of the Al I 396.153-nm line is modulated under the following discharge conditions: an RF forward power of 120 W, a pulsated bias current at a symmetric square wave of 77 Hz (duty ratio of 50%), and a bias current of 11 mA (effective value). Averaging of the FFT calculation was conducted 100 times at a data overlapping of 60%. The resultant spectrum comprises the largest component at a frequency of 77 Hz, which corresponds to the frequency of the pulsated bias current (the fundamental component), and smaller components at frequencies integral-times larger than the fundamental frequency, such as 154 Hz, 231 Hz, and 308 Hz (higher-order components).

According to the theory of Fourier expansion, a square wave function, $F(t)$, can be de-convoluted into a series of sine wave function whose frequencies are integral-times as high as the fundamental frequency of the square wave, f . It can be expressed as

times frequencies; the coefficients for the even-number-times frequencies, such as B and D in Eq. 1, are zero. In the case of the symmetric square waveform, the coefficients in Eq. 1 are theoretically predicted: $A=1$, $B=0$, $C=1/3$, $D=0$, and $E=1/5$, thus implying that the fundamental component becomes much larger than the other frequency components. The result in Fig. 4 well agrees to this prediction.

Figure 5 shows a variation in FFT spectra at the fundamental component with an increase in the bias current, when the emission intensity

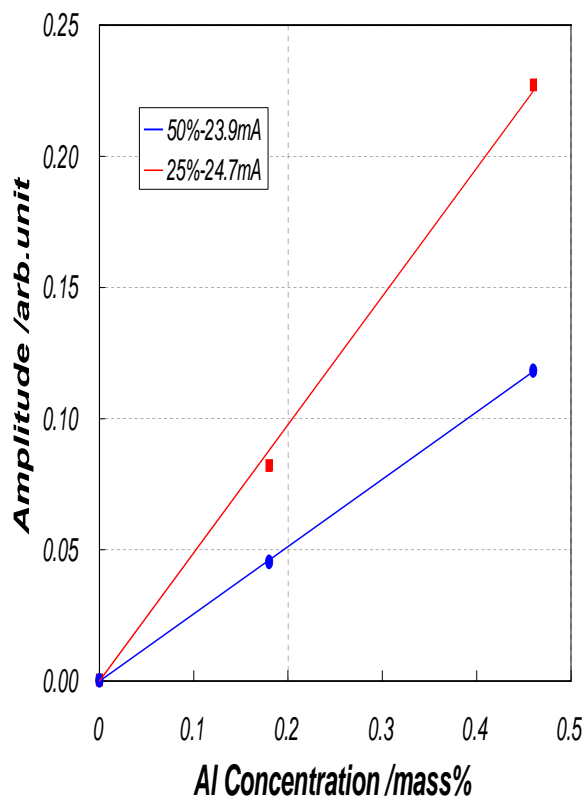


Fig. 7 Calibration curves for Al I 396.153 nm at duty ratios of 25 % and 50 %.

higher-order components would be effective for improving the detection sensitivity for the analytical application. Figure 7 shows a comparison in the calibration curve for the Al I 396.154-nm line, using three steel standard samples including 0.46, 0.18, and less than 0.001 mass % Al, when the duty ratio is pre-determined at 25 % and 50 %. In this case, the pulsed bias current was 24 - 25 mA (effective value). Only the fundamental component was employed at the 50-% duty ratio, whereas the 77-Hz and the 154-Hz components were summed up at the 25-% duty ratio. It can be seen from Fig. 8 that the result of the 25-% duty ratio yields better detection sensitivity than that of the 50-% duty ratio. The pure Fe sample (<0.001 mass % Al) was employed to estimate standard deviations of the blank signal at 396.154 nm. From the slope of the calibration curves, the 3s detection limit can be estimated to be 3.6×10^{-4} mass % Al in the 50-% duty ratio and 8.6×10^{-5} mass % Al in the 25-% duty ratio. In the FFT analysis, the analytical performance could be further improved by selecting the duty ratio of the pulsed bias current appropriately. It is recommended because the duty ratio can be easily varied with maintaining the RF-GD plasma stable as well as without any changes of the other experimental parameters.

6. Conclusions

The intensities of particular emission lines greatly increase by introducing a dc bias current into an RF-GD plasma, while the background intensity is a little changed. Based upon this phenomenon, we developed a new measuring system for RF-GD-OES, which comprised an RF filter, a load resistor, a switching circuit, and an FFT analyser, so that the emission intensities could be selectively measured at very low background levels as well as low noise levels. The FFT analyser computes a power spectrum consisting of the signal components by frequency, and it thus can select only the modulated emission signal when the bias current is periodically varied at a certain frequency. The FFT spectra were strongly dependent on the duty ratio of the pulsed bias current, because each signal component at higher-order frequencies contributed to the FFT spectra in a different manner. The components at the even-number-times frequencies were hardly observed in the FFT spectrum when the duty

of the Al I 396.154-nm line is modulated for the FFT calculation. The measuring conditions were the same as those in Fig. 4 except for the bias current. The amplitude of the FFT spectrum increases with increasing effective bias current up to 22.3 mA, because the Al I emission intensity is much more modulated at larger bias currents.

5. Effect of the Duty Ratio

Figure 6 shows an FFT power spectrum for the Al I 396.154-nm line when the duty ratio for the pulsed bias current is set to be 25 %. The measuring conditions were the same as those in Fig. 4 except for the duty ratio. It should be noted that the amplitude of the second-order component, which appears at a frequency of 154 Hz, becomes much larger than the corresponding component at the 50-% duty ratio (see Fig. 4). This effect is because the coefficients at the even-number-times frequencies in Eq. 1 become non-zero when the duty ratio is asymmetrically determined. Our previous reports have indicated that the amplitude in an FFT power spectrum can be estimated with very small variation and that the background level can be clearly found even when the FFT signal is very faint [7,8]. Therefore, a summation of the fundamental and

ratio was 50 %. However, at a duty ratio of 25 %, the FFT components of fundamental and the twice frequencies were able to be summed to quantify the emission signal for the analytical application. Aluminum in iron-based alloy samples was determined using this method, resulting in detection limits of 3.6×10^{-4} mass % Al in the 50-% duty ratio and 8.6×10^{-5} mass % Al in the 25-% duty ratio, when the Al I 396.154-nm line was employed as the analytical line.

References

- [1] R. Payling, D. G. Jones, A. Bengtson, "Glow Discharge Optical Emission Spectrometry"; 1997; John Wiley & Sons; Chichester.
- [2] K. Marcus, J. A. C. Broekaert, "Glow Discharge Plasmas in Analytical Spectroscopy"; 2003; John Wiley & Sons; Chichester.
- [3] B. Chapman, "Glow Discharge Processes"; 1980; John Wiley & Sons, New York.
- [4] K. Wagatsuma, H. Matsuta, *Spectrochim. Acta*; 1999; 54B; 527-535.
- [5] K. Wagatsuma, *Spectrochim. Acta*; 2000, 55B, 833-838.
- [6] K. Kodama, K. Wagatsuma, *Spectrochim. Acta*; 2004; 59B; 429-434.
- [7] K. Wagatsuma, *Anal. Sci.*; 2009; 25; 157-159.
- [8] K. Wagatsuma, S. Urushibata, *Microchem. J.*; 2010; 95; 107-112.
- [9] Stanford Research Systems, "Operating Manual for SR760 FFT Spectrum Analyzer", 2000; Sunnyvale; USA.
- [10] C. Corliss, W. R. Bozman, "Experimental Transition Probabilities for Spectral Lines of Seventy Elements", 1962; NBS Monograph 53; Washington DC.

INSIGHT INTO THE ROLL GAP– REVEALING HIDDEN PROCESSES BY ANALYTICAL MEANS

Raulf, Martin

ThyssenKrupp Steel Europe AG, Eberhardstrasse 12, D-44145 Dortmund

Abstract

Cold flat rolling of carbon steels is usually done with dilute oil-in-water emulsions. There are a number of theoretical concepts, that try to explain how and why this works quite well. The best known of them is the dynamic concentration theory. There it is assumed, that a continuous oil phase is formed in the roll gap, as long as the emulsion droplets are big enough (i.e. at least in the same order of magnitude as the surface roughness). However the theoretical description of lubrication with emulsions is rather difficult, because numerous factors influence the oil film formation such as pressure, viscosity, rolling speed, oil concentration, surface roughness, etc. and most of these parameters change in each rolling pass.

One important effect occurring in the roll bite is the formation of wear from the strip surface. Different mechanisms of wear formation are presented, such as abrasion, adhesion and tribochemical wear. It is also shown, how effectively lubrication can reduce surface wear and how the mill setup and emulsion care do influence the amount of wear and also the particle size distribution of iron fines.

Tribochemical reactions can effectively improve lubrication in cold rolling. Therefore special additives are present in the rolling oils, which under the influence of temperature and pressure form chemisorbed surface films on the roll or on the sheet. In laboratory trials it could be shown, that it is possible to link the reduction of friction to the formation of tribo-layers from the EP-additives. The reaction mechanisms can be elucidated by detection of the respective reaction products by spectrometrical methods. Moreover the presence of strongly bound surface layers on cold rolled steel surfaces can be demonstrated in cleaning trials. There it could be shown, that a subsequent cleaning of a cold rolled surface with different solvents with increasing polarity only reduces the non polar hydrocarbons. The oxygenated organic substances from can hardly be removed from the surface even with polar solvents.

Background

To claim to be able to provide an insight into the roll gap of a steel cold rolling mill seems arrogant. Too fast are the processes and too extreme the conditions to make valid assumptions for models that describe the roll gap mechanisms. Nevertheless some information can be gathered from chemical analysis results, obtained in regular mill operation, pilot mill trials and also laboratory experiments. In this article some of the results will be reported and the results will be used to deduce information about roll gap processes.

Theory

One speciality in steel cold rolling is, that emulsions are applied as lubricants, which have a typical oil content between 1 % and 5%. Apart from their lubricating properties, they also have the function to cool the work rolls and the strip and to clean the strip and the entire mill from iron fines.

There are a number of theoretical concepts, that can be used to explain, why and how steel rolling with emulsions is working. All of them suffer from the difficulty, that there are numerous parameters, that influence the friction and the lubrication. Moreover all these parameters are changing in each pass, and very often even in the roll bite itself. Some of these parameters are:

- Oil concentration
- Roll and strip roughness
- Temperature
- Speed
- Pressure

One commonly used concept used to describe how emulsions work in the roll bite is the dynamic concentration theory. Here it is assumed, that the oil part of the emulsion is drawn into the roll bite, whereas the water part is squeezed out, so that a continuous lubricant film is formed. This model shows good agreement with experimental results.

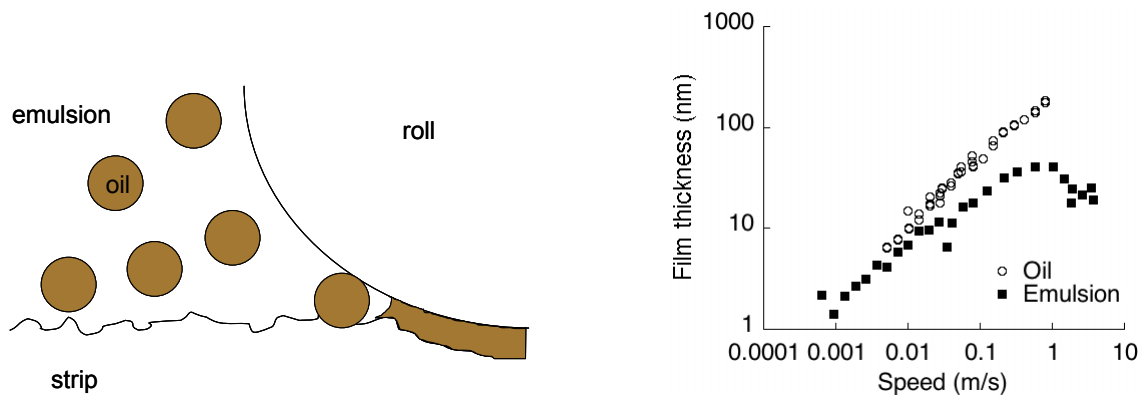


Figure 1: Dynamic concentration theory (left) and starvation in MTM [1] (right) as models for emulsion lubrication in rolling

Figure 1 also gives an example for another phenomenon, that occurs in emulsion lubrication at high speeds. In an experiment with the Mini-Traction-Machine (MTM), a steel ball is rolled on a plate and the oil film thickness is recorded with rising speed. The pure oil shows a linearly increasing oil film thickness over the whole speed range. The emulsion shows a similar behaviour at low speeds, and also the friction level is similar to that of the pure oil. But when a certain speed level is reached, the film thickness drops, because the process is too fast, so that not enough oil can be drawn into the contact. This phenomenon is called starvation and is also observed in industrial rolling processes at high speeds.

Experiments show furthermore, that wetting of the strip surface is an important issue. In order to form a continuous oil film in the contact a rapid wetting of the surface is indispensable.

All this leads to the conclusion, that in the roll bite there is a continuous oil phase instead of a two-phase emulsion. Therefore lubrication in the roll bite can be described to a certain extent by the models that are applied for pure oil lubrication. One important aspect in oil film lubrication is the relative speed of the counterparts and its influence on the friction.

For pure oils, the dependence between speed (v) and friction coefficient (μ) is described by the Stribeck-curve (Figure 3).

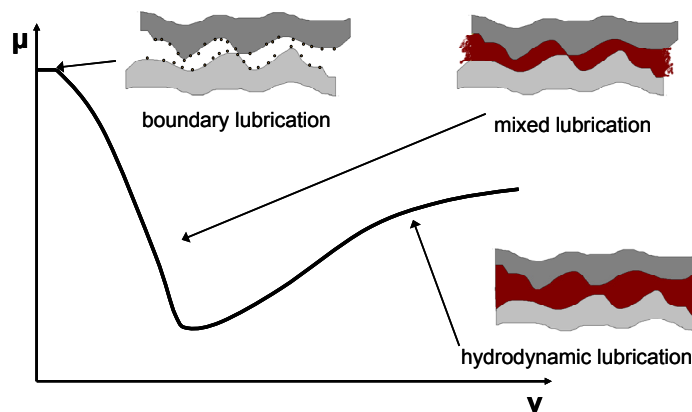


Figure 3: Stribeck curve

At low speeds the friction is relatively high, because there is direct contact between the two friction partners – this regime is called boundary lubrication.

With increasing speed, the friction forces drop, because the amount of hydrodynamic lubrication is increasing, which means that more and more oil is drawn into the contact and the oil film thickness grows, so that a smaller area is in direct metallic contact.

This region is usually called mixed lubrication, because both mechanisms – boundary lubrication and hydrodynamic lubrication are present. This is also the regime, that is predominant in rolling of steel.

With increasing oil film thickness and stronger hydrodynamic lubrication the friction coefficient goes down until it reaches a minimum. At very high speeds, the friction is again increasing, because in a situation with a fully developed fluid lubrication film, the viscosity is the decisive factor for friction forces.

Observations

One strong hint, that mixed lubrication is predominant in steel rolling is the fact, that the amount of wear, that is produced in the roll bite has a strong negative correlation to the oil plate out. This can be seen in Figure 4.

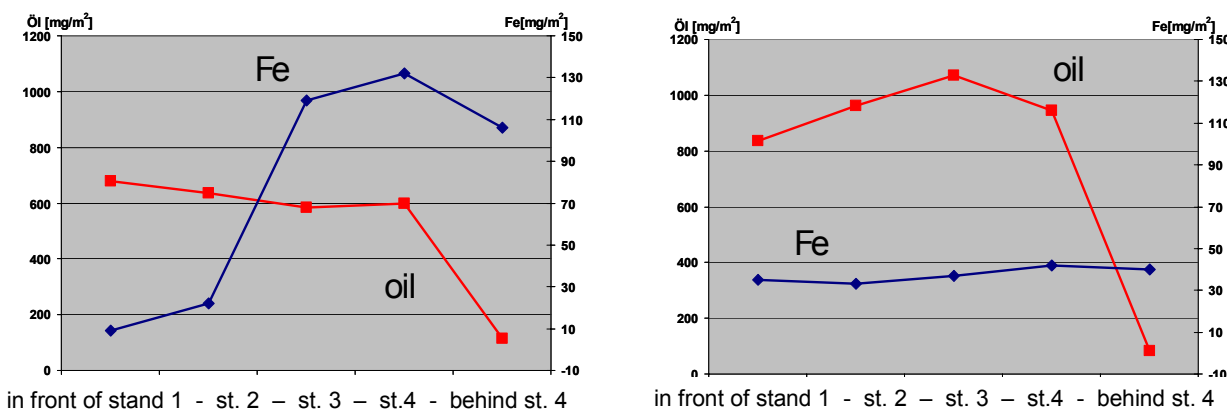


Figure 4: Wear formation in roll gap, with low plate out (left) and higher plate out (right), from iron and oil determination between rolling stands

In a rolling trial in a four-stand cold rolling mill an oil with improved plate out has been used. In order to be able to evaluate the effect on strip cleanliness, a test has been carried out in which the mill has been stopped and the strip has been wiped behind each stand with a wetted glass fiber filter to remove oil and iron fines from the strip surface. Oil amount has been determined gravimetrically after extraction and iron has been determined by AAS after dissolution in hydrochloric acid. It could be shown that the higher plate out of the oil could be clearly observed in

terms of oil amount on the strip and that simultaneously the amount of iron fines on the surface has been reduced by more than 50%.

But abrasion is only one way to produce wear in the roll bite. Other mechanisms are adhesion, e.g. when poor lubrication leads to micro welds between the strip and the roll surfaces, so that material from the strip is torn out. A third mechanism is the tribochemical wear, i.e. when a tribo-reaction takes place between the lubricant and the strip. The lubricating properties of these reaction layers, that partly also consist of strip material, depend mostly on the fact, that they are much softer than the metallic surface and hence can be sheared off much easier than the metal itself. Both effects can be modelled in laboratory friction tests.

The easiest way to learn about wear in the roll bite is to look at the strip surface topography after rolling. Here wear traces can be easily seen in the topography (Figure 5), that indicate abrasive wear from the relative motion between the work roll surface and the strip.

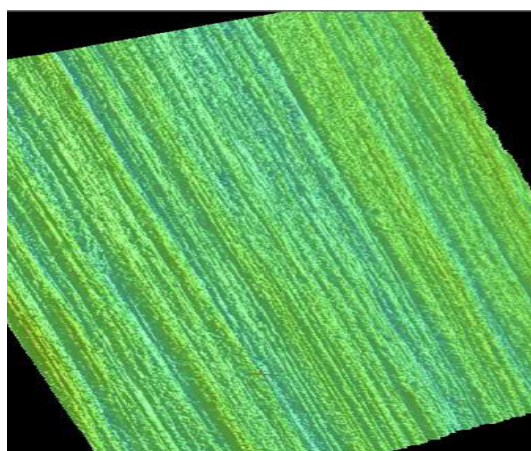


Figure 5: Topography of a cold rolled steel sheet showing abrasive wear

But also the abrasion particles can be examined if isolated from the emulsion.

This can be done by flow cytometry and image analysis of dispersed iron fines, where a classification of particles is done with respect to their size and shape.

When the shape of the iron particles extracted from as rolled steel surfaces is correlated to different size classes it is evident, that the biggest particles are irregular and elongated fibre like structures, whereas the smaller particles become more compact and the smallest particles are more or less spherical.

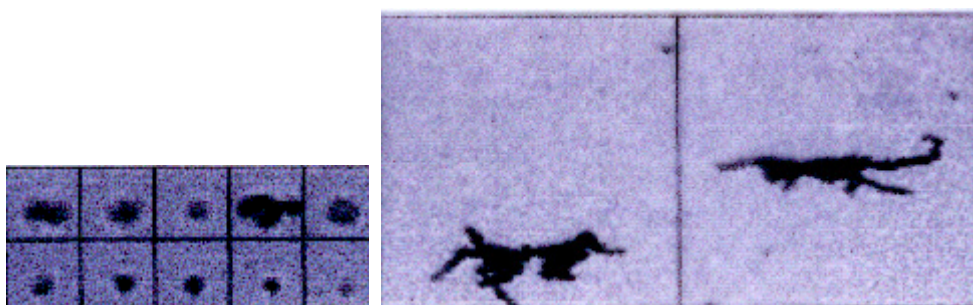


Figure 6: Shape analysis of small wear particles (appr. 1 µm; left) and big wear particles (appr. 10 µm; right)

It is assumed, that the irregular particles are the primary wear particles from abrasive wear in the roll bite. The smaller particles are produced, when the big ones are passing the roll bite over and over again and are strongly sheared and kneaded.

All processes described above could be deduced from the examination of the products and by-products of an industrial rolling mill. Another way to gather information about processes in front of and in the roll bite are laboratory experiments.

In Figure 2 an experimental setup is shown, to simulate and evaluate the wetting of a steel surface in an emulsion with an oil droplet.

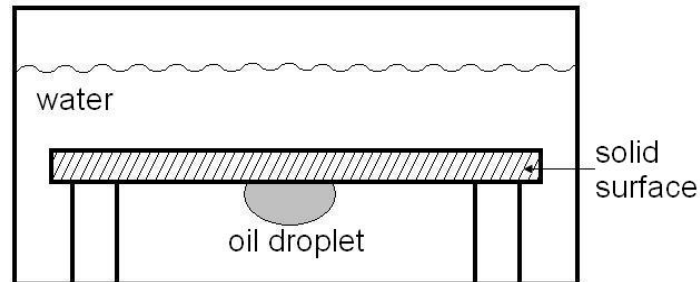


Figure 2: Setup to measure wetting properties of oil droplets in emulsion on solid surfaces [1]

Here the contact angle between an oil drop and the surface in a submerged condition in water is taken as a measure for the ability of the lubricant to wet the surface. It has to be taken into account, that the wetting is not only a property of the lubricant, but strongly influenced by the chemical state of the strip surface (fresh or oxidised) and also its topography. The amount of oil, that is deposited on the surface is often referred to as plate out. It is not only determined by the wetting ability of an oil, but also from the pressure at the nozzles, the viscosity and the ability of the emulsion to form a stable film, that is not easily washed off again, when the emulsion is drained.

Another valuable tool for simulating and analysing friction and lubrication in rolling processes are tribometrical tests especially followed by surface chemical analysis of the friction scars afterwards.

Here the occurrence of tribochemical processes, in which the components of the rolling lubricants are transformed or undergo surface reactions under the influence of pressure and temperature can be confirmed by chemical analysis methods.

One instrument that is used frequently in our laboratory to evaluate the lubricating properties of rolling emulsions is the high frequency friction machine where a steel ball is rubbed on a steel plate in a reciprocating motion. This instrument can also be utilised to identify and describe processes in the roll bite.

As an example, the wear scar on the plate has been examined with infrared spectroscopy. It could be seen, that under the influence of pressure shear stress and temperature in the friction contact iron soaps have formed from the fat component of the rolling lubricant and the steel substrate (Figure 7).

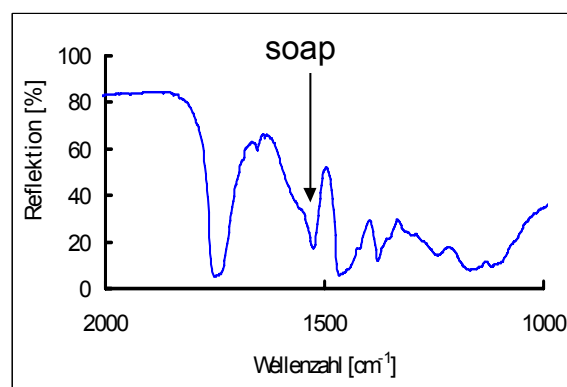


Figure 7: Soap formation in wear scar, detected with FT-IR

This is remarkable, because normally it is assumed, that hydrolysis of the fat in the aqueous environment of the emulsion is the decisive first step in formation of iron soaps. But in the laboratory experiment it could be shown, that soap formation even occurs under dry conditions with pure rolling oil concentrates.

By XPS-analysis of the wear scar it could also be shown, that sulphur- and phosphorus-components form strong covalent bonds to the steel surface in tribochemical reactions. The occurrence of these reaction products could be correlated to the friction coefficient in SRV-tests.

That means, that the starting of a tribochemical reaction e.g. at a certain temperature is accompanied by a drop in friction coefficient and can be proved afterwards by the detection of the respective reaction products in the wear scar.

It can also be shown, that the reactivity and the concentration of EP additives in the rolling oil has a direct influence on the formation of wear.

Therefore a number of lubricants from different suppliers with different levels of P and S-additives have been tested in the high frequency friction machine with the same experimental parameters. The diameters of the wear scars have later been measured and afterwards the surface concentration of P and S has been determined by XPS after degreasing. It could be found, that the concentration of P and S - i.e. the degree of triboreactions that occurred in the contact - was closely correlated to the wear scar diameter (Figure 8)

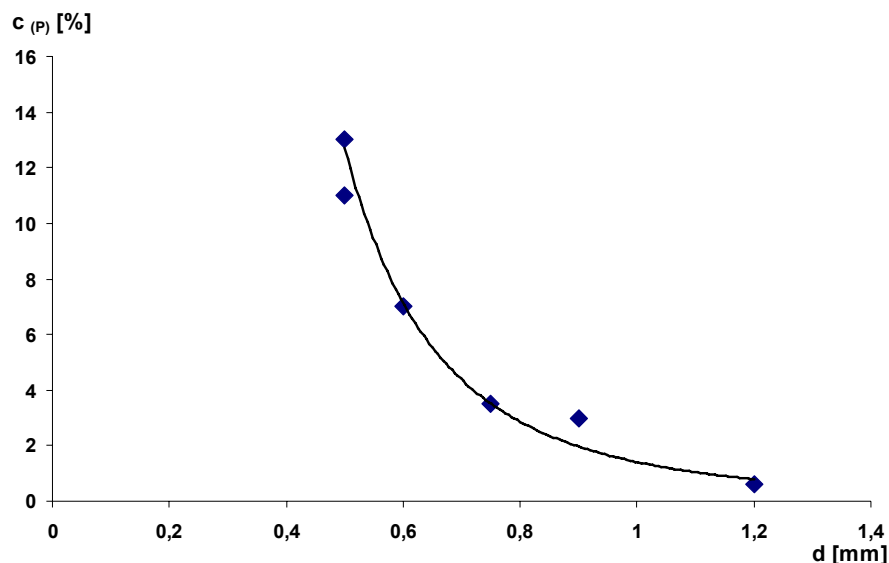


Figure 8: Correlation between wear scar diameter and phosphorus concentration in the wear scar after degreasing

Another experiment with pilot mill material demonstrated, that strong adhesive bonds are formed between the steel surface and the lubricant components in the roll gap. As rolled steel sheets have been analysed by XPS for organic components present on the surface. Different signals have been examined so e.g. the C1s-peak of a C-C-H group as representative for the non polar organic compounds, the C1s-peak for the O-C-O group as representative for the polar organic compounds and the oxygen signal.

Then the surfaces have been cleaned by subsequently stronger rinsing steps, starting with a hexane degreasing, followed by a chloroform degreasing, a toluene degreasing and a degreasing with a mixture of four solvents of different polarity assisted by sonication.

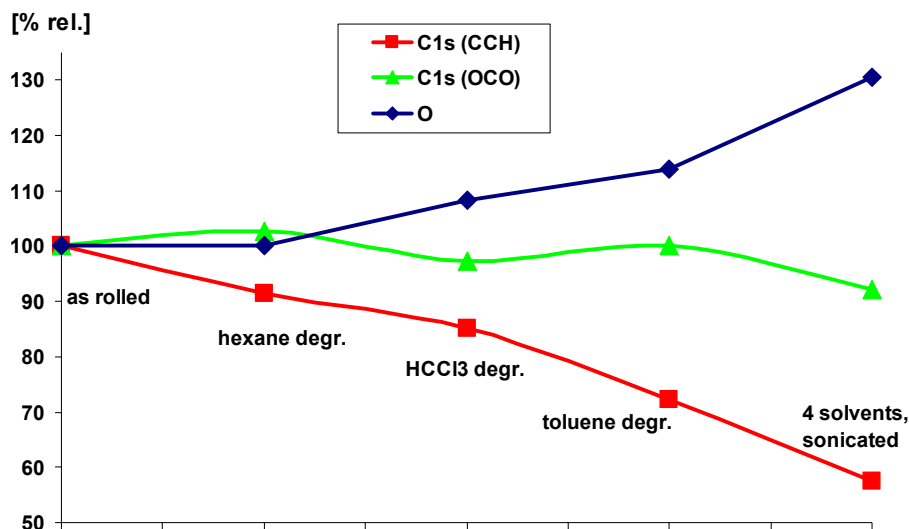


Figure 9: Polar and non polar compounds on as rolled surface after different cleaning steps [2]

It was observed, that the non-polar compounds were decreased in each subsequent cleaning step, whereas the signal for the polar bonds remained on the same level and was hardly influenced by the cleaning. The oxygen signal increased slightly, which is probably due to the fact, that the non polar compounds are washed off and leave the partly oxidised steel surface free.

Conclusions

It could be shown, that the combined effort in analysing the phenomena observed in the emulsion and on the strip in a cold rolling mill, together with results from pilot mill trials and laboratory experiments gives a good opportunity for illuminating the mechanisms that occur in the roll bite.

References

- [1] K. Persson, P. Falk in RFCS-Report Optimisation of rolling lubricants for improved operation of cold rolling mills RFS-CR-04019
 [2] B. Schmitz in RFCS-Report Improved quality of steel sheet by better control and reduction of surface contamination 7210 – PA-E/233

COMBINED APPLICATION OF MICROCLEANLINESS MEASUREMENT DEVICES FOR SUCCESS IN MAGNESIA INCLUSION DETECTION IN SLABS

Egger M.W., Pissenberger A., Aigner St.

*Martin W. Egger, MSc., Research and Development, Steel Plant- Hot strip production
Dr. Andreas Pissenberger, Analytical Process Laboratory, Metallurgy
Dr. Stefan Aigner, Microstructure Surface Analysis
(all at voestalpine Stahl GmbH, voestalpine-Strasse 3, Postfach 3, 4031 Linz, Austria)*

Abstract:

The production of heavy plates for the oil and gas industry requires highest quality levels of the semi finished products like slabs. Calcium-treatment at the end of the steelmaking process is essential. The composition of non-metallic inclusion is changed during this production step. Accurate analysis of inclusions is of main interest. An automated OES-PDA system makes statistical investigations of any steel sample possible. OES-PDA is used to detect the basic micro cleanliness parameters like content and composition. Targeted automated SEM-EDX analysis gives more detailed information about non-metallic inclusions and verifies the OES-PDA data sets. The combination of both results show new detailed information about the process, especially magnesia containing inclusions during solidification of slabs.

1. Overview of the voestalpine group

voestalpine is an international corporate group with a wide variety of specialized and flexible companies who produce, process and further develop high-quality steel products. The corporate group has roughly 360 production and distribution companies in more than 60 countries worldwide. With highest-quality flat-steel products, voestalpine is a leading European suppliers to the automotive, construction, household-appliance and energy industries. The group is the world market leader in railway switch technology, tool steels and special sections, and Europe's number-one manufacturer of rails. The corporate group employs 40,000 employees and consists of five divisions with core segments in leading markets. One of the five divisions, voestalpine Stahl GmbH in Linz, is one of the top three European suppliers of high-quality steel strip and heavy plates for sophisticated applications.

2. Calcium treatment of sour-gas-resistant plates

The production of high sophisticated, sour-gas-resistant pipe plate grades requires an optimized plant system configuration and a high degree of process expertise. Three ladle furnaces and three RH degasser are available for secondary metallurgical treatment of such steel grades. Following deoxidation and pre-alloying of the heat, deep desulfurization of the steel is performed in the ladle furnaces to below 0.0010 mass percent. In the RH degassing plant, nitrogen and hydrogen contents in the heat are reduced to the lowest possible values and fine-alloying is carried out. Following completion of the vacuum treatment, CaSi wire is injected inline and soft bubbling is conducted to completely remove the dissolved residual sulfur (sulfide modification) in the heat. The heats are cast in two continuous casting lines CC5 or CC6 with dynamic soft-reduction technology in order to guarantee high inner quality of the slabs (low porosity, low segregation). The process route is depicted in Figure 1.

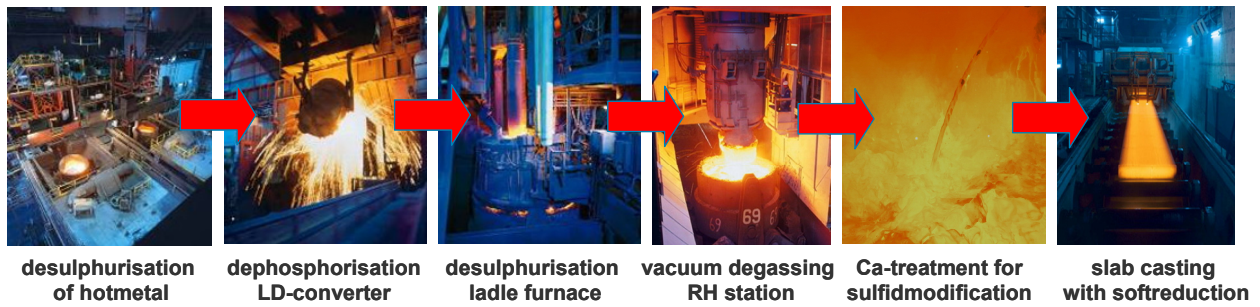


Figure 1: Production process route for sour-gas-resistant plates

3. Microcleanliness measurement

Non-metallic inclusions were analyzed by means of two different methods. In addition to optical emission spectrometry/pulse discrimination analysis (OES-PDA) for rapid online determination of inclusions, automated offline REM-EDX analysis (P-SEM) was also performed in order to determine the chemical composition, size, shape and distribution of a large number of different inclusions.

3.1 OES-PDA determination of cleanliness by means of spark spectrometry

An inclusion analysis by means of optical emission spectrometry with individual spark analysis (OES-PDA) entails inspection of several thousand individual sparks (Figure 2). The results are automatically recorded. Each of these results is a complete analysis of the element concentrations in the steel volume vaporized by the individual spark (approximately 0.0001 mm^3). Both constituents of the steel matrix and microscopic, non-metallic inclusions are analyzed in these volumes. Statistic algorithms are used to register inclusions based on the intensities of the individual sparks, and the types of the inclusion is determined through comparison of the elements aluminum, calcium, magnesium, titanium, manganese, sulfur and silicon with each other.

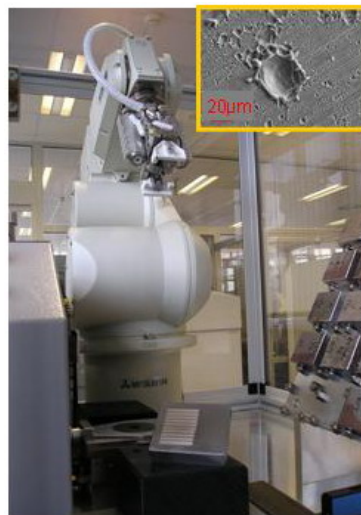


Figure 2: OES-PDA at voestalpine Stahl GmbH

Optical emission spectrometry is used at voestalpine Stahl GmbH both to automatically analyze the chemical composition of all types of steel samples and to determine the microscopic degree of cleanliness. All samples are processed by a fully automatic system in a processing lab. An optimum sample surface is guaranteed by preparing the sample exclusively by means of milling. The analysis itself is conducted by means of OE spectrometers (QSG 750 made by OBLF). The determination of inclusions by individual spark analysis is

completely integrated and incurs no additional expense or time. The quantitative and qualitative inclusion parameter such as the amounts of different elements and the types of inclusions are subsequently automatically calculated by a special software. These values are stored in several different data and quality systems to be accessed at any time. The OES-PDA method has been increasingly used by steelmakers to determine cleanliness characteristics in production process routes and products^[1].

3.2 Automated REM-EDX analysis (PSEM)

Any steel sample (lollipops, slabs, hot-rolled strip, cold-rolled strip and heavy plates) can be measured in a standard way. The sample surface must first be metallographically prepared and must be free of scratches, polishing or grinding residues and alcohol. The automated REM/EDX inclusion analysis system consists of a conventional raster electron microscope (REM) equipped with secondary (SE) and a backscatter electron (BSE) detector. Chemical microprobing by means of an energy-dispersive x-ray (EDX) spectroscopy Si(Li) detector is conducted for each non-metallic inclusion. The EDX results are quantified in accordance with data from certified standards. It is possible based on a variation in the gray values of inclusions and matrix in the BSE image to detect non-metallic inclusions in an automated fashion. Special algorithms supply information on the position, size, shape (length/width) and surface area of the inclusion. EDX analysis on the same particle provides information on the chemical composition while ignoring the excited steel matrix and standardizing the results in mass percent. Depending on the frequency of the inclusion and size of the measured surface, the analytical measurement time varies between one and several hours for non-metallic inclusions $\geq 1\mu\text{m}$.

4. Results

The literature contains a variety of different data on the solubility of magnesium in liquid steel as it depends upon temperature, pressure or the type of refractory material used. There is also a variety different data of MgO, MgO.Al₂O₃ phase ranges. Most sources cite a that MgO precipitation in steel starts at very small amounts of 1 ppm of Mg and 9 ppm of O^[2-7]. The point in time at which MgO is formed, the reaction mechanisms and unique sources are still unclear^[8-10]. In the course of subsequent heats treated with CaSi wire injection in the secondary metallurgy, different methods of cleanliness measurement were combined to analyze this issue.

Operational samples (lollipop) from several heats during CaSi wire injection in the ladle furnace (W1–W3) and in the subsequent soft-bubbling treatment phase (S1–S4) were invariably taken in the same location in the ladle at a bathlevel of roughly 0.6 meters. Steel samples taken from the tundish of the continuous slab caster (T1) correspond to the final molten phase of the heat. The heavy plate samples present the final condition of steel cleanliness after slab casting with dynamic softreduction und hot rolling. The steel samples were first analyzed by means of spark spectrometry, after which the inclusion content was determined by means of an inclusion analyzer (100 mm², magnification of 600 times). In compliance with the rules of quantitative microscopy, measured surfaces of inclusions may be converted into mass content. The bound element content can be calculated from the data by implementing the particle compositions of the elements Al, Mg, Ca, S, Ti, Cr, Nb, Si, Na, K and Cl.

The results of volume-based measurements (OES-PDA) can thus be compared to a surface-based measurement (PSEM). Figure 3 shows the total magnesium content in the samples measured by means of spark spectrometry (OES-PDA) as compared to the bound magnesium content in inclusions (PSEM). Significant differences are shown during CaSi wire injection, soft-bubbling treatment and tundish operation. The measured magnesium content does not coincide well until in the plate samples.

Based on the results of the OES analysis, the magnesium content in the heats increases to 2 ppm through calcium treatment. The source of increased Mg may be due to the CaSi wire, the MgO-saturated ladle slag and the MgO-containing refractory materials in the wall or slag zones of the steel teeming ladle. The PSEM measurement results do not indicate any Mg increase in the inclusions during secondary metallurgical treatment.

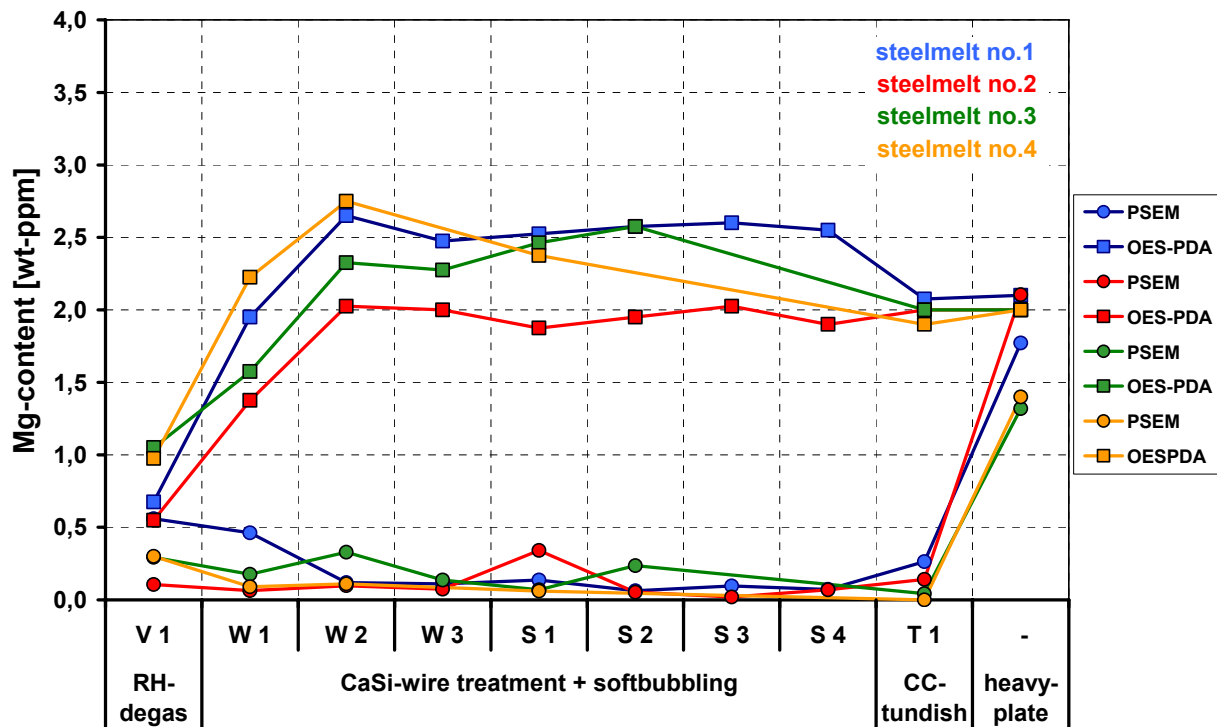


Figure 3: Comparison of measured Mg content by means of OES-PDA and PSEM

It was necessary to analyze in detail the processes during solidification of the continuously cast slab in order to clarify the verified change between the tundish sample and the heavy plate. For this purpose, a sample was removed from a slab across its entire width (285 mm). The cross-section of this sample was analyzed incrementally for a period of 2.5 months from the top side to the bottom side by means of OES-PDA methods. Between 5 to 8 individual measurements were made on each analyzed surface. The distance between the individual levels was 0.4 mm. A total of nearly 4,000 individual measurements were made. Figure 4 shows the continuous increase in Mg-containing inclusions in the first 40 mm of the slab. The inclusions consist of MgO, MgO.Al₂O₃ or CaO.MgO.Al₂O₃. The Mg content remains unchanged across the entire thickness of the slab. This increase is real because the basis for the calculation algorithm for determination of the Mg inclusions from the individual sparks does not change. It coincides with the calculated change in the solidification zone size during controlled solidification of the slab.

Targeted analysis of the individual levels of the slab sample by means of PSEM based on the OES-PDA results also makes it possible to verify continuous inclusion of Mg in complex calcium-aluminate particles (see Figure 5). Directly at the slab surface, the magnesium content in inclusions is up to 20 mass percent and rises up to 40 mass percent in 33 mm slab depth.

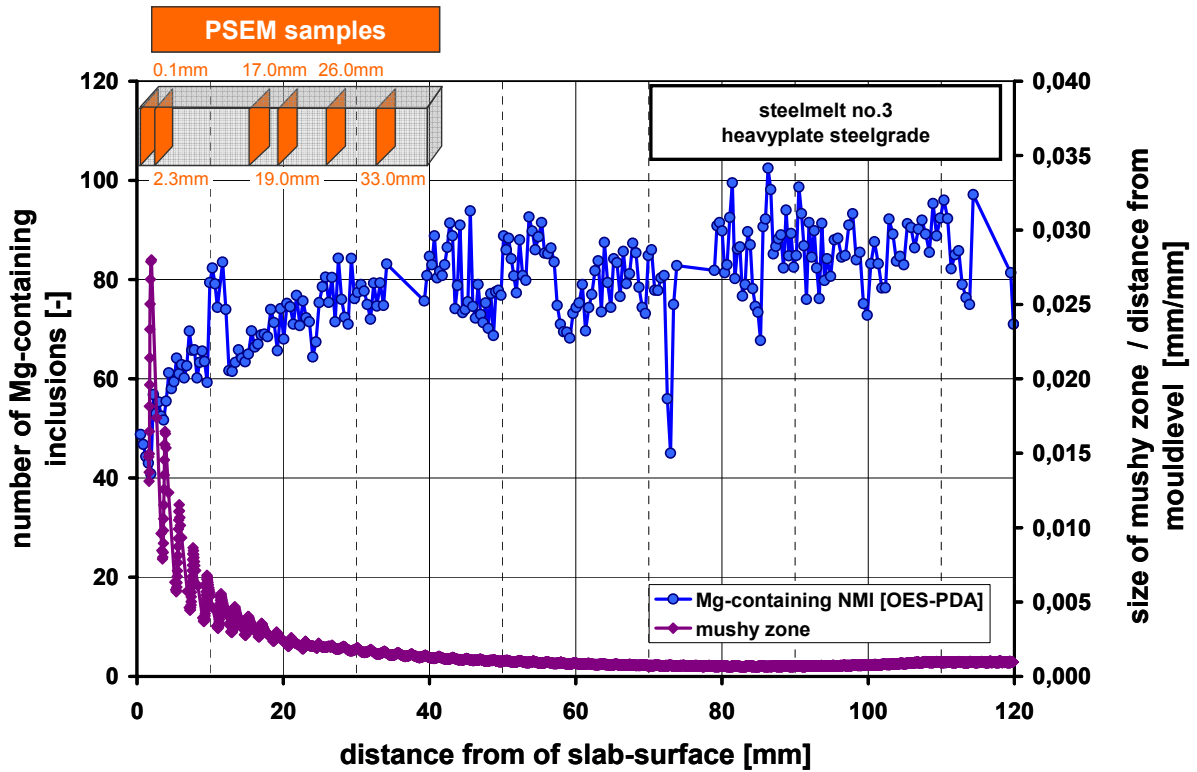


Figure 4: Mg-containing inclusions compared to the calculated solidification interval of the slab

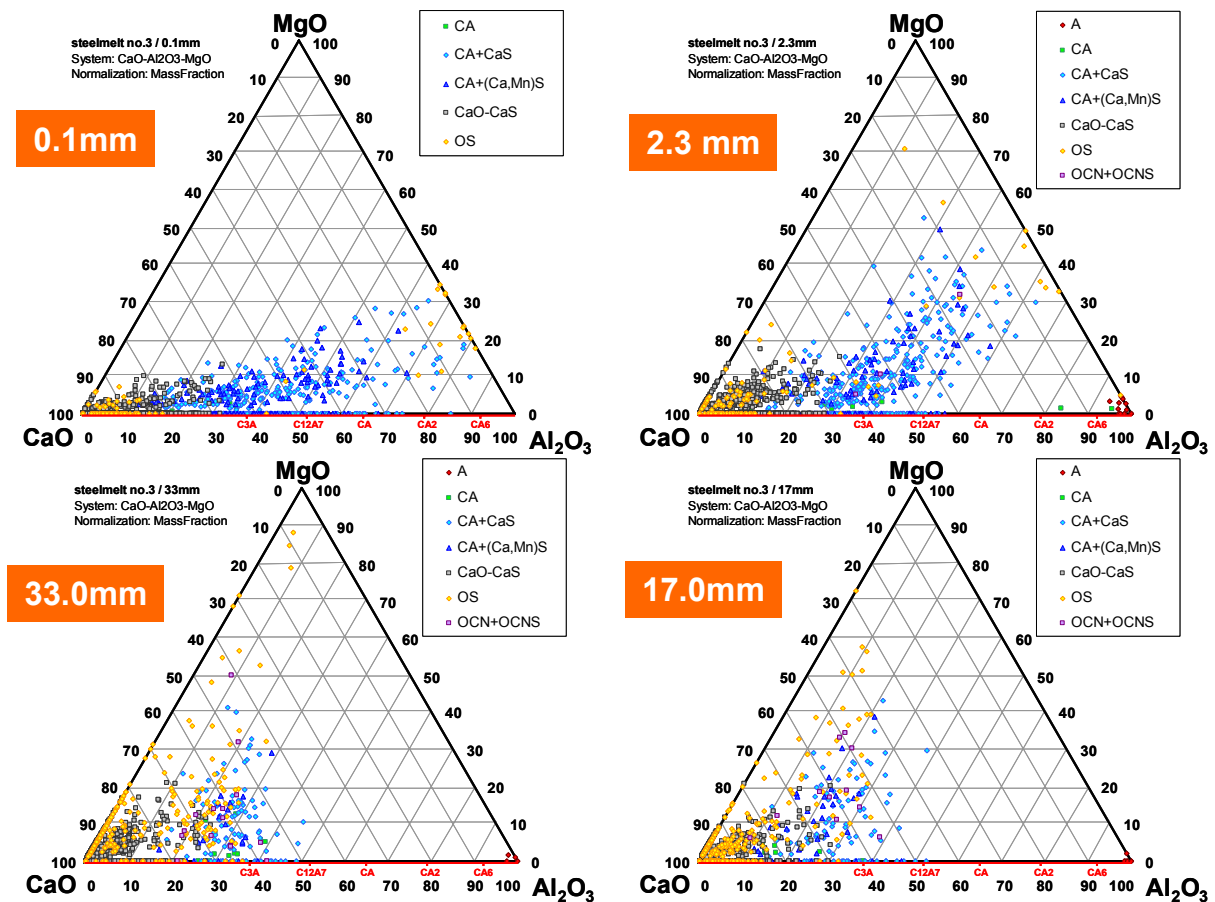


Figure 5: Continuous increase of Mg content in inclusions as dependent on the shell thickness of the slab [PSEM]

5. Conclusion

It has been verified that Mg is absorbed in liquid steel as a result of calcium treatment in the molten steel heat. The magnesium is introduced during reduction with the calcium from various sources in the steel teeming ladle (refractory material or slag). OES-PDA measurement is an important tool in describing MgO precipitation and agglomeration processes during controlled solidification in the continuous casting line. These effects were demonstrated for the first time by a combination of automated inclusion analysis. Determination of a reproducibility factor, here Mg content, between volumetric and surface-based measurement methods forms the basis for comparisons of the measured results. The analyses in this study provide the largest-possible source of information on a slab sample. The newly gained information represent a substantial contribution to our understanding or complex morphological changes in microscopic inclusions. The form in which Mg occurs in liquid steel was not clarified and advances a sophisticated challenge to later analysis. Future TEM analyses will focus on the analysis of sub-microscopic MgO inclusions in more detail. Laboratory investigation can maybe help to identify the source of magnesia under isolated conditions.

References:

- 1) Process based steel cleanliness investigations and rapid metallurgical screening of inclusions by modern PDA techniques; RFCS Project RFS-PR-06036
- 2) Jung, I.H., S.A. Deckerov and A.D. Pelton: Computer applications of thermodynamic database to inclusions engineering, ISIJ, Vol.44, No.3, 2004, 527-536
- 3) Costa e Silva, A.: Calcium and magnesium thermodynamics in steel and its impacts on secondary steelmaking: a computational thermodynamics approach, ATS International Steelmaking Conference, Paris, 2007
- 4) Otha, H., H. Suito: Deoxidation equilibria of calcium and magnesium in liquid iron, Metallurgical and Materials Transactions B , 25B, 1997, 235-244
- 5) Nadif, M., C. Gatellier: Influence of calcium and magnesium content on the solubility of various non-metallic elements in liquid steel, Revue de Metallurgie, no.83, 1986, 377-394
- 6) Seo, W.G., W.H. Han, J.S. Kim and J.J. Pak: Deoxidation equilibria among Mg, Al and O in liquid iron in the presence of MgO·Al₂O₃ spinel, ISIJ International, Vol. 43, No. 2 , 2003, 201–208
- 7) Fuji, K., T. Nagasaka and M. Hinoi: Activities of the constituents in spinel solid solution and free energies of formation of MgO, MgO·Al₂O₃; ISIJ International, Vol. 40, No. 11, 2000, 1059–1066
- 8) Okuyama, G., K. Yamaguchi, S. Takeuchi and K.I. Sorimachi: Effect of Slag composition on the kinetics of formation of Al₂O₃-MgO inclusions in aluminum killed ferritic stainless steel; ISIJ International, Vol. 40 (2000), No. 2, 121–128
- 9) Jansson S., V.Brabie and P.Jönsson: Magnesia-Carbon refractory dissolution in Al-killed low carbon steel, Ironmaking and Steelmaking, Vol33, Nr.5, 2006, 389-397
- 10) Frank, L.A.: Castability – from alumina to spinels, I&SM, April, 1999, 33-39.

RAPID INCLUSION MAPPING TECHNOLOGY FOR SLAB SAMPLE

Yong-Tae Shin*, Chang-Woo Reeu**

* POSCO Technical Research Laboratory, Rolling & Instrumentation Research Group
699, Gumho-dong, Gwangyang-si, Jeonnam, 545-090, Korea

** POSCO Technical Research Laboratory, Rolling & Instrumentation Research Group
1, Goedong-dong, Nam-gu, Pohang, Gyeongbuk, 790-300, Korea

Abstract

In order to develop new manufactured goods of steel, we applied the new inclusion analysis system to new steel making process. Many non-metallic inclusions in steel making process are generated. Because the non-metallic inclusions are very harmful in steel, steel makers try to remove the inclusion in steel. During our effort to remove inclusions in steel, the new inclusion analysis technology has been developed. The characteristics of the new system are to analyze inclusion rapidly and to acquire more inclusion information of steel. We applied this system to improve steel making process. The performance of our developed system has been estimated very excellent. Not only inclusion index information but also inclusion nonhomogeneity information for slab sample size, [100 x 50] mm was measured by the new method. The system has been applied to RH and VTD (Vacuum Tank Degasser) process in steel making process. More high graded quality slabs are produced by the improved steel making process.

1. Introduction

Currently rapid analysis method for inclusion map in steel using the PDA_OES is studied. This method is convenient to analyze inclusion distribution for large area sample rapidly. The new method for inclusion determination had been developed by our research team using PDA_OES in 1998 and the system has been upgraded step by step. We developed the system to measure inclusion distribution of slab sample. According to the characteristics of the continuous casting process in steel industries, inclusions are found at transverse edges of hot-rolled steel products frequently. When making pipes, these inclusions sometimes cause a weakness at the welded area. A rapid inclusion map measurement system is required to verify the occurrence of inclusions by the precise measurement to samples of transverse edges of slab. However, until recently, we had no measurement technique to determine the interior cleanliness of a slab. So we developed the system to determine cleanliness, OASIS (OES Analysis System for Inclusion & Segregation mapping). OASIS to evaluate the purity of a steel slab sample, size [100x50] mm of the surface, causing sequentially electric sparks, analyzing the plasma spectrum, can generate the map of inclusions automatically. OASIS consists of OES (Optical Emission Spectroscopy), SPSA (Sample Positioning & Scanning Apparatus), SSMM (Sample Surface Milling Machine), ISP (Inclusion Signal Processing) and data server. The information of size distribution and inclusion area is provided by OASIS software. Inclusions are classified for several kinds of steel. In the steel making process for pipe steel, it is important to reduce alumina inclusion in steel. Alumina inclusions in steel making process are well generated. But total quantity of inclusion is being reduced and cleanliness of steel is being improved by our efforts. Pipe steel is high cleanliness steel and is sensitive to the Al_Mg oxide inclusion in steel. We do not allow a few inclusions in pipe steel. Therefore size and a number of inclusions in pipe steel should be reduced during the steel making process. The quality level of steel product in the steel making industry is being changed from low-grade to high-grade rapidly. The need of process optimization for the production of clean steel has driven the development of this method for rapid determination of micro-inclusion characteristics. The steel product' quality is decided by steel making process, to remove ingredients and inclusions in molten steel are mainly. In particular, we can select the optimum process by comparing relationship between the steel making processes (LF, RH, VTD) and the occurrence of inclusions. In the past, we could not obtain the information about inclusion which was included in a slab, but in the present we can obtain information about inclusion in a slab using the developed system. We

applied to several kinds of steels at steel making process using the data information of OASIS system and we acquired good results.

2. Experimental work

2-1. Overall Architecture of OASIS

Figure 2-1 shows the overall architecture of OASIS and Figure 2-2 shows sampling position for a slab. It was developed to evaluate cleanness of metals. its components and main functions are as follows.

- (1) OES (Optical Emission Spectroscopy) : This device obtains the light intensity on the surface of a sample by generating electrical sparks according to the specific wavelength of each element.
- (2) SPSA (Sample Positioning & Scanning Apparatus) : Analysis samples should be moved to the OES stand according to the scheduled work orders and placed to the appropriate location on the OES stand. This apparatus controls the robot arms to move the analysis sample.
- (3) SSMS (Sample Surface Milling Machine) : The milling machine treats the surface of analysis sample to provoke sparks.
- (4) ISP (Inclusion Signal Processing) : This converts OES spectral analog signal generated by sparks to digital signal. To calculate the type and the size of inclusions, appropriate algorithms are adopted. And final data of inclusion map is stored at the data server.
- (5) Data Server : Its functions include storing inclusion map data generated by ISP, searching, and retrieving. And also it performs verifying user identification, managing user identification, deploying user application program, etc.

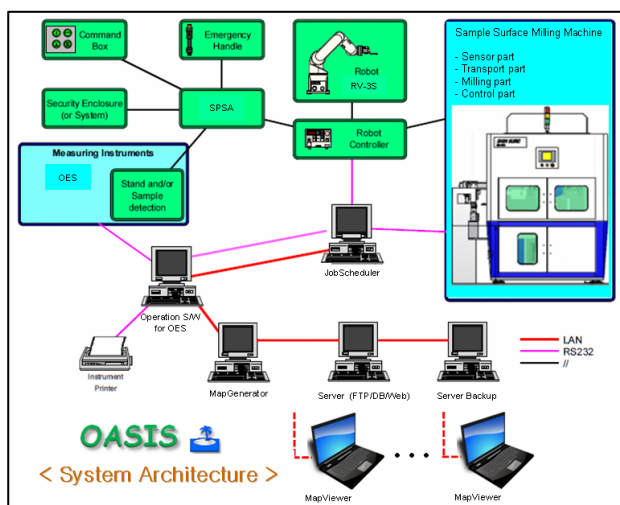


Figure 2-1 The overall architecture of OASIS

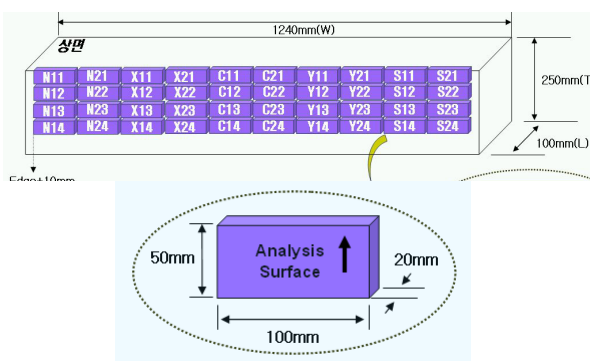


Figure 2-2 Sampling position for a slab

2-2. Procedures of Cleanness Analysis

Once the samples to be analyzed are prepared, you can schedule the analysis job orders and the analysis method using SPSA. The system automatically runs the analysis job based on scheduled job sequence, controls SSMM, OES and IMG (Inclusion Map Generator) to continue its order. When it is completed, the result information can be retrieved by using IMV (Inclusion Map Viewer).

2-3. Deriving Analytical Information

Figure 2-3 shows a picture of sample surface after damaged by sparks. In the picture, you can check spark damaged pattern. Figure 2-4 shows an example of analysis result report, it can be searched by analysis job order.

In Figure 2-5, you can see the inclusion map in case of less distributed at (a), and in case of Many distributed at (b). Figure 2-6 shows an example of three-dimensional analysis map. The same sample is analyzed after milling in the direction of sample thickness.

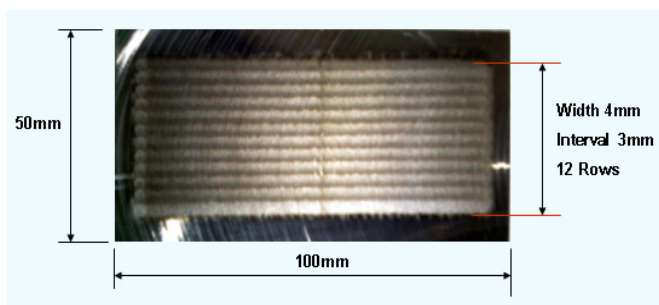


Figure 2-3 Picture of sample surface after damaged by spark

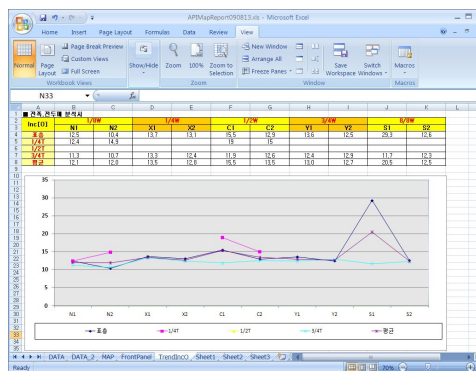
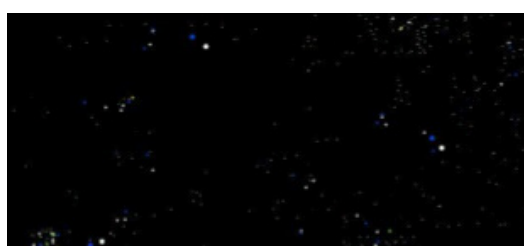
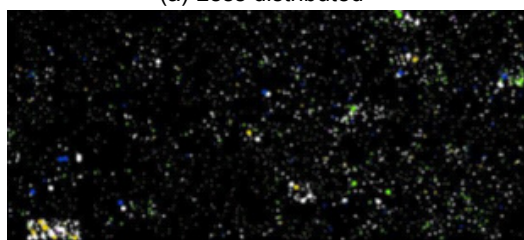


Figure 2-4 Report file of analysis result



(a) Less distributed



(b) Many distributed

Figure 2-5 Examples of Inclusion map

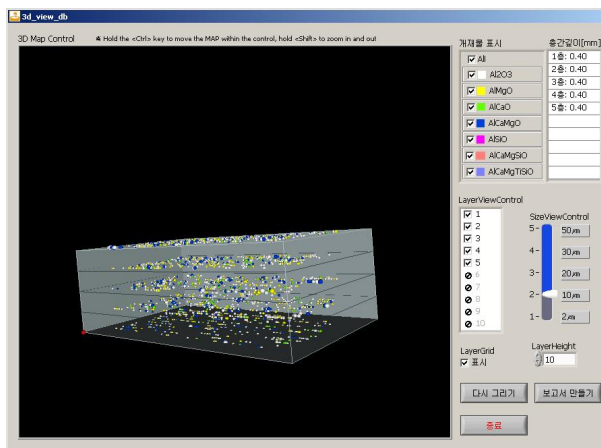


Figure 2-6 An example of 3-D inclusion map

2-4. Performance of the device

Quality control of product was to take the advantage of OASIS, rating cleanness of steel sample in order to quickly assess the sample size. [100x50] mm with the following features for steel production field. The main features and functions are as follows. Analysis results provide information about the sample, content of complex inclusions and composition (Al_2O_3 , $AlMgO$, $AlCaO$, $AlCaMgO$, $AlSiO$, $AlCaMgSiO$, $AlCaMgSiTiO$, etc.), size distribution of complex inclusions (<2 , $2\sim5$, $5\sim10$, $10\sim20$, $20\sim30$, $30\sim40$, $40\sim50$, >50 [μm] / [μm^2] / each), oxygen index of inclusion [ppm], area of inclusions [μm^2], Nonuniform of analysis sample, etc. In addition to the functions of the system, it provides calibration settings and lookup functions (1st, 2nd, etc.), map view function according to the size selection ($>2 \mu m$, $>10 \mu m$, $>20 \mu m$, $>30 \mu m$, $>50 \mu m$), size distribution view of Al family, size distribution view of Si family, signal view according to the selection of element, map view according to the selection of complex inclusion type, DB data view, section view, 3D view, etc.

3. Results

3-1. Cleanness determination application for pipe steel slab

Figure 3 shows mapping data for [N11], [N21], [N12], [N22] 4 slab samples through the conducted experiments. The steel making process during the experiments is [LF] and [RH], the stopper is made from [MC type] material during the continuous casting. The ingredients of the MC type stopper are consisted of Mg oxide and some other

materials. In this case, many inclusions in all around detection areas are found and the oxygen index is high also. We can know that the Al_Mg oxide inclusions are appeared in a slab because of using the stopper material in continuous casting process.

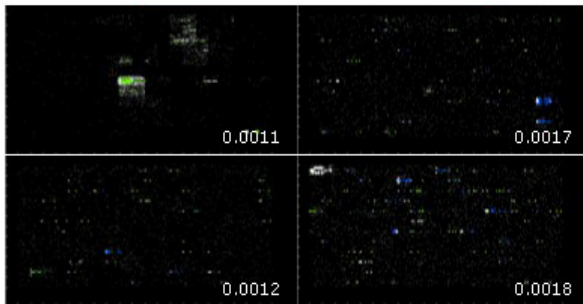


Figure 3 Inclusion map by [LF] + [RH] process, [MC] type stopper

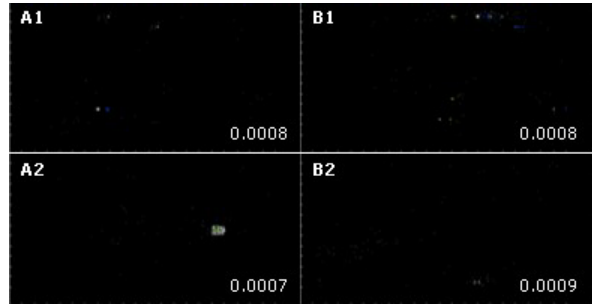


Figure 4 Inclusion map by [RH] + [VTD] process, [AB] type stopper

Figure 4 shows mapping data for [N11], [N21], [N12], [N22] 4 slab samples through the conducted experiments. The steel making process during the experiments was [RH] and [VTD], the stopper is made from [AB type] material. The ingredients of the AB type stopper are consisted of Aluminum oxide and other materials. In this case, only a few inclusions in all around detection areas are found and the oxygen index is low also. We can know that the Al_Mg oxide inclusions are not appeared in a slab during the continuous casting process. Total inclusion quantity is reduced during this process improvement. This pipe steel is vulnerable material to inclusion. If steel has many inclusion in slab like Figure 3, then steel can not be used after manufacturing pipe. The pipe will be destroyed by high petroleum pressure because crack in welding zone will be generated by HIC(Hydrogen Induced Crack). However, If clean steel is made without inclusion like Figure 4, we can make steel for pipe.

3-2. Cleanness determination application for automobile steel slab

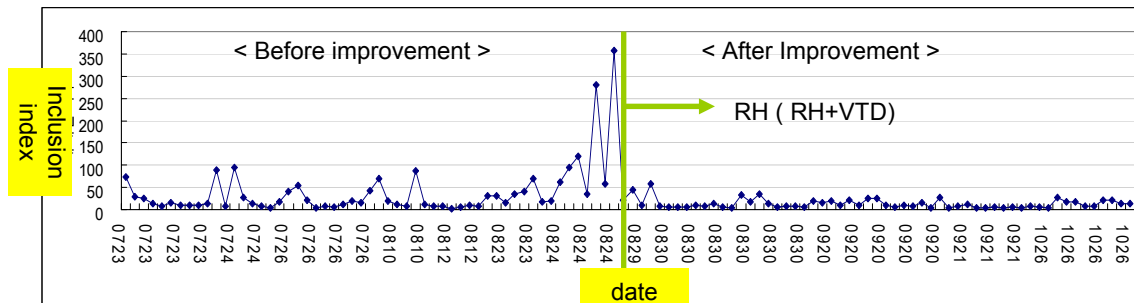


Figure 5. Change of inclusion index on each processes

Figure 5 shows the cleanness index to the automobile steel slab relationship between before and after improvement. In steel making process, before improvement only [RH] treatment is processed. But after improvement, [RH] and [VTD] treatment are processed. We can find rapidly that the cleanness index for the automobile steel slab was improved by the OASIS system.

$$[\text{inclusion Index}] = \text{function of } [\text{Inclusion oxygen quantity, Inclusion nonhomogeneity, number of inclusions in excess size } 20 \mu\text{m}] \quad (1)$$

$$[\text{Inclusion nonhomogeneity}] = [\text{the standard deviation}] \text{ for inclusion area values} \quad (2)$$

Equation (1) shows the definition of inclusion index and inclusion index is a fuction of inclusion oxygen quantity, Inclusion nonhomogeneity and a number of inclusions in excess size 20 μm. Equation (2) shows the definition of

inclusion nonhomogeneity. Figure 5 shows that steel making process is changed from [RH] in Single Process to [RH + VTD] process, the inclusion index can be seen that far smaller.

Figure 6 shows the inclusion distribution map of the before and after improvement. We can see that the quantity of inclusion is reduced after improvement. Level of Inclusion nonhomogeneity is reduced from 254 to 78 and inclusion index is reduced from 62.1 to 8.

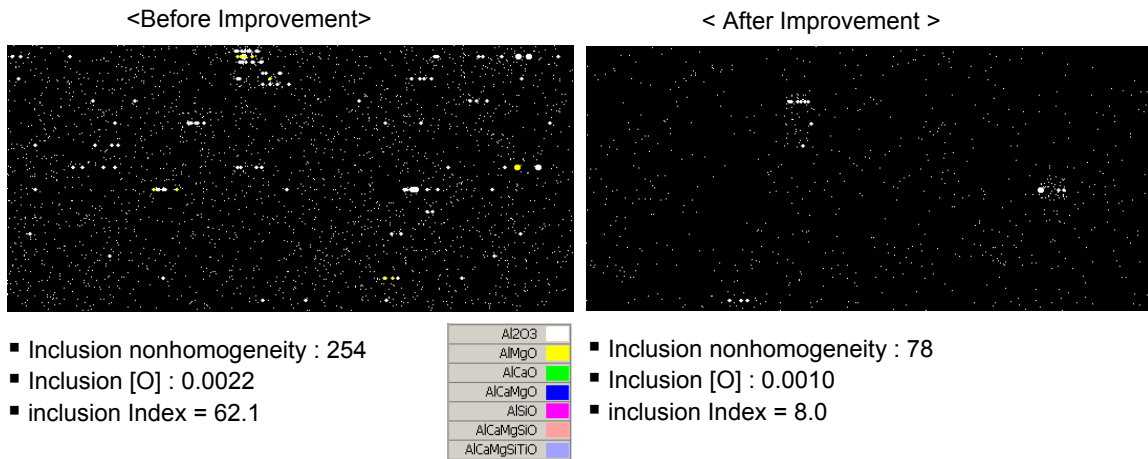


Figure 6 Change of Inclusion Map for process relationship before and after improvement

3-3. Quality Improvement application for the molten steel flow

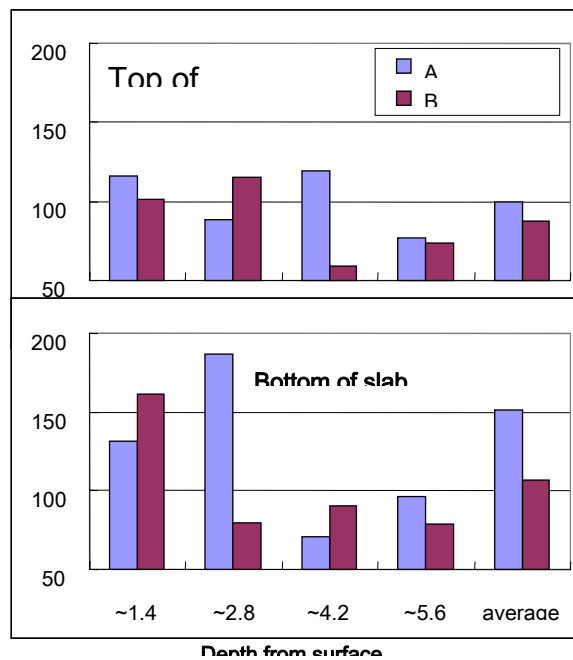


Figure 7 Change of Inclusion nonhomogeneity toward depth

Figure 7 shows the change of inclusion nonhomogeneity through the change of molten steel flow in Mold. The bar A in Figure 7 is presented inclusion nonhomogeneity in EMLS condition of current 340[A] and the bar B in Figure 7 is presented inclusion nonhomogeneity in EMRS condition of current 550[A]. We can see that the bar B about the average of inclusion nonhomogeneity is lower than the bar A about the average of inclusion nonhomogeneity. Inclusion nonhomogeneity to bottom surface for slab is higher than top surface for slab. Inclusion nonhomogeneity of bar A is 151 and bar B is 107 each in bottom of slab. Especially Inclusion nonhomogeneity is high in 2.8mm depth from surface and Inclusion nonhomogeneity is high at EMLS condition. From these data, we can know that inclusions are concentrated in the surface layer part of slab.

4. Conclusion

We developed new inclusion map detection system for slab sample. The performance of the system was very effective to analyze characteristic of inclusion after test of continuous casting process and steel making process. Slab samples are prepared like follow. The thickness of the cross section of slab is divided by 4 parts : surface part, quarter part, half part and 3 quarter part. The width of slab is divided by 8 parts : S11, S21, X11, X21, C11, C21, Y11, Y21, N11 and N21. Analysis area of slab sample is [100 x 50]mm and analysis time of slab sample is about 30 minutes. The inclusion distribution of quarter part toward thickness in slab' cross section is more concentrated than other parts. The inclusion distribution of edge, 1/4 width and center part toward width in slab' cross section is more concentrated than other parts. The Al_Mg oxide inclusions are reduced by [RH] and [VTD] process for pipe steel and we can know that it is kept down to generate inclusion in combined [RH] and [VTD] process for automobile steel. But, the combined [RH] and [VTD] process can not be adapted in other kinds of steel because of no experience. However, we will try to adapt this efforts to other kinds of steel using the OASIS system.

References

- 1) F. Reinholdssen, A. Lind, R. Nilsson, P. Sjodin and P. Jonsson, ISIJ International, Vol. 37 (1997), No.6, p 637 - 639.
- 2) H. Falk, P. Wintjens, Spectrochemica Acta part B 53 (1998) p 49 - 62.
- 3) P. Eggimann, Steel Times International, May (1999), p 46 - 48.
- 4) Y. T. Shin and J. S. Bae, IMTC2003 Instrumentation and Measurement Technology Conference, May 2003, p1583.
- 5) Y.T. Shin, C.W. Reeu, KACC2009, BEXCO Busan, Sep. (2009).
- 6) "Mitsubishi Industrial Robot, RV-3S / 3SJ / 3SB / 3SJB SERIES Manual", Mitsubishi Industrial Robot.

ADVANCES IN THE ULTRA-FAST INCLUSION ANALYSIS IN STEEL BY SPARK OES – PHENOMENOLOGY, IMPROVEMENTS AND CALCULATION OF INCLUSIONS' COMPOSITION AND SIZE

Dr. Jean-Marc Böhlen, Dr. Kaizhen Li, Dr. Jean-Luc Dorier and Edmund Halász

Thermo Fisher Scientific, En Vallaire Ouest C, CH-1024 Ecublens, Switzerland

ABSTRACT

Inclusions analysis with Spark-DAT has become popular in the steel industry, and numerous companies now routinely use it. The main reasons for this success are its analysis speed that allows using it for inclusion control during the steel elaboration process and the negligible extra costs compared with standard spark OES elemental analysis.

With Spark-DAT the raw signal intensities from the elements of inclusions generated during each single spark individually are acquired and converted with the aid of mathematical algorithms into information of interest.

Recent developments and improvements, made in the light of research work allowing a better comprehension of the phenomena related to the sample ablation by the electrical spark, make Spark-DAT even more attractive than before:

- A new statistical principle is used in the algorithms. It allows detecting smaller inclusions, more inclusions being therefore detected
- The same principle also allows better quantifying the soluble/insoluble parts of various elements
- The combined inclusion and elemental analysis is faster than before by 6s, being now performed in barely more than the time necessary for the simple elemental analysis. This is a very important result, because the time needed for combined analysis is now acceptable in most of the contexts of use of the OES instrument
- A novel type of algorithm allows quantifying the average concentration and Equivalent Spherical Diameter (ESD) of various types of inclusions commonly found in steels. The algorithm enables the measurement of the concentration of an element present in a specific type of inclusion by using single spark intensity analysis of the channels measuring the elements forming oxides, sulfides, nitrides or others, such as Al, Ca, Mg, Mn, Ti, Si, etc. The average ESD is then calculated based on the average mass ablated by a single spark and the composition stoichiometry of the inclusion.

Phenomena taking place during the spark ablation process are shown in the presentation. The new developments and improvements are explained and illustrated with examples, demonstrating the extraordinary potential of Spark-DAT for inclusion analysis.

INTRODUCTION

Progress has been made in the ultra-fast inclusion analysis in solid steel samples with the Thermo Scientific ARL 4460 OES spectrometer with Spark-DAT option [1]. Recent methodological and algorithmic developments increase the attractiveness of Spark-DAT and further extend the capability of the OES instrument [2]. The new Spark-DAT-based methods are faster, have better performance and are capable of performing new types of OES determinations, like the quantitative inclusion size analysis and the quantitative analysis of the total oxygen content at concentrations lower than 30ppm.

PRINCIPLES

Spark-DAT is a package composed of acquisition hardware, software and specialized algorithms included in OXSAS analytical software. With Spark-DAT the single intensity values that are generated by typically two thousands single sparks are acquired separately on the optical channels of inclusion elements. Since the Spark-DAT raw dataset is large and complex, fast algorithms are used to calculate the values corresponding to the information of interest. These values can then be handled like conventional OES results by the analytical software OXSAS (e.g. displayed, printed, stored, transmitted, etc.).

The intensity of a Spark-DAT signal depends on the composition of the sample at the position struck by the corresponding single spark. If the concentration of an element in the ablated sample material is significantly higher than the concentration of its soluble form in the matrix, the outcome is an intensity peak. This is typically the case when a spark hits a sample area containing an Al based inclusion (e.g. Al_2O_3), because the Al concentration is much higher than in the metal matrix due to the contribution of the inclusion (Fig. 1). For example, the concentration of Al in an Al_2O_3 particle is $\sim 53\%$, and if an inclusion with a size of $5\ \mu\text{m}$ ESD (Equivalent Spherical Diameter) is contained in the ablated sample material, an apparent rise in the concentration of 0.075% is observed.

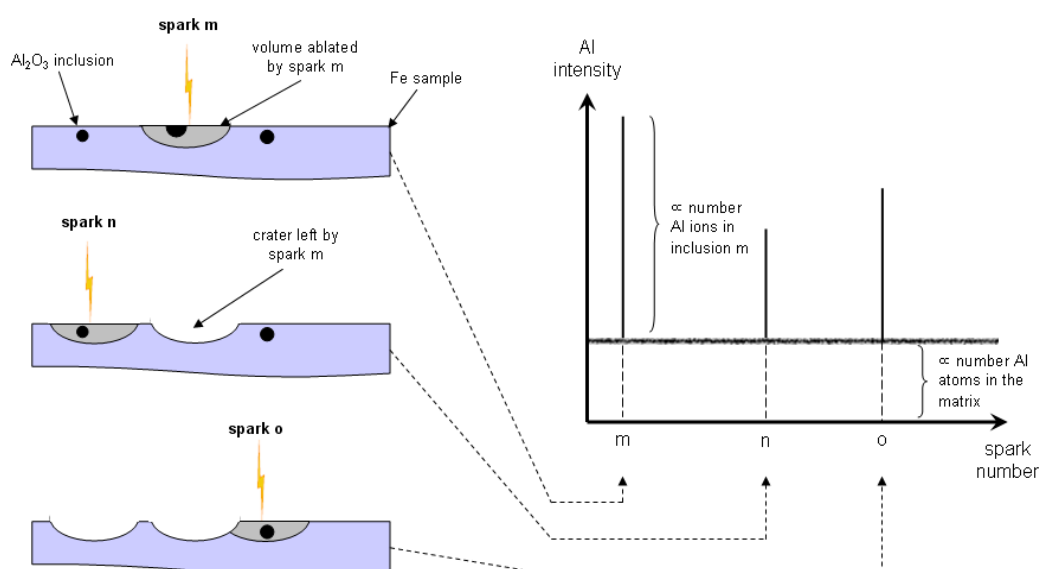


Fig. 1. Principle of Spark-DAT illustrated for a steel sample containing Al_2O_3 inclusions. Three sparks m, n and o striking inclusions of different sizes give rise to Al intensity peaks, due to the high Al concentration in the inclusion.

The intensity of the baseline signal is proportional to the concentration of Al atoms dissolved in the matrix and the intensity of a peak depends on the amount of Al atoms contained in the inclusion(s) ablated by a single spark. Consequently, the number of peaks is related to the number of such inclusions and their intensity to such factors as the inclusion size and the concentration of Al in the inclusion.

PRACTICAL DETAILS

Analysis time: inclusion analysis can be performed stand-alone in about 7s for a single measurement. However, full benefit is obtained when combined with the analysis of the elemental concentrations. The sequence allowing this combined analysis was recently improved and the time necessary for a single measurement was decreased

from 29s to 22s, making inclusion analysis even more attractive than before in the context of production, where costs significantly depend on analysis time. Note that the time needed for the combined analysis is only 3s longer than the standard OES analysis.

Sample preparation: the standard OES sample preparation can be used for Spark-DAT inclusion analysis. However, with paper grinding, the paper should be chosen in order to avoid any influence on the analysis of the inclusions of interest (e.g. using SiC paper when Al_2O_3 inclusions have to be analyzed). For advanced, quantitative Spark-DAT applications, milling is advisable.

EXAMPLES OF INCLUSIONS QUANTIFIABLE WITH SPARK-DAT

Various types of endogenous and exogenous inclusions may be observed in steel with the ARL 4460 equipped with Spark-DAT, e.g. oxides (Al_2O_3 , MgO, CaO, MnO, TiO_2 , SiO_2 ...), spinels (Al_2O_3 -CaO, Al_2O_3 -MgO...), sulfides (CaS, MnS, AIS...) and others.

The detection of an inclusion type is limited mainly by the sensitivity of the analytical lines used, by the size of the inclusion and by the concentration level of the inclusion elements as soluble elements in the matrix: higher line sensitivity and lower soluble content allow determining smaller inclusion ESD's. For example for a steel containing 50ppm of Al the minimum detectable ESD is about $1\mu\text{m}$, while for 0.2% of Al it is $4.5\mu\text{m}$.

BENEFITS

The main benefit of the fast combined analysis is that inclusion analysis is possible during steel elaboration on most of the samples analyzed normally by OES. Other important benefits of using Spark-DAT inclusion analysis are:

- Low investment costs, the spectrometer being capable of performing inclusion analysis in addition to analysis of elemental concentrations
- No additional cost and time for operations compared to the standard OES spectrometer. Maintenance, service, consumables and sample preparation remain the same as for standard OES
- Quantitative inclusion size determinations
- Quantitative determination of the total oxygen content in killed steels

NUMBER AND TYPE OF INCLUSIONS

The algorithm **Peaks** allows the evaluation of the number of inclusions by counting intensity peaks on the channels of elements present in inclusions. A peak is defined as an intensity signal I_{peak} higher than a threshold situated at the mean intensity m of the element dissolved in the matrix plus three times its standard deviation SD:

$$I_{\text{peak}} > m + 3 \cdot \text{SD}_{\text{Imatrix}}$$

Steel samples can easily be classified as clean or dirty according to the number of peaks counted on the channels of the inclusion elements (Fig.2).

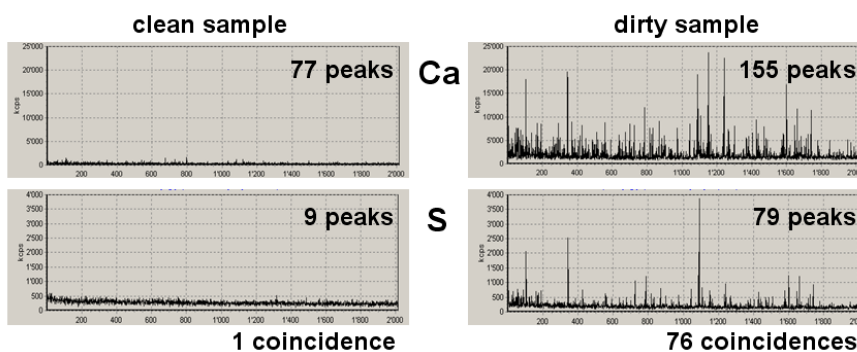


Fig. 2. Comparison of the spark intensity diagrams of Ca and S obtained for a clean and a dirty sample. Intensity peaks were counted with the algorithm *Peaks* and peak coincidences with the algorithm *Composition*.

The algorithm *Composition* allows counting coincidences of peaks, i.e. peaks appearing on the channels of several elements concurrently during the same single spark, as illustrated in Fig. 2. The coincidence of a peak on Ca and S channels means that these two elements are part of the same inclusion, very often a calcium sulfide inclusion. Coincidences of up to four channels can be counted with this algorithm. This enables the chemical formulation of complex inclusions or inclusion clusters. Furthermore, the possibility to check for non-coincident elements in addition to coincident ones helps removing ambiguities between inclusions that have close composition, like Al_2O_3 and Al_2O_3 -CaO or CaO and Al_2O_3 -CaO (Fig. 3).

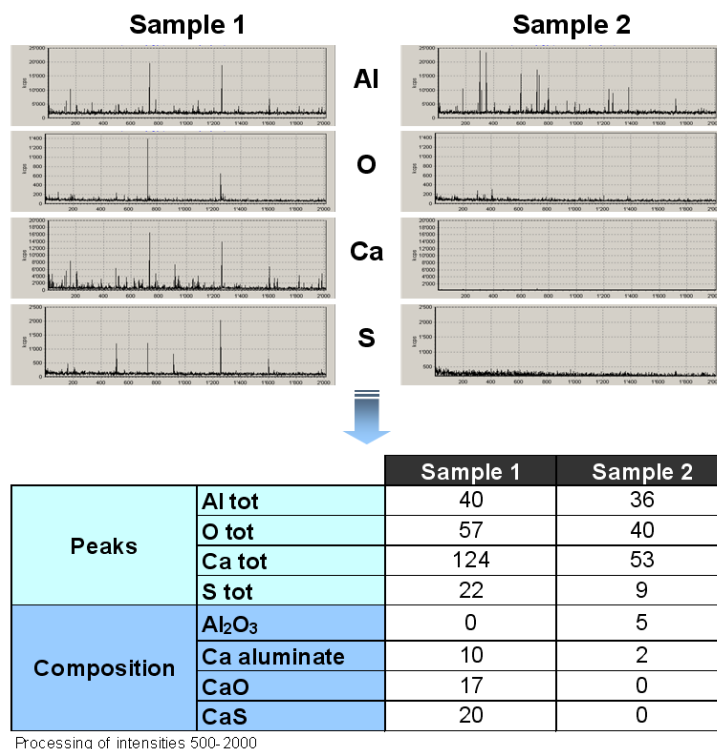


Fig. 3. Application of algorithms *Peaks* and *Composition* for the analysis of two low alloy steel samples of the same grade.

QUALITATIVE INCLUSION SIZE ANALYSIS

Knowing the size of the inclusions and more precisely their size distribution is important, since large inclusions are normally more detrimental to the metal quality. The algorithms *Peaks* and *Composition* can be used in order to count inclusions (signals) belonging to different size (intensity) classes. Setting the threshold 3-SD above the intensity of the element in the matrix allows the counting all the inclusions that are large enough to be detected. Setting it higher, for example at 9 or 15-SD like in Fig. 4, allows us counting inclusions with larger size.

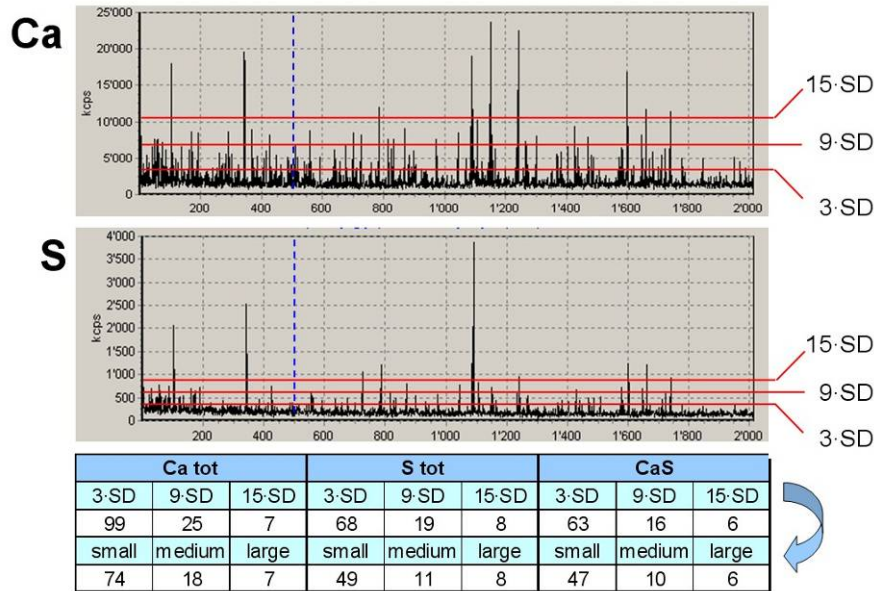


Fig. 4. Count of inclusions in intensity classes. The numbers of intensity peaks and peaks coincidences calculated with thresholds at 3, 9 and 15-SD allow calculating the numbers corresponding to small, medium and large inclusions.

Calculating the inclusions between consecutive threshold values provides the number of inclusions in the size class that they delimit. In the example, the number of peaks and coincidences between 3 and 9-SD correspond to small size inclusions, between 9 and 15-SD to medium size inclusions and higher than 15 to large size inclusions. Such calculations are possible with more than three size classes. This allows generating inclusion size distributions diagrams that are qualitative, but can be extremely useful for example in order to compare the inclusion distributions in samples of different heats.

QUANTITATIVE INCLUSION SIZE ANALYSIS

Traditionally, inclusion sizes are determined by techniques such as optical microscopy and scanning electron microscopy (SEM/EDX). However, the methods are time-consuming, taking typically 2-4h per analysis in a very competent laboratory.

The algorithm **QuIC** (**Q**uantification of **I**nclusion **C**ontent) enables quantitative analysis of inclusions in terms of size and size distribution. With *QuIC*, average ESDs of different inclusion types and size classes may be calculated. Fig. 5 presents an example of size distribution diagram of Al₂O₃, based on the application of the *QuIC* algorithm and size calculation method for several production samples.

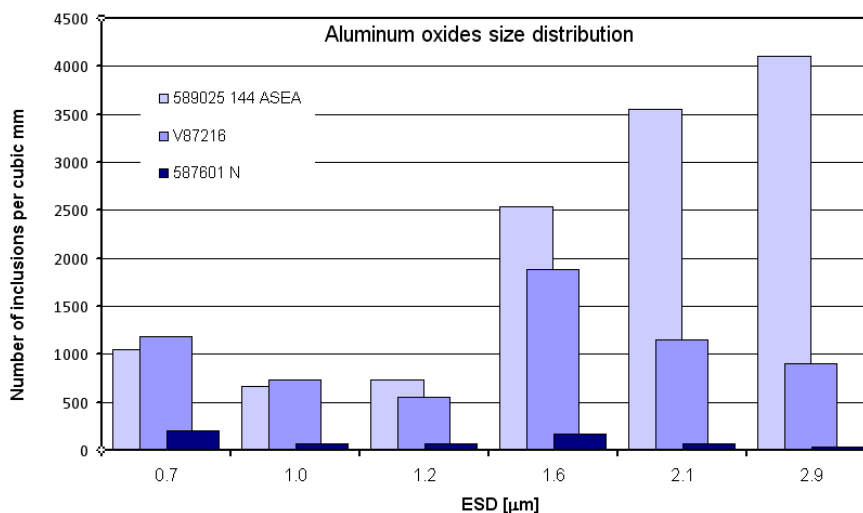


Fig. 5. Size distribution diagram of Al_2O_3 in three low alloy steel samples built up from the results of the algorithm *QuIC*. The horizontal axis represents the average ESD and the vertical axis represents the number of inclusions per cubic mm.

Other parameters like the area fraction of a given inclusion type and the total oxygen content (Fig. 6) can also be calculated from the results of the algorithm *QuIC*.

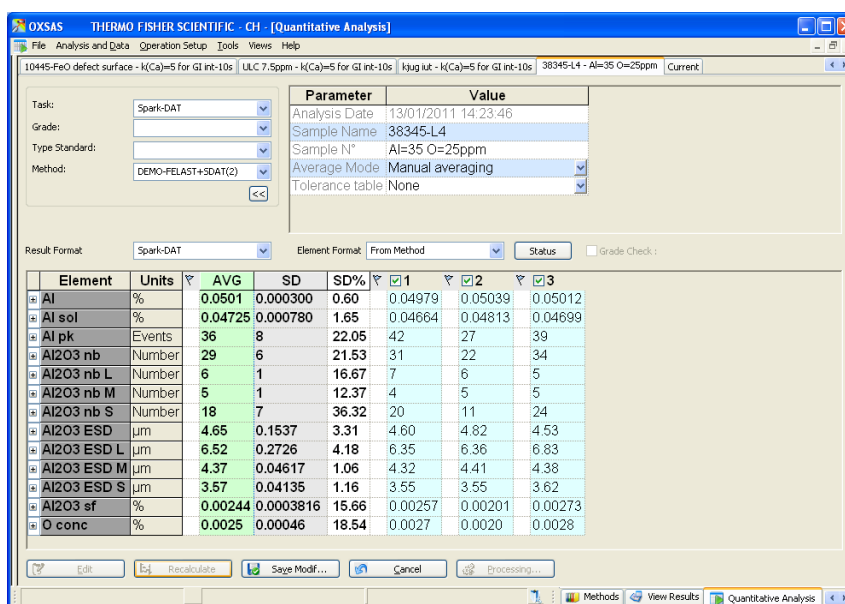


Fig. 6. Analysis screen in OXSAS, with the display of the results of a combined analysis (3-measurements). The elements represent from top to bottom: total and soluble Al concentrations, number of Al peaks, total number, number of large, medium and small Al_2O_3 inclusions, and the corresponding average ESD's, Al_2O_3 area fraction and total oxygen content.

QUANTITATIVE DETERMINATION OF TOTAL OXYGEN CONTENT

Due to the relatively low sensitivity of the analytical line, the standard routine quantitative analysis of total oxygen by OES is still only semi-quantitative below 60ppm and very difficult below 30ppm. In the steel industry, oxygen at very low concentration is therefore normally analyzed using dedicated combustion analyzers.

In killed steels treated with the typical deoxidizers (Al, FeSi, FeMn and Ca, etc.) most of the oxygen is insoluble, more precisely in the form of oxide inclusions. With Spark-DAT the total oxygen concentration can therefore be calculated directly from the amount of oxygen contained in the oxide inclusions measured with *QuIC*. It is important to note that no oxygen optical line is necessary for this determination, which can therefore be referred to as **indirect oxygen measurement**. The method is quantitative and determines total oxygen content well below 30ppm, as demonstrated in Fig.7 and 8.

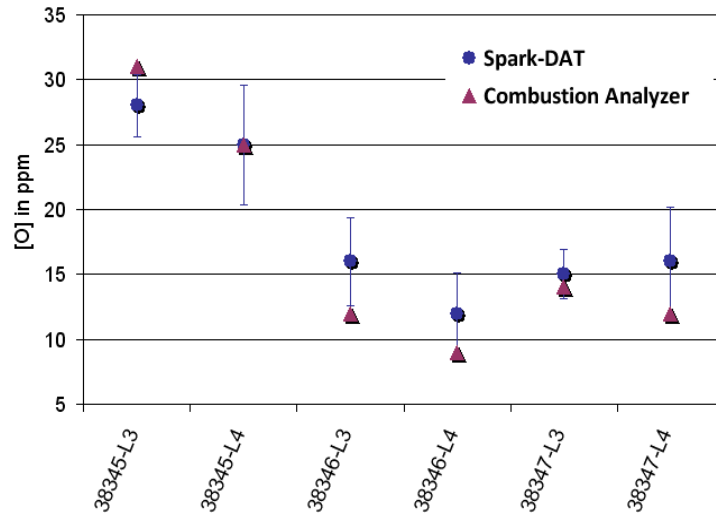


Fig. 7. Comparison of the results based on *QuIC* and those obtained by combustion analysis for low alloy steel samples taken in the continuous casting mould (samples and combustion results with permission of R. Dumarey and F. Medina, from ArcelorMittal, Gent).

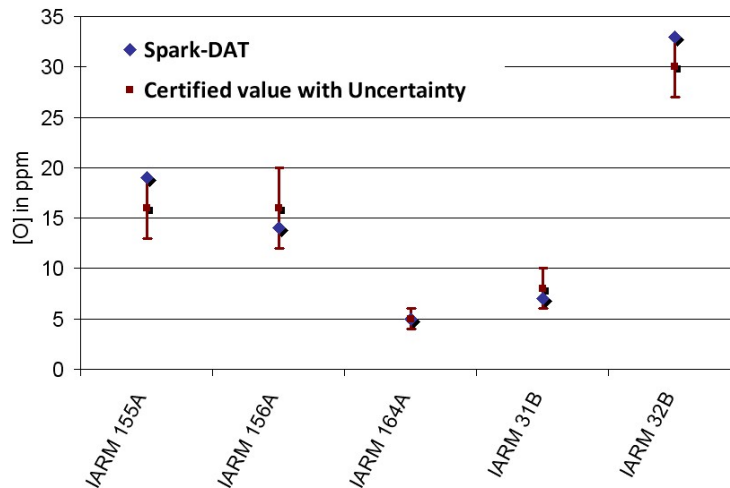


Fig. 8. Comparison of the results based on *QuIC* and the certified oxygen concentration in some low alloy steel reference materials.

CONCLUSIONS

The Spark-DAT option of the ARL 4460 metals analyzer increases the versatility of the OES spectrometer. From routine use to research, Spark-DAT provides quick, simple and cost-effective solutions for inclusion analysis in the steel industry. Among all the inclusions analysis techniques available today, the Spark-DAT based methods are the fastest. Spark-DAT allows ultra-fast on-line counting and identifying of inclusions, determining their size and total oxygen content in a time ranging from several seconds to a few minutes, making it highly effective for controlling inclusions and steel cleanliness during production. The sample and its surface preparation, as well as the instrument maintenance and consumables, are equivalent compared to a standard OES instrument, milling being required for quantitative analysis. This signifies extremely low operation costs compared to the other inclusions analysis techniques that need dedicated instruments. In addition, the ability to obtain elemental analysis information and inclusion contents with a single OES instrument reduces greatly investment and operating costs.

ACKNOWLEDGEMENTS

We are indebted to Rolf Didriksson from SSAB (Oxelösund) for enlightening (sparking) discussions. We acknowledge Ronny Dumarey and Frank Medina from ArcelorMittal (Gent) for extremely valuable help and discussions, and for giving permission to publish the results obtained on their samples.

REFERENCES

- [1] J.-M. Böhlen and R. Yellepeddi, "Combined quantitative analysis and ultra-fast analysis of non-metallic inclusions by optical emission spectrometry", Millenium Steel, 2009, p. 167-171.
- [2] K. Li, E. Halász and J.-M. Böhlen, "Analysis of inclusions in steel and aluminum with the ARL 4460 Spark-DAT – Recent improvements", Metallurgical Analysis, CCATM 2010 Conference Proceedings, Vol. 30, Supplement September 2010, p. 214-217.

STEEL CLEANNESS AND REFERENCE MATERIALS

Gunilla Runnsjö*, Arne Bengtson**, Miroslava Sedlakova** and Torbjörn Engkvist*

**Outokumpu Stainless AB, Box 74, SE-774 22, Avesta, Sweden*

***Swerea KIMAB AB, Box 55 970, SE-102 16, Stockholm, Sweden*

Abstract/ Summary

Several attempts to procure reference materials for assessment of steel cleanliness have been made over a long period of time without success in preparations with additions of synthetic non-metallic particles. The need for reference materials is increasing, especially in relation to refining of instrumental techniques such as OES-PDA and SEM-EDS.

In the present study a number of steel grades containing various inclusion types were chosen by steel companies as possible reference materials. Further, a few commercial, certified reference materials were included. The homogeneity of the material regarding inclusion forming elements was studied using OES and to some extent OPA (Original Position Analysis). The oxygen content was determined with the combustion method. SEM-EDS was used as a reference method for inclusion types and size distribution. Wet chemistry was the reference for insoluble and soluble species. A limited Round Robin was performed and it was realised that the demands in standardised certification (number of laboratories etc) cannot be met for inclusion reference materials. However, some of the materials can be defined as cleanliness reference materials with attached composition and inclusion parameter data.

The cleanliness data are discussed and a layout is presented.

This work is a part of RFCS project RAMSCI.

Introduction

Improved and faster methods for non-metallic inclusion assessment in steel have been developed in several projects. Of special interest are the fast spectrometric methods such as PDA-OES. However, any analytical method needs verification of the results. There has been a lack of suitable reference materials for verification of inclusion assessments. The present work comprises tests and evaluation of candidate reference materials for inclusions in steel. The materials represent a variety of steel grades and inclusion types. The statistical evaluation of results according to international standards is discussed and modified.

Experimental

A set of steels was procured representing various grades – low-alloy to high-alloy stainless steels - with various types of non-metallic inclusions. Some already existing certified reference materials were included.. The compositions, as stated by producers and in certificates, are shown in Table 1.

Table 1: Composition of the RM candidate materials, m%.

Material	C	Si	Mn	P	S	Al	Cr	Ni	Mo	Cu	N
52256	0,1580	0,271	1,384	0,014	0,0004	0,029	0,016	0,035	0,001	0,04	0,007
SE61-50	0,1670	0,337	1,529	0,011	0,018	0,063	0,027	0,028	0,005	0,014	0,005
Sid58504	0,51	0,35	0,95	0,023	0,023	0,028	1,09		0,06		0,009
V27	0,065	0,328	1,58	0,009	0,0010	0,032	0,019	0,013	0,003	0,012	
V28	0,023	0,005	0,20	0,009	0,0110	0,045	0,033	0,032	0,008	0,055	
VRM 22	0,140	0,262	0,23	0,008	0,0015	0,050	1,147	2,715	0,315	0,024	
Riva74933	0,35		1,17	0,013	0,022	0,02	0,2	0,05	0,02	0,18	
ECRM298-1	0,0146	0,262	0,398	0,0197	0,0006	0,0285	24,72	7,056	3,799	0,201	0,263
JK27A	0,0477	0,411	1,589	0,0222	0,0168	0,0169	16,76	12,04	2,531	0,199	0,0629
Material	V	Nb	Ti	Sn	Zr	As	B	Co	Sb	Ca	W
52256	<0,001	0,03	0,001	0,001		0,003	0,0002	0,002		0,005	
SE61-50	0,002	<0,001	0,001	0,001		0,003	0,0001	0,002		0,0006	
Sid58504	0,12									0,0005	
V27	0,027	0,036	0,013	0,001	0,002	0,002	0,0003	0,002	0,001	0,0004	0,003
V28	0,001	0,001	0,001	0,003	0,001	0,004	0,0001	0,003	0,001	0,0001	0,002
VRM 22	0,005	0,004	0,003	0,001	0,001	0,002	0,0002	0,008	0,000	0,0006	0,001
Riva74933	0,05		0,049				0,0023			0,004	
ECRM298-1	0,0607		0,0014				0,0021	0,055			
JK27A	0,041			0,004			0,0018	0,089		0,0033	0,028

The homogeneity of the materials with respect to “inclusion” elements e.g. Al, Ca, Mg and oxygen was an initial examination. Here OES bulk analysis as well as wet chemistry methods were used according to standard procedures. For oxygen the combustion method was used. RSD% was evaluated as basic parameter in the homogeneity test.

In the metallurgical characterisation, the facilities among the partners were used with emphasis on available expertise and special equipment. The characterisation comprised automatic Image Analysis (IA) to get physical parameters (area, size and number of inclusions) and SEM-EDS, where SEM-EDS could deliver both the composition of the inclusions and the physical parameters of their amount and size. From SEM-EDS data, B-factors (wt% of elements present in inclusions) were calculated. However, such calculations are not standardised in the SEM-EDS standard for inclusion assessment ASTM E 2142. The B-factors were evaluated according to established procedure and are calculated as

$$c_{incl}^i \approx B_i = (0.5/A) \times \sum_{j=1}^N (a_j \times c_j^i)$$

where c_{incl}^i is the inclusion related concentration of element i ; A is the total area assessed; a_j is the area of inclusion j ; c_j^i is the concentration of element i in the inclusion j ; N is the number of inclusions. The factor 0.5 is the density ratio between inclusions and the steel matrix.

For certificate purpose, micrographs of typical inclusions were made in relation to the SEM-EDS analysis.

Results

Homogeneity tests as repeated analyses distributed over the specimen area resulted in an estimate that the relative variations of elements forming non-metallic inclusions (NMI) are of the order of 10% from the average. The RSD% obtained for “inclusion” elements in repeated bulk analyses are also in the order of 10%, max.

The obtained oxygen contents are presented in Table 2. There are higher variations than expected. It might be related to heterogeneous inclusion distribution. The two stainless certified materials ECRM 298-1 and JK 27A with previous informative oxygen values, 36 and 27 µg/g, have repeated agreement in the present study.

Table 2: Oxygen determinations (combustion method) as mean values (µg/g) from different laboratories. Values in bold italic are from the same specimen.

Material	Lab 1	Lab 2	Lab 2	Lab 3	Lab 4	Lab 5	Lab 6	Lab 7	Lab 8	Mean
Dill 52256			26	22	<i>(74)</i>	22				23
Dill SE61-50			20	20	37	(48)				26
SID 58504			14	10	14	8		12		12
V27	8	17	24	12	21	15			21	17
V28	24	25	23	15	25	26			28	24
VRM 22	13	25	17	15	<i>(29)</i>	14				17
RIVA T				43		37				40
RIVA L			48?	39	60					50
ECRM 298-1			34		40	32	31			34
JK 27A		26	27	22	32	28	20			26

Wet chemistry was performed at one lab with results in Table 3. Additionally, lab 6 delivered Al-insol and Al-sol results. For ECRM 298-1 the information values of the certificate are used, in italic.

Table 3: Wet chemistry results (m-%).

Laboratory	5	5	6	5	6	5	5	5
Material	S	Al insol.	Al insol.	Al sol	Al sol	Al tot	Mg	Ca
52256	0,0015	0,0007	0,0004	0,0285	0,0287	0,0293	0,0006	0,0050
SE-61-50	0,0203	0,0014	0,0021	0,0611	0,0616	0,0625	0,0003	0,0005
Sid58504	0,0218	0,0013	0,0008	0,0269	0,025	0,0282	0,0001	0,0008
V27	0,0009	0,0009	0,0008	0,0418	0,0308	0,0427	0,0002	0,0002
V28	0,0116	0,0012	0,0012	0,0447	0,0449	0,0459	0,0002	0,0003
VRM22	0,0008	0,0012	0,0013	0,0480	0,0493	0,0492	0,0001	0,0011
Riva	0,0271	0,0011	0,0016	0,0199	0,0223	0,0210	0,0005	0,0042
ECRM298-1		<i>0,0045</i>					<i>0,0008</i>	<i>0,0020</i>
JK 27	0,0169	0,0026		0,0145		0,0171	0,0002	0,0021

Material	Ti tot	Ti sol	Ti -C-N	Ti-ox
52256	0,0010			
SE-61-50	0,0010			
Sidenor	0,0030			
V27	0,0134	0,0011	0,0120	0,0004

V28	0,0003			
VRM22	0,0017			
Riva	0,0515	0,0042	0,0470	0,0000
ECRM298-1				
JK 27	0,0006			

The metallographic characterisation involves several demanding steps as to get the final result. Different local routines are applied at the laboratories to meet specific demands related to own products. The results in the present work are some basic parameters ECD (Equivalent circle diameter, which means the diameter of a virtual circle with the same area as the measured particle), area% and density (number of particles/mm²). Table 4 summarizes the result.

Table 4: Physical parameters obtained in metallurgical characterisation IA and SEM-EDS

1. Image Analysis (IA) of oxides showing density and size.

Analysed area 100 mm²

Sample	Density (number/mm ²)	Mean Incl. Area (μm ²)	Mean Incl. Length (μm)	Max. Incl. Area(μm ²)	Max. Incl. Length (μm)
52256	11	41.1	6.7	560	37.4
SE6150	17	41.2	6.0	1796	86.3
SID58504	11	19.5	4.3	571	48.9
VRM27	5	36.6	6.3	653	25.7
VRM28	1	47.3	7.3	280	23.2
VRM22	10	20.1	4.4	982	33.2
RIVA 2T	53	10.7	3.4	526	28.2
ECRM298	24	12.6	3.6	663	60.5
JK27A	30	15.3	4.3	501	32.3

2. SEM EDS of oxides showing density, size and area %.

Analysed areas 30 – 190 mm² depending on amount.

Oxides	Number density	ECD		Length		Area%
		mean	max.	mean	max.	
Sample	mm ⁻²	μm	μm	μm	μm	
52256	33,1	1,89	40,78	2,41	53,59	0,0125
SE6150	2,5	2,8	11,3	3,8	26,6	0,0190
58504	0,7	2,1	6,4	2,9	12,6	0,0030
V27	1,5	3,0	9,1	3,9	12,9	0,0014
V28	4,8	2,2	8,1	3,1	13,6	0,0023
VRM22	2,4	1,7	5,7	2,2	7,8	0,0007
Riva T	6,1	2,9	15,8	4,9	25,6	0,0060

3. SEM EDS of complex oxy-sulphides showing density, size and area %.

Analysed areas 30 – 190 mm² depending on amount.

Complex Oxy-sulphides Sample	Number density, mm ⁻²	ECD		Length		Area%
		mean µm	max. µm	mean µm	max. µm	
52256	15,8	2,3	25,3	2,8	26,5	0,0097
SE6150	24,4	3,1	12,3	3,9	13,6	0,0210
58504	8,5	3,8	14,9	7,2	67,8	0,0128
V27	3,5	4,5	9,0	5,4	13,4	0,0063
V28	5,5	2,2	8,0	3,1	14,9	0,0024
VRM22	5,4	2,9	12,5	3,6	16,6	0,0048
Riva T	29,8	3,1	17,3	5,38	48,6	0,0304

4. SEM EDS summary of inclusion type(s)

Material	Main type(s)
52256	AlMgCa-ox; oxysulph CaSAlMgO , Al ₂ O ₃ CaS
SE-61-50	MnS; oxysulph Al ₂ O ₃ Ca(Mn)S;
Sid58504	MnS; oxysulph Al ₂ O ₃ Ca(Mn)S
V27	Oxysulph CaSAlMgO; AlMg-ox; CaMnS
V28	Oxysulph Al ₂ O ₃ MnS; Al-ox; MnS
VRM22	Oxysulph CaSAlMgO; AlMg-ox; CaS
Riva	TiN; MnS; oxysulph CaSAlMnO; CaAl-ox
ECRM298-1	AlMg-ox; MgCa-ox;
JK 27	Mn(Ca)S; Oxysulph MgAl ₂ O ₃ MnS; AlMg-ox

The B-factors determined with SEM-EDS are shown in Table 5. For oxygen there are two variants (O and O-calculated) due to different facilities.

Table 5: SEM-EDS B-factors for NMI elements, m%. Oxygen with combustion, µg/g. Al-insol from tab. 3

	O	Mg	Al	Si	S	Ca tot	Mn tot	Ti tot	O-calc	O-Comb	Al-insol
52256		0,0003	0,0009	0,0000	0,0013	0,0037	0,0001	0,0000	0,0019	23	0,0007
SE61-50		0,0002	0,0022	0,0000	0,0013	0,0004	0,0064	0,0001	0,0036	26	0,0014
V27		0,0003	0,0011	0,0000	0,0003	0,0003	0,0002	0,0001	0,0013	17	0,0013
V28		0,0000	0,0012	0,0000	0,0003	0,0000	0,0007	0,0000	0,0011	24	0,0009
VRM22		0,0001	0,0010	0,0000	0,0003	0,0006	0,0000	0,0000	0,0011	17	0,0012
Riva_T		0,0003	0,0032	0,0000	0,0021	0,0027	0,0094	0,0350	0,0061	40	0,0012
Riva_L		0,0002	0,0022	0,0000	0,0017	0,0019	0,0074	0,0359	0,0045	50	0,0011
ECRM											
298-1	0,0036	0,0011	0,0037	0,0001	0,0003	0,0018	0,0000	0,0002		34	0,0045
JK27A	0,0025	0,00013	0,0035	0,0001	0,0158	0,0042	0,0180			26	0,0026

It should be observed that Ca tot, Mn tot and Ti tot are the total concentrations related to *inclusions*. Thus, Ti tot is different from the Ti tot values in Table 3 Wet chemistry. For the low alloy steels oxygen O-calc was stoichiometrically calculated according to well established routines. For O-calc there are some deviations from the mean values of the combustion data, but might be related to non-uniform distributions. For the two certified stainless steels, the oxygen B-factor summarized in column O corresponds very well to the combustion values.

For Al there is a good agreement obtained with Al-insol for the following materials: 52256, SE61-50, V27, V28, VRM22, ECRM298-1, JK27A.

Round Robin tests on the selected materials using PDA-OES

Due to different facilities of the instruments, it is obvious that the same set-ups cannot be used. Further, each partner used their own set of reference materials for the calibration.

Five burns, minimum, were made. Average and standard deviation were reported for selected parameters.

For the data treatment the quantification model refined and harmonised in the project was used. This complete quantification takes into account background subtraction and non-linearity of the calibration curves. A set of inclusion parameters is calculated, including the analytical B-factors and size.

The assessment of B-factors, that is the “inclusion” element concentration related to inclusions, was given high priority in the Round Robin evaluation. During the work the accuracy of the B-factors has been discussed as the best parameter to reveal as a quality index for the PDA-OES assessment. A calculated oxygen index based upon stoichiometry is also important as a fast estimate of the oxygen content in process samples.

The results are presented in a few summarizing tables. Of special interest in low-alloy steel is the Al-oxide group of inclusions. Thus, the PDA B-factors for Al (mean value of six laboratories) are presented in Table 6 together with the Al-insol results. Generally, the low concentrations mean higher scatter, but the biggest RSD% is obtained for ECRM 298-1, a high alloy stainless steel with Al-insol =0,0045%. The Al PDA mean for the Riva sample is considerably higher than the Al-insol.

Table 6: Basic statistical parameters of PDA B-factors (wt%) for Al; comparison with Al-insol

Sample	Al-insol	Mean	s	RSD%
52256	0,0007	0,0008	0,0004	52,6
SE61-50	0,0014	0,0017	0,0003	20,5
Sid58504	0,0013	0,0006	0,0002	41,1
V27	0,0009	0,0010	0,0004	38,5
V28	0,0012	0,0012	0,0002	14,8
VRM22	0,0012	0,0011	0,0003	23,5
Riva-T	0,0011	0,0029	0,0007	25,5
Riva-L		0,0024	0,0004	15,7
ECRM 298-1	0,0045*	0,0041	0,0022	54,9
JK 27A	0,0026	0,0033	0,0011	32,3

*This value is given as information in the ECRM 298-1 certificate

B-factors for other NMI elements (Ca, Mg) can be given similar remarks. Generally, the B-factors for Ca and Mg are lower than those determined by wet chemistry. During the project it was realised that the bulk concentrations of Ca, Mg, could be used as B-factors, because the main part of these elements forms NMI's. This is not introduced in the present results.

One of the applications of the PDA technique is assessment of the oxygen content in process samples by a fast spectrometric method. The outcome of the calculated oxygen indices from the PDA data is promising as shown in Table 7. In the two existing commercial reference materials the calculated PDA oxygen indices are close to the “information” values, 0,0036 and 0,0027 wt%.

Table 7: PDA. Calculated oxygen indices vs. oxygen (combustion) in $\mu\text{g/g}$

Material	Comb mean	PDA	PDA	PDA	PDA
		O-calc Lab 1	O-calc Lab2	O-calc Lab 6	O-calc Lab 8
52256	23	10	20	19	14
SE61-50	26	13	32	9	24
Sid58504	12		9	4	20
V27	17	8	12	12	10
V28	24	9	6	8	14
VRM 22	17	9	21	4	14
RIVA T	40	48	41	43	31
RIVA L	50	52			
ECRM 298-1	34		31	83	29
JK 27A	26		26	24	29

Comments on statistical evaluation of results according to international standards for certification

In certification as RM, e.g. JK material, seven laboratories, minimum, should deliver measured values. The European certification should involve 14 laboratories, minimum. Chemical reference methods should be used. Further, there should be a validation of error in light of historically issued certificates. The error should be given as absolute values in relation to concentration ranges, not as RSD%.

Obviously, it is not possible to perform the evaluation and validation in this conservative way. The quantitative metallography with respect to inclusions needs special qualifications and there are just a few laboratories being able to perform the SEM-EDS analyses over the full range of parameters. As described in this study a comparable parameter set is the B-factors. Other essential parameters are the main inclusion type, the size distribution (as average and maximum size), number density for the main type, area%, volume %, respectively.

In the present study, the B-factors for Al and the total oxygen content are demonstrated as being reliable for "certification". For instance, difficulties to meet levels obtained by established methods (wet chemistry and combustion) are useful in validation of a material as a reference material.

Certification

Figure 1 shows an example of a data sheet.

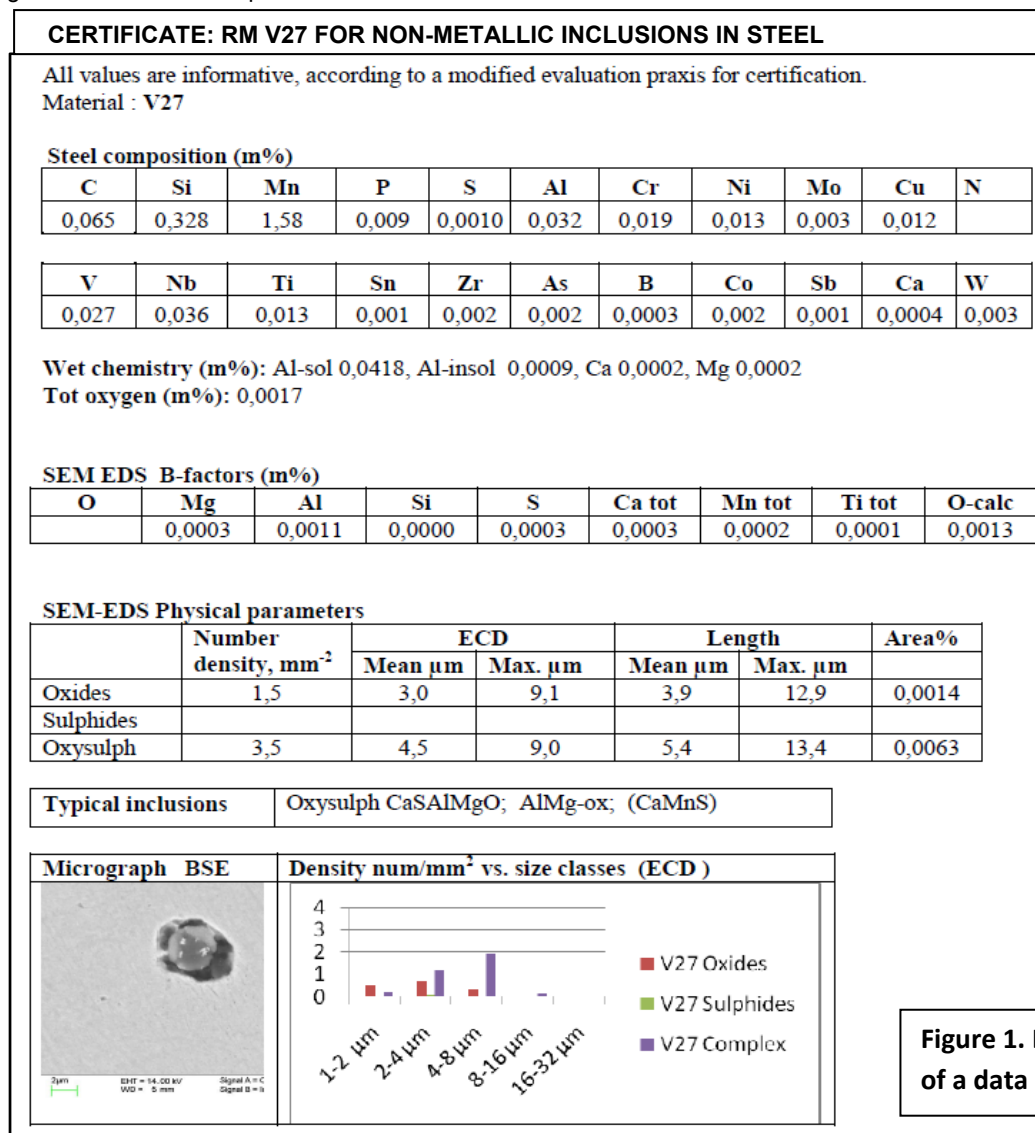


Figure 1. Layout of a data sheet

Conclusion

The present work comprised evaluation of a set of steels as possible reference materials for cleanliness assessment. A modified statistical evaluation of the test results was needed in light of a limited number of partners.

A set of reference materials could be delivered, mainly dedicated to PDA work. A layout for the data sheets was presented. There are applications in verification of analytical results, but also in future standardization of methods. A need for future standardization and implementation of B-factor evaluation in SEM-EDS was identified.

References

1. Mathy H, Tusset V, Lamberigts M (2003). Scanning electron microscopy assessment of steel cleanliness, Steel GRIPS 1, No 3, p 211-218
2. ECSC project 7210-PR/298: Fast characterisation of steel cleanliness by advanced mathematical analysis of spark and laser source optical emission data (ADMATH), completed 2004-12-31

3. Bengtson A, Didriksson R, Sedlakova M, Development of MVA techniques for quantitative determination of non-metallic inclusions in steels by OES/PDA, (2006), In: Proceedings of the 7th International Workshop on Progress in Analytical Chemistry in the Steel and Metal Industries, 16-18 May 2006, Luxembourg, pp 213-218
4. Winkler W, Angeli J, Mayr M (2006). Automated SEM/EDX cleanliness analysis for metallurgical developments. In: Proceedings of the 7th International Workshop on Progress in Analytical Chemistry in the Steel and Metal Industries, 16-18 May 2006, Luxembourg, pp 281-289
5. Runnsjö G, Jonsson JY, Bengtson A, Sedlakova M (2006). An evaluation of stainless reference materials for steel cleanliness. In: Proceedings of the 7th International Workshop on Progress in Analytical Chemistry in the Steel and Metal Industries, 16-18 May 2006, Luxembourg, pp 290-295

THREE-DIMENSIONAL ESTIMATION OF MULTI-COMPONENT INCLUSION PARTICLE IN STEEL

Ryo Inoue¹, Kei Kiyokawa², Koichiro Tomoda², Shigeru Ueda¹ and Tatsuro Ariyama¹

¹ *Institute of Multidisciplinary Research for Advanced Materials, Tohoku University, Sendai 980-8577, Japan*

² *Physical Analysis Technology Center, Toshiba Nanoanalysis Co., Kawasaki 212-8583, Japan*

Summary

Since the estimation of inclusion particles has a relation close to the production of clean steel, various methods were proposed. Recently, the effects of inclusion particles on the control of steel grain growth, which can improve mechanical properties of steel, have been investigated. In those researches, the utilized inclusion particles are very fine and sometimes consist of the chemically unstable multi-component compound.

It is well known that the composition and size of inclusion particles on a cross-section of steel sample are easily estimated using analytical instruments. In comparison with those two-dimensional measurements, the inclusion particles extracted from metal matrix are convenient for the accurate three-dimensional estimation of morphology, size and composition.

In this study, the potentiostatic and galvanostatic extraction methods using nonaqueous electrolytes have been examined for the extraction of various inclusion particles. It was concluded that 4%MS (4v/v% methylsalicylate-1w/v% salicylic acid-1w/v% tetramethylammoniumchloride-methanol) and 10%AA (10v/v% acetylacetone-1w/v% tetramethylammoniumchloride-methanol) electrolytes were suitable to the extraction of TiO_x and $TiAl_2O_5$.

Though those electrolytic extraction methods are available for the extraction of chemically unstable inclusion particles, the position of each inclusion existed in metal cannot be specified because the observation of inclusions is carried out on a film filter after extraction. For the specification of inclusion position in metal, the light etching using halogen-alcohol was applied to appear the inclusion particles near the surface of steel sample, which was deoxidized by Ti and Al. The morphology, size and segregation of elements on the fine inclusion particle were estimated using a scanning electron microscopy and an Auger electron spectroscopy (AES). Then, the micro-segregation of elements on the cross section of fine inclusion particle, which was prepared by a focused ion beam, was estimated using a low acceleration energy-scanning electron microscopy and AES. Based on these results, the formation mechanism of multi-component inclusion particle was discussed.

Keywords: three dimensional estimation, multi-component inclusion, light etching, auger electron spectroscopy, focused ion beam, formation mechanism.

Introduction

The removal of nonmetallic inclusion particles has been of importance for the production of high quality steel. Various methods were proposed in order to evaluate the relatively large inclusion particles^{1,2)}. It was recently reported that some kinds of fine complex inclusion particles had an effect on the minimization of steel grain size, which can improve the mechanical properties of steel³⁻⁵⁾. The exquisite evaluation of the multi-component inclusion particle has become extremely important.

The two-dimensional size and compositional segregation of inclusion particles on a cross section of steel sample correspond hardly to the real size of three-dimensional inclusion particles⁶⁻⁸⁾ and the real micro-segregation of components in the particles, respectively. In comparison with two-dimensional measurements of inclusion particles on a cross-section of metal, the inclusion particles separated from metal matrix are convenient for the accurate three-dimensional estimation of their morphology, size and composition. Furthermore, the quantitative analysis of inclusion amount in metal can be directly obtained by the analysis of those separated

particles. For these purposes, many extraction methods⁹⁻²³⁾ using acids, halogen-alcohol mixture and electrolysis using nonaqueous electrolyte such as 4%MS (4v/v% methylsalicylate-1w/v% tetramethylammoniumchloride-methanol), 2%TEA (2v/v% triethanolamine-1w/v% tetramethylammoniumchloride(or LiCl)-methanol), 10%AA (10v/v% acetylacetones-1w/v% tetramethylammoniumchloride-methanol) were proposed, as listed in Table 1. However, it is disadvantageous that the dissolution loss of inclusions is inevitable during extraction. The electrolysis using the nonaqueous electrolyte has been recommended as a standard method for the extraction of inclusion particles because of good reproducibility, but the dissolution loss of Al_2O_3 ²⁴⁾, nitrides¹⁹⁾ and carbides¹⁹⁾ was only examined in these nonaqueous electrolytes. In present study, the applicability of electrolytic extraction methods using nonaqueous electrolyte have been investigated for Ti_2O_3 and TiAl_2O_5 multi-component inclusion particles. In order to evaluate the three-dimensional segregation of composition in inclusion particles, the cross section of a fine inclusion particle, which was prepared by a Focused Ion Beam (FIB) method, was observed by a Low acceleration Energy-Scanning Electron Microscopy (LE-SEM) and qualitatively analyzed using an Auger Electron spectroscopy (AES). It is well known that the AES method can analyze only the surface of sample, while an Electron Probe Micro-Analysis (EPMA) obtains the all information from the surface to the depth of 1~2 μm . From the present results, the formation mechanism of complex inclusion particle was discussed.

Experimental method of dissolution loss of oxide particles in solution

The Ti_2O_3 reagent and the synthesized TiAl_2O_5 (50mg) were charged into acid (80~90°C), 5v/v bromine-methanol (43~60°C in ultrasonic vibration bath), 14w/v iodine-methanol (43~60°C in ultrasonic vibration bath) or nonaqueous electrolyte (room temperature). The acid and the nonaqueous electrolyte were stirred at intervals of 30 min. After an appropriate time, 5 mL of solution was suction-filtered using a film filter (open pore size 0.1 μm), and analyzed by inductively coupled plasma-mass spectrometry (ICP-MS) or inductively coupled plasma-atomic emission spectrometry (ICP-AES).

Extraction procedure of TiO_x particles from metal

An appropriate amount of Fe-50mass% Ti alloy was added to Fe-10mass% Ni (70g) melted in an Al_2O_3 crucible under deoxidized Ar atmosphere at 1600°C. Then, the melt (Fe-0.15~0.21mass% Ti) was stirred for 10 sec using Al_2O_3 rod. After holding for 60 sec, the crucible containing metal sample was rapidly quenched into water.

A piece of metal sample was sliced to about 10x4x4 mm. The surface of the piece was cleaned by using a micro grinding machine, and washed by acetone in ultrasonic vibration bath. The piece was cut to small granules, following to rinse by acetone and petroleum benzene in ultrasonic vibration bath. The small granules of metal sample were charged in Erlenmeyer flask, and dissolved by $\text{HCl-H}_2\text{SO}_4\text{-H}_2\text{O}$ (4:1:5 in volume ratio) solution or halogen-methanol under the same conditions mentioned in Section 2.1. The solution was suction-filtered using a film filter (open pore size 0.1 μm).

A piece of metal sample was sliced to about 12~15x8~12x3 mm. The surface of the piece was cleaned by using a micro grinding machine, following to rinse by acetone and petroleum benzene in ultrasonic vibration bath before storing in petroleum benzene.

Inclusion particles in metal were extracted by the following electrolytic extraction method: A schematic diagram of the potentiostatic electrolysis device is shown in Fig. 1, where the metal sample was held by Pt tweezers and a pole was a Pt ring. A reference pole was a calomel electrode, which was connected with electrolyte through KCl saturated solution and KCl-agar bridge. In the case of galvanostatic electrolysis, the bridge and the reference pole were unnecessary. After extraction, the electrolyte was suction-filtered using a polycarbonate film filter (open pore size 0.05 μm) for the inclusion observation or a PTFE film filter (open pore size 0.1 μm) for the quantitative analysis of inclusion particles.

The extracted TiO_x inclusion particles on a polycarbonate film filter were observed using an Electron Probe Micro-analyzer with Energy Dispersed X-ray Spectroscopy (EPMA-EDX) after the coating with carbon or Pt.

After the filter containing inclusion particles was fused by $\text{Na}_2\text{CO}_3\text{+B}_2\text{O}_3$ flux in Pt crucible, the contents of elements were determined by ICP-AES. Total O contents in metal were determined by the inert gas fusion-infrared absorptiometry²⁵⁾.

Table 1. Various methods for extraction of inclusion particles reported previously⁹⁻²³.

	I-Methanol	Br-Methanol	Acid	Potentiostatic electrolysis (nonaqueous electrolyte)
Al ₂ O ₃	ok	ok	ok	
3Al ₂ O ₃ ·2SiO ₂	ok	ok	ok	
B ₂ O ₃ , BN	ok	–	bad	10%AA
CaO	bad	bad	bad	2%TEA-BaO
3CaO·Al ₂ O ₃ , 12CaO·7Al ₂ O ₃	ok	not good	bad	2%TEA-BaO, 3%MS 10%AA
3CaO·2SiO ₂ , CaO·SiO ₂	not good	not good	bad	2%TEA-BaO, 10%AA
Cr ₂ O ₃	ok	–	HCl, HNO ₃	
FeO, MnO, (Fe,Mn)O	not good	×	bad	
(Fe, Mn)O·Al ₂ O ₃	ok			
3(Mn,	ok			
(Fe, Mn)O·Cr ₂ O ₃	ok			
FeO·TiO ₂ , FeO·Ti ₂ O ₃	ok			
FeO·V ₂ O ₃	ok			
MgO	bad	bad	bad	
MgO·Al ₂ O ₃			bad	
Nb ₂ O ₅ , NbN, NbC NbCN	ok	–	HCl, H ₂ SO ₄ HNO ₃ , HClO ₄	10%AA
RE-oxide	ok	ok		4%MS
SiO ₂	ok	ok	ok	
TiO ₂ , Ti ₂ O ₃ , TiO	ok	ok	HNO ₃ , HClO ₄	
V ₂ O ₅	not good	–	bad	
ZrO ₂	ok	ok	cold HNO ₃	
AlN, AlO _x N _y	ok			10%AA
CaS, CaS-MnS	not good	bad	bad	2%TEA-BaO, 4%MS
Cr ₂ N, CrN			HNO ₃ , EDTA	10%AA
(Cr,Fe) ₂₃ C ₆ , (Cr,Fe) ₇ C ₃			H ₃ PO ₄	10%AA
(Fe, Mn) C	not good	not good	not good	10%AA
FeS, MnS	not good	bad	bad	TEA, MS, 10%AA
Mo ₂ C, (Fe,Mo) ₃ C			not good	10%AA
RE-sulfide	not good	not good		4%MS
RE-oxysulfide	ok	bad		4%MS
Si ₃ N ₄	ok			10%AA
TaN	ok			
TiN, TiC, TiCN, TiS	ok	ok	not good	10%AA
VN, VC, VCN	ok	–	HCl, H ₂ SO ₄ , HClO ₄	10%AA
ZrN, ZrCN	ok	ok	cold HNO ₃	10%AA
ZrC, ZrS, Zr ₃ S ₄	not good	not good	cold HNO ₃	4%MS, 10%AA

Procedure of three-dimensional observation of Al₂O₃-TiO_x inclusion particle

A Fe-1mass% Al alloy (3g) was added to the Fe-0.1mass% Ti alloy (20g) melted in an Al₂O₃ crucible under deoxidized Ar atmosphere at 1600°C. After holding for 30 sec, the crucible containing metal sample was rapidly quenched into water. The boundary between solid Fe-Al alloy and liquid Fe-Ti alloy was clearly observed on cross section of metal because of insufficient time for complete melting of Fe-Al alloy.

The polished cross section of metal sample was dipped into a 3~5v/v% bromine-methanol solution at room

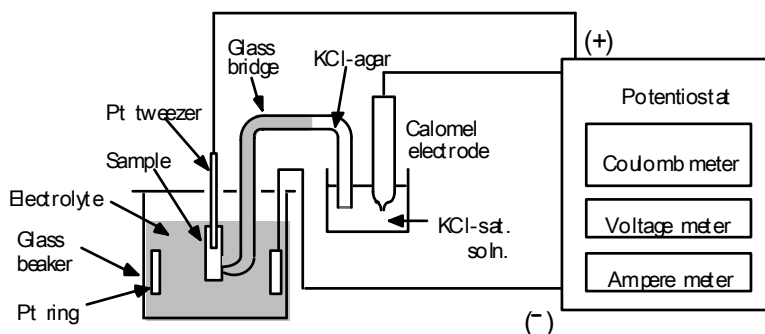


Fig.1 Schematic diagram of the apparatus for potentiostatic extraction method.

temperature, and rinsed by methanol. A particle exposed on metal surface was qualitatively analyzed by AES. Then, the particle was treated using FIB method to obtain the cross section. The cross section of fine particle was observed by LE-SEM and qualitatively analyzed by AES.

Stability of Ti_2O_3 and $TiAl_2O_5$ particles in solution

From the thermodynamic calculation using the standard free energies²⁶⁾ for the formation of TiO , Ti_2O_3 , Ti_3O_5 , Ti_4O_7 and TiO_2 , the free energies for the dissolution of $Ti(s)$ and O_2 into liquid iron²⁷⁾, and the respective interaction parameters²⁷⁾, Ti_2O_3 and Ti_3O_5 are the most stable TiO_x phases at 1600°C in the Ti concentration range of 0.13~0.21 and 0.0003~0.13 mass%, respectively.

Kawamura et al.¹³⁾ reported that the synthesized Ti_2O_3 (7 mg) dissolved completely in hot HCl or hot H_2SO_4 solution after 20 min, but undissolved in iodine-methanol and bromine-methanol at 70°C for 20 min. However, 20 minutes is too short to dissolve an appropriate amount of iron sample. In order to clarify the stability of Ti_2O_3 in solution, the dissolution of Ti_2O_3 fine powder, whose average grain size is 0.4 μm , was examined in halogen-methanol (43~60°C in ultrasonic vibration bath), 4%MS and 10%AA. The variation of the amount of Ti dissolved from fine Ti_2O_3 powder in those solutions with time is shown in Fig. 2. Ti_2O_3 powder is found to be stable in iodine-methanol and nonaqueous electrolytes, but is expected to be stable in bromine-methanol for a short time. It was indicated previously that fine Al_2O_3 reagent was stable in halogen-methanol and nonaqueous electrolytes²⁴⁾.

Though $TiAl_2O_5$ is the equilibrium phase in the limited concentration ranges of Al and Ti in liquid iron²⁷⁾, this compound can be considered to form at the boundary between Al_2O_3 and TiO_x . The dissolution of $TiAl_2O_5$ fine powder with the average grain size of 2.1 μm was examined in halogen-methanol (43~60°C in ultrasonic vibration bath), 4%MS and 10%AA. Figure 3 shows the variation of Ti content in those solutions with time. $TiAl_2O_5$ powder is stable in both halogen-methanol and nonaqueous electrolytes.

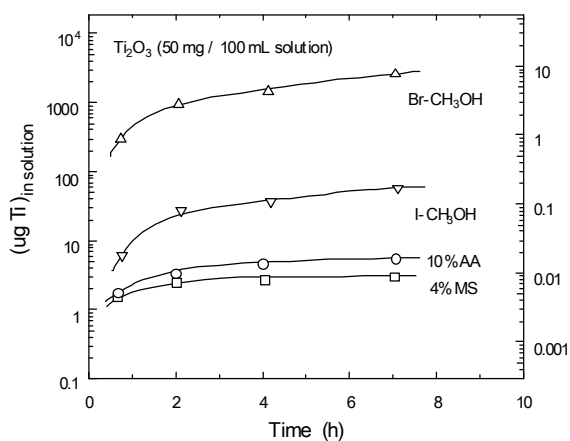


Fig.2 Variation of dissolution of fine Ti_2O_3 reagent in various solutions with time.

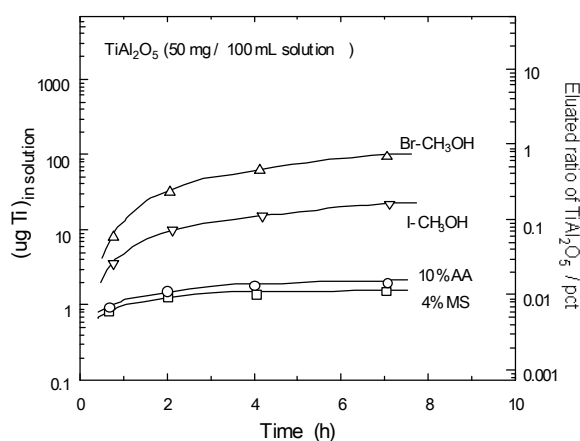


Fig.3 Variation of dissolution of fine $TiAl_2O_5$ powder in various solutions with time.

Extraction of TiO_x inclusion particles

Due to the difference of morphology, size and chemical stability between reagent and actual inclusion particle, it was supposed that the extraction condition obtained using reagent or synthesized compounds cannot apply to the actual extraction from metal^{13,28)}. The amount of Al₂O₃ dissolved in acid was varied depending on the Al₂O₃ crystal structure¹²⁾. Therefore, the applicability of the TiO_x extraction methods should be examined by using Fe sample deoxidized by Fe-Ti alloy in deoxidized Ar atmosphere at 1600°C.

The oxygen content in inclusion extracted by the electrolytic extraction with 4%MS are plotted against that obtained by subtracting the equilibrium oxygen content, which is thermodynamically evaluated by using ΔG° for the reaction: $2[\text{Ti}]+3[\text{O}]=\text{Ti}_2\text{O}_3(\text{s})$ ^{26,27)} and interaction parameters²⁷⁾ from the analyzed total oxygen content in Fig. 4. The validity of potentiostatic electrolysis is obvious because the results obtained by electrolytic extraction using 4%MS agree well with the thermodynamically calculated one. However, the results obtained using HCl-H₂SO₄-H₂O(4:1:5) solution and iodine-methanol deviated from the calculated ones due to the dissolution of inclusion particles. Based on this result along with the other examinations, the extraction methods for various nonmetallic inclusions, the extraction methods for various nonmetallic inclusion particles were verified as listed in Table 2, where 2%TEA-Ba denotes the 2%TEA containing 0.05 ~0.2w/v% metallic Ba.

Three-dimensional observation of inclusion particles

The SEM image of the metal surface after the light etching is shown in Fig. 5. Many inclusion particles are found to be clearly exposed on the metal surface. Using this method, a particle can be easily sampled from grain boundary, finally solidified area, intergranular part, and so on. Figure 6 indicates the SEM image and elementary mapping results of an inclusion particle. The white and gray areas in SEM image correspond to Al₂O₃ and TiO_x, respectively. The presence of TiAl₂O₅ phase at the bound-

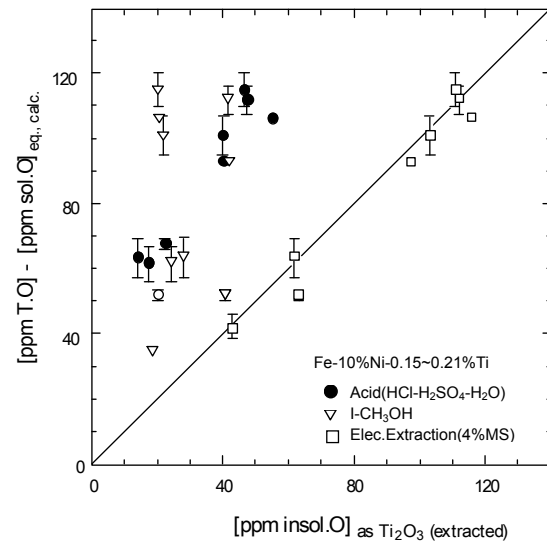


Fig.4 Insoluble O contents obtained from total O and equilibrium soluble O plotted against insoluble oxygen contents estimated from analyzed insoluble Ti.

Table 2 Applicability of various extraction methods for inclusion particles.

	I-methanol	Br-methanol	Hot acid	Recommended electrolysis (nonaqueous electrolyte)
Al ₂ O ₃	not good	not good	bad	4%MS, 10%AA
CaO	bad	bad	bad	
12CaO·7Al ₂ O ₃	not good	not good	bad	2%TEA, 10%AA
3CaO·Al ₂ O ₃	not good	not good	bad	2%TEA-Ba, 2%TEA
CaO·SiO ₂	not good	not good	bad	10%AA
3CaO·2SiO ₂	not good	not good	bad	2%TEA, 10%AA
CeO ₂ , Ce ₂ O ₃	not good	not good	bad	2%TEA
MgO	bad	bad	bad	2%TEA-Ba, 2%TEA
MgO·Al ₂ O ₃	not good	not good	bad	2%TEA-Ba
SiO ₂	bad	not good	bad	2%TEA-Ba, 2%TEA
TiO ₂ , Ti ₂ O ₃	bad	not good	bad	4%MS, 10%AA
ZrO ₂	ok	not good	bad	4%MS, 10%AA
CaS	not good	not good	bad	4%MS, 10%AA
CeS, Ce ₂ S ₃	not good	not good	bad	4%MS, 10%AA
TiN	ok	not good	bad	2%TEA-Ba

ary between TiO_x and Al_2O_3 phases is not clear from Fig.6. Then, this particle was treated using FIB method to obtain the cross section. The LE-SEM image is shown in Fig.7. The mapping analysis on the cross section of the inclusion particle was carried out using AES. The results are also shown in Fig. 7, where the core and rim of the particle consist of TiO_x and Al_2O_3 , respectively.

$TiAl_2O_5$ phase was not identified around the boundary between TiO_x and Al_2O_3 phases by the point analysis of

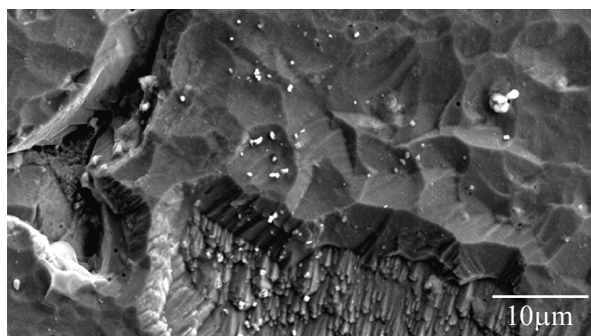


Fig.5 SEM image of metal surface after Br-methanol etching.

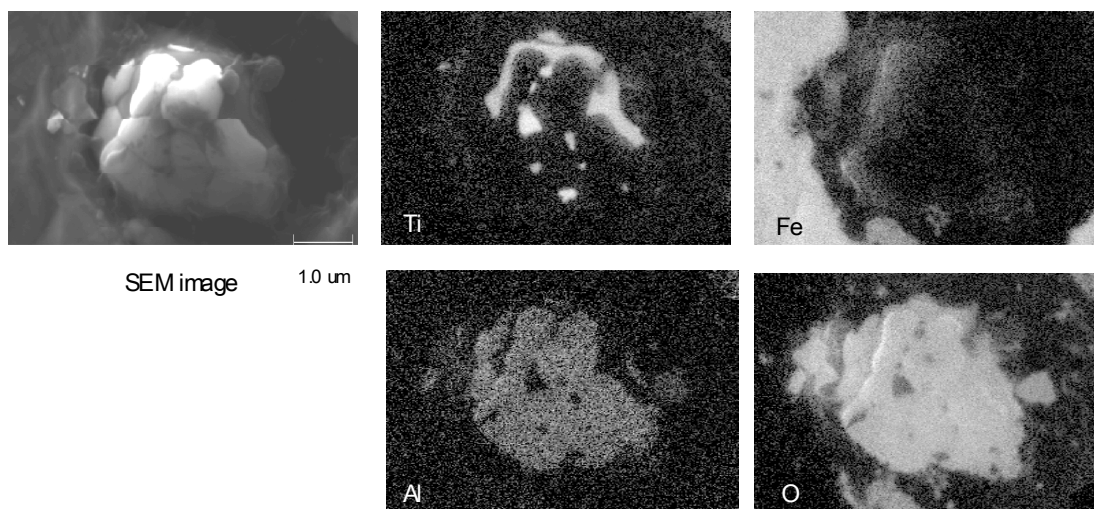


Fig.6 SEM image and the results for elementary mapping analysis on inclusion surface.

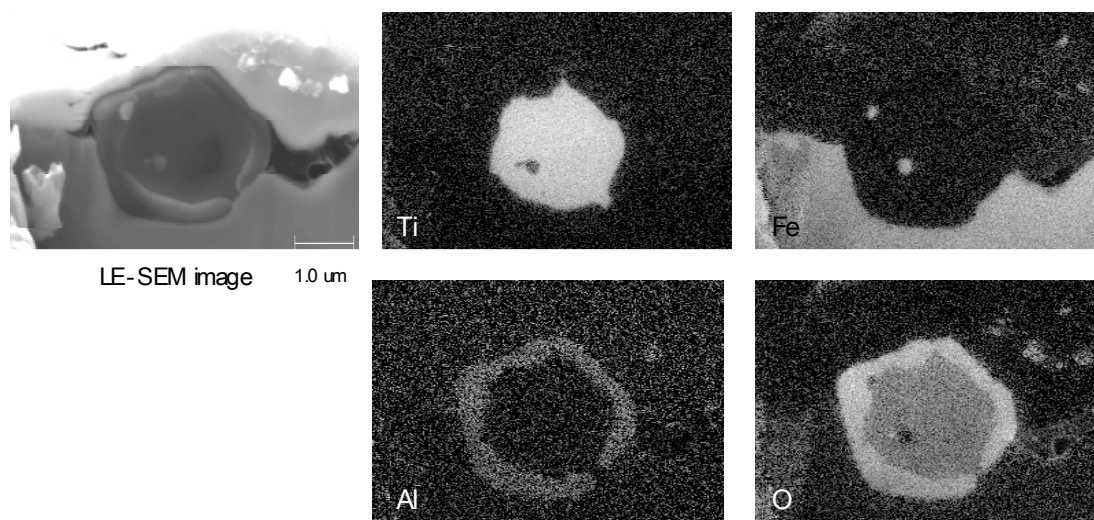


Fig.7 LE-SEM image and the results for elementary mapping analysis on the cross section of inclusion.

EPMA. Matsuura et al.²⁸⁾ reported that $TiAl_2O_5$ phase could form by the reaction of Al_2O_3 with not Ti_2O_3 but Ti_3O_5 . Therefore, TiO_x layer observed in Figs.6 and 7 is expected as Ti_2O_3 .

Formation mechanism of complex inclusion particles

The following two formation mechanisms of $TiO_x-M_yO_z$ complex inclusion particle are expected depending on Ti and M contents in metal, as illustrated schematically in Fig.8.

Case-1: the primary deoxidation product, TiO_x , is reduced from the surface by strong deoxidant M added later according to the reaction: $TiO_x + xy/z[M] \rightarrow x/z M_yO_z + [Ti]$.

Case-2: the primary deoxidation product, TiO_x , is decomposed by the reaction: $TiO_x \rightarrow [Ti] + x[O]$, and then $[Ti]$ and $[O]$ react with M added later according to the reaction: $[Ti] + (x+z)[O] + y[M] \rightarrow TiO_x-M_yO_z$

From the experimental findings in Figs.6 and 7, it is concluded that $Ti_2O_3-Al_2O_3$ complex inclusion particle forms according to Case-1 under the present experimental condition.

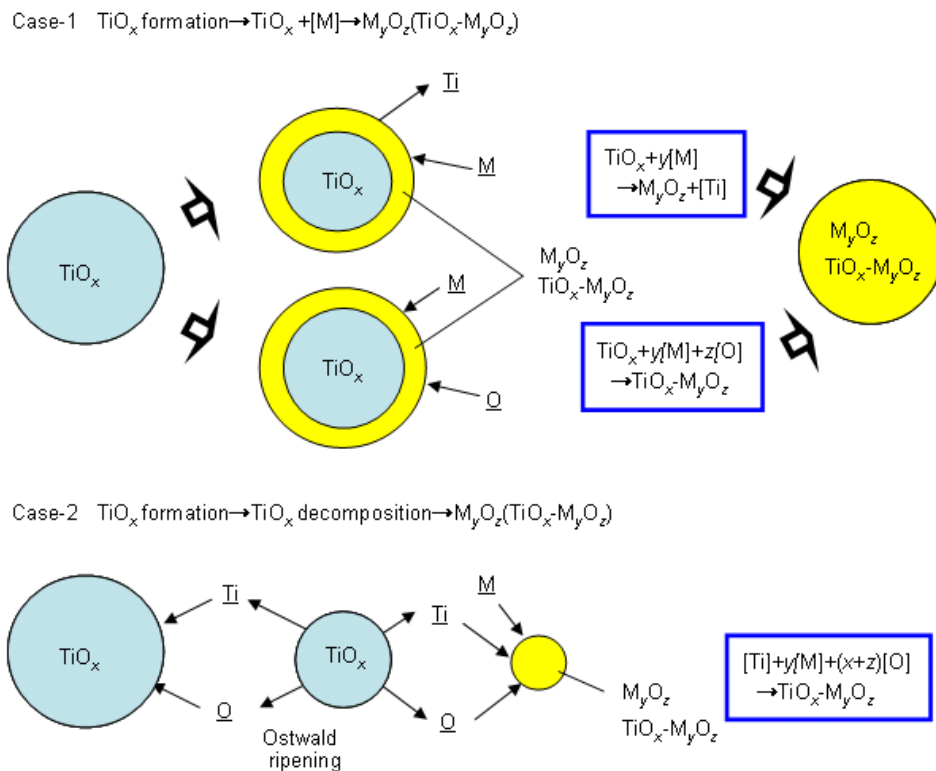


Fig.8 Schematic illustration of formation mechanisms of complex inclusion particles.

Conclusion

The electrolytic extraction is recommended for the stable extraction of inclusion particles in metal, but it is important to choose the electrolyte appropriately according to the inclusion composition. The present method of exposing inclusions by Br-methanol is effective for an easy three-dimensional observation of each particle. The formation mechanism of inclusion particles can be clarified by the evaluation of the cross section of inclusion particle.

References:

- 1) Iron and Steel Inst Jpn eds. Analytical Technologies in iron and steelmaking process of Japan. Tokyo: Iron and Steel Ins. Jpn, 1982.
- 2) Kawai Y, Ishibashi Y, Chino J and Kutsumi T.: Research committee on nonmetallic inclusions in steel eds. Recent development of research on nonmetallic inclusions in steel. Tokyo: Japan Society for the Promotion of Science, 1994, 206-227.

- 3) Takamura J and Mizoguchi S.: Roles of oxides in steels performance, The sixth International Iron and Steel Congress. Nagoya: ISIJ, 1990, 591-597.
- 4) Ogibayashi S. Development in the technology of oxides metallurgy. Shinnittetsu-giho, 32(1994), No.351, 64-69.
- 5) Kojima A, Kiyose A, Uemori R, Minagawa M, Hoshino M, Nakashima T, Ishida K and Yasui H.: Super high HAZ toughness technology with fine microstructure imparted by fine particles. Shinnittetsu-giho, 42(2004), No.380, 2-5.
- 6) Takahashi J and Suito H.: Random dispersion model of two-dimensional size distribution of second-phase particles. Acta Materialia, 49(2001), 711-719.
- 7) Takahashi J and Suito H.: Effect of omitting small sectioned particles with limited cross-sectional area on characterization of secondary phase particles. Mater Sci Tech., 18(2002), 103-110.
- 8) Takahashi J and Suito H.: Evaluation of the accuracy of the three-dimensional size distribution estimated from the Schwartz-Saltykov method. Metall Mater Transactions A, 34A(2003), 171-181.
- 9) Narita K.: On observation, identification and determination of nonmetallic inclusion and precipitate in steel, Tetsu-to-Hagané, 60(1974), 1820-1826.
- 10) Maekawa S.: Study on chemical analysis of nonmetallic inclusion in steel, Tetsu-to-Hagané, 55(1969), 381-401.
- 11) Chino A, Iwata H and Ihida M.: The measurement of particle size distribution of Al_2O_3 inclusion in ultra low oxygen steel, Tetsu-to-Hagané, 77(1991), 2163-2170.
- 12) Honda F and Hirokawa K.: Infrared spectroscopic study of Al oxides in Al-killed steel[J], Tetsu-to-Hagané, 60(1974), 2013-2017.
- 13) Kawamura K, Watanabe S and Uchida T. Study on phase analysis of titanium in steel[J], Tetsu-to-Hagané, 57(1971), 94-104.
- 14) Ishii T and Ihida M.: Analysis of titanium carbide in austenite stainless steel, Tetsu-to-Hagané, 60(1974), 1957-1961.
- 15) Kawamura K, Watanabe S and Suzuki T.: Study on the phase analysis of vanadium in steel, J Japan Inst Metals, 32(1968), 375-378.
- 16) Kawamura K, Watanabe S and Suzuki T.: Study on the phase analysis of niobium in steel, J Japan Inst Metals, 32(1968), 180-183.
- 17) Wakamatsu S.: Metallographic analysis of niobium in high strength steel, Tetsu-to-Hagané, 55(1969), 503-511.
- 18) Kawamura K, Watanabe S and Suzuki T.: Extraction and determination of various precipitates in steel cold nitric acid method, Tetsu-to-Hagané, 58(1972), 2067-2077.
- 19) Yoshida Y, Funahashi Y, I k and Kamino Y.: Determination of non-metallic inclusions in steel at kawasaki steel corp., Kawatetsu-giho, 12(1980), 653-664.
- 20) Kurosawa F, Taguchi I and Matsumoto R.: Observation and analysis of carbides in steels using non-aqueous electrolyte-potentiostatic etching method, J Japan Inst Metals, 44(1980), 1288-1295.
- 21) Narita K.: Fundamental study on isolation and determination of carbide in steel, Tetsu-to-Hagané, 66(1980), 2119-2138.
- 22) Narita K. Isolation and determination of sulphides in steel, Tetsu-to-Hagané, 73(1987), 67-83.
- 23) Yoshida Y, Funahashi Y and Kamino Y.: State analysis of Ca in steel by electrochemical separation technique, Tetsu-to-Hagané, 68(1982), 162-171.
- 24) Inoue R, Ariyama T and Suito H.: Extraction and Evaluation of Inclusion Particles in Steel, Asia Steel International Conference 2009: The Korean Institute of Metals and Materials, 2009, S11-16, 1-9.
- 25) Inoue R and Suito H.: Determination of Oxygen in Iron-Aluminum Alloys by Inert Gas Fusion-Infrared Absorptiometry, Mater Trans JIM, 31(1991), 1164-1169.
- 26) Barin I.: Thermochemical data of pure substances, VCH, Weinheim, 1989.
- 27) Sigworth G K and Elliott J F.: The thermodynamics of liquid dilute iron alloys, Met Sci, 8(1974), 298-310.
- 28) Matsuura H, Nakase K and Tsukihashi F.: Composition of inclusions in Fe-Al-Ti melt at 1873K, CAMP-ISIJ, 23(2010), 956.
- 29) Wakamatsu S.: State analysis of steel, Tetsu-to-Hagané, 57(1971), 656-672.

USE OF ON-LINE EVALUATION OF PDA-DATA AT SSAB AT OXELÖSUND AND OUTOKUMPU STAINLESS AB AT AVESTA

Rolf Didriksson*, Torbjörn Engkvist**, Gunilla Runnsjö**

*SSAB EMEA, 61380 Oxelösund, Sweden

**Outokumpu Stainless, Avesta Works, Box 74, 77422 Avesta, Sweden

Abstract/ Summary

A software for on-line and off-line evaluation of PDA-data has been developed and implemented. As the non-metallic inclusions in stainless steel differ from those in low-alloy steel, the development of suitable software was initially performed at Outokumpu Stainless in Avesta. The basic consideration is result presentations easy to interpret by metallurgists and to some extent operators. Further, statistic parameters are included and presented graphically.

By a modern graphic design showing all the evaluation steps from basic pulsograms to the final results, the tests and further development of the software were facilitated. At the moment an off-line version is used at Avesta Works. The software is integrated in the normal LIMS systems at both laboratories.

An on-line version of the same software is implemented at Oxelösund with the analytical conditions modified in order to incorporate the PDA-measurements with the routine analysis without causing any extra time delay. A summary of the PDA-data are reported together with normal heat analysis.

The software gives the total amount of detected inclusions in weight% (B-factors) and an indication of the size distribution. The result can also be plotted in ternary phase diagrams.

The software, how it is used and the results from the evaluation will be presented.

The work is applied in the RFCS-project RAMSCI and the Swedish project "Innestyr" financed by the Swedish Government through Vinnova.

Introduction

Pulse distribution analyzing technique in optical emission spectroscopy (PDA-OES) is today an established technology for a fast detection of inclusions in steel, but there is a lack of software that presents the results in a user-friendly way. Customers want to know the type and amount of inclusions and their size-distribution. To meet this a software has been developed and integrated in the LIMS systems at Outokumpu (offline) and at SSAB (offline and online). Basic principle of PDA-OES is not described here. The name of the new developed software is Dynalab-PDA and can be adopted to different spectrometers. At Oxelösund it has been adopted to an ARL4460 and at Avesta to an Spectro M10.

Evaluation principle

The SSAB/KIMAB nanogram model (developed during the AFMATH-project, ref 1)) is used and is based on a calibration by ordinary bulk reference samples using the total content and the amount of sputtered material. In this way a calibration between intensity and nano-grams is achieved.

Basic parameters to be evaluated are the following:

- Average concentrations (bulk)
- B-factors (The total weight of each detected inclusion element is summed up and the total concentration calculated from the ablated mass. The results are presented as B-factors).
- Inclusion types
- Compositions of different inclusion types
- Size distributions
- Oxygen index (calculated oxygen content based on stoichiometry)

The steps in evaluation are:

Step#1 Pulsograms

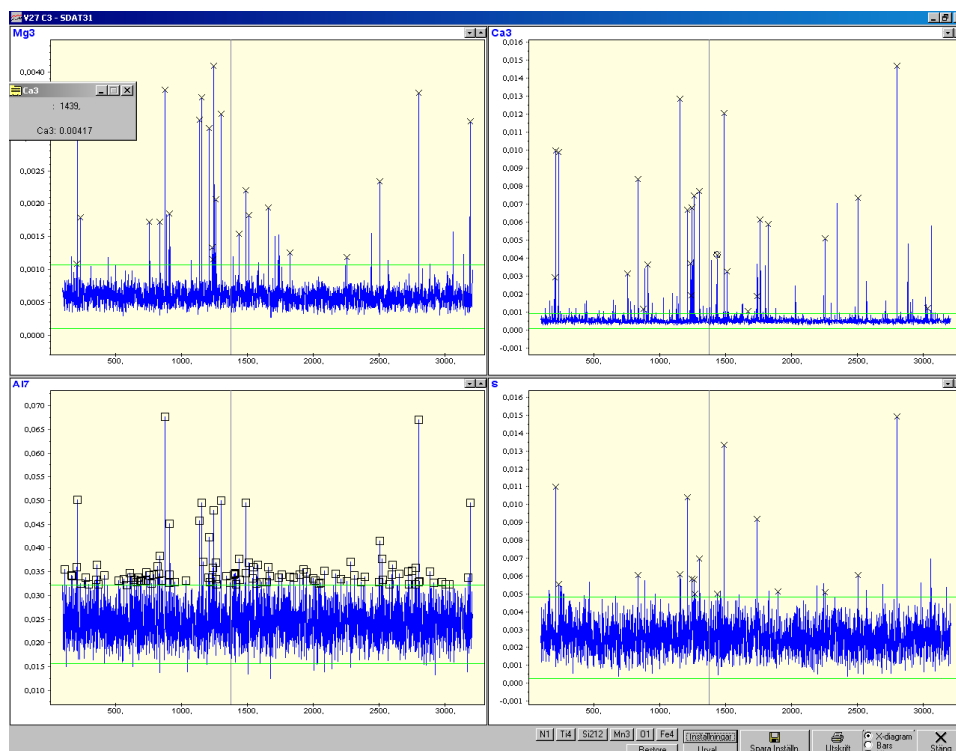


Figure 1 Pulsograms achieved in the new software showing outliers for Mg, Ca, Al and S

Step #2 includes evaluation of outliers using basic statistical procedures as average and standard deviation in sequence. The results are presented graphically as shown in figure 2

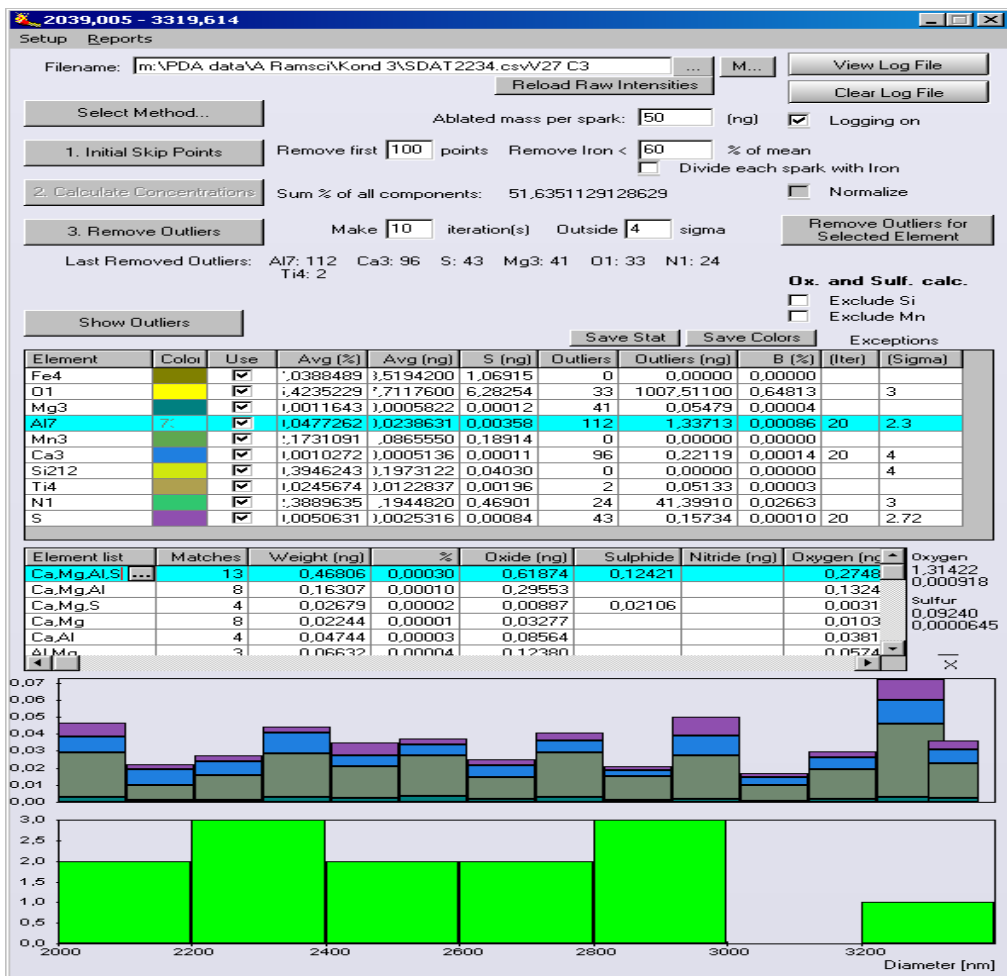


Figure 2. Printout of calculation steps and primary result presentation from Dynalab-PDA software

Calculation steps using combos in figure 2

- "Select" an evaluation method
- "Skip" the first 500 sparks
- "Calculate" bulk concentration
- "Remove outliers" and recalculate new standard deviation limits of the background using several iterations
- "Show outliers" results in primary result presentation

Primary result presentation

- Presentation of composition and B-factors
- Compounds
- Graphs for inclusion composition and a rough size distribution.
- Oxygen is presented as an index

Report layouts

Various report layouts are available, depending on different demands. A SSAB variant is shown in Figure 3.

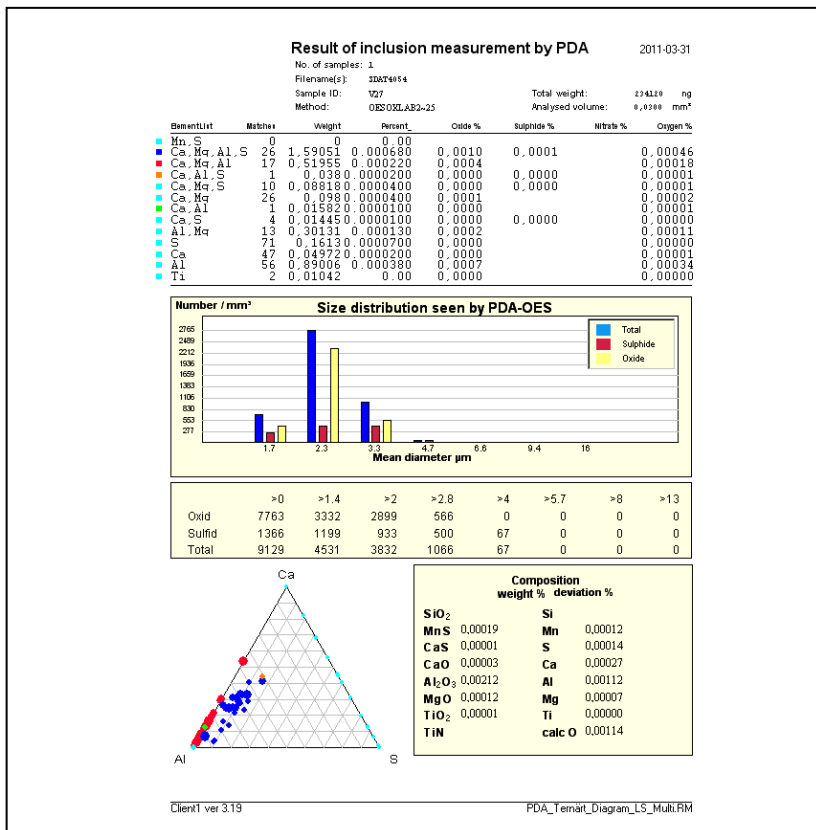


Figure 3. The SSAB report layout including online results.

Here the table on top presents on line the weight% of inclusions (B-factors) reported together with the normal heat analysis. The PDA size distribution is presented in the histogram. The accumulated distribution is given in a table. At the bottom of the report sheet there is a ternary diagram, which can be used as a finger-print for cleanliness of the specific steel. At the bottom to the right, the calculated oxygen index is shown based upon stoichiometry.

Flexibility

Calculation parameters can easily be changed and the measurements recalculated. The software is equipped with different modules for statistical reporting. Figure 4 shows an example of statistical treatment where a dirty steelplate sample is compared with a population of clean steelplate samples of the same grade. The black bars indicate average and 2-sigma levels of the the clean sample population (10 samples) . The dirty sample has levels outside the 2-sigma value for the inclusion types CaAlMg, CaAl and TiN. The software meets the demands in customer related questions.

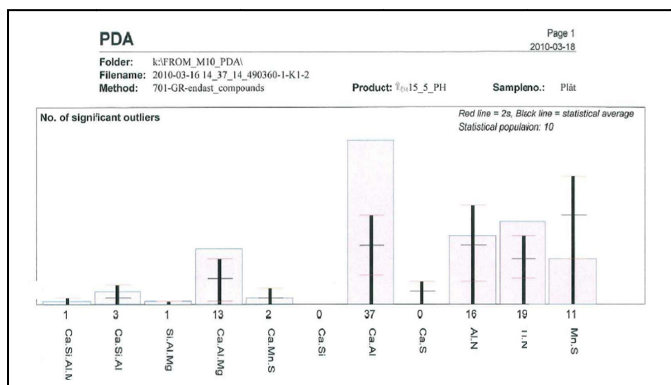


Figure 4. Cleanliness comparison between a dirty sample and a population of clean samples

Changes in instrumental setup in order to implement on-line measurements.

Shortest possible analysis time is necessary for the normal pre-samples. When integrating PDA sequence analysis time, the total analysis time would be too long.

In order to integrate the PDA measurements with normal analysis without losing any response time, both the pre-spark condition and the analyzing condition have been used for PDA-analysis. The sparking frequency had to be lowered for the pre-spark from 600 Hz to 400 Hz as the electronics was not fast enough. The same response function could be used after normalization to ablated mass, which was about 150 ng per spark for pre-spark and about 50 ng per spark for the analyzing condition. Integration of PDA with normal analysis has made it necessary to include a short pre-spark before collecting the PDA-data. In spite of this, still the first 100 sparks have to be excluded before the sparking is stable after changing of condition. The high energy spark is necessary in order to implement nitrogen measurement.

In this way PDA could be included in normal pre-sample analysis without losing more than a few seconds per sample. Comparisons of the two sparking conditions have shown that the evaluated inclusion content in weight% is the same for the two sparking conditions but the size distributions differ. Tests have shown that the pre-spark does not affect the size-distribution. By using the sparking condition at pre-spark (hard 150 ng/spark) and the analyses condition (50 ng/spark) the statistics for routine production samples have been improved. The PDA-data for all production samples are registered and evaluated on line.

Conclusion

Dynalab-PDA is efficient and valuable in evaluation of non-metallic inclusions in process metallurgy. It is unique with respect to flexible graphics presentations in a simple way. Together with the online integrated method of OES-analysis for normal measurement and PDA-measurement it is a new powerful tool in process control.

The present work has shown the potential to interpretate and report data in process control and finished products.

References

- 1) ECSC project 7210-PR/298: Fast characterization of steel cleanliness by advanced mathematical analysis of spark and laser source optical emission data (ADMATH), completed 2004-12-31.
- 2) ECSC project RFSP-CT-2007-00048 : Process based steel cleanliness investigations and rapid metallurgical screening of inclusions by modern PDA (RAMSCI), completed 2010-12-31.

LASER-BASED METHODS FOR CHEMICAL COMPOSITION ANALYSIS OF PARTICULATE EMISSIONS FROM STEELMAKING PROCESSES

C. Fricke-Begemann¹, N. Strauß², R. Noll¹

¹ Fraunhofer ILT, Steinbachstr. 15, 52074 Aachen, Germany

² RWTH Aachen University, Chair for Laser Technology (LLT), Steinbachstr. 15, 52074 Aachen, Germany

Abstract

Increasing evidence of adverse health effects from airborne particulate matter leads to extended legislative efforts on air quality. In order to focus abatement strategies in the most appropriate areas, a broad understanding of particulate emissions, environmental impacts and generating processes is required.

In a joint project of research and industry partners, investigations of particulate matter (PM) from iron and steelmaking processes were carried out. A major aspect of this project was the development and application of novel sampling and analytical techniques, including both real-time *in situ* techniques and laboratory analysis. The advanced measurement methods were applied to characterise fugitive and primary emissions, as well as ambient air samples.

For the analysis of particle composition, laser measurement methods based on laser-induced breakdown spectroscopy (LIBS) were developed by Fraunhofer ILT. The methods can be applied for fast screening analysis of sampled material and for real-time on-line particle analysis. They focus on the time- and size-dependent content of particulate matter. Different metals are found to be enriched in particles of different size for a certain process, e.g. a number of heavy metals like lead can be concentrated in sub-micrometer particles. The size-dependent composition gives a characteristic fingerprint of the emitting process. The on-line measurements with a response time below one second are suited also for process control applications and are sufficiently sensitive to allow for single-particle analyses even of ultrafine particles.

Introduction

In the last years, the importance of controlling particulate emissions has been widely recognized [1]. Whereas the environmental reasons for emission control are of interest to the public, there are also economic reasons for the industry to introduce monitoring measures due to the fact that the emissions can provide fast and accessible indications about the ongoing production processes.

In current governmental regulations mainly the total amount of particulates is considered and in some cases additionally the amount of certain components within the particulate mass. However, it has become evident that the size of the particulate matter in combination with the composition of the individual size classes is of major importance for health issues, due to different modes of action for different sized particles to physiologically affect the organism. For example, the effects of the fine dust, i.e. particles smaller than 2.5 µm, have been studied and published by the WHO and led to numerous consequences for air quality control [1, 2].

Hence, there is a strong need for measurement devices providing direct information about the particulate content of emissions and ambient air. Novel measurement techniques are required for both real-time *in situ* and laboratory investigations. Fraunhofer ILT has developed and validated laser-based techniques for particulate analysis based on laser-induced breakdown spectroscopy (LIBS). This work was partly carried out within a joint project of European partners from industry and research [3].

When considering the inorganic contents of particulate matter, the LIBS technique was considered as a promising measurement tool since it is known to provide multi-element information of material of any aggregation state. It

operates fast and requires only a small amount of sample material which is an important property when airborne particles are to be analysed.

Previous work has led to the development of LIBS microanalysis systems at ILT that can be used to characterise inclusions in solid metallic samples with inclusion sizes down to about 100 nm [4, 5]. Similar particle sizes occur also in particulate emissions where the size range below 100 nm is referred to as ultrafine particles. Due to the short time period for excitation and detection, which is typically in the range of microseconds, the method can also be applied to particles moving within a gas stream. It has been demonstrated before, that LIBS measurements can be carried out directly in the top gas of a blast furnace to continuously monitor the composition of the particulate matter [6]. Such top gas flows contain a high content of particles with sizes up to a few millimetres. The work presented here is focussing to smaller particles, including the size range of fine and ultrafine particles. Currently, for the on-line investigation of such particles, there exists only one type of commercially available instrument, which is an aerosol mass spectrometer being limited to the measurements of the mainly organic compounds of non-refractory material. However, in the steel and metals industry especially the metal content is of interest.

Screening analysis of particulate samples

For emission control it is desired to have an instrument of minimized technical complexity which provides quickly a broad range of particulate information. Today, the deposition of particles on a filter substrate is the most common technique to characterise particulate matter in ambient air. The electrical low pressure impactor (ELPI, Dekati Ltd.) is an instrument collecting particles fractionated by size on impaction plates that can be easily operated at any location (Fig. 1, left panel). The amount of particles for each size fraction is recorded on-line and the sampled material is available on the substrate for subsequent analysis. If this analysis is carried out by standard laboratory methods, it requires a high effort and amount of time for preparation and analysis. For most methods, like ICP-MS, the analyses require the transformation of the particulate matter into a liquid phase first. This involves the uncertainty of losing some material that cannot be resolved completely.

Therefore, a LIBS-based measurement technique was developed (Fig. 1, right panel) that allows the direct analysis of the material sampled on the substrate [7]. The automated measurement of a complete set of 13 ELPI substrates is carried out within about 20 minutes. This provides the possibility to sample a large number of particle streams and still get a measurement result of each sample without a long delay. The components used are compact enough to enable the development of a field deployable analysing system in the near future.

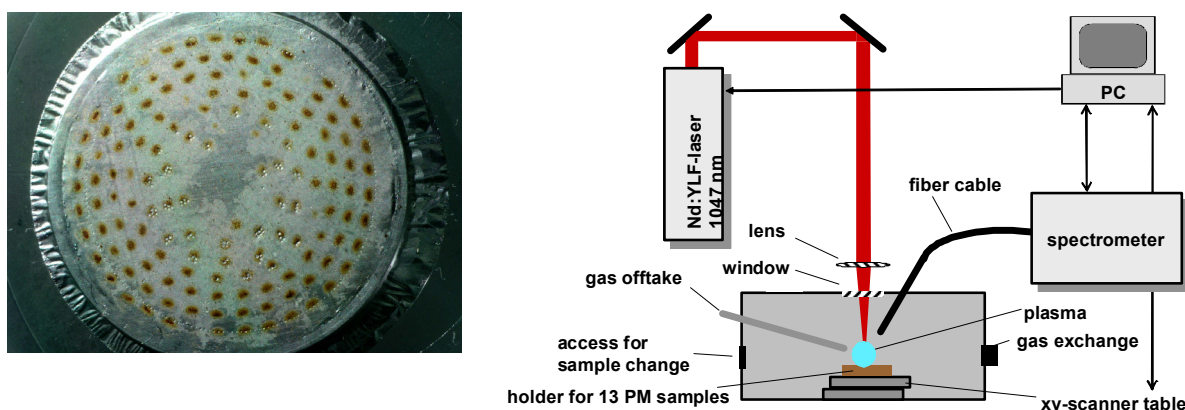


Fig. 1. Left: Aluminium substrate with spots of samples of particulate matter (substrate diameter 25 mm). Right: Set-up for scanning LIBS analysis of filter samples.

The substrates are placed in a sample holder on a pair of linear translation axes. Their movement presents the substrates subsequently to the fixed optical system. The LIBS microanalysis is performed at low pulse energies of about 1 mJ to incorporate primarily the material deposited in a thin layer on the substrate in the measurement. An

automated optical detection ensures that measurements are carried out only in the presence of particles, which are located in between 1 and about 200 spots on the substrates. The system is calibrated with a set of reference samples prepared using artificial aerosol generated from salt solutions, see also Fig. 2 below. For the application to steelwork emissions, the calibration was carried out with a total of 20 metals including iron and calcium as internal standards. A few sets of impaction samples were additionally analysed for metals using ICP-MS for comparison which provided a good agreement between the two independent methods [3].

Characterisation of steelworks emissions

Size fractionated samples of particulate emissions were taken from different steelwork emission sources [3]. As a result from the measurements, the size-dependence of the chemical composition is obtained. As shown in Fig. 2, a size range of particle diameters from about 40 nm to 10 μm is covered by the impactor and for each of the stages the elemental composition is measured independently. The examples in Fig. 2 show that different emission sources have characteristic size-dependences of their composition, even in cases where the average composition is similar.

Two sets of samples were analysed from each a UK and a French sinter plant. In the UK plant particles were sampled from the main stack twice, whereas the French samples were taken upstream and downstream of the back filter (numbers 1 and 2, respectively). Analyses of the ELPI data show the main particle mode with diameters at 0.12 μm . In the size range below 0.3 μm , in total 99 % of the number of particles are detected, which account for 75 % of the mass [3].

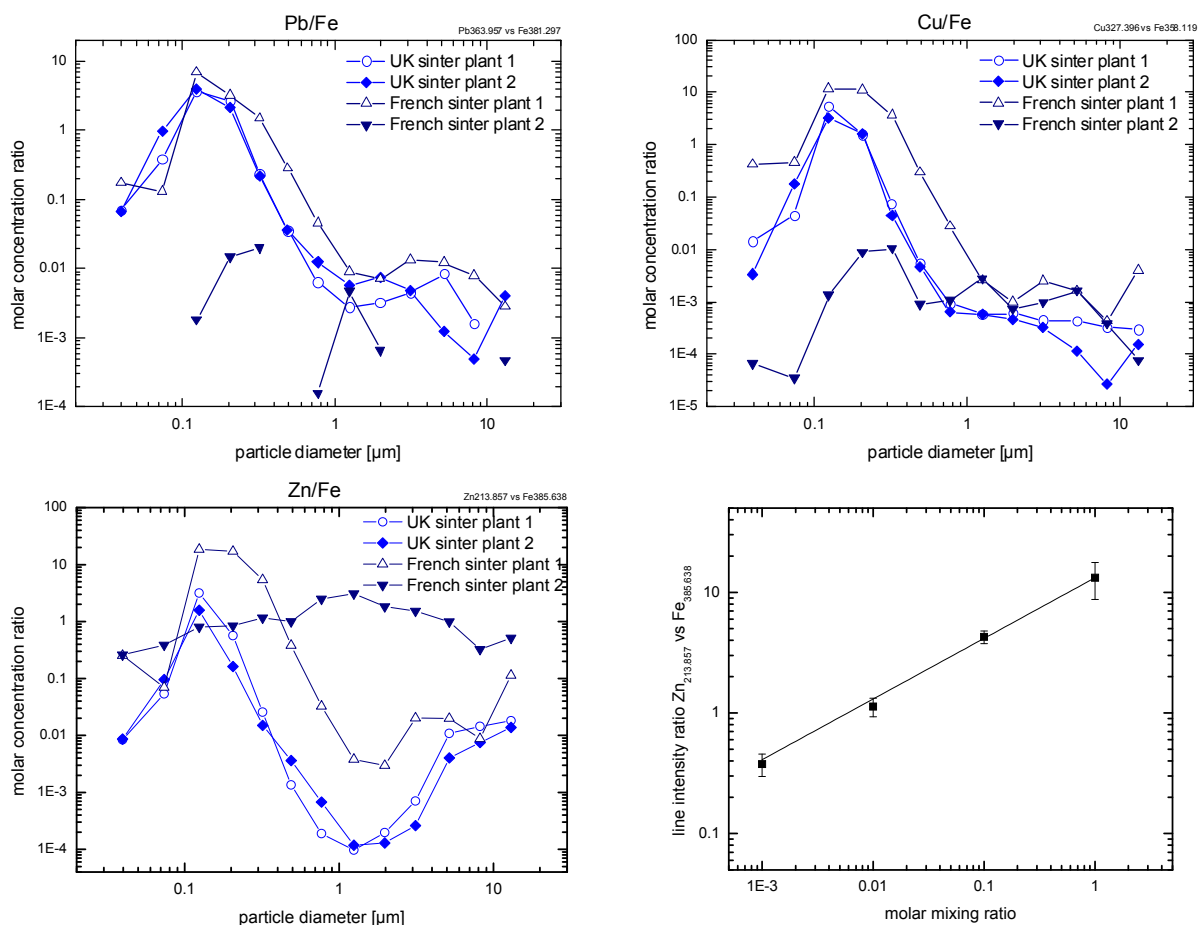


Fig. 2. Concentration ratios of lead (top left), copper (top right) and zinc (bottom left) to iron from sinter plant emission samples analysed using LIBS on sampled particulate matter, data points denoted as “-”-French sinter

plant 2" represent samples taken downstream the backfilter. The calibration curve for the Zn-to-Fe-ratio is shown at the bottom right.

The LIBS analyses, with examples given in Fig. 2, show the relative composition of the particles in the different size ranges. A prominent characteristic of the emissions is the high relative concentration of several metals in the particles with aerodynamic diameters of about 100 to 300 nm.

The list of metals with this characteristic includes Ag, Ba, Cd, Co, Cu, Hg, K, Na, Pb and Zn. The trace metals Hg, Ba and Co were not detectable in all measurements. A different characteristic is measured for Mg, Mn and partly As, where high concentration ratios are also found for the micrometer-sized particles, see also Fig. 3 below. To some degree an increase above 2 μm is also observed for Zn as shown in Fig. 2.

The variation of the composition with particle size is found to be very similar in the UK and French emission samples, although the absolute concentrations can vary between the sources. While the characteristic is observed in the same way for emissions in the different sinter plants, it is significantly different after the back filter. Together with the reduced total concentration, also the composition was changed. For the Cu-to-Fe ratio (Cu/Fe), a strong reduction was observed, especially in the lower size range, where only a weak maximum was preserved. Lower abundances downstream of the filter are similarly observed for a series of metals, including Pb. For Zn, in contrast, the relative abundance after the back filter is relatively high and exhibits only a small variation, with the highest ratio at 1 μm , where the minimum was found before the emission is treated by the back filter.

It can be noted from Fig. 2 that the abundance exhibits variations over several orders of magnitude. Although the calibration was carried out over a range of three or four orders of magnitude for most elements, this range did not cover the whole range occurring in the measurements. As in the example of Zn in Fig. 2, the calibration therefore had to be extrapolated in many cases to higher and lower mixing ratios.

Emission sampling was also carried out for other steelwork sources. Fugitive emissions were sampled on the roof of a BOS plant in the UK. The size-dependent composition obtained from the BOS samples is compared to the sinter plant emissions in Fig. 3. It is apparent that the fugitive BOS emissions are much more homogeneous in relation to the particle size when compared to sinter plant emissions. Beneath this fact, the Cu abundance is again found to be higher in the sub- μm range and for the larger particles. On the other hand, the Mg emissions are found to differ between one another. This is due to the fact that the samples were taken during different periods of the BOS batch process.

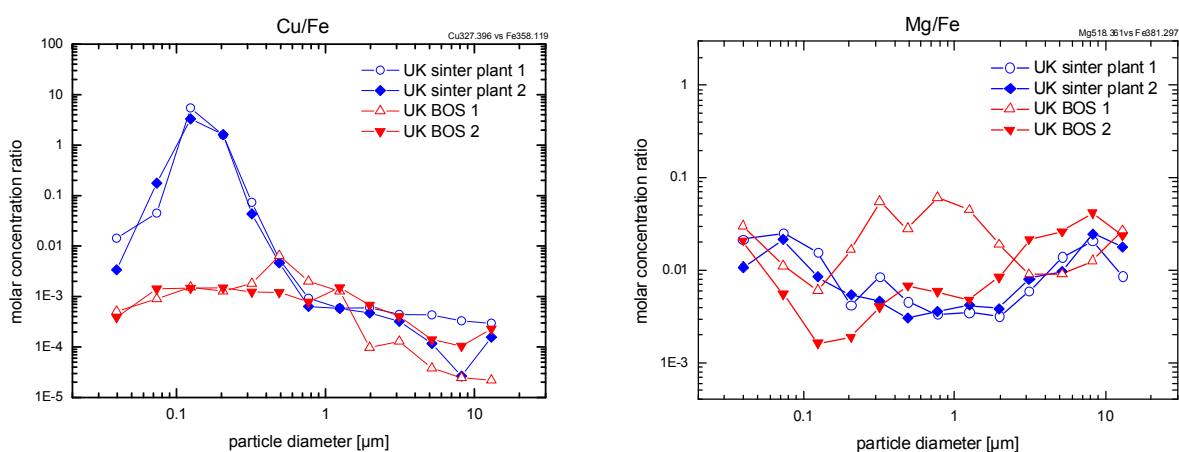


Fig. 3. Concentration ratios of copper (left) and magnesium (right) to iron from sinter plant and basic oxygen steelmaking (BOS) emission samples analysed using LIBS on sampled particulate matter.

In the course of the study, fugitive emission samples were also collected in the vicinity of a coke oven. Since coke making is also a batch process, the chemical compositions are again dependent on the selected sampling period. For example, arsenic was significantly detected only in two of three samples. The size dependent composition shows again specific features for the individual elements which deviate from the ones shown above. This demonstrates that the size-dependent chemical composition of particulate emissions is characteristic for the

emitting process and therefore can be used to identify possible emission sources when particulate matter in ambient air is investigated.

During a 10-day field campaign, ambient air samples were taken in an urban area near a continental integrated steelworks plant. Due to untypical meteorological conditions during the campaign, the wind at the measurement site was only rarely coming from the direction of the steelworks, which were located at a distance of 1 to 4 km. Particulate matter samples were collected over 24-h periods and subsequently analysed for their metal content. As an example, the relative concentrations of zinc and lead are given in Fig. 4, with respect to iron which was found to contribute to about 40 % of the total metals on average [3]. For each sample, the ratios are given for ultrafine ($< 0.1 \mu\text{m}$), fine ($0.1\text{-}2.5 \mu\text{m}$) and coarse ($> 2.5 \mu\text{m}$) particle classes, based on the measurement of the individual stages as before. In the data for lead three days are clearly elevated. The days two and five were also the days with the highest total particle concentrations ($\text{PM}_{2.5} > 30 \mu\text{g}/\text{m}^3$ [3]). On these days, a high concentration of Pb is found similarly in the fine and ultrafine particles. The Zn content, in contrast, was enhanced only on day two, in the coarse particles but not in the ultrafines. These differences show that the measured particles are likely to originate from different processes within the steelworks, which were transported to the measurement site at different wind directions.

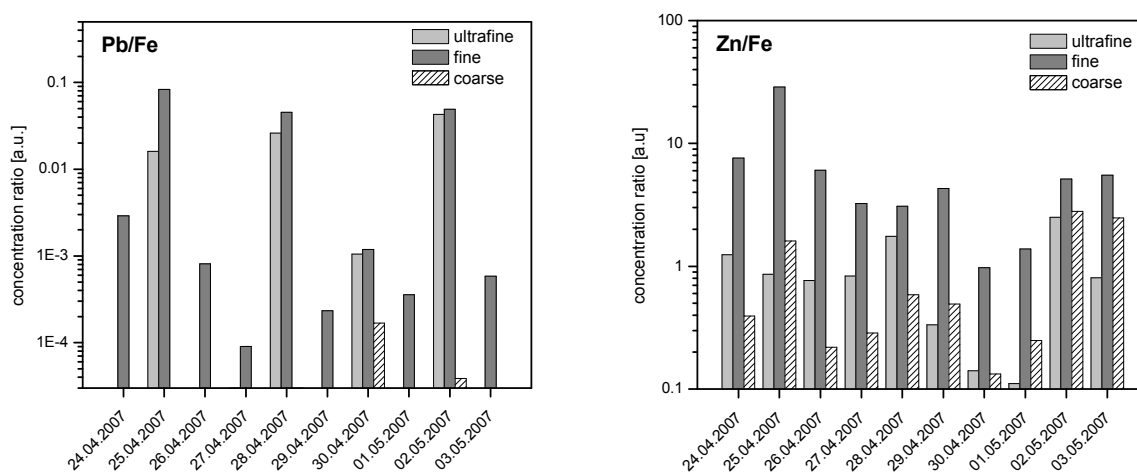


Fig. 4. Concentration ratios on logarithmic scale for lead (left) and zinc (right) in relation to iron for daily ELPI samples near a continental steelwork site.

Particle analysis in gas flows with LIBS

For the investigation of particulate matter it is often desired to perform measurements with a high time resolution. For example, batch processes like oxygen steelmaking and coke making generate particulates, whose character change on a time-scale of a few minutes. Observations in ambient air are strongly influenced by the meteorological conditions. Especially the wind direction can change quickly and transport emissions into a certain direction only for a few minutes, as it was encountered during the measurement campaign described above. When particulate analysis measurements are considered as a tool for process control, a short reaction time of the system is also important and the analysis results have to be provided in real-time.

Therefore we have developed an on-line particle analyser based on the LIBS method. The set-up for on-line measurements differs from that for filter analysis as shown in Fig. 1 and has been described in more detail in [8]. An air or gas stream carrying the particles is directed into a measurement chamber and crosses the focus of the laser beam which is propagating perpendicular to the flow direction. The pulse of a Nd:YAG laser with about 250 mJ induces a plasma in the stream of particles and only the particles which directly interact with the laser beam or the plasma are excited for element-specific emission. Since an individual measurement is carried out

within a few tens of microseconds, the response time of the system is governed mainly by the time constants of the measurement rate and the particle transport within the flow. In the set-up used, the measurement frequency is limited by the pulse repetition rate of the laser source to 10 Hz, whereas the spectrometer and its read-out electronics are capable of analysing individual spectra at rates up to 1 kHz.

Fig. 5 shows the response of the LIBS signal to the injection of salt particles of NaCl and CaCl₂. The particles were injected into the system for a period of a few seconds and with ten seconds separation. The emission signal for the respective metal rises within less than one second and exhibits a decay time of about ten seconds after the end of the injection which is probably due to mixing processes occurring in the gas flow.

In order to obtain size-resolved information about the particle composition, as from the filter samples described above, the measurement chamber is coupled to a differential mobility particle analyser (DMA, TSI Inc.). The DMA separates charged particles in an electrostatic field by their trajectory deflection which correlates to the particle diameter. Fig. 5 (right) shows the size distribution of particles generated from a salt solution and dried using a diffusion dryer. The particles generated are classified and subsequently registered by a particle counter. The size distribution of the number concentration has a maximum at about 50 nm. When the mass concentration is considered, the higher mass of the larger particles causes the maximum of the distribution to be shifted to about 200 nm. When the particle counter is replaced by the LIBS measurement chamber, emission intensities are obtained after temporal averaging which reflect the mass distribution. This demonstrates that the LIBS measurements are capable of determining the particle composition in terms of a mass average of the ensemble of particles included in the measurement.

The on-line LIBS set-up provides in real-time results of the same kind as those obtained from the filter samples. Since the individual particle sizes are measured subsequently when using a DMA, a complete measurement takes approximately one to two minutes.

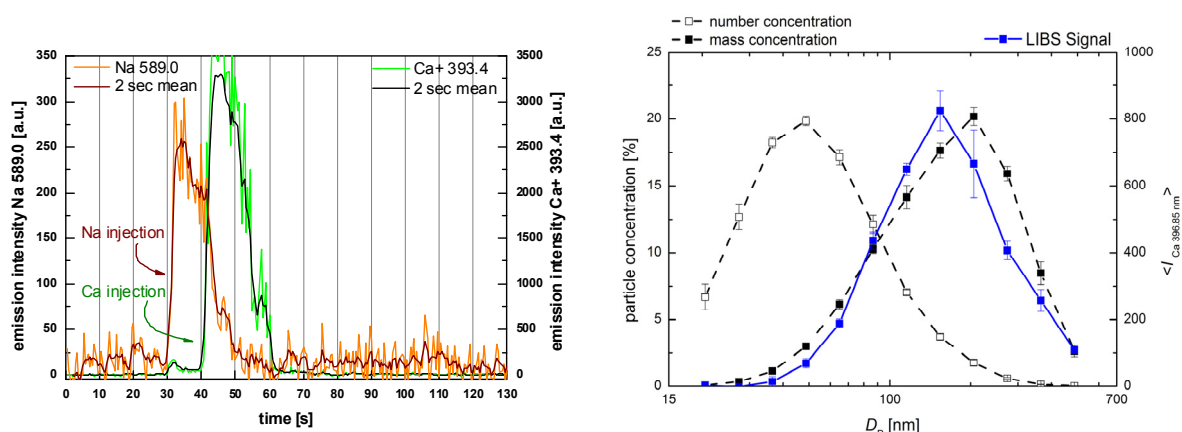


Fig. 5. Left: Temporal evolution of LIBS emission intensities measured from subsequent injection of Na- and Ca-containing particles. Right: particle concentration and LIBS signal as a function particle diameter.

Single particle detection

Particles produced in industrial processes cannot be assumed to be homogeneous and of the same composition in general. This is also the case for ambient air particles which may originate from different sources. For example, emitted particles will always get mixed with the background aerosol present in the air before. A strong interest exists therefore in the analysis of individual particles.

To enable single particle detection even for small particles with the on-line LIBS method, a high efficiency of the measurement system is required. Therefore, a particle inlet was developed which is intended to provide a defined guidance of the particle beam trajectory through the laser focus volume (Fig. 6). The inlet is based on the principle of an aerodynamic lens [9, 10]. This device consists of a series of orifices which separate the trajectories of particles and air mass and have been developed to transfer a particle beam well localized into a vacuum

chamber, e.g., for investigations by mass spectrometry. In contrast, here a pressure gradient of about 30 mbar only is present in relation to the ambient gas pressure.

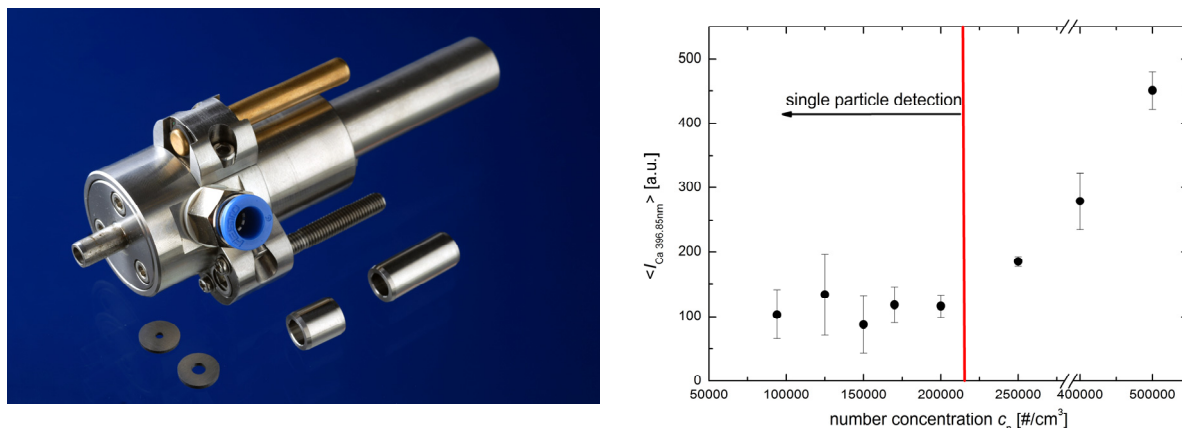


Fig. 6. Left: Photograph of particle inlet. Right: Dependence of emission intensity per particle hit on the number concentration for monodisperse particles of 154 nm diameter.

With this inlet, LIBS measurements of monodisperse particles have been carried out. The number concentration was reduced to identify the transition level below which only single particles are present in the interaction zone defined by the laser beam waist and the plasma. This level is identified by the individual evaluation of each LIBS measurement to discriminate events with particle hits from measurements in pure air. As shown in Fig. 6 (right) the average intensity of particle hits is constant for low concentrations and increases for higher concentrations where the statistical frequency of multi-particle measurements increases.

Measurements of single monodisperse particles at a fixed number concentration below the transition level are shown in Fig. 7. The resulting LIBS signal is strongly increasing with particle size. Single particles of 80 nm in diameter still produce a clearly detectable emission signal. The particle size can be converted into Ca mass with the assumption that they consist of pure CaCl₂ because they were generated from a CaCl₂ solution and dried prior to DMA classification and LIBS measurement ($\rho = 2,16 \text{ g}\cdot\text{cm}^{-3}$). The signal intensity is directly proportional to the calcium mass and the limit of detection can be determined to be in the order of 0.1 fg ($1\cdot 10^{-19} \text{ kg}$). The slope of the curve allows for the first time a determination of the sensitivity of the LIBS system in terms of absolute mass of a certain species within the plasma volume.

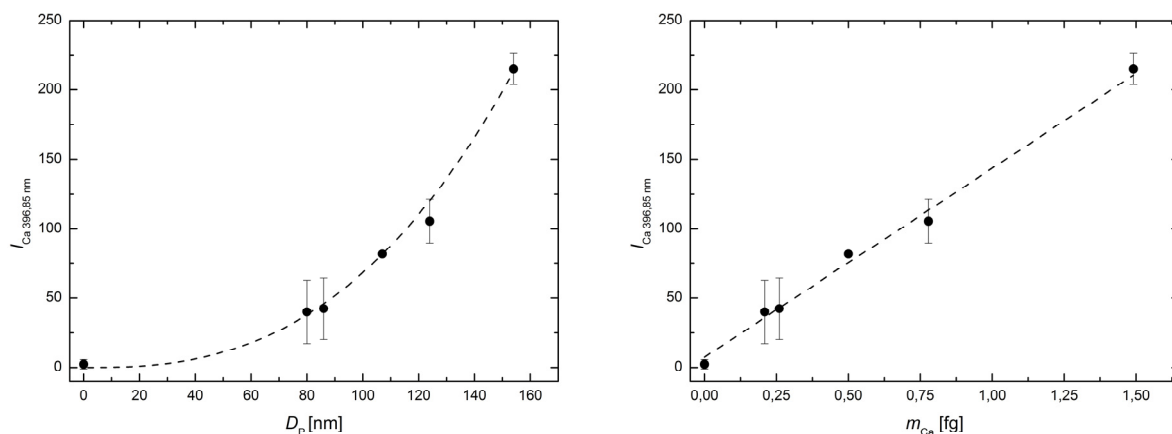


Fig. 7. Emission intensity for LIBS measurements of single particles at a number concentration of $1.25\cdot 10^5 \text{ cm}^{-3}$ as a function of particle size (left) and particle mass (right).

Conclusions

The LIBS method was studied for the analysis of particulate matter. A system was realised which allows fast automated scanning analyses of material deposited on filter substrates. In combination with a multi-stage cascade impactor it was used to analyse the size-dependent chemical composition of emission and ambient air samples. Depending on the emission source, the particles showed a strong variation of metal content in the investigated size range from 40 nm to about 10 μm . In particular, sinter plant emissions were found with a strongly enhanced concentration of several heavy and transition metals in particles of diameters of about 200 nm. The capability for fast multi-element analysis can be used for screening experiments and continuous monitoring applications which require the analysis of large numbers of samples.

As an alternative approach, an on-line LIBS system was developed which analyses the particles directly in the carrier gas stream to provide time-resolved measuring results. With short response times of less than one second, the system is suited for real-time applications which require a fast monitoring of rapidly changing processes. In addition to emission characterisation it can be applied to monitor dust-laden process gases or flue gas to observe continuously process performance and provide feedback for process control. The system is as well able to analyse size-segregated particles. Single-particle analyses even for particles in the ultrafine size range with diameters below 100 nm were demonstrated successfully.

Acknowledgement

Part of the work presented was carried out with financial support from the EU Research Fund for Coal and Steel under contract number RFSCR-04049 and from the Fraunhofer Gesellschaft. We thank our project partners for the cooperation.

References

- 1) World health organisation, *Health aspects of air pollution, results from the WHO project „systematic review of health aspects of air pollution in Europe“*, WHO report E83080, Juni 2004.
- 2) Directive 2008/50/EC of the European Parliament and of the Council of 21 May 2008 on ambient air quality and cleaner air for Europe, Official Journal L 152, 11/06/2008, 1–4.
- 3) D. R. Anderson, M. J. Booth, P. Collins, D. Ciaparra, J. S. Hodges, P. Le Louer, F. Drewick, C. Fricke-Begemann, N. Strauss, M. Dall'Osto, *Ultrafine characterisation of emission and impact of ultrafine particulate*, Final report to RFCS contract No RFSR-CT-2004-00049, EUR 23877, 2009.
- 4) Bette, H., Noll, R., Müller, G., Jansen, H.-W., Nazikkol, Ç., and Mittelstädt, H., *High-speed scanning laser-induced breakdown spectroscopy at 1000 Hz with single pulse evaluation for the detection of inclusions in steel*, J. Laser Appl., 2005, 17, 183-190.
- 5) Kuss, H.M., Mittelstaedt, H., and Mueller, G., *Inclusion mapping and estimation of inclusion contents in ferrous materials by fast scanning laser-induced optical emission spectrometry*, J. Anal. At. Spectrom., 2005, 20, 730-735.
- 6) Sturm, V., Brysch, A., Noll, R., Brinkmann, H., Schwalbe, R., Mülheims, K., Luoto, P., Mannila, P., Heinänen, K., Carrascal, D., Sancho, L., Opfermann, A., Mavrommatis, K., Gudenau, H.W., Hatzia Apostolou, A., and Couris, S., *Online multi-element analysis of the top gas of a blast furnace by LIBS*, CETAS 2006: Progress in analytical chemistry in the steel and metal industries, Verlag Glückauf, 183-188.
- 7) Kuhlen, T., Fricke-Begemann, C., Strauss, N. and Noll, R., *Analysis of size-classified fine and ultrafine particulate matter on substrates with laser-induced breakdown spectroscopy*, Spectrochim. Acta, Part B, 2008, 63, 1171–1176.
- 8) Strauss, N., Fricke-Begemann, C., and Noll, R., *Size-resolved analysis of fine and ultrafine particulate matter by laser-induced breakdown spectroscopy*, J. Anal. At. Spectrom., 2010, 25, 867–874.
- 9) Liu, P., Ziemann, P. J., Kittelson, D. B., and McMurry, P. H., *Generating Particle Beams of Controlled Dimensions and Divergence: I. Theory of Particle Motion in Aerodynamic Lenses and Nozzle Expansions*, Aerosol Sci. Technol., 1995, 22, 293-313.
- 10) Liu, P., Ziemann, P. J., Kittelson, D. B., and McMurry, P. H., *Generating Particle Beams of Controlled Dimensions and Divergence: II. Experimental Evaluation of Particle Motion in Aerodynamic Lenses and Nozzle Expansions*, Aerosol Sci. Technol., 1995, 22, 314-324.

NATURALLY OCCURRING RADIOISOTOPES (POLONIUM-210 / LEAD-210) IN STEELMAKING MATERIALS AND THE IRON ORE SINTERING PROCESS

Franck Dal-Molin, Eric Aries, Raymond Fisher, David Anderson and Simon Johnston

Tata Steel Research Development and Technology, Swinden Technology Centre, Rotherham, S60 3AR, UK

Summary

Iron ores contain naturally occurring radioisotopes arising from the presence of traces of uranium and its decay products, two of which, polonium-210 and lead-210, are volatilised and emitted in the iron ore sintering process. In England and Wales the emissions of polonium-210 and lead-210 from the iron ore sintering process are regulated by the Environment Agency in accordance with the 1993 Radioactive Substances Act. Emissions of polonium-210 and lead-210 are monitored at least twice per annum at all sinter plants operated by Tata Steel's sinter plants. There are no national or international standard methods for the determination of the polonium-210 and lead-210 activity in waste gas emissions from industrial processes. In accordance with the emission limits imposed by the England and Wales Environment Agency, Tata Steel carried out research and development between 2008 and 2010 into the radiochemistry of polonium-210 and lead-210 radioisotopes. In particular, a state-of-the-art analytical radiochemistry laboratory, located at its Swinden Research and Development Technology Centre (Rotherham, UK), was created to accurately measure polonium-210 and lead-210 activities in steelmaking materials and stack particulate emission samples. The analytical methods developed were accredited by the United Kingdom Accreditation Service (UKAS) to ISO 17025 standard in 2010. This paper presents details of the analytical and sampling methods used for measuring both radioisotopes in steelmaking matrices and particulate emission samples. It provides information on sample preparation, analytical instrumentation and quality assurance procedures that have been put in place to fulfil the requirements of the ISO 17025 standard. Finally, it presents data from research carried out to investigate the occurrence of polonium-210 / lead-210 in a range of steelmaking materials.

1. Introduction

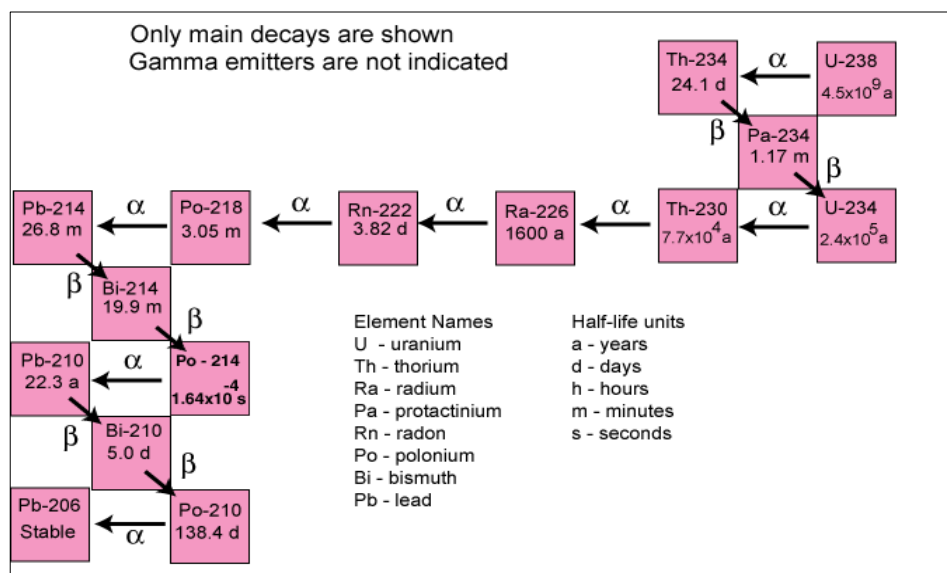
All the raw materials used in the iron ore sintering process contain trace quantities of naturally occurring radioisotopes stemming from the presence of uranium-235, uranium-238 and thorium-232 in the iron ores, coal and minerals used in the process. The natural decay of the parent radioisotopes results in the presence of numerous daughter products according to the respective decay chains. The end product of each decay chain is a stable isotope of lead (Fig. 1). Geological materials, such as iron ores, coal and minerals used in sintering, have been present undisturbed in the ground for many years and, generally speaking, the decay chains are in equilibrium, i.e., all the radioisotopes present have the same rate of decay. The activities of daughter products in a given natural material will be dependent upon the amount of uranium-235, uranium-238 or thorium-232 originally present and the length of time that has elapsed since these radioisotopes were deposited. Several daughter products in the uranium and thorium radioactive decay schemes are volatile and may be evolved and become more concentrated in the off-dusts from thermal processes, such as iron ore sintering. In the sintering process the main radioisotopes are polonium-210 and lead-210 and the emissions of these species from Tata Steel UK (formerly Corus UK) sinter plants have been regulated by the England and Wales Environment Agency since 1998. Similar regulations also apply to the sintering plant at Tata Steel's IJmuiden Works in the Netherlands. Between 1998 and 2008, external accredited laboratories were used by Tata Steel for the analysis of polonium-210 and lead-210 in steelmaking materials and stack particulate emission samples. The determination of polonium-210 requires specific instrumentation for which only a small number of laboratories are equipped in the UK. Most of the UK accredited laboratories involved in radiation analysis were formerly associated with radiation protection agencies or the UK nuclear industry. Tata Steel UK has previously used the Health Protection Agency (HPA) laboratories based at Chilton and Glasgow as external contractors for polonium-

210 and lead-210 analysis. However, from 2008, the HPA laboratories did not always have the capacity to analyse the samples provided by Tata Steel owing to an unusually high sample throughput resulting from the Litvinenko incident (a Russian dissident believed to have been poisoned by ingestion of a large quantity of polonium-210 at a restaurant in London). This coincided with a greater demand for such analyses within Tata Steel owing to the increased research activity on the behavior of polonium-210 and lead-210 in the sintering and blast furnace processes. Consequently, it was decided that Tata Steel would develop and validate in-house radiological methods for the measurement of polonium-210 and lead-210 in steelmaking materials and emission samples. A state-of-the-art radiological laboratory equipped with high resolution alpha and gamma spectrometers was built in 2008. Subsequently, analytical methods were successfully developed by Tata Steel for the measurement of polonium-210 and lead-210 in steelmaking materials, by-products and emission samples. The methods developed were accredited by the United Kingdom Accreditation Services (UKAS) to the ISO 17025 standard in 2010. This paper presents details of the analytical and sampling methods used for measuring both radioisotopes in steelmaking materials and particulate emission samples. It provides information on sample preparation, analytical instrumentation and quality assurance procedures that have been put in place to fulfill the requirements of the ISO 17025 standard. Finally, it presents data from research carried out to investigate the occurrence of polonium-210 / lead-210 in a range of steelmaking materials.

2. Background

In 1898, Marie Curie separated two new elements, radium and polonium, from several tonnes of pitchblende. Polonium was named in honour of Poland, Marie Curie's birthplace. Polonium-210 was only obtained in very small amounts, and conclusions about its chemical nature were made on the basis of the elements with which it co-precipitated. Polonium-210 is a relatively short-lived isotope (Table 1), with a half-life of 138 days. Even though the half-life of polonium-210 is short, it is always present in the environment because it is maintained by its parent nuclide (i.e. lead-210), which decays to polonium-210 by beta emission through the short-live radionuclide bismuth-210 (Fig. 1), and has a half-life of 22.3 years [1].

Fig.1. Uranium-238 decay chain.



Typically, two techniques can be used for the determination of radioisotopes undergoing radioactive decay by alpha particle emission. These are either by direct measurement of the alpha particles emitted in the decay process (alpha-spectrometry) or, in suitable cases, by measurement of gamma-rays accompanying the decay process (gamma-spectrometry). In the case of polonium-210, there is no accompanying gamma-ray emission so that it is only possible to measure the activity of this radioisotope by alpha spectrometry. Lead-210, however, undergoes beta decay to bismuth-210 (half-life 5.4 d), which subsequently decays to polonium-210 by beta

emission. The beta particle decay of lead-210 is accompanied by a weak gamma-ray emission with energy of 46.5 keV, which permits its activity to be measured directly by gamma-ray spectrometry. However, this direct measurement is only possible for samples exhibiting an activity in the Becquerel per gram (Bq/g) range using a high resolution gamma-spectrometer system with a germanium semiconductor detector, but cannot easily be detected for samples exhibiting low activity (i.e. Bq/kg range). For the latter types of sample, lead-210 measurements are carried out by the indirect measurement of the alpha activity of its granddaughter isotope polonium-210 [2]. When alpha spectrometry measurements are carried out, another polonium isotope (polonium-209) is used as an internal standard to determine the chemical recovery and to quantify polonium-210. Polonium-209 can be used as an internal standard because it is an alpha-emitter, has identical physico-chemical properties to polonium-210, has a relatively long half-life ($T_{1/2} = 103$ y) and does not interfere with the analysis in alpha spectrometry.

Table 1. Characteristics of lead-210, polonium-210 and polonium-209.

Isotope	Half-life	Decay mode	Energy (keV)	Gamma emissions
Polonium-210	138.4 days	Alpha	5310	No
Polonium-209	103 years	Alpha	4889	No
Lead-210	22.3 years	Beta	63.5	Yes (46.5 keV)

3. Experimental

3.1 Sampling

There are currently no national or international standardised procedures for the determination of the activities of polonium-210 and lead-210 in waste gas emissions from industrial processes. The sampling from sinter plants can be performed meeting the requirements of either BS EN 13284-1 [3], typically used to determine particulate emissions in waste gases, or BS EN 14385 used to determine trace metals emissions in both particulate and gas phase [4]. The former method is currently used at Tata Steel for sampling and consists in the isokinetic extraction of particulates from the waste gas stream through a sharp edged nozzle. The particulate matter is then trapped on a pre-weighed quartz filter. Sampling is carried out at multiple points in the stack to obtain a representative sample. On completion of sampling, the filter is dried and weighed to determine the mass of particulate collected. During sampling, stack temperature, barometric pressure, water vapour and gas meter temperatures are recorded periodically to allow the volume of gas sampling to be calculated at reference conditions. (0°C, 101.3kPa and either wet or dry gas depending on the permit conditions). The second method is recommended for the determination of emissions of both particulate-bound and gas-phase metals, including As, Cd, Cr, Co, Cu, Mn, Ni, Pb, Sb, Tl, and V, from stationary sources and is the most relevant method to study the partitioning of polonium-210 and lead-210 between the particulate and the gas phase. This method also uses isokinetic sampling to extract a sample of the waste gas, but after collection of particulate matter on a pre-weighed quartz filter the gas is passed through a series of impingers containing nitric acid and hydrogen peroxide in order to trap any metals present in the gas phase. The filter and absorption solutions are then analysed by inductively coupled plasma mass spectrometry to determine the concentrations of the cited metals.

3.2 Analysis

Because of their energy range, alpha particles are completely stopped by the dead layer of human skin or a single sheet of paper. Alpha particles within a solid matrix would be also largely attenuated by the solid matrix itself and only the particles released at the surface of the solid would be detected. Therefore, polonium-210 analysis requires an important sample preparation method to extract selectively the polonium-210 present in the sample prior quantifying it using alpha spectrometry. The sample preparation method developed by Tata Steel is illustrated schematically in Fig. 2. Samples are spiked with a known amount of polonium-209 standard before being digested using a mixture of hydrochloric and nitric acid (*Aqua Regia*) in a microwave-assisted digestion

system. The resulting digests are filtered and evaporated to dryness, and the residues are re-dissolved in concentrated hydrochloric acid (10M). Iron III (Fe^{3+}), a major interference in the analysis of polonium-210 by alpha spectrometry, is extracted from the concentrated hydrochloric acid solution using liquid-liquid extraction with diisopropylether. After extraction of iron (III), the concentrated hydrochloric acid solution is evaporated to dryness and the residue is taken up in 1M hydrochloric acid. A silver disc is placed in the solution for 6 hours at 80°C to allow for the spontaneous deposition of polonium-209 and polonium-210 using a specially designed glass holder and magnetic stirring (Fig. 3). The alpha particles emitted from the decay of radionuclides deposited on the silver disc are counted using an ORTEC Octète Plus Alpha-Spectrometer instrument (Fig. 3). The alpha spectrometer is equipped with a semiconductor detector that is capable of discriminating between alpha particles of different energy in the range 4 to 8 MeV. Owing to the short range of alpha particles in air, the counting is performed in a vacuum chamber (Fig. 3). Typically, ion-implanted silicon or silicon surface barrier detectors having a diameter of ~ 25 mm and a very thin sensitive depth (typically $400\mu\text{m}$) are used for alpha spectrometry applications. Subsequently, additional silver discs are placed in the sample solution to ensure complete depletion of polonium-209 and polonium-210 from the sample. The solution is then stored for typically three months to allow for an in-growth period of fresh polonium-210 (from the decay of lead-210), and the resulting polonium-210 produced by in-growth is plated onto a silver disc as before and determined by alpha spectrometry to obtain indirectly the lead-210 activity of the sample.

Fig. 2. Flow chart of the analytical procedure used for the analysis of polonium-210 and lead-210 in steelmaking materials.

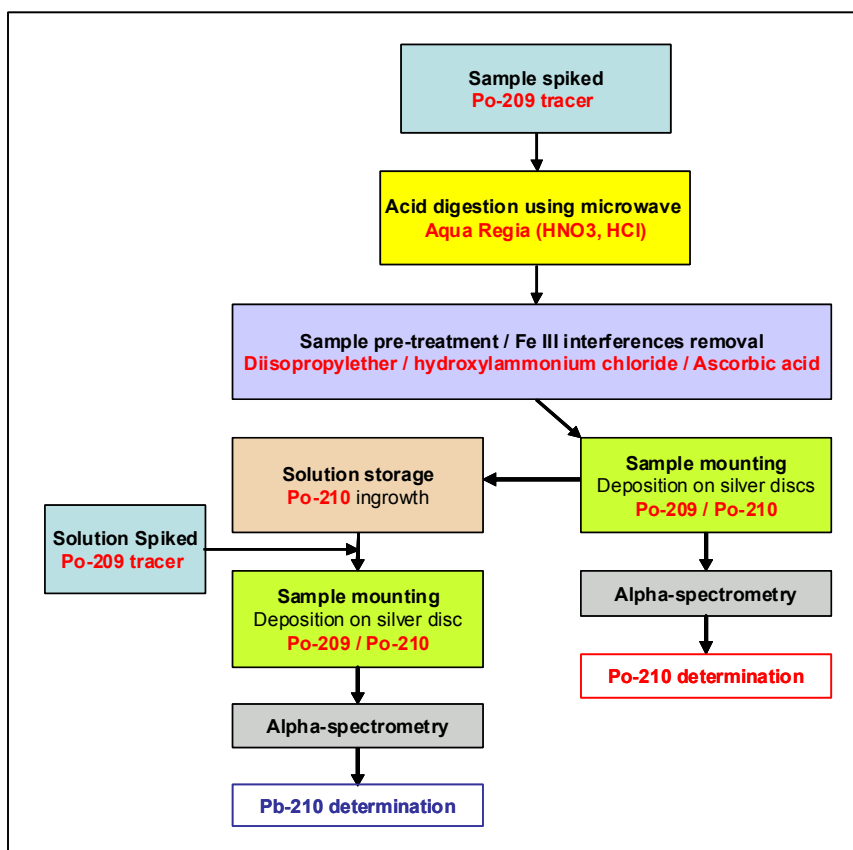
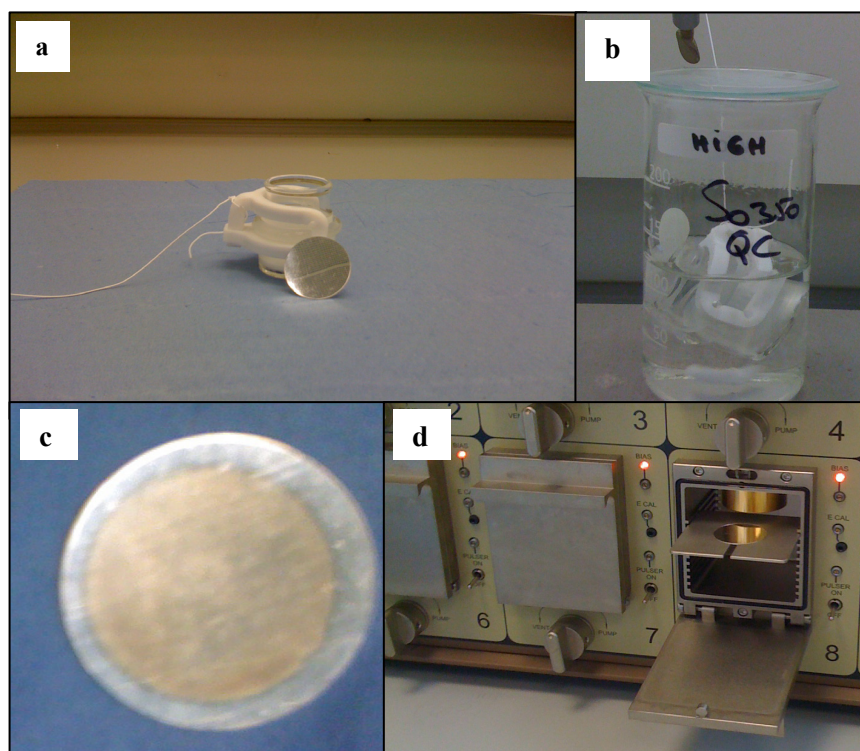


Fig. 3. Pictures of (a) specially designed glass holder used to hold silver discs in the sample solution, (b) sample solution with silver disc during deposition of polonium-210, (c) silver disc after deposition and (d) alpha spectrometry vacuum chamber.



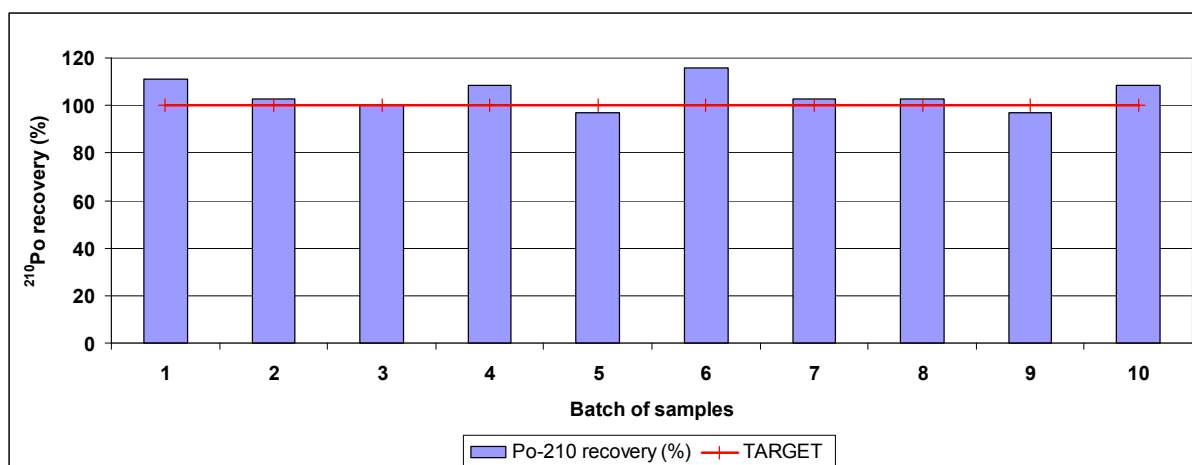
The determination of lead-210 is carried out also by isotope dilution using the polonium-209 as internal standard after an in-growth period of approximately three months. Samples exhibiting a relatively high activity (Bq/g range) are also analysed using an ORTEC High Performance Germanium Detector Gamma Spectrometer (method not described) in order to confirm lead-210 measurements using alpha spectrometry via the polonium-210 in-growth method.

4. Results and discussion

4.1 Method validation

As part of the quality control programme and in accordance with the ISO 17025 accreditation requirements, each batch of samples contains a blank sample in order to control possible contamination and background levels and a quality control sample (QC). The QC sample used in the procedure is composed of a blank sample (pure iron oxide) which is spiked with a known amount of polonium-210 and polonium-209 using certified standard solutions. This QC sample provides the analyst with a measure of the accuracy of the method by comparing the theoretical polonium-210 activity of the sample with the measured polonium-210 activity in the sample. The results obtained from ten replicate analyses of the QC sample are depicted in Fig. 4. It shows that polonium-210 recoveries in the QC samples were very close to the target value of 100% showing very good precision and accuracy for the method.

Fig. 4. Polonium-210 recoveries for a series of ten replicate analysis of a quality control material composed of pure iron oxide spiked with known amounts of polonium-210 and polonium-209.



The method was further validated by analysing the sediment Reference Material IAEA-384 from the International Atomic Energy Agency (IAEA). In total, six replicate analyses of the sample were carried out following the entire analytical procedure. Table 2 summarises the data obtained for these validation experiments.

Table 2. Comparison of the polonium-210 activity reference value in the IAEA-384 marine sediment with the mean value obtained using the analytical procedure developed by Tata Steel.

IAEA-384 Reference Sediment	Polonium-210 activity (Bq/g)	Standard Deviation (Bq/g)
Reference value	0.022	0.001
Measured value (N=6)	0.020	0.002

As may be seen from Table 2, a very good agreement was obtained between the polonium-210 reference value of the sample and the activity determined using the analytical method developed by Tata Steel.

4.2 Partitioning of polonium-210 / lead-210 between particulate and gas phase in sinter plant emissions

In order to verify the assumption that the radioactive species are predominantly found in the particulate phase studies were carried out at two sinter plants to determine the degree of partitioning of polonium-210 and lead-210 between the particulate and the gas phase in sinter plant emissions using the British Standard EN 14385, which affords discrimination between particulate-bound and gas phase metals. The results obtained at sinter plant 1 clearly indicated that both the polonium-210 and the lead-210 were predominantly present in the particulate phase in sinter plant emissions. As may be seen from Table 3, the polonium-210 and lead-210 activities found in the gas phase for the samples ranged from 0.0006 to 0.005 Bq/Nm³ and from 0.003 to 0.008 Bq/Nm³, respectively. These concentrations equate to there being only 0.01 to 0.13% of polonium-210 and 0.23 to 0.66% of lead-210 of the total emission activity of the corresponding radioisotope present in the gas phase. In other words, 99.87 to 99.99% of the polonium-210 and 99.34 to 99.77% of lead-210 are associated with the particulate phase. At sinter plant 2, the polonium-210 activities found in the gas phase for the two samples collected were 0.007 and 0.024 Bq/Nm³, equating to only 0.07% and 0.19% of the total polonium-210 activity present in each sample. Similarly, the lead-210 activities found in the gas phase for these samples were 0.028 and 0.038 Bq/Nm³, equating to 0.42% and 0.46% of the total lead-210 activity. These results show excellent agreement with those obtained at Sinter Plant 1. This means that, on average, approximately 99.9% and 99.5 % of the polonium-210 and lead-210, respectively, was associated with the particulate matter in the emission.

Table 3. Partitioning of polonium-210 and lead-210 in emission samples collected using the British Standard EN 14385 at sinter plants 1 and 2.

	Activity (Bq/Nm ³ , dry)	
	Polonium-210	Lead-210
Sinter Plant 1		
Test 1 (Particulate)	4.0 [99.99%]	1.1 [99.73%]
Test 1 (Gas phase)	0.0006 [0.01%]	0.003 [0.27%]
Test 2 (Particulate)	4.5 [99.93%]	1.3 [99.77%]
Test 2 (Gas phase)	0.003 [0.07%]	0.003 [0.23%]
Test 3 (Particulate)	3.9 [99.87%]	1.2 [99.34%]
Test 3 (Gas phase)	0.005 [0.13%]	0.008 [0.66%]
Sinter Plant 2		
Test 1 (Particulate)	10.01 [99.93%]	6.7 [99.58%]
Test 1 (Gas phase)	0.007 [0.07%]	0.028 [0.42%]
Test 2 (Particulate)	12.65 [99.81%]	8.2 [99.54%]
Test 2 (Gas phase)	0.024 [0.19%]	0.038 [0.46%]

The results of this study demonstrated that both polonium-210 and lead-210 were present in the particulate phase in sinter plant emissions and therefore that the use of British Standard EN 13284-1 is justified for the sampling of these radioisotopes in sinter plant emissions.

4.3 Studies into the occurrence of polonium-210 and lead-210 in steelmaking materials

Sinter plants are part of an operational chain involved in the production of steel via the integrated process route, and their principal purpose is to convert fine iron ores into a clinker-like agglomerate (sinter) that has the essential physical and chemical properties for use in modern high-performance blast furnaces. The sintering process also plays a pivotal role in the recycling of ferruginous materials (reverts) arising from the downstream processes in steel production, thus making a strong contribution to the sustainability of the steel industry by the conservation of natural resources and by minimising the disposal of useful iron-bearing by-products to landfills. In the sintering process, blended iron ore fines, fluxes (e.g. limestone and olivine), fuel in the form of coke breeze and/or anthracite, and some recycled materials such as dusts and grits from downstream processes, are fused together to produce the sinter product. All of the raw materials used in the sintering process contain trace quantities of polonium-210 and lead-210, however little is known about their respective activities. In order to understand the behaviour of polonium-210 and lead-210 within the iron ore sintering process, it was important to have accurate measurements of these radioisotopes in the raw materials and reverts used therein. Accordingly, representative samples of each type of input and output material typically in use at UK sinter plants were collected and submitted for polonium-210 and lead-210 analysis. The results are summarised in Table 4.

Table 4. Polonium-210 and lead-210 activity range for key elements of the raw sinter mix at UK sinter plants.

Component	Polonium-210 activity range (Bq/g)	Lead-210 activity range (Bq/g)
Iron ores	0.001 – 0.099	0.002 – 0.082
Limestone	0.002 – 0.042	0.003 – 0.025
Millscale	0.001 – 0.003	0.002 – 0.004
Coke breeze	0.002 – 0.011	0.004 – 0.006
BF flue dust	0.011 – 0.48	0.043 – 0.93
BF slurry	0.47 – 2.90	0.56 – 3.20

As may be seen from Table 4, amongst all the materials used in the raw sinter mix, the blast furnace revert materials designated as 'BF flue dust' and 'BF slurry' exhibited the highest polonium-210 and lead-210 activities (i.e. Bq/g range). However, these constitute only a small proportion of the overall blend, typically 1 to 3% by weight, so that their contributions to the overall blend activities are small. The relatively high radioactivity levels found in blast furnace (BF) flue dust and BF slurry are explained by the fact that a major part of the lead-210 and polonium-210 input into the process is retained in the product sinter and, hence, carried forward to the blast furnace. The high temperature in the blast furnace causes the lead-210 and polonium-210 to be released with the off-dust and subsequently collected in the dust catcher or wet gas cleaning system. In comparison, other types of revert materials such as millscale originating from the rolling mills exhibit very low activities. With regard to fuels and fluxes, these typically exhibit very low polonium-210 and lead-210 activities.

The 1993 Radiological Substances Act (RSA) defines whether a substance is deemed radioactive. Several exemption orders exist which exempt from the disposal requirements of the RSA some materials containing naturally occurring radioisotope (or NORM: Naturally Occurring Radioactive Material). For steelmaking materials, the most important of these is the Radioactive Substances (Phosphatic Substances, Rare Earths, etc.) Exemption Order 1962. This effectively exempts NORM with elemental activities of radium and polonium below 14.8 Bq/g. All the materials investigated in this study were well below the threshold of 14.8 Bq/g specified in the Radiological Substances Act. Therefore, BF slurries and BF flue dusts are considered as exempt radioactive wastes that do not have to be reported and do not require an authorisation under the RSA.

5. Conclusions

An analytical method was developed by Tata Steel RD&T to determine the activity of polonium-210 and lead-210 in steelmaking materials using alpha spectrometry by isotope dilution following a method accredited to ISO 17025 by UKAS. It was established that the lead-210 and polonium-210 emitted in the sintering process are associated almost entirely with the particulate matter (>99.5% and >99.9%, respectively). Consequently it is necessary only to use a relatively simple particulate sampling method (BS EN 13284-1) for the sampling of radioactivity in sinter plant waste gas emissions, rather than the more complicated two-stage metals sampling method (BS EN 14385). The method was used to investigate the activity of key components of the raw materials used in the iron ore sintering process. Detailed work described here enabled a progressive collaboration in full compliance with the authorities and was designated best practicable means for monitoring and analysing radioisotopes from UK sinter plants in 2010.

Acknowledgements

The authors wish to express their gratitude to the members of the 2011 CETAS conference organisation for accepting this paper. Dr Paul Brooks, Peter Quinn and Louis Brimacombe are also gratefully acknowledged for their helpful comments to prepare this paper.

References:

- [1] K. M. Matthews, C. K. Kim, P. Martin, 2007. Determination of polonium-210 in environmental materials: A review of analytical methodology, review. *Applied Radiation and Isotopes* 65, 267 – 279.
- [2] J. Lehto, X. Hou, 2011. Chemistry and Analysis of radionuclides, *Laboratory Techniques and Methodology*. Ed. Wiley-Vch, 217 – 228.
- [3] BS EN 13284-1 (2002). Stationary source emissions. Determination of low range mass concentration of dust. Manual gravimetric method.
- [4] BS EN 14385 (2004). Stationary source emissions. Determination of the total emission of As, Cd, Cr, Co, Cu, Mn, Ni, Pb, Sb, Tl and V.

SPECIATION OF NI AND CO FOR RECYCLING PURPOSES

A.I. Farinha, X. Vanden Eynde

Center for Research in Metallurgy
Avenue du Bois Saint Jean 21, 4000 Liège, Belgium
farinha@rdmetal.ulg.ac.be, vdeneynde@rdmetal.ulg.ac.be

Abstract

Many techniques have been developed for the speciation of heavy metals for environmental and recycling purposes. ^[1, 2, 3, 4] Several of them use sequential extraction schemes to determine the metal over different fractions. They show that sequential extraction methods are an important approach, although the tiny separation of various chemical forms of heavy metals is difficult. These methods are time-consuming in view of routine method. One widely used method, especially for the quantitative determination of the metallic iron, uses bromine in methanol ($\text{Br}_2 / \text{CH}_3\text{OH}$) to extract metallic iron. ^[1]

The present paper attempts to develop other methods which allow, not only the selective dissolution of the metallic forms, but also the oxides and hydroxides of the studied elements. Pure metallic powders or mixtures of nickel and cobalt oxides were attacked by bromine in methanol and by copper chloride in methanol. After extraction, the amount of metal dissolved for the different elements was determined by Inductively Coupled Plasma Optical Emission Spectroscopy. Study allowed us to compare these two methods.

Metallic species quantification, for both cobalt and nickel, were found to be satisfactory by both methods and we observed that the method by copper chloride in methanol presents better recoveries. It is more difficult to take conclusions for the separation of the oxides from the metallic species.

Based on thermal decompositions, another route or intermediate route has been tested for hydroxides ($\text{Ni}(\text{OH})_2$, $\text{Co}(\text{OH})_2$). In order to obtain the dehydroxylation of these elements and produce the desired oxides and metallic species, mechanisms and temperature of decomposition of pure hydroxide powders of cobalt, nickel are followed with thermogravimetric analyses. The evolution and characterisation of the products of decomposition, at different temperatures, have been characterized by X-ray powder diffraction.

1. Introduction

Toxicity of heavy metals depends decisively on their speciation (Pott et al. 1991).^[3] Two different chemical forms of the same element can have very different toxicity due to its bioavailability and so elemental composition of a product gives only an indication of its degree of pollution, but without some important part concerning the toxicological risks related to the compounds.^[4] This topic is important for many research fields but in particular for recycling purposes and REACH regulation.

Many techniques have been developed for the speciation of heavy metals. Several of them make use of sequential extraction schemes to determine the metal distribution over different fractions, usually including species such as soluble, sulphide, metallic and oxide compounds.^[5]

On the basis of an analytical fractionation of heavy metal compounds, the procedure of Zátka et al. involves a sequential leaching of dust samples by ammonium citrate, hydrogen peroxide/ammonium citrate, and bromine-methanol. With the second step, the authors are able to separate sulphurs (Ni_3S_2 , NiS , Ni_3S_4 ...) from metals and oxides.^[4] Butler et al. have described similar dissolution procedures. Materials tested included refinery dusts, welding fumes and pure salts.^[6]

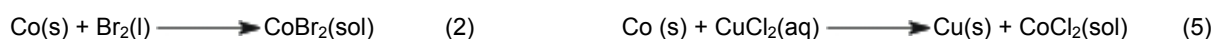
In this work we concentrated on determining the metal distribution over two fractions, for the metallic and oxides species of nickel, cobalt and to initiate hydroxide speciation route.

Hugues et al. described a procedure for the analysis of the metallic phase in multiphase systems. Potassium cuprochloride/tartaric acid phase solutions were used to quantitatively remove elements (Fe, Co, Ni, Mn, Sn, Bi and Sn) from the metallic phase in a multicomponent material.^[7]

Following this study, Matsumoto and al. proposed the determination of nickel oxide in nickel, based on the fact that nickel metal is soluble in potassium cuprochloride solution, while nickel oxide is insoluble.^[8] The nickel metal is dissolved in the aqueous solution while the nickel oxide remained as a residue, and therefore both can be quantitatively determined.

In the present paper we attempted to expand to other compounds and to cobalt, the methods for the determination of the metallic, hydroxides and oxides species. Pure metallic powders or mixtures of nickel and cobalt oxides were attacked by bromine and by copper chloride in methanol.

Based on the chemical reactions, we can dissolve the desired species, for the different methods and elements^[9]:



Br_2 and CuCl_2 are the oxidizing agents for Fe, Ni and Co and Cu is reduced. In addition, another route has been attempted by thermal decomposition of the hydroxides of the different elements (Ni(OH)_2 , Co(OH)_2), in order to obtain the dehydroxylation of these elements and to produce the desired oxides and metallic species.

Frost et al. studied the synthesis and characterization of cobalt hydroxide, cobalt oxyhydroxide, and cobalt oxide by thermal analysis. They reported that the dehydroxylation of the synthetic cobalt hydroxide happened at 130°C , while cobalt oxyhydroxide decomposed at 252°C and the thermal decomposition of Co_3O_4 at 820°C .^[10] Figlarz et al. studied the morphological and topotactical aspects of both reactions $\text{Co(OH)}_2 \rightarrow \text{CoOOH}$ and $\text{CoOOH} \rightarrow \text{Co}_3\text{O}_4$, in an air flow (fixed-bed reactor).^[11]

In this work, the mechanisms and decomposition temperature of pure cobalt and nickel hydroxide powders are followed with thermogravimetric analyses. The evolution and characterisation of the products of decomposition, at different temperatures, have been followed by X-ray powder diffraction.

2. Experimental

Reagents: High purity reagents and distilled water were used for all the analyses.

Powders: Metallic Nickel (99.9%, Johnson Matthey ~100 mesh), Oxide Nickel (anala R, UCB), Metallic Cobalt (99.9%, Aldrich, ~150 μ), Oxide (II) Cobalt (99.9%, Aldrich, ~325 mesh), Cobalt(II,III) oxide (99%, Alfa Aesar), Nickel Hydroxide (II) (Ni content= 61%, Alfa Aesar), Cobalt Hydroxide (99%, Alfa Aesar), Nickel Chloride hexahydrate (anala R, UCB), Cobalt chloride hexahydrate (anala R, VWR)

Solutions: For the preparation of standard solutions (All standards were prepared from reagent grade chemicals):

Nickel Solution: Standard Solution of Ni (Chem-Lab), Cobalt (Chem-Lab), Nitric acid (69%, VWR, Normapur), Chloridric acid (37%, VWR, Normapur)

For the attack by bromine in methanol: 5% Br_2 (VWR Normapur) in CH_3OH (VWR Normapur 99.8%)

For the attack copper chloride in methanol: 5% $\text{CuCl}_2 \cdot 2\text{H}_2\text{O}$ (VWR Normapur) in CH_3OH (VWR Normapur 99.8%)

Apparatus:

The analytical quantification of desired extracted phases is measured by an Inductively Coupled Plasma Optical Emission Spectroscopy (Perkin-Elmer Optima 3000 ICP-OES, with a segmented-array, Charge-coupled device Detector (SCD), which contains a quartz torch and an alumina sample injector). The plasma is oriented horizontally in the sample compartment. The wavelengths used were 231.604nm for the Nickel and 228.616nm for the cobalt.

For thermal decomposition of the hydroxides, the mechanisms and temperature of decomposition of powders were followed by thermogravimetric analyses (TGA), with a TA Instruments analyzer (Q50 with a temperature

control range going from +35°C to 1000°C, weighing capacity (sample) of 1.0 g, a resolution of ~ 0.1 µg and an accuracy < + 0.1%. It allows the following purge gases: Helium, nitrogen, oxygen, air, and argon.

The evolution and characterisation of the products of decomposition were characterized by X-ray powder diffraction, with a Bruker D8 Discover X-Ray diffractometer. The equipment has a Theta/2Theta horizontal goniometer, a Göbel Mirror and a Co Anode.

3. Procedures

The analysis procedure used in detail can be given as follows:

- Method by bromine in methanol (Br₂/ CH₃OH)

Weigh sample and put it in an Erlenmeyer flask. Insert by the top of the condenser the bromine-methanol solution. The attack is carried out under reflux with magnetic stirring for one hour.

Rinse the condenser with CH₃OH and filter the solution with a 0.45µm membrane. Transfer the solution to a 250 ml volumetric flask and bring to volume with CH₃OH. Add ~ 50 ml H₂O to 100 ml of solution and cool it.

Add 10 ml of HNO_{3 conc} and 10 ml H₂O, allow the reaction to cool and then evaporate to dryness. Add 5 ml HNO_{3 conc} + 10 ml HCl_{conc} to solution and less react for some minutes. This residue is again diluted with HCl and heated and finally analysed by ICP-OES.

- Method by copper chloride in methanol (CuCl₂/ CH₃OH)

Samples are treated with 100 ml of the solution CuCl₂.2H₂O in 5% CH₃OH and heated for 1-3h. Hence the solution is filtered with a 0.45 µm filter. The filtrate, solution and rinsings with CH₃OH, is collected in a beaker, washed with HCl and evaporated to dryness. This residue is again diluted with HCl and heated. The solution is diluted if necessary and finally analysed by ICP-OES.

- Thermo analysis

Weighed samples (~20mg) were put in the thermogravimetric analyser, with different flowing atmospheres (40 ml/min of nitrogen or air). The heating rate is fixed at 2.0°C/min (though for some samples different rates were used), up to 400°C and 1000°C.

4. Results

Wet chemistry

Both methods Br₂/ CH₃OH and CuCl₂/ CH₃OH were applied to pure metallic, hydroxides and oxides powders of nickel and cobalt. Nickel and cobalt chloride and hydroxides, were also attacked by methanol to check solubilities.

The results of the analytical quantification measured by ICP-OES, expressed by the dissolution rates of each species are reported in Table 1.

Table 1. Recoveries for different species of Ni and Co, with both methods

	CH ₃ OH		CuCl ₂ .2H ₂ O / CH ₃ OH		Br ₂ / CH ₃ OH	
	Recovery (%)	Standard deviation	Recovery (%)	Standard deviation	Recovery (%)	Standard deviation
Ni°			97.3	1.1	94.2	0.24
NiO			2.1	0.2	-0.97	0.05
Ni(OH) ₂	0.20	0.09	75.2	2.3	10.3	1.4

NiCl₂*6H₂O	100.5	0.01				
Co	0.010	0.002	95.1	0.08	86.2	1.3
CoO	0.020	0.006	77.4	0.55	6.4	0.86
Co₃O₄	0.073	0.004	12.6	1.5	0.90	0.24
Co(OH)₂	0.30	0.02	94.2	1.2	99.3	1.9
CoCl₂*6H₂O	96.4	0.01				

As expected, both nickel and cobalt chloride are totally soluble in methanol (CH₃OH at pH=8.5), all the other species are insoluble in this medium (Table 1).

Nickel:

We can notice that nickel hydroxide presents a significant dissolution in copper chloride-methanol (75.2% ± 2.3). However it is only slightly soluble with bromine-methanol attack (10.3% ± 1.4).

Concerning metallic nickel analysis with both methods, it presents a good recovery, which means that we are able to extract the metallic nickel (Ni⁰) and quantify it with a good recovery (97.3% ± 1.1). We can observe that the method by copper chloride in methanol presents better recoveries.

Nickel oxide is not soluble by any of the methods, which means that when in presence of a mixing of oxide and metallic nickel, we can eventually make the speciation by recovering each one of the species, respectively in the filter (NiO) and in the filtrate (Ni⁰).

Cobalt:

For metallic cobalt (Co⁰), the bromine-methanol attack presents lower recovery (86.2% ± 1.3), than the copper chloride-methanol method, which is very good (95.1% ± 0.1).

For cobalt hydroxide, we can see that it is totally soluble in both media and therefore another way should be found.

For the CoO we can notice that it is slightly soluble by the bromine-methanol attack (6.4% ± 0.9) and with the copper-chloride attack CoO is soluble, even though it is not fully dissolved in hour of reaction (recovery: 77.4% ± 0.6). For the Co₃O₄ it is insoluble for the bromine-methanol attack, but it is slightly soluble by the copper-chloride in methanol attack, so we face the same problem. This partly disagrees with ref [7]. The dissolution of the cobalt(II) oxide in copper-chloride solution might be due to the acidic medium (pH~1.75). Tests are ongoing, to try to perform the metal dissolution at higher pH.

Thermogravimetry

Fig.1, a, b, c and d shows TGA curves for cobalt and nickel hydroxides (heating the samples to 400°C and 1000°C, in different atmospheres (air and nitrogen)). The transformation temperatures and the weight losses determined by TGA for cobalt and nickel hydroxides and products of transformation are summarized in Table 2.

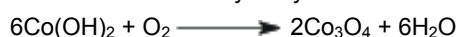
As regarding Ni(OH)₂ (fig. 1a and 1b) one single transformation step (weight loss of ~19%) is observed in agreement with the literature ^[9], that stoichiometric β-Ni(OH)₂ is expected to undergo a single step decomposition as



Nevertheless, the temperature of decomposition can slightly vary in the literature (according to different authors).

In our case, we can obtain NiO, at T= 245.2°C with a mass loss of 19.2% and T= 282.6°C with a mass loss of 18.89%, respectively in air and nitrogen. In TGA curves of nickel hydroxide (fig.1 a and 1b), we notice that even though decomposition temperature is lower than 300°C, the reaction is incomplete and mass loss is observed continuously up to 400°C. This might be due to the powder diameter implying a diffusion process.

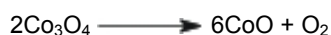
For the Co(OH)₂ three transition steps are observed in TGA performed in air and only two when powder is in nitrogen atmosphere. In sample heated with air, the first decomposition at T=135°C with a mass loss of 5.8% is not identified and might be related to CoOOH formation. By including the second step (at T= 226.9°C), the observed weight loss (~14%) can be attributed to the dehydroxylation according to the reaction



As already mentioned Frost et al. (2010) ^[10] studied the synthesis and characterization of Cobalt Hydroxide, Cobalt Oxyhydroxide, and Cobalt Oxide and reported that cobalt oxyhydroxide decomposed at 252°C. Figlarz et al. ^[11] studied the morphological and topotactical aspects of both reactions Co(OH)₂ → CoOOH and CoOOH → Co₃O₄, in an air flow (fixed-bed reactor) for five hours at 250°C and indicated that these reactions can occur simultaneously.

In our case, we can obtain CoO, at T= 890.1°C with a mass loss of 20.1% in air atmosphere.

The third major loss step is attributed to the formation of CoO through loss of oxygen according to the reaction



In agreement with literature, Co₃O₄ oxide converts into CoO at high temperatures. ^[13]

In order to identify the phases at different stages of the treatment and to better understand the decomposition products, samples of Co(OH)₂ were heated in air at 600°C and 900°C for two hours and characterised by XRD. It has not been possible to identify the intermediate compound, CoOOH in any of these patterns. At 600°C in air the Co₃O₄ phase is detected without CoO and at 900°C, mostly CoO. These XRD have confirmed interpretations of TGA steps.

In sample heated with nitrogen, we can identify two decomposition steps. First step at T= 184°C with a mass loss of 18.9% and second step at T=942°C with a mass loss of 37%. At the end of first step decomposition, we should already have the CoO compound (from calculation, 19.6% weight loss). By treating cobalt hydroxide in nitrogen atmosphere until 1000°C, metallic cobalt is finally formed.

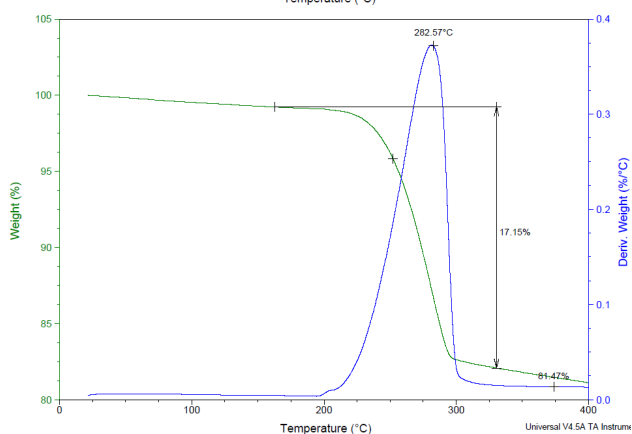
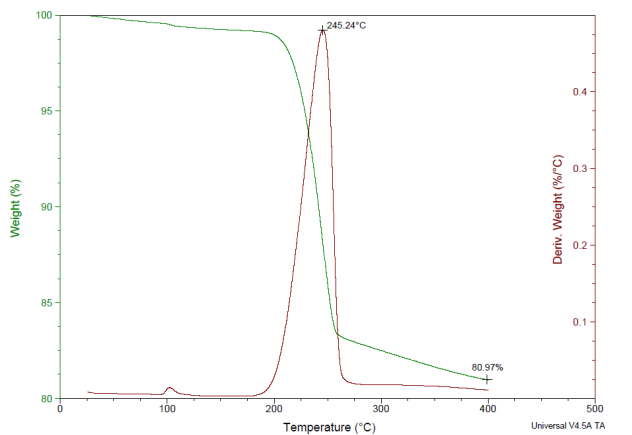


Fig.1 a) TGA curves for Ni(OH)₂ with air

Fig.1 b) TGA curves for Ni(OH)₂ with nitrogen

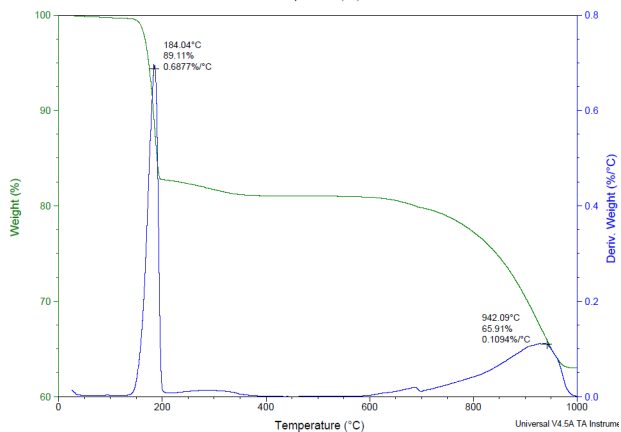
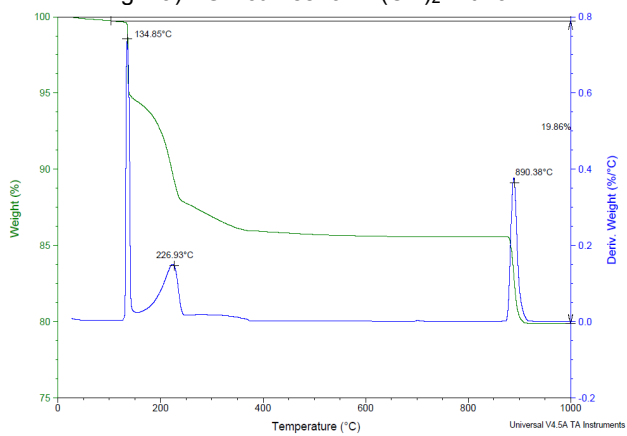


Fig. 1 c) TGA curves for Co(OH)₂ with air

Fig.1 d) TGA curves for Co(OH)₂ with nitrogen

Table 2. Temperatures of transformation and weight loss for Ni(OH)₂ and Co(OH)₂ by thermal decomposition with TGA

Species	Atmosphere	T of transformation (°C)	Weight loss (%)
Ni(OH) ₂	Oxidation (air)	245.24	19.18
	N ₂	282.57	18.89
Co(OH) ₂	Oxidation (air)	134.85	5.82
		226.93	14.39
		890.38	20.13
	N ₂	184.04	18.94
		942.09	37.00

Theoretical weight loss		
From	to	Weight loss (%)
Ni(OH) ₂	NiO	-19.4
	Ni	-36.7
Co(OH) ₂	CoOOH	-1.3
	CoO	-19.6
	Co ₃ O ₄	-13.9
	Co	-36.9

5. Discussion

Zatka et al. (1992) already showed that the salts (chloride, sulphate) are soluble by ammonium citrate (NH₄.2C₆H₆O₇ solution 0.1M at pH=4.4). In our case, we will do it in methanol. Study could be presumably extended to nitrate and sulphate.

In summary:

Ni speciation		Co speciation	
CuCl ₂ .2H ₂ O / CH ₃ OH	Br ₂ / CH ₃ OH	CuCl ₂ .2H ₂ O / CH ₃ OH	Br ₂ / CH ₃ OH
<ul style="list-style-type: none"> - Possible to separate metallic (soluble) from oxide (insoluble) - Possible to separate oxide (insoluble) from hydroxide (soluble) - Not possible to separate metallic from hydroxide (both soluble) 	<ul style="list-style-type: none"> - Possible to separate metallic (soluble) from oxide (insoluble) - Difficult to separate oxide (insoluble) from hydroxide (~insoluble) - Difficult to separate metallic from hydroxide (~insoluble) 	<ul style="list-style-type: none"> - All species are soluble, impossible to separate them by this method only 	<ul style="list-style-type: none"> - Possible to separate metallic (soluble) from oxides (insoluble) - Possible to separate oxides (insoluble) from hydroxide (soluble) - Not possible to separate metallic from hydroxide (both soluble) - Not possible to separate CoO from Co₃O₄(both insoluble)

In the second part of this work, we studied thermal decomposition of cobalt and nickel hydroxides, in order to transform the hydroxide towards oxide species by dehydroxilation.

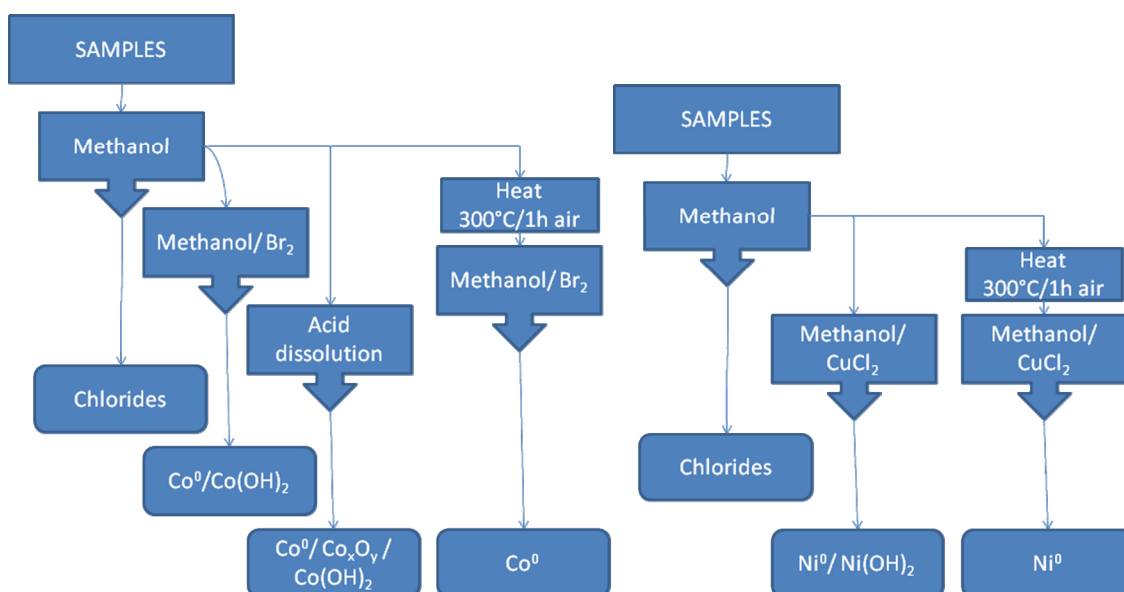
After analysing the results for both methodologies in the context of chemical speciation (by chemical dissolution and by thermal decomposition), a combination gives a first indication of a wet chemical speciation of cobalt or nickel compounds.

For nickel speciation, if we have a sample with different nickel species (chlorides, hydroxide, oxide and metallic), we start dissolving the chlorides in methanol. In a second step, the residue can be heated until 300°C, this way we will transform the hydroxides and obtain a product with a mixture of NiO and Ni metallic. After that, by both attacks (bromine-methanol or copper-chloride) applied to this mixture, the oxide part is separated from the metallic part.

For cobalt speciation, we can act the same way for the chlorides; after this, if we use only chemical dissolution, we notice that for the copper-chloride method, all the species are soluble and with bromine-methanol, we can separate the oxides (CoO and Co₃O₄) from the metallic and the hydroxide. After heating in air until 300°C, hydroxides will form Co₃O₄ and then by the bromine-methanol attack we can extract the metallic cobalt. Although, Co oxidation up to 300°C is low enough ^[12], we need to check if when submitting the sample to a heating treatment, the metallic cobalt will not be too much affected by this treatment. The selective extraction between CoO and Co₃O₄ is not achieved yet.

The extension of the method to other compounds should be performed. We can expect that sulphate and nitrate will follow chlorides in the first methanol wash. Concerning carbonates, oxalates and phosphates, it is more difficult, since they are not soluble in water and methanol.^[13]

The following graphs summarize the first routes for Ni and Co speciation.



6. Conclusion

In this work we attempted to develop and compare two methods by selective dissolution of different species. Pure metallic powders and oxides were attacked by bromine in methanol and by copper chloride in methanol. Metallic species quantification, for both cobalt and nickel, were found to be satisfactory by both methods and we observed that the method by copper chloride in methanol presents better recoveries.

For the cobalt, the method copper chloride in methanol is not the best solution, because all the species are soluble in this solution. For the bromine-methanol attack, separation of metallic from oxides is possible although some CoO is leached.

Mechanisms and temperature of decomposition of pure hydroxide powders of cobalt, nickel are followed with thermogravimetric analyses. Depending on the conditions, it is possible without affecting metallic part to transform hydroxide to oxides. These transition steps are interesting to evaluate the presence of hydroxide in samples.

When combining both methodologies, we can realise that, for nickel speciation, we are able to separate 4 different nickel species. Although the route is more complex, the chemical speciation of cobalt seems also feasible.

Study is still ongoing. In the future we will study the effect on mixtures composed of Fe, Co, Ni species. For the cobalt speciation, it is more difficult to take conclusions, especially when trying to separate CoO and Co₃O₄.

Acknowledgements

The authors thanks J. C. Goffin, Y. Gagliardi, A. Dupont and students from the Faculty of Chemistry, University of ULg, Liège, Belgium for their work in the laboratory as well as Pr B. Gilbert.

Bibliography

- [1] Baliza S.V., da Costa Pereira E.A., « Détermination de la composition minéralogique de minerai de fer » ; ISO 5416:2006 « Direct reduced iron -- Determination of metallic iron -- Bromine-methanol titrimetric method ».
- [2] Bolt H.M., Noldes C., Blaszkewicz M., Fractionation of nickel species from airborne aerosols: practical improvements and industrial applications, *Int Arch Occup Environ Health* (2000) 73: 156-162
- [3] Pott F., Rippe R.M., Roller M., Rosenbruch M., Huth F. (1991) Vergleichende Untersuchungen über die Kanzerogenität verschiedener Nickelverbindungen und Nickellegierungen. Schriftenreihe der Bundesanstalt für Arbeitsschutz, Dortmund, Fb 638. Wissenschaftsverlag NW, Bremerhaven
- [4] Zarka V.J., Warner J.S., Maskery D., Chemical speciation of nickel in airborne dusts: analytical method and results of an interlaboratory test program *Environ Sci Technol* (1992) 26: 138-144 ; Perdrix E., Spéciation des particules atmosphériques, *Ecole des Mines de Douai - Département Chimie et Environnement* (2000)
- [5] Führtjohann L., Jakubowski N., Speciation of nickel in airborne particulate matter by means of sequential extraction in a micro flow system and determination by graphite furnace atomic absorption spectrometry and inductively coupled plasma mass spectrometry", *J. Environ. Monit.* (2001) 3: 681–687
- [6] Butler O.T., Bradley S.D., Howe A.M., Development of a method for the sampling and analysis of nickel and inorganic compounds of nickel in a workplace air using atomic absorption spectrometry, *Analyst* (1995) 120: 2089-2095
- [7] Hughes T.C., Hannaker P., Metallic phase analysis of multicomponent systems using a potassium cuprochloride-tartaric acid leach, *Analytical Chemistry*, (1978) 50/8: 1197
- [8] Matsumoto K., Matsuki M., Terada K., Determination of Nickel Oxide in and on High-Purity Nickel Metal, *Fresenius Z. Anal. Chem.* (1981) 309: 399-400
- [9] Pascal, P. "Cobalt and Nickel." *Nouveau traité de chimie minérale*, 17 (2eme fascicule) (in french).
- [10] Frost L., Yang J., Liu H., Synthesis and Characterization of Cobalt Hydroxide, Cobalt Oxyhydroxide, and Cobalt Oxide Nanodiscs *J. Phys. Chem. C* (2010) 114: 111–119
- [11] Figlarz M., Guenot J., Tournemolle J-N., Oxidation of cobalt (II) hydroxide to oxide hydroxide: solids evolution during reaction, *Journal of Materials Science* (1974) 9: 772-776
- [12] Tompkins H.G., Augis J.A., The Oxidation of Cobalt in Air From Room Temperature to 467°C, *Oxidation of Metals*, (1981) 16 5/6: 355-369.
- [13] Fletcher E. (coordinator) "Cobalt Monograph" Edited by Centre d'information du Cobalt: Belgium, 1960 (in English).

DEVELOPMENT OF A NEW METHOD FOR THE DETERMINATION OF PARTICLE-BOUND PAHs BASED ON DIRECT THERMAL EXTRACTION - GAS CHROMATOGRAPHY - MASS SPECTROMETRY

Diane Ciaparra

Tata Steel RD&T, Swinden Technology Centre, Moorgate, Rotherham S60 3AR, UK.

Summary

A new method for the determination of particle-bound polycyclic aromatic hydrocarbons (PAHs) was developed based on direct thermal extraction (DTE) - gas chromatography (GC) - mass spectrometry (MS). DTE-GC-MS is an emerging analytical method that is increasingly being adopted as an alternative to solvent extraction (SE) for the analysis of particle-bound organic species collected on filters from emission sources and ambient air monitoring studies. The replicate analysis of a certified reference material (NIST 1649a) showed good precision of the method with individual PAH relative standard deviations around or below 15%, and good agreement between measured and certified mass fraction (typical recoveries of 90%-120%). Limits of detection were low, typically 0.5 ng/m³ of benzo[a]pyrene for the analysis of a single punch on a filter collected using a high-volume sampler after sampling for 24 h. In-house comparison of the developed method with SE revealed that DTE generally exhibited higher recoveries than SE, especially for low molecular weight PAHs that are relatively volatile. The proposed method can be applied to characterise emission sources, workplace exposures in the steel industry, and to investigate the effect of the iron and steel making operations on the ambient air quality.

Introduction

Thermal extraction (TE) - gas chromatography (GC) - mass spectrometry (MS) is an emerging analytical method that is increasingly being adopted to identify and quantify individual particle-bound organic species, including PAHs, in emission sources and ambient air. Some of the advantages associated with the method include its relatively low cost, increased automation, reduced sample preparation and improved sensitivity. The method allows increased temporal resolution of aerosol composition making it adequate for particulate matter (PM) exposure assessments. In comparison, conventional methods used to determine PAH concentrations in airborne particles require several expensive and time-consuming extraction and clean-up steps. Since 1985, a number of TE investigations have endeavoured to improve the methodology, for example studies have been undertaken to minimise sample handling and eliminate difficulties associated with sample introduction to the TE oven [1]. In addition, prior work with standard reference material has assured the applicability of the TE technique for the analysis of PAHs in particulate matter [2]. Comparison of TE with solvent extraction (SE) methods showed good agreement for the analysis of PAHs and n-alkanes, showing that the TE method was more efficient at extracting PAHs from filter sections by approximately 5-10% [1]. Quantitative delivery of organics from the oven to the GC is still an issue and is typically achieved via a heated transfer line, where maximum temperatures of approximately 300°C are maintained to minimise adhesion and chemical reactions. Despite recent developments, transfer losses of polar compounds still remain an issue [3], and more recent work has successfully demonstrated the use of direct sample introduction where TE is performed at the inlet of the GC eliminating the need for a transfer line [4, 5]. The so-called direct thermal extraction (DTE) techniques have demonstrated the capability to extend the range of compound classes identified and quantified by oven methods, and to date Jeon et al [5] have presented the most comprehensive list including the identification of sterane and hopane molecules in ambient air samples [5]. In spite of these advancements, a number of specific areas still need further development. Previous work has focused on ambient air aerosol characterisation; however characterisation of primary emission sources is also needed, especially when source apportionment studies are to be carried out [3]. In this paper a description is

given of work carried out to develop and validate a method based on DTE-GC-MS in order to measure PAHs in aerosol samples collected in the vicinity of steelworks to characterise emissions, workplace air and ambient air.

Terminology

The 4th Daughter Directive (2004/107/EC) of the Air Quality Framework Directive has established a target value for benzo[a]pyrene (BaP), a marker for the carcinogenic risk of polycyclic aromatic hydrocarbons (PAHs), of 1 ng/m³ in the PM₁₀ fraction in ambient air expressed as an annual mean [6]. PAHs are a large group of organic compounds consisting of two or more aromatic rings fused together. They are formed by incomplete combustion of organic material containing carbon and hydrogen. In the steel industry, PAHs are released during coke manufacturing, sintering, ironmaking, casting, and steelmaking. Because of their low vapour pressures, some PAHs are present at ambient temperatures in air, in both gaseous form and in association with particles. Lighter PAHs, such as naphthalene, are found almost exclusively in the gas phase, whereas the heavier ones, such as benzo[a]pyrene (B[a]P) are almost totally adsorbed onto particles, especially the finest particulate fractions. Several PAHs are classified as highly carcinogenic or mutagenic. Among these, a group of 16 PAHs has been identified as priority pollutants by the US Environmental Protection Agency [7]. A list of the targeted PAHs in this study is presented in Table 1.

Table 1: Targeted PAHs and molecular weight

Compound	Molecular weight
Phenanthrene	178
Anthracene	178
Fluoranthene	202
Pyrene	202
Benz[a]anthracene	228
Chrysene	228
Triphenylene	228
Benzo[b]fluoranthene	252
Benzo[j]fluoranthene	252
Benzo[k]fluoranthene	252
Benzo[e]pyrene	252
Benzo[a]pyrene	252
Perylene	252
Indeno[1,2,3-cd]pyrene	276
Dibenzo[a,h]anthracene	278
Dibenzo[a,c]anthracene	278
Benzo[g,h,i]perylene	276

Materials and methods

The analytical system used by Tata Steel consists of a direct thermal extraction (DTE) system mounted on an Agilent gas chromatograph with inert source mass spectrometry detection (GC6890/MS5973). The DTE system (Gerstel, Germany) consists of a cooled injection system (CIS 4), a multipurpose sampler (MPS 2), and an automated liner exchange (ALEX) system. The ALEX allows liners to be exchanged automatically during an analysis sequence. The system mainly consists of a special sampling head, a gripper and a tray with a transport adapter. The liners are mounted manually by the operator in the transport adapter and then positioned in the

ALEX tray (14 positions), where they are stored free from contamination. For automated liner exchange, the gripper removes a liner from the tray and inserts it into the sampling head where it is held by a pneumatic lock.

Fig. 1 describes the analytical procedure used by Tata Steel for the validation of the method. Dust materials were typically introduced directly into the pre-conditioned CIS liners using a small spatula. With regard to filter samples, filter sections were cut using a 1.5 mm diameter micropunch (Harris, US) and inserted in the CIS liners which were subsequently placed into the ALEX liner tray. A small plug of conditioned quartz wool was used to prevent dust from contaminating the GC column. Gloves were worn at all times and liners and filters were handled with clean forceps to avoid contamination. The ALEX gripper removes the liner from the tray and inserts it into the sampling head where it is held by a pneumatic lock. At that stage, injection of a standard solution can be performed by the MPS syringe through the septum of the transport adapter of the liner. The CIS temperature was then increased from 40 to 360°C at a rate of 12°C/min allowing all analytes to be thermally desorbed, transferred, and concentrated onto the GC column. The analytes were then separated by a DB-5MS 60 m x 0.25 mm x 0.25 mm column (JW, USA) and detected by mass spectrometry with the ion source set at 300°C. Targeted compounds were detected in single ion monitoring (SIM) mode. Quantification of the target PAHs was performed by internal calibration by injecting onto empty CIS liners increasing amounts of the analytes prepared in nonane from native PAH solutions (S-4083 mix, Chiron, Norway) and perdeuterated compounds (S-4081 mix, Chiron, Norway). For the dust samples, an internal standard solution (S-4081 mix, Chiron, Norway) was introduced by automated syringe injection directly in the liner containing the sample prior to thermal extraction. All the data were analysed using Masslynx software (Waters, Manchester, UK).

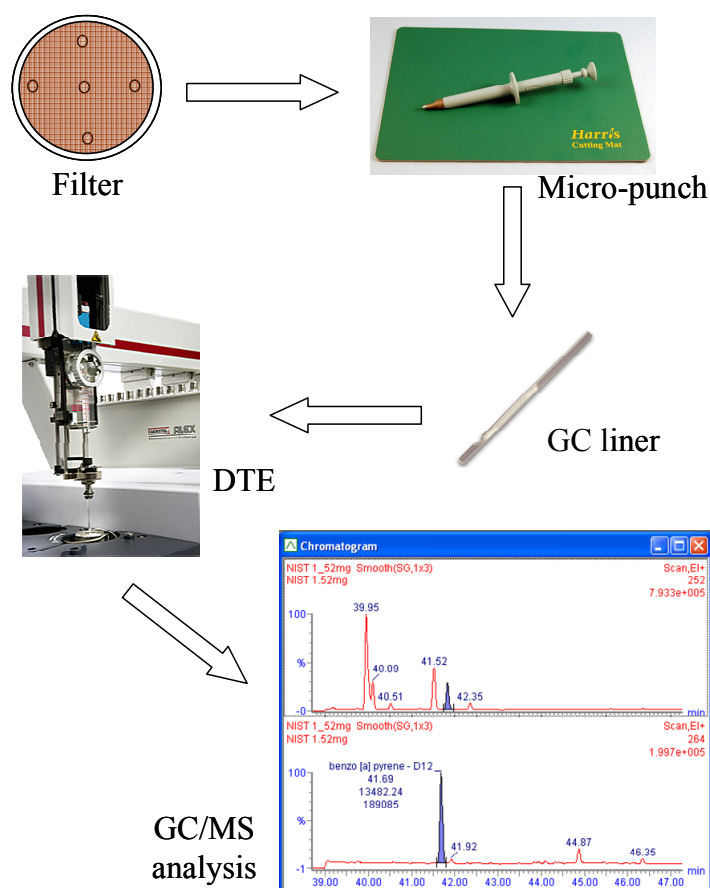


Fig. 1: Experimental procedure for the analysis of particle bound PAHs collected on filters using direct thermal extraction (DTE) - gas chromatography (GC) - mass spectrometry (MS)

Method validation

The performance of the method was evaluated by assessing several parameters such as linearity, recovery and detection limits), and by analysing a standard reference material urban dust obtained from the US National Institute of Standards and Technology (NIST SRM1649a).

- Precision of the method

The replicate analysis of 6 samples of approximately 0.5 to 2 mg of NIST SRM1649a exhibited good precision of the method with relative standard deviation typically around or below 15% for all PAH compounds.

- Accuracy of the method

Results for the replicate analysis of 6 samples of 0.5 to 2 mg of NIST SRM1649a and comparison with the certified values are presented in Fig. 2. Results for all analytes showed good agreement between the certified and measured values. For most compounds, the measured range of concentrations (95% confidence) was well within the certified values. Only anthracene appeared to be measured in higher concentrations than expected. This was attributed to the co-elution of anthracene with unidentified compound(s).

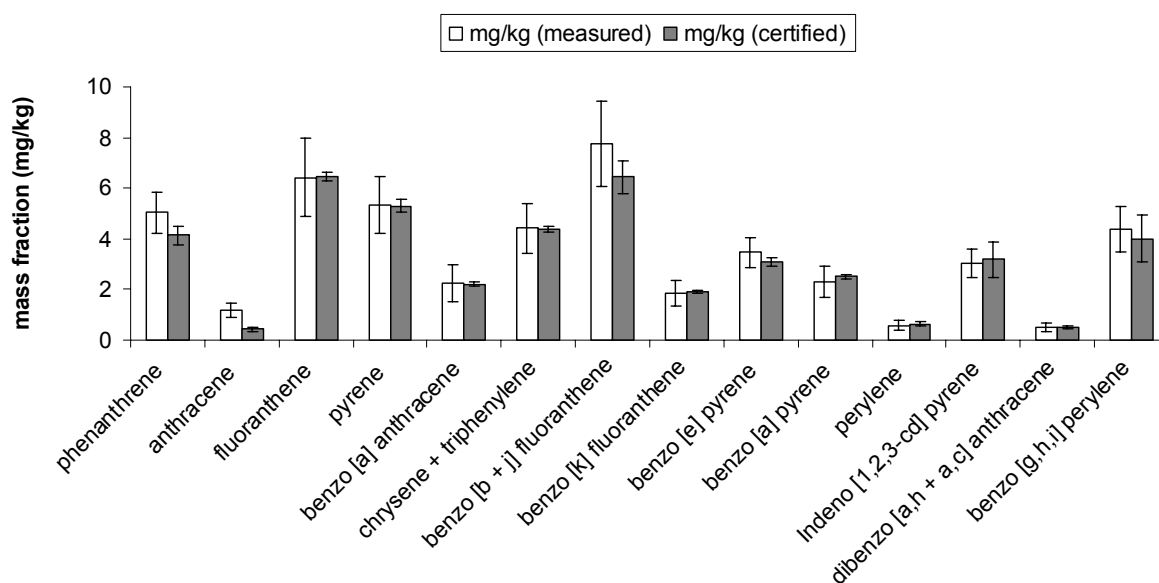


Fig 2: Comparison between certified values and measured values for the quantification of PAHs in the NIST SRM 1649a. Average mass fractions and confidence intervals were determined by the analysis of 6 replicate samples ($m = 0.5$ to 2 mg).

- Analysis of filter samples

Two types of particulate samples were collected: PM₁₀ and inhalable dust. The PM₁₀ sample was collected on a 150 mm quartz filter using a Digital DHA-80 high volume sampler (Digital, Switzerland) at an urban location in Rotherham, UK (flow rate: 30 m³/h; sampling time: 24 h). Inhalable dust was collected on a 25 mm silver membrane filter using a low volume sampler equipped with a seven-hole head (SKC, US) at a Tata Steel coke plant in the UK (flow rate: 2 l/min; sampling time: 5 h). For each sample type, five different sub-sample punches of the same filters obtained as described in the operating procedure were analysed by DTE-GC-MS. Replicate analysis of the five punches exhibited an excellent agreement between sub-samples with a relative standard deviation ranging from 5% to 9% for all compounds. This showed that the sample preparation technique was applicable to both types of air samples, namely low- and high- volume samples.

- Limits of detection

Limits of detection (LoDs) were determined by sequential analysis of 10 replicate tubes with a low-level spike (2 ng/tube). The LoDs were obtained by applying the following formula: $LoD = SD \times t_{0.99}$ where SD was the standard deviation of the replicate measurements and $t_{0.99}$ is the t-distribution factor for 99% confidence with a degree of freedom (N-1), in that case $t_{0.99} = 3$. Detection limits for all targeted PAHs are presented in Table 2, and were in the range 0.05-0.25 ng/tube. Table 2 also presents the equivalent LoDs as concentrations in air when analysing a single punch of a filter after sampling for different time periods using a high-volume sampler for ambient air studies and an inhalable dust sampler for occupational studies. The LoDs of the method were generally low and were greatly limited by the sampling technique itself. In the case of ambient air studies using a high volume sampler, the LoD for B[a]P (0.023 ng/m³) was well below the EU target value of 1 ng/m³. There are currently no workplace exposure limits for PAHs in the UK. However, the LoD for B[a]P when using an inhalable dust sampler can be compared to the French 8-h time-weighted average threshold limit value of 150 ng/m³ defined for B[a]P in the workplace [10]. With the B[a]P LoD found to be less than 3 ng/m³ it is shown that the method was also applicable to workplace exposure studies. It is important to note that the LoD can be significantly improved simply by increasing the number of punches analysed.

Table 2: Limits of detection (LoD) for the developed DTE-GC-MS method in ng/sample and as equivalent concentrations in air for target PAHs when analysing a single punch (punch diameter of 1.5 mm)

Type of study		Ambient air	Occupational hygiene
Type of sampler		Hi-Vol ¹	7-hole head sampler ²
Sampling period		24hr	8hr
	ng/sample analysed	ng/m ³	
Phenanthrene	0.05	0.006	0.74
Anthracene	0.15	0.019	2.35
Fluoranthene	0.09	0.011	1.37
Pyrene	0.12	0.016	1.93
Benzo [a] anthracene	0.22	0.029	3.56
Chrysene + triphenylene	0.14	0.019	2.28
Benzo [b + j] fluoranthene	0.20	0.026	3.22
Benzo [k] fluoranthene	0.20	0.026	3.18
Benzo [a] pyrene	0.18	0.023	2.87
Indeno [1,2,3-cd] pyrene	0.22	0.029	3.52
Dibenzo [a,h + a,c] anthracene	0.24	0.032	3.91
Benzo [g,h,i] perylene	0.23	0.030	3.70

¹ Digital DHA-80 high-volume samplers: 30 m³/h flowrate; 140mm disposable filter surface [8]

² 7-hole head inhalable dust sampler: 2 lpm flowrate; 23 mm disposable filter surface [9]

- Comparison with solvent extraction technique

Solvent extraction (SE) is the conventional technique used to prepare filter samples prior to GC-MS analysis. Two inhalable dust samples (samples 1 and 2), that were collected on 25 mm silver membrane filters using a low volume sampler equipped with a seven-hole head (SKC, US) at a Tata Steel coke plant in the UK, were cut in half, with one half undergoing SE-GC-MS, and two replicate punches of the other half undergoing DTE-GC-MS. The SE was performed by Tata Steel RD&T following a UKAS accredited method for the preparation of environmental samples involving the use of an accelerated solvent extraction apparatus (Dionex ASE 100) and concentration apparatus (Zymark Turbovap II). Comparison of the results from both techniques is presented in Fig. 3. In general, both methods were in good agreement with a very good correlation for heavy molecular weight (MW) PAHs (MW = 252 or over), whereas for medium MW PAHs (MW = 228 or below), there were some

discrepancies with higher levels measured by DTE in comparison with SE-GC-MS. This can be explained by the fact that using solvent extraction, recovery efficiencies are usually lower for low- to medium-MW PAHs owing to evaporation losses during the concentration steps. This shows that DTE-GC-MS has similar performance to SE-GC-MS for high-MW PAHs, but actually lead to obtain higher recovery than SE-GC-MS for medium-MW PAHs.

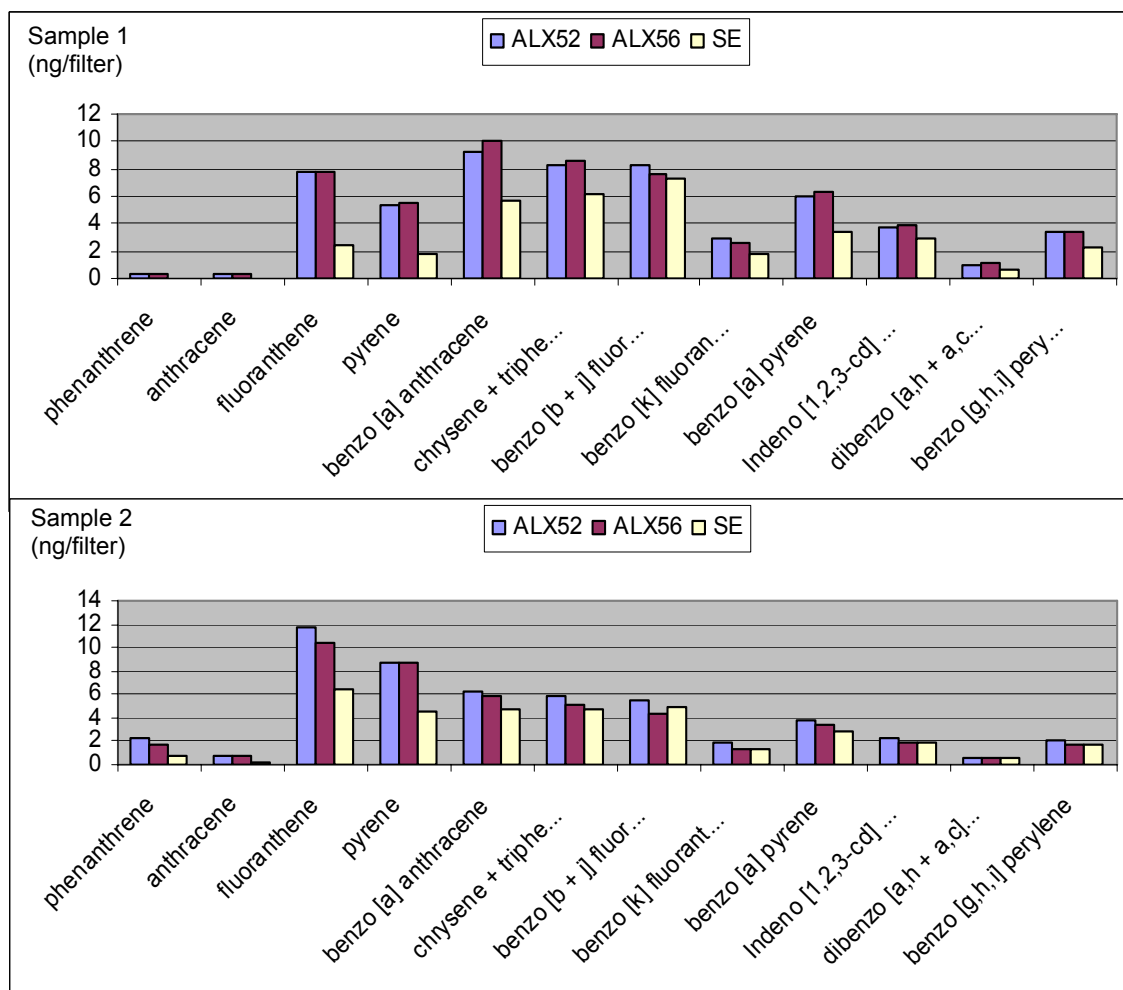


Fig. 3: Comparison of PAH masses measured by DTE-GC-MS and SE-GC-MS for two inhalable dust samples (Sample 1 and Sample 2) collected on filters. In the case of DTE, two separate punches of the same filters were analysed (ALX52 and ALX56).

Conclusions

A new method to determine particle-bound PAHs was developed based on direct thermal extraction (DTE) - gas chromatography (GC) - mass spectrometry (MS). Owing to its low cost and minimal sample preparation requirement, DTE-GC-MS is the method of choice when analysing particle-bound PAHs collected on filters. The method has been validated against key criteria including accuracy, precision, limits of detection and by analysing certified reference material. A comparison with the reference method of solvent extraction (SE) -GC-MS was also made using samples collected at a steelmaking site, showing equivalence and even improved performance in comparison to the reference method dependent upon the volatility of the individual PAHs. The applicability of the DTE-GC-MS method has been demonstrated for the analysis of emission samples, environmental materials and occupational exposure samples. Following its validation, the method has been successfully applied to aerosol samples collected from emissions arising from steelworks' operations and it is planned to use the method on

ambient air samples to help determine the environmental impact of steelmaking operations in order to develop a strategy for reducing their impact on the local area.

Acknowledgements

I would like to thank the Research Fund for Coal and Steel for sponsoring the work as part of the research project ASEMIS (Grant agreement number: RFSR-CT-2009-00029). I am also very grateful to Tina Conroy for collecting samples at the coke ovens and Jie Chen for performing the SE-GC-MS analyses. Finally, I would like to thank Dr Eric Aries, Ray Fisher and Dr David Anderson for their helpful comments.

References:

- [1] Greaves, RC, Barkley, R M and Sievers, R E: Rapid sampling and analysis of volatile constituents of airborne particulate matter, *Anal. Chem.*, Vol. 57, 2807-2815, 1985
- [2] Watermann D., Horsfield B., Leistner F., Hall K., Smith S., Quantification of polycyclic aromatic hydrocarbons in the NIST standard reference material (SRM1694a) urban dust using thermal desorption. *Anal. Chem.*, 72, 3563-3567, 2000
- [3] Hays M.D., Lavrich R.J., Developments in direct thermal extraction gas chromatography mass spectrometry of fine aerosols. *Tr. Anal. Chem.*, 26 (2), 88-102, 2007
- [4] Ho S.S.H., Yu J., In-Injection Port Thermal Desorption and Subsequent Gas Chromatography-Mass Spectrometric Analysis of Polycyclic Aromatic Hydrocarbons and n-Alkanes in Atmospheric Aerosol Samples. *J. Chromatogr. A* 1059, 121- 129, 2004
- [5] Jeon S.J., Meuzelaar H.I.C., Sheya S.A.N., Lighty J.S., Jarman W.M., Christian K., Sarofim A.F., Simoneit B.R.T., Exploratory studies of PM10 receptor and source profiling by GC/MS and principal component analysis of temporally and spatially resolved ambient samples. *J. Air Waste Manag. Assoc.*, 51, 766 - 784, 2001
- [6] OJ, 2004. Directive 2004/107/EC of the European Parliament and of the Council of 15 December 2004 relating to arsenic, cadmium, mercury, nickel and polycyclic aromatic hydrocarbons in ambient air. *Official Journal of the European Community L 23*, 26/01/2005, 3-16
- [7] US EPA, 1989. US Environmental Protection Agency Risk Assessment Guidance for Superfund, Human Health Evaluation Manual
- [8] Information available from http://www.digitel-ag.com/Frameset_engl.htm, website accessed on 02/03/2011
- [9] MDHS 14/3, 2000. General methods for sampling and gravimetric analysis of respirable and inhalable dust, Health & Safety Executive
- [10] Maitre, A, Collot-Fertey, D, Anzivino, L, Marques, M, Hours, M and Stoklov, M, Municipal waste incinerators: air and biological monitoring of workers for exposure to particles, metals and organic compounds, *Occupational and Environmental Medicine*, 60, 563-569, 2003

RESISTANCE SPOT WELDING FUMES OF COATED STEEL

Veerle Van Lierde, Philippe Legros

*ArcelorMittal Global R&D Gent (OCAS NV)
Pres. J.F. Kennedylaan 3, B-9060 Zelzate*

Summary

A metallic steel plate coated with a Thin Organic Coating (TOC) was tested on the release during spot welding of possible hazardous compounds in order to perform a risk assessment. The main questions were: what are the main volatiles released during welding and is there a potential hazard related with it?

Before performing a real welding test, the coating was submitted to pyrolysis at 500 °C and 800 °C in order to simulate the welding conditions. The pyrolysis coupled with GC-MS is a laboratory test representing worst case conditions and allows estimating the main volatile organic compounds that may be generated during welding (according to ISO15011-5). This screening test gives qualitative and semi-quantitative results concerning the degradation products endangering human health. These data are useful in order to define a sampling strategy at workplace or during welding. A small amount of the coating was scraped off the metal plate in order to perform the pyrolysis. All of the degradation compounds released during pyrolysis were identified using Gas Chromatography - Mass Spectrometry (GC-MS). The pyrolysis method allowed detection of specific target compounds before a real welding test was even performed.

From the pyrolysis of the TOC, a lot of potentially hazardous compounds were identified such as benzene, 1,3-butadiene, phenol, formaldehyde and isocyanates. This result led to the performance of a spot welding test in our Toxibox in which specific gas sampling for these target compounds was performed, together with sampling of the particulate matter. Full quantification of the sampled gases was performed. For instance, liquid (HPLC) and gas chromatography (GC) were used for the determination of the target compounds isocyanates, benzene, phenol, formaldehyde and 1,3-butadiene.

Also the particulate matter released during welding was sampled and analyzed. The weight and composition of the particulate matter was determined with special interest in particle size (distribution), morphology, metal content and soluble organic matter.

Based on the results obtained from the pyrolysis and the welding test of the TOC in the Toxibox, a risk assessment was made. This allowed estimation of the possible health risk by comparing the possible concentration of the major pollutants with the respective exposure limits. It was concluded that (i) concerning the gases, the concentrations of the pollutants were at least 50 to 200 times below the exposure limits and (ii) concerning the particulate matter, the concentrations were higher but remained below the exposure limits.

Full article

1.1. Introduction

Thin Organic Coatings (TOCs) offer very high corrosion resistance based on a barrier effect. They are designed to retain good weldability by means of metallic particles included in their organic matrix. Steels with organic coatings are protected from corrosion, have a high quality surface and can be readily shaped and welded. They are therefore recommended for numerous automotive and industrial applications. Thin organic coatings are applied over metallic coated steel. They can be applied on one or both sides.

Spot welding tests have been carried out on metallic steels coated with Thin Organic Coatings (TOC) and /or oils. The main objectives of the welding trials were (i) to identify and quantify the dust (Particulate Matter) and gases and (ii) to compare the results obtained by pyrolysis of the coatings and the gas sampling during welding. Sampling and analysis of dust and gases have been performed.

1.2. Methodology

The general methodology used for welding fumes analysis is summarized in Figure 1.

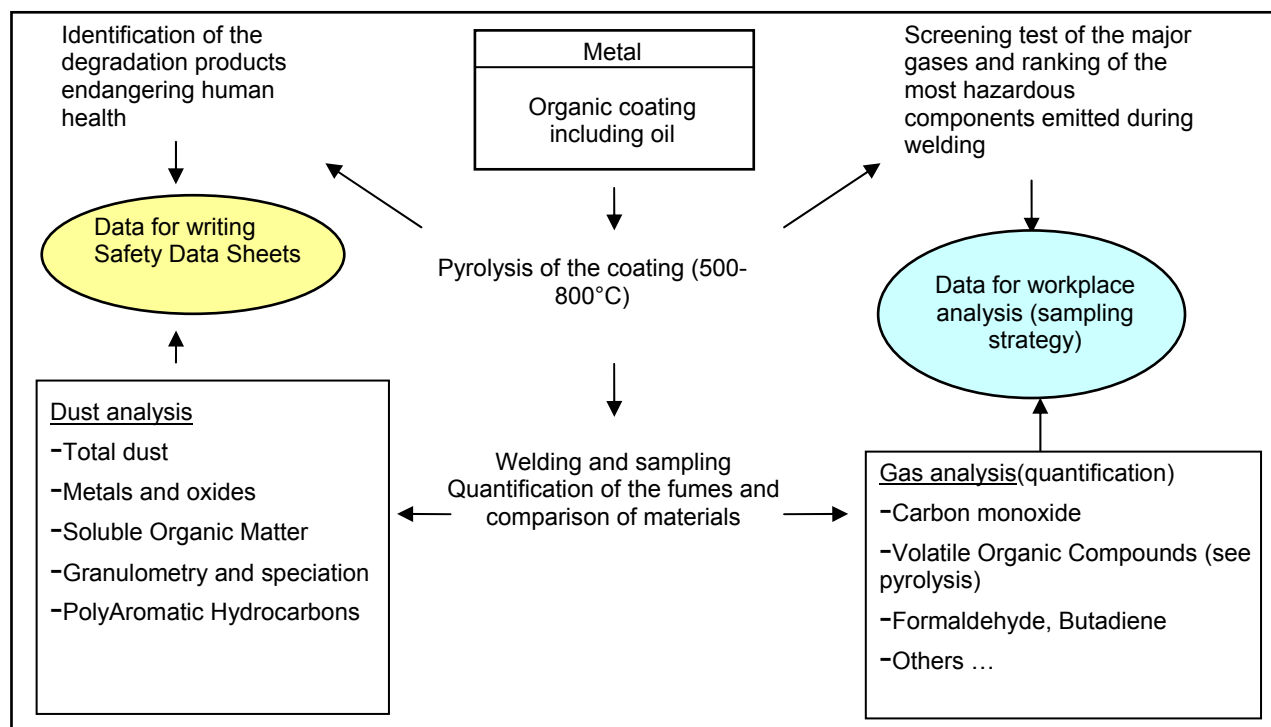


Figure 1: Methodology of welding fumes analysis

Generally, the methodology can be divided into three steps:

- Pyrolysis of the coating for the first screening of the organic gases emitted during welding;
- Welding test and sampling of the dust and the gases for quantification;
- Analysis at workplace using the previous results from the pyrolysis and the laboratory welding tests.

1.3. Results and discussion

1.3.1. Pyrolysis of the coatings

Pyrolysis coupled with Gas Chromatography and Mass Spectrometry (Py-GC-MS) is a laboratory test which allows estimation of the main volatile organic compounds (VOCs) that may be generated during welding. This screening test gives qualitative and semi-quantitative results concerning the degradation products endangering human health. These data are useful in order to define a sampling strategy at workplace or during welding and are also helpful when preparing Safety Data Sheets.

Pyrolysis at 500°C and at 800°C of two oils (oil I and oil A) and two Thin Organic Coatings (TOC A and TOC I) were performed. The corresponding major hazardous compounds in terms of relative concentration are summarized in Table 1.

Table 1: Ranking of the major hazardous components in terms of relative concentration based on the pyrolysis results

Ranking	Oil I	Oil A	TOC A	TOC I
1	Semi-volatile hydrocarbons (>C ₁₆)	Semi-volatile hydrocarbons (>C ₁₆)	Semi-volatile hydrocarbons (>C ₁₆)	Methyl methacrylate
2	Benzene	Benzene	Benzene	Ethyl acrylate
3	1,3-butadiene	1,3-butadiene	1,3-butadiene	Benzene
4	Toluene	Toluene	Toluene	1,3-butadiene
5	Xylenes	Xylenes	Xylenes	Toluene
6	Styrene	Styrene	Styrene	Xylenes
7	Ethylbenzene	Ethylbenzene	Ethylbenzene	Cresol
8	Naphthalene	Naphthalene	Naphthalene	Methyl acrylate
9			Phenol	
10			Cresol	

Pyrolysis of oil results in emission of volatiles which consist of 80-90% aliphatic and aromatic hydrocarbons. As for the oils, regarding the TOC A, the major part is composed of semi-volatile hydrocarbons (>C₁₆). Concerning the TOC A, the presence of a lot of alkenes (C₃-C₇) and aromatic hydrocarbons, in particular benzene, 1,3-butadiene, toluene, styrene and xylenes is significant.

An increase in pyrolysis temperature causes (i) a decrease of semi-volatile hydrocarbons, phenol and cresol and (ii) an increase of alkenes and aromatics.

Observing the TOC I, the major compound at 500°C and at 800°C was methyl methacrylate. At 500°C, about 50% of the volatiles are acrylates, namely methyl methacrylate and ethyl acrylate. The acrylates concentration at

800°C, is lower but new compounds appear, especially 1,3-butadiene, benzene, toluene, xylenes, cresol, naphthalene. Compared with the oils and the TOC A, benzene and butadiene were also detected.

1.3.2. Welding experiments

Sampling of welding fumes

The welding experiments were carried out in the laboratory using a specially designed sampling box (Figure 2). This box was positioned around the electrodes of the welding equipment to sample the welding fumes. Four sampling points are present on the front side of the box. For the gas sampling, 100 spotwelds were done and for the dust sampling 300 spot welds.



Figure 2: Sampling box of 60 litres made of glass and stainless steel

The gases were sampled on specific adsorbents with a filter or quartz wool in front to protect the adsorbent from the dust. Dust was sampled onto specific filters depending on the subsequent analysis technique.

Analysis of gases and dust

Table 2 presents a summary of the amount of emitted gases and dust obtained for 100 welding spots.

Table 2: Quantity of gases and dust emitted for 100 spots

Gases for 100 spots	Oil I	Oil A	TOC I	TOC A + Oil A
Carbon monoxide in mg	0.2	0.2	1.6	2.6
Formaldehyde in mg	0.005	0.004	0.024	0.028
Butadiene in mg	0.034	0.027	0.054	0.058
Benzene in mg	0.019	0.004	0.009	0.377
Ethyl acrylate in mg			0.541	
Methyl methacrylate in mg			1.000	
Benzo(a)pyrene in µg	0.010			0.01
Dust for 100 spots	Oil I	Oil A	TOC I	TOC A + Oil A
Total dust in mg	1.5	0.7	4.9	2.5
Zn in mg	0.064	0.018	1.64	0.24
Fe in mg	0.174	0.003	1.19	0.41
Cu in mg	0.002	0	0.78	0.012
SOM, Soluble Organic Matter in mg	0.84	0.43	0.84	1.32

The coated steels with Thin Organic Coatings have emitted more fumes than the oiled steels. The major pollutant in the fumes is the total respirable dust. Regarding the dust, the most important part is organic, except for the TOC I because of the large amount of metals due to the difficulty to weld and the expulsions.

In case of the TOCs, the gases are of great importance because of the hazard and the low exposure limit of some compounds such as benzene, formaldehyde, carbon monoxide or benzo(a)pyrene.

A good correlation exists between the pyrolysis and the welding results, especially for the Thin Organic Coatings (TOCs): detection of the acrylates in the TOC I and the aromatic hydrocarbons for the TOC A.

The important part of Soluble Organic Matter analysed in the dust probably corresponds to the semi-volatile hydrocarbons found during the pyrolysis of the two oils and the TOC A.

1.4. Conclusion

Taking into account a scenario of a welding of 1800 spots/hour in a room of 100 m³, a risk assessment was performed. In this way, an estimation of the possible risk could be made by comparing the possible concentration of the major pollutants with the exposure limits.

Risk assessment in real conditions (hypothesis: 100 m³ air, 1800 spots/hour) in case of absence of exhausting system (worst case):

Gas concentration mg/m ³	Oil I	Oil A	TOC I	TOC A + Oil A	⁽¹⁾ TLV	⁽²⁾ OEL
Carbon monoxide	0.036	0.036	0.29	0.47	55 mg/m ³	23 mg/m ³
Formaldehyde	0.0009	0.0007	0.004	0.005	0.61 mg/m ³	
Benzene	0.003	0.007	0.002	0.07	3.25 mg/m ³	3.25 mg/m ³
Ethyl acrylate			0.1		20 mg/m ³	21 mg/m ³
Benzo(a)pyrene in µg/m ³	0.002			0.002	max 0.15 µg/m ³	
Dust concentration mg/m ³	Oil I	Oil A	TOC I	TOC A + Oil A	⁽¹⁾ TLV	⁽²⁾ OEL
Total dust	0.27	0.13	0.88	0.45	5 mg/m ³ respirable	
Cu			0.14		0.2 mg/m ³	0.2 mg/m ³

(1) France : Valeurs limites d'exposition professionnelle aux agents chimiques en France, ED 984, 2011

(2) European Union : Occupational Exposure Limit, 2011

Concerning the gases, the concentrations of the pollutants are at least 50 to 200 times lower than the exposure limits.

Concerning the dust, the concentrations are higher but remain below the exposure limits.

Depending on the system and according to the current results, an air analysis of the total dust and one or two gases emitted at the workplace could be performed in order to determine the "real" air quality.

THE MEASUREMENT OF GAS PHASE REACTIONS AT STEEL SURFACES USING A MASS SPECTROMETER PROBE

Heinz Falk¹, Martin Falk¹, Martin Norden², Frédéric Huber³ and Wolfgang Bleck³

¹(Falk Steuerungssysteme GmbH; Stadthagen, Germany)

²(DOC Dortmunder Oberflächencentrum GmbH; Dortmund, Germany)

³(RWTH Aachen University, Department of Ferrous Metallurgy, Germany)

Abstract

A mass spectrometer probe incorporated in a thermal reactor which is used to measure the concentrations of gas phase components will be described. The steel samples have been exposed to various oxidizing and reducing gas flows at pressures between ambient pressure and 2 bar. The species in the gas phase of foremost interest are H₂O, H₂, CO, CO₂ and NH₃ to observe the processes going on during the annealing, oxidation and reduction as well as the decarburization or nitriding. By applying linear temperature ramps from ambient up to 900°C to the sample, the activation energies of the respective chemical reactions could be evaluated. Additional investigations of the samples after thermal treatment, such as GDOES, have been carried out. The gas phase concentrations as a function of the processing time are correlated to the changes of the respective concentrations within the treated samples. Also, since steels differ in their alloying concept, steels behavior during the process could be compared. This applies in particular to the decarburization and nitriding processes. The measurement of the concentrations of the gaseous components during the thermal treatment of steel samples allows the optimization of the relevant process steps.

1. Background

High strength steels have to undergo several steps in the annealing atmosphere to prepare them for the respective application. Crucial points are the zinc wettability of the surface, carburization/decarburization and nitriding of surface near layers the so called sub-surface of the steel. The processes during the annealing treatment of high strength steel under various concentrations of hydrogen and water vapor has been studied theoretically and with a laboratory hot dip simulator by Shastry et al. [1]. After the treatment the samples have been investigated with different surface analysis methods such as SEM, XPS, GDOES and optical microscopy. The authors could interpret the experimental findings with the theoretical predictions, particularly with respect to selective oxidation of the alloying elements Mn, Si and Al. It is a limitation of the investigation by Shastry et al. [1] that the theoretical model used assumptions about the dew point at the surface which is not supported by measurements. Such data can be provided by in-situ measurements of the gas phase concentrations using a mass spectrometer probe [2]. The determination of the gas phase concentrations of the reactive components at the steel surface allows the quantification of the components involved and, consequently, to control the process.

If the annealing treatment of the steel is accomplished with NH₃ present besides H₂, then the zinc wettability will be improved as well as the mechanical characteristics of the sub-surface [3-6]. Also in this case, the in-situ measurement of the gas phase components near to the steel surface can be used to control this process.

The basic arrangement of the experimental set-up of the mass spectrometer probe to study surface reactions has been described in a former publication by H. Falk and M. Falk [2]. The feasibility of this method has been shown by some application results for the reduction as well as for the decarburization of steel samples [2]. In this paper experimental results for the thermal treatment of selected steel grades with the in-situ measurement of the gas phase concentrations will be reported.

2. Experimental

With respect to the former paper by H. Falk and M. Falk [2] only the schematic of the set-up is shown here in Fig. 1. Very important for the analytical capability of the mass spectrometer connected to the thermal reactor is the construction of the MS-probe. The sampling of the gases to be analyzed takes place in the vicinity of the metal surface. Consequently, the dilution of the analytes by diffusion into the carrier gas will be minimized. Additionally, the carrier gas flow is transported by a ceramic tube, which contains the entrance capillary of the mass spectrometer. In this way, the reaction products formed at the metal surface will be collected at the entrance capillary, resulting in low limits of detection.

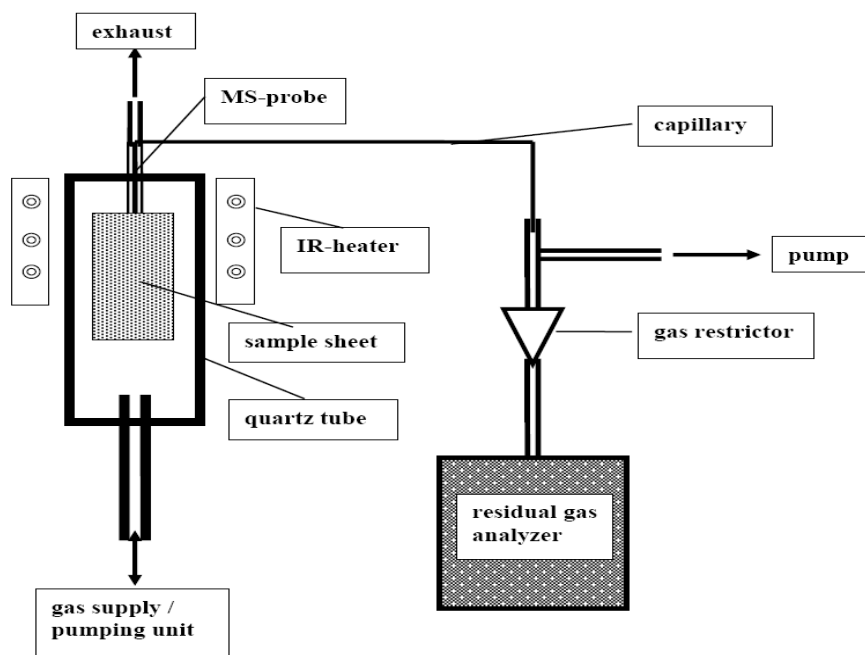


Fig. 1. Scheme of the experimental reactor [2].

The chemical composition of the steel samples used for the experiments in this study is presented in Tab. 1. and the temperature programs in Tab. 2.

element (mass-%)					
steel grade	C	Si	Mn	Al	Cr
DP	0.07	0.1	1.4	0.05	0.5
High Mn	0.3	0.2	22	0.01	0.1
TRIP Al	0.2	0.1	1.6	1.55	0.1
TRIP Si	0.16	1.5	1.6	0.05	0.02

Tab. 1. Main components of the steel samples investigated in this study.

	gas	T1; R1 (°C; K/s)	T2; t2 (°C; s)	R2; T3 (K/s; °C)	T3; t3 (°C; s)
oxidation	air	100; 10	500; 3 - 20		
reduction	Ar-H ₂ ; 95-5	100; 10	300; 20	1; 900	
nitriding	Ar; NH ₃ 0.5 – 4.5 %	100; 10	300; 20	1 - 6; 750 - 900	750 – 900; 1 - 200

Tab. 2. Experimental conditions for thermal treatment of the steel samples.
Gas pressure: ca. 1.3 bar.

The following processes listed in Tab. 3 were studied by monitoring the gaseous species via the mass spectrometer.

process	reaction	No.
hematite oxidation/reduction	$3 \text{H}_2 + \text{Fe}_2\text{O}_3 \leftrightarrow 3 \text{H}_2\text{O} + 2 \text{Fe}$	(1)
hematite oxidation/reduction	$\text{H}_2 + 3 \text{Fe}_2\text{O}_3 \leftrightarrow \text{H}_2\text{O} + 2 \text{Fe}_3\text{O}_4$	(2)
magnetite oxidation/reduction	$4 \text{H}_2 + \text{Fe}_3\text{O}_4 \leftrightarrow 4 \text{H}_2\text{O} + 3 \text{Fe}$	(3)
bulk carbon oxidation/reduction	$\text{C} + \text{H}_2\text{O} \leftrightarrow \text{CO} + \text{H}_2$	(4)
nitriding	$2 \text{NH}_3 \leftrightarrow 2 \text{N} + 3/2 \text{H}_2$	(5)
dissociation	$2 \text{NH}_3 \leftrightarrow \text{N}_2 + 3/2 \text{H}_2$	(6)

Tab. 3. Gas phase reactions at the surface of a steel sample.

Before the reduction measurements were carried out, the steel surfaces were treated using various conditions as shown in Tab. 2. While heating the oxidized samples at a constant heating rate of 1 K/s starting at 300 °C in a reducing atmosphere, the formation of the water vapor according to equation (1) to (3) as well as the consumption of the hydrogen could be observed via the mass spectrometer. Similarly, if a wet atmosphere was applied, the formation of hydrogen and carbon monoxide as well as the consumption of water vapor could be measured. The presupposition for this measurement was the use of argon as the carrier gas instead of the nitrogen, which is usually applied. This is due to the fact, that CO and N₂ have coinciding masses. Since neither N₂ nor Ar is taking part in the respective chemical reaction, the result with respect to the carbon oxidation is not influenced. Ar as the carrier gas was also reasonable for the nitriding process, since besides the diffusion of atomic nitrogen into the steel matrix according to equation (5), some ammonia is dissociated resulting in nitrogen and hydrogen gas according to equation (6). Because the hydrogen stemming from dissociation does not contribute to the nitriding, it has to be subtracted via the measurement of the formation of nitrogen during the thermal treatment. Besides the molecules of interest the respective fragments, for example C and O from CO, were measured simultaneously. The intensity ratio of the fragments to the parent molecule was checked to identify the possible influence of coinciding masses.

Generally, the size of the steel sheets was 80 x 20 mm², thickness: 1 to 1.5 mm.

3. Results

3.1 Oxidation by water vapor

The presence of water vapor causes oxidation of the iron surface according to equation (1) and (2) as well of carbon within a surface-near layer according to equation (4). Fig. 2. shows the hydrogen concentration at two High Mn samples for time regimes differing in the duration of the temperature hold time as a reproducibility test. Considering Fig. 2. the differences between the temperature characteristics of the hydrogen concentrations shown in Fig. 3. for different samples appear to be significant. It can be noticed that different steel qualities differ with respect to the rising edge of the hydrogen production rate which implies different reaction mechanisms. The CO formation resulting from the bulk carbon oxidation shown in Fig. 2 starts much later than the metal oxidation at the surface. This explains the second rise of the hydrogen peak at higher process times. The quantification of the hydrogen and carbon monoxide amounts formed during the oxidation process can be carried out by integrating over the pressure peaks.

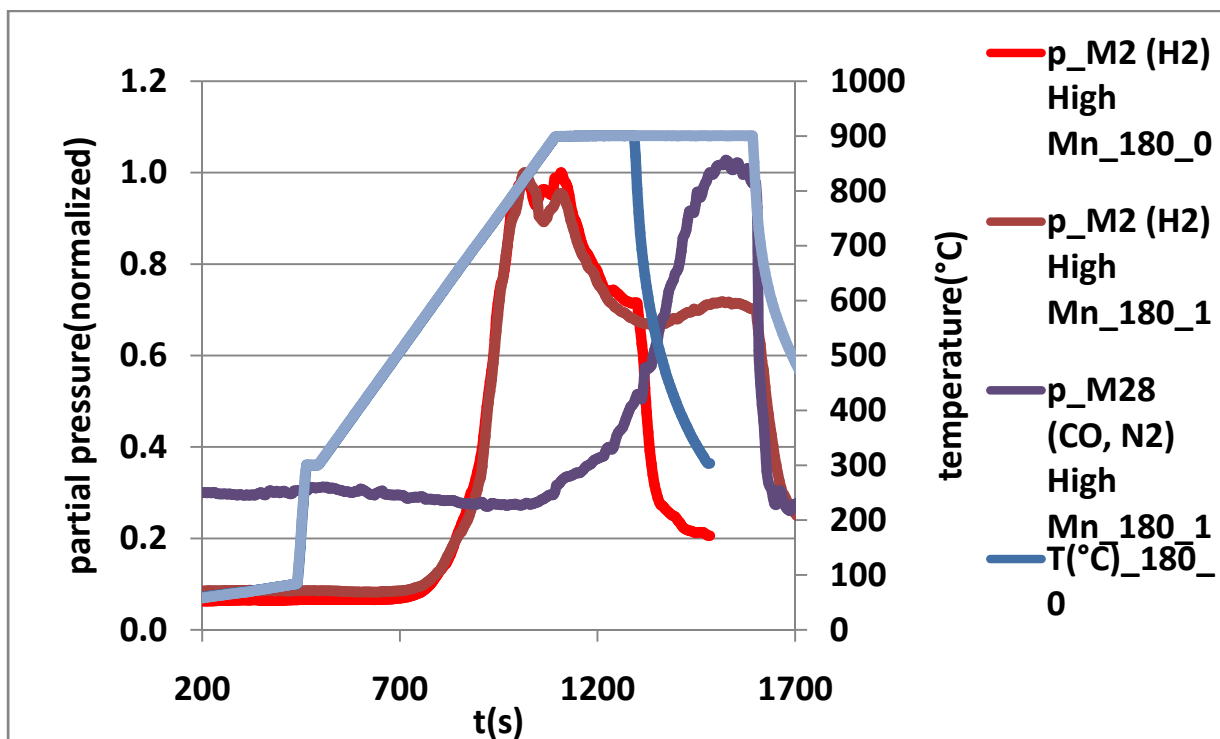


Fig. 2. Reproducibility of the hydrogen signal formed via oxidation of two High Mn samples. Ar-flow: 0.3 l/min., $T_p = 30^\circ\text{C}$, ramp rate: 1 K/s.

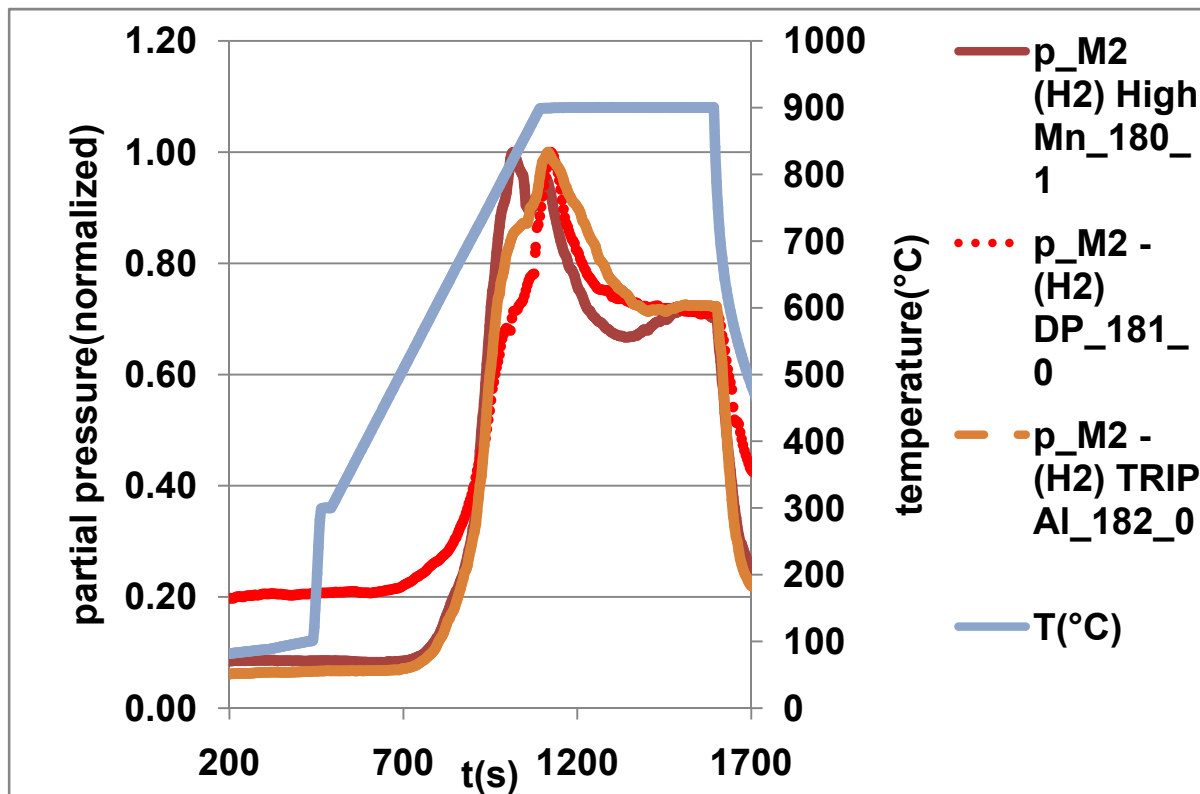


Fig. 3. Hydrogen signals formed via oxidation of three different steel samples. Ar-flow: 0.3 l/min, $T_p = 30^\circ\text{C}$, ramp rate: 2 K/s.

3.2 Reduction of surface oxides

Surface oxides were formed either via humidity as described above, or by exposing the steel samples to air while heating up to 500°C . The water vapor formed by the reduction with hydrogen is shown in Fig. 4. As an example. Besides mass 18 for water the fragment mass 17 the hydroxyl molecule is displayed in Fig. 4. From the time dependence of the water signals it can be noted that the reduction process is completed at the process time of 800 s, when the thermal treatment could be finished in further experiments. The rising edge of the H_2O and OH signals allows evaluating the activation energy for the reduction reaction using an Arrhenius plot.

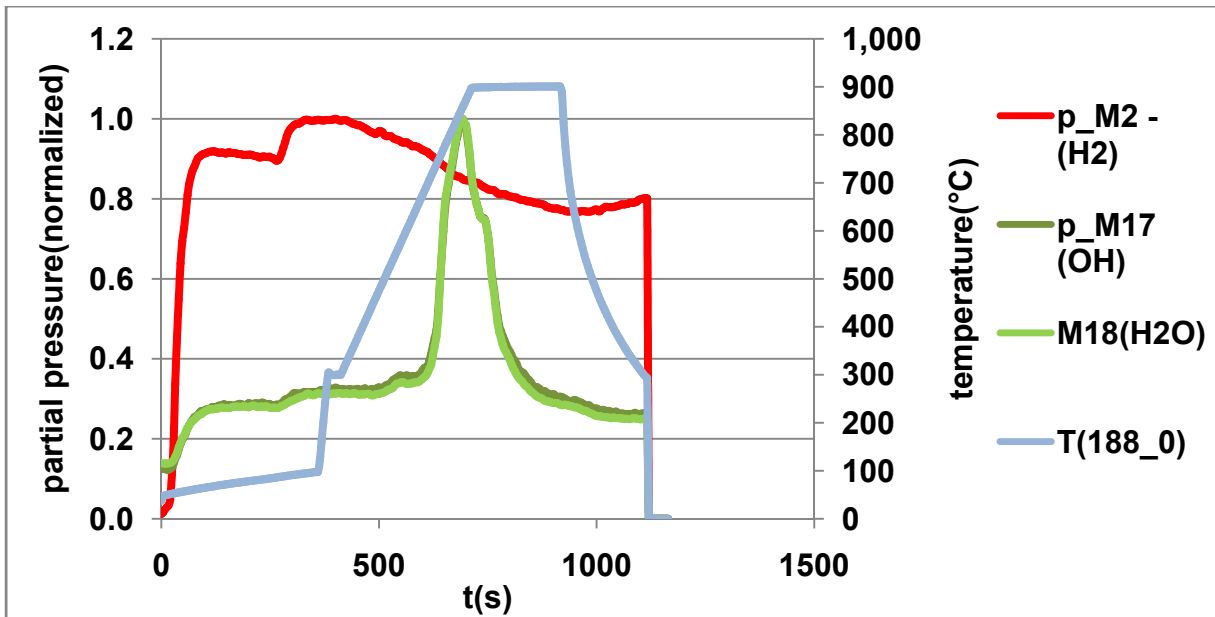


Fig. 4. Measurement of the water vapor formation during the reduction of an oxidized steel surface (air oxidation at 500 °C). 2 l/min Ar (95 %), H2 (5 %), ramp rate: 2 K/s.

3.3 Analysis of the final product

The findings of the in-situ MS-probe measurements were compared with the surface analysis of steel samples after the completion of the thermal treatment. Besides structural analysis the GDOES depth profiles of the element concentrations allows a kind of calibration of the gas phase data. Fig. 5. shows an example of decarburization and hydrogen formation curves after oxidation in a wet atmosphere.

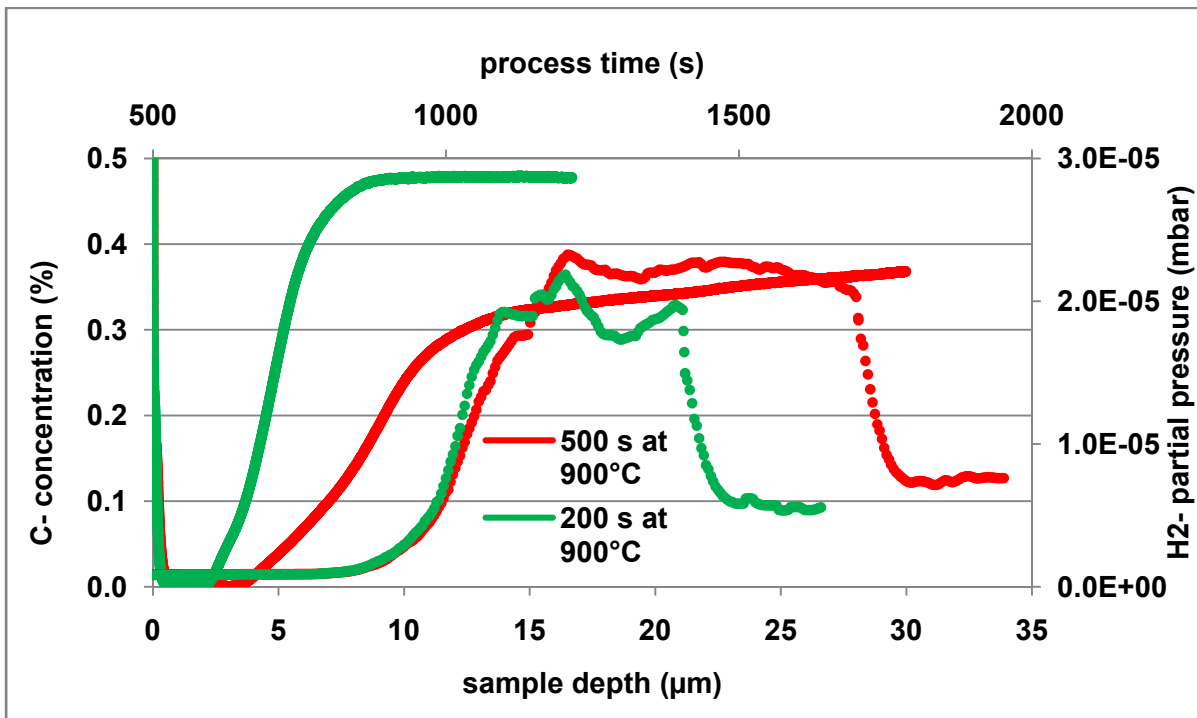


Fig. 5. Carbon depth profiles from GDOES and the respective hydrogen formation peaks for two exposition times at 900 °C and wetness $T_p = 30$ °C. Sample: High Mn (0.5 % C).

4. Conclusions

With help of the MS-probe the gas phase processes at steel surfaces during annealing and surface conditioning can be followed up. The MS-probe takes the samples near to the steel surface avoiding analyte dilution. The evaluation of the temperature dependences of the chemical reactions between steel surface and reactive gases allows controlling the surface conditioning process. The analysis, e.g. by GDOES, of the steel after the completion of the thermal treatment is compatible with the results of the in-situ measurements using the MS-probe, but the latter is much faster. The process parameters evaluated from the measurements on steel samples using an experimental reactor with the MS-probe can be used to simulate the operation of a production plant.

References

- [1] C. R. Shastry, J. A. Totole and T. W. Kaiser; "Characterization of selective oxidation of alloying elements in an advanced high strength steel from theoretical and experimental viewpoints", Galvatec '07, 403 - 408 (2007).
- [2] H. Falk and Martin Falk; steel research int. 81 (2010) No. 4, 320.
- [3] B. Schuhmacher, S. Staudte, D. Beste and S. Claessens, Projekt der European Coal and Steel Community, 2002, Projektreferenz: 7210-PR/257.
- [4] J. Staudte, Surface Conditioning of High-Strength Steels, Dissertation RWTH Aachen; Shaker Verlag Aachen, 2003 (Berichte aus dem Institut für Eisenhüttenkunde; Bd. 4/2003).
- [5] W. Bleck, D. Beste and J. Staudte, Galvatech '04, 6th Int. Conf. on Zinc and Zinc Alloy Coated Sheet Steels, 04.-07.04.2004, Chicago, USA. Warrendale, PA: AIST 2004, S. 349-360.
- [6] F. Luther, A. Dimiyatl, D. Beste, W. Bleck and J. Mayer, Advanced Engineering Materials 9 (2007) Nr. 4, S. 274-279.

DETERMINATION OF ARGON IN TITANIUM ALLOY & NANO POWDER BY INERT GAS FUSION-TIME-OF-FLIGHT MASS SPECTROGRAPH METHOD

Wang Peng*, Hu Shaocheng, Yang Zhigang, Shen Xuejing, Ma Hongquan, Wang Haizhou

*China Iron & Steel Research Institute Group, Beijing NCS Analytical Instruments Co., Ltd.
Beijing, China 100081*

Abstract:

Studies have been done for years on how to analyze gas elements such as O, N and H in metallurgical materials. Traditional methods used are the inert gas fusion-infrared absorption and thermo-conductivity method. There is no standard method documented to analyze Argon or Helium in metallurgical materials. Since the content of Argon in metal is very limited and the conductive coefficient of Helium is too close to that of Hydrogen, traditional thermo-conductivity method can not succeed in the analyses of these two elements. To solve this problem, we developed Inert Gas Fusion-Time-of-flight Mass Spectrograph Method to analyze not only O, N, and H, but also Argon and Helium. TOF-MS is simple in theory and has a fast response. By using TOF-MS as detector, the results of O, N, H, Ar/He, etc can be got simultaneously. The lower limit of TOF-MS can be ppb.

The Certified Reference Materials (CRMs) of Argon/Helium are hardly to find. So a gas dosing calibration equipment is setup. The reserved gas dose interface on the analyzer is used. Based on the calibration curve built up by gas dosing, Argon in titanium and nano powder is analyzed by using Helium as the carrier gas. The differences among titanium materials were found. Argon in some specimens can be up to 700ug/g, but in the others content of Argon is too low to be detected. The detection limit of Argon by Inert Gas Fusion-Time-of-flight Mass Spectrograph Method is got by results of gas dosing.

Keywords: Argon, Oxygen, Nitrogen, Hydrogen, gas dosing, TOF-MS, Inert gas fusion

With researches and developments of the new materials, requirements become more and more strict for the properties of the metal, alloy, and nano powder, etc. The effect of trace gas elements such as C, S, O, N, H, Ar and He is more and more focused on by material workers, and accordingly demands and requirements are raised for the detection of trace gas elements. The traditional pulse heating -inert gas protecting-infrared absorption /thermo - conductivity detection method has successfully solved the problems of the detection within normal range of O, N and H in the material, and relevant method researches and applications are relatively mature and are widely used in various laboratories and research institutes. However, there are few analysis methods^[3,4,5] and researches applied for the inert gas elements Ar and He in the material. Although the content of Ar and He is very low in metal, alloy and nano powder, in order to improve and strength the properties of the new materials the detection of Ar/He has become a new demand for gas element analysis. In this article, an Inert Gas Fusion-Time-of-flight Mass Spectrograph Analyzer^[1,2] is used to conduct the analysis method research of Ar. Analysis method of Ar based on Inert Gas Fusion-Time-of-flight Mass Spectrograph is established, and is applied on titanium alloy and nano powders. The analysis results comply with the expected values of the technologists.

1. Inert Gas Fusion-Time-of-flight Mass Spectrograph Method

1.1 Operation Theory

Inert Gas Fusion-Time-of-flight Mass Spectrograph (TOF-MS) Method is a new combination technology, which combines traditional inert gas fusion method with advanced time-of-flight mass spectrograph method. There are three units in this analyzer, sample pretreatment unit, TOF-MS detection unit and the interface between two units. Fig. 1 shows the structure of Inert Gas Fusion-Time-of-flight Mass Spectrograph Analyzer.

The sample pretreatment unit adopts the traditional inert gas protecting-pulse heating furnace, which is

provided by Beijing NCS Analytical Instruments Co. Ltd. (China). Inert gas is adopted as the carrier gas. The sample drops in and is heated and fused instantly in the graphite crucible, which is located between the upper and lower electrodes of the pulse heating furnace and can be heated to over 3000°C within 10 s by high current. Reduction reactions take place between oxides and nitrides in the sample and C of the crucible. CO, N₂, H₂ and Ar or He are released from the reaction. After being filtered and dehydrated, the mixed gases released are carried by the inert gas into the subsequent detection unit.

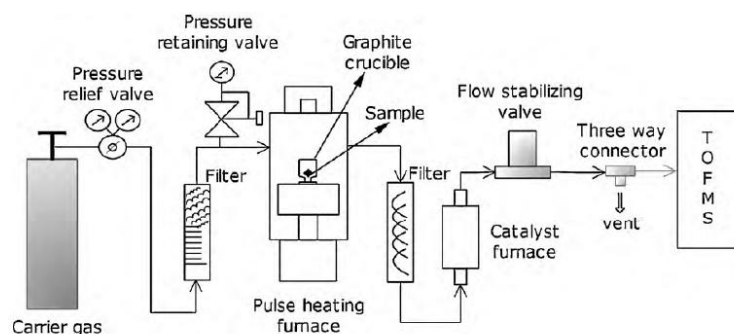


Fig. 1 The schematic flow chart of the Inert Gas Fusion-TOF-MS Analyzer

The mixed gases enter the detection unit through the coupling interface between two units. The coupling interface can fulfill the flow control transition from a large-flow process analysis to diffusely tiny-flow control demanded by TOF-MS. The interface adopts a branch diffusion structure, and a capillary tube is used to lead a trace of gas into the Time-of-flight Mass Spectrograph detector for detection.

A time-of-flight Mass Spectrograph Detector is used as the detection unit, which is provided by Hexin Analytical Instrument Co., Ltd. It consists mainly of einzel lens and mass analyzer. A trace of to-be-detected gas is introduced from the branch diffusion capillary tube into the high vacuum system of the Time-of-flight Mass Spectrograph detector, and impacted by the electrons in the ionization chamber and turned into ions. When passing through an accelerated electric field with a constant potential, the ions with the same original kinetic energy are thrown out. The ions are separated in the field-free drift tube according to different m/z . Signals are generated on the microchannel plate (MCP). Finally, a TDC/ ADC is used to collect the signals generated through the impact of the ions on the detector, and perform amplification, A/D conversion, statistics, integration and other mathematic operations.

1.2 Selection of TOF-MS Spectral lines

During applications different spectral lines (carrier gas conditions and detection conditions) are selected according to the analytical demands of the samples. For the detection of O, N, H and Ar, high purity He is needed as the carrier gas. The selection of spectral lines is shown in Table 1:

Table 1 Spectral lines for O, N, H, and Ar

Elements to Be Detected	Analyzed Objects	Spectral lines (m/z)
H	H ₂	2
O	CO	12
N	N ₂	14
Ar	Ar	40

Due to the overlapping of CO⁺ and N₂⁺, H₂⁺, C⁺, N⁺ and Ar⁺ spectral lines are selected. Thus the interference between CO⁺ and N₂⁺ is avoided. The process that converts CO into CO₂ is not needed, thus possible error caused by the exchange efficiency is prevented. And the gas conduit system of this method is simple.

However, the sensitivity of fragment ions C⁺ and N⁺ are comparatively lower than the corresponding molecule ions and may affect the detection limit of O and N when the contents are super low (< 10ppm). Therefore, CO₂⁺ ($m/z=44$) can be selected as the spectral line of O and N₂⁺ can be selected as the spectral line for N. For this condition, the gas mixture carried out will pass through Schutz reagent or copper oxide catalyst furnace, where CO

is selectively oxidized into CO₂. Therefore the detection limits of O and N can be remarkably lowered by adopting molecular ion peaks as the spectral lines. The selection of spectral lines for super low content of O&N is shown in Table 2:

Table 2 Spectral lines for super low content of O&N

Elements to Be Detected	Analyzed Objects	Spectral lines (m/z)
H	H ₂	2
O	CO ₂	44
N	N ₂	28
Ar	Ar	40

For the detection of O,N,H and He, the selection of spectral lines is similar, except that high purity Ar is used as the carrier gas. The selection of spectral lines is shown in Table 3:

Table 3 Spectral lines for O, N, H, and He

Elements to Be Detected	Analyzed Objects	Spectral lines (m/z)
H	H ₂	2
O	CO/CO ₂	12/44
N	N ₂	14
He	He	4

2. Experiment

2.1 Instruments and Materials

PMA1000 Inert Gas Fusion-Mass Spectrograph Analyzer

Self-made gas dosing equipment; self-made quantitative tube

High-purity He (>99.999%), dehydrate, and graphite crucible

Standard gas 1[#] (H₂: 0.000925%; CO: 0.00217%; Ar: 0.000101%; He: 0.0099680%)

Standard gas 2[#] (H₂: 0.00115%; CO: 0.00287%; N₂: 0.00161%; Ar: 0.000297%; He: 0.0099407%)

Titanium alloy

Nano powder

2.2 Experimental Conditions

High-purity He is used as the carrier gas. The flow rate is stabled at 400ml/min and the pressure is set to be 0.15MPa. The parameters of the pulse heating furnace are set as shown in Table 4.

Table 4 Configuration of the pulse heating furnace

Power (W)		Time (s)	
Outgassing power	2,500	Outgassing time	20
Purging power	2,000	Purging time	30
Waiting power	2,000	Waiting time	30
Heating power	2,000	Heating time	60

The working conditions of Time-of-flight Mass Spectrograph Detector are set as shown in Table 5.

Table 5 Working conditions of Time-of-flight Mass Spectrograph Detector

Vacuum pressure	3.0×10 ⁻⁴ Pa	Trigger level	-0.5 V
Ion source transmission current	200μA	MCP voltage	-1,750 V
Diameter of the capillary tube	50μm	Push-out frequency	12,000
Length of the capillary tube	20mm	Threshold voltage	13m V

2.3 Experimental Method

2.3.1 Blank Value and Detection Limit

A home-made high-temperature crucible is used to detect Ar blank value of the system, and analysis is performed for 11 times, wherein a new crucible is used for each time. Results are shown in table 6. The average blank value of the analyzer is 0.03 $\mu\text{g/g}$, and the standard deviation is 0.02 $\mu\text{g/g}$. Usually detection limit of the analyzer is determined by three times of the standard deviation. So the detection limit of Ar is 0.06 $\mu\text{g/g}$ and the analyzed limit is 0.2 $\mu\text{g/g}$, which is 10 times of the standard deviation.

Table 6 Blank value of the graphite crucible

Ar Content ($\mu\text{g/g}$)	Average ($\mu\text{g/g}$)	SD ($\mu\text{g/g}$)
0.01, 0.08, 0.04, 0.01, 0.01, 0.03, 0.01, 0.03, 0.05, 0.06, 0.03	0.03	0.02

2.3.2 Gas Dosing Calibration Model

Because there are no certified samples of Ar nowadays, gas dosing equipment is used in the experiment. And the corresponding calibration model is established. With gas dosing method, the influences of sample materials, pretreatment and fusion etc. can be avoided and the process of analysis can be simplified too.

The standard gas with known content of Ar is selected as the object. Sample gas is directly injected into the inert gas fusion system without starting up the heating system. The standard gas injection system is shown in Fig. 2. A chromatogram six-way valve is used. The pressure and the flow rate are set to match with those of the analyzer. The self-made quantitative tubes are used for injecting the standard gas with certain volumes into the flow channel along the direction of carrier gas so as to simulate the actual release of the sample.

According to the gas equation, in a certain injected volume of standard gas 1[#] or standard gas 2[#] the mass content of Ar corresponding to the spectra lines is calculated as follows:

$$W(\text{Ar}) = V \cdot 0.0101 \cdot 28 / 22.4 \cdot 1000 \quad (1)$$

$$W(\text{Ar}) = V \cdot 0.0297 \cdot 40 / 22.4 \cdot 1000 \quad (2)$$

According to the equations (1) and (2), the relationship between the injection volume and Ar content is shown in Table 7.

Table 7 Relationship between the injection volume of the standard gas and the content of Ar

Injection Volume (μL)	Content of Ar in Standard	
	Gas 1 [#] ($\mu\text{g/g}$)	Gas 2 [#] ($\mu\text{g/g}$)
250	0.10	0.308
500	0.15	0.440
1,000	0.24	0.705
2,000	0.42	1.236
5,000	0.96	2.827
10,000	1.86	5.479
20,000	3.67	10.782
30,000	5.47	16.086
40,000	7.27	21.389

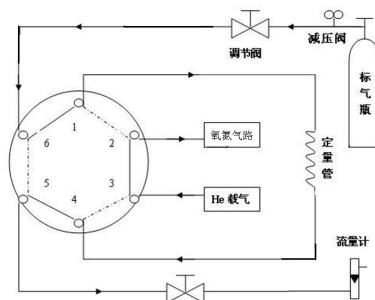


Fig. 2 Gas dosing equipment

2.3.3 Calibration curve of Ar

Quantitative dosing tubes with different volumes are used for injecting the standard gases to simulate the test points with different contents. Analysis is performed for at least three times with the same volume, and the average value is taken. Calibration data are shown in table 8. According to the instrument instructions and based on the data in table 8, the calibrating procedure is performed, and a calibration curve is established between Ar content and the integrated number of ions detected through mass spectrograph detector, as shown in Fig. 3. It can be seen from the Figure that the correlation coefficient of the fitting curve is above 0.99. The linearization between Ar content and the ion number is good.

Table 8 Calibration data

Ar content(%)	Ion number	Average
0.000031	967.85, 1025, 1397	1129.95
0.000071	1528.286, 1607.572, 1856.714	1664.19
0.0001244	3085.715, 3117.714, 3244.715	3149.38
0.0002847	6347.857, 6484, 6618	6483.29
0.0005517	12489.71, 12614.43, 12710.24	12604.79
0.0010858	24286.57, 24345.43, 24354.01	24328.67

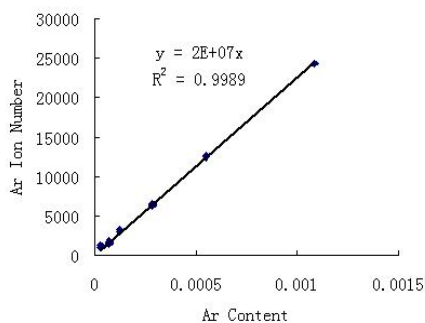


Fig.3 Ar calibration curve

2.3.4 Stability of the Analyzer

A quantitative dosing tube with a volume of 15.0ml and standard gas 2[#] are adopted. The quantitative gas is injected for 11 times to inspect the stability of the analyzer. According to the equation (2) in 2.3.2, the absolute content of Ar in 15ml standard gas 2[#] equals to 0.000813% Ar in 1g material. Repetitive results of gas dosing are shown in Table 9. The average value is 0.0008382%. The standard deviation is 0.000012%, and the relative standard deviation is 1.44%. From the results the stability of the analyzer can match the demands of analysis.

Table 9 Results of repetitiveness determined by dosing 15.0ml of standard gas 2[#]

Found of Ar (%)	Average (%)	SD (%)	RSD (%)
0.000817, 0.000835, 0.000858, 0.000848, 0.00085, 0.000833, 0.000835, 0.00083, 0.000849, 0.000839, 0.000826	0.0008382	0.000012	1.44

3. Results and discussion

3.1 Analysis Procedure

Two types of samples were analyzed which have requirements for Ar content, namely, titanium alloy and nano powder. According to different forms and alloy components, a compound bath is used as a fusing assistant during the analysis, and 0.10g-0.30g of sample is taken, which is accurate to 0.0001g. The samples are packed with a nickel foil and placed in a nickel basket, which is then put into the sample adding unit. The analysis conditions are set according to 2.2.

3.2 Results of Ar in Titanium and Titanium Alloy

The analysis results of Ar in three types of titanium alloys are shown in Table 10, and the releasing plots are shown in Fig. 4-Fig. 6. As can be seen from the analysis results of Table 10, the Ar content in the samples ranges from less than 3µg to 700µg, and the releasing process is complete. Among the samples, sample 3# is the product during processing without Ar injected, while sample 1# and 2# are products during processing with Ar injected. The analysis results are consistent with the values from theoretical calculations which are expected. It is proved that the differences between the processing with Ar injected and the processing without Ar injected do exist.

The results obtained in this test are basically the same as those determined through the pulse heating thermo-conductivity method, as shown in Table 11. Because there are no reference materials, the data deviation is probably caused by selection of different reference standards.

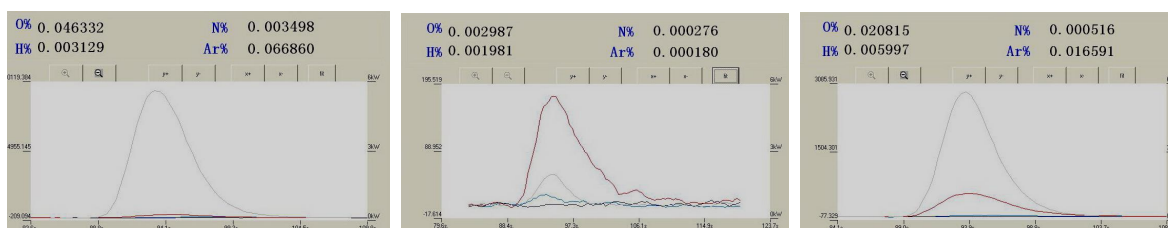


Fig. 4,5,6 Releasing plots of Ar (Sample1#, 2#, 3#)

Table 10 Results of Ar in titanium and titanium alloy

Sample	Weight (g)	Found (%)	Average (%)	RSD%
1#	0.1094,0.1229, 0.1097	0.014940, 0.017388, 0.016543	0.01629	7.63
2#	0.0941, 0.1280, 0.1250	0.000207, 0.000180, 0.000158	0.00018	13.51
3#	0.1206, 0.1093, 0.0939	0.067464, 0.067178, 0.066860	0.06717	0.45

Table 11 Comparison between the inert gas fusion-TOF-MS method and the pulse heating thermo-conductivity method

Sample	PMA1000	Pulse heating Thermo-conductivity Method
1#	0.0163	0.020
2#	0.00018	-
3#	0.0672	0.072

3.3 Results of Ar in Nano Alloy Powders

Ar contents in six types of nano alloy powders were analyzed, and the results are shown in Table 12. It is generally considered that Ar exists in the nano alloy powder by adsorption, its content is relatively low. However, some technologists also raise the question whether there is a trace of Ar existing in the form of a compound. From the data in table 12, Ar contents are really very low, the highest one is less than 3 $\mu\text{g/g}$. For this range the traditional pulse heating thermo-conductivity method can not fit.

Table 12 Results of Ar in nano alloy powders

Sample	Sample Weight (g)	Found ($\mu\text{g/g}$)	Average ($\mu\text{g/g}$)	SD ($\mu\text{g/g}$)
powder-01	0.0250, 0.2911, 0.1365, 0.1770	0.23, 0.10, 0.18, 0.67	0.29	0.26
powder-02	0.2286, 0.2815, 0.0919	0.85, 0.88, 0.19	0.64	0.39
powder-03	0.1958, 0.0879	0.17, 0.33	0.25	0.11
powder-04	0.0968, 0.0722, 0.1161, 0.1071	2.27, 2.16, 2.95, 2.4	2.45	0.351
powder-05	0.0892, 0.1086, 0.1108, 0.1472, 0.1333	0.93, 0.88, 0.63, 0.81, 0.94	0.838	0.13
powder-06	0.1455, 0.1920, 0.1322, 0.1733, 0.1630	0.9, 0.81, 1.1, 0.92, 0.99	0.944	0.11

4. Conclusion

In this article, the PMA1000 Inert Gas Fusion-Mass Spectrograph Analyzer is used to achieve the quantitative analysis of Ar in metal materials. Self-made gas dosing equipment and standard gases with different contents are used to replace the reference material of Ar, and the calibration curve of Ar is built in the material detected through the Inert Gas Fusion-Mass Spectrograph Method. Meanwhile, for the analysis demands for titanium alloy and nano powder, corresponding analysis methods such as pulse heating and multi-element bath are established.

According the calculation method of the system blank standard deviation, the analyzed lower limit of Ar is 0.06 $\mu\text{g/g}$ in the Inert Gas Fusion-Mass Spectrograph Method, and the detected lower limit is 0.2 $\mu\text{g/g}$. In this article, the Inert Gas Fusion-Mass Spectrograph Method is used to three types of titanium alloy samples, and the analysis results are basically the same as those obtained through the traditional pulse heating thermo-conductivity method and comply with the technical theory values. Also, the Inert Gas Fusion-Mass Spectrograph Method is used to solve the problem that the traditional pulse heating thermo-conductivity method cannot be used for analyzing Ar with a super-low content, and six types of nano alloy powders are analyzed, wherein the contents of Ar are mostly less than 1 $\mu\text{g/g}$.

References:

- [1] P. Wang, X.J. Shen, S.C. Hu, et al. Inert Gas Fusion-Time-of-flight Mass Spectrograph - A Novel Analytical Instrument of Gas in Metallurgical Materials. ICASI2008 International Conference and Exhibition on Analysis & Testing of Materials, Beijing, 2008
- [2] S.C. Hu, X.J. Shen, P. Wang, Chin. Metall. Anal. 29 (2009) 34.
- [3] Y.J. Zhu, Q. Wang, X.Y. Geng. Determination of argon in metals by impulse heating thermal conductivity method. ICASI2008 International Conference and Exhibition on Analysis & Testing of Materials, Beijing, 2008.
- [4] K.S. Zhang, X.Y. Zhang. Study on calibration technique for analysis of gas in metal. Metallurgical Analysis. Vol.28, Suppl.2, 2008.
- [5] Y.J. Zhu, S. Liu, S.J. Li. Study on release of helium and hydrogen in metals by impulse-program heating method. Metallurgical Analysis. Vol.28, Suppl.2, 2008.

CORRECTION METHOD OF MASS SPECTRAL INTERFERENCE OF CO^{++} TO N^+ AND ITS APPLICATION IN SIMULTANEOUS ANALYSIS OF OXYGEN AND NITROGEN

ShenXuejing, Wang Peng, Hu Shaocheng, Yang Zhigang, Ma Hongquan, Wang Haizhou

*China Iron & Steel Research Institute Group, National Analysis Centre for Iron & Steel;
Beijing, China 100081*

Abstract:

As well known the serious mass spectral interference exists between CO^+ ($m/z = 28$) and N_2^+ ($m/z = 28$). For this reason it is not easy for inorganic mass spectrometer to analyze gaseous CO and N_2 simultaneously. Usually under this condition C^+ ($m/z = 12$) and N^+ ($m/z = 14$) are selected as the detection objects for CO and N_2 , respectively. Even so, it has been found that the interference from the double charged ion of CO, CO^{++} ($m/z = 14$) on N^+ ($m/z = 14$) will influence the measurement precision of N_2 on a certain extent. In this article a correction method for the above described interference has been established. Firstly, the linear equation between the ion intensity of CO^{++} and C^+ was established by measuring a series of CO-He standard gas mixtures with different contents on the mass spectrometer. For a gas sample which contains both of CO and N_2 , the total ion intensity at the mass peak $m/z = 14$ includes the contribution of CO^{++} and N^+ . At the same experimental condition, the former could be calculated by the above linear equation and the ion intensity of C^+ . The ion intensity produced by N^+ was easy calculated and the content of N_2 in the sample was obtained based on its calibration curve made in advance. On a self-patented pulse-heating time of flight mass spectrometric gas elements analyzer, the method has been applied to simultaneous and precise analysis of O and N in metal samples. The method also could be used for on-line analysis of CO and N_2 in industrial process gases.

Keywords: mass spectral interference; correction method; carbon monoxide; nitrogen; simultaneous analysis

Introduction

As a new analysis method for gas elements, Inert Gas Fusion-Time-of-flight Mass Spectrograph Method has been used in the analysis of O, N, H, Ar/He, with its unique superiority. In order to avoid the overlapping of the spectral peaks between CO^+ and N_2^+ , Inert Gas Fusion-Time-of-flight Mass Spectrograph Method adopts C^+ ($m/z = 12$) and N^+ ($m/z = 14$) as the detection spectral lines for the tested components of CO and N_2 , but falls into troubles during the analysis of N. The results of N in iron & steel chips and titanium alloy samples can not match the results obtained through traditional Inert Gas Fusion-Thermo-conductivity method^[3,4,5,6], which are over high. In this paper, the interference produced by CO^{++} ($m/z = 14$) at the spectral line of N^+ ($m/z = 14$) was determined. And by analysis with standard gases and pure substances, the correction method to eliminate the interference produced by CO^{++} ($m/z = 14$) at the spectral line of the N^+ ($m/z = 14$) was established.

1. Inert Gas Fusion-Time-of-Flight Mass Spectrograph Method^[1,2]

Inert Gas Fusion-Time-of-Flight Mass Spectrograph Method is a new combination technique, which combines the traditional pulse heating technique with the high precise Time-of-Flight Mass Spectrograph detection technique. The spectrograph analyzer comprises three components: sample pretreatment unit, detection unit and coupling interface between the two units. The pulse heating technique is used for fusing the samples, and then the reduction reaction is taken place between the oxides or nitrides in the sample and C in the graphite crucible, in which CO and N_2 are released from the reaction; the inert elements such as H, Ar, He emit in the form of H_2 , Ar, He. The gas mixture to be tested is led into the Time-of-Flight Mass Spectrograph detection unit through the tributary diffusion coupling interface. A trace of tested gases is sucked into the high vacuum system of the Time-of-flight Mass Spectrograph detector, and is bombarded by the electron beam in the ionization area, and transformed to the ions with the positive charge. According to the differences of m/z among the ions, the ions are separated out in the drift space without field, with the voltage signals generating on the microchannel plate, and finally the ion information with different m/z (spectral line) is obtained.

TOF-MS spectral lines are selected according to the analytical demands of the samples in Inert Gas Fusion-Time-of-flight Mass Spectrograph Method. Generally, the simultaneous detection of O, N, H and Ar need to use He as the carrier gas. The selection of spectral lines is shown in Table 1:

Table 1 TOF-MS spectral lines for O, N, H, and Ar

Elements to Be Detected	Analyzed Objects	Spectral Line (m/z)
H	H ₂	2
O	CO	12
N	N ₂	14
Ar	Ar	40

H₂⁺, C⁺, N⁺ and Ar₄₀⁺ are selected as the detection lines respectively, so as to avoid the overlapping of the CO⁺ and N₂⁺ detection lines. However, the sensitivity of the fragment ions of C⁺ and N⁺ is relatively low, and would affect the detection limits of the O and N when the content is ultralow (<10ppm), and therefore the CO₂⁺(44) can be selected as the detection line of O. Hence, after the gas mixture released from the heating furnace being filtered and dehydrated, CO is selectively oxidized into CO₂ by Schutz reagent or rare earth copper oxide and then introduced into the TOF-MS Analyzer for analysis. Thus the detection limits of O and N can be remarkably lowered by adopting molecular ion peaks as the spectral lines for 4 compositions.

2. Issues

This article tests and validates the selections and practical applications of the spectral lines by using Inert Gas Fusion-Time-of-flight Mass Spectrograph Method. The steel materials and titanium alloy materials which are common in gas analysis are used as the application objects to analyze the O, N results particularly.

2.1 Application on O & N analysis in Iron & Steel Samples

The data shown in the Table 2 are the analysis results of O, N in the steel material by adopting the Inert Gas Fusion-Time-of-flight Mass Spectrograph Method, with 6 samples in total analyzed. It can be obtained from the analysis results that the O, N analysis results from the first four samples (GSB03-1680-2004, GSB03-1065-99, GSB03-1680-2004 and GSB03-1678-2004) conform to the certified value basically. While the detection results of N from the other two samples (GSB03-1679-2004 and Sample 6#) are higher than the certificated value.

Table 2 O and N founds of iron & steel samples

Sample	Found of O (μg/g)	Average (μg/g)	Certified of O (μg/g)	Found of N (μg/g)	Average (μg/g)	Certified of N (μg/g)	O/N
GSB03-1680-2004	49.8, 46.5, 46.6	47.6	48.1	451.1, 444.4, 447.0	447.5	455.0	0.018
GSB03-1065-99	49.0, 61.9, 61.9	57.6	63.8	158.4, 160.3, 163.4	160.7	164.5	0.388
GSB03-1680-2004	76.1, 70.9, 77.1	74.7	74.0	351.7, 358.2, 357.5	355.8	351.0	0.21
GSB03-1678-2004	86.8, 87.7, 90.4	88.3	86.4	35.4, 36.0, 34.7	35.3	31.4	2.75
GSB03-1679-2004	114.0, 115.8, 117.2	115.7	111.8	35.5, 34.4, 36.4	35.4	24.3	4.6
Sample 6#	198.2, 195.5, 197.6	197.1	195.0	96.1, 99.4, 97.7	97.73	73.0	2.67

2.2 Application on O & N analysis in Titanium Samples

The data shown in the Table 3 are the analysis results of O, N in the titanium alloy material by adopting Inert Gas Fusion-Time-of-flight Mass Spectrograph Method, with 4 samples in total analyzed. It can be obtained from the analysis results that the O, N analysis results from the first three samples (LECO996, sample2#, and LECO657) conform to the certified value basically. However, the detection results of N from sample 4# are obviously high. The certificated value is 127ug/g, while the found is 238.5ug/g.

Table 3 O and N Results of titanium samples

Sample	Weight (g)	Found of O (μg/g)	Average (μg/g)	Certified of O (μg/g)	Found of N (μg/g)	Average (μg/g)	Certified of N (μg/g)	O/N
LECO 996	0.1189,0.1198	2047, 2000	2023.5	1940	376, 368	372	360	5.39
Sample 2#	0.0319, 0.0641	1410, 1305	1357.5	1190	250,249	249.5	270	4.4
LECO 657	0.1147, 0.1136	780, 824	802	970	152, 144	148	140	6.9
Sample 4#	0.0973, 0.0979	1867, 2011	1939	1990	241, 236	238.5	127	15.7

2.3 Interference Issues

From the analysis results for the iron & steel material and titanium alloy by adopting the Inert Gas Fusion-Time-of-flight Mass Spectrograph Method, the oxygen analysis results conform to the certificated value basically, while the abnormal results of nitrogen are much more, and the common characteristic of these abnormal results of nitrogen is that the oxygen content is relatively high, that is, the ratio of O, N content is great.

The reason is probably that there is other ions' interference at the N⁺ position. By analyzing the ions produced by the tested gas mixture, it is found that only the CO⁺⁺ may generate the overlapping interference at the position where m/z = 14.

Generally, the oxygen content in the iron & steel material samples is low, which is not so different from the nitrogen content, and the O/N content ratio in the samples used in this article is around 5 times, where so little deviation is produced that is difficult to be observed. While the O/N difference in the titanium alloy is much greater, which reaches 10 times, and the influence on the N is increased significantly, which almost double its content.

3. Validation of Interference between CO⁺⁺ and N₁₄⁺

3.1 NIST Standard Mass Spectrum

Fig. 1 is the NIST standard mass spectrum of CO. CO is bombarded by the electrons produced from the ion source into the fragment ions such as C₁₂⁺, C₁₄⁺, O₁₆⁺, CO⁺ etc. The abundance of each kind of fragment ions is listed in Table 3. Among the ions produced by CO, the abundance of CO⁺ is the highest, and the following is C₁₂⁺. From the mass spectrums, there indeed exists the ion interference of CO⁺⁺ at the position where m/z = 14. But the abundance of CO⁺⁺ is very small, only 7 while C₁₂⁺ is 88.

Fig. 2 is the NIST standard mass spectrum of N₂. The N₂ is bombarded into the fragment ions such as N₁₄⁺, N₂⁺ etc. In Table 3 the abundance of each kind of fragment ions is listed, the abundance of N₂⁺ produced by N₂ is the highest, and the following is N₁₄⁺.

As can be gathered from the two mass spectrums, selecting the low sensitivity fragment ions of C₁₂⁺ and N₁₄⁺ as the analysis spectral lines is practical in theory. And there is interference between CO⁺⁺ and N₁₄⁺

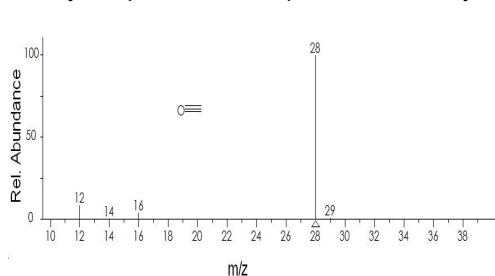


Fig. 1 Mass spectrum of CO

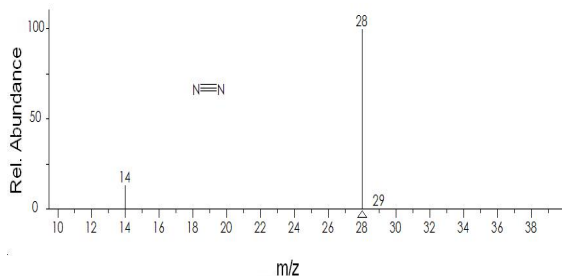


Fig. 2 Mass spectrum of N₂

Table 3 Masses and abundances of CO spectrum

Masses	12	14	16	28	29
Abundances	88	7	44	999	11

Table 4 Masses and abundances of N₂ spectrum

Masses	14	28	29
Abundances	137	999	7

3.2 Experiments

Pure oxide is adopted to validate the interference. It is considered that there is no N in pure oxide. So it is analyzed and the signal changing at $m/z=14$ is observed to inspect the interference of CO^{++} .

Fig. 3 shows the mass spectrum collected by mass spectrum detector when only the carrier gas exists before performing the sample determination, and there are no obvious signal peaks at the position $m/z = 12$ and $m/z = 14$, which means that the blank values on these two positions are stable and very low against the background of carrier gas.

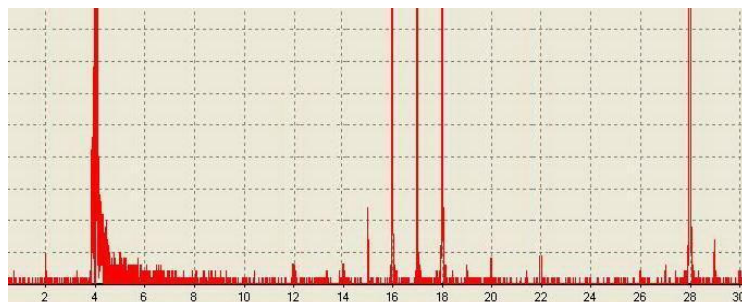


Fig. 3 Baseline of TOF using He as carrier

Fig. 4 is the mass spectrum collected by the mass spectrum director when the pure substance W_2O_3 is analyzed. It can be read from the figure that there are obvious signals at the positions where $m/z = 12$ and $m/z = 14$. It means that the double charged fragment ions produce the interference signals at the position where $m/z = 14$.

In order to validate the conclusion, the catalyst furnace is added into the system, which would oxidize CO released from fusion into CO_2 through the rear earth copper oxide. And the mass spectrum detected after CO oxidized into CO_2 is shown in Fig. 5. There are obvious signals at the position where $m/z = 12$ and $m/z=44$, and no signals at the position where $m/z = 14$ can be got. The signal intensity at the position where $m/z = 44$ is the greatest. It means that there are no other fragment ions producing interference signals at the position where $m/z = 14$ after CO is converted into CO_2 .

These two tests above can validate that in the case of using N_{14}^+ as the spectral line to analyze N, the higher analysis results are caused by the interference of CO double fragment ions at the position of $m/z=14$.

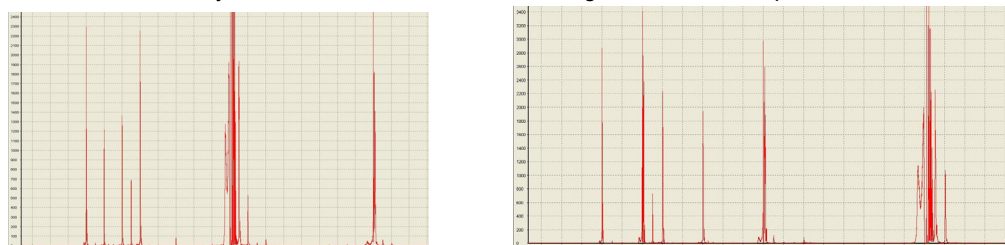


Fig. 4,5 Spectrum of W_2O_3 without & with catalyst Furnace

4. Establishing the Mathematical Model for Interference Correction of CO^{++} at the Position Where $m/z = 14$

4.1 Instruments

PMA1000 Inert Gas Fusion-Time-of-flight Mass Spectrograph Analyzer

Standard gases (0.1% CO+He, 0.2% CO+He, 0.4% CO+He, 0.8% CO+He, 1.6% CO+He)

Gas dosing equipment

4.2 Experimental Method

Inject the standard gas of certain concentration for 1min each time, and average the number of the collected fragment ions C_{12}^+ and CO^{++} .

4.3 Results

Table 6 lists the signals produced by the C_{12}^+ and CO^{++} fragment ions, which are generated from the standard gases with different contents at the positions where $m/z = 12$ and $m/z = 14$.

Table 6 C₁₂⁺ and CO⁺⁺ ions collected from standard gases with different contents

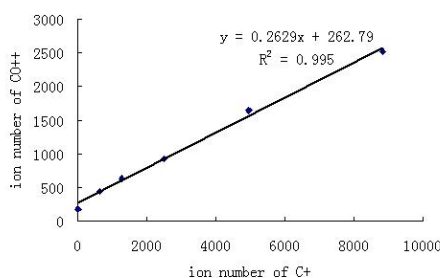
Standard gas content (V/V)	C ₁₂ ⁺	CO ⁺⁺
0.0%	18	182
0.1%	641	445
0.2%	1283	634
0.4%	2508	931
0.8%	4954	1650
1.6%	8819	2525

4.4 Establishing the Mathematical Model for Removing Interference

After the molecules of CO being ionized, there exists constant proportion correlation among the intensities for each fragment ion peaks in theory. According to the average number of the fragment ions C₁₂⁺ and CO⁺⁺ from standard gases, the corresponding mathematical relationship between them was studied and shown in Fig. 6. There exists the linear relationship between ion numbers of C₁₂⁺ and CO⁺⁺. The linearization function is got in formula (1).

$$y = 0.2628x + 262.83 \quad (1)$$

The linear related coefficient is 0.995. According to this mathematical model, the interference of CO⁺⁺ to N₁₄⁺ can be obtained indirectly from C₁₂⁺, and thus the interference can be corrected through the mathematical method to obtain the accurate measurement of N.

Fig. 6 Correlation between C₁₂⁺ and CO⁺⁺

5. Applications of the Interference Correction Method

5.1 Establishment of Calibration Curve of N

Simultaneous analysis on O and N is tested using high purity helium as the carrier gas, recording the ions data of C⁺ (m/z = 12), N⁺ (m/z = 14). By using the interference correction equation developed in section 4.4, and according to the ion information of C⁺ (m/z = 12), the interference of the fragment ions CO⁺⁺ to N⁺ could be obtained, and thus the accurate information of N⁺ (m/z = 14) could be obtained.

YSB C 11931-2007 (0.0084% N), YSB C 11930-2007 (0.0055% N), GSB 03-1678-2004 (0.0032% N), GSB 03-1679-2004 (0.0025% N), and AR1648 LOT#061501 (0.0073% N) were analyzed, and the analysis results are shown in table 7. Results of N with interference of CO⁺⁺ are much higher than those after correction.

Table 7 Results of N for calibration curve

Sample	Certified of N (μg/g)	Found of N (μg/g) (with interference)	Found of N (μg/g) (without interference)
YSB C 11931-2007	84	104.65, 105.29	83.47, 83.23
YSB C 11930-2007	55	86.63, 87.51	53.58, 52.36
GSB 03-1678-2004	32	50.12, 51.14	32.86, 33.89
GSB 03-1679-2004	25	49.27, 50.16	27.72, 27.91
AR1648 LOT#061501	73	108.83, 109.21	73.83, 74.27

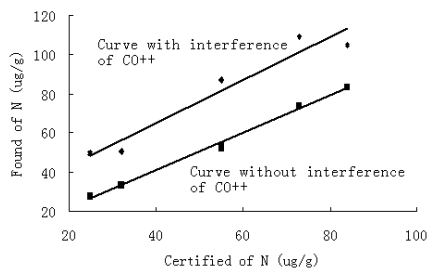


Fig. 7 Calibration curve of N

The calibration curve of N was drawn according to the data of Table 7 which is shown in Fig. 7. There are two lines in fig.7. The upper line is drawn based on the data with CO⁺⁺ interference, while the lower line is drawn according to the data after interference correction. As can be seen, after correction the interference of fragment ion CO⁺⁺ on N⁺ could be removed and the data points deviated from the calibration curve could be pulled back to the curve. Both the linearization and the disperse become better after the interference correction. And thus the accurate quantity analysis of N using N⁺ spectral lines can be obtained.

5.2 Interference Correction Method used in O&N Analysis of Standard Gases and Pure Oxides

Using the interference correction method developed in section 4.4 to remove the interference of CO⁺⁺ to N⁺, tests are carried out on the standard gases, pure oxides and iron & steel samples respectively. Releasing plots of C⁺ and N⁺ got from CO standard gas (the background is He) and pure oxide are drawn in Fig.8 and Fig.9. Fig. 8-1 shows the plots of standard gas without interference correction and Fig. 8-2 shows the plots after correction. Under these two conditions, the plots of C⁺ have no changes, while the plot of N⁺ in Fig.8-2 turns to zero after removal. Similarly, effects of interference correction on the analysis of WO₃ are compared in Fig. 9-1 and Fig. 9-2. From the plots, it is confirmed that the interference correction method really acts and removes the ion interference from N⁺.

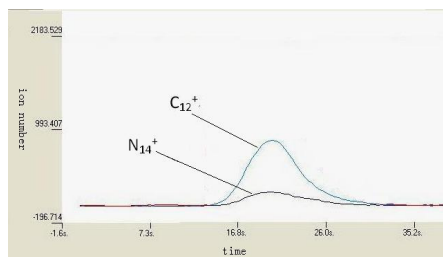


Fig. 8-1 Plots of standard gas with interference

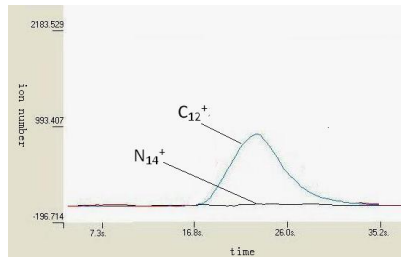


Fig. 8-2 Plots of standard gas without interference

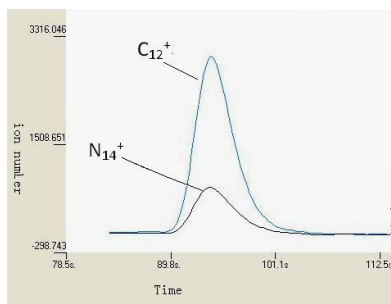


Fig. 9-1 Plots of WO₃ with interference

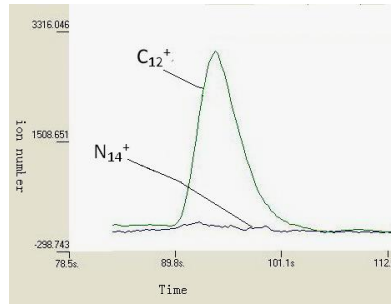


Fig. 9-2 Plots of WO₃ without interference

5.3 Interference Correction method used in O&N Analysis of Iron & Steel Samples

The analysis results of nitrogen in chips are always over high before interference correction, and different from the results in pins. Fig. 10 is the difference between N calibration curves based on chips and pins without correction, the rates of slope are significantly different. According to the conclusion in this article, this phenomenon is caused by the introduced CO⁺⁺ interference to the results of N⁺, due to the high oxygen content in chips. Determine N in chips by using the interference correction method, with the results shown in Table 8. Analyze N in

pins with the same method, with the results shown in Table 9. Fig. 11 is the calibration curve of N based on chips and pins with correction. The results of the two groups of samples are on the same line, with the correlation coefficient of 0.9978, which means that the CO⁺⁺ interference to the results of N⁺ is removed after interference correction.

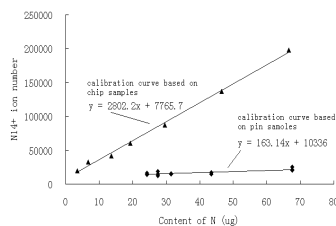


Fig. 10 Difference between N Calibration Curves Based on Chips and Pins without Correction

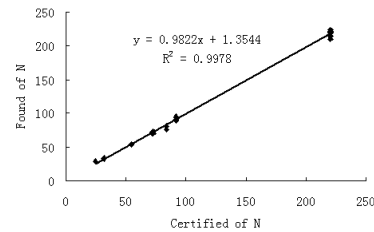


Fig. 11 N Calibration Curves Based on Chips and Pins with Correction

Table 8 N results of chips without interference of CO⁺⁺

Sample	Found of O(µg/g)	Certified of N (µg/g)	Found of N(µg/g)
Chips N72	1489.29, 1251.23, 1233.02,	72	71.34, 71.10, 70.76, 73.32,
	1402.67, 1291.21, 1203.47		71.92, 71.10
Chips N92	984.95, 899.84, 784.14,	92	95.95, 89.38, 93.83, 90.62,
	706.79, 1084.73, 817.22		94.44, 92.23
Chips N220	217.15, 185.19, 267.18,	220	218.38, 221.35, 215.06, 231.37,
	347.34, 190.79, 190.20, 193.72		210.01, 223.90, 215.43

Table 9 N results of Pins with/without Interference of CO⁺⁺

Sample	Weight(g)	Found of N (µg/g) (with interference)	Found of N (µg/g) (without interference)	Certified of N (µg/g)
Blank Value	1.0000g	0.01,0.31	0.01,0.25	0
O 112 N 84	0.5000g	104.65,103.29	81.38,80.27	84
O 197 N 55	0.5000g	86.63, 87.51	54.58, 53.91	55
O 88 N 32	0.9820g	50.12, 51.14	33.3, 34.25	32
O 115 N 25	0.9720g	49.27, 50.16	28.95, 29.6	25
O 195 N 73	1.0000g	104.83, 109.21	70.23, 73.85	73

5.4 Interference Correction method used in O&N Analysis of Titanium Alloy Samples

As to the problems in the N analysis of titanium alloy samples, O, N in the titanium alloy samples are analyzed again using the interference correction method. Results are shown in Table 10. After interference correction, the analysis results of nitrogen in the titanium alloy samples are in conformity with the certificated value.

Table 10 O and N Results of Titanium Alloy Samples after Correction

Sample	Certified of O (µg/g)	Found of O (µg/g)	Certified of N (µg/g)	Found of N (µg/g)
Titanium1#	1190	1261, 1438, 1221	270	284, 288, 276
Titanium 2#	1990	1958, 1972, 1919	127	121, 126, 120

6. Conclusion

The applications of Inert Gas Fusion-Time-of-flight Mass Spectrograph Method in simultaneous O, N analysis were carried out by analyzing iron & steel samples and titanium samples. The results of N in the chips of iron & steel and the titanium alloy samples are over high. Spectral lines selected in Inert Gas Fusion-Time-of-flight Mass Spectrograph Method are studied. In order to avoid the overlapping of the peaks between CO⁺ and N₂⁺, Inert Gas Fusion-Time-of-flight Mass Spectrograph Method adopts C⁺ (m/z = 12) and N⁺ (m/z = 14) as the detection spectral lines for the tested components of CO and N₂, while falls into troubles of the interference of CO⁺⁺ on N⁺. By analyzing pins of iron & steel, the interference effect on N is small and can be forget. But when the ratio of O/N is higher than 5, the interference is obvious. Through the tests of standard gases (CO+He) and pure oxides, CO⁺⁺

($m/z = 14$) produced interference on the peak of N^+ ($m/z = 14$) is validated, that is, the signals obtained from the peak ($m/z = 14$) is consisted of two kinds of ions, CO^{++} and N^+ .

The correction method for removing the interference produced by CO^{++} ($m/z = 14$) on the peak of N^+ ($m/z = 14$) is established:

- (1) the linear relationship between C^+ ($m/z = 12$) and CO^{++} ($m/z = 14$) is established by standard gases with different CO concentration.
- (2) According to the ion information of C^+ obtained during the sample analysis, the interference intensity of CO^{++} can be calculated through the linear relationship.
- (3) Remove the interference intensity of CO^{++} from the ions intensity obtained at the spectral line $m/z = 14$, then get the accurate N^+ ion intensity information.

Tests on the iron & steel samples and titanium alloy samples are conducted by using the interference correction method above. Results illustrate that the correction method developed in this article solve the problems in N analysis by Inert Gas Fusion-Time-of-flight Mass Spectrograph Method, and is capable to get the accurate results of N content. This method is also available in the industrial online analysis of CO and N_2 .

References

- [1] P. Wang, X.J. Shen, S.C. Hu, et al. Inert Gas Fusion--Time-of-flight Mass Spectrograph-A Novel Analytical Instrument of Gas in Metallurgical Materials. ICASI2008 International Conference and Exhibition on Analysis & Testing of Materials, Beijing, 2008
- [2] S.C. Hu, X.J. Shen, P. Wang, Chin. Metall. Anal. 29 (2009) 34.
- [3] ASTM E 1409. Standard Test Method for Determination of Oxygen and Nitrogen in Titanium and Titanium Alloys by the Inert Gas Fusion Technique.
- [4] GB/T 11261-2006. Steel and Iron - Determination of oxygen content - The pulse heating inert gas fusion-infra-red absorption method.
- [5] GB/T 223.82-2007. Steel and iron-Determination of hydrogen content-Inert gas impulse fusion heat conductivity method.
- [6] ASTM E 1019. Standard Test Methods for Determination of Carbon, Sulfur, Nitrogen and Oxygen in Steel and in Iron, Nickel, and Cobalt Alloys.

ORIGINAL POSITION STATISTIC DISTRIBUTION ANALYSIS BY LASER INDUCED BREAKDOWN SPECTROSCOPY

CHEN Ji-wen, ZHAO Lei, YAO Ning-juan, HAN Peng-cheng, YUAN Liang-jing, CHEN Yong-yan,
QU Huayang, WANG Hai-zhou

China Iron & Steel Research Institute Group, National Analysis Centre for Iron & Steel, Beijing 100081, China

Abstract:

With Laser-induced breakdown spectroscopy (LIBS), there is no need to prepare samples and a non-contacting analysis is used for materials over sample surfaces. In this paper, LIBS-OPA, a new method and instrument, was developed to characterize the original statistic distribution in non-flat and irregular-shaped materials. Irradiation from a Nd-YAG laser was focused on the sample and therefore induced plasma spectrum. Then, the LIBS-OPA statistical distribution analysis was carried out combining with a movable excitation platform under the protection of Ar. Based on unusual spectrum signals of multi-element by laser induced breakdown spectroscopy, quantitative and statistical information about original position in fracture sample and welding seam were collected, representing position distribution, degree of statistic segregation and maximum degree of segregation for every material element. The results of depth and defect parts for the galvanized sheet obtained by LIBS-OPA were consistent with those by glow discharge optical emission spectrometry (GD-OES) and scanning electrical microscopy (SEM), showing that LIBS-OPA could be used to analyze depth profile and distinguish origin of defect for coated sheets. With these analyses and results, LIBS-OPA was proved a technique offering performance and quality criteria for research of new materials and technics.

Key words: Original statistic distribution analysis; Laser Induced breakdown spectroscopy; Irregular-shaped metallurgical materials; Galvanized sheet

Laser is the invention of great significance in 20th century and a kind of newly arisen means for material composition analysis[1]. Its principle based on a kind of coherent ray radiation produced, which is stimulated emission and enlarged. Laser has the high brightness, wonderful monochromaticity and coherence. Original position statistic distribution analysis by the laser induce breakdown spectroscopy (LIBS-OPA) has not only the advantage of non-contact measurement, micro probe analysis and depth analysis for LIBS, but also the original position character of original position statistic distribution analysis technique. It could do any point scanning, linear dimension scanning, one-dimensional depth scanning and two-dimensional area scanning. With these advantages, laser is now used to achieve accurate localization and analysis on sample surfaces.

The fracture is a couple of mutually matched breaking surface and external appearance acquired after the metal broken and always occurs at the weakest place in metal organization which records a lot of valuable information during the whole breaking process. Therefore, fracture has been attached great importance in cracking research. Welding defect is the flaw that does not accord with the request of design and craft at the welding junction during the process of welding. Such defects primarily include longitudinal cracking, porosity, undercutting, incomplete penetration, incomplete fusion, slag inclusion, weld beading and inclusion, etc. The component statistic distribution should be done with the elements at the fracture and welding place by LIBS-OPA, offering criteria for fracture analysis and improvement of the welding craft.

During the steelmaking procedure, the defects on steel rolling board can reduce the quality of steel product. Therefore, it is extremely important to confirm origin of defects to instruct craft of steel production. Compared with the traditional test, such as EPMA, a time-consuming method while preparing samples, LIBS is considered an effective method in analyzing steel defects.

1 Experiment

LIBS-OPA developed in this research used high-energy Nd-YAG pulsed laser (Continuum SureliteIII-10, 12ns pulsed widths, 10Hz repetitive frequency) as radiation source. When the laser was focused on samples, the plasma spectrum was produced through the lens. Its pulsed energy was 300mJ/pulse and wavelength was 1064nm. The emitted atomic spectrum signal was dispersive by the polychromator with focus distance of 750mm, then the instant spectrum signal was recorded by photomultipliers and quantitative analysis was completed by emitted spectrum intensities. The original statistic distribution analysis had been done when the sample was set on the two-dimensional moving stand protected with argon. Based on the design of this new instrument, the author analyzed fracture sample, the surface component distribution of welding metal, the surface component depth distribution of coated sample and component difference between normal part and defect part on galvanized sheet. Analytical lines selected were listed in Table1.

元素 Element	波长 λ (nm)
C	193.1
Si	212.4
Cr	266.7
Ni	231.6
Al	396.1
Ca	393.3
Na	588.9
Zn	334.5
Fe	273.0

2 Results and discussion

2.1 Original position statistic distribution analysis by LIBS on welding sample

Fig.1 illustrated a welding sample used by LIBS-OPA. The position of every spark point was set previously by program through laser configuration. Every point should be focused anew to ensure every spark point was on the focus point. Spark surface pattern of the sample was remade through position and focus value of every spark points corresponding to their surface depth coordinate.

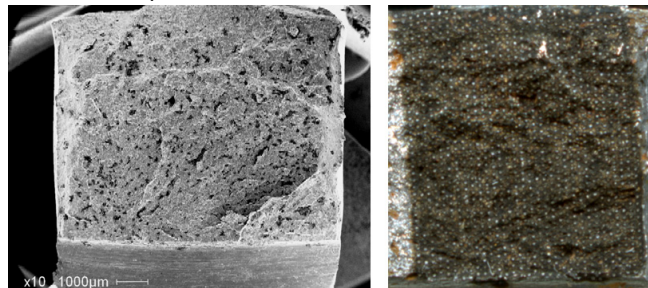


Fig. 1 Fracture samples used in LIBS-OPA experiment

At the same time three-dimensional graph and two-dimensional contour map were obtained and degree of statistic segregation of every element was counted. Figure 2 described three-dimensional view and segregation degree of Aluminum.

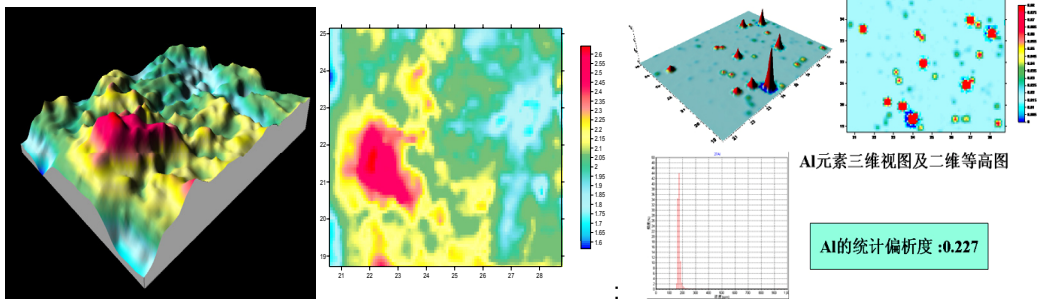


Fig. 2 Analysis results of fracture samples by LIBS-OPA method

2.2 Chemical constitution distribution analysis of welding metal

Both Figure 3 and Figure 4 gave component distribution of Cr and Ni in welding samples. The three- and two-dimensional section drawings of component distribution clearly described variance of Cr and Ni at different positions of welding seam (including base materials, weld junction and heat-affected zone), which offered foundation for improving welding technique and quality.

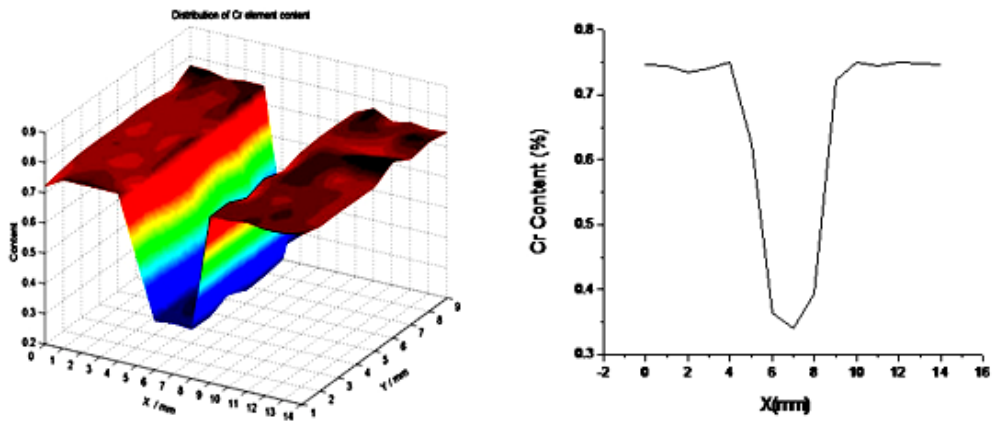


Fig.3 Cr analysis results of welding sample by laser-OPA method

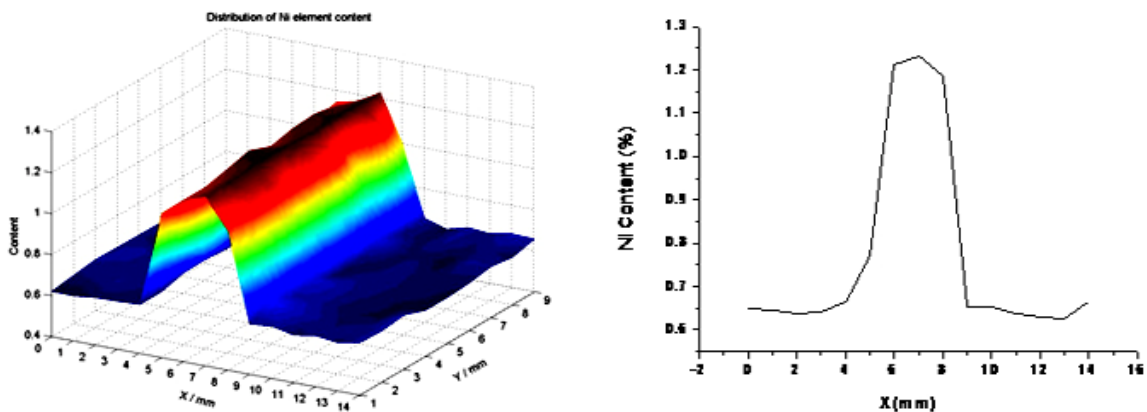


Fig. 4 Ni analysis results of welding sample by laser-OPA method

2.3 The surface component depth distribution of coated sample

The galvanized sheet is a type of thin steel plate that is coated by a layer of zinc on the surface, which can prevent the steel surface from being corroded and extend its service life. It has been, widely used for the household appliance industry and auto industry. At present, it is usually used by glow discharged spectrometry (GDS) to analyze the coated-film of galvanized sheet. However, the ablative point is quite big and the sample is damaged badly. Moreover, the sample has to be fixed on the spark stand. By using LIBS, samples are damaged slightly at micrometer level and the high powerful laser acts on the surface of material non-contact while using LIBS. The galvanized sheet was tested by GDS and LIBS individually and the results showed in Fig.5.

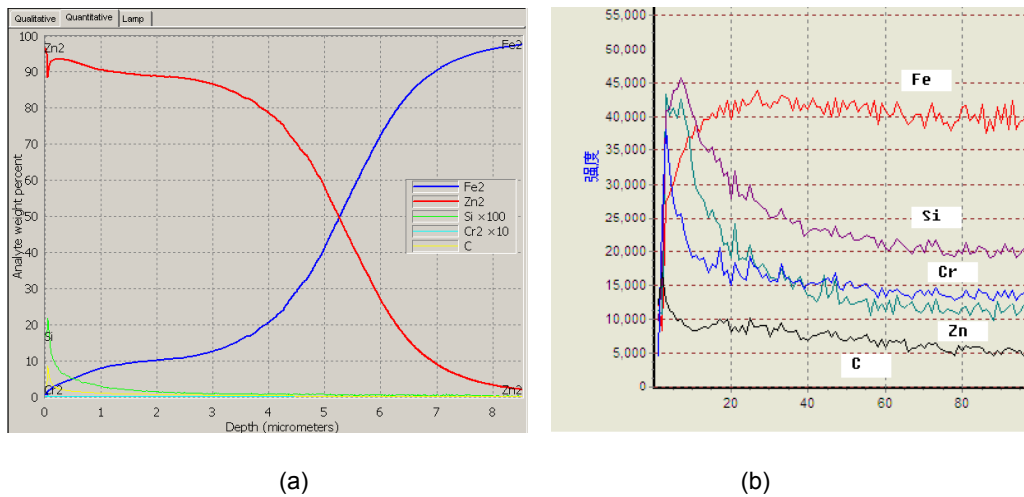


Fig.5 Contrast of results of galvanized sheet by GDS and LIBS
(a) GDS (b) LIBS

The results of galvanized sheet by GDS were showed in Fig.5-a. With the coating was stripped, zinc contained in the surface was reduced continuously and transited to matrix of Fe, in which contents of two foreign elements, C and Si, varied from being low to high and then backed to low level again. This result coincided with the ones tested by LIBS (Fig.5-b).

2.4 Defect Analysis of galvanized sheet

Fig.6 gave a galvanized sheet, showing a apparent banding defect on the surface. Using the method of depth distribution analysis, the variety of the intensities following the change of the pulse number on the defect part of the sample indicated the relation between element content and depth. Comparing the normal part to the defect part, the difference of element content on the surface and in the depth direction was ascertained and the type of defect was therefore determined.

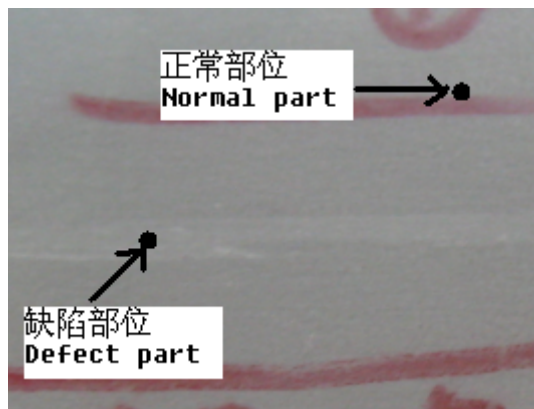
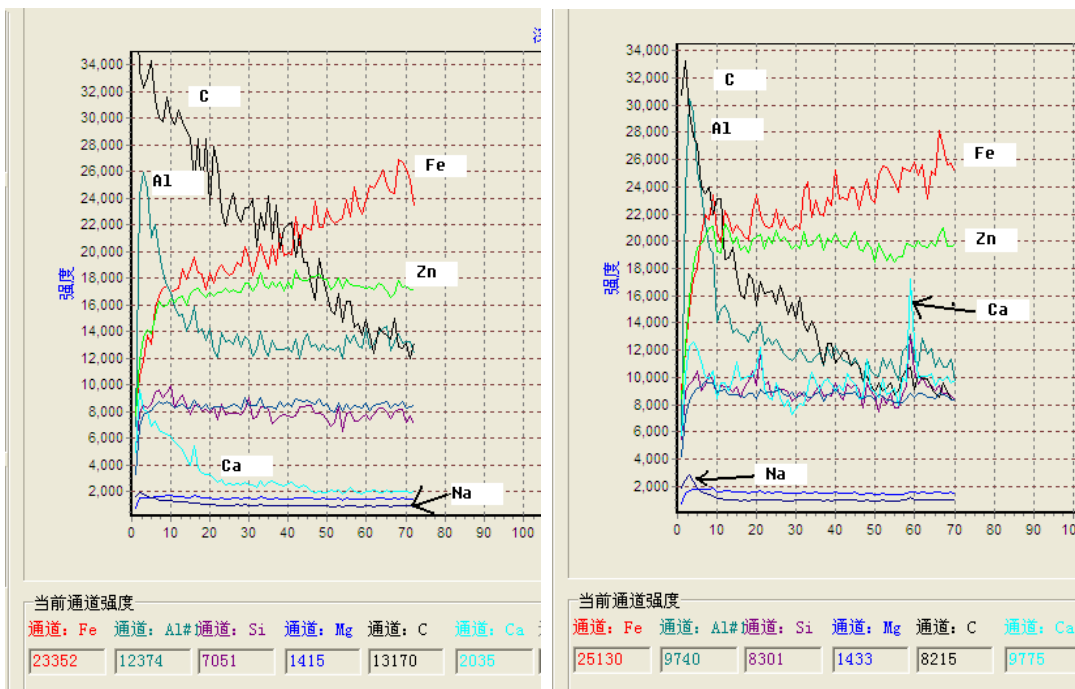


Fig.6 Sample with defect

As shown in Fig.7, the contents of Ca and Al on the defective part were distinctly higher than those on the

normal part. Also, contents of Si and Na on the defective part were observed little higher than those on the normal part. The defect was so considered a kind of protecting slag.



(a) (b)

Fig.7 Depth analysis by LIBS for galvanized sheet

a. Normal part b. Defective part

Fig.8 described results of the galvanized sheet contrasting of defective part and normal part in the depth direction tested by GDS. It showed that the content of C on the normal part was much higher than that on the defective part, while both the contents of Fe and Si were lower, which consisted with the ones tested by LIBS.

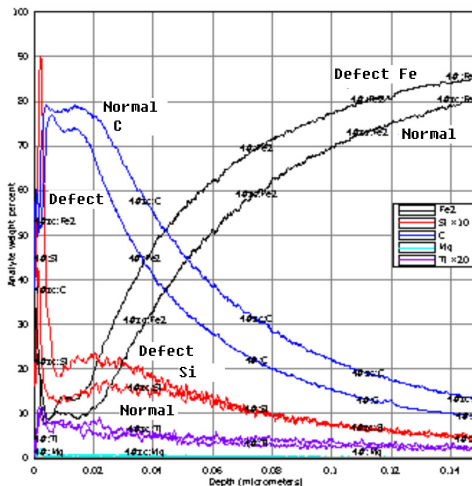


Fig.8 Contrast of defective part and normal part by GDS for galvanized sheet

Fig.9 and Fig.10 showed results of the galvanized sheet tested by SEM on the normal part and the defect part respectively. The analytical results indicated that there Si and Ca significantly existed on the defective part, which consisted with the ones that obtained by LIBS.

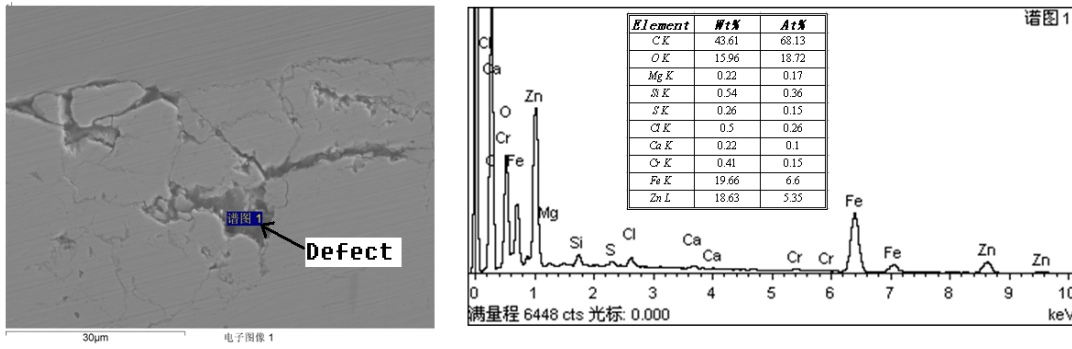


Fig.9 Results of defective part by SEM

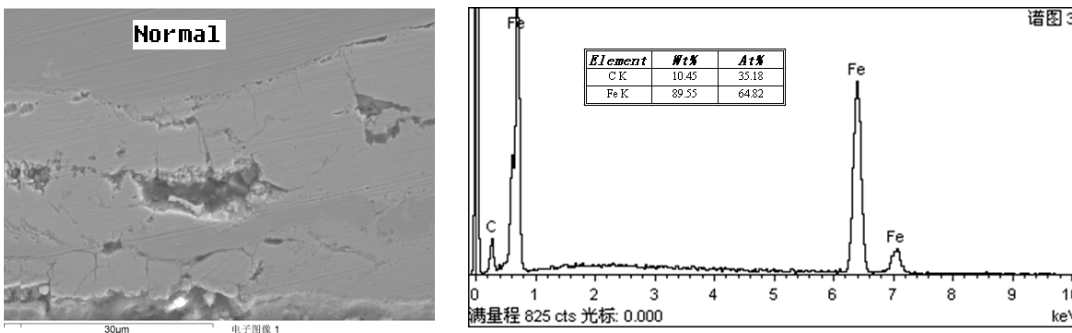


Fig.10 Results of normal part by SEM

3 Conclusions

In this research, LIBP-OPA reflected component distribution in fracture and welding samples well. Plus, with advantages of non-contacting measurement and slight damage to the sample, LIBP-OPA was expected to embrace bright development in coating analysis.. The difference of content on the normal part and defect part could be showed rapidly by LIBS-OPA and the origin of the defect could be decided by the variety of content of elements or associated varying trend of several elements. In summary, it is confirmed that LIBS-OPA would be critical to upgrading quality and output of metallurgic products.

Reference

[1] D.Romero and J.J. Laserna.Surface and tomographic distribution of carbon impurities in photonic-grade silicon using laser-induced breakdown spectrometry[J].J. Anal. At. Spectrom,1998,13,557-560

ToF-SIMS ANALYSIS OF ANTICORROSION ADDITIVES ON TECHNICAL SURFACES

D. Poerschke^{1*}, S. Janssen¹

¹ThyssenKrupp Steel Europe AG FuE C-O, Eberhardstr. 12 44145 Dortmund

*Corresponding author: David.Poerschke@thyssenkrupp.com

Secondary ion mass spectrometry is used to characterize anticorrosion additives like triazoles on technical surfaces. To define the initial state of selected technical surfaces like electrolytically zinc coated steel and uncoated steel, these samples have been characterized with ToF-SIMS after cleaning with a technical alkaline product. In a second step triazoles have been prepared as self assembling monolayer on similar cleaned technical surfaces and characterized as well. It was found out, how most triazoles chemically bind to uncoated steel and electrolytic zinc coated steel. Additionally a method could be established to check the chemical reactivity of anticorrosion additives on technical surfaces.

In development of new coatings and steel surfaces it is important to ensure corrosion protection during delivery to and storage at the automotive customer. Usually common corrosion protection oils are used to prevent surfaces temporarily. However in some cases conventional corrosion protection oils were insufficient on newly developed metallic surfaces. The development of new concepts for corrosion protection oils by trial and error failed. So it is necessary to understand how corrosion protection oils react with technical surfaces like zinc coatings, to be able to find new specific and efficient corrosion protection concepts.

Corrosion protection oils are normally mixtures of mineral oil and additives. The mineral oil base acts as a barrier against humidity and other environmental influences. The additives form an additional interface layer by adhesively bonding to the metallic surface. In order to properly understand the mechanisms of corrosion protection, we do have to analyse individual components of these complex oils. Especially important for the performance of oil are the anticorrosion additives. In addition to the prevalent sulfonates, triazoles are an important class of anticorrosion additives which are used in aqueous and oily process media especially for corrosion protection of non-ferrous metals. Three different triazoles, labelled with Irgamet 30™, Irgamet 34™ and Irgamet 39™ are prepared as self assembling monolayer on electrolytic zinc coating and uncoated steel to analyse them with ToF-SIMS.

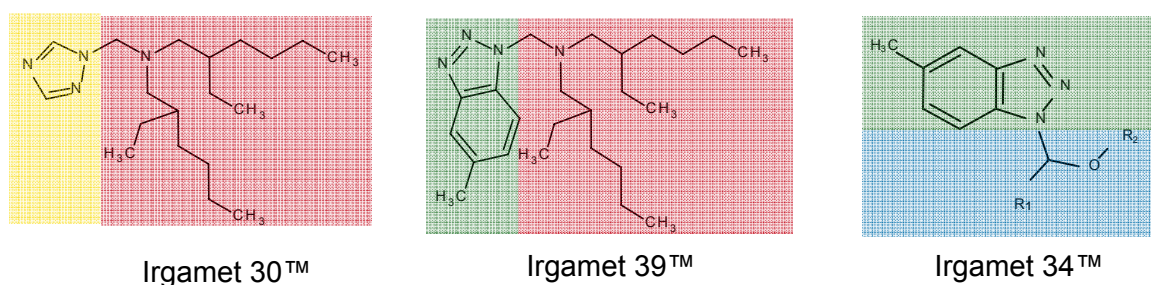


Figure 1: chemical structure of three analysed triazoles; distribution by BASF (former CIBA Specialty Chemicals) [1, 2]

The three triazoles Irgamet 30™, Irgamet 34™ and Irgamet 39™ are shown in Figure 1. The chemical structure of them can be separated in two parts, the principal basis structure and the side chain. The principal basis structure is supposed to be the surface active component and the side chain is held responsible for the solubility of the additive in different process media. The principal basis structure of triazole Irgamet 30™ (in Figure 1 yellow coloured) is a five ring compound with three nitrogen- and two carbon-atoms. The side chain (in Figure 1 red coloured) is non-polar and therefore suitable for oily process media. The triazole Irgamet 39™ has the same side chain like Irgamet 30™ and is also applicable in oily process media. The principle basis structure of Irgamet 39™

(in Figure 1 green coloured) is tolyltriazole, known as a good anticorrosion additive for copper [1]. The triazole Irgamet 34™ has the same principal basis structure as Irgamet 39™, but its side chain (in Figure 1 blue coloured) is more polar so for this reason its better adaptable to aqueous process media.

The experiments were performed with an ION-TOF GmbH (Münster, Germany) ToF-SIMS 5.spectrometer equipped with Bi-liquid metal ion gun generating a focused 25keVBi₃⁺- ion beam (radial dimension 1-2µm diameter) of about 0,4pA in high current-bunched mode. The feasibility of imaging the local molecular dispersion on scanned areas (256pixelx256pixel) image data were taken by mapping a field of view of about 400µmx400µm. The acquisition time has been about 200s at a repetition rate of 10 kHz in random raster mode to prevent charging. The total static primary ion dosage is about 3x10¹¹cm⁻² and is for that reason under the static limit. [3] For getting a statistically relevant statement on each sample, minimum 5 measurements at different places should be conducted. Mass spectra in both polarities were taken from 0.5m/z to 800m/z and calibrated on well known mass peaks like hydrogen, carbon and zinc. The spectra are analysed with SurfaceLab 6 Software from ION-TOF GmbH (Münster, Germany).

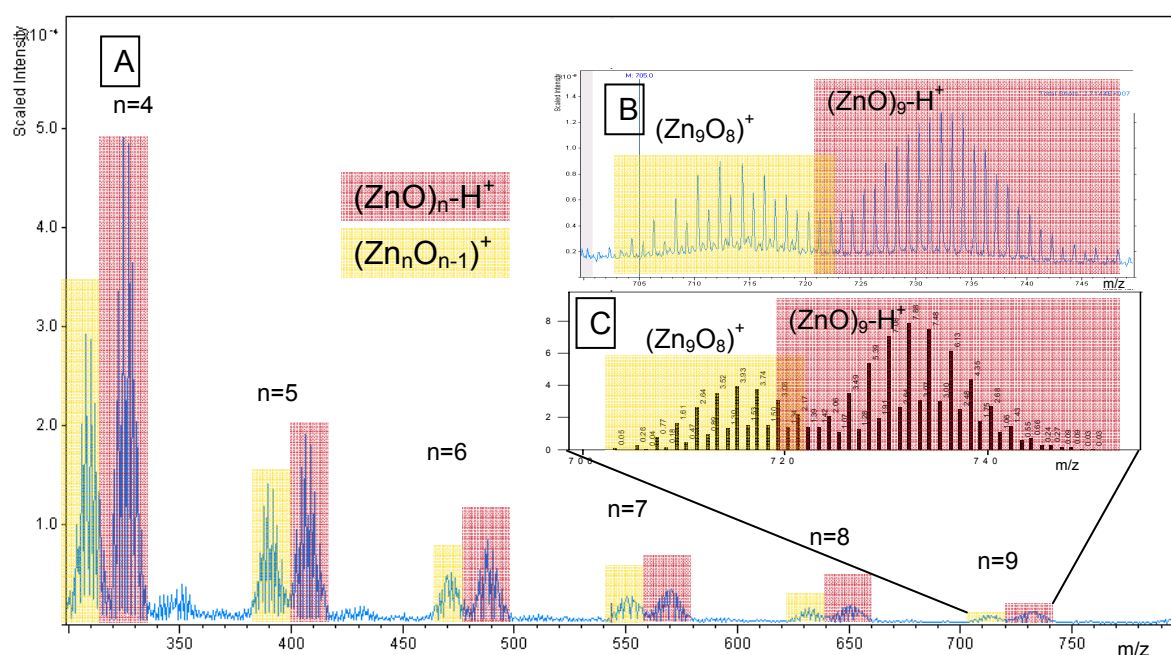


Figure 2: A ToF-SIMS positive spectrum (m/z 300-800), of electric zinc surface showing $(Zn_nO_{n-1})^+$ - (yellow coloured) and $(ZnO)_nH^+$ -cluster (red coloured) n=4-10; **B** Cut-out of A showing $(Zn_9O_8)^+$ -and $(ZnO)_9H^+$ -cluster; **C** Theoretical pattern of $(Zn_9O_8)^+$ - and $(ZnO)_9H^+$ -cluster in ratio of 0.5 to 1.0.calculated with SurfaceLab 6.

In a first step technical surfaces have been cleaned with an alkaline cleaner like Ridoline C72™, which is a NaOH based product from Henkel AG&Co. KGaA [4]. After that alkaline bath the surfaces have been rinsed with distilled water to reduce the alkaline residue. The cleaned samples, zinc coated steel and uncoated steel, were measured with ToF-SIMS measuring parameters as described above to define the initial state. In the mass spectra in both polarities several clusters were detected. In the ToF-SIMS mass spectra measured from the technical electrolytic zinc surface $(Zn_nO_{n-1})^+$, $(ZnO)_n^+$, $(ZnO)_nH^+$ & $(ZnO)_nOH^-$ cluster till n=9 are significant (Figure 2). By intensity comparison the protonated $(ZnO)_nH^+$ -cluster are more dominant as the unprotonated $(ZnO)_n^+$ -cluster. On the uncoated steel surface $(FeO)_n^+$ & $(FeO)_nO^-$ -cluster till n=8 has been detected. These clusters are identified by there characteristic pattern. Zinc-oxide-cluster-pattern is dominated by three (⁶⁴Zn, ⁶⁶Zn, ⁶⁸Zn) of five stable atomic zinc isotopes (⁶⁴Zn 48,268%; ⁶⁶Zn 27,975%; ⁶⁷Zn 4,102%; ⁶⁸Zn 19,024%; ⁷⁰Zn 0,631%) [5] and as well iron-oxide-cluster-pattern is dominated by three ⁵⁴Fe, ⁵⁶Fe, ⁵⁷Fe of four stable atomic iron isotopes (⁵⁴Fe 5,845%; ⁵⁶Fe 91,754%; ⁵⁷Fe 2,119%; ⁵⁸Fe 0,282%) [5]. The oxygen- and hydrogen-atoms of the protonated metal-oxide-

clusters influenced slightly the ratio of the peaks, due to the fact that atomic oxygen and hydrogen are nearly mono isotopic (^{16}O 99,757%, ^{17}O 0,038%, ^{18}O 0,205%; ^1H 99,985%, ^2H 0,015%) [5]. For identification of bigger molecule-cluster it can be helpful to calculate the isotope-pattern of these molecule clusters and then compare these theoretical values to measured signals. As an example $(\text{Zn}_9\text{O}_8)^+$ and $(\text{ZnO})_9\text{-H}^+$ (Figure 2 C) in ratio of 0.5 for $(\text{Zn}_9\text{O}_8)^+$ to 1.0 for $(\text{ZnO})_9\text{-H}^+$ has been calculated with the SurfaceLab6 analyzing software. As shown in Figure 2 B, the calculated pattern looks nearly similar to the measured mass spectra, but within the intensity distribution not negligible differences are shown, which are caused by the unprotonated $(\text{ZnO})_9^+$ -cluster. Due to the fact that these metal-mono-oxide-clusters are significant for both surfaces especially up to the high mass range (up to 300u), according to K. Wittmaak [9] we assume the FeO-stoichiometry on uncoated Steel and ZnO-stoichiometry on electrolytic Zinc

In the second step to study the binding of the triazoles to the surface of uncoated steel and electrozinc coated steel the three different triazoles are prepared on similarly cleaned samples. For that purpose the triazoles Irgamet 30™ and Irgamet 39™ were solved in n-hexane and Irgamet 34™ in isopropanol. The sample sheets are dipped in the bath of the triazole solution, dried at room temperature and rinsed with the corresponding solvent to remove surplus solution. The resulting ToF-SIMS mass spectra from the triazole wetted samples are compared to the ToF-SIMS spectra of the samples which were not treated with triazoles to identify significant signals of triazole and polymorphic triazole fragments. The identification of the main triazole fragments of Irgamet 30™, Irgamet 39™ and Irgamet 34™, can be done by analysing the differences in the intensities at the significant nominal masses of the respective ToF-SIMS mass spectra.

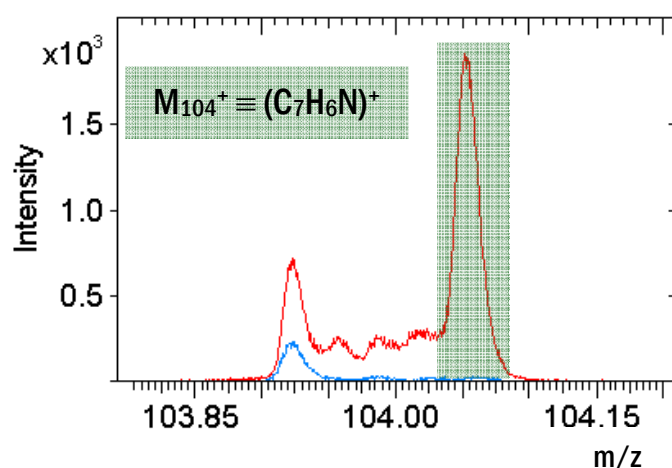


Figure 3: significant fragment of the triazoles Irgamet 39™ and Irgamet 34™ (green coloured), blue line: mass spectrum of a cleaned electric zinc surface without triazole coating, red line: mass spectrum of an Irgamet 39™ coated electric zinc surface.

At first the triazoles Irgamet 34™ and Irgamet 39™ measurements are discussed. For both triazoles intact of the un/protonated molecules couldn't be found, however in contrary, dozens of characteristic fragments are detectable in mass spectra. In positive mass spectra at the nominal Mass 104 m/z a significant signal for both triazoles on both substrates could be found. Due to the fact, that both triazoles Irgamet 34™ and Irgamet 39™ have the same principal basis structure and moreover the fragment M_{104}^+ didn't appear in mass spectra of triazole Irgamet 30™, the resultant implication is, that the nominal Mass 104 m/z must be a fragment of the principal basis-structure, which is identified as $(\text{C}_7\text{H}_6\text{N})^+$ (see Figure 3). Furthermore significant signals of Irgamet 34™ and Irgamet 39™ on the electrolytic zinc substrate pointed out a characteristic zinc-pattern (^{64}Zn 48,6%; ^{66}Zn 27,9%; ^{68}Zn 18,8%), which are exemplified at the nominal masses 184 m/z, 186 m/z and 188 m/z (see Figure 4). Due to the fact that a ZnO-stoichiometry is assumed, the mass of Zinc-Oxide (80 m/z, 82 m/z, 84 m/z) have to be subtracted from the nominal mass of the zinc-pattern based triazole molecules, so that the nominal mass 104 m/z

resulted as further identified $(C_7H_6N)^+$. So the signals, caused by the triazoles Irgamet 34™ and Irgamet 39™ at masses 184 m/z, 186 m/z, 188 m/z can be identified as fragment $(ZnO-C_7H_6N)^+$, a triazole linked to the metal surface.

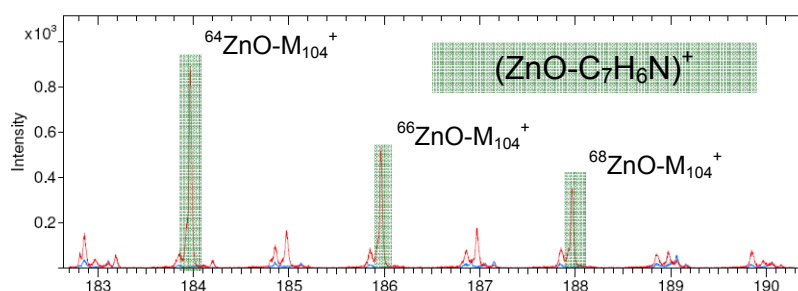


Figure 4: chemical bond between ZnO-substrate and triazole Irgamet 39™ (green coloured), blue line: mass spectrum of a cleaned electric zinc surface without triazole coating, red line: mass spectrum of an Irgamet 39™ coated electric zinc surface.

Based on Benninghoven's precursor model, it can be assumed that if a molecule- or cluster-ion is found in a ToF-SIMS spectrum, there had been a chemical bond between the constituents of the cluster already on the surface before bombardment [10, 11]. In our case that means, that a chemical, covalent bond between the surface ZnO and the fragment of the anticorrosion additive $(C_7H_6N)^+$ existed before analysis.

On the uncoated Steel substrate with a monolayer of Irgamet 39™ the fragment $(FeO-C_7H_6N)^+$ is found, whereas no fragments like this are found on the same substrate with an Irgamet 34™ coating. Therefore it is assumed that triazole Irgamet 34™ does not react on FeO-substrates, likely caused by the polar side chain.

In the mass spectra of triazole Irgamet 30™ prepared on ZnO- and FeO-substrates, a significant fragment at nominal mass 70u of the principal structure is found in both polarities. Due to the fact that this fragment does not appear on surfaces prepared with Irgamet 39™, this fragment is attributed to the basis structure (yellow coloured in Figure 1) of the Irgamet 30™ and could be identified as $(C_2H_4N_3)^+$. For the electrozinc surface, this triazole fragment is also found in chemical bond with the zinc oxide as $(ZnO-C_2H_4N_3)^+$. Just as the zinc oxide linked Irgamet 30 molecule fragment $(ZnO-C_2H_4N_3)^+$. The determination of the mass fragment $(FeO-C_2H_4N_3)^+$ points out the chemical bond of this triazole fragment to the uncoated steel surface.

Conclusion

Generally each surface could be characterized by analyzing clusters of surface molecules.

First of all to document the initial state of the surfaces and as necessary requirement for reference measurements the important discovery and statement of these ToF-SIMS measurements on different substrates was to find out and to define the dominated stoichiometry of the substrate surface. The main stoichiometry of an electrolytic zinc coated steel is specified by $(Zn_nO_{n-1})^+$ and $(ZnO)_n-H^+$ -clusters; also the $(FeO)_n^+$ - & $(FeO)_nO^-$ -cluster indicated a FeO-stoichiometry.

It was found out, that the triazoles Irgamet 30™, Irgamet 39™ chemically bind on both surfaces in different ways. Furthermore Irgamet 34™ is a good example that side chains not only influences solubility, but moreover influences the chemical activity on surfaces.

At least with ToF-SIMS a method is found to check easily the chemical activity of anticorrosion additives on different technical surfaces and to determine the chemical binding of different polar molecule fragments. However for the identification of the chemically bonded molecules it is very helpful to know their chemical structure.

References

- [1] M. Levin, P. Wiklund, H. Arwin, Appl. Surface Sci. 254 (2007) 1528
- [2] © Ciba Specialty Chemicals 2004 Pub. No. PA 8765M1204 job#04-32
- [3] J.C. Vickerman in ToF-SIMS Surface Analysis by Mass Spectrometry, Ed by J.C.Vickerman and D. Briggs IM Publications and SurfaceSpectra Limited, Huddersfield, UK, 1 (2001)
- [4] Henkel online available safety data sheet German version, RidolineC72 Sicherheitsdatenblatt gemäß (EG) Nr. 1907/2006 (February 2011)
- [5] J.R. de Laeter, J.K. Böhlke, P. de Bievre, H. Hidaka, H.S. Peiser, K.J.R. Rosman, P.D.P. Taylor PURE APPL. CHEM., Vol. 75, No. 6, 683 (2003)
- [6] M. Winter online isotope cluster calculator winter.group.shef.ac.uk/.../isotopes.html (March 2011)
- [7] Y. Junhua online isotope cluster calculator <http://yanjunhua.tripod.com/pattern.htm> (March 2011)
- [8] Scientific instrument services, online isotope cluster calculator, <http://www.sisweb.com/mstools/isotope.htm> (March 2011)
- [9] K. Wittmaak, Surface Sci 89 (1979) 668
- [10] A. Benninghoven, in secondary Ion Mass Spectrometry (SIMS II), Ed by A. Benninghoven, C.A. Evans, R.A. Powel, R. Shimizu and H.A. Storms, Springer, Berlin, Germany, 116 (1979)
- [11] A. Benninghoven, in Ion Formation from Organic Solids, Springer Series in Chemical Physics, Vol. 25. Springer, Berlin, Germany, 77 (1983)

EXPERT SYSTEMS FOR PREDICTION OF CORROSION PROPERTIES OF ZN-BASED COATINGS FROM THE CHEMICAL ANALYSIS

Arne Bengtson¹, Lars Hildebrand²

¹Swerea KIMAB AB, Drottning Kristinas väg 48, SE-114 28 Stockholm, Sweden

²Technical University of Dortmund, Computer Science I, Otto-Hahn-Str. 16, D-44221 Dortmund, Germany

Summary

The purpose of the work is to develop a general method, to predict the corrosion resistance of Zn-based coatings, expressed as total mass loss in an accelerated salt spray test. The method is to be based on just three analytical parameters: the total coating weights of Zn, Al and Mg. The reason for this restriction is that determination of these three parameters is possible in on-line analysis. The predicted corrosion resistance could then be included in a process control system.

Accelerated corrosion tests have been carried out by Swerea KIMAB IC (Institut de Corrosion) in Brest, and CRM in Belgium. Test were run according to the Renault ECC1 test D172028/--C (12 weeks), the neutral salt spray according to ISO 9227 8CRM) and an accelerated cyclic corrosion test developed by CRM. The materials were divided into four corrosion classes according to total mass loss.

- class 4 (very good), mass loss < 20 mg/cm²
- class 3 (good), mass loss >= 20 mg/cm² and <30 mg/cm²
- class 2 (fair), mass loss >= 30 mg/cm² and <40 mg/cm²
- class 1 (poor), mass loss >=40 mg/cm²

All corrosion experiments show clearly the well documented positive influence of magnesium and aluminium. In relation to the masses of these elements in the coatings, the influence of both elements is considerably higher than the influence of zinc alone. For this reason, a new quantity is introduced, called "equivalent Zn coating weight ($Zn_{eq\ cw}$)". This measure is a linear combination of the coating weights of zinc, aluminium and magnesium:

$$Zn_{eq\ cw} = Zn_{cw} + a \cdot Al_{cw} + b \cdot Mg_{cw}$$

The next assumption is that the total mass loss can be expressed as a potential function of the equivalent zinc coating weight. A regression analysis has determined the coefficients a and b as follows:

$$Zn_{eq\ cw} = Zn_{cw} + 4,6 \cdot Al_{cw} + 59 \cdot Mg_{cw}$$

The calculated value for $Zn_{eq\ cw}$ was used in combination with the coating weights of Zn (Zn_{cw}), AL (Al_{cw}), and Mg (Mg_{cw}), as an input to the data treatment model. The model, based on a combination of regression analysis and a "decision tree" algorithm was able to correctly classify 25 out of 27 materials based on just the three analytical parameters: the total coating weights of Zn, Al and Mg.

In conclusion, the approach shows that an accurate prediction of the corrosion behaviour is possible even on-line. For purposes of material development, the expert system can be expanded to include additional analytical parameters.

This work is part of the RFCS-project RFSR-CT-2006-00034

1 Introduction

Because of the steadily thinner sheet materials used in automobile manufacture, ever greater importance is being attached to corrosion protective surface coatings. Different zinc alloy coatings can have pronounced beneficial effects, therefore a worldwide trend to alloy coatings with two (e.g. Zn-Al, Zn-Fe) or even more components is observed. For the continuous galvanising of steel strip, hot-dip coating and electrolytic deposition are well established methods. However, both processes are strongly limited with respect to the selection of possible alloy coatings for technical as well as for economical reasons. These can be overcome by introducing a combined coating process. Binary or ternary alloy coatings can be produced by:

- co-deposition by PVD and subsequent thermal treatment
- direct coating by hot dipping into zinc alloy bath
- conventional hot-dip or electrolytic deposition followed by PVD deposition of an additional metallic coating and subsequent diffusion-annealing.

It is by now well established that Zn-Mg and Zn-Al-Mg alloy coatings offer excellent corrosion protection in unpainted as well as in the painted state. Interesting economical aspects arise from such new zinc alloy coatings, since through their application the corrosion protection of conventional zinc coatings may be achieved with significantly thinner alloy coatings.

There is a need to be able to characterise these new types of coatings with both fast and analytically comprehensive techniques. The most comprehensive characterisation is needed for better understanding of the material and product development. The fast characterisation is needed for production quality control and troubleshooting. Obviously, one of the most important properties to determine is the corrosion resistance. Since there is a dependence on the corrosive environment and other factors, the corrosion resistance must be defined based on an accepted test procedure. The purpose of this work was to develop a general method for prediction of the corrosion resistance of Zn-based coatings, *expressed as total mass loss in an accelerated salt spray test*. The method was to be based on just three analytical parameters: the total coating weights of Zn, Al and Mg. The reason for this restriction is that determination of these three elements is possible in on-line analysis. The predicted corrosion resistance could then be included in a process control system.

1.2 Expert systems

An expert system is a computer application that is able to perform tasks which are normally performed by human experts. Expert systems are made to assist humans as well as to replace humans. Assisting systems can be found in medical areas, where an expert system can diagnose human illness and give advice for proper treatment. The expert system suggests treatment only, the person in charge will always be the doctor. Other areas, e. g. traffic control, are fully automated. Results from actual traffic analysis are directly used to control traffic signs. No human interaction is needed [5]. A typical definition of an "expert system" in the computer science is as following:

A program that uses available information, heuristics, and inference to suggest solutions to problems in a particular discipline.

The actual realisation of an expert system normally includes a number of different parts, e.g. data pre-processing, regression analysis to fit data to mathematical models, classification software to sort data based on specific properties. The classification software can be grouped in "supervised" and "unsupervised". In supervised classification, the expert system has to be trained using training examples with already known results. The expert system learns the relationship between input and output variables and is able to generalize this relationship in the case unknown data is presented. In unsupervised classification, the software automatically sorts the data in sets with similar properties.

There are several types of computational models for these purposes: Artificial neural networks, self-organising maps, similarity trees, decision trees etc. An expert system is designed in such a way that it can be “trained” on a given set of data, similar to a calibration in regular analytical software. The training sets up a number of rules that can be used for prediction and thereby suggest a solution to a problem. The rules can be expressed in mathematical terms, like sets of intervals, but also in a linguistic way, which is close to natural languages [4].

2 Experimental

The experimental tests included 29 coated steel sheet samples. Most of them were produced in pilot plants for the purpose of coating development R&D, but a few coatings produced in full-scale factory trials were also included. In addition, two pure Zn coatings were included as reference.

A total of 15 materials (“PVD” type) were produced by a multistep technique: Electrolytic deposition of a pure Zn layer (2 – 9 μm) followed by PVD deposition of a thinner Mg layer and subsequent thermal treatment.

A total of 12 materials (“HD” type) were produced by hot dipping into zinc alloy bath, with varying admixtures of Mg and Al.

2.1 Determination of coating weights

All materials were analysed by glow discharge optical emission spectrometry (GD-OES) [1], examples of quantitative compositional depth profiles (CDP) are shown in figure 1. The coating weights (CW) of Zn, Al and Mg, expressed in g/m^2 , were calculated from the depth profiles.

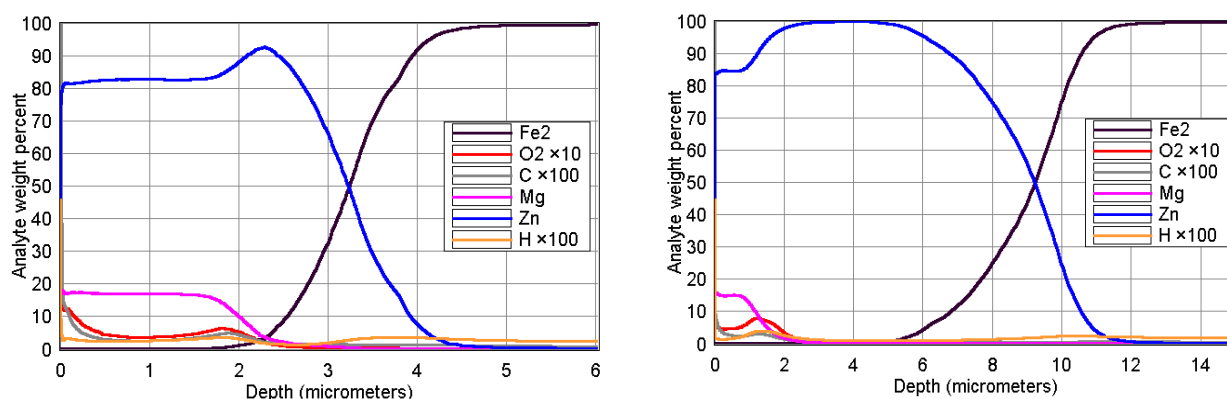


Figure 1: Compositional Depth Profiles of two PVD type coatings: left a relatively large amount of Mg on a thin Zn base coating; right a medium amount of Mg on a thick Zn base.

For a substantial number of the materials, the CW of Zn, Al and Mg were also determined by wet chemical analysis (ICP-OES analysis of coating dissolved in inhibited hydrochloric acid) at Swerea KIMAB, ThyssenKrupp Steel (TKS) and CRM in Liege. The agreement between the methods was found to be very good. In table 1 below, the average determined CW of all three elements are given for the 29 materials.

2.2 Corrosion tests

Accelerated corrosion tests have been carried out by Swerea KIMAB IC (Institut de Corrosion) in Brest. Tests were run according to the Renault ECC1 test D172028/--C (12 weeks).

The materials were divided into four corrosion classes according to total mass loss.

- class 4 (very good), mass loss < 20 mg/cm^2
- class 3 (good), mass loss $\geq 20 \text{ mg}/\text{cm}^2$ and <30 mg/cm^2
- class 2 (fair), mass loss $\geq 30 \text{ mg}/\text{cm}^2$ and <40 mg/cm^2
- class 1 (poor), mass loss $\geq 40 \text{ mg}/\text{cm}^2$

The total mass loss and corrosion class for each material is given in table 1.

Table 1: Numerical data for the test samples used to model corrosion resistance.

Sample No.	Type	Zn cw (g/m ²)	Al cw (g/m ²)	Mg cw (g/m ²)	Mass loss (mg/cm ²)	Corrosion class
1	PVD	16,40	0,00	0,24	93,0	1
2	PVD	29,20	0,00	0,21	81,0	1
3	PVD	16,20	0,00	0,61	74,0	1
4	PVD	52,60	0,00	0,20	54,5	1
5	PVD	15,00	0,00	0,94	47,0	1
6	PVD	16,80	0,00	0,59	36,5	2
7	PVD	16,66	0,00	1,54	33,5	2
8	PVD	17,46	0,00	0,59	31,0	2
9	PVD	14,81	0,00	1,51	30,5	2
10	HD	55,10	0,57	1,14	27,0	3
11	HD	47,10	15,23	0,00	26,5	3
12	PVD	58,30	0,00	0,40	26,5	3
13	HD	62,43	0,19	1,28	26,0	3
14	HD	54,53	1,15	1,72	22,0	3
15	PVD	73,00	0,00	0,00	21,5	3
16	HD	55,89	0,58	1,75	20,0	3
17	PVD	58,30	0,00	1,43	20,0	3
18	HD	47,00	2,53	2,19	16,0	4
19	HD	25,20	26,19	0,00	16,0	4
20	HD	44,90	7,52	2,06	16,0	4
21	PVD	50,65	0,00	1,02	15,5	4
22	HD	32,00	5,25	1,46	15,0	4
23	HD	39,40	7,15	1,92	15,0	4
24	HD	36,90	7,16	1,78	15,0	4
25	HD	41,70	2,29	1,63	13,5	4
26	PVD	61,00	0,00	1,91	13,0	4
27	PVD	63,00	0,00	2,55	10,0	4
HDG 10 ref	HD	73,00	0,00	0,00	40,0	1
HDG 20 ref	HD	146,00	0,00	0,00	35,0	2

3 Results

All corrosion experiments show clearly the well documented positive influence of the alloying elements Mg and Al. In relation to the masses of these elements in the coatings, the influence of both elements is considerably higher than the influence of Zn alone. For this reason, a new quantity is introduced, called “equivalent Zn coating weight” $Zn_{eq\ cw}$. This quantity is defined as a linear combination of the coating weights of Zn, Al and Mg:

$$Zn_{eq\ cw} = Zn_{cw} + a \cdot Al_{cw} + b \cdot Mg_{cw} \quad (1)$$

Where Zn_{cw} , Al_{cw} , Mg_{cw} , are the coating weights of Zn, Al and Mg respectively; a and b are constants.

The next assumption is that the total mass loss M_l can be expressed as a potential function of the equivalent zinc coating weight.

$$M_l = A \times Zn_{eq\ cw}^B \quad (2)$$

Inserting equation (1) in equation (2), the coefficients a , b , A and B were determined by iterative regression analysis:

$$a = 4,6 \quad b = 59 \quad A = 2483 \quad B = -0,98$$

The high value of b reflects the very beneficial influence of Mg on the corrosion resistance. It is also interesting to note that the best fit to the exponential B is very close to -1, which means that the total mass loss is essentially inversely proportional to the quantity $Zn_{eq\ cw}$.

The final fitted curve of M_l vs. $Zn_{eq\ cw}$ is shown in figure 2. The correlation coefficient is 0,794, which must be considered very good considering the rather large statistical uncertainty in the mass loss determination from the corrosion test.

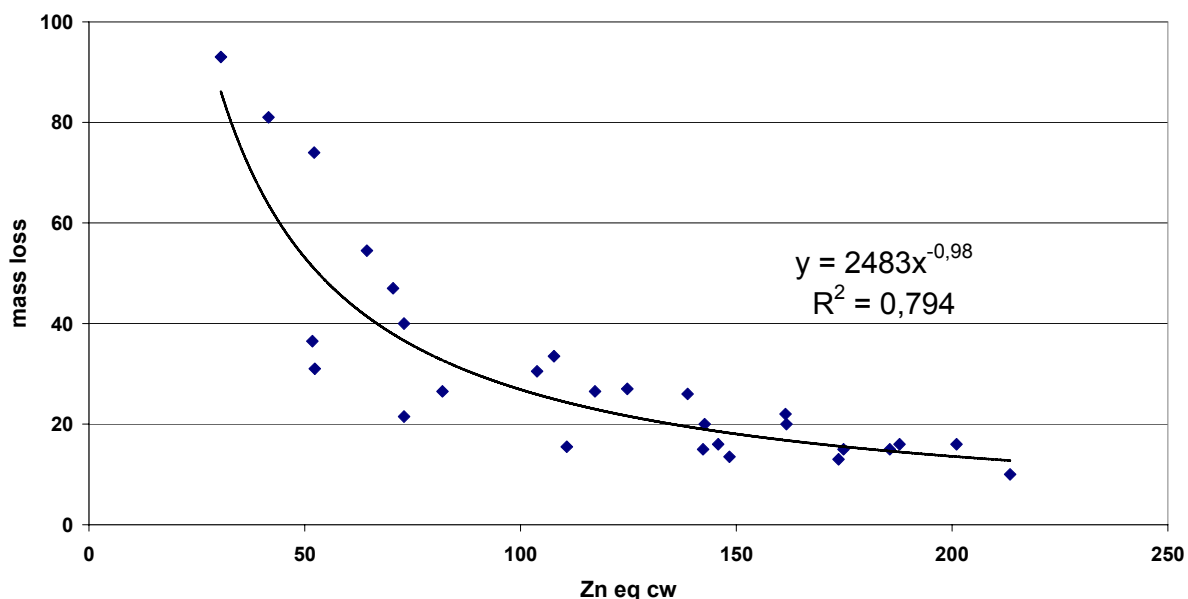


Figure 2: Measured corrosion mass loss vs “Zinc equivalent coating weight”.

3.1 Evaluation with the expert system

The data was evaluated with an expert system developed within the framework of the RFCS project ADCTEC. In this system, there are several alternative classification methods available.

The calculated value for $Zn_{eq\ cw}$ was used in combination with the coating weights of Zn, Al, and Mg as input to the expert system. The model used is based on a combination of regression analysis and a “decision tree”

algorithm (the J48 decision tree algorithm, an implementation of Quinlan's C4.5 decision tree [6, 7]). The method has been extended to allow an interactive operation [8].

Based on the input of just these 4 parameters, the decision tree is able to correctly predict the corrosion classes of 25 out of 29 samples, with only 4 misclassifications. The introduced quantity $Zn_{eq\ cw}$ is the major criterion to distinguish between the classes "good" and "very good", as it is used as the first decision condition in the tree, see figure 3.

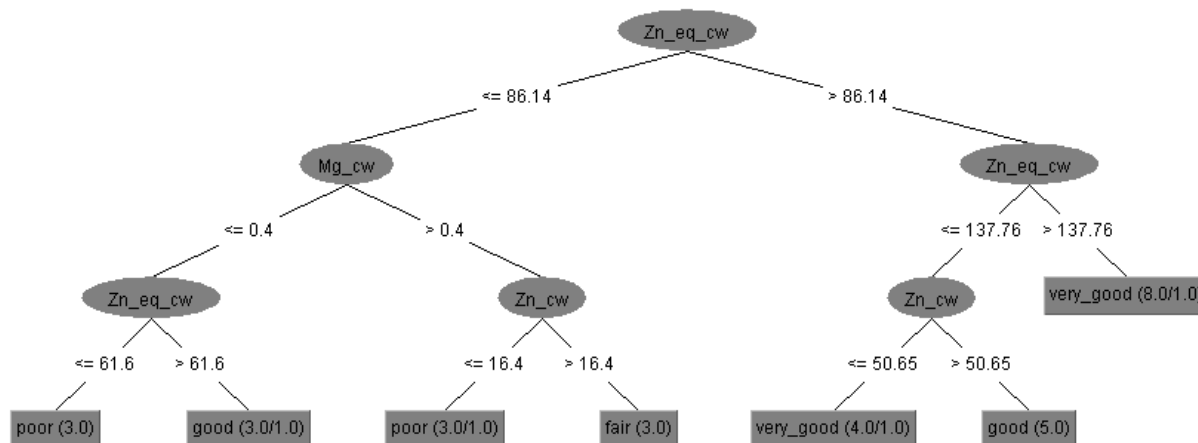


Figure 3: : Decision tree for classification of corrosion resistance.

The classification is correct for the following 25 samples:

- classification "very good", Samples 18 – 27
- classification "good", Samples 10, 12 - 17
- classification "fair", Samples 6 – 8
- classification "poor", Samples 1 - 5

The following four samples have been misclassified:

- HDG10, classified as "poor", correct class is "fair"
- Sample 9, classified as "poor", correct class is "fair"
- HDG20, classified as "very good", correct class is "fair"
- Sample 11, classified as "very good", correct class is "good"

Of these four misclassified samples, two (HDG10 and HDG20) are pure zinc references provided by IC for the corrosion test. Of the actual project samples, only two out of 27 are misclassified.

4 Discussion

This successful result of the regression fit to a mass loss function and subsequent decision tree classification is quite remarkable, considering that the only analytical input data are the coating weights of the three major elements in the coating. It therefore appears that a quite reliable prediction of the corrosion resistance can be obtained in this simple way.

The possible industrial applications of this work are several. Within the project ADCTEC and previous RFCS projects [2, 3], it has been demonstrated that Zn, Al and Mg can be rapidly determined on-line with LIBS systems. This means that assessment of the corrosion resistance can also be done on-line with an expert system. More

likely is perhaps that the technique will be further developed to include more analytical parameters for prediction of the corrosion resistance, as a useful tool in the development of new coating types.

Concerning the results for the set of test samples used for this work, there are at least two important observations:

- For the accelerated salt spray test, there is no difference in corrosion performance between the two main coating types HD and PVD.
- In spite of the improvement in corrosion performance from the alloying elements, very thin coatings < 4 μm do not perform satisfactory.

5 Acknowledgements

This work is part of the RFCS-project RFSR-CT-2006-00034 ADCTEC, and the financial support from the European Commission is gratefully acknowledged.

The authors also wish to thank all the colleagues participating in the projects ADCTEC for their contributions to the work and many valuable discussions.

6 References

- [1] Bengtson A and Nelis T: "The concept of constant emission yield in GDOES", Analytical and Bioanalytical Chemistry, Springer, 385, no. 3, pp. 568-585, 2006.
- [2] Ruiz J., González A., Cabalín L.M., Laserna J.J.; *On-Line Laser-Induced Breakdown Spectroscopy Determination of Magnesium Coating Thickness on Electrolytically Galvanized Steel in Motion*; Appl. Spectrosc. 64, 12 (2010), 1342-1349.
- [3] H. Balzer, M. Hoehne, V. Sturm and R. Noll; Spectrochimica Acta Part B, 60 Nr 7 – 8, 1172 – 1178, 2005.
- [4] Hildebrand, L.; Fathi, M.; *Linguistic color processing for human-like vision systems*, in: proceedings "Electronic Imaging 2000, IS&T/SPIE 12th International Symposium", San Jose, USA, 2000.
- [5] Hildebrand, L.; Michalski, C.; Wickrath, M.; Valentin, H.; *Strategy implementation for mobile robots using the pipes & filters architecture*; in: proceedings "FIRA Robot World Congress 2003", Wien, 2003.
- [6] Ross J. Quinlan: Learning with Continuous Classes. In: 5th Australian Joint Conference on Artificial Intelligence, Singapore, 343-348, 1992.
- [7] Ross J. Quinlan: C4.5: Programs for Machine Learning. Morgan Kaufmann Publishers, San Mateo, CA, 1993.
- [8] Winter, J.; Hildebrand, L.; *Interactive Decision Trees and Artificial Neural Networks*; in: proceedings International Conference on Knowledge Management for Composite Materials; Germany, 2007.

EXPLORATION AND VALIDATION ABOUT CHARACTERISATION OF THIN COATING ON STEEL SURFACE IN INDUSTRY APPLICATION

LI Lei ,ZHANG Sheying ,SHEN Jie ,WANG Junxiang

Test, Analysis and Inspection Center, BaoSteel Industry Inspection Corp., Shanghai, China

ABSTRACT

Generally, to meet the different customer demand, different kinds of coating will be spreaded or treated on the steel sheet surface. The main chemical composing and thickness of the coating are key parameters which will affect usage of the steel sheet product directly. Therefore, how to characterise the thin coating fast, correctly and reliably is important in industry. In the literature, there are various methods to meet the characterisation of the thin coating which is made up of inorganic, organic or complex compound. The methods which can be used in industry to characterise the coating could be described as: (1) solving the coating by chemical reagent or electrochemistry method, then determining the mass or thickness by gravimetry, or determining the chemical composite by UV or ICP or other method. (2) observing the composite and thickness of the coating by SEM, or β ray etc. (3) measuring the intension of the representative element in the coating by XRF, calculate the concentration, then the mass or thickness of the coating can be determined by the calibrated density relation. XRF is widely used in industry because it is quick and suit for testing batches of samples. However, the results obtained from XRF should be validated or verified by other ways since it's relative. The author tried to describe tests of the thickness of several representative steel sheet samples with thin coating. The results are verified by direct measuring methods such as SEM.

1. INTRODUCTION

Generally, during the latter process in the steel plate production, to meet the different customer demand, different kinds of coating (from a few micron to teen micron) will be spread or treated on the steel sheet (galvanized or uncovered steel sheet) surface. For example, since some galvanized steel sheet may be rusted in the air, especially in the high wet and hot environment, these sheets must be chromate-treated to form a passivation film to increase the anti-corrosion ability. Some galvanized steel sheet will be phosphated to meet the needs of industrial application such as domestic automobiles, chemical engineering, shipping and aviation. Because the phosphating is the important preprocess before the metal component are spread. An anti-fingerprint galvanized steel sheet are marketed to avoid the fingerprint staying on the product surface. The sheet has good electrical grounding properties, adequate anti-fingerprint properties and anti-corrosion properties. So it will be widely used in electrical appliances, information technology, especially in computers, images, and acoustics fields. Also electric engine, transformer iron core producer need those steel sheet which with insulating film, to reduce the eddy current loss and increase the electromagnetic excitation.

The types and thickness of the coating will affect the use property of the customer directly. Thus, how to character the thin coating trustly is the important tache in the steel-making works.

2. TYPES OF COATING

In order to characterise the coating, we need to know the composition of the coating first of all. Different of dope may be used for different aim to form the different coating in the works. For example, high or middle concentration of hexavalent chromium solution is treated on the steel sheet surface for a long time. Recently however, green solution without using chromate or with trivalent chromate are used more and more because of the toxicity of the hexabalent chromium. Some passivation solution is mainly made up of molybdate, phosphate, silicon

dioxide, titanium sulfate etc^[1]. Some composition of passivation solution is lanthanum, vegetal acid etc^[2]. The components of phosphating solution is a kind of phosphate with Zn^{2+} , Mn^{2+} , Ni^{2+} etc^[3]. The components of anti-fingerprint paint also is very complex. The Nippon steel corporation developed the organic anti-fingerprint steel by applying organic composite coating on the passivation layer. The patent EP 1426466A1 introduced some kind of paint which is the mixture of cation or non-ion polyurethane, acrylic ester resin, epoxy resin, polyester resin, polyamide resin, particular structure resin, compound of Zr, Ti, Mo, W, Mn, Ce and water. This organic paint is environmental friendliness^[4]. The insulative coating is mostly semi-inorganic coating. The patent US 4618377 introduced one mixture of insulate inorganic and organic paint, the dope is made up of inorganic solution, glue resin, grain of organic resin and separate accelerant. The components of inorganic solution is phosphate, chromate and bichromate of Ca, Mg, Al etc. The grain of inorganic resin is the copolymer or mixture of polyethylene and polypropene. The patent of JP 7268641 expound one kind of organic insulative coating containing phosphate, macromolecule emulsion and proper solidify reagent. The patent CN 101029196 explained one insulating dope which has the main component of bichromate with bivalent metal, the rest component is boric acid, inorganic reducer and resin emulsion^[5].

Thus it can be seen that the coating system on the surface of the steel sheet mostly include organic, inorganic and semi-inorganic coatings. The makeup of the coating is so complex that it is not the simple inorganic or organic compound. Different dope producers provide different formula dope to obtain the similar effect. For instance, there are many companies which can supply the different passivation dope to the same aim.

3. METHODS OF CHARACTERISATION

It is difficult to characterise the coating only by chemical method because of the complexity of the coating. At present, there are several methods to explain the component and the thickness of coating in the manufactory application. (a) Dissolving the coating using chemical reagent or electrochemical method, then determining the coating mass by gravimetry and attaining the component of the coatings by UV, ICP or other ways. (b) Measuring the intensity of representative element in the coating by XRF, and deduce to the coating mass by calibration curve, then calculating the coating thickness by dint of density. (c) Observing the components and the thickness of the coating by SEM, β ray reflect method and so on.

These methods all have its own characters in classification. The key of Method (a) is to find the proper solvent to solve the coating. Method (b) is widely used in the works because it is not need to prepare the sample and it is fast and convenience. Usually the coating mass is controlled in the range by ways that preparing the dope and spreading it on the steel surface according to the demand of the dope producer. The factories usually expressed the coating thickness with g/m^2 or mg/m^2 to control the coating thickness. Since the component of the coating is organic or inorganic, the XRF method only can measure the intension of the representative element in the dope, then the final result can be obtained by the calibration curve. Because the different direction of the dope contain the different representative element, the standard sample is diverse. For example, to gain the similar effect on steel sheet, the provider A and B will supply the different standard sample to establish the calibration curve. The representative element may be Cr, Si or Ti in the passivation coating. Other element such as Si or Zr can be seen in the anti-fingerprint coating and Ca, P or Cr can be seen in the insulating coating. This is the limit of the Method (b). It can be used just as a way of technical control. Commonly, the result of method (a) and (b) is the coating mass, the thickness must be calculated by the density of the coating which is very difficult to get. If the customer wants to know the exact thickness of the coating, the better answer is come from the method (c).

4. ILLUSTRATION

Determining the coating mass by XRF

(1) Determining the coating mass of four types of steel sheet with thin coating by XRF with the same instrument, the results can be seen in table 1.

Tab.1: Results of same type of coating by different dope producers(unit:g/m²)

Name of samples	Sample a (with passivation coating)	Sample b (with phosphating coating)	Sample c (with anti-fingerprint coating)	Sample d (with insulating coating)
Results	0.16 (by calibration curve of dope producer A)	0.002 (by calibration curve of dope producer A)	0.16 (by calibration curve of dope producer A)	6.76 (by calibration curve of dope producer C)
	2.17 (by calibration curve of dope producer B)	1.40 (by calibration curve of dope producer B)	2.36 (by calibration curve of dope producer B)	3.89 (by calibration curve of dope producer D)

(2)From table 1, it can be seen that to the same sample, different value will be given when using different standard samples of dope producer. The final result do not reflect the actual coating mass if the ingredients of the dope are unknown. Users can validate the result by gravimetry but it is difficult to choose the proper solvent and the precision of gravimetry is insufficient.

Observing the coating thickness by SEM

Preparation of sample

Selecting four typical samples with insulating coatings of different producers and types, treating them by incrustation, rubbing and polishing (corrupting the sample 1 with 3% HNO₃-HCl solution). Spray the enchased samples except 1 with Au powder to meet good vision impression.

Instrument

Hitch S-3400N Scan Electron Microscope, Horiba Energy Disperse Spectroscopy.

Experimentation

First, observing the samples by SEM and getting the clear borderline with backscattered electron image. Then, selecting five eyeshot with same magnifying multiple every 3mm of every sample. Finally, measuring the length of the coating (μm) in the eyeshot.

To affirm the coating, the samples were analyzed by EDS. All of the pictures are as follows.

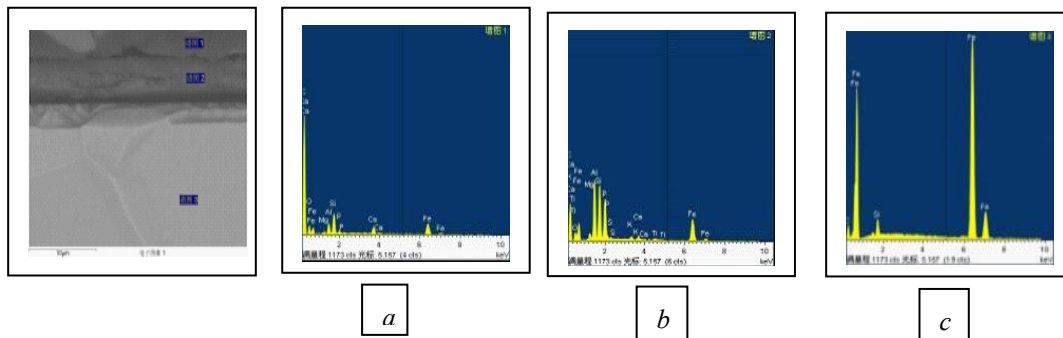


Fig1:SEM photo and EDS photo of sample1 (a: incrustation powder, b: coating, c: steel)

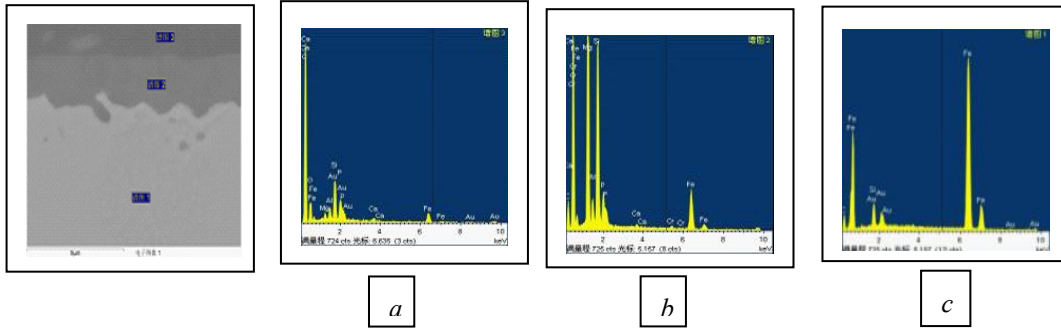


Fig2:SEM photo and EDS photo of sample2 (a: incrustation powder, b: coating, c: steel)

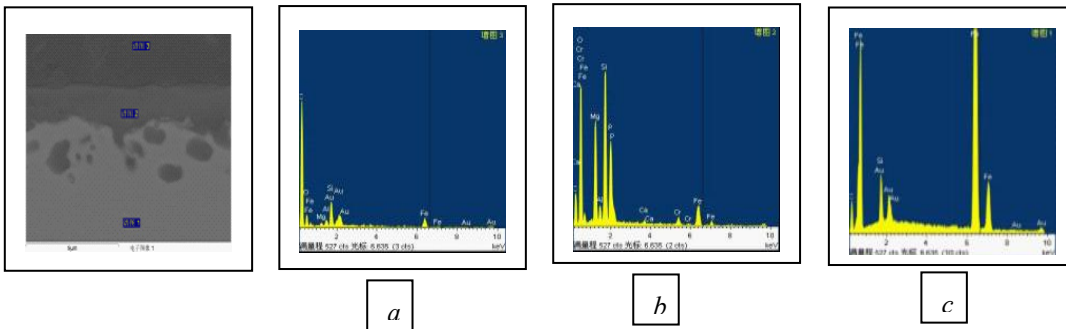


Fig3:SEM photo and EDS photo of sample3 (a: incrustation powder, b: coating, c: steel)

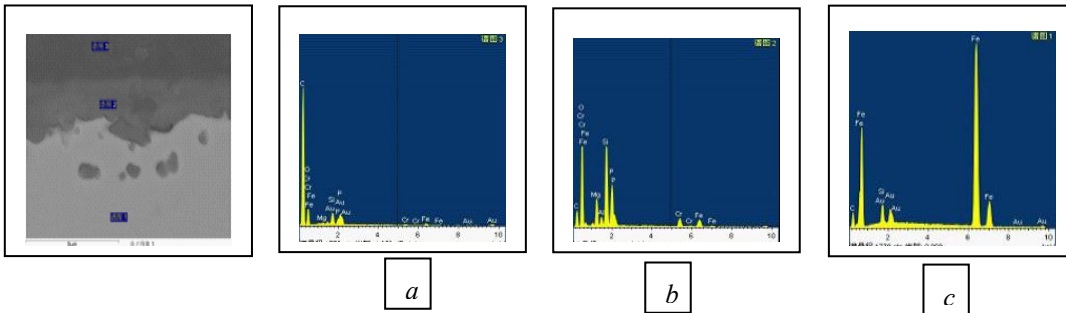


Fig4:SEM photo and EDS photo of sample4 (a: incrustation powder, b: coating, c: steel)

Explanation: There are Au in the EDS photos of sample2~4, because samples are treated by spraying Au powder.

Results

- (1) Method of calculation: the area of the coating can be get by integral. The thickness of the coating=area/length. The finally result was averaged by 5 thickness of 5 eyeshots.
- (2) Main factors to affect the results: pitch of cross section of enchased samples, pitch of surface of rubbed samples, distortion of the coating, errors of staff guage of SEM and calculation errors etc.
- (3) The thickness of 4 samples can be seen as table 2.

Tab.2: Results of thickness of samples(unit:μm)

Name of samples	Sample 1	Sample 2	Sample 3	Sample 4
Results	2.4	3.2	3.6	2.8

5. CONCLUSION

This paper not only introduced several methods to characterise thin coatings on steel sheet surface but also summarized the merit and the demerit of these methods. Since the coating mass value determined by XRF is relative to the calibration curve, the result by XRF cannot express the actual coating mass because of XRF's relativity. The author tried to observe the coating thickness of some samples with insulating films by SEM, and validated the credibility of the results by EDS. Also, the result by XRF can be validated by customers. The paper only gave some examples of insulating coatings due to the variety of the coating types. It has not make the progress on how to observe the passivation and anti-fingerprint films yet. This will be studied in the next step.

BIBLIOGRAPHIES

- [1] GongLi, LuYarrping, (2007) Modification and Corrosion Resistance of Molybdate Passivation Film on Hot Dip Galvanized Steel Sheet. In: *Journal of Iron and Steel Research*; 19, 88-92.
- [2] Ding Nan, Yang Fei & Zhu Li Qun, (2008) The effects of parameters of passivating process on the colour and lustre of titanium passivation film of galvanized steel sheet. In: *Materials Protection*; 41, 46-48.
- [3] Zhou Mo Yin, (1999) The factors Affecting Phosphating Coating Growth on Galvanizing Layers. In: *Electroplating & Pollution Control*; 19, 21-24.
- [4] Zou Zhong Li, Li Ning & Li De yu, (2008) Generalization of anti-fingerprint treatment on galvanized steel sheet. In: *Electroplating & Pollution Control*; 28, 1-4.
- [5] Han Xiao guang, Zhang Dun ming, (2008) Progress in the Study of Insulating Coating for Non-Oriented Silicon Steel. In: *Science & Technology Information*; 25, 276-277.

ANTI-CORROSION PROPERTIES OF ORGANOSILICON PLASMA POLYMER COATINGS FILLED WITH CERIUM NANOPARTICLES DEPOSITED FOR PROTECTION OF GALVANIZED STEEL

Julien Bardon*, Doriane Del Frari, Jérôme Bour, Claire Arnoult, David Ruch

*Laboratoire de Technologies Industrielles, Centre de Recherche Public Henri Tudor (CRPHT), Rue de Luxembourg 70, L4221 Esch sur Alzette, Luxembourg
Fax number : +352 425991 555
E-mail address : julien.bardon@tudor.lu*

Keywords : coatings, corrosion, dielectric barrier discharges (DBD), hexamethyldisiloxane (HMDSO), nanocomposites, particles

Summary

Innovative Ce-containing nanoparticles in plasma polymerized (pp) HMDSO layers have thus been deposited and studied. This combination allows to afford a good physical barrier effect and active properties. Gas/aerosol mixture of liquid organosilicon and cerium-based particles is injected into an atmospheric pressure DBD where plasma polymerization of organosilicon precursor occurs. Corrosion resistance of these different coatings is compared by electrochemical impedance spectroscopy (EIS). Potential self-healing property afforded by cerium incorporation in the layer was studied by associating EIS measurements and nanoscratch controlled damaging. Combination of nanoscratch damaging of layers with EIS experiments allows to measure the active protection property of such layers: when particles are incorporated, a decrease of the global corrosion resistance is observed immediately after a scratch; however, after a longer immersion, the resistance increases and tends to the initial value.

Introduction

Spherical inorganic nanoparticles have been successfully used as fillers to obtain enhanced properties of polymer matrices. Specific surface area of such particles is high, which drastically enhance the change in properties of such a nanocomposite. Particles of interest are mainly metal oxides, which can afford better mechanical^[1], thermal^[2], tribological^[3] or anticorrosion properties to the polymer matrix. Their isotropic shape and small size allow an easier processing of the composite and a reduced effect on matrix cross-linking, and hence on final properties.

Sol-gel^[4] and solvent deposition^[5] processes have been considered to elaborate organosilicon anticorrosion coatings. Furthermore, it has been reported that the specific incorporation of a small amount (1-5% in weight) of nanoparticles in organic and organosilicon polymers can lead to improvements in properties of polymer coatings. For instance, Ooij et al.^[5] have shown that silane (organosilicon chemical including alkoxy groups) based polymer films with silica particles incorporation could be used to replace the toxic chromate-based treatment for aluminum alloys. However, dry processes, such as plasma polymer deposition, should be preferred because they are solvent free and therefore more environmentally friendly. Simultaneous incorporation of nanoparticles into a coating during plasma polymer deposition is reported.^[6,7] This process allows direct and easy deposition of the nanocomposite coating on the target surface.

Coatings based on plasma polymerization of organosilicon precursors for anticorrosion purpose have been studied by several authors. Most of these treatments are carried out in vacuum reactors.^[8-11] Recently, organosilicon coatings performed in plasma discharges at atmospheric pressure have shown promising corrosion protection properties.^[11-13] Such treatments are suitable to replace harmful chromate process for the corrosion protection of metal parts because of their good barrier properties. However, self-healing properties provided by chromates cannot be reproduced by these organosilicon coatings. Since cerium is known to afford similar active properties than chromium,^[14] incorporation of cerium oxide compounds into the layer could be beneficial for the corrosion protection properties.^[15] Indeed, cerium oxides and cerium hydroxides are reported as cathodic inhibitors and have been also proposed as effective species for the protection of metals from corrosion^[16-18].

Moreover, it seems that the pitting auto-repair process takes place when high amounts of cerium and silicon are present^[19].

In this study, hybrid layers are deposited onto metal parts for anticorrosion purpose. AlCeO_3 particles are homogenized within liquid HMDSO. The mixture is atomized and injected into a DBD plasma discharge reactor. Coating shows incorporation of particles into ppHMDSO. Particles aggregates are measured by means of SEM in backscattering mode. This work and complementary studies were discussed in a previous article^[20].

Experimental part

Deposition plasma process

During one coating experiment, samples are threefold.

Metal surface to be coated for corrosion purpose is hot dip galvanized steel from Arcelor Mittal Dudelange (Aluzinc®, 55wt% Al – 43,3wt% Zn – 1,6wt% Si).

Glass slides are dedicated to thickness measurements by interferometry.

Polished silicon pieces (from wafers) are used for SEM analysis.

Deposition experiments are performed in a semi-dynamic DBD reactor at atmospheric pressure. The plasma set-up of the reactor was described in a previous article^[13] and is schematically described in figure 1.

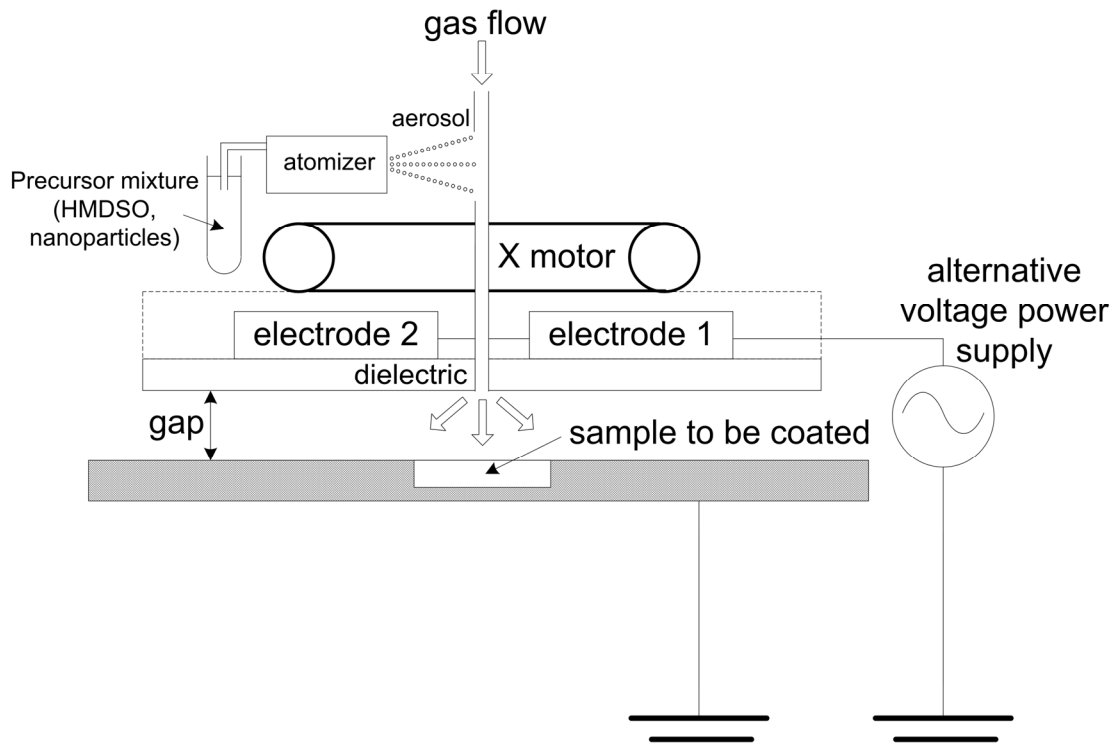


Figure 1: Schematic drawing of a semi-dynamic DBD reactor to perform plasma coatings at atmospheric pressure

Alternative voltage power supply is currently a G10S generator from AFS. Frequency is set to 1,5 kHz and voltage is a sinusoid signal as a function of time. Power is set to 480W, which corresponds to a power density over the electrodes close to $0,8 \text{ W/cm}^2$.

AlCeO_3 nanoparticles (Aldrich, 99%) is made up of some aggregates with diameter varying between a few nm (< 25nm) and 300 nm, according to SEM analysis of the AlCeO_3 powder. They are added to hexamethyldisiloxane (Aldrich, HMDSO > 98% grade). 3% in weight of nanoparticles are added to the liquid mixture. Solutions were homogenized by means of ultrasonic stirring at room temperature during 30 min.

Mixture is atomised in a TSI 3076 device. Atomisation pressure is set to 2 bar, which correspond to a precursor consumption of 2,0 mL per experiment. Atomization output is constant with time. Precursor aerosol is injected into the carrier gas. It flows into the plasma area where a plasma polymer layer is deposited onto the samples.

Experiment parameters are given in table 1.

Table 1: parameters of the three studied plasma treatment experiments

Experimental parameter	Experiment A	Experiment B
Carrier gas	N ₂ (19.4 L/min, 97%) O ₂ (0.6 L/min, 3%)	N ₂ (19.4 L/min, 97%) O ₂ (0.6 L/min, 3%)
Treatment time	136s	136s
Precursor (concentration weight)	HMDSO (100%)	HMDSO (97%) AlCeO ₃ (3%)

Electrochemical measurements

Electrochemical experiments on galvanized steel samples were performed by means of a GAMRY 600 potentiostat/galvanostat with a PC4 Controller Board.

Tests were carried out in a 35 g/L NaCl non-deaerated aqueous solution, using a three-electrode electrochemical cell, consisting of the working electrode (1 cm² of exposed area), saturated calomel electrode (SCE) as a reference and platinum grid as a counter electrode. The measurements were performed at room temperature.

The open-circuit potential (OCP) is the potential measured after a 3h stabilization period in the solution. Electrochemical impedance spectroscopy curves (EIS) are measured in a frequency range from 100 kHz down to 10 mHz, with a 10mV amplitude sinusoidal voltage at the OCP.

Self-healing coatings are characterized by their ability to still provide corrosion protection when the barrier property of the layer failed. Layer artificial failure is simulated in this study by controlled scratching of the coating. Such a scratch is deeper than the layer is thick and is performed by means of a nanoscratch (NST, CSM instruments) apparatus.

Results and discussion

All coatings appear to be visually transparent and homogeneous.

Thickness measurement

Coating thickness is estimated on glass slides from a step height measurement by means of white light interferometry^[13].

Thickness values are given in table 2.

Table 2: Thickness measurements

	Experiment A	Experiment B
Thickness values	260nm	320nm

Deposition rate slightly increases in case of nanoparticles incorporation (experiment B).

Scanning electron microscopy

Preliminary experiments performed on ppHMDSO layers filled with AlCeO₃ nanoparticles demonstrated that nanoparticles aggregation occurs. Such aggregates can be observed by SEM in backscattered electrons mode. Aggregates are embedded into the ppHMDSO matrix and, as observed in cross cut sections, they form

“protuberances” since layer is locally thicker where these aggregates lie. These results are described in details elsewhere.^[21]

Distribution of aggregates within the layer appears to be homogeneous for experiment B, as observed in figure 2.

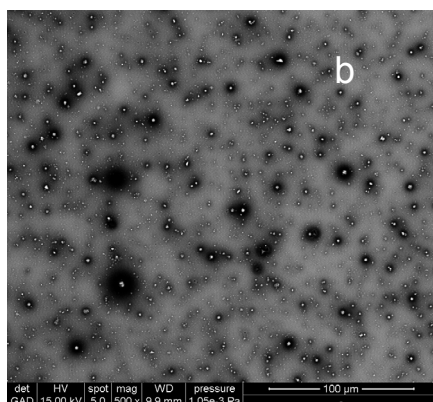


Figure 2: SEM pictures of ppHMDSO filled with AlCeO_3 particles, experiment B. Particles aggregates are observed as white dots surrounded by dark rings.

Electrochemical measurements

Bode plots obtained from EIS measurements on coated aluzinc samples are given in figure 3. Effect of cerium oxide particles incorporation and influence of these particles dispersion within ppHMDSO are tested.

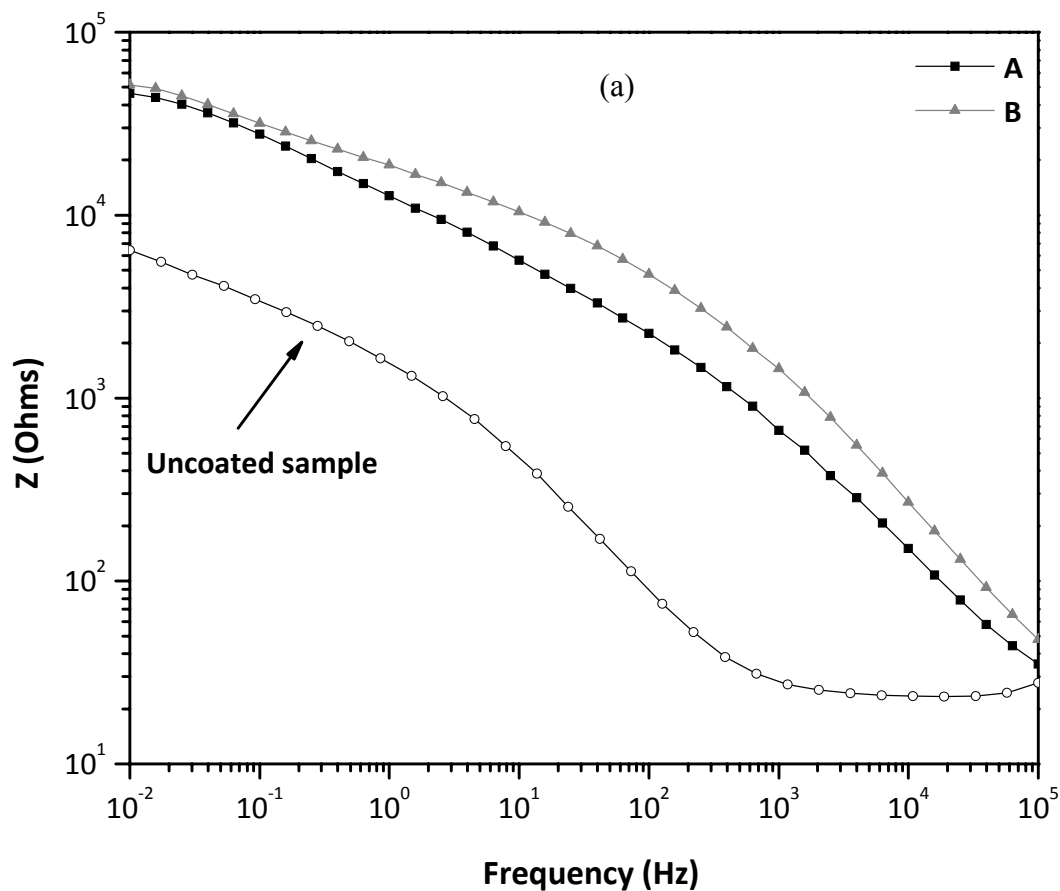


Figure 3 : Bode plots : Impedance modulus vs frequency of layers deposited on aluzinc: experiment A (sheer ppHMDSO), experiment B (ppHMDSO filled with 3% AlCeO₃). Results on bare aluzinc (uncoated sample) are given for the sake of comparison

The two (A and B) curves have similar shape and values. Both curves show that significant corrosion protection is afforded by layers A and B compared to uncoated sample. Moreover, a slight increase in the impedance value for curve B is observed at intermediate frequencies, in the range 10-100Hz. This could be interpreted as an increased corrosion resistance provided by B layer because of a self-healing effect coming from cerium incorporation.

Total corrosion resistance of samples, i.e. from coating and substrate, is given on bode plots by the impedance value at low frequency.

According to Montemor et al.^[22], cerium oxide (CeO₂) nanoparticles can act as corrosion inhibitors due to their ability to complex species responsible for the loss of passivation at the galvanized film surface. Such an effect can be expected to provide self-healing properties from aluminum-cerium oxide particles incorporation.

Self-healing properties are tested. It is expected to detect such property on samples B since they contain aluminum-cerium oxide. Zheludkevich et al.^[23] suggest to follow the impedance value at low frequency to investigate self-healing mechanism of hybrid layers. Therefore, relative variation of this value when immersion time is increased and when coating failure is simulated by scratching is recorded. Results are given in table 3.

	Sample A (only HMDSO), Impedance values (%)	Sample B (3% AlCeO ₃), impedance values (%)
After 3h immersion	100% (initial reference value)	100% (initial reference value)
After 24h immersion	80 %	92%
After 24h immersion, scratch damaging, 3h immersion	47%	36%
After 24h immersion, scratch damaging, 24h immersion	41%	54%

Table 3: Self-healing measurements

Sample A shows a strong decrease of its impedance value after scratching. Further immersion after scratching of sample A gives a further decrease of this value. This behavior is related to samples which do not provide any self-healing property.

Conclusion

Hybrid coatings based on plasma polymerised HMDSO with AlCeO₃ particles incorporation have been deposited by means of a DBD reactor onto galvanized steel samples.

Deposition rate slightly increase with nanoparticles incorporation.

Structure analysis has demonstrated that nanoparticles form aggregates which are embedded in the ppHMDSO matrix. A self-healing property, and hence an increased corrosion protection, is provided by cerium based particles incorporation.

Further investigations to improve such hybrid layers are twofold. First, particles dispersion shall be improved by means of suitable mixture and homogenisation method. Then, complementary characterization techniques shall be applied on such hybrid layers to determine more precisely the electrochemical phenomena involved in corrosion protection provided by these coatings.

Acknowledgements

The authors would like to thank Mr. Fiorucci and Mr. Kloos (Arcelor Mittal Dudelange) for constructive discussions and for providing galvanized steel samples.

This work was carried out in the frame of the TRASU project and was sponsored by the Luxembourg research funding association FNR (Fonds National de la Recherche).

References

- [1] B. R. K. Blackman, A. J. Kinloch, J. Sohn Lee, A. C. Taylor, R. Agarwal, G. Schueneman, S. Sprenger, *J. Mater. Sci.* **2007**, *42*, 7049
- [2] A. Laachachi, M. Cochez, M. Ferriol, J.M. Lopez-Cuesta, E. Leroy, *Materials Letters*, **2005**, *59*, 36
- [3] Polymer Composites, K. Friedrich, S. Fakirov, Z. Zhang, **2005**, Springer US, chapter 10 "Tribological characteristics of micro- and nanoparticle filled polymer composites"
- [4] T.P. Chou, C. Chandrasekaran, S.J. Limmer, S. Seraji, Y. Wu, M.J. Forbess, C. Nguyen, G.Z. Cao, *J. Non-Crystal Sol.* **2001**, *290*, 153.
- [5] V. Palanivel, D. Zhu, W. J. Van Ooij, *Progress in Organic Coatings* **2003**, *47*, 384.
- [6] C. Nastase, F. Nastase, A. Dumitru, M. Ionescu, I. Stamatina, *Composites*, **2005**, *36*, 481.
- [7] F. Nastase, I. Stamatina, C. Nastase, D. Mihaiescu, A. Moldovan, *Progress in Solid State Chemistry* **2006**, *34*, 191.
- [8] G. Grundmeier, M. Stratmann, *Materials and Corrosion* **1998**, *49*, 150.
- [9] E. Vassalo, A. Cremona, L. Laguardia, E. Mesto, *Surf. Coat. Technol.* **2006**, *200*, 3035.
- [10] F. Fracassi, R. d'Agostino, F. Palumbo, E. Angelini, S. Grassini, F. Rosalbino, *Surf. Coat. Technol.* **2003**, *174*, 107.
- [11] C. Petit-Etienne, M. Tatoulian, I. Mabile, E. Sutter, F. Arefi-Khonsari, *Plasma Process. Polym.* **2007**, *4*, S562.
- [12] M. Simor, A. Fiala, D. Kovacik, A. Wypkema, R. Kuipers, P. Hlidek, *Surf. Coat. Technol.* **2007**, *201*, 7802.
- [13] J. Bardón, J. Bour, H. Aubriet, D. Ruch, B. Verheyde, R. Dams, S. Paulussen, R. Rego, D. Vangeneugden, *Plasma Process. Polym.* **2007**, *4*, S445.
- [14] F. Mansfeld, *Journal of Applied Electrochemistry* **2000**, *36*, 1063.
- [15] A. S. Hamdy, *Surf. Coat. Technol.* **2006**, *200*, 3786.
- [16] M. Dabala, E. Ramous, M. Magrini, *Mat. Corros.*, **2004**, *55*, 381-390
- [17] F. Mansfeld, *J. Electrochem.*, **2000**, *36*, 1063-1069
- [18] C. B. Breslin, C. Chen, F. Mansfeld, *Corros. Sci.*, **1997**, *39*, 1061-1073
- [19] A. S. Hamdy, *Surf. Coat. Tech.*, **2006**, *200*, 3786-3792
- [20] J. Bardón, J. Bour, D. Del Frari, C. Arnoult, D. Ruch, *Plasma Process. Polym.* **2010**, *6*, S655.
- [21] D. Del Frari, J. Bour, J. Bardón, O. Buchheit, C. Arnoult, D. Ruch, *J. Nanosci. Nanotechnol.*, **2010**, *10*, 2611–2619
- [22] M.F. Montemor, M.G.S. Ferreira, *Electrochimica acta*, **2007**, *52*, 6976
- [23] M.L. Zheludkevich, K.A. Yasakau, A.C. Bastos, O.V. Karavai, M.G.S. Ferreira, *Electrochemistry Communications*, **2007**, *9*, 2622

XRF VERSUS GDOES IN STEEL INDUSTRY APPLICATIONS

Myriam Madani

OCAS N.V, Pres. J.F. Kennedylaan 3, 9060 Zelzate, Belgium, Myriam.madani@arcelormittal.com

Ocas offers among others support to ArcelorMittal production plants, both for quality control as for defectology on finished products. Another objective is to develop new products and solutions.

Both in the development of new substrates, metallic coatings, environmentally friendly passivation layers and so on, quality control of production processes and defectology, GD-OES and XRF are valuable tools.

GDOES is mainly applied for elemental depth profiling with a very high depth resolution (down to a few nm). The method is very versatile, as it can be used for bulk analysis as well. Conductive and non conductive samples as well as tube shaped samples can be analysed. The analysis is in principle qualitative, however when calibration panels are available or when sputter rates are known, quantitative information can be obtained. One of the drawbacks in using GD-OES for quantitative analysis is the necessity of matrix matched calibration panels. Furthermore, the measurements are destructive and the calibration panels need to be measured prior to each analysis.

An alternative for this application is XRF. The measurements are still matrix dependent, however not as critical as in GD-OES. Furthermore, since XRF is non destructive the calibration panels aren't consumed.

In this presentation we will discuss the specifications, advantages and drawbacks of both techniques are discussed. Their added value is illustrated based on some examples and case studies.

Description of the equipment

The XRF system consists of a 50 Watt Pd tube Energy Dispersive XRF system (Spectro Xepos). The use of a silicon drift detector allows for higher count rates and high energy resolution compared to other X-ray detection systems. It is a table top model which can be transported to industrial sites to verify layer thicknesses during industrial trials for development of new products. Other applications are bulk analysis of solid samples, liquids, powders and pellets.

Although the XRF system at OCAS is of the energy dispersive type, due to the polarizing targets the background is lower compared to regular ED systems, resulting in better detection limits (cf. picture 2).

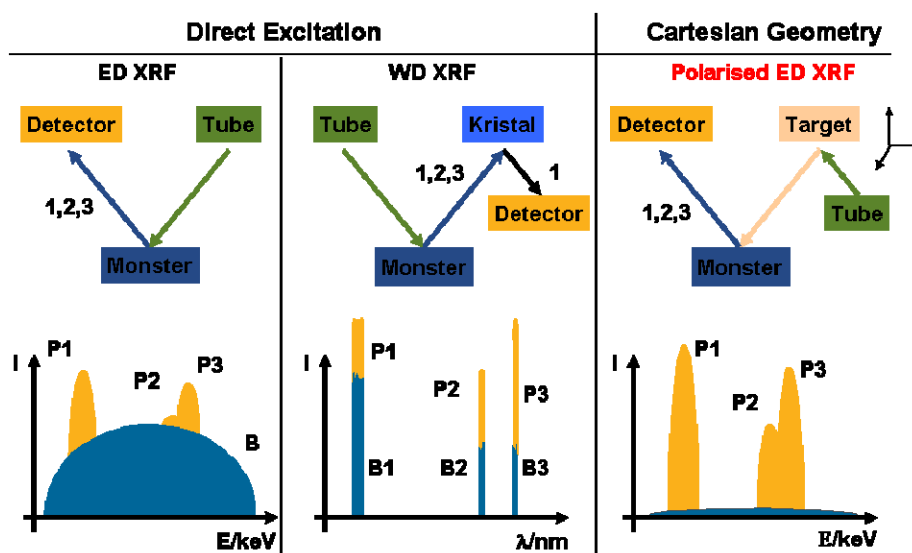
The setup is shown in picture 1. With the use of the sample tray, which can be used for samples up to 40mm diameter, 12 samples can be measured in one run (sequentially). However for smaller samples or bigger samples that can't be cut to the adequate shape, the samples can be measured directly on the shutter, allowing samples sizes from 1x4cm² up to 10x15cm².

As mentioned above one can also measure liquids and powders. For this purpose inert cups covered with prolene foil are being used.

In general the sample preparation is limited and the measurements are very fast (3 to 15 minutes depending on the application).



Picture 1: illustration of XRF system used at OCAS



Picture 2: illustration of the effect of polarised XRF measurements

The GD-OES system consists of a SPECTRUMA GDA 750, with a GRIMM type lamp and a 750mm polychromator detection system. Up to 64 emission lines can be detected with the selected PM tubes and the sensitivity of the PMT's can be adjusted. Due to the high vacuum of the polychromator vessel, elements such as N, C, S, H and P can be easily detected as well. Detection limit ranges between 0.1 and 50ppm and the depth resolution lies in the nanometer range.

A CCD camera is also installed, however hardly used.

The GD-OES can be operated in DC (direct current) or RF (radio frequency) mode, allowing analysis of conductive samples and non-conductive materials and coatings such as glass, ceramics, varnish and paint layers. In DC mode three different measurement spot sizes are available: 2.5, 4 and 8mm. In RF mode this is only 2.5 and 4mm. The shape and size limit of the samples is extended with the universal sample unit for small samples (up to 1 mm) and tubes (cf. picture 4)



Picture 4: illustration of the different sample holders in GD-OES

Applications

The main application of the XRF at OCAS is the determination of coating weights of thin and thick organic and inorganic layers. The procedure here starts with characterizing a set of calibration samples. The calibration samples can be either lab scale or produced by industrial lines. The layer is selectively removed by etching and the content of a tracer element determined with ICP. A calibration line is made based on those samples allowing a rapid quantification of unknown samples (3 minutes per sample; 12 samples in one run).

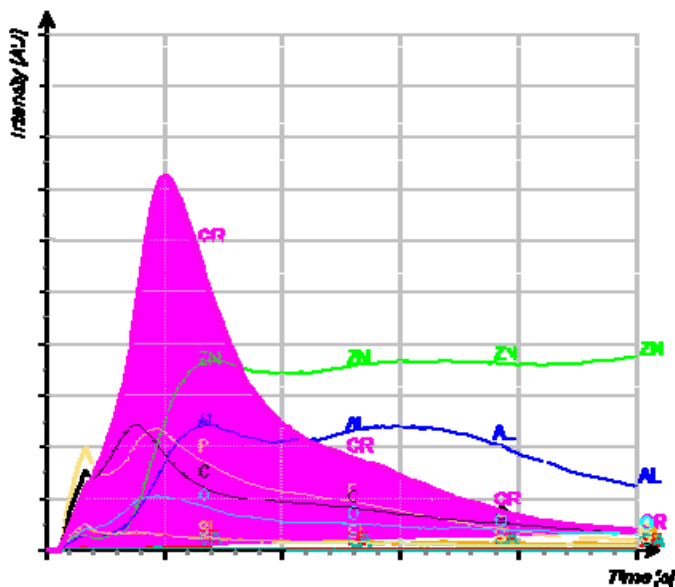
The same procedure can be applied with GD-OES. However, the main drawback here is that the calibration line has to be measured before each measurement series, which is not the case with XRF. Furthermore, the GD-OES measurements are destructive. The calibration samples are hence consumed after some time and it is not always easy to obtain a set of homogeneous calibration samples for each type of layer.

Moreover, since XRF is less matrix dependent compared to GD-OES, it is not necessary to have calibration panels for each different application. Similar type of applications can be quantified based on the same calibration line.

This advantage can be valuable from several points of view:

- there are no calibration panels available for a certain application
- there is no time for the etching procedure (a rapid answer is often needed in defectology or even in product development)
- the sample has an unknown type of layer, coating ...
- the layer isn't homogeneously soluble in acids and can hence not be measured with ICP.

With GD-OES, samples with unknown layers can only be analysed qualitatively. The added value of GD-OES measurements however is the ability of depth profiling. In multi-layer systems this allows the characterization of the different layers, determining the different elements present in each of the layers and at the interface (cf. picture 5). This can help to identify the type of layer prior to quantification with XRF. In such cases XRF and GD-OES give complementary information.



Picture 5: example of a depth profile

Another characteristic of GD-OES is that it can measure more locally compared to XRF (2.5 mm compared to 10mm in XRF). In cases of defectology it can be important to measure the coating weight in different localized areas. For example on a stained sample, the stains might be due to differences in layer thickness, or due to the presence of contamination, or it can be some kind of oxidation. With GD-OES the cause of the stains can be identified, which is not possible with our XRF system. Note that μ XRF systems are available on the market; however, the detection limits would, in most cases, not meet the requirements. Furthermore, light elements such as O and C can't be measured with the current μ XRF systems and in the case of contamination elements it wouldn't be possible to know from which layer the elements are originating.

With the universal sample holder (GD-OES) as shown above, it is also possible to measure depth profiles or relative layer thicknesses on tube shaped samples and wires.

Next to the determination of layer thicknesses the XRF system is used as a fingerprinting technique, for non destructive bulk analysis, or for fast quantification of exotic materials which can not be measured with SS-OES. The main drawback here is that elements with an atom number lower than Na can't be measured. And since the XRF measurements are performed in vacuum and not in helium the quantification of light elements such as Si is not very accurate.

Next to solid material it is also applied as a fast quantification technique for powders and liquids. In this case it is not possible to measure in vacuum for obvious reasons, so there the deviation for lighter elements will be relatively high. Keeping those limitations in mind, for the main elements, in all type of samples, a deviation of less than 5 % is obtained.

An example of a quantitative analysis of Zr in an unknown solution is shown in table 1. As can be seen, there is a good agreement with ICP-MS measurements. Certainly when taking into account that the calibration of the XRF is meant to be semi quantitative.

Note that the quantification is based on a factory calibration. In order to improve the accuracy for specific applications, own calibration lines are implemented. This of course requires adequate calibration samples.

Table 1: comparison Zr content in an unknown solution measured with XRF and ICP-MS

Solution X	g/l Zr ICP-MS	g/l XRF
batch A	2,0	1,9
batch B	1,2	1,1
REF	1,9	1,9

The GD-OES is ideal for concentration profiles analysis and surface analysis. All kinds of surface treatment processes can be monitored by analyzing the surface and near-surface areas of the material. For example the influence of heat treatment, forming, thermal oxidation and anodizing processes and so on. The depth profiles can give valuable information on the presence of segregations, enrichments or depletion of certain elements near or below the surface.

With GD-OES bulk quantification of solid materials is also possible. However, since we have a lot of analytical techniques are available which are better suited for bulk quantification (ICP-MS, ICP-OES, SS-OES, Combustion...), this is only used as a complementary alternative. The GD-OES can provide accurate quantitative information for very demanding applications but this gives only an added value where no alternative technique for rapid analysis exists.

For coated materials it can be summarized that the XRF is mainly used for quantification purposes, whereas the GD-OES gives added information in depth (chemical composition of the different layers and the interfaces). Furthermore, with GD-OES, more local information can be obtained which is essential in defectology.

In metal characterization XRF is useful for non destructive quantification, fingerprinting and rapid quantification of exotic materials. In this domain GD-OES is more applicable for concentration profiles analysis and surface analysis.

IN SITU XPS FOR SURFACE SPECIATION DURING ANNEALING OF STEELS

X. Vanden Eynde, L. Bordignon

*Centre de Recherches Métallurgiques
Domaine Universitaire du Sart-Tilman, P59
Avenue du Bois Saint-Jean, 2
B 4000 Liège (Belgium)*

ABSTRACT

Surface segregation during recrystallisation annealing is related to the oxidation potential present in the furnace atmospheres. The qualification of such surface segregation is important for the following steps of the process, especially the hot-dip galvanisation. X-ray photoelectron spectroscopy (XPS) is able to differentiate the chemical states at the uppermost surface. The annealing furnace connected to the spectrometer allows us to finely determine the chemistry of the surfaces after annealing. Its direct connection to the XPS spectrometer allows us to analyse the surface and to limit the artefacts due to air oxidation. The surface segregation of Mn and Si is studied for TRIP-Si steel grade as a function of the maximum temperature and oxidation potential. At low oxidation potential, the silica formation is favoured. By contrast, at higher oxidation potential, the manganese-silicon oxide formation is observed. The nitride/oxide formation at surfaces of boron bearing IF steel is followed as a function of the oxidation potential and the atmosphere composition. The interpretation of the oxide/nitride formation based on XPS in-situ experiments is discussed

KEYWORDS

XPS, surface segregation, boron, silicon, TRIP

INTRODUCTION

Boron is added in IF steel grades for several reasons. In rephosphorised IF steel, added boron prevents P grain boundary segregation, which induces secondary cold-work embrittlement (SCWE).ⁱ Unfortunately too high B concentration is not effective in preventing SCWE.^{ii,iii,iv} Moreover, Boron has a strong effect on the austenite-ferrite transformation (kinetics and microstructure changes) and, thus, depending on the process conditions, affects the mechanical and processing properties.^v Boron exhibits other metallurgical properties in carbon steels but this is not the topic of our contribution.^{vi,vii} In a recent ECSC-RFCS project, the importance of boron in the external selective oxidation has been enlightened.^{viii} With very small boron content (in ppmwt. range), impressive external selective boron oxidation and boron nitriding have been observed. This contribution gives important details on the phenomena taking place for boron surface annealing under recrystallisation annealing and their effects on galvanisation are discussed.

To improve mechanical properties mainly for automotive applications, new High strength steel grades are developed by the industry. In this context, it is well known that, unfortunately, steels containing significant amount of silicon are difficult to hot dip galvanised. Indeed, external selective oxidation of silicon in silicon dioxide hampers the adequate reactivity between the annealed substrate and the liquid zinc (Zn with 0.2-0.3%Al at 460°C). Various alternative methodologies have been developed to adequately galvanise such steel strips (metallic pre-deposits, pre-oxidation/reduction, pre-oxidation/maturation ...).^{ix,x,xi,xii} This contribution will give some insights in the evolution of the surface segregation during heating and annealing.

EXPERIMENTAL SECTION

Two steel grades are presented in this study. Their respective chemistry can be summarized as follows (wt%):

- TRIP-Si : 0.154C-1.64Mn-1.4Si-0.07P and
- IF-B 0.002C-0.150Mn-0.011Si-0.0058P-0.040Al-0.068Ti-0.0015B

XPS analyses are performed in a PHI-Quantum 2000 spectrometer from Physical Electronics directly connected to the UHV annealing preparation chamber, so that undesired sample transfer-associated surface contamination be always avoided. The spectrometer is characterised by a monochromatised Al K_{α} primary X-ray beam and a photoelectron takeoff angle of $\pi/4$ against the sample normal direction. Analysis quantification was based on sensitivity coefficients proposed by the equipment manufacturer. Charge effects are systematically compensated by broad beams of low energy electrons and argon ions.

A PHI-680 Scanning Auger electron microprobe equipped with a Field Emission Gun (SAM-FEG) from Physical Electronics is used to establish element distribution maps with a lateral analysis resolution of 20 nm. Primary electron beam energy is fixed at 10 keV for secondary electron imaging and Auger mapping. It is also worth mentioning here that all the element distribution maps commented on below were established after sputtering the first 0.1 nm of material from the specimen surface.

RESULTS AND DISCUSSION

To investigate the selective oxidation phenomena of these steels, the water vapour content of the atmosphere has been varied between -60 to 10°C . The surface chemistry is analysed in-situ with the XPS spectrometer. The core-level spectra are displayed in Figure 1 and quantified in the following graph (Figure 2).

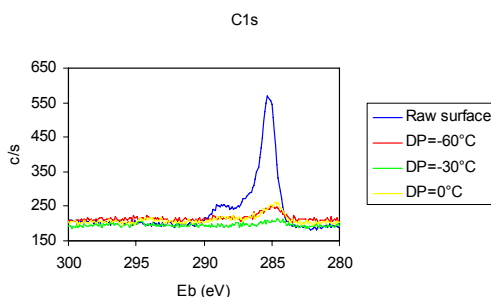
Except the raw surface, the iron peak (Fe2p spectral window, Figure 1) shows characteristic metallic peak shape and binding energy {Fe2p $_{3/2}$; BE= 706.9 eV}. The Mn2p manganese signal appears only after annealing. At very low dew point (DP= -60°C), a slight metallic peak can be discerned {Mn2p $_{3/2}$; BE= 639 eV}. In all the other cases, the manganese signals are quite similar in shape but vary in intensity. Niobium oxide shows distinct characteristic peaks for its two oxidation state: {Nb3d $_{5/2}$ for NbO; BE= 202.8-204.7 eV} and {Nb3d $_{5/2}$ for Nb $_2$ O $_5$; BE= 207.5eV} or as nitride species {Nb3d $_{5/2}$ for NbN; BE= 203.7 eV}.^{xiii} At DP = -60°C , the niobium soaring at the sample surface is observed as NbO or NbN. By contrast, when water vapour is added in the atmosphere, the signal is weaker but it seems more characteristic of Nb $_2$ O $_5$. Phosphorus shows two intense photoelectron peaks, P2p and P2s at BE= \sim 130 and \sim 188 eV, respectively while boron oxide exhibit one single peak, {B1s; BE= \sim 189eV}. Therefore, when boron and phosphorus are present simultaneously, an interference is possible between the P2s and B1s. To overcome this problem, the ratio of the phosphorus peaks has been determined on a boron free steel. The intensity due to the P2s photoelectrons has been subtracted from the intensity of the peak observed at the B1s characteristic binding energy. In Figure 1, the B1s core-level spectrum for the 1X14 sample annealed in N $_2$ -5%H $_2$ with DP= $+10^{\circ}\text{C}$, is indeed only due to the P2s peak. The boron core-level spectra show different component as a function of the dew point in the annealing atmosphere. When the dew point is above -60°C , only one component is observed and is related to B $_2$ O $_3$ {BE= 192-193.3 eV}.^{xiii} At DP = -60°C , two components are detected: an oxide one at BE=192-193.3 eV and another with lower binding energy. The boron nitride binding energy is fixed at BE= 190.5 eV in the literature. In another reference^{xiv}, the binding energies for an oxynitride boron compound BN-O is about 192 eV, which seems in agreement with the observed component. This oxynitride boron can be directly related to the nitrogen peak at {N1s; BE= 399eV}. Its binding energy is characteristic of nitride species.^{xiii} This specific point (DP= -60°C) will be discussed in more details in the following section. The boron peak width after the annealing at DP= -60°C also confirms that two boron environments are present. Aluminium is significantly observed after annealing in a very dry atmosphere (dew point about or below -60°C). This aluminium appearing at the top surface is mostly located at the grain boundaries. Significant peaks

are also observed in the S2p and Zn2p3 spectra. These elements are assumed to come mainly from the cold-rolling process as it has been determined in another ECSC project.^{xv} O1s oxygen signal is quite complex owing to the fact that all the oxide species give their own components. The intense peak at BE= 530 eV is directly related to the iron oxide. This component disappears when annealing is applied. The other peaks present in the raw surface spectrum could be related to the iron hydroxyde and other oxygen containing hydrocarbon contamination as already indicated in the C1s spectrum. At high dew point, one component is observed and could be related to the manganese and phosphorus oxides. By contrast, at intermediate dew points, another component at higher binding energy makes the O1s peak wider. This component is clearly related to both boron and aluminium oxides. In the same spectral window, the two peaks surrounding the oxygen one are related to the two energy levels of the 3d orbitals of antimony (Sb3d 5/2 and Sb3d 3/2). This element is present in its metallic state in all our in-situ annealing experiments.

In Figure 2, the different elements present at the strip surface are quantitatively plotted as a function of the dew point. Manganese surface segregation exhibits a maximum at a dew point between -30 to -10°C. R.M. Hudson et al. also determined such maximum at DP~-40°C in binary Fe-Mn alloys.^{xvi} On the contrary, the boron signal decreases with the dew point increase whatever the species created at the strip surface. Therefore the boron segregation is changed from external to internal by the water vapour increase in the N₂-5%H₂ atmosphere. At DP=+10°C (1.2 vol%H₂O in N₂-5%H₂), no more boron (signal below the detection limit) reaches the surface. The metallic iron signal increases with the enhancement of the internal oxidation phenomena. At high dew point, the boron external segregation is replaced by phosphorus one (from DP=-10°C). The sulphur content is almost similar for all the surfaces (about 2-3 at%) as well as sodium in the 1 at.% range.

The boron-manganese selective oxides are mainly located at the grain boundaries and exhibit needle shape (**Figure 3**). Nodules can also be observed but at the ferrite grain surface. Such surface with major metallic iron content in the vicinity of the surface will obviously be favourable for hot dip galvanisation.

In Figure 4, SEM and SAM mappings of the 3X14 sample (1X14 with complementary thickness reduction, 50%, by cold-rolling) annealed in N₂-5%H₂ with DP=-30°C show another surface morphology. Acicular boron-manganese oxides are still observed but boron oxide film has been locally formed. The boron covers homogeneously some of the grains. Such film can be directly related to the higher amount of boron oxide, ~22at%, detected in the XPS simulation (Figure 2 and Figure 5). It seems quite obvious that such film can strongly hamper the zinc wettability. The boron films are surrounded by manganese oxides located at the grain boundaries. It seems that there is a correlation between the acicular manganese oxides and these boron films. Indeed, the relative concentration in boron and manganese could influence the formation mechanisms of the oxide crystals. This could be related to the preferential growth along cristalline axis of the mixed oxides.



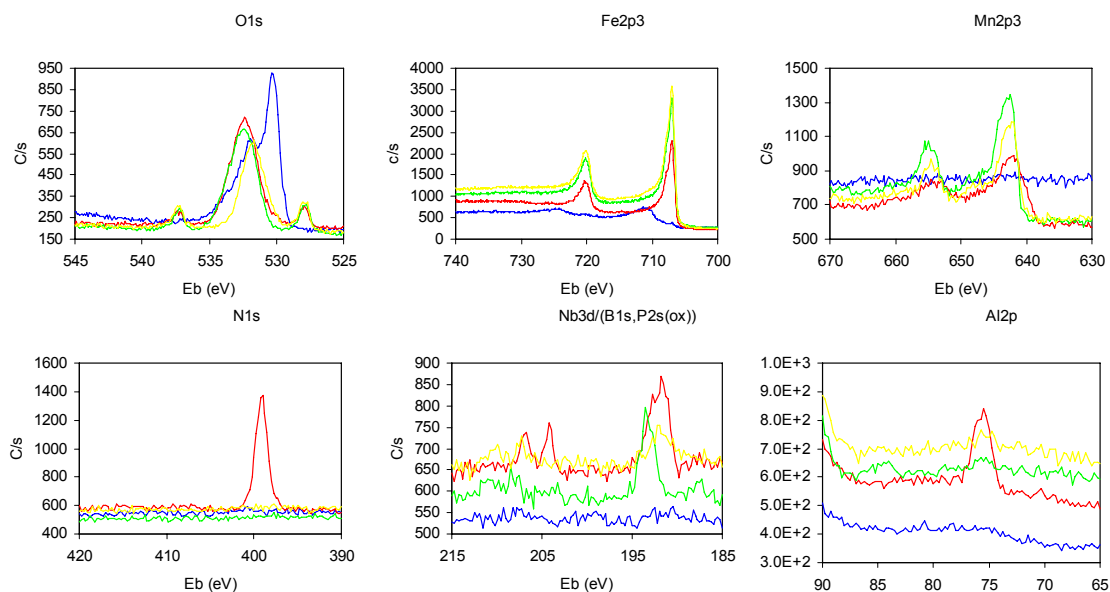


Figure 1: XPS core-level spectra of 1X14 sample annealed in $N_2-5\%H_2$ at $800^\circ C$ with various dew points. The initial acetone degreased surface is given as a reference state. Other elements such as Ca, Na and As were also detected.

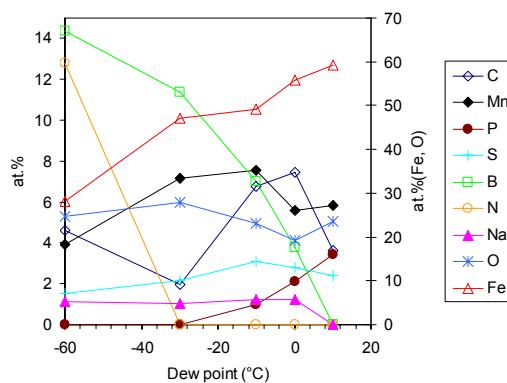


Figure 2: 1X14 annealed at $800^\circ C$ in $N_2-5\%H_2$ with various dew points for 60 seconds.

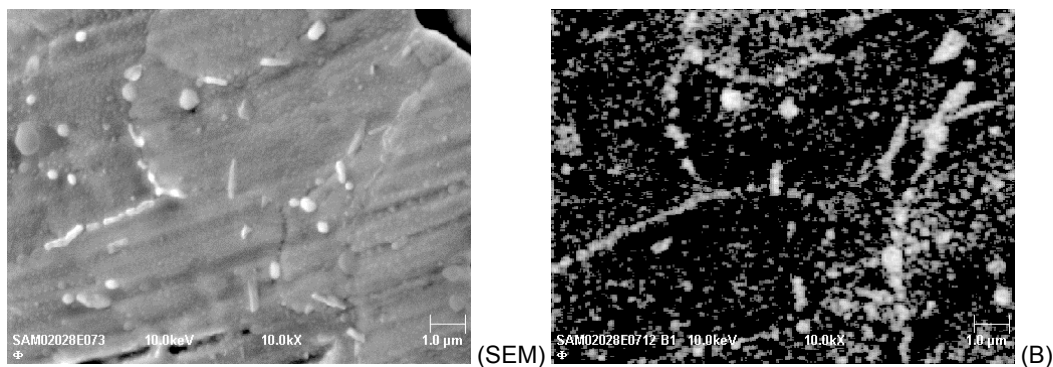


Figure 3: SAM mappings of the sample surface annealed at $800^\circ C$ in $N_2-5\%H_2$ with $DP=-30^\circ C$ with 60 seconds of soaking.

The comparison between 1X14 and 3X14 shows that for similar bulk concentration, an additional preparation step can induce very different surface state after annealing. Nevertheless, when the dew point is increased in the annealing atmosphere of the 3X14 (Figure 5), the external oxidation trends are similar to what is observed for the 1X14 (Figure 2). Meanwhile, the magnitude of the boron selective oxidation is much higher, by a factor of two, for the 3X14 than for the 1X14. On the contrary, the manganese selective oxidation is much less affected. As a matter of fact, the obvious differences at $DP=-30^\circ C$ between the 3X14 and 1X14 samples disappear when the annealing is performed in a more humid atmosphere, $DP=+10^\circ C$ (Figure 2 and Figure 5).

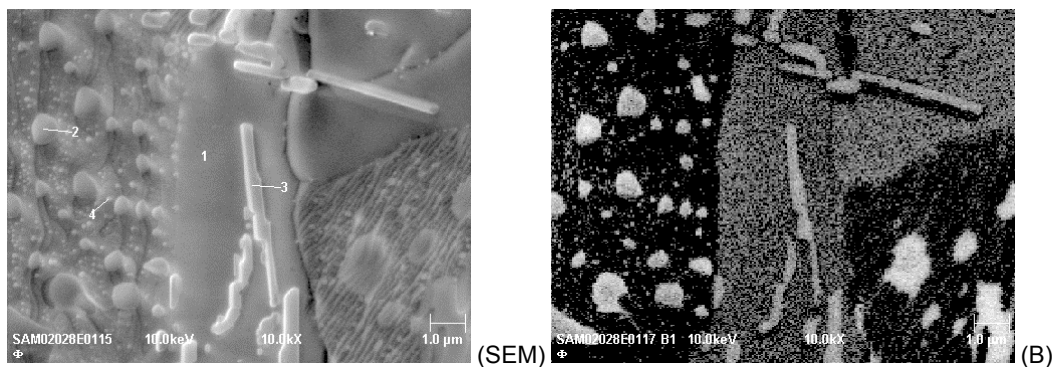


Figure 4: SEM image and SAM mappings of the 3X14 sample annealed at 820°C in N₂-5%H₂ at DP=-30°C.

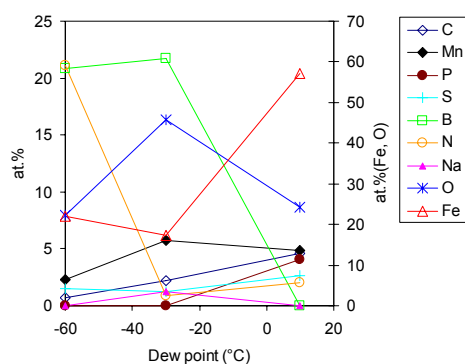


Figure 5: 3X14 annealed at 800°C in N₂-5%H₂ with various dew points for 60 seconds.

The surface states after annealing of the 1X14 and 3X14 are given in Table 1. With no additional pre-treatment (called “As received” in Table 1), these two sample surfaces are quite dissimilar meanwhile the base steel grade is exactly the same. When the samples are polished, no more influence of the thickness reduction on the external selective oxidation is discerned. Therefore, as expected, we can assume that the strain-hardening has no significant influence on the amount of external selective oxidation. The most affected elements are boron, iron and oxygen. It seems that the external selective manganese oxidation is less affected.

Table 1: *in-situ* XPS analysis of samples annealed at 820°C in N₂-5%H₂ with dew point at -30°C.

		C	N	Mn	Si	Al	P	S	B	Na	Nb	Sb	Sn	As	O	Fe
1X14	As received	1.9		7.2				2.2	11	1		0.4	0.1	0.73	27.9	47.2
	As received /polished	0.9		5.8	1.4			1.8	21	0.4		0.05		0.08	44.3	24.4
3X14*	As received	2.2	0.9	5.7	1.9	1.3		1.3	22	1.3		0.08			45.7	17.4
	As received /polished			6.9	1.3			1.1	21		0.5	0.07			48.4	21

*3X14 is the cold-rolled 1X14 steel sheet (50% thickness reduction).

One question risen from previous experiments described previously is: “how could we explain the boron oxynitride formation at very low dew points?”. Two hypotheses are proposed. The first possibility is the influence of steel soluble nitrogen to form the boron nitride film. The second hypothesis was the nitrogen pick-up in the nitrogen-hydrogen atmosphere.

The 3X14 steel grade is chosen owing to the fact that strong surface selective nitrogenation/oxidation has already been observed after annealing with this steel grade (Figure 1 and Figure 2). In order to investigate the influence

of nitrogen in the annealing atmosphere, it has been exchanged with argon. In a preliminary step, no water vapour was added to the gas mixture (maximal nitrogenation conditions). This means a residual water vapour content, which exhibits a dew point below -60°C . Afterwards, higher dew point (-30°C) has been tested as well. This study has been, exclusively, performed with the *in-situ* XPS preparation chamber.

In Figure 6, the XPS spectra of 3X14 samples annealed in three different gas mixtures are displayed. No water vapour is added to the feeding gas and thus, the dew point is below -60°C . The interpretations of the peak positions have been deeply presented in previous sections. In all conditions, only metallic iron appears at the free surface, even under free hydrogen annealing. The samples annealed in both nitrogen atmospheres exhibit the lower iron peak intensities. Aluminium signal is intense in all conditions. This segregation is related to the residual of solute aluminium present in the steel, which segregates mainly through the grain boundaries and is oxidised at this place at the free surface. This selective oxidation is stronger under Ar-10%H₂ or N₂-10%H₂ annealing than N₂. This is due to the increase of the oxygen potential.^{xvii} Manganese oxide is detected at all surfaces and is more intense for the Ar-10%H₂ annealing. Pure nitrogen annealing exhibits more metallic manganese than nitrogen-hydrogen atmosphere. Niobium oxide or nitride (NbO-NbN) is also detected. Boron and nitrogen signals are intense for N₂ and N₂-10%H₂ annealing atmospheres. Boron nitride or oxynitride has been formed in these two specific gases. On the contrary, nitrogen peak is absent when the sample is annealed in Ar-10%H₂. Therefore no boron nitriding occurs when nitrogen is absent from the annealing gas but boron selective oxidation still occurs. A titanium signal is observed only for the Ar-10%H₂ annealing.

The background on the iron peaks indicates that such boron nitride appears as films covering the surface of the sample. It has been shown that, thank to such film, no atmosphere oxidation can be observed at the annealed strip surface.

Similar heat treatments have been applied in atmospheres with dew point fixed at -30°C . In these conditions, we impose the competition between selective nitriding and oxidation. The most important point is that no nitrogen peak is present and thus, the nitriding reactions of the alloying elements are completely suppressed. In this case, the surfaces exhibit similar manganese selective oxidation. Nevertheless, the iron signal is higher for Ar-10%H₂ than for N₂-10%H₂. Boron peaks show the opposite behaviour. The niobium is detected in its higher oxidation state (Nb₂O₅) as it was already mentioned in the previous paragraph.

Table 2: Quantitative surface analysis of 3X14 annealed at 820°C for 60 seconds in various atmosphere conditions.

Gas mixture	Dew point (°C)	C	N	Mn	Al	S	Ti	B	Nb	O	Fe
Ar-10%H ₂	-60	2.72	0.7	3.18	15	1.5	1.3	3.3	0.42	37	33
Ar-10%H ₂	-30	2.15	0	7.39	1.5	2	0	11	0.16	31	44
N ₂ -10%H ₂	-60	2.13	25	1.14	8.9	0.8	0	24	0.14	23	14
N ₂ -10%H ₂	-30	0.89	0	6.91	2.9	2	0	14	0.35	35	34
N ₂	-60	1.37	20.9	1.75	7.2	0.8	0	24	0.1	26	17

From these experiments, it can be concluded that the observed nitriding effects at DP= -60°C can occur in nitrogen-hydrogen annealing atmosphere. Several elements seem to react with the nitrogen gas, aluminium and boron. Meanwhile, if the dew point is increased, this effect of nitrogen on the selective surface segregation is strongly decreased.

Nitrogen of iron in N₂ atmosphere has already been described in the literature.^{xviii} Such nitrogenation decreases with the increase of the pH₂O/pH₂ ratio or the dew point increase at constant hydrogen content. The amount of

dissolved nitrogen in pure iron is 42 wt. ppm in α -iron and 250 wt. ppm in γ -iron at 890-1000°C. Such nitrogen is dissolved in the iron substrate according the reversible reaction $N_{2(gas)} = 2N_{(diss.)}$. We could assume that these nitrogen atoms in solid solution remain close to the surface and will reacts to form the most stable compounds. When oxygen activity in the gas is increased, the nitride formation is no more the most favourable path and external/internal selective oxidations are the main phenomena.

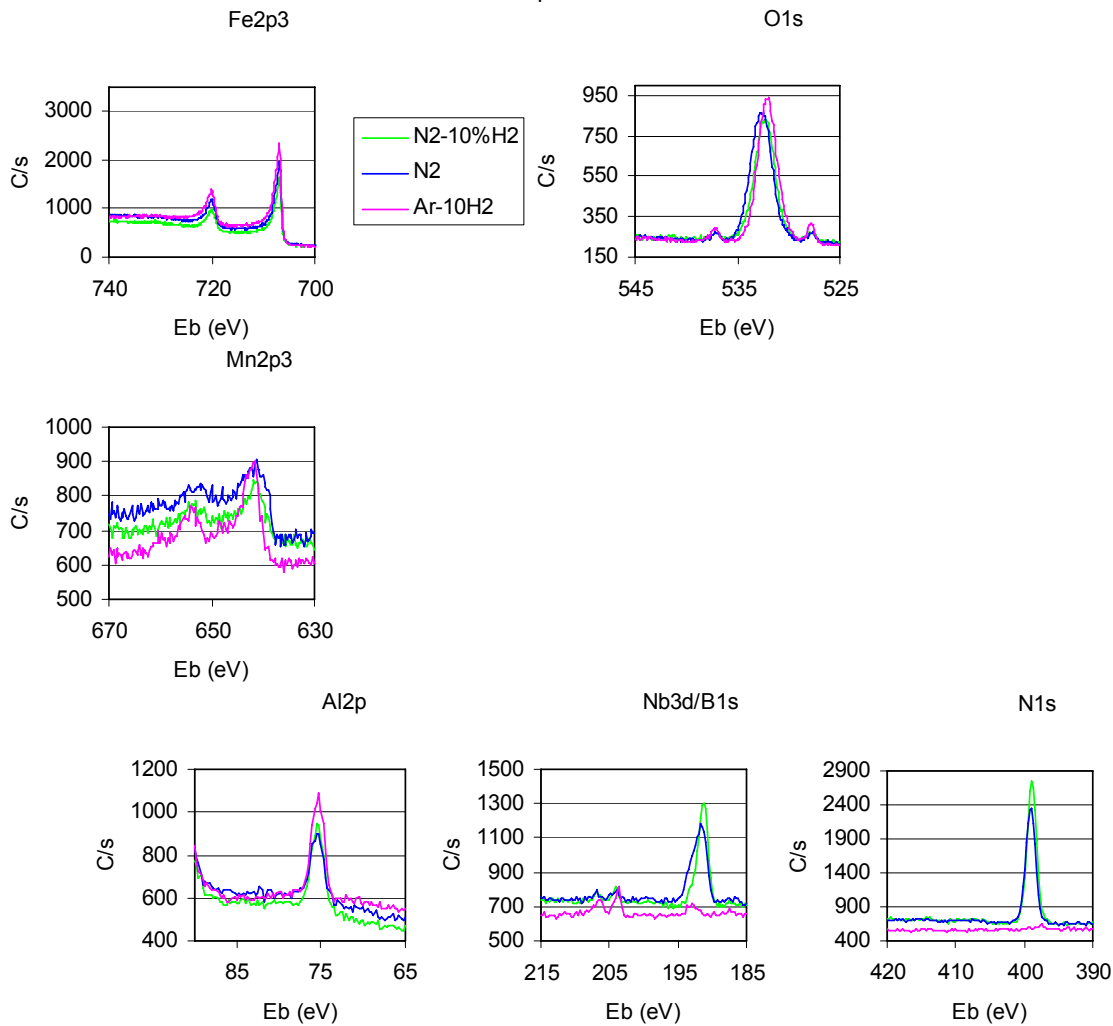


Figure 6: XPS surface analyses of 3X14 annealed at 820°C in various atmospheres with fixed dew point (DP=-60°C).

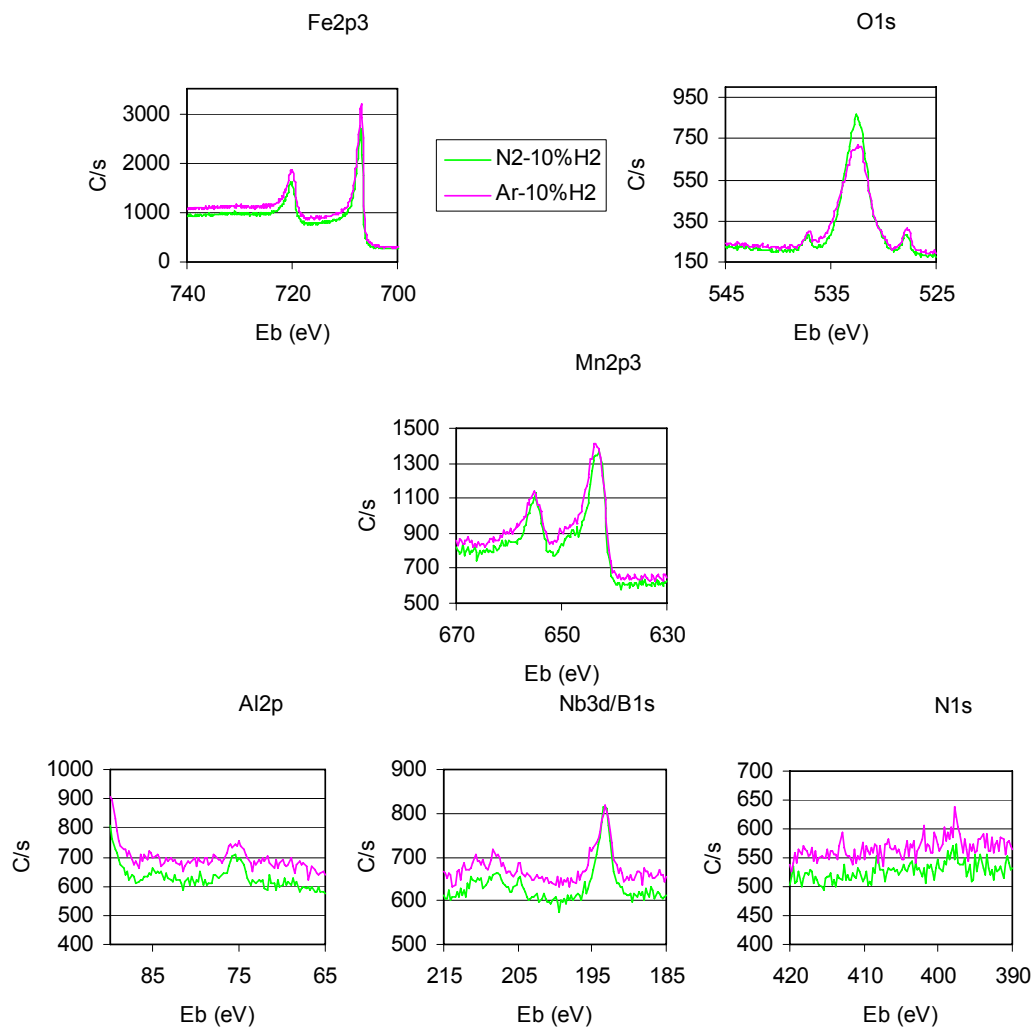


Figure 7: XPS surface analyses of 3X14 annealed at 820°C in various atmospheres with fixed dew point (DP=-30°C).

The last section is dedicated to the surface segregation phenomena taking place during the heating and soaking stages of the inter-critical annealing cycle for TRIP-Si. Heating speed of 10°C/s has been chosen.

In a classical annealing atmosphere composed of N₂-5%H₂ with DP=-30°C, the strip surface evolves with the maximum of temperature reached in the heating ramp (10°C/s) as shown by the XPS surface spectra in **Figure 8**. The iron is metallic in nature at all tested temperatures (500-1050°C). Iron signal decreases with the temperature increase. Manganese present as an oxide remains almost constant or slightly decreases above 700°C. No clear chemical shift can be observed for the manganese peak meaning that its oxidation state is not drastically changed within the experimental conditions. On the contrary, an additional peak is observed in the silicon spectra when the sample is heated above 750°C (**Figure 8**). The only component below 750°C is characteristic of a mixed oxide presumably Mn₂SiO₄. The other component above 750°C is related to silicon dioxide. The quantitative interpretation of the XPS spectra is given in **Figure 9**. The increase of the selective oxidation at the free surface obviously decreases the metallic iron content. Moreover, the silicon dioxide component is detected and increases from 750 to 1050°C at the expense of the manganese and iron contents.

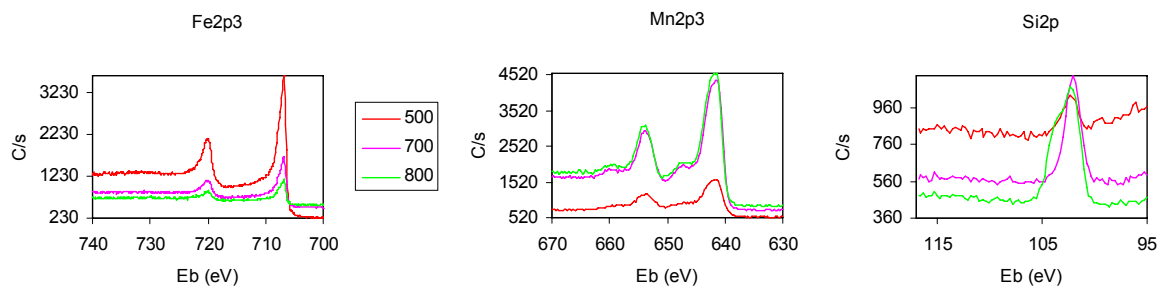


Figure 8: TRIP-Si annealed 1 second in N₂-5%H₂ DP=-30°C at various temperatures.

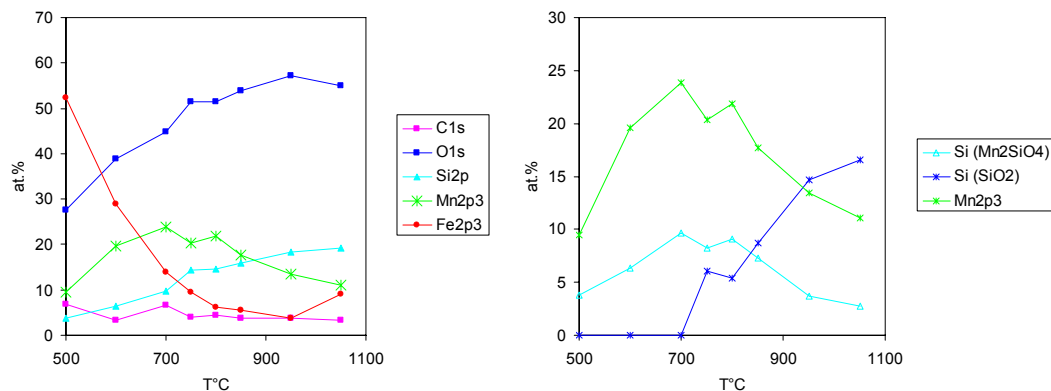


Figure 9: XPS quantitative analysis of the short annealing cycles from 500 to 1050°C in N₂-5%H₂ DP=-30°C.

Similar experiments have been performed at higher dew points, 0 and 13°C (**Figure 10** and **Figure 11**). At DP of 0°C, the iron is mainly metallic at low temperature but at higher temperature an oxidised iron component appears as well as a silicon dioxide component (**Figure 10**). The XPS quantitative analyses show a similar trend than at DP=-30°C. The decomposition of the iron XPS peak clearly indicates an obvious transition at about 700-750°C from mainly metallic iron to a mixture with oxidised iron. This oxidised iron is assumed to be part of a mixed oxide, presumably fayalite. Conversely to lower DP, at DP+13°C, silicon dioxide is not formed but oxidised iron peak is clearly evidenced (**Figure 12**). At heating speed of 10°C/s, there exist a threshold between 700-750°C at which the silicon segregation and selective oxide formation are enhanced. The silicon oxide type is temperature and dew point dependent. At low temperatures (below 700°C) only mixed manganese-silicon oxide are observed whatever the used DP. At higher temperatures, the silicon oxide formed is clearly dependent on the atmosphere DP, silicon dioxide/manganese-silicon oxide or fayalite/manganese-silicon oxide for DP=-30°C or +13°C, respectively.

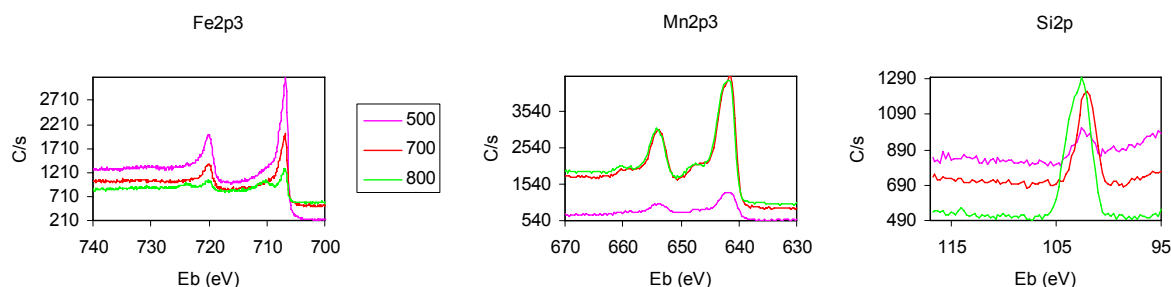


Figure 10: TRIP-Si annealed 1 second in N₂-5%H₂ DP=0°C at various temperatures.

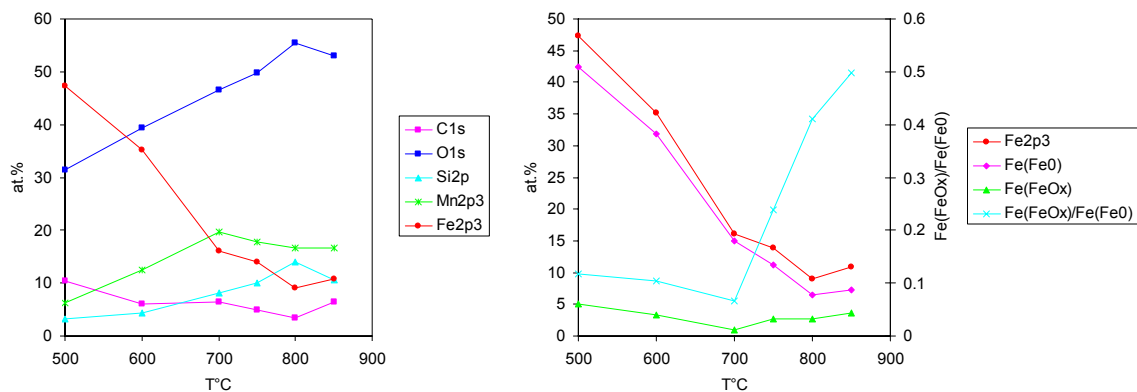


Figure 11: XPS quantitative analysis of the short annealing cycles from 500 to 850°C in N₂-5%H₂ DP=0°C.

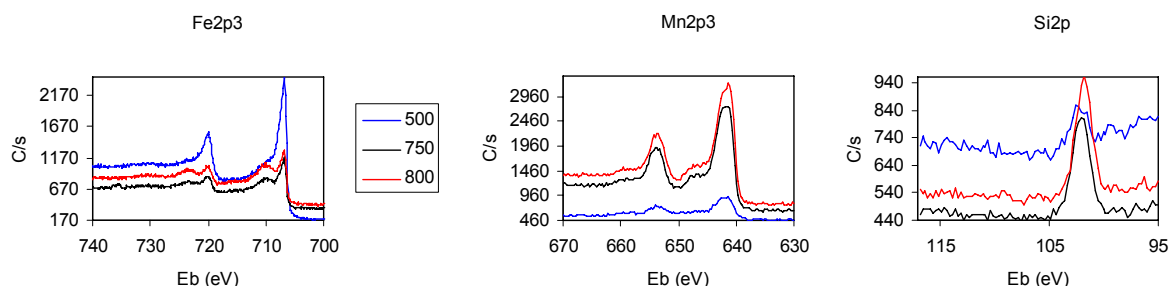


Figure 12: TRIP-Si annealed 1 second in N₂-5%H₂ DP=13°C at various temperatures.

In order to establish if the surface is at equilibrium in the heating ramp, several simulations have been undertaken at fixed temperatures, 700 and 800°C but longer soaking times (up to 6000 seconds), with heating ramp fixed at 10°C/s.

At 700°C, no silicon dioxide is observed after 1 and 10 seconds of soaking time. The silicon dioxide formation after 60 and 600 seconds appears at the expense of the metallic iron. Up to a certain soaking time, a balance between silicon and manganese exists which is in favour of manganese. Therefore mixed silicon-manganese oxide is favoured compared to silicon dioxide. The selective oxidation growth at the free surface implies a loss of metallic iron for the galvanisation reaction.

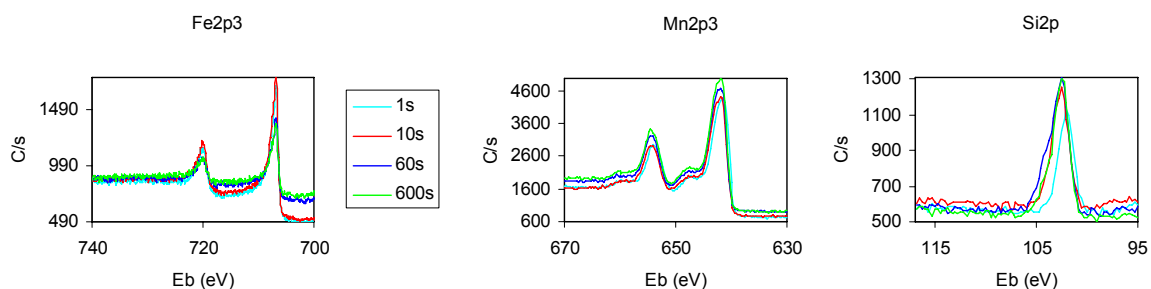


Figure 13: TRIP-Si annealed in N₂-5%H₂ DP=-30°C at 700°C for increasing times.

As mentioned earlier, silicon dioxide appears already at the early stage of the soaking period at 800°C in N₂-5%H₂ with DP=-30°C (**Figure 8** and **Figure 14**). Significant silicon dioxide component in Si2p XPS spectrum increases from 1 to 10 seconds of soaking but it has disappeared after 6000 seconds at 800°C (**Figure 16**). We can assume that the silicon dioxide film rearrange in order to form the more stable mixed manganese-silicon oxide. These last oxides are much less covering the steel substrate as shown by the increased amount of metallic iron at the free surface for long soaking time (**Figure 15**).

CONCLUSIONS

In-situ XPS allows to observe and determine the amounts of species present at surfaces as well as the bonding types, the elemental speciation. The two examples presented are representative of industrial research programs. Thanks to the in-situ capabilities, these surface analyses are almost free artefact for the interpretation of the chemical shift observed in XPS.

ACKNOWLEDGMENTS

P. Bastin and P. Henkinet are gratefully acknowledged for their technical assistance in the course of these studies.

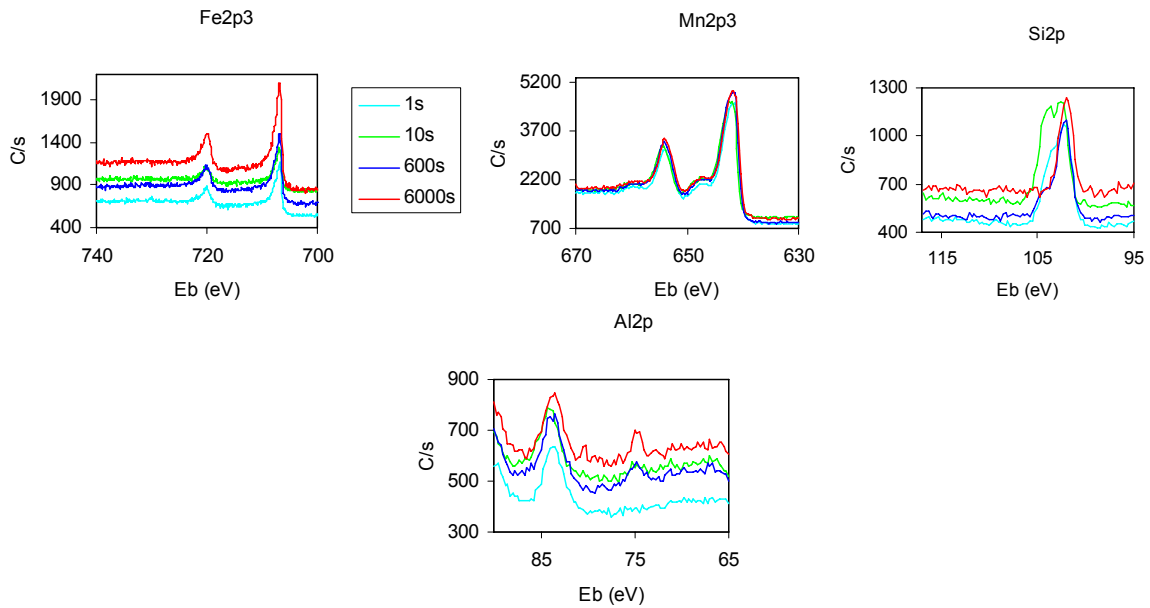


Figure 14: TRIP-Si annealed in N₂-5%H₂ DP=-30°C at 800°C for increasing times.

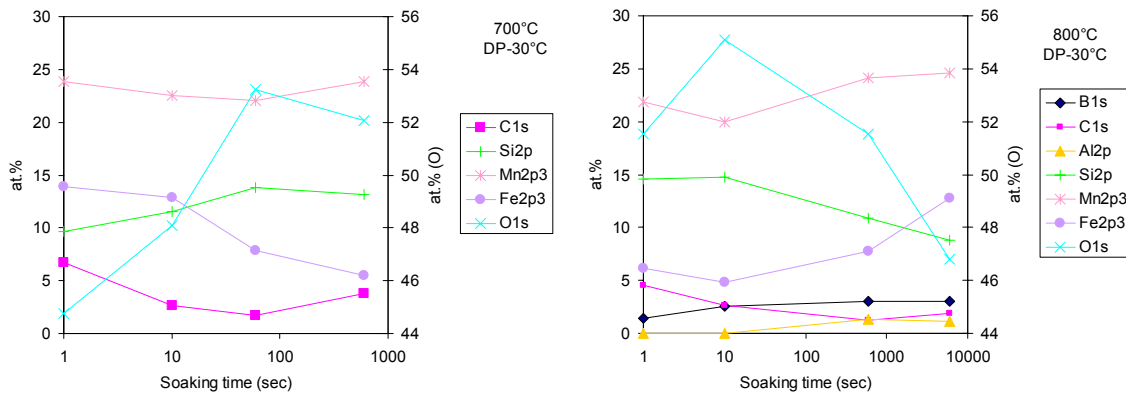


Figure 15: Quantitative surface analysis of XPS spectra of TRIP Si annealing at 700 and 800°C for increasing soaking times in N₂-5%H₂ with DP= -30°C.

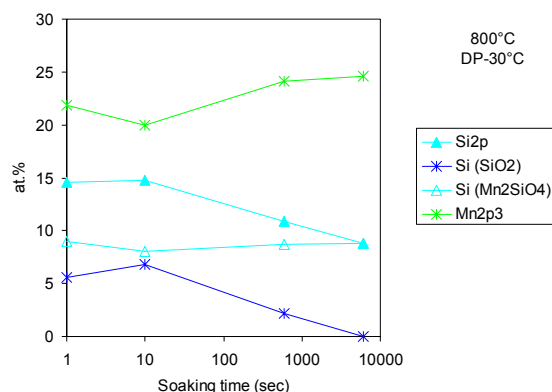


Figure 16: Si2p peak decomposition for TRIP-Si annealed in $N_2-5\%H_2$ with DP = $-30^\circ C$ at $800^\circ C$.

REFERENCES

- ⁱ J. Neutjens, J.C. Herman, V. Leroy, In "Modern LC and ULC Sheet Steels for Cold Forming: Processing and Properties" Conference book ed. by W. Bleck, RWTH: Aachen (1998) 591-602.
- ⁱⁱ T. Mega, J.-I. Shimomura, E. Yasuhura, *Mat. Trans. JIM* **36** (1995) 1206-1213.
- ⁱⁱⁱ T. Mega, J.-I. Shimomura, K. Seto, *Mat. Trans. JIM* **37/3** (1996) 323-329.
- ^{iv} C.M. Liu, T. Nagoya, K. Abiko, H. Kimura, *Met. Trans. A* **23A** (1992) 263-269.
- ^v M. Baetens, D. Vanderschueren, J. Dilewijns, In "Modern LC and ULC Sheet Steels for Cold Forming: Processing and Properties" Conference book ed. by W. Bleck, RWTH: Aachen (1998) 579-590.
- ^{vi} C. Mesplont, S. Vandeputte, B.C. De Cooman, "Dilatometric study on the effect of soluble boron on the continuous and isothermal austenite decomposition in 0.15C-1.6Mn steel" *Z. Metallkd.* **93/11** (2002) 1108-1118.
- ^{vii} X.M. Wang, X.L. He, *ISIJ Int.* **42** (2002) S38-S46.
- ^{viii} X. Vanden Eynde, L. Bordinon, ECSC technical report n°4.
- ^{ix} L. Bordinon, X. Vanden Eynde, A. Hennion, Influence of strip surface quality during hot dip galvanising and application to HSS, ECSC Steel Workshop, Galvanizing of Steel Strip, Luxembourg, February 27-28, 2002.
- ^x L. Bordinon, G. Angeli, H. Bolt, R. Hekkens, W. Maschek, J. Paavilainen, X. Vanden Eynde, Enhanced hot dip galvanising by controlled oxidation in the annealing furnace, 44th MWSP Conference, Orlando, September 2002.
- ^{xi} X. Vanden Eynde, J.P. Servais, M. Lamberigts, *Surface and Interface Analysis*, **35** (2003) 1004-1014.
- ^{xii} X. Vanden Eynde, L. Bordinon, M. Lamberigts, Galvatech'04 conference proceedings, AIST, ed. by R.E. Ashburn, M.A. Baker (2004) 361.
- ^{xiii} J.F. Moulder, W.F. Stickle, P.E. Sobol, K.D. Bomben, "Handbook of X-ray Photoelectron Spectroscopy", Ed. by J. Chastain, Perkin-Elmer Corporation:Eden Prairie (1992).
- ^{xiv} T. Klotzbücher, W. Pflöging, D.A. Wesner, M. Mergens, E.W. Kreutz, *Diamond Rel. Mater.* **5** (1996) 525-529.
- ^{xv} B. Schmitz, X. Vanden Eynde, ECSC Technical report n°?, (2002-2003).
- ^{xvi} R.M. Hudson, H.E. Biber, E.J. Oles, C.J. Warning, *Metall. Trans. A.* **8A** (1977) 1713.
- ^{xvii} X. Vanden Eynde, J.P. Servais, M. Lamberigts, *Surf. Interface Anal.* **33** (2002) 322-329.
- ^{xviii} H.J. Grabke, "Kinetics of Gas-Solid Interactions" *Mat. Sci. Forum* **154** (1994) 69-86.

HYDROGEN DETERMINATION IN STEEL AT VOESTALPINE

Dipl.-Ing. Dr. Hubert Duchaczek, Dipl.-Ing. Florian Zwettler

Environmental- and Analytical Chemistry, voestalpine Stahl GmbH, Linz, Austria

Abstract:

Hydrogen analytics at voestalpine is implemented with melt and hot extraction. Both methods are validated. The hot extraction analyser can be calibrated with standard reference materials (SRM) and test gas. For low level calibration, standard reference materials and for high level calibration, test gas is used. The limit of detection (LOD) of the hot extraction method was determined by measuring samples with low hydrogen content. LOD was determined by Validation Software SQS 2000 as 0,16 ppm hydrogen. Hot extraction is used for analysing steel sheets, filler wire, weld samples,....

Melt extraction is calibrated with standard reference materials. The LOD of the melt extraction method was determined as 0,18 ppm hydrogen. The performance of the measurement method was determined by several round robin tests. Melt extraction is used for steel sheets, coated steel samples, casting samples, flakes, ...

Introduction:

Development of new high strength steel products leads to an increasing risk of embrittlement induced by hydrogen. The small quantities involved (typically from 0,1 to several mass ppm) and the nature of hydrogen with very special physical properties make this task difficult to perform [1]. To deliver satisfying results, calibration is of major importance. Hydrogen measurement was tested by several round robin tests. Since welding "causes hydrogen uptake" its influence is also studied at voestalpine and some results are presented.

Hot Extraction:

The analyser, Leco DH 603, can be operated at a maximum temperature of 1100 °C. The sample is heated up in a fused quartz tube. As carrier gas nitrogen is used. The detection of hydrogen is done in a thermal conductivity cell. A big advantage of this method is that in contrast to melt extraction, larger samples with maximum dimension of 25x110 mm can be analysed.

The instrument is equipped with gas dose calibration. Helium is used as test gas and 2 loops, A and B, with volumes of 7 µl and 30 µl are available. High level calibration is done with test gas. Low level calibration is done with SRM. Four different standard reference materials are available for the calibration. The calibration is done with three standard reference materials on different ppm levels. One SRM is used to control the calibration and the result is listed in a control chart. In case of an out-of-control situation of the control chart the measurement has to be calibrated again.

Furthermore the LOD was determined by measuring samples with low hydrogen contents. For this purpose the samples were cut with a plate shear to reach lower hydrogen contents. As shown in Figure 1, LOD was calculated with Validation Software SQS 2000, and 0,16 ppm hydrogen was determined.

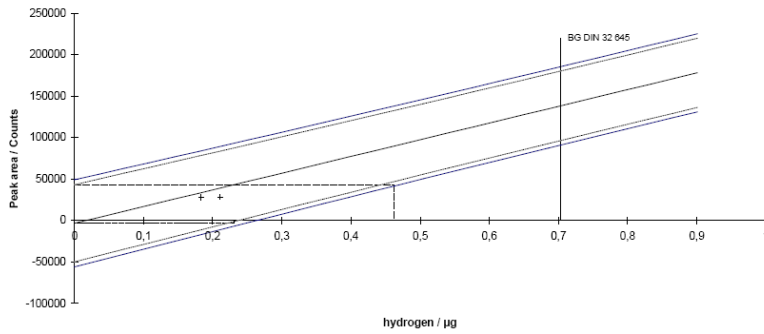


Figure 1: Calculation of LOD

The instrument is designed to work at constant temperature but it is also possible to study thermal desorption of hydrogen from steel products with heat programmes. As can be seen in Figure 2, measurements of reference materials (Leco 502061 $2,19 \pm 0,35$ ppm) with continuous and stepwise heat programmes showed according to the set value satisfying results.

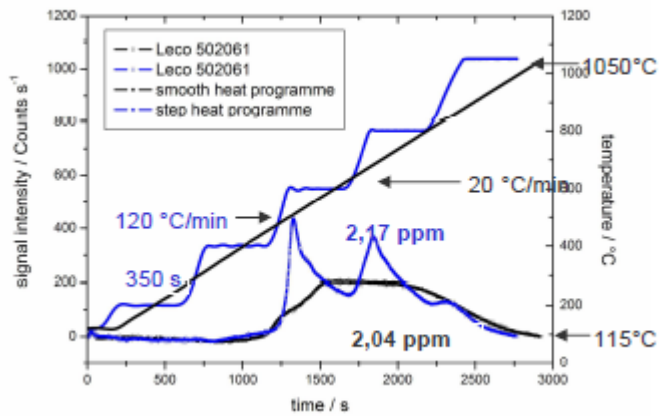


Figure 2: Thermal Desorption Analysis (TDA) of Leco 502061 $2,19 \pm 0,35$ ppm

Since welding “causes hydrogen uptake” therefore its influence is also studied at voestalpine. The measurement is implemented according to the standard method ANSI/AWS A4.3-93 [2]. As specimen a degassed steel sample with dimensions of 80x25x12 mm is used. After the welding experiment the sample is immediately cooled in liquid nitrogen and transported to the analyser where the measurement is carried out at 400 °C. The method was studied through a comparison measurement with another laboratory. The results can be seen in Figure 3.

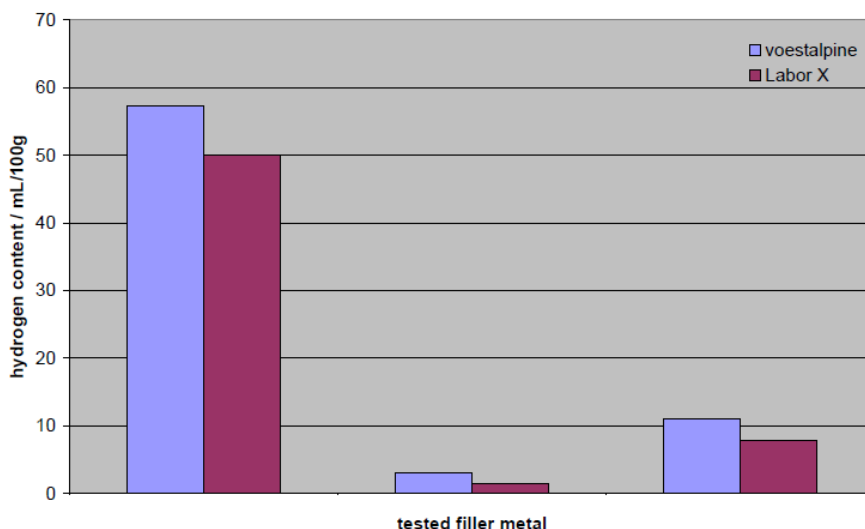


Figure 3: Comparison measurement of three different filler wire samples

Melt Extraction:

The analyser, Leco TCH 600, can be operated at a maximum temperature of 2400 °C. The sample (max. dimension 10x8 mm) is melted in a graphite crucible. The detection of hydrogen is done in an infrared cell after hydrogen is oxidised to water. Leco TCH 600 allows the simultaneous detection of nitrogen, oxygen and hydrogen. The calibration is carried out with one reference material Leco 501529 ($6 \pm 0,2$ ppm), controlled with standard Leco 762747 ($1,8 \pm 0,4$ ppm) and the test sample is once more listed in a control chart. In contrast to hot extraction, also zinc coated samples can be analysed here. The limit of detection was determined as 0,18 ppm hydrogen. The measurement was studied by several round robin tests (Steelinstitut VDEh, Working group FA II. 66, Determination of hydrogen in steel products). As can be seen in Figure 4 a sample with a set value of $1,9 \pm 0,2$ ppm was measured by six participating laboratories.

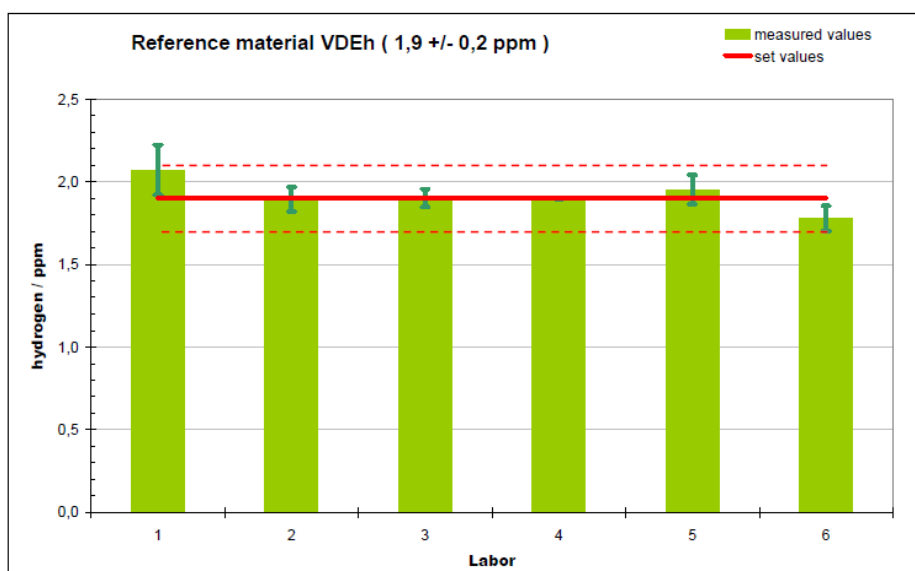


Figure 4: Round Robin test carried out by VDEh

Conclusion:

Melt and hot extraction method are used in daily routine work. Hot extraction has the advantage that relatively large samples with a maximum dimension of 25x110 mm can be analysed compared to only 10x8 mm in the melt

extraction. When analysing hydrogen contents below 1 ppm it is a clear advantage to use larger samples with higher mass.

Both methods were validated and the limit of detection was determined with as below 0,2 ppm hydrogen. Hot extraction is capable to perform thermal desorption measurements which according to Figure 2 show satisfactory results related to quantification of hydrogen. Due to dimensions of the fused quartz tube, welded samples can be measured as well. Melt extraction has the advantage that zinc coated samples can be analysed whereas for hot extraction the zinc layer has to be removed prior to analysis.

With both validated analytical methods voestalpine has high potential to analyse hydrogen (low and high levels) in various steel products.

References

[1] RFCS-CT-2007-00018 "Methodology of hydrogen measurement in coated steels",
2007-2010

[2] Standard ANSI/AWS A4.3-93 November 12, 1992. Standard Methods for Determination of the Diffusible Hydrogen Content of Martensitic, Bainitic, and Ferritic Steel Weld Metal Produced by Arc Welding

DETERMINATION OF HYDROGEN IN STEEL BY THERMAL DESORPTION MASS SPECTROMETRY

Karin Bergers, Ingo Thomas, Jörg Flock

ThyssenKrupp Steel Europe AG, Kaiser-Wilhelm-Straße 100, 47166 Duisburg, Germany

Hydrogen embrittlement has been observed since high-strength steels have been produced in the nineteen thirties. Several different analytical methods have been developed to quantify the total and diffusible hydrogen in steel, but many aspects of hydrogen determination are still to be explored. Purely quantitative determination of hydrogen is not sufficient to fully characterize the steel regarding its resistance against embrittlement.

Thermal Desorption Mass Spectrometry (TDMS) allows the investigation of hydrogen absorption and desorption mechanisms to characterize hydrogen traps in different kinds of steel microstructures. This provides valuable information for the development of new materials with a higher resistance against hydrogen embrittlement. Additionally TDMS allows the quantitative determination of very small concentrations of hydrogen ($< 0.05 \mu\text{g/g}$). Such low detection limits can not be reached with other methods. Due to time-consuming analysis and a rather complex construction, thermal desorption mass spectrometry is not usually applied for hydrogen determination in German steel mills.

At ThyssenKrupp Steel Europe AG a thermal desorption spectrometer was developed by adapting a compact quadrupole mass spectrometer to a commercially available hot solid extraction analyzer, which has proven to be a simple and efficient solution for the determination of diffusible hydrogen in steel.

Sensitivity and accuracy of the developed instrument for both quantitative analysis and trap characterization were evaluated by standard validation methods. The analysis of certified reference materials yielded valuable information about the quality of the applied desorption model and analytical methodology, showing the great potential of the developed thermal desorption mass spectrometer as a reliable tool in routine analysis.

Hydrogen embrittlement

Hydrogen has a large field of application in the industry, such as in the chemical industry as a hydrogenating agent, in the metallurgy as a reducing agent and in different fields as an energy source, such as in welding, astronautics and in the automotive industry [1].

Most of these applications involve the interaction of hydrogen with steel, which can lead to the absorption of hydrogen by the steel lattice. The adsorption and/or absorption of hydrogen in the steel can occur at the following conditions: exposure to pressurized hydrogen at high temperatures, atomic hydrogen originating from corrosion reactions, galvanic metal deposition and cathodic corrosion protection; exposure to air moisture and hydrocarbon during casting, forging and welding as well as heat treatment of the steel material.

In view of the higher solubility of hydrogen in steel at high temperatures, especially in molten steel, internal microcracks (flakes) can develop during the cooling of large forgings. In this case, conglomerates of recombined hydrogen molecules (H_2) are formed in the lattice's imperfections leading to high pressures, which results in microcracks. But also atomic hydrogen which is dissolved inside the crystal lattice can cause crack formation (figure 1). There are several mechanisms which are being discussed in literature in order to explain this phenomenon [2-7].

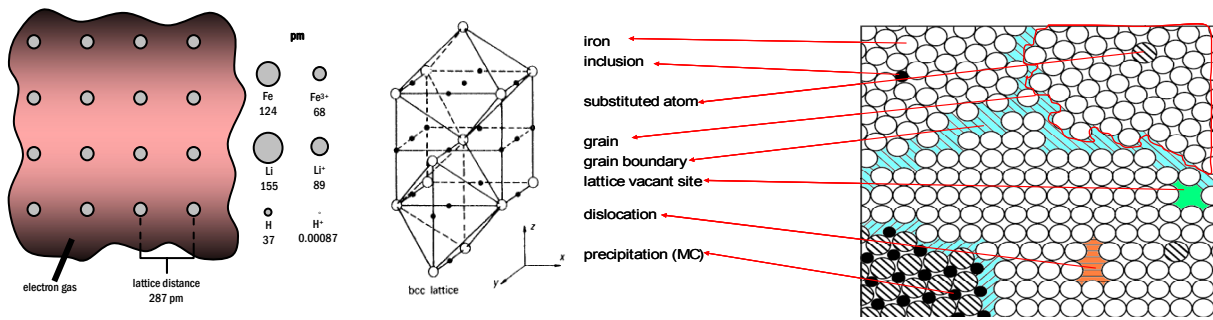


Figure 1: Interaction of hydrogen and microstructure of steel

Hydrogen in high-strength steels

High-strength multiphase steels are widely applied in the automotive industry, mostly as flat steel for cold working. Multiphase steels are generally characterized by a mixture of several grain types in their microstructure, such as ferrite, bainite, martensite and retained austenite. Apart from being appropriate for body construction, which involves plastic deformation, cutting, welding and corrosion protection, these materials must have special mechanical properties, which are very important for the stability and crash-safety of the steel structure [8]. Furthermore, high-strength steels allow a drastic weight reduction of up to 30% in car bodies contributing to the reduction of fuel consumption.

Hydrogen embrittlement plays a major role in the application of high-strength steels. Hydrogen can be absorbed by the steel during the steelmaking process, during galvanizing, during welding and by exposure to H₂ in gaseous phases in the presence of promoters such as H₂S and in acid solutions.

High strength steels are susceptible to hydrogen embrittlement as they show a high level of residual stresses after cold forming. Additionally the high strength level itself makes the steel very sensitive towards crack formation in general (figure 2).

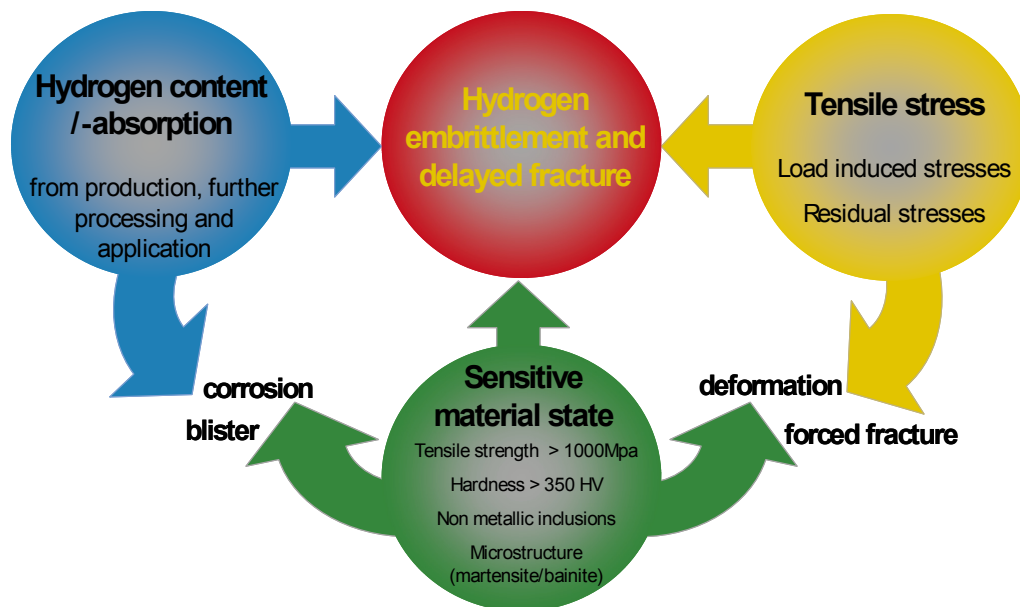


Figure 2: Correlation of hydrogen embrittlement, steel characteristics and microstructure and production process

TDMS methods

Some commercial equipments are available for the routine determination of bulk and diffusible hydrogen in metallic samples. They are based upon solid and melt extraction methods using thermal conductivity or infrared detection for the quantification of hydrogen. The calibration of the analyzers is usually done by gas calibration or with certified reference materials.

Several efforts have been made in the last decades to develop a method, which is able not only to quantify, but also to characterize the mobility of the detected hydrogen in order to better evaluate the susceptibility of the material to hydrogen embrittlement.

There are two main techniques, which are usually applied in TDMS equipments: the carrier gas or the ultrahigh-vacuum (UHV) method.

The ultrahigh-vacuum equipment consists in an integrated construction, in which all the components are located in a sealed chamber subjected to ultrahigh-vacuum. The hydrogen particles released from the sample are then directly ionized and accelerated through the mass analyzer into the detector. By the carrier gas method, the gases released from the sample are carried by an inert gas, such as nitrogen, into the detector.

The integrated ultrahigh-vacuum system has the advantage of a faster response to changes in desorption rate and a higher sensitivity, due to the absence of a carrier gas. Furthermore, the influence of retrapping and diffusion of hydrogen can be avoided, which leads to a more accurate determination of the activation energies. This system is, however, much more sensitive to pressure changes, requiring an elaborate control of the vacuum inside the UHV chamber. One important disadvantage of ultrahigh-vacuum systems is that they can not be used to measure the hydrogen content of materials which show high lattice diffusivity for hydrogen like ferritic steels for example. In this case significant parts of the dissolved hydrogen are already desorbed by the sample during the evacuation of the system and before the measurement can be started.

The carrier gas system, on the other hand, is relatively simple and less expensive. However, due to the longer path between the furnace and the mass analyzer and the influence of the carrier gas flow, this system can present a variety of unknown variables, which can decrease substantially the quality of the thermal desorption analysis, especially at very low heating rates.

TDMS instrument at ThyssenKrupp Steel Europe

While many TDMS equipments involve a rather complex design, requiring a robust construction for ultrahigh-vacuum, it is intended to develop a simpler solution, based on the carrier gas method. A solid extraction analyzer was therefore adapted to a quadrupole mass spectrometer, which allows the use of resources initially available for the isothermal analysis.

Commercially available solid extraction analyzers are usually equipped with a thermal conductivity detector and designed for short isothermal analysis with a purely quantitative approach. Thermal desorption spectrometry on the other hand requires a very long analysis time and a more sensitive and stable detection, capable of determining very small changes in the desorption rate of hydrogen.

Mass spectrometers are able to selectively determine hydrogen with a higher sensitivity and a lower drift throughout the thermal desorption analysis and are therefore more appropriate for TDS. The use of thermal desorption mass spectrometry (TDMS) for the determination of hydrogen in steel has been described by some publications [9,10] and is being recently explored in some research laboratories.

The analyzer G4 Phoenix DH (in the past called H-MAT 221) from the company Bruker - Elemental is designed for the determination of diffusible hydrogen in metallic materials by the carrier gas hot extraction method with thermal conductivity detection (TCD). The main elements of the analyzer are the furnaces with quartz tubes for hot storage of the sample, the TCD, the reagents, the gas calibration device and the membrane pump.

This instrument is equipped with an infrared and a resistance furnace with a temperature range of up to 950° respectively 1050°C. Pure nitrogen (99,99 %) flowing through the quartz tube inside the furnace carries the gases

released from the sample through a Schütze reagent and a molecular sieve into the TCD. This separation step removes other sample gases such as carbon oxides and H₂O allowing the determination of hydrogen through the TCD. A membrane pump maintains a constant volume flow of the carrier gas system, which is also crucial for the thermal conductivity determination. The calibration is done with a gas calibration device, which is able to work with 10 different volumes of calibration gas.

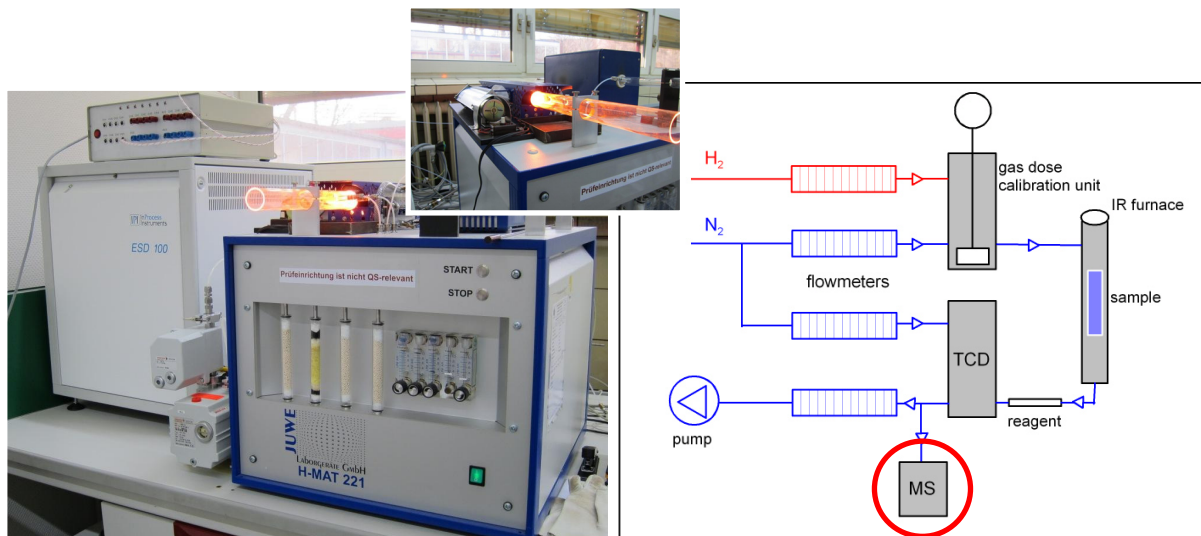


Figure 3 : TDMS equipment at ThyssenKrupp Steel Europe and flow chart

The quadrupole mass analyzer is the most common type of available. This instrument is more compact and less expensive than other mass spectrometers and allows high scan rates, being suitable for continuous Multiple Ion Detection (MID).

The mass spectrometer currently used for combination with the elementary analyzer is the compact quadrupole mass spectrometer ESD 100 from the company Inprocess Instruments IPI. It has been developed for simple capillary coupling to reactions, furnaces, elementary analyzers, thermobalances and other analytical methods. It is particularly suitable for the sensitive detection of light elements and stable isotopes. Both channeltron and faraday transducers are available for ion detection. A turbomolecular pump generates an ultimate pressure of about 10⁻⁸ mbar in the UHV chamber. For the adaptation of the mass spectrometer, a T-junction was installed after the TCD in the equipment (figure 3).

Calibration of TDMS instrument – Determination of diffusible hydrogen

In order to determine the relation between the raw signal from the thermal conductivity detector and the amount of hydrogen released from the sample, the elementary analyzer is equipped with a gas calibration module, which is capable to inject precisely defined volumes of calibration gas through a special valve into the carrier gas.

The injected calibration gas is then carried by nitrogen through the quartz tube into the TCD, which gives a signal proportional to the amount of calibration gas in the carrier gas. For the calibration of the TCD, either helium or hydrogen can be used as calibration gas, with the appropriate correction of the thermal conductivity of helium.

For the calibration of the MS, which is the more selective detector, only hydrogen or mixtures of hydrogen in nitrogen can be applied as calibration gas.

The temperature and pressure of the injected hydrogen volume is internally measured during the calibration and used to calculate the correspondent mass of hydrogen through the ideal gas law ($p \cdot V = n \cdot R \cdot T$).

$$f_c = \frac{\text{Integral}}{m_{H_2}}$$

$$m_{H_2} = \frac{p \cdot V \cdot \tilde{M}}{R \cdot T}$$

where

f_c : calibration factor; m_{H_2} : mass of hydrogen; V : volume of hydrogen; p : pressure in the instrument;
 T : temperature in the instrument; \tilde{M} : molecular mass, R : gas constant

The raw signal of the mass spectrometer is integrated in order to calculate the calibration factor.

To calculate the hydrogen amount in analysed samples the detected peaks are integrated and compared with those of the gas calibration peaks (multi point calibration, figure 4). Usually, the five lowest volumes of gas dose calibration unit are used for calibration. In combination with a low concentrated mixture of hydrogen in nitrogen (e.g. 2%) the typical level of diffusible hydrogen amount in routinely analysed samples is approached. The results are presented in $\mu\text{g/g}$ (ppm).

According to experience the diffusible hydrogen is analysed in a temperature range from room temperature to nearly 450 °C. Here, differentiated peaks could be observed and integrated. Usual rate of heating is 1200 K/h.

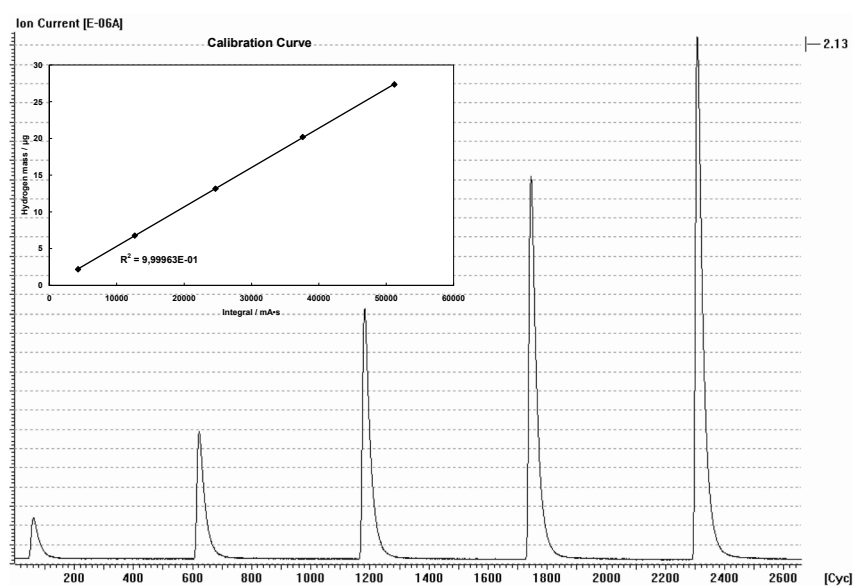


Figure 4: Calibration with pure hydrogen (99,9999%)

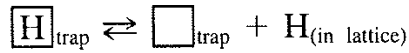
The limit of detection (LOD) was calculated by the signal-to-noise ratio S/N of the lowest volume measured with a mixture of 2% hydrogen in nitrogen. Concerning to a 1 g sample and a ratio of S/N = 5, the limit of detection for this method is then 0.05 $\mu\text{g/g}$ (ppm). Samples with higher mass and the same concentration of diffusible hydrogen release a higher absolute amount of the analyte, thus increasing the sensitivity of the instrument, when only the concentration is taken into consideration. A 10 g sample, for instance, theoretically implies a LOD 10 times lower than the one for a 1 g sample.

Calculation of desorption energies

One approach to prevent hydrogen embrittlement, besides e.g. thermal diffusion, is the implementation of small second phase particles such as metal carbides into the microstructure. These particles attract hydrogen which is dissolved in the lattice and therefore can avoid the diffusion of hydrogen into active regions in the material. This process is called “hydrogen trapping”.

Thermal Desorption Mass Spectrometry has been used, in combination with a mathematical model of the desorption process, to calculate desorption activation energies of multiple traps in steel. These energies, in combination with metallographic data and the chemical composition of the steel, can be attributed to specific traps and provide valuable information for the development of new steel materials.

One of the models, proposed by Choo and Lee [9], is based on the adsorption/desorption kinetics of hydrogen:



The lowest energy level in the desorption process is the trap. The difference between the trap and the lattice energy level is the binding energy between the trap and the hydrogen. The trap activation energy is then the sum of the binding energy and the saddle point energy around the trap. Finally, there is the diffusion energy which is not considered by this model.

A hydrogen escape rate can be derived from the Polanyi-Wigner equation, which involves a desorption rate of n^{th} order and a rate constant described by the Arrhenius equation as shown below [11].

$$r_{\text{des}} = \frac{d\Theta}{dt} = \nu_n \cdot \exp\left(-\frac{E_a}{R \cdot T}\right) \cdot \Theta^n$$

where

r_{des} : desorption rate, Θ : surface coverage or trap occupation, ν_n : frequency factor, E_a : desorption activation energy, n : order of the desorption rate, R : gas constant, T : absolute temperature.

The desorption energy can then be calculated from the gradient of the above equation:

$$\frac{\partial \ln\left(\frac{\Phi}{T_p^2}\right)}{\partial\left(\frac{1}{T_p}\right)} = -\frac{E_a}{R}$$

Some important simplifications were made in the model proposed by Choo and Lee [12]:

The diffusion of hydrogen from the interior to the surface of the material, as well as the surface impedance is not considered to be rate-controlling processes; the traps are sparsely distributed, so that there is no interaction between them; the retrapping of hydrogen is neglected. These simplifications imply some practical limitations concerning the sample size and geometry, surface characteristics, heating rate and hydrogen concentration.

A more detailed derivation is described in [12] and [13].

Experiments

Sample preparation

Because of the characteristics of hydrogen, especially concerning its diffusibility, sample preparation is a non-negligent aspect of TDMS measurement. Basically, it is important to cut the samples without using cooling liquid and to avoid heating of the samples. So, plate shears or laser devices instead of saws are recommended. In case of laser devices it is necessary to take the further specimen in enough distance to the area, where the laser had maybe heated the sample. Removal of coatings should be done by chemical methods like etching with hydrochloric, for example, and not by mechanical removal.

Furthermore, in particular for ferritic materials, the samples have to be cooled in liquid nitrogen from beginning of sampling to analysis. The necessary cold chain must not be interrupted. For this, different cooling boxes for the different applications could be used (figure 5).

Sample cleaning occurs in ultrasonic bath with solvents like water free acetone or, in case of very oiled sheets, with alkaline solvents like e.g. Ridoline.



Figure 5: Cooling equipment: (a) **Arperge 110** with rolls and 4 x 9 cryoboxes (long time storage), Airliquid ; (b) **Voyager 12** with two round clip boxes (transport), Airliquid ; (c) **Dewar 2I** (short time storage of readily prepared samples)

Determination of desorption energies

Several pieces of a high-strength steel of same size and weight were heated up with five different heating rates from 0.1 K/s to 0.75 K/s in a temperature range of nearly 25 °C to 950 °C.

Assuming hydrogen release from a single desorption site and supposing Gaussian distribution on the peaks, they were integrated and calculated as described above (page 5 and figure 6).

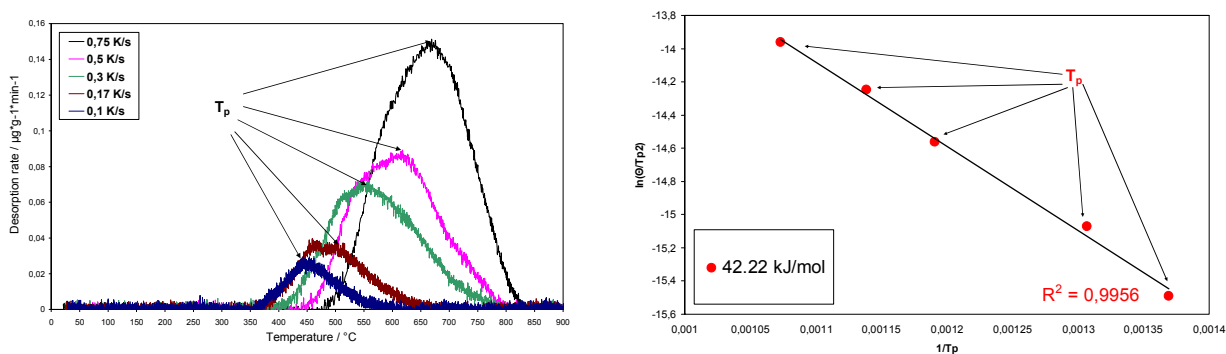


Figure 6: TDMS of a high-strength steel (five rates of heating) and Arrhenius plot

It was obviously possible to determine a desorption energy of 42.2 kJ/mol by TDMS method. But the further interpretation concerning steel characteristics and behaviour is not possible without detailed information obtained by metallographic analysis of microstructure and comparison of this value with some of those found in literature.

Influence of exposure time at room temperature

A metal formed constructional element, made of high-strength steel was analysed by TDMS. The samples were cut in centre by laser beam cutting, cleaned with water free acetone and analysed with a rate of heating of 1200 K/h. The determined amount of diffusible hydrogen was 0.5 µg/g. The whole constructional element had been stored for nine days at room temperature. Then the same procedure was repeated. TDMS measurement shows, that the diffusible hydrogen decreased in that time more than half of the value (figure 7).

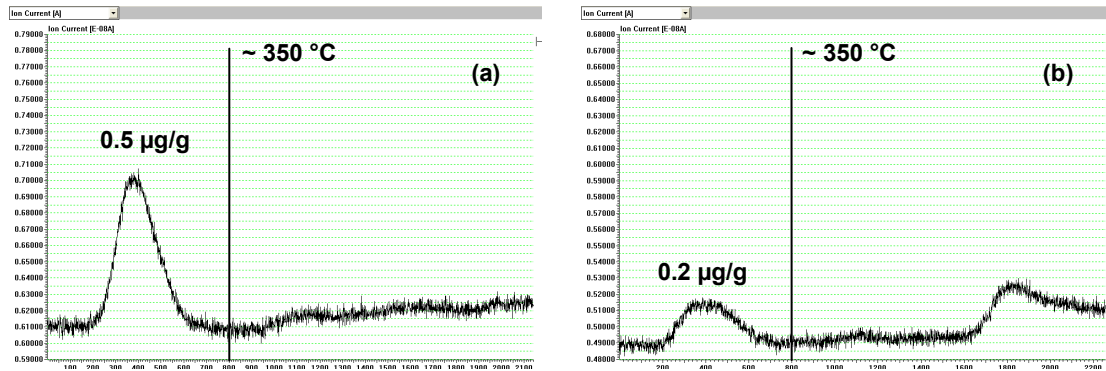


Figure 7: TDMS of a constructional element at initial state (a) and after nine days of exposure (b)

This effect could be a hint to the assumption, that diffusible hydrogen, which is possibly adsorbed during metal forming process, could be decrease by storing the constructional elements at room temperature for a certain time. That could maybe avoid problems in the further manufacturing process. Alternative applying of thermal effusion is possible.

A further example of the influence of exposure time on the diffusible hydrogen content is shown in figure 8.

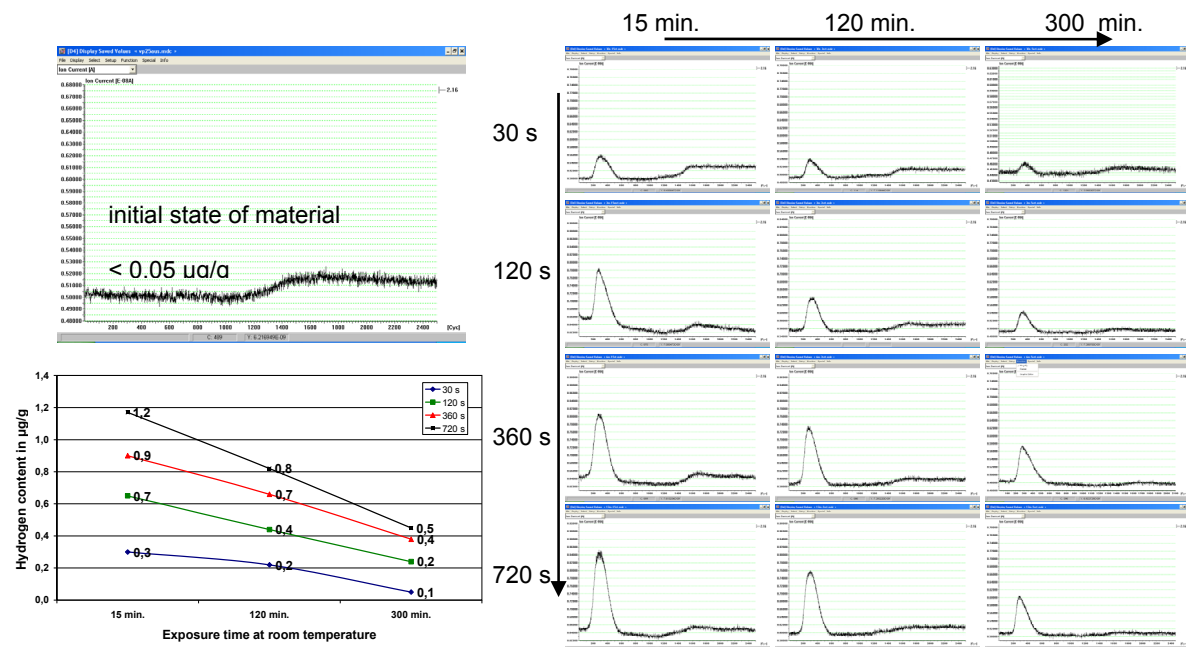


Figure 8: TDMS of a high-strength steel, pickled for different times (y-axis) and stored for different periods (x-axis)

In laboratory four stripes of plates (15 x 100 mm, high-strength steel grade) were pickled under in-plant conditions of push pickling for four different times (30, 120, 360 and 720 s). After pickling they were immediately stored in

liquid nitrogen. Directly before TDMS measurement each stripe was cut in three equal pieces. The first one was directly analysed (15 min.). The others were stored for two and five hours at room temperature. Within five hours of storage at room temperature the diffusible hydrogen decreased to nearly the third of the initial amount of diffusible hydrogen.

Influence of microstructure and sample form

Two different dual phase steels with different tensile strength (material 1: 1000 MPa; material 2: 500 MPa) were analysed by TDMS after charging with three different methods. Additionally the microstructure was examined. The measurement conditions and results are shown in table 1 and figure 9.

Table 1 : Determination of diffusible hydrogen in dual phase steel after applying different charging methods (n=6)

Charging methods		Material 1 (tensile strength 1000 Mpa) size 20 x 50 x 1.4 mm weight ~ 11 g H in µg/g	Material 2 (tensile strength 500 Mpa) size 20 x 50 x 0.75 mm weight ~ 6 g H in µg/g
variation 1	24 h, 0.1 N HCl at room temperature	0.06 ± 0.02	0.05 ± 0.04
variation 2	5 min., 20 % HCl at 80°C	1.09 ± 0.19	2.93 ± 0.67
variation 3	10 min. at 10 mA/cm ² with 1N H ₂ SO ₄ + 20mg/L Thiourea	1.38 ± 0.14	2.34 ± 0.37

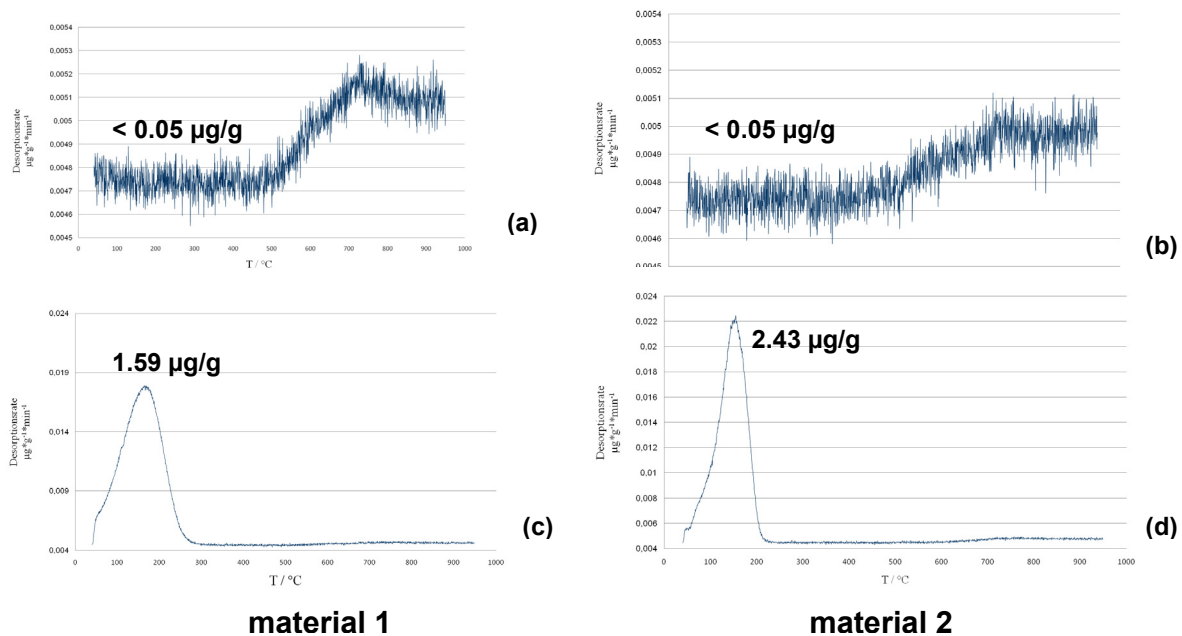


Figure 9: Determination of diffusible hydrogen of two dual phase steel plates at initial state (a,b) and after charging method 3 (c,d)

After charging different behaviour of the two materials could be observed. With the first charging method at room temperature marginal diffusible hydrogen was detected. Using more concentrated hydrochloric acid and temperature treatment, alternatively cathodic charging, both sample types could be sufficiently charged. Furthermore, in case of effective charging the second material obviously absorbed more hydrogen than the first

one, but the standard deviation increased to more than the double value. Possible reasons could be the half thickness and weight of the samples or maybe another microstructure.

Metallographic analysis showed that the first material mainly consisted of ferrite and bainite. Additionally small amounts of martensite and traces of perlite and eventually traces of retained austenite could be found. The high amount of bainite was quite uncommon for dual phase steel grades. The material showed clear center segregation. The second material mainly consisted of ferrite. Small amounts of martensite and traces of perlite could also be found. Additionally, the presence of traces of retained austenite could not be excluded.

Conclusion

Through a simple adaptation of commercially available instruments it was possible to develop a compact TDMS equipment, which has proven its efficiency in both quantitative and qualitative determination of hydrogen.

Among mechanical tests and other analytical methods TDMS is able to provide the highest amount of information regarding the susceptibility of steel materials to hydrogen embrittlement. The determination of bulk hydrogen concentration in steel alone is not able to fully characterize the probability of hydrogen embrittlement, since in some steels a high amount of inactive hydrogen residing in irreversible traps contributes to the total concentration. With a determined limit of detection of 0.05 µg/g hydrogen and the possibility to analyze relatively large samples of up to 30 g, the developed instrument is able to determine extremely low concentrations in steel and inherently low hydrogen desorption rates.

First exploratory analysis showed, that the determination of activation energies from the Polanyi-Wigner equation with the assumption of a first order desorption rate yielded to satisfactory results. Individual location and characterisation of hydrogen traps added to the base-alloy of high-strength steels seems to be possible in future.

There are several aspects involved in the determination of diffusible hydrogen and the activation energies, which are still to be more deeply explored, such as the effects of microstructure, trapping elements, sample geometry, surface treatment, the influence of tailing in the deconvolution with Gaussian peaks, the effects of background drift and polynomial normalization. With regards to the construction of the TDMS instrument the optimization of temperature measurement is one other point of view.

Above all, the great potential of thermal desorption mass spectrometry as a routine analytical tool in the steel industry was shown. Furthermore, the relatively simple concept of the developed TDMS instrument could set the basis for a wider application of this type of analysis in many laboratories.

References:

- 1) K.-H. Tostmann: Korrosion Ursachen und Vermeidung, Wiley-VCH Verlag, Weinheim, 2001, pp. 134-144.
- 2) R. Troiano, The Role of Hydrogen and other Interstitials in the Mechanical Behaviour of Metals, Trans. ASM 52 (1960), pp. 54-80.
- 3) R.A. Oriani, A Mechanistic Theory of Hydrogen Embrittlement of Steels, Ber. Der Bunsengesellschaft 76 (1972), pp. 848-857.
- 4) H.G. Nelson, Hydrogen Embrittlement, Treatise on Materials Science and Technology, Vol. 25 (Ed. C.L. Briant, S.K. Banerji), New York (1983), pp. 275-359.
- 5) G.M. Bond, I.M. Robertson, H.K. Birnbaum, Effects of hydrogen on deformation and fracture processes in high-strength aluminium alloys, Acta Metallurgica, 36 (1988), No. 11, pp. 830-834.
- 6) J.S. Wang, The thermodynamic aspects of hydrogen induced embrittlement, Engineering Fracture Mechanics, 68 (2001), pp. 647-669.
- 7) K. Nibur, D. Bahr, B. Somerday, Hydrogen effects on dislocation activity in austenitic stainless steels, Acta Materialia, 54 (2006), pp. 2677-2684.
- 8) H. Berns, W. Theisen: Eisenwerkstoffe – Stahl und Gusseisen, Springer-Verlag Berlin, Heidelberg, 2008, pp. 1-16, 124-128, 153-178.
- 9) M. Mizuno, H. Anzai, T. Aoyama and T. Suzuki: Mat. Trans. Vol. 35, No. 10 (1994), p. 703
- 10) F. G. Wie, T. Hara and K. Tsuzaki: Met. And Mat. Trans. B, Vol. 35B (2004), pp. 597.
- 11) S. L. M. Schroeder and M. Gottfried: Temperature-Programmed Desorption (TPD) / Thermal Desorption Spectroscopy (TDS), Advanced Physical Chemistry Laboratory, FU Berlin (2002).
- 12) W. Y. Choo and J.Y. Lee: Metall. Trans. A, 13A (1982), p. 135.
- 13) K. Bergers, E. Camisão de Souza, I. Thomas, N. Mabho, J. Flock, Determination of hydrogen in Steel by Thermal Desorption Mass Spectrometry, steel research international, Wiley-VCH Verlag GmbH&Co. KGaA (2010), Vol. 81, pp. 499-507

DESTRUCTIVE AND NON-DESTRUCTIVE DETERMINATION OF HYDROGEN IN METALS WITH SPECIAL EMPHASIS ON STEELS

Reiner Kirchheim

*Institut für Materialphysik, Universität Göttingen, Friedrich-Hund-Platz 1
D-37077 Göttingen, Germany*

Abstract:

After describing the motivation for analyzing hydrogen in metals and especially in steels a new technique for non-destructive hydrogen analysis or a novel hydrogen probe, respectively will be presented. The probe has been applied to measure hydrogen uptake in an iron and in a steel sample which were charged electrochemically with hydrogen. For many of the standard methods of destructive hydrogen analysis the reliability of analytical results depends on the reliability of reference materials which is a serious problem at low hydrogen contents at and below 1 μg or 1 weight ppm, respectively. A new type of reference material in this concentration range will be introduced. Results obtained by hot extraction analysis of reference samples containing hydrogen ranging from about 0.5 to 10 μg are presented.

Introduction

Hydrogen in metals has been a subject of intensive research regarding positive aspects like the storage of hydrogen as a secondary energy carrier [1] as well as negative aspects like hydrogen embrittlement [2]. Hydrogen embrittlement means a deterioration of the mechanical strength of a metal usually revealed by a remarkable decrease of fracture strain. Among metallic alloys steels are especially susceptible to H-embrittlement and the higher the strength of the steels the more severe the problem becomes. Research in this area is hindered by two experimental obstacles.

(1) Embrittlement of steels occurs at low H-concentrations of a few ppm (here and in the following ppm refers to weight ppm) which are difficult to be determined. The analytical techniques applied are mostly destructive and/or do not allow an in-situ determination during an embrittlement experiment.

(2) Due to the high mobility of hydrogen atoms in steel the hydrogen content of a sample may change in a short time depending on the external conditions. Thus during an experiment or in between the experiment and the following destructive analysis the hydrogen content may vary.

Besides the experimental difficulties the interpretation of mechanical properties and their dependence on hydrogen is complicated as well, because a variety of different models has been proposed explaining H-embrittlement [3]. Many of these models require detailed information about hydrogen mobility, i.e. how the hydrogen diffusion coefficient depends upon the microstructure of the steel. Microstructural features are grain boundaries, carbide/metal interfaces, inclusions, dislocations, vacancies and solute atoms. All of them provide trap sites where hydrogen atoms are bound stronger when compared with the normal interstitial site of the iron matrix. Thus H-atoms stay longer in these traps and, therefore, their overall mobility is reduced. Despite the fact that the microstructural features mentioned before have different binding energies giving rise to different magnitudes of the loss of H-mobility, only two types of traps are very often considered, i.e. irreversible and reversible traps. The latter are assumed to release hydrogen at ambient temperatures leading to so-called diffusible hydrogen. The term diffusible hydrogen remains to be ambiguous, because the amount of this type of hydrogen depends on temperature and time allowed for its desorption.

Regarding the experimental determination of hydrogen two new inventions will be presented in the present study which help to overcome some of the problems mentioned before. The first one relates to a hydrogen probe which can be attached to a sample containing hydrogen. The probe continuously absorbs hydrogen from the sample

and the absorbed amount is measured in-situ within the probe. Depending on the geometry of sample and probe the method allows the determination of the concentration of diffusible hydrogen and its diffusion coefficient. The second invention relates to the development of a new type of reference material for hydrogen analysis. Hydrogen in this reference material is bound strongly and, therefore, will remain within the sample during years of storage.

A novel hydrogen probe

The functioning of the new probe is based on thermodynamics and kinetics of hydrogen transport. If two materials of different thermodynamic affinity to hydrogen are brought into contact, hydrogen moves from the material of lower affinity (sample) to the one of higher affinity (probe). If the ratio of the probe volume to the sample volume is small, the hydrogen concentration in the probe material becomes larger than in the sample and its determination may become easier. A schematic presentation of this scenario is shown in Fig. 1.

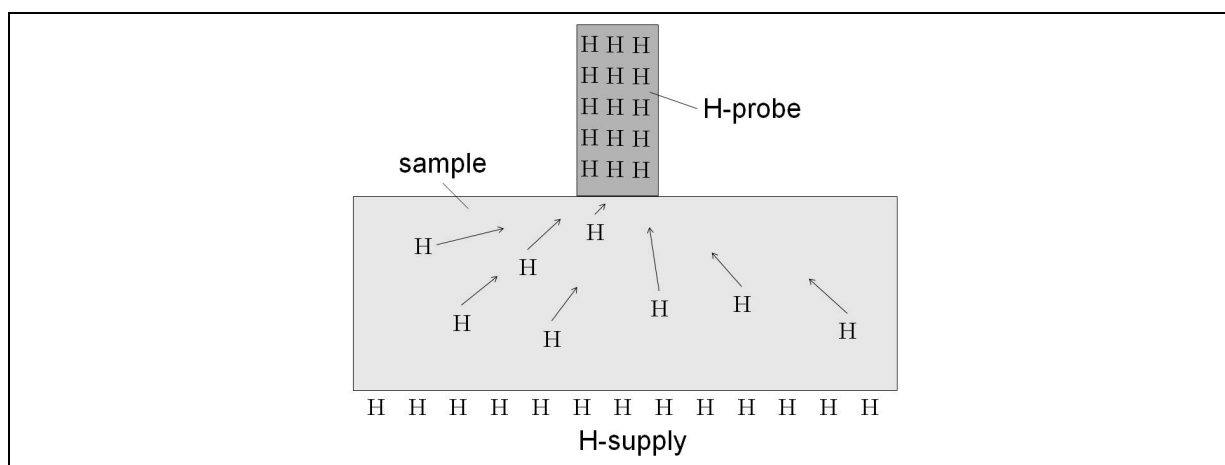


Figure 1:

Schematic presentation of the functioning of the novel hydrogen probe. Because of the higher affinity of the probe material to hydrogen the latter is absorbed out of the sample into the probe. If there is no supply of hydrogen from outside, all the hydrogen of the sample will be concentrated within the probe and will be determined there. If hydrogen enters for instance the sample at the side adjacent to the probe, the hydrogen concentration in the probe increases continuously and its in-situ determination yields information about the hydrogen flux within the sample or the hydrogen concentration at the bottom side of the sample.

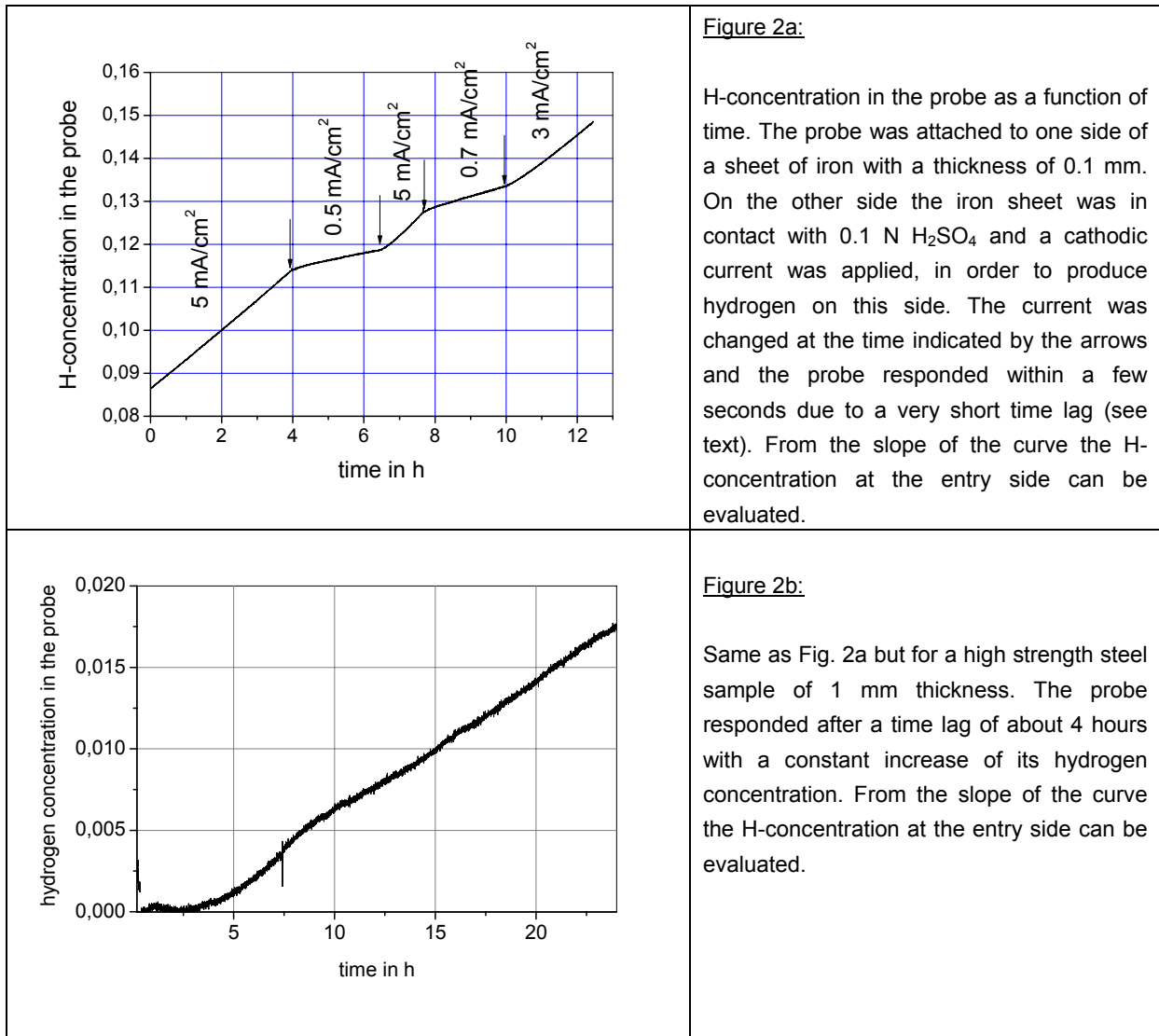
Appropriate probe materials are transition metals and their alloys, where hydrogen has a high solubility and high mobility, e.g. Ti and V. H-concentration within the probe material can be determined in-situ by a variety of different methods, e.g. X-ray diffraction, volume change, resistivity change etc.. The hydrogen probe is commercially available from KircTec GmbH.

Figure 2a shows results for a probe which was attached to a 0.1 mm thick iron sheet. Adjacent to the contact area the steel sample was charged with hydrogen by a cathodic current passed through 0.1 N H₂SO₄. A few seconds after switching on the cathodic current or changing the current the probe responded by a linear increase of its hydrogen content. The time required for hydrogen to diffuse from its region of production to the probe is called break-through time and it is related to the H-diffusion coefficient D and the sample thickness d by the following equation [4]

$$(1) \quad D = \frac{d^2}{6t_b}$$

The diffusion coefficient of hydrogen in iron is $9 \cdot 10^{-5} \text{ cm}^2/\text{s}$ [5] which yields a value of $t_b=0.18 \text{ s}$. Reducing the cathodic current density leads to lower H-concentration on the entry side and a smaller slope of the curves and vice versa as demonstrated in Figure 2a.

The probe was also applied to a high strength steel sample (cf. Fig. 2b). After a break-through time t_b of 4 hours the H-concentration within the probe increases linearly with time which corresponds to a H-diffusion coefficient of $D = 1.2 \cdot 10^{-7} \text{ cm}^2/\text{s}$ for the 1 mm thick sample. The linear increase of the H-concentration in the probe is equivalent to a flux of about $10 \mu\text{A}/\text{cm}^2$ or a H-concentration of diffusible hydrogen of 6 ppm.



For a closed sample (without hydrogen entering through the surface) of volume V_s and H-concentration c_s and a probe of volume V_p all of the diffusible hydrogen will be absorbed by the probe and its H-concentration increases by

$$c_p = \frac{V_s}{V_p} c_s .$$

Thus the sensitivity of the probe can be tailored by choosing an appropriate volume ratio.

A novel hydrogen reference material

Mostly all of the analytical techniques for hydrogen determination provide a signal which is an unknown function of hydrogen concentration and, therefore, require the use of reliable reference materials with known and unchanging hydrogen contents. In addition, small hydrogen contents between 0.1 ppm and several ppm are indispensable for steel samples. At these very low H-concentrations three problems arise:

- Hydrogen may leave the reference material by degassing or by reaction with oxygen
- Hydrogen may enter during corrosion of the reference material
- Hydrogen on the surface of the reference material bound in an adsorbed water layer will contribute to the hydrogen signal as well.

All of these three issues may affect the measured hydrogen concentration of the reference material to a small extent only, but their negative influence on the reliability of a reference material will dramatically increase when the H-content of this material is low. In order to minimize the effect of these problems the following strategy was developed for a new reference material. In order to avoid H-losses the H-atoms were bound strongly in the reference material. Deep traps are especially suited as they also decrease the H-mobility dramatically and thus minimize H-losses, too, by reducing the kinetics of degassing. In addition, a low H-solubility in normal interstitial sites of the reference material is favourable, because this reduces the pick-up of atomic hydrogen during corrosion reactions. These conditions are fulfilled with a novel reference material consisting of a silver matrix with deep trap sites for H-atoms.

Hydrogen losses occur usually by reaction with oxygen and concomitant water formation on the sample surface. Knowing the trap site concentration, their binding free energy to hydrogen and the H-diffusion in the matrix allows an evaluation of the outward diffusion of hydrogen. This is expressed in terms of a hydrogen free depth extending from the surface to a depth where the traps still contain their bound hydrogen. An example with solid silver as a matrix and strong traps of a concentration of about 0.3 at.-% is presented in Fig. 3.

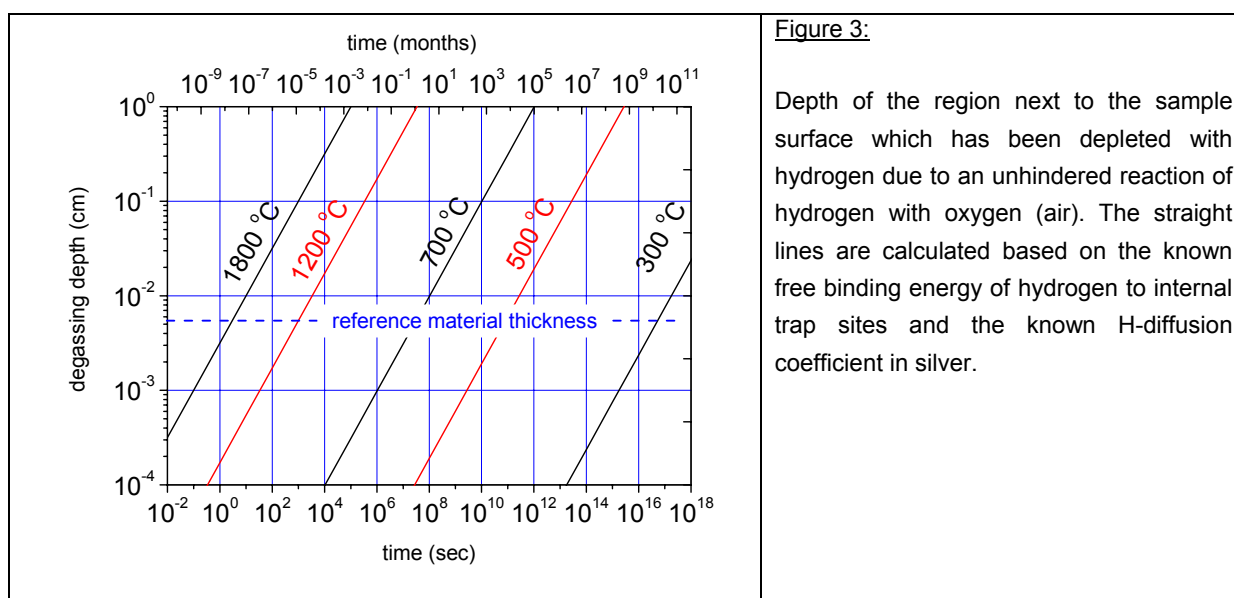
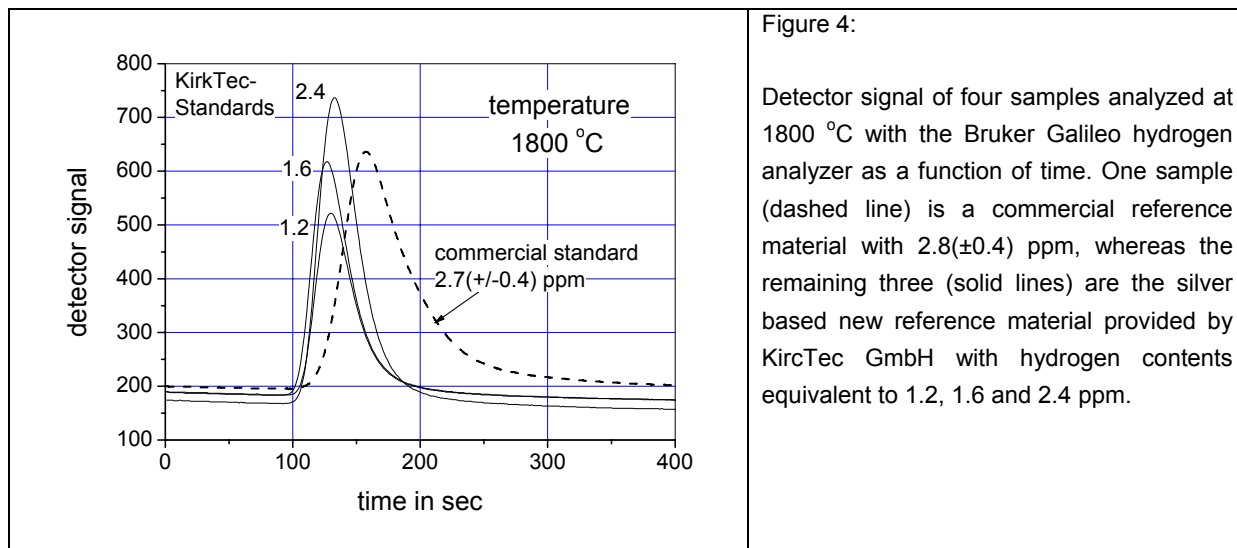


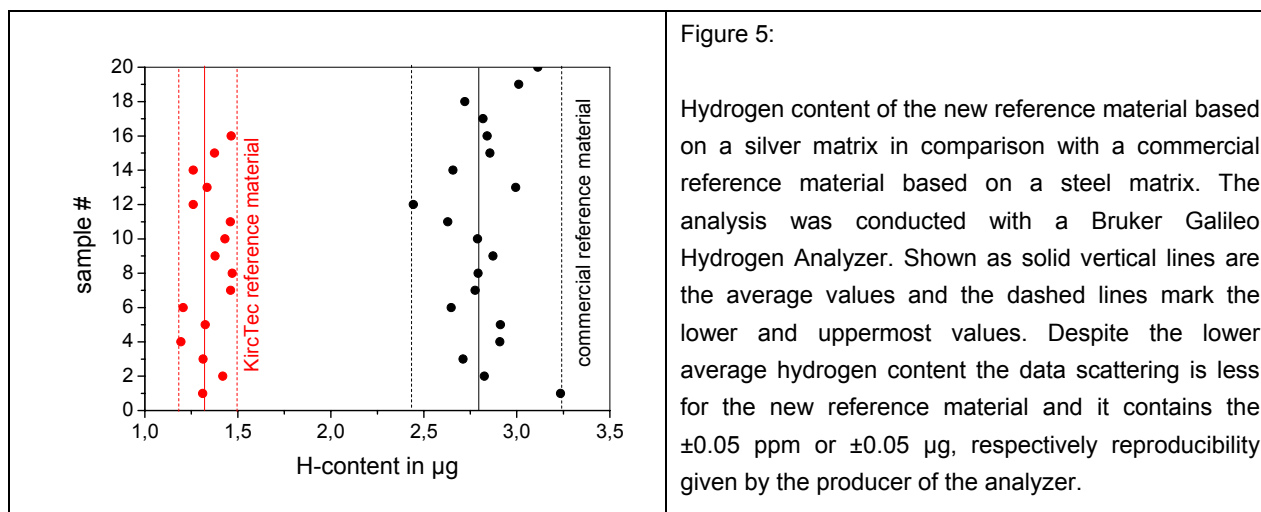
Fig. 3 reveals that virtually no hydrogen losses occur at room temperature for the proposed reference material and samples could be kept on shelf for decades without measurable H-depletion. Our first samples were prepared about one year ago. Measuring the hydrogen content after preparation and one year later by hot extraction analysis yielded the same values within experimental error. Even an annealing treatment of this new reference

material in vacuum at 450 °C for 5 hours did not lead to a measurable hydrogen loss. However at elevated temperatures, namely when silver is melting, hydrogen is leaving the sample. This is demonstrated by hot-extraction experiments at 1800 °C using the Bruker Galileo hydrogen analyzer. Compared to a commercially available reference material provided as 4 mm thick steel pins the silver based new reference material was used in the form of discs of 110 μm thickness. The hydrogen peaks obtained for the two types of reference material are shown in Fig. 4.

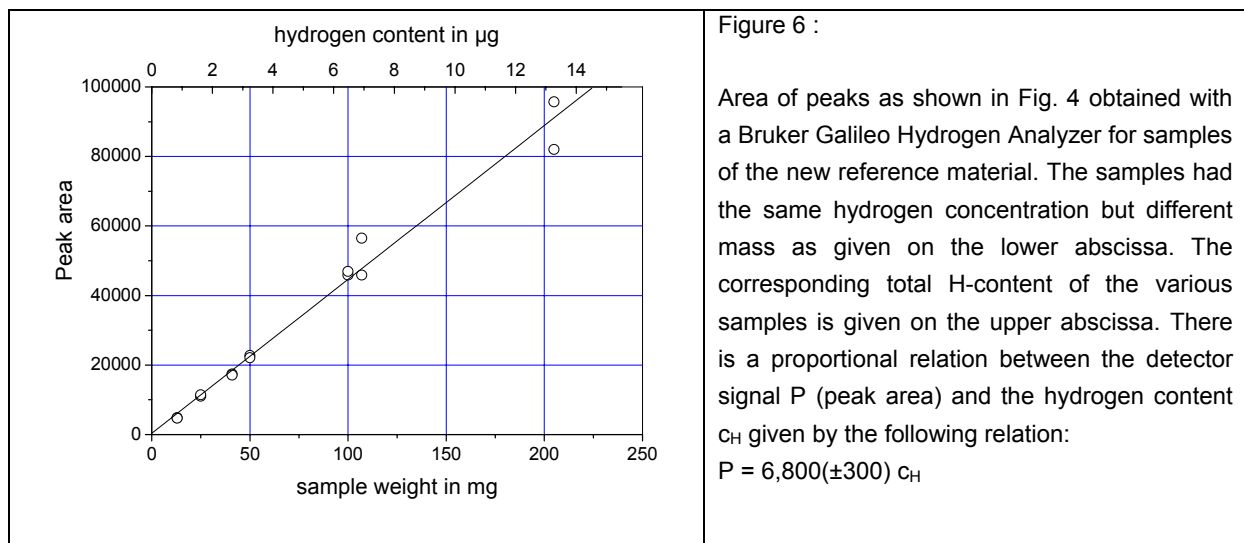


The larger width of the commercial reference material is probably due to its larger dimensions and the corresponding larger time for hydrogen to diffuse out of the sample.

Although commercial reference materials based on steel are covered with thin copper and nickel layers acting as permeation barriers and corrosion resistant coatings, their susceptibility to hydrogen absorption or desorption during production and/or during shell life remains to be a problem. This may be the reason why the relative error bars given for their average hydrogen content are in the range of ±40% for about 1 ppm and ±0.4 ppm for an average of 2.8 ppm. Several sample of the commercial reference material with 2.8±0.4 ppm were analyzed in comparison with the silver based materials of the KircTec GmbH. The results are shown in Fig. 5.



As proven by the results in Fig. 5 the new silver based reference samples yield reliable results at low hydrogen contents. The results are also independent of the weight of the reference material as shown in Fig. 6 yielding a proportional relation between detector signal or peak area respectively (cf. Fig. 4).



Conclusion

a) a new hydrogen probe is described which allows an in-situ and non-destructive determination of hydrogen in iron and steel. Two examples are given where the probe was monitoring the input hydrogen concentration as produced by cathodic charging in an iron and a steel sample.

b) a new reference material for hydrogen analysis at low H-concentrations was presented and compared with a commercially available reference material. The reproducibility of the measured hydrogen content of the new material was much better than the commercial one despite a much lower hydrogen content. Due to its thermodynamic and kinetic properties the novel material has a long shelf life without picking up or losing hydrogen.

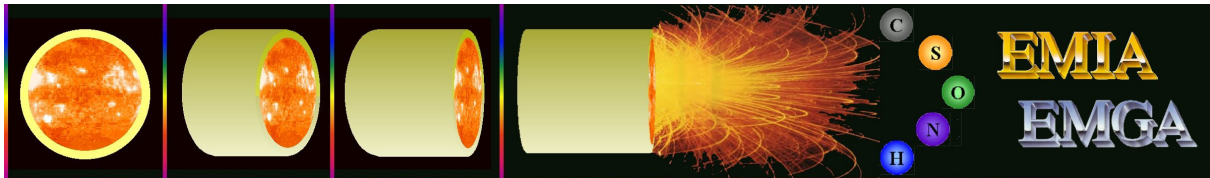
References:

- 1) L. Schlapbach and A. Züttel. Nature (2001) 414, 353-358
- 2) "Hydrogen Effects on Materials Behavior and Corrosion Deformation Interactions", edited by N.R. Moody, A.W. Thompson, R.E. Ricker, G.W. Was and R.H. Jones, (2002) TMS Warrendale, USA
- 3) R. Kirchheim, Scripta Mater. (2010) 67-70
- 4) J. Crank „The Mathematics of Diffusion“, Oxford University Press 2nd edition (1975) 44 ff
- 5) H.J. Grabke and E. Riecke, Mater. Tehnol. (2000) 34 331-342

APPLICATION AND INNOVATIONS FOR CS AND ONH ANALYZERS SURFACE CARBON SEPARATION WITH HIGH FREQUENCY HOT EXTRACTION AND CARRIER GAS ANALYSIS

Alain SALAVILLE

HORIBA Scientific, 16-18, rue du Canal, 91165 Longjumeau, France
Tel. +33 (0)1 64 54 13 18 ~ Fax +33 (0)1 69 09 90 88 ~ Mobile +33 (0)682 584 197
alain.salaville@horiba.com ~ www.horiba.com/scientific



INTRODUCTION

Hot extraction and gas analysis is currently in use in the iron and steel industry to measure C, S, O, N, and H in solid samples. The specifications of the products are becoming tighter, mainly at low concentrations due to market demand. The basic combustion method without special preparation does not produce good results due to surface contamination. By combining the advantages of an induction furnace with the programmable temperature curve capability of a resistance furnace it is possible to separate the concentrations from the surface and the sample without sample preparation and with the easiness and the speed of a conventional High Frequency (HF) analyzer.

PRINCIPLE

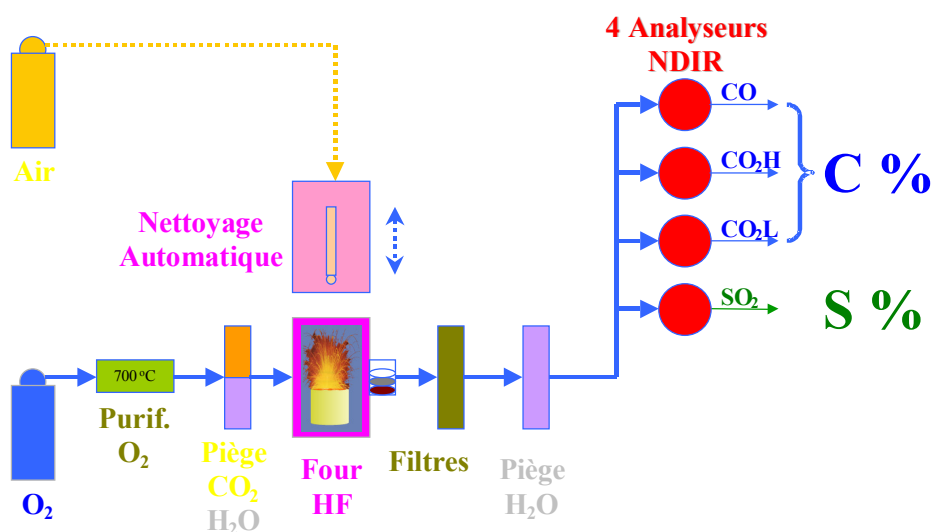


Figure 1: Principle of the Carbon Sulfur analyzer,
Using 4 Infra-red detectors for simultaneous analysis of all the gases.

INSTRUMENTATION

The instrument used for these analyses is the EMIA-920V2 made by HORIBA (Principle fig.1). The Elemental Metal Infrared Analyzer (EMIA) Series offers a variety of models to determine the carbon and sulfur contained in solid samples (powders, blocks of metal, chips...). Main applications are metals, especially steels alloys, for the iron industry where concentrations of C and S directly affect the properties of the products. Other materials can also be analyzed: ceramics, rocks, ores, semiconductors and new materials.

The sample (about 1 g) is placed in a ceramic crucible in a high frequency induction furnace, swept with purified oxygen and heated using a unique programmable temperature feature for optimum combustion. Gases produced during this combustion are then analyzed using four Infrared detectors, after removal of dust and moisture. Sulfur concentration is determined by the direct analysis of SO₂ while carbon is determined by the analysis of CO and CO₂ (low and high).

The induction furnace benefits from unique Plate Current Control (PCC). This feature allows the operator to create very easily any kind of custom temperature curves including up to 10 steps.

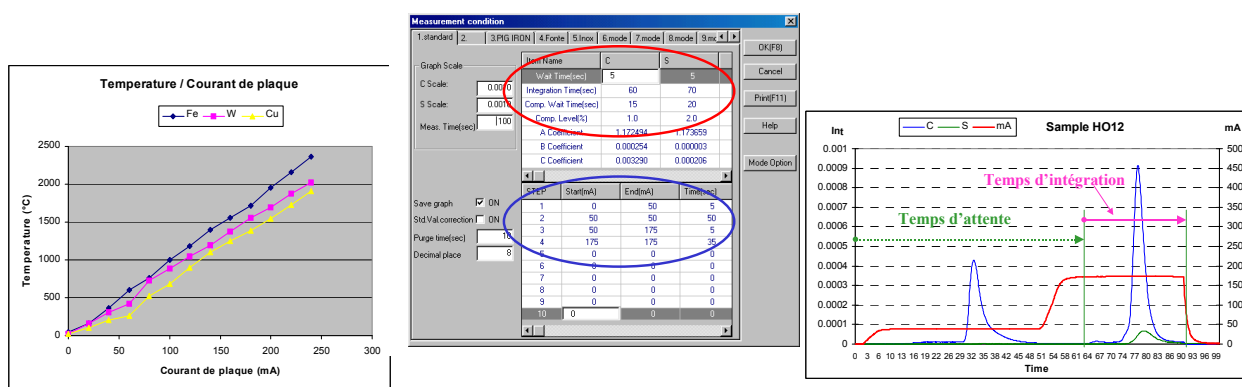


Figure 2: Correlation between plate current and temperature inside the crucible (left). The temperature curve can be set very easily (centre blue), as well as integration parameters (centre red). These settings produce a multi steps curve (right), up to 16 modes and curves can be stored in the software.

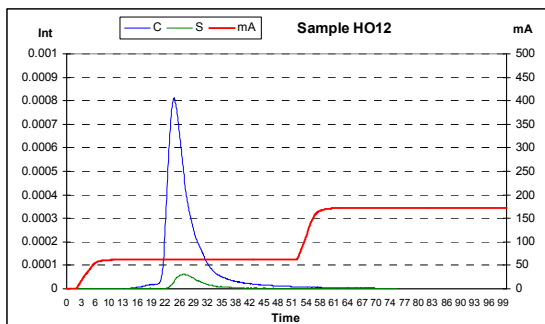
OPTIMISATION of the CONDITIONS

The target of peak separation method is to adjust the level, the duration and the shape of the temperature curve in order to visualize different peaks of carbon. In this case, it is adjusted in order to separate the carbon from the surface to the inner carbon of the sample.

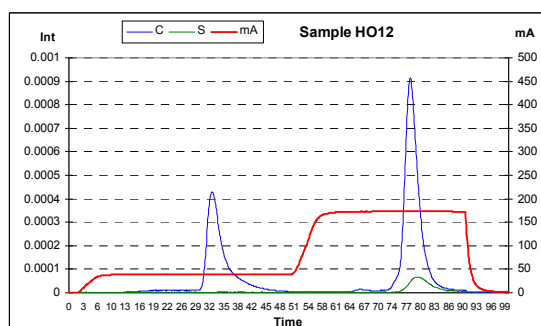
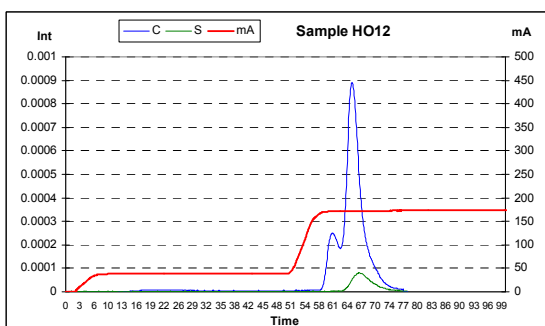
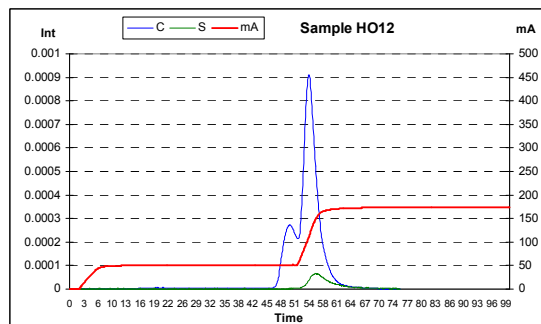
The measurement conditions are optimized based on different parameters such as weight and type of sample, quantity of accelerators used (W, Fe, Sn, ...) as well as the data of interest (integration area). Figures 3(a) to 3(d) explain the method to determine ideal conditions for the analyses done hereafter.

Peaks separation method

(a) 60 mA : Temperature at first step is too high.: All is extracted at once



(b) 50 mA : 2 peaks are visible, but not enough separated



(c) 40 mA : Temperature at first step is too low : Extraction is too late

(d) 45 mA : Optimum conditions : the 2 peaks are well separated.

Figure 3 : Optimization of the measurement conditions

EXPERIMENTATION

This work was carried out using pure iron chips as sample.

The sample is divided in 2 lots:

Lot 1 : Sample with heat pre-treatment for complete decontamination

Lot 2 : Same sample without pre-treatment. "As it is"

Three measurement series have been made:

Run # 1: Lot 1 with standard method

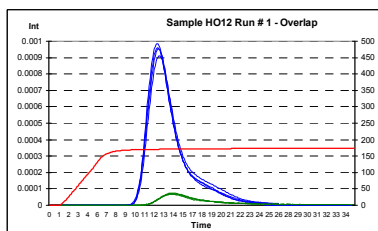
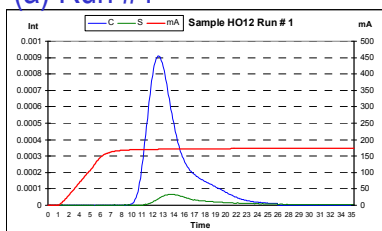
Run # 2: Lot 2 with standard method

Run # 3: Lot 2 with peak separation method

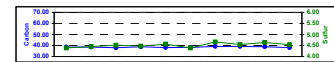
RESULTS

For each run, the figure 4 hereunder present one extraction curve, the overlap of 4 extraction curves and quantitative results with statistical graph.

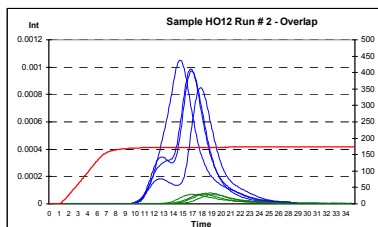
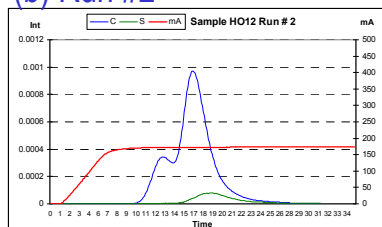
(a) Run #1



Sample	Weight	Mode	C carbon (ppm)	Sulfur (ppm)
HO 12 Lat 1	0.9920	Standard	38.64	4.39
HO 12 Lat 1	1.0102	Standard	38.65	4.45
HO 12 Lat 1	1.0151	Standard	37.94	4.51
HO 12 Lat 1	1.0111	Standard	38.12	4.56
HO 12 Lat 1	1.0086	Standard	38.26	4.39
HO 12 Lat 1	1.0055	Standard	39.87	4.66
HO 12 Lat 1	1.0147	Standard	39.11	4.54
HO 12 Lat 1	1.0086	Standard	38.86	4.64
HO 12 Lat 1	1.0234	Standard	38.89	4.55
Average			38.56	4.51
Standard deviation			0.42	0.09
RSD (on %)			1.09%	2.00%



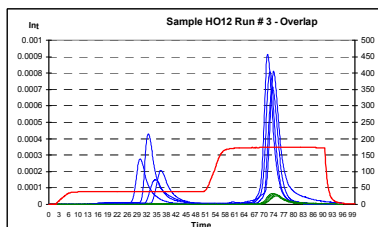
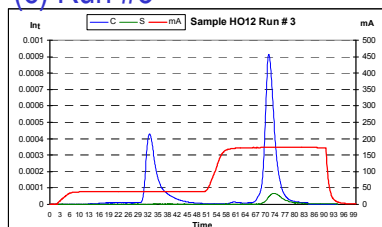
(b) Run #2



Sample	Weight	Mode	C carbon (ppm)	Sulfur (ppm)
HO 12 Lat 2	0.9382	Standard	40.98	4.66
HO 12 Lat 2	0.9354	Standard	41.40	5.17
HO 12 Lat 2	0.7081	Standard	41.95	5.57
HO 12 Lat 2	0.9257	Standard	41.75	4.69
HO 12 Lat 2	0.8126	Standard	41.28	4.52
HO 12 Lat 2	0.9678	Standard	41.74	4.92
HO 12 Lat 2	0.9188	Standard	41.10	4.44
HO 12 Lat 2	0.9169	Standard	53.89	4.87
HO 12 Lat 2	0.9824	Standard	41.81	4.52
HO 12 Lat 2	0.9884	Standard	48.18	5.08
Average			46.60	4.77
Standard deviation			6.85	0.42
RSD (on %)			14.70%	8.81%



(c) Run #3

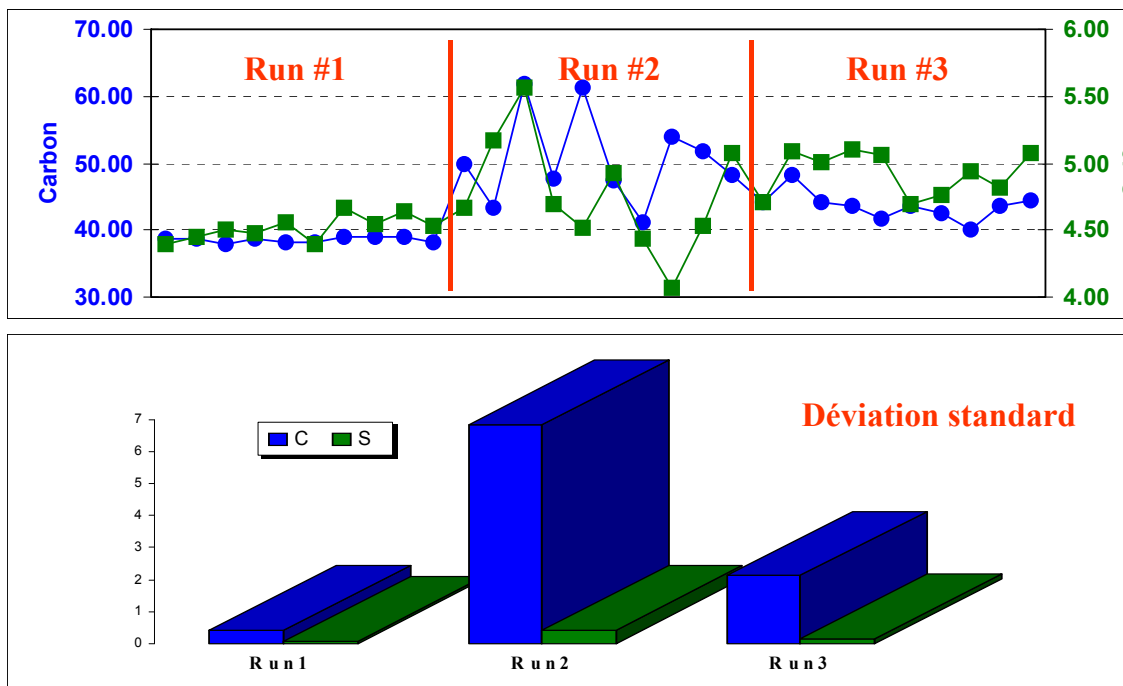


Sample	Weight	Mode	C carbon (ppm)	Sulfur (ppm)
HO 12 Lat 2	0.9237	Peak separation	44.87	4.71
HO 12 Lat 2	0.9260	Peak separation	48.26	5.09
HO 12 Lat 2	0.9772	Peak separation	44.27	5.01
HO 12 Lat 2	0.9251	Peak separation	43.50	5.18
HO 12 Lat 2	0.9983	Peak separation	41.79	5.06
HO 12 Lat 2	0.9255	Peak separation	43.79	4.69
HO 12 Lat 2	0.9679	Peak separation	43.52	4.76
HO 12 Lat 2	0.9210	Peak separation	39.98	4.94
HO 12 Lat 2	0.9298	Peak separation	43.54	4.82
HO 12 Lat 2	0.9338	Peak separation	44.70	5.08
Average			43.69	4.93
Standard deviation			2.12	0.17
RSD (on %)			4.86%	3.46%



Figure 4 : Results for the 3 runs

CONCLUSION



- ✓ Results from Run #1 are the reference, but require tedious sample preparation.
- ✓ Results from Run #2 are the best expectable results using the standard method and without sample pre-treatment.
- ✓ Results from Run #3 show a big improvement on repeatability and accuracy, still without sample preparation. This method also offers the advantages of no increase in cost and analysis time. For the operator, it is totally transparent: even without doing sample preparation, the instrument will separate the contamination itself and only the inner carbon concentration will be reported.

TATA STEEL IJMUIDEN LAB MADE FIT FOR THE FUTURE

Casteren van H.F.P.M. , Heemskerk R.B.

Tata Steel, Wenckebachstraat 1, IJmuiden, The Netherlands

Summary:

In April 2009 a new automated laboratory became operational at Tata Steel in IJmuiden. The extensive process which led to the automation is described as are its goals, benefits and properties. Two years of experience with the system shows that the goals are achieved and that the expectations were met. The changing demands of the internal customers can be met with relative ease due to the flexibility of the system. This shows that the Tata Steel process control laboratory in IJmuiden is fit for the future.

Article:

In 2009 the two process control laboratory automations were replaced by a new one. Goals were to improve reliability, speed, capacity, accuracy and efficiency for the handling of steel, iron and slag samples. This in the context of an expected growth in steel production. Almost all ultra low carbon and nitrogen analyses should be done with optical emission spectrometry to fulfil some of the main conditions.

Essential to achieving the desired functionality of the design was getting input from many users and technicians inside and outside Tata Steel. Also open discussions with the supplier of the automation (Panalytical) proved very useful. One of the most important conclusions was that there should be no "single point of failure" in the system. Known and reliable components of other automations were again applied in the new one. Components that were giving problems, were replaced with other commercially available ones. In some cases totally new machines were developed.

A software simulation of the automation was used to assess its speed and capacity. This also helped to test the proposed design of the automation. These simulations included assessing the consequences of failures in parts of the system and confirmed the quality of the design.

The new automation consists of 17 airtube sending stations, 11 airtube receiving stations, 5 ABB robots, 8 discharge stations, 3 millers, 3 optical emission spectrometers, 2 slag preparation lines, 2 XRF's. In addition to that there are camera's, weighing stations, printers, pyrometers, cooling stations and radio activity measurement systems.

Getting from the conceptual phase to an operational automation took about 3 years. It has been operational since April 2009 and fully replaced the existing automations in July 2009.

Because of the system architecture and inbuilt redundancy a very high availability of the system is achieved. Maintenance and repair are also much easier in this new system. Response times are better than before and they are more predictable. Also some improvements in analytical accuracy were achieved.

The expected cost reductions in manning and maintenance have been achieved. Manning was reduced by five in the shifts and one in the support group. Furthermore internal and external costs for maintenance and repairs were also reduced significantly.

Almost 100% of the ultra low carbon and 98% of the nitrogen analyses are now done with optical emission spectrometry. This results in faster reporting to the steel plant as well as lower costs for the analyses because of the reduction of consumables.

Conclusion:

Good preparation and innovation have resulted in a highly reliable automation and goals that were envisioned for this automation are achieved. This makes the new process control laboratory of Tata Steel IJmuiden "Fit for the Future".

INTEGRATION OF THE ROBOTIZED BORATE FUSION TECHNIQUE FOR THE XRF ANALYSIS IN THE FERROALLOY INDUSTRY

Luc Bérubé¹, Sébastien Rivard² & Mathieu Bouchard¹

Corporation Scientifique Claisse, Québec, CANADA¹
Corporation Scientifique Claisse - DIVISION EUROPE, Paris, FRANCE²

Abstract

Ferroalloys are high added-value materials used as raw materials in the steel industry to adjust the final composition of steel and provide its physical and chemical properties. A careful management of the quantities of ferroalloys added in the steel making process leads to significant savings. Moreover, impurities in ferroalloys can also affect the properties of steel. Proper characterization of ferroalloys is necessary since it has important impacts on the quality of steel production and also important financial impacts for the steel manufacturing companies.

Sample preparation by borate fusion coupled with XRF analysis is an effective and renowned technique for accurate and precise determination of major, minor and some trace elements in a wide range of ferroalloys. High performance fusion instruments can be integrated to robotized systems, rFUSION, allowing fused disks preparation to run completely independently from manual operations. Production wise, the automated fusion system rFUSION increases and stabilizes analysis output rates. Still, quality of results is never compromised over productivity and the rFUSION ensures standardization of the fusion process and brings consistency and uniformity over the results. The automated fusion system, rFUSION, by its effective and modular design, low cost of ownership and great return on investment ensures significant savings.

Introduction

Various metals such as V, Ni, Mo, Cr to name a few, are added quantitatively into liquid steel in their ferroalloy form, to produce various grades of steel that have different physical and chemical properties. Since ferroalloys are high added-value raw materials, a careful management of the quantity added within the steel process leads to significant savings. A very accurate and precise characterisation of their content is therefore needed. For example, it has been demonstrated¹, that an error of 1% in the determination of the Cr in FeCr was sufficient for a ferroalloy manufacturer or a steel maker to lose several hundreds of thousands of dollars in only year. In addition to the direct losses, important arbitration costs are to be expected in case of a dispute between the manufacturer and the steel maker over the composition of the ferroalloy. Impurities in ferroalloys also need to be characterized because they can affect the properties of steel.



Figure 1: Glass disks prepared by borate fusion.

Sample preparation by borate fusion², coupled with X-Ray Fluorescence spectrometry (XRF) is a preferred and well proven technique used by the steel industry to analyze ferroalloys and other raw materials of steel and ferroalloys. The preparation of borate fused disks (figure 1) is valuable since it offers the most precise and accurate multi-elemental composition determination for major, minor and a wide range of trace elements. The borate fusion preparation technique is preferred over the pressed pellet technique because it eliminates the particle size and the microstructure effects that can lead to significant accuracy problems for ferroalloys^{2,3}.

Ferroalloys are known to be difficult samples to prepare using borate fusion. They need to be completely oxidized in order to become soluble into the lithium borate melt. Moreover, if the oxidation is not completed or well controlled, the metals within the sample can form low melting point alloys with the platinum of the crucible resulting in important damage or total destruction of the crucible⁴. Hence, fusion specialists have developed reliable and platinum safe methods over the years to overcome these challenges^{1, 5, 6}. These methods are now used routinely by a growing number of ferroalloy testing laboratories all over the world.

A growing number of industrial laboratories are looking into robotized systems to automate their XRF sample preparation by fusion. Robotic automation allows laboratories to increase and stabilize their production rates, while decreasing labour costs, risk of injuries and errors associated with repetitive tasks. Several mining and cement testing laboratories are already equipped with robotized fusion preparation systems and are benefiting from the advantages of automation. In part because of the challenges of the fusion technique for ferroalloys, automation is not yet employed in ferroalloy testing labs. In fact, many world class leaders of the steel industry are still performing fusions using completely manual methods in a muffle furnace.

This paper demonstrates how to combine the dry oxidation technique and the Claisse rFUSION (Figure 2) to integrate the ferroalloy fusion preparation routine into a simple and totally automated robotized system. rFUSION is a line of automation products entirely dedicated to fusion. Even though the first advantages of automation that come to mind are related to increased productivity and labour savings, the rFUSION philosophy is to put the first priority on obtaining the quality results that are so important for the ferroalloy industry. rFUSION is designed to automate the manipulation steps that have the most impact on result quality and time saving while remaining easy to use and maintaining maintenance requirements and downtime to the lowest levels yet seen in fusion automation.



Figure 2: The rFUSION system for the automation of borate fusion.

Overview of the rFUSION System

A Claisse rFUSION workstation suitable for borate fusion for ferroalloys is illustrated in figure 3. It is composed of the rFUSION Weighing Station and the rFUSION M4 Fusion Station. Each station is composed of modules which serve specific functions as per described in the following.

The rFUSION Weighing Station performs the weighing of the flux according to a programmed sample-to-flux ratio. It contains a robot, racks for crucibles and glass disks, a mixing device as well as a control panel. It is the core of any rFUSION workstation:

- Robotic Arm - A six-axis electro-servo-driven industrial robot equipped with optic-fiber sensors for crucible detection.
- Claisse TheAnt Weigher and Dispenser - An automatic flux weigher and dispenser with a maximum accuracy of 0.1mg that is

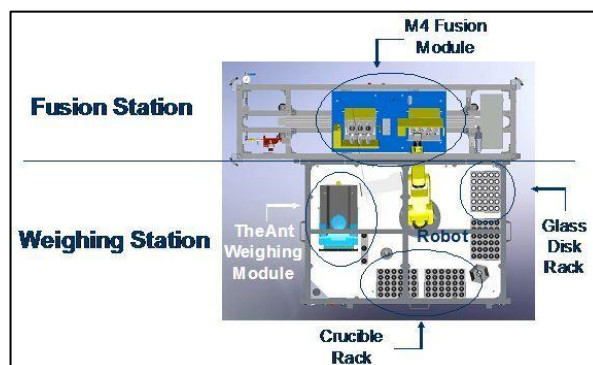


Figure 3: Overview of a Claisse rFUSION workstation suitable for ferroalloys preparation by fusion.

equipped with detectors for flux level and crucible presence and a high performance analytical balance with a maximum precision of 0.1mg and overload protection for vertical and horizontal loads.

- Claisse VortexMixer - A homing vibration mixer with programmable speed.
- Control panel - An HMI touch screen capable of storing up to 10 automated programs.
- Crucible and glass disk racks - Four, 30-position removable racks to hold crucibles or glass disks.

The rFUSION M4 Fusion Station is an add-on for the rFUSION Weighing Station. It performs the fusions:

- Claisse M4 Fluxer - A 3-position gas fusion instrument with programmable heating and agitation by rotation on an inclined axis. Capable of multi-temperature fusion cycles of up to 15 steps. The M4 fluxer does not require the use of compressed air or oxygen. A choice of one or two M4 fluxers can be installed in the rFUSION to obtain a maximum of 6 fusion positions.
- Artificial vision - A 3D smart-camera that provides 10 000 profiles per second and designed to operate in tough industrial environments.

The Weighing Station can be used alone or linked with the M4 Fusion Station. Since the system is modular, the user can upgrade the automation of his fusion operations step by step over the course of time. For example, a user could upgrade his TheAnt Weigher and Dispenser and M4 fluxer stand alone units to an rFUSION Weighing Station and then later upgrade by adding an rFUSION M4 Fusion Station.

The downtime of the rFUSION is greatly reduced in case of a breakdown or scheduled maintenance because the stations are composed of modules that can be used independently; TheAnt Weigher and Dispenser and the M4 fluxer units can be used with or without the robot and the Weighing Station can be used with or without the M4 Fusion Station.

The only significant moving part of rFUSION being a heavy duty industrial robot makes the maintenance requirements of the rFUSION simple and time-saving compared to what is generally expected of laboratory fusion automation.

Integration of the fusion of ferroalloys into the robotic rFUSION system

The use of the dry oxidation technique⁷ to prepare the ferroalloys by borate fusion is essential to the successful automation of ferroalloys. It is the simplest, quickest and is the most convenient oxidation method for ferroalloys⁵. The dry oxidation technique allows the oxidation and the fusion to take place in sequence during a single cycle, using only one instrument without the intervention of an operator. Generally, the sample is mixed with a small portion of flux and a solid oxidizer (hence the designation of dry oxidation) like a carbonate or a nitrate at the bottom of a platinum crucible.

The rest of the flux is added on top of the mix. The use of a non-wetting agent (bromide or iodide) is recommended to allow complete pouring of the melt into the mold, facilitate the cleaning of the crucibles between runs and ease the release of the glass disks out of the mold. It is recommended to use a flux with integrated non-wetting agent to eliminate a weighing step, thus eliminating a potential source of error. This sample-flux-oxidizer setup ensures a good contact between the sample and the oxidizer and contributes in obtaining total oxidation of the ferroalloy. The flux layer on top reduces the sputtering or overflowing of the material that can occur because of the exothermic reaction and the release of gases during the oxidation step. The crucible is then heated at low temperature to perform the oxidation process while the borate flux is still in a solid form. The oxidation steps are

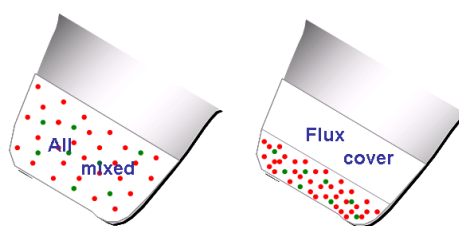


Figure 4: Two sample (green) – flux (white) – oxidizer (red) preparation setups for the dry oxidation technique.

followed by a careful and gradual increase of the temperature to allow the flux to melt and the fusion reaction to occur at around 1 000°C.

The design, the flexible operations as well as the technical performances of the different modules of the rFUSION, are also essential to the successful automation of ferroalloy fusion. Depending on the type of ferroalloy, two different preparation setups of sample-flux-oxidizer can be chosen to perform the fusion (figure 4). As it will be detailed below, the rFUSION system is capable of preparing these two types of setups. Additionally, to get successful fusions of ferroalloys using the dry oxidation, a fluxer capable of executing temperature plateaus at various levels in sequence in a controlled and repeatable manner is also needed. Figure 5

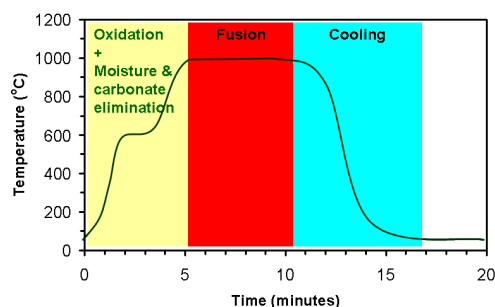


Figure 5: Typical heating cycle for the dry oxidation technique.

illustrates a typical temperature cycle for the fusion of a ferroalloy using the dry oxidation technique. Gas fluxers such as the Claisse M4 fluxer will provide the optimal flexibility to heat crucibles from a temperature plateau to another.

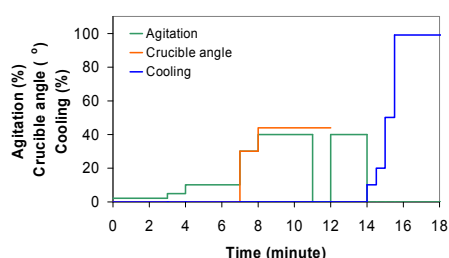


Figure 6: Programmed sequence of agitation, crucible angle and cooling rate in a ferroalloy fusion program on the Claisse M4 Fluxer.

The specially designed burners of the M4 fluxer also ensure stable oxidizing flames that do not reduce the efficiency of the oxidizing reaction in the crucibles. Other fusion parameters must also be controlled and programmed throughout the different steps of the fusion as shown in figure 6. A Claisse M4 Fluxer fusion cycle may contain as many as 15 different steps; therefore a user can easily program the rotation agitation speed, agitation angle, temperature level and the cooling rate which must be executed precisely to achieve successful fusions with optimal oxidation, without loss of material by sputtering or overflowing.

Here follows the methodology to prepare FeMo by borate fusion and the corresponding automation sequence on the rFUSION. The preparation of many other ferroalloys such as FeV, FeCr, FeMn, FeNi only to name a few may also be integrated to the rFUSION using similar dry oxidation techniques^{1, 6}.

1. First, two empty 30-position racks are removed from the station and brought to the weighing room of the laboratory by an operator;
2. The operator weighs $0.200 \pm 0.002\text{g}$ of FeMo (grinded under $125 \mu\text{m}$) in a clean ceramic crucible;
3. The operator then weighs $2.00 \pm 0.01\text{g}$ of NaNO_3 in a clean platinum crucible;
4. Both the ceramic crucible containing the sample and the platinum crucible containing the oxidizer are then placed onto the rFUSION racks by the operator. Up to 30 samples in their ceramic crucible and their corresponding platinum crucibles can be prepared and placed onto the rFUSION at once;
5. The racks are then placed into the rFUSION system and the sliding doors are closed by the operator;
6. The operator chooses the FeMo weighing and fusion programs using the rFUSION control panel and then presses the *Start* button;
7. The doors lock magnetically and the cycle begins. From this point on, up to 30 glass disks of FeMo are processed without the intervention of the operator;
8. The robot begins the fusion process by taking the platinum crucible (containing oxidizer) and places it on the balance of TheAnt Weigher and Dispenser. The tare weight is measured and a programmed first amount of flux (LiT/LiBr; 99%/1%) of 2g is poured into the platinum crucible.
9. The robot then takes the platinum crucible (now containing the first amount of flux and oxidizer) and places it on the transfer station.

10. The robot takes the corresponding ceramic crucible (containing the sample) and pours its content into the platinum crucible that is sitting on the transfer station. The platinum crucible now contains the unmixed sample, oxidizer and first amount of flux;
11. The robot then takes the platinum crucible to the VortexMixer for mixing;
12. Once mixed, the robot brings the platinum crucible back onto TheAnt Weigher and Dispenser balance where the weight of the sample is accurately measured;
13. According to the exact sample weight recorded, TheAnt Weigher and Dispenser pours the exact amount of flux needed to reach the programmed sample-to-flux ratio into the platinum crucible. The sample is now ready for fusion;
14. The platinum crucible is placed on the Claisse M4 Fluxer to start the fusion;
15. First, the oxidation step is executed at a low temperature and low agitation. A gradual temperature increase follows until the decomposition of the excess oxidizer is completed. Faster agitation follows once the fusion temperature is reached. The melt is poured into a pre-heated mold after complete homogenization and the cooling cycle starts;
16. At the end of the cooling cycle, the robot uses the vacuum suction cup to remove the glass disks and finally places them onto the glass disk rack.

When several samples are processed together, the multi-task ability of the robot allows for time-saving and also increases the throughput.

Accuracy and repeatability of the dry oxidation method for FeMo

To evaluate accuracy and repeatability of the fusion method used for FeMo, calibration curves for elements Mo, Si, Cu and Fe were created using reference materials SL-20-03, SL-20-06, SL-20-07, SL-20-08, SL-20-09, SL-20-11 and SL-20-12 from Dillinger and ECRM 578-1 from BAS. Six replicates of SL-20-12 were prepared as unknowns to evaluate the repeatability. The glass disks were prepared on a Claisse M4 Fluxer and the analyses were performed on a Philips PW 1404 WD XRF spectrometer. Other data obtained using the Claisse M4 Fluxer for the fusion of FeCr and FeV are also available^{1,6}.

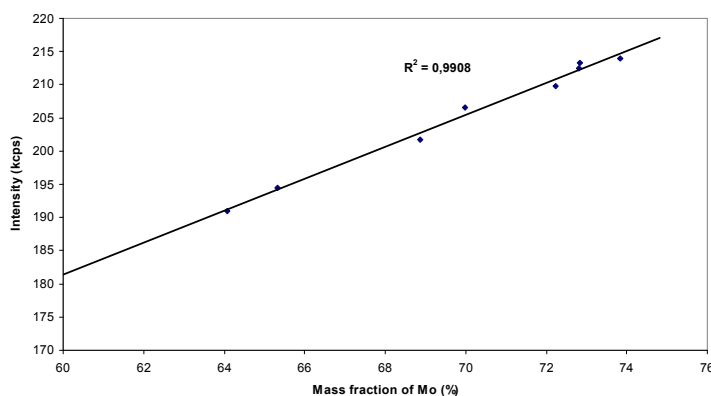


Figure 7: XRF calibration curve for Mo in FeMo using the dry oxidation technique and the Claisse M4 Fluxer.

Replicate	%Mo	%Cu	%Si	%Fe
SL-20-12-1	69.83	0.38	0.77	27.79
SL-20-12-2	69.93	0.37	0.74	27.81
SL-20-12-3	69.95	0.37	0.74	27.77
SL-20-12-4	69.94	0.38	0.74	27.80
SL-20-12-5	70.08	0.36	0.72	27.62
SL-20-12-6	69.52	0.38	0.73	27.70
Average	69.87	0.37	0.74	27.75
Std. Dev.	0.19	0.01	0.02	0.08
RSD (%)	0.28	1.5	2.5	0.27
Certified Value	69.99	0.390	0.790	27.82

Table 1: Accuracy and repeatability of the XRF measurement of Mo, Cu, Si and Fe in FeMo using a Claisse M4 Fluxer.

The calibration curve for Mo can be seen in figure 7. The Mo curve indicates adequate linearity and good coefficient of determination (R^2) at 0.9908 for a Mo concentration range of 64.07% to 73.83%. Table 1 indicates the measurements obtained for the six SL-20-12 replicates. The repeatability and accuracy are excellent for all four tested elements. The accuracy and repeatability for Mo recorded here is comparable to what can be found elsewhere in the literature for other fusion methodologies for FeMo and other ferroalloys^{8, 9}. Our repeatability and accuracy obtained by fusion is also in the same order of magnitude of what is expected for the ISO-4173 gravimetric standard method¹⁰.

The advantages of using rFUSION automation for the fusion preparation of FeMo

The total error of an analytical method is known to equal the root sum of squares of all errors of each step of the procedure. For an XRF method with sample preparation done by fusion, errors can be generated mainly by the spectrometer, the fusion instrument, the quality of the molds used, the manipulation of the sample and the weighing. The methodology and good practices for the monitoring of the performance of the XRF spectrometer are well known and work well. The same care needs to be applied to monitor the performance of the fusion instrument¹¹ and the effect of the quality of the molds used during fusion¹². The Claisse Fusion Monitor is a new tool designed to monitor the mold effect and the performance of the fusion instrument¹³. As for the manipulation of the sample and weighing, the use of the rFUSION allows limiting and nearly eliminating the errors associated to these crucial steps.

As seen above in the methodology description, nearly all the operations involved with the preparation of the sample before, during and after fusion are done by the robot when rFUSION is used. With a robotic system, the manipulations are always done the same way without forgetting any step and without interchanging samples. The automation of the fusion manipulations also means that training is simplified for new operators.

Now that most modern XRF labs are equipped with automatic fluxers like the Claisse M4 Fluxer, manual weighing has become the most hated and tedious task associated with borate fusion. Because it is tedious and repetitive, operators are prone to make mistakes or take bad decisions when fatigue sets in. The problem is that small weighing errors can introduce significant bias in the final results. In fact, incorrect weighing has a direct influence on sample dilution in the specimen analyzed in the fusion technique and dilution affects the measurement of the intensities, especially for major elements like Mo in FeMo for example. For the fusion of ferroalloys, the absolute error on the sample weight has the largest impact on the final dilution. Extra care needs to be taken during the manual weighing of the sample. The precision tolerance for ferroalloy sample weighing should weigh no more than $\pm 0.0001\text{g}$ when it is done manually. The second largest impact on dilution will come from flux weighing and a precision of $\pm 0.001\text{g}$ will be required when it is done manually. Such tight precision requirements will require much concentration and will also require perseverance from the operator when the task is repeated several times during the day. For the oxidizer NaNO_3 , the precision required will be less at $\pm 0.01\text{g}$ since only 36% of the mass will remain after the fusion (only Na_2O remains after N_xO_y gases are generated and lost during heating).

Because of the impact of weighing on the total error of the method, the module TheAnt Weigher and Dispenser (figure 8) of the rFUSION Weighing Station is a major contributor to the accuracy and repeatability of the robotized ferroalloy fusion method. TheAnt Weigher and Dispenser is already used in several industrial laboratories as a table top stand alone instrument and can also be used online in the robotized fusion system rFUSION. It has been proven to be a performing instrument that ensures consistent and accurate weighing while simplifying the work of the operator¹⁴. TheAnt Weigher and Dispenser measures the exact weight of the sample ($\pm 0.0001\text{g}$), calculates the amount of flux to add to reach the exact programmed sample-to-flux ratio and finally dispenses the flux with great accuracy (up to $\pm 0.0001\text{g}$). For the preparation of ferroalloys it means that the sample-to-flux ratio will always be the same even if the sample weight is not exactly on the target (oxidizer is included in the tare weight). Since the weight measures of the sample and the flux have the largest impact on dilution, it means that TheAnt Weigher and Dispenser eliminates the largest part of the error associated with weighing (Note: the weight of the oxidizer is included in the tare weight so it has no impact on the sample-to-flux ratio adjustment made by TheAnt Weigher and Dispenser and its effect on the final dilution is much less than for the sample and the flux since 64% of its mass is lost during fusion). Because of the ratio adjustment made



Figure 8: Claisse TheAnt Weigher and Dispenser.

automatically, the precision required for weighing of the sample becomes $\pm 0.002\text{g}$ instead of $\pm 0.0001\text{g}$ which makes a big difference in terms of the probability to make an error.

The use of rFUSION drastically reduces the labour time needed to prepare ferroalloy glass disks for XRF analysis. The first reason is that most of the steps are automated which totally frees the operator's time as soon as the *Start* button is pressed. The second reason is that less precision is required for the weighing of the sample as it is explained above and therefore less time is needed to execute this task. In table 2, an evaluation of the labour time savings associated with the use of rFUSION is proposed. The only tasks that have to be done by the operator using the rFUSION is to weigh the sample at $\pm 0.002\text{g}$ precision and the oxidizer at $\pm 0.01\text{g}$ precision which should take about 75 seconds total per sample. In manual mode (manual weighing with the use of a Claisse M4 Fluxer), the sample needs to be weighed with a high precision and all the other steps are done manually for a total of 6 minutes (360 seconds). This means that the use of the rFUSION leads to labour time savings of 80%.

Operation steps	Labour time (s)	
	Manual mode	rFUSION robotized mode
Sample weighing	120	45
Oxidizer weighing	30	30
First flux weighing	60	auto
Mixing	30	auto
Second flux weighing	60	auto
Crucible installation in fluxer	20	auto
Glass disk removal	20	auto
Crucible removal	20	auto
TOTAL TIME	360	75

Table 2: Evaluation of the labour time savings associated with the use of the rFUSION robotized system for the borate fusion of ferroalloys.

Conclusion

The Claisse approach to robotics and the dry oxidation methodology now makes it possible to integrate the preparation of ferroalloys by fusion into a fully automated system. Equipped with the M4 fluxer, a high performance fusion instrument, and a TheAnt Weigher and Dispenser, the Claisse rFUSION system allows users to fully benefit from the advantages of automation such as increased and stabilized throughput rates and decreasing labour time, while ensuring consistent glass disk quality and accurate and repeatable results. The use of rFUSION eliminates most of the potential errors associated with weighing and sample manipulation that can have important impacts on the quality of the results. The accuracy and the precision obtained with the Claisse fusion methods for ferroalloys meet the requirements of the industry and the use of the rFUSION ensures that these quality results are always obtained independently from the operator.

References:

- 1) Berube L., XRF and AA/ICP analysis of FeCr: The power of borate and peroxide fusion sample preparation, CCATM 2010, Beijing, China.
- 2) Corporation Scientifique Claisse, Glass disks and solutions by fusion for users of Claisse fluxers, 2nd edition, 2003, 67 pages.
- 3) Eivindson T., Mikkelsen O., Problems by using pressed powder pellets for XRF analysis of ferrosilicon alloys, *Advances in X-Ray Anal.*, 2001.
- 4) Lupton D. F. *et al.*, The correct use of platinum in the XRF laboratory, 19th Durham Conference on X-Ray Analysis, Durham, England, 1995.
- 5) Berube L., Minimizing time and manipulations for the preparation of ferroalloys by fusion, Duisburg X-Ray Fluorescence User Meeting, Duisburg, Germany, 2007.
- 6) Rivard S., Preparation of ferroalloys for XRF analysis using the borate fusion and the dry oxidation technique, Dortmund X-Ray Fluorescence User Meeting, Dortmund, Germany, 2010.
- 7) Berube L., Borate fusion of samples containing semi or non oxidized element: The solid dry oxidation technique, Denver X-Ray Conference, Denver, USA, 2006.
- 8) Coedo *et al.*, X-ray fluorescence determination of major and minor elements in ferrotitanium, ferroniobium and ferrovanadium from compressed pellets and fusion beads, *X-Ray Spectrom.*, 2002.
- 9) Rutherford R.T., Ferro-alloy analysis by X-Ray fluorescence spectrometry, *X-Ray Spectrom.*, 1995.
- 10) ISO-4173, Ferromolybdenum – Determination of molybdenum content – Gravimetric method, 1980.
- 11) Gagnon J-P., Gendreau L., Evaluation of an electric fluxer, *International Cement Review*, August 2007.
- 12) Corporation Scientifique Claisse, ASTM C-114 Qualification test method to improve analytical results using the fused beads technique, ICMA, 2001.
- 13) Levesque D. *et al.*, Error free monitoring, *International Cement Review*, August 2009.
- 14) Berube L. *et al.*, XRF fusion precision with TheAnt, *International Cement Review*, March 2008.

THE IMPORTANCE OF SAMPLE PREPARATION AS PART OF LABORATORY WORKFLOW AUTOMATION SOLUTIONS

Bassin Marc, Dolezal Ludwig, Hagen François

Thermo Fisher Scientific SARL, 1024 Ecublens, Switzerland

Abstract

The preparation of metals samples for process control purposes in the iron and steel industry has undergone a significant evolution in recent years. With milling becoming the preferred preparation technique, new opportunities are available to users:

First, the use of universal CNC machining centers broadens the range of available solutions.

On the other hand, local manufacturers in India and China for instance, have specialized in this field and offer preparation machines designed specifically for the purpose.

A review of the most important parameters affecting the performance of modern sample preparation machines as part of fully automated laboratories will help understanding better their contribution. The tighter integration of sample preparation in the new generation of automated Thermo Fisher Scientific Optical Emission Spectrometers (OES), X-Ray Fluorescence spectrometers (XRF) and Fire Assay Analyzers (FAA) allows exploiting the full potential of modern sample preparation systems in terms of speed and throughput, flexibility, cost of ownership and lifetime.

Fully aware of the market expectation to have a choice of solutions and brands, the new Thermo Fisher Scientific open automation architecture on the sample preparation side allows customers to select the best solution depending on their needs, preferences and budgets.

1) Introduction

The preparation of metals samples for process control purposes in the iron and steel industry has undergone a significant evolution in recent years.

Milling has become the preferred preparation technique with the following advantages:

- It is suitable for both iron and steel samples
- It reduces contamination between samples which is essential for low and ultra low C and N₂ analysis.
- There is no grinding paper contamination (Al₂O₃ or CaO)
- No conditioning of abrasive belts is necessary which saves time
- A deburring capability is available for standards
- No sophisticated dust aspiration is needed, saving on maintenance and increasing uptime
- It produces perfectly flat and constant quality surfaces with reduced roughness fluctuations over time
- Samples do not heat during preparation. Cold samples have not to be cooled before analysis

With milling, new opportunities are now available to users:

- First, the use of universal CNC machining centers broadens the range of available solutions.
- On the other hand, local manufacturers in India and China for instance have specialized in this field and offer preparation machines designed specifically for the purpose

Sampling and sample preparation are essential components of the laboratory workflow contributing directly to the quality of results. The best spectrometer will never be able to produce meaningful results out of poor or badly prepared samples.

Closely related to the analysis which is the ultimate goal of the process and the only deliverable, sample preparation must operate as a peripheral device of the spectrometer, readily available when samples or standards have to be re-prepared. Therefore, in the optimized Thermo Fisher Scientific automated laboratory workflow, sample preparation is always integrated in the automated spectrometer cell rather than in the sample transport or in a separate intermediate workflow component, as explained below.

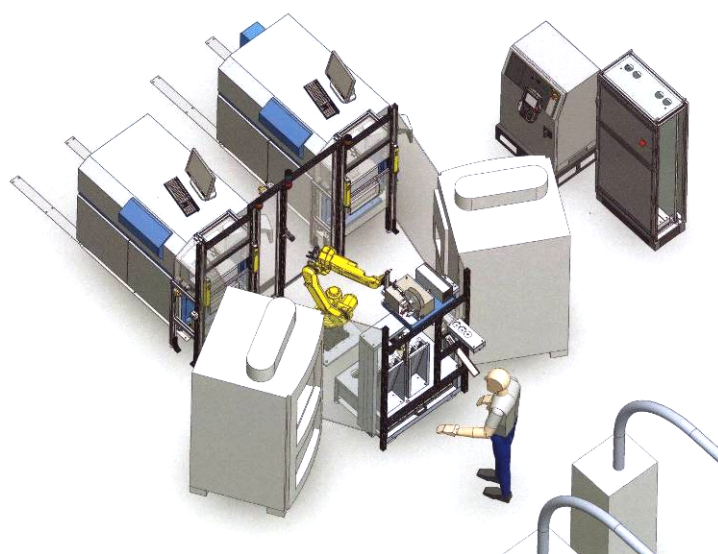
2) Major criteria in the evaluation of milling machines

We will now review the most important parameters affecting the performance of modern sample preparation machines as part of fully automated lab. This will help understanding better their contribution.

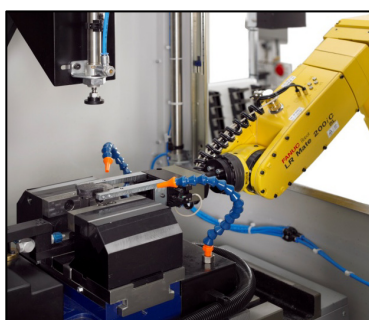
The first and probably most important criteria in iron and steel applications is:

2.1) Speed and sample throughput

In the automated laboratory example below including two ARL Metals Analyzers and two sample preparation machines, the automation robot has a direct access to the milling machines to save time. Electromechanical sample transfer systems are eliminated which reduces sample turnaround times and increases uptime.



Automated laboratory example with ARL SMS-3500



The ARL SMS-3500 robot accesses the two milling machines directly for sample pick-up and place via an additional side door. For maintenance or semi-automatic operation, convenient access to the milling machines is maintained via the front doors, avoiding having to switch off the complete robotic system.

Short sample preparation times are important to increase throughput when several samples of different priorities have to be processed at the same time.



In this application, samples are unloaded manually from the air tubes and introduced in the system via a single introduction position.

A sample introduction magazine provides for the storage of incoming production samples. This simplifies operators work and automated air tubes interfaces:

- The next sample can be immediately introduced
- The samples are automatically processed by priority
- No extra mechanical moving parts are required, the robot providing for a high speed random access in the fixed magazine

The automation system manages the samples based on their priorities and on the available sample preparation and analysis resources to optimize response times. No more than 8 seconds are required to load samples in the preparation machine.

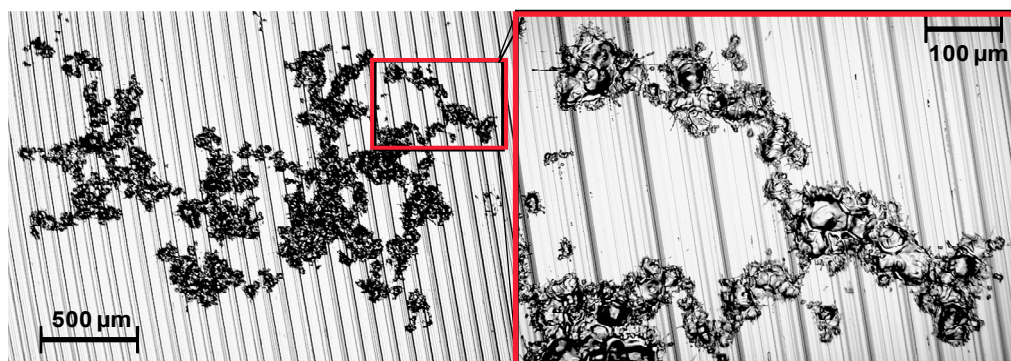
In larger laboratories, multiple ARL SMS-3500 automated cells are used to cope with higher sample volumes while providing full redundancy to maximize availability of automated sample preparation and analysis.

Another important factor contributing to the global performance is the total milling cycle time.



The highest speed obtained today is using a Haas vertical machining centre called Mini Mill: 22 to 27 seconds for iron and steel samples depending on the type of sample. This is the total time between closing the sample introduction door and unlocking it to pick-up the prepared sample; it includes the sample surface positioning using a fast sample height measurement system, sample clamping, milling and sample release.

2.2) The preparation quality and reproducibility



The ablation pattern produced by single spark on the surface of the RE12 pure iron standard

The zoomed view of the selected area

This shows the effect of the first spark at the surface of a prepared RE12 pure iron standard using an ARL Metals Analyzer. The milling grooves (pattern left by the milling tool) are clearly visible in the background as parallel lines. A single spark consists of several hundreds of cathode craters spread over more than 2.5 mm. Several thousand sparks are produced during the homogenization phase called pre-integration.

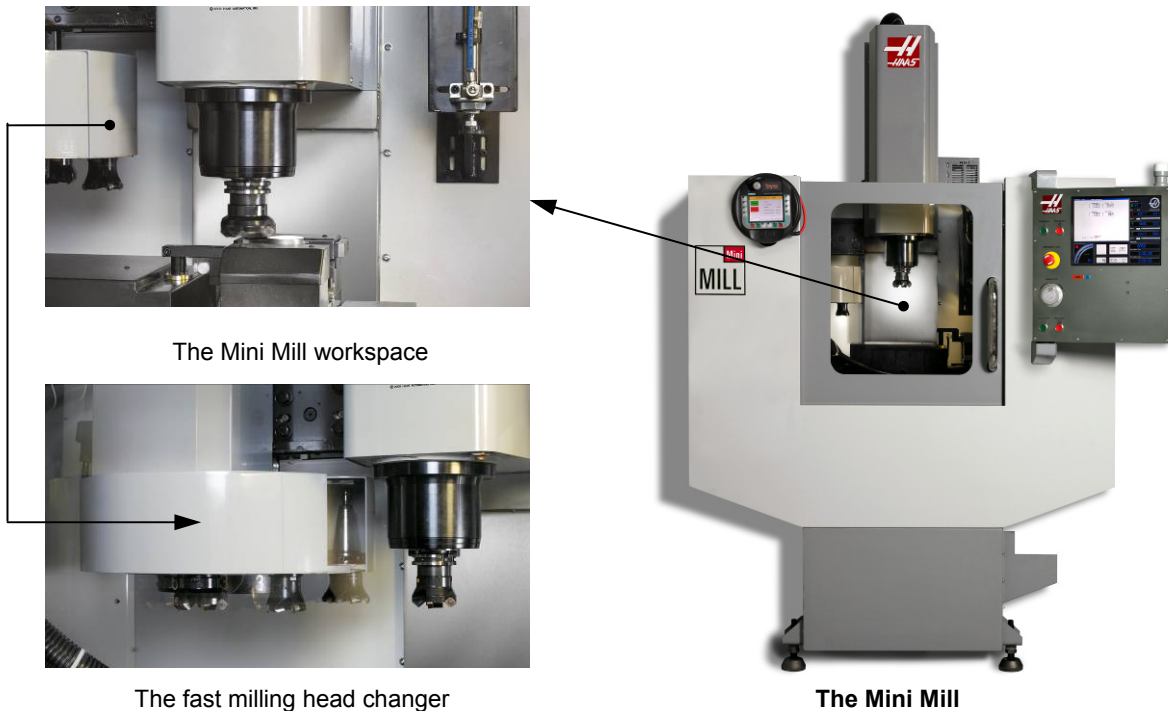
A fully reproducible sample preparation ensures measuring samples under strictly identical conditions.

Of particular importance is the prepared surface roughness which is targeted below 2 Ra [μm] for OES and XRF analysis (this is the roughness of the surface expressed in μm as the arithmetic average of the absolute roughness values).

To achieve high and constant quality prepared samples surfaces, the compliance of the milling machine with milling best practices is an important evaluation criterion, as explained hereafter.

2.3) Customization potential and system autonomy

This shows the Haas Mini Mill workspace with its surface positioning system on the right and its internal storage magazine for up to 10 milling heads.



The Mini Mill workspace

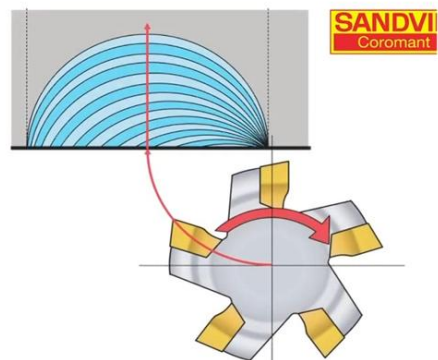
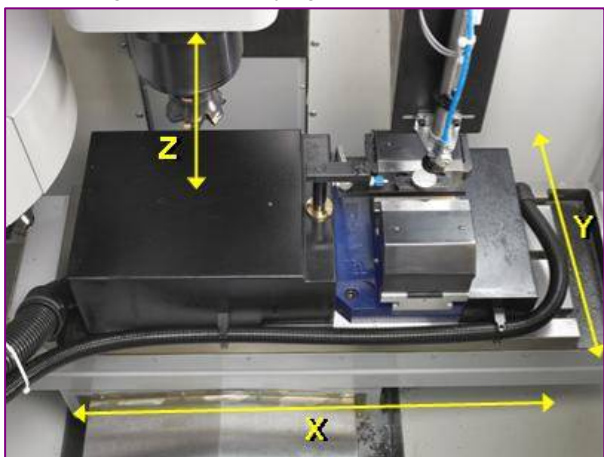
The fast milling head changer

The Mini Mill

This ultra fast and reliable umbrella tool changer performs milling head changes in 5 seconds. This increases the sample preparation autonomy and reduces maintenance interventions as milling heads can be automatically changed after a user defined number of production samples and standards have been processed. More milling heads can also be used to optimize the milling process for specific material qualities. The milling machine must be compatible with all sample shapes and dimensions typical of the iron and steel industry. A deburring facility must be available for the perfect preparation of soft setting-up, control samples and type standards as well as for production samples of symmetric shape.

2.4) Operating costs and service

The cutting tips lifetime is critical in terms of operating costs. To achieve the highest speed and longest cutting tips lifetime, the machine must comply with milling best practices (golden rule of milling). This requires a true 3-axes milling machine applying the roll-in technique (as explained for instance in the Sandvik Coromant web site).



The Mini Mill: a true 3-axes (X-Y-Z) milling machine producing thick chips on entry and thin chips on exit

The robustness of the milling machine is another key issue as the cutting tips lifetime depends on the rigidity of the machine. Flex and damp vibrations must be eliminated by the use of a cast-iron frame. This must not be done at the expense of speed.

The milling machine must be designed for a 24/7 continuous operation and long lifetime to cope with the sample workload peaks typical of the iron and steel industry.

Beside the machine price, which is important in the evaluation of any product, the machine upgradability is another important evaluation criterion which has a direct impact on the cost of ownership. Even when used in a semi-automatic mode initially, a full automation and integration in a robotized spectrometer system must be possible anytime at affordable costs.

Regular maintenance and efficient local service support are other critical requirements to ensure uptime.

2.5) Ease of set-up and operation

Ease of set-up and simple operation is also important to consider when evaluating milling machines.

This shows the swivelling control terminal of a Herzog milling machine. It provides all the necessary facilities to operate the preparation machine in semi-automatic mode.



The operator control terminal

The Herzog HS-FF2000 milling machine

The milling machine must be very easy to set-up and operate for the specific sample preparation application. No special knowledge must be required to define the relevant machining parameters (the choice of milling head, the milling depth, the milling spindle feed rate and the milling head rotation speed). For complex applications requiring fine tuning, the number of preparation programs available for the user should not be limited.

3) Conclusion

Sampling and sample preparation quality are essential for the analytical performance of Optical Emission and X-Ray Fluorescence spectrometers.

With sample preparation automation, the variability of the prepared samples surfaces is drastically reduced. Differences between operators are eliminated.

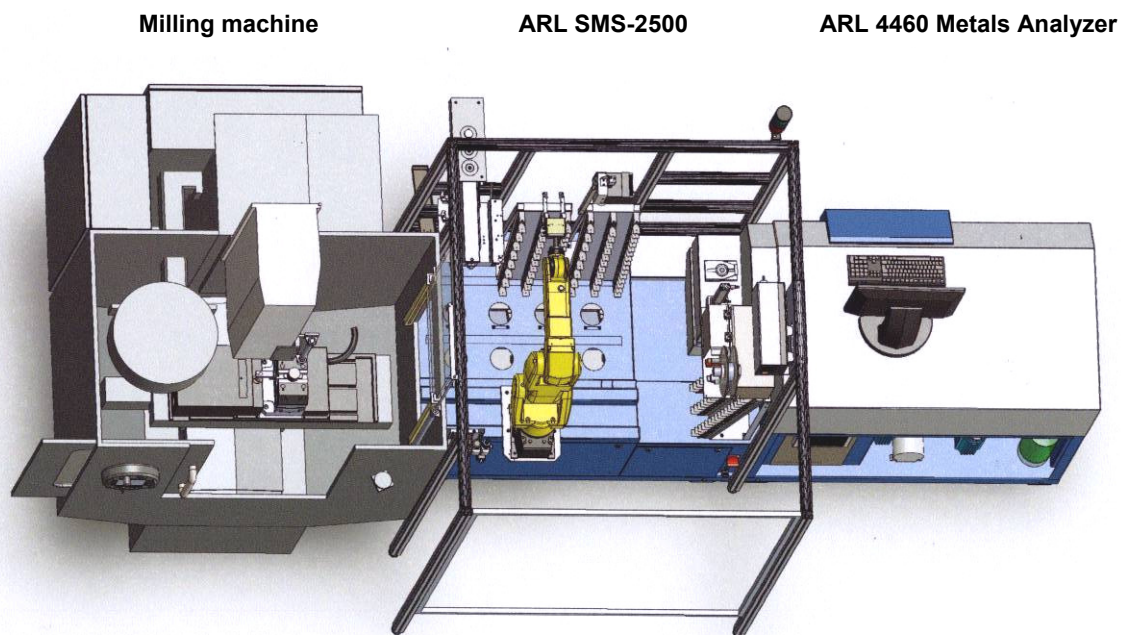
A more consistent and reproducible prepared surface quality improves both the short term analysis repeatability and the long term reproducibility. Both aspects contribute to the instrument precision that is an essential measure of the analytical performance.

In addition, sample preparation automation leads to significant time savings. This allows delivering metals qualities within tighter specifications. Savings in alloying materials and faster production turnover are other major quantifiable benefits.

As designer of the instrument that produces the elemental analysis, which is the only deliverable of the process, Thermo Fisher Scientific is better able to take the responsibility of the entire system including accessories such as sample preparation. Fully aware of the market expectation to have a choice of solutions and brands, the new Thermo Fisher Scientific open automation architecture on the sample preparation side allows customers to select the best solution depending on their needs, preferences and budgets.

Using innovative technologies, scalable and optimized for the best analysis quality and the shortest sample turnaround times, the new automation architecture is the ideal base to build instrument and laboratory workflow automation:

This shows the latest addition to our range of spectrometer automation systems with sample preparation integrated as a peripheral of the OES or XRF spectrometer: The ARL SMS-2500 is based on a mid-size Fanuc robot standing on a chassis.



The compact and optimized automated ARL Metals analyzer with ARL SMS-2500

This ultra fast sample processing system is capable of delivering a single run analysis in just about 60 seconds (from sample introduction to analytical result transmission)

The automation of production control laboratories in the iron and steel industry offers new perspectives and real opportunities for the metals industry. These are summarized as a conclusion of this presentation:

- To give priority to quality while not compromising volume
- To better control critical manufacturing phases
- To work closer to the low grade specification limits and save on expensive alloying material
- To cope with increasingly severe and tighter product specifications
- To eliminate bottlenecks
- To reduce manufacturing costs (energy, refractory) leading to a more competitive cost of the ton of metal

- To participate to production rationalization efforts
- To minimize scrap and rework resulting of human mistakes

Nowadays, automation is increasingly considered as a necessary contribution to the integrity of a production process and the final quality of its output

A NEW GENERATION IN SPARK EMISSION SPECTROMETRY

J. Niederstraßer, B. Overkamp

*OBLF – Gesellschaft für Elektronik und Feinwerktechnik mbH, Salinger Feld 44, 58454 Witten, Germany,
www.oblf.de*

Abstract

Sample analysis using spark emission spectrometry requires taking at least two readings at various positions on the sample surface to ensure any inhomogeneities such as inclusions and blow holes are detected and a realistic average can be calculated. Since the sample has to be repositioned between measurements, the total analysis time is therefore made up of the time taken for the readings and for moving the sample.

As the response times governing steel production in steel mills are growing ever shorter and at the same time more and more analyses need to be performed on a single batch, reducing analysis time has become a major objective within the field of spark emission spectrometry. To this end, this paper intends to present practical experience gained using a spark stand plus a measurement data acquisition system with whose help simultaneous readings can be taken at various positions on the sample surface. This means the total analysis time can be reduced to the time taken for a single measurement – and without having to reposition the sample on the spark stand.

Introduction

Spark emission spectrometry has been the preferred analysis method used by process laboratories serving the steel industry for many years now. The advantages of the method include the possibility of being able to analyse all elements required for process control purposes – including carbon, sulphur and nitrogen – in a single step, its suitability for automation as well as its speed.

However, process laboratories are expected to enable ever shorter analysis times and therefore pass this demand on to spectrometer manufacturers. While a single sparking still took 60 s forty years ago, the same sparking takes no more than 15 to 25 s today, depending on the necessary number of exposure times. In this regard, the additional sparking time required for nitrogen and ultra-low carbon (ULC) is a point in case. Up to now, analysis time was reduced by, among others, introducing a high-energy pre-spark (HEPS) period, as a result of which the so-called stationary sparking condition is reached more quickly, or by increasing the spark frequency. While older spectrometer systems were only capable of generating a spark frequency of 50 Hz, frequencies of many hundred Hertz are possible today. Within the steel industry, a typical value would be in the region of 800 Hz – a 16-fold increase on the frequency used years ago. However, there are limits to both methods of reducing analysis time. Experience has shown that time plays an important role in achieving the stationary sparking condition. It is, for instance, not possible to increase the discharged energy to the extent that the pre-spark time would take no more than a single second. Using a commonly available spark stand, it is currently not possible to increase the spark frequency beyond 800-1000 Hz for both excitation- and time-related reasons since the time between individual discharges has to be long enough to permit the discharge gap between the sample and the electrode to be fully purged of plasma. If this period of time is not long enough, the individual discharges will interfere with each other.

Another way of reducing analysis time is by decreasing the number of sparkings that are required for calculating a mean value. As a general rule, two reproducible readings are used to calculate the mean. Cutting out one of these sparkings will therefore halve the analysis time. However, in so doing one also increases measurement uncertainty, since the reading may, for instance, have been caused by an inclusion or a blow hole. Plausibility tests can be performed on the analysis results, based on the cast quantity or cast history, to help to detect such inhomogeneities or raised concentrations of typical inclusion elements such as Ca. If at all, this method is applied by steel mill laboratories nowadays only for testing particularly time-critical preliminary samples. If such a degree of uncertainty is unacceptable for whatever reason, further readings have to be taken at various positions on the sample surface. The total analysis time is therefore made up of the time taken for both sparkings plus the time taken to reposition the sample and clean the electrode. If we take an analysis including nitrogen and ULC as an example, we arrive at the following times:

- 1. Sparking: 3 s Purge time + 8 s Pre-spark time + 14 s Exposure time = 25 s
- Repositioning the sample (incl. cleaning the electrode): 6 s
- 2. Sparking: 3 s Purge time + 8 s Pre-spark time + 14 s Exposure time = 25 s
- Total: 56 s

During the so-called purge time, the spark stand is purged with argon to fully remove any air. The pre-spark time is used to condition the spark spot. The 14-second exposure time is made up of a period for standard elements, a high-energy period for nitrogen excitation and an exposure time characterised by special measuring conditions to enable accurate ULC determination. It therefore takes about a minute to take two readings from a single sample. While it may be possible to save another second or two by optimising the pre-spark and exposure times – but not without simultaneously compromising the statistical reliability of measurements taken – the question here is whether there are any other ways of reducing analysis time. The following goes to prove that alternative options certainly do exist.

Experimental

Fig. 1 shows a diagram of a spark stand consisting of an upper plate, on which the sample is positioned to rest above the spark stand opening, and the spark chamber that, among other things, houses the electrode. The spark chamber is purged with argon while the reading is taken. After an electric spark has been ignited by an excitation source, a plasma is created between the electrode and the sample. While this takes place, sample material is split into atoms and thermally excited in the hot plasma. The light that is generated enters the optical system. A spark spot is left on the sample.

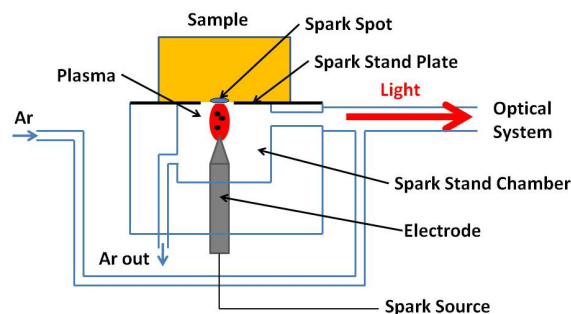


Fig. 1: Standard spark stand

But if the spark stand opening were oval instead of being circular and if the spark chamber contained two and not just one electrode, as shown in Fig. 2, the sample would no longer need to be repositioned to take two readings – which amounts to a major advantage and cuts analysis time by about six seconds. This is of particular value if sample readings are taken using a robot-controlled automated system because the robot does not need to wait for the first reading to be completed before repositioning the sample and cleaning the electrode. Should no more than two sparkings be required, the robot only has to deliver and collect each sample once.

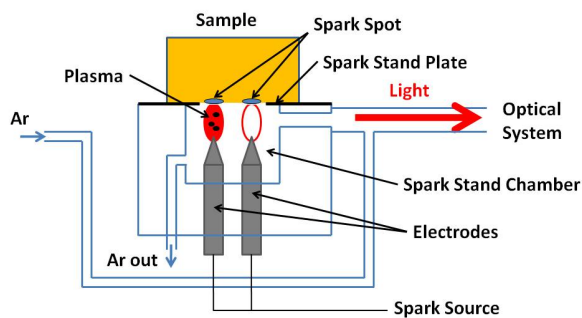


Fig. 2: Double electrode spark stand

The following Figs. 3 and 4 show photos of such a double electrode spark stand, once without a sample and once with a sparking in progress and the sample only half covering the spark stand opening. The two plasmas – which actually alternate – are easy to see. They are both visible at the same time due to the longer exposure time of the camera. Fig. 5 shows the two resulting spark spots.

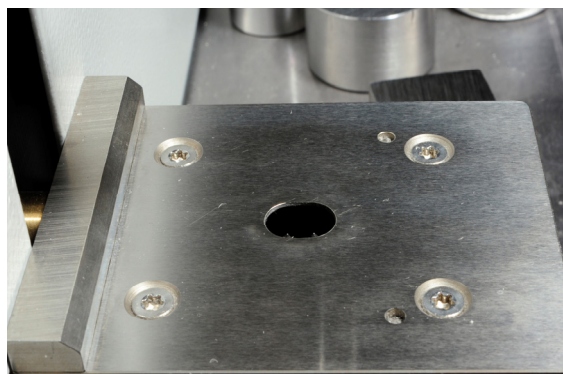


Fig. 3: Spark stand plate with oval opening

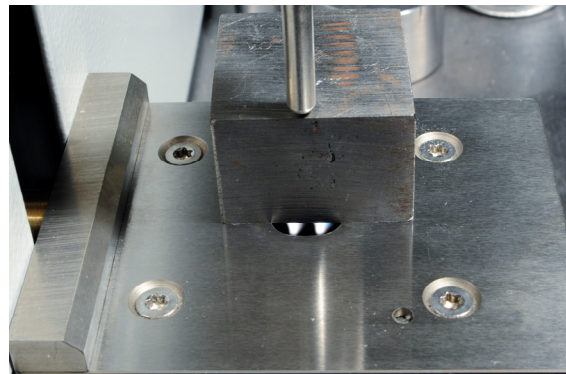


Fig.: 4: Both plasmas

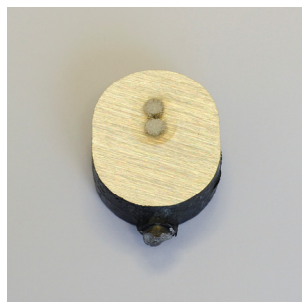
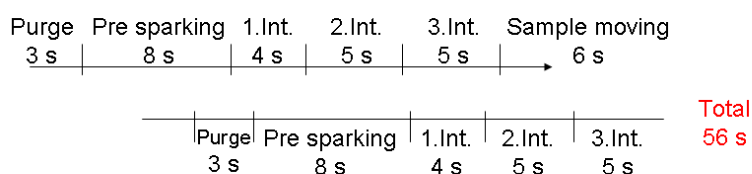


Fig. 5: Both spark spots

The possible time saving is not limited to these six seconds, though. As an example, only one purge period is required to remove atmospheric air from the spark chamber. And then there is the pre-spark time. As no readings are taken during this time, the measurement data acquisition system is not involved in this step. The electrodes are spaced far enough away from each other to enable alternating operation at a frequency higher than 800 Hz. Tests conducted with a new and more powerful excitation source have shown that twice the frequency can be used, i.e. 1600 Hz. This means that both spark spots can be conditioned during the eight-second pre-spark time. Pre-sparking is carried out alternately on both electrodes quasi simultaneously at a frequency of 1600 Hz, with the subsequent integrations being carried out consecutively. Going back to the example of an analysis for nitrogen and ULC, the time taken to perform two sparkings is reduced from 56 to 39 seconds. The precise timings are shown in Fig. 6.

Standard spark stand



Double electrode spark stand

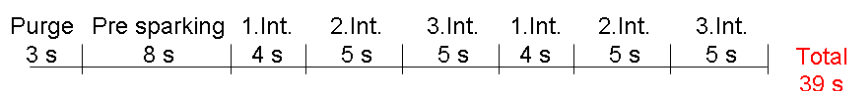


Fig. 6: Breakdown of the time saving

Analytical Performance Data

Let us now look at the analytical performance data of a double electrode spark stand. As the degree of masking at each of the two electrodes can be subject to slight variation, BEC (Background Equivalent Concentration) values were initially determined. As an example, the results for a number of key steel elements along with standard performance data are shown in Table 1.

Tab.1: Comparison of BEC Values

Element	Wavelength / nm	BEC / ppm Electrode 1	BEC / ppm Electrode 2	BEC / ppm Standard
C	193.1	390	383	380-440
Si	251.6	956	942	940-1100
Mn	293.3	153	150	136-165
P	178.3	99	97	95-120
S	180.7	73	70	52-75
Cr	286.3	723	712	710-810
Ni	225.4	1160	1130	1000-1200
Mo	202.0	710	686	520-720
Al	396.2	49	48	42-50
Ti	337.3	54	53	44-58
B	182.6	28	28	23-30

For most elements, the BEC values are identical or vary only very little, which means there is no significant difference between the degree of masking. In comparison to standard values delivered by the same spectrometer type, all values lie within the measuring interval. The requisite analytical conditions are therefore given.

In the next step, calibrations were carried out for both electrode systems using just a few certified samples. The time to take the readings necessary for calibration purposes is almost the same as the time taken for a normal reading since measurements are taken at both electrodes when the “start” button is pressed. The evaluation is naturally performed separately for both electrodes. Examples of analysis function (reverse of calibration function) of chrome and nickel in low-/medium-alloy steel are shown in Figs. 7-10. The analysis functions themselves differ only slightly, while the standard deviation and the Ni matrix interference on Cr are almost identical. Separate calibrations should still be used, though, to ensure the measurements at both electrodes are as accurate as possible.

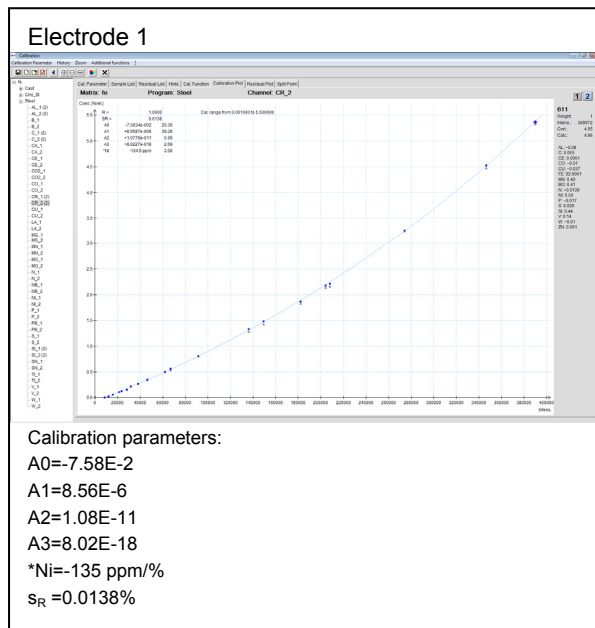


Fig.7: Analysis function Cr, Electrode 1

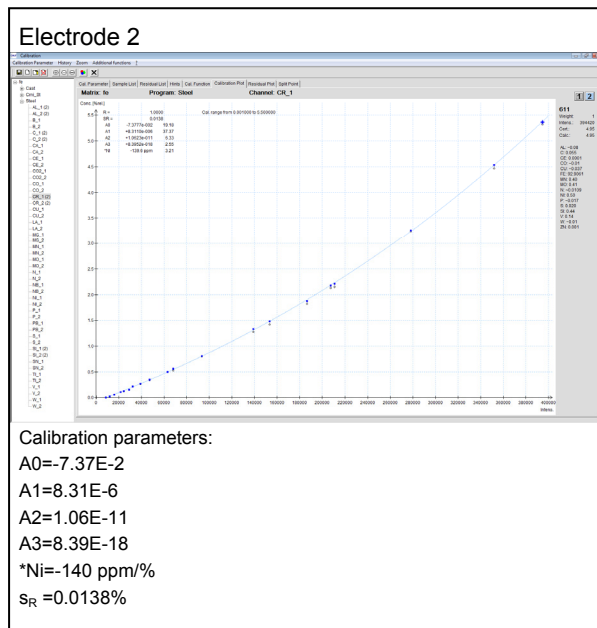


Fig.8: Analysis function Cr, Electrode 2

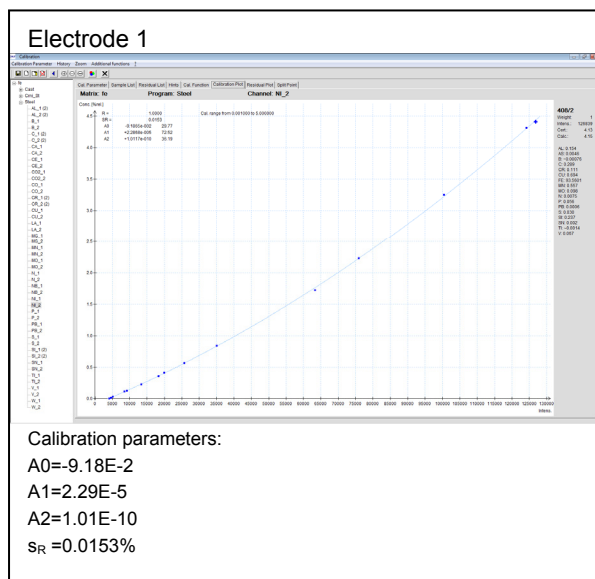


Fig.9: Analysis function Ni, Electrode 1

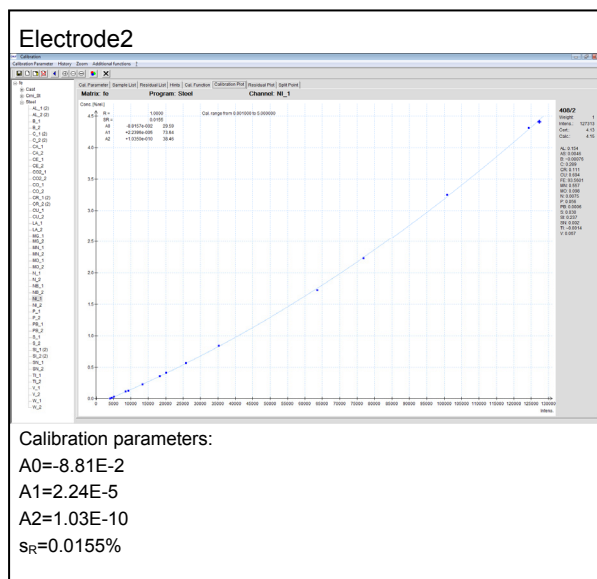


Fig.10: Analysis function Ni, Electrode 2

After the calculation of the analysis functions they are imported into the analysis programs to check the results for congruence. Thanks to performing 10 sparkings on the Fe 2/1 sample used, repeatability data were also delivered. The results are detailed in Table 2. The calculated mean values are comparable for all elements. Obviously, they do not perfectly match since they were performed using two different calibrations. But as these values must lie between the repeatability values obtained using a standard spectrometer and those obtained using different spectrometers – calibrated using the same set of samples – this requirement has more than been satisfied.

Tab.2: Comparison of Mean Values and Repeatability Data

Element	Electrode 1		Electrode 2	
	Mean / %	SD / %	Mean / %	SD / %
C	0.3752	0.0014	0.3789	0.0019
Si	0.3615	0.0015	0.3608	0.0013
Mn	0.6200	0.0020	0.6200	0.0021
P	0.0387	0.0002	0.0392	0.0002
S	0.0102	0.0002	0.0103	0.0002
Cr	0.6063	0.0017	0.6047	0.0015
Ni	0.6793	0.0024	0.6805	0.0030
Mo	0.3179	0.0010	0.3168	0.0009
Al	0.0431	0.0006	0.0440	0.0004
Ti	0.0406	0.0001	0.0397	0.0001
B	0.0038	0.0002	0.0039	0.0001

Overlap of Exposure Times

The only part of the analysis that still needs to be performed twice is the actual reading. Up to now, readings have been taken at both electrodes consecutively. But what if this could also be optimised? Given a spark frequency of 800 Hz, there is a time slot of 1.25 ms for each spark. However, a spark discharge and the resulting emission only takes about 0.25 ms, which means that signals only have to be actually measured and processed in a fifth of the integration time – leaving the measuring system “idle” for four fifths of the time. So to keep the system busy during this time, a bright idea was born in 2010. While we would have liked to patent the process, we unfortunately found out that someone else had already done so several years ago. In fact, Franz-Josef Brüning from Hattingen in Germany filed a patent application for this idea in 1983. However, as far as we know, a commercial spectrometer with this special feature has never come on the market.

The idea itself is as simple as it is effective and involves using the “idle” times of the integration system to supply it with information from a second measuring point. A schematic of the idea is shown in Fig. 11.

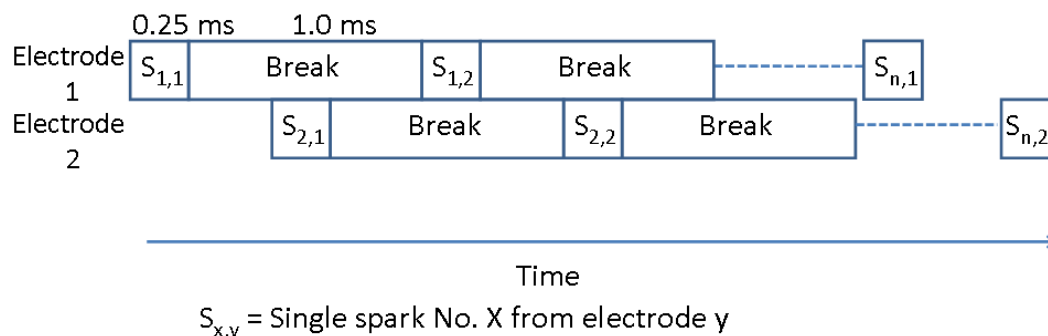
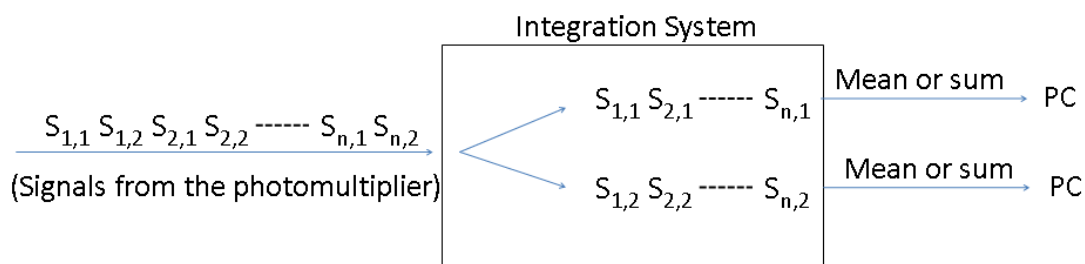


Fig. 11: Timing of sparking two electrodes and taking readings

The first individual spark and the associated emission are generated at electrode 1. During the pause between the first and the second individual spark, another spark is ignited at electrode 2, which results in the emission of light. Once this emission has fully died down, the second spark is generated at electrode 1 – and so on. The alternating light emissions generated in this manner therefore do not interfere with each other. All light impulses are measured in the optical system with the help of photomultipliers. These photomultiplier signals are ultimately captured by the measurement data acquisition system, as illustrated in the diagram at Fig. 12 below. Each individual spark signal must be separately integrated and the values saved specific to each electrode. A mean value or the sum of all values can then be viewed on a PC, with the values measured at both electrodes displayed as separate sparkings. Further, it must remain possible to define an individual time window for each measuring channel (key word: TRS = Time Resolved Analysis).



$$S_{x,y} = \text{Single spark No. X from electrode y}$$

Fig. 12: Schematic of signal separation

The total time saving detailed at Fig. 6 can, however, be maximised still further due to the fact that the exposure times also occur simultaneously, as shown in the breakdown at Fig. 13.

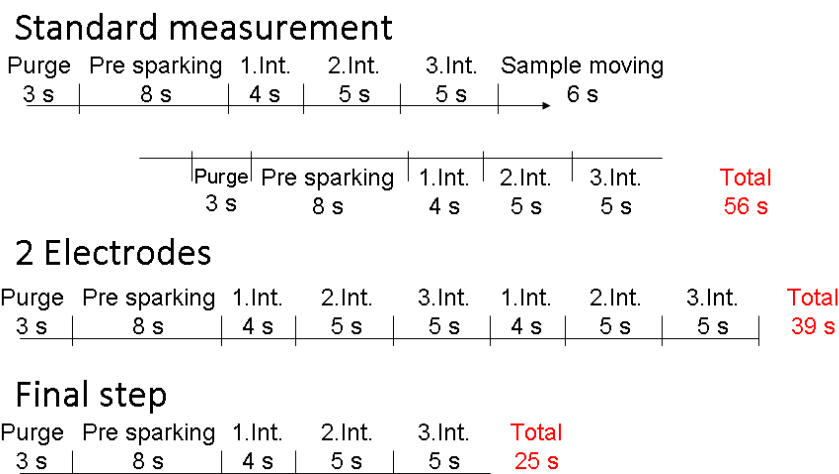


Fig. 13: Schematic of the time saving (II)

The time taken for a double measurement including nitrogen and ULC can therefore be reduced from 56 to 25 s, which puts it on a par with the time it takes to perform a single sparking.

Conclusion

Thanks to the introduction of a double electrode spark stand plus intelligent software and a measurement data acquisition systems for control, signal readout and signal separation purposes, a process was developed with which an analysis comprising two sparkings can be carried out in the same time it takes to perform a single sparking. This should help process laboratories that serve the steel industry to perform sample analyses considerably more quickly than was possible up to now.

Once further manual-operation tests have been completed, all necessary measures will be taken to ensure this new generation of spectral analysis can also be used with automated spectrometer systems.

Bibliography

[1] Brüning, F. J., Patent application DE 3703928 A1

SAMPLING METHODS AND SAMPLE PREPARATION

Maria Pelé

CTIF, 44 av Division Leclerc, 92310 Sèvres, France

Abstract

This presentation aims to recall "old" concepts and instructions, regarding sampling methods and sample preparation.

Information on the procedures used in other fields of the metallurgical analysis, besides that of steel, will be given. However, these concepts and procedures are mostly linked to the foundry industry knowledge rather than to other possible fields requiring specific operations (if any).

Sampling by itself is an "useless" action: it has to be taken as a corner of a "triangular" process, where the other two are the matrix under concern and the technique(s) to be used.

A fourth "dimension" – the preparation of the sample – will also be detailed regarding its suitability, taking into account the alloy and the analytical technique (or method) supposed to be used.

In cases of samples taken from a "piece", warning on the re-melting possibilities and limits will be reminded.

Some particular cases related with the preparation of divided samples will also be underlined.

In parallel, the expertise (or rather, the lack of expertise) of operators in charge of these tasks will be reminded, together with that of customers sending "all kind of sample" to a laboratory (namely the third party ones).

At last, the existing standards on "Sampling and sample preparation" will be pointed out, together with a "complaint" regarding the content of these documents, as some of them are not enough "mandatory": they may lead therefore to some "bad" practices.

Introduction

In metallurgical analysis, "sampling" can be defined as a chain of operations carried out in order to obtain a "sample suitable for analysis" that SHALL represent the chemical composition of a melt.

In the foundry industries (at least in almost cases), sampling is performed from the molten metal at the moment when the metal is poured into the moulds. The composition of these samples should be representative of that of the castings produced.

Irrespective of the alloy, this operation has a critical importance regarding the reliability of the results of any further analysis.

This implies that the sampling instructions be strictly followed in all circumstances.

Sampling instructions

Most of the controls of the chemical composition are carried out by "optical emission spectrometry" (or less usually by X-ray fluorescence spectrometry) directly on a solid sample.

Consequently, it is of paramount importance to obtain samples with a structure as similar as possible to that of the Reference Materials used for the calibration of the instruments used: the sample to be poured *should therefore have a structure and a grain size as fine as possible*.

For this purpose, it is necessary to cast the sample in a die that should be cold, clean and free of imperfections, whilst paying attention to the place (in the ladle) where the molten metal is taken (areas with slag shall be avoided, for example).

The solid samples

The shape and the size of the solid samples may depend:

- on the alloy to be analysed;
- on the excitation source that will be used.

But... in all cases, such samples shall:

- be free of imperfections and other macroscopic heterogeneities;
- be correctly machined;
- be correctly labelled.

Figure 1 schematizes the unbroken interconnection between "sampling and sample preparation", the matrixes and the techniques.

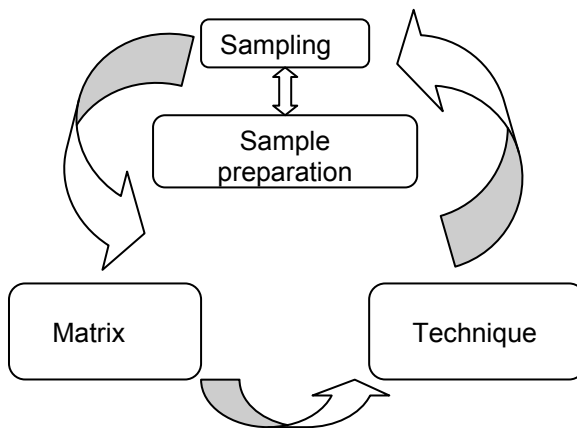


Figure 1 – Sampling "triangular process"

Cast iron solid samples

The related structure shall be necessarily WHITE. For this, the discs to be obtained shall be THIN as, for example, those described in EN ISO 14284:2002 [1] or in the French standard NF A 01-800:1986 [2].

The surface of these discs should be prepared by means of a **grinding machine**, regardless of the analytical technique to be used.

The analysis of these solid samples can be carried out either by S-OES¹, GD-OES² or XRF³. The related suitability may be schematized as:

Low alloy cast irons	Performances rather equivalent	}	GD-OES
			XRF
	Less suitable	⊘	S-OES
Alloyed cast irons	To be used preferentially	⊘	XRF
	Less appropriate	±	GD-OES
	Much less appropriate	⊘	S-OES

However... most of the laboratories use spark optical emission spectrometry, independently of the material grades, for reasons mostly linked with the cost of the equipment and related maintenance and with the required training level of the staff...

Steel (casting) solid samples

In most cases, suitable samples are obtained either by pouring the metal in a tapered mould (as shown in Figure 2) or by immersing a suitable device (sampling probes) [1] in the molten metal.

¹ Spark optical emission spectrometry

² Glow discharge optical emission spectrometry

³ X-ray fluorescence spectrometry

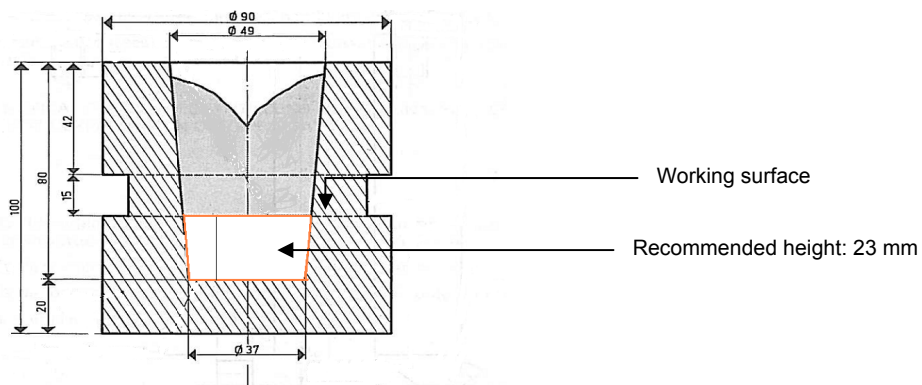


Figure 2 – Tapered mould [2]

Killing (often with aluminium) is mandatory, in both cases.

The surface of the steel samples should be prepared by means of:

- grinding machines, if glow discharge or spark optical emission spectrometry is used;
- turning or milling machines, if X-ray fluorescence spectrometry is used.

For steel samples, the "recommended" analytical techniques are:

Low alloy steels	<i>To be used preferentially (better sensitivity)</i>	↗	S-OES
	<i>Performances rather equivalent</i>	}	GD-OES
			XRF
Alloyed steels	<i>To be used preferentially</i>	↗	XRF
	<i>Less appropriate than X-ray fluorescence</i>	±	GD-OES
	<i>Much less appropriate</i>	↘	S-OES

Copper and copper alloys

The solid sample should be thin and it should be cast in a mould having a shape that will avoid (or at least minimize) segregation (namely radial).

ISO 1811-1 [3] and ISO 1811-2 [4] give specifications for the selection and preparation of samples for chemical analysis.

However, these specifications are widely related with the preparation of samples for wet chemistry analysis: there is no EN or ISO standard specifying shape(s), size(s) and mould(s) for copper and copper alloys specimens for "solid sample analysis".

CTIF recommends the use of "mushroom" discs (60 mm diameter and 5 to 6 mm thickness), as represented in Figure 3.



Figure 3 – Copper alloy "mushroom" disc

Sometimes used for copper-aluminium alloys, discs casted using the "top pouring" (or "spout pouring") method should be avoided. Figure 4 gives a schema of such specimens and shows the corresponding segregation zone (inappropriate for analysis).

The surface of the copper and copper alloys solid samples should be prepared by means of turning (or milling) machines, regardless of the analytical technique to be used.

Polishing shall be avoided for samples with lead content greater than about 0,5 %.

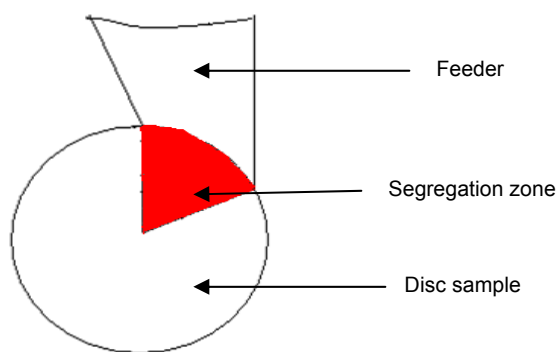


Figure 4 – Top poured specimen

For copper and copper alloys, it is appropriate to classify the recommended analytical techniques as:

Determination of traces and minor elements contents	<i>To be selected preferentially (better sensitivity)</i>	↗	S-OES
	<i>Performances rather equivalent</i>	}	GD-OES
			XRF
Determination of alloying elements contents	<i>To be used preferentially</i>	↗	XRF
	<i>Less appropriate than X-ray fluorescence</i>	±	GD-OES
	<i>Much less appropriate</i>	↘	S-OES

Aluminium and aluminium alloys

As for copper alloys, the sample should be thin and it should be cast in a mould having a shape that will avoid (or at least minimize) segregation (namely radial).

EN 14361 [5] specifies: "The form of the sample shall ensure, after sample preparation, a correct analysis. If S-OES is used, the sample shall allow as many sparks as required according to preliminary tests and prEN 14726⁴, to guarantee the compliances with specifications. The sample form shall allow a portion of drillings, millings or small pieces to be taken that are known, by pre-testing to be representative of the average composition of the whole sample (e.g. a longitudinal segment) for wet chemical analysis."

Nevertheless, this European standard does not specify the shape(s), size(s) and mould(s) suitable for obtaining an aluminium or aluminium alloy specimen for "solid sample analysis".

For such purposes, CTIF recommends [6] the use of "mushroom" discs (40 or 60 mm diameter and 5 to 6 mm thickness), as represented in Figure 5.

⁴ EN 14726, published in December 2005



Figure 5 – Aluminium alloy "mushroom" discs

As for copper and copper alloys, the surface of the aluminium or aluminium alloys solid samples should be prepared by means of turning (or milling) machines, regardless of the analytical technique to be used.

For aluminium grades, the recommended analytical techniques should be:

Aluminium-silicon alloys	<i>To be selected</i>	↗	S-OES
	<i>Less appropriate than S-OES</i>	±	GD-OES
	<i>Inappropriate: structure effects</i>	× ×	XRF
Other aluminium alloys grades	<i>To be used preferentially</i>	↗	S-OES
	<i>Performances rather equivalent</i>	}	GD-OES
			XRF

Zinc alloys

Concerning the sample moulds, EN 12060 [7] indicates: "*Designed to produce homogeneous samples representative of the product metal. The form and the size of the mould are very important. Moulds shall have a sufficient cooling rate, to cause the rapid solidification of the metal and avoid the segregation of the components. Moulds shall be chemically inert, not affecting the molten metal.*"

However in spite of the real importance of the size and shape of the moulds (and of the samples to be poured into), this standard does not propose drawings.

For zinc and zinc alloys sample shapes (and also for the preparation of the related surface), the CTIF recommendation [6] is the same as for aluminium and aluminium alloys.

As for copper-aluminium alloys, discs cast by the "top pouring" method are often prepared. However, they should be avoided for the segregation reasons already underlined.

Spark optical emission spectrometry remains the most suitable technique for all zinc grades, but glow discharge optical emission spectrometry and X-ray fluorescence spectrometry can be used with equivalent performances.

Sampling from the castings

The sample obtained cannot be representative of the composition of the whole product, for reasons related with segregations, grain size effects ...

For some alloys, re-melting operations may help (at least to minimize grain size effects), provided that some limits are respected:

- *Cast irons*
Re-melting under argon atmosphere is appropriate; BUT, losses of C, Mg, Pb, Zn ... in all cases.
- *Steels*
Re-melting is appropriate with suitable devices, under the same conditions as for cast irons and with the same restrictions ...

- *Copper alloys*
Re-melting **is not appropriate** (losses of Zn, Pb, Sn, ...). Direct analysis on a test piece should be restricted to low contents determinations on a semi-quantitative basis.
- *Aluminium alloys*
Aluminium alloys can be re-melted under normal atmosphere (the melt is well protected by the formation of an Al₂O₃ layer). Nevertheless ... loss of Na, Ca, Sr ...
- *Zinc alloys*
Zinc alloys can be re-melted under normal atmosphere; as far as we know, only Zn losses may occur.

The divided samples

The surface of the solid sample from which the chips are taken should be perfectly clean.

The tools (mill, drill...) **shall** be clean and in good condition and they **shall be** chosen taking into account the hardness of the material to be machined.

Lubrication and/or cooling products **should be avoided**.

Overheating should be avoided.

The chips, drillings, turnings or millings obtained should be stocked in suitable containers: *clean, dry, hermetic, chemically inert and abrasion resistant*.

Cast irons

- Divided samples from white structure materials are mostly obtained by drilling (or crushing for carbon and sulphur determination purposes)
- If the materials have a grey structure, the divided samples are prepared by drilling: the chips obtained shall be THICK in order to minimize graphite losses.

Steels

- Drilling, milling and turning are appropriate. The use of chip breaker devices is often recommended.

Aluminium, copper and zinc alloys

- A suitable surface of the sample should be machined (milling):
 - an **entire** sector of a disc;
Care should be taken if the disc was cast by the "top pouring" method (sometimes used for Cu-Al or for zinc alloys)
 - an **entire** surface of a cylinder;
 - an **entire** piece;
 - **all** bits of pieces taken from a casting.

Specific cases

- *Carbon determination*

For cast iron white structure materials, the carbon determination is carried out on chips (drillings) or on small pieces obtained by crushing.

If the materials have a grey structure, pieces with suitable dimensions (2 mm thickness and 5 to 8 mm length) should be cut by means of a saw in order to minimize the graphite separation from the bulk. *Chips, even when THICK, shall be AVOIDED.*

For steels and copper-nickel alloys, any kind of well prepared chips is suitable.

Care should be taken when dealing with steel specimens having undergone carburisation or decarburisation treatments: the sampling shall be carried out in a suitable core zone of the piece.

- *Nitrogen determination*

For steels, samples in the form of chips, small pieces obtained by punching or machined cylinders [$\varnothing \sim 4$; $h \sim 8$ mm] are appropriate.

Care should be taken when dealing with steel specimens having undergone nitriding treatments: the sampling shall be carried out in a suitable core zone of the piece.

For cast irons, if the structure is white, small pieces obtained by crushing or chips are to be used: machining cylinders is rather difficult for hardness and brittleness reasons.

When materials have a grey structure, machined cylinders [$\varnothing \sim 4$ mm; $h \sim 8$ mm] or chips are suitable.

- *Oxygen determination*

For steels as well as for cast irons, only machined cylinders or punched pieces are allowed. These preparations are to be carried out just before the analysis.

This also means that it is quite difficult to determine the oxygen content in white structure cast irons, as the machinability of small cylinders is not easy to achieve from a bulk test piece.

To "solve" this problem, a test piece as that represented in Figure 6 can be used. The mould presents a cylindrical extra device, allowing obtaining a pre-machined cylinder.



Figure 6 – Cast iron test piece with lateral cylindrical device

Conclusions

Let us try to bear in mind that a good and suitable sample preparation is the basis of a "good determination".

Unfortunately, this operation is often performed by insufficiently trained staff.

This point is critical within third party laboratories as they have no control of the initial sampling.

Lacks of knowledge regarding sampling and sample preparation are also shown by some customers: requiring good oxygen determination on "blue" chips taken from steel or an accurate carbon determination on grey cast iron thin chips...

In some circumstances, we have to declare that some samples are inappropriate for particular determinations, regardless of some "bad economical consequences".

The absence of short and clear guidelines describing appropriate moulds and specific sampling and sample preparation procedures is to be underlined: wrong, incomplete or misunderstood sampling instructions are the first linkage of the uncertainty chain associated to a result of an analysis!

Some material standards (for cast irons, namely) give mould drawings for mechanical test pieces and the related instructions are respected.

Why should it be different when dealing with sampling for the purpose of a determination of chemical analysis?

References:

- 1) EN ISO 14284:2002, Steel and iron - Sampling and preparation of samples for the determination of chemical composition (ISO 14284:1996)
- 2) NF A 01-800 (Sept 1986), Produits de fonderie — Prélèvement et préparation des échantillons destinés à la détermination de la composition chimique — Fontes et aciers moulés
- 3) ISO 1811-1:1988, Copper and copper alloys — Selection and preparation of samples for chemical analysis — Part 1: Sampling of cast unwrought products
- 4) ISO 1811-2:1988, Copper and copper alloys — Selection and preparation of samples for chemical analysis — Part 2: Sampling of wrought products and castings
- 5) EN 14361:2004, Aluminium and aluminium alloys — Chemical analysis — Sampling from metal melts
- 6) Recommandation technique n° 354-01 du Bureau de Normalisation des Industries de la Fonderie, Analyse spectrométrique des alliages d'aluminium de fonderie – Echantillons massifs
- 7) EN 12060:1997, Zinc and zinc alloys – Method of sampling – Specifications

IMPROVEMENT OF THE SAMPLING FOR CLEANNESS MEASUREMENT AT LIQUID STEEL STAGE

F. Ruby-Meyer¹, S. Evrard¹, M. Vergauwens², P. Balland³

¹ ASCOMETAL CREAS, Avenue de France, BP 70045, F-57301 HAGONDANGE Cedex

² HERAEUS ELECTRO-NITE Belgique, 27a Grote Baan, B-3530 HOUTHALEN

³ HERAEUS ELECTRO-NITE France, Beau Vallon, Illange, BP 90025, F-57971 YUTZ Cedex

Summary (abstract)

Development of steel grades for high performance products or for safety components conducts to more and more severe requirements in terms of steel quality, inclusions control and cleanliness. Such requirements include all types of characteristics in the fields of long life fatigue, contact fatigue, mechanical properties, machinability... As a consequence, steel makers need to know very early during steelmaking process the amount of oxides present at the liquid stage in order to improve the melting steps before casting to achieve the aimed final product quality.

Today several inclusion assessment methods are available in the steel plants and quick cleanliness control is possible (total oxygen analyser, optical emission spectrometry coupled with PDA). But it will be shown that erroneous results can be obtained due the lack of reliability of the conventional liquid steel samples. In fact, the inclusions observed in the conventional liquid steel samples are not always the inclusions present in the liquid steel at the moment of sampling. Slag entrapment or steel re-oxidation can occur during sampling.

Therefore, the sampling device IDCAS, of Heraeus Electro-Nite, has been tested in the ladle and in the tundish in Ascometal's steel plants. New sampler shapes were tested and compared to the conventionally used lollipop sampler.

The comparison of the results of the total oxygen analyses on conventional samples and on new samples is discussed. The advantages of the Heraeus Electro-Nite's sampling device are demonstrated. The sampling with argon blowing improves clearly the reliability of the total oxygen measurements. The advantages and weaknesses of the different sample shapes are also presented.

This research has been partly founded by the European Commission.

Full article

Introduction

Development of steel grades for high performance products or for safety components conducts to more and more severe requirements in terms of steel quality, inclusions control and cleanliness. Such requirements include all types of characteristics in the fields of long life fatigue, contact fatigue, mechanical properties, machinability... As a consequence, steel makers need to know very early during steelmaking process the amount of oxides present at the liquid stage in order to improve the melting steps before casting and to achieve the aimed final product quality.

Today several inclusion assessment methods are available in the steel plants and quick cleanliness control is possible (total oxygen analyser, optical emission spectrometry coupled with PDA, automatised SEM). These techniques give reliable results on rolled product but, often, on liquid steel samples taken in the tundish or in the ladle, the dispersion of the analyses is high. Ascometal has undertaken a study on the representativeness of the liquid steel samples particularly, for the improvement of the total oxygen measurements. The conventional sampling was compared to new sampling techniques and new sample shapes.

Description of the conventional samples used in Ascometal

Two types of samples are generally taken in Ascometal's plants at liquid steel stage: the double thickness lollipop and the massive LUS sample (figure 1).

As it is shown in figure 2, there are often porosities in those samples, due to the steel shrinkage at the end of solidification or due to an incomplete filling of the samples. It can conduct to erroneous results if the total oxygen measurement is done in an area where these kinds of porosities are present. In the case of PDA-OES (optical emission spectrometry) measurements, it can conduct to an unstable signal and a wrong interpretation of the analysis.

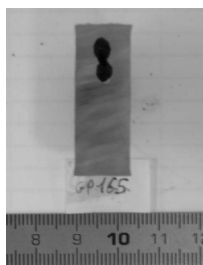


Double thickness Lollipop
12/4 mm



Massive LUS sample

Figure 1: Samples conventionally taken in Ascometal's plants.



Porosity/shrinkage in the central part of a lollipop



Porosity/shrinkage in the upper part of a LUS

Figure 2: Example of location of porosities in the conventional samples.

All over the years, the characterisations of conventional samples by light optical microscopy (LOM) and by secondary electron microscopy (SEM) have shown that large oxides which have the same composition as ladle slag or tundish powder (depending at which stage the sample has been taken) can be found. Inclusions which composition can correspond to re-oxidation of the steel are also observed. Typical examples are presented in figure 3.

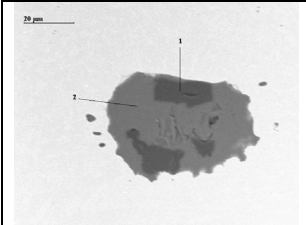
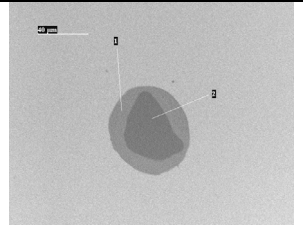
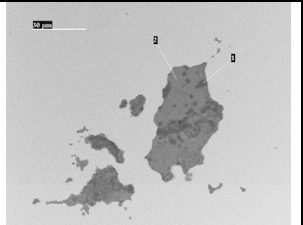
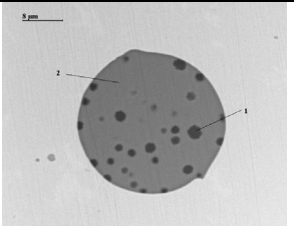
			
45%Al ₂ O ₃ - 43%CaO - 2%SiO ₂ - 5%MgO oxide with spinel crystals and traces of F	6% Al ₂ O ₃ - 45% SiO ₂ - 45%MnO oxide with internal SiO ₂ phase	6%Al ₂ O ₃ - 62%CaO - 27%SiO ₂ - 2%MgO with MgO crystals	2% Al ₂ O ₃ - 45% SiO ₂ - 46%MnO with SiO ₂ crystals
Slag entrapment partially reduced by Al of steel	Acid tundish powder entrapment (partially reduced)	Basic tundish powder entrapment (partially reduced)	Inclusion formed from steel re-oxidation by air entrapment

Figure 3: Type of exogenous inclusions found in the conventional liquid steel samples.

In fact, during the sampling, it is needed to go through the slag or tundish powder. So it is possible to entrap some particles. In addition, the turbulences of the steel created during the sampler immersion can conduct to air entrapment and so steel re-oxidation during sample filling.

The presence of these inclusions, which are often larger than 20 μm , can disturb the analyses and conduct to erroneous results. For improving the inclusion assessment at the liquid steel stage, it was necessary for Ascometal to improve the sampling procedure.

New sampling device

The sampling device IDCAS, introduced by Heraeus Electro-Nite, has been tested in the ladle and in the tundish in two of Ascometal's steel plants (Figure 4). The IDCAS system works as follows:

- Argon carrier gas is sent in the steel over the sampler. Its amount and flow is ensured by the IDCAS system.
- The argon will clean the sampler of air and also avoid slag pick up in the sample.
- The argon is already blown before entering the melt and removes the slag when entering the melt.
- Once the system finds the correct immersion depth, a vacuum is applied over the sampler. The sampler is filled by steel. The sampling procedure will be stopped by an acoustic signal and the red light switches on.
- The sampler is taken out of the steel bath, stripped and the sample sent to the steel laboratory.

The immersion depth is controlled by a sensor integrated in the probe holder of the sampling lance, detecting the slag/steel interface. The sample will only be filled as soon as the slag/interface has been found by this sensor. This results in a constant immersion depth of at least 25 cm. This technique not only ensures a constant immersion depth, it also eases the life of the operator and makes the sampling consistent.



Figure 4: IDCAS system (left) - sampling lance (right).

Test of IDCAS sampler

Heraeus Electro-Nite has proposed to test different shapes of samples with IDCAS system. The samples presented in figure 5 were tested and compared to the conventional lollipop sampler:

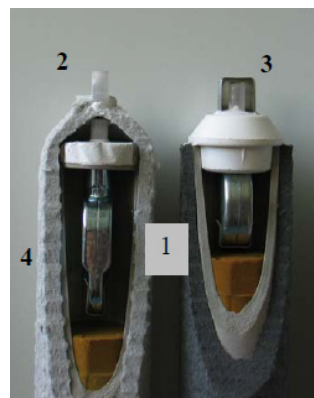
- double thickness 12/4 mm lollipop with steel entrance on thick part,
- squaf 24 mm with steel entrance on the side,
- "björnborg sample" with 5 mm pencil for oxygen measurements,
- "massive sampler" well known in other countries but taken without IDCAS system.

Figure 6 shows the cross section of two types of samplers (1). For tundish sampling, the sampler inlet is a quartz tube (2). For ladle sampling, the quartz tube is protected by a cap (3). The sampler is also equipped with a non splash material (4).



Figure 5: Shapes of samples tested in collaboration with Heraeus Electro-Nite.

Figure 6: Cross section of some argon samplers with different moulds (1), Quartz capping (none) (2), slag cap with hole (3), non-splash material (4).



Results

Sampling campaigns were carried out in two of Ascometal's steel plants:

- In steel plant 1, in the ladle, before and after vacuum treatment, and in the tundish during the casting of the same heats.
- In the steel plant 2, in the tundish during continuous casting.

Porosities

In the double thickness lollipop, the macro-porosity is always located at the frontier between the thick and the thin part of the sample that means in an area where no analyses are carried out. On the contrary, in the squaf 24 mm, the location of the porosity is more unpredictable. Sometimes it is located in the middle of the sample and is very small but sometimes it is larger and goes from the centre up to the top of the sample (figure 7). These large porosities can disturb the total oxygen analysis on the squaf 24 mm.



Figure 7: Location of the macro-porosity in the double thickness lollipop (left) and squaf 24 mm sample (right) taken with IDCAS.

Exogenous inclusions

In order to check if there is a decrease of the number of "exogenous" inclusions in the samples taken with IDCAS device, they were observed by LOM (Light Optical Microscopy) and then the chemical composition of the larger inclusions analysed by SEM-EDS (Scanning Electron Microscopy with Energy Dispersive Spectroscopy). This assessment is highly time-consuming. It was done on two sets of ladle samples from plant 1, on two sets of tundish samples from plant 1 and on five sets of tundish samples from plant 2.

As it can be observed in tables 1 to 3, the conventional lollipop sample and the massive sampler contain a larger number of inclusions $> 20 \mu\text{m}$ than the samples taken with argon (IDCAS). The large inclusions are re-oxidation oxides or slag or powder entrapments. The argon lollipop presents never re-oxidation inclusions or slag entrapment. The argon Squaf 24 mm contains, in a very few cases, re-oxidation inclusions.

number of inclusions / 1000 mm ²	Ladle before vacuum treatment		Ladle after vacuum treatment	
	Conventional lollipop	Argon lollipop	Conventional lollipop	Argon lollipop
Slag entrapment	4.4	0	0	0
Re-oxidation	12.2	0	3.3	0

Table 1: Number of exogenous inclusions ($> 20 \mu\text{m}$) in liquid steel samples sampled in the ladle (number of inclusions / 1000 mm²) - plant 1 – 2 heats.

Number of inclusions / 1000 mm ²	First half of casting			Second half of casting			
	Conven. lollipop	Argon lollipop	Argon Squaf 24	Conven. lollipop	Argon lollipop	Argon Squaf 24	Massive sampler
Slag or Powder entrapment	0	0	0	1.1	0	0	0.5
Re-oxidation	7.7	0	0	7.7	0	0	13.8

Table 2: Number of exogenous inclusions ($> 20 \mu\text{m}$) in liquid steel samples sampled in tundish (number of inclusions / 1000 mm²) - plant 1 – 2 heats.

Number of inclusions / 1000 mm ²	Conventional lollipop	Argon lollipop	Argon Squaf 24
Slag/Powder entrapment	0	0	0
Re-oxidation	7.0	0	0.25

Table 3: Number of exogenous inclusions ($> 20 \mu\text{m}$) in liquid steel samples taken in tundish in plant 2 at mid-casting – average value obtained on 5 heats (number of inclusions / 1000 mm²).

Total oxygen

The total oxygen content is assessed on the thin part of the conventional lollipop sample, on the thin part of the argon lollipop sample, on the upper (top) and lower (bottom) part of the argon squaf 24 mm sample, on the pencil of the argon björnborg sample and at three positions in the massive sampler (10, 20 and 30 mm from the bottom) as described in figure 8. Three analyses of total oxygen are carried out on each part. The mean value and the standard deviation of the 3 analyses are calculated.

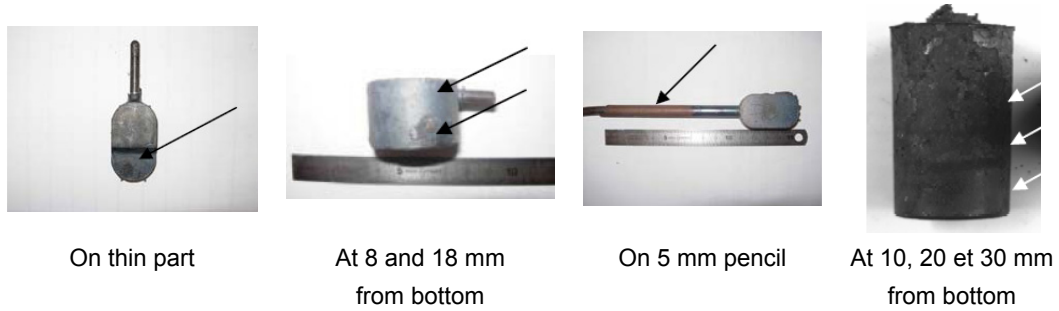


Figure 8: Part of the samples where the total oxygen measurements are carried out.

The results obtained on sampling campaign in plant 1 are presented as an average of the total oxygen mean values obtained on the different types of samples taken in 6 heats. The dispersion correspond to ± 1 standard deviation (figure 9 corresponds to the ladle samples; figure 10 corresponds to the tundish samples).

For the plant 2, a high number of argon samples were taken in tundish, before and after the sampling of the conventional lollipop. The results, obtained on 2 heats, are presented in figure 11. Each value corresponds to the mean value of 3 analyses and the dispersion corresponds to ± 1 standard deviation.

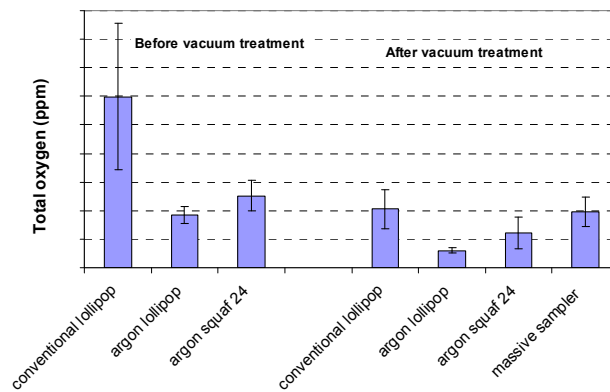


Figure 9: Average total oxygen value and mean standard deviation (dispersion bars) obtained on each type of sample before and after vacuum treatment (6 heats).

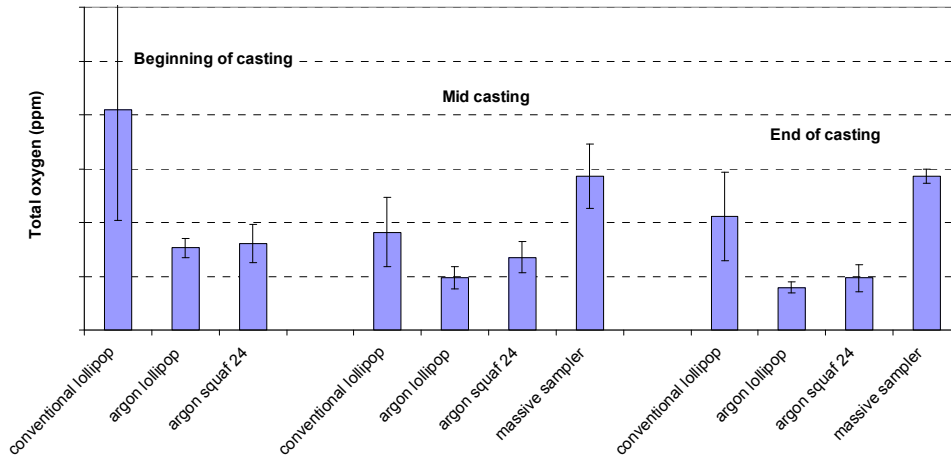


Figure 10: Average total oxygen value and mean standard deviation (dispersion bars) obtained on each type of sample at beginning, middle and end of casting (6 heats).

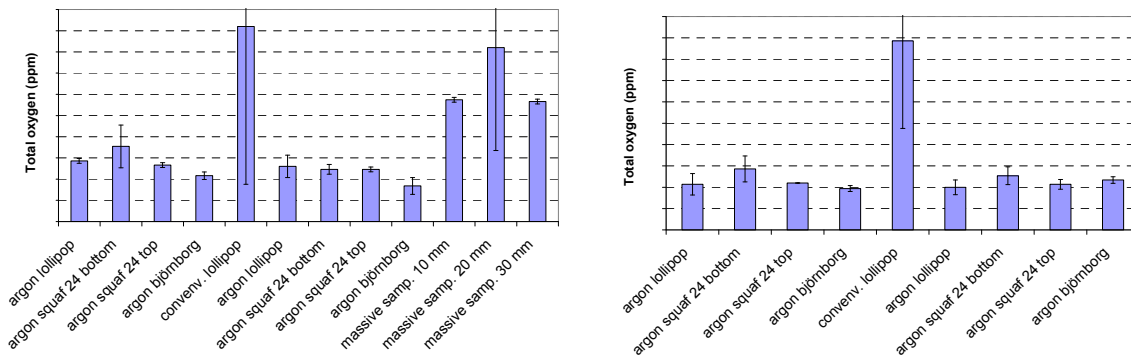


Figure 11: Total oxygen content (mean value and standard deviation) in the conventional samples and in the argon samples from heat A (left) and heat B (right).

The lollipop and the björnborg sample taken with argon give very reproducible results (very narrow standard deviation, less than 3 ppm). The oxygen values obtained on those samples (thin part of the lollipop and pencil of the björnborg sample) are in agreement with the oxygen level attended at the corresponding production stage. The squaf 24 mm conducts to oxygen values more dispersed and sometimes higher than the argon lollipop. The total oxygen values obtained on the thin part of conventional lollipop sample and on the massive sampler are, in all cases, higher than the values obtained on the argon lollipops. The standard deviation is always higher (> 5 ppm). It means that those two types of samples, which are taken manually without argon, are more heterogeneous than the samples taken with argon.

The dispersion of the total oxygen measurements in the conventional lollipop sample and massive sampler has probably as origin the presence of the large exogenous oxides described in table 1, table 2 and table 3. The sampling with IDCAS, by avoiding the entrapment of those inclusions, gives more reliable samples.

Conclusion

The comparison of the results of the total oxygen assessment on conventional samples and on new samples shows that there is a large improvement of the reliability of the total oxygen measurements on the samples taken with the IDCAS device, as well in the ladle as in the tundish. In fact, the sampling with argon blowing improves clearly the representativeness of the liquid steel samples by avoiding exogenous slag or powder entrapment and steel re-oxidation during sampling. The controlled immersion depth obtained with the IDCAS sampler will also contribute to improve the reliability of the sampling.

Between the different sampler shapes which were tested with IDCAS device, the double thickness lollipop 12/4 mm shape will be preferred to the Squaf 24 mm and the Börnborg sample for following reasons:

- In the Squaf 24 mm, the internal porosity can be located in an area where total oxygen measurements are carried out whereas in the double thickness lollipop it is located in an area where no oxygen measurements are carried out.
- The pencil of the Börnborg sample can not be analysed directly, it must be turned from 5 mm to 3 mm before total oxygen measurement.
- The double thickness lollipop 12/4 mm shape is already used as the production sample for bulk analysis. So both analyses can be carried out on the same sample, one on the thick part, the other one on the thin part.
- Inclusion assessment by PDA-OES technique is also optimised for the lollipop sample shape. The reliability of this kind of analyses will be improved by the reduction of unreliable measurements due to presence of exogenous inclusions.

The lollipop 12/4 mm and the Squaf 24 mm samples were studied more in detail by SEM and PDA techniques in the frame of the SOPLIQS project which is founded by the European Commission.

INVESTIGATION OF THE POSSIBILITIES TO CHANGE SAMPLE PREPARATION FROM GRINDING TO MILLING FOR FE- AND NI-BASE ALLOYS.

Peter Henningsson, Linn Johansson

*AB Sandvik Materials Technology
811 81 Sandviken
Sweden*

Abstract

Since some 10 years ago, grinding has successively been replaced by milling as a sample preparation technique for analysis of steels by XRF- and sparkOES. This has been an ongoing process, connected to development of efficient automation solutions within low-alloyed steel production laboratories. However, there are very few applications where milling has been studied as a sample preparation step before analysis of high-alloyed steels and Ni-base alloys.

Sandvik Materials Technology is a producer of steels and Ni-base alloys for demanding applications and the product mix covers grades from low-alloyed steels, chromium steels, high alloyed steels and Ni-base alloys. As a first step, in our laboratory's planning for replacement of our first generation of laboratory automation, the use of milling for sample preparation has been investigated.

Samples have been milled on a standard milling-machine in one of our work-shops. During the development of suitable milling-methods different parameters (rotation-speed, feed, cutting-tools, and milling-heads) have been tested. The hardness (HRC) has been measured on a number of samples and the surface structure (Ra and Rz) have been measured on all milled samples. Correlations between hardness and surface structure have been checked for both milling and grinding. Analytical data have been compared between milled surfaces and ground surfaces, using the same samples. For most elements, results for milled samples fits very well on a calibration based on ground samples, but for some elements there are big systematic errors. The repeatability is about the same for most elements, but for a few elements a big improvement is achieved when the sample is milled. When comparing real samples from the melting-process, some unexpected results occurred. The first sample in the process (after melting the scrap in an arc-furnace) shows very big differences in Cr and Ni, when milled and ground samples are compared. These samples normally have very high carbon-concentrations, between 1-2 %. For all other samples taken in the melt shop-process, the results fits with those obtained using homogeneous bars. Results obtained will be presented and reasons for deviations will be further discussed.

Full article

Not available

Conclusion

Apart from one problem, it seems that milling can replace grinding as sample preparation-method for spark-OES and XRF. The differences in measured concentrations between milled and ground surfaces have been compared and are generally small. However, the first sample in the melt-shop process (after melting the scrap in an arc-furnace) shows very big differences in Cr and Ni, when milled and ground samples are compared. These samples normally have very high carbon-concentrations, between 1-2 %. The reason for this deviation is not yet known.

References:

No references

EFFECT OF SAMPLING CONDITIONS ON INCLUSION CHARACTERISTICS IN SAMPLES FROM LIQUID STEEL

Ola Ericsson¹, Andrey Karasev², Pär Jönsson²

¹*Suzuki Garphyttan, Bruksvägen 3, SE-719 80 GARPHYTTAN, Sweden*

²*Royal Institute of Technology, Applied Process Metallurgy, Materials Science and Engineering, SE-100 44 STOCKHOLM, Sweden*

Abstract

During the steelmaking process, samples are taken from the liquid steel, mainly to obtain the chemical composition of the steel. Recently, methods for rapid determination of inclusion characteristics have progressed to the level where they can be implemented in process control. Here, inclusions in steel can have either good or detrimental effects depending on their characteristics. Thereby, by determination of the inclusion characteristics during the steelmaking process it is possible to steer the inclusion characteristics in order to increase the quality of the steel. However, in order to successfully implement these methods it is critical that the samples taken from the liquid steel represent the inclusion characteristics in the liquid steel at the sampling moment.

The purpose of this study is to investigate the changes in inclusion characteristics during the liquid steel sampling process. The dispersion of the total oxygen content in the samples (Lollipop and Björneborg) was evaluated as a function of sample geometry and type of slag protection (metal-cap-protection and argon-protection). In addition, in order to determine the homogeneity and representativity of the industrial samples, the dispersion of inclusion characteristics in different zones and layers of the samples were investigated. Inclusion characteristics were determined on sample cross-sections and on film filters after electrolytic extraction of steel sample.

It was concluded that the type of slag protection has a significant effect on the sampling repeatability. Furthermore, it was shown that top slag can contaminate the samples. Therefore, the choice of slag protection type is critical to obtain representative samples. In addition, the study revealed that both secondary and primary inclusions are heterogeneously dispersed in the industrial samples. In general, the middle zone of the surface layer is recommended for investigation of primary inclusions.

Keywords: liquid steel sampling, inclusion characteristics, sampling conditions, sample homogeneity.

INTRODUCTION

In the last decades the steel industry has experienced a markedly increase in production efficiency and steel quality. A vast range of tools are nowadays available for process control, with increased possibilities to reach optimum parameters for casting, as well as obtaining tailored material properties for each specific application. Specifically, temperature, chemical composition and inclusion characteristics (size, number, composition and morphology) are the main parameters controlled during the steelmaking process.

Commonly used tools are online and continuous measurements of temperature, as well as online determinations of oxygen activity and hydrogen content directly in the melt. The chemical composition is usually determined from samples taken from the liquid steel at the different steps in the steelmaking process. Therefore, a range of different techniques for sampling during the steelmaking process have been developed, from handheld metal scoops to the nowadays commonly used, disposable samplers.

During immersion, filling, cooling and solidification of the liquid steel sample, several factors can affect the inclusion characteristics. First, on its way down into the liquid steel, the sampler passes through a slag layer. At this moment it is critical that slag is not allowed to enter and pollute the sample. Second, when the liquid steel (and inclusions) flows into the sample mold, the sample geometry and filling velocity can affect the fluid flow, which can affect the inclusion dispersion and collision frequency.[1] Third, during cooling and solidification of the liquid steel sample, the decreased solubility of inclusion-forming elements (e.g. S, N and O) can lead to precipitation of sulfides, nitrides and oxides.[2-5] These can significantly change the characteristics of the existing inclusions in the steel sample.

Therefore, an increased understanding of the changes in inclusion characteristics which can occur during sampling of the liquid steel and the effect of different sampling conditions are key points for this study. In general, numerous studies have been published on changes in inclusion characteristics due to casting, treatment time, slag composition, etc. However, few studies have focused on the representativity of the samples taken from liquid steel. It should be mentioned that even though it has not been the main objective of the studies, researchers [6-8] have observed that primary inclusions can be heterogeneously dispersed in the obtained steel samples. The purpose of this study is to investigate the sample quality with respect to reoxidation by exogenous inclusions and the distribution of secondary (formed during cooling and solidification) and primary inclusions (existing in the melt at the sampling moment) in different zones of the final sample. For this purpose the commonly used Lollipop and Björneborg samples are used. In addition, metal-cap-protected and argon-protected sampling is evaluated.

EXPERIMENTAL METHODS

Analysis of total oxygen content in different industrial samples

Analysis of the total oxygen content in the different zones of the metal sample provides a rough estimation of the dispersion of oxide inclusions. The body, pin and inlet parts of the industrial metal samples from three heats of the S32304 stainless steel grade were cut into small specimens (0.5~1 g). The analyzed zones of the body, pin and inlet in the different samples are shown in **Figure 1**. The specimens were prepared by filing, cleaning in alcohol in an ultrasonic bath and drying. Directly after preparation they were analyzed by the inert gas fusion method using a Leco TC600 instrument.

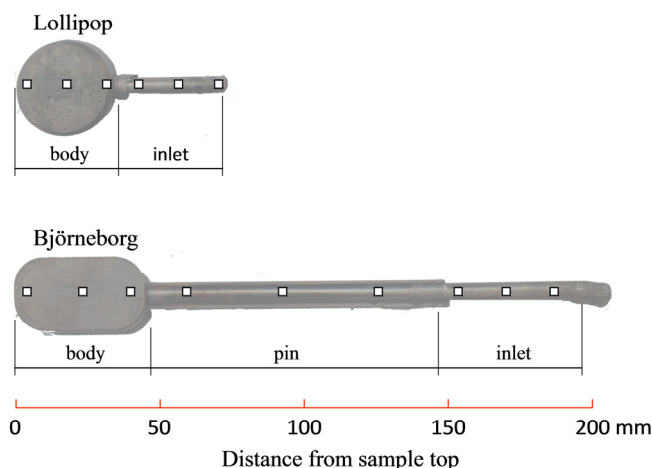


Figure 1. Schematic illustration of the different zones (white squares) for determination of the total oxygen content in the metal samples.

Investigation of inclusion dispersion in industrial samples

The dispersion of inclusions in different zones and layers of the LP-6 and LP-12 samples taken from stainless 316L liquid steel were evaluated on cross-sections (CS) and on film filters obtained by electrolytic extraction (EE). A detailed analysis procedure is described in a previous paper [9]. The different zones (top, middle and bottom) in the samples analyzed by electrolytic extraction and cross-section methods are shown in **Figure 2**.

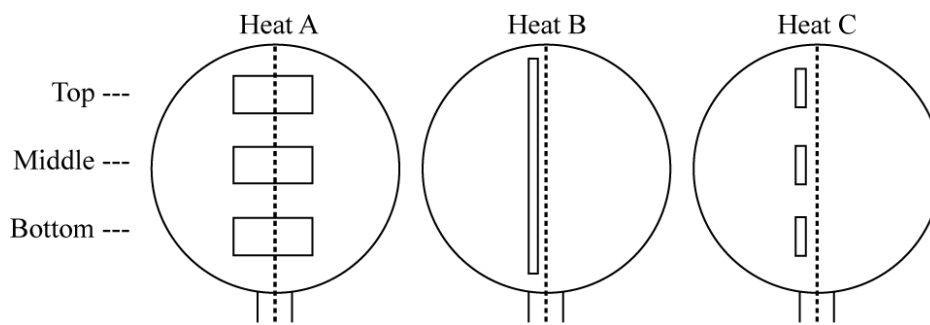


Figure 2. Schematic illustration of zones for determination of inclusion characteristics in LP-6 and LP-12 samples from heats A, B and C, determined by EE (heat A) and CS (heats B and C) methods.

The sample mold is filled by the molten steel through the inlet located at the bottom end of the samplers. For the extraction method, metal specimens were cut from the marked positions in the steel samples from heat A, as shown in Figure 2. For cross-section method, the appropriate marked zones of the steel samples from heats B and C were polished and investigated in 2-D. Samples from heat A and C were analyzed in “surface” (0.1~0.3 mm under original sample surface) and “center” (~3 mm for LP-6 and ~6 mm for LP-12 under original sample surface) layers, which were parallel to the original surface of the steel samples. The sample from heat B was only analyzed in the “surface” layer.

RESULTS AND DISCUSSION

Homogeneity of total oxygen content in industrial samples

The total oxygen content in different zones of the argon-protected and metal-cap-protected Björneborg, LP-6 and LP-12 samples was investigated to test the dispersion of oxide inclusions within the samples and to detect possible contamination from exogenous inclusions. **Figure 3** show typical photographs of the surface of metal-cap-protected and argon-protected LP-6 samples.

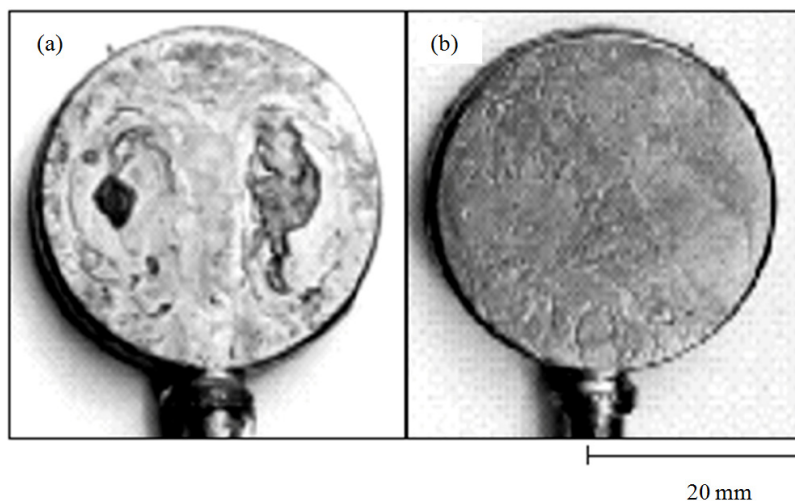


Figure 3. Photographs of typical metal-cap-protected (a) and argon-protected (b) LP-6 samples.

From the photographs it can be seen that the surface of the argon-protected Lollipop sample is considerably smoother and more flat than the surface of the metal-cap-protected sample. In addition, the metal-cap-protected sample is partly covered by a dark layer. This indicates that the filling of argon-protected samplers is more uniform and continuous.

Figure 4 shows the average total oxygen content in different samples depending on geometry and type of slag protection. The error bars in this figure represent the arithmetic standard deviation values. As seen, most of the argon-protected samples contain on average 25-35 ppm of oxygen. However, the total oxygen content in the metal-cap-protected samples is significantly higher, particularly in the Lollipop samples (on average 45-80 ppm). Moreover, the standard deviations values for the results obtained with metal-cap-protected samplers are significantly larger in comparison to the argon-protected samplers. It was found that the oxygen content in the end part of the inlet (Figure 1) in all the samples was drastically higher. This is most likely because of reoxidation and/or entrapment of top slag during withdrawal of the sampler from the melt. Therefore, this end part does not represent the melt and these values are excluded from further discussion.

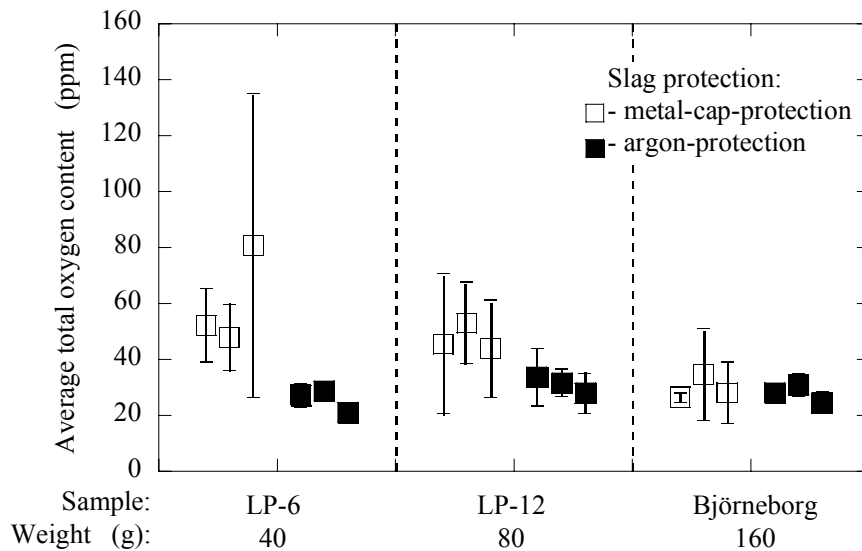


Figure 4. Average total oxygen content in LP-6, LP-12 and Björneborg samples depending on type of slag protection.

As seen in Figure 4, for the metal-cap-protected samples, the average value of the total oxygen content increases significantly with a decreased sample weight. For the argon-protected samples the value of the total oxygen content is independent of the sample geometry.

Therefore, possible entrapment of slag particles during sampling was investigated on metal cross-sections of a LP-6 sample by optical and scanning electron microscopy. In large parts of the investigated sample area, there were large dark particles. Both in form of spherical particles with diameters up to almost 400 μm , and as large irregular particles up to 100 μm in length. By using SEM-EDS analysis, these particles were confirmed to be oxide particles. The spherical particles corresponded well to the composition of the top slag during ladle treatment. However, the irregular particles had an unusually high Cr_2O_3 content (17~23 %). One possible source for the irregular particles is Cr_2O_3 rich converter slag which was transferred from the converter to the ladle treatment.[10] Thereafter, the top slag froze on top of the metal cap during immersion of the sampler. As a result the top slag particles were pushed into the sample body by the liquid steel flowing into the sample mold when the metal cap melted.

Homogeneity of inclusion characteristics in different zones and layers of industrial samples

The dispersion of oxide inclusions in different zones (Figure 2) and layers of industrial LP-6 and LP-12 samples was investigated by using EE and CS methods. Based on the size, composition and morphology of the inclusions they were separated into secondary ($d < 0.6 \mu\text{m}$, Al-Ti-O and Al-Mg-O), formed during cooling and solidification of the melt in the sample mold, and primary ($d \geq 0.6 \mu\text{m}$, Ca-Si-Al-Mg-O) inclusions, present in the melt at the sampling moment.

In order to facilitate comparison of the inclusion number in the different sample zones, a relative coefficient of inclusion dispersion, K_N , was estimated as follows:

$$K_N = \frac{N_A}{\bar{N}_A} \quad (1)$$

where N_A is the number of inclusions per unit area in the appropriate zone (mm^{-2}) and \bar{N}_A is the average number of inclusions per unit area in all investigated zones (mm^{-2}) obtained by the CS method. The corresponding K_N value for the inclusion number per unit volume is estimated by using the same procedure for the results from the EE method. With the assumption that all of the primary inclusions ($d \geq 0.6 \mu\text{m}$) are counted and do not change during sampling, the average inclusion number should correspond to the number of inclusions present in the liquid steel. Therefore, if $K_N \approx 1$ the inclusion number in that zone represents the inclusion number present in the liquid steel at the sampling moment. It should be noted that for secondary inclusions ($d < 0.6 \mu\text{m}$), the K_N value

shows the relative frequency as they are not present in the liquid steel at the sampling moment. The experimental values for primary inclusions are shown in **Figure 5** together with predicted values using a fluid flow model based on the sampling conditions used in the present study.[11-13] It can be seen that the obtained experimental results are confirmed by the calculated K_N values from the model.

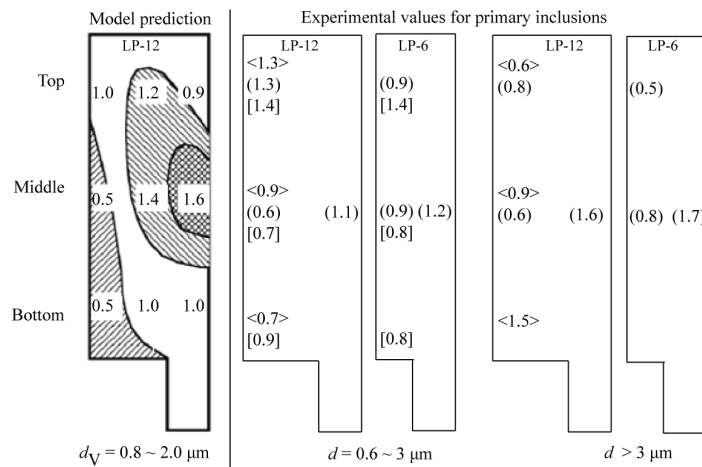


Figure 5. The relative coefficient of inclusion dispersion, K_N , calculated from model [11] and experimental results obtained in the present study. The analyzed heats are represented individually as [heat A], <heat B> and (heat C), where A was obtained by the EE method and B and C with the CS method.

Going from the surface layer through to the center layer in the middle zone, the K_N value tends to increase in both the LP-6 and LP-12 samples. Particle size distributions of the respective layers showed no significant difference between the layers, particularly for the LP-6 sample. Furthermore, in the LP-6 sample the K_N values for primary inclusions in the size range 0.6 to 3 μm are quite stable (0.9-1.2). However, for inclusions larger than 3 μm , the K_N value increases significantly, from 0.8 in the surface layer to 1.7 in the center layer. A similar tendency was obtained for the LP-12 sample. Specifically, from the surface to the center layer, the K_N value increases from 0.6 to 1.1 and 0.6 to 1.6 for primary inclusions in the size range 0.6-3 and > 3 μm , respectively.

Dispersion of secondary inclusions in industrial samples

The dispersion of secondary inclusions ($d < 0.6 \mu\text{m}$) in LP-6 and LP-12 samples from heat A obtained by the EE method were compared in the top, middle and bottom zones of the surface layer, as well as in the bottom and middle zone of the center layer. In **Figure 6** the experimentally obtained K_N values for secondary inclusions are summarized.

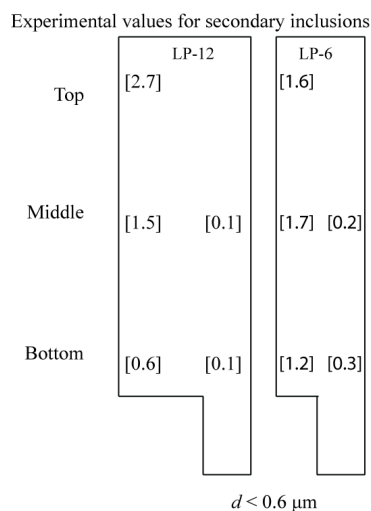


Figure 6. The relative coefficient of inclusion dispersion, K_N , of secondary inclusions in heat A obtained by the EE method.

In the surface layer of the LP-6 sample, the K_N value is evidently more stable than in the LP-12 sample. Specifically, the K_N value ranges from 1.2 to 1.7 in the LP-6 while the corresponding value in the LP-12 sample is 0.6 to 2.7. In both samples, the K_N value decreases drastically to a level of 0.1~0.3 in the center layer. In addition, a slight shift towards larger d_V values was noticed in the center layer. The smaller amount of secondary inclusions in the center layer may be explained by a lower solidification rate in the center layer of the sample, which gives the secondary inclusions a possibility for heterogeneous precipitation onto surfaces of the primary inclusions as well as additional time to grow. Based on the obtained results, it can be concluded that the secondary inclusions can grow and/or precipitate heterogeneously in the center layer of both LP-6 and LP-12 samples. This can have a significant effect on the size and composition of the primary inclusions. However, the number of primary inclusions should not be affected considerably.[9] In this case, it can be difficult to separate the secondary and primary inclusions for separate analysis. On the other hand, in the surface layer most of the secondary inclusions in the top, middle (LP-6 and LP-12) and bottom (LP-6) zones can be separated by size from the primary inclusions in order to separately analyze the inclusion characteristics.

Recommended zones for investigation of primary inclusions

Based on the results, the overall tendencies are similar in both LP-6 and LP-12 samples, but the overall inclusion dispersion in the LP-6 is more homogenous. In **Table 1**, the K_N values for primary and secondary inclusions are summarized for both sample types, depending on layer and zone.

Table 1. K_N values for primary and secondary inclusions in different zones and layers of LP-6 and LP-12 samples from heats A, B and C.

Sample zone	Layer			
	Surface		Center	
	K_{N-Prim}	K_{N-Sec}	K_{N-Prim}	K_{N-Sec}
Top	0.9-1.4 (0.5-0.8)	1.6-2.7 *		
Middle	0.7-0.9 (0.8-0.9)	1.5-1.7 *	1.1-1.2 (1.6-1.7)	0.1-0.2 **
Bottom	0.7-0.9 (1.5)	0.6-1.2 **		0.1-0.3 **

() values for primary inclusions with $d > 3 \mu\text{m}$

* - Possible separation of primary and secondary inclusions by size (two peaks in particle size distributions)

** - Possible heterogeneous precipitation of secondary inclusions on primary inclusions and growth of secondary inclusions

It can be seen that in most cases, the K_{N-Prim} value is close to one (0.7-0.9) in the middle and bottom zones of the surface layer, which resembles the average number of inclusions in the sample. Furthermore, in the middle and top zones, the K_{N-Sec} values are significantly larger than one (1.5-2.7), which indicates an easier separation of primary and secondary inclusions by size. Based on the obtained results, the middle zone of the surface layer in the LP-6 sample can be recommended for determination of inclusion characteristics ($K_{N-Prim} \approx 1$ and $K_{N-Sec} \approx 1.7$).

On the other hand, in the center layer, the number of primary inclusions is larger and more scattered, particularly for inclusion larger than $3 \mu\text{m}$ ($K_{N-Prim} = 1.6-1.7$). In addition, the number of secondary inclusions is markedly lower ($K_{N-Sec} = 0.1-0.3$), which indicates that secondary inclusions can grow and/or precipitate heterogeneously on the surface of primary inclusions. In this case the characteristics of the primary inclusions may change during sampling. As a result, it is difficult to separate primary and secondary inclusions by using size or composition.

CONCLUSIONS

Based on the results it is clear that the sampling equipment, type of sample, and the analyzed zone and layer has to be clearly defined in the analysis of inclusion characteristics from liquid steel samples.

The higher total oxygen content in the metal-cap-protected samples cannot be explained by reoxidation during sampling. However, large size oxide particles (30~400 μm) are present in the metal-cap-protected samples. These are entrapped in the sample from the top slag during the sampling. Furthermore, the total oxygen content in the metal-cap-protected samples increases with a decreased sample weight (especially for LP-6 and LP-12). Therefore, it is critical to use argon-protection to obtain samples which represent the total oxygen content in the liquid steel.

For analysis of primary inclusions, the middle zone in the surface layer of LP-6 sample can be recommended. In this region the number of primary inclusions corresponds satisfactorily well with the average number of primary inclusions in the sample, i.e. the relative coefficient of inclusion dispersion $K_N \approx 1$, which value corresponds well with the real number of primary inclusions present in the liquid steel at the sampling moment. The inclusion characteristics in the center layer of the LP-6 and LP-12 samples may change drastically during sampling because of the lower amount of secondary inclusions ($K_{N-Sec} = 0.1-0.3$) in this layer, which indicates that they may have time to grow or precipitate heterogeneously onto the surface of primary inclusions. Thus, it is difficult to separate secondary and primary inclusions. Moreover, the number of primary inclusions is higher than the average value ($K_{N-Prim} = 1.1-1.2$), especially for inclusions larger than 3 μm ($K_{N-Prim} = 1.6-1.7$).

REFERENCES

- 1) M. Söder, P. Jönsson and J. Alexis: *Scand. J. Metall.*, 31 (2002), 210-220
- 2) M. Van Ende: Formation and Morphology of Non-Metallic Inclusions in Aluminium Killed Steels, Leuven, Belgium, 2010 (Ph.D. Thesis)
- 3) M. Zhongting and D. Janke: *ISIJ Int.*, 38 (1998), No. 1, 46-52
- 4) K. Oikawa, H. Ohtani, K. Ishida and T. Nishizawa: *ISIJ Int.*, 35 (1995), No.4, 402-408
- 5) M. Suzuki, R. Yamaguchi, K. Murakami and M. Nakada: *ISIJ Int.*, 41 (2001), No. 3, 247-256
- 6) M. Göransson, F. Reinholdsson and K. Willman: *Ironmaking and Steelmaking*, May (1999), 53-58
- 7) P. Sjödin, P. Jönsson, M. Andreasson and A. Winqvist: *Scand. J. Metall.*, 26 (1997), 41-46
- 8) L. Huet, P. Jönsson and F. Reinholdsson: *Steel Times Int.*, Nov (1997), 47-50
- 9) O. Ericsson: An Experimental Study of a Liquid Steel Sampling Process, Stockholm, Sweden, 2010 (Ph.D. Thesis)
- 10) Personal communication with Tord Pettersson, Outokumpu Stainless AB, 2010-06-21
- 11) Z. Zhang, A. Tilliander, A. Karasev and P.G. Jönsson: *ISIJ Int.*, 50 (2010), No. 12, 1746-1755
- 12) Z. Zhang, A. Tilliander and P.G. Jönsson: *Steel Res. Int.*, 81 (2010), No. 9, 749-758
- 13) Z. Zhang, A. Tilliander, M. Iguchi and P.G. Jönsson: *ISIJ Int.* 49 (2009), No. 10, 1522-1529

DETERMINATION OF BORIC ANHYDRIDE IN ASCHARITE ORES BY INDUCTIVELY COUPLED PLASMA ATOMIC EMISSION SPECTROMETRY

Wen Xiang-dong, Chen Shi-hua, Shao Mei, Zhu Ying

Research and Development Center of Wuhan Iron and Steel (Group) Corp. , Wuhan ,China

Abstract:

Inductively coupled plasma atomic emission spectroscopy was applied to the determination of boric anhydride in ascharite ores. Pretreatment method, reagents used for acid decomposition and the interferences from matrix and coexistent elements were discussed in details respectively. The analytical spectral lines were selected while experimental parameters were optimized. The results indicated that after the samples were completely dissolved and collected with hydrochloric acid (1+1) in a sealed container with a reflux condenser by the low-temperature heating method, they could be directly analyzed and determined with ICP-AES at optimized operating parameters. The relative standard deviation of the method is less than 0.9% within the measurement range of 0.1% ~ 40% and the recovery rate is in the range of 98.1% ~ 101.0%. The method was proved satisfactory with wide linear range, low detection limit and also high sensitivity and accuracy.

Key words: inductively coupled plasma atomic emission spectroscopy, ascharite ores, boric anhydride

It is the tenor of boron that determine the use of ascharite ores, suggesting that the content of boric anhydride is one of the significant factors for valuation of ascharite ores as well as the key parameters in the production. Consequently, the accurate and rapid determination of boric anhydride in ascharite ores is by far important.

At present, the determination of boric anhydride in ascharite ores only adopts GB/T 3447.3-82^[1]: boric anhydride was dissolved and titrated with standard solution of sodium hydroxide. However, the method has many disadvantages, including complicated and time-consuming operation procedures, unobvious titration endpoint, which make the results variable and can not meet the requirements of modern enterprise production.

Inductively coupled plasma atomic emission spectroscopy (ICP-AES) has become an important testing method in analysis of raw materials^[2-14]. In this study, after the samples were completely dissolved in a sealed container with a reflux condenser by the low-temperature heating method, they could be directly analyzed and determined with ICP-AES. The method with wide linear range, low detection limit and also high sensitivity and accuracy has been proved satisfactory.

1 Experimental

1.1 Instrumentation

The experiments were performed with a TJA IRIS Advantage model inductively coupled plasma optical emission spectroscopy (Thermo Fisher Scientific, US) with a CID semiconductor solid-state detector, whose measurement range is 168 ~ 860nm while resolution is 0.007nm (at 200nm).

The operating conditions and instrumental parameters for the ICP-AES are given in Table 1.

Table 1 ICP-AES operating parameters

RF power (w)	Nebulizer pressure (psi)	Auxiliary gas flow (L/min)	Pump rate (r/min)	Wavelength(grade) (nm)	Integral time (s)
1150	28	0.5	120	208.893 { 160 } , 208.959 { 161 }	Long wavelength 5 , Short wavelength 10

1.2 Reagents

Hydrochloric acid (1+1); aqua regia (1+1); sulfuric acid (1+1); standard solutions of boric anhydride: 200.0 μ g/mL and 4.00mg/mL; iron oxide power with purity of 99.99%. Standard solutions were prepared by dissolving certified reference material of boric anhydride. All other reagents were prepared from analytical grade chemicals and deionized water was used throughout.

1.3 Decomposition procedures

Ascharite ores were dissolved as follows: powdered sample of 0.2000g (with precision of 0.0002g) with 15mL hydrochloric acid (1+1) in a sealed 250mL container with a reflux condenser was heated and kept boiled for 20 ~ 30min. After cooling, the reflux condenser was rinsed with water and the wash solution and the sample solution were collected and subsequently diluted with water to 100mL. The blank sample containing the acid used for decomposition was prepared in the same way. The experiment apparatus is shown in Figure 1.

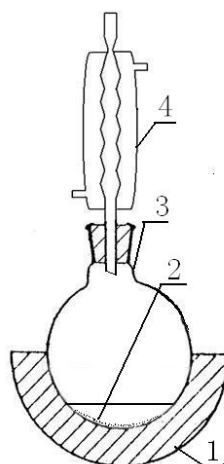


Figure 1 Chemical experiment apparatus

1.4 Calibration curve

Seven parts of 0.143g iron oxide power (with purity of 99.99%) were weighted. After 20mL hydrochloric acid (1+1) was added, the solution was heated to dissolve the sample completely and transferred into a 100mL volumetric flask. Different amount of standard solutions of boric anhydride were added into the set of the samples separately and then diluted to the mark with water. Calibration was carried out with samples weighed 0.2000g containing 0% , 0.10% , 0.50% , 4.00% , 10.00% , 20.00% , 40.00% of boric anhydride.

1.5 ICP-AES analysis

The ICP-AES determination was performed with optimized parameters and the accuracy was improved by using two selected analysis lines for boron: 208.893nm and 208.959nm, between which 208.893nm is better. The intensities of calibration solutions and testing solutions were measured and measuring point was defined by Intensity-Wavelength curve. The content of boric anhydride could be calculated from calibration curve directly after background correction.

2 Results and discussion

2.1 Blank control

The blank values of new chemical glass ware could be up to 0.2% ~ 0.3% because of high boron content and usually variable. All glass ware used in the experiments were kept in the acid such as hydrochloric acid, nitric acid, sulfuric acid or mixed acid, of which hydrochloric acid(1+1) was determined to be best, for at least 12 hours or in other way rinsed with the previously described kinds of acid over low heat and subsequently with water before use. The blank value would be reduced to 0.005% when saturated with hydrochloric acid(1+1) for over 12 hours.

2.2 Decomposition procedures

2.2.1 Selection of acid used for decomposition

Iron oxide, boric anhydride, silicon oxide and magnesium oxide are the principal components of ascharite ores, which could be dissolved in hydrochloric acid, sulfuric acid or aqua regia. It was found that when 15mL hydrochloric acid(1+1), 15mL aqua regia(1+1) and 15mL sulfuric acid(1+1) were added respectively, the dissolved rate of hydrochloric acid was quicker than aqua regia, and the nebulization efficiency would be reduced when sulfuric acid was used. Therefore, the samples used in the present study were dissolved in 15mL hydrochloric acid(1+1).

2.2.2 Selection of sample preparation method

As boric acid are volatile, when powdered sample with 15mL hydrochloric acid (1+1) in an open container was heated and kept boiled, the solution was evaporated to nearly dryness in no more than 10 minutes. However, 40mL of hydrochloric acid(1+1) was added into the solution by several times for further decomposition. After boiled for 30 minutes, the sample was decomposed completely. The results of duplicate ICP-AES analysis were inconsistent and obviously on the low side. Heating the sample and 15mL hydrochloric acid(1+1) in a sealed container with a reflux condenser and keeping the solution boiled for 30min and then collecting the solution after complete dissolubility is the best way for decomposition.

2.3 Optimization of operating conditions

3mL standard solution of boric anhydride was added into the blank solution prepared according to the method described in section 1.3. The solution was diluted to 100mL with water and then introduced into ICP by carrier gas. A number of parameters including RF power, nebulizer pressure (carrier gas pressure), auxiliary gas pressure (plasma gas pressure) and pump rates have been studied. The emission intensity of boron was enhanced with high signal-to-background ratio at RF power of 1150w. The signal-to-background ratio kept almost invariant at different nebulizer pressure of 26psi, 28psi and 30psi, auxiliary gas flow rate of 0.5L/min and 1.0L/min as well as pump rate of 100r/min, 120r/min and 150r/min. And the optimized operating parameters are: RF power was 1150w, nebulizer pressure 28psi, auxiliary gas flow rate 0.5L/min and pump rate 120r/min.

2.4 Selection of analysis spectral line

Linearity of calibration curve and spectral interferences at different wavelength are listed in Table2.

Table 2 Interference and calibration curve at different boron analytical wavelength

Boron analytical wavelength (nm)	Relative intensity	Correlation coefficient for calibration curve	Conceivable spectral interference wavelength (nm)	Relative intensity of interference wavelength
182.591 { 184 }	290	0.99999	S 182.624	□ 50.0
			B 182.641	□ 660.0
182.641 { 183 }	660	0.99999	B 182.591	□ 290.0
			S 182.624	□ 50.0
208.893 { 160 }	750	0.99992	Sc 182.682	□ 0.0
			Pb 208.843	□ 3.0
			V 208.856	□ 1.0
			Cl 208.858	□ 350.0
			Ta 208.867	□ 10.0
			Pt 208.871	□ 3.5
			Hf 208.877	□ 15.0
			Ir 208.882	□ 60.0
			Pt 208.893	□ 0.0
			Y 208.900	18.0
Os 208.903	13.0			
Pt 208.905	□ 0.0			
Ni 208.907	□ 2.0			

			W 208.914	<input type="checkbox"/> 40.0
			Os 208.921	<input type="checkbox"/> 0.0
			Hf 208.938	<input type="checkbox"/> 5.0
208.959 { 161 }	1500	0.99991	W 208.914	<input type="checkbox"/> 40.0
			Os 208.921	<input type="checkbox"/> 0.0
			Hf 208.938	<input type="checkbox"/> 5.0
			Rh 208.948	<input type="checkbox"/> 1.2
			Os 208.950	12.0
			Mo 208.952	<input type="checkbox"/> 12.0
			Ta 208.960	1.0
			Th 208.992	<input type="checkbox"/> 1.5
			Hf 208.995	<input type="checkbox"/> 4.0
249.678 { 135 }	2000	0.99999	Cr 249.631	<input type="checkbox"/> 8.0
			Zr 249.648	<input type="checkbox"/> 10.0
			Fe 249.653	<input type="checkbox"/> 4.0
			Ta 249.664	<input type="checkbox"/> 1.8
			W 249.664	<input type="checkbox"/> 25.0
			Pd 249.669	<input type="checkbox"/> 1.0
			Co 249.671	<input type="checkbox"/> 4.0
			Nb 249.697	<input type="checkbox"/> 1.0
			Hf 249.699	<input type="checkbox"/> 80.0
			U 249.720	1.0
			Os 249.721	<input type="checkbox"/> 1.8
249.773 { 134 }	4000	0.99997	W 249.748	<input type="checkbox"/> 25.0
			Co 249.750	2.0
			Th 249.756	<input type="checkbox"/> 2.0
			Sn 249.772	<input type="checkbox"/> 1.0
			Ta 249.777	<input type="checkbox"/> 10.0
			Fe 249.782	<input type="checkbox"/> 3.0
			Ge 249.796	<input type="checkbox"/> 15.0
			Re 249.822	<input type="checkbox"/> 1.2

The effects of spectral symmetry, background and interferences of coexistent elements and matrix were investigated. High level background interferences in the presence of sulfur were registered around B182.591nm { 184 } and B182.641nm { 183 }. Obvious matrix background interferences in the presence of iron were registered around B249.678nm { 135 } and B249.773 nm { 134 } which can be selected only on the condition that the amount of iron-base is equal to that of sample and of same background correction. Based on studied on spectral line sensitivity, interferences and correlation coefficient of the standard curve, B208.893 nm { 160 } and B208.959 nm { 161 } were selected.

2.5 Effect of solution acidity

Five parts of iron standard solution (10.0mg/mL) used as matrix each were put into five 100mL flask. 3.00mL of standard solutions of boric anhydride (4.00mg/mL) was added to each flask, followed by 4mL, 10mL, 15mL, 20mL, 25mL, 30mL of hydrochloric acid(1+1) respectively, and then diluted to the mark. The prepared solutions with different volume fraction of 2%, 5%, 7.5%, 10%, 12.5% and 15% were determined under instrumental working conditions for boron. The results obtained are listed in Figure 2. It is seen that ICP-AES is free from acid matrix interference when volume fraction of hydrochloric acid varied from 2% to 5%. 15mL of hydrochloric acid is recommended for sample dissolution.

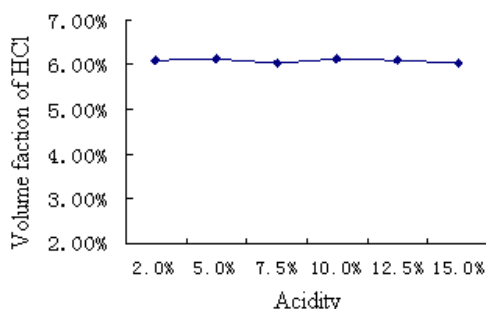


Figure 2 Effect of solution acidity

2.6 Effect of matrix and interference elements

Iron, one of the main components in ascharite ores used in metallurgical production, was more than 55%. Comparison experiments were carried out as different amounts of iron-base were added into solutions containing the same content of the standard solution of boric anhydride. The results indicated that the content of iron in ascharite ores ranged from 10% to 65% do not have remarkable matrix effect in the ICP-AES determination around B208.893nm and B208.959 nm.

Four reference solutions used for the interference determination of the coexist elements including silicon, aluminium, calcium and magnesium were prepared respectively on the basis of a solution containing 3mL standard solution of boric anhydride and 15mL hydrochloric acid(1+1) . The ICP-AES analysis results showed that silicon, aluminium, calcium and magnesium do not interfere with the determination of boron around B208.893nm and B208.959 nm when the maximum relative error is 5%.

2.7 Accuracy, precision and recovery test of method

According to the sample pretreatment method described above, the certified reference material and actual samples of ascharite ore were analyzed. The results obtained are listed in Table 3.

The results on certified reference material half weighing test, certified reference material three-quarters weighing test and standard recovery test are listed in Table 4.

Table 3 Comparison of the certified reference material and actual sample analytical results (%)

Sample	Valid certified value	Measured values	Mean value	Standard deviation	RSD
Certified reference material	5.65	5.579、5.545、5.622 5.601、5.640、5.584	5.60	0.0357	0.64
Sample 1 #	/	18.22、18.12、18.18、 18.25、18.10、18.28	18.19	0.072	0.39
Sample 2 #	/	1.02、1.00、1.01、 1.03、0.99、1.01	1.01	0.014	1.4

Table 4 Results on the certified reference material (YSB1674-05) of ascharite ores (%)

Certified reference material	Valid certified value	Addition amount	Measured values	Recovery rate
Half weighing of YSB1674-05(0.1000g)	2.825	0	2.80	/
three-quarters weighing of YSB1674-05(0.0500g)	1.413	5	4.91	98.2
YSB1674-05	5.65	1.00	1.01	101.0
YSB1674-05	5.65	10.00	9.89	98.9

YSB1674-05

5.65

20.00

20.13

100.6

The relative standard deviation of this method is less than 1.4% within the measurement range of 0.1% ~ 40 % and the recovery rate is in the range of 98.1 % ~ 101.0 %.

3 Conclusion

A simple method with wide linear range, low detection limit and also high sensitivity and accuracy has been developed in this study. After the samples were completely dissolved and collected with hydrochloric acid(1+1) in a sealed container with a reflux condenser by the low-temperature heating method, they could be directly analyzed and determined with ICP-AES at optimized operating parameters. The results obtained in the determination of boron in the certified reference material and actual samples agree well with the corresponding values obtained by the other certification methods (GB3447.3-82,etc.). This method is proved to be simple, rapid and accurate, which could offer effective technical supports for quality control and the actual production.

References :

- [1] GB3447.3-82 Ascharite ores-determination of boric anhydride content-volumetric method[S].
- [2] Yang L.F. , Li Y. , Su M.Y. Determination of gold, platinum and palladium in chromium concentrate by inductively coupled plasma atomic emission spectrometry after separation and enrichment with D290 resin and active carbon[J].Metallurgical analysis , 2010 , 30(6) : 12 - 15.
- [3] Zhao Q.L. Determination of Al₂O₃, CaO, TFe₂O₃, MgO, MnO, SiO₂,TiO₂ in Limestone and Dolomite by ICP-AES[J]. Analysis and testing technology and instruments,2009(15) 3:179 - 181.
- [4] Peng H. , Wang Y.M. , Li C.Y. Determination of phosphate rock components by microwave dissolving sample of enclosed system and ICP-AES [J]. Phosphate & compound fertilizer, 2010(25)3:71 - 72.
- [5] Wen X.D. , Zhao X.W. , Wen.B.etc. Determination of low content silicon dioxide in fluorite by inductively coupled plasma atomic emission spectrometry [J] . Metallurgical Analysis , 2008 , 28 (3) : 61 - 63.
- [6] Isil Aydin, Sefik Imamoglu, Firat Aydin etc. Determination of mineral phosphate species in sedimentary phosphate rock in Mardin, SE Anatolia, Turkey by sequential extraction[J]. Microchemical Journal 91 (2009) :63 - 69.
- [7] Wen X.D. , Cao H.Y. , Yang Y. Determination of oxides of silicon, aluminium, calcium, manganese and sulphur in iron oxide powder by ICP-AES[J].Research on Iron and steel , 2008 , 36 (4) : 45 - 47
- [8] GB/T6730.63-2006 Iron ores—Determination of aluminum calcium magnesium manganese phosphorus silicon and titanium content—Inductively coupled plasma atomic emission spectrometric method [S]
- [9] Liu W. , Luan Y.L. , Wu L.P.. ICP-AES Determination of Nb and Ta in products of oredressing of spodumene.[J] Physical Testing and Chemical Analysis Part B:Chemical Analysis,2006,42(9):715.
- [10] Song W.L. , Zhang L. , Zhao X.W. Determination of oxides and total iron in metallurgical slag by ICP-AES[J]. Metallurgical Analysis,2004 , 24 (2) : 70 - 72.
- [11] Li B.,Ma X.R.,Yang H.X.,etc. Determination of boron, arsenic and sulfur in geological samples by inductively coupled plasma atomic emission spectrometry with sample treatment by pressurized decomposition[J].Rock and mineral analysis,2003,22(4):241.
- [12] Osamu Fujino, Shigeo Umetani, Eiji Ueno etc. Determination of uranium and thorium in apatite minerals by inductively coupled plasma atomic emission spectrometry with solvent extraction separation into diisobutyl ketone[J]. Analytica Chimica Acta 420 (2000) :65–71.
- [13] V. Padmasubashini, M.K. Ganguly, K. Satyanarayana etc. Determination of tungsten in niobium–tantalum, vanadium and molybdenum bearing geological samples using derivative spectrophotometry and ICP-AES[J]. Talanta 50 (1999): 669–676.
- [14] Kazuaki Ito, Fuminori Masukawa, Qinglu Mao etc.Inductively coupled plasma-atomic emission spectral fitting analysis of rare-earth elements in ion-adsorption type ores[J]. Analytica Chimica Acta 362 (1998) :241 - 245.

PROGRESS ON ANALYTICAL METHODS FOR COMPOSITION OF NICKEL-BASE ALLOYS IN CHINA

Shao Xiaodong, Liu Yangqin, Wu Jian

CNPC Tubular Goods Research Institute, No. 32 Dianzier Road, Xi'an 710065, China

Abstract:

The progress of analytical methods was reviewed for chemical composition in nickel-base alloys in recent years. The basic characteristics and application instances of existing determination methods were introduced, including atomic emission spectrometry, atomic absorption spectrometry, spectrophotometry, atomic fluorescence spectrometry, X-ray fluorescence spectrometry, infrared absorption spectroscopy, mass spectrometry, electroanalytical chemistry and chemical analysis method. The advantages, disadvantages and applicable scopes of these methods were compared. The development trend of this field was also outlined as follows: from chemical method and single element analysis to instruments analysis and simultaneous determination of multi-elements.

Keywords: Nickel-base alloys, Chemical composition, Analytical method, Review

Introduction

The energy supply is growing day by day, more and more acid oil-gas fields are exploited. The maximum temperature in acid deep well can be up to 320°C, and the maximum pressure is up to 100MPa. Meanwhile, the partial pressure of hydrogen sulfide and carbon dioxide is very high. During exploitation, the elemental sulfur may be separated out. The concentration of chloride solution is very high. In order to meet the exploitation requirements of these oil-gas wells with high temperature, high pressure and high partial pressure of hydrogen sulfide and carbon dioxide, the oil well pipes must adopt alloy materials with excellent resistance to high temperature and corrosion, good strength, plasticity, toughness, metallurgical stability, workability and solderability. The application scope in industry of nickel-base alloys is increasing, for example, in aerospace, nuclear power and ship products [1]. Many nickel-base alloys have excellent heat resistance, and become the ideal selection for resistance to corrosion and high temperature. The nickel-base alloy oil well pipes have excellent resistance to corrosion. This is because that the formed passive film on surface isolate the further contact between matrix and aggressive medium, protecting the matrix. It not only has lower metal loss, but also can be subject to local corrosion, especially for resistance to hole corrosion or crevice corrosion, intergranular corrosion and stress corrosion. Therefore, the nickel-base alloys will be widely used in the exploitation of oil-gas wells [2].

Continuous improvement of metallurgy and manufacturing technology promotes the development of nickel-base alloys. The content of chemical elements in nickel-base alloys directly influences the properties of alloy materials. Therefore, the accurate determination of chemical components in nickel-base alloys is important to ensure its development, application and production. In order to control the quality of nickel-base alloy products and meet the requirements of the new products, the contents of trace impurities and alloy elements in nickel-base alloys should be determined. During the analysis and testing of nickel-base alloys, every testing step should be noticed to reduce the error factors. It has very important significance to guide the production and development of new nickel-base alloys and control the product quality. In this paper, the progress in analytical methods of elements in nickel-base alloys was reviewed, including atomic emission spectrometry, atomic absorption spectrometry, spectrophotometry, atomic fluorescence spectrometry, X-ray fluorescence spectrometry, infrared absorption spectroscopy, mass spectrometry, electroanalytical chemistry and chemical analysis. In the future, the analysis method of chemical composition in nickel-base alloy will be focused on rapidness, high accuracy and sensitivity, high automation, on-line analysis of elements in smelting process and so on. These researches will boost the analysis of chemical elements in nickel-base alloy to a newer and higher level.

Atomic emission spectrometry

Atomic emission spectrometry (AES) has wide application in material analysis. Because of its high sensitivity, good

stability, little interference, wide linear range, rapid analysis speed, simultaneous determination or sequential determination of multi-elements. AES has become the indispensable and important method in metallurgical analysis [3]. AES is the most widely used method in analysis of nickel-based alloys. Its largest advantage is the simultaneous determination of multi-elements with little sampling amount. According to the difference in light source, it can be classified into direct current arc, alternating current arc, electric spark and inductively coupled plasma atomic emission spectrometry (ICP-AES). Among these methods, the application of ICP-AES is the most extensive. Ye investigated the spectral interference of matrix nickel and coexisting elements [4]. They used vanadium as internal standard solution, and established the analysis method of 10 elements (including aluminum, boron, cobalt, chromium, iron, hafnium, molybdenum, tantalum, titanium and tungsten) by ICP-AES. Feng studied the determination of trace boron in nickel-base and iron-nickel-base superalloy by ICP-AES [5]. They investigated the effect of matrix and alloy elements in DZ125 nickel-base alloy and GH4169 iron-nickel-base alloy on the determination. The interference of iron, tungsten, niobium and tantalum was eliminated by fractional precipitation separation method. The analytical line of boron was 249.67nm, and the measured content of boron in sample was 0.002~0.05% (mass fraction). Li adopted QSN-750 photoelectric direct reading spectrometer to determine nine alloy elements in nickel-base alloys, including carbon, sulfur, phosphorus, silicon, manganese, chromium, molybdenum, iron and vanadium. The analytical lines of each element, the analytical parameters for measurement, the sample preparation and the fitting of calibration curve were tested and optimized. The selected internal-standard line was Ni 218.55nm [6]. The determination of chemical compositions in nickel-base alloys using atomic emission spectrometry were listed in Table 1.

In recent years, some researchers in our country did in-depth research in the application of spectroscopy (spectrograph) in the analysis of components in nickel-base alloys. By combining with visible spectrum digital analysis techniques, the spectroscopy was successfully applied to the matrix determination, and qualitative, semi-quantitative and quantitative analysis of components in nickel-base alloys. Under the conditions that photoelectric direct reading spectrometer is in an important role in market, it broadens the application of spectroscopy [7]. Liu studied the visible spectrum digital analysis technology of cobalt in nickel-base alloys [8]. The analytical lines including Co 481.35nm and Co 645.02nm were digitally treated. The quantitative analysis and trademark identification of visible spectrum for cobalt in nickel base alloys were conducted using visible spectrum digital analysis system. The proposed method was applied to the qualitative analysis, quantitative analysis and trademark identification of cobalt in nickel-base alloys. They also applied visible spectrum digital analysis technique to the qualitative and quantitative analysis of chromium, molybdenum, tungsten, titanium and aluminum in nickel-base alloys [9-13].

Atomic absorption spectrometry

Atomic absorption spectrometry (AAS) was used in analytical chemistry since 1955, and it has

Table 1 Determination of chemical composition in nickel base alloys using AES

Excited source	Element	Limit of determination (%)	Reference
Hollow cathode discharge source	Pb, Bi, Te, Tl, Ag	0.0019	[14]
ICP	Nb	0.0066	[15]
ICP	La, Y	0.012 μ g/mL	[16]
Direct current arc	Pb, Bi, Ag, Tl	0.00001	[17]
Hollow cathode discharge source	As, Te, Sb, Pb, Sn, Bi, Tl, Ag	0.000002	[18]
ICP	B	0.0005	[19]
ICP	Mn, Cr, Cu, Co, Ti, Mo, Fe, Nb, Ta	0.0013	[20]
ICP	Al	0.0026	[21]
Electric spark	La, Ce	0.0001	[22]

ICP	Al, B, Ce, Co, Cr, Cu, Fe, Hf, La, Mg, Mo, Nb, Ta, Ti, W, Zr	2.6µg/L	[23]
ICP	Ta, Zr, Hf	0.027	[24]
Electric spark	Si, Mn, P, C, S, Cr, Al, Cu, Fe, Ti,	0.008	[25]
ICP	Fe, Mo, V, Ti, Mn, Al, Ce, Nb, W, Zr	0.0023	[26]
ICP	Cu	0.001	[27]

evolved into a mature analytical technique [28]. At present, it is widely applied to the metallurgical analysis due to its high selectivity, high automation and intelligentization, and little interference. In nickel-base alloy industry, AAS is mainly used for the analysis of metal elements in nickel-base alloys. AAS mainly includes two kinds: flame atomic absorption spectrometry (FAAS) and graphite furnace atomic absorption spectrometry (GFAAS). The former is a mature and widely used analytical technique, which is mainly applied to the analysis of trace elements. It has many advantages such as simple operation, rapid analysis speed, little interference and stable signal. The latter has higher sensitivity and lower detection limit, and it is a commonly used analytical method of trace elements. Guo used graphite furnace atomic absorption spectrometry to determine arsenic, lead, tin, antimony and bismuth in iron-nickel base superalloy combining with extraction separation method [29]. In this method, these five elements could form complex with iodide ion, which could be separated from matrix by methylsobutylketone extraction. The effect of extraction conditions and residual matrix after extraction on testing elements was investigated. Meanwhile, the interference of tungsten, niobium and tantalum was eliminated by masking. Under the selected experimental conditions, the measured recoveries of arsenic, lead, tin, antimony and bismuth were 93~99%. The common flames for FAAS are air-acetylene, nitrogen monoxide-acetylene and air-hydrogen. Xue adopted nitrogen monoxide-acetylene flame to determine the tin in high temperature nickel-base alloys [30]. The optimal determination conditions and the concentration of linear range were investigated. The resonance line at 286.3nm was used for analysis. The interference factors in sample were considered. The tin in range of 1~80mg/L could be determined with detection limit of 0.05mg/L. In addition, AAS also includes hydride generation atomic absorption spectrometry (HGAAS). Its sensitivity is similar with GFAAS. HGAAS has many advantages such as little matrix interference, high loading efficiency, low detection limit and direct state analysis of elements. Yu used HCF-I hydride generator to determine trace bismuth in iron-nickel-base alloy by HGAAS [31]. The interference of matrix elements (Fe and Ni) on the determination of trace bismuth was investigated. By using thiourea as inhibiting reagent, the interference of nickel, copper and cobalt could be eliminated. The detection limit was 0.00077µg/mL. Several iron-nickel base alloys and steel standard samples were determined. The results were consistent with the certified values. The determination of chemical compositions in nickel-base alloys using atomic absorption spectrometry were listed in Table 2.

Table 2 Determination of chemical composition in nickel alloys using AAS

Analytical method	Element	Limit of determination (%)	Reference
HGAAS	Bi	0.0011	[32]
GFAAS	Se	0.000858µg/mL	[33]
FAAS	Mo	10.36mg/L	[34]
FAAS	Si	2µg/mL	[35]
GFAAS	Ag	0.00023	[36]
HGAAS	Se, Sn	0.0001	[37]
GFAAS	Sb	0.00005	[38]
GFAAS	Se	0.0025	[39]
FAAS	Fe	4.80	[40]
GFAAS	As	0.000027	[41]
GFAAS	B	0.0014	[42]
HGAAS	Te	0.00002	[43]

FAAS	Bi	0.1µg/mL	[44]
GFAAS	Pb, Sb	0.000013	[45]
HGAAS	Se	0.00045	[46]
GFAAS	Bi	0.00003	[47]
GFAAS	Te	0.00005	[48]
GFAAS	Tl, Te	1.0ng	[49]
GFAAS	Cd	0.0000024	[50]
GFAAS	Cu	1.9pg	[51]
FAAS	Mg	0.5ng/g	[52]

Spectrophotometry

National standard method of spectrophotometric determination of phosphorus in nickel-base alloys is phosphorus vanadium molybdate yellow spectrophotometry. In this method, the sample is dissolved in HCl and HNO₃ mixed acid. For insoluble substances or samples with high content of silicon, HF is added to enhance the dissolution. After perchloric acid smoking and chromium volatilization with HCl, the phosphorus in sample is converted into phosphorus vanadium molybdate yellow heteropolyacid, which is then measured at 355 nm. The phosphorus vanadium molybdate yellow is extracted with methylisobutylketone. The compound containing arsenic can be complexes with citric acid. This method is applicable for the determination of phosphorus (0.0005~0.05%) in nickel, ferronickel and nickel-base alloys. Hsu used acetylchlorophosphonazo (CPApA) as coloring reagent for spectrophotometric determination of cerium in nickel-base alloys [53]. The results were satisfied. Zheng also used CPApA as a coloring reagent to study the optimal conditions for the determination of cerium and yttrium [54]. Since the absorption spectra of cerium and yttrium were severely overlapped, the authors adopted partial least squares method for the mathematical correction of measured results. This method realized the simultaneous determination of cerium and yttrium in synthetic samples and actual samples. The spectrophotometric determination of chemical compositions in nickel-base alloys were listed in Table 3.

Table 3 Determination of chemical composition using spectrophotometry

Chromogenic reaction	Element	λ_{\max} (nm)	Linear range (µg/mL)	Reference
Ce-Dibromocoboxyarsenazo	Ce	632	0~0.2	[55]
Zr-Arsenazo III	Zr	660	0.040~0.132%	[56]
Fe-Phenanthroline	Fe,	508	0.1~6	[57]
Mo-NH ₄ SCN	Mo	460	0.10~2.00%	[57]
Mo-H ₂ O ₂	Mo	330	0~80	[58]
Si-(NH ₄) ₆ Mo ₇ O ₂₄ - (NH ₄) ₂ Fe(SO ₄) ₂	Si	660	0.010~3.00%	[59]
Cerium subgroup rare earths- CPApA-CPC-OP	Cerium subgroup rare earths	675	0~0.56	[60]
		692		
Fe-EDTA-H ₂ O ₂	Fe	530	2.5~7.5%	[61]
Fe-1-nitroso-2-naphthol	Fe,	445	0.5~2.5	[62]
Ni-1-nitroso-2-naphthol	Ni	455	0.2~1.0	[62]
Ni-Carmine-KIO ₄	Ni	510	0.0004~0.032	[63]

Atomic fluorescence spectrometry

Atomic fluorescence spectrometry (AFS) is a spectrometric analysis technique proposed and developed since middle 1960s. It combines the advantages of atomic absorption spectrometry and atomic emission spectrometry. Moreover, it overcomes some shortcomings. AFS is a kind of good trace analysis technique [64]. AFS has the advantages such as simple instrumental structure, high sensitivity, low detection limit, little gas phase interference and applicable for multi-elements analysis. AFS is especially suitable for the analysis of elements with fluorescent

lines between 200nm and 290nm, including arsenic, antimony, bismuth, mercury, selenium, tellurium, lead, tin, germanium, zinc and cadmium. AFS has been widely used in the analysis of environment, biomedicine, geology and metallurgy [65,66]. However, there are few reports about the analysis of chemical compositions in nickel-base alloys by AFS. Xie used AFS-220A dual-channel atomic fluorescence spectrometer to establish the determination of trace bismuth in nickel-base superalloys by hydride generation-atomic fluorescence spectrometry [67]. The fluorescence intensity showed linearity with the concentration of bismuth in range of 0~30.0 μ g/L. The detection limit was 0.29 μ g/L. This method was applied to the determination of trace bismuth in DZ125 and 849-1 nickel-base superalloys. The precision and accuracy could meet the requirements of actual testing. Zhang B. studied the analysis method of trace selenium in nickel-base superalloys by hydride generation-atomic fluorescence spectrometry [68]. The instrumental working conditions, pH, concentration of reducing reagent, the interference and to elimination of coexisting elements were investigated. The linear range of this method was 1~90ng/mL. The proposed method was applied to the analysis of GH4169 nickel-base alloy samples, and the results were satisfied. Jian studied the analysis method of trace selenium and tellurium in nickel-base superalloys by hydride generation-atomic fluorescence spectrometry [69]. The optimal conditions for hydride generation, pH, the dosage of reducing reagent and the interference of nickel and cobalt under discontinuous flow conditions were tested. The interference was inhibited by citric acid. A direct, rapid and accurate analysis method of selenium and tellurium in nickel-base superalloys was finally established. The determination low limits of selenium and tellurium were up to 1.00ng/L. The proposed method was applied to the determination of selenium and tellurium in DZ125, GH141, K77 and K3 nickel-base superalloys.

X-ray fluorescent spectrometry

Since 1980s, the X-ray fluorescent spectrometry (XRF) gradually becomes a kind of mature, high precision and rapid analysis method. At present, XRF is widely used in geology, metallurgy, chemical industry and material science. The papers published by domestic researchers mainly focus on the geological and ore analysis [70]. In recent years, the papers about the application in metallurgical analysis are rising. Wang also used XRF to analyze the components in nickel-base alloy [71]. The nickel-titanium alloy standard block sample was prepared for daily analysis in laboratory. The non-uniformity was less than 0.05%. The design content of standard components could be directed used as standard data. By using PW-1400 full automatic X-ray fluorescent spectrometer, and the measuring method of reciprocal internal standard method and sample optimization, the relative standard deviation (RSD) of analytical results could be controlled at 0.02%. The results of this method were consistent with gravimetric analysis.

Infrared absorption spectroscopy

The application of infrared absorption spectroscopy in nickel-base alloy is the analysis of carbon and sulfur. The experimental facility is a special analysis instrument combining infrared source, gas absorption cell, high-temperature heating furnace (generally high frequency induction heating furnace) and detector [72]. The carbon and sulfur in sample were gasified at high temperature and then converted to CO₂ and SO₂. The content was quantitatively determined by infrared absorption spectroscopy [73]. In recent years, the infrared gas analysis technique has rapid developed. Many analytical instruments using high frequency induction heating and infrared spectrum absorption principle are also produced. The infrared absorption spectroscopy has been used as the national standard method for the analysis of carbon and sulfur in nickel-base alloy. The carbon (0.001~0.5%) and sulfur (0.001~0.1%) in nickel-base alloy could be measured. For the determination of carbon and sulfur by high frequency combustion infrared absorption spectroscopy, the crucible, the dryness of sample, electromagnetic induction, physical dimension, sample amount, the type of fluxing reagent, mixture ratio, adding order and dosage, reagent for purifying gas (anhydrous magnesium perchlorate) and the setting of blank value should be considered. At present, the reports of carbon and sulfur in nickel-base alloy by infrared absorption spectroscopy were few. Song used infrared carbon-sulfur analyzer to determine the trace sulfur in superalloy [74]. The main factors influencing the determination of trace sulfur in superalloy were investigated. By shortening washing interval, prolonging residence time and analyzing other samples, the samples with low content of carbon and sulfur were measured. The absorption of tin dust to sulfur was reduced by diluting the tin dust concentration in combustion

system, increasing the accuracy and precision. An analysis method of trace sulfur in nickel-base superalloys was established. The determination range of sulfur was 0.0001~0.0005% (mass fraction). This method was applied to the analysis 11 kinds nickel-base alloy samples (LECO 501-673, S₈₂, SUJ-1, M1702, M17, DZ17G, M41A, DZ17GL-2, In738, M91 and GH169). The determination results were satisfied.

Mass spectrometry

Mass spectrometry (MS) is also a kind of important instrumental analysis method [75]. However, its application in metallurgical analysis especially the analysis of nickel-base alloy is rarely reported. Hu J. and Wang H. combined laser ablation solid sampling technique and inductively coupled plasma mass spectroscopy (CP-MS) for the analysis of 20 kinds trace elements in superalloys [76]. The used instrument was VG PQII Turbo ICP-MS and VG Laser Lab sampling system. The instrumental conditions were optimized: By lay-lay ablation, the low boiling point elements in superalloys were stably evaporated. A stable element signal response curve with good repeatability was established. ⁷¹Ga was used as the internal standard element to establish the analysis method of trace elements in superalloy by LA-ICP-MA internal standard quantitative method. The proposed method was applied to the determination of elements with content at µg/g level or lower. Gan used dynamic reaction cell (DRC) hydride generation (HG) to enrich germanium, arsenic and selenium [77]. The gas liquid separator reduced the interference of nickel and cobalt during the hydride generation of three elements. The optimal conditions for hydride generation were: 2.0g/L of NaBH₄ was used as hydrogen generator; 20g/L of cysteine was used as masking and sensitivity enhancing reagent; the flow rate of gas was controlled at 0.95mL/min. A determination method of germanium, arsenic and selenium in nickel-base alloy by HG-DRC-ICP-MS was established. The detection limits were 0.003pg/L, 0.001pg/L and 0.002pg/L, respectively.

Electroanalytical chemistry

The potentiometry is an important branch of electroanalytical chemistry method. Under zero current conditions, the potential difference between two electrodes is analyzed and measured. In recent 30 years, the method with ion selective electrodes is rapidly developed. Its instrument is simple, lightweight and portable. This method is applicable for field measurement and easily expanded with good selectivity. The fluoroborate electrode was successfully developed in 1970s in China, and it has been applied to the determination of boron in steel [78]. Jia used fluoroborate ion-selective electrode to determine trace boron in novel nickel-base superalloy [79]. The pH in study was 5.0~6.0, and the electrode response time was 2~3min. A large amount of common ions such as nickel, molybdenum, tungsten, cobalt, titanium, aluminum and iron in alloy had no interference with the determination of boron. Cr(III) did not interfere with the determination. However, the interference of Cr(VI) was serious. And the electrode potential was instable, even unable for measurement. When the sample was dissolved with hydrochloric acid and little nitric acid using sulphuric acid smoking, the chromium was usually in low valency state. When the smoking was large, some chromium ions would be oxidized to high valency state. 0.5mL of 60g/L ferrous sulphate could be added to reduce high valency chromium to eliminate the interference. Under the experimental conditions, 2% (mass fraction) of hafnium has no interference. However, tantalum interfered with the determination of boron. The interference was more and more severe with the increase of tantalum. When Ta/B≤20, it could be considered that there was no interference. For the interference of tantalum, it could be eliminated by adding same amount of tantalum into testing solution during the preparation of standard solution for plotting calibration curve. The precision test indicated that RSD was less than 1.54%. The proposed method was applied to the analysis of alloy samples, and the results were satisfied.

Titrimetry

The titrimetry is a classical method of analytical chemistry. Feng established EDTA titrimetric analysis method of high-content nickel in superalloy [80]. In ammonia solution containing citrate, the nickel was separated from chromium, iron, aluminum, tungsten, molybdenum, vanadium and manganese using dimethyl glyoxime. The nickel precipitation and filter paper were decomposed with HNO₃ and HClO₄. The sample solution was titrated at pH with EDTA standard solution using murexide as indicator. The content of nickel was calculated based on the consumed volume of EDTA solution. The nickel in mass fraction of 50~80% could be measured. The optimal conditions were: 15g/L of dimethyl glyoxime, 20mL of 500g/L citric acid solution and precipitation temperature of 70~80°C. The

recovery of standard addition was above 99%. The precision and accuracy tests were conducted using D105 and D150 nickel-base alloys. The found values were consistent with the standard values with $RSD \leq 0.09\%$. This method solved the analysis problem of matrix element in nickel-base superalloy. Yu used thiourea to rapidly mask palladium-EDTA complex at room temperature [81]. The separated EDTA was titrated with zinc standard solution. This method realized the rapid determination of palladium, and it has been applied to the determination of palladium in nickel-base alloy, hard solder and electroplating liquid.

Conclusions

In recent years, the analysis method of chemical composition in nickel-base alloy has been rapidly developed. The analysis method is becoming diversity. The sensitivity and selectivity of method are higher and higher. Atomic emission spectrometry is the most widely used analytical method of elements in nickel-base alloy due to ties low interference, good precision and simultaneous determination of multi-elements. ICP-AES becomes the main determination method of elements in nickel-base alloys in production departments. The application of atomic absorption spectrometry in determination of elements in nickel-base alloys is gradually increasing. Due to the different characteristics, the FAAS, GFAAS and HGAAS all achieved good development. The spectrophotometry and titrimetry have some disadvantages such as complicated operation and long analytical period, so they are not stable for the requirements of modern production. However, they have great advantages for the analysis of elements with high content. The application of infrared absorption spectroscopy in nickel-base alloys is mainly for the determination of carbon and sulfur. This method has good accuracy, wide analysis range and good stability, and it has been used as the national standard method. With the application and development of ICP-MS, it has many advantages in the analysis of trace and super-trace elements in nickel-base alloy, and paid much attention to. However, the researches about it are mainly at abroad, and relatively few at home. The ion-selective electrode method in electroanalytical chemistry is also applied to the determination of chemical composition in nickel-base alloy. It could be seen from the references that, the analytical method of chemical composition in nickel-base alloy is developing from chemical analysis and single element to instrumental analysis and simultaneous determination of multi-elements. Although the researches of nickel-base alloy have yielded impressive results, the national standards about the analysis of nickel-base alloys are rare in China. The analytical method is single, so it should be further studied in future. The analysis method of chemical composition in nickel-base alloy will be focused on rapidness, high accuracy and sensitivity, high automation, on-line analysis of elements in smelting process and so on. These researches will boost the analysis of chemical elements in nickel-base alloy to a newer and higher level.

Acknowledgments

The authors gratefully acknowledge the CNPC Tubular Goods Research Institute, and China National Quality Supervision, Testing and Inspection Center of Oil Tubular Goods.

Reference

- [1] Guo X D, Li J L, Zhou B, *et al.* *Journal of Shanghai Jiaotong University*, 2009, 43(1): 79-83.
- [2] Zhang C X, Zhang Z H. *Baosteel Technology*, 2008, 26(5): 35-38.
- [3] Jiang Z C, Hu B, Peng T Y. *Chinese Journal of Analysis Laboratory*, 2001, 20(2): 101-108.
- [4] Ye X Y, Li F. *Journal of Materials Engineering*, 2002, 47(12): 23-24.
- [5] Feng Y Y, Yang B W. *Chinese Journal of Spectroscopy Laboratory*, 2000, 17(2): 195-198.
- [6] Li W X. *Journal of Gansu Science*, 2008, 20(2): 86-88.
- [7] Liu P, Yang J H. *Modern Instruments*, 2007, 13(1): 63-65.
- [8] Liu P, Yang J H. *Modern Instruments*, 2008, 53(11): 46-48.
- [9] Liu P, Yang J H. *Development and Application of Materials*, 2008, 23(5): 64-66.
- [10] Liu P, Yang J H. *Journal of Aeronautical Materials*, 2008, 28 (5): 100- 102.
- [11] Liu P, Yang J H. *Modern Instruments*, 2008, 14(4): 45-47.
- [12] Liu P, Yang J H. *Analytical Instrumentation*, 2008, 39(3): 23-25.
- [13] Liu P, Yang J H. *Modern Scientific Instruments*, 2008, 25(5): 49-51.
- [14] Pang X H. *Modern Scientific Instruments*, 2007, 24(5): 93-95.
- [15] Tang M S, Dou Z W, Ma X, *et al.* *Journal of Harbin University of Commerce*, 2006, 22(3): 80-81
- [16] Wang B R. *Chinese Journal of Spectroscopy Laboratory*, 1999, 16(2): 161-164.
- [17] Li D X, Du Z X, Sun J Y, *et al.* *Metallurgical Analysis*, 1995, 15(6): 54-56.

- [18] Wang B R. *Journal of Materials Engineering*, 1999, 44(8): 42-43.
- [19] Ye X Y, Yang C S, Xie S J. *Chemical Analysis and Meterage*, 2008, 17(4):31-32.
- [20] Liu Y Z, Liu Z M. *CFHI Technology*, 1997, 36(3): 62-64.
- [21] Tang M S, Dai D, Meng X B. *Journal of Harbin University of Commerce*, 2003, 19(5): 80-81.
- [22] Su Z. *Journal of Xingjian Normal University: Natural Sciences Edition*, 1998, 17(3): 22-25.
- [23] Li F, Ye X Y. *Spectroscopy and Spectral Analysis*, 2003, 23(6): 174-176.
- [24] Zhang B S, Jia J Z. *Journal of Materials Engineering*, 1996, 41(2): 37-39.
- [25] Su Z. *Xinjiang Nonferrous Metals*, 1995, 24(1): 35-37.
- [26] Liu F H, Sun G P, Wang C G, et al. *Turbine Technology*, 2004, 46(3): 236-237.
- [27] Shi X L, Zhang B S. *Metallurgical Analysis*, 2008, 28(6): 63-65.
- [28] Zhu M H. *Instrumental Analysis* [M]. Beijing: Higher Education Press, 2000.
- [29] Guo J X, Xu S K, Li X Z, et al. *Spectroscopy and Spectral Analysis*, 2006, 26(6): 167-169.
- [30] Xue G R. *Chemical Word*, 2007, 62(1): 658-660.
- [31] Yu F L, Zhou S K. *Metallurgical Analysis*, 1998, 18(2): 56-58.
- [32] Takase I, Luna A S, Campos R C. *Talanta*, 2003, 61(5): 597-602.
- [33] Pang X H, Yang J H, Liu P. *Modern Scientific Instruments*, 2006, 23(5): 96-97.
- [34] Xue G R. *Modern Scientific Instruments*, 2007, 24(3): 95-97.
- [35] Xue G R. *Shanghai Measurement and Testing*, 2004, 32(1): 15-17.
- [36] Geng D F, Yan Y M, Chang Z J. *Ordnance Material Science and Engineering*, 2002, 25(3): 70-72.
- [37] Chen T Y, Wang Z. *Chinese Journal of Analysis Laboratory*, 2001, 20(2): 14-16.
- [38] Luo C, Sun Y, Zhao S R. *Metallurgical Analysis*, 1999, 19(4): 51-52.
- [39] Geng D F, Luo H, Yan Y M, et al. *Ordnance Material Science and Engineering*, 2002, 25(4): 48-58.
- [40] Xu G H, Sun Y, Ma H B. *Chinese Journal of Spectroscopy Laboratory*, 1997, 14(4): 47-49.
- [41] Xie W B, Yao J Y. *Physical Testing and Chemical Analysis Part B: Chemical Analysis*, 1997, 33(3): 107-108.
- [42] Liu Y M, Gong B L, Xu S L et al. *Spectroscopy and Spectral Analysis*, 1995, 15(1): 75-78.
- [43] Peng Y Q, Yao J Y. *Physical Testing and Chemical Analysis Part B: Chemical Analysis*, 1995, 31(2): 75-76.
- [44] Yang J L. *Physical Testing and Chemical Analysis Part B: Chemical Analysis*, 1994, 30(4): 242-243.
- [45] Xie W B, Yao J Y, Hu Q L. *Chinese Journal of Applied Chemistry*, 1995, 12(4): 108-110.
- [46] Peng L Q, Yao J Y. *Chinese Journal of Analytical Chemistry*, 1994, 22(11): 1135-1137.
- [47] Xie W B, Yao J Y, Hu Q L, et al. *Chinese Journal of Analysis Laboratory*, 1995, 14(2): 64-67.
- [48] Yao J Y, Duah H F, Yun Z M, et al. *Spectroscopy and Spectral Analysis*, 1994, 14(6): 83-86.
- [49] Tsai S J, Jan C C. *Analyst*, 1993, 18(9): 183-191.
- [50] Tsai S J, Chang L L, Chang S I. *Spectrochimica Acta Part B: Atomic Spectroscopy*, 1997, 52(1): 55-65.
- [51] Tsai S J, Shiue C C, Chang S I. *Spectrochimica Acta Part B: Atomic Spectroscopy*, 1997, 52(9-10): 55-65.
- [52] Tsai S J, Bae Y L. *Analyst*, 1993, 18(3): 301-302.
- [53] Hsu C G, Li H, Pan J M. *Talanta*, 1994, 41(8): 1357-1361.
- [54] Zheng J, Pan J M, Zhou W L. *Chinese Journal of Analysis Laboratory*, 1998, 17(5): 25-27.
- [55] Chen L R, Jin W. *Journal of Shanghai Iron & Steel Research*, 1995, 22(2): 50-53.
- [56] Dong S Q. *Locomotive & Rolling Stock Technology*, 1994, 31(6): 13-14.
- [57] Li Q X, Tan L Q, Wang J G, et al. *Metallurgical Standardization & Quality*, 2006, 44(5): 15-17.
- [58] Fan S Y. *Physical Testing and Chemical Analysis Part B: Chemical Analysis*, 1998, 34(7): 327-328.
- [59] Bao D J, Zhou Y Q. *Design and Manufacture of Diesel Engine*, 1994, 14(4): 47-51.
- [60] Li H, Xu Z J, Pan J M. *Journal of East China Normal University: Natual Science*, 1995, 41(2): 55-59.
- [61] Bao D J. *Design and Manufacture of Diesel Engine*, 1996, 16(2): 30-37.
- [62] Xia C B, He X Z, Li X. *Materials Protection*, 2006, 39(3): 72-74.
- [63] Li L M, Zhang X F. *Metallurgical Analysis*, 2007, 27(9): 64-66.
- [64] Winefordner J D, Vickers T J. *Analytical Chemistry*, 1964, 36(1): 161-165.
- [65] Morita H, Tanaka H, Shimomura S. *Spectrochimica Acta Part B: Atomic Spectroscopy*, 1995, 50(1), 69-84.
- [66] Stchur P, Yang K X, Hou X. *Spectrochimica Acta Part B: Atomic Spectroscopy*, 2001, 56(9): 1565-1592.
- [67] Xie S J. *Physical Testing and Chemical Analysis Part B: Chemical Analysis*, 2005, 41(6): 381-382.
- [68] Zha B S. *Chinese Journal of Spectroscopy Laboratory*, 1999, 16(4): 37-37.
- [69] Jia J D. *Physical Testing and Chemical Analysis Part B: Chemical Analysis*, 2001, 37(3): 104-106.
- [70] Zuo S J. *Chinese Journal of Analysis Laboratory*, 2009, 28(7): 112-122.
- [71] Wang S L, Chui G H, Li M J, et al. *Chinese Journal of Analysis Laboratory*, 1999, 18(1): 96-97.
- [72] Chao D F. *Physical Testing and Chemical Analysis Part B: Chemical Analysis*, 1999, 35(6): 249-253.
- [73] Wang B L, Guo H T. *Chemical Analysis and Meterage*, 2007, 16(1): 65-67.
- [74] Song W D, Sun Y, Chen M. *Metallurgical Analysis*, 2004, 24(4): 51-59.
- [75] Houk R S. *Analytical Chemistry*, 1986, 58(1): 97A-105A.

- [76] Hu J Y, Wang H Z. *Metallurgical Analysis*, 2008, 28(1): 1-5.
- [77] Gan N, Li T H, Wang L Y, *et al.* *Metallurgical Analysis*, 2008, 27(1): 7-11.
- [78] Zhang G X, Fu H Z, Chen W X, *et al.* *Acta Chimica Sinica*, 1980, 38(3): 223-226.
- [79] Jia J Z, Zhang B S. *Journal of Materials Engineering*, 1998, 43(9): 42-45.
- [80] Feng Y Q, Bai W J. *Chinese Journal of Analysis Laboratory*, 2008, 27(Suppl.): 351-354.
- [81] Yu Y G. *Metallurgical Analysis*, 2000, 20(6): 20-21.

METALLURGICAL AND MECHANICAL CHARACTERIZATION OF Cu ELECTROLYTIC COATING ON ALUMINIUM ALLOYS

K. Brunelli, I. Calliari, I. Rampin, , M. Magrini, , M. Dabalà

University of Padua, Dept. of Chemical engineering processes, Via Marzolo 9, Padua, Italy

Aluminium and its alloys are attractive for many applications in chemical, automotive and aerospace industries because of their excellent properties as height– to– weight ratio, high electrical and thermal conductivities and good formability.

In this work, a surface hardening process based on Cu electrolytic coating and subsequent diffusion heat treatments was studied for 7075 and 2024 aluminium alloys.

The effect of temperature and time on the microstructure and the depth of hardening was studied by SEM, EDS, XRD and HV tests. The increasing of hardness and depth of hardening have been correlated to formation of different intermetallic phases in the surface coatings.

Introduction

Aluminium alloys are widely used in automotive and aerospace due to their low specific weight and high thermal conductivity. Their major limitation is the low surface hardness and poor wear resistance. In recent years various studies have been conducted to address this to make up for this limitation, using surface coatings obtained using different techniques and different coating materials. The techniques used most often have been PVD [1,2], CVD [3], electrochemical deposition and the use of lasers [4,5]. The elements most commonly used for coating aluminium alloys are nickel [6-9], chromium [10,11], and iron [12].

The alloys chosen for this study are 2024 and 7075, two of the most common aluminium alloys and of greater interest due to their high mechanical properties, improvable with an appropriate heat treatment. This consists of a solution treatment followed by quenching and aging [13-19].

The purpose of this research is to characterize the microstructure and the mechanical properties of two Cu coated aluminium alloys after heat treatment. The choice of copper is related to the fact that the interaction of this element with aluminium leads to the formation of intermetallics with increased hardness and wear resistance. The type of intermetallics that form and the thickness of their layer depends on the amount of copper that diffuses into the sublayer and the type of alloy treated.

Experimental

In Tab. 1 the chemical compositions of alloys 2024 and 7075 are shown. The samples obtained were coated by electrolytic deposition of Cu and then submitted to heat treatment. The treatments were carried out in a tube furnace, in an inert atmosphere, at different temperatures and for different periods of time.

Lega	Si	Fe	Cu	Mn	Mg	Zn	Cr	Altri
2024	0,50	0,50	3,8-4,9	0,3-0,9	1,2-1,8	0,25	0,1	0,20 Ti+Zr
7075	0,4	0,50	1,2-2,0	0,3	2,1-2,9	5,1-6,1	0,18-0,28	0,25 Ti+Zr

Tab.1. Chemical composition of the AA2024 and AA7075.

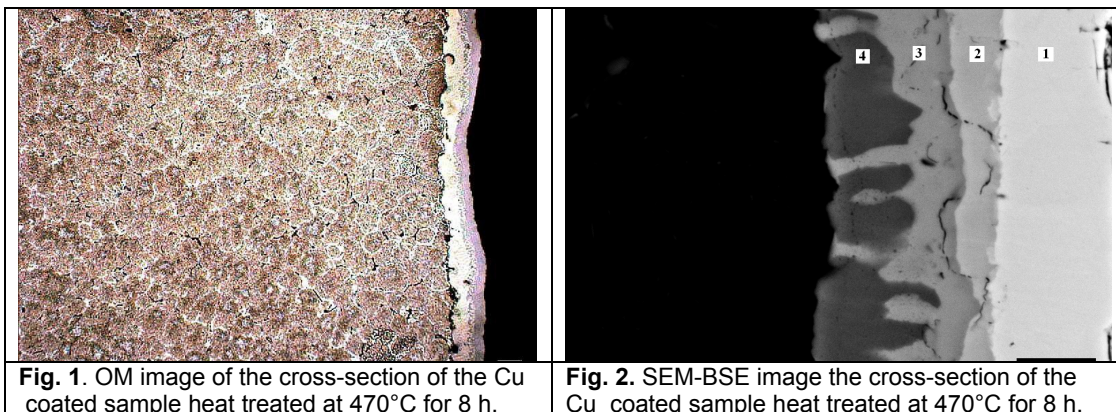
The morphological and microstructural characterization of the samples was conducted using Leitz microscope analysis, electron microscopy with a Cambridge Stereoscan 440 SEM equipped with a Philips PV800 EDS microprobe, and X-ray diffraction with a SIEMENS D500 diffractometer (Cu K α).

Microhardness profiles were obtained with a Leitz-Werlag Microdurometer applying a 100 g load.

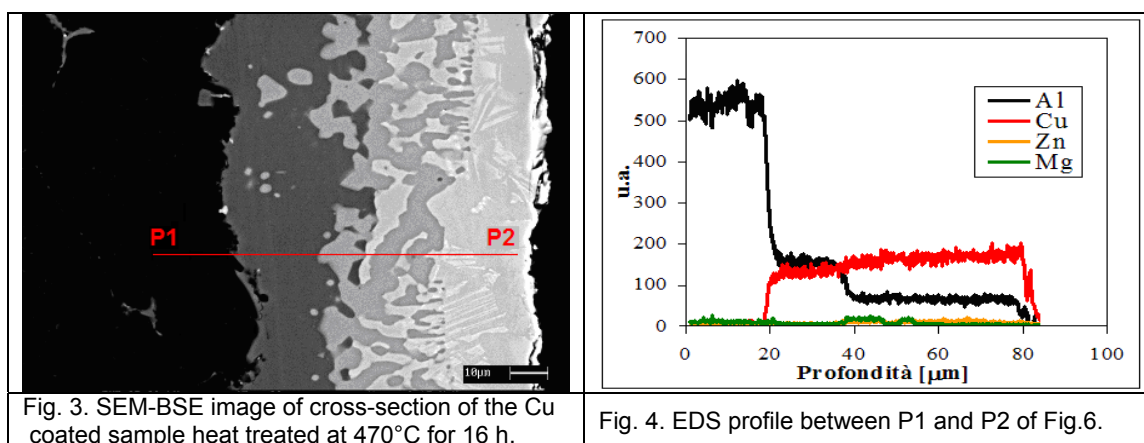
Results and discussion

Alloy 7075

In the sample treated at 8 h at 470 °C the OM and SEM observations reveals that Cu diffused in the substrate and intermetallic layers with various amount of Cu formed (Fig.1, Fig.2). From SEM-EDS analysis, the outer layer, 10 μm thick, is composed of Al 41 at.%, Cu 56 at.% and Zn 3 at.%, that suggests the formation of the compounds θ - Al_2Cu and η - AlCu . The intermediate layer is 5 μm thick and contains 50.5 at.%, Cu 43 at.% Zn 2 at.% and Mg 4.5 at. %. In the third layer the following composition is found: Al 55 at.%, Cu 32 at.%, Zn 2 at.% and Mg 11 at.%. In the fourth layer there is: Al 77 at.%, Cu 19 at.%, Zn 1 at.% and Mg 3 at.%.



By observations at OM and SEM it resulted that after the heat treatment at 470° for 16 h the intermetallics layer reached the thickness of 70 μm . In Fig. 4 is shown the EDS profile between the points signed P1 and P2 the trend of Al, Zn, Cu and Mg across the intermetallics layer, from which it results that zinc is present in greater quantities in the outermost layers of diffusion while magnesium is present in greater quantities in the intermediate layers, where there it reaches.



By observations at OM and SEM it resulted that after the heat treatment at 470° for 16 h the intermetallics layer reached the thickness of 70 μm . In Fig. 4 is shown the trend of Al, Zn, Cu and Mg across the intermetallics layer, from which it results that zinc is present in greater quantities in the outermost layers of diffusion while magnesium is present in greater quantities in the intermediate layers, where there it reaches.

The surface hardness of the samples treated at 470 °C reached very high values with a maximum of 850 $\text{HV}_{0.1}$ for the longer treatment (Fig.5). The hardness values achieved can be related to the presence of phases AlCu and Al_2Cu . The sample treated at 470°C for 16h shows high values of hardness (800 $\text{HV}_{0.1}$) in the external layer which

is characterized by the presence of a greater amount of zinc present in solid solution or more likely as the intermetallic compound.

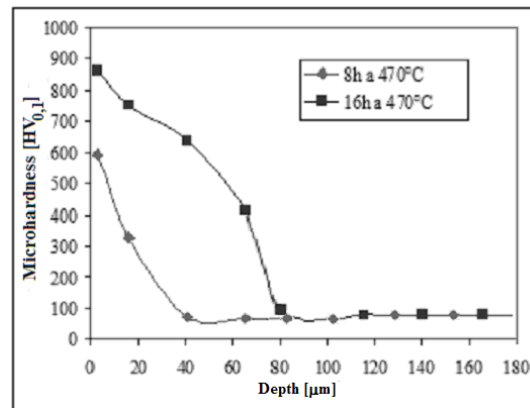


Fig. 5. Microhardness profile of Cu coated samples of AA7075 after different heat treatments.

Alloy 2024

The OM analysis of the Cu coated samples heat treated at 495°C for 24 revealed the formation of an intermetallic layer: the diffusion heat treatment induces the migration of copper inside the sublayer and the diffusion of aluminium and alloying elements towards the surface (Fig. 6).

The SEM analysis with backscattered electrons and the EDS analysis revealed that after a compact 40 μm layer was formed at the interface between the sublayer and layer of undiffused deposited copper, characterized by a concentration of 71 at.% of Al and 29 at.% of Cu (Fig. 7). Based on the Al-Cu phase diagram, it can be stated that this layer is mainly composed of the Al₂Cu (θ) intermetallic compound. The XRD analysis confirmed the presence of this intermetallic.

Along the interface between the intermetallic and the sublayer there are some areas where there was an enrichment in Fe and Mn. (Fig. 8). The lack of homogeneity in the vicinity of the sublayer is due to the different distribution of the elements. During the heat treatment there is not only the diffusion of copper towards the inside of the piece but the alloying elements are also subject to the same process even when present in small amounts. The diffusion of aluminium and its high affinity for copper lead to the formation of a compact outer layer consisting of practically only these two elements. The iron and manganese elements are less diffused but still create areas of mixed compounds

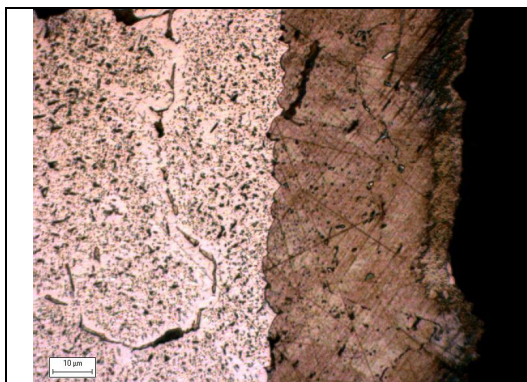


Fig. 6. OM image of the cross-section of the Cu coated sample heat treated at 495°C for 24 h.

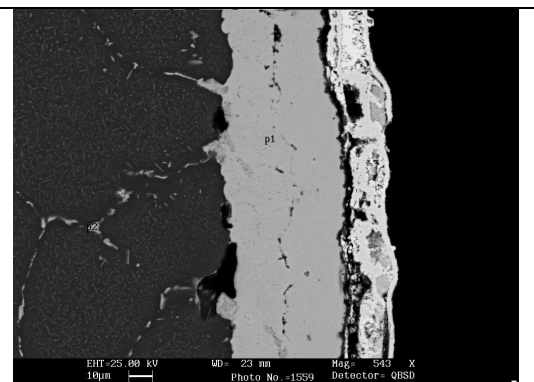
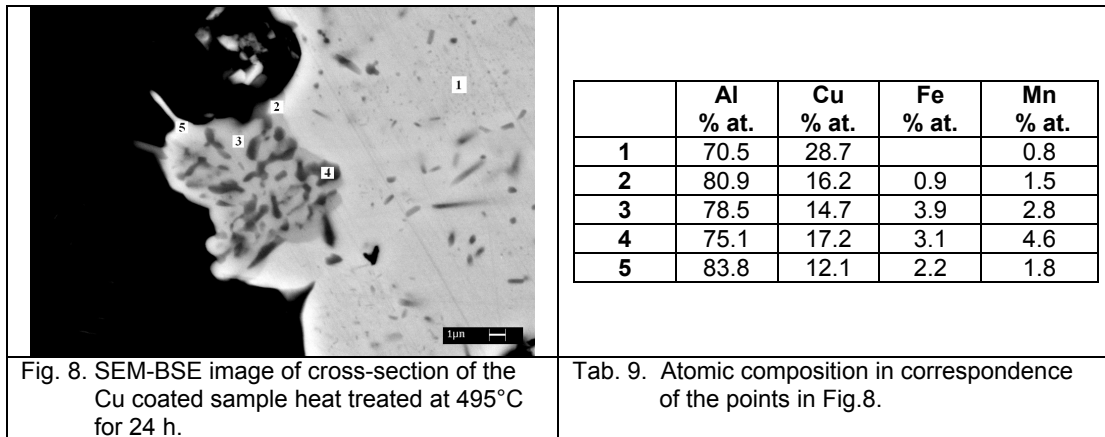


Fig. 7. Fig. 3. SEM-BSE image of cross-section of the Cu coated sample heat treated at 495°C for 24 h.

Along the interface between the intermetallic and the sublayer there are some areas where there was an enrichment in Fe and Mn. (Fig. 8). The lack of homogeneity in the vicinity of the sublayer is due to the different distribution of the elements. During the heat treatment there is not only the diffusion of copper towards the inside of the piece but the alloying elements are also subject to the same process even when present in small amounts. The diffusion of aluminium and its high affinity for copper lead to the formation of a compact outer layer consisting of practically only these two elements. The iron and manganese elements are less diffused but still create areas of mixed compounds.

In this alloy the layer formed by the intermetallic compound is clearly separated from the sublayer. EDS analysis revealed that there was no diffusion of copper along the grain boundaries and that the precipitates found are typical of the 2000 series alloys.



The microhardness analysis performed on samples before and after diffusion treatments are shown in Fig.10. The high surface hardness of the layer rich in copper is due to the presence of the Al₂Cu intermetallic phase (characterized by microhardness in the order of 400-600 HV_{0,1}.)

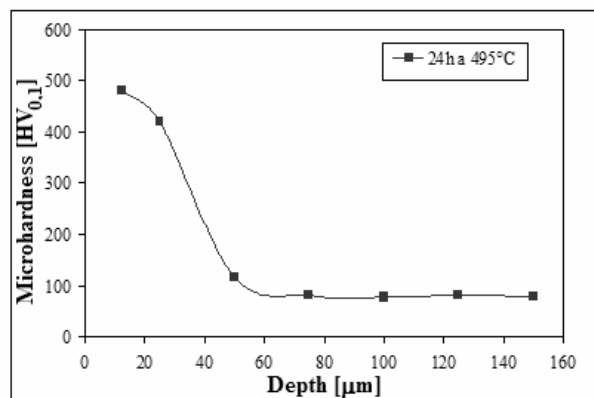


Fig. 10. Microhardness profile of Cu coated samples of AA2024 after heat treatment.

Conclusions

The observations carried out by OM and SEM equipped with EDS of the Cu coated sample of aluminum alloys (AA7075 and AA2024) after heat treatments revealed the formation of intermetallic layers. In the case of Cu coated AA 7075 the heat treatment at 470°C induces the formation of a multilayered diffusion zone composed of AlCu and Al₂Cu. By treating the samples for 8 hours the diffusion layer reaches a thickness of about 30 µm and with a microhardness of about 600 HV_{0,1}, attributed to Al-Cu intermetallic compounds. The 16-hour treatment leads to the formation of a 70 µm diffusion layer. In this case, the surface hardness reaches 850 HV_{0,1}, a value much higher than the typical 600 HV_{0,1} of Al-Cu intermetallic compounds. This phenomenon can be explained by

the presence of a greater amount of Zn present in solid solution or more intermetallic compound, favoured by the greater diffusion time of the alloy elements toward the interface with the layer of deposited copper. In the case of Cu coated AA 2024 the diffusion treatment at 495°C for 24 h leads to the formation of a layer primarily constituted by Al₂Cu (θ) intermetallic compound which achieves a hardness of 500 HV_{0,1}.

References

- [1] E. LUGSCHEIDER, G. KRAMER, C. BARIMANI, H. ZIMMERMANN, Surf. Coat. Technol 74-75 (1995), p. 497.
- [2] M. H. STAIA, Y. Y. SANTANA, Z. DEL V. MARCANO, Surf. Eng. 20 (2004), p. 128.
- [3] K. T. RIE, A. GEBAUER, J. WOHL, Surf. Coat. Technol. 86-87 (1996), p. 498.
- [4] L. DUBOURG, H. PELLETIER, D. VAISSIERE, F. HLAWKA, A. CORNAT, Wear 253 (2002), p. 1077.
- [5] L. DUBOURG, F. HLAWKA, A. CORNAT, Surf. Coat. Technol. 151-152 (2002), p. 329.
- [6] K. BRUNELLI, M. DABALA, C. MARTINI, Metallurgia Italiana 7-8 (2006), p. 37.
- [7] I. APACHITEI, J. DUSZCZYK, Surf. Coat. Technol. 132 (2000), p. 89.
- [8] J. ALEXIS, D. ADRIAN, T. MASRI, J. A. PETIT, Surf. Eng, 20 (2004), p. 121
- [9] D. VOJTECH, M. NOVAK, M. ZELINKOVA, P. NOVAK, A. MICHALCOVA, T. FABIAN, Appl. Surf. Sci. 255 (2009), p. 3745.
- [10] A. ALMEIDA, M. ANJOS, R. VILAR, R. LI, M.G.S. FERREIRE, W.M. STEEN, K.G. WATKINS, Surf. Coat. Technol. 70 (1995), p. 221.
- [11] Y.Y. QUI, A. ALMEIDA, R. VILAR, Scripta Metall. Mater. 33(6) (1995), p. 863.
- [12] W.J. TOMLINSON, A.S. BRANSDEN, J. Mater. Sci. Lett. 13 (1994), p. 1086.
- [13] L. LASA, J. M. RODRIGUEZ-IBABE, Mat. Charact. 48 (2002), p. 371.
- [14] M. ARAVIND, P. YU, M. Y. YAU, DICKON H. L. NG, Mat. Sci. Eng. A 380 (2004), p. 384.
- [15] I.N. KHAN, M. J. STARINK, J. L. YAN, Mat. Sci. Eng. A 472 (2008), p. 66.
- [16] S. C. WANG, M. J. STARINK, Acta Mat. 55 (2007), p. 933.
- [17] T. J. BASTOW, S. CELOTTO, Acta Mat. 51 (2003), p. 4621.
- [18] S. W. KIM, D. Y. KIM, W. G. KIM, K. D. WOO, Mat. Sci. Eng. A 304-306 (2001), p. 721.
- [19] S.C. WANG, M. J. STARINK, N. GAO, Scripta Mat. 54 (2006), p. 287.

MICRO-STRUCTURAL AND CHEMICAL CHARACTERIZATION OF ELECTRIC ARC FURNACE SLAG

D. Mombelli¹, C. Mapelli¹, A. Gruttadauria¹, F. Magni², P.L. Levrangi³, P. Simone⁴, Claudio Baldizzone¹

¹ *Dipartimento di Meccanica, Politecnico di Milano, 20156 Milano, Italy*

² *Feralpi Siderurgica, Lonato (BS), Italy*

³ *Ferriera Valsabbia, Odolo (BS), Italy*

⁴ *Società Montana, Milano (MI), Italy*

Abstract

Steel slag can represent an excellent opportunity for their use as alternative cement materials. In particular black slag produced during the melting process in EAF (Electric Arc Furnace) can be used as adjunct in the operation of land-filling, in the building operation of road grounds and in the production of concrete. Their use limitation is due to the presence of polluting chemical elements, including Cr, Ba, V, Mo, etc, that can be dangerous for human and environment, resulting by using of polluted scraps (i.e. painted, lubricated or polymeric compound scraps).

Several experimental trials have been performed on the slag produced by two Italian steelmaking plants producing reinforcing bars. The chemical compositions of the final obtained slag belong to a range in which the slag has shown a releasing behaviour that is significantly different as a function of the different ratios among the fundamental constituting chemical species, i.e. CaO, SiO₂, Al₂O₃, MgO etc.. The chemical composition has been characterized through the optical basicity and the slag has been investigated from a microstructural point of view through scanning electron microscopy techniques that has permitted to identify the main phases contained in the slag and to characterize their chemical composition and the dangerous polluting elements solved in each phase. The combination of the data coming from chemical analysis, micro-structural examination and data coming from the releasing tests have permitted to identify a chemical range that allows to avoid dangerous chemical releasing and this statement has provided the possibility to identify a correct procedure for treating and modifying the slag.

Introduction

In every steelmaking industrial process is implied the production of a relevant amount of slag. The industrial world struggled long in order to design a practical application for this by-product, however this effort has been often hindered by different applicative problems. Specifically, this study deals with the presence of polluting chemical elements, including Cr, Ba, V, Mo, etc, that can have dangerous consequences for both the human health and the environment.

The report RFCS 7210-CB/115 [2] stressed the conclusions that due to the recent severe modifications in the Dutch legislation, it is extremely difficult to use steelwork slag for application as a granular aggregate in mineral sealing products. The applicative problem is related to size distribution and high alkalinity of the slag. However, after this statement any other effort to decrease the alkalinity has not been performed and the application prospect of such a material has not been taken into consideration, as a systematic plan to realize a chemical conditioning lacks.

According to literature, the total amount of steel slag generated from the EAF route is about 16.5 million tonnes, and in this amount 29% is produced by Electric Arc Furnace and 9% comes from secondary metallurgical operations. About 72% of the produced slag is used on qualified fields: 3% fertilizer, 15% internal recycling, 17% interim storage, 11% final deposit, 3% armour-stones for hydraulic engineering, 44% road construction, 1% cement production and 6% for other applications. Nearly the total amount of 28% unused slag comes from EAF route, because the alloying elements contained in the scraps are usually transferred to the slag and they can

cause the leaching of chemical species considered dangerous and so the slag of EAF and secondary metallurgy are defined as waste [1].

A general chemical or crystallographic characterization is not enough to state the attitude of a slag to capture the polluting elements, instead such an achievement implies a careful morphological, microstructural and chemical characterization in order to detect the solved elements within the different structural constituents that can release them. Specifically, the study involves the use of optical basicity to characterize synthetically the basicity of the slag. Although, some limitations in the use of this tool were required, as the system lacks in reliability.

In RFCS 7215 PP/044 [3] the study of immobilization of chromium has been performed focusing the attention on EAF slag. The studied slag comes from the production route of stainless steel production, in which the leaching of chromium has been felt as the main problem, since chrome is one of the major constituents of stainless steel. The chrome contained in the slag should be bound in stable mineral phases to suppress the leaching of chrome, since the environmental compatibility is very important for the use of slag from stainless steelmaking. The most effective binding for chrome is found in the natural magnesite-chrome-spinels. The composition of a typical magnesiochrome oxide ($MgCr_2O_4$) is about 14%wt.MgO, 13%wt.FeO, 12%wt. Al_2O_3 , 6%wt. Fe_2O_3 , 0.5%-wt.MnO and 55%wt. Cr_2O_3 . Owing to this composition of a natural mineral, which is known to bind the chrome stable, tests to bind chrome into stable slag phases of a similar composition have been successfully started. The most effective binding has been achieved by creating a composition with the main spinel formers iron oxide, MgO and Al_2O_3 nearly in the composition described for natural chrome oxides. This study reports interesting results, such as an indication that a chemical species can be bound efficiently through the formation of specific structural constituents and allow to state the polluting level of a slag through a specific chemical parameters called "factor sp" defined as:

$$\text{factor } sp_{opt.} = 0.2 * MgO + 1.0 * Al_2O_3 + x_{opt.} * FeO_n - 0.5 * Cr_2O_3 \text{ [%wt.]} \\ (\text{where } x_{opt.} \text{ depends from the oxidation state of the EAF-slag})$$

The relationship between "factor sp" (factor associated with the sum of spinel forming elements) and the leaching behaviour of chrome has been described with consideration of the weight of influence. Three domains have been distinguished:

- values of "factor sp" < 5 %-wt. implies no or only few chrome containing spinels;
- values of "factor sp" 5 to 25 %-wt. allow the formation of chrome spinels;
- values of "factor sp" > 25 %-wt. implies nearly no chrome leaching.

Though fulfilling all the requirements for road construction aggregates, the authors of the indicated report denounced that slag was still mostly dumped, because authorities were not convinced that this treated slag is a good product and no wastes. The report has been delivered in 2004 and now, the doubt of the authorities might be even strengthened by the very low release extent set by the authorities, especially in the presence of sea-water and potable-water reserve. Moreover, the regulation concerning leachate solutions set especially low level for barium, selenium, vanadium etc. (Table 1).

Limits of chemical elements considered dangerous								
[mg/l]	F^1	SO_4^{2-}	Cl^1	CN^1	<i>Ba</i>	<i>Cu</i>	<i>Zn</i>	NO_3^{-1}
<i>PH</i>	1,5	250	100	0,05	1	0,05	3	50
5.5-12	<i>Co</i>	<i>Ni</i>	<i>V</i>	<i>As</i>	<i>Cd</i>	<i>Cr</i>	<i>Pb</i>	<i>Be</i>
[μ g/l]	250	10	250	50	5	50	50	10

Table 1: Limits of chemical elements considered dangerous.

Moreover, the MgO slag concentration seems to be favourable for the immobilization of chrome but detrimental for the leaching of other polluting elements, i.e. barium, selenium, vanadium tend to follow a solution behaviour expressed by the parabolic law function of CaO and MgO concentration, while the dependence on silica

concentration is expressed described by a linear law [4]. The decrease of the CaO and MgO concentration can produce an excessive decrease of the alkalinity that does not represent a favourable condition to grant a correct quality level of the steel, above all for the impossibility to remove phosphorus and the need to preserve the integrity of refractories [5,6].

Experimental procedure

The micro-structural and morphological characterizations have been performed by SEM (Scanning Electron Microscopy) used in two different modalities:

- SEM-EBS (Scanning Electron Microscopy set in the modality of Electron Back-Scattering Diffraction) allows performing a morphological characterization of the solidified slag and, after grinding and polishing, it permits to distinguish correctly the structural constituents formed in the slag;
- SEM-EDS (Scanning Electron Microscopy exploiting the equipment for Energy Dispersive Spectrometry) permits performing localized chemical analysis on each recognized single structural constituent and to identify the presence of possible solute elements.

One hundred coupons of slag have been taken from two steelmaking plants equipped by electric arc furnace. The analysed coupons have been sampled over three months and they have undergone the micro-structural characterization and the chemical analysis through leaching test according to EN 12457, and in this case the versions EN 12457-1 and EN 12457-3 have been followed, because those standards impose critical conditions for the size of slag granules or fragments.

Results

The experimental work consists in a micrographic description and analysis of the specimen employed in the leaching tests. Regardless of the release finding, both the samples showing lower or larger release extent of hazardous elements were characterized and the results were then compared in order to identify eventual features that might affect the leaching process. The analysis performed by electronic scanning microscopy have always pointed out the presence of the following structural constituents:

- $2\text{CaO}\cdot\text{SiO}_2$ often associated with $3\text{CaO}\cdot\text{SiO}_2$;
- $\text{MgO}\cdot\text{FeO}$ (magnesio.wustite) associated with significant presence of MnO;
- $(\text{FeO}\cdot\text{MnO}\cdot\text{MgO})\cdot\text{Cr}_2\text{O}_3$ spinel that is the phase showing the highest content of chromium concentration;
- a calcium silicon aluminate compound with a stoichiometric ratio corresponding to $2\text{CaO}\cdot 2\text{SiO}_2\cdot\text{Al}_2\text{O}_3$ that is probably associated to an intermediate eutectic compound in the region between anorthite ($2\text{SiO}_2\cdot\text{CaO}\cdot\text{Al}_2\text{O}_3$) and gehlenite ($2\text{CaO}\cdot\text{SiO}_2\cdot\text{Al}_2\text{O}_3$) featured by a melting temperature in the range of 1265°C - 1390°C .

Barium and vanadium are generally combined with $2\text{CaO}\cdot\text{SiO}_2$ ($3\text{CaO}\cdot\text{SiO}_2$) and with the calcium silicon aluminate (Figure 1, Figure 2). In several samples the micro-structural analysis have pointed out the presence of clear lamellae (Figure 3) rich in FeO and these are certainly the consequence of the eutectic formation during the solidification and cooling process.

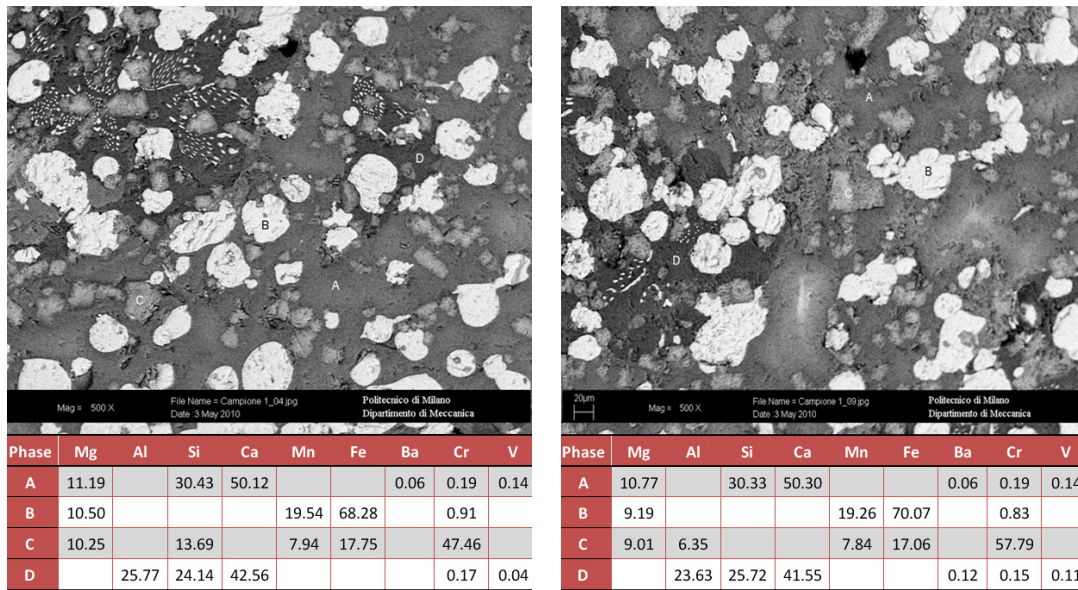


Figure 1. Examples of the microstructure of a slag that overcomes the leaching limit indicated in Table 1 (left: CaO 28.86% - SiO₂ 14.5% - FeO 36.98% - Cr₂O₃ 2.8% - Al₂O₃ 9.64% - MnO 6.54% - BaO 0.21% - MgO 3.77% - V₂O₅ 0.18%; right: CaO 25.82% - SiO₂ 15.93% - FeO 37.68% - Cr₂O₃ 2.54% - Al₂O₃ 9.88% - MnO 6.4% - BaO 0.19% - MgO 4% - V₂O₅ 0.14%).

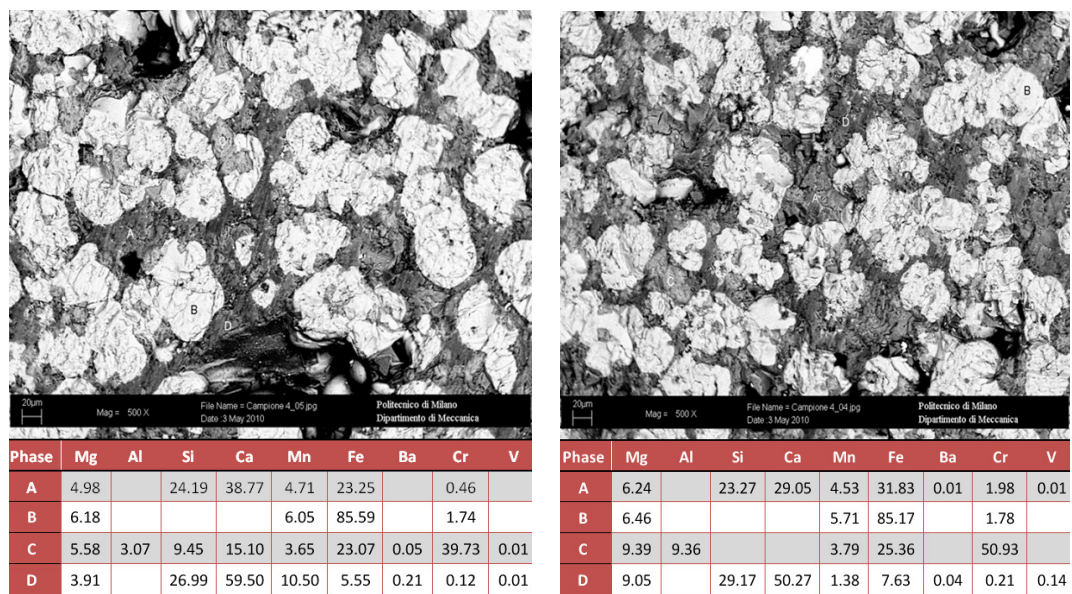


Figure 2. Example of the microstructure of a slag that is under the leaching limit indicated in Table 1 (left: CaO 27.2% - SiO₂ 16.8% - FeO 37.7% - Cr₂O₃ 3.02% - Al₂O₃ 8.8% - MnO 5.4% - BaO 0.25% - MgO 3% - V₂O₅ 0.19%; right: CaO 20.1% - SiO₂ 21% - FeO 39.2% - Cr₂O₃ 4.02% - Al₂O₃ 7.8% - MnO 7.4% - BaO 0.3% - MgO 2.4% - V₂O₅ 0.35%).

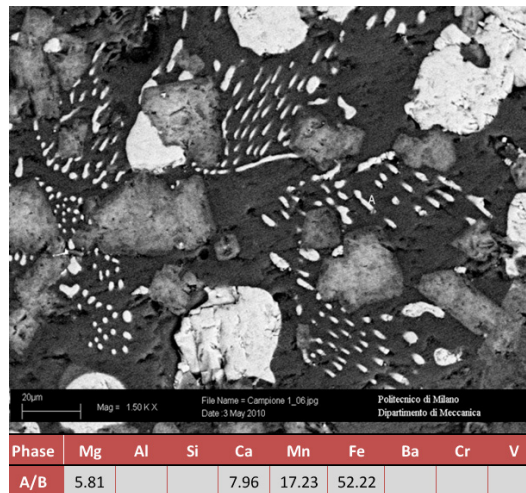


Figure 3. Details of the lamellar structural constituents mainly constituted by wustite combined with CaO, MgO and MnO.

Of the whole test batch the experimental trials provided thirty-four samples showing a safe behaviour and indicating a release of chemical elements under the constraints indicated in [Table 1](#). The chromium concentration does not exceed the safety limits in any leaching solution in which the analysed slag coupons have been tested. Thus, in the analysed cases, the barium and vanadium are considered the elements to be captured in order to make slag safe. The released amounts of barium and vanadium found to be exceeding the regulations mentioned before are reported in [Figure 4](#) and [Figure 5](#): 24 slag coupons do not respect the limit of vanadium and 59 are featured by an excessive release of barium (17 samples release both the polluting elements in concentrations higher than the imposed maximum limits).

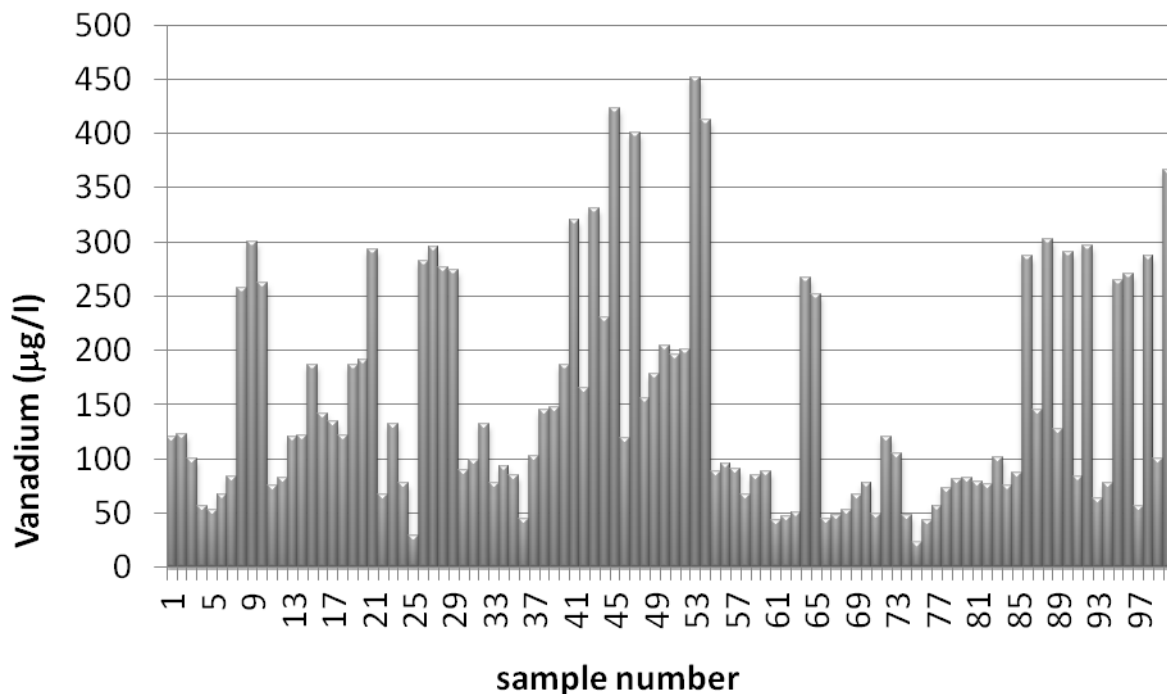


Figure 4. The concentration of Vanadium in leaching solution as a function of the different slag samples

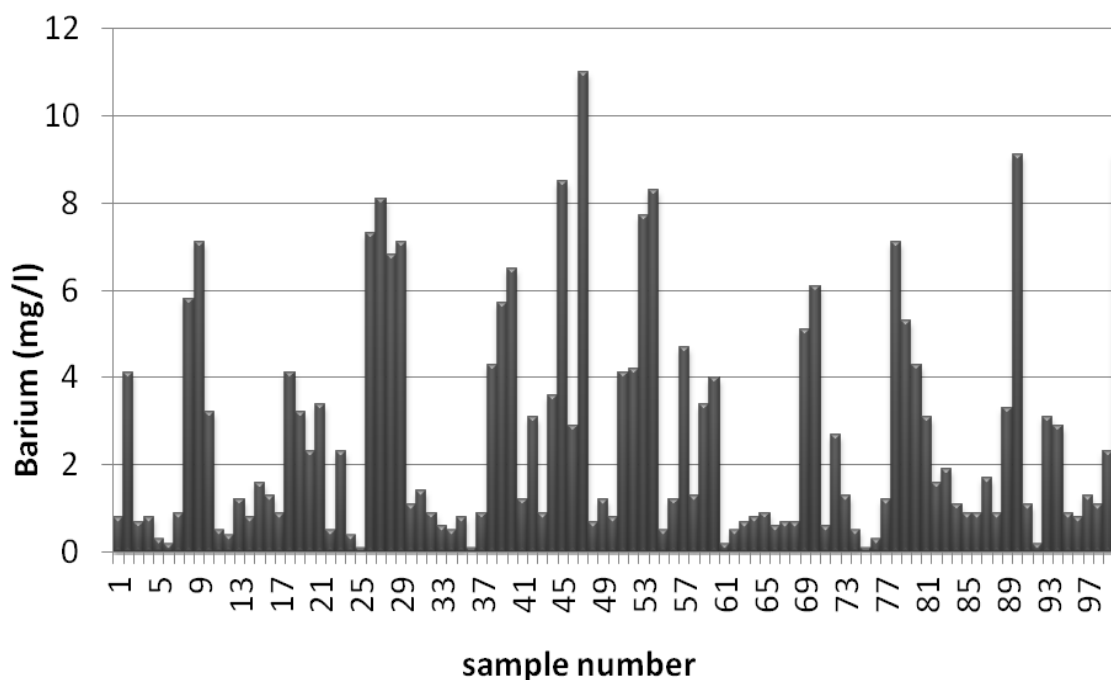


Figure 5. The concentration of Barium in leaching solution as a function of the different slag samples

Discussion

The micro-structural and chemical characterization performed by the scanning electron microscopy indicates that:

- chromium is mainly dissolved in the spinel constituents formed by $(\text{MnO} \cdot \text{FeO} \cdot \text{MgO})\text{Cr}_2\text{O}_3$ and this explains the absence of high value of chromium in the solution of leaching tests, confirming the results obtained in RFCS 7215 PP/044 [3];
- barium and vanadium are mainly contained in $2\text{CaO} \cdot \text{SiO}_2$ and in the calcium silicon aluminates phases, so it is the behaviour of such structural constituents that determines the release of polluting elements.

The SEM results are consistent with the process background. In details, the main source of vanadium is associated with its concentration as alloying and micro-alloying elements of the steel constituting the scrap while the presence of barium is due to its content in the proler (barium is present in the coloured coating of car steel) or to the contamination of the charged lime.

As reported in the introduction, the study involves also the use of optical basicity as a tool to characterize chemically the slag and the results were further compared with the release tests. The correlation between optical basicity [7,8] and the retention the polluting elements, i.e. barium and vanadium, shows a decrease in release extent with the acidity the slag. In other words, the most acid slag seems to present the best attitude for capturing the dangerous elements mentioned above (Figure 6, Figure 7). On the other hand, this statement does not represent a general and reliable rule because in some cases there is an excessive leaching although the optical basicity belongs to a range that in most cases seems to grant a safe condition (points representing concentration over the maximum limits). Thus, the decrease of the optical basicity points out a favourable capturing trend but it is not a parameter reliable enough to permit the discrimination of a slag and it has to be integrated with the information provided by micro-structural analysis.

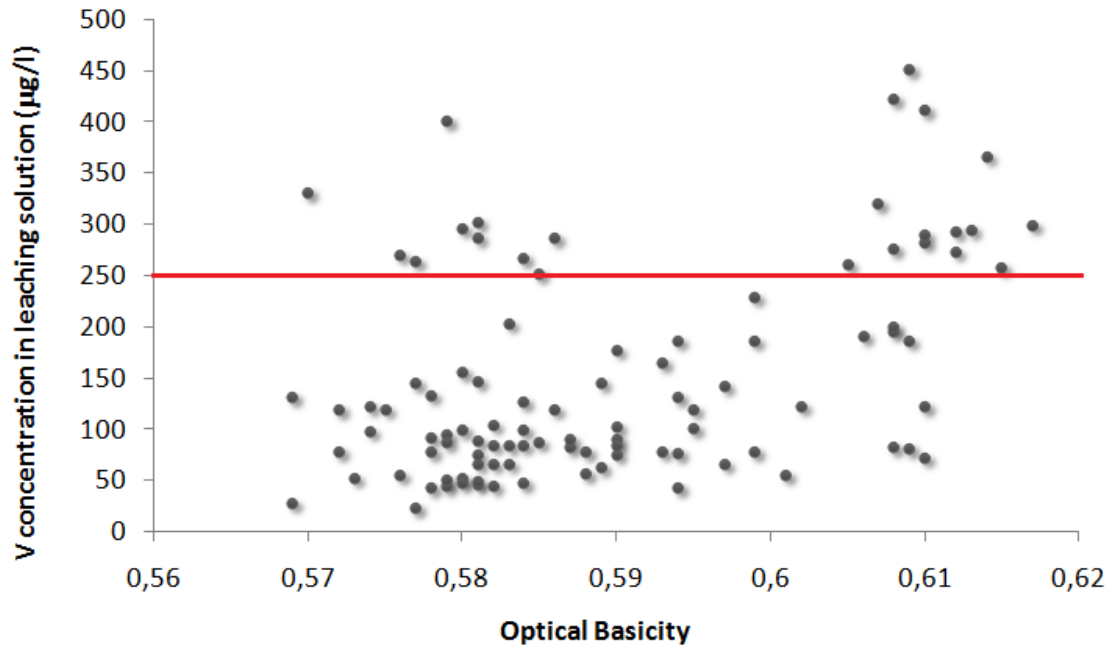


Figure 6. Relation between optical basicity and the concentration of barium in the leaching solution (the line represents the limit of the maximum allowed concentration).

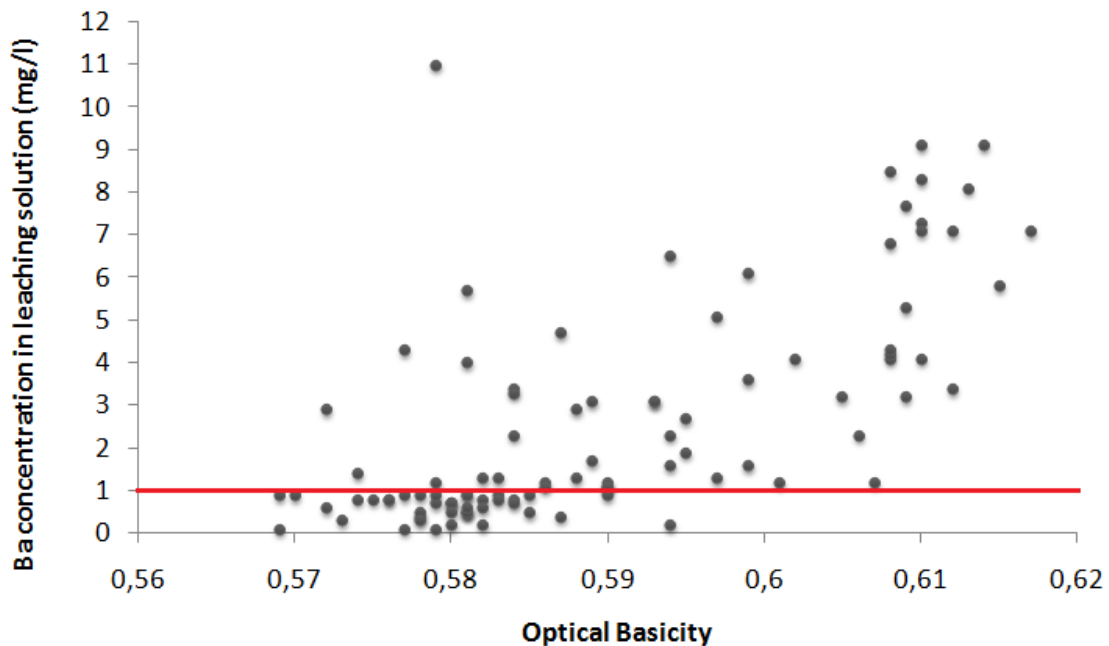


Figure 7. Relation between optical basicity and the concentration of barium in the leaching solution (the line represents the limit of the maximum allowed concentration).

All the samples showing a concentration of barium and vanadium of leachate solution under the maximum allowable limit show a concentration of MgO in the $2\text{CaO}\cdot\text{SiO}_2$ structural constituents lower than 6.8%, while the chemical composition of calcium silicon aluminate is nearly invariant in all the samples. The favourable capturing behaviour of calcium silicon aluminate (that seems not to be responsible for any release, notwithstanding the presence of barium and vanadium) can be expected thanks to its low melting point that favours a vitrification of the compounds and the consequent capturing attitude. So, the composition of $2\text{CaO}\cdot\text{SiO}_2$ and especially the concentration of solved MgO in this phase appears to be the ruling factor of the releasing behaviour of polluting elements. The role played by MgO can explain why the optical basicity does not clearly indicate the tendency of

the release of barium and vanadium contained in the steel. Actually, the optical basicity associated to MgO (0.78) on the basis of data proposed by Duffy and Ingram [7] is lower than the one of CaO and this aspect combined with relatively contained variation of MgO in the slag causes a little variation of slag basicity that cannot be clearly associated to the variation in the capturing and leaching attitude of the slag. On the other hand, the experimental observation has pointed out that MgO content represents a very critical factor to determine the slag behaviour and this is due to the lowering effect in solubility of other chemical species featured by basic characteristic (i.e. BaO), actually the introduction of MgO tends also to increase the activity of CaO and BaO [9,10], decreasing their tendency to be maintained in liquid and solid solution.

Provided that the preservation of dolomite refractory of EAF imposes to work in the condition of MgO saturation (MgO content between 6-9%), the right chemical modification of the slag needs to be performed after the scorification of the slag from EAF. This condition is also imposed by the need to avoid an excessive acidification of the slag that can lower its metallurgical efficiency dephosphoration capacity.

Conclusions

- the chromium release is hindered by the presence of spinel, confirming the previous results obtained for the slag coming from the production of stainless steels;
- the $2\text{CaO}\cdot\text{SiO}_2$ ($3\text{CaO}\cdot\text{SiO}_2$) are the main structural constituents containing and sometimes releasing the identified dangerous chemical species, i.e. barium, vanadium;
- the decrease of MgO concentration in di-calcium silicate represents a favourable conditions for decreasing the release of polluting elements;
- the whole effect of the basic chemical species has to be taken into account in order to fulfil a complete capture of the dangerous polluting elements;
- a chemical parameter involving optical basicity and concentration of MgO can be developed and applied for stating whether a slag that can be considered as a safe product or by-product coming from the melting process in EAF;
- formation of eutectic structural constituents can improve the capturing attitude of the slag, as pointed out by the not releasing behaviour of the detected calcium silicon aluminate belonging to the region of region between anorthite ($2\text{SiO}_2\cdot\text{CaO}\cdot\text{Al}_2\text{O}_3$) and gehlenite ($2\text{CaO}\cdot\text{SiO}_2\cdot\text{Al}_2\text{O}_3$).
- optical basicity can provide a good estimation of the slag ability for retaining polluting elements, although the test presents some limitations due to a scarce reliability;
- the attitude to capture dangerous element, i.e. vanadium and barium, seems to increase as the optical basicity decreases.

References

- 1) H. Motz and J. Geiseler: *Waste Manag.*, 21 (2001), 285
- 2) RFCS 7210-CB/115, Utilisation of fine-grained steel slag for mineral sealing products - laboratory and practical investigation
- 3) RFCS 7215 PP/044, Chrome immobilisation in EAF slag from high alloy steelmaking - Development of a slag treatment process
- 4) K. Shinoda, H. Hatakeda, N. Maruoka, H. Shobata, S. Kitamura and S. Suzuki, 'Chemical State of Chromium in CaO-SiO₂ Base Oxides Annealed under Different Conditions', *ISIJ International*, Vol. 48 (2008), No. 10, pp. 1404-1408
- 5) K. Pillay, H. von Blottnitz and J. Petersen: *Chemosphere*, 52 (2003), 1771
- 6) S.Yokoyama, A. Suzuki, N. B. M. North. Kanematsu, A. Ogawa, T. Takahashi, M. Izaki, M. Umemoto, 'Serial Batch Elution of Electric Arc Furnace Oxidizing Slag Discharged from Normal Steelmaking Process into Fresh Water', *ISIJ International*, Vol. 50 (2010), No. 4, pp. 630-638
- 7) J.A. Duffy, Ingram M.D., Establishment of an Optical Scale for Lewis Basicity in Inorganic Oxyacids, Molten Salts and Glasses, *J. Amer. Chem. Soc.*, 1971,93,6448-6455
- 8) J.A. Duffy, M.D. Ingram, I.D. Sommerville, Acid-Base Properties of Molten Oxides and Metallurgical Slags, *J. Chem. Soc. Faraday Trans. 1*, 1978,74,1410-1419
- 9) R. Markus, O. Grega, 'EAF Slag Treatment Technology', *Acta Metallurgica Slovaca*, 12, 2006, (269 - 276)
- 10) T. Mori, On the Phosphorus Distribution Between Slag and Metal, *Bull. Jpn. Inst. Met.* 1984,23, (5), 354-361

COMPREHENSIVE ANALYSIS OF PRECIPITATES IN Cr – RICH STEELS BY MEANS OF ELECTRON ENERGY LOSS SPECTROMETRY SPECTRUM IMAGING

M. Albu¹, P. Mayr³, F. Hofer^{1,2} and G. Kothleitner^{1,2}

¹Graz Center for Electron Microscopy and Nanoanalysis, Steyrergasse 17, A-8010 Graz

²Graz University of Technology, Institute for Electron Microscopy, Steyrergasse 17, A-8010 Graz

³Graz University of Technology, Institute for Materials Science and Welding, Kopernikusgasse 24, A-8010 Graz

Summary

This paper give insight into the microstructural evolution during heat treatment and creep testing of a boron alloyed 9 wt.% Cr steel, with special emphasis on the role of boron, by using advanced analytical transmission electron microscopy methods. Electron energy loss spectrum images acquired in scanning transmission electron microscopy mode provide full elemental information in the form of compositionally quantified maps (atoms/nm³) of C, N, Fe, Cr, V and B with high spatial and energy resolution. MX precipitates embedded in the M₂₃(C,B)₆ particle were identified and analysed with respect to their boron concentration. Energy filtered TEM elemental maps have been processed by applying bivariate histogram analysis in order to recognise an early stage transformation of vanadium nitride particles to the complex nitride named modified Z phase.

Moreover, pre-austenite grain boundaries in the creep tested specimens have been charted and the phases were identified via energy filtering TEM, electron energy loss and X-ray spectrometry.

1. Introduction

Energy saving and, therefore, new materials development has become an important issue for research and industry in the least years. Rise of the energy efficiency of thermal power plants, for example, by enabling higher steam temperatures and pressure, can be achieved by using improved boron-alloyed tempered martensitic 9-12 wt.% Cr steels, which are currently in development [1-2]. Boron addition should help retarding the progression of microstructural degradation, namely coarsening of the M₂₃C₆ particles, an effect which causes a drastic drop in the creep strength of tempered martensitic Cr rich steels after long-term high temperature service in the creep regime [3]. Other effects promoting an inhomogeneous microstructural evolution are: destabilization of the martensitic lath structure, especially in the vicinity of prior austenite grain boundaries and precipitation of large AlN, BN, M₆X and Z-phase [3-7].

Because the very low concentration of boron (< 200 ppm) does not favor the formation of M₂₃(C,B)₆ inside the grains, boron enriched carbides have, so far, only been found at former austenite grain boundaries and been investigated through Auger spectroscopy [8]. Other measurements on ferritic low-carbon steels using small-angle neutron scattering (SANS) and neutron powder diffraction reveals very fine (5 to 60 nm) BN, Fe₃(C,B) and MnS particles surrounded by BN layers [9]. Other authors suggest that boron atoms segregate at the interface of growing precipitates with the matrix reducing the coarsening rate of Ostwald ripening of M₂₃C₆ carbides near prior austenite grain boundaries. This mechanism mainly depends on diffusion, solid solubility and interfacial energy. Up to now, neither experimental evidences for a significant drop in the diffusion coefficient or the solid solubility nor any enrichment of boron at the carbide-matrix interface was given.

Advanced analytical transmission electron microscopy investigations have been performed on the boron-nitrogen balanced 9Cr3W3CoVNb steel specimens at four different stages: end of cooling after 4 h at 770 °C – "as received" condition, long-term tempering 50 h at 770°C (quenched) as well as after creep exposure at 650°C - 130 MPa for 8971 hours and at 650°C - 100 MPa for 23997 hours. The present investigations were focused on verifying the boron distribution along the pre austenite grain boundaries and its impact on the microstructure changes of this steel during the tempering and creep testing. Therefore dual electron energy loss spectrum images [10-12] have been processed from different areas containing large chromium carbides with small boron amounts and without, and the interface with the matrix. Phase transformation of fine VN into the modified Z phase

in the short time creep tested specimen was investigated by energy filtering combined with bivariate histogram analysis as well as by electron energy loss spectrometry line scans in scanning mode of the transmission electron microscope.

2. Experimental

The boron-nitrogen balanced 9Cr3W3CoVNb steel was produced by vacuum induction melting. Boron and nitrogen concentrations were kept very low, 120 ppm boron versus 130 ppm nitrogen, in order to promote the formation of vanadium nitrides and inhibit the precipitation of large boron nitrides.

Table 1 presents the exact chemical composition of the test melt, Mayr (2008) [10]. The material has been homogenized by forging in the temperature range of 950°C to 1150°C to its final dimensions. The final heat treatment, characteristic for steam pipes, consisted of normalizing at 1150°C (250°C h⁻¹) for one hour followed by air cooling and tempering at 770°C for 4 hours (250°C h⁻¹). Additionally, an alternative long-term tempering for 50 hours at 770°C applying the same heating rates was processed.

Table 1. Chemical composition of the boron alloyed 9Cr3W3CoVNb test melt in wt. % (balanced Fe) [13].

C	Si	Mn	Cr	W	Co	V	Nb	B	N
0.074	0.29	0.44	9.26	2.84	2.95	0.21	0.056	0.012	0.013

The investigated samples correspond to the heat treatment stages and creep tests described in table 2. Cubes of the material, with a side length of 40 mm, were heated at 770°C in a laboratory furnace. In order to freeze the microstructure, samples removed from the furnace at elevated temperatures were quenched in water. The creep tested specimens were provided by uniaxial constant load creep experiments at 650°C and 130 MPa for 8971 hours and at 650°C and 100 MPa for 23997 hours. Detailed information on the creep testing results has been published by Mayr (2010) [14].

Table 2. Studied specimen conditions.

Heat treatment		Creep tested specimens	
end of cooling after 4 h at 770 °C – "as received"	long-term tempering 50 h at 770°C <i>quenched</i>	650°C - 130 MPa - 8971 h	650°C - 100 MPa - 23997 h

Transmission electron microscopy (TEM) as well as high resolution TEM (HRTEM), energy filtering TEM (EFTEM), electron energy loss spectroscopy (EELS) and energy dispersive X-ray spectroscopy (EDX) investigations were performed on ion milled samples and precipitate extracted specimens. Due to chemical reactions during the extraction process, Laves phase particles (Fe₂W) could only be identified in the ion milled specimens. The prior austenite grain boundaries (PAGB) were clearly visible in the extraction and therefore investigation of the grain boundary precipitates chemistry was possible.

Standard measurements have been performed by using a fully equipped analytical Philips CM20 / scanning TEM, operated at 200 kV with a LaB₆ cathode. For electron energy loss spectra an integrated CCD camera, and for the X-ray spectra a Noran HPGe detector in scanning TEM (STEM) mode with a probe diameter of 7 nm, have been used. All micrographs and spectra, acquired with a beam convergence angle of 6.4 mrad and a collection half angle of 7.6 mrad, were processed with Gatan's Digital Micrograph, and were corrected for dark current and gain variations. Only particles having thicknesses in the range of 0.2 – 0.5 times the inelastic mean free path, have been used for analytic investigations. Core-loss analysis of EEL spectra was done employing the elemental edges of B-K, Nb-M_{4,5}, C-K, N-K, V-L_{2,3}, O-K, Cr-L_{2,3} and Fe-L_{2,3}.

More advanced STEM measurements have also been performed by using a high resolution monochromated microscope, FEI Tecnai F20, TEM/STEM (200 kV) equipped with a Schottky field emission gun, an X-ray detector, a Gatan bright field/annular dark field (ADF) detector, a Fischione high-angle annular dark field (HAADF)

detector, and the last generation of a Gatan imaging filter (GIF Quantum™) with a dual energy range EELS acquisition system (DualEELS) [10-12].

DualEELS STEM spectrum image (SI) allows the acquisition of both, low- and core- loss optimized EELS spectra for each pixel, defined by the small probe scanned over a one- or two- dimensional region of the sample, nearly simultaneously. The advantages of this technique are the high spatial and energy resolution, the possibility of spatial and energy drift corrections as well as a full elemental quantification in the form of volumetric or areal densities (atoms/ nm³ or atoms/ nm²).

The EELS SI, presented in this paper, has been acquired with a beam diameter of 5 Å and a current of 213 pA. The system was controlled by Gatan Inc.'s Digital Micrograph™, with the spectrum imaging plug-in, and DigiScan-scanning device. For the zero loss alignment and multiple linear least square (MLLS) fitting procedure the commercial plug-ins implemented in the DM software have been used.

Edge overlaps and/or edges which are too closely positioned in the EEL spectra are a common problem which needs special treatment for a correct integration of the element specific intensities. Two energy regions were affected by this inconvenience in our specimens: 180 - 380 eV of B-K (188 eV), Nb-M_{4,5} and M_{2,3} (205 – 363 eV) and C-K (284 eV) and 500 – 675 eV of V-L_{2,3} (513 eV), O-K (532 eV) and Cr-L_{2,3} (575 eV). By using a multiple linear least squares (MLLS) fit approach, fitting a set of reference spectra as a linear combination to the unknown, the respective intensities could be correctly extracted. Thereby conditions have considered, as described by Riegler and Kothleitner 2010 [15]. The thickness map, experimental determined ionization cross sections and calculated mean free paths for each phase, were in addition needed to compute the concentrations of all involved elements, in form of volumetric densities (atoms/nm³) [16-17].

3. Results and Discussion

The specimens from before-, start- and end- of austenitization conditions showed only some needle shaped cementite precipitates containing iron and chromium ((Fe,Cr)₃C and/or epsilon carbide) with lengths ranging from 200 nm in 'as forged' to 30 - 50 nm at the end of normalizing and 100 – 200 nm after cooling from normalizing temperature. Some primary manganese sulfides (MnS) with a diameter of around 400 nm were identified in the specimen quenched when reaching normalizing temperature.

The specimens in "as received"- and after long term tempering- conditions have been prepared by both ion milling and as extraction. The creep loaded specimens have only been prepared as an extraction replica in order to allow the mapping of the prior austenite grain boundaries in TEM.

Chromium carbides (Cr,Fe,Mo,W)₂₃C₆, NbC, VN and (VN)(CN) with increasing dimensions as the tempering time increase have been found in all conditions along the tempering process. During the short creep test, nitrogen and chromium diffuses and the VN particles with increasing nitrogen deficit start to transform to modified Z phase. However, this phase fraction is very low thus, only a few mod Z phase particles would be present and their observation in the TEM became very difficult. The precipitates were identified via EFTEM, EELS and X-ray spectroscopy. Their dimensions are listed in Table 3.

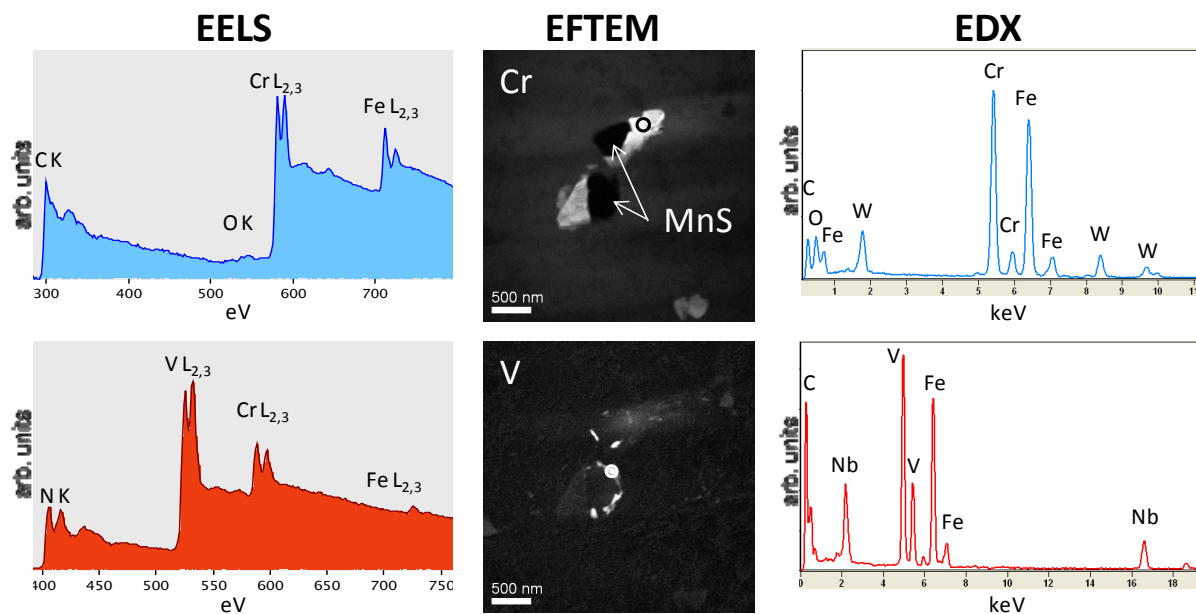
Figure 1 presents typical results from analytical electron microscopy investigations (AEM): energy filtered micrographs together with the EELS and X-ray point analysis spectra specific to (Cr,Fe,Mo,W)₂₃C₆ and MX particles. Two large manganese sulfides MnS (600 nm) surrounded by two chromium carbides (Cr,Fe,Mo,W)₂₃C₆ (600 nm) and two VN of about 50 to 150 nm can be observed, in the near of one VN a NbC has been identified, see the X-ray spectrum. The element specific edges are indicated.

Quantification of EELS point analysis, by using the MLLS procedure, provided a boron content of 2 at.% in the M₂₃(C,B)₆ particles observed only after the long-term tempering for 50 hours. Starting from this experimental finding, DualEELS spectrum images (DualEELS SI) in the scanning mode (STEM) were applied in order to clarify the enrichment of boron at the prior austenite grain boundaries and/or at the interface.

By using this method the thickness map together with different elemental maps for all involved elements Fe, Cr, V, Nb, N, C and B were calculated. Furthermore, by invoking the mean free path of each phase and the ionizations cross sections of each element, see table 4, specific volumetric density maps in atoms/nm³ could be generated. Examples of thickness map and volumetric densities are summarized in figure 2.

Table 3. Dimensions of different particles in the studied specimen conditions

Sample Condition / Precipitate (mean dimension)	long-term tempering 50 h at 770°C	end of cooling after 4 h at 770 °C	650°C - 130 MPa 8971 h	650°C - 100 MPa 23997 h
$(\text{Cr,Fe,Mo,W})_{23}\text{C}_6$	< 600 nm + Boron	150 -250 nm	< 1000 nm	> 1000 nm
NbC	< 100 nm	< 30 nm	< 100 nm	< 100 nm
VN	< 100 nm	< 100 nm	< 600 nm	< 100 nm
(VNb)(CN)	< 50 nm	< 30 nm	~ 30 nm	~ 30 nm
MnS	~ 600 nm (E)	x	x	x
$\text{B}_{0.38}\text{C}_{0.62}$ & $\text{BC}_{0.36}\text{Si}_{0.04}$	x	< 50 nm	x	x
Fe_2W	x	x	< 600 nm	> 1000 nm
Modified Z phase	x	x	< 200 nm	> 1000 nm (PAGB) < 200 nm (MLB)

Figure 1. EFTEM maps of Cr and V with EELS- and EDX- point analysis of the $(\text{Cr,Fe,Mo,W})_{23}\text{C}_6$ and VN phases.

A large carbide with two embedded particles VN and a (V,Nb)(C,N) can be recognized. Due to carbon contamination the derivation of the real carbon content was not possible. The low boron concentration in the $(\text{Cr,Fe,Mo,W})_{23}(\text{C,B})_6$ particle yielded a rather noisy volumetric density map with an average of $\sim 3 \pm 0.85$ atoms/nm³. The investigations reveal so far an almost homogenous distribution of boron inside the carbide and no obvious enrichment at the interface with the matrix. Instead, enrichment of silica and sulfur at the interface were recognized. Moreover, in the high resolution micrographs observed stacking faults and crystal dislocations are likely to accommodate boron atoms.

Table 4. Ionisation cross sections of each element and mean free paths of each phase for 200 kV, $\beta = 10.8$ mrad, $\Delta E=100$ eV. For the B, C, N and Nb the cross sections have been converted from experimental data by Hofer (1991) [18] and (1996) [19], and for V, Cr and Fe from data by Albu (2008) [20].

Element	eV	σ (10^{-7} nm ²)	Phase	λ (nm)
B K	188	11.11	martensite	103.1
Nb M _{4,5}	205	17.80	Cr ₂₃ C ₆	109.5
C K	282	4.88	VNbN	107.2
N K	401	2.63	VN	117.9
V K	513	4.55		
Cr L _{2,3}	575	3.82		
Fe L _{2,3}	708	2.17		

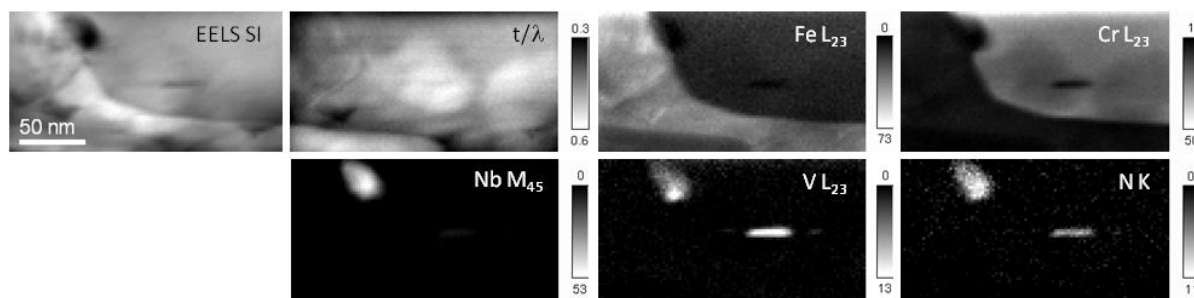


Figure 2. STEM EELS spectrum image, t/λ relative thickness map and the calculated volumetric density maps in atoms/nm³ for iron L_{2,3}, chromium L_{2,3}, niobium M_{4,5}, vanadium L_{2,3} and nitrogen K.

In the "as-received" condition, apart from the M₂₃C₆ and finely distributed MX precipitates, mainly along the grain boundaries, other boron carbides phases (B_{0.38}C_{0.62} and BC_{0.38}Si_{0.04}) with tetragonal and trigonal crystallographic structures, were identified. A more detailed study about the investigation of this specific specimen together with the respective EELS and EFTEM results has already been submitted for publication [21].

The short time creep exposed condition, 650°C - 130 MPa - 8971 h, shows coarse chromium carbides (Cr,Fe,Mo,W)₂₃C₆, laves phase (Fe₂W), VN and Cr₂N. Moreover, fine core-shell particles of modified Z phase surrounded by a thin VN layer, have been assessed by using the bivariate histogram method applied to EFTEM elemental maps, EELS and X-ray spectroscopy. Figure 3a presents the Cr and V jump ratios acquired from an area in the near of a PAGB. The respective scatter diagram for Cr and V jump ratios is shown in figure 3b. Three distinct clusters were identified: the most lightening cluster corresponds to the hole, the right-up cluster corresponds to the chromium carbide and the left-bottom cluster corresponds to vanadium nitride. The elongated form of the clusters is related to the thickness variation of the particles. The diffusely distributed region next to the vanadium nitride cluster with a higher and almost constant Cr intensity corresponds to the modified Z phase. After cluster extraction as a new phase map, the core-shell particle could be identified, as seen in figure 3b. Moreover, the comparison of the N-K edge fine structure (ELNES) in the EELS spectra with a modified Z phase ELNES reference and STEM EELS spectrum imaging line scan investigations, confirms these findings.

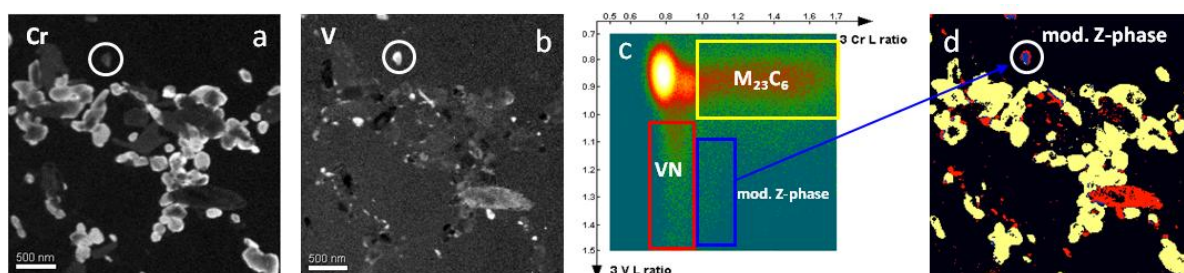


Figure 3. Cr (a) and V (b) jump ratios, (c) respective scatter diagram, (d) the extracted phase map: yellow - $M_{23}C_6$, red - VN and blue - modified Z phase core.

Microstructure changes along pre austenite grain boundaries (PAGB) in the 650°C - 100 MPa – 23997 h creep exposed sample were investigated on the a-C extractions. The particles at the PAGB which were fine distributed during the heat treatment and in the short creep exposed specimen became now significantly large. Remarkable sizes $> 1\mu\text{m}$, were reached by the $M_{23}C_6$, tungsten-rich laves- and modified Z- phases. Figure 6 shows a montage of a couple of TEM micrographs acquired along the PAGB (indicated by the white line) at the lowest magnification allowed by the CM20 microscope. Energy filtered micrographs have also been recorded. An RGB picture (red V-, green Cr-, blue N- jump ratios) from the upper right region with some of the noticed phases is presented. Due to the fact that the large particles were entirely extracted from the matrix, and thus not transparent for the electron beam, some particle regions in the RGB picture are dark. Nevertheless, at the $M_{23}C_6$ boundaries, for example, where the thickness is lower than 200 nm, the green color corresponding to chromium intensity, can be observed. A small Cr_2N particle and modified Z phase particles with different sizes are, as well, present.

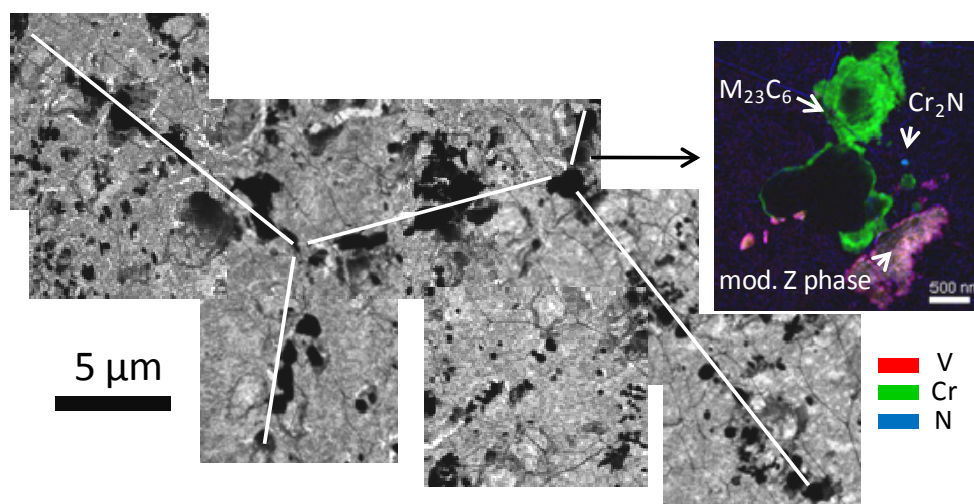


Figure 4. The PAGBs are charted by mounting a couple of zero loss filtered micrographs, EFTM map of Cr, V and N were acquired from selected regions. An RGB (red - V, green - Cr and blue - N) picture from the upper right region is also presented. A small Cr_2N particle and larger $M_{23}C_6$ and modified Z phases can be recognized.

EELS point analysis of some large modified Z phases also reveals a very low boron amount ($< 2\%$) as figure 5 shows. Apart from Nb, V, N and Cr, a high amount of carbon and oxygen appear. Those are caused by the amorphous carbon sustaining the particles and by surface oxidation. The iron signal can also be due to the incomplete etching of the matrix.

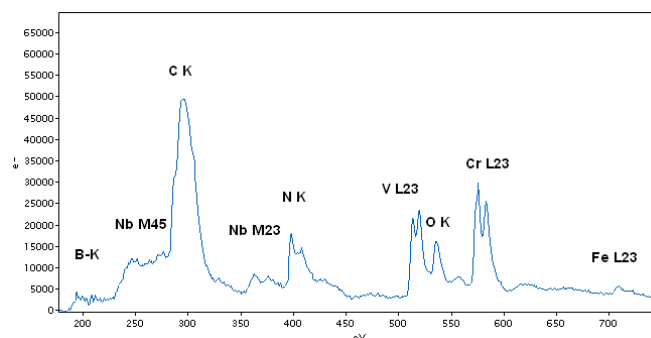


Figure 5. EEL spectrum acquired from a large modified Z phase at the PAGB. The respective B, Nb, C, N, V, O, Cr and Fe edges are indicated. The high amount of carbon is due to the amorphous carbon replica, and the high oxygen amount is due to surface oxidation of the particle.

However, fine particles (< 500 nm) mostly chromium carbides and complex nitrides, but also few VN, NbC and Cr_2N were still present being mostly distributed at the martensite lath boundaries (MGB), see figure 6. Despite of the remarkable sizes reached by the particles at the PAGB the creep property of this steel seems not to be much influenced so far. This fact is quite surprising, since the formation of complex nitrides, namely modified Z phases, with such a high dimensions, causes the disappearance of the strengthening VN and NbC precipitates.

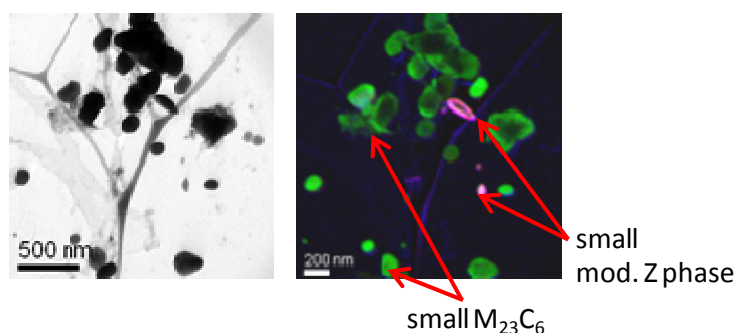


Figure 6. A zero loss filtered TEM micrograph and the RGB (red - V, green - Cr and blue - N) from a region containing small particles far from the PAGB.

4. Conclusions

This paper presents a comprehensive analysis of the precipitation sequence during the heat treatment and short and long time creep testing of the boron nitrogen balanced 9Cr3w3CoVNb steel.

Advanced analytical electron microscopy such as STEM DualEELS spectrum imaging has been applied with the aim of verifying boron enrichment and quantification inside the chromium carbides and at the matrix interface. Moreover, energy filtering TEM and bivariate histogram analysis, was employed to identify of early stage phase transformation to modified Z phase in the short time creep tested sample, 650°C - 130 MPa – 8971 h.

It has been found that some large M_{23}C_6 particles after long time tempering (50 h at 770°C), contain a small evenly distributed amount of boron, approximately 3 atoms / nm^3 . No enrichment of boron at the particle-matrix interface was detected. Unexpected other boron containing phases like boron carbide have been discovered, thus reducing even more the amount of boron available for carbide or matrix-particle interface enrichment. Fine modified Z phase – VN core-shell particles have already been found in the short creep exposed specimen, confirming once again the influence of mechanical stress on the diffusion process of nitrogen and chromium.

Furthermore, pre austenite grain boundaries in the 650°C - 100 MPa – 23997 h creep tested sample were TEM charted and a number of regions along the PAGB were analyzed by FTEM and EELS revealing very large (> 1 μm) carbides, tungsten-rich laves- and modified Z- phases. A low signal of boron has been detected in the EEL spectra of the modified Z phases.

Few fine (< 100 nm) VN, NbC and Cr₂N and many fine chromium carbides and Z phase particles were mostly observed along the martensite lath boundaries.

References

1. Abe F., "Precipitate design for creep strengthening of 9% Cr tempered martensitic steel for ultra-supercritical power plants", Sci. Technol. Adv. Mater. **9** (2008) 013002 (15pp)
2. Staubli M. et al, "European Collaborative Evaluation of Advanced Boiler Materials" Mat. Adv. Power. Eng. 1998, 87-103
3. Golpayegani A. et al, "A study on Z-phase nucleation in martensitic chromium steels", Mater. Sci. Eng. A (2008) p 310
4. M. Hättestrand et al., "Boron distribution in 9.12% Cr steels", Mater. Sci. Eng. A **270** (1999) p 33
5. Semba H. et al., "Alloy design and strength of advanced 9% Cr steels USC boiler steels containing high boron", Mat. Adv. Power Eng. (2006), 1041
6. Siradek-Hahn K. et al., "Boron added 9% Cr steel for forged components in advanced power plants", Advances in Mat. Tech. for Fossil Power Plants, Book 0770, (2001) 165
7. Tabuchi M. et al, "Improvement of type IV creep cracking resistance of 9Cr heat resisting steels by boron addition", Creep Cracking of 9Cr steels with boron, OMMI Vol. 3-3 (2004)
8. Abe F., "Effect of boron on creep deformation behavior and microstructure evolution in 9% Cr steel at 650°C", Int. J. Mat. Res. **99** (2008) p 387
9. Seong et. al, "Study of the effect of nano-sized precipitates on the mechanical properties of boron-added low-carbon steels by neutron scattering techniques", J. Appl. Cryst. (2008). 41, 906-912
10. Trevor C. J. et al, "An experimental ultra fast shutter for a spectrometer", Proceedings book, EDGE 2009 Banff
11. Kothleitner G. and Thomas P.J., "Accurate chemical shift measurements using a post column spectrometer equipped with an experimental electrostatic shutter", Proceedings book, EDGE 2009 Banff
12. Tencé M. et al, "Towards systematic single scattering EELS analysis with improved energy resolution. A new detection scheme.", Proceedings book, EDGE 2009 Banff
13. Mayr P. et al., "Direct observation of phase transformation in the simulated heat-affected zone", Int. J. Mat. Res. **99** (2008) p 381
14. Mayr P. et al., "Correlation of creep strength and microstructural evolution of a boron alloyed 9Cr3W3CoVNb steel in as-received and welded condition." Materials at High Temperatures 2010; 27-67.
15. Riegler K. and Kothleitner G., "EELS detection limits revisited: Ruby - a case study", Ultramicroscopy 110-8 (2010), 1004-1014
16. Kothleitner G. et al., "Toward more quantitative electron energy-loss spectroscopy by nearly simultaneous acquisition of low and high losses", in preparation for Ultramicroscopy (2011)
17. Scott J. et al., "Near-simultaneous dual energy range EELS spectrum imaging", Ultramicroscopy 108 (2008) 1586– 1594
18. Hofer F., "Determination of inner-shell cross-sections for EELS-quantification", Microsc. Microanal. Microstruct. **2** (1991) 215 – 230
19. Hofer F. et al., "Ionization cross-sections for the L23-edges of the elements Sr to Mo for quantitative EELS-analysis", Ultramicroscopy 63 (1996) 239-245
20. Albu M. et al., "Compositional characterization and thermodynamic modeling of nitride precipitates in a 12% Cr steel", J. Mat. Res. **99** (2008) 422
21. Albu M. et al., "The influence of boron on the microstructure of a 9 wt.% Cr ferritic steel ", submitted to Mat. at High Temp. (2011)

MAGNETIC AND METALLOGRAPHIC INVESTIGATION OF PHASE TRANSFORMATIONS IN DUPLEX STAINLESS STEELS

.I.Calliari[°], A.Miranda Perez[°], G.Tortoreto* I.Meszaros[^]

[°] University of Padova, Dept.of Chemical engineering processes, Via Marzolo 9,
* Tifast Terni, Italy, ^ Budapest University of Technology and Economics 1111 Budapest, Hungary

Heat treatment and cold working -induced microstructural processes were studied by metallography and different non-destructive magnetic in commercial lean, duplex and superduplex stainless steels.

In DSS and SDSS the metastable ferrite can decompose to a sigma phase and secondary austenite due to heat treatment. All the mechanical, corrosion resistance and magnetic properties are strongly influenced by this microstructural changes. The capabilities of magnetic measurements allow a quantitative correlation between measured harmonics and mechanical properties obtained from destructive tests.

In lean duplex the substitution of Ni by N and Mn in lean grades may result in austenite phase instability, and this phase tends to transform to metastable martensite. The cold rolled samples were examined with OM, SEM, XRD and Magnetic measures. Three different magnetic tests were applied for determining the magnetic behaviour of DSS samples. The effect of cold rolling is on grains size and shape and the magnetic tests suggest the martensite presence in 2101.

1. Introduction

Duplex Stainless Steels (DSSs) have a bi-phased structure of austenite (γ) and ferrite (δ), with a ferritic matrix in which the austenitic phase and other alloying elements (chromium, nickel, molybdenum, manganese, silica) are present. The differences between DSSs and other stainless steels are their weldability, which is better than ferritic stainless steels, and their resistance to stress corrosion cracking, that is higher than austenitic stainless steels. DSSs are also not affected by the intergranular corrosion. They have higher pitting and crevice corrosion resistance than ferritic stainless steels and a resistance in strong acid environment similar to austenitic steels but the main advantages is their resistance to chloride stress corrosion cracking. The optimal temperature to use these steels is between 50-250°C, because the toughness decreases too much below the minimum value, and the ferrite δ starts to be unstable above 250°C [1-3]. The pitting resistance of stainless steels is primarily determined by their composition. The three main elements which have a significant beneficial effect are chromium, molybdenum, and nitrogen. The dual phase structure of duplex could rise to both phase transformation : the sigma, chi and nitrides formation mainly involve the ferrite by diffusion mechanism and lattice arrangement, while in austenite could occur a martensite transformation induced by cold working , as well known in fully austenitic stainless steels [4-6].

The recently introduced low Ni duplex grades, characterized by a decrease of Ni which is substituted by Mn and by N, are extensively used in industrial application. On the contrary their physical metallurgy and phase stability are less known. Many tests have been carried out in order to study their microstructure stability after thermal treating, and the main results are the absence of sigma and chi precipitation and a moderate presence of nitrides at grain boundaries. The impact toughness after solution annealing treatment is very good and after isothermal treatment the impact energy is never lower than 50 J. Furthermore, the substitution of Ni with Mn and N may induce the instability of the austenite, as suggested in previous researches, which report of a probable transformation to martensite during cold forming [7]. There are many factors that can influence the austenite-martensite transformation: e.g. the chemical composition, the grain size of the austenite, the temperature and the strain rate. In 2101, the gamma-former power of Ni is partially compensated by Mn and N, but the total austenite-stabilizer effect is less than with Ni. The deformation mode and the strain rate are other important factors.

It is well known [8] that two types of martensite can form from metastable austenite: epsilon - hcp paramagnetic and α' bcc ferromagnetic martensite, where the α' phase is more stable than ϵ -martensite. The diffusion less

transformation from γ -phase, paramagnetic, into α' phase, strongly ferromagnetic, can be detected studying the magnetic properties of the cold rolled material. The austenite-martensite transformation and ferrite decomposition can be deeply investigated by metallographic techniques (SEM, TEM and XRD). The different magnetic properties of duplex phases could be used to monitor such phase's transformation. In the present work the capabilities of some magnetic tests are illustrated. The microstructural evolution produced by cold rolling and heat treatment in lean and traditional duplex stainless steels has been investigated. The effect of cold deformation on microstructure and grain refining has been investigated through metallographic technique (OM, SEM) on a 2101 grade. Magnetic measurements and XRD have been performed to assess the amount of strain-induced martensite after cold rolling with different thickness reductions. The effect of heat treatment on a cold rolled 2507 is studied by metallography (OM, SEM) and magnetic tests [9, 10].

2. Experimental

In the present study a lean and super duplex (chemical composition Table 1) have been considered. The 2011 grade was received as hot rolled plates of 8 mm in thickness, solution annealed at 1050°C and, WQ.

The 2507 grade was received as hot rolled of 1.5 mm, solution annealed at 1100°C and WQ.

Plastic deformation of the solution annealed materials was carried out by RT cold rolling (10-85%TR). The 2101 was examined only in rolled condition while the cold rolled 2507 samples were heat treated at 900°C for 40 minutes to investigate the influence on cold rolling on secondary phase's precipitation. A single stand reversing mill, with 130mm diameter rolls was used. The plates were cold rolled in one direction, through many constant passes, to gradually reduce its thickness by compression. Seven cold rolled samples were obtained applying different thickness reductions in the range of 10-80%. Metallographic samples were prepared with conventional grinding, polishing and etching with Beraha's etchant. Microstructural analysis was carried out using a light optical microscope and scanning electron microscopy (SEM, Leica Stereoscan 440, and Image Analysis)

For the identification of the phases, X-ray diffraction was performed using a Cr-K α radiation ($\lambda=2.2897 \text{ \AA}$, operating at 30kV and 20mA), in step scan mode with step size of 0.025° and time per step of 5s. First magnetization curve and hysteresis loops were measured in a double-yoke DC magnet-steel tester. The predecessor equipment was firstly described by Stäblein and Steinitz. Our equipment is characterized by two E-shaped soft iron yokes, opposite one another with an air-gap between each of the three pairs of transverse limbs. Equal magnetizing windings are placed on each half of the long arms of both yokes. Hence the equipment has a perfect symmetry. The introduction of a specimen in one gap causes an imbalanced symmetry; an additional flux is needed to complete the circuit mainly across the central air-gap, the flux in which is thus closely proportional to the magnetization (M) of the specimen. The apparatus for measuring the strength of the applied field H may be calibrated in any known field, and is found to give accurate readings of the value of H applied to the specimen [11, 12]. The maximum applied external field was of 210 kA/m. The present form of the measuring setup is developed at the Department of Materials Science and Engineering of the BUTE and it applies up-to date field sensors and data acquisition apparatus. AC measurements of the minor hysteresis loops were carried out by using a specifically designed permeameter type magnetic property analyzer, with a maximum applied external field of 2450 A/m. For each cold rolled sample the relative magnetic permeability values were derived from the resulting magnetizing curves. The coercivity (H_c) was measured by a high-accuracy Förster coercimeter (Type 1.093) equipment, based on the compensation of the own remnant magnetic field of the samples. The coercivity was measured magnetizing the samples along their rolling direction. Vickers hardness (HV) tests were also performed using a Buehler MMT-3 digital micro hardness tester. All measurements were carried out using a load of 0.5 Kg on each sample.

Element	C	Si	Mn	P	S	Cr	Ni	Mo	Cu	N
2507	0.015	0.24	0.83	0.023	0.001	24.8	6.89	3.83	0.23	0.27
2101	0.028	0.78	3.41	0.026	0.01	21.72	1.13	0.15	0.32	0.13

Tab.1 Chemical composition of the investigated duplex stainless steels [wt. %]

3. Results and discussion

The as received materials in the solution annealed condition is characterized by coarse grains, elongated in longitudinal direction due to the previous hot rolling. Indeed the grains are equiaxial in the transversal cross section, perpendicular to rolling direction. The phase volume fractions in 2101 are 20.4 % of austenite and 79.6 % of ferrite, while in 2507 are 41.5% of ferrite and 59.5 of austenite.

2101 grade

The first effects obtained by cold rolling on both steels were a strong grain refining and changing in shape compared to the solution annealed sample microstructure. In the 2101 samples the SEM-BSE and SE micrographs (2000-4000X) evidenced a microstructural modification in the austenite grains. It could be indicate a presence of a new phase with the typical platelet martensite morphology (Fig.1)

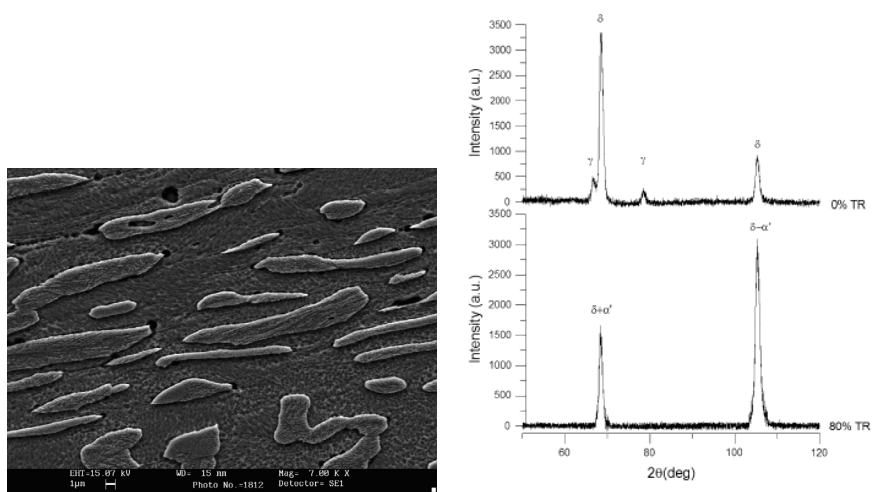


Fig.1 SEM-BSE micrograph of 2101 cold rolled (80% or 65% T.R.) with platelet in austenite grains

Fig.2: X-Ray diffraction of as received (up) and cold rolled sample (80% T.R.)

The identification and quantification of martensitic phase was not possible through classical metallographic technique because the tested etchants were not able to unequivocally isolate lath martensite.

Therefore X-ray diffraction and magnetic measurements allowed to suggest the presence of α' - martensite. X-ray spectrum of the strongest deformed sample (80% Thickness Reduction) is shown in Fig.2.

It is not possible to distinguish the peaks of ferrite (δ) and α' - martensite because the two phases have the same crystal lattice so the same reflections. Over the detection limit, the peaks of austenite completely disappear after the maximum thickness reduction applied. Therefore at this deformation condition all the detectable austenitic phase could be transformed into α' - martensite. The saturation magnetic polarization is known to be linearly proportional with the amount of ferromagnetic phase. In the non-deformed condition only a ferromagnetic phase (δ – ferrite) was present. The saturation magnetic polarization in this case was $\mu_0 M_s (\delta) = 0.752$ T, and remained at a constant value during cold rolling. As the material was subjected to cold deformation another ferromagnetic component was introduced in it. This could be to the appearance of α' - martensite, which increased with cold deformation up to a complete detectable ferromagnetic structure made of 79.6% of ferrite, 20.4% of α' - martensite and 0% of austenite. The saturation magnetic polarization ($\mu_0 M_s$) seems to have almost the same value at the lowest cold deformation (up to 30% of thickness reduction) (Fig.3). Increasing thickness reduction at room temperature a stronger and gradual increase in saturation magnetic polarization was highlighted.

The amount of the new phase, at the moment called α' - martensite, was calculated from the saturation induction values can be seen in Tab.2.

Thickness Reduction [%]	0	10	20	30	40	50	60	70	80
New phase [%]	0	0.1	0.3	1.0	7.7	8.3	12.4	16.9	20.4

Tab.2 New phase quantification

Maximum relative magnetic permeability values were derived from AC normal magnetization curves (Fig.3). Magnetic permeability is an index of how well a material concentrates the magnetic field. The results show a relationship between the reciprocal of maximum relative magnetic permeability and the amount of the hypotized strain induced martensite. Therefore relative magnetic permeability could be a possible parameter derived from non destructive tests to detect martensitic transformation in the duplex stainless steel considered.

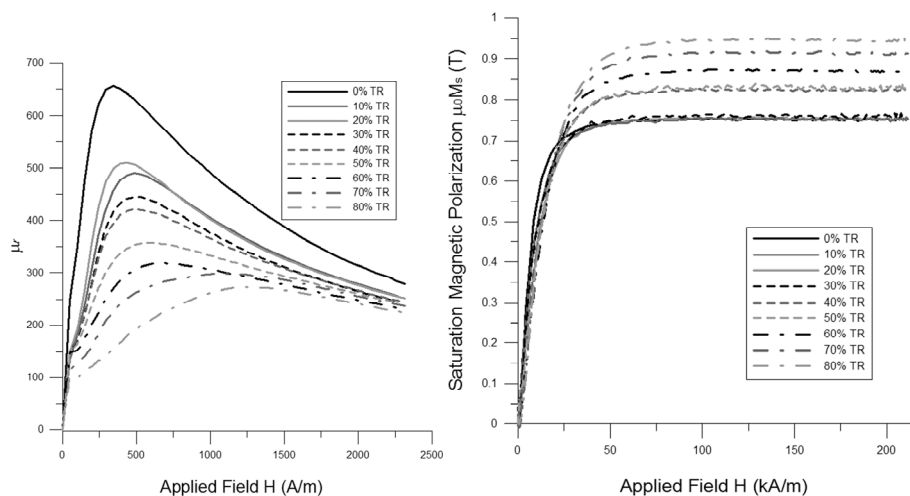


Fig.3 Initial magnetization curves for each thickness reduction vs.. applied field

Fig.4: Maximum Relative Magnetic Permeability for each thickness reduction vs. Applied Field

2507 grade

The cold rolling affects only grain's size and shape. Deformation effect is evident along longitudinal direction as stretching and thinning of austenitic and ferritic grains, and a packaging of them. The effect on the transversal direction is a crushing of austenitic and ferritic grains, while no new phases inside the austenite grains was detected by metallographic techniques and magnetic tests. The investigation on heat treated samples evidenced that the previously deformed samples have an higher amount of secondary phases than the solution annealed ones. In fig. 5 it is possible to appreciate the huge precipitation of sigma phase and secondary austenite. The sigma phase (white particles) is mostly placed at the primitive ferrite/austenite boundary of the as-received material, but also some not negligible amount of sigma particles are observed into the austenitic grains, partitioning them. This happens at very important level from the 25% thickness reduction up to the most deformed. In that case, the partition is strong, and also due to the very fine microstructure the distinction between different grains is now very difficult.

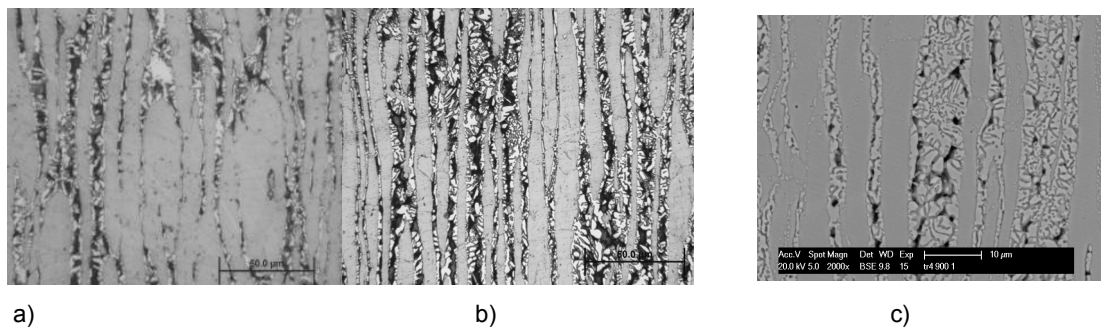


Fig.5 OM micrograph, 500x Effect of heat treatment at 900°C for 40min , a) base material, b)25% TR, c) SEM micrograph, 50%TR with the partition of the austenite grains by the sigma precipitates, and the great decomposition of the ferrite.

The results of magnetic tests confirm that the in cold rolled samples the amount of magnetic phase is not affected by cold rolling while in heat treated samples its decreasing is evidenced.

Stäblein-Steinitz measurement is a closed loop DC measurement which is based on a symmetrical magnetic bridge yoke. It is able to supply an excitation field over 200'000A/m, greater than AC measurement test.

It is enough to saturate a hard magnetic material such as this SDSS.

About the first magnetization curves the little shift that can be noticed is due only to the instrument (positioning of sample, noise etc. So, this confirms again that in this steel there is no difference in the amount of ferromagnetic phase after several degrees of cold rolling. The same conclusion can be drawn watching the hysteresis loops that are exactly the same for each sample, again, all the sample reach the same value of magnetization and the little shift are only due to the device problem.

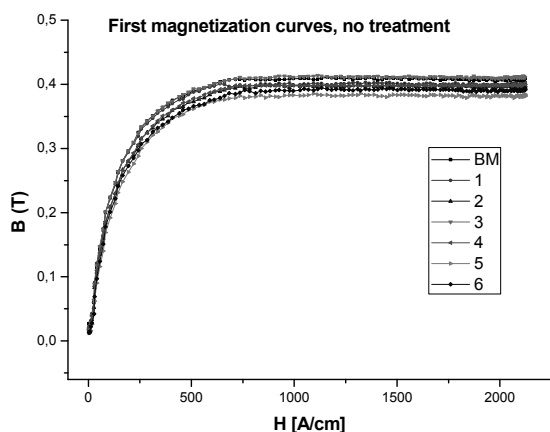


Fig.6 First magnetization curves of the samples at only cold rolled state: there no detection of further ferromagnetic phase..

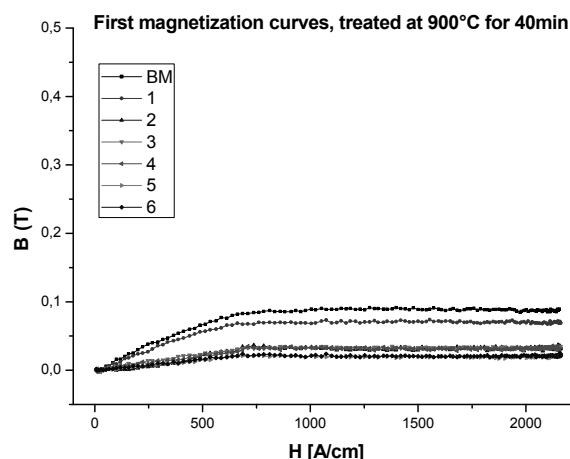


Fig.7 First magnetization curves of the samples after the treatments. The device detect appreciable ferromagnetic phase only on the first two samples.

Conclusions

The effect of cold rolling on the microstructures of a superduplex and a low Ni duplex stainless steel can be summarized as follows:

2101

- A strong grain refining and hardness with increasing cold deformation.
- Magnetic and X-ray data confirm that the $\gamma \rightarrow \alpha'$ transformation could take place after cold rolling from 20% thickness reduction
- A strict relation between microstructure and magnetic properties was revealed.
- A strong dependence between coercivity and the new phase, may be α' - martensite, content has been highlighted.
- The definitive identification of the new phase can be done by TEM and electron diffraction investigation

2507

- The SAF 2507 does not show any α' martensite presence after each rate of plastic deformation. This result is validated by the two different magnetic tests very sensible to any variation of amount of ferromagnetic phase.
- In the samples deformed at 50% and 85% was found at the SEM into the austenite grains, stripes and bands brighter than the neighbour, anyway after EDS analysis no differences in composition was found.
- The precipitation of sigma phase is enhanced by the plastic deformation, magnetic tests found that in the sample cold rolled at 50%, 65% and 85% the ferrite is almost totally disappeared to give $\sigma + \gamma_2$
- It seems that the eutectic decomposition of ferrite does not give sigma phase and austenite in the same percents, but it depends on the strain rate. This is confirmed also by the decrease in Mo in the sigma phase. Anyway these topics require further investigations.
- Magnetic tests demonstrate the possibility to find a quantitative correlation between measured harmonics and metallurgical data in lean duplex and superduplex stainless steels.

References

1. J.O. NILSSON , Materials Science & Technology, 8(1992) , p.685
2. I.CALLIARI, M.ZANESCO; E. RAMOUS, Journal of Materials Science,41, (2006) p. 7643
3. H.SIEURIN, R.SANDSTROM Mat. Sci. Eng., **A444**, 271 (2007)
4. K.H. LO, C.H. SHEK, J.K.L. Lai, "Recent developments in stainless steels", Materials Science and Engineering R, MSR-371; No of Pages 66
5. TAVARES SSM, NETO JM, DA SILVA MR, VASCONCELOS IF, ABREU HFG, " , Mater Charact **59 (2008)p.:90**
6. MILAD M, ZREIBA N, ELHALOUANI F, BARADAI J Mater Process Technol **203 (2008)p.:80**
7. CHOI JY, JIN W Scr Mater **36 (1997):99-104**
8. SEETHARAMAN V, KRISHNAN P J Mater Sci **16 (1981)p.:523**
9. MÉSZÁROS I, PROHÁSZKA J , J Mater Process Technol **161 (2005)p.:162**
10. TAVARES, PARDAL, DE SOUZA, NETO, DA SILVA, Journal of All.and Compounds 416 (2006) p. 179.
11. TAVARES SSM, DA SILVA MR, PARDAL JM, ABREU HFG, Gomes AM), J Mater Process Technol **180 (2006)p.:318**
12. KRONMÜLLER H, FÄHNLE M (2003), "Micromagnetism and the Microstructure of ferromagnetic Solids", Cambridge University Press
13. I.MÉSZÁROS, *Magnetic characterization of duplex stainless steel*, Physica B 372 (2006) pp 181–184.

METHOD FOR IMPROVED DETERMINATION OF CARBON IN CAST IRON

Roland van Driel¹, Bruno van Stuivenberg², Heinz-Gerd Joosten¹

¹ *Spectro Analytical Instruments GmbH, Kleve*

² *With Spectro Analytical Instruments GmbH, Kleve, during the period of the experimental work*

Abstract

Carbon is the most important element in cast iron. It therefore has to be constantly monitored during the casting process. Sample taking is critical, too slowly chilling produces graphite inclusions. However, it is well known that spark emission spectrometers need completely graphite-free samples to produce accurate results. The reasons for this requirement are investigated and discussed. Finally the principles and capabilities of a new carbon determination method are described. This method improves the accuracy of the carbon determination in suboptimal cast iron samples, and indicates if poorly taken samples are measured.

Introduction

Up to the 80th of last century a volumetric method was used as a standard procedure for total carbon determination in ferrous materials. A small amount of cast iron or steel (approx. 0.5 g) was chipped, heated to 1150 °C and burnt in an atmosphere of pure oxygen. The gaseous reaction products, most of it CO₂, and the surplus O₂ replaced a part of the water of a washing bottle. The CO₂ dissolves into water and causes a contraction of volume, which can be measured by reading a burette. It is possible to directly calibrate the burette's scale to weight-% of carbon. The procedure described existed in different variations. In most cases, the way of detecting CO₂ was affected. The CO₂, for example, was absorbed by natron asbestos and weighted using a scale. Again, the scale can be directly calibrated in weight-% carbon. Nowadays the CO₂ is usually measured optically, based on the absorption of infrared radiation. Up to now, automated combustion analyzers of this type are used in steel mills and cast iron foundries.

Starting during the 60th of last century the C-determination was also carried out by spark emission spectrometers (S-OES) and glow discharge optical emission spectrometers (GD-OES). Especially spark emission spectrometers are much faster than the combustion process. Chipping of the sample is not required and analysis takes only one minute for a double burn. Also GD-OES doesn't need chipping, but according to Weiss [Wei1996] due to the low sputter rates of graphite the analysis time can be as long as ten minutes.

All methods for total carbon detection are based on proper sample taking. For the combustion procedures this means to care for sufficiently raw chips, if the samples are containing globular graphite. Otherwise there might be a significant loss of graphite inclusions due to the fact that they tend to fall off the surface or they are torn off during the process of chipping.

Especially for spark spectrometry sample taking is critical. It is of utmost importance, that the sample is free of graphite. This can be achieved by chilling relatively thin sample disks using a heavy copper mold. Sometimes elements like bismuth are added to inhibit formation of graphite. Reproducible and correct sample taking can only be carried out by an experienced operator. These problems were described frequently in literature, for example by Kipsch [Kip1974], Horvath/Répási/Szabo [Hor1973] and Weiss [Wei1996].

There is a simple reason why the sample has to be graphite-free: Before the actual integrating measurement starts, there is a pre-spark period consisting of around 4000 high energy sparks. This pre-spark period is required to remelt and homogenize the sample's surface. If there are big inclusions of graphite, a spark causes sublimation of big portions of graphite. This amount of carbon vanishes and is no longer available during integration time. The C-values show up too low. Graphite inclusions can be found in components made of grey cast irons, malleable irons and in globular cast irons. In grey cast irons, graphite inclusions have a lamellar structure. Parts made of malleable iron are containing carbon in the form of iron carbide after solidification, the graphite is intentionally

formed later on by annealing. Globular cast iron contains small amounts of magnesium or cerium. Carbon is gathering around single Mg or Ce atoms, forming small globes of diameters between few micrometers up to 50 μm . It is not easy to prevent this globe-forming process during sample taking. Therefore, here is a constant danger of error. In this paper, we concentrate on globular cast iron, because here the problem of sample taking quality is the most difficult one.

Instrumentation

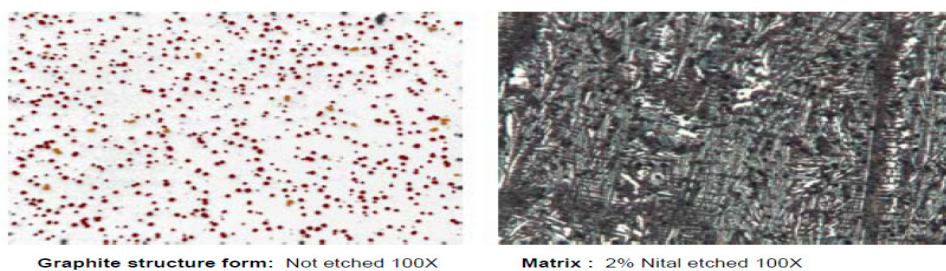
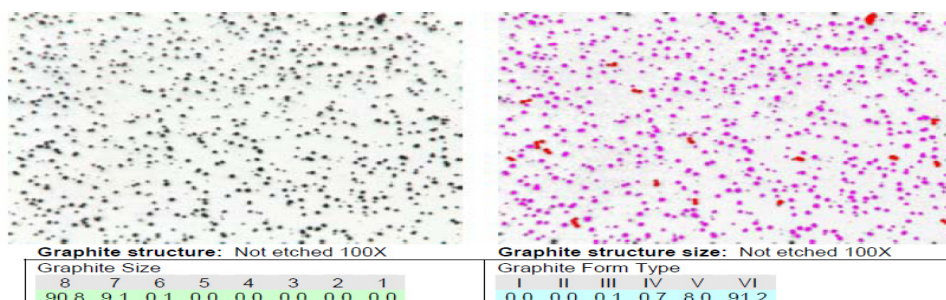
The metallographic investigations of fig. 1 and 2 were made using the particle analysis software of dhs (dhs Dietermann & Häuser GmbH, Greifenstein-Beilstein, Germany) at Gieterij Doesburg, the Netherlands. We are grateful for the kind support of Mr. Cor van Ettinger, lab manager of Gieterij Doesburg. Fig. 3 and 4 were made at SPECTRO using a Keyence VX500-F computerized microscope. All spectroscopic investigations were made on a SPECTROLAB LAVM10 (SPECTRO Analytical Instruments GmbH, Kleve, Germany). The SPECTROLAB contains a source unit capable of performing up to 600 sparks per second, each of them with a power of up to 2500W at a resolution of 0.125 W. The SPECTROLAB's optical system offers a high resolution of 9pm and covers the spectral range between 120 and 780nm. It is equipped with two types of sensors: Photomultiplier tubes make it possible to use time resolved spectroscopy. CCD-sensors enable a full coverage of a wide spectral range and provide flexibility of spectral line usage.

Experimental

For a series of 16 different heats a sample pair was taken for each heat. The first sample of one pair was chilled slowly, the second one very slowly. As a result, all samples were containing free graphite, with the expectation that the second samples of a pair are containing more graphite inclusions.

Figure 1 is showing an example of such a very slowly chilled globular cast iron sample. The microstructure was made visible by polishing the sample and etching it using a 2% Nital solution. Viewing the result through a microscope showed that there were a lot of graphite inclusions. The microscope was combined with the dhs particle analysis software to count and classify the size of the inclusions. As a result, 6.55% of the sample's volume was occupied by graphite. There was a particle density of 1660 per mm^2 . Figure 2 shows another sample, chilled a little bit faster. Here, the graphite inclusions are smaller and less frequent (1126 per mm^2), reducing the graphite phase fraction to 3.28%. Here, most of the inclusions (95.5%) have a diameter of less than 15 μm . The remaining 4.5% are between 15 and 30 μm .

Structure analysis according to EN ISO 945



Sample related Measurement Data		
Date of Evaluation:	06.05.2008 11:43	Phase fraction Graphite [%]: 6.55
Standard for Evaluation:	EN ISO 945	Number of Particles (absolute): 5254
Measurement fields unetched:	8	Particle Density [1/mm ²]: 1660
Measurement fields etched:	0	Size Class: 6
Sample area unetched [mm ²]:	3.16	Nodularity Index [%]: 63.8
Sample area etched [mm ²]:		Ferrite/Pearlite Ratio [%]:

Fig. 1 Very slowly chilled globular cast iron sample

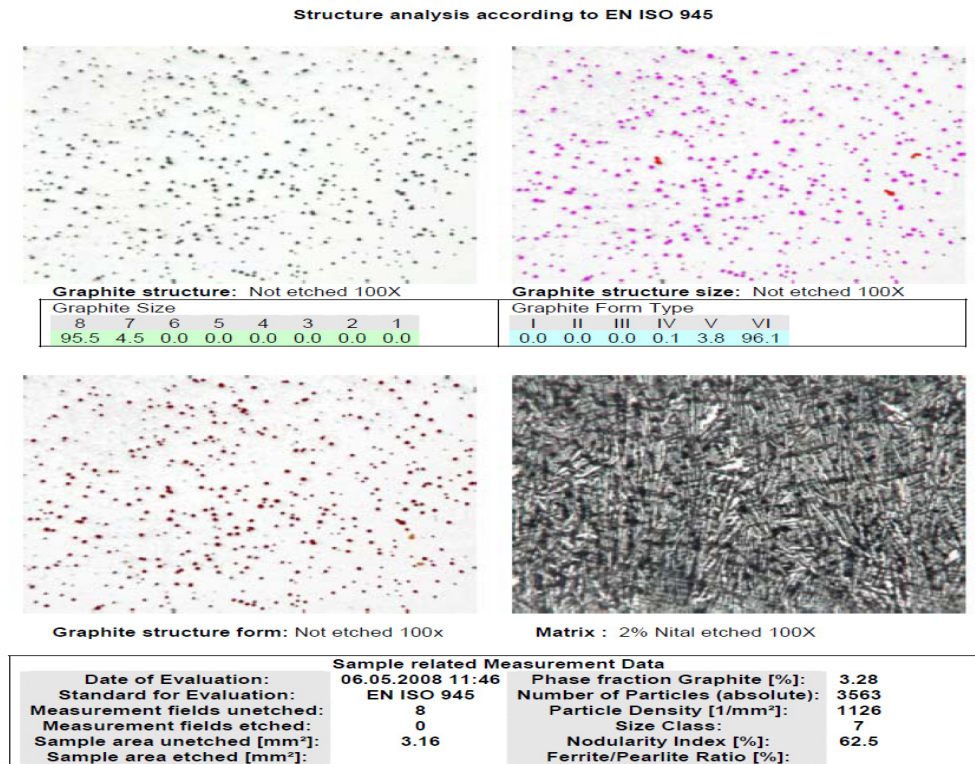


Fig. 2 Slowly chilled globular cast iron sample

Figure 3 shows a photo of a single spark crater, created using prespark source conditions. Its total diameter is around 30 μm , the diameter of the vaporized area is approx. 12 μm . The vaporized area is surrounded by a belt of remelted metal of 3.5 μm width. It is important to record, that in general the inclusions are much smaller than the crater of a single spark. This implies a high probability, that a spark crater completely covers a graphite inclusion.

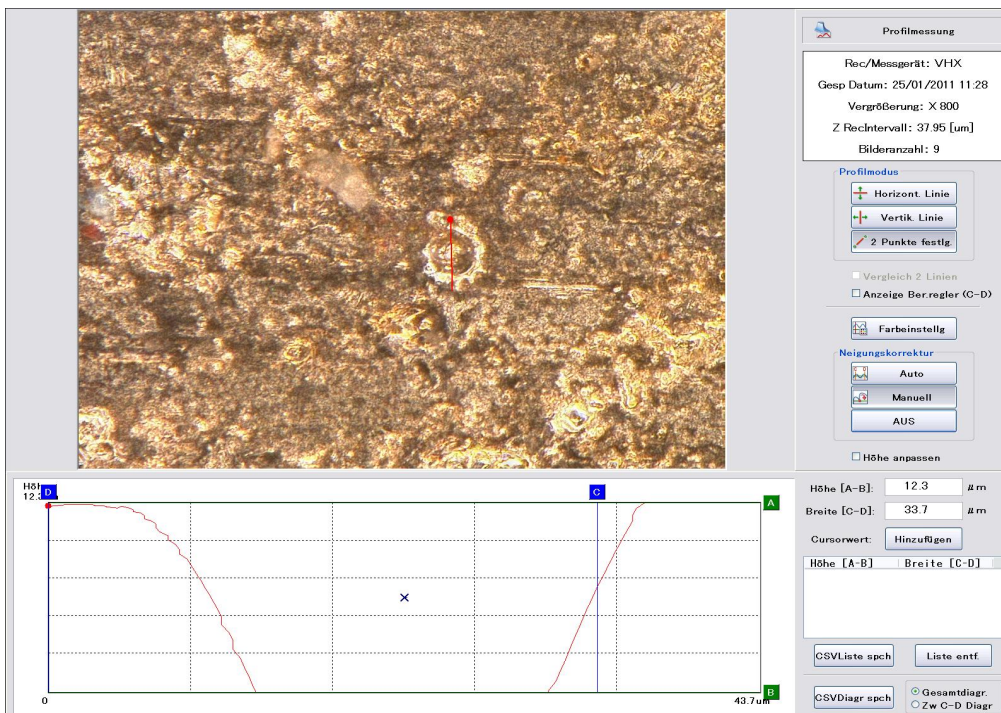


Fig. 3 Diameter and depth of a spark crater

Figure 1 to 3 support the theory mentioned in the introduction: If a graphite inclusion is hit, there is a statistical high chance that the whole inclusion is affected. The chance is high, that the whole graphite inclusion is sublimating immediately. Therefore, the preburn-spark cannot do the job to transport Carbon into the metallic matrix. That means that such a spark can vaporize smaller inclusions totally. There might remain relics of bigger graphite inclusions. However, a second impact on the remainder will erase it completely. As a consequence, most of the free graphite leaves the sample during a very long-lasting preburn period. Figure 4 shows the result of such a preburn period on a sample containing globular graphite inclusions. After applying a preburn phase, the sample was re-ground and re-polished. The center of the burn spot (dark-brown areas) should be ignored, because is not 100% flat. Here the concentration of spark impacts and the ablation rate is maximal. However it can be easily seen, that around this centre there is a belt without any graphite. This area is the one, where the measurement normally takes place after preburn. It is obvious, that the depletion of graphite inclusions causes the carbon content to be determined too low.

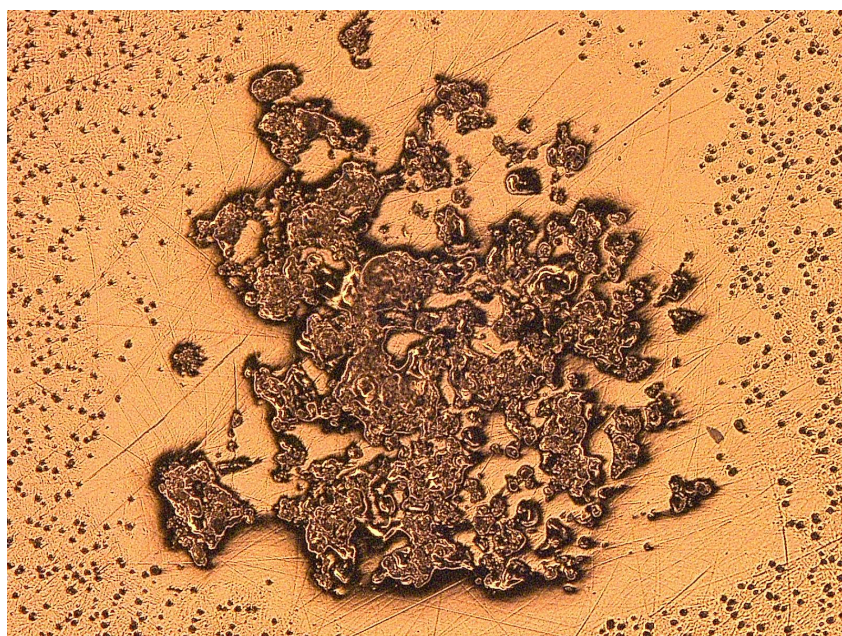


Fig. 4 Depletion of graphite inclusions after preburn

Off course, in a real preburn situation, not all graphite inclusions are hit. Also, ablation of materials leads to deeper levels of material, where new graphite-inclusions come into the spark during the measurement phase.

Table 1 shows some numbers that are useful to quantify the errors obtained for the samples of figure 1 and 2.

Table 1: Errors in C detection due to grey solidification of cast iron

Sample of fig.	Real value (Weight-%)	Measures conventionally (Weight-%)	Difference (Weight-%)	Graphite inclusions, approx. (Weight-%)
1	3.63	3.07	0.57	1.8
2	3.65	3.46	0.19	0.9

Please note, that such high errors are not real life. They only can be produced by completely inadequate sample taking! However, small mistakes during sampling can produce errors of more than a tenth of a percent in total carbon. It would be useful to modify the method of cast iron determination in a way to be warned if the sample's

quality is poor. It also would be useful to get a corrected carbon value for such samples, even if it is a little bit less accurate than those obtained for a good sample. Therefore, a procedure for improved Globular Cast Iron determination will be described. It is a straightforward approach as a result of the perceptions gained up to now. The information of the last paragraph makes it clear that we have to have a look on the C-signal during the preburn time. Normally, the carbon is measured using the spectral line C 193 nm and an appropriate iron line as an internal standard, for example Fe 187.7 nm. During preburn time, there are different excitation conditions. Therefore, here the line pair C 148 nm and Fe 149 nm is better suited. The SPECTROLAB makes it easy to add additional spectral lines using its CCD-segment. At preburn time, the intensities of every ten subsequent sparks are combined into packages. That means there are 500 packages for 5000 sparks. It is now possible to plot the package intensities against the packet numbers.

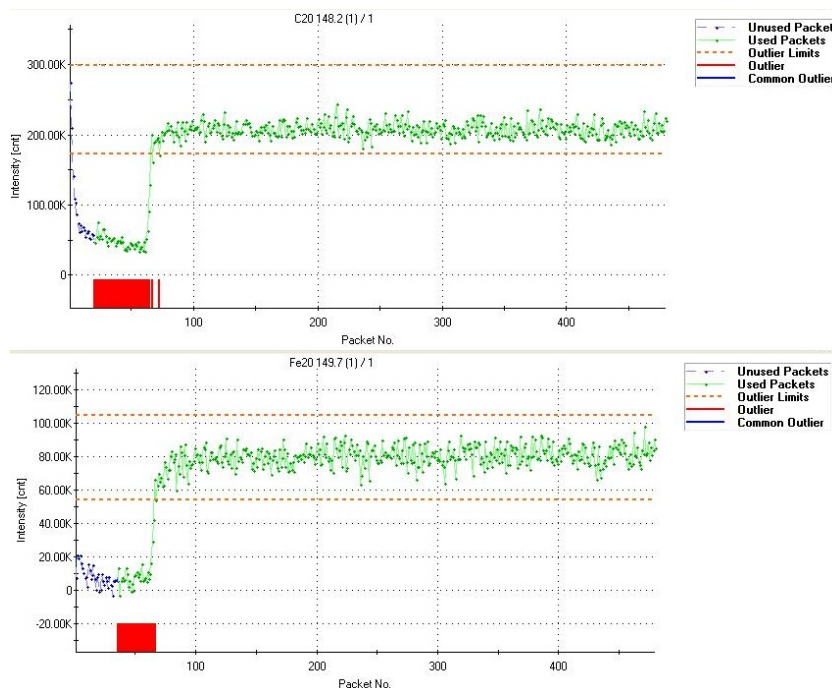


Fig. 5 Package intensities for C and Fe of a graphite –free sample (SUS 5/45)

Figure 5 shows a typical picture of a complete graphite-free sample. After a stabilizing phase of 700 sparks (70 packages), the packet intensities become stable. They are staying on a constant level. For a sample containing 0.5% weight-% graphite, the situation is different (see fig.6). It can be seen easily, that, after the stabilization phase, there is a super-elevation of the carbon intensities between packet 50 and packet 150. This super-elevation is caused by spark impacts on graphite inclusions. It can be used to calculate the corrected total carbon content. The first step of this procedure is to determine, where the usable packages start. For this purpose the average of the last 3/8 of all C 148 - packages is formed. The first package that exceeds this average is the first usable one. In figure 6 this start package is around 40. All C- and Fe packages before this start point are ignored. The remaining phases are separated into eight parts (see figure 7). The standard deviation sd of the last 3/8 packets is formed. sd is multiplied by constant factors f_u and f_l to determine a valid lower limit $ll = a - f_l \cdot sd$ and a valid upper limit $ul = a + f_u \cdot sd$. For iron the factors f_u and f_l usually can be set to identical values. In the case of carbon factors f_u has to be higher than factors f_l , because of the expected super-elevation caused by graphite inclusion. All packages outside the interval $ll \dots ul$ are rejected. If more than 20% of the packages are outside, the whole burn is rejected. In this case, the measurement has to be repeated.

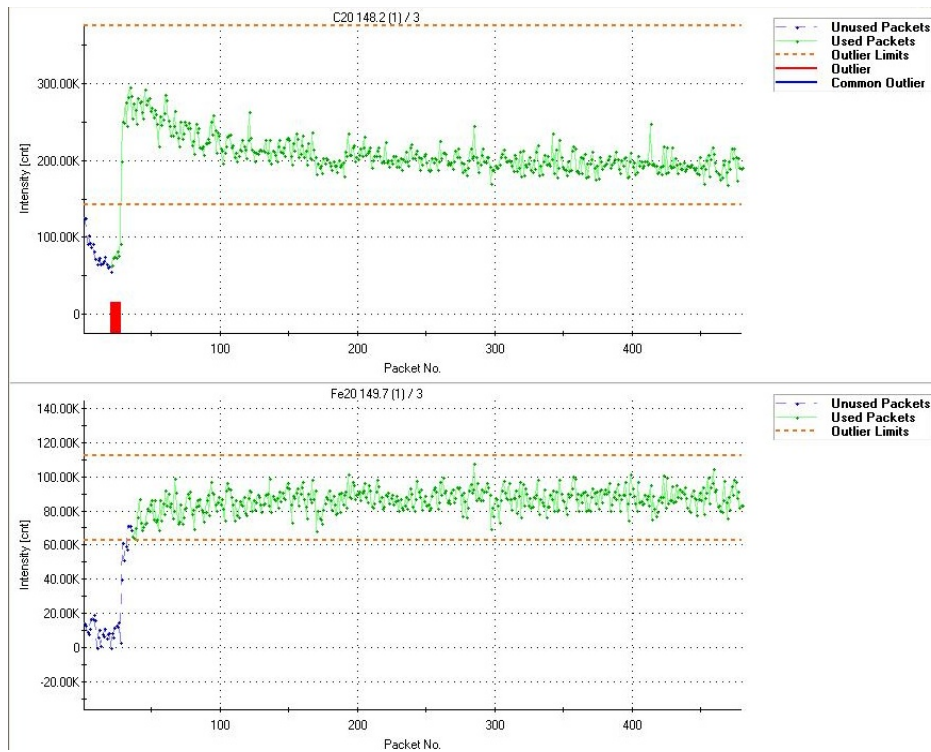


Fig. 6 Package intensities for C and Fe of a sample containing 0.5% graphite

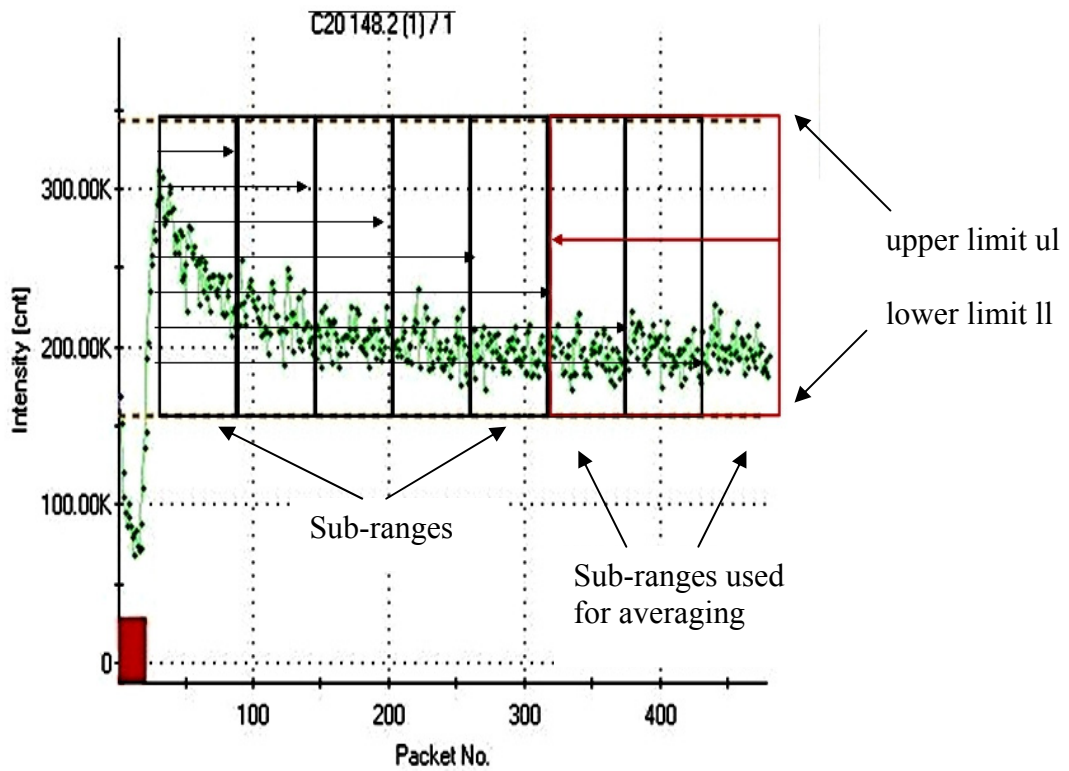


Fig. 7 Division of packets into eight parts

The next step is to calculate a series of eight carbon concentrations by using a curve for the C148 / Fe149 line pair:

- First input value for this series is the sum of all phase-1 C 148 intensities divided by the sum of all phase 1 Fe 149 intensities.
- Second input value is the sum of all phase-1 and all phase-2 C 148 intensities divided by the sum of all phase-1 and all phase-2 Fe 149 intensities.
- Third input sums up all phase-1, phase-2 and phase-3 intensities and so on.

The last point of the sequence represents the concentration calculated from the line pair C148/Fe149 using all valid sparks of the preburn time. It will be used later on.

If there is free graphite, there is a decay. The function of this decay can be fitted by a polynomial of second degree. Figure 8 shows an example. The coefficients a_2 and a_1 of this polynomial can be used to form a classification number $k = -a_2/a_1$.

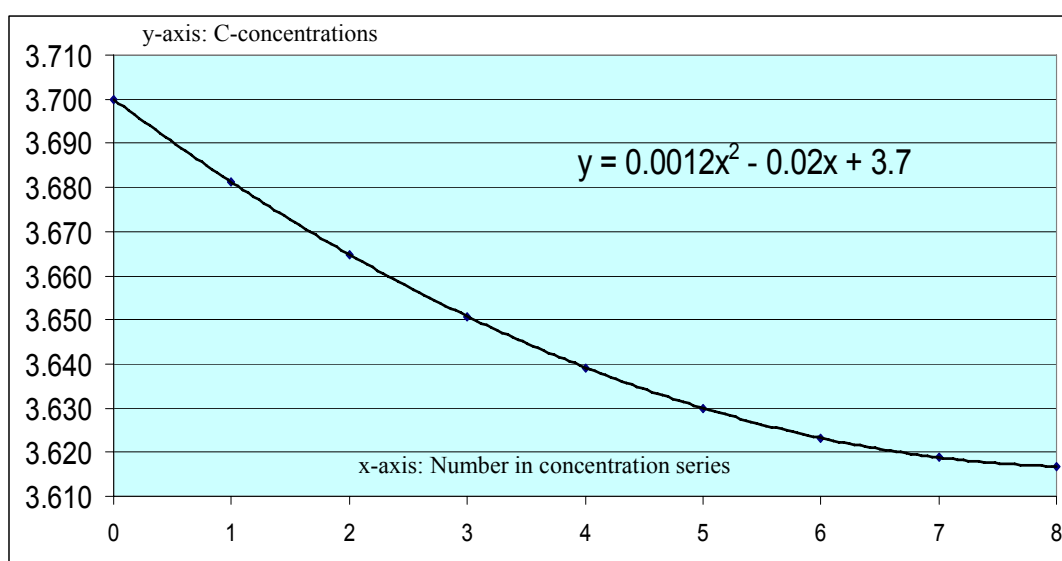


Fig. 8 Decay of C/Fe concentrations

In the case that there is no free graphite at all, a_2 and a_1 both are zero and also k is zero. A strong decay always will cause a high k . Finally, three limit-levels I_1 , I_2 and I_3 are determined empirically. There are four cases to distinguish.

$k < I_1$ or no Mg and no Ce present:

Carbon is calculated the conventional way using C193/Fe187.7 after preburn

$I_1 < k < I_2$:

C is calculated as an average of the conventional C193/Fe187.7 line pair and the preburn line pair C148/Fe149

$I_2 < k < I_3$

C is calculated using the preburn line pair C148/Fe149

$k > I_3$

The burn is rejected. The sample has to be re-measured

Using the method described, all of the 16 sample pairs showed a good accuracy in carbon determination.

Table 2: Results of the new method compared to combustion determination

Sample	C (conventionally measured by S-OES)	C (determined using new method of this paper)	C (combustion)
1a (slowly chilled, <= 0.2% graphite)	3.54	3.63	3.623
1b (very slowly chilled, >=0.5 % graphite, same heat as sample 1a)	3.19	3.64	3.679
Difference	0.350	-0.010	-0.056
8a (slowly chilled, <= 0.2% Graphit)	3.58	3.66	3.589
8b (very slowly chilled, >=0.5 % graphite, same heat as sample 8a)	3.29	3.62	3.664
Difference	0.290	0.040	-0.075
16a (slowly chilled, <= 0.2% graphite)	3.52	3.69	3.599
16b (grey, >=0.5 % graphite, same heat as sample 16a)	3.15	3.68	3.666
Difference	0.370	0.010	-0.067

Conclusions

The method described makes it possible to detect if there is any free graphite in real life samples. It is possible to create a warning signal as soon as a sample is containing a critical level of graphite. Graphite-caused C-determination errors could be reduced significantly. The differences to the results of the combustion methods were below 0.1% for all samples examined.

Literature

- [Kip1974] Kipsch: Lichtemissions-Spektrometrie, VEB Deutscher Verlag für Grundstoffindustrie, Leipzig 1974, pages 97ff
- [Hor1973] Horvath/Répási/Szabo: OE Patent No 341 809 vom 20.3.1973, page 2, line 35 - page 3, line 5
- [Wei1996] Weiss, Z. : Analysis of graphitized cast irons by optical emission spectroscopy, Spectrochimica Acta Part B, 1996 Vol. 51, Issue 8, pages 863f and 870-876

TRACEABLE ANALYSIS OF IMPURITIES IN METALLIC REFERENCE MATERIALS USING GD-MS

Sebastian Recknagel, Heinrich Kipphardt, Britta Lange, Marion Hoppe

*BAM Federal Institute of Materials Research and Testing;
Richard-Willstätter-Str. 11 - D-12489 Berlin, Germany*

The traceability requirements for certification analyses of reference materials are much more stringent than for routine analysis, where certified matrix reference materials (CRM) can be used for calibration and to establish traceability. Although the ISO-Guides related to CRM production and certification are not fully clear concerning calibration, many established CRM-producers do not accept matrix-CRMs for calibration in case of certification analyses, e.g. to avoid circular reasoning. These requirements limit the methods used for certification to those that can be calibrated using standards of known high purity and stoichiometry or mixtures of such standards. Powerful solid sampling techniques such as glow discharge mass spectrometry (GD-MS) or spark-optical emission spectrometry (SOES), where usually compact CRMs are used for calibration, seem not be applicable for certification analyses. Especially GD-MS is a powerful tool for trace element determination of solid samples. Beside metallic impurities the use of specific gas mixtures enables also the determination of interesting non-metallic impurities such as sulfur and phosphorus. Within BAM a calibration approach, was developed which enables to use mixtures of standards of known high purity and stoichiometry also for GD-MS. Analogue to matrix adaption in solution based techniques, the calibration approach is based on doped pressed powder pellets. Approach and application on the certification analyses of copper and steel CRMs are presented.

Introduction

Glow discharge mass spectrometry (GD-MS) is an excellent tool to determine very low mass fractions of analytes in different materials and can be favourably used for the analytical characterization of semiconductor materials and of high-purity metals [1], such as highly purified copper or iron. Benefits are the extremely low limits of quantification (LOQs), the wide multi-element capability, and the direct solid-sampling technique avoiding losses and contamination caused by wet-chemical pre-treatment. A drawback of the method are the rather high LOQs for non-metallic elements when only Ar is used as discharge gas. This is due to the high ionisation potentials of many non-metallic elements (e.g. P, S) which leads to a rather low ionisation efficiency. A possible approach to overcome this problem is the use of Ar-He-mixtures as discharge gas.

A second drawback of the method is, as for all solid sampling techniques, the necessity to calibrate with solid calibration samples of known composition and which are similar to the samples to be analyzed, which can be realized by e.g. existing certified reference materials (CRM) of similar matrix.

If solid sampling techniques should be used for certification analysis of reference materials, specific requirements for calibration exist to achieve metrologically traceable results. The use of matrix CRM for calibration purposes is often undesirable for certification analysis. ISO 35 defines direct traceability to SI units as preferred option to establish traceability of a certified reference material [2]. Following common understanding this can best be achieved by using pure substances and avoiding matrix-CRMs for calibration. A promising approach for the application in solid sampling techniques is the preparation of doped pressed powder samples.

Preparation of calibration samples

In our investigation metal powders doped with solutions of analytes were used to ensure a very fine grained distribution of the analytes in the samples and later on in the plasma. The calibration samples were prepared from high purity metal powders (Alfa Aesar, Johnson Matthey) doped with definite trace contents of analytes, dried and then pressed to pellets. The purity of the metal powders was 99.999% (metals basis) and the grain size was <150 µm. The calibration samples were prepared by wet doping of the pure metal powder with defined volumes of

multielement standard solutions prepared from monoelemental stock solutions (Merck KGaA; Teknolab A/S; Alfa Johnson Matthey). The doping procedure was carried out in a clean bench (class 10). The matrix metal powders were deposited in plastic vessels and then doped with the standard solutions using microliter pipettes. Each doping step was followed by a drying step of the doped powder sample using an infrared lamp. The masses of the powder samples (3-5 g) and the volumes of the solutions (400-500 μL) used for doping of the powders were taken such that on the one hand no part of the doped volumes of solutions could contact the walls of the plastic vessels and that on the other hand more than half of the volume of powder samples was saturated by the doped volumes of solutions. These conditions were regarded as prerequisites to achieve quantitatively doped and homogeneous calibration samples at the end of the sample preparation. Losses of analytes would have been expected if the doping solutions had contacted the walls of the plastic vessels. On the other hand the homogenisation process of the final powder samples was supposed to be impaired if the penetrated portion of powder volume was much smaller than 50% [3].

GD spectrometer and working conditions

An Element GD (Thermo Fisher Scientific) glow discharge mass spectrometer was used for these investigations. It is a double-focusing mass spectrometer enabling mass resolutions of 400 (low resolution), 4,000 (medium resolution), and 10,000 (high resolution). The spectrometer is equipped with a Grimm type fast-flow glow discharge cell appropriate for the analysis of electrically conductive samples with a flat surface. Argon 6.0, additionally purified by a MP-2000 (Sacral Instruments, UK) rare gas purifier, was used as discharge gas. The instrument used here was equipped with an additional gas kit, to have the possibility to add another gas (in this investigation helium 6.0) to the argon discharge gas [4]. The working conditions of the GD-MS instrument are given in Table 1.

Table 1: Element GD working conditions

Parameter	Values
GD current	50 - 60 mA
GD Ar gas flow rate	280 - 450 mL min ⁻¹
GD He gas flow rate	0 - 300 mL min ⁻¹
GD voltage	600 - 1400 V
Peltier cooling	15° C
Cones	Nickel
Flow tubes, caps	Steel

Certification of BAM-M390, BAM-M391 and BAM-M392

In the years 2004 to 2006 BAM certified a set of pure copper calibration CRMs with different contents of up to 20 trace elements [5,6]. Since the mass fractions (w) of P, Fe and Sn of these CRMs were rather high, an additional set of three CRMs with lower contents were produced. The aim was to get CRMs with $w(\text{Fe}) < 1 \text{ mg kg}^{-1}$, $w(\text{Sn}) < 1 \text{ mg kg}^{-1}$ and $w(\text{P})$ of 1 mg kg^{-1} , 3 mg kg^{-1} and 7 mg kg^{-1} . The determination of phosphorus below mass fractions of 10 mg kg^{-1} is not an easy task. ICP-OES with a sensitive instrument and photometric methods are suitable. Beside these wet chemical methods GD-MS can be used as alternative method. To enhance the sensitivity especially for the element phosphorus, a mixture of Ar and He was used as discharge gas. Fig. 1 shows the signal enhancement for phosphorus (7.2 mg kg^{-1}) after addition of He to the Ar discharge gas (chart (c)). Chart (b) which shows the signal enhancement after increasing only the discharge current from 50 to 60 mA is given for the purpose of comparison. Chart (a) shows the original peak intensity under the discharge conditions usually applied. The comparison showed that even for phosphorus with its relatively low ionization potential helium addition led to a greater intensity increase (factor 2.5) than observed with the increase of the discharge current.

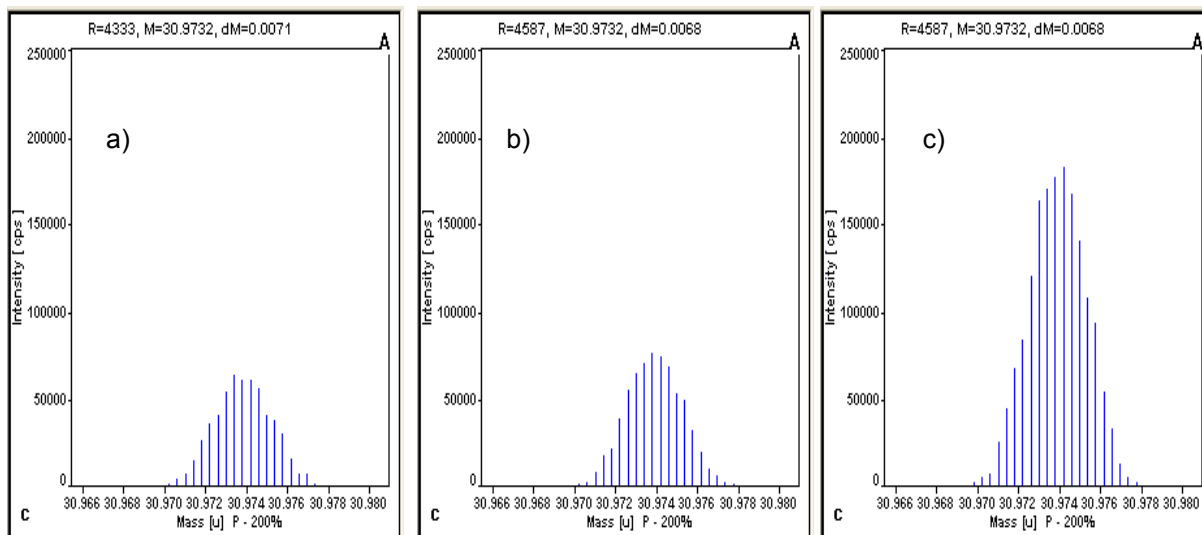


Fig. 1: Influence of discharge current (DC) and He-addition (Ar: 370 mL min⁻¹) on the intensity of the phosphorus-signal [4]

a) DC: 50 mA; He: 0 mL min⁻¹ b) DC: 60 mA; He: 0 mL min⁻¹ c) DC: 50 mA; He: 100 mL min⁻¹

Fig. 2 shows the results of the certification interlaboratory comparison for phosphorus in BAM-M390. In total seven laboratories participated in this certification project. It can be seen that GD-MS results were in good agreement with the results received from wet chemical methods. The same holds for the element iron, GD-MS results agreed well with the results of wet chemical methods (ICP-OES, ICP-MS, graphite furnace atomic absorption).

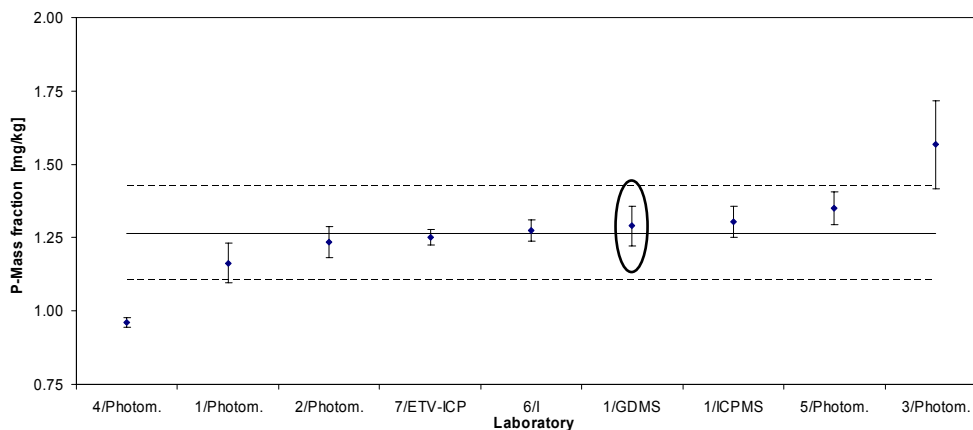


Fig. 2: Results of the certification interlaboratory comparison of BAM-M390 (element: phosphorus)

Table 2: Certified values in BAM-M390, -M391 and -M392

	BAM-M390	BAM-M391	BAM-M392
P	1.3 ± 0.4	3.3 ± 0.5	7.0 ± 0.5
Fe	0.79 ± 0.20	0.90 ± 0.21	0.80 ± 0.17
Sn	(< 0.1)	(< 0.1)	(< 0.1)

Tin as the third element of interest was present in the three CRMs only below 0.1 mg kg⁻¹. It was therefore only detectable with GD-MS and ICP-MS. The certified and informational mass fractions of P, Fe and Sn in the CRMs

BAM-M390, -M391 and -M392 are given in Table 2. The CRMs are available in form of discs (diameter: 40 mm, height: 30 mm).

Certification of ECRM 270-1 high alloy steel 1.4835

Within the framework of the EURONORM CRM Producers Group ECRM 270-1 was produced and certified, managed by the Nordic CRM Working Group. Beside the typical steel elements (C, Si, P, Mn, S, Cr, Ni etc.) also La and Ce were certified. In addition several rare earth elements were determined by two of the participating laboratories, BAM used GD-MS, another laboratory used HR-ICP-MS. For calibration of the GD-MS instrument doped powder pellets were used. Table 3 shows the composition of the pellets used for calibration. The matrix of the steel was simulated using pure metal powders (21 % Cr, 11 % Ni; 1.5 % Si; 66.5 % Fe) which were mixed very thoroughly before doping the mixture with aqueous standard solutions. A blank sample was produced using only the metal powder mixture, doped with pure acid instead of elemental standard solutions.

Table 3: Mass fractions of the calibration set used for measurement of ECRM 270-1 by GD-MS

	w(Std 1) / %	w(Std 2) / %	w(Std 3) / %	w(Std 4) / %
Ce	37.5	75	300	600
Dy	0.0625	0.125	0.5	1
Er	0.000625	0.00125	0.005	0.01
Gd	6.5	12.5	50	100
Ho	0.000625	0.00125	0.005	0.01
La	25	50	200	400
Lu	0.000625	0.00125	0.005	0.01
Nd	6.5	12.5	50	100
Pr	3.125	6.25	25	50
Sc	0.00625	0.0125	0.05	0.1
Sm	0.003125	0.00625	0.025	0.05
Tb	0.03125	0.0625	0.25	0.5
Tm	0.000625	0.00125	0.005	0.01
Y	0.00625	0.0125	0.05	0.1
Yb	0.000625	0.00125	0.005	0.01

Matrix: 21 % Cr; 11 % Ni; 1.5 % Si; 66.5 % Fe

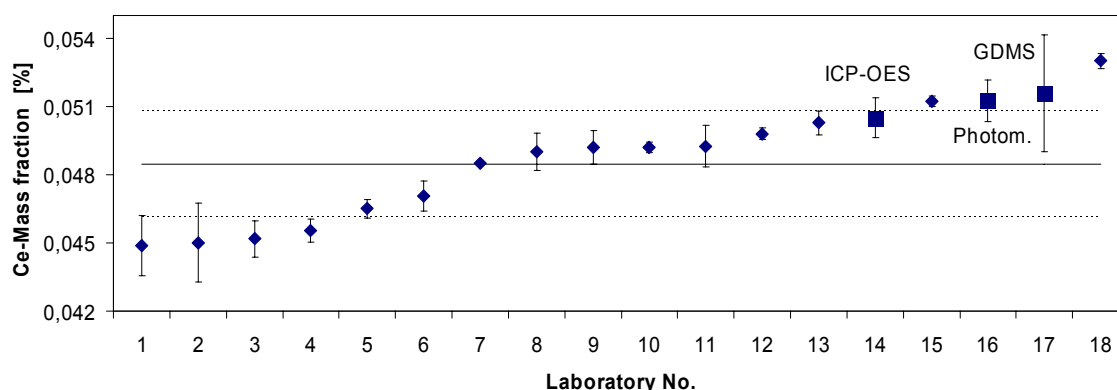


Fig. 3: Results of the certification interlaboratory comparison of ECRM 270-1 (element: cerium; ■ BAM-result) GD-MS results for Ce (see Fig. 3) as well as for La agreed well with the results of other laboratories. In addition Ce was determined using ICP-OES and spectrophotometry and the results showed good consistency. In Table 4

the results of GD-MS analysis of several rare earth elements are compared to results obtained with high resolution ICP-MS after decomposition. Except of Gd, Sm and Y the results agreed well.

Table 4: Comparison of mass fractions in % obtained by GD-MS vs. HR-ICP-MS

	HR-ICP-MS	GD-MS	ICP-OES
Dy	0.014	0.015	
Er	0.0038	0.0046	
Gd	< 0.2	1.3	
Ho	0.0015	< 0.002	
Lu	< 0.001	< 0.002	
Nd	73.5	78.8	74.5
Pr	29.5	29.5	
Sc	< 0.02	< 0.006	
Sm	0.079	< 0.006	
Tb	< 0.045	0.033	
Tm	< 0.002	< 0.002	
Y	0.18	0.014	
Yb	< 0.003	< 0.001	

Conclusion

If reference materials are characterised in a certification interlaboratory comparison it is always desired and advantageous to use different analytical techniques for the determination of the different constituents. Today most of the laboratories use ICP-OES since it is a robust and time saving method suitable for multi element analysis. In this study it was demonstrated that GD-MS is a valuable tool for certification analysis of metallic materials. In addition GD-MS as solid sampling technique offers the opportunity to avoid possible errors of wet chemical analysis techniques, e.g. caused by incomplete dissolution of the test sample. Applying pressed powder samples doped with solutions of analytes allows a calibration with rather direct SI traceability which is a requisite for certification analysis of reference materials. However, the doping procedure of the metallic powder samples must be carried out without losses of analytes at the walls of the plastic vessels and without contamination. With argon-helium plasma gas, linear calibration curves for phosphorus down to the $\mu\text{g kg}^{-1}$ range could be established with high sensitivity and very good linearity using pressed powder samples for calibration. Calibration for such a low mass fraction range was impossible when pure argon alone was used as discharge gas. The LOQs (9s) of phosphorus could be decreased about threefold.

References:

- [1] A.P. Mykytiuk, P. Semeniuk, S. Berman, Spectrochim Acta Rev 13 (1990) 1–10
- [2] ISO Guide 35 Reference materials: General and statistical principles for certification; ISO/REMCO, 2006
- [3] R. Matschat, J. Hinrichs, H. Kipphardt, Anal. Bioanal. Chem. 386 (2006) 125-141
- [4] B. Lange, H. Kipphardt, R. Matschat, Anal. Bioanal. Chem. 389 (2007) 2287-2296
- [5] B. Lange, S. Recknagel, M. Czerwensky, R. Matschat, M. Michaelis, B. Peplinski, U. Panne, Microchim Acta (2008) 160: 97–107
- [6] B. Lange, S. Recknagel, S. Richter (2006) Certification report BAM-M381 - 384. Certificates. BAM, Berlin, http://www.rm-certificates.bam.de/en/certificates/non_ferrous_and_alloys/copper/index.htm

THE EVOLUTION OF MINIMUM SAMPLE MASS OF RMS BY HOMOGENEITY STUDY

Xu Jianping¹, Hu Xiaoyan², Xue Nan³

¹ Wuhan University of Science and Technology,

² Central Iron & Steel Research Institute,

³ China Metallurgical Information & Standardization Institute

Abstract:

The formula (7) for evaluating the minimum sample mass was deduced. The results are reasonable in practical use for evaluating the minimum sample mass in Chinese RMs (powder or chips).

1 INTRODUCTION

Homogeneity testing is an essential task in the preparation and certification of reference materials (CRMs). The homogeneity study includes between-bottle and within-bottle testing, in ISO guide 35. The between-bottle homogeneity study has been carried out in the preparation of CRMs, but the within-bottle homogeneity study has been tested seldom. So the problem is that the minimum sample mass are conservative and unreasonable in the certificates of CRMs. It is much greater than the real one. Another problem is some less sample consume micro-analytical techniques need use RMs and want to know how much sample mass can be sampled.

For some very sensitive or micro-analytical techniques such as electrothermal atomic-absorption spectrometry (ETAAS), particle-induced X-ray emission (PIXE), neutron activation (NAA), etc., who require only minute amounts of material (sub-mg to several mg) for single determination, the minimum sample mass should be studied in the preparation and certification of reference materials. Papers[2-7] report the evaluation of the minimum sample mass for the use of RMs in sensitive or micro-analytical techniques. But these minimum sample mass is not on the certificate of RMs and is much smaller than that on it. There are some reports about it in China. Paper[3,14] report that the sample size of many elements of NIST RM2703 were 0.8 to 1.4mg, which were the results of analysis of NAA and judged with Ingamells model. Paper[10] reports that the minimum sample mass of Chinese Geostandards reference Materials may be about 20mg, rather than 100mg (which means as the minimum sampling mass of geological reference materials widely used). The paper[11] reports that if a soil sample was pretreated under high temperature and grinded repeatedly until 99 % of the sample powder is $\leq 30\mu\text{m}$ in size, the minimum analytical mass may be 1mg.

The real minimum sample mass can be find out with some less sample consume micro-analytical techniques methods such as mentioned above, if the sample mass decrease to that size with a high precision balance. The first, getting the micro-analytical techniques and a high precision balance prepared and having within-bottle homogeneity tested are not the general tasks for most RMs producers. And then, the real minimum sample mass is not necessary in most cases. So evaluating the minimum sample mass from the existent data of the between-bottle homogeneity test is a useful work.

2. BETWEEN-BOTTLE HOMOGENEITY STUDY

Homogeneous means no difference between the values of this characteristic from one part (item) to another. However, in practice a material is accepted to be homogeneous with respect to a given characteristic if a difference between the values of this characteristic from one part (or item) to another is negligible when compared to the uncertainty component from characterization. The between-bottle homogeneity test always has been carried out in preparation of RMs according to the model recommended by ISO Guide 35. So S_{bb} , S_{among} , S_{within} ect. can be evaluated by using analysis of variance. The sampling variance (S_{sh}) can also be evaluated if paying attention to separate the measurement method variance from the total variance (S_T). S_T is the total variance of

homogeneity test. The total standard deviation combine of sampling standard deviation with measurement standard deviation in the sample size of homogeneity test. This means as formula(1). The s_m is the variance of measurement.

$$s_{sh}^2 = s_T^2 - s_m^2 \quad (1)$$

3. THE MINIMUM SAMPLE MASS AND EVALUATION

The minimum sample mass is the smallest test portion that when drawn correctly, can be considered as being representative for the RM within the certified uncertainty. It should be relative to inhomogeneity of in-bottle. J. Pauwels[8] recommended that a different test portion sizes be examined with the micro-analytical techniques and evaluate the minimum sample mass from the testing data. Rossbach M.[5] report the results in table 1. The M(mg) is the minimum sample mass evaluating by the Pauwels formula(2)

$$M = \left(\frac{k_2' \cdot RSE}{UNC} \right)^2 m \quad (2)$$

Tab.1 Homogeneity determination of Pb, Cd in RM(lichen) by SS-AAS

Bottle No	Weight(mg)	Mean(ug/g)	M(mg)	Bottle No	Weight(mg)	Mean(ug/g)	M(mg)
041	0.191	108.2	2.51	012	0.339	0.447	13.5
121	0.222	98.0	3.85	041	0.315	0.457	8.8
161	0.222	106.4	3.71	081	0.342	0.455	8.5
191	0.211	106.0	1.92	121	0.342	0.468	6.45
Mean	0.211	103.9	3.81	161	0.335	0.426	6.1
				191	0.343	0.45	9.4
				Mean	0.336	0.451	5.6

In table 1, the minimum sample mass M is greater than the real balance weight. It means that the real balance sample mass cannot represent the total mass, but you can find out the total RSD were 4.33%(Pb), 3.11%(Cd). The sampling RSD be <1% if the measurement RSD are taken out. If so, the Ingamells model say that the "m" can be taken as the minimum sample mass. So the Pauwels formula is too conservative.

In fact, another testing for minimum sample mass is not only costly and time-consuming but also unnecessary. Even if you have a micro-analysis equipment, the minimum sample mass can not really be found, due to the lack of high-precision balance and clean laboratory environment, and the measurement or sampling error cannot be separated completely. So the minimum sample mass should be a statistical evaluated value.

The homogeneity study must be done in preparation of RMs. As a general rule, do it as ISO Guide 35 providing. If doing so, s_{bb} can be obtained by using analysis of variance. The s_{bb} often be used to evaluating homogeneity. Here, a parameter s_{sh} is used for evaluation of the minimum sample mass.

Set the sampling mass in homogeneity study is M_h , the minimum sample mass is M_m . The sampling variance due to heterogeneity is inversely proportional to the sample mass, the formula (3) and (4) is reasonable.

$$\frac{M_m}{M_h} = \frac{s_{sh}^2}{s_{ss}^2} \quad (3) \quad \text{and} \quad s_{ss}^2 = \frac{M_h}{M_m} s_{sh}^2 \quad (4)$$

Where s_{sh}^2 is the variance of sampling for homogeneity test and can be evaluated by homogeneity study. s_{ss}^2 is the variance of the minimum sample mass. The s_{ss}^2 is unknown for the minimum sample mass can not be tested. But we know that s_{ss}^2 is the variance of that sample size. The minimum sample mass of RM means that when drawn correctly, the measurement value is consisted with the certified value. The variance homogeneity should be compared if we want to know the means consistence in statistics.

4. ANALYSIS OF VARIANCE

In statistics, analysis of variance (ANOVA) is a collection of statistical models, and their associated procedures, in which the observed variance is partitioned into components due to different sources of variation. In its simplest form ANOVA provides a statistical test of whether or not the means of several groups are all equal.

Typically, however, the one-way ANOVA is used to test for differences among at least three groups, since the two-group case can be covered by a t-test (Gosset, 1908). When there are only two means to compare, the t-test and the F-test are equivalent; the relation between ANOVA and t is given by $F=t^2$.

5. WHY F-TEST AND THE POSITIONS OF VARIANCES IN F-TEST

The minimum sample mass can be used means that the measurement value of that sample size is consisted with the certified value. The means consistence can be tested by ANOVA in statistics, so F-test can be used. s_{ss} and s_{char} are equal in statistics means that F is near to 1. The s_{ss} may be very smaller than s_{char} when the sample size is equal or larger than that in characterization, so

$$F = \frac{s_{ss}^2}{s_{char}^2} \tag{5}$$

On the other hand s_{ss} may increase as the sample size decrease, when the s_{ss} is much larger than s_{char} ANOVA says the variances is not homogenous. F_{α} is a limit. $F > F_{\alpha}$ means that s_{ss} is far more than s_{char} and the measurement value of that sample size is not consisted with the certified value. So the bellow formula can be used as to evaluate the minimum sample mass

$$F_{\alpha} = \frac{s_{ss}^2}{s_{char}^2} \tag{6}$$

Let formula (5) into formula (6), the formula (7) can be found bellow:

$$F_{\alpha} = \frac{s_{ss}^2}{s_{char}^2} = \frac{M_h}{M_m} \frac{s_{sh}^2}{s_{char}^2} \text{ then } M_m = M_h \frac{s_{sh}^2}{F_{\alpha} s_{char}^2} \tag{7}$$

Where F_{α} is constant from F-test table; s_{char} comes from characteration for certified value.

6. THE EVALUATION OF s_m

In formula (7), M_h and s_{char} can be found in characterization F_{α} can be found in F-test table. The s_{sh} is relative with s_m . The s_m can be evaluated bellowing.

Case 1 The homogeneity is not a problem between units. Formula (8) can be used for evaluating s_m . because s_m contains some sampling error, and 3 times sampling may decrease the sampling error to near 0. Where MS_{among} is the average variance between units.

$$s_m = \sqrt{\frac{MS_{among}}{3}} \tag{8}$$

Case 2 The homogeneity is a problem between units. The s_m more approximate to swithin. In this case the s_{bb} should be a smaller item otherwise the characterization cannot be going on, and the s_{sh} contains s_{bb} , so the minimum sample is more conservative.

6. EXPLANATION

The formula (7) shows that the less s_{sh}^2 (the variance of sampling of the test) is the less of minimum sample mass. If $s_{sh}=s_{char}$,

$$M_m = \frac{M_h}{F_{\alpha}} \tag{9}$$

for $F_{\alpha} > 1$, than $M_m < M_h$. It means that the sampling mass (M_h) can be reduced to

$$\frac{M_h}{F_{\alpha}} \quad (10)$$

for there is no significant difference between the two sizes sampling mass.

In the practice, s_{char} always greater than s_{sh} 3-5 times, $F_{0.05} = 2-3$, so the minimum sample intake of many Chinese RMs (powder or chips) maybe 20mg to 1mg. The papers [10-12] show that is true.

CONCLUSION

The minimum sample mass evaluating from formula (3) is based on statistical assumptions and statistical data, so the rationality comply with the law of statistics.

ACKNOWLEDGEMENTS:

This work is supported by The National Natural Science Foundation of China (No. 50874083), the Foundation for Distinguished Young Scientists of Hubei Province of China (No. 2009CDA044) and the Foundation of Hubei Educational Committee (No. Q20091110)

Please number tables consecutively (Tab. 1, Tab.2, ...) Do not forget to refer to the tables in the text. Place the title of the table above the table.

Reference

- [1] Certification of reference materials General and statistical principles ISO Guide 35 (2008)
- [2] Pauwels J., Vandecasteele C., Determination of the minimum sample mass of a solid CRM to be used in chemical analysis, *Fresenius J. Anal. Chem.*, 1993; 345:121-123.
- [3] Pauwels J., Hofmann C., and Vandecasteele C., On the usefulness of SS-ZAAS for the microhomogeneity control of CRM's, *Fresenius J. Anal. Chem.*, 1994, 348:418-421
- [4] Rossbach M., E. Zeiller, Assessment of element-specific homogeneity in reference materials using microanalytical techniques, *Anal. Bioanal. Chem.*, 2003, 377: 334-339
- [5] Rossbach M., Karl-Heinz, Grobecker, Homogeneity studies of reference materials by solid sampling AAS and INAA, *Accred. Qual. Assur.*, 1999, 4: 498-503
- [6] Thomas P. J., Linsinger, Pauwels J., et al, Homogeneity and stability of reference materials, *Accred. Qual. Assur.*, 2001, 6:20-25
- [7] Štupar J., Dolinšek F., Koren U., Estimation of the homogeneity of reference materials by SS-ETAAS and use of the "tape-sandwich" sample-introduction technique, *Anal. Bioanal. Chem.*, 2002, 374: 968-976.
- [8] Pauwels J., Lamberty A., Schimmel H., Homogeneity testing of reference Materials, *Accred. Qual. Assur.* 1998; 3: 51-55
- [9] Adriaan M.H. Linsinger T., Pauwels J., Uncertainty calculations in the certification of reference materials.2. Homogeneity study, *Accred. Qual. Assur.* 2001; 6:26-30.
- [10] Wang, Y M, Wang X H, He H L et al., The minimum sampling mass of Geostandards reference materials. *Geological Bulletin of China*, 2009, 28(6):804-807
- [11] Feng S. L, Cheng L., Lei Y. et al., Study on Microanalysis Reference Material for X-Ray Fluorescence Analysis, *Rock and Mineral Analysis*, 2004;23(3):179-182
- [12] Chen Y. H., Wang H.Z. Investigation on sample preparation and quantitative method for analysis of small-scale iron, steel and alloy by laser ablation inductively coupled plasma mass spectrometry. *Metallurgical Analysis*, 2009, 29(2):127
- [13] HUANG D.H., WANG P.S., TIAN W. Z. et al., Sampling Behavior of Multielements in Candidate NIST RM 2703 by Using Neutron Activation Analysis, *Journal of Nuclear and Radiochemistry*, 2009, 31(1):61-64
- [14] HUANG D.H., XIAO C. J., NI B. F. et al, Preliminary Study on Reference Material for Microanalysis Quality Control, *Atomic Energy Science and Technology*, 2009, 43(12):1123-1127

STANDARDISATION OF ICP-OES ROUTINE METHOD(S) FOR LOW ALLOY STEEL ANALYSIS

Maria Pelé

CTIF, 44 av Division Leclerc, 92310 Sèvres, France

Abstract

By itself, this presentation has not a technical content related to the ICP-OES technique. It is the "anatomy" of a process for passing from a "single idea" until the standardisation of "Multi-elemental method(s) of analysis of low alloyed steels by ICP-OES".

The idea "grew" from the following thought: "When wet chemistry determinations are carried out in steel industry laboratories, the analytical method most commonly used is the ICP-OES. Laboratories have developed and validated in a more or less extensive way their own method. In case of disputes, such in-house methods are not always accepted. There is no standard treating this subject."

In parallel, at the 2006 CETAS conference, during the discussions on the presentations in the field of "Certification, Traceability, Standardization", the lack of availability of recognized routine methods, like ICP-OES, namely - was deeply underlined.

Since 2006, two methods were registered, related with "Low alloy steel analysis by ICP-OES" within the ECISS/TC 102 work program: one is published now and the other remains at the "working draft" stage, whilst its precision test is achieved and evaluated.

The presentation will therefore deal with:

- The organisational part of these developments;
- Evaluation technique of the results of the related precision tests;
- Advantages and disadvantages of each method.

The difficulties met when developing multi-elemental methods will also be discussed.

The conclusion will deal with the projects for continuing the issue of standards related with the ICP-OES technique for the analysis of steel: mono and multi-elemental analysis, either on a routine or on a referee basis.

Introduction

In the title of this paper, we can find the words like "ICP-OES", "Routine method" and "Low alloy steels". The term "multi-elemental" could also be added.

This presentation deals rather with the topics above and not strictly with performances and/or recent improvements of the ICP-OES technique.

The EN standard 10351:2011, titled "Chemical analysis of ferrous materials - Inductively coupled plasma optical emission spectrometric analysis of unalloyed and low alloyed steels - Determination of Mn, P, Cu, Ni, Cr, Mo, V, Co, Al (total) and Sn [Routine method]" is freshly published.

The reason to develop such a method was because ICP-OES is the most widely used technique for wet chemistry analysis of steels. Only a few standardisation works were carried out and fewer standards were published.

The published "standards" in the field of the ICP-OES analysis of steel are:

- ISO/TR 17055 Steel — Determination of silicon content —Inductively coupled plasma atomic emission spectrometric method [0.02 to 5 %]. Issued as a Technical Report, for unsuitable precision data.
- ISO 10278 Steel — Determination of manganese content —Inductively coupled plasma atomic emission spectrometric method [0.002 to 1.5 %].
- ISO 13891-2 Steel and iron — Determination of nickel, copper and cobalt contents — Inductively coupled plasma atomic emission spectrometric method — Part 2: Determination of nickel content [0.001 to 0.3 %].
- ISO 13891-3 Steel and iron--Determination of nickel, copper and cobalt contents--Inductively coupled plasma atomic emission spectrometric method--Part 3: Determination of copper content [0.001 to 0.4 %].

- ISO 13891-4 Steel and iron — Determination of nickel, copper or cobalt contents — Inductively coupled plasma atomic emission spectrometric method —Part 4: Determination of cobalt content [0.001 to 0.1 %].
- ISO/TS 13899-1 Steel--Determination of Mo, Nb and W contents in alloyed steel--Inductively coupled plasma atomic emission spectrometric method--Part 1: Determination of Mo content [0.03 to 8.5 %]. Issued as a Technical Specification, because "commercial" standard solutions were used during the precision test.
- ISO 13899-2 Steel--Determination of Mo, Nb and W contents in alloyed steel--Inductively coupled plasma atomic emission spectrometric method--Part 2: Determination of Nb content [0.005 to 5 %]
- ISO/TS 13899-3 Steel--Determination of Mo, Nb and W contents in alloyed steel--Inductively coupled plasma atomic emission spectrometric method-- Part 3: Determination of W content [0.1 to 20 %]. Issued as a Technical Specification, as the number of participating laboratories to the precision test was insufficient.

The available standards listed here above only concern referee mono-elemental methods and only for five elements.

This appeared widely insufficient, taking into account that most of the ICP-OES instruments, for routine purposes, allow the determination of ten or more elements simultaneously.

Undertaking actions within the European Standardisation Organisation (ECISS, for steel) in order to prepare recognised method(s) describing suitable practices appeared essential, then.

Bearing in mind that the major part of the analysis work is done on routine basis, the standard(s) to be developed would be prepared regarding such aim.

What is a "routine method"?

For a better understanding, the definitions of "referee method" and "routine method" are given here below:

Referee method

Stoichiometric method or a method calibrated against pure metals or stoichiometric compounds. To be used for certification analysis or in case of arbitration.

Routine method

Method calibrated against reference materials or certified reference materials, or against standard solutions commercially available. It is widely used for control purposes (day-to-day analysis).

In both cases, the validation of the methods shall be carried out against the performances of each apparatus: sensitivity, linearity, resolution (where relevant), stability, limit of detection and also regarding the accuracy required.

These whole actions allow then the definition of the corresponding scope.

It is then easy to understand that the validation of a "routine method" requires the same steps as a "referee method".

This "requirement" is not always well taken into account when dealing with "routine method", even by laboratories participating to exercises such as the precision tests for the preparation of a standard.

Lacks of linearity of the calibration curves, or lacks in connection with the sensitivity criteria were brought to light during the precision tests. The laboratories concerned have justified these problems, stating that "routine methods" do not require full optimization of instrumental parameters...

What is unalloyed or low alloyed steel?

When developing a method of analysis, the composition of the samples to be treated with, has to be defined and limits shall be specified, in order to:

- minimise the matrix effects;
- check the availability and the suitability of the procedure of sample solution preparation.

When defining the scope of EN 10351, it appeared that definitions exist [1], [2] regarding the boundary between non alloy and alloy steels, whereas CEN/TR 10317 [3] specifies more precisely what unalloyed and low alloyed steel are:

- Unalloyed steel: Normally no element has a mass content greater than the limit values in the following list: $Si \leq 1.0 \%$; $Mn \leq 1,5 \%$; Cr and $Ni \leq 0,5 \%$; Co , Cu and $W \leq 0,3 \%$; other elements $\leq 0,10 \%$ each; B , C , P , Pb and S no limit value.

- Low alloy steels: The content of one or more elements is greater than the limit for unalloyed steels but none exceeds 5 %. The sum of these alloying elements remains under 10 %.

The scope of EN 10351 partially "respects" the definitions given above: however, the iron content was set at a minimum content level of 95 %. This restriction is widely based on the scope of the first method proposed as candidate.

The method(s)

A method developed in CTIF, describing the determination of thirteen elements in low alloy steel and cast irons by ICP-OES was distributed for comments and preliminary approval within ECISS/TC 102¹.

Its principle, for the sample solution preparation, is based on that of EN 29658 [4].

Originally, the elements included were Mn, P, Cu, Ni, Cr, Mo, Ti, V, Co, Al_{total} , Sn, Mg and Ce, but Mg and Ce were removed, as they rather belong to cast irons compositions.

The most important criticism the proposal got concerned its impossibility regarding the determination of silicon.

A proposal for issuing a second standard, specifying a routine multi-elemental method including the determination of this element (together with that of Mn, P, Cu, Ni, Cr, Mo, Sn and $Al_{soluble}$) was therefore made by Corus Ijmuiden. Figures 1 and 2 represent the principles of each method.

These principles and the related fields of application well show the limits brought by the sample preparation procedures, regarding the "extent" of each "multi-elemental" method.

The ICP-OES instruments capacities (in terms of number of elements likely to be measured) are much wider than that of the dissolution procedures, namely when these procedures do not include the use of hydrofluoric acid or fusion reagents as sodium peroxide.

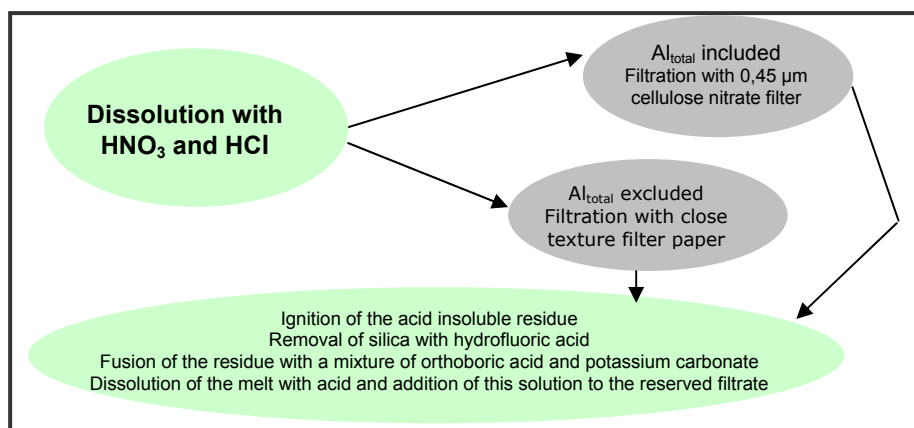


Figure 1 – Method proposed by CTIF

¹ Former ECISS/TC 20

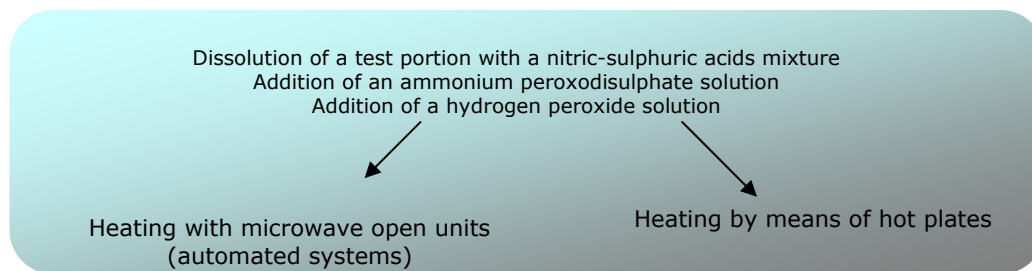


Figure 2 – Method proposed by Corus Ijmuiden

The organisation of the precision test

Table 1 summarises the scope of the method described in EN 10351, at the precision test stage.

Table 1 – Scope of EN 10351 at its precision test stage

Element	Range (%)	Element	Range (%)
Mn	0.002 - 2.00	Ti	0.002 - 0.40
P	0.005 - 0.10	V	0.002 - 0.40
Cu	0.005 - 0.80	Co	0.002 - 0.10
Ni	0.005 - 2.00	Al	0.003 - 0.30
Cr	0.005 - 1.60	Sn	0.001 - 0.10
Mo	0.005 - 0.80		

For the preparation of the precision test program, an attempt to follow the "rules" listed below was made:

- no more than 15 samples,
- inclusion of Certified Reference Materials, as much as possible,
- selecting "two samples for each range of values to be determined",

whilst respecting the specification regarding the iron content of the samples ($\geq 95\%$).

Soon, it was found that some ranges could not be properly covered. For example, samples containing about 0.005 % nickel or about 0.02 % vanadium or even about 0.05 % tin were unavailable.

The rule concerning the number of samples was respected, but lacks regarding the full covering of the scope had to be "accepted" within the precision test program.

Even if the range of each element reported in Table 1 appears relatively narrow, it is arduous to optimise the selection of the samples together with a regular distribution of the contents within each of the eleven ranges. Such selection represents one of the major steps when preparing precision tests for multi-elemental methods, but can't be perfectly achieved when the number of samples to be handled is "intentionally limited".

The experimental design of the precision test launched was a "three factor staggered-nested", with three determinations for each sample and from each laboratory:

- two determinations in repeatability conditions called 'Day 1,1' et 'Day 1,2';
- a supplementary determination in reproducibility conditions called 'Day 2'.

The participation and results

16 laboratories from 8 European countries reported results.

Keeping in mind that there were 15 samples, 11 elements and 16 laboratories, each of them producing 3 results, the number of data to handle would be of 7 920.

All the laboratories did not determine all the elements (or taken all the samples) and some samples were only appropriate for some elements (the others being below the low limit of the scopes); the number of data to be really evaluated was of about 5 000, by the end.

Some results were referred back, even if such policy is not a common one in contexts linked to the validation of a method for standardisation purposes.

The evaluation of the results

The evaluation was carried out by applying the methodology for handling the ISO 5725-1, -2 and -3:1994 standards, described in the CEN/TR 10345:2008 [5].

Usually, the statistical evaluation of a "three factor staggered-nested" design is:

- Cochran test for "Day 1,1/Day 1,2" and for "Day 1,1/Day 2", and then
- Grubbs test for "Day 1,1/Day 1,2" and for "Day 1,1/Day 2"

The methodology specified in CEN/TR 10345:

- Cochran test for "Day 1,1/Day 1,2", then
- Grubbs test for "Daily mean from Day 1/Day2", then
- Grubbs test for the "Laboratory mean value"

However, some of the results were removed before starting the statistical evaluation.

This practice it's not a common rule (even if "allowed" by the ISO 5725 standard), as it may be "interfered" by a part of subjectivity...

Nevertheless, could we "accept" as "normal" results as those shown in bold in Table 2?

The CEN/TR 10345 recommends that "a first graphical evaluation of the raw data may be performed in order to test the intra laboratory repeatability consistency by using Mandel's k test (all data included): its only purpose is to get an overview of the data population", before starting the statistical evaluation.

For some elements, this Mendel's graphical representation led to the removal of ALL the data produced by one laboratory, for the element under concern.

Table 2 – Some results for manganese (precision test of EN 10351)

	Sample D		Sample F	
Lab Z	0.0054 0.0053	0.0059	0.0287 0.0289	0.0288
Lab Y	0.0044 0.0042	0.0047	0.0153 0.0159	0.0154
Lab X	0.0079 0.0129	0.0080	0.0267 0.0265	0.0269
Lab W	0.0066 0.0064	0.0069	0.0201 0.0204	0.0218

Figure 3 illustrates such kind of situation: for eight samples on fourteen, one laboratory shown "insufficient" repeatability consistency: all its results for manganese were therefore removed.

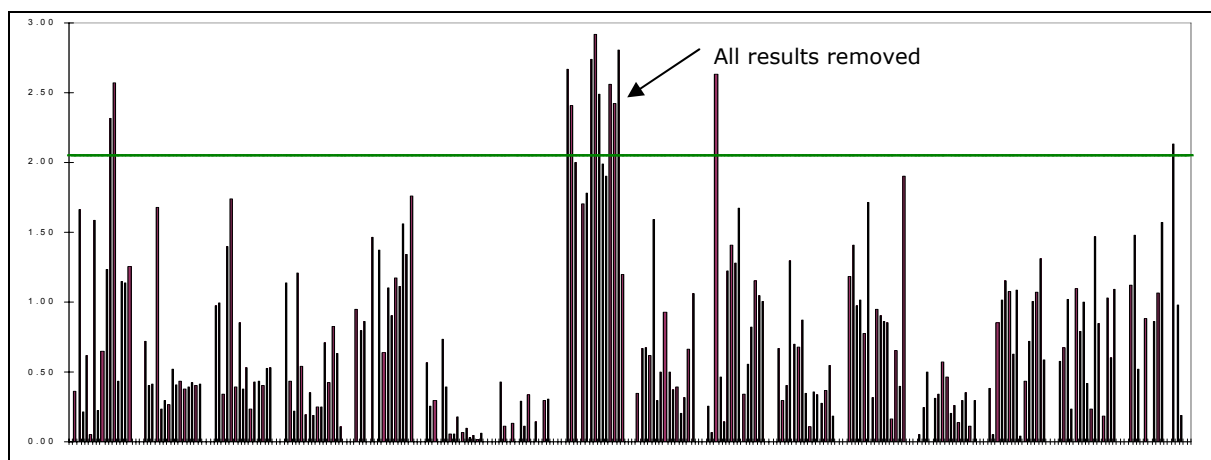


Figure 3 - Mandel's k test for the intra laboratory repeatability consistency (Mn – EN 10351)

Cochran and/or Grubbs tests lead to the removal of outliers, sample by sample. Each time all the samples related with one element are fully submitted to both these tests, a critical "inter sample" examination is done.

Such examination may result on the removal of all data from one or more laboratories, if multiple outlier or straggler values are found for these laboratories...

For example, from the statistical evaluation of manganese results related with the precision test of EN 10351, one laboratory appeared as an outlier and/or a straggler for 9 samples, whilst 15 were under examination. From this statement, the removal of all the data produced by this laboratory for the element concerned (Mn) was done and a complete second statistical evaluation of the "remaining" population had to be carried out.

The whole evaluation aims to:

- determine the mean value and the associated precision parameters "r - R_w - R", together with CV (R), Aim CV(R) and Max CV(R)²;
- evaluate the relationship between "r", "R_w" and "R" and the mean value³;
- "derive" the smoothed values of "r, R_w and R", together with that of "CV (R), Aim CV(R) and Max CV(R)";
- check if "r < R_w < R" **IN ALL CASES**;
- compare the smoothed values of "R" with that available from other published standards;
- to get an assessment of the trueness.

Figure 4 shows the relationships between lg r, lg R_w and lg R and lg m related with the manganese determination specified in EN 10351: the coefficients of correlation of each relationship are "satisfactory" (as they are widely above 0.7).

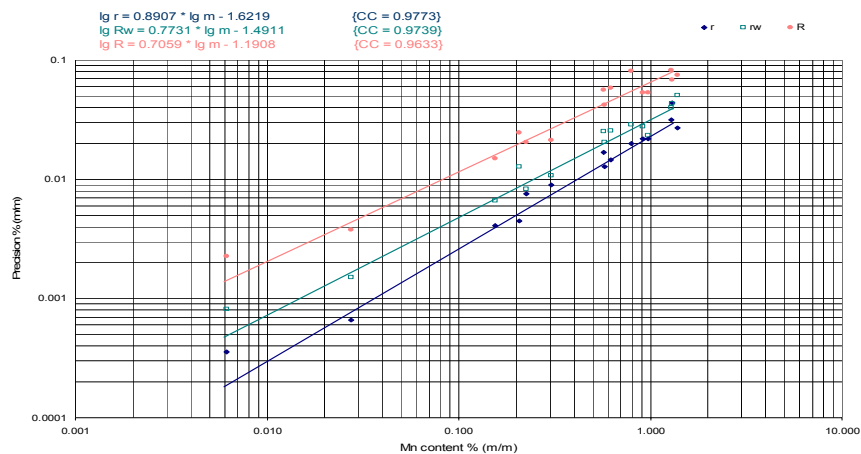


Figure 4 - Relationships between lg r, lg R_w and lg R and lg m (Mn – EN 10351)

The relationships shown above allowed therefore the calculation of the smoothed values of the precision parameters, collected in Table 3. These values, demonstrate that:

- the condition "r < R_w < R" is fulfilled for all levels;
- all CV(R) values are < Max CV(R).

Table 4 gives an example of the comparison between the smoothed values for R (V – EN 10351) with those corresponding to other standardised methods. For vanadium, EN 10351 shows reproducibility data that are equivalent or even better than that characteristic of ISO 4942, which is a spectrophotometric referee method.

Concerning the assessment of the trueness, among the eleven elements treated, it was found that the data available for titanium were insufficient. Table 5 illustrates this lack.

These unsatisfactory results led to the removal of titanium from the scope of EN 10351.

Other adjustments of the initial scope of EN 10351 were also carried out, as shown in Table 6.

² r: repeatability limit; R_w: intralaboratory reproducibility limit; R: reproducibility limit; CV(R) = $\sigma R \cdot 100 / \text{mean value}$; Aim CV(R) = $(\text{mean value})^{-0.3466} \cdot 1.477$; Max CV(R) = $(\text{mean value})^{-0.3466} \cdot 3.247$

³ The coefficient of correlation of each of these three relation shall be at least 0.7

Table 3 – Smoothed values of the precision parameters (Mn - EN 10351)

Content (%)	r	R _w	R	CV(R)	Aim CV(R)	Max CV(R)
0.005	0.0002	0.0005	0.0015	10.93	9.27	20.37
0.01	0.0004	0.0009	0.0025	8.92	7.29	16.02
0.02	0.0007	0.0016	0.0041	7.27	5.73	12.60
0.05	0.0017	0.0032	0.0078	5.55	4.17	9.17
0.1	0.0031	0.0054	0.0127	4.53	3.28	7.21
0.2	0.0057	0.0093	0.0207	3.69	2.58	5.67
0.5	0.0129	0.0189	0.0395	2.82	1.88	4.13
1	0.0239	0.0323	0.0644	2.30	1.48	3.25
2	0.0443	0.0552	0.1051	1.88	1.16	2.55

Table 4 – Comparison between the smoothed values for R (V – EN 10351) with those corresponding to other standardised methods

Content (%)	EN 10351	ISO 4942 [MAS]	EN ISO 4947 [Potentiometric titration]	ISO 9647 [AAS]
0.003	0.0017			
0.005	0.0022	0.0021		0.0016
0.01	0.0032	0.0032		0.0024
0.02	0.0045	0.0049		0.0037
0.05	0.0072	0.0087		0.0064
0.1	0.0103	0.0134	0.0061	0.0099
0.2	0.0146	0.0207	0.0092	0.0151
0.5	0.0233	0.0367	0.0156	0.0264

Table 5 – Assessment of the trueness (Ti – EN 10351)

Sample	Label	Referee value (%)	Value found (%)	Comment
A	ECRM 035-2	0.0030 [s : 0.0002]	0.0031	
C	IRM R8	0.23 (not certified)	0.2214	
F	ECRM 191-1	0.0088 [s : 0.0016]	0.0040	Too low
J	CRM BCS 453/1	0.073	0.0705	Low tendency
K	CRM BCS 452/1	0.031	0.0275	Low tendency
N	IRM 66	0.003 (not certified)	0.0014	

Table 6 – Scope of EN 10351

Element	Initial range (%)		Final range (%)
Mn	0.002 - 2.00	↘	0.005 - 2.00
P	0.005 - 0.10	↘	0.005 - 0.05
Cu	0.005 - 0.80	=	0.005 - 0.80
Ni	0.005 - 2.00	↘	0.01 - 2.00
Cr	0.005 - 1.60	↘	0.01 - 1.60
Mo	0.005 - 0.80	=	0.005 - 0.80
Ti	0.002 - 0.40		Removed from the scope
V	0.002 - 0.40	=	0.002 - 0.40
Co	0.002 - 0.10	=	0.002 - 0.10
Al _{total}	0.003 - 0.30	↘	0.02 - 0.30
Sn	0.001 - 0.10	=	0.001 - 0.10

The method proposed by Corus Ijmuiden, stills under validation. Its scope is not yet completely fixed. However, Table 7 summarises the possible changes.

Table 7 – Draft scope of Corus Ijmuiden method

Element	Initial range (%)		Final range "draft" (%)
Si	0.01 – 0.50	↘	0.05 – 0.45
Mn	0.005 - 2.00	↘	0.005 – 1.40
P	0.005 - 0.10	=	0.005 - 0.10
Cu	0.005 - 0.60	=	0.005 - 0.60
Ni	0.005 - 2.00	↘	0.01 – 2.00
Cr	0.005 - 1.50	↘	0.01 – 0.90
Mo	0.005 - 0.80	↘	0.005 - 0.60
Sn	0.001 - 0.10	↘	0.01 - 0.10
Al _{soluble}	0.005 - 0.20		To be removed from the scope ??

The following main remarks can be made:

- the sample preparation described can't completely dissolve samples having a combination of high chromium and substantial carbon, which leads to chromium carbide in the steel. This incomplete dissolution can also affect the determination of manganese and molybdenum in these samples. This fact represents an important weak point regarding its "robustness".
- its reproducibility is more satisfactory than that of EN 10351 for Mn, Cu, Ni, Cr, Mo and Sn (but within narrower ranges, for some elements);
- the method is not enough satisfactory (for precision reasons) for the determination of aluminium (soluble).

Conclusions

From the works described, the following should be underlined:

- When leading projects as those described in this paper, modesty should be kept in order to guarantee an objective acceptance regarding a possible "reduction" of the fields of application of the methods proposed or even a downgrading of the expected status.
- Besides the "quality" of the method itself, a precision test also shows the level of "expertise" of the participating laboratories and the "capability" of the instruments available.
- Some laboratories (a few, luckily) shown insufficient criticism on the results provided: sets somewhat inconsistent regarding their repeatability or their intra-laboratory reproducibility.
- No links between models of the spectrometers and the correspondent instrumental criteria (stability, BEC, DL...) could be found: the "quality" of the results is not related with these instrumental criteria, but rather with the skills of the staff involved.
- A personal "feeling" that spectrometers equipped with CCD detectors "seem" less "performing" than those equipped with photomultipliers rose.

In all cases, the publication of EN 10351 is to be taken as a success that encourages continuing the works for:

- issuing the second method;
- preparing other pertinent ICP-OES standards in the field of the analysis of steels.

References:

- 1) ISO 4948-1:1982, Steels – Classification – Part 1: Classification of steels into unalloyed and alloy steels based on chemical composition
- 2) EN 10020:2000, Definition and classification of grades of steel
- 3) CEN/TR 10317:2009, Iron and steel — European standards for the determination of chemical composition
- 4) EN 29658:1991, Steel — Determination of aluminium content — Flame atomic absorption spectrometric method (ISO 9658:1990)
- 5) CEN/TR 10345:2008, Guideline for statistical data treatment of interlaboratory tests for validation of analytical method

CHARPY IMPACT PROFICIENCY TEST IN MECHANICAL TESTING LABORATORIES

Gao Yifei, Deng Xinglin, Chenwu

Central Iron & Steel Research Institute, Beijing 100081, China

Abstract:

Mechanical lab proficiency test is quite different with chemical lab proficiency test. The key different point is chemical sample can be attained homogeneity through mixing or dissolution, but actually mechanical sample must be non-homogeneous in reality. So preparation of mechanical test sample is crucial for laboratory proficiency testing. There are main factors such as raw materials preparation, non-homogeneity testing, statistical design and the determination of the uncertainty of measurement of robust statistical value in mechanical laboratory proficiency test. This paper offers an example for Charpy impact proficiency test (high energy level and ultra-high energy level) using special design arc-shaped side test piece instead of a V-notch in order to ensure high repeatability, see Fig 1. According to robust statistical value, special method for evaluating the non-homogeneity of testing material and the uncertainty of measurement of robust statistical value are offered in this paper. Non-homogeneity of testing material can be determined according to equation $s_r(\bar{x}_m) \leq 0.3 \bullet s_R(\bar{x}_n)$. Among the equation, $s_r(\bar{x}_m) = s_r(x_i) / \sqrt{m}$, repeatability standard deviation; $s_R(\bar{x}_n)$, the reproducibility standard deviation of the lab number p for n times measurement average value (for the proficiency test is normalized IQR); $s_r(x_i)$, the repeatability standard deviation for single measurement; m is the m times duplicate measurements. Standard uncertainty for robust statistical value can be evaluated according to $u = 1.25 \times s^* / \sqrt{p}$, s^* is robust standard deviation, p is lab number in the equation.

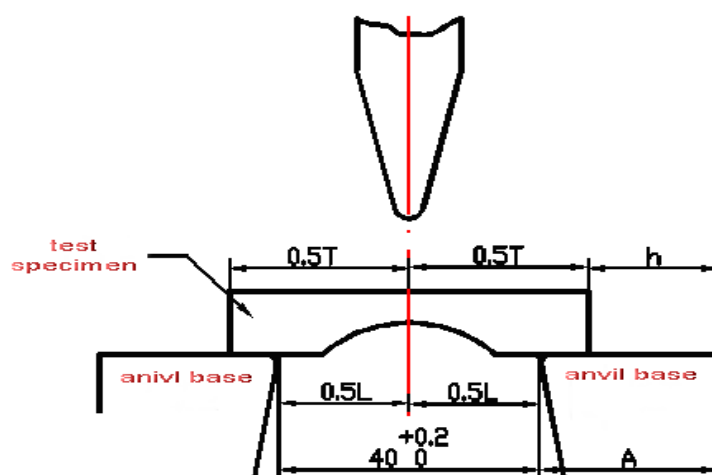


FIG. 1 Application of Reference Impact Test Specimen

INTRODUCTION

Usually the preparation of the samples for proficiency test can refer to ISO Guide 35: 2006^[1] and the statistical methods are detailed in ISO 13528^[2]. The requirements of this International Standard call for a demonstration of “sufficient homogeneity” with valid statistical methods. Because the solid metals are heterogeneous materials, actually mechanical sample must be non-homogeneous in reality. So preparation of mechanical test sample is crucial for laboratory proficiency testing. There are main factors such as raw materials preparation,

non-homogeneity testing, statistical design and the determination of the uncertainty of measurement of robust statistical value in mechanical laboratory proficiency test. Here offers an example for Charpy impact proficiency test (high energy level and ultra-high energy level) using special design arc-shaped side test piece instead of a V-notch in order to ensure high repeatability, see Fig 1.

1 The preparation of the mechanical samples

1.1 Deciding on the quantities of samples

The amount of test pieces prepared shall be sufficient to cover the non-homogeneity tests and the proficiency experiment, including some in reserve. It is preferable to prepare with one batch of commercial material. If it is possible, the test pieces can be heat-treated for stabilization and homogenization.

1.2 The machining of the mechanical samples

The test piece shall be cut and machined with precautions to minimize sample superficial work hardening and to avoid over-heating of the material probably to change the mechanical characteristics.

2 Non-homogeneity testing

When measurements have to be performed on metals and the measurements cannot be repeated on the same test piece, non-homogeneity in the test materials will form an essential component of the standard deviation of the measurement. In general, the non-homogeneity of the mechanical property value is larger than the precision (measuring error) and it is the main source of the uncertainty, because the metal is heterogeneous material. The mechanical property is affected by chemical component of the test pieces, processing, heat treatment and so on.

2.1 Characteristic number for describing the non-homogeneity

The mathematical test is the widely used method for homogeneity test. It may be of interest to perform a mathematical test for heterogeneous materials to see if the variation of property between test pieces is statistically significant. But it is not enough to use such a test to decide if the variation between test pieces can be acceptable in proficiency test program.

The non-homogeneity of the materials is described by standard deviation. Standard deviation is characteristic number for describing the non-homogeneity. The dispersion of different mechanical testing property is different. For example, the repeatability of the impact absorbed energy for reference test pieces is poor. The standard deviation of absorbed energy measured on at least 10 reference test pieces less than 5% (when absorbed energy ≥ 40 J) in ISO 148-3:2008^[3]. The maximum allowed repeatability value is 15% certified absorbed energy value of the reference material used in the indirect verification.

For example, there are n number labs to attend proficiency test, each lab offers m times duplicate measurements results.

$$s_r(\bar{x}_{in}) = \sqrt{\frac{1}{n} \cdot \sum_1^n s^2(x_i)} \quad \text{(equation 1)}$$

$$s_r(\bar{x}_m) = \frac{s_r(\bar{x}_{in})}{\sqrt{m}} \quad \text{(equation 2)}$$

2.2 Determination of acceptability for non-homogeneity

Assessment of non-homogeneity is required to establish the degree of non-homogeneity to demonstrate fitness for proficiency test program. Methods for determination of acceptability for non-homogeneity obtained under both repeatability and reproducibility conditions. The guideline is that, if the standard deviation of the average of m replicate measurements is less than (or equal to) one third of reproducibility standard deviation (here is normalized IQR), then the effect of repeatability of the test pieces can be negligible. It is $s_r \leq 0.3\sigma$ guideline.

$$s_r(\bar{x}_m) \leq 0.3 \cdot NIQR \quad \text{(equation 3)}$$

where

$$s_r(\bar{x}_m) = \frac{s_r(x_i)}{\sqrt{m}} \quad \text{Standard deviation of the average of } m \text{ replicate measurements}$$

NIQR Normalized Inter-quartile range

$s_r(x_i)$ Repeatability standard deviation

Usually the number of replicate measurements in a mechanical proficiency test is 3. The justification for the factor of 0.3 is that when this criterion is met, the repeatability standard deviation contributes no more than about 10% of the NIQR for proficiency testing. If the requirement of $s_r(x_m) \leq 0.3 \cdot NIQR$ is not met, then the number of replicate measurements made by each laboratory can be increased, or the results of the proficiency test shall be interpreted with caution. It is obvious that when we first time conduct a proficiency testing program, the reproducibility standard deviation can not previously been determined, so we do not know whether the repeatability deviation can meet the guideline, then there is a risk that repeatability variation will cause the result of the program to be erratic. So it is important that further useful information can be extracted from the data by carrying out supplementary calculating proficiency results.

3 Statistical design

When the measuring repeatability is poor, Cochran's test have to be applied to verify that no significant differences exist. It is a common experience when testing data from experiments to find data that are on the borderline between straggles and outliers, so that judgments may have to be made that affect the results of the calculation. The robust statistical methods allow the data to be analyzed in such a way that it is not required to make decisions that affect the results of the calculations. The median and normalized IQR, which are measures of the center and spread of the data (respectively), are used similarly to the mean and standard deviation. As robust statistics, the median and normalized IQR are less influenced by the presence of extreme results in the data.

For heterogeneous materials, because of the variability of the material, the test pieces can be a main source of variation, the values of repeatability standard deviation produced will not be representative of the variability experienced by test procedure. So programs designed with uniform pairs or split pairs in chemical proficiency test in order to assess within-laboratories, are unreasonable for mechanical proficiency test. Usually the statistical result for mechanical test proficiency programs is the variation between-laboratories.

4 Evaluating the measurement uncertainty of robust statistical value

The measurement uncertainty of robust statistical value is

$$u = 1.25 \times s^* / \sqrt{p} \quad [2] \quad \text{(equation 4)}$$

where : s^* robust standard deviation

p the number of laboratories

Level of confidence 95% Coverage factor $k=2$

The extended measurement uncertainty is

$$U = 2u \quad \text{(equation 5)}$$

5 An example for Charpy impact proficiency test (high energy level and ultra-high energy level)

Here offers an example for Charpy impact proficiency test (high energy level and ultra-high energy level) using special design arc-shaped side test piece instead of a V-notch in order to ensure high repeatability, see Fig 1.

5.1 Charpy impact test result data and statistic analysis

A total of 31 laboratories have participated in this proficiency test program.

Seven summary statistics (number of results, median, normalized inter-quartile range (NIQR), robust coefficient of variation (CV), minimum, maximum and range.) are calculated to describe the data. Based on robust summary

statistics, Z-score is used to evaluate the participants' results, see Table 1.

$$Z = \frac{(\text{result} - \text{median})}{NIQR} \quad (\text{equation 6})$$

Table 1 Charpy impact proficiency testing result

Code	1	2	3	Mean	Z(UH)
01	228	238	238	235	1.01
02	223	224	230	226	0.00
03	240	244	244	243	1.91
04	222	220	216	219	-0.79
05	230	240	230	233	0.79
06	232	235	235	234	0.90
07	226	225	222	224	-0.22
08	223	232	239	231	0.56
09	221	214	217	217	-1.01
10	220	220	220	220	-0.67
11	264	261	261	262	4.05§
12	256	255	265	259	3.71§
13	217	212	219	216	-1.12
14	216	217	216	216	-1.12
15	249	252	252	251	2.81*
16	223	222	226	224	-0.22
17	222	226	228	225	-0.11
18	211	225	232	223	-0.34
19	230	235	231	232	0.67
20	233	232	234	233	0.79
21	208	214	212	211	-1.69
22	222	227	225	225	-0.11
23	224	228	227	226	0.00
24	228	226	228	227	0.11
25	232	235	241	236	1.12
26	244	242	243	243	1.91
27	228	233	230	230	0.45
28	222	224	223.5	223	-0.34
29	230	226	225	227	0.11

30	222	218	220	220	-0.67
31	223	220	217	220	-0.67
No of results				31	
median				226	
normalized IQR				8.896	
robust CV				3.936%	
robust standard deviation				7.117	
minimum				211.0	
maximum				262.0	
range				51.0	

Using the labs repeatability data in proficiency test, repeatability standard deviation is calculated according to **equation 1** as followed:

$$s_r(\bar{x}_{in}) = \sqrt{\frac{1}{n} \cdot \sum_1^n s^2(x_i)} = 3.7517$$

Repeatability standard deviation for the average value of three times duplicate measurements is as followed according to **equation 2**:

$$s_r(\bar{x}_m) = \frac{s_r(\bar{x}_{in})}{\sqrt{m}} = 2.1661$$

According to equation 3 and Normalized IQR in Table 1:

$$s_r(\bar{x}_m) / NIQR = 2.1661 \div 8.896 = 0.243 < 0.3$$

The result means the non-homogeneity of samples is satisfied with equation3 requirement. It also means this proficiency test is successful.

Test result uncertainty for this proficiency test

The measurement uncertainty of robust statistical value is as followed according to **equation 4**:

$$u = 1.25 \times s^* / \sqrt{p} = \frac{1.25 \times 7.117}{\sqrt{30}} = 1.624$$

Level of confidence 95% Coverage factor k=2

The extended measurement uncertainty is:

$$U = 2u = 3.248$$

References:

- [1] ISO Guide 35:2006 Reference materials-General and statistical principles for certification
- [2] ISO 13528:2005 Statistical methods for use in proficiency testing by inter-laboratory comparisons
- [3] ISO 148-3:2008 Metallic materials-Charpy pendulum impact test-Part 3:Preparation and characterization of Charpy V-notch test pieces for indirect verification of pendulum impact machines

ANALYTICAL TREATMENT OF UNCERTAINTIES FOR A MACROSCOPIC TRIBOLOGY INSTRUMENTATION

M. Merlin, C. Soffritti, R. Vazquez, V. Mazzanti, G. L. Garagnani

Engineering Department, University of Ferrara, via Saragat 1, 44122 Ferrara, Italy

Abstract

In tribology, friction coefficient and wear rate are usually determined experimentally. The present work is aimed at investigating the measuring uncertainties associated with the evaluation of these two parameters. In particular, a standard pin-on-disk tribometer, having two pins constrained to a counterface, has been used. Varying normal load, sliding distance and test duration, a total of twenty tests have been carried out. Environmental temperature and relative humidity have been maintained constant. After the tests, a stylus profilometer has been used to acquire the wear scar profiles on the cross-sections of the disks. The wear rates have been subsequently calculated by measuring the area of the wear track cross-sections and evaluating an average wear volume.

The experimental results show that the load measurement uncertainty strongly affects the evaluation of both friction coefficient and wear rate. The information obtained are useful to optimise the experimental apparatus and/or to develop suitable procedures aimed at reducing measurement uncertainties.

1. Introduction

In the tribology field, simple testing devices known as *tribometers* are used to obtain practical data on friction, lubrication and wear. The results are always affected by scatter of data, so their reliability should be evaluated. In particular, it is common for different laboratories using similar machines and test methods to get to contradictory results. Some authors show that any change in the experimental conditions can significantly affect data repeatability and reproducibility [1,2]. Almond and Gee [3] demonstrated that the repeatability within individual laboratories is usually better than the reproducibility between laboratories and the variability in wear parameters is generally high.

Laboratory experimentation remains the most common practical method employed for the identification of friction coefficients for arbitrary material pairs. Burris et al. [4] and Schmitz et al. [5] argue that the measure of the friction coefficient is strongly sensitive to any equipment misalignment: for example, for materials with friction coefficients below 0.05 the alignment becomes hopelessly difficult if the goal is to have uncertainties below 1%. Moreover, the friction coefficient measurement depends on the material, surface, environment and measuring equipment.

The wear rate evaluation is also fundamental to predict service life of the mechanical components in relative motion. Even for nominally identical tests, the wear rate variation may be due to many factors, such as the intrinsic properties of the material pairs, surface conditions, experimental apparatus and procedure employed. Accordingly, all these factors must be necessarily taken into account for the calculation of uncertainty [6,7,9,10].

The aim of this paper is to calculate the uncertainties of the measured friction coefficient and wear rate for a given experimental apparatus as a function of uncertainty of the measured input quantities. These information can then be used for redesigning the equipment and/or the procedure in order to reduce the measurement uncertainty.

2. Materials and methods

In this experimental study a Multispecimen Tester tribometer produced by DUCOM Instruments has been used to create a reciprocating sliding contact between the two surfaces of interest. The equipment allows the user to test four different contact geometries: pin on disk, ball on disk, cylinder on disk, ball on ball and disk on disk. A wide range of test parameters, such as normal load, speed rotation, test duration, lubrication, temperature and relative humidity can also be selected. The data acquisition system permits to set the input parameters like normal load, speed rotation, temperature, and test duration using a simple interface. The output parameters like frictional torque, friction coefficient, temperature, wear, rotational speed and test duration are acquired, recorded and

displayed. In this work several wear tests have been performed using a pin-on-disk configuration, in accordance with ASTM G99-05 “Standard test method for wear testing with a pin-on-disk apparatus” [8]. A plasma-sprayed Cr_2O_3 ceramic coating with a thickness of 150 μm (powder: Amperit[®], -45 +22.5, fused and crushed) on an about 20 μm -thick Ni-20%Cr bond coat (powder: Metco 43CNS, -106 +45 μm) to improve the ceramic material adhesion, have been deposited onto circular steel plates (80 mm in diameter and 6 mm in thickness). Cylindrical steel pins of 6 mm in diameter and 22 mm in height have been used as counterpart material; all the surfaces of the pins have been also cemented for about 500 μm in thickness. Before the wear tests all the samples have been cleaned in an ultrasonic bath. The disks have been subsequently characterised by means of the portable Handysurf E35_A ZEISS-TSK rugosimeter in order to calculate the roughness parameters (R_a and R_z). Microhardness measurements (3 N load and 15 s loading time) have been carried out on polished cross-sections of the coating by a Future-Tech FM-model Vickers microindenter. The Vickers microhardness of the pins has been also determined (1 N load and 15 s loading time) on properly cleaned cross-sections, at a distance of 100 μm from the coupling surface. A mean of 15 indentations have been performed for each microhardness measurement. Microhardness and roughness of the ceramic coating and of the steel pins are collected in Table 1.

Table 1 - Microhardness and roughness of the samples.

	$\text{HV}_{1\text{N}}$ (GPa)	$\text{HV}_{3\text{N}}$ (GPa)	R_a (μm)	R_z (μm)
Cr_2O_3	-----	11.88 ± 0.45	0.15 ± 0.02	1.78 ± 0.19
Pins*	6.70 ± 0.05	-----	-----	-----

* Vickers microhardness is evaluated on the pin cross-section, at a distance of 100 μm from the coupling surface.

The LEICA MEF4M Optical Microscope (OM) on properly polished cross-sections has been employed in order to characterise the microstructure of the samples. In Fig. 1a and 1b are reported the micrographs showing the microstructure of a ceramic coating and a steel pin near the coupling surfaces. As can be seen, the investigated Cr_2O_3 coating shows the typical lamellar microstructure of a plasma-sprayed ceramic coating, while the cemented layer of the steel pin exhibits a martensitic microstructure with a little amount of carbides.

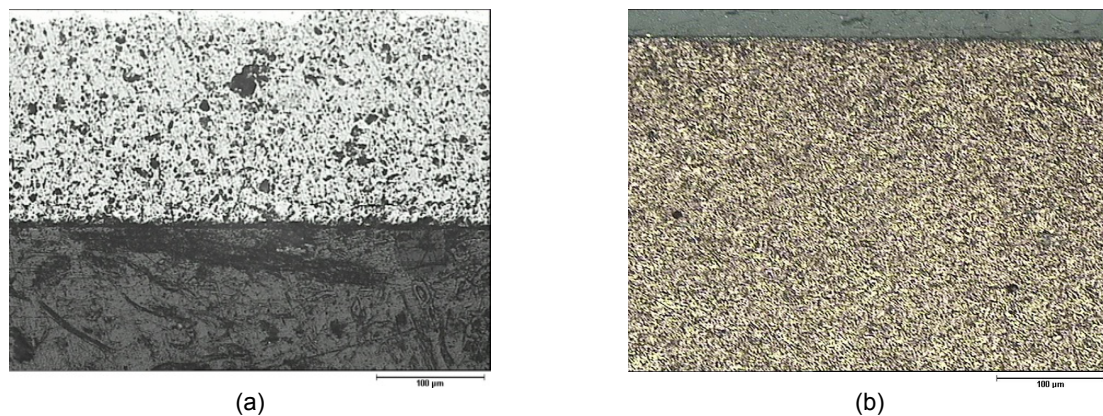


Figure 1 - Optical micrographs showing microstructure of the samples: (a) Cr_2O_3 cross-section, (b) steel pin cross-section in the cemented zone.

A total of 20 wear tests have been carried out under different test conditions. In particular, two different sets of tribological parameters have been used, varying the normal load, speed rotation and test duration. In the first one, normal loads have been fixed at 5 and 50 N, respectively, whereas a rotational speed of 100 rpm and a test duration of one hour have been maintained constant. In the second one, the values of 250, 450 and 650 N of the normal load have been selected, whereas a speed rotation of 477 rpm and a test duration of two hours have been unchanged. All tests have been performed with a relative humidity of 20%, at room temperature and in dry

conditions. Friction coefficient is an output of the equipment. Wear rate of disks has been evaluated by measuring the area of the wear track cross-section by a Hommelwerk T2000 profilometer. Each area has been used to calculate the wear volume.

The uncertainties associated with the calculation of friction coefficient and wear rate have been determined in agreement with UNI CEI ENV 13005:2000 "Guida all'espressione dell'incertezza di misura" [11]. In general, the result of a measurement is an approximation of the value of the specific quantity subject to measurement, that is the *measurand*; thus, the result is complete only when accompanied by a quantitative statement of its uncertainty. The uncertainty of the result of a measurement consists of several components, which may be grouped into two categories according to the method used to estimate their numerical values:

- Type A: those which are evaluated by statistical methods. In agreement with the Type A evaluation of uncertainty, consider an input quantity Y_i , whose value is estimated from n independent observations $Y_{i,k}$ of Y_i obtained under the same conditions of measurement. The standard uncertainty $u(y_i)$ is the estimated standard deviation of the mean:

$$u(y_i) = s(\bar{Y}_i) = \left(\frac{1}{n-1} \sum_{k=1}^n (Y_{i,k} - \bar{Y}_i)^2 \right)^{1/2} \quad (1)$$

where

$$\bar{Y}_i = \frac{1}{n} \sum_{k=1}^n Y_{i,k} \quad (2)$$

- Type B: those which are evaluated by other means, e.g. by assigning a probability distribution.

Both type of uncertainty can be indicated in terms of absolute or relative error. The absolute error is expressed by using the relevant unit and is defined as the size of the values' range in which the true value of the measurement probably lies. The relative error is usually expressed in percent, parts per thousand or parts per million and is defined as the ratio of the absolute uncertainty of a measurement to the best estimate.

In many cases a *measurand* Y is determined indirectly from n other quantities X_1, X_2, \dots, X_n through a functional relation f :

$$Y = f(X_1, X_2, \dots, X_n) \quad (3)$$

where the function f should express not simply a physical law but a measurement process, and in particular, it should contain all quantities that can contribute to a significant uncertainty on the measurement result. The combined standard uncertainty of a measurement result, suggested symbol u_c , is taken to represent the estimated standard deviation of the result. It is obtained by combining the individual standard uncertainties u_i , whether arising from a Type A evaluation or a Type B evaluation, using the usual method for combining standard deviations. This method is often called the *law of propagation of uncertainty*. An estimate of the *measurand* Y , denoted as y , is calculated from Eq. (3) using input estimates x_1, x_2, \dots, x_n for the values of the n input quantities X_1, X_2, \dots, X_n . The combined standard uncertainty of the measurement result y is defined as:

$$u_c(y) = \sqrt{\sum_{i=1}^n \left(\frac{\partial f}{\partial x_i} \right)^2 u^2(x_i)} \quad (4)$$

where the partial derivatives $(\partial f / \partial x_i)$ are often referred as *sensitivity coefficients*.

2.1 Friction coefficient uncertainty

The friction coefficient is defined as the ratio between the tangential frictional force (F_t) and the applied normal force (F_n):

$$\mu = \frac{F_t}{F_n} \quad (5)$$

The normal load is selected by the user into the software and applied by the load cell, while the tangential frictional force is calculated by means of the frictional torque (C_a) measured by a torsional load cell. Considering the arm length ($b = 40$ mm), the tangential force is determined as follows:

$$F_t = \frac{C_a}{b} \quad (6)$$

From Eqs. (5) and (6) the friction coefficient is a function of three parameters, that is:

$$\mu = f(F_n, C_a, b) \quad (7)$$

Therefore, the uncertainty of the friction coefficient is the combined standard uncertainty u_c of all the input quantities in Eq. (7), and its value is calculated by the following Eq. (8):

$$u_c(\mu) = \sqrt{\left(\frac{\partial \mu}{\partial F_n}\right)^2 u^2(F_n) + \left(\frac{\partial \mu}{\partial F_t}\right)^2 u^2(F_t)} \quad (8)$$

2.1.1 Normal force uncertainty

The uncertainties associated with the measurement of the normal force applied are of both Type A and Type B. The data acquisition system records the values of the normal load with a frequency of 45 Hz, subsequently the Type A uncertainty is evaluated in accordance with Eq. (1). Two different uncertainties of Type B are individuated based on the available information given by the instructional manual of the equipment. These uncertainties are associated with the resolution of the digital device and with the accuracy of the equipment. Accordingly, the total uncertainty associated with the normal force is:

$$u(F_n) = \sqrt{(u_A^2(F_n) + u_{B1}^2(F_n) + u_{B2}^2(F_n))} \quad (9)$$

2.1.2 Frictional force uncertainty

The uncertainties associated with the measurement of the frictional force are of both Type A and Type B. The software displays the values of the tangential frictional force, subsequently the Type A uncertainty is evaluated in agreement with Eq. (1). Three different uncertainties of Type B are individuated; the first one is related to the resolution of the caliper used for evaluating the arm length, the last ones, associated with the frictional torque measurement, are based on the available information given by the instructional manual of the equipment. The total uncertainty associated with the tangential frictional force is:

$$u(F_t) = \sqrt{(u_A^2(F_t) + u_B^2(F_t))} \quad (10)$$

2.2 Wear rate uncertainty

The wear rate (W) is calculated as the ratio between the volume of material removed by wear (V_{loss}) and the product of the normal load applied (F_n) and the sliding distance (d):

$$W = \frac{V_{loss}}{F_n \cdot d} = \frac{(2\pi r A)}{F_n \cdot (2\pi r t \omega)} = \frac{A}{F_n \cdot (t \omega)} \quad (11)$$

The variables that directly affect the calculation of the wear rate are: the area of the wear track cross-section, normal force applied, test duration and the rotational speed. Therefore, from Eq. (11) the wear rate is a function of four parameters, that is:

$$W = f(A, F_n, \omega, t) \quad (12)$$

The uncertainty of the wear rate is the combined standard uncertainty u_c of all the input quantities in Eq. (12), and its value is calculated by the following Eq. (13):

$$u_c(W) = \sqrt{\left(\frac{\partial W}{\partial A}\right)^2 u^2(A) + \left(\frac{\partial W}{\partial F_n}\right)^2 u^2(F_n) + \left(\frac{\partial W}{\partial t}\right)^2 u^2(t) + \left(\frac{\partial W}{\partial \omega}\right)^2 u^2(\omega)} \quad (13)$$

2.2.1 Wear track cross-section's area uncertainty

The area of the wear track cross-section is calculated by means of the trapezoid integration method, applied on the wear scar profile measured by a stylus profilometer. The area is determined as follows:

$$A = \sum_{i=1}^{n-1} \frac{(y_i + y_{i+1}) \cdot (x_{i+1} - x_i)}{2} \quad (14)$$

where x_i and y_i are the radial distance and the depth of the trace, respectively. The Type B uncertainties of x_i and y_i are equal and given by the instructional manual of the profilometer.

The total uncertainty of the wear track cross-section's area can be expressed as:

$$u(A) = u \cdot \sqrt{\left((n-1) \frac{\Delta x}{2}\right)^2 + \left(\sum_{i=1}^{n-1} \frac{(y_i + y_{i+1})}{2}\right)^2} \quad (15)$$

2.2.2 Test duration uncertainty

This uncertainty can be determined by combining the two Type B uncertainties related to the resolution of the acquisition system timer and to the resolution of PC clock. Accordingly, the total uncertainty of the test duration is:

$$u(t) = \sqrt{u_{B1}^2(t) + u_{B2}^2(t)} \quad (16)$$

2.2.3 Rotational speed uncertainty

The uncertainties associated with the measurement of the rotational speed are of both Type A and Type B. The software displays the values of the speed rotation, subsequently the Type A uncertainty is evaluated according to Eq. (1). The Type B uncertainties, available from the instructional manual, are associated with the resolution of the data acquisition system and with the accuracy of the equipment. The total uncertainty of the rotational speed is:

$$u(\omega) = \sqrt{u_A^2(\omega) + u_{B1}^2(\omega) + u_{B2}^2(\omega)} \quad (17)$$

3. Results and discussion

3.1 Friction coefficient

In Table 2 are collected the friction coefficient under different normal load conditions and the corresponding values of the absolute and relative uncertainties. When a 5 N normal load is applied the friction coefficient is very low and equal to 0.02, then increases proportionally to the normal load up to a value that remains almost constant for the normal loads applied of 250, 450 and 650 N. The absolute uncertainties lies in a range of values between

± 0.01 and ± 0.03 , while the relative uncertainty decreases with increasing normal force from a value of approximately 100% to 2.47%.

Table 2 - Friction coefficient under different normal load conditions and corresponding absolute and relative uncertainties.

F_n (N)	5	50	249	451	649
μ	0.02	0.09	0.38	0.41	0.41
$u(\mu)$	0.02	0.01	0.03	0.02	0.01
$u(\mu)/\mu$	100%	6.65%	6.59%	5.34%	2.47%

In order to understand and reduce these uncertainties, the analysis of the single quantities in Eq. (5) has been performed. In Figure 2 are reported the normal force (F_n) and tangential frictional force (F_t) variations under different normal load conditions. For the lowest load applied (Figure 2a) a significant amount of noise is overlapped to the signals of normal force and tangential frictional force. In particular, the plot of the normal force versus the test duration shows random peaks probably due to the control of the pneumatic system. With increasing of the normal load (Figure 2b and 2c) the noise overlapped to the signals of the tangential frictional force is the same of the previous case, while the plots of the normal force versus the test duration show quasi-periodic peaks. Moreover, when a 250 N normal load is applied, the tangential frictional force remains constant at very low value until the test duration of about 1.5 h. Then rises rapidly until it reaches the value of about $F_t = 90$ N at the end of the test. The same behaviour can be observed for a 450 and 650 N normal loads applied (Figure 2d and 2e).

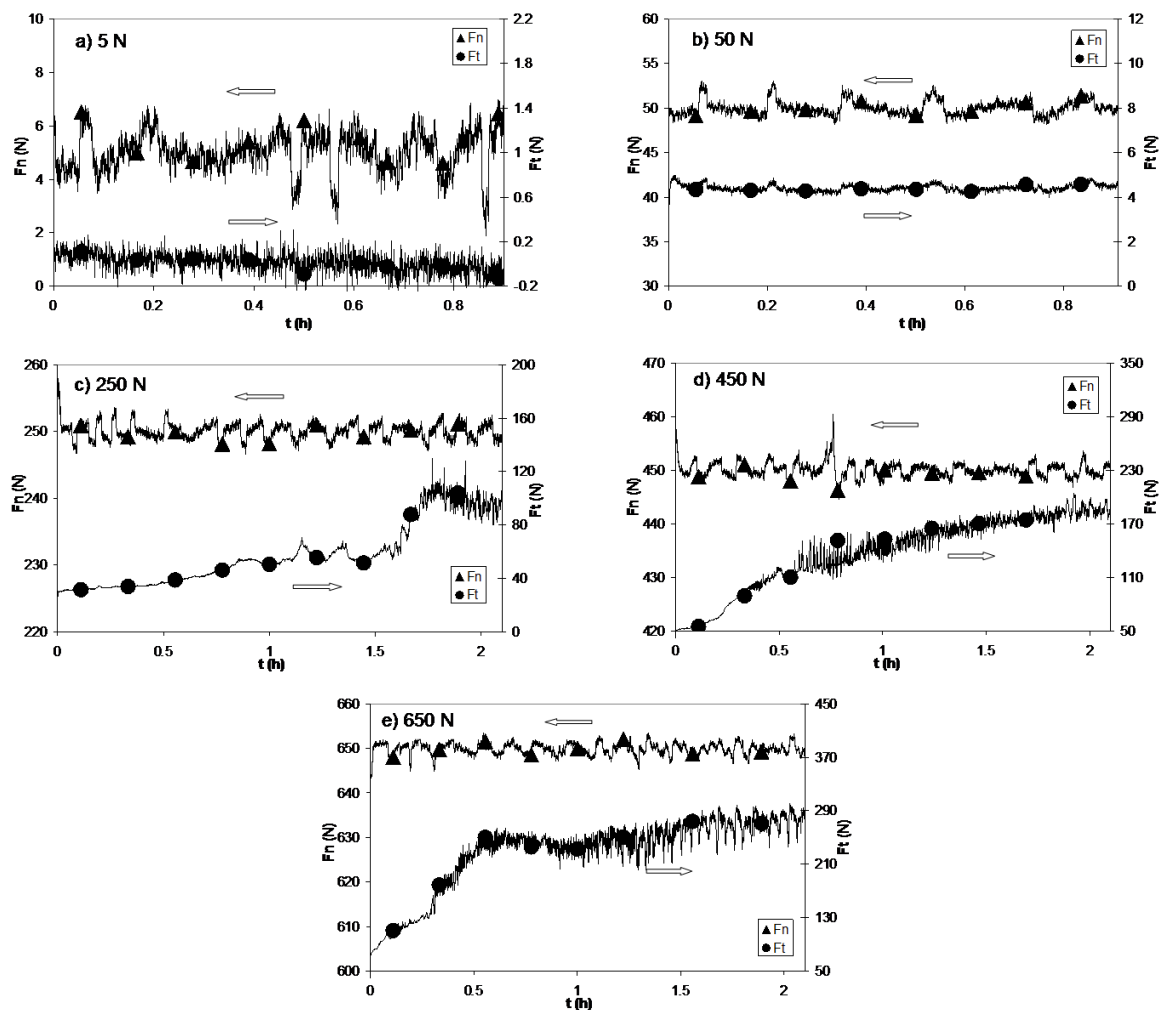


Figure 2 - Normal force and tangential frictional force variations in different conditions of normal load applied.

3.2 Wear rate

In Table 3 are listed the wear rate under different normal load conditions and the corresponding values of the absolute and relative uncertainties. The absolute uncertainty lies in a range of values between $\pm 6.10 \times 10^{-7}$ and $\pm 4.43 \times 10^{-8} \text{ mm}^3/(\text{Nm})$, while the relative uncertainty decreases with increasing normal force from a value of approximately 24.31% to about 1.30%.

Table 3 - Wear rate under different normal load conditions and corresponding absolute and relative uncertainties.

F_n (N)	5	50	249	451	649
W (mm^3/Nm)	2.51×10^{-6}	6.85×10^{-7}	5.15×10^{-7}	6.46×10^{-7}	3.46×10^{-6}
$u(W)$ (mm^3/Nm)	6.10×10^{-7}	2.25×10^{-8}	6.56×10^{-9}	8.32×10^{-9}	4.43×10^{-8}
$u(W)/W$	24.31%	3.29%	1.27%	1.29%	1.28%

In order to understand and reduce these uncertainties, the analysis of the single quantities in Eq. (11) has been performed. The total uncertainty of the speed rotation for the wear tests carried out under the lower normal loads (5 and 50 N) and for the higher normal loads applied (250, 450 and 650 N) is about $\pm 1.10 \text{ rpm}$ and ± 4.92 , respectively. The Type A uncertainty associated with the measurement of the rotational speed is in a range between $\pm 0.10 \text{ rpm}$ and $\pm 12.22 \text{ rpm}$. At lower normal loads the total uncertainty of speed rotation is mainly affected by the Type B uncertainty related to the resolution of the data acquisition system. In contrast, at higher normal loads the most important contribution is the Type B uncertainty associated with the accuracy of the equipment. For all wear test the total uncertainty of the test duration is equal to $6.50 \times 10^{-3} \text{ s}$. In particular, the Type B uncertainties of test duration are related to the resolution of the acquisition system timer and to the resolution of PC clock. With increasing the normal load applied, the area of the wear track cross-section proportionally rises in a range between 5.75×10^{-11} and $1.35 \times 10^{-7} \text{ m}^2$. In this case, the total uncertainty is in the range of $\pm 1.64 \times 10^{-12}$ and $7.12 \times 10^{-11} \text{ m}^2$.

3.2.1 Wear scar area

With the measurement of the scar area an interesting methodology has been suggested. The number of acquired points in the profile can be optimised in order to control the measurement uncertainty. The target is to identify the number of acquisitions that gives the lowest uncertainty. The evaluation of the area of the wear track cross-section (Eq. (14)) needs to determine both depth and width of the trace; only the negative depth contributions must be taken into account. The wear trace appearance strongly depends on the normal force. Generally, if the normal load applied produces a well-defined wear scar a low number of acquisition points is preferable; on the opposite, if the wear track is barely evident a high number of acquisition points is recommended. Moreover, for a limited number of points the wear trace profile can be imprecise; on the contrary, if the number of acquisition points increases the uncertainty can show a great increase too. As an example, profiles of Figure 3a and Figure 3b have been obtained by the profilometer, but with a different number of acquisition points (253 and 23, respectively).

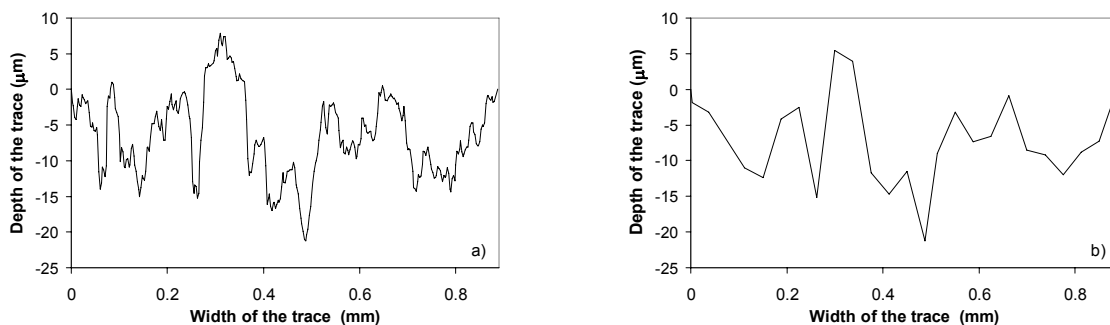


Figure 3 – Wear scar profiles obtained with: (a) 253 acquisition points, (b) 23 acquisition points.

As a function of the acquisition points, in Figure 4a are collected the relative uncertainties calculated for the wear scar area, after a wear test carried out on the Cr_2O_3 coating and under a normal load of 5 N. It is evident a minimum in the middle part of the range; on the contrary, the uncertainty is very high at both the extremes of the range. In Figure 4b are reported the contributions of both depth and width contributions to the area uncertainty; as can be noted, the best compromise for the combined uncertainty is in the range of 100-150 acquisition points.

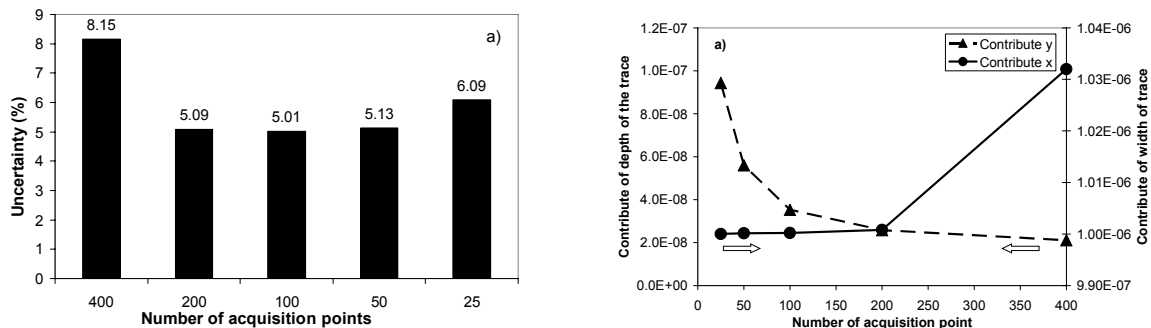


Figure 4 – Cr_2O_3 coating after the wear test performed with a normal load of 5 N: (a) uncertainty percentage and (b) depth and width contributions to the area uncertainty as a function of the number of the acquisition points.

4. Conclusions

This work shows the complexity of the tribological experimentation carried out in order to calculate the friction coefficient and wear rate for an arbitrary material pairs. The following conclusions can be drawn:

- the friction coefficient measurement is principally affected by uncertainty of the tangential frictional force, while for the wear rate the main contribution to uncertainty is the normal force;
- in order to obtain a significant result and to design the appropriate procedure necessary to reduce the uncertainty, is important to know the metrological performances of the equipment;
- the total uncertainty of the area of the wear track cross-section can be minimised by controlling the number of acquisition points.

References:

- 1) J.M. Cunningham, C. Garcia Marirrodiga, A practical assessment of data repeatability & reproducibility in tribometer tests for space applications, Proc. Sixth European Space Mechanisms & Tribology Symposium, Technopark, Zurich, Switzerland, 4-6 October 1995, 35-43.
- 2) S. Guicciardi, C. Melandri, F. Lucchini, G. de Portu, On data dispersion in pin-on-disk wear tests. *Wear* 252 (2002) 1001-1006.
- 3) E.A. Almond, M. Gee, Results from a UK inter-laboratory project on dry sliding wear. *Wear* 120 (1987) 101-116.
- 4) D.L. Burris, W.G. Sawyer, Addressing practical challenges of low friction coefficient measurements, *Tribol. Lett.* 35 (2009) 17-23.
- 5) T.L. Schmitz, J.E. Action, J.C. Ziegert, W.G. Sawyer, The difficulty of measuring low friction: uncertainty analysis for friction coefficient measurements, *J. Tribol.* 127 (2005) 673-678.
- 6) T.L. Schmitz, J.E. Action, J.C. Ziegert, W.G. Sawyer, Wear-rate uncertainty analysis, *J. Tribol. Trans. ASME* 126 (2004) 802-808.
- 7) K.C. Ludema, *Friction, wear, lubrication: a textbook in tribology*, CRC Press (1996).
- 8) ASTM G 99-05 "Standard test method for wear testing with a pin-on-disk apparatus".
- 9) R.S. Figliola, D.E. Beasley, *Theory and design for mechanical measurements*, Wiley 4th edition.
- 10) D.L. Burris, W.G. Sawyer, Measurement uncertainties in wear rates, *Tribol. Lett.* 36 (2009) 81-87.
- 11) UNI CEI ENV 13005:2000 "Guida all'espressione dell'incertezza di misura".

EXPRESSING THE MEASUREMENT UNCERTAINTY IN SPARK-OES ANALYSIS WITH APPLICATION FOR THE MATERIAL CONFORMITY PROBABILITY CALCULATION

Edmund Halász and J-M Böhlen

Thermo Fisher Scientific, Ecublens, Switzerland

ABSTRACT

Every year and increasing number of the laboratories using OES (Optical Emission Spectroscopy) spectrometers gets accredited according to ISO 17025. The compliance with ISO 17025 has elevated the importance of estimating and reporting measurement uncertainty. The Guide to the expression of uncertainty in measurement (GUM) provides guidelines for conducting an uncertainty analysis. Unfortunately, the implementation of these guidelines can be a daunting task, especially if one is not familiar with the necessary mathematical and statistical concepts. Consequently, testing and calibration personnel must often find off-the-shelf tools that meet their analysis requirements.

The paper presents the way the calculation of the measurement uncertainty is implemented in Thermo Scientific OXSAS analytical software. It also describes the usage of the measurement uncertainty in order to calculate the product conformance probability.

INTRODUCTION

Measurement uncertainty plays an important role in making decisions after measuring materials characteristics, managing risk related to non-conform materials, developing tolerances, selecting measurement methods, developing capability statements, achieving laboratory accreditation, hypothesis testing, establishing calibration intervals and communicating technical variables. Therefore, uncertainty estimates should realistically reflect the measurement process under investigation or evaluation.

While the Guide to the expression of uncertainty in measurement (GUM) provides general rules for analyzing and communicating measurement uncertainty, it does not focus on providing step-by-step instructions for evaluating very specific measurement processes. As a result, testing personnel may find the measurement uncertainty assessment difficult or may be confused trying to apply these principles to specific measurement scenarios.

SOME THEORETICAL ASPECTS REGARDING MEASUREMENT ERROR AND MEASUREMENT UNCERTAINTY

The GUM method evaluates and combines error distribution variances and calculates the effective degrees of freedom of the uncertainty estimate for the combined measurement error. The convolution method uses a mathematical approach for combining error distributions. In any given measurement scenario whereby the value of a quantity is estimated, each measured quantity is also accompanied by measurement error. The basic relationship between the measured quantity x and the measurement error ε_x is given in Eq. (1).

$$x = x_{true} + \varepsilon_x \quad (1)$$

The error model, described by the algebraic expression in Eq. (2), defines the total error in the value of a measured quantity as the sum of all the relevant measurement process errors encountered during the measurement. Thus, the total error ε_x of the measured quantity x is

$$\mathcal{E}_x = \sum_{i=1}^k \mathcal{E}_i \quad (2)$$

where the numbered subscripts signify the different measurement process errors.

Measurement uncertainty can be seen as the quantification of our lack of knowledge of the sign and magnitude of measurement error. The uncertainty of measurement is a parameter associated with the result of a measurement that characterizes the dispersion of the values that could be reasonably attributed to the measurand. As a comment, the parameter may be, for example, a standard deviation or the half width of an interval having a stated level of confidence.

The errors of the measurement process are the basic elements of uncertainty analysis. Once these fundamental error sources have been identified, we can begin to develop uncertainty estimates. For modern OES spectrometers these errors can be grouped in four important categories, presented in figure Fig.1:

- Sampling error
- Random error
- Analytical bias
- Spurious errors

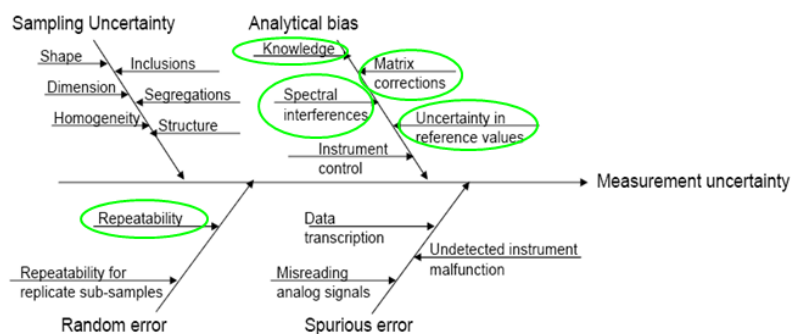


Figure 1. Error categories contributing to the measurement uncertainty for modern OES spectrometers. Highlighted in green are those sources of error that can be directly calculated.

Among these categories there are two types of errors that are mainly relevant: the analytical bias, or the calibration uncertainty, and the repeatability and their impact on the measurement uncertainty can be calculated with mathematical algorithms.

The calibration uncertainty for OES spectrometers has the following potential sources of uncertainty:

- incomplete knowledge of factors having critical impacts on measurement accuracy
- lack of correction or incomplete correction for matrix effects
- lack of corrections or incomplete correction for spectral interferences
- reference value not accurate for reference materials used for calibration; usually the reference materials exhibiting unacceptable bias during the calibration process are discarded
- instrument resolution or discrimination threshold
- inadequate control of environmental conditions needed for instrument operation

The points a) to d) are all related to the calibration process, while the points e) and f) are related to the instrument, to its maintenance and environment.

The repeatability is a random error that manifests itself as differences in measured value from measurement to measurement during a measurement session. It is important to note that, random variations in a measured quantity are not separable from random variations in the reference attribute or random variations due to other error sources.

MEASUREMENT PROCESS UNCERTAINTY

The measurement processes uncertainty or the measurement uncertainty is the standard deviation of the probability distribution for the measurement process error. The standard deviation of an error distribution is the square root of the distribution's statistical variance. If $f(\varepsilon)$ represents the probability density function for an error distribution, and μ_ε represents the mean value of the distribution, then the variance or mean square error is given by

$$\text{var}(\varepsilon) = \int_{-\infty}^{\infty} f(\varepsilon)(\varepsilon - \mu_\varepsilon)^2 d\varepsilon \quad (3)$$

and the standard deviation becomes

$$\sigma_\varepsilon = \sqrt{\text{var}(\varepsilon)} \quad (4)$$

There are two types of estimates of the standard deviation of an error distribution. Type A estimates involve data sampling and analysis. Type B estimates use engineering knowledge or recollected experience of measurement processes. For OES spectrometry, the calibration uncertainty and the repeatability are type A estimates.

COMBINED UNCERTAINTY

The variance addition is employed to obtain a method for combining uncertainties that accounts for possible correlation between errors. For the optical emission spectrometers we consider the error in measurement of a concentration quantity x , for a given element, that involves errors due to repeatability and measuring equipment bias, ε_{rep} and ε_{bias} .

ESTIMATING CALIBRATION UNCERTAINTY FROM THE CALIBRATION DATA

The GUM (appendix E3) shows an application to calculate uncertainty for linear least square calibration. For a relationship between the instrument response y and the analyte x like:

$$y = b_0 + b_1 x \quad (5)$$

the predicted, or measured concentration of the analyte is obtained from the observed response y_{obs}

$$x_{pred} = (y_{obs} - b_0) / b_1 \quad (6)$$

The uncertainty $u(x_{pred}, y)$ in a predicted value x_{pred} due to variability in y can be estimated as the sum of the variance from the observation or the measurement and the variance from the least square calibration of a set of n data points (x_i, y_i) :

$$\text{var}(x_{pred}) = \frac{\text{var}(y_{obs})}{b_1^2} + \frac{S^2}{b_1^2} \cdot \left(\frac{1}{\sum w_i^2} + \frac{(x_{pred} - \bar{x})^2}{\sum (w_i x_i^2) - (\sum w_i x_i)^2 / \sum w_i} \right) \quad (7)$$

where

$$S^2 = \frac{\sum w_i (y_i - y_{fi})^2}{n - 2}$$

is the equivalent of the standard error of measure, n is the number of data points in calibration, b_1 is the calculated best fit slope, w_i is the weight assigned to y_i and \bar{x} the mean of the n values x_1, x_2, \dots, x_n .

For unweighted data, where $\text{var}(y_{obs})$ is based on p measurements, equation Eq. 7 becomes:

$$\text{var}(x_{pred}) = \frac{S^2}{b_1^2} \cdot \frac{1}{p} + \frac{S^2}{b_1^2} \cdot \left(\frac{1}{n} + \frac{(x_{pred} - \bar{x})^2}{\left(\sum (x_i^2) - (\sum x_i)^2 / n \right)} \right) \quad (8)$$

The reference values may each have uncertainties which propagate through to the final result. In practice, uncertainties in these values are usually small compared to uncertainties in the system responses y_i , and may be ignored.

At a careful look the second member in equations Eq.7 and Eq.8 represents the square of the so called confidence interval's limit expression.

Our calibration model for the Thermo Scientific OES spectrometers is based on the following equation:

$$C = \left(\sum_{i=0}^{\max 3} A_i I^i + \sum_j^n a_j C_j \right) \left(1 + \sum_k^m m_k C_k \right) \quad (9)$$

where A_i are the polynomial coefficients multiplying the powers of the intensity I , a_j ($a_j < 0$) are the additive correction coefficients multiplying the concentration of the interfering elements C_j and m_k are the multiplicative correction coefficients multiplying the concentration of the interfering elements C_k . All the coefficients (polynomial and corrections) are calculated with a multivariable regression routine in the same time.

In very rare cases the calibration model is linear, without corrections, for example for the calibration curves of ultra-trace concentration levels in pure metals and in precious metals. In all the other cases the calibration model is far from linear and the confidence interval can't be directly calculated. However, despite the complexity of the calibration model, there is an equation that is linear and this is the calibration correlation curve equation:

$$C_{calculated} = a \cdot C_{certified} + b \quad (10)$$

where a is the slope of the curve and b is the intercept. For a perfect correlation a equals 1 and b equals 0.

Our method is based on the use of this correlation curve and it calculates the calibration uncertainty through the confidence interval of the curve described by equation Eq. 10 instead of trying to calculate for the complex equation described by Eq. 9.

We note the confidence interval CI . We calculate $1/2CI(C)$, the half width of the confidence interval or the confidence interval's limit at the concentration level C as a function of the concentration level C , as described by Eq. 11:

$$\frac{1}{2} CI(C) = t_{\alpha/2, n-k} \cdot SEE \cdot \sqrt{\frac{1}{n} + \frac{(C - \bar{C})^2}{\sum_{j=1}^n (C_{certified_j} - \bar{C})^2}} \quad (11)$$

where:

$$SEE = \sqrt{\frac{\sum_{j=1}^n (C_{certified_j} - C_{calculated_j})^2}{n - k}}$$

is the Standard Error of Estimate of the calibration curve, n is the number of samples used in regression, k is the total number of coefficients for polynomial (curve degree) and corrections (interferences) used in regression, t is the Student factor for $\alpha/2$ confidence level (and $1-\alpha$ double sided probability) and $n-k$ degrees of freedom, $C_{certified_j}$ is the certified concentration of sample j and

$$\bar{C} = (\sum_{j=1}^n C_{certified_j}) / n$$

is the average of the certified concentrations of the n samples.

The confidence interval has a minimum difference between the confidence limits at the concentration level \bar{C} write lower and has a larger difference at the low and high concentration values.

The factors that affect the confidence interval are the desired confidence level 1- α , the statistical sample size n and the SEE. More samples are used in the calibration and better the SEE, the width of the CI decreases. This shows the importance of the quality of the calibration process.

The confidence interval estimate gives an indication of how much uncertainty there is in our estimate of the true mean. The narrower the interval, the more precise is our estimate [2].

The advantage of this approach is that the correlation curve is independent on the mathematical model and has the same SEE as the calibration curve. The number of the degrees of freedom is reported from the concentration versus intensity calibration curve. In fact SEE is decoupled from the calibration model and reflects the goodness of the fit.

COMBINING THE REPEATABILITY AND THE CALIBRATION BIAS UNCERTAINTY

The GUM method evaluates and combines the variances of each measurement process error distribution. The combined uncertainty is computed by taking the square-root of the combined variance. In our case, as repeatability and calibration uncertainty are non correlated input quantities, this leads to:

$$u = \sqrt{SD^2 + CI^2} / 4 \tag{12}$$

The expanded uncertainty will be U=2u. The measurement result is reported by using the Eq. 8:

$$C_{result} = C_{measured} \pm 2\sqrt{SD^2 + CI^2} / 4 \tag{13}$$

The combined uncertainty is reported in the analysis screen of the analytical software OXSAS as in the example in Figure 2.

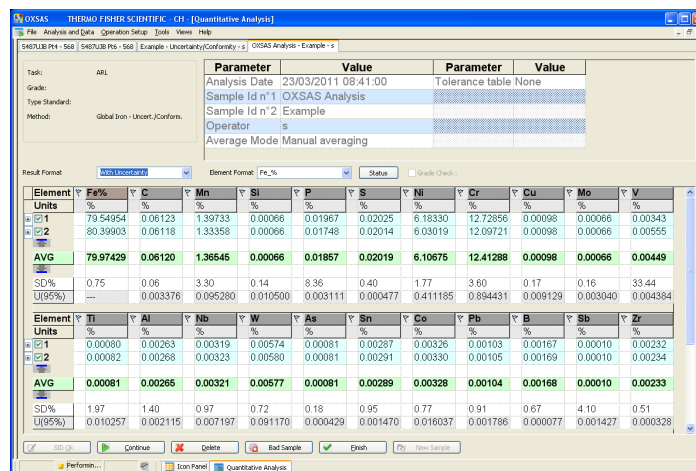


Figure 2. Example of analytical measurement screen reporting the standard deviation and the U(95%) in the analytical software OXSAS.

As we said before, the same approach can be applied to any other comparative (not absolute) measuring method, which needs calibration. As an example, for an X-Ray instrument the equation Eq. 12 can be rewritten as:

$$C_{result} = C_{measured} \pm 2\sqrt{(b \cdot N)^2 + CI^2 / 4} \quad (14)$$

where b is the calibration constant and N is number of the counted X-ray photons for a given wavelength or energy (Poisson statistics applies in this case).

COMPLIANCE PROBABILITY FOR CONFORMANCE TESTING

The conformance testing procedure we propose to use is based on the technical report ASME B89.7.4.1-2005 [3]. It is applied in work-pieces inspections, instrument verification and general conformance tests where uncertain numerical test results are compared with specific requirements.

From chemical composition point of view, a given product for a set of given elements is considered compliant or conforms to a specification, if the result of the analysis is within the specification limits. For a given element, the specification limits are defined by the upper limit T_U and the lower limit T_L .

The probability that for a given element the measurement result x_m is compliant to a specification is expressed through the probability for conformance P_C :

$$P_C = \Phi\left(\frac{T_U - x_m}{u_c}\right) - \Phi\left(\frac{T_L - x_m}{u_c}\right) \quad (15)$$

where Φ is the standard normal cumulative distribution function and u_c is the combined standard uncertainty defined by the Eq. 13. The standard normal cumulative distribution function $\Phi(z)$ gives the probability that a standard normal variable assumes a value in the interval $[0, z]$

$$\Phi(z) = \frac{1}{\sqrt{2\pi}} \int_0^z \exp(-x^2 / 2) dx \quad (16)$$

The product is considered to conform to a specification if all the elements are within the specification ranges. However, due to the measurement uncertainty, when the measurements result is near to any specification limit, the conformance probability is less than 100%.

This functionality is also implemented in OXSAS for the official limits of the grade specification and, when selected, for the inner control limits. Figure 3 is an example of the analysis screen when grade assessment is performed: the elements outside the specification range are highlighted and the compliance probability is shown together with the measurement uncertainty.

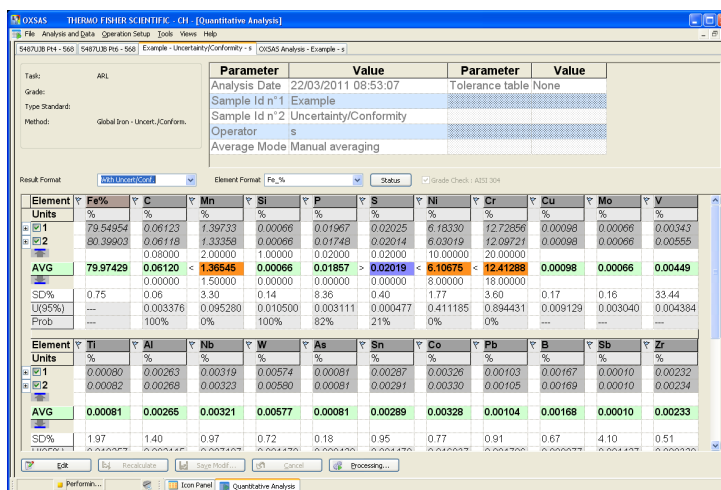


Figure 3. Example of analysis screen in OXSAS with conformance probability calculation together with the material specification limits.

In order to understand the case when the measurement's results lie near the specification limit we created a numerical example, presented in the Table 1. The simulation of the conformance probability applied for the elements Cr and Ni in the AISI 304 alloy, for which the specifications for Cr is between 18 and 20% and for Ni is between 8 and 10.5%.

We have evaluated the uncertainties at 19% Cr and at 9.25% Ni (i.e. in the middle of the range) on a sample measured with a Thermo Scientific ARL 3460 instrument, as being $u_{Cr} \sim 0.15\%$ and $u_{Ni} \sim 0.07\%$, respectively. With these values we can calculate the product conformance probability (between 0% and 100%) in function of the results that can be measured inside the specified ranges:

Cr	Measured concentration [%]	18	18.1	18.2	18.3	18.4	18.5	...	19.5	19.6	19.7	19.8	19.9	20
	Conformance probability [%]	50	74.2	90.3	97.7	99.5	100	100	100	100	99.5	97.7	90.3	74.2
Ni	Measured concentration [%]	8	8.05	8.1	8.15	8.2	8.25	...	10.25	10.3	10.35	10.4	10.45	10.5
	Conformance probability [%]	50	75.8	91.9	98.2	99.7	100	100	100	99.7	98.2	91.9	75.8	50

Table1. Conformance probability for AISI 304 in function of the measured content of Cr and Ni with a Thermo Scientific ARL 3460.

Obviously for values outside the specification range the conformance probability goes fast to 0%.

The information obtained from the conformance probability can be further used for setting the stringent acceptance zones or the inner quality limits.

CONCLUSIONS

The new features that were added to the proprietary analytical software OXSAS driving the Spark-OES spectrometers allows calculating the measurement uncertainty. This is an important step forward towards the compliance to the requirements of ISO 17025 for accredited laboratories.

BIBLIOGRAPHY

- [1] ISO/IEC Guide 98-3:2008 Guide to the Expression of Uncertainty in Measurement (GUM)
- [2] Snedecor, George W. and Cochran, William G. (1989), Statistical Methods, Eighth Edition, Iowa State University Press
- [3] ASME B89.7.4.1-2005 (Technical Report) Measurement Uncertainty and Conformance Testing: Risk Analysis

ORIGINAL POSITION STATISTIC DISTRIBUTION ANALYSIS OF TRACE ELEMENT SEGREGATION IN NICKEL-BASE SUPER ALLOY BY LA-ICP-MS

CHEN Ji-wen, ZHAO Lei, YAO Ning-juan, HAN Peng-cheng, YUAN Liang-jing, CHEN Yong-yan, QU Huayang, WANG Hai-zhou

China Iron & Steel Research Institute Group, National Analysis Centre for Iron & Steel, Beijing 100081, China

Abstract: A new original position statistic distribution analysis method to reflect the different composition distributions and segregations in nickel-base super alloy was developed by laser ablation inductively coupled plasma mass spectrometry (LA-ICP-MS). The distribution of more than 20 trace elements at intragranular solid solution phase and crystal boundary in wrought super alloy GH698 was investigated using the micro-area analysis of LA-ICP-MS technique. For most of the trace elements, no significant difference was found between the content in the crystalline grain and that at the crystal boundary. Only a few elements such as Mg, Zr, B and P showed slight segregation at crystal boundary. However, according to the compositional two-dimensional isohypsic chart and statistic degree of segregation, which was obtained by original position statistic distribution method combined with LA-ICP-MS, the segregation of As, Mg and Te was more serious in the cross section scope (10 mm*10 mm) of the wrought super alloy sample. Moreover, the segregation of Mg, P, Zn, As, Sb, Ce and Hf was higher in cross section scope (ϕ 5 mm) of the cast super alloy K002 sample. The results showed that the original position statistic distribution analysis results were in good agreement with the crystal boundary segregation and eutectic structure enrichment obtained by metallographic analysis.

Key words: laser ablation; inductively coupled plasma mass spectrometry; original position statistic distribution analysis; super alloy; trace element; segregation

The super alloys are important parts and components materials of aircraft engines and various industrial gas turbines due to their excellent high-temperature strength and mechanical properties. The chemical composition of super alloys is very complicated. In general, more than 20 elements should be accurately analyzed, and the content range is up to six or seven orders of magnitude. For example, the content of Bi may be low to 0.000001 %. Since 1990s, the developed inductively coupled plasma mass spectrometry^[1-4] can well meet these analytical requirements. However, the super alloys easily cause composition segregation due to high alloying extent. The local enrichment of trace elements caused by segregation may have great influence on the high-temperature mechanical properties of super alloys^[5]. Therefore, the original position distribution of trace elements will provide important information to evaluate material performance. As a kind of high-sensitivity and semi-quantitative surface analysis method, auger electron spectroscopy (AES) plays important roles in crystal boundary segregation analysis. However, it has limitation in accurate quantification of trace elements and distribution analysis of element content with large dimension range.

Therefore, based on the original position statistic distribution analysis techniques^[6-7] and combined with the solid original position analysis characteristic of laser ablation, we used inductively coupled plasma mass spectrometry with powerful quantitative abilities to study the composition distribution and segregation of trace elements in nickel-base super alloy in this paper. The aim was to establish a new method to reflect the different composition distributions and segregations in super alloy, which could provide new criterion for performance study of materials.

1 Experimental

1.1 Instruments and parameter settings

In this study, the Newwave UP213 solid-state laser and Thermo X series II CCT quadrupole ICP-MS were used. The optimized operation parameters of LA-ICP-MS were listed in Table 1.

Table 1 Operation parameters of LA-ICP-MS

Parameter of laser system	Value	Parameter of ICP-MS	Value
Laser wavelength	213 nm	RF power	1200 W
Laser mode	Q-switched	Cool gas	13.0 L/min
Laser energy	80~100%	Auxiliary gas	0.80 L/min
Laser frequency	15 Hz	Ar carrier gas	0.95~1.10 L/min
Laser spot size	100 μm	Signal acquisition mode	TRA
		Signal collect time	45 s

1.2 Samples and pretreatment

Standard samples: super alloy GH167 series of GBW01619 ~ GBW01623, and super alloy GH169 series of GBW01636 ~ GBW01640.

Analytical samples:

(1) wrought super alloy GH698, which was a kind of precipitation strengthening nickel-base super alloy and mainly used to manufacture turbine disks. Its manufacturing process was as follows: smelting of master alloy \rightarrow casting and forming \rightarrow thermal treatment (air-cooled at 1120 $^{\circ}\text{C}$ for 8 h, air-cooled at 1000 $^{\circ}\text{C}$ for 4 h, air-cooled at 775 $^{\circ}\text{C}$ for 16 h). The dimension of sample: one piece of sample was cut from turbine disk outer ring after thermal treatment with quadrate cross section of about 10 mm*10 mm. The sample was then polished after burnishing with abrasive paper above 400-mesh.

(2) Cast super alloy K002, which was a kind of normal precision casting nickel-base super alloy and mainly used to directly cast (cast directly?) into turbine blade and countervanes. K002 usually needed aging treatment with following thermal treatment process: air-cooled at 870 $^{\circ}\text{C}$ for 16 h. In this study, one piece of sample was cut from tension specimen with round cross section: the diameter was about 5 mm. The sample was edged with dental base acrylic resin powder, and then polished after burnishing with abrasive paper above 400-mesh.

2 Results and discussion

2.1 Investigation on crystal boundary segregation

The sample could be amplified by 300 times using the equipped micro camera device in laser ablation system, so the chemical compositions in super alloy could be analyze by original position microprobe method. The wrought super alloy GH698 sample surface was burnished, polished and treated by corrosion, and then put into sample cell. The parameter settings were as follows: beam spot of 100 μm , energy of 100 % and impulse frequency of 15 Hz. The sampling began after pre-ablation for 12 s in the areas of crystalline grain and crystal boundary. It was repeated for 12 times. The segregation of elements at the areas of crystalline grain and crystal boundary in wrought super alloy GH698 sample was investigated. The surface morphologies of samples before and after ablation were shown in Fig.1.

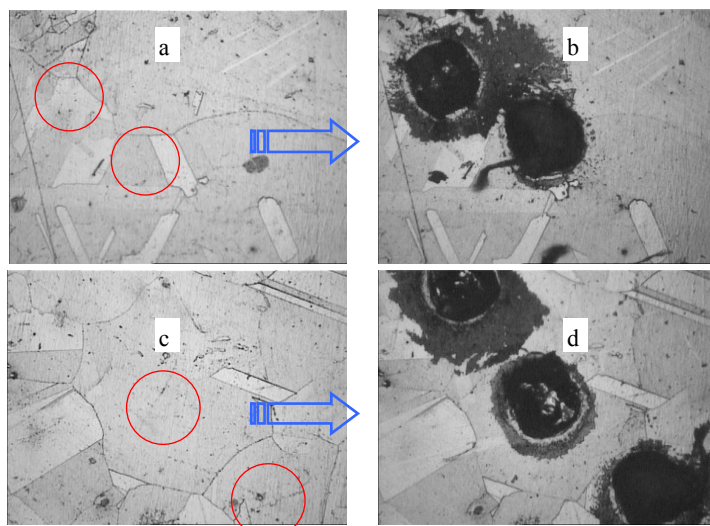


Fig. 1 Sample surface morphologies before and after ablation

a) crystal boundary area before ablation ; b) crystal boundary area after ablation ;
c) crystalline grain area before ablation ; d) crystalline grain area after ablation

More than 20 trace elements including B, Mg, Al, P, Si, Cu, Zn, Ga, Ge, As, Se, Nb, Zr, Ag, Cd, In, Sn, Sb, Te, Ti, Pb and Bi were studied. The results showed that the distribution of most trace elements in this sample had no significant difference at crystalline grain and crystal boundary. Only Mg, Zr, B and P showed slight segregation at crystal boundary. The comparison of analytical results was listed in Table 2.

Table 2 Analytical results of the elements at the areas of crystalline grain and crystal boundary in wrought super alloy

Element	Ref. (w,%)	Average (w,%)	Crystalline grain area		Crystal boundary area	
			Found (w,%)	RSD (%)	Found (w,%)	RSD (%)
¹⁰ B	<0.005	0.0014	0.0012	25.52	0.0017	18.76
²⁴ Mg	0.0027	0.00289	0.00266	14.39	0.00284	3.89
³¹ P	0.0026	0.0015	0.0014	19.96	0.0017	21.25
⁹⁰ Zr	0.033	0.0372	0.0360	10.76	0.0388	9.64

2.2 Large-area original position statistic distribution analysis of trace elements in wrought super alloy

2.2.1 Original position statistic distribution analysis scanning of trace elements

The translatory velocity of sample stage in laser ablation system was 100 $\mu\text{m/s}$. The interval of each sampling track was 300 μm . The cross section surface (10 mm*10mm) of wrought super alloy GH698 sample was scanned point-to-point and line-by-line to obtain tens of thousands data. The collected signals were one-to-one corresponded to the points on sample surface according to the timing sequence. The signal intensity presented the content of chemical composition at this point. The typical two-dimensional isohypsic charts of the content of some trace elements wrought super alloy GH698 were shown in Fig.2.

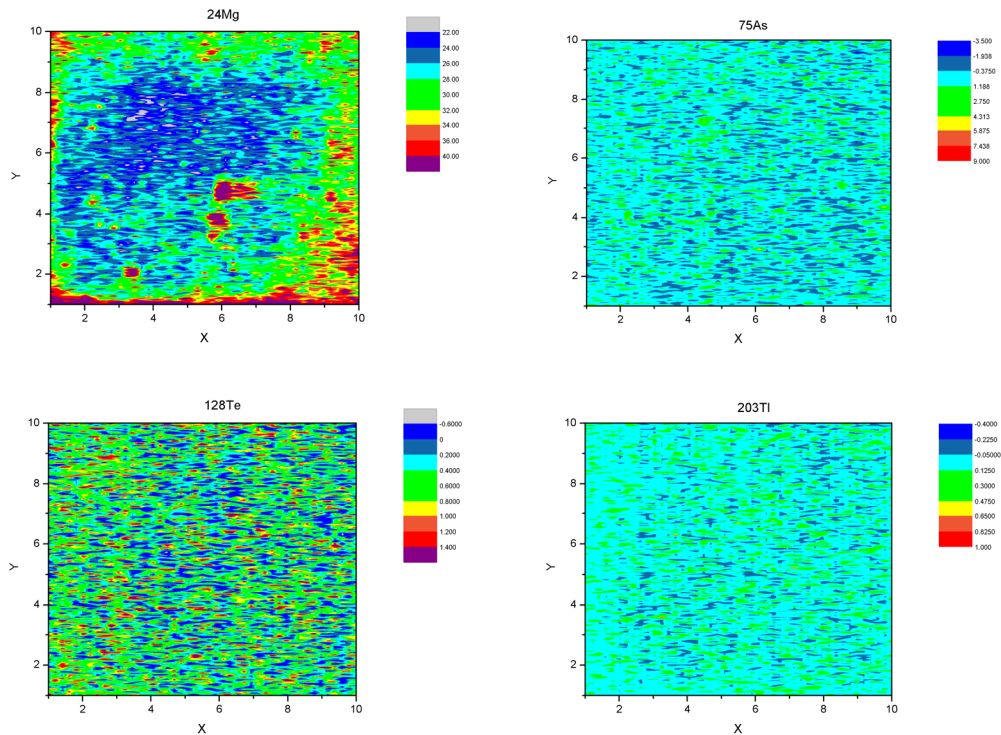


Fig. 2 Typical two-dimensional isohypsic charts of some trace elements in wrought super alloy GH698

The intensity of each signal presented the original state of each chemical composition in this position. By resolving these signals systematically, the quantitative statistic distribution information of each composition in tested sample at large dimension (10 mm*10mm) could be obtained. It was a relatively visualized quantitative analysis method for the distribution of trace elements. According to the distribution charts of all the elements, the segregation of As, Mg and Te was more serious.

2.2.2 Statistic analysis of segregation degree for trace elements

The quantitative statistic distribution information of each composition in tested sample could be intuitively and quantitatively described by two-dimensional isohypsic chart or three-dimensional cubic chart. Moreover, the statistic segregation degree and maximum segregation degree were also the important characterization data to evaluate the distribution of one sample on sample surface in recent years^[8]. High statistic segregation degree indicated serious distribution segregation of this element in material. If necessary, the value of maximum segregation degree could be calculated, and its accurate position on material surface should be marked. In general, the calculation formula of statistic segregation degree^[9] was:

$$S = (C_2 - C_1) / 2C_0 * 100\%$$

Where, $(C_2 - C_1)$ was the content range using median (C_0) as center with confidence coefficient of 95 %.

The calculation formula of maximum segregation degree was $P = C_{\max} / C_0 * 100\%$.

Where, C_{\max} was the maximum content, and C_0 was the median or average of all obtained contents.

The segregation statistic analysis results of cross section in the wrought super alloy sample were listed in Table 3.

Table 3 The segregation statistic analysis results of cross section in the wrought super alloy sample

Element	Ref. (w,%)	Average (w,%)	Statistic segregation degree (%)	Maximum segregation degree (%)
²⁴ Mg	0.0027	0.0029	7.00	3.65*10 ³
⁴⁵ Sc	<0.00005	0.000038	0.05	5.10*10 ²
⁵³ Cr	13.0~16.0	13.15	0.02	1.42*10 ²
⁷⁵ As	<0.0012	0.00003	10.00	2.71*10 ³
⁹⁰ Zr	0.033	0.037	2.90*10 ⁻⁴	1.51*10 ²
⁹³ Nb	1.8~2.2	1.74	0.01	1.45*10 ²
⁹⁵ Mo	2.8~3.2	3.13	0.02	1.28*10 ²
¹⁰⁷ Ag	<0.00005	0.000036	0.23	4.01*10 ³
¹²¹ Sb	<0.00005	0.00004	0.35	7.57*10 ²
¹²⁸ Te	<0.00005	0.000023	3.00	1.66*10 ³
¹⁷⁸ Hf	0.0005	0.00068	0.19	1.87*10 ²
²⁰⁵ Tl	<0.00005	0.000005	0.18	9.27*10 ²

Based on the compositional two-dimensional isohypsic chart and statistic segregation degree of each element in the wrought super alloy GH698, it could be seen that the segregation of As, Mg and Te was more serious, while the segregation of Sc, Cr, Zr, Nb, Mo, Ag, Sb, Hf and Tl was relatively light.

2.2.3 Metallographic analysis of sample

In order to study the reason of composition segregation, the scanning surface was treated by burnishing and polishing. Then, it was corroded using FeCl₃ (supersaturated hydrochloric acid) and the metallographic phase was observed under microscope. No segregation region and abnormal structure were observed in metallographic analysis. However, the grain size of this material was relatively heterogeneous. The grain size was Grade one with large diameter (50 μm~200 μm). Fig.3 presented the metallographic images of sample before laser ablation.

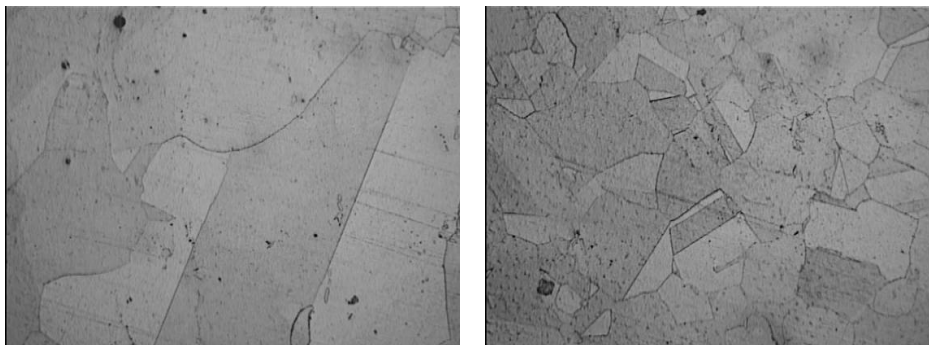


Fig. 3 Ablation area with big crystalline grain (Left: *300) and small crystalline grain (Right: *300)

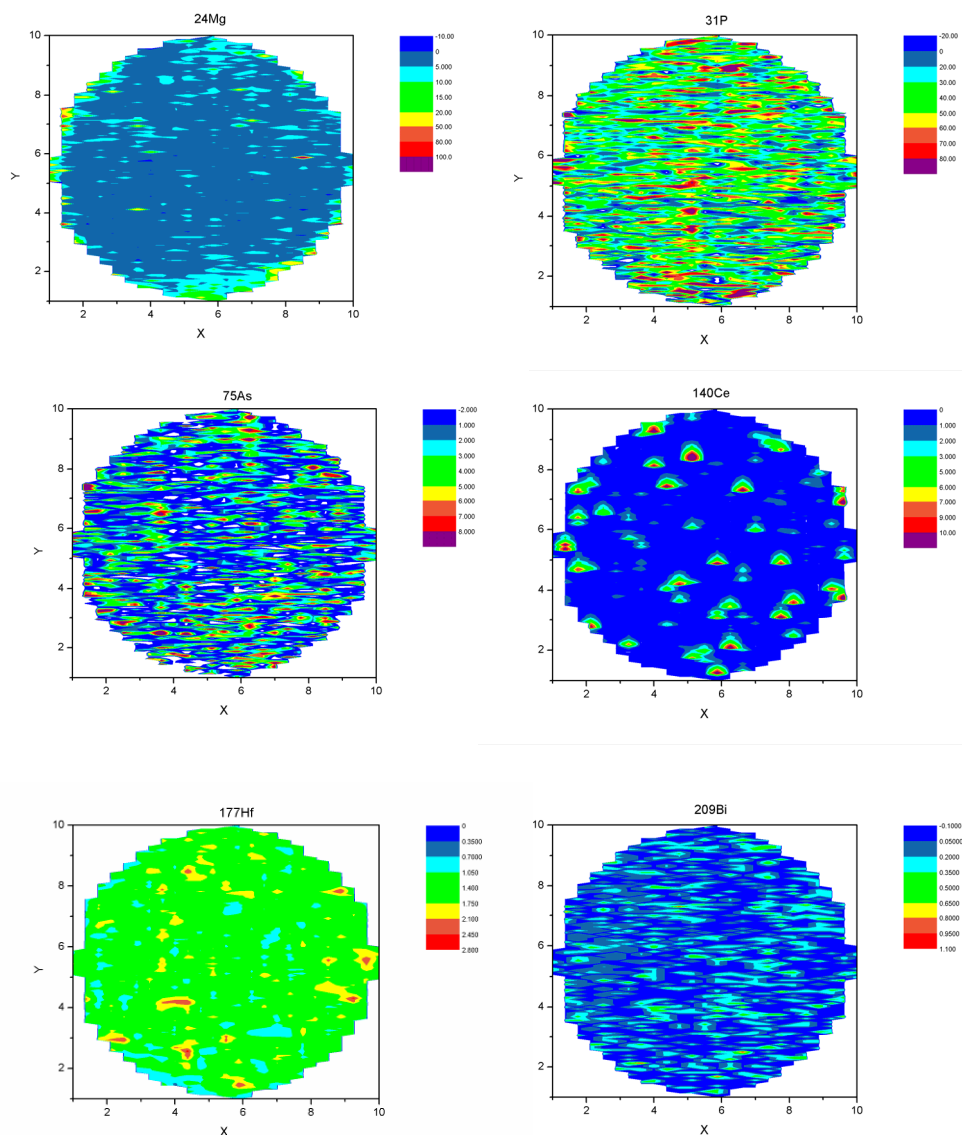
In transverse scanning of laser ablation process, the track interval was 300 μm and the spot diameter was 100 μm, so the signals in band regions with actual interval of 200 μm were selected. In longitudinal scanning, the translatory velocity of sample stage was 100 μm/s, and the counting interval of detector in ICP-MS was 66.3 ms, so the step length between sampling points was 100 μm/s×66.3 ms=6.63 μm. Therefore, the contained quantity of crystal boundary in each laser ablation spot was different. The segregation of elements in crystal boundary

may cause the fluctuation of content of tested elements, resulting in the composition segregation of elements in large dimension scope.

2.3 Large-area original position statistic distribution analysis of trace elements in cast super alloy

2.3.1 Original position statistic distribution analysis scanning of trace elements

The translatory velocity of sample stage in laser ablation system was 50 $\mu\text{m/s}$. The interval of each sampling track was 200 μm . The cross section surface (ϕ 5 mm) of cast super alloy K002 sample was scanned point-to-point and line-by-line. The collected signals were one-to-one corresponded according timing sequence and points on sample surface. The obtained two-dimensional isohypsic charts of composition distribution of elements were shown in Fig.4.



The two-dimensional isohypsic charts of elements indicated that, many discontinuous local enrichment zones existed in sample for the elements such as B, Mg, Sc, Zn, Ga, Ge, As, Sb, Ce, Hf, Tl and Bi, and also many discontinuous local depletion zones existed in sample for Si and P.

2.3.2 Statistic analysis of segregation degree for trace elements

According to the original position statistic distribution analysis method, the results of sample cross section were listed in Table 4.

Table 4 The segregation statistic analysis results of cross section in cast super alloy sample

Element	Ref. (w,%)	Average (w,%)	Statistic segregation degree (%)	Maximum segregation degree (%)
¹¹ B	0.01~0.02	0.0078	6.32×10^{-2}	2.11
²⁴ Mg	≤0.003	0.00050	0.81	89.35
³¹ P	≤0.01	0.0038	0.83	8.1
⁴⁵ Sc	<0.00005	0.000012	5.70×10^{-3}	14.73
²⁸ Si	≤0.20	0.19	3.56×10^{-2}	18.26
⁶⁶ Zn	0.0011	0.0012	0.7	17.79
⁶⁹ Ga	0.0016	0.0018	1.14×10^{-2}	3.53
⁷² Ge	0.00027	0.00030	7.56×10^{-2}	26.94
⁷⁵ As	0.00022	0.00019	0.16	14.06
¹²¹ Sb	<0.00005	0.000047	0.16	154.24
¹⁴⁰ Ce	0.00008	0.000091	0.23	24.58
¹⁷⁷ Hf	1.3~1.7	1.38	12.87	1.9
²⁰⁵ Tl	<0.00005	0.000012	1.23×10^{-2}	11.91
²⁰⁹ Bi	≤0.00005	0.000012	1.70×10^{-2}	8.87

It could be seen from the statistic segregation degrees of elements in Table 4 that, the segregation degree of Mg, P, Zn, As, Sb, Ce and Hf was higher, while that of B, Sc, Si, Ga, Ge, Tl and Bi lower.

2.3.3 Metallographic analysis of sample

For K002 sample, a lot of tiny γ' phases were usually uniformly precipitated in γ matrix during the ageing treatment process. Moreover, there were also many eutectic structures ($\gamma+\gamma'$) with large diameter (about 50 μm) in alloy. The distribution of alloying elements in different structures had great influence on the properties of materials. The metallographic structure of cast super alloy K002 was shown in Fig.5.

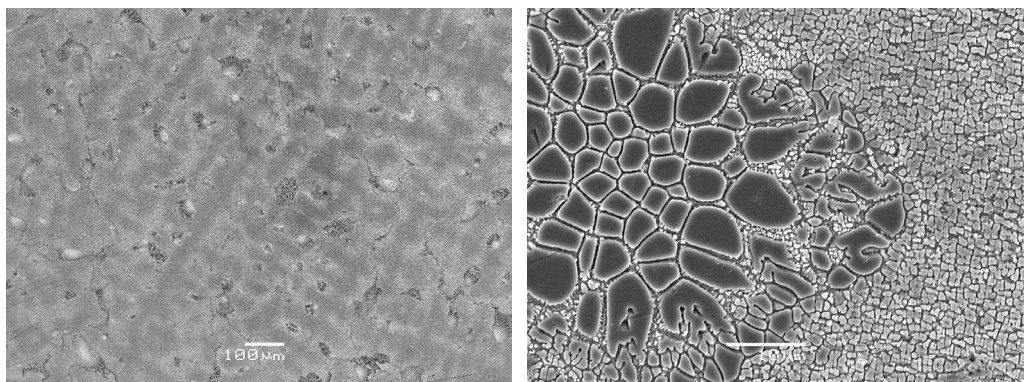


Fig. 5 Metallographic structure of cast super alloy K002 (Left: *100; Right: *2000)

Since the metallographic structure of cast super alloy K002 was the many dispersed and distributed eutectic structure regions ($\gamma+\gamma'$) with large diameter in alloy, we could inferred that the heterogeneous composition distribution was caused by the nonuniform distribution of elements in each phase of structure. Mg, Zn, As, Sb, Ce and Hf may be enriched in eutectic structure ($\gamma+\gamma'$), causing the content fluctuation of elements and resulting in the composition segregation of elements in large dimension scope.

3 Conclusion

Based on the microprobe analysis of LA-ICP-MS and the results of original position statistic distribution analysis, and combined with the metallographic analysis of wrought super alloy and cast super alloy, it was found that some elements had obvious segregation in the both alloys. The original position statistic distribution analysis results were in good agreement with the crystal boundary segregation and eutectic structure enrichment obtained by metallographic analysis. With the further improvement of this method, LA-ICP-MS may become a kind of powerful tool to accurately and intuitively analyze the original position statistic distribution and micro segregation of trace elements in materials.

References :

- [1] ISHIBASHI Y. Rapid analysis of steel by inductively coupled plasma -atomic emission spectrometry and mass spectrometry with laser ablation solid sampling[J]. ISIJ Int, 1997,37(9): 885-891.
- [2] MÜLLER G, STAHNKE F, BLEINER D. Fast steel-cleanness characterization by means of laser-assisted plasma spectrometric methods[J]. Talanta, 2006, 70(5): 991-995.
- [3] Han Mei, Hu Jing-yu, Chen Yu-hong, Wang Hai-zhou. Determination of trace elements in super alloy by LA-ICP-MS. Metallurgical Analysis, 2010, 30(3): 1-6.
- [4] Hu Jing-yu, Wang Hai-zhou. Determination of 17 Trace Elements in Nickel-base Superalloy by Laser Ablation Inductively Coupled Plasma Mass Spectrometry [J]. Journal of Instrumental Analysis, 2010, 29(4):359-363.
- [5] Yang Shu-lin, Sun Wen-ru, Wang Zhao-kun. Effect of Simultaneous Adding of Phosphorus and Boron on Mechanical Properties of GH761 Alloy. Rare Metal Materials and engineering, 2006, 35(6) : 929-932.
- [6] Chen Yu-hong, Yuan Liang-jing, Wang Hai-zhou. Investigation on original statistic distribution analysis of flat bulb steel by laser ablation inductively coupled plasma mass spectrometry. Metallurgical Analysis, 2009, 29 (9): 1-5.
- [7] Yuan Liang-jing, Yu Lei, Han Mei, Wang Hai-zhou. Original position statistic distribution analysis of low alloy steel rupture by laser ablation inductively coupled plasma mass spectrometry. Metallurgical Analysis, 2010 30 (6): 1-6.
- [8] Wang Hai-zhou. A new method of statistic characterization of specific properties of materials ——Original position statistic distribution analysis. Physical Testing and Chemical Analysis Part B: Chemical Analysis, 2006(42): 1-5.
- [9] Wang Hai-zhou, Zhao Pei, Chen Ji-wen. Study on original position statistic distribution analysis of low alloy steel billet. Science in China (Series E Engineering & Materials Science), 2005, 35(3): 260-270.

SUPERMAGNAG : A NEW MAGNETIC SENSOR FOR AN ON-LINE MONITORING OF THE SINTERING PROCESS

C. Mathy, B. Vanderheyden, J.-C. Pierret,
F. Stas, W. Holbrecht, W. Lumen

*Centre for Research in Metallurgy, avenue du Bois Saint-Jean 21, B-4000 Liège
ArcelorMittal Gent, John Kennedylaan 51, B-9042 Gent*

Abstract

The SuPerMagnag system is an innovative magnetic sensor able to monitor the sintering degree continuously, directly on the sinter strand and over the whole bed width.

The core sensor measures the magnetic permeability of the sinter cake, directly correlated with the bivalent iron content of the sinter product and its physical quality. Positioned on top of the strand, on a ski-type support, it moves transversely to provide a complete and continuous mapping of the upper layer sinter quality. Sensible to changes in the sintering degree due to variations of the solid fuel input but also of the ignition conditions, it supplies real-time information, much earlier than with any other monitoring system. The complete system has been installed on the No.2 sinter strand at ArcelorMittal Gent, who took in charge the assembly and installation of the mobile supporting structure.

This sensor can help the operators to select in a more reactive way the solid fuel input or the mix charging and ignition conditions, and to improve the process regularity and minimise the transverse heterogeneities. Transverse information can be used as an alarm signal to detect abnormal loading conditions, ignition failures or maintenance needs. Important gains in terms of energy savings, productivity, quality and environmental impact might be obtained with a pay-back period of only a few months.

SuPerMagnag observations have already been one of the factors that have led to the choice of a new set point concerning the solid fuel input level for the Gent sinter strand. This modification has reduced the overheating hazard, enhanced sinter quality and decreased solid fuel consumption. Further improvements are expected from the ongoing SuPerMagnag integration into the semi-automatic solid fuel control system of the sinter plant at ArcelorMittal Gent.

Introduction

Sinter plants have to maintain high and stable performances at lowest possible production costs in various operating situations. This requires a high level of flexibility with respect to requested production rate (high or low demand), energy sources (coke breeze or anthracite) and use of reverts and more challenging ores (finer, high gangue content, variable quality ...). Enhanced process control tools are essential to reach this goal.

CRM developed for that purpose the patented SuPerMagnag sensor.^[1] Measuring on-line the evolution of the sinter quality with a very short response time compared with conventional methods, it allows optimisation of the sintering energy consumption, in particular in combination with semi-automatic solid fuel control systems.

Principle

The core sensor, developed by CRM, is based on a magnetic permeability measurement, this magnetic property of the sinter cake being a direct image of its bivalent iron content ^{[2] [3]} and thus of its sintering degree. As can be seen on Figure 1, the measurement is made directly on the sinter strand. As a point of comparison, the Permagnag system (previously developed by CRM ^{[4] [5] [6]}) is using a similar principle but with the magnetic measurement carried out on the produced return fines. The positioning system, engineered by ArcelorMittal Gent, allows the sensor to be moved transversely to scan the full width of the strand. So, it provides a continuous mapping of the upper layer sintering degree.

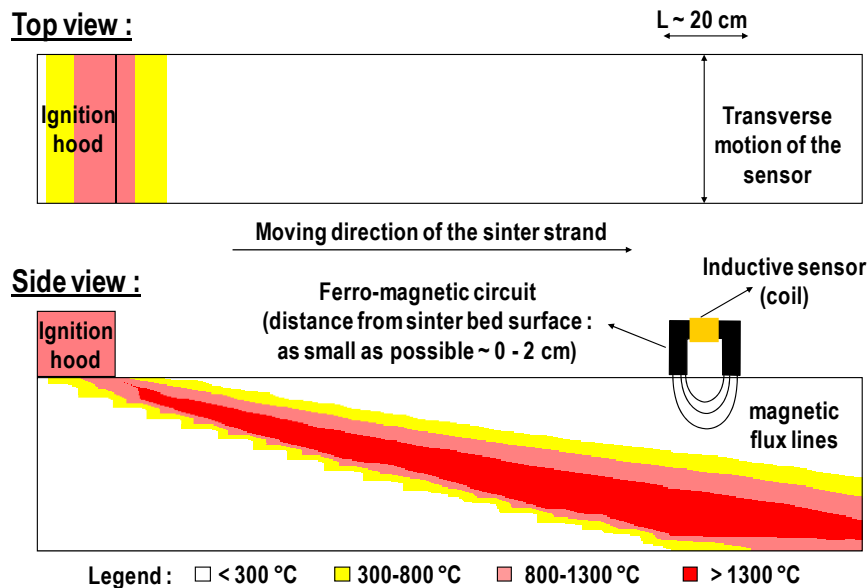


Figure 1: Schematic view of the SuPerMagnag system

Sensor development

Preliminary studies

Preliminary studies allowed to check the measurement principle and to determine the new sensor optimal characteristics and working conditions.

Measurements carried out on different sinters allowed first establishing the potential variation range of the sinter relative magnetic permeability: between 1.2 and 2.5.

Preliminary tests were also dedicated to the study of the temperature dependency of this value. Figure 2 points out the necessity to measure only on an already cooled sinter for which the signal deviation is relatively low and constant.

It was therefore decided to place the sensor near the discharging end of the sinter strand, where the upper sinter layer is already cooled. A simple temperature correction allows in this case obtaining a stable measurement.

A numerical 3D simulation tool of electromagnetic systems was used to design the sensor. Its size and shape, as well as the electric characteristics, were optimised to maximise the sensitivity and the transverse resolution, and to minimise the air gap effect (i.e. the effect of the gap between the sensor and the sinter cake surface).

Sinter pot tests

The new sensor was firstly tested at the sinter pot pilot installation in CRM.

As foreseen from numerical simulations, the air gap effect appeared to be very important. The graph of Figure 3 shows that the raw sensor signal difference between two different mixes decreases quickly when the sensor is moved away from the sinter. The sensor has thus to be maintained at a distance as close and as constant as possible from the sinter cake surface to provide a sufficiently discriminating signal. The measured raw voltage is then converted to magnetic permeability value thanks to a fitted conversion law taking into account the actual gap. Sinter pot tests demonstrated that with an air gap of about 15mm, SuPerMagnag is sensitive to little variations of the top layer sintering degree down to 50 mm depth. Moreover, the repeatability was proven to be very good: on Figure 3, four different measurements are stacked for each mix and gap.

An extensive pot test campaign was then carried out at CRM using different coke rates and different ignition times for several types of sintering mix. For those tests, the Permagnag sensor was used as a reference system. Resulting sensor sensitivity curves are presented in Figure 4. Those trials proved that SuPerMagnag is as sensitive as Permagnag to changes in the coke input, while it is much more sensitive to changes of the ignition conditions.

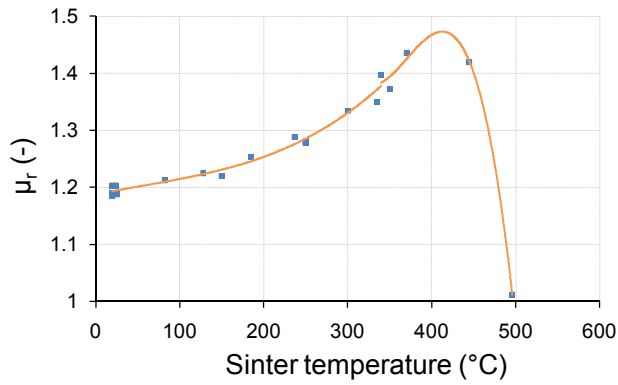


Figure 2: Temperature dependency of the relative magnetic permeability

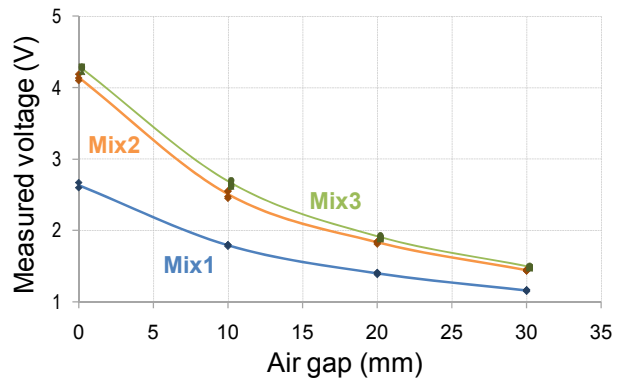


Figure 3: Effect of the air gap on the new sensor sensitivity

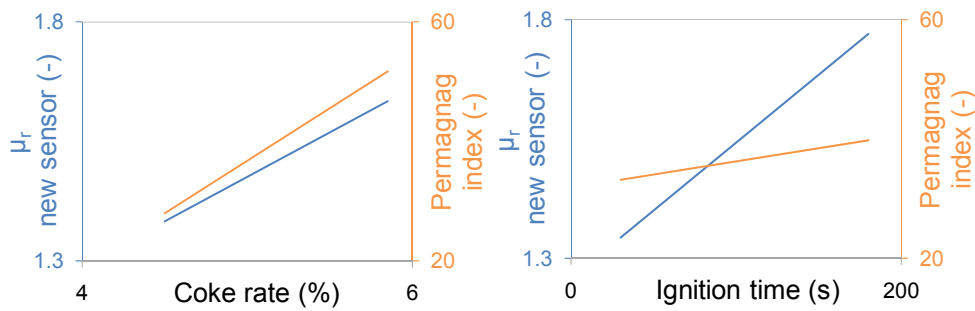


Figure 4: Comparison of the sensitivity of Permagnag and SuPerMagnag

The direct link with the sinter quality was also checked during pot trials. Figure 5 shows the relation between magnetic properties of the sinter, Fe⁺⁺ content and sinter strength (fraction above 6.3mm after tumble tests) for a typical sinter mix of ArcelorMittal Liège. To facilitate comparisons, the magnetic permeability measured by SuPerMagnag is converted to a “Permagnag” relative scale.

Those sinter pot results confirmed the interest of this new measurement technique and it was thus decided to carry on the sensor development towards an industrial application.

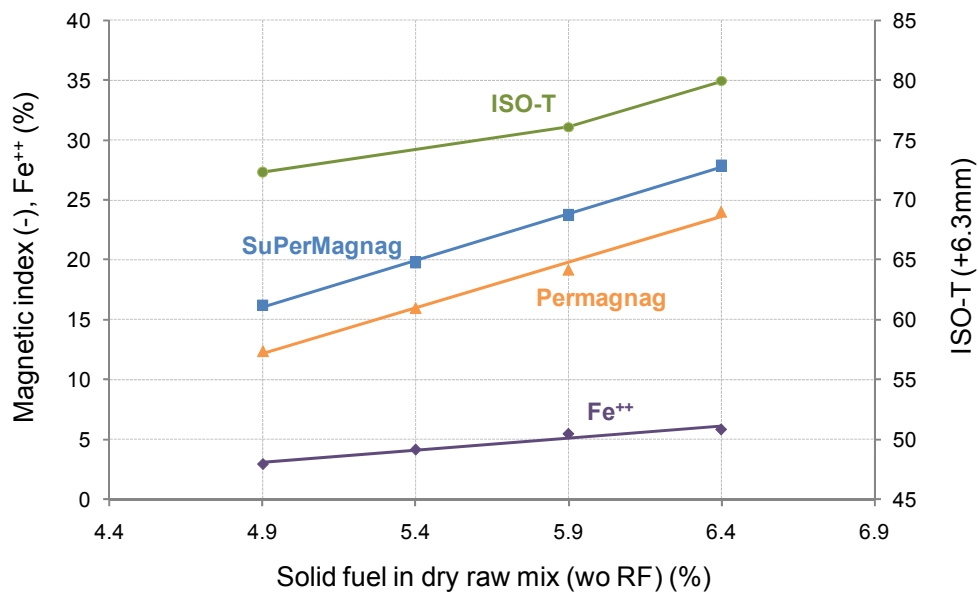


Figure 5: Correlation between magnetic properties and quality indices

Industrial prototype

The solution chosen to control the air gap between the sensor and the sinter top layer consists in positioning the sensor on a well-suited support “skiing” on the sinter cake. As can be seen on Figure 6, it is equipped with a counterweight in order to minimise the wear of the ski plate. Those wearing elements have been carefully studied (in what concerns the material and the mechanical conception) in order to obtain a sufficiently robust and handy system. An ancillary laser sensor, measuring the distance to the sinter surface, allows adapting the SuPerMagnag level to the layer height variations. This solution allows a continuous measurement at a constant distance with only little maintenance work: just the replacement of the wear plates when needed.

The mobile structure, engineered by ArcelorMittal Gent and installed at their sinter strand n°2 (see Figure 7), ensures the transverse motion across the sinter strand, and allows measuring about 18 transverse profiles per hour.

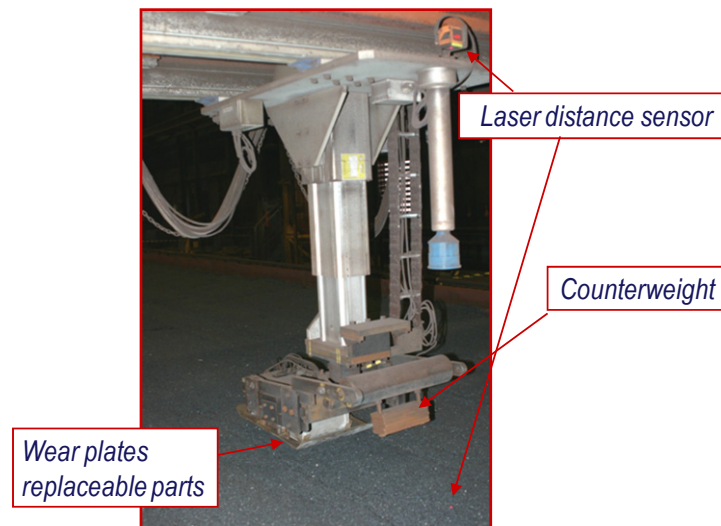


Figure 6: SuPerMagnag sensor moving on sinter strand SIFA2 at ArcelorMittal Gent



Figure 7: SuPerMagnag system installed on sinter strand SIFA2 at ArcelorMittal Gent

Regulation and alarm ancillary sensors, combined with diagnosis systems, allow a safe operation, taking into account progressive or discontinuous sinter cake level variations or an accidental stoppage of the sinter strand.

The system also includes an automatic calibration procedure. Standard blocks were built with a known and homogeneous magnetic permeability. Calibration curves, as a function of the sensor distance, were determined for each of those blocks. During the measuring process, the sensor is regularly brought back to its calibration position and corrective factors are calculated. An automatic cleaning procedure is performed during this phase.

Thanks to this automatic calibration, measurements given on the sinter strand are automatically corrected to take into account the wear of the ski plate and a possible electronic drift. A supplementary second order correction is also applied continuously to take into account the influence of the temperature.

The implemented signal processing allows extracting reliable information even when permeability bars are in operation. In this case indeed, the strand surface is more undulating and an envelope curve extraction is useful to compensate for higher air gap variation. This signal processing also includes on-line wear and temperature corrections mentioned here before. The data logging system is integrated in the plant monitoring system so that sensor measurements can be easily related to other process parameters.

Control of the complete system and basic visualisation of results is made through a dedicated screen in the control room.

A mean value is calculated for each profile and the monitoring of this averaged value temporal evolution is included inside the global control screen used by operators for process regulation guidance. In Gent, the continuous regulation of the solid fuel input is mainly based on the Permagnag measurements. An alternative control system has been implemented, based on the current Permagnag control, but working with the SuPerMagnag signal. This system calculates the needed solid fuel input adaptations based on the SuPerMagnag measurements.

In parallel, the monitoring of the transverse profile information is made through a screen allowing the follow-up of the current profile evolution and the comparison with a reference curve, which can be chosen as the average on a previous period.

All those elements make up a complete system available for long term industrial campaigns.

Industrial application

On the whole, the SuPerMagnag system on the No.2 sinter strand at ArcelorMittal Gent has been measuring during more than 4000 hours. The maintenance consists in the replacement of the wear parts when necessary (an alarm is given by the system itself). The life time corresponds to at least 40 days continuous work, which is sufficient to ensure continuous measurements between two programmed plants shut down. The replacement of the wear parts is an easy operation that can be carried out without any special tool in only a few minutes.

To validate the information provided by the new sensor, different tests have been organised.

Global sintering degree evolution

The first trials concerned the evolution of the mean sintering degree (the average value of each transverse profile). During these campaigns, voluntary variations of the solid fuel rate and of the ignition power were performed.

For what concerns coke rate evolution, a clear correlation with SuPerMagnag signal can be seen on Figure 8. To complete this validation campaign, specific sinter samples were extracted from the bed top layer (core sampling 50mm depth) and they were analysed. Their bivalent iron content was compared to corresponding SuPerMagnag measurements. The coherence between both provided a supplementary proof of the new sensor validity. All SuPerMagnag measurements were also compared to the magnetic index of the return fines, measured by the Permagnag. Both evolutions are really similar, with a clear gain of more than one hour for SuPerMagnag to get information on the sintering degree. This delay corresponds to the time needed for the sinter to go from SuPerMagnag position to Permagnag sampling point. For sintering plants using more classical characterisation means (chemical analyses on sinter samples), this time gain would even be higher.

Concerning the influence of the ignition conditions, specific trials were organised, for which hood temperature was modified between 1290 and 1200°C. The effect on SuPerMagnag signal is obvious, with a variation higher than 10 rel.% per 100°C (see Figure 9), and a delay of about 25 minutes, corresponding to the distance between the ignition hood and the sensor. On the other hand, the effect on Permagnag signal is very weak. This behaviour confirms perfectly, at industrial scale, the results from sinter pot trials previously presented.

A long term comparison between the chemical analyses of the sinter samples (the magnetite content on the Figure 10) and the averaged SuPerMagnag values shows a real correlation. The correlation coefficient is of course not so high, but it must be pointed out that the sampling procedure intrinsically brings some errors.

To enhance this quality prediction, the influence of some other process parameters (such as the produced return fine rate) has to be carefully studied, for each particular configuration, keeping in mind that the sensor is measuring mainly the quality of the sinter cake upper-layer.

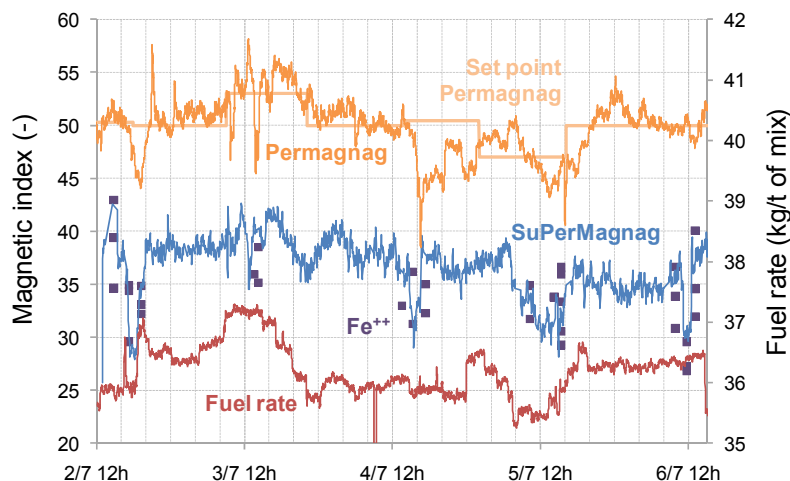


Figure 8: Sintering degree evolution compared to solid fuel input and Fe^{++} content of sinter

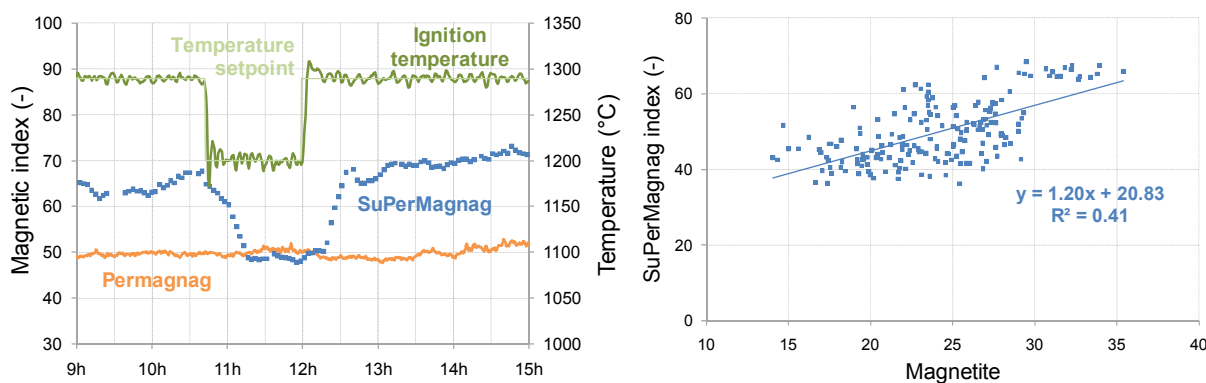


Figure 9: Effect of ignition temperature modification on magnetic indices

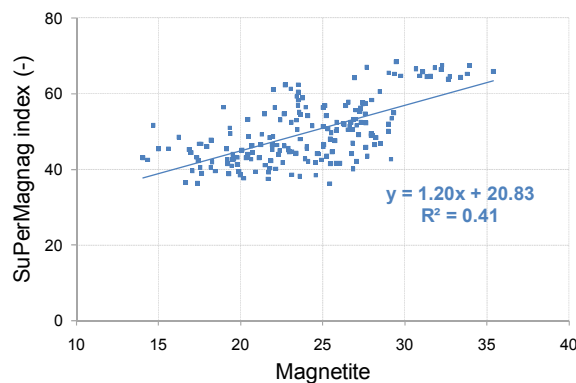


Figure 10: Correlation between magnetite content of sinter samples and SuPerMagnag

At ArcelorMittal Gent, in the current configuration, the SuPerMagnag system can be used as an indicative tool allowing a short loop monitoring of the sintering process, in combination with other signals. For example, if an important variation of the current SuPerMagnag mean value occurs, other relevant signal progressions must be observed carefully. Depending on their relative evolutions, inadequate heat input, vertical heterogeneity or even overheating situations can be detected and corrective actions have to be taken on the solid fuel input, on the ignition or on the charging conditions.

To upgrade this system to a tool for an effective “semi-automatic” process control, it is thus necessary to combine existing monitoring means of the sinter quality (Permagnag system or classical off-line analyses), relevant process parameters and new SuPerMagnag information and to fit optimised control rules adapted to the varying input mix composition. At Gent, the optimisation of those control rules is currently in progress.

A full exploitation of this monitoring tool should of course be facilitated by a plant configuration including supplementary action means such as a vertical segregation control.

Transverse profile information

Besides this global monitoring, specific verification campaigns were also dedicated to the assessment of the transverse profile information.

The system is designed to measure approximately 18 profiles per hour (3 minutes for each transverse movement and some minutes for calibration every hour). As there is some noise on the measurements (remaining influence of the relief, cracks ...), looking at individual curves does not provide reliable data but averaging some successive profiles allows obtaining readable information.

On Figure 11, the sintering degree profile is given for two different periods, each curve being the result of an average on 18 minutes (which corresponds to 6 successive profiles). During those periods, several samples were extracted from the bed top layer at different transverse locations. Their bivalent iron content analysis (represented by the squared points) confirms an important transverse variation (here up to 23 relative percent) and a fluctuating shape. This example clearly shows that besides the average level for each period, the SuPerMagnag is able to supply a real on-line sintering degree profile.

This transverse information of the SuPerMagnag can be used by the operators as a diagnosis tool. Depending on the measured shape and its evolution, different actions can be prescribed. Here are some examples:

- If the gradient at the wall increases sharply, operators have to check possible air in-leaks in the hood.
- For any local disturbance, ignition burners have to be checked.
- If the dissymmetry left/right rises up, operators have to check the bed level, the feeding system and the burner's temperatures.
- If the profile standard deviation increases, the cleanliness of the segregation plate has to be checked. Figure 12 illustrates this case, with a clear positive effect on the process homogeneity after a cleaning of the charging bin and of the segregation plate. The standard deviation can thus be used to optimise the cleaning practice.

Further modifications in the strand infrastructure at ArcelorMittal Gent will provide more actuation means; for example more regulation possibilities with a new ignition burner system.

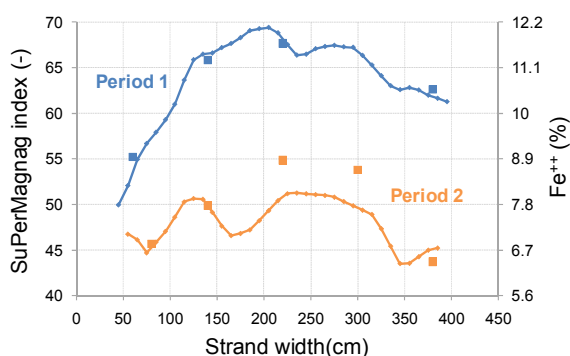


Figure 11: Consistency of the transverse profile information

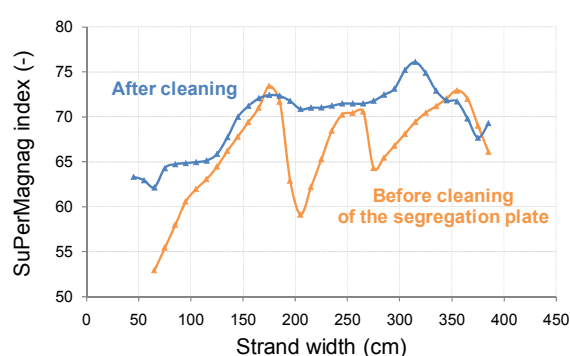


Figure 12: Transverse profile measurement as a diagnosis tool

Evaluation of the industrial benefits

A completely integrated SuPerMagnag system provides a useful tool to the operator that allows him selecting in a very reactive way the solid fuel input or the mix charging and ignition conditions. The consequence is an improved process regularity and a minimisation of the transverse heterogeneities.

Based on those considerations, important gains in terms of energy savings, productivity, quality and environmental impact are estimated. Figure 13 details those potential gains, including the impact of sinter quality improvement on blast furnace operation^[7]. The corresponding economic gain is expected to be in the range 0.3 - 1 € per tonne sinter, depending on specific characteristics of each plant and on available action means.

Considering an investment of approximately 300 to 500 kEUR for a complete system (including sensor and accessories, sensor moving structure and control, preliminary sensitivity study, support to implementation and set-up tests), the pay-back period would be only a few months.

Even if those gains have still to be proved during a long term evaluation, SuPerMagnag observations have already been one of the factors that have led to the choice of a new set point concerning the solid fuel input level for the Gent sinter strand. This modification has reduced the overheating hazard, enhanced sinter quality and decreased solid fuel consumption. Further improvements are expected from the ongoing SuPerMagnag integration into the semi-automatic solid fuel control system of the sinter plant.

Impact on plant performances**Sinter plant**

Solid fuel saving	2 - 5	kg/ t _{sinter}
Electricity saving	0.2 - 0.5	kWh/ t _{sinter}
Productivity increase	3 - 7	%

Blast furnace

Coke saving	1 - 2	kg/ t _{hot metal}
-------------	-------	-------------------------------

Impact on pollutant emissions

(specific reductions : per tonne sinter)

Sinter plant

CO	4 - 12	%
SOx	3 - 10	%
NOx	1 - 4	%
PCDD/F	3 - 10	%
VOCs	2 - 7	%
CO ₂	3 - 8	%

GHG emissions**(sinter plant + blast furnace)**

CO ₂	11-20	kg
-----------------	-------	----

Figure 13: Potential gains with SuPerMagnag measuring system

The transferability of the measurement principle has been checked by tests carried out with a prototype portable version of the measuring device at ArcelorMittal Liège. Results obtained on their DL5 sinter strand have proven the validity of this technique for a higher basicity sinter (1.7 instead of 1.4 for Gent). However, it must be noted that in extreme cases of atypical sinter mix composition (for ultra high basicity above 2.5 or very high magnetite ore content in the sinter mix) the sensitivity of the magnetic properties versus sintering degree has to be checked.

Conclusion

A new on-line monitoring tool is provided for a better control of the sintering process. It allows improving its regularity and minimising the transverse heterogeneities.

Indeed useful information can be obtained concerning the sintering degree, comparable to those given by traditional techniques, but with numerous advantages:

- First of all, the response time is considerably shorter, allowing a much more reactive process control.
- It allows the detection of modified ignition conditions.
- A very useful transverse information is supplied that can be used as an alarm signal to detect abnormal loading conditions, ignition failures or maintenance needs.
- The measurements should also be sensitive to vertical segregation (to be confirmed by segregation trials).

This highly promising technique is still in an optimisation phase based on long term collaboration between CRM and ArcelorMittal.

References:

- 1) Belgium Patent, delivered on 07/10/03, n° 1014405, "Procédé et dispositif pour le contrôle en ligne de la qualité de l'allumage et/ou du degré de cuisson d'un gâteau d'agglomération de minerais de fer"
- 2) Knott, A.C.; Scaife, P.H.: Sinter plant control using magnetic permeability to measure FeO in sinter; IISI Technology Committee meeting, March 1981
- 3) Vidal, R.; Poos, A.; Meunier, G.; Lückers, J.; Boelens, J.: Le contrôle et la régulation du processus d'agglomération sur grille, Revue de Métallurgie, CIT, Avril 1980, pp. 285-292
- 4) Poos, A.; Lückers, J.: Contribution to the automatic control of a sintering strand, Stahl und Eisen, 1975, Nr. 15, July 17, pp. 683-689
- 5) Fleming, G.; Hofmann, P; Cappel, F.; Hastik, W.: Use of a process control computer in a new ore preparation plant; Stahl und Eisen, 1975, Nr. 15, July 17, pp.677-683
- 6) Depaye, P.; Mathonet, Ch.; Vanderheyden, B.; Manassis, E.: Expert System for Sinter Plant Control; 3rd European Ironmaking Congress, Gent, September 16-18, 1996, pp. 193-201
- 7) Inkala, P.; Karppinen, A.: Rautaruukki's sinter quality and testing methods; Meeting of Young Blast Furnace Engineers (European Blast Furnace Committee), May 1991, Sidmar

DEVELOPMENT OF AN ON-LINE LIBS-BASED SENSOR FOR MONITORING THE HOT METAL COMPOSITION IN THE BLAST FURNACE RUNNERS

G. Monfort, L. Bellavia, B. Vanderheyden, V. Tusset

CRM Group, Liege, Belgium

Summary

This paper is devoted to the description of a sensor developed at CRM in the field of the Iron and Steel Making. This sensor, based on the LIBS technique is dedicated to the continuous measurement of the composition and temperature in the blast furnace runners. The goal is to assess on-line the composition of the hot metal, mainly Fe, C, Si and Mn and its temperature. For the slag, the concentration in CaO, MgO, SiO₂, Al₂O₃ and MnO can also be determined as well as the presence of iron particles, which is an important issue for safety reasons. This sensor has been submitted to feasibility tests at the ArcelorMittal Gent blast furnace.

Potential advantages of using such a sensor for the process control are also presented.

Introduction

Blast furnaces need a lot of skill to be operated, mainly because of the complexity of the reactions taking place in a multi-phase process with interactions of heat and mass transfer. Moreover, due to the size of this reactor, a long time is needed before the changes resulting from control actions are effectively observed. As a consequence, it is important to base these control actions on process data as accurate as possible.

One of the key factors to take into account in order to ensure a smooth running of the blast furnace is the silicon concentration in the hot metal. Indeed, beside its importance for the metal quality, this element is related to the thermal state of the hearth. On the other hand, as demonstrated by several studies, the silicon concentration is far from being constant during one cast [1,2], while only one or two samples are usually taken for its analysis. In the same way, most of the time, only one temperature measurement is made, while variations are observed depending on the origin of the hot metal inside the furnace [3].

As far as the slag is concerned, it can be important to assess its composition in order to evidence possible mistakes in loading minerals. However, the main interest of a continuous measurement at that level is probably linked to the safety. Indeed, if some hot metal (iron particles) flows in the slag runner, explosion can occur during the subsequent water granulation. A continuous monitoring of the presence of iron matter could avoid accidents which, even if they rarely occur, can be very heavy and damageable for the personnel and the material.

For all these reasons, CRM has started the development of a sensor able to continuously monitor the composition and the temperature of the hot metal and slag in the blast furnace runners. This sensor is based on the LIBS technique and is aimed at operating with the minimum of maintenance and of human intervention.

Principle of the LIBS

LIBS stands for Laser Induced Breakdown Spectroscopy. This method is mainly used when chemical analysis has to be made at stand-off, due to difficulties resulting from environmental conditions. It is particularly useful for measurements on hot materials, in radioactive areas or in poorly accessible or confined zones.

Figure 1, based on a commercial equipment, the TeleLis [4,5], supplied by a German company, illustrates the principle of the LIBS method as applied at CRM. To make things simple, a high energy Nd-YAG pulsed laser emits short pulses of light at a frequency of 20 Hz. The beam is focused by a suitable optics on a target, located 2 to 12 metres away. At the focal point, the energy density is such that the material is vaporised, plasma is formed and expands at high speed. This plasma emits a UV-Visible spectrum, with lines specific to the chemical elements present in the target. The intensity of each line is a function of the concentration in the corresponding element. The light of the plasma is collected by a 30 centimetre diameter telescope and focused back on the

entrance slit of a spectrometer. After a suitable calibration, the intensity of relevant spectral lines gives the concentration of the elements to be analysed.

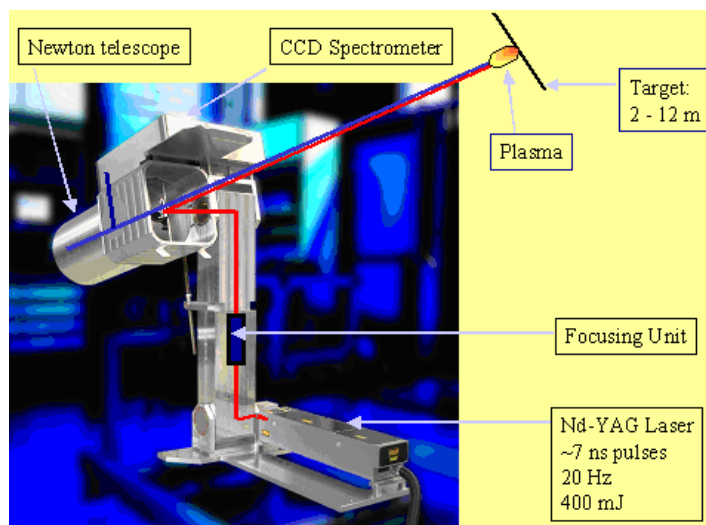


Figure 1: Principle of the LIBS for stand-off measurements (Example of *TeleLis*)

Preliminary tests

Before being able to demonstrate the feasibility of LIBS measurements at stand-off on liquid metal in an industrial environment, it was useful to determine the best measuring conditions in laboratory conditions. To this aim, the TeleLis was used for measurements on solid samples as well as on liquid metal in a CRM pilot installation.

Measurements on solid samples

In a first attempt, the effort is devoted to the analysis of silicon, because of its importance to the process and because it represents a challenge for the following reasons:

- the silicon concentration in the hot metal is rather low, from about 0.2 to 0.8%;
- the most sensitive spectral line of silicon is surrounded by very close and rather intense iron lines. As a result, a spectrometer with a very good resolution is needed;
- the sensitivity of the silicon line, while acceptable, is not very high: a powerful laser as well as a sensitive spectrometer are thus needed;
- stand-off measurements imply low amounts of collected plasma light and consequently rather high background noise.

Tests were carried out on samples supplied by ArcelorMittal Gent and ArcelorMittal Dunkirk, taken from various casts to cover the range between 0.2 and 0.8% of silicon content.

The measurements were performed at a distance of 4 metres and 200 laser pulses were used for each measurement. An optimising procedure allowed removing the background noise and performing an outlier rejection. After defining the best operating conditions, i.e. laser and spectrometer settings as well as focusing position, the results depicted in Figure 2 were obtained. A relative accuracy of about 10% can be stated in the full range of investigated concentrations, compared to the classical laboratory XRF method.

Measurements at the pilot stage

After these tests, it was necessary to verify that the liquid state of the hot metal and its high temperature will not deteriorate the sensitivity and the precision of the results.

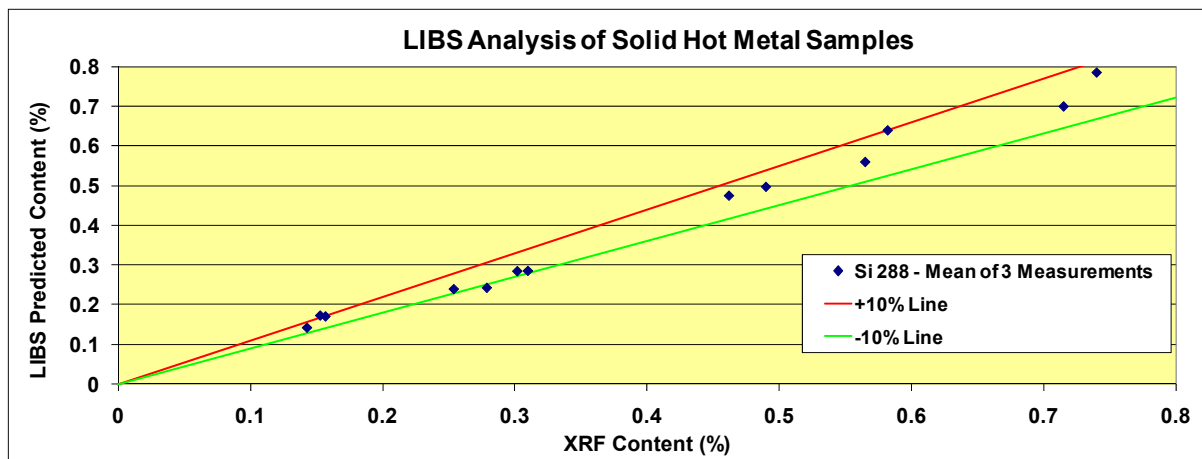


Figure 2: Results of LIBS analysis on solid hot metal samples

Pilot tests were carried out at CRM. A 10-kg induction furnace allowed to melt a commercially available cast iron and to heat it to 1400°C. The TeleLis was placed on a lift table and fitted with a 3 metres long tube to protect the personnel from the laser beam and to provide confinement for an inert atmosphere. A view of the set-up is given in Figure 3. The initial silicon content was expected to be 0.2% but XRF analyses showed that it was about 0.7%. During the test, several additions of silicon were done and, each time, LIBS analyses were performed.



Figure 3: View of the pilot set-up for LIBS measurements on liquid hot metal

As shown in Figure 4, the accuracy of the results is satisfactory and similar to the one obtained on solid samples, even if the level of silicon concentration is slightly higher than expected. This test proved that the radiated heat from the high temperature liquid metal does not substantially interfere with the measurements. Moreover, splashing of the liquid due to plasma expansion or large deviations of the spectral line width were not observed. From these encouraging results, it was decided to carry out tests at the blast furnace runners.

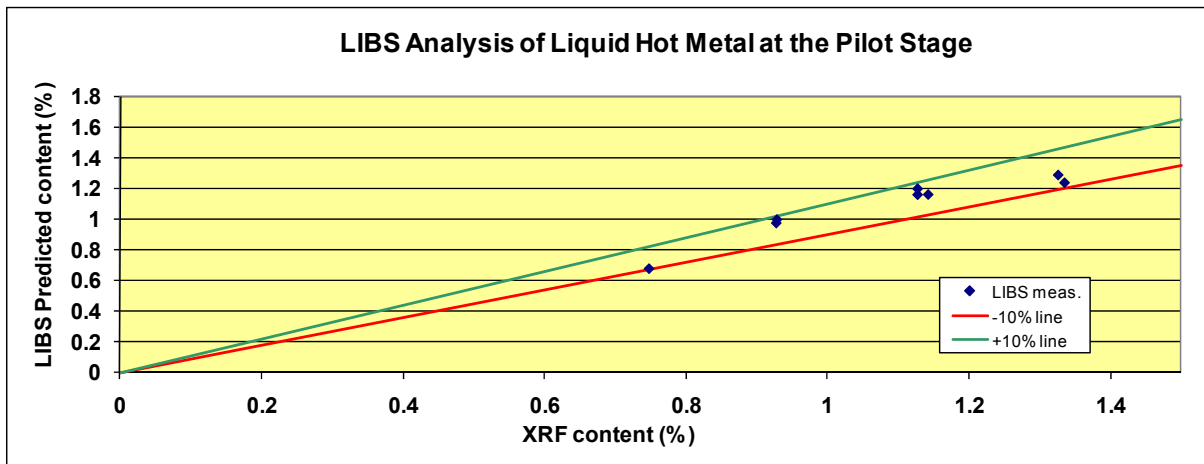


Figure 4: Results of LIBS analysis on liquid hot metal at the pilot stage

Industrial tests

The industrial tests were performed at the ArcelorMittal Gent blast furnace with the support of their operational staff.

Due to the harsh conditions prevailing at the industrial site, the TeleLis cannot be used as such. The development of a remote sensor head able to be placed on top of the runner was thus started.

A special attention was devoted to the cooling system and to the management of fumes and dust. In a first stage, the size of the sensor was not optimised since the aim was mainly to prove the feasibility of the analysis.

Figure 5 shows the principle of the measuring head: an optical cabinet and its cooling system are fitted with a refractory nozzle dipping in the liquid metal. It only contains the laser head, the optics for laser beam focusing, the optics for the plasma light collection and ancillary electronics. All the controls for laser firing, the spectral line analysis and the result display and storing are done remotely at five to ten metres from the runner, far from the hot and dusty area.

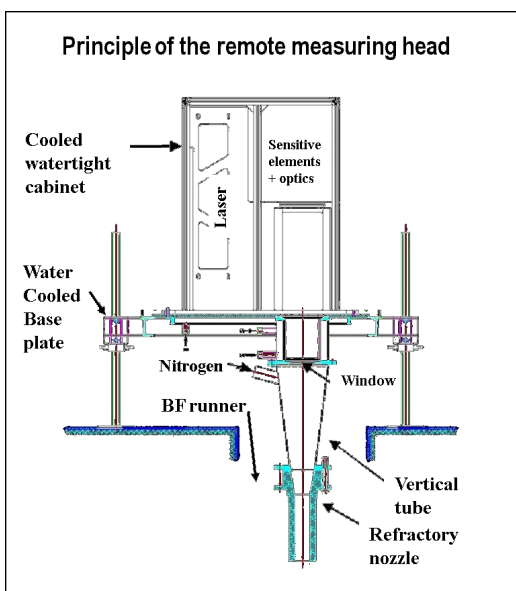


Figure 5: Principle of the LIBS remote measuring sensor

The optics for laser focusing and plasma light collection is optimised by the ZEMAX software in order to ensure that the energy density always remains below the damage threshold of the optics while being maximised on the liquid metal. The design also ensures that the amount of light measured by the spectrometer is maximised while keeping a reasonable size for the dimensions of the optics.

Dummy tests

Before completing real measurements, a dummy test of the new CRM measuring head, without the sensitive optical components, has been carried out at the ArcelorMittal Gent blast furnace B. The aim of this test was to determine whether it is possible to keep the temperature inside the optical cabinet below 40°C. The reason is that the laser will not operate above this temperature.

The results were very satisfactory: the recorded temperature at the location where the laser has to be fitted remains below 15°C, at a distance to the liquid hot metal lower than one metre. Only the fused silica window closing the cabinet reached 110°C, far below its maximum operational temperature.

A webcam, installed to monitor the atmosphere inside the nozzle in contact with the liquid metal, confirmed that the design of the measuring head allows performing analyses on a clean liquid and that the atmosphere above is reasonably free of fumes, owing to especially designed nitrogen blowing.

Industrial LIBS tests

A full scale measurement campaign was then scheduled for which the laser, the optics and the control electronics were placed in the measuring head. A complete risk analysis has been previously performed together with the ArcelorMittal Gent staff in order to address all possible issues that could occur due to the use of a class IV laser in an industrial environment. This procedure allowed defining a series of hardware and software improvements so that the final system is extremely safe for the personnel.

The measuring head was directly located on top of the runner, at a distance of about 75 centimetres from the liquid metal at 1500°C (Figure 6). Despite these very difficult conditions, the temperature inside the cabinet was kept below 25°C while the optics and mainly the exit window remained as clean as at the beginning of the test.

The overall duration of this trial was more than 9 hours and two successive casts were monitored.

During the first cast, which stood for one and an half hour, measurements were taken about each 1.5 to 2 minutes.



Figure 6: View of the LIBS measuring device on top of the ArcelorMittal Gent blast furnace runner - to the right, views of the nozzle during and after the test.

The sensitivity of the analysis is very good and similar to what was obtained in the lab. A remote focusing device allows maintaining the quality of the signals in spite of the variations of the liquid metal level.

The whole system was left on the runner during the time between the first and second cast, i.e. about 2 hours and the temperature of the optics remained constant. During the beginning of the second cast, measurements were taken each minute during 40 minutes with the same sensitivity as during the first cast.

All analyses were performed with 100 laser pulses per measurement, with laser energy of 400 mJ and a 10 Hz repetition rate. Owing to software optimisation, a complete measuring cycle including firing 100 laser pulses, spectral data processing, display and storing of the results takes less than 30 seconds.

For illustration purposes, Figure 7 summarises the results of the LIBS analyses during the second cast for silicon, carbon and manganese. The agreement with the classical sampling method ("Lollipop" samples) is quite good.

A deeper evaluation of the results, a careful examination of the spectra recorded during these industrial tests and further comparisons with the slag composition prove the feasibility of liquid hot metal and liquid slag analysis by LIBS, even if a mixture of slag and hot metal is present at the surface of the runner.

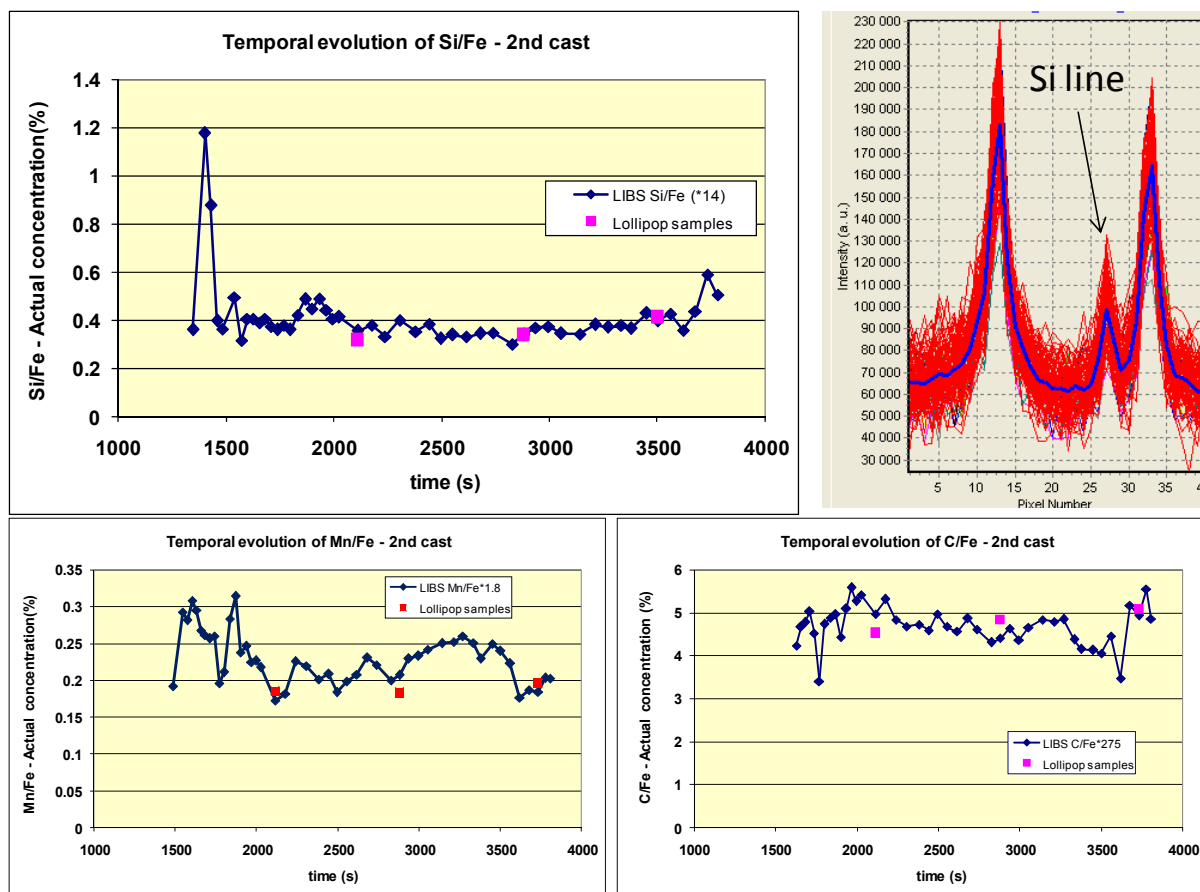


Figure 7: Comparison between LIBS measurements and classical sampling. An example of silicon spectrum is given in the upper right part of the Figure.

Work currently in progress

Considering the success of this first measuring campaign, it has been decided to test the system during longer periods of time. However, longer runs impose more constraints on the unit to be used. Indeed, the analyses have to be carried out unattended and all the safety measures have to be taken to ensure that people, not trained to work with lasers, cannot be injured due to a faulty operation. Moreover, at the request of the staff from the casting floor, temperature measurement has to be added to the LIBS analysis. Such measurements can obviously be done with a classical pyrometer. However, it is possible to use the already existing LIBS optics to send the visible and infra-red radiations from the liquid metal to a dedicated spectrometer. With suitable data processing software, this technique allows true multi-wavelength pyrometry while remaining economical since no dedicated optics has to be added.

Another constraint is to keep the dimensions of the remote sensor as small as possible to avoid disturbing the blast furnace operators in their day-to-day tasks. Such a system and the corresponding control software are now nearly completed and extensive tests are planned in the next months.

The new measuring head is equipped with a lot of sensors to ensure the personnel safety as well as to evaluate the operating parameters. From these data, a fully optimised sensor could be manufactured by an equipment builder for implementation in routine use at the steel industry level.

Possible applications of the LIBS sensor for the blast furnace process control

In parallel to the sensor development, a bibliographic study, corroborated by discussions with blast furnace specialists gives some information on the way a continuous monitoring of the hot metal composition could improve the process control.

Tsuchiya et al. [6] have identified variables influencing the silicon content of the hot metal at short term, middle term and long term. If a continuous measurement of the silicon concentration is available, a faster evaluation of the effect of variations in these process parameters can be obtained and the silicon content can be kept more constant.

Another approach could consist in feeding an autoregressive vector (ARV) model [7], able to predict the evolution of silicon at short term, based on a previous series of measurements. The more measurements are carried out, the more accurate is the prediction.

Generally speaking, a more precise evaluation of the silicon content of the hot metal leads to energy savings by allowing a lower average silicon concentration. Moreover, a better control of the blast furnace induces less hot metal temperature fluctuations which results in an increase of the cast floor refractory life-time as well as reduction of excessive hearth cooling.

Since the continuous measurement can be done during nearly 100% of the tapping time, the representativeness of the analysis is better and less sampling could be necessary, resulting in benefits in personnel costs as well as gains at the steel shop by a decreased variability of the hot metal composition.

Moreover, on-line measurements could be beneficial to the estimation of the liquid levels in the furnace by the EMF method. Indeed, since this technique is influenced by the silicon content [8,9], an automatic correction could be applied on-line.

Finally, as far as the slag analysis is concerned, a continuous monitoring of the iron content could avoid explosion hazards during granulation and help maintaining the iron level below the limit value for slag valorisation notably by the cement industry.

Conclusions

This paper describes the methodology applied at CRM for the development of an industrial LIBS sensor devoted to the on-line composition and temperature measurement of the hot metal and the slag directly in the blast furnace runners. The effort was mainly devoted to the analysis of silicon due to its importance on the process control but other important constituents of the hot metal and the slag were also analysed. The first tests have proved the feasibility of the measurements despite the very harsh environment and the tough constraints to address in order to get enough sensitivity while ensuring small sensor dimensions, long lasting and personnel safety. A bibliographic study in parallel with the sensor development has given some hints for an efficient use of such measurements, as far as return on investment is concerned.

Acknowledgments

The authors gratefully acknowledge the financial support of the CRM affiliated companies, mainly ArcelorMittal and Tata Steel. The help and involvement of the ArcelorMittal Gent blast furnace staff during the whole duration of this research are also particularly acknowledged.

References

- [1] R. Vidal et al., "Contribution to the Fundamental Study of the Blast Furnace - Evolution of the Slag and Hot Metal Compositions", Revue C.N.R.M. n°24, September 1970, pp.14-19
- [2] Fedulov, "Change in the Silicon and Sulfur Content of Pig Iron", Metallurg, n° 7, pp. 17-19, July 1981 (trad. Plenum, 1982)

- [3] A. Andersson et al., "Variation of Hot Metal and Slag Composition during Tapping of Blast Furnace", *Ironmaking and Steelmaking*, Vol 31 (2004), n°3, pp. 216-226
- [4] Reinhard Noll and Cord Fricke-Begemann, "Stand-Off Detection of Surface Contaminations with Explosives Residues Using Laser-Spectroscopic Methods", in *Stand-Off Detection of Suicide Bombers and Mobile Subjects*, NATO Security through Science Series, 2006, 2006, 89-99, DOI: 10.1007/1-4020-5159-X_12
- [5] LSA Company web site: <http://www.lsa-systems.de>
- [6] N. Tsuchiya et al., "The transfer of Silicon from the Gas Phase to Molten Iron in the Blast Furnace", *Metallurgical Transactions B*, September 1976, pp. 315-320
- [7] H. Saxen and L. Karilainen, "Model for Short-Term Prediction of Silicon Content in the Blast Furnace Process", *51st Ironmaking Conference Proceedings, Toronto Meeting, April 5-8, 1992*, pp. 185-191
- [8] V. Dubovik, et al., "Automatic Monitoring of the State of the Blast Furnace Well", *Izv. V.U.Z. Chernaya Metall.*, 1982(4), pp. 4-6
- [9] P. Lebed, L. Safina, V. Demidenko, A. Semenko, I. Pochedkailo, "Evaluating Work of Blast Furnace Hearth from the Nature of EMF Variation", *Steel in the U.S.S.R.*, Vol. 20, February 1990, pp. 59-61

ELEMENT ANALYSIS OF OXIDE MATERIALS IN STEEL INDUSTRY BY LASER-INDUCED BREAKDOWN SPECTROSCOPY

J.D. Pedarnig 1, J. Heitz 1, B. Praher 1, P. Kolmhofer 1, N. Huber 1,
R. Rössler 2, H. Wolfmeir 2, E. Arenholz 2

*1 Christian Doppler Laboratory for Laser-Assisted Diagnostics, Institute of Applied Physics,
Johannes Kepler University Linz, A-4040 Linz, Austria*

2 voestalpine Stahl GmbH, A-4031 Linz, Austria

SUMMARY

Laser-induced breakdown spectroscopy (LIBS) is an attractive method for fast and quantitative materials characterization that can be employed for in-line monitoring in industrial processes. We report on the application of LIBS to the analysis of multi-component oxide materials. Slag from industrial steel production, certified reference materials and mixed oxide test materials are analyzed by LIBS and the concentration of oxides is determined by a calibration-free (CF) method. For all materials investigated we find good match of CF-LIBS concentration values with reference values. The relative errors are < 15 % for major oxides, larger errors are observed for minor oxides. The concentration values are stable against large variations of measurement parameters. Our results indicate that LIBS has significant potential for innovative analytical sensing in steel industry.

1. INTRODUCTION

Laser-induced breakdown spectroscopy (LIBS) is a versatile technique for fast multi-element compositional analysis of gaseous, liquid and solid materials [1 - 6]. This method is employed in various fields including materials identification, environmental monitoring, detection of hazardous materials, and for different on-site and in-line industrial applications. For quantitative composition analysis of sample materials univariate or multivariate regression models are commonly employed. Matrix-matched reference materials and sample materials are measured under similar experimental conditions in order to calibrate the employed LIBS measurement system. Calibration-free LIBS (CF-LIBS) methods, on the other hand, determine the composition of sample materials directly from measured spectra by modelling the laser-induced plasma and the optical plasma emission [7 - 8]. This approach is of interest as calibration samples are not required and constraints regarding the control of experimental parameters are less stringent. Various materials such as metal alloys rocks and biological samples have been analyzed by CF-LIBS.

Oxides are key materials for different industrial branches and the measurement of oxide concentration is essential in various technical processes. LIBS has been employed for the investigation of oxide materials like slag, ore, cement, and concrete. The concentration of oxides in metallurgical slag and ores has been determined by multivariate and univariate regression procedures. Major oxides in rocks and soils have been quantified by artificial neural network methods.

In this contribution, we report on the application of CF-LIBS method for the quantitative compositional analysis of different types of oxide materials. Homemade mixed oxides are investigated by LIBS in order to test the CF-LIBS algorithm developed. Industrial slags from steel production are measured and analysed by our CF-LIBS system. The compositional analysis of slag is important for the process control in steel production and for the use of slag as secondary raw material.

2. EXPERIMENTAL

Figure 1 shows the experimental setup that is employed for LIBS measurements. The pulsed radiation of a Nd:YAG laser (Continuum Surelite I-20, wavelength $\lambda = 1064$ nm, pulse duration $\tau_L \approx 6$ ns, laser pulse energy around 100 mJ if not stated otherwise, repetition frequency 5 - 10 Hz) is employed for ablation of sample materials. The samples are placed on a rotation stage and all measurements are performed in air background.

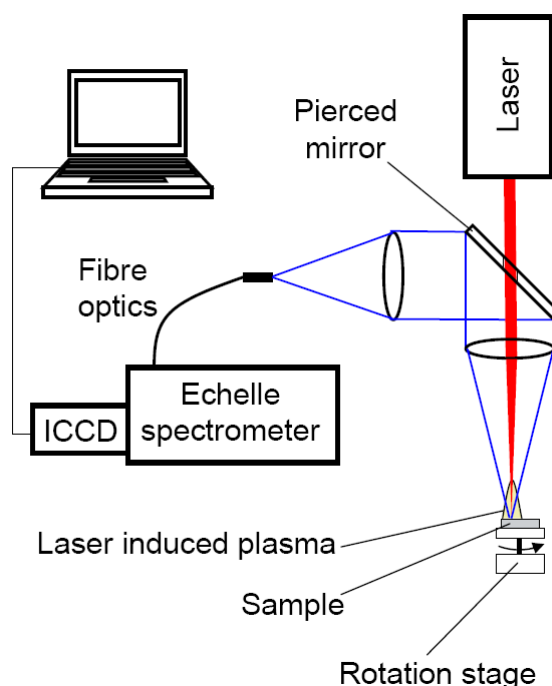


Figure 1: Schematic of experimental setup for LIBS measurements of multi-component oxide materials (slag).

The plasma emission is collected by lenses, a pierced mirror, and a quartz fiber, and LIBS spectra are measured with an Echelle spectrometer and a gated intensified CCD camera (LTB, model Aryelle). For one spectrum the plasma emission is accumulated over many laser pulses (typically, 100 shots). For CF-LIBS analysis several spectra are averaged for each sample.

The mixed oxide samples were prepared from three powder materials (Fe_2O_3 , MgO , CaO) by mixing and hydraulic pressing. For different samples the concentration of powders was varied in the range 9.8 - 33.3 wt % (Fe_2O_3), 7.6 - 33.3 wt % (MgO), and 33.3 - 81.2 wt % (CaO) [9]. The slag materials contained at least seven different oxides (CaO , Al_2O_3 , MgO , SiO_2 , FeO , MnO , TiO_2 , Cr_2O_3) with concentration values in the range 10^{-3} - 54.4 wt % for different samples [10].

3. RESULTS

The CF-LIBS determination of concentration of elements from measured optical emission spectra requires several calculations [9]. The measured spectra are corrected for the spectral response of spectrometer and detector and are deconvolved by the instrumental function. Emission lines showing low self-absorption are selected for all relevant elements. The number densities of neutral $N_j^{(I)}$ and singly-ionized $N_j^{(II)}$ plasma species (multiplied by an unknown experimental parameter) are obtained from Saha-Boltzmann analyses for all elements (j). The concentration of an element is assumed to be proportional to $N_j^{(I)} + N_j^{(II)}$ and the concentration of the corresponding oxide is determined by using stoichiometric factors. The summation over all analyzed elements

determines the unknown experimental parameter and yields the weight content of oxides in the sample material investigated.

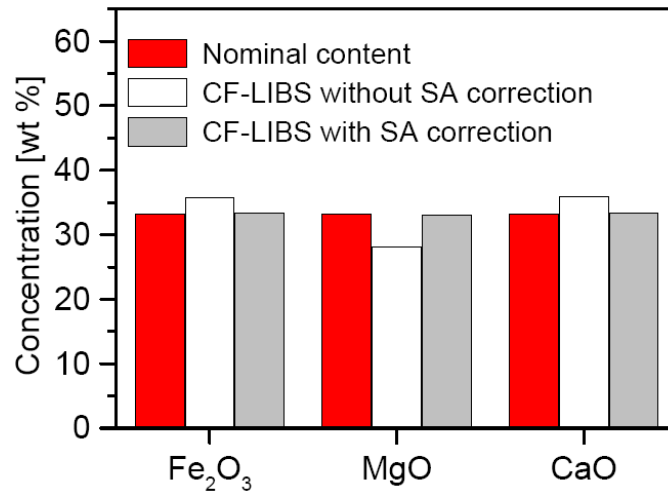


Figure 2: Comparison of the nominal composition with the composition calculated by CF-LIBS for a tertiary mixed oxide sample. The CF-LIBS calculation is performed with and without self-absorption (SA) correction for comparison [9].

Figure 2 compares the nominal concentration of oxides C_N with the CF-LIBS calculated concentration of oxides C_{CF} for a homemade tertiary sample. The CF-LIBS data are calculated directly from the measured LIBS spectra. A good match of nominal and calculated concentrations and small absolute errors, $e_a = |C_{CF} - C_N| < 1 \text{ wt \%}$, are achieved when self-absorption effects are taken into account in the calculation. Without self-absorption correction the observed absolute errors are significantly larger.

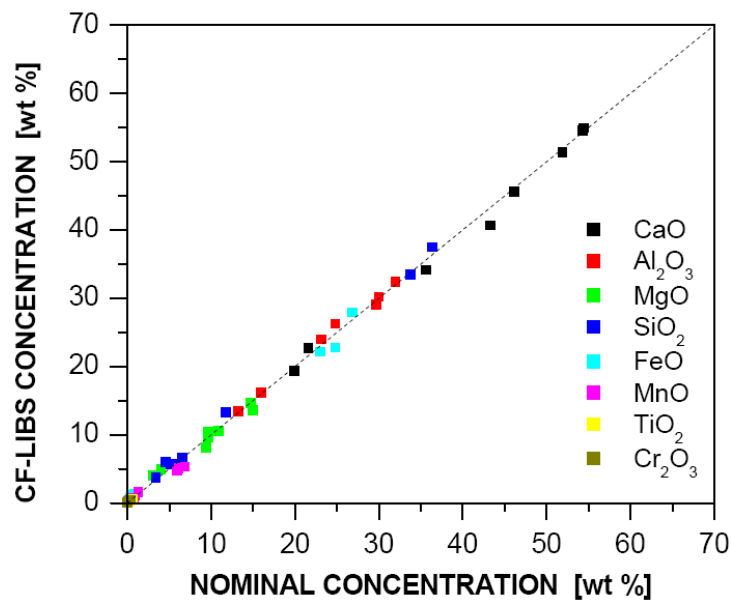


Figure 3: Nominal (C_N) and CF-LIBS (C_{CF}) calculated oxide composition of industrial slag samples [10]. The broken line indicates the ideal case ($C_{CF} = C_N$).

Figure 3 compares the nominal and the CF-LIBS calculated oxide composition of industrial slag samples [10]. Self-absorption correction is taken into account in the CF-LIBS calculation. Eight different samples were analysed

each containing at least seven different oxides. For all slag samples and all oxides investigated a good match of the CF-LIBS concentration with the nominal concentration is found. The broken line indicates the ideal case of perfect match ($C_{CF} = C_N$). For the major oxides ($C_N \geq 10$ wt %) the relative errors $e_r = |C_{CF} - C_N| / C_N$ are less than 10 %. For minor oxides the relative errors are larger and trace oxides cannot be reasonably determined.

For technical applications the stability of CF-LIBS results against fluctuations of experimental parameters is decisive. In order to test our method we have varied the laser pulse energy over broad range (70 – 325 mJ) and we studied the variation of CF-LIBS concentrations with pulse energy. For major oxides we find small errors and small variations of errors with energy ($e_r < 10$ %).

4. CONCLUSIONS

LIBS is a promising technique for fast analysis of multi-component materials. The calibration-free LIBS method allows for quantitative compositional analysis of such materials without the need for matrix-matched reference materials. From our results we conclude a lower limit for CF-LIBS quantitation of about 1 wt % for individual oxides in slag. Our results indicate that the LIBS method and the calibration-free evaluation of spectral LIBS data have significant potential for innovative analytical sensing in steel industry.

Acknowledgements

Financial support by the Austrian Federal Ministry of Economy, Family and Youth and the National Foundation for Research, Technology and Development (Christian Doppler Laboratory LAD) is gratefully acknowledged.

References

- [1] A.W. Miziolek, V. Palleschi, I. Schechter (Eds.), *Laser-Induced Breakdown Spectroscopy (LIBS), Fundamentals and Applications*, Cambridge University Press (2006).
- [2] D. A. Cremers, L. J. Radziemski, *Handbook of Laser-Induced Breakdown Spectroscopy*, John Wiley & Sons Inc (2006).
- [3] *Laser Induced Breakdown Spectroscopy*, ed. J. P. Singh and S. N. Thakur, Elsevier (2007).
- [4] R. Noll, V. Sturm, Ü. Aydın, D. Eilers, C. Gehlen, M. Höhne, A. Lamott, J. Makowe, J. Vrenegor, *Laser-induced breakdown spectroscopy - From research to industry, new frontiers for process control*, *Spectrochimica Acta B* 63 (2008) 1159 – 1166.
- [5] L.M. Cabalín, A. González, J. Ruiz, J.J. Laserna, *Assessment of statistical uncertainty in the quantitative analysis of solid samples in motion using laser-induced breakdown spectroscopy*, *Spectrochimica Acta B* 65 (2010) 680 – 687.
- [6] S. Laville, M. Sabsabi, F.R. Doucet, *Multi-elemental analysis of solidified mineral melt samples by Laser-Induced Breakdown Spectroscopy coupled with a linear multivariate calibration*, *Spectrochimica Acta Part B* 62 (2007) 1557 - 1566.
- [7] A. Ciucci, M. Corsi, V. Palleschi, S. Rastelli, A. Salvetti, E. Tognoni, *New procedure for quantitative elemental analysis by Laser Induced Plasma Spectroscopy*, *Applied Spectroscopy* 53 (1999) 960 – 964.
- [8] E. Tognoni, G. Cristoforetti, S. Legnaioli, V. Palleschi, A. Salvetti, M. Mueller, U. Panne, I. Gornushkin, *A numerical study of expected accuracy and precision in Calibration-Free Laser-Induced Breakdown Spectroscopy in the assumption of ideal analytical plasma*, *Spectrochimica Acta Part B* 62 (2007) 1287 – 1302.
- [9] B. Praher, V. Palleschi, R. Viskup, J. Heitz, J.D. Pedarnig, *Calibration free laser-induced breakdown spectroscopy of oxide materials*, *Spectrochimica Acta Part B* 65, 671 - 679 (2010).
- [10] B. Praher, R. Rössler, E. Arenholz, J. Heitz, J.D. Pedarnig, *Quantitative determination of element concentrations in industrial oxide materials by laser-induced breakdown spectroscopy*, (submitted for publication in *Analytical and Bioanalytical Chemistry*).

SRM: AN INDUSTRIAL ON-LINE TOPOGRAPHY MEASUREMENT

Wolfgang Bilstein¹, Genevieve Moreas²

¹*Amepa GmbH, Karl-Carstens-Str. 12, D 52146 Wuerselen (Germany)*

²*CRM group, Avenue du Bois Saint Jean 21, B 4000 Liège (Belgium)*

Summary

Complex metal forming, high level protection, more and more stringent customer requirements and the necessity to increase productivity are some of the numerous reasons that confront the steel makers to a delivery problem of guaranteed high surface quality strips.

Although major improvements have been achieved during the last years, the strip surface, and especially roughness (Ra), was not yet under control.

To continuously control and so improve the surface properties, a surface roughness sensor (SRM) has been developed by CRM and industrialized by AMEPA to measure roughness parameters along the whole length of the strip on various industrial lines. The selected measurement method is based on the principle of triangulation: a very thin line is projected on the surface and the relief is determined by analyzing the deformation of the line.

The method has been validated by comparison with mechanical stylus reference measurement. The correlation between SRM and stylus is in a range of +/-10% which is far good.

SRM has been installed on various lines and so on various products: continuous annealing line, tandem (oiled surface), galvanising line (high reflective surface), roll shop (high reflective and roughness surface). As well coated, un-coated, random (e.g. EDT) and deterministic (e.g. EBT) surfaces are concerned.

The final result is so an on-line sensor for assessing topography. This sensor is presently used in Europe in daily production by Arcelor Mittal, Salzgitter Flachstahl and Voestalpine others lines.... Four sensors are installed in China in Shougang Cold Rolling Co, Ltd on continuous galvanising line and on continuous annealing line.

This leads to a better understanding of the influence of the various production parameters on the strip surface with the possibility to directly control the process.

Key words

Roughness, Ra, SRM, topography, on-line, sensor, continuous, industrial

Biography of authors

Wolfgang Bilstein: 45 years old, mechanical engineer from University of Aachen (PhD in 2001). Senior engineer at Amepa GmbH, Research and Development.

Genevieve Moreas: 44 years old, electronic civil engineer from University of Liege (1990). Program leader at CRM Group, CRM Liege in "Advanced sensors" department.

INTRODUCTION

Rising demands of the automotive industry in quality of sheet surface make it necessary to control continuously the roughness of strip steel. Moreover, the optimization of the deep drawing process requires sharp tolerances in the tribological behavior of the material to achieve higher production rates. High-strength steel and aluminum sheet can only be deformed without defect under optimized conditions. Homogeneity of the surface roughness is an important factor to reach the best product.

The on-line measurement of the roughness parameters enables not only a complete documentation as expected by ISO 9000 but also a more economic production. The immediate availability of roughness data allows the direct correction of process parameters if the quality of the surface roughness is out of its tolerance range. This avoids a cost and time intensive second milling of the product.

Today the roughness is measured with a mechanical stylus manually on samples taken from head or tail of the coil. This measurement does not give a representative value for the roughness distribution over the length of the coil because rolling force and speed are reduced when the welding passes the skin pass.

The optical on-line roughness measurement provides a measurement over a significant part of each coil and could be used for a more complete documentation of this important product property. The on-line measurement could not only be used for sharper production tolerances but it could also be used as a tool for a more precise trigger for the change of the texturing rolls.

Here we will present the development, laboratory results and on-line measurements of the industrialized version by Amepa based on the original development by the Center for Research in Metallurgy (CRM) in Liège, Belgium /1, 4/.

MEASURING PRINCIPLE

The presented roughness measurement system uses the two-dimensional triangulation, also known as light-section measurement. The CRM has refined this principle for the on-line roughness measurement on strip steel. Successful tests were done at Arcelor Flat Carbon Steel, Gent /1/.

For the roughness measurement a laser line is projected under a certain angle onto the surface. Due to the surface topography this line is distorted if it is observed under a different angle than the projection. This distortion allows a direct calculation of the surface profile and hence the surface roughness. Figure 1 shows the correlation between distortion of the line and the topography of the surface. A more detailed description can be found in /1/.

As an example the projected laser line is shown in Figure 1 on an EBT texturized galvanized surface. The background illumination is not necessary for the measurement but gives the user the opportunity to validate the result. Even the fine structures of the zinc layer can be resolved by the distortion of the laser line.

On-line roughness measurement systems that use a laser spot for the roughness measurement depend on the movement of the strip to achieve data in the second dimension. Therefore these devices are only able to measure parallel to the rolling direction. The light section principle – used in the Amepa SRM - allows an arbitrary orientation of the line and so roughness can be measured perpendicular or under 45° to the rolling direction as SEP 1940 and DIN EN 10049 /3/ demand.

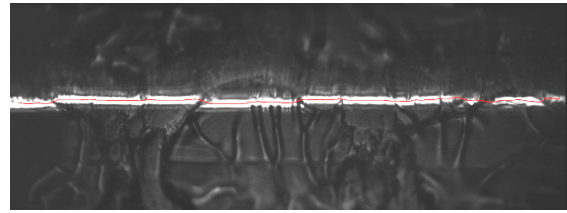
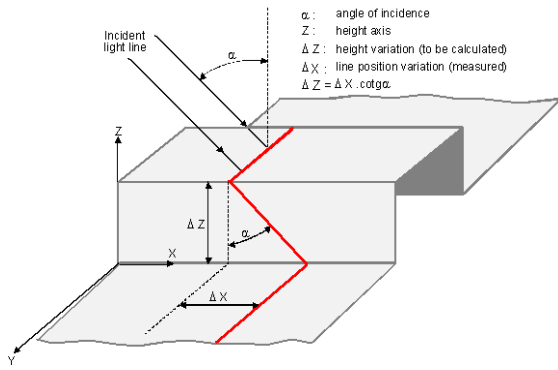


Figure 1 Geometrical correlation between topography and line distortion /1/

The other advantage of the line projection is the fixed correlation between all points of the line. When the exposure time is short enough the system is not affected by vibrations or the velocity of the strip.

The image series in Figure 2 shows the wide range of optical properties of coated and uncoated steel sheet which can be measured by the SRM. The system adjusts automatically to the different reflectivity of e.g. galvanized (highly reflective, fig. 2b) or galvanized (perfect scattering surface, fig. 2c). This is very important because both products are manufactured alternating in the same production lines.

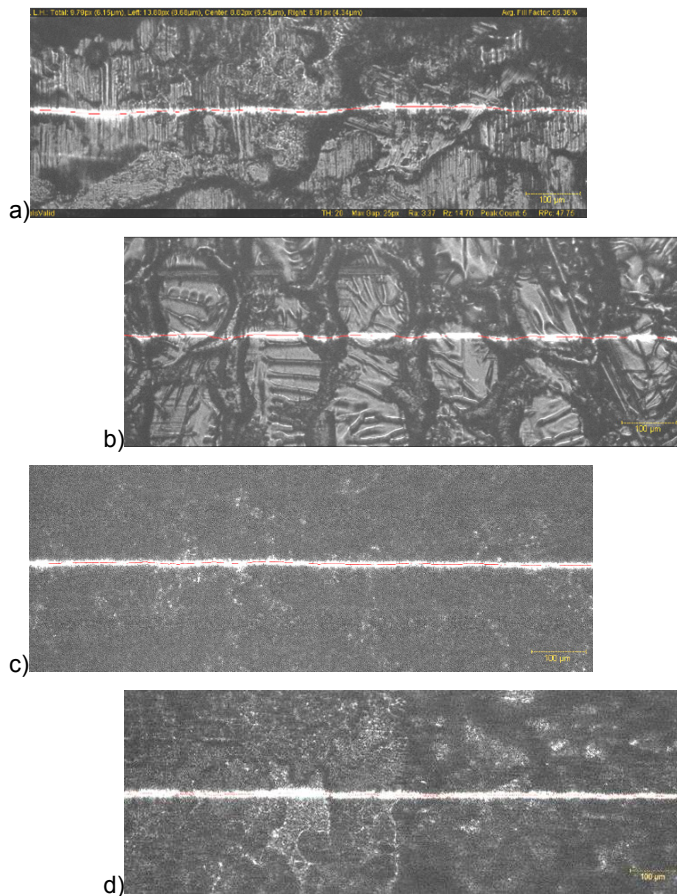


Figure 2 Example images of different textures and coatings: a) EDT annealed, $R_a = 3.5\mu\text{m}$; b) EBT galvanized, $R_a=1.4\mu\text{m}$; c) EDT galvanized, $R_a = 1.1\mu\text{m}$; d) EDT electrolytic galvanized, $R_a = 1.2\mu\text{m}$.

SYSTEM DESIGN

The sensor consists of a laser system for line projection and of a microscope with a high resolution CCD-camera for the observation of the distorted line. An additional laser is used for background illumination enabling a direct inspection of the microscopic image of the strip surface which can be done normally only in laboratory.

The used diode laser system is maintenance free and guarantees a long lifetime of the system. The lasers are equipped with special driver electronics which enable not only the control of the pulse energy but also the variation of the pulse duration which could be decreased down to 8 ns. This means in combination with the used optical setup that even at speeds up to 1500 m/min no reduction of image quality could occur. Two times higher velocities should not affect the result of the measurement itself. The other advantage of this electronics is the possibility to set the illumination of the laser diodes to the optimum point for each sheet surface with very different scattering properties from nearly black to highly reflective.

A very high resolution and magnification of laser line and image is necessary to measure surface structures in the micrometer range. The small depth of field of the required microscope objectives leads to high demands in the positioning accuracy of the sensor. To match this task, the sensor is equipped with a precise distance sensor which triggers the lasers and the image acquisition process when the strip surface is within the focus of the microscope. The sensor is placed above a roll where the strip is held in a defined position. To make sure that the strip is well aligned, an angle of contact of 5 degree is sufficient. A special version of the sensor, developed for use in skin pass mills, is even able to measure on free swinging strip due to its high speed distance measurement.

For the necessary adjustments of the optical system fully motorized stages are used. This means the settings for installation or corrections can be changed whenever necessary. No production stop is required. An installation at nearly inaccessible locations is possible as well. These properties guarantee a high availability and a flexible operation.

LABORATORY RESULTS

The laboratory results can be divided in two sections. The most important are the comparative measurements with the stylus on different textures and surface qualities over a wide range of roughness. Optical roughness measurements on roughness standards used for the calibration of stylus systems are also possible. These two groups allow a comparison of the optical measured statistic roughness values with the results of a stylus and with the values of the calibration standards (Table 1).

Roughness Standard	Nominal Ra [μm]	Optical measured Ra [μm]
Halle KNT 2058/2	0.45	0.49
Halle KNT 2058/2	1.1	1.07
Mitutoyo Specimen No 178-601	2.97	2.91

Table 1 Optical measurement on roughness calibration standards /4/

Sheet Samples

The results of laboratory measurements with the stylus and the optical system show a very good correlation (Figure 4). The investigated samples cover a wide range of roughness, but also stochastic and deterministic

textures (EDT, Pretex, EBT) and different surface qualities (cold rolled, annealed, galvanized, galvanized and electrolytic galvanized) as well.

This collection of 130 different samples was measured with the same optical setup and identical software settings. This means that there are no texture specific settings necessary. The only parameter which has to be adjusted is the laser intensity to avoid over- or underexposed images due to the very different reflectivity of the analyzed surfaces.

For most samples the deviation was less than 5% which is in the same order than the deviation of stylus measurements done by different operators with different stylus systems /4/.

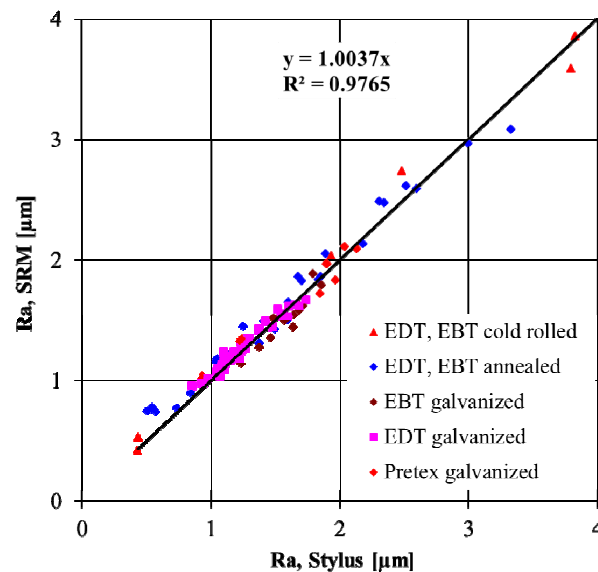


Figure 3 Comparison of the optical roughness measurement (SRM) with stylus on different sheet samples with different textures and surface qualities

ON-LINE MEASUREMENTS

For on-line measurements the system was installed at Arcelor Flat Carbon Steel, Ghent (Sidmar). These online measurements were overseen by the Rolling Annealing Finishing (RAF) group of Arcelor Research. The Amepa system was tested on different production lines. In the beginning, the sensor was installed behind the skin-pass at the exit of the continuous annealing line (CAPL). To test also its performance on polluted surfaces, the sensor was installed at the entrance of the CAPL. Since spring 2006 the system is installed at the exit of the galvanizing line at Arcelor Mittal Ghent.

Exit of Continuous Annealing Line

For the first on-line test the prototype of the roughness measurement system was installed at the exit of the continuous annealing line behind the skin pass mill. In Figure 6, the mechanical off-line and optical on-line roughness measurements of one production day are shown. For the mechanical roughness three stylus measurements were done at the end of each coil at the strip position where the optical sensor was installed. The optical measurements were saved in the plant database and the mean value of the last 10% of the coil was calculated for the comparison with the stylus results.

The SRM system got no information about texture or material qualities that were produced. This means all different surface qualities are measured and analyzed with the same set of parameters. Only the illumination intensity is automatically adjusted to avoid overexposed images of the sheet surface.

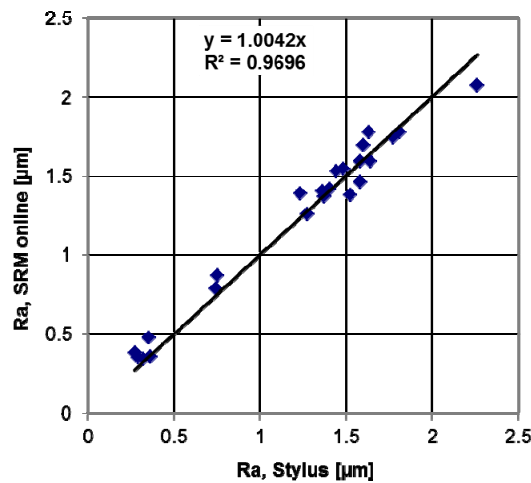


Figure 4 On-line results at the continuous annealing line at Sidmar, including the complete product range (EDT, EBT, polished rolls).

Test Measurements at a Tandem Mill

The SRM sensor was installed directly after the last stand next to the thickness measurement gauge. To stabilize the sheet surface to take focused images of the texture the support of the flatness measuring roll was used. With this configuration the SRM was able to measure at strip speeds up to 1450 m/min. In Figure 7 the result of a step test is shown, where a coil was rolled in the tandem mill with increasing rolling forces in the last stand of the mill. Afterwards the roughness was measured manually in the inspection line with a stylus.

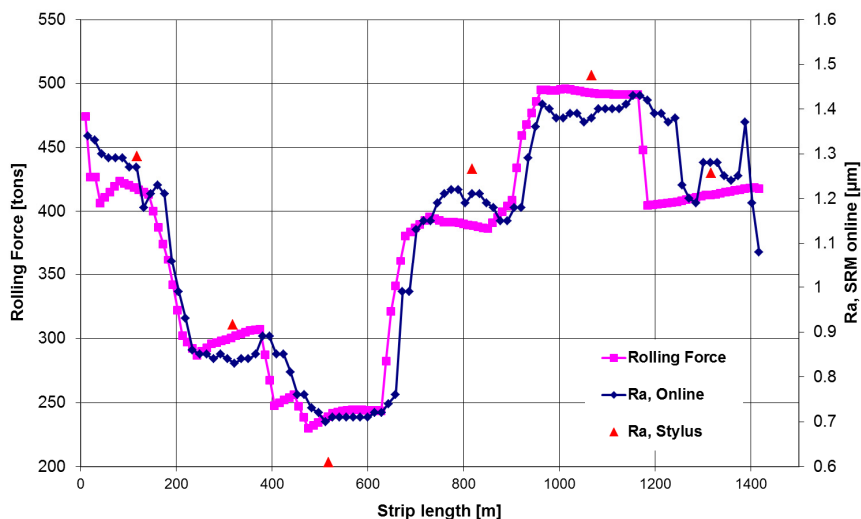


Figure 5 EDT surface, rolled with different rolling forces in the tandem mill: comparison of optical and mechanical roughness measurement.

Free standing Skin Pass

The SRM system can also be used in free standing skin pass mills. A blower unit was developed to keep the optics clean from cooling emulsion. First experiences have shown that cleaning intervals of 30 days can be achieved.

Another important feature of the skin pass sensor is the increased dynamic behavior. While a tandem mill has high strip speeds product properties and production are still quite stable, the skin pass has higher requirements regarding the dynamic behavior of a measuring system. Strip thickness and optical properties may differ very much so focus settings and laser power must be adjusted for each coil to achieve the best image quality. Due to high accelerations and short production cycles these adjustments have to be very fast to ensure stable data over the complete length of the coil.

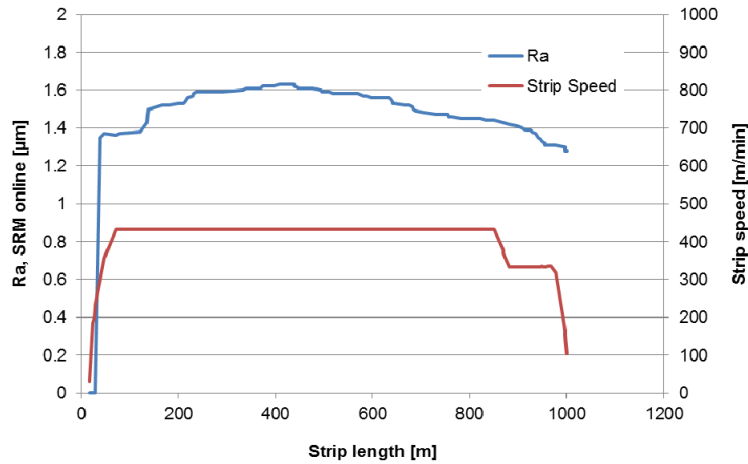


Figure 6 Dynamic behavior of the online roughness measurement inside a free standing skin pass mill

The graph in Figure 6 shows the fast reaction of the system. It takes only between 20 and 50 m after insertion of the coil into the skin pass that the sensor adjusts itself and is ready for measurement.

Exit of Galvanizing Line

Online tests on galvanized sheet were performed at the galvanizing line (Sidgal) at Arcelor Flat Carbon Steel, Ghent. Production of automotive exposed sheets requires a high level of quality.



Figure 7 SRM Sensor at galvanizing line

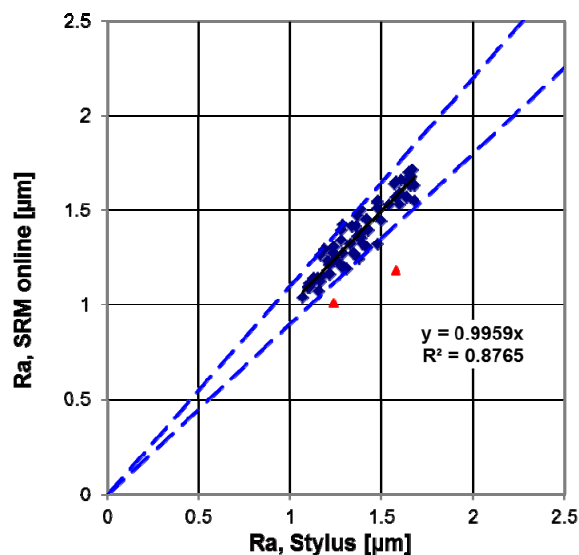


Figure 8 Online results on a galvanized EBT surface. In between the blue dotted line the deviation between online measurement and stylus is smaller than 10%.

CONCLUSION

Amepa has developed, based on the CRM prototype, an industrial online roughness measurement system. Its results show a good agreement with the stylus measurements in laboratory and in on-line trials as well. It delivers roughness information over the complete length of the coil. This opens the possibility of process optimization during cold rolling and a complete documentation of this product property.

The here described measuring principle enables a roughness measurement perpendicular or under 45° to the rolling direction (SEP 1940 and DIN EN 10049) unlike optical systems which calculate the roughness out of a series of punctual measurements measuring always in rolling direction. The Amepa SRM system works independent of the investigated surface, of its roughness, coating or texture, therefore no calibration is required. For a verification of the system performance it is possible to use the same roughness standards used for stylus systems as well.

The first permanent installed system, at ArcelorMittal Flat Carbon Steel, Ghent (Belgium), was installed in June 2006 at the exit of the continuous annealing line. Today numerous lines in Europe and China for galvanized, galvannealed, electrolytical galvanized and annealed products are equipped with the SRM system

REFERENCES

- 1) G. Moreas et al., "Advanced sensor for on-line topography in continuous lines", 26th Journées Sidérurgiques Internationales, Paris, 2005
- 2) A.W. Koch et al., "Optische Messtechnik an technischen Oberflächen", Renningen-Malmsheim: expert-Verlag, 1998
- 3) EN 10049
- 4) W. Bilstein et al., "Two systems for on-line oil film and surface roughness measurement for strip steel production", ATS Steel Rolling Conference, Paris, 2006

WAVIMETER: ON-LINE MEASUREMENT OF WAVINESS

Genevieve Moreas

CRM Group, Liege, Belgium

Abstract

The mastering of the waviness is becoming a major issue for making high quality coated steel, especially for the automotive users. Indeed, if the waviness of a steel sheet is above defined limits, the steel user does not generally accept the annealed and galvanised product for high added value application because it can cause poor aspect and surface quality, notably after the finishing and painting operations.

Presently, when waviness is measured, it is in a static way and quasi always on samples taken at the exit of galvanising or annealing line from coil head or tail, not necessarily representative of all the coil length. As a consequence, an on-line measurement appears mandatory to fully evaluate the surface quality all along the coil and to potentially control the production parameters.

In that aim, the concept of a Wavimeter sensor has been developed by CRM inside a RFCS project to continuously measure in real time the waviness during the production. The method has been tested in industrial lines by comparison with mechanical reference measurements.

The sensor is able to measure as well roughness and waviness parameters. Its principle and the industrial results will be presented.

Key words

Waviness, roughness, Ra, Wa, topography, on-line, sensor, continuous, industrial

Biography of authors

Genevieve Moreas: 44 years old, electronic civil engineer from University of Liege (1990). Program leader at CRM Group, CRM Liege in "Advanced sensors" department.

1. Introduction

If the waviness of the steel sheet is above defined limits, the steel user does not accept the product because it causes rejection or downgrading in the further processing steps (such as deep drawing, painting or brushing). As waviness, except for high glossy surfaces, is mostly not eye visible before painting, a measurement is required to evaluate its level. Nowadays, this is done by the use of profilometers on static samples from the tail or the head of some coils. However, this measurement is not available for the whole coil and, moreover, is only realised on some ones (1 on 5 in average). Nevertheless, the waviness is becoming more and more important for the customers, specially the automotive ones, who require better surface and aspect quality to put less painting on the steel product. So, as nothing exists today, an on-line system, measuring the waviness, has been developed by CRM in the frame of a RFCS project where industrial partners were Arcelor Mittal and Segal Tata Steel.

Basically, the surface topography refers to the horizontal and vertical information on the height variation of the surface and can be divided into (micro) roughness and waviness. Generally, the roughness is defined to include only the height variations having a horizontal spacing or wavelength up to 0.8mm or 2.5mm in case of steel. In case of 2.5mm cut-off, following standards, it concerns measurement length of 12.5mm.

The waviness, on the other hand, refers to structural components with longer wavelengths.

Waviness means, in general, the shape deviation of a surface in the wavelength range above the roughness (Fig.1).

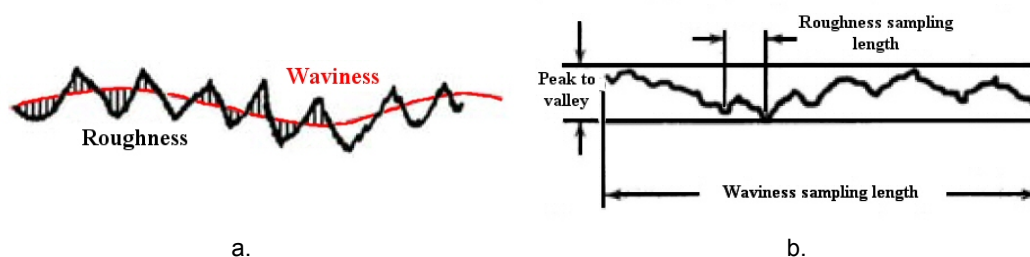


Fig.1 Waviness

The reference is mechanical stylus measurement. Following the literature and the results of previous RFCS project, a length of 30mm and values of 1mm and 5mm have been respectively chosen for the low and high cut-off values for waviness measurement to filter the basic profile.

2. Wavimeter

2.1. Principle

Wavimeter method is based on high precision triangulation principle, overlapping images grabbing and stitching algorithm using on-line microscope sensor.

The triangulation principle, also known as light-section measurement, at a microscopic scale, has been implemented in the Surface Roughness Measurement sensor (SRM, commercialised by Amepa GmbH, under license of CRM). A very thin laser beam line is projected on the surface and the deformation of the observed line is directly in relation with the height of each point of surface by which the laser beam line is reflected. (Fig. 2 and Fig.3). To reach the required precision in roughness measurement, the observed field of view has a maximum of 1200 μ m width.

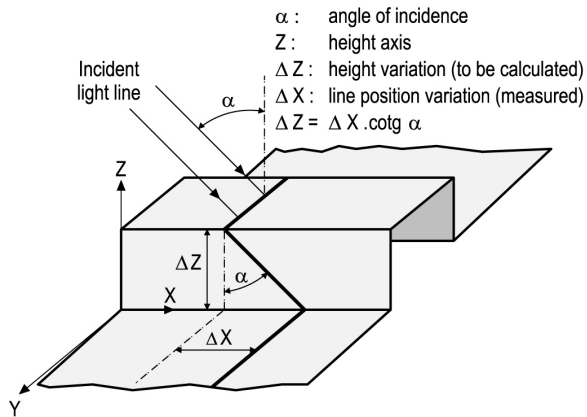


Fig.2 Principle of height measurement

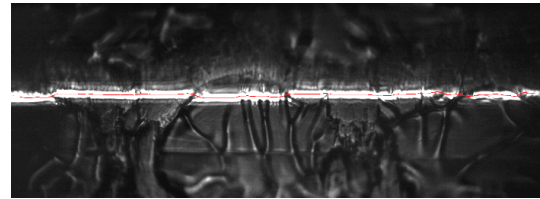


Fig.3 Galvanised EBT textured surface with distorted line; Image area 530µm x 200µm

Waviness requires at least the same precision than roughness but a minimum of 30mm of measurement length. To reach both these specifications, the chosen technique consists in grabbing images that overlap on a small part of the field of view and in stitching all of them to get the required measurement length (Fig.4).

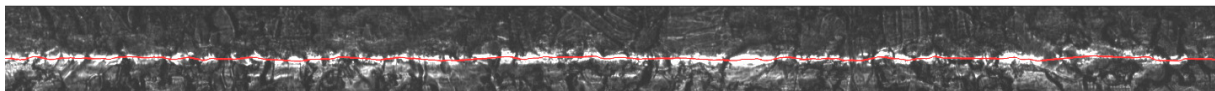


Fig.4 Sample of stitching result

Stitching algorithms refer to a set of techniques used to recover a large image from a set of smaller one. It is commonly used for instance to recover a full panorama based on a set of pictures taken with a camera

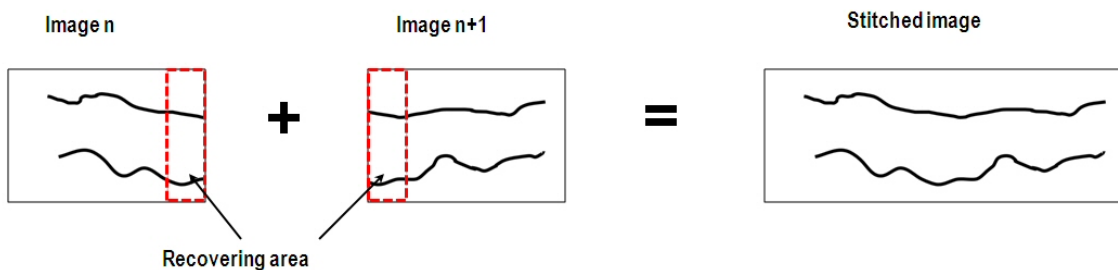


Fig.5 Stitching principle

The basic principle of stitching algorithms (Fig.5) involves usually several steps:

- Pre-processing of the images
- Estimation of a transformation from one image to another (usually, the transformation is a parametric model whose parameters have to be estimated)
- Mixing of the two images based on the estimated transformation to reconstruct a stitched image
- Post-processing of the images to obtain higher-level data.

The role of the pre-processing step is to correct possible artefacts that would prevent the transformation computation to be accurate enough for the target application. In the case of a usual camera to reconstruct panorama for instance, a transformation model involving variation of position, orientation and zoom of the camera has to be taken into account.

The mixing of two images is a kind of data reconciliation to obtain a final result as accurate as possible. The post-processing consists in the exploitation of the stitched images to recover the topographical information (profile and W_a).

To measure the waviness, the line is projected in the rolling direction and the sensor will take profit of the movement of the strip to get images of the surface on overlapping areas. So, considering that the strip follows a simple translation displacement, the translation model, which is one of the simplest transformations in the stitching paradigm, has been used.

The transformation normalizes the illumination level enabling so to take into account variation of global illumination from one image to another (due for instance to flash non-homogeneity).

The translation model is directly associated to the maximization of the correlation function between a patch of image I_0 and a patch of image I_1 using FFT techniques.

In summary, the used stitching method is based on:

- A simple translation transformation model
- The displacement vector estimated between two consecutive image using a correlation technique and FFT algorithms.
- The fusion of data on the recovering area is done by averaging the two images.
- The iteration of the process to stitch several images.

1.1. Implementation

To get high quality images with small overlapping on moving products, high speed camera and illumination source have been used. The system is synchronised with the line speed to reach a constant user defined overlapping and so optimise further processing. (Fig.6)

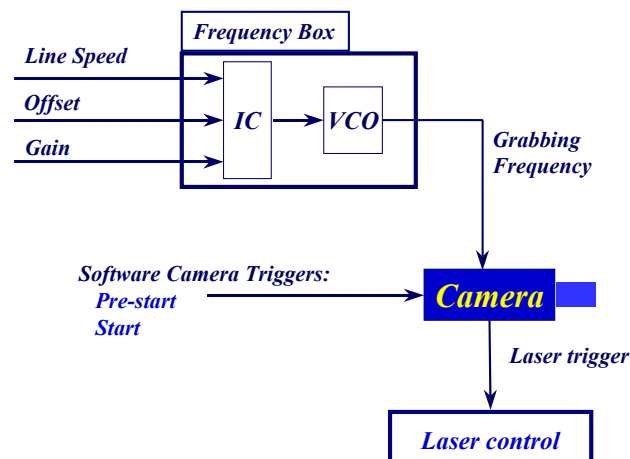


Fig.6 Scheme for synchronisation signal

A high speed PC is used to control the whole system.

Considering that n images are required to cover the desired length with a defined recovery amount. The camera is used in cycle mode. In a first step, the camera is pre-triggered by the PC. It will acquire images and store them in a cycle buffer of n images size.

When a complete cycle of acquisition is done, the first time the focus point is reached, the PC triggers the camera again. This second step is completed when $n/2$ images are acquired.

In that way, the buffer of the camera consists in $n/2$ images acquired before focus and $n/2$ images acquired after focus. A priori, this is the best way to obtain a line of images greater focused.

The most noticeable feature is the orientation of the laser line compared to the strip direction. Ideally, the laser line would be exactly projected in the direction of the strip movement, so that acquiring several successive images would be equivalent to project a longer laser line on a larger field-of-view.

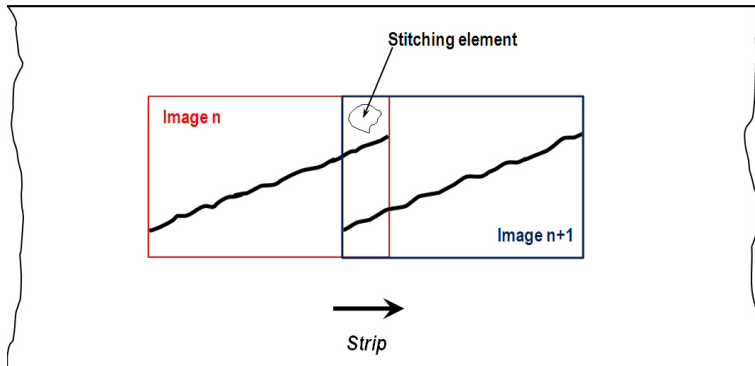


Fig.7 Slight misalignment in line

To align perfectly the system, the line direction is adjusted through the use of a precise rotation table combined to an FFT analysis of the resulting stitched image.

Indeed, if the line is not perfectly in the rolling direction (Fig.7), it will result in the stitched image in a profile with steps appearing at the length of stitching (which is constant as the grabbing frequency is directly linked to the speed product). These steps will appear in the FFT profile of both W_a and R_a profiles. Orientating the line in the rolling direction will result in the extinction of the concerned peak. (Fig.8)

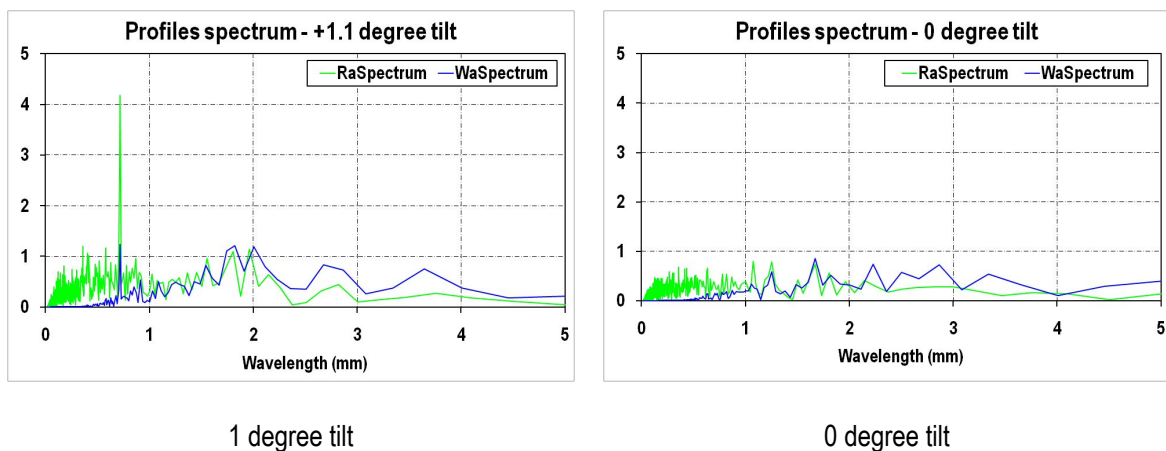


Fig.8 Spectrum analysis for line position adjustment

The quality of the stitching is directly linked to the quality of the background image. So, illumination has been homogenised and correlation is done on zones without the projected line.

The stitched image is then processed to isolate the profile of the projected line from which roughness and waviness parameters can be extracted.

To calculate waviness and separate it from the roughness, the Gaussian filter has been chosen as this is phase correct i.e. it does not introduce phase distortion into the transmitted wave.

1.2. Validation on industrial samples in laboratory

The method has been validated on static samples by:

- displacing the sample in the line direction to simulate on line moving,
- taking an image after each displacement,
- stitching all the grabbed images,
- analysing the resulting image to find the line and get the profile,
- filtering the profile with adequate cut-offs,
- calculating the Ra and Wa,
- comparing the got values with the measurements given by classical off line laboratory methods.

The global results for Wa calculated with a low cut-off of 1mm and a high cut-off of 5mm are shown in Fig.9.

The X axis is the mechanical stylus reference. Two sets of data are displayed: blue and orange points. They correspond to two different mechanical stylus references.

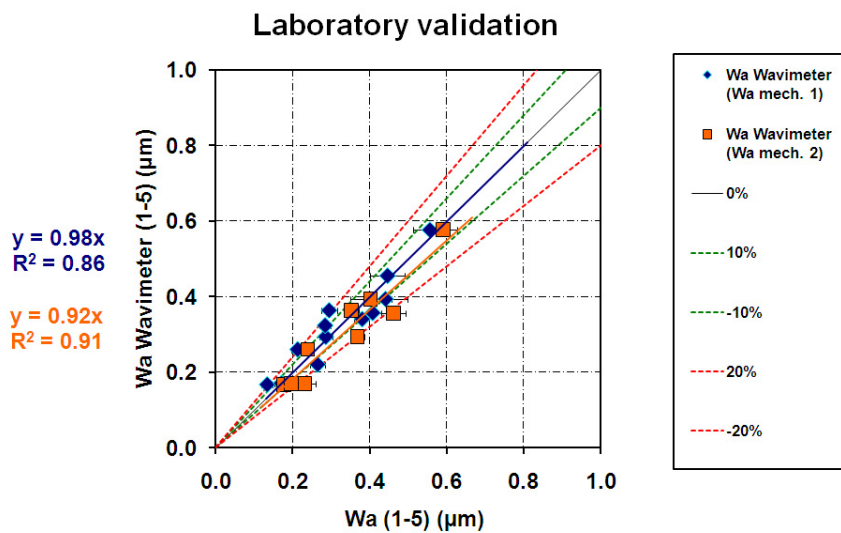


Fig.9 Wavimeter Wa in function of mechanical stylus Wa

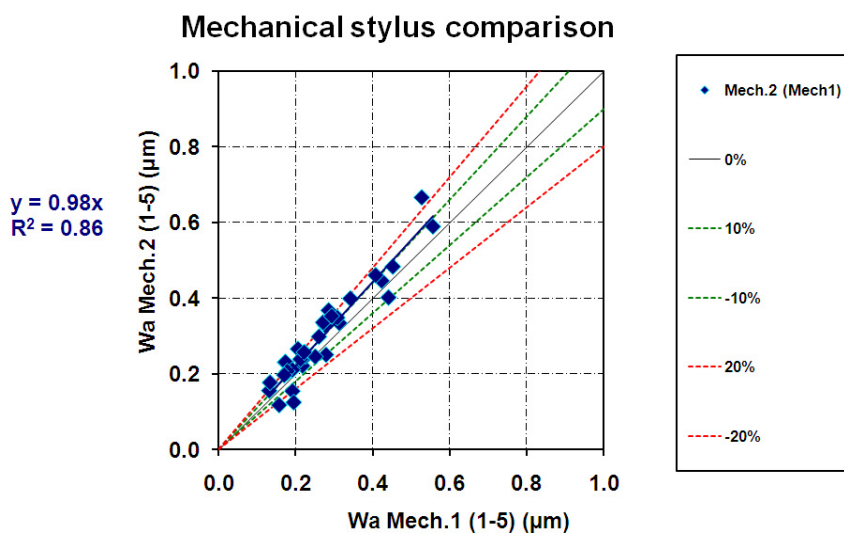


Fig.10 Comparison of mechanical stylus Wa

It appears clearly that the differences between two different mechanical stylus references (Fig.10) are of the same order than the ones existing between Wavimeter and each of the mechanical reference. The correlation coefficient and the dispersion are of the same order.

The profile got by image processing gives the complete profile of the surface and so, it allows also to measure roughness parameters as, for example, Ra. Indeed, to measure roughness parameters with a cut-off of 2.5mm, the minimum length of measurement is 12.5mm which is lower than the length required for Wa. The Fig.11 shows the correlation between Ra calculated with the Wavimeter and Ra measured with stylus reference with a very good correlation (0.92).

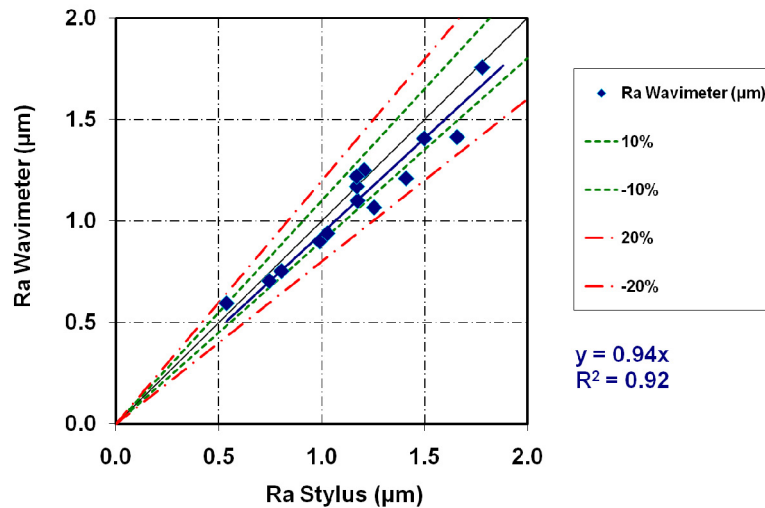


Fig.11 Wavimeter Ra in function of mechanical stylus Ra

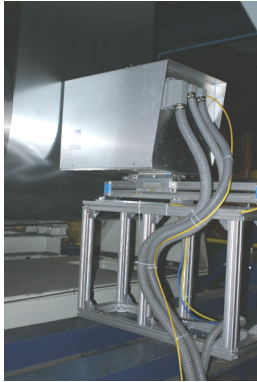
All these results have validated the method in laboratory, as well for the image stitching as for the image processing and for profile filtering. The precision (mainly in +/-15%) and the correlation with mechanical stylus measurement are good.

2. Integrated on-line strip surface waviness measurements in galvanising lines

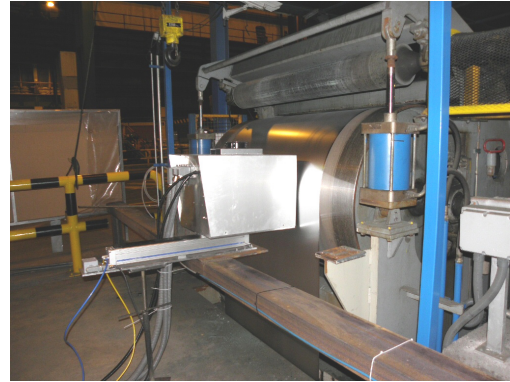
2.1. Mechanical implementation

The mechanical support of the sensor places the optical axis of the Wavimeter in such a way it passes through the axis of the roll. In that way, the optical axis is perpendicular to the surface assuring that the image is well focussed.

Fig. 12 shows the sensor installed on two different galvanising lines (Segal Tata Steel and Arcelor Mittal Spain).



Segal Tata Steel



Arcelor Mittal Spain

Fig.12 Wavimeter on industrial galvanising lines

2.2. Check on static samples

In order to validate the measurements done by the Wavimeter, samples of coils were taken and measured manually. For each sample, three mechanical measurements were done on the same side and at the same location as the waviness sensor. The average data has been calculated for comparison with Wavimeter measurement.

Considering the data got by averaging the last 4 measurements, the correlation appears very good and the variations are in +/-10% related to the TS Wa (mechanical measurement) (Fig. 13). This is a very good result considering for the correlation factor of 0.71 that it is influenced by the small range of data (from 0.28 to 0.42 μm).

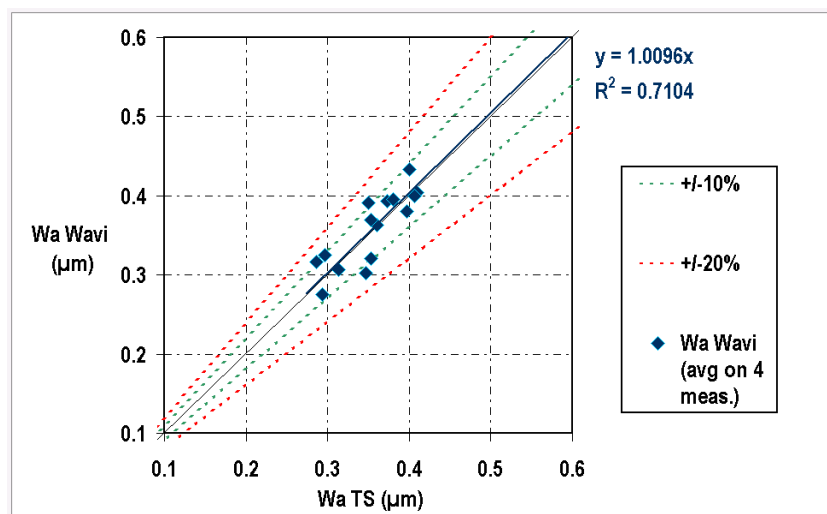


Fig.13 Comparison between Wa from Wavimeter and TS mechanical measurements

2.3. Industrial following

Numerous coils have been followed during industrial campaigns. This has been used, coupled with samples from coils to check the Wavimeter measurements in comparison with mechanical data during variation of production parameters. Fig.14 shows such a measurement campaign. The light blue triangles, corresponding to Wavimeter data, follow well the dark blue triangles, corresponding to mechanical stylus data.

This figure shows two well distinguished levels of Wa well assessed by the Wavimeter. This validates the possibility to monitor variations due to process conditions.

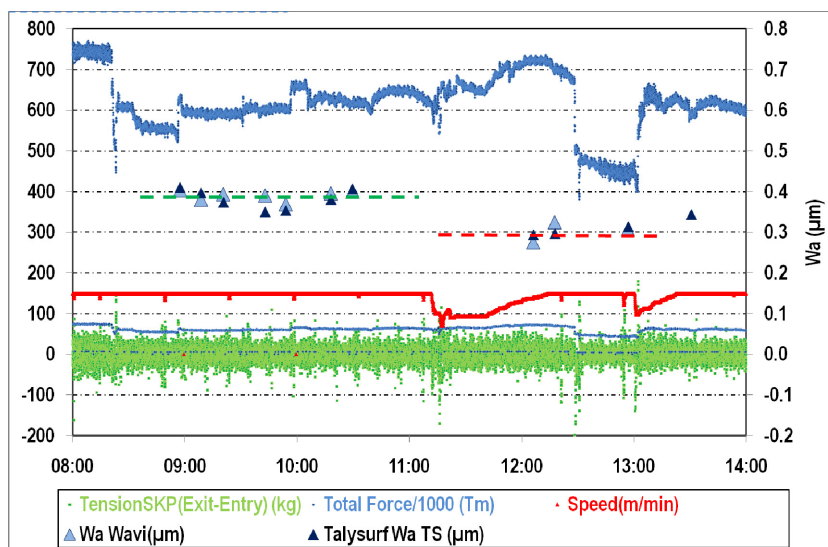


Fig.14 Wavimeter versus mechanical during variation of production parameters

3. Conclusions

A new sensor able to measure roughness and waviness parameters on industrial line in real time has been developed. It has been validated and checked in laboratory and on line using mechanical stylus reference. The correlation is very good on Ra and on Wa (as small as $0.27\mu\text{m}$).

This new sensor, called Wavimeter, will be helpful to follow the waviness and roughness variations on line and so to control the process conditions to reach the customer requirements.

In collaboration with Amepa GmbH in Germany, a second generation designed for a complete industrial application will be developed in the frame of a pilot project supported by the RFCS program.

4. References

- [1] On-line continuous assessment of the surface roughness of cold rolled steel strip, ECSC-STEELDEM 2C, 7215-GB/201
- [2] Surface roughness measurement on steel strip in rolling mill, ECSC-STEELRES 8C, 7210-GB/122
- [3] Characterizing the surface waviness of hot dip galvanised steel sheets for optical high-quality paintability, RFS-CR-03046
- [4] Development of a waviness measurement for coated products, RFSR-CT-2006-00016

5. Acknowledgment

This development has been realised with the financial support of the European RFCS program.

ON-LINE DETERMINATION OF Mg COATING THICKNESS ON ELECTROLYTICALLY GALVANIZED STEEL IN MOTION USING A LIBS DEMONSTRATOR

J. Ruiz¹, A. González², L.M. Cabalín², G. Müller³, Ch. Schwerdt³, J.J. Laserna^{2*}

¹ Department of Applied Physics, University of Málaga, Campus de Teatinos s/n, 29071, Spain

² Department of Analytical Chemistry, University of Málaga, Campus de Teatinos s/n, 29071, Spain

³ ThyssenKrupp Steel Europe AG, R&D, Eberhardstrasse 12, 44145 Dortmund, Germany

*Corresponding author: Prof. J.J. Laserna, Fax +34952132000, E-mail: laserna@uma.es

ABSTRACT

A relevant part of the development process in an industry is the design of an adequate production control, guaranteeing a fast and reliable analytical characterization. In the case of the steel industry, the determination of coating thickness is of paramount importance. For this goal, many complementary analytical technologies can be used. In the recent years, several applications using laser-induced breakdown spectrometry (LIBS) have been reported. Outstanding features of laser-based methods for this application include capability of achieving fast surface chemical analysis, the absence of sample preparation, and ease of deployment in factory.

In this work, a portable LIBS system for the on-line determination of coating thicknesses in the production line has been optimized and evaluated. A field campaign has been carried out in the *ThyssenKrupp Steel Europe* (TKSE) pilot plant in Dortmund. The LIBS demonstrator is based on an axial dual-pulse Q-switched Nd:YAG laser, operated in its fundamental wavelength. This portable LIBS system generated plasmas on the coated steel surface after the annealing process. The LIBS intensity was monitored in order to measure the thickness of Mg on electrolytically galvanized steel in motion. For variable Mg thickness (depending on the speed of the production process, in the range 100 - 1200 nm), and for a fixed Zn thickness, a good agreement between LIBS measured results and data from laboratory chemical analysis (dissolution of the metallic coating and subsequent ICP-OES analysis) has been achieved. Corrosion and tribological tests with specimen with and without laser craters in the surfaces demonstrated no significant effect of laser craters on the materials corrosion tendency and tribological characteristics.

Research supported by the Research Fund for Coal and Steel, under contract number RFCS-CT-2006-00034.

INTRODUCTION

The number of applications of zinc-coated sheet steel is increasing more and more in the last years (automotive industry, structural building products and metal building roofing, wire cables, etc.). The quality requirements for these galvanized and galvanized sheets are also growing up: there is a tendency to produce thinner sheet materials to be used in different industries, but without a significant loss of corrosion protection; this protection is given attaching coatings of different nature to the steel sheet. By these reasons, the coating industry is developing new products and processes to meet the specific needs of the end users, particularly demanding better mechanical properties and improved resistance against corrosion of the finished surfaces.¹

There is also a real need to be able to characterize these new families of coatings in a fast way. In these manufacturing processes of galvanized steel sheets, on-line monitoring of the coating thickness and elemental composition during the production process is essential. One of the analytical tools to characterize Zn-based alloy coatings during the continuous manufacturing process is laser-induced breakdown spectrometry (LIBS). This technique fulfils the need to measure the coating thickness without contact with the steel strip, and with satisfactory levels of accuracy and reliability.^{2,3}

The capability of LIBS to quantitative resolve complex depth profiles has been demonstrated successfully⁴ in different areas of industrial interest,^{5,6} for metallic samples (thicknesses up to 10 μm), but also in the case of monitoring of coatings on steel.⁷⁻¹⁵

The situation changes when a sample in motion has to be analyzed. In this case, all the information about the coated sample has to be obtained with only one laser pulse on each specific spatial position, and not from a series of sequential laser pulses. Noll et al.¹⁶ have reported that significant improvements to the analytical performance of a LIBS experiment is achieved by the use of laser double pulses in each spatial position to ablate and excite the sample material to be analyzed. By using a double pulse mode, the thickness of a Zn coating, with a thickness resolution of around 400 nm has been demonstrated.^{2,3} In a different work, this research group characterized Al depth profiles of hot-dip galvanized coatings, with the use of triple laser pulses.¹⁷ The thickness resolution obtained optimizing experimental conditions (the energy deposited on the sample, and a careful and systematic selection of the spectral lines) could be improved to 140 nm.¹⁸

In the present work, a laser-based method has been used for remote on-line quality control and fast product characterization of Zn-bases alloy coatings. The samples consist in steel covered by an inner variable-thickness layer (2-9 μm) of Zn, and an outer thinner layer (of several hundreds of nm) of Mg. The measurements campaign was carried out in the pilot plant that ThyssenKrupp Steel Europe (TKSE) has in Dortmund, Germany¹ by using a portable LIBS system. After the field campaign, corrosion and tribological test studies have been carried out, and it will be discussed.

EXPERIMENTAL

Instrumentation. Two Q-switched Nd:YAG lasers have been mounted in an axial dual-pulse configuration in order to carry out LIBS measurements, as it is shown in Fig. 1. Both lasers sources were operated at its fundamental mode (1064 nm) at a repetition rate of 5 Hz. The first laser has a flat energy profile (Big Sky Laser, CFR200 model, pulse width 13 ns, beam diameter 6 mm), and can be operated at a maximum energy of 50 mJ, and at a maximum repetition rate of 50 Hz. The second laser, also exhibiting a top hat energy profile (Big Sky Laser, Ultra CFR model, pulse width 8 ns at 1064 nm, beam diameter 2 mm), provided a maximum pulse energy of 50 mJ at 10 Hz, the highest repetition rate allowed for this laser. According to the manufacturer, the jitter of both lasers is lower than 1 ns.

The two laser beams were combined by means of a quartz beam splitter, after the reflection of the second laser beam in a mirror, and then guided with a beam-expander and a dichroic quartz mirror to the sample. The 5x-beam expander consisted of a couple of 1064 nm antireflection-coated lenses with optical focal lengths of 25-mm (concave, diameter 25.4 mm) and 125-mm (convex, diameter 50.8 mm), respectively. The dichroic quartz mirror (with high reflectivity at 1064 nm, transparent for the plasma light, and diameter 38.1 mm) has been inserted in the optical path in order to observe the plasma, along the same axis. Finally, a 150-mm focal length fused-silica lens (diameter 50.8 mm) focuses the combined laser beams onto the surface of the samples to be studied, at normal incidence.

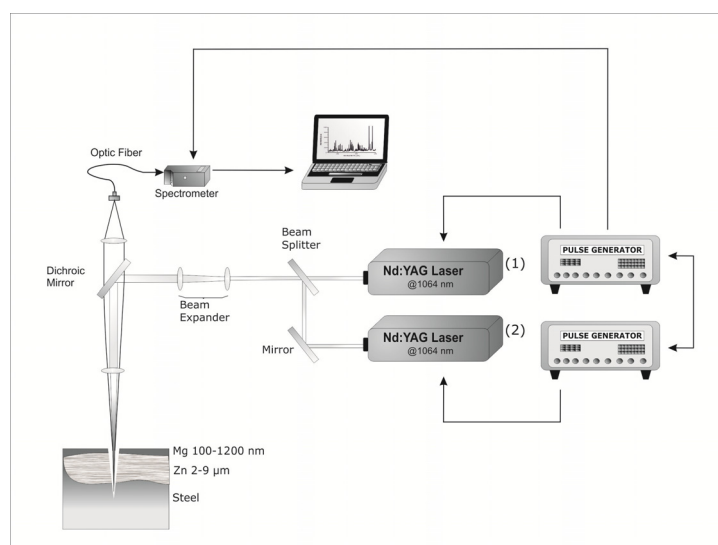


Fig. 1. Experimental set-up showing the LIBS system in the dual-pulse configuration used for on-line determination of Mg coating thicknesses. The arrangement dimensions are not to scale.

The optical emission collected reaches finally a planoconvex quartz lens (50-mm focal length, diameter 25.4 mm), focusing the emission onto the input aperture of an optical fiber. The output of the optical fiber (length = 2 m, diameter = 200 μm , NA = 0.22) is then coupled onto the entrance slit of a high-resolution miniature spectrometer (Ocean Optics HR2000) of 1/10 m, detecting the dispersed light with an integrated linear CCD array of 2048 pixel elements. The grating installed in the spectrometer has 2400 grooves per mm, and the slit width is of 10 μm , providing a spectral resolution of 0.08 nm (FWHM) in the selected spectral region. The spectral range chosen for this application covers from 450 to 525 nm, allowing the detection of several adequate spectral lines of Mg and Zn. The spectral lines used for Mg and Zn thickness evaluation have been indicated. Finally, the spectrometer interfaces to a personal computer via its USB port.

The two pulsed lasers were externally controlled by means of two digital delay/pulse generators (Stanford Research Systems, model DG535) triggered at the same time, allowing energy control for both lasers through the delay between flash-lamp and Q-switch firing, inter-pulse delay between both lasers, and synchronization with the spectrometer. The beam quality is not degraded significantly by increasing the Q-switch delay at the settings needed in these experiments. The CCD aperture is placed just after the arriving of the first laser beam, and the integration time was fixed at 2 ms, the minimum integration width allowed. The inter-pulse separation was varied in the range 0-10 μs , optimizing the performance of the dual-pulse configuration to estimate thicknesses.

A dedicated computer program was designed in our laboratories to allow real-time spectra acquisition and data processing. This software (written in LabVIEW) allows control of the spectrometer, real time visualization of spectra, measurement of Mg and Zn signal, construction of calibration curves, and finally, on-line determination of Mg and Zn thicknesses. The signal corresponding to each atomic line was evaluated calculating peak areas.

The described experimental setup was mounted on a robust and portable box, in order to be able to move the equipment and to install it in an industrial environment. Fig. 2A shows a schematic drawing of the TKSE pilot line, illustrating the position in which the LIBS system has been installed. Fig. 2B is a photograph of the LIBS demonstrator as mounted in the field trials carried out in TKSE.

For tribological and for corrosion tests, excessive numbers of laser craters were prepared on samples from the on-line trials. For this purpose a LIBS system available at TKSE was utilized. The system comprises a Q-switched Nd:YAG laser working at its 1064 nm fundamental wavelength, maximum 2 mJ/pulse energy, maximum 1 kHz pulse repetition rate, about 7 ns pulse duration (FWHM), diffraction-limited measure M^2 factor < 1.3, motor controlled x-y- stages for scanning sample movement with <1 μm positioning precision, raster with 100 μm step width in x and y direction. More details are given elsewhere ¹⁹.

Samples. Two kinds of samples have been studied in these experiments: in a first step, several Zn-based alloy coated samples sets to be considered as a set of reference materials for calibration purposes; and on the other hand, the real Zn-based coating strips, manufactured in the TKSE pilot plant, in Dortmund (Germany), during the field campaign.

The first set of samples is formed by individually produced materials by PVD (physical vapour deposition) on a laboratory scale in TKSE, and they have been characterized by GD-OES. These samples were produced by deposition on cold steel sheets of a variable amount of Zn, followed by deposition of the Mg layer (of variable

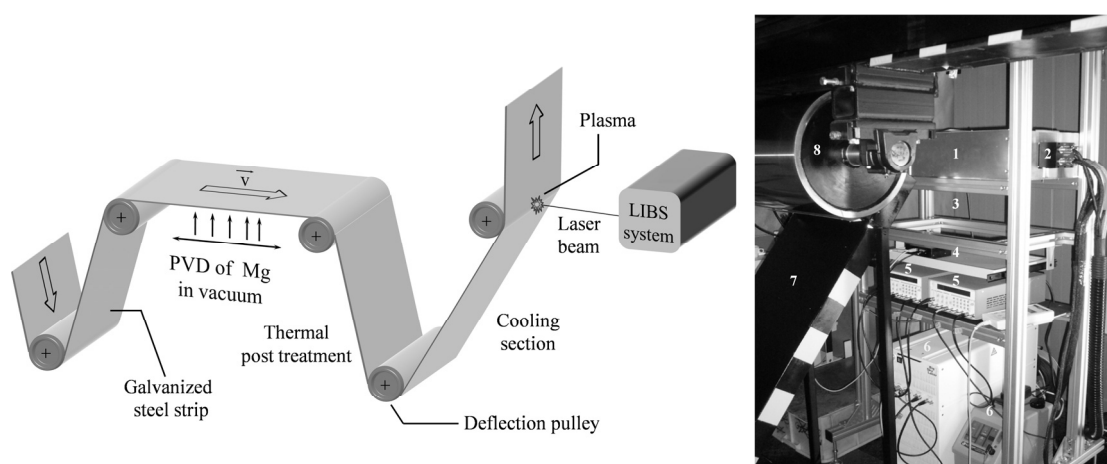


Fig. 2. A) Scheme of the TKSE pilot line, showing the zone where the experimental setup was installed, and B) Photograph of the LIBS demonstrator as installed during the field trials developed in TKSE: (1) Optical system, (2) Laser heads, (3) Optical fiber, (4) Spectrometer, (5) Pulse generators, (6) Power supplies, (7) Steel strip, and (8) Deflection pulley.

Table I. Set of electrolytically Zn coated samples with variable Mg PVD coating, provided by TKSE, considered as reference materials for LIBS thickness calibration.

Experimentally GD-OES thickness values have been determined by TKSE.

Sample denomination	GD-OES Zn thickness (μm)	GD-OES Mg thickness (nm)
1A	2.4	82
1B	2.4	286
P7	2.2	696
P8	2	1176

coating thickness) in a vacuum chamber. The coatings were partly annealed to produce the intermetallic MgZn_2 interphase. **Table I** summarizes the GD-OES thicknesses, both for Mg and Zn layers, obtained for this set of reference samples.

The coated steel sheets considered in the on-line factory trials have been described elsewhere.¹ A zinc coated steel sheet is Mg vapour deposited; the resulting two-layer stack is subjected to a specific short-term thermal annealing, producing intensive interdiffusion reaction between the two layers.²⁰ The strip consists of a 0.75 mm low carbon steel sheet, coated in one side by 2 or 9 μm of Zn, and a second coating of variable Mg thickness (depending on strip speed of the manufacturing process). The maximum continuous pilot line speed is 60 m min^{-1} , the strip width is 300 mm, and its length 1700 m.

RESULTS AND DISCUSSION

Optimization of experimental conditions. Prior to the field campaign, a systematic work has been done in order to investigate the optimal experimental conditions required for Laser-Induced Breakdown Spectrometry (LIBS) determination of the thickness of Mg on electrolytically galvanized steel in real time during the production process. In the optimization of the working conditions (in terms of pulse energies of both laser beams and inter-pulse delay), two aspects were taken into account: i) the need to improve sensitivity and figures of merit, obtaining sensitive calibration curves to make possible thickness measurements for Mg or Zn, and ii) the need to minimize the optical damage to the sample. Strip damage is of special concern, since craters produced during LIBS measurements could affect the corrosion resistance of the Zn-based coating.

The effect of the pulse energy of both laser beams on the LIBS signal for Mg and Zn, and on the calibration curves (dependence between spectral intensity and laser energy) was studied. For this purpose, several combinations of pulse energies were evaluated for the first and for the second laser, fixing the value for the inter-pulse delay. In this way, an energy combination of 5.0 mJ/5.6 mJ has been measured to be the optimum set to obtain a good signal to background ratio, with the best sensitivity in the calibration curves for Mg thickness determination. This same dependence has been measured for Zn, obtaining a combination of energies of 5.0 mJ and 9.6 mJ for optimum Zn thickness determination. The fact that higher energies are required to optimize Zn calibration curves seems reasonable, because in this case, it is necessary to deep further in the Zn layer.

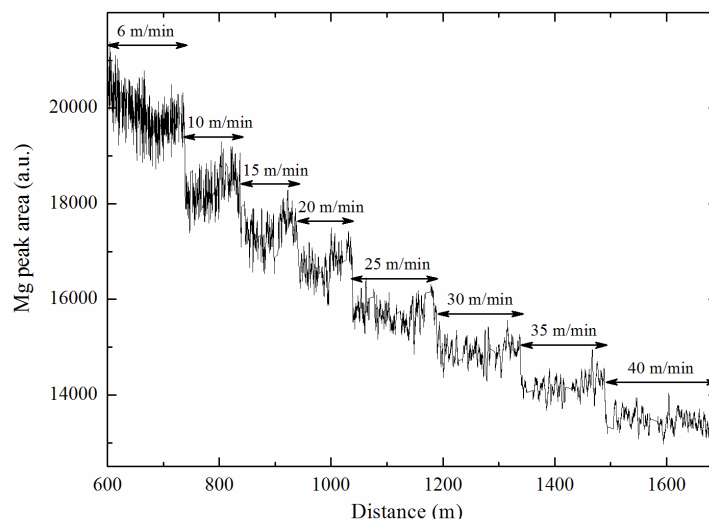


Fig. 3. Mg intensities versus position in the strip. The spectral intensities for Mg were calculated integrating below the peak at 517.27nm.

The effect of the inter-pulse delay between both laser beams on the analytical signal, and on the behaviour of the calibration curves (sensitivity, linearity, saturation effects) has also been studied. On the basis of these studies, an inter-pulse delay of 0.5 μs has been selected in order to improve the sensitivity, but avoiding the saturation of the signal. Similar results were found for Zn.

Field tests. Finally, the suitability of a laser-based device to on-line control the thickness of a coating was tested in a field campaign developed in November 2008 on the TKSE pilot plant in Dortmund, Germany. The goal of the field campaign was to measure the thickness of the Mg coating added to the steel sheet (with a predetermined and known Zn coating already deposited) when this coating is being supplied to the strip. Several environmental factors affecting LIBS signal had to be taken into account. The LIBS equipment was installed in the production line after the thermal treatment (annealing) of the steel strip. As established in the above, an inter-diffusion phase appears after the annealing process supplied to the strip. The meaning of coating thickness when this diffusion process takes place is confusing, but it is used also in the case of laboratory measurements of the coating thickness (GD-OES), and it is in any case a measurement of the amount of Mg in the overall coating as the manufacturer needs.

Moreover, in order to minimize the effects of the mechanical vibrations of the strip on the focusing conditions of the laser beams, an adequate region of the steel strip was chosen to be analyzed by LIBS. The region of the strip less affected by vibrations was a rolling cylinder used to drive the motion of the steel strip (deflection pulley on Figure 2A). Finally, temperatures measured on the steel sheet (backside of the strip, near the position of the laser ablation) changes from 22°C (when the strip moves at a speed of around 6 m/min) to 39°C (when the strip speed is of 40 m/min). The effects of sample temperature in the properties of the laser-induced plasma have been studied in a much wider range (25 to 1200°C) elsewhere.²¹ The variation in temperature in our case is less than 20°C, leading to a negligible effect on the intensities measured, and then, on the thickness determination.

The laser repetition rate used during the on-line trials was 5 Hz. Under these conditions, the separation between adjacent sampling positions varied from 2.0 cm (at a strip speed of 6 m/min) to 13.3 cm (at a strip speed of 40 m/min). This guarantees that there is no overlapping between craters.

Mg thickness was monitored by means of the three spectral lines already described. Fig. 3 shows the Mg intensities (computed from the area below Mg peak at 517.27 and background subtracted -one of the three spectral lines studied-) versus the distance travelled by the strip. The experimental points shown have been smoothed averaging the intensities for 21 adjacent values. The speed of the strip varies from 6 m/min to 40 m/min, modifying in this way Mg thickness of the coating. The results cover more than one kilometre of length, where more than 15,500 laser shots have been delivered onto the strip surface, showing a small, but significant change in spectral intensities, allowing in this way the utilization of the LIBS signal for thickness determination, as expected.

As it has been described previously, for each spectral line, a calibration curve was measured (using the TKSE reference materials labelled 1A, 1B, P7 and P8, with common nominal Zn thickness of 2 μm and different Mg

Table II. Mg coating thickness in field campaign: comparison of LIBS with nominal and ICP-OES values. The relative error is calculated considering ICP-OES value as true, except where not available (nominal value is considered then as true). ICP-OES values were measured at TKSE after the experiment was finished, by digesting several portions of the sample, taken from different positions along the strip.

Strip speed (m min ⁻¹)	Nominal Mg thickness (nm)	LIBS Mg thickness (nm)	ICP-OES Mg thickness (nm)	Rel. error (%)
6	1200	1290±200		(7.5)
10	720	852±220	696	22.4
15	480	535±104		(11.4)
20	360	366±7	337	8.6
25	288	296±25		(2.7)
30	240	243±11	235	3.4
35	206	195±14		(5.3)
40	180	182±17	178	2.2

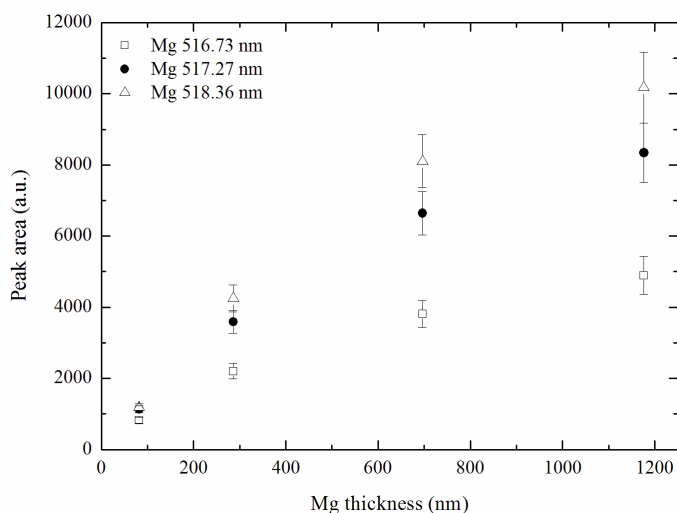


Fig. 4. Calibration curves obtained for different spectral lines of Mg, using TKSE standards, using laser energies of 5.0 mJ/5.6 mJ. Inter-pulse delay has been fixed to 0.5 μ s.

thicknesses) just before the field trials, in the same experimental conditions (Fig. 4). The vertical bars correspond to the standard deviation calculated for fifteen replicate measurements each on a fresh sample position. The calibration curves were fit to a hyperbolic model. The fit was good enough to adjust the experimental points, although the R^2 value (better than 0.99) is not significant, due to the low number of available points for the fitting (only four standards). After the experiment was finished, another set of calibration curves was acquired, in order to be sure that the focusing conditions had not changed during the measurements.

Finally, from the averaged LIBS intensities for Mg at 517.27 nm, the corresponding thicknesses have been determined. Fig. 5 shows the final results obtained at each speed regime of the strip. In this figure, these LIBS experimental values for Mg thickness are compared with the nominal and laboratory measurements when available (made by ICP-OES subsequent to the dissolution of the metallic coating system) in **Table II**. The relative error is also shown for each speed regime. Mg thickness determined by LIBS agrees satisfactorily with ICP-OES and with nominal values at different strip speeds, that is, for different Mg thickness values (including the value corresponding to 6 m/min, obtained slightly extrapolating outside the calibration curve range). The deviations observed are surely due to the limited number of standards available for a precise definition of a good calibration curve. Moreover, it has been assumed that the ICP-OES values measured for the process samples are the true

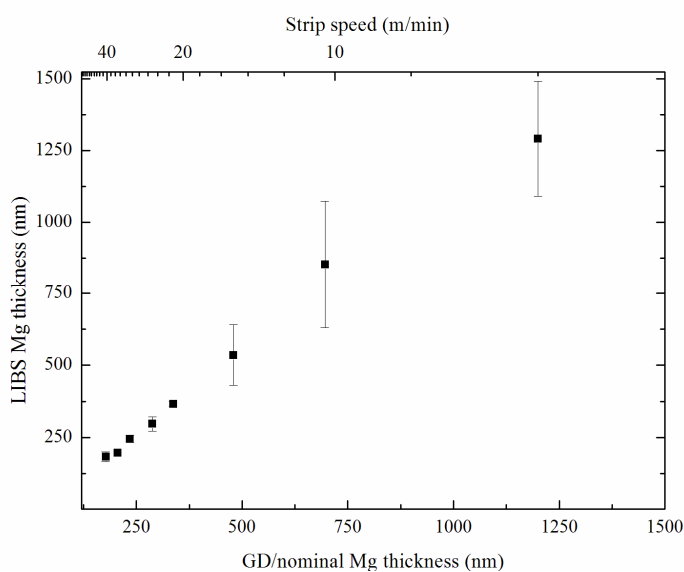


Fig. 5. Mg thickness obtained by LIBS averaging the available points for each speed regime of the strip, versus experimental (ICP-OES) or nominal thicknesses (bottom axis), and speed of the production line (top axis). See Table II for details.

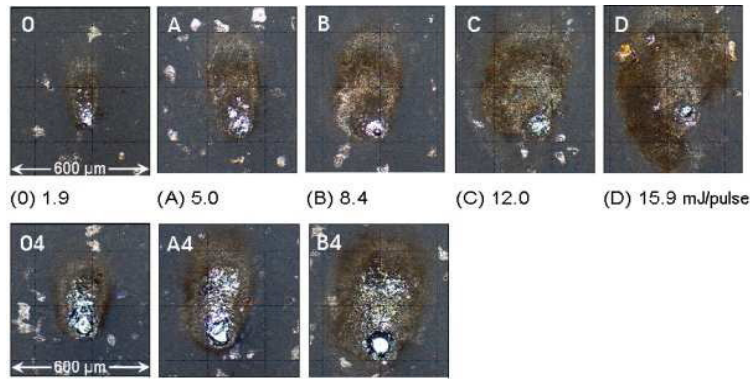


Fig. 6. LIBS craters obtained after dual pulse excitation on an alloyed steel sheet with 8.4 μm Zn + 750 Mg at given pulse energies. Upper row: single pulses, lower row: 4 successive pulses at same position.

values, but it is clear that these values are also affected by experimental errors. Taking this into consideration, the accuracy obtained for the LIBS prototype working in an on-line process is good enough for control purposes. It should be noted that minimal damage on the sample surface has been generated in terms of the crater produced by the dual pulse delivered onto the sheet steel. In fact, it was not possible to find any crater after the experiment by visual examination, although more than fifteen thousand laser shots were delivered to the strip.

Effect of surface damages after LIBS measurements on tribology and corrosion resistance of Zn-Mg coatings on steel sheet. It should be remarked that the damage produced on the sample surface by the dual-laser pulse delivered onto the sheet steel is minimal. In fact, it was not possible to find any crater after the experiment by visual examination and at tenfold LOM magnification. Nevertheless, any possible adverse effects of laser ablation craters in coated steel surfaces were studied.

The shape and geometry of dual pulse laser ablation craters from LIBS system under different pulse energies were studied (a) for 1 laser pulse and (b) for 4 subsequent pulses focused on same position on a steel sheet with 8,4 μm Zn + 750 nm Mg after the alloying step. The entire energies of the first and second partial pulse of the dual pulses with identical energies are given in Figure 6.

Finally, the corrosion tendency of annealed ZE-Mg coated steel samples from the on-line LIBS trials was tested by comparing two sheets with and two sheets without laser craters. The criterion for corrosion resistance is the duration until the start of red rust formation could be observed. In order to magnify the possible effects of laser craters, the number density of laser craters was significantly increased: (a) A field of 100 x 10 craters in a raster (10 x 1 mm²) and 2.0 mJ/pulse, (b) 3 craters, each from 4 subsequent pulses and 2.0 mJ/pulse, (c) 3 craters, each from 4 subsequent pulses and 1.6 mJ/pulse, (d) 3 craters, each from 4 subsequent pulses and 1.2 mJ/pulse were allocated in the same way (Figure 7) on all of the sheets with laser craters. The purpose was to observe the initial steps of white and red rust formation. Salt spray test according to DIN ISO EN 9227 was carried out for the comparison of the corrosion tendency of material with and without laser craters. Samples with different Zn and Mg coating thicknesses and with and without laser craters were compared with respect to the duration until red rust

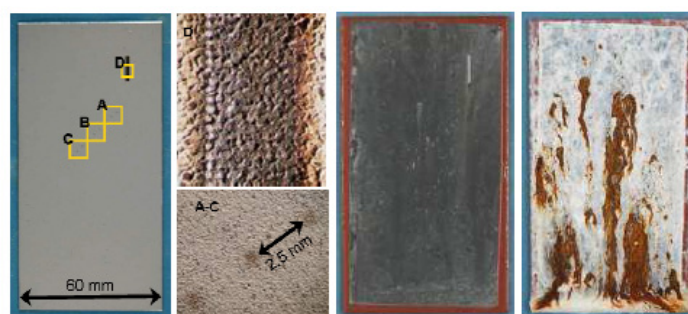


Fig. 7. Allocations of laser craters on a sample with 7.5 μm Zn and 250 nm Mg "with craters" after 0, 48 and 2376 hours (from left to right) in a salt spray corrosion test.

formation begins in the salt spray test (Figure 7). The results show that there is no significant enhancement of corrosion due to laser craters for the various coated samples.

For testing the possible influence of laser craters on forming processes, ZE-Mg coated strips from above mentioned online trial material were treated with the laser at Malaga University at 12 mJ/pulse resulting in two parallel 40 mm long lines of 20 separate laser craters each. As a reference, again strips without laser craters were used. For strip drawing tests at 2 MPa constant surface load and 6 m/min. drawing speed, the samples with and without laser craters were oiled with 1.5 g/m² lubricant Anticorit RP4107S (Fuchs, Frankfurt, Germany). Friction coefficient using 1.2379 high alloy steel tools is reduced from $\mu = 0.15$ to 0.11 after this laser treatment. Reduction of friction in the case of craters present in the surfaces could be explained by conveying more oil towards the tools resulting in better lubrication in the sample-tool-interface.

CONCLUSIONS.

The results demonstrate the potential of a LIBS-based method for on-line production control of the thickness of a coating in steel industry. A portable LIBS system has been designed and optimized for thickness measurements, and installed and tested at TKSE factory in Dortmund. Field trials have been performed, and show that such a LIBS-based device is able to successfully on-line determine thickness measurements. The effect of environmental conditions on field measurements, such as temperature, mechanical vibrations, and moisture on the strip surface, has been demonstrated to be negligible. The experimental results obtained in the field campaign are in good agreement with respect to the thickness estimated by other analytical techniques, such as ICP-OES. The craters delivered were so small that they could not be visually detected; even with a 10 times magnification in a microscope. Corrosion tests showed no difference between areas with and without laser craters. A tribological test also showed no adverse impact on surface friction.

ACKNOWLEDGEMENTS

This work was financially supported by the Research Fund for Coal and Steel under contract RFCS-CT-2006-00034 of the European Commission, and by project CTQ2007-60348-E/BQU of the Spanish Ministerio de Educación y Ciencia.

References:

- 1) B. Schuhmacher, W. MÜschenborn, M. Stratmann, B. Schultrich, C.-P. Klages, M. Kretschmer, U. Seyfert, F. Förster and H.-J. Tiller, *Adv. Eng. Mater.* 3, 681 (2001).
- 2) H. Balzer, M. Hoehne, V. Sturm and R. Noll, *Spectrochim. Acta B* 60, 1172 (2005).
- 3) 7210-PR/360: On-line characterization of zinc coatings (LIBSCOAT).
- 4) J. M. Vadillo and J. J. Laserna, *J. Anal. At. Spectrom.* 12, 859 (1997).
- 5) M. D. Mowery, R. Sing, J. Kirsch, A. Razaghi, S. Bécharde and R. A. Reed, *J. Pharm. Biomed. Anal.* 28, 935 (2002).
- 6) G. Asimellis, A. Giannoudakos and M. Kompitsas, *Appl. Opt.* 46, 935 (2007).
- 7) D. R. Anderson, C. W. McLeod, T. English and A. T. Smith, *Appl. Spectrosc.* 49, 691 (1995).
- 8) J. M. Vadillo, J. M. Fernández Romero, C. Rodríguez and J. J. Laserna, *Surf. Interface Anal.* 26, 995 (1998).
- 9) J. M. Vadillo, C. C. García, S. Palanco and J. J. Laserna, *J. Anal. At. Spectrom.* 13, 793 (1998).
- 10) C. C. García, M. Corral, J. M. Vadillo and J. J. Laserna, *Appl. Spectrosc.* 54, 1027 (2000).
- 11) C. C. García, J. M. Vadillo, S. Palanco, J. Ruiz and J. J. Laserna, *Spectrochim. Acta B* 56, 923 (2001).
- 12) V. Margetic, M. Bolshov, A. Stockhaus, K. Niemax and R. Hergenroeder, *J. Anal. At. Spectrom.* 16, 616 (2001).
- 13) M. P. Mateo, L. M. Cabalín and J. Laserna, *Appl. Opt.* 42, 6057 (2003).
- 14) L. St-Onge and M. Sabsabi, *Spectrochim. Acta B* 55, 299 (2000).
- 15) A. Hrdlicka, V. Otruba, K. Novotny, D. Günther and V. Kanicky, *Spectrochim. Acta B* 60, 307 (2005).
- 16) R. Noll, R. Sattmann, V. Sturm and S. Winkelmann, *J. Anal. Atom. Spectrom.* 19, 419 (2004).
- 17) H. Balzer, M. Hoehne, R. Noll and V. Sturm, *Anal. Bioanal. Chem.* 385, 225 (2006).
- 18) H. Balzer, S. Hoelters, V. Sturm and R. Noll, *Anal. Bioanal. Chem.* 385, 234 (2006).
- 19) H.-M. Kuss, H. Mittelstaedt, G. Mueller, *J. Anal. Atom. Spectrom.* 20, 730 (2005).
- 20) B. Schuhmacher, C. Schwerdt, U. Seyfert and O. Zimmer, *Surf. Coat. Tech.* 163-164, 703 (2003).
- 21) S. Palanco, L. M. Cabalín, D. Romero and J. J. Laserna, *J. Anal. Atom. Spectrom.* 14, 1883 (1999).

ORIGINAL POSITION STATISTIC DISTRIBUTION ANALYSIS FOR THE SULFIDES IN GEAR STEELS

Li Dongling, Xiao Guohua, Jia Yunhai, Wang Haizhou

Central Iron & Steel Research Institute, Beijing 100081, China

Abstract:

The sulfides in some different gear steels were analyzed by original position statistic distribution analysis technique. The abnormal high intensity signals emitted by the inclusion elements were identified by the statistic method. The determination method of the threshold value for the inclusion containing S, Ca, Al, Mn and Si element was presented. The relationship between the proportion of the frequency of high intensity signals and the content of total sulfur and total oxygen in samples has been investigated. It was found that the proportion of the frequency of high intensity signals emitted by S element increased with the rise of the content of total sulfur. Meanwhile the proportion of the number of high intensity signals emitted by Al element increased with the rise of the content of total oxygen. Multi-elemental correlation on high intensity signals has been performed in order to obtain the composition and proportion of different type of sulfides. It was found that the proportion of simple sulfide was more than that of oxide-sulfide duplex inclusion in six gear steel samples. The ratio of the oxide-sulfide duplex inclusion to the total sulfides were determined by the present method and the results had good coincidence with the value obtained by quantitative metallographic method and scanning electronic microscopy. The influence of the content of Ca on the composition of the sulfides was investigated. It was found that the relative proportion of the complex inclusions of Al-Ca-Mn-O-S increase with the rise of the content of Ca in gear steels. The ratio of the content of Ca to the content of S (Ca/S) also had great effect on the relative proportion of the oxide-sulfide duplex inclusion.

Keywords: Sulfide, Gear steel; Original position statistic distribution, Multi-elemental correlation;

1. Introduction

Gear steel has been widely used in the manufacturing field of automobile, railway and shipping. It is important for the gear steel to possess high fatigue properties and good machinability. In order to improve the production efficiency, some countries are devoting their efforts to the study of easy-cutting gear steels, and the exploitation of easy-cutting gear steels with latest type is the development trend of gear steels technology. The non-metallic inclusion in gear steels are mainly composed of sulfides and oxides. Sulfide is the one of the most important inclusion and can affect the mechanical properties in anisotropic property and greatly improve the machinability of steels. But the extend of the influence on properties depends on the type, composition, shape, quantity, size and distribution of sulfides in steels. So the determination of the composition, quantity and distribution of sulfide is very important for the improvement of steelmaking technique and properties of gear steels [1].

There are many conventional methods [2-3] for the analysis of sulfide in steel such as electrolysis extraction method, optical microscopy, scanning electronic microscopy combined with energy spectrum analysis. The electrolysis method has the disadvantages of long analytical period, trivial operation and a little loss of some fine and instable non-metallic inclusion. Optical microscopy and scanning electronic microscopy can be used to observe the microstructure and determine the composition of sulfide, but these methods still belong to microscopic analysis with the disadvantages of limited observed area and are not enough to represent the state of the sulfides in a large area of whole sample. On the basis of the research on the characterization of dissolved and combined aluminum in steel by Optical Emission Spectrometry (OES) [4-6], Irisd has developed a rapid multielement method for the determination of non-metallic inclusions in steel, which is called OES-CDI. This method has been used for the quick analysis of the content and size distribution of the oxides. But this method only excited a fixed point of the sample with a 20mm² surface and is unable to continuously analyze the inclusions in a large area of the samples.

Original position statistic distribution analysis (OPA) is a novel statistic characterization method for the quantitative distribution of different chemical composition and also can investigate their states of components on a large area of material [7-10]. Moreover it can be used for the determination of inclusions by collecting and discriminating the signals produced by single spark discharge in the way of no pre-sparking, scanning and emitting continuously. In this paper, the sulfides of some different gear steels were analyzed by original position statistic distribution analysis technique and the multi-elemental correlation on high intensity signals has been investigated in order to obtain the composition and proportion of different type of sulfides. The results determined by the present method are in good agreement with the value obtained by quantitative metallographic method and scanning electronic microscopy.

2. Experimental

2.1 Chemical composition of the samples

The testing samples are from cast ingot of 18CrNiMo7-6. The main composition is presented in Table 1.

Table 1 Main composition of the testing samples (wt %)

No.	C	Si	Mn	P	S	Cr	Ni	Mo	Alt	Ca	[O]
1	0.16	0.06	0.54	0.005	0.037	1.51	1.40	0.25	0.0094	0.0002	0.0019
2	0.14	0.10	0.53	0.005	0.033	1.62	1.48	0.26	0.0051	0.0013	0.0041
3	0.14	0.16	0.53	0.004	0.032	1.58	1.47	0.26	0.0090	0.0020	0.0049
4	0.15	0.08	0.52	0.005	0.031	1.66	1.43	0.25	0.0032	0.0006	0.0030
5	0.15	0.08	0.52	0.004	0.008	1.65	1.45	0.26	0.0049	0.0005	0.0034
6	0.14	0.14	0.56	0.005	0.025	1.64	1.46	0.25	0.0180	0.0017	0.0042

2.2 Original position statistic distribution analysis of samples

The slice of sample with the size of $\Phi 90 \times 15$ mm was cut out from the middle of the cast ingot in the transverse direction. The surfaces of samples were ground on the resin paper with the size of 46 meshes. The scanning mode is linear at a continuous scanning speed of 1mm/s along X-axis. Step model is used along Y-axis with an interval of 2 mm. The parameters of OPA are as follows: Exciting frequency: 480Hz; exciting capacitance: 7.0 μ F; exciting resistance: 6.0 Ω ; spark gap: 2.0mm; purity of argon: 99.999%; flux of argon: 80ml/s; material for electrode: tungsten electrode with 45 corner angle and the diameter of 3mm. The spectrum signals are processed by a specially software. The scanning area of 50 \times 56mm is shown as Figure 1. In order to get a comparable area with metallographic method, the region with the area of 16 \times 10mm in the position of half of radius was chosen as the analytical region. The area analyzed by OPA is scaled out in the white frame of Figure 1.

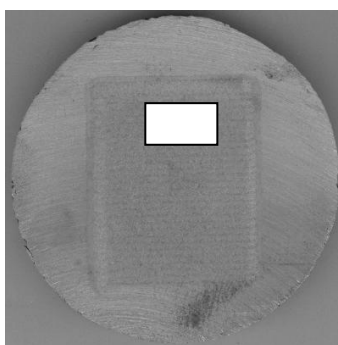


Figure 1 Scanning area and analytical area of testing sample

2.3 Microstructure and energy spectrum analysis of inclusions in samples

The Morphology of the sulfides was observed by Hitachi S - 4300 scanning electronic microscope and the composition of the sulfides was determined by energy dispersive spectrometer. The area percentage of sulfides and the number of different type of sulfides were quantitatively measured at a magnification of 500 by Zeiss 40MAT optical microscopy and the observed area of each microphotograph was 0.049 mm².

3 Results and discussion

3.1 Identification of light signals emitted by sulfides

The number of the light signals from each elemental discharge is up to 48000 when the analytical area is 160mm² and it is necessary to resolve the light signals emitted by different state of the element. Sulfur in steels is usually in the presence of sulfide and there is little dissolved sulfur in the matrix of steel. So the light signals of sulfur can be divided into two parts: the low intensity signals corresponding to noise of the instrument and the blank of the matrix from S channel and the high intensity signals corresponding to sulfur in sulfides. For the first part the value of the low intensity can be obtained by the determination of the sample with a low content of sulfur ($S \leq 0.001\%$). The sum of average intensity and two times of standard deviation from the low sulfur sample was regarded as the threshold value distinguishing the signals emitted by sulfides. Calcium in steels is mainly in the presence of calcium oxide and calcium sulfide. So the determination method of the threshold value of Ca-channel distinguishing the signals emitted by Ca inclusion is just the same as S element.

Al, Si and Mn are in the presence of dissolved and combined states and two populations of the signals can be defined. The low intensity signals correspond to Al, Si and Mn element dissolved in the steel. Whereas the high intensity signals are related to Al, Si and Mn element contained in the inclusions. The statistic method that was used to analyze the dispersed data was adopted to process the intensity data of spectrum signal from Al, Si and Mn channels. A confidence probability was given and the confidence region could be found. The data out of the confidence region can be considered as an abnormal data that is beyond the normality distribution. The relationship can be expressed as follows:

$$|x_i - \bar{X}| > K \cdot \sigma_{(X)} \quad (1)$$

Where x_i is the value determined, \bar{X} is the average value, K is a coefficient related to the confidence probability and $\sigma (X)$ is the standard deviation. When K is 2.0, the confidence probability is 95.5%. In this study K was given as 2 and the abnormal intensity data above the value ($\bar{X} + 2\sigma (X)$) was identified and considered as the light signals emitted by the elements containing in the inclusions. The value of $\bar{X} + 2\sigma (X)$ was thought as a threshold value distinguishing the signals emitted by the inclusions containing Al, Si and Mn.

3.2 Relationship between the high intensity signals and the quantity of inclusions

Because most of the sulfur element in steel is in the presence of sulfide, the content of total sulfur in steel may represent the quantity of the sulfides. Similarly, the content of total oxygen in steels will reflect the quantity of the oxides. Because the testing samples are deoxidized by Al element, the oxides in the samples are made up of alumina. So the relationship between the relative proportion of the high intensity frequency to total light signals and the total sulfur and oxygen content in samples has been investigated. It was found that the relative proportion of the high intensity frequency of S-signal increased with the rise of the content of total sulfur. The relationship curve is shown in Figure 2. Meanwhile the relative proportion of the high intensity frequency of Al-signal increased with the rise of the content of total oxygen. The relationship curve is shown in Figure 3. So it can conclude that the relative proportion of the high intensity frequency of S-signal and Al-signal have close relationship with the sulfides and oxides.

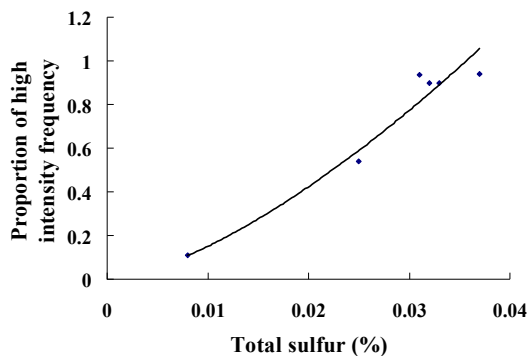


Figure 2 Relationship between the relative proportion of the high intensity frequency of S-signal and the content of total sulfur in samples

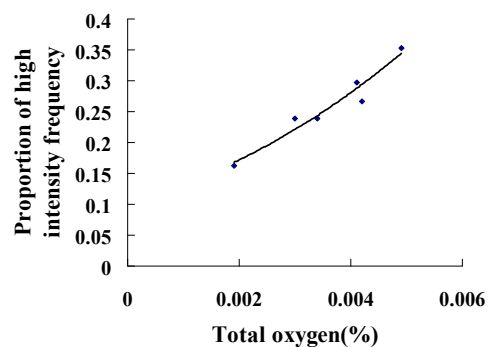


Figure 3 Relationship between the relative proportion of the high intensity frequency of Al-signal and the content of total oxygen in samples

3.3 Multi-elemental correlation of high intensity signals

The abnormal high intensity signals of S, Mn, Ca, Al and Si elements were investigated considering that they are the main components of the sulfides and oxides. It was found that some abnormal signals with high intensity simultaneously appeared in the spectra channels of S, Mn, Ca, Al and Si elements, which indicated the composition of the inclusion in the discharge position. So the composition and the quantity of inclusions can be determined by multi-elemental correlation of high intensity signals emitted by the inclusions containing S, Mn, Ca, Al and Si elements. The correlation of five spectra channels in the first 1000 discharge for No.4 sample is shown in Figure 4. In No.1 point excited by a spark discharge, abnormal high intensity signals in the spectra channels of Al, Ca, Mn and S simultaneously appear and we can conclude the composition of the inclusion in this point is Al-Ca-Mn-S. Because Al element is in the presence of alumina, the inclusion in this point is actually composed of Al, Ca, Mn, S and O elements. And in No.2, No.3 and No.4 point the inclusions are Mn-Ca-S, Mn-S and Al-Ca-Si-Mn-S-O separately. Furthermore it should be considered that Fe element is also the main component of the sulfide but it is not suitable for Fe to correlate with other spectra channels as a matrix element. The microstructure and composition of the inclusions in YC2 sample were analyzed by scanning electronic microscope combined with energy dispersive spectrometer. It was found that the inclusions were composed of simple sulfides and oxide-sulfide duplex inclusion. The results are shown in Figure 5 and Figure 6, which were in good coincidence with the results by OPA. The statistic of the number of the discharge points just like No.1 point are performed and the proportion of the inclusions with the composition of Al, Ca, Mn, S and O in total sulfides can be calculated.

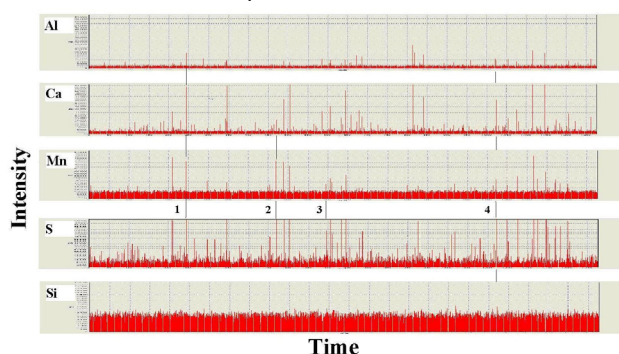


Figure 4 Multi-element correlation of high intensity signals for No.4 sample

- 1) Al-Ca-Mn-S ; 2) Ca-Mn-S ; 3) Mn-S ; 4) Al-Ca-Si-Mn-S

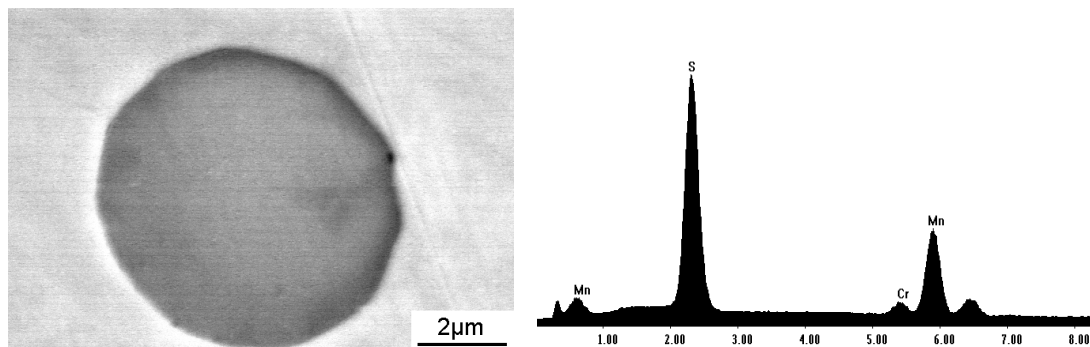


Figure 5 Morphology and composition of the Simple sulfide in No.4 sample

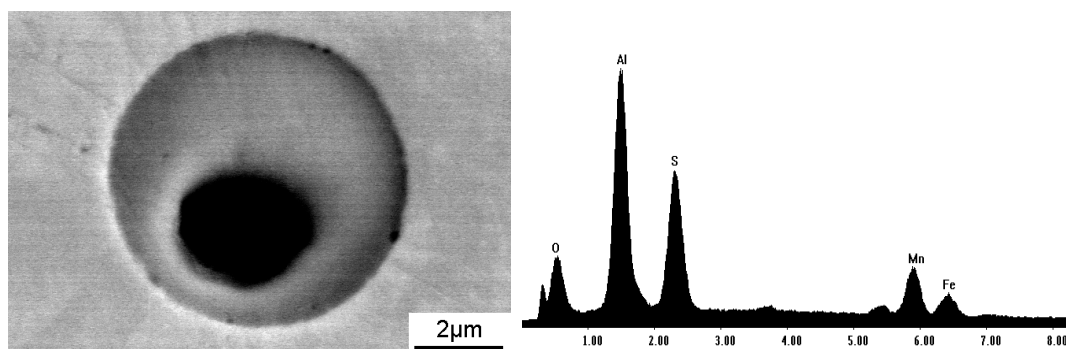


Figure 6 Morphology and composition of the oxide-sulfide duplex inclusion in No.4 sample

3.4 Statistic of the different type of sulfides

The correlation of five spectra channels from other five samples in the first 1000 discharge points are shown from Figure 7 to Figure 11. It was found that there were a lot of high intensity signals simultaneously appeared in the spectra channels of S and Al, which indicate that there are a large amount of complex inclusions of sulfide and alumina in gear steels. The abnormal high intensity signals from Ca channels increased with the rise of the content of Ca in steel and the discharge points in which the abnormal signals of Al, Ca and S simultaneously appear also increased. It indicates that the quantity of the inclusions with the composition of Al, Ca, Mn, and S also increase. The proportion of different type of the sulfides in total sulfides determined by OPA is shown in Table 2. It was found that quantity of simple sulfide was more than the oxide-sulfide duplex inclusion. The relative proportion of the simple sulfide and oxide-sulfide duplex inclusion were calculated and listed in Table 3. The area percentage of the sulfides (A) and the comparison of the results determined by quantitative metallographic analysis were also presented in Table 3. It was found that the relative proportion of the simple sulfide and oxide-sulfide duplex inclusion for six samples was in good agreement. The relative proportion of the high intensity frequency of S-signal also had close relationship with the area percentage of the sulfides. The relationship curve is shown in Figure 12.

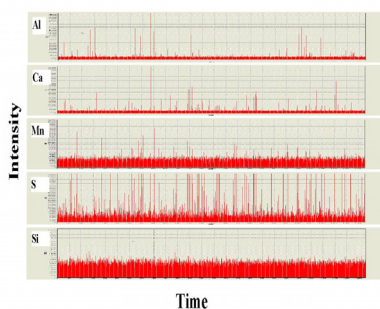


Figure 7 Multi-element correlation of high intensity signals for No.1 sample

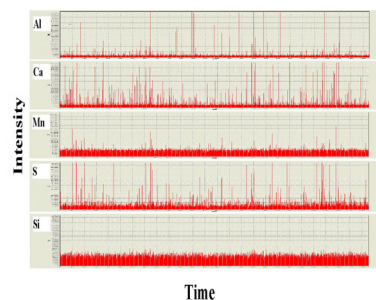


Figure 8 Multi-element correlation of high intensity signals for No.2 sample

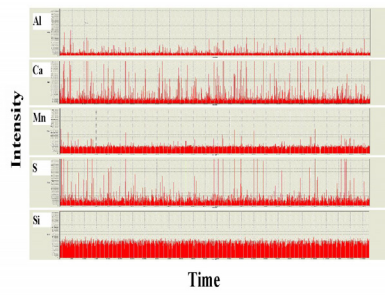


Figure 9 Multi-element correlation of high intensity signals for No.3 sample

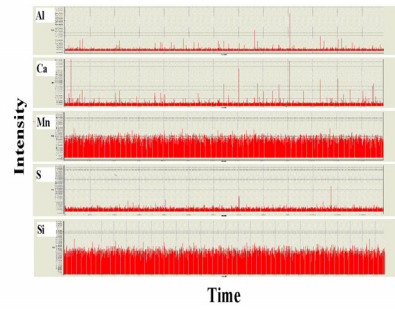


Figure 10 Multi-element correlation of high intensity signals for No.5 sample

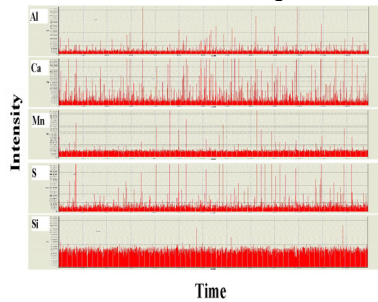


Figure 11 Multi-element correlation of high intensity signals for No.6 sample

Table 2 Proportion of different type of sulfides in total sulfides (%)

No.	1	2	3	4	5	6
(Mn, Fe) S	78.66	68.65	63.18	74.44	57.38	65.32
(Ca, Fe) S	1.53	0.25	0.78	0.11	0.04	1.49
(Ca,Mn, Fe)S	0.68	0.08	0.07	0.07	0	0.11
Al-Mn-O-S	12.38	11.50	8.84	15.42	19.23	4.76
Al-Ca-Mn-O-S	1.33	16.59	25.75	6.97	9.33	14.51
Al-Si-Mn-O-S	1.22	0.38	0.15	0.73	2.90	0.66
Al-Ca-Si-Mn-O-S	1.02	1.84	0.71	0.88	8.14	11.84
Others	3.18	0.71	0.52	1.38	2.98	1.31

Table 3 Comparison of the relative proportion of the simple sulfide and oxide-sulfide duplex inclusion between metallographic analysis and OPA (%)

No	AA /%	metallographic analysis		OPA	
		Simple sulfide	oxide-sulfide duplex inclusion	Simple sulfide	oxide-sulfide duplex inclusion
1	0.161	86.7	13.3	80.9	16.0
2	0.153	70.1	29.9	69.0	30.3
3	0.129	59.8	40.2	64.0	35.5
4	0.161	74.6	25.4	74.6	24.0
5	0.028	60.9	39.1	57.4	39.6
6	0.098	67.6	32.4	66.9	31.8

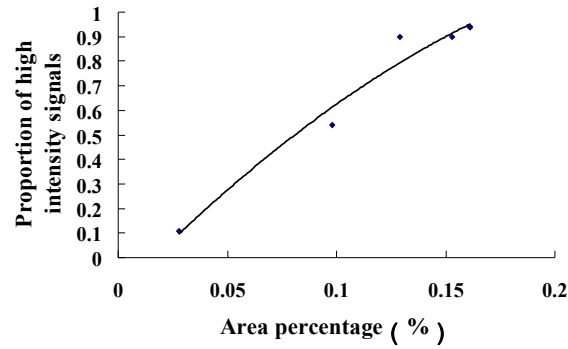


Figure 12 Relationship between the relative proportion of high intensity frequency of S-signal and the area percentage of the sulfides.

3.5 Influence of the content of Ca on the type of sulfides

The influence of the content of Ca on the composition of the sulfides was investigated. It was found that the proportion of the complex inclusions of Al-Ca-Mn-O-S increased with the rise of the content of Ca in gear steels, the relationship was shown in Figure13. The ratio of the content of Ca to the content of S (Ca/S) also had great effect on the relative proportion of the oxide-sulfide duplex inclusion. Figure14 Shows that the relative proportion of the oxide-sulfide duplex inclusion increase with the rise of the ratio of Ca to S.

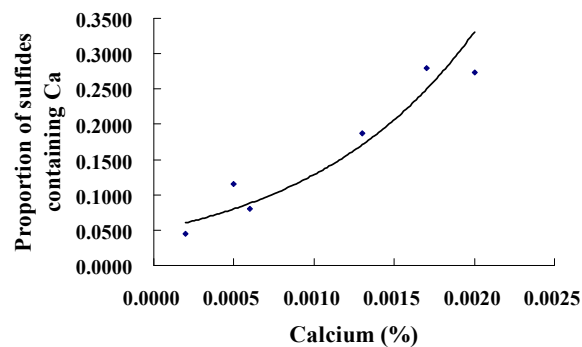


Figure 13 Relationship curve between the content of Ca and the proportion of the complex inclusions of Al-Ca-Mn-O-S

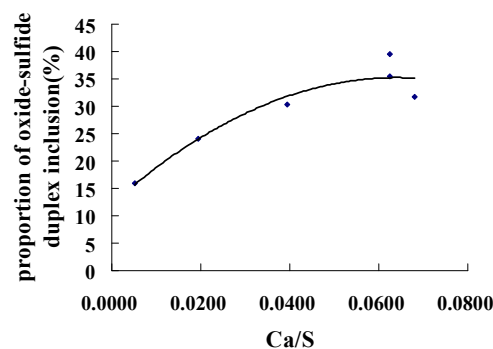


Figure 14 Relationship curve between the ratio of Ca to S and the oxide-sulfide duplex inclusion.

4 Conclusion

- (1) In this paper, the sulfides in some different gear steels were analyzed by original position statistic

distribution analysis technique. The abnormal high light signals emitted by the inclusion elements were identified by the statistic method. The determination method of the threshold value for distinguishing the inclusion containing S, Ca, Al, Mn and Si element was presented.

- (2) The relationship between the proportion of the number of abnormal light signals in total light signals and the content of total S and total O in samples has been investigated. It was found that the proportion of the number of abnormal light signals emitted by S element increased with the rise of the content of total S. At the same time the ratio of the number of abnormal light signals emitted by Al element increased with the rise of the content of total O. So it can conclude that the ratio of high intensity signals from S and Al has close relationship with the quantity of sulfides and oxides.
- (3) Multi-elemental correlation on high intensity signals has been performed in order to obtain the composition and proportion of different type of sulfides. It was found that the proportion of simple sulfide was more than the oxide-sulfide duplex inclusion in six gear steel samples. The ratio of the oxide-sulfide duplex inclusion to the total sulfides were determined by the present method and the results had good coincidence with the value obtained by quantitative metallographic method and scanning electronic microscopy.
- (4) The influence of the content of Ca on the composition of the sulfides was investigated. It was found that the relative proportion of the complex inclusions of Al-Ca-Mn-O-S increase with the rise of the content of Ca in gear steels. The ratio of the content of Ca to the content of S (Ca/S) also had great effect on the relative proportion of the oxide-sulfide duplex inclusion.

References

- [1] Gladman T. (1992) Developments in inclusions control and their effects on steel properties. *Ironmaking and Steelmaking* 19 (6) : 457-463
- [2] Auclair G, Meilland R, Meyer F. (1996) Methods for assessment of cleanliness in super clean steels. *La Revue de Metallurgie-CIT* 93(1): 119-130
- [3] Masahiro K, Toshihiko N, Toshihide T et al (1999) Characterization of relieved non-metallic Inclusions in stainless steel by image processing of micrographs. *ISIJ International* 39(2):164-170
- [4] Yongtae S, Bae J S, Statistical signal processing of optical emission spectroscopy for micro inclusion detection in steel, *IEEE Instrumentation and Measurement Technology Conference*, 1089 ~ 1092 May 2001
- [5] Ruby-Meyer F, Willay G, (1997) Rapid identification of inclusions in steel by OES-CDI technique, *La Revue de Metallurgie-CIT* 94(3):368-377
- [6] Kuss H, Lungen S, Muller G (2002) Comparison of Spark OES methods for analysis of inclusions in iron base matters. *Anal. Bioanal. Chem* 374:1242 ~ 1249
- [7] Wang H Z, (2007) Original position statistic distribution analysis(OPA)-novel statistic characterization method of different chemical composition and its states of the materials *Materials Science Forum* 539-543:4446-4451
- [8] Jia Y H, Wang H, Wang H Z (2007) Correlation analysis of MnS inclusion composition using Original Position Statistic Distribution Analysis. *Materials Science Forum* 15-17:810-815
- [9] Li D L, Wang H Z, (2007) Determination of inclusions of boron and titanium in steel by original position statistic distribution analysis technique. *Materials Science Forum* 539-543:4272-4276
- [10] Zhang Q Y, Wang L T, Wang X H (2008) Non-metallic inclusion distribution in surface layer of IF steel slabs. *Journal of Iron and Steel Research, International* 15(1):70-74

BRIEF OF THE QUALITY CONTROL OF THE AUTOMATIC ANALYSIS SYSTEM IN STEEL-MAKING INDUSTRY

LE Yang

Baoshan Iron & Steel Co., Ltd. Shanghai 200941, China

Abstract

With the development of the Analysis equipment and automatic, full automatic quick analysis system has been used much more in Steel-making industry, especially in ladle analysis. The system can finish the analysis job with out manual operations, but most of the quality control works have to be done by operators manually. By modifying and improving exciting system, some quality control methods have been used and some functions have been set up in order to develop the automatic quality control capability of the system. This paper centers on the analysis quality control of the automatic analysis system, particularly on the steel analysis which is the biggest part in a ladle analysis laboratory.

1. Introduction

With the development of the Analysis equipment and automatic, full automatic quick analysis system has been used much more in Steel-making industry. Progress of the Analysis equipment let the analyzing to be more accurate, quicker, and with more elements at the same moment. And the cooperation with mechanical automation not only reduces the manpower but also make the analyses more stable, both in the period and the result quality. Now, full automatic quick analyses system is getting popular in Chinese Steel-making factories, especially in ladle analysis.

Baosteel, one of the biggest iron and steel making company in china, have built several Full Automatic Systems in past ten years , and the processes of each system is similar with each other. Specimens are sampling in steel-making site and are send to laboratory via pneumatic tubes by sample carrier. The automatic system discharges the specimens and send them to sample prepare units, which usually are mills, cutters and belt machines. Then the specimens will be distributed to each analysis instruments. There are usually a number of OES for the steel sample, XRF for the Iron and slag sample. Sometimes we also have some automatically gas analyzer at the end of the system. Finally, the result will be made by instruments and sent back to the work site via network automatically.

Stricter the composition control of steel is required, more accurate the analyses results need to be. Today laboratory plays a key part in the production and the quality control of analyzing is also very important. Though the automatic analysis system, claimed to be automatic and intelligent, can finish the job full automatically, and the central computer is powerful enough to find a rational path which the sample should go through by detecting which equipment is busy or which one is out of order. But it's still not clever enough to care the quality control of analyzing. Lots of Manual works, like selecting applications, detecting the sample quality, monitor the state of sparking and checking the results, are still necessary to prevent departures and error results in an automatic laboratory.

To exert the calculation capability of the system, we try to make the system treat with the big amount of quality control data by itself and make response automatically and timely. Here are some solutions, among which some of them are existed already and some others are what we are trying to reach.

2. The control of the analysis instruments

To get a high quality control over the laboratory, make instruments work under a satisfied state is most important. With the improvement of software and automatic fittings, instruments like OES and XRF can monitor itself with out manual works. The robot can select and take the standard samples to make standardization and verification periodically. Data can be ingathered by the instrument's computers or be sent to Central Computer of the system. The result will be checked and the warning will be given if they can not fulfill the control limits. This function shows one of the biggest advantages of automatic systems, powerful computing capability, to process the quality control data. Operators just need to check the status of the instrument when the warning occurs, saving time on the data collection and verification. Also we use SPC to monitor the status of equipments, abnormal situation will be feedback timely by performing the tests for specialties, and system can let individual equipment out of work automatically when the tests fail, before a deviation of result accruing.

To get accurate analysis results, instruments may have several curves or applications for different grade of steel. Calibrate and verify all the curves and applications will consume a large amount of standard samples and a lot of time, also bring a lot of work to processing data and increase the probability of instruments down as dissatisfy the verification. To deal with this problem, we make the centre computer to communicate with the higher level system, which release the production plan. By Compared with the database which contains the composition demand of every steel grades and the method of standardization for each grade, the centre computer sends the message to each instrument and to organize the standardization and verification in a best way. Because of the production plan being released much earlier than the verification made, the system can make fully preparation for the coming samples with different composition and saving time and cost.

In additional, it is necessary to spot-check the analysis results frequently. To finish this job automatically, the system must be designed to have ability to storage a number of samples, which can be re-taken from the instruments after analyzing and re-prepared by the system. The system could take the samples periodic or take a sample from certain amount. The analysis will be done again several hours later, or after a shift or standardization. Also the analysis could be done with another instrument. The result will be collected and be verified with the original and if the results do not fall within the control limits, an error message will be given and the system will relieve the instruments automatically.

3. The control of the sample quality

Sampling quality is also an important factor in Ladle analysis. The quick analysis system needs stable and homogeneous specimens to fulfil the high requirement of the analysis speed and accuracy.

Compared with the manual operation, it is difficult for the full automatic systems to find out the defects in the specimens. There are commonly two ways to discover the defects in an automatic system. One of them is to calculate the deviation between each excitation. A bad sample is recognized if the deviation exceeds the limit, and bad sample information will be sent out. Then the sample will be re-prepared by the system or another sampling will be done on site. This way is suitable to discover an inhomogeneous specimen. (Chart-1)

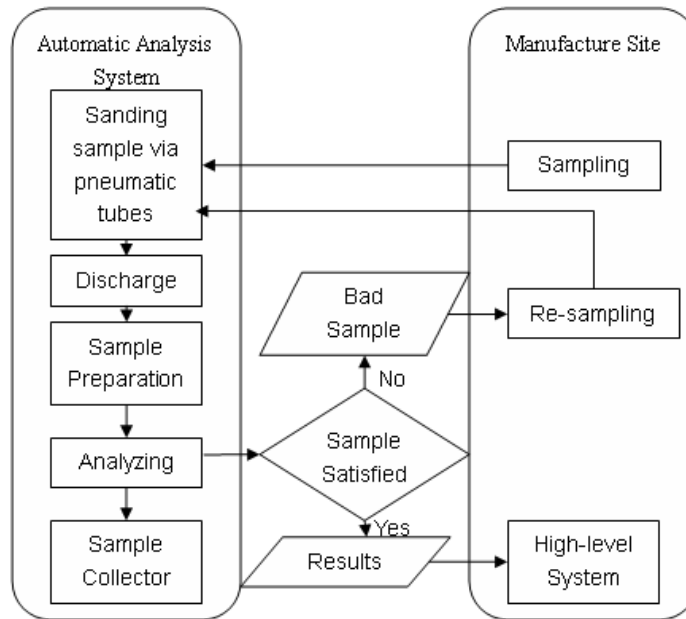


Chart-1 Bad Sample Discovered by Instruments

Other one is to scan the surface of the specimens. With the development of digital imaging technique, nowadays OES systems usually have a digital camera to monitor the surface of each specimen. It takes 2~4 seconds and picks out the defective regions where can not be sparked. Then the robot will avoid the defects following the monitoring results. Some camera can find out the defects as small as 0.25mm.

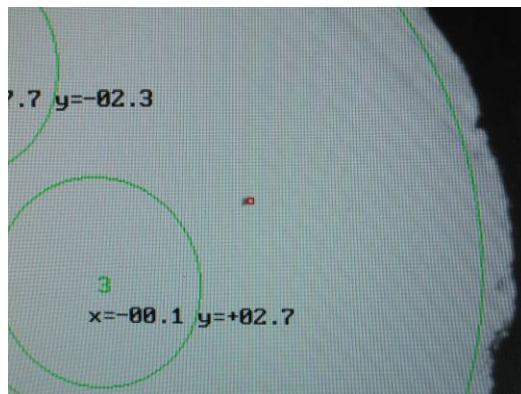


Chart-2 A small defect was recognized by digital camera

In contrast with the first one, the second method can select satisfied regions of the specimen been excited. It saves the time on re-sampling or re-preparation, and avoids the wrong results by sparking on bad area. This method can deal with a bad sample if only the defects are on the surface. But some kind of badness inside the specimen can not be detected even by the digital camera. Sometimes the hollows under the surface and the inclusions inside could also make the samples unsuitable for analysis.

As the specimens are always uniform-sized, the weight of the specimens will also be an important index. We have weighed amount of specimens and counted them in QAS No.3, one of the automatic analysis system in Baosteel. For example, the flat sample usually is 70g to 85g. The test shows that the samples below 75g, which could caused by less sampling time and sampling depth not meeting the requirement, will be potentially a bad-sample (Table-1). To keep the bad sample within the out of the laboratory, we set a weight limit at the sampling site. The specimens can be sent to the laboratory only over 75g, which should be weighed on an electronic balance.

Weight of the Specimens (g)	Specimens	Bad Samples	Bad Sample Rate
80 to 85	364	8	2.2%
75 to 80	131	10	7.6%
70 to 75	77	13	16.8%
Less than 70	20	7	34.5%

Table-1 Weight and Bad Sample Rate

Though weighing the specimens, sometimes including cooling, will take 10 to 30 seconds each, but the promotion of the sample quality and the raise of the success analysis rate is obviously. On another hand, this work will save a lot of time of re-preparing and re-sampling after a bad sample turns up. The effect could be more outstanding where the sampling quality is highly instable. (Chart-3)

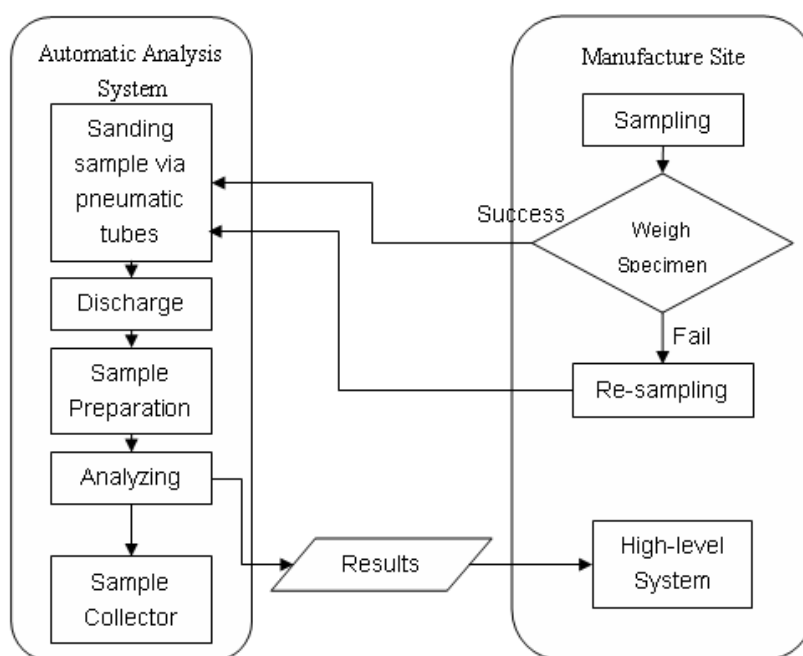


Chart-3 Bad Sample Discovered by Weight

We also try to merge this function into the full-automatic systems, and then specimens could be weighed by the units, which like sample-carriers and sample-transport. But there are still some problems as how to weigh the specimens quickly and exactly, how can the units weigh the specimen when the specimen is moving fast, and what shall the system do when the specimen is detected to be too light.

However, the sampling quality should be keep improved and be guaranteed for a automatic analysis system, A bad sample will delay interfere the analyzing whether it has been recognized or not.

4. The control of the excitation and measurement

In a manual ladle analysis laboratory, operators always take care of the analyzing and the result obtained, but the automatic system usually release the analysis data just behind the analyzing finished with out any confirmation. Now some means have been set up to make the system more responsible.

As each step of the steel-making have a specification limits of component, each sample also have a components limits corresponding with each production procedure. In manual analyzing, operators usually compare the result with the specification limits of the sample. If the value is without of the limits, the analysis process will be checked and a retest will be done in order to prevent a potential error.

Now for automatic systems, each sample has its own number which include the information about where the sample come from, which process the sample was taken, and which grade sample is. A table has been established including information about steel grades and specification limits of each process. Every result will be checked with the table via its sample number. If the result is out of the limits, as options, the system can keep the result and make another measure by another spectrometer, or make a warning for operators to check the analysis process and the state of the spectrometer.

Technically, this function will not control the quality of the measurements and the instruments directly, but in where the steel-making process is stable and mature, this function can find out irregular issues timely.

Another difference from manual operation and automatic system is the checking of the sparked area. With spectrometers, a properly excited specimen should exhibits a dark ring around the pitted sparked area. A characteristic dark ring indicate a successful excitation, and if there is any smooth, white, texture burn, there could be some interferences and irregularities during the excitation, like argon gas leak, impurities or water on specimen surface, small holes in the specimen. In all such instance, the result could be wrong or instable.

As the digital imaging system, mentioned before, installed in front of the instrument and monitoring the surface of the specimens before analyzing, could also be used as a detector to monitor the surface after the analyzing. With digital image-identify-techniques, it is easy to recognize a burn with a dark ring automatic. As a successful analysis need at least two sparks, the system also need find out two spots with characteristic dark ring after an analyzing. If not, the system could keep the result from sending out and release a message to operator. In the same way, the system could make a retest by itself and calculate the two values to decide whether to send out the result. (Chart-4)



Chart-4 Characteristic Dark Rings

5. Conclusion

With the quality control functions mentioned before, the automatic system could be much smarter and can finish the analysis job more autonomous. During the analysis operations, the system could collect quality control data and calculate those at the same time by its powerful calculate ability. So system can become aware of the abnormalities and instability much quicker than human when the logic have been setup and could make responses as soon as the abnormalities happening. It will be a great advantage particular in Ladle analysis which requires a short period and generates a big amount of data.

At the same time, there is still many problems need to be solved. Since each instrument from different manufacturers have its own quality control functions and controlled by different software, it's easy to collect data from instruments but it's hard to send quality control orders to each instrument. And, however, many confirmations and investigation works still need to be done manually after a warning being released. Some kind of functions, like retesting and re-preparation of the samples, cost a lot of time. Some others, like weighing the specimens, could give only a message but no suitable solution. There still will be a long way for an intelligent system but not only an automatic one.

References:

- 1) LIAO Li-ping, XIANG Xiu-zhi. The application of SPECTRO direct –reading spectrograph in automated analysis system, 1003-0514(2005)06-0017-06.
- 2) CHEN Zhi-min. Application of full automatic quick analysis system in steel chemical composition analysis of Baosteel, 1000-7059(2006)05-0046-05

QUALITATIVE AND QUANTITATIVE ANALYSIS OF PRECIPITATE PHASES IN 2205 DUPLEX STAINLESS STEEL WITH DIFFERENT ISOTHERMAL TREATMENT SITUATION

Miao Lede, Zhang Yi

Research Institute, Baoshan Iron & Steel Co. Ltd., Building 5, No.889 Fujin Road, Baoshan, Shanghai, 201900, China, Email: miaolede@baosteel.com, Phone: 0086-021-26648710

ABSTRACT:

Due to isothermal heat treatment or welding, duplex stainless undergoes a variety of decomposition processes at a temperature ranging from 300-100 °C, which could form inter-metallic phases like σ phase and χ phase, as well as Cr_2N and M_{23}C_6 , etc. These processes are not only influenced by temperature and cooling speed, but also are affected by alloy element content. The purpose of the research was to work out the qualitative and quantitative analysis of precipitate phases in 2205 duplex stainless steel with different isothermal heat treatment situation. After choosing the electrolyte and electrolytic systems, we use electrochemical method to extract precipitate phases from the matrix. Scanning electron microscope (SEM) and X-ray diffraction (XRD) were used to examine their modality and structure. Particle size distribution was performed by dynamic laser scattering sizer (DLS-Sizer). Furthermore, oxygen-nitrogen analyzer and carbon-sulfur analyzer were applied to measure the content of nitrogen and carbon in precipitate phases. Separation and quantitative analysis of precipitate phases were carried out by wet chemical analysis and inductively coupled plasma spectrometry (ICP). In a word, combining chemical and physical methods, our research reveals the transformation of precipitate phases' species, content, elemental composition and particle size distribution during different isothermal heat treatment situation.

KEY WORDS: duplex stainless steel; inter-metallic phases; isothermal treatment; qualitative and quantitative analysis

1 INTRODUCTION

Compared with austenitic stainless steel, duplex stainless steel possess significant effect on inter-granular corrosion, spot eroding, clearance corrosion, especially, on stress-corrosion cracking caused by chloride. They are being increasingly used as structural material in oil, chemical, petrochemical, nuclear and marine industries [1]. However, due to containing higher Cr, Ni and Mo, after isothermal heat treatment, the carbide phase, inter-metallic phase and nitride precipitate phase were generally formed during the transformation process from ferrite to austenite in duplex stainless steel. These precipitated phases in alloy would cause the embrittlement of stainless steel, the remarkable decrease of plasticity, ductility and corrosion resistance of steel. In addition, particle size and distribution of precipitates also seriously affect mechanical property of the steel, such as compressive creep and fatigue properties [2-3]. Therefore, qualitative and quantitative analyses of those precipitates phases are important for the performance improvement through the optimization of alloying and heat treatment processing, as well as for research and development of high-grade duplex stainless steel [4-6].

For the qualitative and quantitative analysis of precipitated phase of 2205 duplex phase stainless steel with different heat treatment time, the electrolysis results of duplex stainless steel with different electrolysis systems were firstly studied. After selecting proper electrolysis system, the precipitated phase was separated from the matrix by electrolysis separation. The topography and structural change process of precipitated phase after extraction were qualitatively investigated by scanning electron microscope (SEM) and X-ray diffraction (XRD). The size distribution of precipitate phase was analyzed by laser particle analyzer. Moreover, the content of nitrogen in

precipitated phase was measured by oxygen-nitrogen analyzer. The content of carbon in residue after acid treatment was analyzed by carbon-sulfur determinator. The content of alloy elements in solution after chemical separation was tested by inductively coupled plasma-mass spectrometry (ICP-AES). By combining the content of nitrogen and carbon, the elemental composition and content of different precipitated phases were calculated. Finally, the effect of aging time on the precipitated phase was discussed. The inter-metallic phase χ phase firstly formed during the beginning of aging. χ phase decreased with the prolonging of heat treatment time, while σ phase gradually formed and finally predominated the precipitated phases.

2 EXPERIMENTAL

2.1 Materials and heat treatment specifications

The material used was a 2205 steel plate (25mm thick) with composition as given in Table 1. All the samples were subjected to solution anneal at 1050°C for 30 min in order to achieve homogeneity and cooling in water. Next isothermal heat treatment was performed at different temperature, and then cooled in air. Details as follows: specimen No.1 was after solution treatment; specimen No.2-7 were performed at 850°C for 45min , 2h , 4h , 6h , 10h,24h ; specimen No.8-12 were performed at 750°C for 1h , 2h , 5h , 7h,24h ;

Table 1 Chemical composition of 2205 duplex stainless steel (wt.%)

Element	C	Si	Mn	P	S	Cr	Mo	Ni	N
Content (Wt%)	0.024	0.62	1.4	0.023	0.001	21.07	3.01	5.36	0.155

2.2 Instruments and reagent

Potentiostat/Galvanostat: 273A/10A, Princeton Applied Research;

Laser particle sizer: Mastersizer 2000, Malvern;

ICP-AES:IRIS Intrepid II, Thermo;

XRD: RINT2500/PC, Rigaku;

Metallurgical microscope: Axioplan2, Zeiss;

SEM: S-4200, Hitachi;

Oxygen/nitrogen analyzer: TC600, Leco.

Carbon/sulfur analyzer: 444LS, Leco.

All reagents are analytically pure and water is double distilled.

2.3 Experimental methods

Sample preparation: Electrolysis was performed after preparing the specimen as $\Phi 10 \times 100$ mm round stick. Polarization cure was performed after preparing the specimen as $\Phi 10 \times 1$ mm slice and examination of the as-polished specimen. In the electrolytic system, platina was used as the cathode material. The specimen for optical microscopy and SEM were performed after eroding specimen No1 and No2 with size $10 \times 10 \times 5$ mm in 4% picric acid alcohol solution.

Extraction and analysis of precipitation phases: The electrodes and temperature were same as the above. Electrolysis was carried out with current density 25 mA/cm² for 2h. Then, the extracted residues were ultrasonic cleaned in alcohol and filtrated by 0.02 μ m film. The collected precipitates were analyzed by XRD, Laser particle sizer and so forth and they could be also separated into species of different phases by wet chemical method [9].

3. RESULTS AND DISCUSSION

3.1 Morphological observation and percentage of precipitates at different aging situation

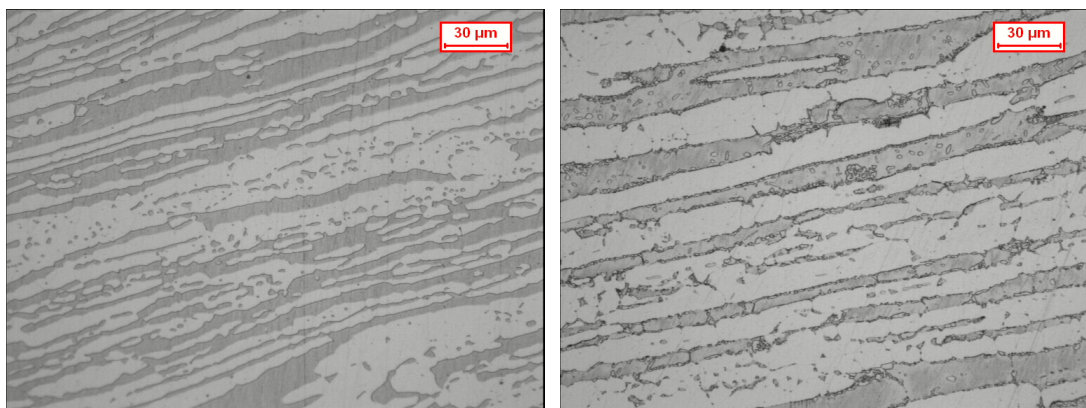


Fig.1 OM micrographs of specimen No.1(solution-treated state) and No.2(850°C , 45min)

In order to evaluate the consistency of precipitates appearance during electrolysis progress, the specimens No.1 and No.2 etched in 4% picric acid alcohol solution were observed in OM and SEM. The results showed that he specimen before heat treatment did not contain any precipitate either within ferrite grains or at grain boundary (Fig.1, left). During 850°C/45 min tempering, precipitation occurred firstly at grain boundary. Fig.1 and 2 also showed clearly the presence of precipitates at the ferrite / austenite interfaces, the preferential nucleation sites for heterogeneous precipitation. Their formation in duplex stainless steels is a result of δ ferrite decomposition through an eutectoid transformation.

In an attempt to assess the precipitation phase percentage of specimen with different time of heat treatment at 750°C/850°C, the electrolysis loss and the residue weight were determined. The precipitates were extracted using electrolysis method, and the residue was separated using a membrane filter with 0.05 μm pores. Therefore, the electrolysis loss Δm as well as the precipitate percentage f of specimens with different aging time at 750°C/850°C were shown on Fig. 3. The calculation of Δm and f could be expressed as:

$$\Delta m = m_0 - m_t \text{-----1}$$

$$f = (m_c / \Delta m) \times 100\% \text{-----2}$$

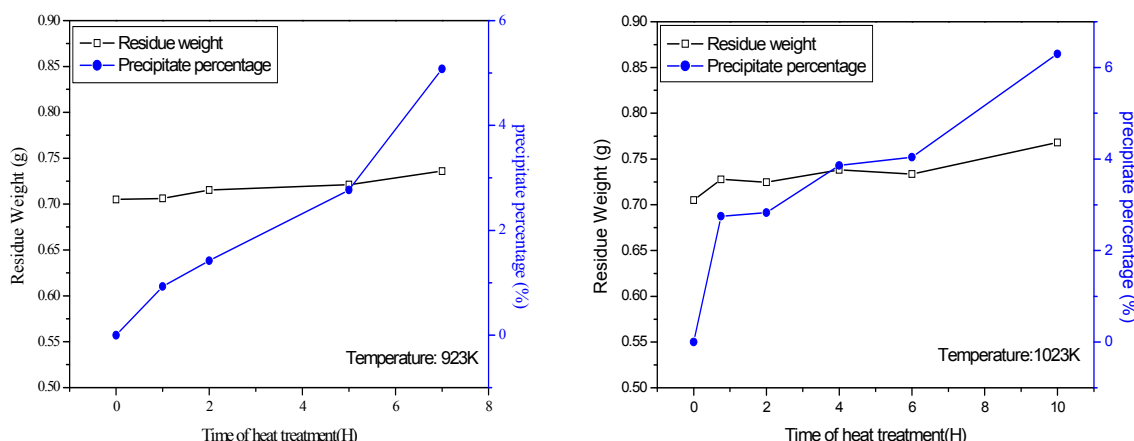


Fig. 2 Relation between aging time at 750°C/850°C and electrolysis loss as well as the precipitate percentage

Where, m_0 is the original mass of specimen before electrolyzing and m_t is the final mass of specimen after electrolyzing, m_c is the mass of precipitates extracted from the specimen.

The results (as shown in Fig 2) revealed that the electrolysis loss of different specimens with the same electrolysis situation changes little (Δm of specimen with different time of heat treatment at 750°C/850°C was among 0.70g to 0.76g). However, the precipitation phase percentage of specimens aged at 750°C/850°C had largish increment with ascending aging time: at 750°C, the precipitation phase percentage increased from 0.93% to 5.08% with aging

time ascending from 1h to 7h; at 850°C, the precipitation phase percentage increased from 2.75% to 6.30% with aging time ascending from 45min to 10h. In addition, for specimen No.1 (without aging process), the electrolysis loss was about 0.71g in same electrolysis situation, which showed little discrepancy with aging specimens. However, hardly any electrolysis residue of specimen No.1 suggested that precipitate phases were formed after aging process.

3.2 Transformation of precipitate phases in different aging process

The extracted residue powder was analyzed by Rigaku D/max-2550 X-Ray diffractometer with CuK α radiation and graphite monochromators. The diffraction data was collected for each specimen from 30 to 90° 2 θ with a step width of 0.02° and a count time of 2.0 s per step. In order to study the forming temperature and aging time of precipitate phases, specimens aging at 550°C/650°C with 2h and 24h were performed. The results indicated that most of these precipitate phases are carbide phases, containing a small quantity of nitride phase and inter-metallic phase. All of these precipitate phases were not stable, and their crystal structure was not integrity. Figs. 3 showed the XRD spectra of specimen No.8-12, aging at 750°C for different time. It was shown that precipitate phase had formed at the initial state of aging, and then, the transformation of precipitate phase occurred with prolonged aging. After aging 1h, the precipitate phases mostly contained M₂₃C₆ and Cr₂N, as well as a few meta- stable χ phase; to 2h, meta- stable χ phase increased; till 5h, some σ phases formed; and then, χ phase decreased with the prolonging of heat treatment time, while σ phase gradually formed and finally predominated the precipitation phases at 24h. The whole transformation process could be described as: M₂₃C₆, Cr₂N, χ phase \rightarrow χ phase, Cr₂N, M₂₃C₆ \rightarrow χ phase, Cr₂N, σ phase \rightarrow σ phase, Cr₂N, χ phase. It was suggested that M₂₃C₆ firstly formed at the initial state of aging. The precipitation of M₂₃C₆ could lead to the loss of Cr in ferrite near the crystal boundary, which could accelerate the original α/γ phase boundary transfer to ferrite crystal and create situation for forming inter-metallic phases [7-8]. For inter-metallic phases, the meta-stable χ phase had formed at the initial state of aging, and then, χ phase decreased with the prolonging of aging time, while σ phase gradually formed and finally predominated the precipitate phases.

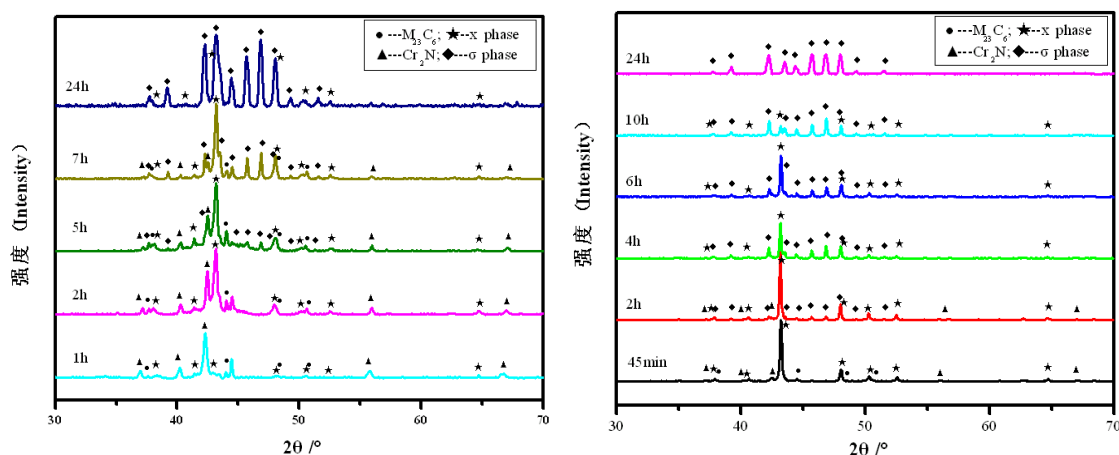


Fig.3 XRD spectrums of electrolytic residues collected from specimens treated at 750 °C with different heat treatment time

Fig.4 XRD spectrums of electrolytic residues collected from specimens treated at 850 °C with different heat treatment time

Fig.4 showed the XRD spectrums of electrolytic residues collected from specimens treated at 850 °C with different aging time. The whole transformation process could be described as: χ phase, Cr₂N, M₂₃C₆ \rightarrow χ phase, σ phase, Cr₂N \rightarrow χ phase, σ phase \rightarrow σ phase, χ phase \rightarrow σ phase. The structure of χ phase is cube crystal, and the composition of χ phase mainly contains Fe, Cr, Mo. χ phase is meta-stable phase, which is formed with aging temperature from 700°C to 900 °C and decrease with the prolonging of aging time. The forming χ phase induces

ullage of Cr and Mo in the region, which also cause the remarkable decrease of toughness and corrosion resistance of steel. Due to coexistence with σ phase, it is very hard to distinguish the influence of χ phase and σ phase. Besides, σ phase is the most harmful precipitate phase, which could significantly decrease of plasticity, ductility and corrosion resistance of steel. Fig.5 showed SEM photographs of electrolytic residues collected from specimens treated at 850 °C with different aging time. The energy spectrum results indicated that spiculate part mainly contained Fe, Cr, Mo, without Ni; and nubby part included Fe, Cr, Mo, Ni, Si. It is primarily concluded that the spiculate part is χ phase, and the nubby part is σ phase. The SEM results coincide with XRD spectra, both of them revealed that inter-metallic phases' transformation from χ phase to σ phase. The SEM results also concluded that χ phase and σ phase are coexistence in transition process, and χ phase decreased with the prolonging of aging time, while σ phase gradually formed and finally instead of χ phase.

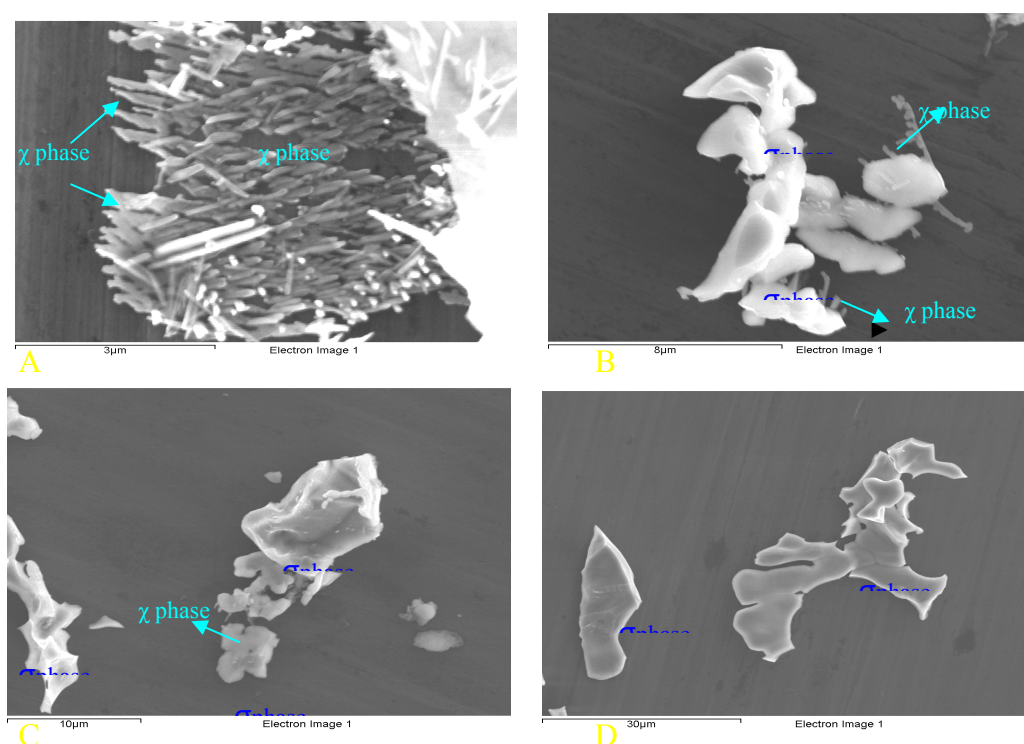


Fig.5 SEM photographs of electrolytic residues collected from specimens treated at 850 °C with different heat treatment time (A : 45 min , B : 2H , C : 10H , D : 24H)

3.3 Chemical quantitative analysis of precipitate phases

In an attempt to separate the nitride phase, carbide phase and inter-metallic phase of precipitate phase, different acid solution methods were performed. Wet chemical analysis indicated that nitride phase and partial inter-metallic phase were easily dissolved in weak acidity solution. So, it is impossible to separate nitride phase and inter-metallic phase by solution's different acidity. XRD results indicated that all of the nitrogen in the residue was shown as Cr_2N , so, the content of nitride phase could be calculated when the nitrogen in the residue was measured. In our experiment, $\text{HCl-H}_2\text{O}_2$ solution system was performed to dissolve both of nitride phase and inter-metallic phase, after dissolution, the carbide phase was separated using a membrane filter with 0.05 μm pores. The content of alloy elements in solution after chemical separation was tested by inductively coupled plasma-mass spectrometry (ICP-AES). Table2 showed the elemental composition and content of precipitation of specimens aged at 750 °C with different time. The results were concluded that the content of inter-metallic phase increased with the prolonging of aging time, increasing from 0.55% at 1h to 3.67% at 7h. Inter-metallic phase mostly included Fe, Cr, Mo, also containing some Ni, Mn, Si; however, carbide phase mostly included Fe, Cr, hardly containing Ni, Mn. In addition, the composition of χ phase contains Mo, hardly any Ni, so, the

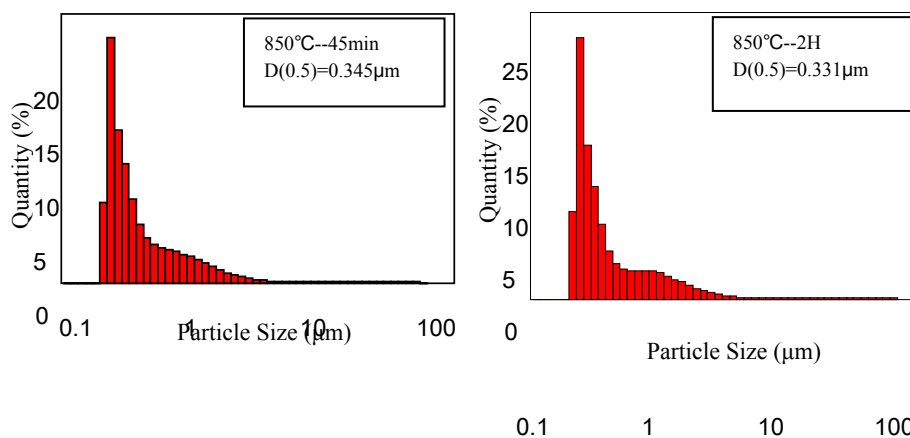
transformation of χ phase and σ phase could be described by the change of the content of Mo and Ni. After aging 1h, the inter-metallic phase hardly contained Ni, and the elemental composition ratio of Cr: Fe: Mo approximately equal to 2: 4: 3; at 5h, the ratio approximately equal to 2: 4: 2; and till 7h, the ratio approximately equal to 2: 4: 1. The change was consistent with XRD analysis result. The inter-metallic phase χ phase firstly formed during the beginning of aging. χ phase decreased with the prolonging of aging time, while σ phase gradually formed and finally predominated the precipitate phases.

Table2. The elemental composition and content of precipitation of specimens aged at 750 °C with different time (WT%)

Precipitate phase	Aging time (h)	Cr	Fe	Mo	Ni	Si	Mn	C	N	SUM
Cr ₂ N	1	0.13							0.017	0.14
	5	0.17							0.023	0.19
	7	0.12							0.016	0.14
Inter-metallic phase	1	0.11	0.22	0.17	0.01	0.03	0.01			0.55
	5	0.43	0.94	0.56	0.05	0.07	0.02			2.07
	7	0.93	1.81	0.70	0.08	0.11	0.04			3.67
Carbide phase	1	0.13	0.01	0.04	0.00	0.01	0.00	0.017		0.20
	5	0.12	0.03	0.01	0.00	0.05	0.00	0.024		0.24
	7	0.12	0.03	0.01	0.00	0.05	0.00	0.024		0.24

3.4 The size distribution of precipitate phases

Laser particle size analysis was performed to establish the size distribution of precipitate particles in samples tempered for different time at 850°C. Fig6 showed precipitation phase's size distribution of electrolytic residues collected from specimens treated at 850 °C with different aging time. The results from laser particle sizer suggested that the aging time influenced the mean diameter of precipitates. After aging 45min, the quantity distribution D (0.5) value (median particle diameter of quantity distribution) is 0.345 μ m, and most of particle were less than 1 μ m. The size distribution of precipitate particles changed little with the aging time increased from 2h to 6h, the D (0.5) value equaled to 0.430 μ m at 6h. However, the size increased significantly after aging 10h, D (0.5) value equaled 1.235 μ m. This remarkable change was consistent with the precipitate percentage change at 850°C (shown on Fig.3). Till aging 24h, D (0.5) value equaled 2.099 μ m, and most of particles were larger than 1 μ m.



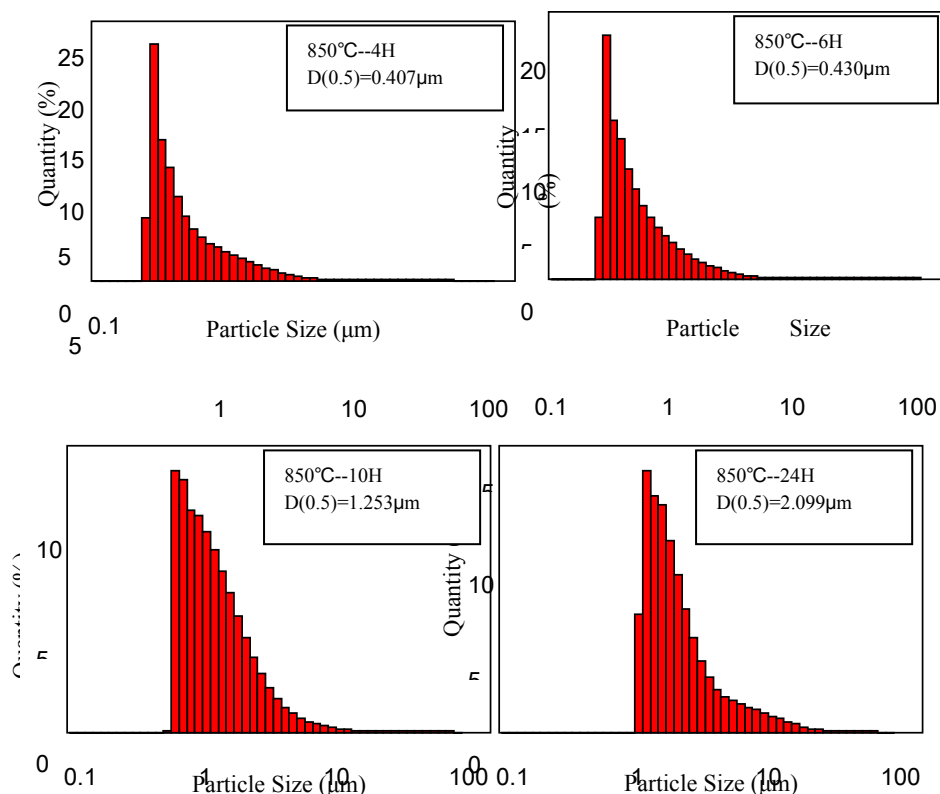


Fig6. Precipitation phase's size distribution of electrolytic residues collected from specimens treated at 850 °C with different heat treatment time

4 CONCLUSIONS

① Chemical and physical methods were performed to research the species, content, elemental composition and size distribution of precipitate phases in 2205 duplex stainless steel. χ phase is meta-stable phase, which is formed with aging temperature from 700°C to 900°C. χ phase decreased with the prolonging of aging time, while σ phase gradually formed and finally predominated the precipitate phases.

② After aging 45min, the quantity distribution $D(0.5)$ value is 0.345 μm , and most of particle were less than 1 μm . However, the size increased significantly after aging 10h, $D(0.5)$ value equaled 1.235 μm . This remarkable change was consistent with the precipitate percentage change at 850°C. Till aging 24h, $D(0.5)$ value equaled 2.099 μm , and most of particles were larger than 1 μm .

③ The nitride phase, mainly existing as Cr_2N , was formed in a temperature range from 600 to 850°C, especially at 750°C. And the carbide phase mostly included Fe, Cr, hardly containing Ni, Mn. The carbide phase was formed quickly, which could lead to the loss of Cr in ferrite near the crystal boundary, and create situation for forming inter-metallic phases.

④ The composition of χ phase contains Mo, hardly any Ni, so, the transformation of χ phase and σ phase could be described by the change of the content of Mo and Ni. After aging 1h, the inter-metallic phase hardly contained Ni, and the elemental composition ratio of Cr: Fe: Mo approximately equal to 2: 4: 3; at 5h, the ratio approximately equal to 2: 4: 2; and till 7h, the ratio approximately equal to 2: 4: 1.

5. BIBLIOGRAPHIES

[1] Gao wa, Luo jianmin, Yang jianjun,.(2005) *Research progress and application of double phase stainless steel.*

- Ordnance Material Science and Engineering, 28 (3) :61
- [2] Lu shiyong. (1995) *Stainless steel*. Beijing : Atomic energy publishing company, 161-179,312-319.
- [3] Xiao jimei. (2006) *Metallic issue on stainless steel*. Beijing : Metallurgy industry publishing company, the 2nd edition:49-107.
- [4] Karlsson L.(1999) *Intermetallic phase precipitation in duplex stainless steel and weld metals*, WRC Bulletin,438 :1 ~ 23
- [5] Karlsson L.(2000) *Welding duplex and super-duplex stainless steels*. Welding inter, 14(1):5-11
- [6] Kuroda T. (2000) *Precipitation behavior of σ phase in duplex stainless steels and weld metals*. Welding in the World, 44(2):17-21
- [7] Lee C., Cho H., Choi D..(2006) *Effect of isothermal treatment of SAF 2205 duplex stainless steel on migration of δ/γ interface boundary and growth of austenite*. Mater Charact,285:156-161
- [8] Michalska J., Sozanska M..(2006) *Qualitative and quantitative analysis of α and χ phases in 2205 duplex stainless steel*. Mater Charact, 56:355-362.
- [9] Miao Lede, Zhang Yi, Wang Zhiyu and Wu Junfei.(2009) *Electrochemical extraction and the analysis of intermetallic phases and nitrides in tempered duplex stainless steels*, Baosteel Technical Research, 3(2):52-57.

PRECIPITATION STUDY ON TI-NB-MO CONTAINED HIGH STRENGTH STEELS

N. Cai, X. H Ju, Y Meng, J. L. Hao, W. P. Liu

Shougang technical research institute, Beijing 100043

ABSTRACT:

Steels with the yield strength higher than 700 MPa have been achieved through Ti, Nb and Mo microalloy technique and TMCP process. The high strength is greatly attributable to the nano-sized Ti, Nb and Mo precipitates. In this work, Thermo-calc software was employed to calculate the thermodynamic equilibrium phases. The morphology, distribution, size and component changes of Ti, Nb and Mo precipitates in cast slabs and hot-rolled plates were studied by using SEM and TEM, respectively. It was found that after hot-rolling, precipitates with diameter (D) larger than 120 nm grow bigger and those with D between 40 to 120nm dissolved partially and downsized. The number of the precipitate smaller than 10nm increases obviously after hot-rolling. Most of the precipitates are composed with Ti, Nb and Mo carbides. The smaller is the precipitate size, the higher the content of Mo is. In summary, TMCP process has different influences on different sizes of precipitates. Through precise temperature controlling of TMCP process, the size and the distribution of precipitates can be controlled and therefore, different strength level can be achieved.

KEYWORDS : High strength steels, Microalloy technique, Nano-sized precipitates

1 INTRODUCTION

High strength steels have attracted more attentions for its wide usages in the automobile, machinery industry and great buildings or bridges [1]. Adding micro-alloy elements of Ti, Nb, V and Mo is a standard method to strengthen mechanical properties through grain refinement and precipitation hardening [2]. Such elements can interact with the microstructure evolution in different ways depending on the reheating conditions, deformation history and parameters as well as cooling conditions [3]. Most of these elements can react with carbon to form carbides, which will lead to an additional increase in strength. The combination of chemical composition and thermomechanical processing parameters determines the formation of microstructure which controls the mechanical properties. This paper is aimed to study the precipitates variation of Ti, Nb, Mo carbides from cast state to hot-rolled one.

2 EXPERIMENTAL PROCEDURE

Tab. 1: Chemical compositions (unit: wt%)

C	Si	Mn	P	S	Al _T	Mo	Ti	Nb	N
0.08	0.12	1.51	0.009	<0.002	<0.040	<0.15	<0.09	<0.05	0.003

The steels used in the experiments were manufactured by a steel company with continuous cast process. The cast slab was 1300mm in width and 230mm in thickness, and cooled to room temperature. Re-heat in 1250°C for 30 minutes, then hot-rolled into plate of 9.7 mm thick. Hot rolling process started at 980 °C, and ended at 830 °C. Curling temperature was controlled at 600 °C. Specimens were cut from the cast slab and the hot-rolled plate at the quarter of the width. Standard grinding and polishing techniques were employed and specimens were etched with 3% nitric acid in ethanol. Scanning electron microscopy (SEM, JEOL-7100F) imaging techniques were used to examine the microstructure at low magnification. Precipitates were observed using TEM (JEOL-2100F). TEM sample was the carbon replica film with extractive precipitates prepared using standard fabrication process. Carbon was evaporated onto the etched SEM sample using high vacuum evaporator (Polaron E6500 mini high vacuum evaporator). The chemical compositions of the steels were presented in Table 1.

3 RESULTS AND DISCUSSIONS

3.1. Microstructures

Fig. 1 a and b are SEM images illustrating the microstructures of the cast slab and hot-rolled plate, respectively. In cast state, the microstructure was composed with ferrites and pearlites, and the mean grain size of ferrite was about 100 μm . Whereas, in hot-rolled state, microstructure changed to tiny granular bainite, and the mean grain size was as small as several micrometers.

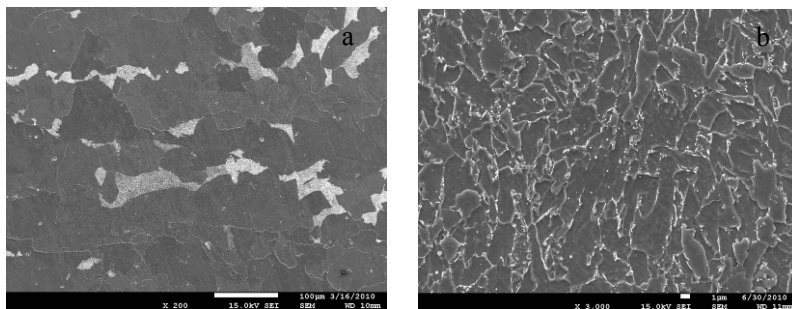


Fig. 1 SEM images of the microstructure in a) the cast slab, and in b) the hot-rolled plate.

3.2. Precipitates analysis and discussions

In FEG-SEM images with high magnification, larger than 100nm carbide particles can be seen usually. Fig. 2 a and b showed us such inclusions distributed in the matrix of cast state and hot-rolled one, respectively. In cast state, there were large amount of precipitates, and partially precipitated along prior austenite grain boundary; while in hot-rolled slab only a few of particles can be seen. Why only few of particles were seen? Where did the added alloy elements go?

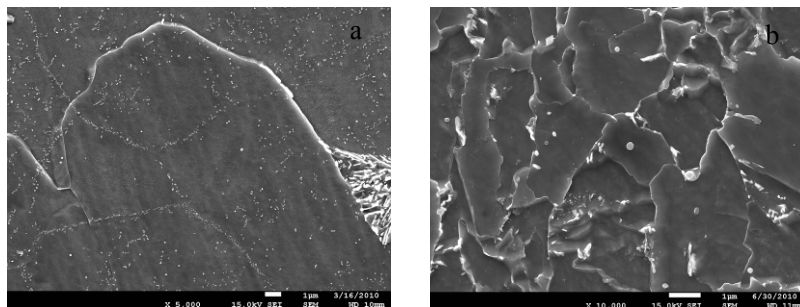


Fig. 2 SEM photos for precipitates distribution in a) the cast slab, and b) the hot-rolled plate.

Transmission electron microscope equipped with EDX was used to identify the size and the components of precipitates. Fig. 3 showed some typical images of carbon film replica samples with extraction of precipitates from the cast ingot and the hot-rolled slab. Fig. 3 a and b showed the precipitates distribution in cast state, while fig. 3 c and d for hot-rolled state. In cast state, numerous precipitates can be seen, and they can be classified into two types. One was as big as 60~100 nm around, another was 20 nm around. The bigger precipitates usually were polyhedral with sharp edges, and the small ones were often spherical. The precipitates in hot-rolled state can also be sorted into two kinds. One was as big as 100~200 nm around, another was smaller than 10 nm. All of the particles in hot-rolled state were round without sharp edges. Compared with cast state, bigger precipitates decreased in number, while smaller precipitates increased. With low magnification (shown in fig 3 b and d), there were much more particles in the cast state than hot-rolled state, which is consistent with Fig. 2. Whereas, with higher magnification (shown in fig 3 a and c), we can see plenty of tiny inclusions about several nano-meters in hot-rolled state, whereas rare in the cast one. Such tiny precipitates can not be observed with nether normal SEM nor FEG-SEM.

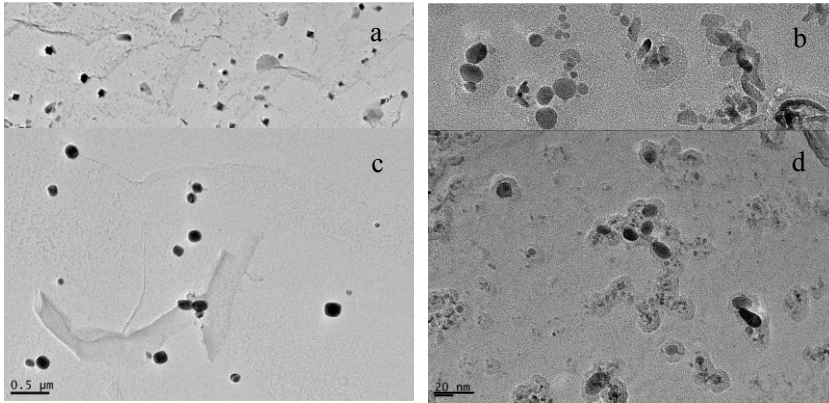


Fig. 3 TEM photos for precipitates distribution in a, b) the cast slab, and c, d) the hot-rolled plate.

EDX analysis was used to determine the chemical compositions of typical precipitates. Fig. 4 gave us the images of some typical precipitates. The chemical compositions of particles marked in figure 4 are listed in Table 2. Since the TEM sample was carbon replica film which would lead to extra carbon content in element quantifying, chemical composition of carbon in table 2 is deleted manually. All these particles were carbides of Ti, Nb and Mo with a little Cr doped.

A thermodynamic calculation was made with the thermo-calc software to predict the theoretical precipitates in this alloy system. The predicted inclusions and their precipitating temperature listed in table 3. According to the theoretical calculation, there was no Ti, Nb and Mo co-precipitates existed. That disagrees with the experimental results. Further investigation is needed to determine the actual molecular formula and the structure of such carbides.

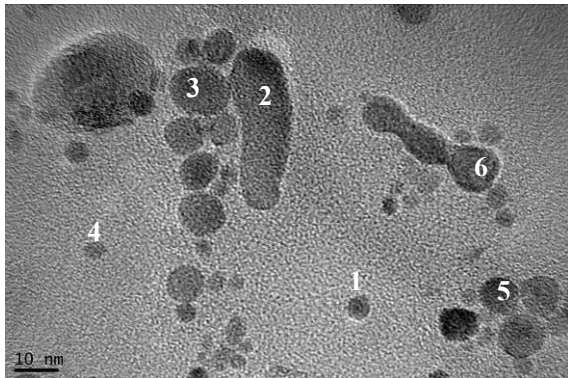


Fig. 4 TEM image of precipitates in cast state.

Tab. 2: EDX analysis results of Fig. 4

Position in Fig. 4	Element and its atom percentage (%)				Total
	Ti K	Cr K	Nb K	Mo K	
1	48.99	/	/	51.01	100
2	46.65	2.05	19.16	32.14	100
3	51.98	2.28	20.49	25.25	100
4	28.87	4.51	14.72	51.89	100
5	42.67	3.16	1.63	52.55	100
6	37.10	2.62	15.72	44.56	100

Tab. 3: Precipitating temperatures of each phase calculated by Thermo-calc

Precipitates	Precipitating temperature
Ti(N,C)	1505
Ti ₄ C ₂ S ₂	1490
(Ti,Nb)(C,N)	1271
(Mo,V)C	682
MoC	620
(Mn,Fe,Mo) ₇ C ₃	575
(Mo,Mn) ₂ C	492

For each sample five different views were recorded with such magnifications, 5K, 50K, 100K, 200K, respectively, to analyse the amount and the size of the precipitates. The statistic results were shown in Fig. 5. In the cast state, the sizes of precipitates were distributed in a rather narrow range from several nano-meter to 170 nano-meter, while in the hot-rolled slab the sizes vary in a wide range from several nano-meter to 300 nano-meter. After homogenization and hot-rolling process, the size distribution changed obviously. Compared with that in the cast state, the number of the precipitates larger than 120 nm increases slightly, while those between 40 to 120 nm decrease in number distinctly. As well, particles smaller than 10nm increase in number in hot-rolled state which maybe the results of large deformation induced precipitation. How to explain these changes. According to the experimental results (shown in figure 4 and table 2), large precipitates (>120nm) were mainly composed with titanium carbides accompanied with some niobium and molybdenum replacement, and they did not dissolve in the reheating process but growing up. However, with the decrease of carbides' size, the content of niobium and molybdenum increased. As we know, the dissolved temperature of niobium carbide and molybdenum carbide is lower than titanium carbide. According to the thermo-cal calculation shown in table 3, (Ti,Nb)(C,N) is dissolved at 1271 °C, and MoC is dissolved at 620 °C, therefore, MoC was completely dissolved accompanied with NbC mostly absorbed at reheating stage. At hot-rolling process, (Ti,Nb)(C,N) precipitated out, and MoC appeared at curling and cooling process. The accelerated cooling caused the downsized precipitates, which lead to the precipitates' distribution function changes.

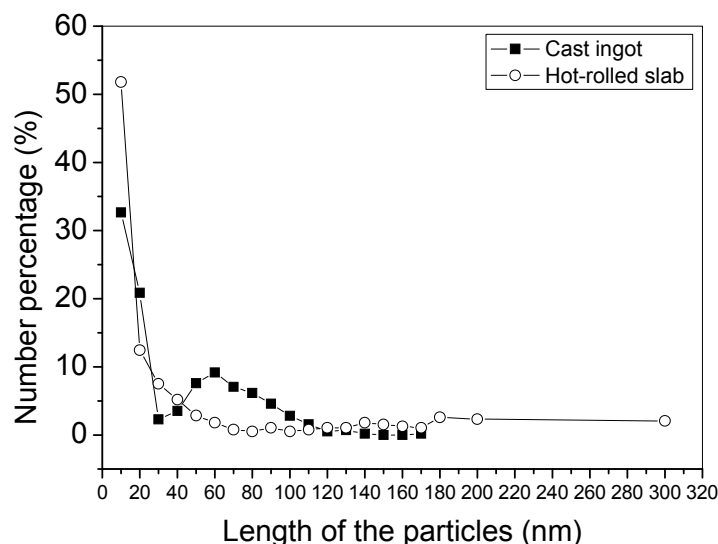


Fig. 5 Size distribution of the precipitates in the cast ingot and in the hot-rolled sheet

4 CONCLUSION

In this paper the precipitates variation of Ti, Nb, Mo carbides in the cast to hot-rolled state has been studied, and the following conclusions can be obtained.

1. Ti(N,C), $Ti_4C_2S_2$, (Ti,Nb)(C,N), MoC, Mo_2C will precipitate in turns in a static cooling procedure according to the Thermo-calc calculations.
2. Most of the precipitates are composed with Ti, Nb and Mo carbides according to the EDX analysis.
3. After hot-rolling, precipitates with diameter (D) larger than 120 nm grew bigger and those between 40 to 120nm solved partially and downsized. The number of the precipitate smaller than 10nm increases obviously after hot-rolling. With the decreasing of precipitation size, the content of Mo increases.

In summary, TMCP process has different influences on different sizes of precipitates. Through precise temperature controlling of TMCP process, the size and distribution of precipitates can be controlled and therefore, different strength level can be achieved.

5 REFERENCES

- [1] Timokhina, I. B. Hodgson, P. D. Ringer, S. P. Zheng R. K. & Pereloma, E. V. (2007) Nano-scale microstructured characterization of modern high strength steels for the automotive industry, In :*Intl. Conference on Microalloyed Steels: Processing, Microstructure, Properties and Performance*, pp. 305-312.
- [2] Raabe, D. Ponge, D, Dimitrieva O. & Sander, B. (2009) Nanoprecipitate-hardened 1.5 GPa steels with Unexpected High Ductility. *Scripta Materilia* 60, 1141-1144.
- [3] Funakawa, Y. Shiozaki, T. Tomita, K. Yamamoto T. & Maeda, E. (2004) Development of high strength hot-rolled sheet steel consisting of ferrite and nanometer-sized carbides, *ISIJ International*, 44, 1945-1951.

MONITORING OF HEAT TREATMENT PROCESSES WITH HIGH ENERGY X-RAYS

**Thomas Rieger¹, Klaus Herrmann¹, Dagmar Carmele², Stephan Meyer², Thomas Lippmann³,
Andreas Stark³, Wolfgang Bleck¹, Uwe Klemradt²**

¹Department of Ferrous Metallurgy, RWTH Aachen University, D-52056 Aachen, Germany

²II. Institute of Physics B, RWTH Aachen University, D-52056 Aachen, Germany

³Institute of Materials Research, Helmholtz-Zentrum Geesthacht (HZG), Max-Planck-Straße 1,
D-21502 Geesthacht, Germany

Abstract

Advanced high strength steels are based on multiphase microstructures on a submicron scale. The decisive production process is the heat treatment to adjust the desired microstructure. Especially TRIP-assisted steel grades depend on the phase composition as strength and ductility are significantly improved by the deformation-induced transformation of retained austenite into martensite (TRIP effect).

Established methods for microstructural characterization are usually applied after completion of the heat treatment process (ex-situ) and comprise typically optical and/or electron microscopy and x-ray analysis with laboratory tubes. Both methods can severely suffer from artifacts such as metastable phase components, e. g. retained austenite, may be affected by the metallographic preparation procedure. Furthermore, the accessible volume or surface area limits the statistical significance of the results.

In the last decade synchrotron facilities have become available to academic and industrial users that offer very hard x-rays with wavelengths in the range of 0.01 nm, equivalent to photon energies of about 100 keV. These new x-ray sources open up new possibilities for the in-situ observation of heat treatment processes owing to the unique combination of extremely high x-ray intensities with large penetration depths (mm scale). Typically, large representative macroscopic volumes (mm³) can be investigated in one exposure, while sophisticated sample environments allow for complex in-situ experiments. The current time resolution is on the scale of a few seconds, with subsecond resolution becoming accessible in the near future.

Only recently a commercial dilatometer of type Bähr Dil805AD has become available for in-situ experiments at the HARWI-II beamline operated by HZG at the Hamburg Synchrotron Laboratory (HASYLAB) at DESY. The experimental setup was used for the in-situ investigation of the Quenching and Partitioning (Q&P) process in TRIP steels. The process involves interrupted quenching to the quench temperature QT between M_s and M_f. It is followed by a partitioning treatment to foster carbon diffusion from martensite to austenite, stabilizing the latter during subsequent cooling to room temperature.

The x-ray experiments are performed in transmission geometry at a wavelength of 0.0124 nm. Debye-Scherrer rings are observed that result from statistical grain distributions characteristic for each microstructure. The time-resolved in-situ measurements of temperature-dependent diffraction rings with high angular resolution allows conclusions about the phases present in the sample, their lattice parameters and crystallographic isotropy as well as the grain size. The resulting transformation kinetics and microstructural evolution will be discussed.

INTRODUCTION

Advanced high strength steels (AHSS). The microstructure features are decisive for the mechanical properties of steel materials. Influencing factors are the phase fractions and the local chemical composition, for example. Possible constituents of multiphase steels are polygonal ferrite, bainitic ferrite, carbides, martensite and retained austenite. The latter plays a distinct role for TRIP-assisted advanced high strength steels (AHSS). During plastic deformation retained austenite may transform to martensite. The martensitic transformation is accompanied by an increase in the volume which causes a plastic deformation in the surrounding ferritic regions. The induced mobile dislocations and the hard martensitic particles lead to a significant local strain hardening. On the macroscopic

scale an elevated uniform elongation is observed at an elevated strength level and accorded to this so-called TRIP effect (transformation induced plasticity).

The development of steel materials is fostered by the automotive industry where the safety exigencies increase constantly. Simultaneously the demand for reduced fuel and exhaust gas emissions, respectively, requires the reduction of the vehicle weight. Both demands are matched by high strength steels exhibiting good ductility. Recent innovations in steel materials resort on the advantageous combination of multiple phases. The first generation of AHSS extended the range of mechanical properties to very high strength levels at relatively low elongation values in martensitic steels to reduced strength levels favoring higher elongation values (TRIP steels), ferritic-martensitic dual phase (DP) steels and complex phase (CP) steels. The second generation used the stabilization of austenite by manganese alloying resulting in very high strength and elongation values. Current research activities aim to establish the third generation of AHSS providing medium strength and ductility levels reduced production costs and the uncomplicated integration in existing process chains, Figure 1. In this context the so-called 'Quenching and Partitioning' process was proposed in 2003. [1-5]

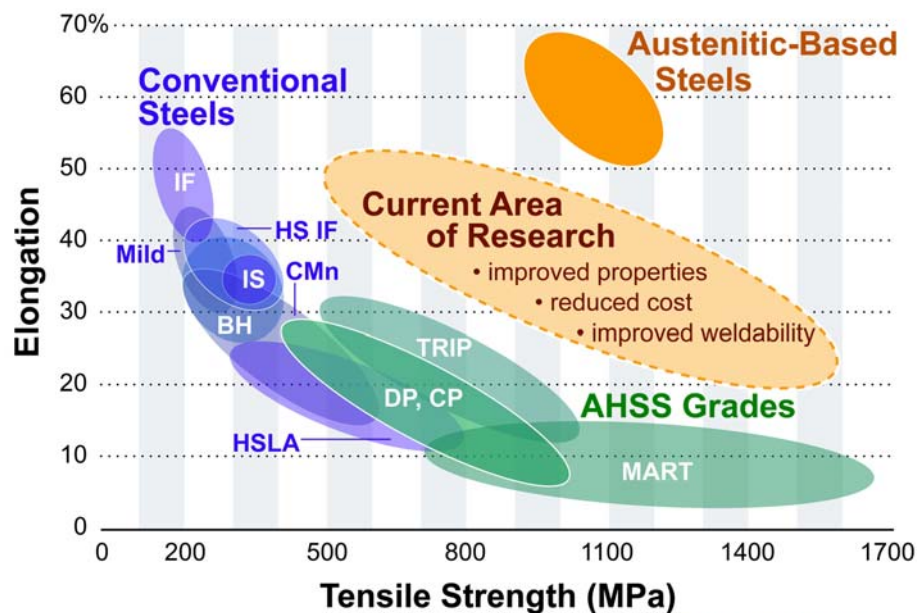


Figure 1: Property range of established and emerging steel grades (www.worldautosteel, 25.03.2011).

The 'Quenching and Partitioning' (Q&P) concept. The 'Quenching and Partitioning' (Q&P) concept defines a heat treatment procedure designed to stabilize retained austenite in a matrix of carbon depleted martensite, Figure 2. The latter is a substitute for the polygonal and the bainitic ferrite in conventional TRIP-assisted steels. The martensitic matrix is expected to increase the global strength level while retained austenite assures a satisfying ductility due to the TRIP effect. The heat treatment process involves partial or complete austenization which is followed by an interrupted quenching to QT. QT signifies the quench temperature which is between martensite start temperature M_s and martensite finish temperature M_f . After this first quenching an isothermal holding period follows at QT (1 Step Q&P) or at an elevated partitioning temperature PT (2 Step Q&P). Meanwhile carbon diffuses from supersaturated martensite to austenite reducing its M_f temperature below room temperature. Consequently austenite remains stable during the concluding quenching to room temperature.

The heat treatment concept is accompanied by an adequate alloying concept typical for TRIP-assisted steel grades. Crucial are additions of aluminium or silicon because both elements are known to retard the formation of carbides. Carbides are undesired because their precipitation might occur during isothermal holding (partitioning) and hence consume carbon intended to chemically stabilize the retained austenite. Furthermore the global carbon content is limited especially for automotive sheet steel not to deteriorate the weldability. Manganese acts as solid solution strengthener and reduces the critical cooling rate. [2,5-10]

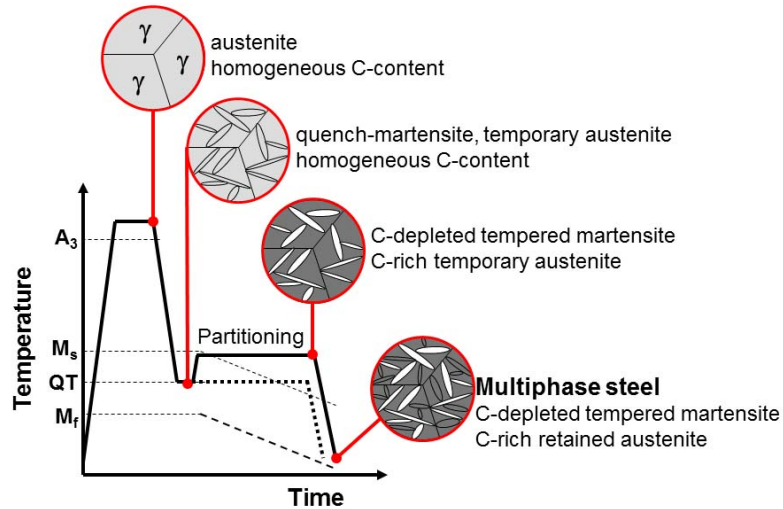


Figure 2: Schematic microstructure evolution during "Quenching and Partitioning".

Investigation of AHSS microstructures by traditional methods. The final microstructure of a steel grade is controlled by its chemical composition and by a sophisticated heat treatment process. Hence the alloying concept, the appropriate heat treatment, the final microstructure and the resulting mechanical properties are closely linked. Therefore a range of characterization methods is established in scientific and industrial practice comprising optical and electron microscopy, dilatometry, diffraction methods and magnetic measurements.

Usually microscopy and diffraction with laboratory X-ray tubes demand a prior metallographic preparation. Specimens are cut after completion of the heat treatment and embedded in polymers for grinding, polishing with abrasives (silicon carbide paper followed by diamond particles in aqueous suspensions) and finishing by electrolytic polish. For optical microscopy and SEM investigations the contrast of the microstructure constituents is developed by selective etching or phase sensitive deposition of chemical reactants on the specimen surface (color etching). Dilatometric methods use the change in length as an indication for phase transformations: the deviation from a linear relation between elongation and temperature is accorded to the occurrence of another phase. Diffraction methods like electron backscatter diffraction (EBSD) and X-ray diffraction with laboratory tubes clearly distinguish the present phases by their crystallographic features. In AHSS austenitic parts (face centered cubic, fcc) are reliably separated from body centered cubic (bcc) microstructure constituents. It is noted that the latter may contain bainitic ferrite with high crystallographic imperfection and tetragonally distorted martensite. For TEM (transmission electron microscopy) thin foils on the submicron scale are prepared in intense and delicate preparation procedures. The phase contrast is based on the crystallographic structure while the different energy absorption of elements allows the distinction of chemical elements. Magnetic methods distinguish the non-magnetic austenitic volume fractions from the remaining magnetic constituents, i. e. polygonal and ferritic ferrite and martensite. [11-14]

Still the established methods suffer from severe disadvantages. Phases with similar chemical potential (like bainite, martensite and retained austenite) are hard to distinguish by color etchants for optical microscopy or for SEM. Also both methods are limited in their resolution and the phases are often identified based on the experience of the investigator instead of objective and precise criteria. The phase fractions are often estimated. Except the magnetic measurements, all mentioned methods investigate the surface or surface near region of the specimens which remains relatively small. Furthermore the preceding sample preparation may affect especially the metastable microstructure constituents like retained austenite. Only the magnetic measurements are applicable to bulk specimens without prior preparation. Still none of the methods is used at elevated temperatures, in particular not in-situ during heat treatment cycles including fast cooling.

The promising Q&P heat treatment results in martensitic/austenitic microstructures on a submicron scale. Therefore classic etching techniques are not directly applicable and more sophisticated techniques (SEM, TEM, EBSD) have to be applied. Still only the final phase composition at room temperature is accessible to the investigation, direct evidence on the microstructure evolution during the processing is lacking so far. [14, 15]

Motivation. In the present work the in-situ characterization of heat treatment processes by diffraction experiments with high-energy synchrotron radiation is discussed. The advantages of the approach are presented based on exemplary investigations of the Q&P process.

METHODIC APPROACH

Firstly the interest of using high energy synchrotron radiation (100 keV) for diffraction experiments is illustrated by the comparison to diffraction experiments with Co-K α (6.9 keV) radiation produced in a laboratory tube. Secondly the methodology is applied to monitor the evolution of the austenite phase fraction during Q&P.

Investigated steel grades. Two diffractograms of the standardized automotive TRIP-steel HCT690T [16] were obtained from diffraction of Co-K α and of synchrotron radiation (100 keV) and compared to each other. For the in-situ experiments with synchrotron radiation the Si/Ni alloyed TRIP steel QPSN was investigated. While the contents of carbon, silicon and manganese correspond to industrialized TRIP-assisted steels, the alloy QPSN was alloyed with nickel to further decrease the critical cooling rate. The chemical compositions of the investigated steels are given in Table 1.

Table 1: Chemical composition of the investigated steels [mass-%].

Alloy	C	Si	Mn	P	S	Al	N	Ni
HCT690T	0.248	0.036	1.623	<0.120	<0.015	1.246	n.a.	0.01
QPSN	0.200	1.910	1.640	<0.002	<0.01 0	n.a.	0.002	3.10

The alloy QPSN was melted in a laboratory vacuum furnace and cast to ingots of 140 mm x 140 mm x ca. 500 mm. To destroy the as-cast microstructure the ingots were cut in two pieces of around 250 mm, reheated to 1 200 °C and deformed to a cross section of 70 mm x 70 mm. After normalization (austenizing at 970 °C for 60 min., air cooling), specimens of 7 mm x 4 mm x 1.3 mm were machined from bulk material in a distance of 6.5 mm to the surface.

Experimental setup for laboratory diffraction experiments. For the laboratory diffraction experiments the specimens were moulded in cold hardening resin and metallographically prepared. The preparation procedure consisted of grinding (SiC abrasives), polishing with diamond particles (6 μ m / 3 μ m) in aqueous dispersion and finishing in an electrolytical polishing machine. The diffraction experiments were effectuated in a diffractometer in reflection geometry using Co-K α radiation (6.9 keV) with a collimator (0.3 mm) and an integration time of 2000 s for the entire experiment.

Experimental setup for synchrotron experiments. The diffraction experiments were effectuated in transmission geometry at the High Energy Materials Science beamline HARWI-II operated as an outpost of HZG at DESY (Deutsches Elektronensynchrotron), Hamburg. The beamline was tuned to a photon energy of 100 keV which corresponds to a wavelength of 0.124 Å. Debye-Scherrer rings were recorded during the exposure time of 1 s with a flat panel detector of type MAR555. Powder diffractograms were obtained by azimuthal integration and evaluated by a Rietveld refinement using the commercial software TOPAS in the academic version 4.0. From the refined pattern the phase fraction of austenite and the austenite lattice parameter were extracted to monitor the phase transformation and the carbon content which is related to the austenite lattice parameter. The heat treatment was effectuated in a state-of-the-art dilatometer (Baehr Thermoanalyse 805AD) which was modified for the demands of the Synchrotron diffractometer. Inductive heating with 25 K/s and Ar gas cooling with a controlled $t_{8/5}$ -time of 17 s were applied. Results are presented for 2 Step Q&P of the alloy QPSN with a quench temperature QT=280 °C and a partitioning time of 70 s at the partitioning temperature PT=450 °C.

RESULTS AND DISCUSSION

Penetration depth. An advantage of the common X-ray tube based characterization methods for AHSS is the penetration depth on the micron scale. For comparison electron backscatter diffraction only investigates few nanometers underneath the surface. In Figure 3 (a) the penetration depth of X-ray radiation in iron is shown as a function of the photon energy. The dip at 7.2 keV is caused by the K absorption edge of iron. Laboratory X-ray tubes use the characteristic radiation which is emitted by the target material. The photon energy is on the order of magnitude of several keV, typical anode materials for the investigation of steel are copper, cobalt or molybdenum with photon energies (K_{α} -lines) of 8.0 keV, 6.9 keV and 17.4 keV, respectively. Hence the penetration depth remains on the micron scale for the mentioned radiation energies. [17]

In contrast to laboratory X-ray tubes the photon energy at synchrotron radiation sources is arbitrary and reaches photon energy levels up to some 100 keV. For energies above 60 keV the penetration depth is on the millimeter scale. Consequently macroscopic volumes of sheet steel can be transmitted. [18]

Photon flux. The photon flux at synchrotron sources is extensive. In Figure 3 (b) it is shown as function of the photon energy exemplary at the beamline HARWI-II. There the photon energy is adjustable between 60 keV and 240 keV. Compared to the photon flux of laboratory tubes it is obvious that the displayed flux of the synchrotron source is several orders of magnitude higher in the entire energy range. As a result the exposure time may be reduced to seconds compared to minutes / hours necessary with X-ray tubes. Improvements of high energy detector technology are expected to allow a time resolution on the subsecond scale in the near future.

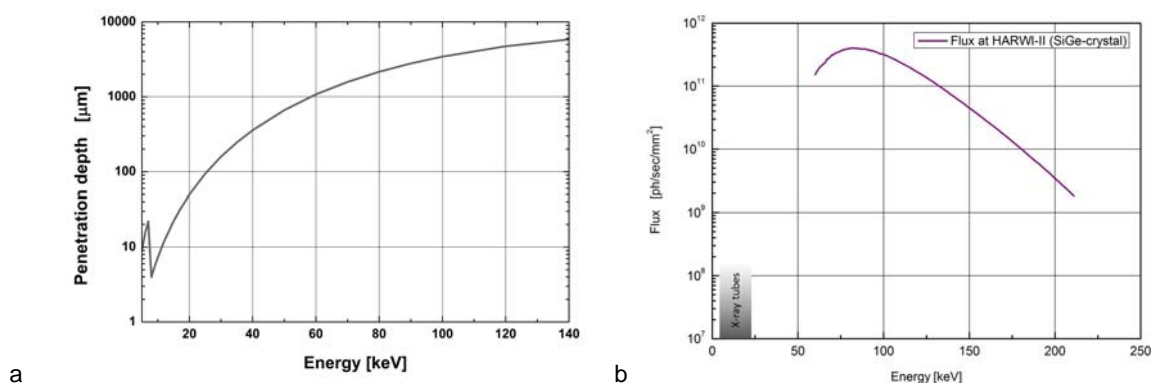


Figure 3: Penetration depth as function of the photon energy (a) and photon flux of beamline HARWI-II (HZG outpost at DESY, Hamburg) compared to the characteristic lines of laboratory X-ray tubes (b).

Resolution. The photon energy of 100 keV used at the HARWI-II beamline results in a wavelength of 0.124 Å. Consequently a larger part of the reciprocal space is experimentally accessible; i. e. the resolution of higher indexed lattice planes is possible. [18]

In Figure 4 two diffractograms of the automotive TRIP-steel HCT690T are displayed which were obtained by diffraction experiments with synchrotron radiation at 100 keV and by Co- K_{α} radiation (6.9 keV). Though the angular range is much smaller for the high energy radiation the larger number of detected peaks is obvious. Additionally, the peaks are more distinct, for example peak $\{220\}_{fcc}$ is clearly separated by the synchrotron radiation but hardly distinguishable from the background in the Co experiment. Hence a better quantitative analysis of the diffraction pattern can be expected from the synchrotron experiment.

Investigation of Q&P processing. The microstructure evolution was in-situ investigated during 2 Step Q&P processing of the alloy QPSN. Figure 5 shows the time-temperature cycle with markers for the moments of diffraction experiments. The time between two exposures was limited by the detector thus the experiment was once repeated (open marker symbols) to comprehensively monitor the sensitive steps of the heat treatment. The measured time-temperature cycles of both experiments coincide.

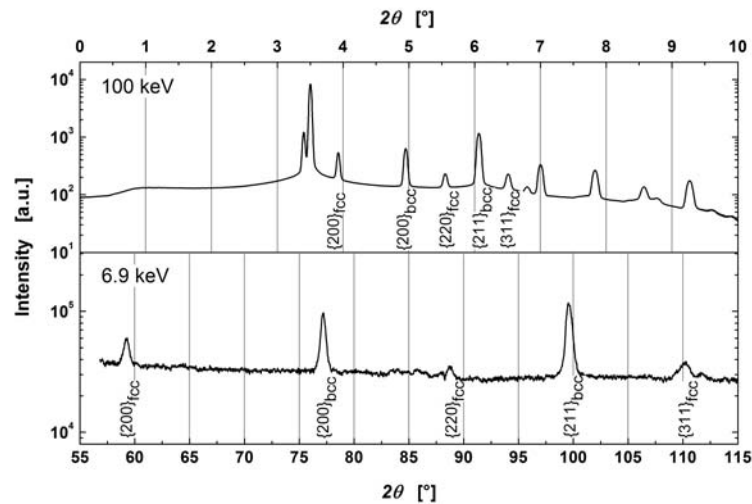


Figure 4: Diffractograms of TRIP steel HCT690T obtained by diffraction experiments with synchrotron (100 keV) and Co- K_{α} (6.9 keV) radiation.

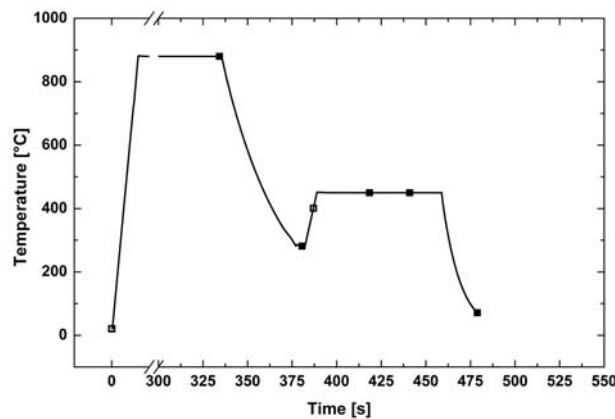


Figure 5: Measured time-temperature cycle of 2 Step Q&P (steel QPSN) with markers for diffraction experiments.

Qualitative evaluation of experimental results. In Figure 6 a/b, exemplary 2D diffraction patterns are shown which were recorded at the austenizing temperature AT and at room temperature RT after Q&P processing. For the quantitative analysis, the diffraction patterns were azimuthally integrated resulting in powder diffractograms, Figure 6 c. The displayed data allow a qualitative evaluation of the experiments. First the intensities clearly show the pattern of Debye-Scherrer rings though the rings are not completely occupied at AT. This is not surprising as individual grains may coarsen during the holding time at the elevated temperature of 950 °C. As a result locally high intensities appear. This information on the texture may be used to qualify the austenizing especially for cold rolled steel strip which is heat treated to properly adjust the desired microstructure. For homogeneous properties the rolling texture should be significantly reduced which can be validated by the occupation of the Debye-Scherrer rings. In the course of the heat treatment the change of the peak positions and intensities is obvious for both the Debye-Scherrer rings and the integral diffractograms. The decisive steps of the microstructure evolution are hence visible at a glance and a starting point for further investigation can easily be identified.

Quantitative evaluation of experimental results. Quantitative results obtained by Rietveld refinement are displayed in Figure 7. The austenite fraction decreases during continuous cooling from AT to QT and during cooling from PT to RT due to phase transformations. Additionally an isothermal phase transformation is observed at PT. The reheating from QT to PT has a negligible effect on the austenite fraction compared to the isothermal

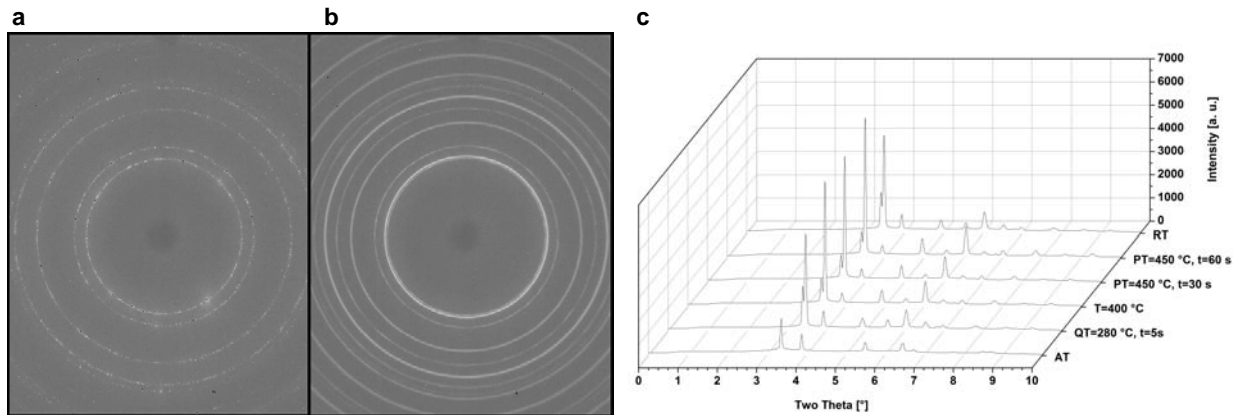


Figure 6: Recorded diffraction patterns at austenizing temperature AT (a) and after Q&P processing at room temperature (b); diffractograms at various process steps obtained by azimuthal integration (c)

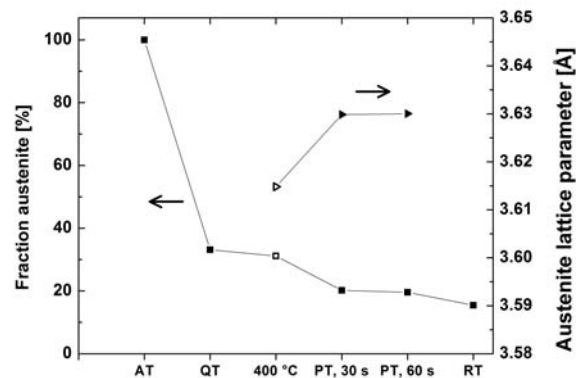


Figure 7: Austenite fraction and lattice parameter during Q&P processing (AT=950 °C/300 s, QT=280 °C/5 s, PT=450 °C/70 s). Open data points indicate a measurement in a repeated experiment.

decrease in the first 30 s at PT. Between 30 s and 60 s at PT only a marginal change in the austenite fraction is measured. At room temperature more than 15 % retained austenite are stabilized. The austenite lattice parameter depends on the temperature. This is illustrated by the severe jump from ca. 3.615 Å at 400 °C to around 3.630 Å at 450 °C. Furthermore is an indicator for the austenite carbon content: the larger the lattice parameter, the higher the carbon content. The two measured values of the austenite lattice parameter at the partitioning temperature do not change significantly. This suggests that no (further) carbon enrichment of austenite occurs after 30 s for the given Q&P conditions.

CONCLUSIONS

In summary the use of synchrotron X-ray radiation provides an ideal instrument for the investigation of the microstructure evolution during sophisticated heat treatment processes like “Quenching and Partitioning”:

- The reliable and quantitative distinction of fcc phase constituents is given.
- The accessible photon energy of more than 60 keV results in a penetration depth on the mm scale and allows the investigation of a representative specimen volume.
- The transmission of sheet steel is possible for thicknesses corresponding to commercialized steel grades (millimeter scale). The prior specimen preparation and hence, eventual preparation artifacts are avoided.
- By the combination of a short wavelength and an experimental setup in transmission geometry with flat panel detector a larger volume of the reciprocal space is covered in one experiment. As a result more (higher indexed) peaks are detected and accessible for analysis.

- Due to the high photon flux the exposure time is reduced to few seconds allowing for the in-situ monitoring of the microstructure development during heat treatment processes. A subsecond time resolution is within reach for the next detector generation.

The methodology was successfully applied for the investigation of a Si-/Ni-alloyed TRIP steel. An austenite transformation during continuous cooling and during isothermal partitioning was observed and quantified. The nearly constant austenite lattice parameter indicates that no further carbon enrichment took place after 30 s at PT for the investigated Q&P conditions.

In the next steps the results will be compared to further Q&P conditions at a higher time resolution. The experiments will be extended to the mechanical properties of the resulting microstructures.

Acknowledgments. The authors gratefully acknowledge funding by Exploratory Research Space (ERS) at RWTH Aachen University (OPPa110) and especially the support in TOPAS Academic by Dr. Lars Peters.

References

- [1] International Iron & Steel Institute - Committee on Automotive Applications, Advanced High Strength Steel (AHSS) Application Guidelines, version 4.1, www.worldautosteel.org, (06/2009), last accessed 25.03.2011.
- [2] D.V. Edmonds, D.K. Matlock, J. Speer, in: Proc. Int. Conf. Advanced Steels 2010, edited by Y.Weng, H.Dong, Y.Gan, Metallurgical Industry Press, Beijing (2010), pp. 229.
- [3] H. Hofmann, D. Mattissen, T. W. Schaumann: *Mat.-wiss. u. Werkstofftech.* 37, No. 9 (2006), p. 716.
- [4] D.K. Matlock, J. Speer in: *Microstructure and Texture in Steels and Other Materials*, edited by A. Haldar, S. Suwas, D. Bhattacharjee, Springer, London (2009), pp. 185.
- [5] J. Speer, D.K. Matlock, B.C. DeCooman, J.G. Schroth, *Acta Mat.*, Vol. 51 (2003), pp. 2611.
- [6] D.V. Edmonds, K. He, F.C. Rizzo, B.C. De Cooman, D.K. Matlock, J. Speer: *Mat. Sc. Eng. A*, Volumes 438-440 (2006), pp. 25.
- [7] D.V. Edmonds, K. He, M.K. Miller, F.C. Rizzo, A. Clarke, D.K. Matlock, J. Speer: *Microstructural features of 'Quenching and Partitioning': a new martensitic steel heat treatment*, *Mat. Sc. Forum*, Vols. 539-543 (2007) pp. 4819.
- [8] P. Jacques, E. Girault, T. Catlin, N. Geerlofs, T. Kop, T., S. van der Zwaag, F. Delannay: *Mat. Sc. Eng. A*, Volumes 273-275 (1999), pp. 475.
- [9] J. Speer, D.K. Matlock: *J. Jpn. Soc. Heat Treatment*, Vol. 49 (2009, Vol. 2), pp. 415, Special Issue on the 17th IFHTSE Congress, October 27-30, 2008, Kobe, Japan.
- [10] C.Y. Wang, J. Shi, W.Q. Cao, H. Dong: *Mat. Sc. Eng. A*, Vol. 527 (2010), pp. 3442.
- [11] J. Angeli, E. Fuehrer, M. Panholzer, A.C. Kneissl: *Prakt. Metallogr.*, Vol. 43, No.10 (2006), pp. 489.
- [12] E. Fuehrer, C. Voit, J. Pühringer, M. Pohl: *Prakt. Metallogr.*, Vol. 47, No.7 (2010), pp. 375.
- [13] S. Melzer, J. Moermann, in: *Microstructure and Texture in Steels and Other Materials*, edited by A. Haldar, S. Suwas, D. Bhattacharjee, Springer, London (2009), pp. 267.
- [14] L. Zhao, N.H. van Dick, E. Brueck, J. Sietsma, S. van der Zwaag: *Mat. Sc. Eng. A*, Vol. 313 (2001), p. 145.
- [15] M.J. Santofimia, L. Zhao, R. Petrov, J. Sietsma: *Mat. Char.*, Vol. 59, Issue 12 (2008), pp. 1758.
- [16] prEN 10338:2010 Hot rolled and cold rolled non-coated products of multiphase steels for cold forming - Technical delivery conditions.
- [17] J.A. Bearden: *Review of Modern Physics*, Vol. 39 (1967), p. 78.
- [18] K.-D. Liss, A. Bartels, A. Schreyer, H. Clemens: *Textures and Microstructures*, Vol. 35, No. 3/4 (2003), pp. 219.

APPLICATION OF LASER ABLATION ICP MASS SPECTROMETRY FOR RAPID ANALYSIS OF OXIDE PARTICLES IN METAL SAMPLES

Andrey V. KARASEV¹, Ryo INOUE² and Pär G. Jönsson¹

¹ Department of Materials Science and Engineering, Royal Institute of Technology, 100 44 Stockholm, Sweden.

² Institute of Multidisciplinary Research for Advanced Materials, Tohoku University, Sendai, 980-8577, Japan.

Abstract

Online analyses of inclusion characteristics (such as size, number and composition) in steel samples during steelmaking are very helpful for improvement of final steel quality. Therefore, the development of rapid analytical methods, which can give the accurate and complete information on inclusion characteristics in metal samples, is very important to enable online correction of operation parameters during ladle treatment of steel.

It is known that a Laser Ablation-Inductively Coupled Plasma Mass Spectrometry (LA-ICP-MS) is one of the potential methods for rapid evaluation of inclusions. In this study, the LA-ICP-MS was applied for the analysis of oxide inclusion particles on a surface of glass holders and in Fe-10%Ni samples deoxidized with Mg and/or Al. The analytical methods for determination of composition, number and size of inclusion particles by the LA-ICP-MS were examined. The obtained results were compared with those from three-dimensional (3D) SEM investigations of particles collected on film filters after electrolytic extraction of metal samples (EE method). It was found that the differences between the average contents for Al₂O₃, MgO and CaO in complex particles obtained from LA-ICP-MS, EPMA and chemical analysis were less than 2%. The deviation of the particle size estimated from LA-ICP-MS by using the size calibration lines for Al₂O₃ and MgO from that determined from SEM investigation was found to be smaller than 10% for most of the Al₂O₃ and MgO particles and not greater than 20% for most of the complex CaO-Al₂O₃-MgO and CaO-Al₂O₃ particles. For the metal samples with a total content of Mg ≤ 0.025% and of Al ≤ 0.09%, the particle size distributions obtained by LA-ICP-MS method were in good agreement with those from the EE method in the range of $d_v \geq 1 \mu\text{m}$. Therefore, it was concluded that the LA-ICP-MS technique could be successfully applied for a rapid analysis of oxide inclusion particles in metal samples.

KEY WORDS: LA-ICP-MS, steel, non-metallic inclusions, inclusion composition, particle size distribution.

1. Introduction

It is well known today that the negative or positive effect of inclusions on the final properties of steel products depends on the inclusion characteristics such as size, number and composition. Therefore, online analysis of inclusion characteristics in metal samples during steelmaking is very helpful for the improvements of the final quality of steel. Thus, the development of rapid analytical methods, which can give accurate and complete information on inclusion characteristics in metal samples obtained from liquid steel, is very important to enable the online correction of operational parameters during ladle treatment of steel. A Laser Ablation-Inductively Coupled Plasma Mass Spectrometry (LA-ICP-MS) is one of the potential methods for rapid evaluation of inclusions. In recent years the LA-ICP-MS was applied for direct analysis of steels and alloys such as for determination of the total bulk composition¹⁻⁴⁾, content of soluble and insoluble elements^{3,4)}, spatial and surface distribution of elements in steels and alloys^{4,5)} and for mapping and analysis of inclusions⁶⁻¹⁰⁾. However, some points of application and limitation of the LA-ICP-MS technique are not clear for investigation of inclusions in steels and alloys up to now.

In this study, the LA-ICP-MS was applied for the analysis of non-metallic oxide inclusion particles (such as Al₂O₃ and MgO) on a surface of glass holders and on a cross section of metal samples of Fe-10%Ni alloy deoxidized with Mg and/or Al. The analytical methods for the determination of composition, size and number of inclusion particles by the LA-ICP-MS were examined by using the respective calibration lines obtained originally. The results from the LA-ICP-MS analysis were compared with those obtained from three-dimensional (3D) SEM investigations of particles, which were collected on film filters after electrolytic extraction of metal samples (EE

method). The analytical error by the determination of composition, size and number were estimated for LA-ICP-MS technique. Moreover, the content of soluble elements in steel were considered and discussed as a limitation factor for analysis of particles by the LA-ICP-MS.

2. Experimental

2.1. Instrumentation and LA-ICP-MS measurements.

The inclusion characteristics (such as composition, size and number) were analyzed on polished cross sections of metal samples by using the Hewlett-Packard HP-4500 inductively coupled plasma mass spectrometer (ICP-MS) equipped with a laser ablation system (CETAC LSX-100). A schematic illustration of the LA-ICP-MS is shown in **Figure 1**. For the investigation of inclusions, a metal sample is placed and sealed in an ablation chamber. The Nd:YAG laser beam is focused onto the surface of the metal sample via the objective lens. The metal surface is irradiated and melted by a laser beam. A fine sample aerosol formed by the laser beam is supplied by the stream of Ar carrier gas (1.4 L/min) from the ablation chamber to the ICP torch and ionized in an Ar plasma. The number of ions with different mass is determined by a Quadrupole mass spectrometer. The sample surface during laser ablation process is viewed directly on a computer monitor by using a color CCD camera at the magnification from 20 to 200.

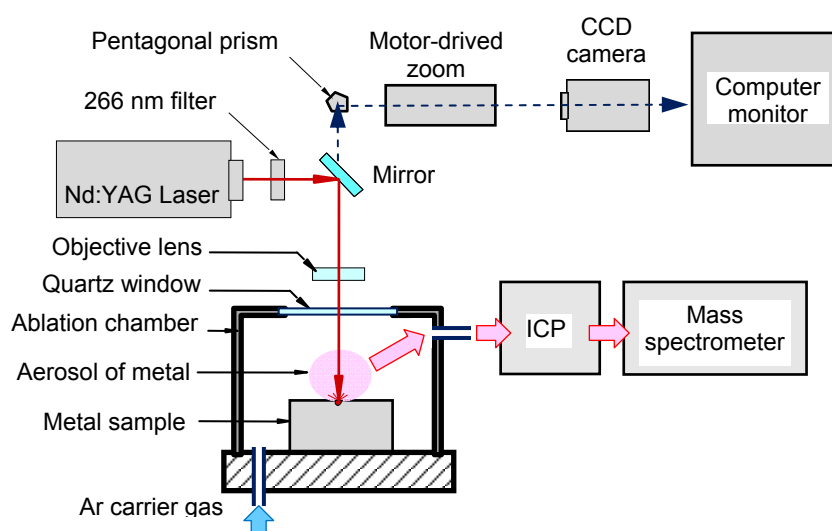


Figure 1. Schematic illustration of LA-ICP-MS system.

In this study, all samples are analyzed by using line ablation pattern. The main instrumental conditions and ablation parameters are given in **Table 1**. During ablation, the laser beam is fixed and the sample is moved horizontally along with chamber at a constant rate. In this case, the laser scan rate of metal sample is 0.01 mm/s.

Table 1. Main instrumental conditions and ablation parameters by LA-ICP-MS measurements.

Parameters of LA-ICP-MS	Values
RF power (W)	1100
Type of laser	Nd:YAG (Q-swth)
Wavelength (nm)	266 (UV light)
Laser scan rate (mm/s)	0.01
Laser energy (mJ/shot)	2.0-4.0
Frequency of the laser shots (Hz)	20
Defocus of laser beam (mm)	0
Integration time (s)	0.01-0.10

By using the integration time of 0.01 and 0.1 s, the ion intensity of one isotope is determined for every 0.1 and 1.0 μm of laser track, respectively. The parameters for laser irradiation and scan rate of metal samples were selected so as every time during ablation to keep a stable melting zone on metal surface. The experimental and standard samples were analyzed by LA-ICP-MS at the same operating parameters. The correction of concentration calibration lines was carried out by the analysis of standard samples after every one-two hours. A detailed description of analytical procedures and selection parameters are given in separate articles.^{3,6)}

2.2. Sample preparation and SEM analysis of inclusion characteristics.

The glass samples (GS-0 to GS-5, matrix glass composition is 13%NiO-72%B₂O₃-15%Li₂O) with different contents of elements (**Table 2**) were prepared. Percent represents mass%, here and hereinafter. Homogeneity of major elements and absence of inclusions in these samples were examined by LA-ICP-MS.³⁾ These samples were used as the standards for determination of concentration calibration lines (CCL), which are used for the quantitatively composition analysis of ablated oxide particles.

Table 2. Chemical composition of standard and experimental samples (in mass%).

Sample	Mg _{total}	Mg _{sol}	Mg _{insol}	Al _{total}	Al _{sol}	Al _{insol}
GS-0	<0.001	-	-	0.003	-	-
GS-1	0.035	-	-	0.042	-	-
GS-2	0.069	-	-	0.086	-	-
GS-3	0.132	-	-	0.162	-	-
GS-4	0.289	-	-	0.354	-	-
GS-5	0.456	-	-	0.532	-	-
Exp.1	0.0104	0.0002	0.0102	0.0833	0.0732	0.0101
Exp.2	0.0122	<0.0001	0.0122	0.0579	0.0513	0.0066
Exp.3	0.0085	0.0001	0.0084	0.0885	0.0772	0.0113

The standard powders of pure Al₂O₃ (Al₂O₃ \geq 99%, Japanese Industrial Standards Z 8901 No. 3, 4 and 5 which correspond to the size of 7 \pm 2, 13 \pm 3 and 27 \pm 6 μm , respectively) and particles of pure MgO (MgO \geq 99%, the size range of 10 to 40 μm) were used for getting a size calibration line (SCL). Furthermore, synthetic particles such as 12CaO·7Al₂O₃ (12C7A), MgO·Al₂O₃ (MA) and CaO·MgO·Al₂O₃ (CAM) were used for the examination of obtained CCL and SCL lines. The synthetic 12C7A and MA particles were obtained by sintering a pressed mixture of appropriate amount of CaCO₃ or MgO and Al₂O₃ powders at 1300°C for 72 hours in a Pt crucible followed by crushing and sieving. CAM particles (35%CaO-57%Al₂O₃-8%MgO) were obtained by melting a mixture of CaCO₃, Al₂O₃ and MgO powders at 1580°C for 10 minutes by using a MgO crucible. The particles in the size range from 7 to 40 μm were fixed on a surface of glass (60%SiO₂-21%B₂O₃-19%Li₂O) holders.³⁾

The LA-ICP-MS was applied for rapid quantitative analysis of inclusions characteristics in Fe-10% Ni alloy deoxidized with Mg and Al (Exps.1 to 3 in Table 2). The preparation of these metal samples is described in details elsewhere.⁷⁾ The contents of soluble and insoluble Mg and Al in the metal samples were determined after the dissolution of metal samples (0.3-0.5g) by using a potentiostatic electrolytic extraction method with a 10%AA electrolyte. For the analysis of inclusions in these metal samples, 0.2-0.3 g of each metal sample was dissolved by electrolytic extraction with 10% AA. The inclusions on a membrane polycarbonate film filter (an open pore size of 0.1 μm) after filtration were investigated by using the scanning electron microscope (SEM) with the electron probe microanalysis (EPMA).

3. Results and Discussion

3.1. Particle composition

The glass samples (GS-0 to 5) were used as the standards for the quantitative analysis of the particle composition. More details are given elsewhere.³⁾ It was found that the mean ion intensity of each isotope (\bar{I}_M) increases linearly with an increased total content of element *M* in an ablated zone of the sample. Therefore, the

concentration calibration line for M element, which was obtained by ablation of the GS samples, can be expressed by

$$\bar{I}_{M(GS)} = a_{M(GS)} + b_{M(GS)} \cdot [\%M]_{(GS)} \quad (1)$$

where $\bar{I}_{M(GS)}$ and $[\%M]_{(GS)}$ are the mean ion intensity of isotope and the total content of M element in the GS sample, respectively. $a_{M(GS)}$ and $b_{M(GS)}$ are the constants of the concentration calibration line for M element.

The representative CAM particle on the surface of the glass holder and the respective ion intensity chart for ^{24}Mg , ^{27}Al and ^{43}Ca isotopes during laser ablation are shown in **Figure 2**. The area of the ion intensity peak for M element, A_M^P , is proportional to the amount of this element in an ablated particle and can be calculated as follows:

$$A_M^P = \sum_{i=1}^n I_{M,i}^P - I_M^{blank} \cdot n \quad (2)$$

where $I_{M,i}^P$ is the ion intensity of the i -th segment in a peak for a M isotope, n is the total number of the ion intensity segments in a peak and I_M^{blank} is the average ion intensity of M element in the matrix.

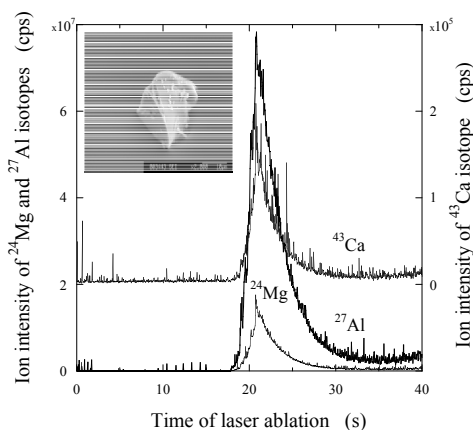


Figure 2. Typical CAM particle on surface of glass holder and the ion intensity chart of ^{24}Mg , ^{27}Al and ^{43}Ca isotopes during LA-ICP-MS analysis of this particle.

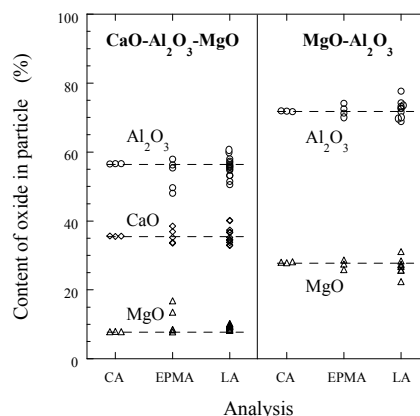


Figure 3. Contents of Al_2O_3 , MgO and CaO in synthetic CAM and MA particles obtained by chemical analysis (CA), EPMA and LA-ICP-MS (LA).

The total content of M element in a homogeneous or heterogeneous complex particle, $[\%M]^P$, is proportional to the area of ion intensity peak and can be evaluated from Eq.(1) and Eq.(2) as follows:

$$[\%M]^P = \frac{A_M^P}{b_{M(GS)}} \quad (3)$$

The final content of M_xO_y oxide was calculated from $[\%M]^P$ value by normalizing the contents of all oxides to 100%. A detailed description for determination of particle composition by LA-ICP-MS analysis was given elsewhere.^{3,10)}

Figure 3 shows the contents of Al_2O_3 , MgO and CaO in CAM and MA particles determined by chemical analysis (CA), EPMA and LA-ICP-MS (LA). It can be seen that the results measured by LA-ICP-MS agree reasonably well with those by the chemical analysis and EPMA. In this case, the relative differences between the average contents for Al_2O_3 , MgO and CaO obtained from LA-ICP-MS, EPMA and chemical analysis are less than 2%. A deviation of some points from LA-ICP-MS and EPMA may be explained by the slight heterogeneity of composition among the measured synthetic particles.

3.2. Particle size

The size of an ablated oxide particle can be determined by using the respective size calibration line (SCL) and A_M^P values for all M elements in this particle. A detailed description of the calculation of the intensity peak area is described elsewhere.^{3,10)}

Figure 4 shows the relationships between the area of the ion intensity peak, A_M^P , and mass of Al_2O_3 and MgO in ablated particles, m_{MxOy}^P . The value of m_{MxOy}^P for each particle was determined by using the value of equivalent diameter, $d_{V(MxOy)}$, measured by SEM and the content of M_xO_y in ablated particle obtained by LA-ICP-MS.^{6,10)} It can be seen that the A_M^P value is direct proportional to the amount of m_{MxOy}^P in an ablated oxide particle and can be expressed as follows by assuming a spherical particles:

$$A_M^P = k_{MxOy} \cdot m_{MxOy}^P = (k_{MxOy} \cdot \rho_{MxOy} \cdot \frac{\pi}{6}) \cdot d_{V(MxOy)}^3 \tag{4}$$

where k_{MxOy} is the constant estimated from the slope of SCL line for M_xO_y in Figure 4 and ρ_{MxOy} is the density of M_xO_y particle.

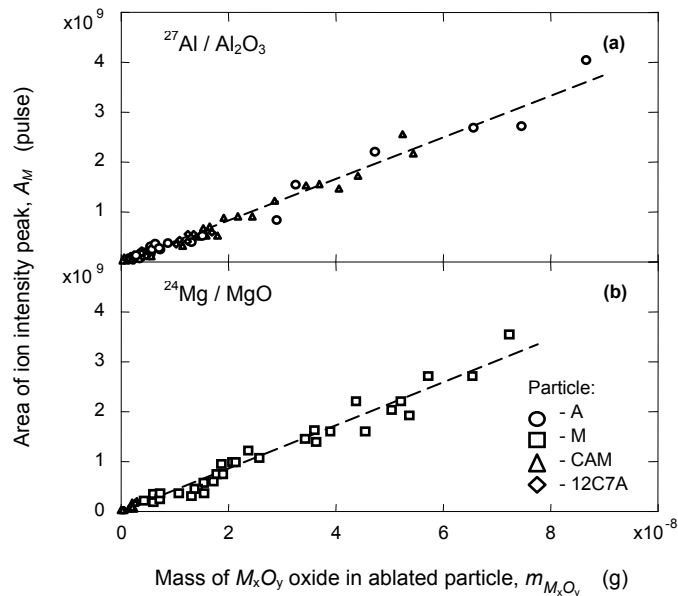


Figure 4. Relationship between the mass of M_xO_y oxide in ablated particle and the area of ion intensity peak on time chart.

The following relationships for Al_2O_3 and MgO particles were obtained from the experimental results:¹⁰⁾

$$A_{Al}^P = 66620 \cdot (d_{V(Al_2O_3)})^{3.04} \quad r = 0.985 \tag{5}$$

$$A_{Mg}^P = 67040 \cdot (d_{V(MgO)})^{3.04} \quad r = 0.972 \tag{6}$$

It is apparent that the experimental relationships expressed by Eqs.(5) and (6) are similar to Eq.(4). The correlation coefficients, r , for these relations are satisfactorily high. Therefore, these relationships for ^{27}Al and ^{24}Mg isotopes were used in present study as the calibration lines for the size determination of oxide particles containing Al_2O_3 and MgO . It should be pointed out that these size calibration lines for Al_2O_3 and MgO oxides can be used for the estimation of size for complex inclusions such as $CaO-Al_2O_3-MgO$, $12CaO \cdot 7Al_2O_3$ and other oxides.^{6,10)}

The deviations of some data points from the size calibration lines in Figure 4 may be explained by the error arising from the size estimation for irregular particles as the equivalent-area diameter of the spherical particle, $d_{V(MxOy)}$, and/or some compositional variation of synthetic particles. In this case, the volume and mass of the irregular particle calculated from the $d_{V(MxOy)}$ value can be different to the real volume and mass of ablated particle, which are direct proportional to the A_M^P value. The deviation from the size calibration line, Δd_V , for various particles such as Al_2O_3 , $CaO-Al_2O_3-MgO$, $12CaO \cdot 7Al_2O_3$ and MgO are shown in **Figure 5** as a function of particle size. In this case, the Δd_V value was determined from Eq.(7).

$$\Delta d_V = \frac{|d_{V(LA-ICP-MS)} - d_{V(SEM)}|}{d_{V(SEM)}} \cdot 100\% \quad (7)$$

where $d_{V(LA-ICP-MS)}$ and $d_{V(SEM)}$ are the size of a particle obtained by LA-ICP-MS and SEM measurements, respectively.

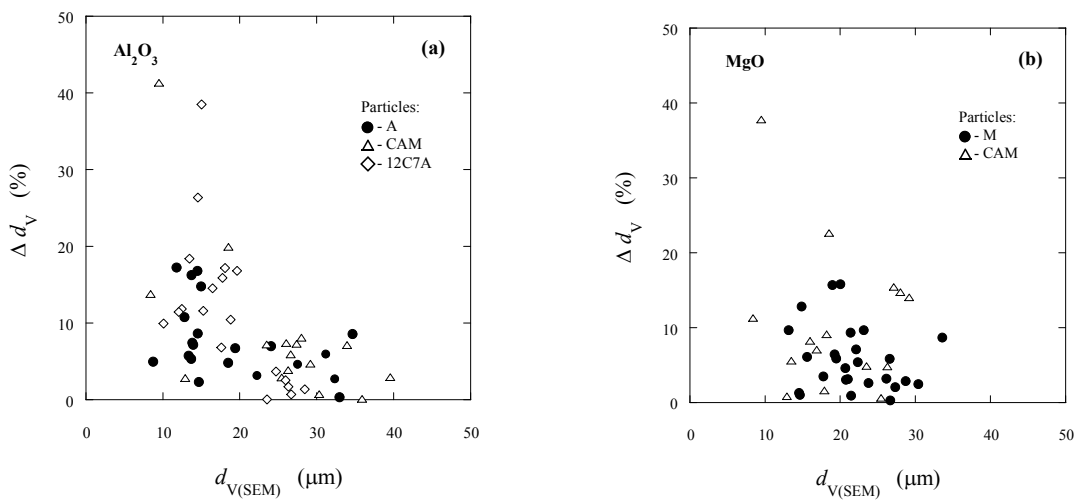


Figure 5. Deviation of particle size, Δd_V , obtained by LA-ICP-MS from size calibration line for various particles: A - Al_2O_3 , CAM - $CaO-Al_2O_3-MgO$, 12C7A - $12CaO \cdot 7Al_2O_3$ and M - MgO .

It can be seen that the Δd_V value tends to decrease with an increased size of the ablated particles. Moreover, the Δd_V values for pure Al_2O_3 and MgO particles (filled circles) are significantly smaller in comparison with the complex CAM and 12C7A particles, in which concentration of Al_2O_3 and MgO oxides is smaller. Thus, most Al_2O_3 and MgO particles have a deviation value for size estimation smaller than 10%, while the Δd_V values for most CAM and 12C7A particles are not greater than 20%.

3.3. Number and size distribution of inclusions in metal sample

An analysis of inclusion number and size distribution in metal samples by using LA-ICP-MS was carried out in Fe-10% Ni alloy deoxidized with Mg and Al (Exps.1to 3). Typical time charts of ion intensity obtained by laser ablation of metal samples are shown in **Figure 6**. The number of ion intensity peaks on time chart corresponds to the number of analyzed inclusions during laser ablation of the metal sample. The number of inclusions per unit volume in a metal sample, $N_{V(LA-ICP-MS)}$, can be determined from LA-ICP-MS measurement as follows:⁷⁾

$$N_{V(LA-ICP-MS)} = n^P / V_{anal} = n^P / (V_{abl} / k_{abl}) \quad (8)$$

where n^P is the number of analyzed inclusions, which corresponds to the number of peaks on the time chart.

V_{anal} is the volume of analyzed metal, which is swept from melt surface during laser ablation and delivered by a stream of Ar carrier gas directly to the ICP-MS. V_{abl} is the volume of ablated metal by laser irradiation of sample surface and depends on the parameters of laser ablation. k_{abl} (=11.8) is the ablation coefficient which is related to the profile of laser track, ablated and analyzed volumes of metal.

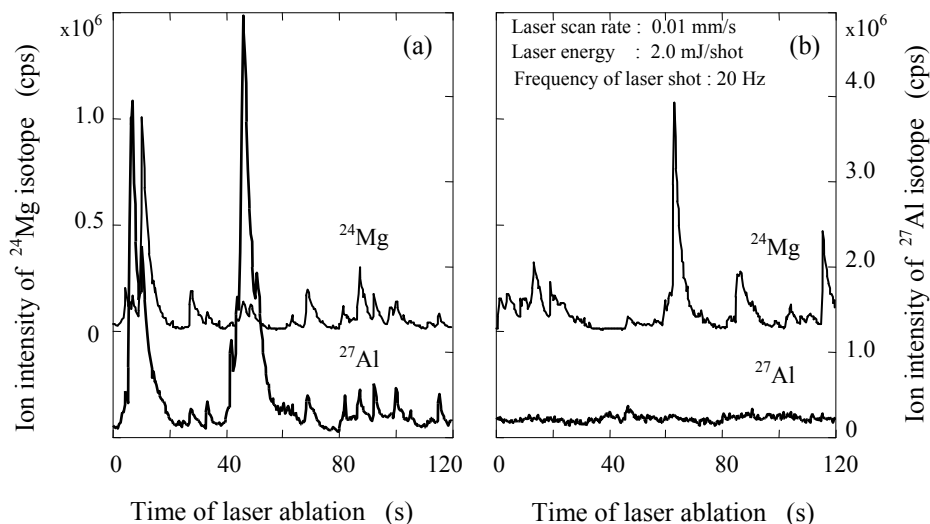


Figure 6. Typical ion intensity charts obtained by LA-ICP-MS analysis of inclusions in Fe-10% Ni alloy deoxidized with Mg and Al in Exps.1 (a) and 3 (b).

According to the present results, it was found that the complete information (composition, number and size) for 40-200 typical inclusions can be obtained automatically during 5-25 minutes of the LA-ICP-MS analysis. It should be noted that the number of inclusions per unit time of LA-ICP-MS measurement significantly depends on the number of inclusions in steel and laser ablation settings.

Figure 7 shows (a) the typical inclusion size distribution in metal sample and (b) the difference, ΔN_V , between the N_V values obtained by LA-ICP-MS and SEM analysis for the inclusions large than $d_{V(min)}$. The SEM

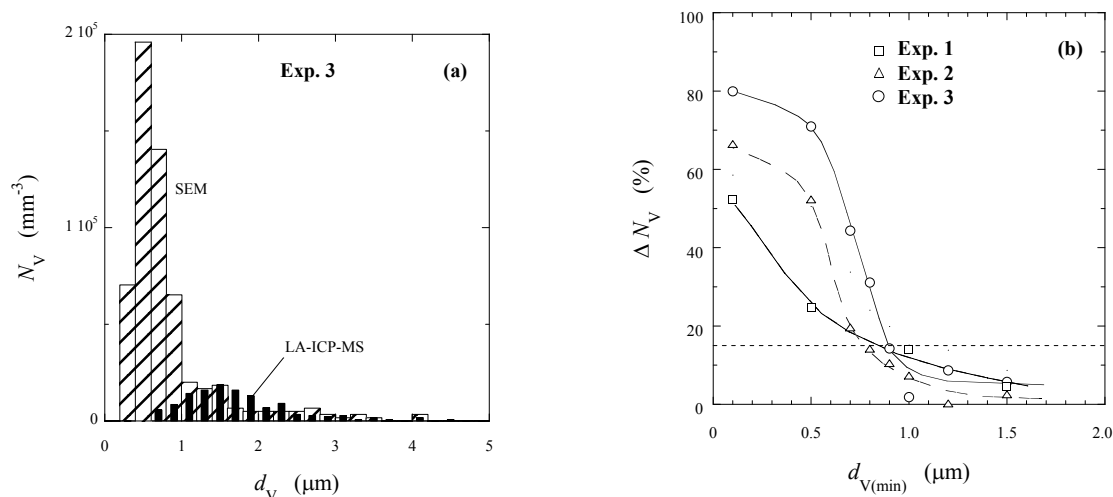


Figure 7. Inclusion size distributions (a) and difference between results (b) obtained by SEM and LA-ICP-MS analysis.

observation was carried out regarding to the inclusions on film filter after electrolytic extraction. It can be seen that the inclusion size distributions in the range of $d_v \geq 1 \mu\text{m}$ obtained from LA-ICP-MS measurements agreed reasonably well with those from SEM observations. In this size range, the ΔN_v values for all experiments are smaller than 15%. The large difference between the inclusion size distributions in the range of $d_v < 1 \mu\text{m}$ obtained from LA-ICP-MS and SEM can be explained by a simultaneous ablation of two or more inclusions at same moment. Therefore, the minimum size of inclusions, which is detected and analyzed in steel sample by LA-ICP-MS method, depends on the number of small size inclusions in steel and laser ablation settings.

4. Conclusions

Some aspects for application of Laser Ablation-Inductively Coupled Plasma Mass Spectrometry (LA-ICP-MS) for rapid analysis of oxide inclusions in metal samples were considered and discussed. The inclusion characteristics such as composition, size, number and particle size distribution were obtained by LA-ICP-MS method, and were compared with those from three-dimensional SEM observations of particles on film filters after electrolytic extraction from metal samples. The most important conclusions may be summarized as follows:

1. The obtained concentration and size calibration lines for Al_2O_3 and MgO were successfully applied for LA-ICP-MS analysis of inclusion characteristics in Fe-10%Ni alloy deoxidized with Mg and Al.
2. The relative differences between the average contents for Al_2O_3 , MgO and CaO oxides in synthetic complex particles obtained from LA-ICP-MS, EPMA and chemical analysis are less than 2%. The deviation of particle size estimated by LA-ICP-MS from that by SEM investigation is smaller than 10% for most Al_2O_3 and MgO particles and not greater than 20% for most complex CaO- Al_2O_3 -MgO and CaO- Al_2O_3 particles.
3. For metal samples with total content of Mg $\leq 0.025\%$ and Al $\leq 0.09\%$, the particle size distributions obtained by LA-ICP-MS method are in good agreement with those from three dimensional SEM investigations of particles on film filter after electrolytic extraction in the range of $d_v \geq 1 \mu\text{m}$.
4. During 5-25 minutes of the LA-ICP-MS analysis, the complete information of composition, number and size can be obtained automatically for 40-200 typical particles ($d_v \geq 1 \mu\text{m}$) in steel samples.

References:

- 1) Y. Ishibashi: *ISIJ Int.*, **42** (2002), S137-S139.
- 2) A.G. Coedo, I. Padilla and M.T. Dorado: *Appl. Spectrosc.*, **58** (2004), 1481.
- 3) A.V. Karasev, R. Inoue and H. Suito: *ISIJ Int.*, **41** (2001), No.7, 757-765.
- 4) G. Müller, F. Stahnke and D. Bleiner: *Talanta*, **70** (2006), 991-995.
- 5) A.G. Coedo, T. Dorado, I. Padilla and J.C. Fariñas: *Talanta*, **71** (2007), 2108-2120.
- 6) A.V. Karasev and H. Suito: *ISIJ Int.*, **44** (2004), No.2, 356-363.
- 7) A.V. Karasev and H. Suito: *ISIJ Int.*, **44** (2004), No. 2, 364-371.
- 8) C. Dubuisson, A.G. Cox, C.W. Mcleod, I. Whiteside, R. Jowitt and H. Falk: *ISIJ Int.*, **44** (2004), No. 11, 1859-1866.
- 9) A.G. Coedo, T. Dorado, I. Padilla and R. Usero: *ISIJ Int.*, **48** (2008), No. 2, 194-199.
- 10) A.V. Karasev and R. Inoue: *Mater. Trans. JIM*, **50** (2009), No.2, 341-348.

DETERMINING INCLUSION SIZE DISTRIBUTIONS FROM OES/PDA DATA

G. Nastasi¹, R. Wester², V. Colla¹, R. Noll²

¹*Scuola Superiore Sant'Anna(IT)*, ²*Fraunhofer ILT, Aachen (DE)*

Abstract

The determination of types and size distributions of inclusions in steel samples from OES/PDA (Optical Emission Spectrometry with Pulse Discrimination Analysis) data requires advanced mathematical tools. The main task is to filter out those OES/PDA events that correspond to inclusions in contrast to volume events, i.e. to find reliably the outliers in the data sets. The distribution functions of intensities and even more of the masses are non-normal. Thus the data are fitted to non-normal distributions and the outliers are determined as events not belonging to this distributions. After determining the outliers this information is used to find clusters of data points corresponding to distinct inclusion types. For this purpose self organizing maps (SOM) proved to be well suited. With the information about outliers and inclusions types mass distributions and further size distributions of the different inclusion types can be calculated.

Work carried out with a financial grant from the European Coal and Steel Community.

1 Introduction

OES-PDA data have long been used for bulk analysis of steel samples. More challenging is to use PDA data for determination of inclusions. First the signals due to inclusions have to be identified and subsequently the inclusion signals have to be classified and quantified.

Most of the OEF-PDA signals are correlated with bulk material, only a few percent of the signals are caused by inclusions. But also the inclusion signals normally contain a large amount of signal content stemming from the bulk material. Identification of inclusion signals out of all signals means to find outliers in the data. OEF-PDA data are in general non-normally distributed and the outliers caused by inclusions are not located isotropically around a center (data mean) but lie at high intensity values. This makes necessary to adapt existing outlier detection algorithms that have been developed for normally distributed univariate or multivariate distributions.

After identifying outliers the identified signals have to be assigned to certain inclusion types. Inclusion types can be discriminated by means of the signal heights of different measuring channels. This can be done in different ways. One way is to use black-box classifiers like artificial neural networks to discriminate among different inclusion types. For this to work a large number of sample data for supervised learning have to be supplied. Another possibility is to use unsupervised schemes like Kohonen maps or clustering algorithms. In that case the found cluster types have to be identified afterwards. In either case it is necessary to incorporate expert knowledge.

After identifying outliers and assigning outlier events to certain outlier types the data have to be used to quantify the amount of inclusion material present in the steel sample. Besides the total mass fraction the knowledge of the size distribution of inclusions is important to determine the steel grade at hand.

2. Robust Outlier Detection Methods

In the following two different approaches to determine outliers are discussed. The first one starts from the assumption that the total data distribution is a normal distribution plus some outlier events. In order to identify the outliers the parameters location and scale of the underlying normal distribution has to be found while excluding the not yet known outliers. This is done using robust location and scale estimators. Neither the mean nor the standard deviation are robust estimators because even a single outlier can change their respective values considerably. In case of univariate data a robust location estimator is given by the median and a robust estimator of the scale is given by the **Median Absolute Deviation**:

$$\mathbf{MAD} = \mathbf{median}(|X_i - \mathbf{median}(X_j)|)$$

Another robust estimator for location and scale is the **Minimum Covariance Determinant** which can also be used in cases of multivariate data. The **MCD** is defined as follows:

- find a subset h of all data-points (usually $h = (n + p + 1)/s$) for which the determinant of the covariance matrix taken with this subset has a minimum.

Robust estimators of location and scale are then the usual mean and covariance matrix computed with this subset. In one dimension ($p=1$) this is a trivial task. In higher dimensions computation times increase drastically. The **FastMCD** (7) algorithm attacks this problem.

With known location and scale the outlier flag is assigned to those data points that are given by:

$$\frac{\mathbf{I} - \mathbf{location}}{\mathbf{scale}} > n$$

n usually is 3-4.

The above described outlier detection relies on the assumption that the main part of the distribution of data is a normal or near-normal distribution. In many cases of interest this is a bad assumption. An alternative way to identify outliers is to fit the real data by known non-normal distribution function as e.g. . Non-Normal, skew distributions that decrease strongly with increasing $(I - I_i)^2$ (I is the intensity and I_i the mean intensity of the i 'th Gaussian) can very well be fitted by a sum of Gaussians or a Gaussian mixture model:

$$f(I) = \sum_{i=1}^n a_i \frac{1}{\sqrt{2\pi}s_i} \exp\left(-\frac{1}{2} \frac{(I - I_i)^2}{s_i^2}\right)$$

There are 3 n fit parameters a_{1-n} , m_{1-n} and s_{1-n} that have to be calculated. The fit parameters can be found by different algorithms:

1. General purpose optimization algorithms.
 - Quasi-Newton
 - Conjugate Gradient
2. Specialized algorithms for multiple Gaussian fits.
 - EM (expectation maximization) (1)

After finding the parameters of the distribution discriminate outlier points from points that belong to the distribution:

- Define a limit:

$$\int_{-\infty}^{I_{limit}} f(I) dI = q$$

with

$$\int_{-\infty}^{\infty} f(I) dI = 1$$

and take e.g. $q = 0.997$ (in case of a normal distribution this corresponds to 3s)

- Sharp discrimination: all events above I_{limit} are outliers. The number of outliers is given by:

$$N_{outlier} = \sum_{I > I_{limit}} 1$$

- Soft discrimination: take the $N_{outlier}$ events with the highest intensities as outliers with:

$$N_{outlier} = \sum_{I > I_{limit}} 1 - \int_{I_{limit}}^{\infty} f(I) dI N_{sparker}$$

Figure 1 shows the histogram and fitting curve of the data of a the Mn masses per spark. On the left the whole curve is shown whereas on the right an enlarged region shows the tail of the distribution where the outliers are located. With sharp discrimination all sparks above the mass limit indicated by the red line are counted as outliers. In the case of soft discrimination the number of outliers is given by the area below the fitting curve (green line) right to the mass limit (red vertical line).

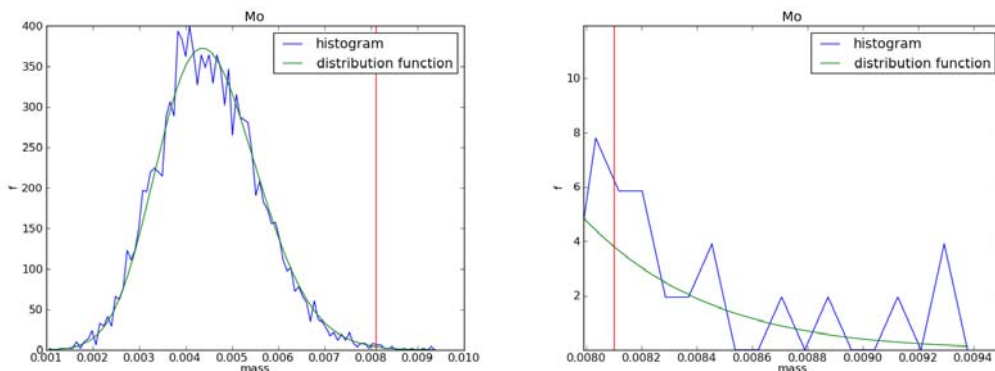


Figure 1: Fitting of non-normal data.

3. Classification and Clustering

In this section some techniques will be discussed for the classification and for the clustering of outliers. The main distinction between these two approaches is that typically classification algorithms are *supervised*, i.e. they need to be trained on reference data, generally called targets, (e.g. SEM analyses), while clusterization algorithms are *unsupervised*, i.e. they subdivide input data into groups just by analyzing the characteristics and features of the input data themselves.

3.1. Supervised classification

By means of a classification model it would be possible to assign inclusions type to PDA analyses. Nevertheless, the main issue in the application of supervised methods is that the number of required reference data in such a complex task as inclusions evaluation is very high. In fact, a typical PDA analysis is composed by at least 10 channels, corresponding to 10 chemical elements, each of which can combine with one or more of the other elements in order to form an inclusion. In order to cope with this kind of data, complex classification models should be employed, but, by increasing the number of parameters that need to be trained, we also increase the number of required targets. In the case of inclusions assessment, reference data can be obtained for instance by SEM analyses, which, unfortunately, are very slow (4-8 hours per analysis), so it's very difficult to have at disposal such a high number of SEM results as it would be required for a correct training of the model.

There are several models in literature to accomplish the classification task, for instance:

- Decision Trees (2);
- Neural Networks (3) such as Multi Layer Perceptrons (MLPs);
- Learning Vector Quantization (LVQ) (4).

Each of these algorithms has different characteristics and features and each is trained by means of a dedicated learning algorithm. Different algorithm may provide very different results, depending on data features, so more than one algorithm should be tested and results compared in order to make a choice.

3.2. Clustering

A partial solution to the issue described in the previous subsection can be provided by unsupervised clusterization algorithms. This kind of models in fact does not require target data, but they divide input data into clusters on the basis of their own spatial disposition and/or location, or on the basis of certain features, depending on the particular employed model. The problem with this approach is that the user/operator must check the results and assign a label (an inclusion type) to each cluster. In order to gradually automate the classification task, it would be possible to couple to the selected clusterization algorithm an expert system that will progressively learn how to assign labels to clusters by means of the choices made by the human operator. In this way it is possible to overcome the lack of reference data at the cost of a longer training procedure and lesser automation, at least in a first period.

An unsupervised model based on a Self Organizing Map (SOM) (5) and the K-means clusterization algorithm (6) has been developed that is able to subdivide a dataset of PDA analyses in groups which has similar features on the base of α -factors. As depicted in figure 2, the algorithm is composed by 4 steps. In the first step, α -factors of all PDA analyses in the input dataset are calculated (e.g. by means of the Robust Outlier Detection Methods described in Sec. 2) and stored in a matrix where each row represents a different sample. An α -factor for each single element and for a subset of combined elements are calculated. In order to lessen the dimensionality and to cancel some redundancy, a Principal Component Analysis (PCA) is performed, where the components whose weight is less than 5% are discarded, by thus reducing the input variables to 6. Afterward, a Self Organizing Map (SOM) (5) is trained on the resulting matrix: a SOM is a particular paradigm of Artificial Neural Network (ANN) that is able to produce a low-dimensional (typically two dimensional), discrete representation of the input space of the training samples, called map, that preserve the input space topology and to find clusters which are represented by means of a prototype neuron. In the last step a further clusterization is performed on the SOM neurons by means of the K-means clusterization algorithm (6) in order to identify clusters of neurons and to have a cleaner and more interpretable output, because SOM neurons can sometimes be redundant.

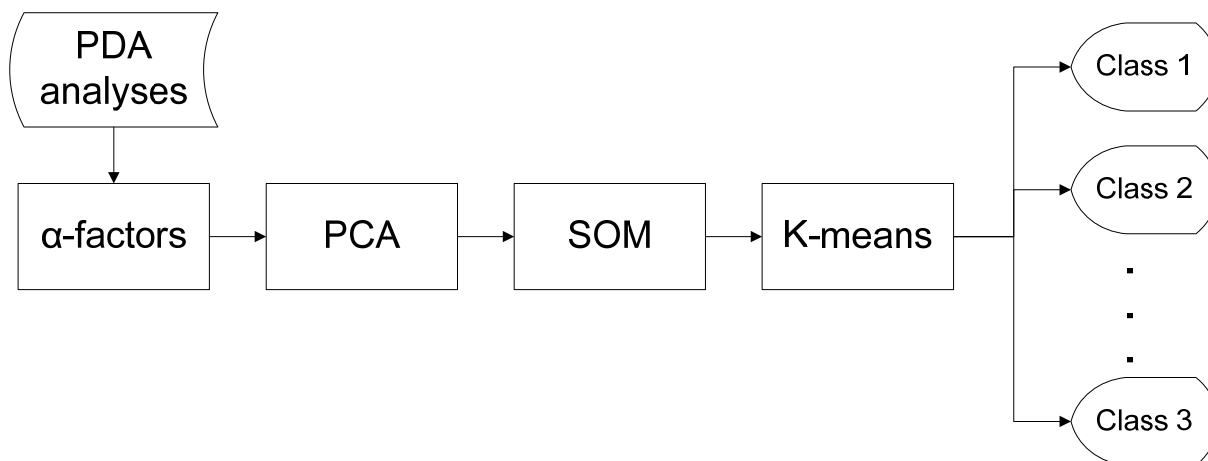


Figure 2: SOM based model.

In figure 3 an example of the output of the SOM based model is shown. Each hexagonal cell is a SOM neuron, the number within each cell is the number of samples that was recognized by that neuron, and each group of cells with the same colour is a different cluster identified by the K-means algorithm. The number of final clusters is automatically calculated by minimizing the quantization and the topographic errors. Thank to this model is thus possible to divide PDA analyses in different groups where each group is composed by samples having similar inclusion contents. The operator can then apply a different label to each cluster. When new analyses are performed, it can be passed to the trained model which will return the class of the sample. Finally, in order to obtain better results, it would be better to train different models for each different steel grade.

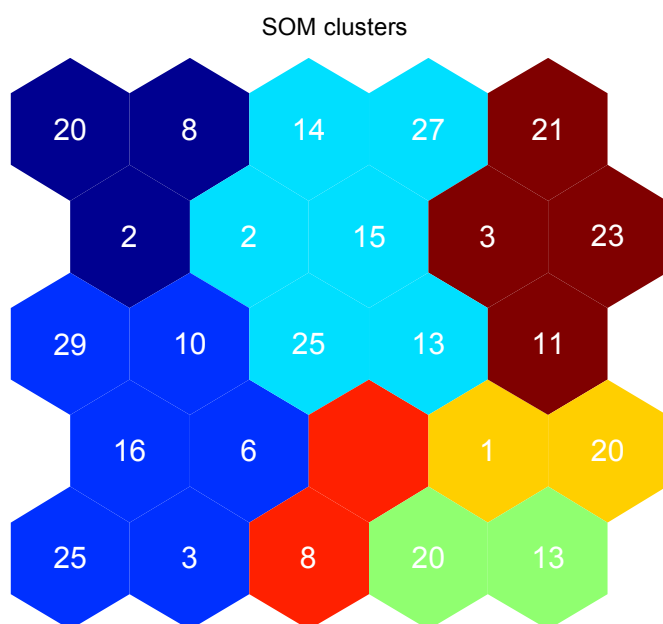


Figure 3: SOM based model output.

4.Computation Steps

The following calculation steps were proposed by Arne Bengtson of KIMAB. The objective of the computational procedure outlined below is analyzing PDA data to find outliers, inclusion types, determine size distributions of the inclusion types found and calculate B-factors. The calculation steps are implemented in a software tool. Many of

the algorithms described in the preceding chapters are included. The main steps are (omitting some intermediate steps):

1. Eliminate sparks with very low iron-signal (typically < 30%)
2. Calculate the mass (in ng) of all elements in each spark using calibration functions
3. Calculate the normalized concentrations of all elements in each spark
4. Subtract background
5. Identify outliers
6. Compute normalized concentrations of the selected elements
7. Classify outliers
8. Re-calculate the mass per element of the inclusions based on the stoichiometry of the inclusion class
9. Calculate the diameter (figure 4 shows as an example the calculated diameter distribution of Al_2O_3 and CaO)
10. Calculate B-factors (ratio of the mass of an element confined in the inclusions to the total mass of the respective element):

$$B_e = \frac{\sum_{i=1}^n m_{e,i}(I)}{\sum_{i=1}^n m_{e,i}(I)}$$

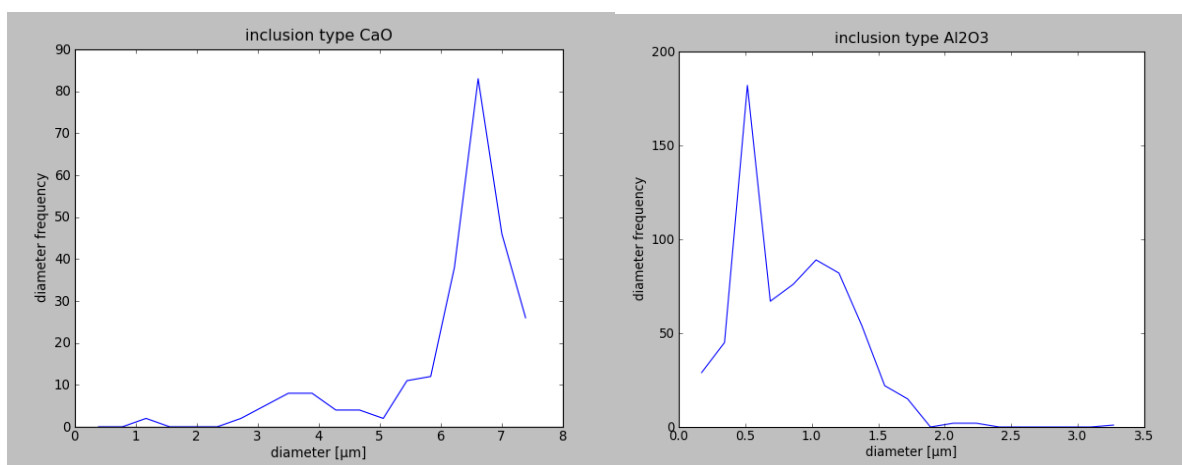


Figure 4: Computed size distributions of CaO and Al_2O_3 inclusions.

Conclusions

The computation of characteristic numbers for inclusion detection and quantification from OES/PDA data makes necessary the use of advanced mathematical methods. We outlined robust outlier detection algorithms that can also reliably find outliers in skew, non-normally distributed measuring data. The next step in inclusion detection is to cluster and/or classify the found outliers according to their elemental composition. Quantification of inclusions with respect to size and B-factors is performed in a series of computational steps that include the above mentioned outlier detectors and classifiers. The mathematical algorithms have been implemented in software tools that can be used on-line to analyze the data gained from PDA/OES measuring systems.

References

- 1) G. McLachlan and T. Krishnan, "The EM Algorithm and extensions", New York: John Wiley Sons, 1997
- 2) Breiman, Leo; Friedman, J. H., Olshen, R. A., & Stone, C. J. (1984). Classification and regression trees. Monterey, CA: Wadsworth & Brooks/Cole Advanced Books & Software. ISBN 978-0412048418
- 3) Haykin, S. (1999) Neural Networks: A Comprehensive Foundation, Prentice Hall, ISBN 0-13-273350-1

- 4) T. Kohonen. Learning vector quantization. In: M.A. Arbib, editor, *The Handbook of Brain Theory and Neural Networks.*, pages 537–540. MIT Press, Cambridge, MA, 1995.
- 5) T. Kohonen. *Self-Organizing Maps*. Springer, Berlin, 1997.
- 6) Hartigan, J. A. (1975). *Clustering Algorithms*. Wiley. ISBN 0-471-35645-X
- 7) P.J. Rousseeuw and K. van Driessen, "A fast algorithm for the minimum covariance determinant estimator", *Technometrics*, 1999, vol. 41, no3, pp. 212-223

TRUE SIMULTANEOUS ELEMENTAL ANALYSIS FOR RAPID PROCESS CONTROL BY XRF

Kai Behrens, Dominique Porta

Bruker AXS, Oestliche Rheinbrueckenstrasse 49, 76187 Karlsruhe, Germany

Abstract

The analytical task for rapid process control in metal production is clearly defined. The aim is to achieve the best possible accuracy and precision within the shortest measurement time for a given range of relevant elements. While most of the traces and minor elements are analyzed with optical emission spectrometry (OES), X-ray fluorescence spectrometers (XRF) add the precision for elements in higher concentration ranges and for materials with high silicon and carbon concentrations such as pig iron. XRF contributes in addition with the analysis of raw materials and slags. The slag analysis is of special interest by giving additional information about the actual furnace condition.

Traditionally simultaneous wavelength dispersive XRF instruments (WDXRF) are used for the rapid process control. Unrivalled is the analytical speed for single elements, but this kind of instrument is not flexible regarding the material range and elements which are analyzed. For this purpose typically scanners and/or goniometers are integrated, which are no longer operating simultaneously.

A new full simultaneous operating X-ray fluorescence spectrometer combines the analytical precision with integrated flexibility matching the analytical demands for ferrous and non-ferrous metal production. Due to the integration of latest technology this new spectrometer provides the complete information about the elemental range without prolonging the measurement time – quick feedback on the process is ensured. Examples for different steel alloys and copper are shown, the achievable precision is in the range of 0.04% relative for major elements, typical detection limits are in the range of 1-2 ppm.

Article

The full paper was not available at time of printing.

ONLINE MONITORING OF HOT DIP GALVANIZING BATH BY LIBS TECHNIQUE

Sophie JACQUES, Norbert WIZENTY, Alain LAMANDE, Marie SIMONNET

*ArcelorMittal Global R&D Maizières, Voie Romaine, BP30320
F-57283 MAIZIERES-LES-METZ Cedex*

ABSTRACT

Pot chemistry management during Hot Dip Galvanizing (HDG) is fundamental to ensure both the quality of coated steel sheets and the efficiency of the process.

Today, zinc bath analysis is possible by ICP-OES (Inductively Coupled Plasma – Optical Emission Spectroscopy) analysis on solid samples taken in the bath. Analyses are however delivered after a time and they do not give any information about precipitates (Fe-Al diagram in rich Zn-region is needed in that case) or fast bath modification.

Thanks to measurements performed directly inside the bath by adapted LIBS (Laser Induced Breakdown Spectrometry) technique, called GalvaLIBS, it will be possible to analyse high (Al, Fe) and traces (Pb, Sb...) elements content and to evaluate the cleanliness of the bath (drosses precipitation).

The first step consists in the calibration of the GalvaLIBS equipment for the different elements of interest: determination of system optimal conditions (lance position, laser power, argon flowrate...) and following addition sequence in a bath furnace where the metal is molten. Precise concentrations were determined by ICP-OES.

The next step consists in the validation of the elements calibration by analysing an industrial bath and comparing results with other common techniques.

Some trials were also achieved to compare the GalvaLIBS analysis on liquid and solid samples.

Keywords: galvanizing bath, LIBS, on-line analysis

1. INTRODUCTION

In order to protect them against corrosion, steel sheets are often coated with a layer of zinc. During continuous hot dip galvanization (HDG), the steel strip is immersed in a molten zinc bath containing small amounts of aluminium (usually 0.2 wt%). Due to dissolution phenomenon, iron is also present in the bath (around 0.03 wt%). Other trace elements can also be found in the pot (Pb, Sb, Sn...).

Pot chemistry is usually controlled by taking samples which are analyzed afterwards in lab by various techniques, such as ICP-OES (Inductively Coupled Plasma – Optical Emission Spectroscopy). The drawback of this method is the time needed to perform the analysis. If the analysis highlights a shift in Al composition for example, the change in bath ingot feeding to solve this issue will be delayed due to the time needed for the chemical analysis.

The technology proposed in this paper relies on the LIBS (Laser Induced Breakdown Spectrometry) principle and allows a continuous measurement of HDG bath composition. The so-called GalvaLIBS system has been developed by Institut des Matériaux Industriels (IMI) from Montreal (Canada) [1,2]. It is commercialized by TECNAR company [3]. The GalvaLIBS measurement principle is presented in Figure 1 [4,5]: it consists in focusing a pulsed laser beam on the material to evaluate. The laser beam is led to the surface to analyze through a lance immersed in the molten metal. Some argon is injected in the lance to renew the analysed surface. The volume of the target is vaporized and ionized to produce plasma. The optical emission of the plasma is analyzed by a spectrograph to obtain quantitative information about its atomic composition.

The advantage of this technique is that it does not need any special sample preparation and allows the simultaneous analysis of different elements in solution in the molten zinc. Moreover if we apply a special treatment to the emitted signal, we can reach some information regarding precipitates presence in the analysed

volume. Such information about precipitates content is critical for bath control since it relates to the bath cleanliness and further to the risk of drosses entrapment by the strip which can lead to aspect defaults.

We describe in this paper, ArcelorMittal Global R&D experience on GalvaLIBS use in lab furnace. In a first part, we will present the experimental setup and the calibration curves for different elements (main elements and traces). The second part of the paper is devoted to the study of the sample state (liquid/solid) influence on calibration curve. Then we validate the determined calibration curves on Certified Reference Materials and a comparison of GalvaLIBS results with ICP-OES analysis results is performed.

2. EXPERIMENTAL SET-UP

2.1. DESCRIPTION OF GALVALIBS

The GalvaLIBS system (Figure 1, Table 1), usable both in solid and in liquid environments, is composed of:

- a cabinet equipped with laser control box (filled by deionised water with a specific device), filter for deionised laser water, computer, spectrometer, ICCD camera (detector), urgency stop button, keys to start equipment and laser, lamp to indicate laser state,
- a chiller to control the laser temperature,
- a laser box equipped with laser head, optic systems,
- cables in which optic fibres, water system and argon (5.0 grade) tube linked to cabinet are present,
- a SiAlon probe which can be immersed in zinc bath (cleaned with alcohol and dried over the bath), protected by a stainless steel tube.

In liquid environment, an argon flow rate injected through the lance is used to refresh the sampling surface directly in the liquid zinc bath.

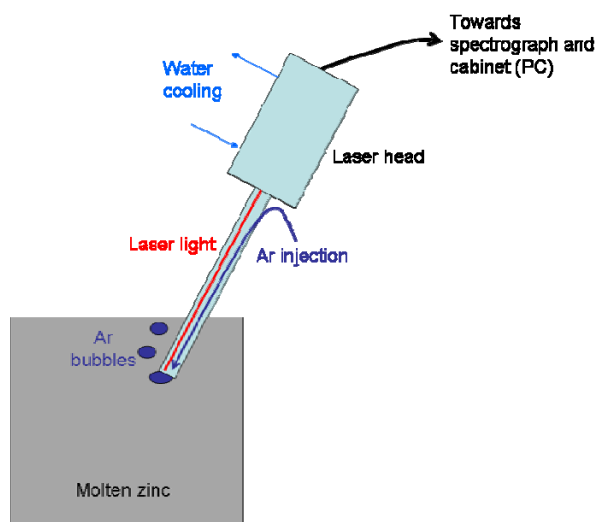


Figure 1 – GalvaLIBS technique for on-line analysis of molten metal composition [4]

Laser system Nd:YAG laser at 1064 nm	
Laser energy	~100 mJ
Repetition rate	1 Hz
Voltage	750 V (~800 V max)
Q-Switch	148 μs
Argon flow	0.75 L/min
Detection system Spectrometer PI Acton	
Focal length	350 mm
Effective wavelength range	250 - 800 nm
Grating	1800 and 3600 grooves.mm ⁻¹
Width of analysis window	12 and 24 nm
Spectral resolution	0.02 nm

Table 1 – Characteristics of GalvaLIBS and standard conditions used for calibrations

The laser used in the GalvaLIBS is a class IV laser. This means that a lot of safety aspects need to be considered, in conformity with the regulations.

2.2. LAB EXPERIMENTS AND CALIBRATION DESCRIPTION

This experiment consists of a bath furnace in which the metal is melt; the LIBS probe is immersed by the top surface.

The calibration of the GalvaLIBS has been done on molten metal contained in lab furnace. Al, Fe, Sn, Sb and Pb have been added gradually in order to cover the standard range of GI galvanizing compositions (Figure 2 and Table 2). It was necessary to stay in the liquid solution domain to avoid composition perturbation by precipitates.

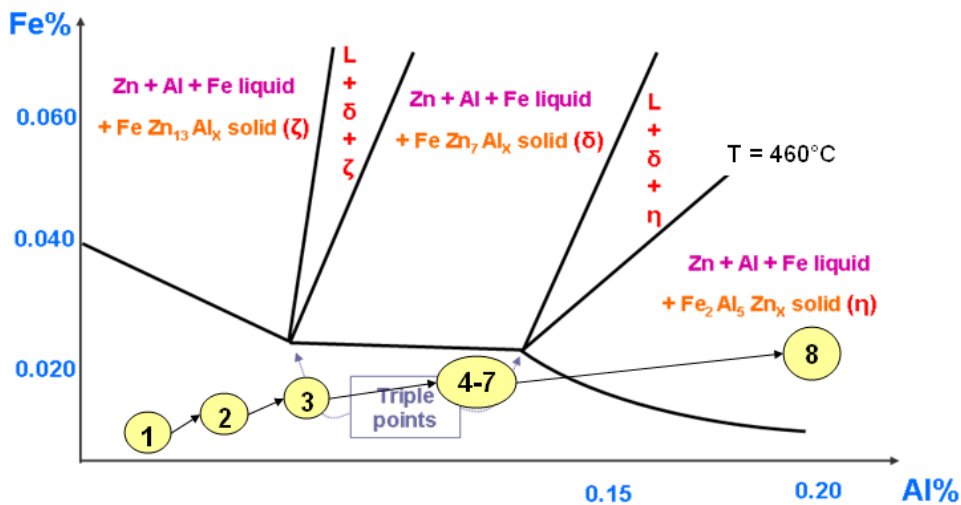


Figure 2 – Additions realised during lab trials

One type of sampling has been performed during the calibration of the GalvaLIBS: disk (sample A and B) water quenched.

Additions	Al (%)	Fe (%)	Sn (ppm)	Pb (ppm)	Sb (ppm)
Ao1	0.02	0.003			
Ao2	0.06	0.01			
Ao3	0.1	0.016			
Ao4	0.12	0.02			
Ao5			50	50	50
Ao6			150	150	150
Ao7			300	300	300
Ao8	0.2	0.02			

Table 2 - Additions realised at zinc pot temperature of 450°C

The equipment presents two gratings and the width of analysis windows is 12 and 24nm. It is thus necessary to determine different windows to analyse the different elements (Table 3).

Aluminium and iron wavelengths were advised by the supplier TECNAR who has a wide experience of zinc bath analysis. For these two elements, a zinc wavelength was also selected to determine the ratio between the element and the zinc intensity, because some conditions can change during measurements (bubble effect, lower intensity due to a different morphology of the bubble...) and effects are reduced by considering intensities ratio.

For traces elements, wavelengths were selected according to literature and to be able to analyse these three elements in the same window, without analysing zinc wavelength. Indeed, as the matrix is zinc, the intensity of zinc is too high and it was not possible to well observe traces intensities. Detector parameters were modified to be able to analyse traces and to avoid a problem of signal saturation on detector ($I_{max} \sim 65000$ conts) and risk of detector damages (zinc can not be analysed with these conditions).

Elements	Window	Zn	Al	Fe	Pb	Sn	Sb
λ (nm)	1	303.5	308.5				
	2	275		259.6			
	3				283.3	284.0	287.8

Table 3 – Selected wavelengths

The classification by increasing intensities allows separating dissolved element and precipitates (Figure 3), the linear part is treated to determine calibration curves.

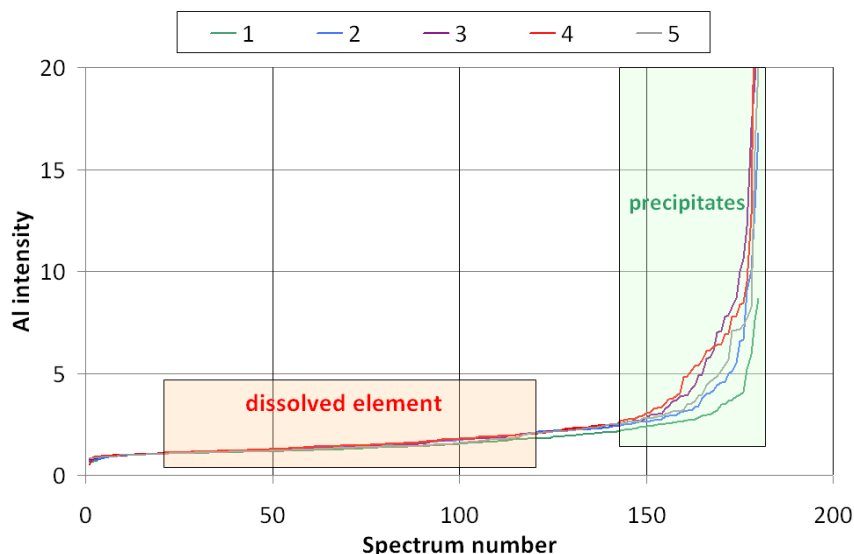


Figure 3 – Example of classification by increasing intensity to separate dissolved elements from precipitates

3. RESULTS AND DISCUSSION

3.1. CALIBRATION CURVES

To elaborate calibration curves, the LIBS signal was treated as described in paragraph 2.2. and corresponding samples were analysed by ICP-OES. Results are presented in Table 4 .

Samples	Al		Fe		Sn		Pb		Sb							
	%	% (theory)	%	% (theory)	%	% (theory)	%	% (theory)	%	% (theory)						
Ao1A	0.027	0.02	0.007	0.003												
Ao1B	0.027		0.007													
Ao1Bis	0.027		0.007													
Ao2A	0.063	0.06	0.007	0.010												
Ao2B	0.061		0.007													
Ao3A	0.099	0.10	0.027	0.016												
Ao3B	0.101		0.027													
Ao4A	0.111	0.12	0.026	0.020							0.005	0.005	0.008	0.005	0.0035	0.005
Ao4B	0.121		0.027								0.008					
Ao5A	0.121		0.029								0.015	0.015	0.018	0.015	0.0067	
Ao5B	0.122		0.029		0.015	0.017	0.0059									
Ao6A	0.119		0.030		0.029	0.029	0.031	0.015	0.0101							
Ao6B	0.116		0.029						0.031	0.0109						
Ao7A	0.118		0.031		0.029	0.030	0.031	0.030	0.0061							
Ao7B	0.119		0.031						0.029	0.0063						
Ao8A	0.173		0.029		0.028	0.029	0.032	0.030	0.0067							
Ao8B	0.176		0.028						0.031	0.0064						
Ao8C	0.172	0.028	0.029													
Ao8D	0.174	0.029	0.029													

Table 4 – ICP-OES results on disks samples

Calibration curves are presented below and good calibration are observed: Figure 4 and Figure 5.

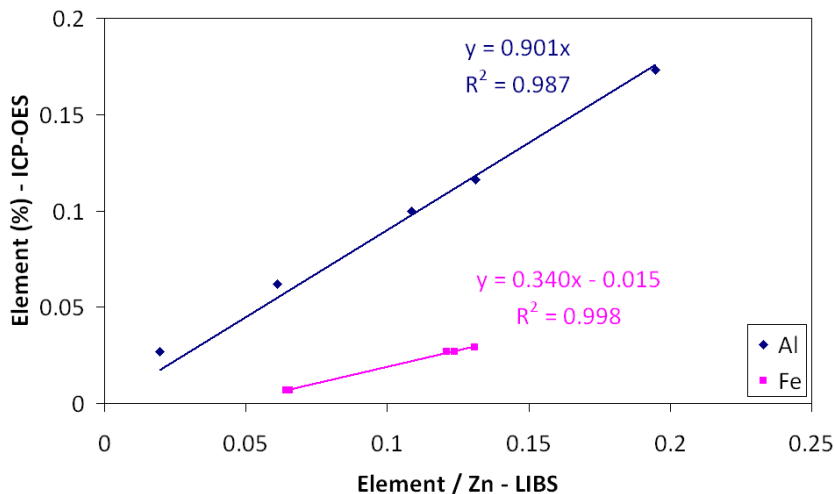


Figure 4 – Liquid calibration curves of aluminium ($\lambda\sim 308.5\text{nm}$) and iron ($\lambda\sim 259.6\text{nm}$)

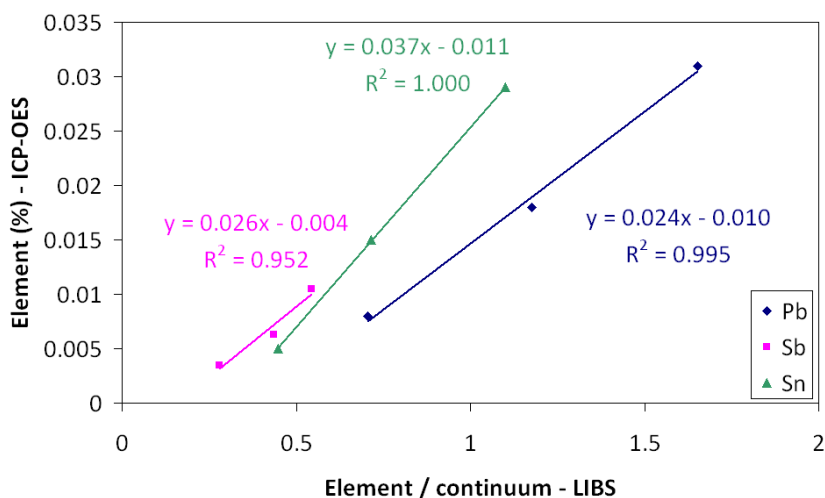


Figure 5 – Liquid calibration curves of lead ($\lambda\sim 283.3\text{nm}$), antimony ($\lambda\sim 287.8\text{nm}$) and tin ($\lambda\sim 284.0\text{nm}$)

Figure 6 shows the aluminium calibration curves obtained at two laser power. We clearly see a large difference between these two curves and that the intensity is widely linked to laser power and maybe other parameters, such as lance angle or depth.

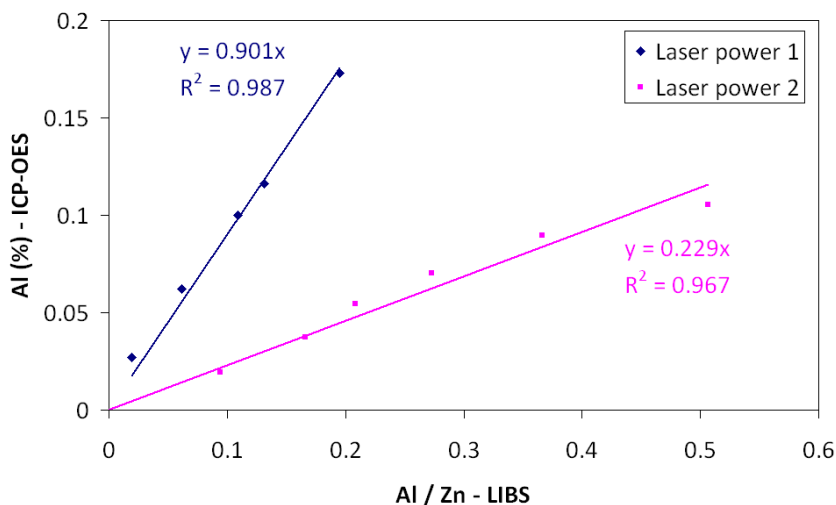


Figure 6 – Liquid calibration curve of aluminium obtained at two different laser powers

3.2. EFFECT OF SAMPLE STATE ON CALIBRATION CURVES

Solid samples (polished surface) were analysed by GalvaLIBS to compare the intensity of the elements between liquid and solid state.

We can see that Al – Fe – Sn calibration curves depend slightly on sample state (liquid/solid) and that Pb – Sb calibration curves depend greatly on sample state (Figure 7).

These results can be linked to the melting temperatures of the traces elements. Sn has indeed the lowest melting point (232°C) compared to Pb (328°C) and Sb (631°C) and the Sn calibration curves for solid and liquid samples are very similar. For Sb which has the highest melting point, the slopes of the calibration curves for liquid and solid analysis are the most distinct.

The discrepancies observed between solid and liquid calibration curves can also be linked to the sampling method (especially sample cooling and elements segregation).

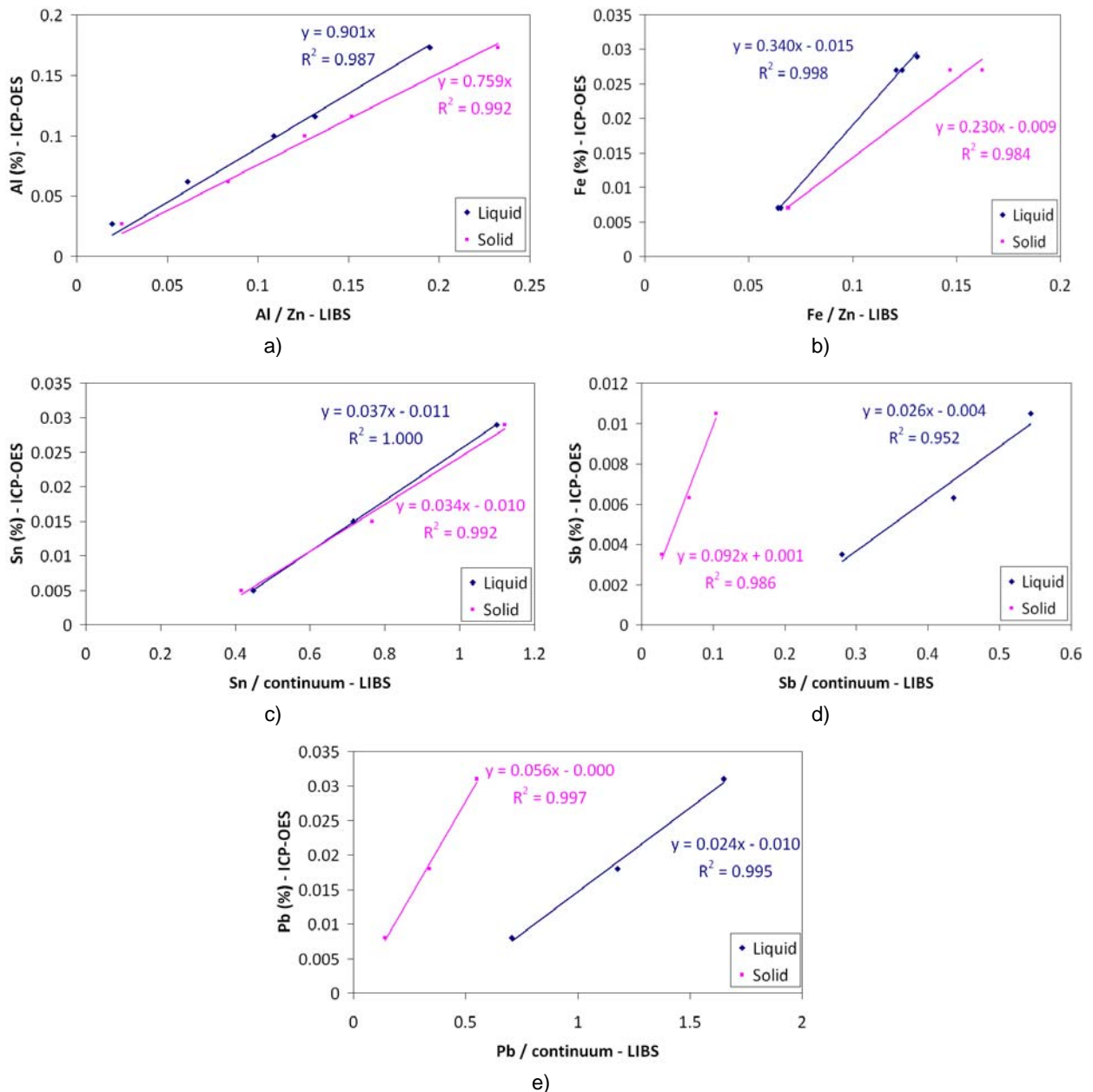


Figure 7 – Effect of liquid and solid state on calibration curves

To summarize the influence of sample form on GalvaLIBS measurements, we can say that:

- for main elements (mainly Fe and Al in standard hot dip galvanizing baths), the same calibration curve can be used for solid and liquid measurements,
- for traces elements:
 - if melting temperature is very low compared to bath temperature (as it is the case for Sn), the calibration curve for solid and liquid samples is the same,
 - if melting temperature is of the same order of magnitude (Pb case) or higher (Sb case), the calibration curve needs to be adapted to sample state.

3.3. VALIDATION OF SOLID CALIBRATION CURVES

Using calibration curves presented above, solid samples have been analysed with GalvaLIBS. Results obtained according to solid calibration were compared to ICP-OES results and to certified values (Figure 8).

For all elements, ICP-OES analysis matches certified values. We observe that the results obtained by LIBS are not really precise but values are in the same order for main elements.

The differences can be attributed to the size of the sample analyzed: while ICP-OES analyses a few grams of matter, GalvaLIBS measurements is only related to millimetric laser spots diameter.

Al	LIBS on solid (%)		ICP (%)	Certified value (%)
	mean	sd		
41X0336Zn1(K)	0.009	0.001	0.014	0.014
41X0336Zn2(K)	1.63	0.08	1.53	1.55
41X0336Zn3(J)	0.33	0.10	0.41	0.43
41X0336Zn4(B)	1.65	0.02	1.36	1.39
41X0336Zn5(A)	0.032	0.001	0.036	0.035
41X0336Zn6(A)	0.138	0.003	0.103	0.105
De2B	0.032	0.002	0.037	-
De4B	0.059	0.002	0.070	-
De8B	0.16	0.01	0.11	-
De11B	0.30	0.01	0.24	-

a) example of Al

Sn	LIBS on solid (%)		ICP (%)	Certified value (%)
	mean	sd		
41X0336Zn1(K)	0.0030	0.0002	0.0038	0.0053
41X0336Zn2(K)	0.032	0.001	0.038	0.04
41X0336Zn3(J)	0.084	0.006	0.105	0.111
41X0336Zn5(A)	0.203	0.010	0.204	0.21
De7B	0.008	0.001	0.005	-
De8B	0.013	0.001	0.010	-
De9B	0.018	0.000	0.015	-
De10B	0.032	0.002	0.029	-

b) example of Sn

Figure 8 – Results comparison on solid samples

4. CONCLUSION

In the studied range, a linear answer of LIBS intensity is observed for the 5 studied elements, at wavelengths determined with the help of the supplier TECNAR. But this answer is closely linked to analyses conditions; it seems that calibration curves are only valuable in calibration conditions.

This equipment can also be used on solid sample. The LIBS answer depends on the element and for some of them, the answer is equivalent between liquid and solid state. Such solid analysis could be use to control equipment before industrial trials.

At present time, the equipment is composed of two different gratings, which allow the measurement in a window of 12 or 24nm. This can induce a problem during on-line measurements because until now, it is not possible to measure in the same time Al, Fe, Sb, Sn and Pb.

The next steps will be to validate the calibration on a lab furnace containing industrial matter and to realise on-line measurements in industrial conditions.

Acknowledgement

The authors acknowledge the European Commission for the financial support through the contract RFSR-CT-2008-00043.

References:

- [1] M. Sabsabi, R. Héon, J. Lucas, "Method and apparatus for in-process liquid analysis by laser induced plasma spectroscopy", U.S. Pat. No. 6,700,660 issued Sept. 2003
- [2] J. Lucas, M. Sabsabi, R. Héon, "Method and apparatus for molten material analysis by LIBS", Application to US patent 20030234928, June 2002
- [3] A. Nadeau, L. Ozcan, F. Nadeau, M. Sabsabi, P. Bouchard, C. Dewey, "Online monitoring of dross and effective aluminium", The Asia-Pacific Galvanizing Conference, Korea, 2009
- [4] M. Sabsabi, L. St-Onge1, V. Detalle, J.M. Lucas, "Laser-Induced Breakdown Spectroscopy: A new tool for process control" (available on website: http://www.ndt.net/article/wcndt2004/pdf/in-process_ndt-nde/679_sabsabi.pdf)
- [5] E. Baril, L. St-Onge, M. Sabsabi, J. Lucas, M. Gagné, "On-line chemical analysis of CGL baths using Laser-Induced Breakdown Spectroscopy", 96th Galvanizers Association Meeting, Charleston, South Carolina, October 2004

DIRECT DETERMINATION OF TRACE ELEMENTS IN STEEL BY LASER ABLATION/ICP-MS

Tomoharu Ishida, Takanori Akiyoshi, Akiko Sakashita, Satoshi Kinoshiro, Kyoko Fujimoto

Steel Research Lab., JFE Steel Corporation, 1 Kokan-cho, Fukuyama, Hiroshima 721-8510, Japan

ABSTRACT

A new laser ablation (LA) system for quantitative analysis with ICP-MS has been developed. The system has a high frequency Q-switched laser and 2 scanning mirrors for moving the ablation spot in an adequate area. Elemental fractionation (non-stoichiometric generation of vapor species) can be eliminated with repeated laser irradiation in an adequate area without vacant space by a developed laser ablation (LA) system. Particles generated with this system were induced to inductively coupled plasma mass spectrometry (ICP-MS) for quantitative determination of trace elements (B, As, Sb, Pb) in steel samples. Analytical performance of the developed LA-ICP-MS was investigated with standard reference materials of iron, NIST steel SRMs. The analytical results showed that this method has sufficient precision, sensitivity and accuracy for the analysis of steel samples in the $\mu\text{g/g}$ level concentration of trace elements.

INTRODUCTION

For quantitative analyses of metals, spark discharge AES and X-ray Fluorescence spectrometry are commonly applied as routine analyses in metal manufacturing. These methods are speedy because they analyze solid samples directly. But when analytical requirements are at the trace concentration level, analytical methods are changed to more sensitive analytical techniques such as inductively coupled plasma mass spectrometry (ICP-MS) and electro-thermal vaporization/cold vapor atomic absorption spectrometry. Laser ablation (LA) method is attracting attention since it can simultaneously meet the two needs for high sensitivity and rapidity.

In order to solve two main problems in applying LA-ICP-MS to quantitative analysis, many articles have been published¹⁾⁻¹⁰⁾ The first is the elemental fractionation of ablated particles (non-stoichiometric generation of vapor species), and the second problem is the quantity of generated ablated particles. Developed laser ablation system, combining a pulse laser having a high repetitive frequency and a galvanometer scanner, can generate fine particles whose composition is the same as that of the base material sample⁽¹¹⁾. This time, an examination was made into the application of LA-ICP-MS to the four elements B, As, Sb, and Pb.

EXPERIMENT

Apparatus

Laser Ablation System

An outline of the system is shown in Figure. 1. An Nd:YVO₄ laser of the Q-switched type capable of oscillating with a maximum average output of 10 W at a pulse frequency of 50 kHz (wavelength: 1064 nm, T40-Z20-106Q, made by Spectra-Physics, Inc.) was used as the system laser. An optical system of beam irradiation, which is composed of a beam expander, two galvanometer scanners (M2S made by GSI Group.) and a condenser lens, was adjusted so that the spot diameter of the laser became 50 μm or less. The ablation cell is of a coaxial double tube construction; a quartz window for transmission is installed on the incoming side of the laser

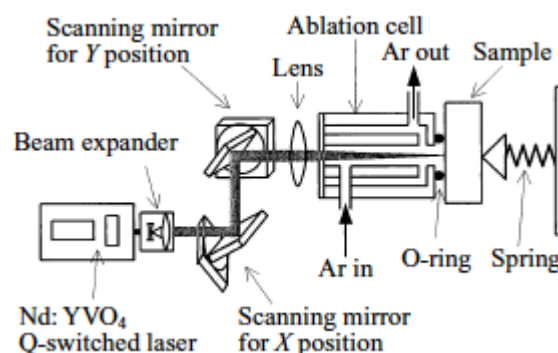


Figure 1¹¹⁾. Schematic diagram of the developed LA system

light and an opening is provided on the opposite side. Ar gas for transferring vaporized fine particles is introduced from the window side of the inner tube and discharged from an opening of the outer tube. A sample is set in the opening via an O-ring.

ICP-MS

A VG PQ ExCell (made by Thermo Electron K.K) was used. NIST SRM 1765 (a low-alloy steel, Co = 0.006%: reference value, NIST: National Institute of Standards and Technology, SRM: Standard Reference Materials) was used for the analysis of LA samples and the sensitivity was adjusted by using ^{59}Co .

Experimental Method

Measurements by LA-ICP-MS

Sample surfaces were polished using a zirconium-based abrasive belt (Z76X, grain size: 60, made by Riken Corundum Co., Ltd.). The laser pre-irradiation time was set at 30 s, the total integration time per ion was set at 3 s, and the cleaning time after the finish of an analysis was set at 30 s. The analytic conditions are shown in Table 1. The analytical performance of LA-ICP-MS was investigated using the steel standard reference materials shown in Table 2.

Table 1. Apparatus and analytical conditions for the developed LA-ICP-MS

Laser ablation	
Laser	Nd :YVO ₄
Wavelength	1064nm
Average power	0.6W
Pulse frequency	10kHz
Pulse width	10ns
Beam expander	× 5
Focal length	100mm
Spot diameter	50μ m
X- scan length	2.0mm
Y- scan length	2.0mm
X- scan frequency	43Hz
Y- scan frequency	2.5Hz
Ar flow	1.0L/ min
Diameter of O- ring	22mm
ICP	
Coolant gas flow	12L/ min
Auxiliary gas flow	1.0L/ min
RF power	1.4kW
Carrier gas flow (for solution analysis)	0.4L / min
Mass spectrometer	
Dwell time	10 ms/ channel
Channels per mass	3
Sweeps	100
Pre laser radiation	30s
Cleaning	30s
Monitor for tuning	
Solution- ICP- MS	In (1ng/ ml)
LA- ICP- MS	Co (NIST1765)

Table 2. Composition of NIST, Brammer and JSS SRM samples

sample	(%)			
	B	As	Sb	Pb
(a)				
NIST- 1765	0.0009	0.0010	0.0010	0.0003
NIST- 1766	0.0004	0.0035	0.0005	0.003
NIST- 1767	0.0010	0.0005	0.0020	<0.0001 ^a
(b)				
BS 61C	0.00005 ^b			
NIST- 1265a	0.00013			
NIST- 1261a	0.0005			
BCS/ SS 112	0.0007			
NIST- 1767	0.0010			
(c)				
BS 250		0.003	0.0004	
NIST- 1768	<0.0002 ^a	<0.0001 ^a	<0.0001 ^a	<0.0001 ^a
JSS 1000- 1	0.00002 ^a	<0.0002 ^a	<0.00002 ^a	<0.00001 ^a
(d)				
NIST- 1265a	0.00013	0.0002 ^a		0.00001
BS 250		0.003	0.0004	
BS 3941		0.003	0.0007 ^a	0.0010
BS 61C	0.00005 ^b	0.003	0.0004	0.00003
BS 61D	0.0004	0.005		0.0003
BCS/ SS 112	0.0007	0.0021		
FCRM 097- 1D	0.0003	0.051		

^a Not certified but informed value

^b Analytical value by conventional method

Chemical Analyses of Steel Samples

Chips were sampled from the steel standard reference materials and after the acidolysis of the samples, B was analyzed by solvent extraction/curcumin absorptiometry and the other elements were analyzed by electrothermal vaporization AAS.

EXPERIMENTAL THEORY[11]

The chemical composition of a generated particle is not the same as that of the original substance because thermal characteristics differ from element to element. However, if thermal irradiation is repeated on the same area of a sample, this non-uniformity will be gradually eliminated as below.

For the sake of simplicity, the following assumptions are made. (1) The heated area is large enough to be able to neglect the effect of a side area; and (2) during laser irradiation, irradiation with thermal energy is spatially and temporally uniform.

A sample initially consists of an element, S and a matrix element, m. $C_s(0)$ is the initial concentration of S in a solid.

$$C_s(0) = X_0/V_0 \dots\dots\dots (1)$$

where V_0 is the quantity of the thermally-affected zone in the solid (= a vaporized part V_v + a melted part V_m), and X_0 is the quantity of the component to be analyzed S in V_0 .

The vaporized part and the melted part are generated by the first irradiation. That is, X_0 is divided into X_v and X_m . X_0 is the quantity of the component to be analyzed S in the vaporized part V_v and X_m is the quantity of the component to be analyzed S in the melted part V_m . The value of X_v/V_v differs from $C_s(0)$ because fractionation occurs. Therefore, the fractionation coefficient, f defines the degree of non-uniformity.

$$f = (X_v/V_v)/(X_0/V_0) \dots\dots\dots (2)$$

The difference of the vaporized quantity from the original quantity remains in the melted part.

$$X_m = X_0 - X_v = X_0(1 - f \cdot V_v/V_0) \dots\dots\dots (3)$$

Because the thermal energy that is given is constant, the same quantity as in the first radiation is thermally affected also in the second laser irradiation. That is, in addition to the quantity of the melted part V_m that remained after the first laser irradiation, a quantity corresponding to the vaporized quantity V_v in the base material not previously thermally affected is newly thermally affected. The quantity of the element $X_0(2)$ present in the new thermally-affected zone due to this second laser irradiation is given by the following equation:

$$X_0(2) = X_m(1) + C_s(0) \cdot V_v = X_0(1) \cdot (1 - f \cdot V_v/V_0) + X_0(0) \cdot V_v/V_0 \dots\dots\dots (4)$$

Hence, the quantity of X that is vaporized, $X_v(2)$, and the quantity that remains in the melted part, $X_m(2)$, are respectively given as follows:

$$X_v(2) = f \cdot X_0(2) \cdot V_v/V_0 \dots\dots\dots (5)$$

$$X_m(2) = X_0(2) - X_v(2) = X_0(2) \cdot (1 - f \cdot V_v/V_0) = X_0(1) \cdot (1 - f \cdot V_v/V_0)^2 + X_0(0) \cdot V_v/V_0 \cdot (1 - f \cdot V_v/V_0) \dots\dots\dots (6)$$

When the inductive method is adopted, the quantity of the element S that is affected by the $(n + 1)$ th laser irradiation, $X_0(n + 1)$, is given as follows:

$$X_0(n + 1) = X_m(n) + C_s(0) \cdot V_v = X_0(1) \cdot (1 - f \cdot V_v/V_0)^n + X_0(0) \cdot V_v/V_0 \cdot \sum_{k=0}^{n-1} (1 - f \cdot V_v/V_0)^k$$

$$= X_0(1) \cdot (1 - f \cdot V_v/V_0)^n + X_0(0) \cdot V_v/V_0 \cdot \left\{ \frac{1 - (1 - f \cdot V_v/V_0)^n}{f \cdot V_v/V_0} \right\} \dots\dots\dots (7)$$

$$X_v(n + 1) = f \cdot X_0(n + 1) \cdot V_v/V_0 = X_0(1) \cdot (1 - f \cdot V_v/V_0)^n \cdot f \cdot V_v/V_0 + X_0(0) \cdot V_v/V_0 \cdot \left\{ 1 - (1 - f \cdot V_v/V_0)^n \right\} \dots\dots\dots (8)$$

Because $|1 - f \cdot V_v/V_0| = |1 - X_v/X_0| < 1$, $(1 - f \cdot V_v/V_0)^n$ approaches 0 as n increases. Therefore, $X_v(n + 1)$ can be approximated to $X_0(0) \cdot V_v/V_0$. It follows that the fractionation coefficient, f converges gradually to 1 as thermal irradiation is repeated.

The above equations hold only when a region, in which a melted part remaining after laser irradiation, and a base material that has not been thermally affected, coexist, is subjected to the next laser irradiation. On the other hand, in order to ensure that all substances are vaporized, it is necessary that the heated spot reach to a sufficiently high temperature of 6000 K or more.

From the foregoing, it is possible to eliminate fractionation in LA by irradiating a sufficiently wide region by a pulse laser having an appropriate output repeatedly and without a vacant space. As a result of thermal conductivity simulation, the conditions of laser ablation were determined as shown in Table1.

RESULTS AND DISCUSSION

Investigation of Stability of Ion Intensity

The stability of ^{57}Fe ion intensity is shown in Figure. 2 compared with the results of a solution analysis method. Owing to the use of the galvanometer scanners and a control system of very good position control capability and the optimization of conditions such as scanning speed, the dispersion of ion intensity in LA-ICP-MS became 2.4% as a relative standard deviation (RSD) and almost reaches the stability as in the solution analysis method.

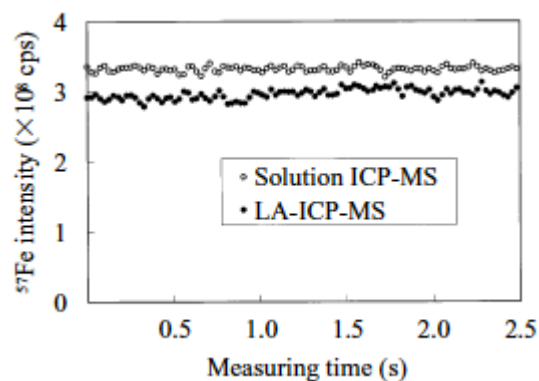


Figure 2¹¹⁾. Intensity-time profile of ^{57}Fe measured by the developed LA-ICP-MS compared with solution ICP-MS

Precision And Sensitivity of LA-ICP-MS

The correlation between the contents and ion intensities or intensity ratios of each element to ^{57}Fe was investigated to verify the analytical precision and sensitivity of LA-ICP-MS for steel samples, using the steel standard reference materials NIST 1765, 1766 and 1767 (Table 2(a)). The results of the investigation are shown in Figure. 3. In the LA method, the ion intensity of Ar gas was used as a blank value, and the intensity ratio was found after the subtraction of the ion intensity of the Ar gas for each sample from the ion intensities of the elements to be analyzed and of ^{57}Fe . Repetitive analytical precision is also shown in Figure. 3 by an error bar (1σ , $n = 5$). The results show that the Fe internal standard method was effective.

For B, the coefficient of correlation between the concentration and ion intensity ratio in the trace concentration region of 4 to 10 $\mu\text{g/g}$ was 0.9993 and a good linear relationship was thus obtained. RSD of 4% or less were obtained in the ion intensity ratio to ^{57}Fe , although some samples showed variations of 6% in RSD for ion intensity.

For As, the coefficient of correlation was 0.9991 in the region of 5 to 40 $\mu\text{g/g}$ and the RSD of the ion intensity ratio was 2% or less.

For Sb, the coefficient of correlation between the certified value in the region of 5 to 20 $\mu\text{g/g}$ and ion intensity ratio was 0.989 and the linear relationship was somewhat poor compared to the other elements, although the repetitive measurement precision of the ion intensity ratio was 2%, which is good in terms of RSD. However, when chips were taken from block samples, and the analytical values were found from electro-thermal vaporization AAS after the dissolution of the chips in an acid, and the analytical values were plotted as abscissa, the coefficient of correlation improved to 0.996. Thus, a linear relationship that substantially intersects the origin was obtained.

For Pb, both the linear relationship of the correlation curve in the range of 1 to 30 $\mu\text{g/g}$ (the coefficient of correlation: 0.9994) and the repetitive analytical precision (RSD < 2%) were good.

The lower limit of determination of each element was calculated. The samples prepared as high-purity irons, which

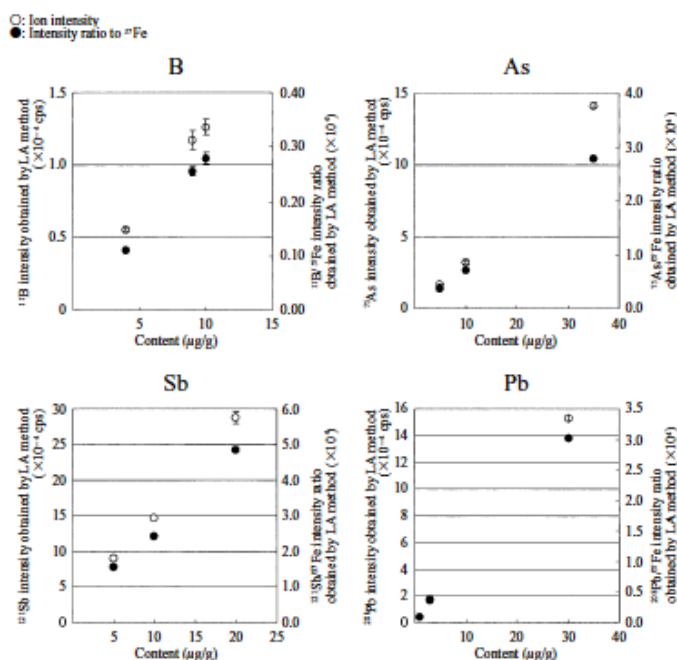


Figure 3¹¹⁾. Correlation between contents and ion intensities or intensity ratios of each element to ^{57}Fe

are shown in Table 2(c), were analyzed by using the correlation shown in Figure.3 as the calibration curve. And a value that is ten times as high as the standard deviation (10σ) was regarded as the lower limit of determination. The results are shown in Table 3. It became apparent that the determination is possible with high sensitivities, which are on the level of several tens of ng / g for B and As and several ng / g for Sb and Pb.

Table 3. Lower limits of determination in steel by LA-ICP-MS

Element	LLD of LA-ICP-MS ($\mu\text{g/g}$)
B	0.06
As	0.02
Sb	0.004
Pb	0.005

Accuracy of Analytical Values in LA-ICP-MS

To verify the accuracy of the analyses of trace elements in steel by this method, steel standard reference materials were used. The samples shown in Table 2(d) were determined by using the correlation shown in Figure.3 as the calibration curve. The results are shown in Figure. 4. Here, the value analyzed by the wet chemical analysis about each sample was used for the horizontal axis of graph. In all of the elements, a good correlation of 0.995 or more in terms of the coefficient of correlation was observed between the two kinds of analytical values. This shows that the LA-ICP-MS can be utilized as a direct determination method for trace elements in steel samples. The value of σd obtained was 0.2 $\mu\text{g/g}$ for B and Pb, 1.4 $\mu\text{g/g}$ for As, and 0.7 $\mu\text{g/g}$ for Sb.

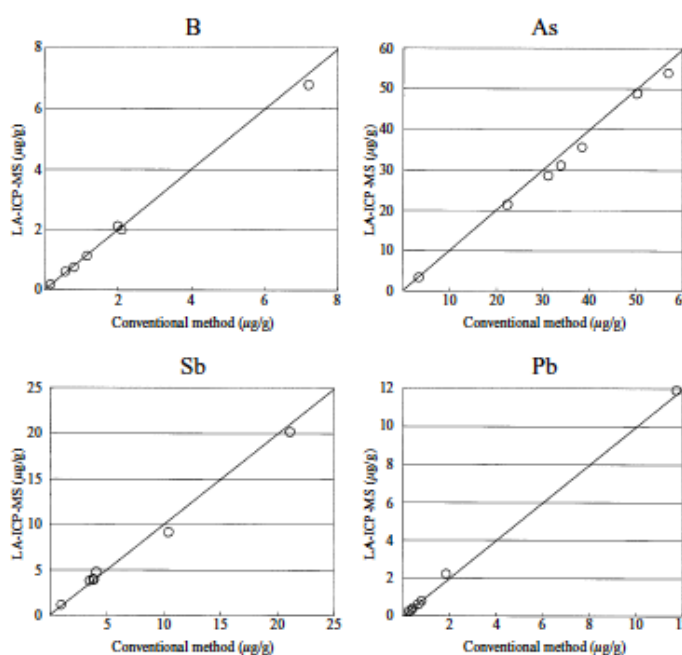


Figure 4¹¹⁾. Correlation of analytical value between conventional method and LA-ICP-MS

Evaluation of Practicality of Boron Analysis

Among the four elements, the analysis of trace amounts of B requires the longest time to perform. Particularly in the region of infinitesimal amounts of 2 $\mu\text{g/g}$ or less, it is necessary to perform the separation of B by its distillation from other components. This preparation requires half a day or a whole day. With direct analysis by LA-ICP-MS, the measuring time is only a minute or so for each sample, and it is possible to complete the analysis within 1 hour, including the time required for pretreatment (polishing work)

to obtain a smooth surface and the preparation of calibration curves. Therefore, the direct analysis by LA-ICP-MS can contribute greatly to the shortening of the analysis time if satisfactory analytical precision can be obtained. Accordingly, the tolerance of repeatability by the LA-ICP-MS method was compared with the values described in JIS G 1227, "Iron and Steel-Methods for Determination of Boron Content." The results are shown in Table 4. R-value was used for accuracy evaluation of LA method. R value shows the difference of two analysis results when the same sample was analyzed twice repeatedly in a short time.

R values below the tolerance are obtained at or below the 5 $\mu\text{g/g}$ level, whereas R is larger than the tolerance in the concentrations of 0.5 $\mu\text{g/g}$ and 1.3 $\mu\text{g/g}$. Since R value of the sample with a concentration of 1.3 $\mu\text{g/g}$ is larger

than others, it could be thought that B exists inhomogeneously within the sample. For this reason, the trial for decreasing an analysis error was carried out. Specifically, the area to which a laser is applied was expanded quadruple (4 mm × 4 mm). The results are also shown in Table 4. In order to eliminate the elemental fractionation, the laser pre-irradiation time was also increased to 120 s. About all samples shown in this table, better precisions were obtained.

B concentration ($\mu\text{g/g}$)	Repeatability($\mu\text{g/g}$)		
	JIS G 1227	LA-ICP-MS	
		2mm \times 2mm	4mm \times 4mm
0.5	0.01	0.02	0.01
1.3	0.04	0.42	0.07
5	0.31	0.17	0.07
7	0.51	0.25	0.11
10	0.85	0.33	0.17

Table 4. Comparison of repeatability between conventional method and LA-ICP-MS

CONCLUSIONS

The following knowledge was acquired as a result of investigating the analysis characteristic of the LA-ICP-MS method for B, As, Sb and Pb.

(1) Analytical Precision: By using a internal standard method for taking a ratio with ^{57}Fe , developed LA-ICP-MS is capable analyzing $\mu\text{g/g}$ concentration levels in less than 3% of RSD.

(2) Sensitivity: The lower limit of determination is estimated at a range from several $\mu\text{g/g}$ to dozens of $\mu\text{g/g}$.

(3) Accuracy of Analytical Values: The results obtained by the LA method were well in agreement with the results analyzed by a wet chemical analysis method. 0.995 or more correlation coefficients were able to be obtained.

REFERENCES

- [1] A. L. Gray : *Analyst.*, 110, 551 (1985)
- [2] N. J. G. Pearce, W. T. Perkins, R. Fuge : *J. Anal. At. Spectrom.*, 7, 595 (1992)
- [3] C. Lelope, P. Marty, D. Dall'ava, M. Perdereau : *J. Anal. At. Spectrom.*, 12, 945 (1997)
- [4] Arrowsmith : *Anal. Chem.*, 59, 1437 (1987)
- [5] M. Guillong, D. Günther : *J. Anal. At. Spectrom.*, 17, 831 (2003)
- [6] T. Hirata, Y. Asada, A. Tunheng, T. Ohno, T. Iizuka, Y. Hayano, M. Tanimizu, Y. Orihashi : *Bunseki Kagaku.*, 53, 491 (2004)
- [7] S. E. Jackson, D. Günther : *J. Anal. At. Spectrom.*, 18, 205 (2003)
- [8] T. Hirata : *Anal. Chem.*, 75, 228 (2003)
- [9] R. E. Russo, X. L. Mao, O. V. Borisov, Haichen Liu : *J. Anal. At. Spectrom.*, 15, 1115 (2000)
- [10] S. M. Eggins, L. P. J. Kinsley, J. M. G. Shelley : *Appl. Surf. Sci.*, 129, 278(1998)
- [11] T. Ishida, T. Akiyoshi, A. Sakashita, S. Kinoshiro, K. Fujimoto, A. Chino : *Bunseki Kagaku.*, Vol. 55, 4, 229 (2006)

CHARACTERIZATION OF THIN FILMS ON ROUGH STEEL SUBSTRATES: WHICH METHOD FITS BEST?

Ann De Vyt, Chris Xhoffer

OCAS NV, John Kennedylaan 3, 9060 Zelzate, Belgium

Summary

To support the development of new, innovative coatings with a thickness in the nanometer range many questions are raised concerning the correct way to analyze them. Thickness, composition, lateral distribution, depth homogeneity ... are important parameters. The world of micro electronics has a lot of experience in this subject. A material such as steel is however more difficult to characterize since the surface is very rough.

A full assessment of the possibilities of several conventional and less conventional techniques, both regarding their technical and cost capabilities, was performed - the effect of roughness on the analytical capabilities of the techniques being an important feature.

Three different coatings were studied dealing with three levels of analytical difficulties:

- Cr^{III} passivation layers that are inorganic wet applications. Cr is a relatively easy element to analyze and the layer is inorganic. This makes this coating rather easy to analyze.
- CVD SiO₂ layers that are inorganic vapor deposited layers. Due to their inorganic nature and their homogeneous distribution across the surface, they are fairly easy to analyze.
- Silane layers that are organic wet applications. Because of their organic nature and their heterogeneous distribution across the surface, they are very difficult to study.

In general the techniques used to characterize these coatings can be divided in 2 classes: local analysis techniques and bulk techniques. Both are essential because the information they give is complementary. Quantification is difficult and remains dependent on the presence of good standard samples. The table below shows the advantages and disadvantages of the techniques used in OCAS.

Local Technique	Advantage	Disadvantage
FIB	Reference because thickness is visible	Small sampling area, time consuming, expensive
XPS	Nanometer resolution in depth and micrometer resolution laterally. Bonding information: good to detect variations in chemical identity	Small sampling area, time consuming, quantification depends on matrix matched standards, expensive
FTIR	Both local and bulk analysis is possible, cheap, chemical (organic) information	Quantification problems, quantification depends on matrix matched standards, peak shifts with thickness
Bulk Technique	Advantage	Disadvantage
ICPMS/OES	Reference technique because of large sampling area and complete destruction of the coating	Destruction of the coating not always straightforward, time consuming, expensive, elemental information
GDOES	Fast technique giving both depth profiling information and thickness information	Quantification depends on matrix matched standards
XRF	Fast technique with low matrix dependency, non destructive	Only mean thickness is measured

Introduction

Coating characteristics such as corrosion resistance, weldability, hardness and visual appearance define the use and value of today's steel products by their high economically added value. Future advanced products rely on the implementation of emerging nanotechnologies to increase these characteristics. As such new and innovative coating technologies are more and more focused on films having a thickness inferior to $1\mu\text{m}$. For such thin films, in/off-line inspection, the quality control and the after sale support is not evident anymore because there is in general lack of methodology, knowledge and Certified Reference Materials (CRM's). In order to gain a competitive advantage, not only new tools for production, but also the characterisation on the nanometer scale should follow this switch towards nanotechnologies. The world of micro electronics has a lot of experience in this subject. A material such as steel is however more difficult to characterize since the surface is very rough.

This study summarizes the comparison of various analytical techniques concerning their technical capabilities to determine thickness, composition and distribution of a thin coating on a rough substrate.

It shows the results obtained by OCAS in the course of an RFCS project (THINFILM, RFSR-CT-2005-00048). The general conclusions comprise the full results of the RFCS project.

Sample description

To assess both the influence of coating and of roughness, 3 types of coatings were applied to a set of hot dip galvanized (HDG) substrates with different roughness ranging from $R_a 0.4\mu\text{m}$ to $R_a 1.59\mu\text{m}$. The selection of the applied coatings was based upon the expected distribution of the coating on top of the rough steel substrate.

- Chemical Vapour Deposited (CVD) coatings. Only minor variations in layer thickness with surface topography are anticipated in these coated samples (as illustrated in Fig.1a).
- Silanes. These layers are applied as a liquid and are anticipated to show „filling up“ effects, as illustrated in Fig. 1b.
- Pre-treatments: Cr III passivation layers. Not only final thickness control but the appropriate build-up of the layer are key factors to guarantee the properties aimed for.

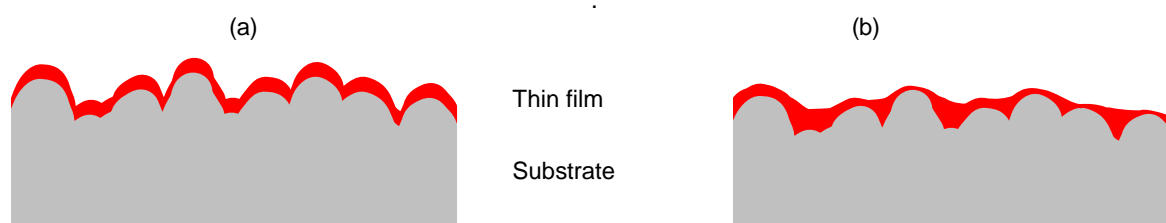


Fig. 1: Two extreme examples of a thin film distribution on top of a rough substrate

Experimental

Both micro and macro techniques were used to study the thin coatings.

Micro techniques are techniques with a lateral resolution smaller than the width of the substrate roughness. This means they enable local analysis. The following instruments were tested in OCAS:

- XPS X-ray Photoelectron Spectroscopy instrument PHY Quanterra with a minimum probe size of $10\mu\text{m}$. The surface of the sample is studied and thickness is measured by depth profiling.
- FIB Focused Ion Beam technique that enables local slicing of the sample surface. This is combined with either SEM or TEM imaging to visualize the thickness of the coating. Lateral resolution is in the nanometer range.
- FTIR Fourier Transform Infrared Spectroscopy Thermo Nicolet6700 with Continuum microscope using a spot size of $20\mu\text{m}$. The surface of the sample is studied and local mappings can show the lateral distribution of the coating.

Macro techniques are bulk techniques that are used to determine quantitatively the surface coverage of the coating on the substrate. The following instruments were tested in OCAS:

- ICPMS Inductively Coupled Plasma Mass Spectrometry Thermo Element II is used to quantify the surface coverage after selective removal of the coating from the substrate. The sampling width is a few square centimeters.
- GDOES Glow Discharge optical Emission Spectrometry Spectruma GDA750 enables fast depth profiling. The sampling width is 15 square millimeters.
- XRF X-ray Fluorescence Spectro Xepos is also used to quantify the surface coverage. The sampling width is a few square centimeters.

Results

I. Analysis of CVD SiO₂ coated samples

Regarding the **composition of the coating** all the techniques give valuable information. Some of them, such as XRF and ICPMS, result merely in the concentration of Si. Others, such as GDOES and XPS give also information of the presence of other elements than Si and O, and enable the determination of the Si/O ratio. XPS, FTIR and Raman give information about the chemical bonding of Si.

Regarding the **homogeneity of the coating in depth and laterally**, several techniques are interesting. All sputter techniques used (GDOES, XPS) give information about the coating variation in depth. However, care must be taken with sputter techniques because the substrate roughness deteriorates the depth resolution at the interface, which could lead to misinterpretations.

Micro analysis techniques such as XPS (with focused X-ray beam), FIB-TEM and FTIR all gave information about the lateral homogeneity of the coating (see fig. 2). For these substrates, where the roughness is broader than the lateral resolution of the techniques, local information could be obtained.

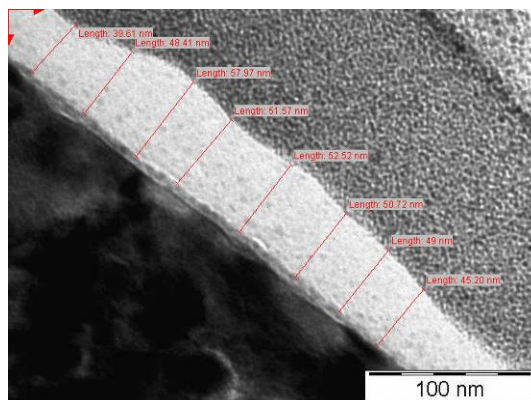


Fig. 2: FIB lamella of a thin CVD layer studied with TEM

Concerning the **thickness of the coating**, all techniques were able to give a signal response that correlates with thickness. Because of the uniform thickness of these coatings, both macro- and micro-analytical techniques are suited to reveal the average coating thicknesses and/or coating weights. The quantification of the signal is however not evident. Ideally FIB-TEM and wet chemical analysis by ICPMS are reference techniques because they either visualize the coating thickness directly or, dissolve the coating quantitatively regardless of the underlying substrate. Fortunately the coating chemistry is very similar to SiO₂ which means that standard thermally grown SiO₂ on Si wafers can also be used as calibration samples.

An average thickness of all quantified techniques is given below.

Ra (μm)	average coating thickness (nm)	standard deviation	relative scatter (%)
0.4	85	13	15
0.81	72	13	18
1.15	54	6	12
1.59	49	9	19

The **effect of roughness** on the technical capabilities of the techniques is rather low. The depth resolution (or sharpness of the interface) is deteriorated by the roughness for sputtering techniques. However in this case it did not lead to incorrect conclusions.

The influence of the roughness on the **CVD deposition system** is shown in Fig. 3 where thickness is plotted as a function of substrate roughness (only those techniques were selected for which at least 3 or 4 different samples were analyzed). The left graph represents the macro-analytical techniques. The graph on the right represents the micro-analytical techniques. The FIB data is shown in both graphs as a reference. For all techniques, a decrease in thickness with increasing roughness is observed. It is remarkable that for the micro-analytical techniques, also a very good agreement is obtained.

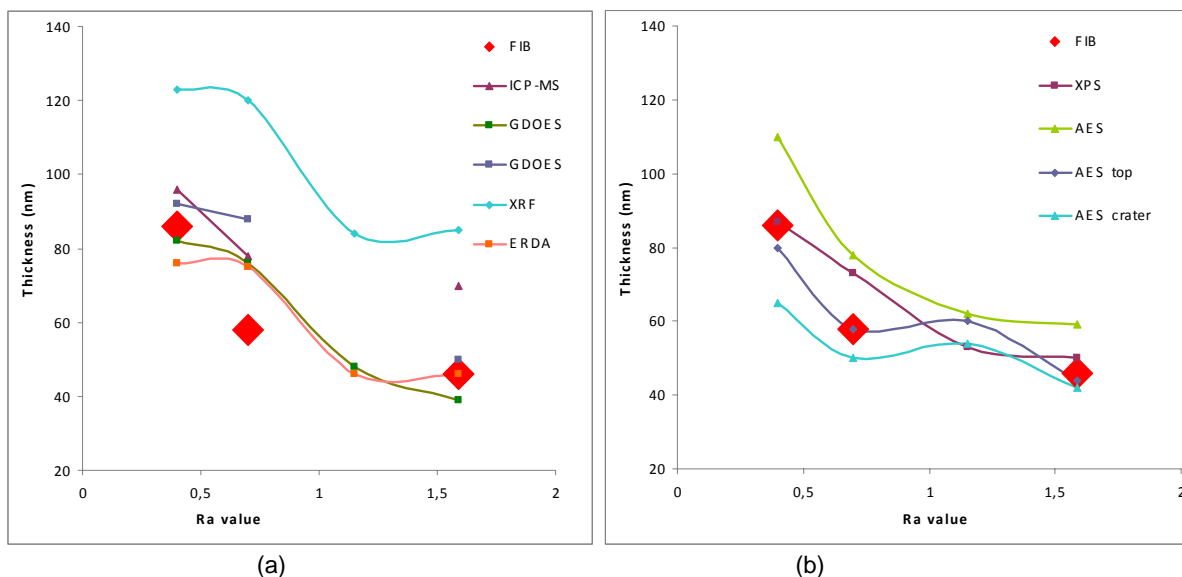


Fig. 3: Measured thickness of the SiO₂ CVD coating as a function of the roughness (Ra-value) obtained with (a) macro-analytical techniques and (b) micro-analytical techniques.

Although not all techniques find the same absolute values, all techniques converged to the same general conclusions.

1. The SiO₂ coating is continuous and appears to be homogeneously distributed across the surface of the substrate.
2. The thickness of the SiO₂ coating is constant regardless of the measurement position. This means that the coating application follows the substrate roughness as shown in fig. 1a.
3. All analyses are consistent i.e. that the composition of the CVD coatings is homogeneous throughout the whole thickness. No organic compounds are detected. C is only present as a surface contamination. This means that the organic precursors of the CVD process are completely burned into CO₂ and H₂O.

4. Quantification of the measurements to obtain thickness values is possible using thermally grown SiO₂ on Si wafer for most techniques. The typical thickness ranges from 20-100 nm.
5. A negative correlation exists between substrate roughness and coating thickness. This means that rougher substrates have a thinner coating. This tendency was confirmed by a large number of techniques. This can be explained as follows: during a stable CVD process where a gas to solid deposition reaction occurs, the amount of vapor deposited remains constant. If the surface roughness is higher, the projected area contains the same amount of deposit (mg/m²), but for a higher roughness, the specific surface increases and therefore the thickness has to decrease.

II. Analysis of Silane coated samples

Regarding the **composition of the coating** all techniques give a variety of useful information as stated for analysis of CVD samples.

Regarding the **homogeneity of the coating in depth and laterally**, several techniques are interesting as stated for analysis of CVD samples.

Concerning the **thickness of the coating**, all techniques were able to give qualitative response that correlates with thickness. However, the characterization of thin silane coating on rough steel substrates is far from evident. There is a strong local variation of the silane coating thickness (see fig. 4). Tops and valleys of the roughness show very different thicknesses. This was confirmed by all techniques able to perform small area measurements. The silane coatings fill up substrate cavities during application and the coating thickness on rougher substrates is significantly higher than for samples having less roughness. Because of the heterogeneity of the coating thickness induced by the roughness of the substrate, macro-analytical techniques can only reveal the average coating thicknesses and/or coating weights. Also it is virtually impossible to compare the results of micro and macro analytical techniques and as such determine the accuracy of the results.

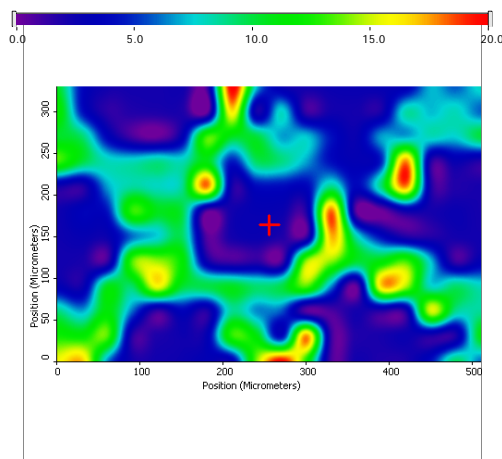


Fig.4: FTIR mapping acquired by Continuum microscope.

The **effect of roughness** on the technical capabilities of the techniques is rather low and comparable to the analysis of CVD samples.

The major problem for the analysis of silane coatings is **quantification**. Silanes are much more difficult to analyze in a consistent way than SiO₂. The cause of this is their partial organic nature and the large variations of the thickness. Most techniques need matrix matched standards for quantification, and for silanes they are not available. Only FIB gives absolute thickness values but due to the heterogeneity of the thickness, the FIB results can not be compared to macro analytical results. The scatter is just too large.

The other reference technique, wet chemical analysis, did not succeed due to incomplete digestion of the etched coating. No standards exist and in-house standards are difficult to prepare because they degrade in time.

Also the comparison between techniques that determine the surface coverage (such as GDOES, XRF,...) with techniques that determine the absolute coating thickness (such as FIB, XPS,...) is impossible because the molar mass and the density of the coating are not well known or even unknown.

It is thus irrelevant to correlate absolute results of various techniques with each other.

In the table below the possibilities of each technique used at OCAS are summarized.

ICPMS	The etching did not lead to stable solutions. The results are not reliable and have to be improved.
GDOES	GDOES intensities correlate well with other techniques. Density and sputter rate of silanes differ from those of SiO ₂ . This means that unknown errors are introduced in the quantification.
FTIR	FTIR intensities correlate well with other techniques but no possibilities for quantification are found. Moreover, thicker coatings can give rise to peak shifts and thus to wrong results. For higher thicknesses (> 500 nm) a non linear relationship might occur.
XRF	This technique is probably the least matrix dependent. Quantification is possible using silica standards. However, the standards used have a steel substrate as opposed to the Zn substrate of our samples. This probably induces errors as well.
XPS	XPS gives local information which is indispensable. Towards the quantification of thickness they have the same problem as GDOES and other sputtering techniques: the sputter rate is only indicative.
FIB	FIB remains a reference technique if the exact thickness needs to be determined. However due to the large local variations of thickness, no correlation with other techniques could be obtained.

The effect of the surface roughness on the **silane deposition system** is shown in Fig. 5 below where various techniques are compared. Although the absolute values of thickness or coating weights are not identical for all techniques, the same trend is found by all partners namely: lower roughnesses have a thinner coating, high roughnesses have thicker coatings.

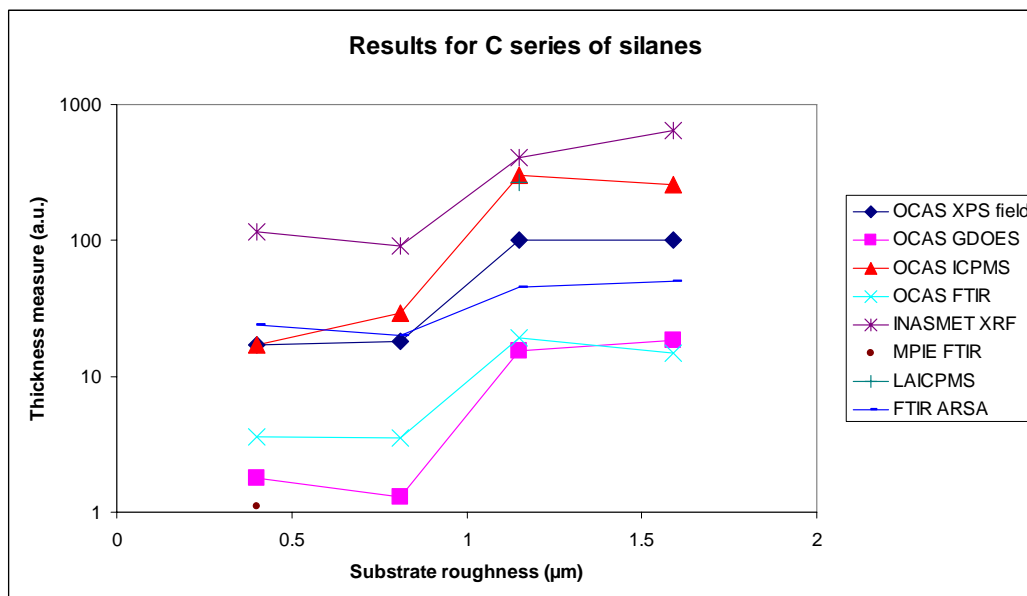


Fig. 5: Intensity versus roughness for silanes

Although not all techniques find the same absolute results, all techniques converged to the same general conclusions.

1. The silane coating is very heterogeneously distributed across the surface of the substrate.
2. The thickness of the silane coating varies a lot depending on the measurement position. Craters (or valleys) in the roughness show thicker coatings than on the tops of the roughness. This means that the coating application fills the substrate roughness as schematically demonstrated in fig. 1b.
3. All analyses are consistent i.e. that the composition of the silane coatings is homogeneous throughout the whole thickness.
4. Quantification of the measurements to obtain thickness values is very difficult because of the absence of standard/reference samples. A reference technique such as ICPMS was not available to provide in-house standards. FIB-TEM is a valid reference technique, but due to the large heterogeneity of the thickness it is statistically not relevant enough. The typical estimated thickness ranges from 40-1000 nm.
5. A positive correlation exists between substrate roughness and coating thickness. This means that rougher substrates have a thicker coating. This tendency was confirmed by a large number of techniques. This is opposite to what was observed for the CVD coatings and can be explained by the filling of the craters.

III. Analysis of Cr(III) coated samples

In industrial environments, the concentration of Cr in a chromate coating is expressed as a surface specific coating weight (mg/m^2 of Cr). In this way, the Cr-content is directly measurable by most analytical techniques and no knowledge of the coating density or chemical formula is required for conversion into thickness. Where possible, the Cr-content of the passivation is expressed as a surface specific concentration (mg/m^2).

Using ICP-MS, it is possible to measure the Cr-content in absolute values. Especially on HDG substrates, the Zn-coating is selectively dissolved from the steel substrate, including the Cr-layer in this process. This technique is therefore used as the reference method and can provide reference samples for other techniques as XRF, GDOES and FTIR. The standard deviations for the determination on the Cr-concentrations are very low: $5 \text{ mg}/\text{m}^2$ absolute or less than 10% relative which is extremely good.

In order to have an idea of the absolute thickness of these E-passivation layers, a FIB cross section was made. The thickness of these chromate coatings is typically below 200nm (see fig. 6).

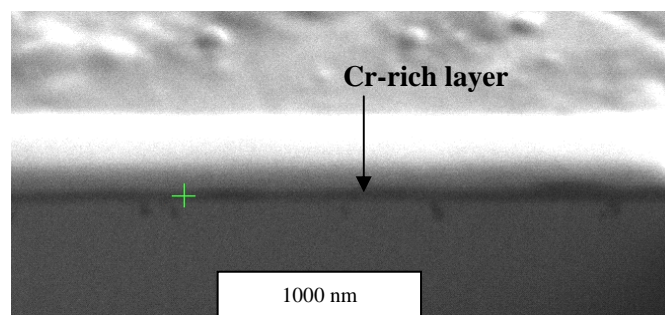


Fig. 6: FIB cross section of an approximate 200 nm Cr(III) passivation layer.

General conclusions

During this project 3 different coatings were studied dealing with three levels of analytical difficulties:

- Cr^{III} passivation layers which are inorganic wet applications. Cr is a relatively easy element to analyze and the layer is inorganic. This makes this coating rather easy to analyze.
- CVD SiO₂ layers which are inorganic vapor deposited layers. Due to their inorganic nature and their homogeneous distribution across the surface, they are fairly easy to analyze.
- Silane layers which are organic wet applications. Because of their organic nature and their heterogeneous distribution across the surface, they are very difficult to study.

A broad variety of techniques was used to study them. In general the techniques can be divided in 2 classes: local analysis techniques and bulk techniques. Both are indispensable because the information they give is complementary. Quantification is difficult and remains dependent on the presence of good standard samples.

The table below shows a comparison of all techniques used. In blue 2 reference techniques are highlighted that are indispensable for methodology purposes. In green XRF is highlighted as an easy, cheap, accurate and industrially applicable technique.

Technique	Micro	Macro	Quantification	Analysis time	Cost
ICPMS/OES		+	Mostly possible	Slow	Medium
FTIR	+	+	Matrix matched standards needed	Fast	Low
GDOES		+	Matrix matched standards needed	Fast	Low
XRF		+	Standards needed	Fast	Low
FIB	+		Absolute	Slow	High
XPS	+		Matrix matched standards needed	Slow	High

Acknowledgments

We owe our sincere thanks to the European Commission for this RFCS project (THINFILM, RFSR-CT-2005-00048) and to the partners within this project (Thyskrup, Arcelormittal global R&D Maizières, Swerea Kimab AB, Chemical research center of the Hungarian academy of sciences, Inasmet, Vrije Universiteit Brussel, MPIE and ISAS). All colleagues from the OCAS chemistry department who were involved in this project are greatly acknowledged.

MECHANICAL RESISTANCE OF ALUMINIUM-EPOXY ASSEMBLIES AS A FUNCTION OF ALUMINIUM SURFACE TREATMENT WITH ATMOSPHERIC PLASMA

J.A.S. Bomfim¹, C. Sperandio^{1,2}, J. Petersen^{1,3}, J. Bardon¹, A. Laachachi¹, H. Aubriet¹, D. Ruch¹

¹ AMS - Centre de Recherche Public Henri Tudor - 66 Rue de Luxembourg BP 144,
L-4002 Esch-sur-Alzette, Luxembourg

² LMOPS, CNRS UMR 7132-Université Paul Verlaine Metz, Supélec, 2 Rue Edouard Belin 57070 Metz, France

³ IPCMS, CNRS UMR 7504, Université de Strasbourg, 23 rue du Lœss, 67034 Strasbourg Cedex 2, France

ABSTRACT

Adhesive bonding is providing superior assembly properties regarding its enhanced fatigue properties, good corrosion resistance, and ability to seal or damp the assembly. For instance, recent technological breakthroughs were achieved in the field of lightweight automotive bodies from extruded aluminium sections bonded using advanced structural adhesives. Hence, aluminium-epoxy system is widely studied for structural adhesive bonding. This work reports the influence of aluminum plasma surface treatment on its surface properties and on adhesive bond strength. Two different atmospheric plasma treatments were carried out: surface activation with air(oxygen plasma and organic coating with plasma polymerized allylamine. Both atmospheric plasma treatments showed an improvement of mechanical properties of the assembly. Several points are discussed to explain the effects of atmospheric plasma treatments on adherence.

Keywords: epoxy adhesive, assembly, aluminium, plasma, surface treatment, plasma polymerisation

I- INTRODUCTION

Epoxy adhesives are widely used for the assembly of metal parts because of their excellent adhesion, chemical resistance and good mechanical properties. Aluminium-epoxy assembly bond strength and reliability is highly dependent on the substrate surface properties. Some studies describe cold plasma treatment as an efficient and environmentally friendly tool to increase the wettability of aluminium [2] and to improve the bond strength on aluminium [3]. Atmospheric Pressure Dielectric Barrier Discharge (APDBD) constitutes a promising alternative compared to low pressure processes, being able to afford an in-line deposition process. These discharges are usually generated in the space between two parallel electrodes covered with a dielectric layer. This dielectric barrier allows the control of the charge, the energy and the distribution of the micro-discharges over the entire electrode [4].

While plasma activation aims at surface modification, plasma polymerization may be best described as a surface coating method, and thus is considered as a straightforward and versatile technique allowing implementing organic coatings with tuneable functional properties. Plasma polymer coatings are known to be pinhole free, highly adherent, with low solubility in various common solvent and having good thermal stability.

The first part of this work deals with the surface treatment of aluminium adherends by N₂/O₂ atmospheric plasmas to generate oxide and hydroxide-rich surfaces on aluminium substrates. The second part explores the formation of organic coatings by atmospheric plasma initiated polymerisation. To deposit amino groups, different approaches have been used, such as plasma polymerization of N-containing monomers or the plasma copolymerization of hydrocarbons in mixtures with N-containing gases such as N₂ or NH₃. For this work we chose allylamine (AA), which is a good candidate to functionalize surfaces with a high retention of primary amino groups.

II. EXPERIMENTAL DETAILS

The metal substrates were 1.5 or 4.0 mm thick aluminium specimens (1024 alloy); the substrates were cleaned and degreased by sonication in acetone for 10 min. The epoxy resin was diglycidyl ether of bisphenol A (DGEBA) mixed with a diamine curing agent diethylenetriamine (DETA). Allylamine (99%) was used without prior purification.

Plasma activation treatment

Aluminium pieces were ultrasonically cleaned in acetone for 10 min, followed by plasma treatment using cold plasma ignited in a semi-dynamic dielectric barrier discharge (DBD) reactor, as shown in Figure 1. The DBD discharge was generated between an earthed bottom aluminium plate and two high-voltage aluminium top plates protected by a glass plate which serves as a dielectric barrier; the substrates were positioned at the bottom electrode.

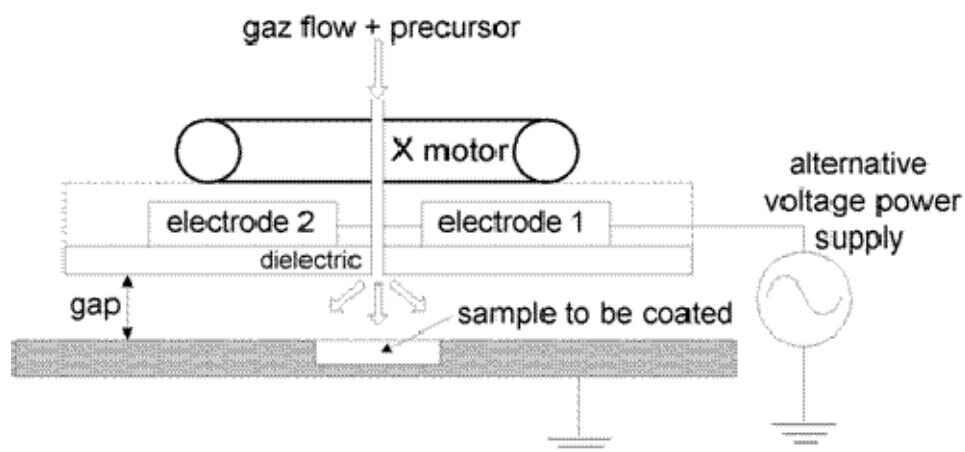


Figure 1, Schematic diagram of DBD reactor used for deposition experiments

A N_2/O_2 gas mixture with different concentrations was injected into the plasma and controlled by mass flow controllers with set points of: 10, 20 and 30 % of O_2 . All experiments were carried out at atmospheric pressure and ambient temperature. During a deposition experiment, the top electrode block moved over the sample at a constant speed (4 m/min) and plasma discharges were generated by an AC power supply.

Plasma polymerisation of allylamine

Plasma polymer allylamine (pPAA) films were deposited using the semi-dynamic DBD reactor described above. The gap between the electrodes was set at 1,7 mm. and Yasuda's parameters were varied during this work. The precursor was atomized at different flow rates and injected into the gas before entering the plasma zone. The carrier gas composition, which was set by mass flow controllers, consisted of a N_2 with a gas flow of 30 slm. During the experiment, the top electrode block moved over the sample at a constant speed (4 m/min). For the coating process, the thickness of the film was controlled by the number of passes. Electrical discharge was varied during each deposition ranging from 21 kV to 30 kV, which corresponded to a power density over the electrodes in the range on 0,6 – 1,6 W/cm^2 .

Assembly processing

Two different kinds of assembly were prepared: single-lap joints for shear testing and dolly-to-surface butt joints for pull-of testing (Figure 2).

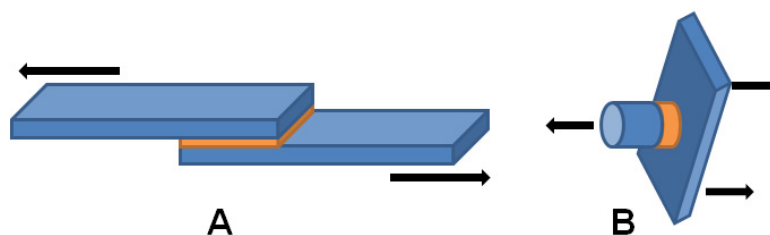


Figure 2, Adhesive assemblies: (A) single-lap and (B) Dolly-to-surface

Measurements

Study of the aluminium surface wettability

The surface energy of the aluminium substrate was calculated by static contact angle measurements using a sessile drop method. A measurement with three liquids was performed after each plasma experiment (i.e. within a couple of minutes). Surface energy was calculated using the Owens-Wendt-Rabel-Kaelble (OWRK) method, where surface energy was split into two components, namely a polar and a dispersive fraction.

Characterization of the aluminium native surface bonds

The atomic composition of the aluminium surface and its chemical bonding states were investigated using XPS (Specs Phoibos 150). During the analysis, the sample was placed in an ultrahigh vacuum environment ($5 \cdot 10^{-9}$ mbar) and exposed to a monochromatic Al K α (1486.7 eV) source operating at 200 W with an anode voltage of 12 kV.

Characterization of shear strength of the adhesive assembly

The video-controlled mechanical testing method utilized was the most recent version of the VideoTraction® system, developed by Apollor SA (Vandoeuvre, France), which gave access to the plastic response of polymers under uniaxial tension from video measurements performed locally at the centre of the specimen. All tests were performed at room temperature under displacement control mode at a crosshead speed of 0.5 mm/min in order to determine the typical load-displacement curve as a function of the surface treatment type.

Characterization of mechanical strength of the adhesive assembly by pull-off testing

Pull-off adhesion tests were performed with a Positest AT-A Automatic Adhesion Tester using 20mm-diameter Al dollies over plasma polymer-coated Al adherends. The epoxy adhesive was cured at room-temperature over 36h. The reported results are an average of at least 6 measurements and compared reference assemblies with Al dollies glued directly over acetone-degreased Al adherends.

ppAA functional group determination

To determine the surface amine density of the plasma polymer allylamine film, UV-Visible absorption spectrometry was used. In an argon atmosphere, films deposited on glass slides were allowed to react with excess 4-nitrobenzaldehyde in anhydrous ethanol solution during 3 hours at 50°C. After the Schiff base reaction, the substrate was thoroughly washed and sonicated with absolute ethanol and dried in vacuum.

III. RESULTS AND DISCUSSION

PART 1: Atmospheric plasma activation

Influence of plasma treatment on aluminium wettability

Surface energy values were visibly different when the oxygen concentration in plasma carrier gas was varied, Figure 3. The aluminium surface degreased with acetone showed a surface energy of 20 mN/m containing a higher dispersive energy (~ 18 mN/m) in comparison to the polar energy (~ 2 mN/m). The polar energy was increased by the plasma activation compared to the AL-DA surface. Surface energy increased with oxygen

concentration; however, at 20 and 30 % of oxygen, a stabilization of the surface energy was observed. Plasma with a high content of oxygen seemed to confer an enhanced hydrophilic character to the native surface.

Surface energy values were visibly different when the oxygen concentration varied in the plasma carrier gas. The polar component, and hence the surface energy, tended to increase with oxygen concentration.

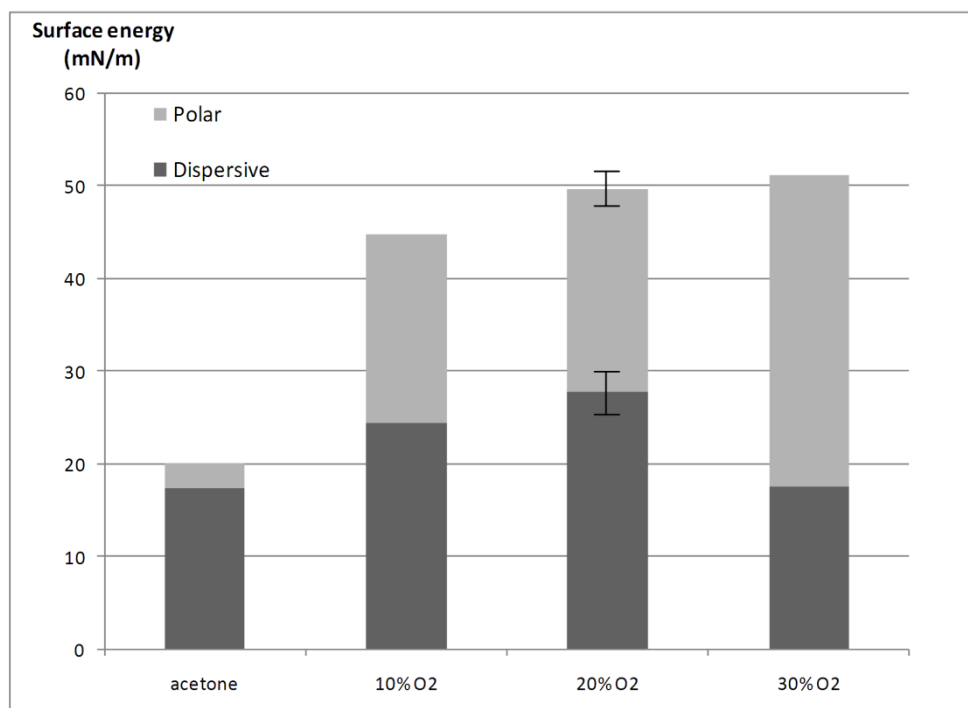


Figure 3, Surface energy (polar and dispersive components) measured on aluminium surface according to the surface treatment type and O₂ concentration in the plasma carrier gas.

Influence of N₂/O₂ ratio on aluminium surface chemistry

In order to understand the adhesion and the interphase formation mechanisms taking part in this study, it is important to know the nature of the aluminium surface chemistry. The peak fitting parameters for C 1s and O 1s peaks decomposition were similar to those determined previously by Debontridder [5].

XPS results obtained for aluminium surface treated in different conditions are given. Figure 4 presents the evolution of the C 1s, O 1s and Al 2p concentrations versus acetone degreasing and N₂/O₂ gas mixture surface treatments (with 10, 20 or 30% O₂).

Carbon was less detected after plasma treatment in comparison to acetone degreasing. At an oxygen concentration higher than 20%, The C 1s concentration is quite similar. The decrease of C 1s detection after plasma treatment can be explained by a decrease of the contamination layer thickness or by an increase of the passivation layer thickness (aluminium oxide).

Both behaviours, the decrease of the contamination layer thickness and the increase of the passivation layer thickness, had an impact on the substrate surface energy. These can be explained, on one hand, by the growth of the passivation layer due to oxygen bonds and explained by the increase of the O 1s peak after plasma treatment; and on the other, by possible etching of the contamination layer of the aluminium substrate by plasma treatment. Such etching could consume amorphous carbon species to form CO, CO₂ and H₂O, which were released in the plasma reactor. It is difficult to conclude on collateral reactions occurring inside the plasma prototype because of the various ions and radicals formed during the plasma treatment. However, results from surface energy and XPS measurements indicate that more oxygen is detected and involved in bonds after plasma treatment, leading to significant increase of the polar contribution to the surface energy.

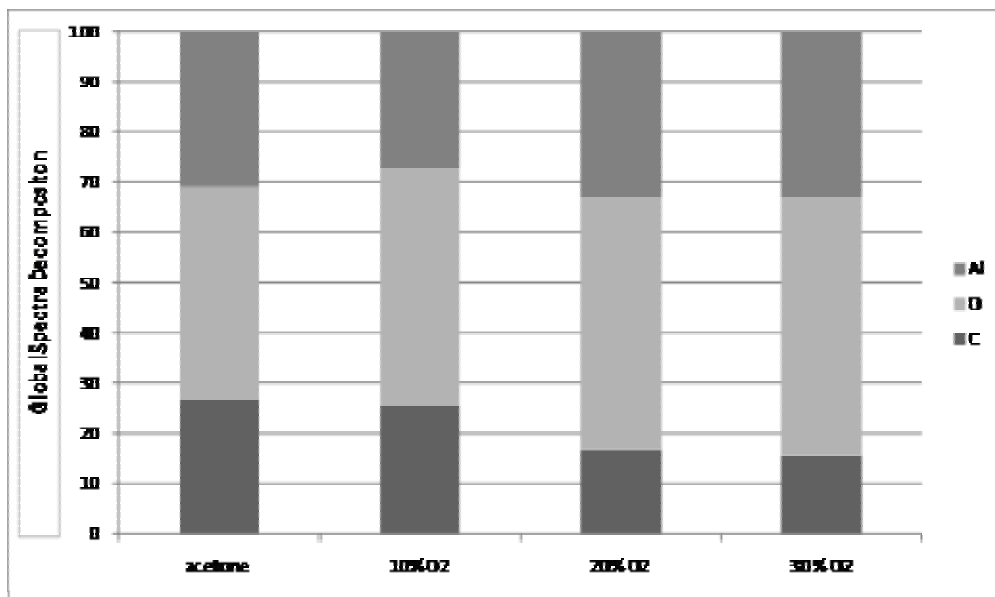


Figure 4, Evolution of the C 1s, O 1s and Al 2p concentrations versus acetone and N₂/O₂ gas mixture surface treatments (10, 20 and 30% O₂)

A greater quantity of aluminium and oxygen was detected by XPS after plasma treatment. This could be explained by growth of the aluminium surface oxide layer. This phenomena has been reported by many authors [6,7,8]. Indeed, oxygen plasma is often used in order to grow the oxide layer of a metallic substrate. This leads to an increase of the hydroxide and/or oxy-hydroxide hydrophilic species and consequently of the surface wettability by the increase of the polar energy fraction.

Load-displacement behaviour of the adhesive assembly

Five samples in each condition were tested to measure mechanical stiffness properties of assemblies. The first series of samples were obtained with substrates treated by acetone (Al acetone/ER/Al acetone), and the second series by atmospheric plasma treatment (Al plasma/ER/Al plasma). The ultimate strength of the assemblies was defined as the value of sample failure (force and strain at break).

Plasma treatment appeared to significantly improve the displacement and strain at break values, compared to the assembly degraded by acetone (which serves as reference sample). Indeed, the average strain increased by 163% for plasma (strain equal to 1,2% versus 0,5% for substrates degraded by acetone). Likewise, force to break values increased from 130 N (degraded adherends) to 350 N (plasma-activated adherends). The plasma treated system stored a much greater mechanical energy before failure.

Plasma treatment increased the hydrophilic character of aluminium substrate by increasing the concentration of aluminium oxy / hydroxide groups. Therefore it increased the adsorption energy in absolute value.

PART 2: Plasma-polymer coating

At first, plasma-polymer films were deposited from allylamine monomer at atmospheric pressure on silicon substrates at different plasma conditions for characterizing the coatings compositions. In this study, flow rate parameters are constant and applied powers varying between 0,9 W/cm² and 1,6 W/cm². Kinetic observations coupled to MALDI-TOF and FTIR analysis of the plasma-polymerised coatings revealed the presence of large allylamine oligomers as well as chemical moieties arising from collateral or secondary reactions, such as imide and nitrile groups [9]. Figure 5 shows the relationships between plasma (Yasuda) parameters and the mass deposition rate of plasma-polymerised coatings and the final primary amine content of the coatings.

The NH₂ content of the plasma polymer is believed to have great importance to the performance of the coating as these primary amino groups should react with epoxy resin and thus create covalent bonds between the

coating and the adhesive. “Soft” plasma conditions lead to lower fragmentation of the monomer/precursor molecules, which may be interpreted as lower reactivity and thus lower mass yields. On the other hand, these same conditions yield amine-rich coatings, with 2 to 5 times more chemically-accessible NH₂ groups (as measured after chemical derivatisation). Indeed, ESI and MALDI-TOF studies have identified several allylamine oligomers in the coatings with structures similar to what would be expected by conventional addition polymerization [9].

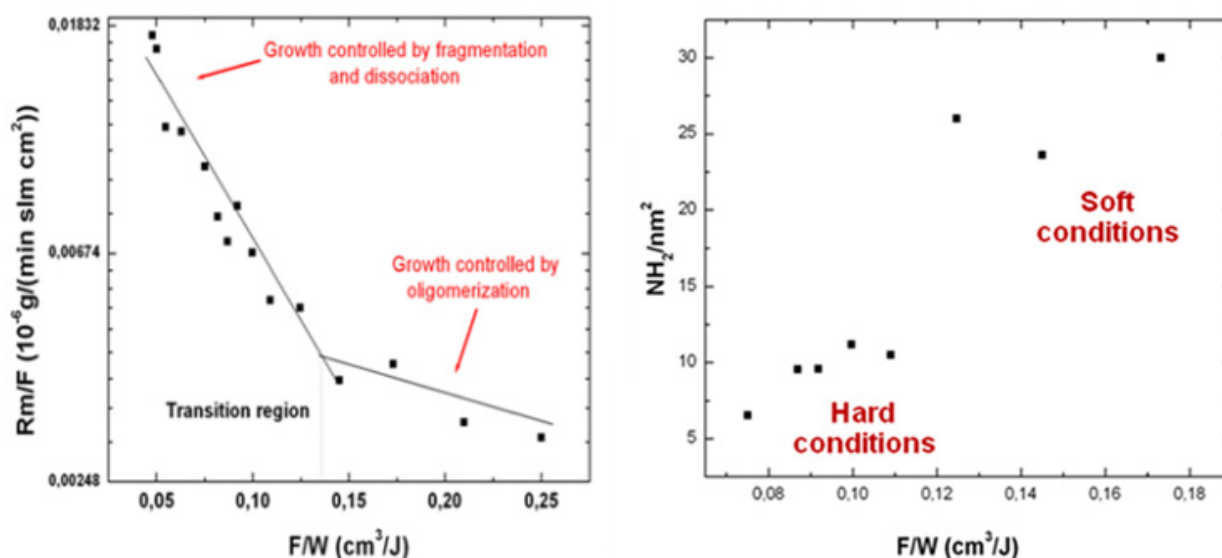


Figure 5, Plasma (Yasuda) parameters influence on reaction mechanism as observed by (left) mass deposit rate and (right) primary amine content on coating

A series of Al adherends was coated with pPAA under different deposition conditions, ranging from hard to soft conditions. Dolly-to-surface assemblies have been prepared and the adhesion force measured as the pull-off strength. The results show a remarkable increase in the stress-to-break for the coated samples, going from 2,9 MPa (uncoated) to 3,5 MPa (high fragmentation) and 4,3 MPa (low fragmentation), as shown in Figure 6. As the mode of fracture for uncoated assemblies was interfacial, between aluminium and epoxy adhesive, the improved results for pPAA-coated samples clearly indicate a gain in performance for the surface-treated samples.

On the one hand, this result also indicates that the concentration of amino groups play a direct role in the adhesion properties of this coating. But, on the other hand, the fracture type observed for all samples was interfacial, between the pPAA coating and the aluminium adherend, which suggests that the adhesion coating-substrate is weaker than coating-adhesive. This could arise not exactly from the concentration of amino groups but from a more resistant coating obtained with low fragmentation conditions. Further experiments are been carried to elucidate this.

A second series was based on the preparation of new pPAA coatings over Al adherends at low fragmentation/soft conditions but changing the number of passes in order to control the thickness of the coating. In the range of 0 to 60 nm, a maximum of adhesion strength was observed for coatings 15 nm thick: 4,4 MPa (Figure 6). Again, an interfacial mode of fracture was observed for all specimens, with a breakage in the coating-adherend plane.

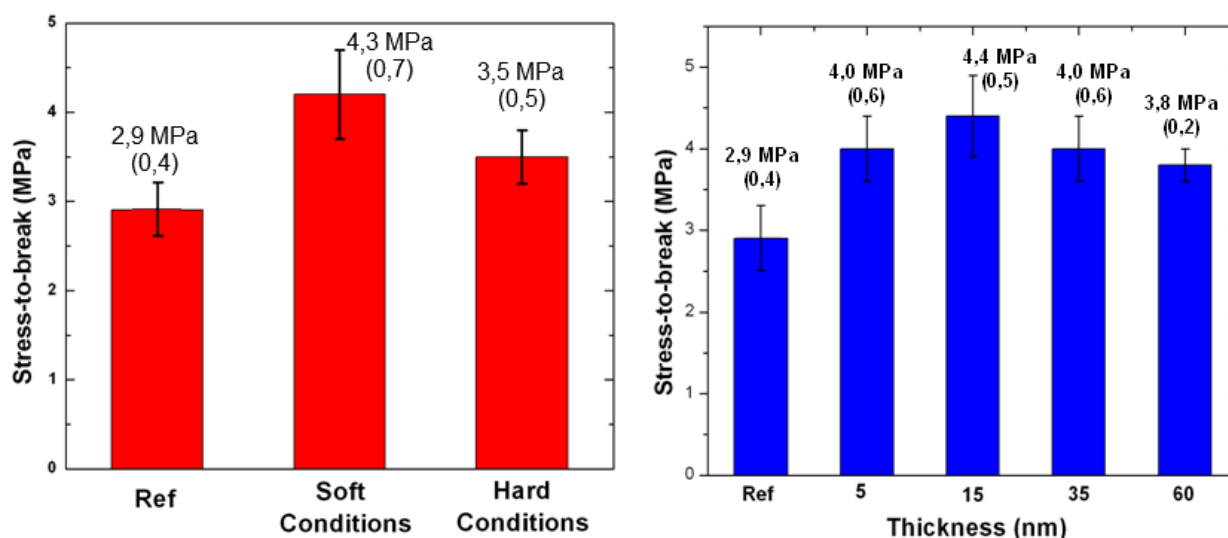


Figure 6, Pull-off mechanical test results for pPAA coatings prepared under different plasma conditions (left) and with different coating thickness (right), standard deviations in brackets.

IV. CONCLUSION

Two different types of plasma-treatment were applied to promote the adhesion between aluminium adherends and epoxy adhesive: oxidative plasma treatment and plasma-initiated polymerization for coating.

In the first part, the mechanical properties of epoxy assemblies with aluminium substrates degreased with acetone and treated with atmospheric pressure plasma were reported. The conditions of the plasma treatment were optimized for aluminium surface wettability; it was shown that mechanical strength of assembly after plasma activation with 20% O₂ is significantly improved. The increase in surface energy of aluminium after plasma surface can be explained either by a decrease of the contamination layer thickness or by an increase of the passivation layer thickness (aluminium oxide). Both effects are assumed to allow the creation of stronger bonds between treated aluminium and adhesive.

In the second part, we demonstrate that the implementation of atmospheric plasma DBD deposited allylamine coatings is an attractive tool for adhesion properties. In a first step, macromolecular studies reveal that the W/F parameter controls the amount of primary amine groups. Pull-off tests highlighted an increase of adhesion properties of aluminium /epoxy assemblies. Indeed, covalent bonds are expected to form between epoxy functional groups and primary amines groups from the adhesion primers.

Further plasma coatings based on plasma polymer layers can provide stronger bonds between aluminium substrate and the layer, and/or the layer and the adhesive. Such layers are currently being developed following this study. The durability of plasma-polymerized adhesion promoters is also being assessed.

ACKNOWLEDGEMENTS

The authors gratefully acknowledge the financial support of the Fonds National de la Recherche (FNR) du Luxembourg.

References:

1. Sperandio, C., Bardon, J., Laachachi, A., Aubriet, H., Ruch, D. Journal of Adhesion & Adhesives 2010;30:720
2. Rider AN, Olson-Jaques CL, Arnott DR. Surf and Interface Anal 1999;27:1055
3. Polini W, Sorrentino L. International Journal of Adhesion & Adhesives 2007;27
4. J. Tang, Y. Duan and W. Zhao, Appl. Phys. Lett. 2010, 96, 191503
5. Debontridder F, PhD thesis defended in Université Paris 11, 2001.

6. Halverson DE, Cocke DL. Thin Solid Films 1987;155:133
7. Cocke DL, Johnson ED, Merrill RP. Catal Rev Sci Eng 1984;26:163
8. Halverson DE, Cocke DL, J Vac Sci Technol A 1989;7:40
9. J.Petersen, J. A. S. Bomfim, T.Fouquet, M.Michel, V. Toniazzo, A. Dinia and D. Ruch, "Plasma polymerized allylamine by means atmospheric DBD process for as adhesion primers adhesion for Aluminium/epoxy assemblies". Manuscript in preparation.

USE OF GLOW DISCHARGE SPECTROMETRY FOR BULK AND COATING ANALYSIS AT HOT-DIP GALVANIZING LINES

Thomas Brixius, Marcel Gosens, Juan Müller, Michael Stang, Nicole Weiher

ThyssenKrupp Steel Europe AG, Kaiser-Wilhelm-Strasse 100, D-47166 Duisburg

Summary

During the production of surface-coated flat steel products a lot of parameters are required to carry out an optimum process control. Among other things the chemical composition of charge materials and the chemical composition of the metallic layer as well as its thickness are of great importance. Further more, the analysis of in-line applied near-surface passivation and pre-treatment coatings is necessary. The required results must be rapidly available to enable an optimum process control. Complex wet chemical analysis with the need of special labs is not the best choice in this case.

Nowadays, state of the art glow discharge spectrometry is a good approach for the wide range of analytical applications at steel strip coating lines. In general the robust design of the glow discharge spectrometry is serviceable for at-line analysis. The applicability of this method goes from bulk analysis of charge materials such as zinc, aluminium alloys and steel over quantitative depth profile analysis of metallic layers up to the analysis of non-conductive coatings with the RF-source.

Our in house developed and realized technical adaptations make glow discharge spectrometers ready for the at-line use at strip coating lines in steel industry. Using the example of hot dip galvanizing lines the special requirements of at-line analysis by means of glow discharge spectrometers as well as necessary adjustments are shown. The main focus will be laid on

- simple operation of the glow discharge spectrometer
- bulk analysis of steel and zinc-pot samples
- coating analysis of passivation, pre-treatments and anti-fingerprint coatings on galvanized steel
- high availability and low operating costs

The key benefits are a simple operation of the spectrometer, a good accuracy of the analytical results and a high availability. Since 1999 glow discharge spectrometers with this conception are successfully used at several locations of strip coating lines in Germany, Spain, USA and China.

Introduction

In steel industries optical emission spectrometry is a common method to get the chemical composition of solids and liquids¹. Different sources like spark, arc, icp and glow discharge are used for special applications. The capability of simultaneous analysis in a short time makes it convenient for process control. Especially the spark emission spectrometry with an easy sample preparation has a wide spreading. Fully automated process control labs equipped with spark emission spectrometers meet the requirements in making steel². Within a few minutes the whole procedure from sampling, transportation, preparation and analysis of the melt is done. Continuous casting, hot rolling and cold rolling are the next steps to get flat steel for automotive, construction and home appliance industries.

Most of these flat steel products are coated with zinc, zinc-aluminium-alloys, zinc-magnesium-alloys, aluminium or tin to prevent the steel against corrosion. Continuous electro-plating and hot-dip galvanizing lines are used to coat the steel with a homogeneous metallic layer. In addition nowadays a pre-treatment, post-treatment or paint is

applied in-line. To get a high quality product an optimum processing is required. Therefore a lot of parameters like chemical composition of charge materials, thickness of coatings and treatments as well as chemical composition of layers are important. Many in-line sensors are used, but to control these complex processes, typically a minimum of two offline or at-line instruments for bulk and coating analysis are necessary. The glow discharge spectrometry with its layer by layer sputtering of the sample has the capability to do both, bulk and depth profiling analysis, but usually commercial available instruments are designed for lab use and not for at-line use.

Glow Discharge Spectrometry for bulk and coating analysis at hot-dip galvanizing lines

Using the example of a hot-dip galvanizing line three main applications were found:

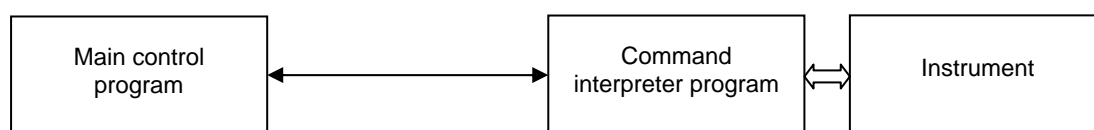
- chemical composition of steel (substrate)
- chemical composition of charge metals (e.g. zinc)
- chemical composition of coatings (depth profile analysis)

From the view of techniques an adaptive concept of a fully automated lab is conceivable, but it is difficult to match the economics. To handle different sample types with different analytical requirements a complex and expensive system is necessary, so most of the industries use single instruments in manual operation mode.

Typically for at-line use are spark emission spectrometers for bulk analysis and X-ray fluorescence spectrometers (XRF) for coating analysis. Also atomic absorption spectrometers (AAS) or inductively coupled plasma spectrometers (ICP) are often used instead of spark emission spectrometers, but therefore special labs for wet chemical analysis are required. Due to the fact that established XRF Spectrometers are liable to interfering effects (e.g. Cr, Ti) of the substrate in coating analysis, it was not so far to seek that layer by layer sputtering of the glow discharge technique could help to solve these problems.

First tests with a commercial glow discharge spectrometer³ including a Grimm type source⁴ showed us that the results for both bulk analysis and coating analysis are comparable to current techniques. To make the glow discharge spectrometer ready for at-line use some adaptations were required which are described as follows.

One of the difficulties to setup an instrument for at-line analysis is the control software. As time passed this software becomes more and more powerful. A lot of functions are implemented to fulfil the requirements for all analytical applications. Today this software is complex and designed for specialists, but not for operators at production lines. To fix this problem we developed in cooperation with the manufacturer of the instrument an easy to use desktop software package consisting of two parts, a command interpreter program^I and a main control program^{II}. Each sequence of an analysis, like loading a method, loading a sample, measuring a sample etc. is separated in short commands. These commands are integrated into the command interpreter program developed by the manufacturer. The main control program is connected via a serial line interface to the command interpreter program and drives the instrument. This main control program developed by ThyssenKrupp Steel Europe enables a full access to all functions of the instrument to setup an individual analysis system for special requirements of each strip coating line.



Among the strict user guidance a lot of tests are done in the background during the analysis. Fundamental parameters of the instrument are also checked as well as the results of each measurement. The main topics of the software are:

- User dependent program access (Figure 1).
With the logon procedure of the main control program each user gets its own access rights for analysing samples, performing drifts and modifying method settings. This ensures a save program administration.
- Operator guidance step by step through the analysis with a powerful online help system (Figure 2)
A special program toolbar enables the user to perform an analysis without the knowledge of the instrument operation in detail. Messages during the analysis and a context sensitive help system provide useful information.
- Permanent instrument diagnostics.
During operation as well as in standby mode important parameters like pressures, temperatures, voltages and flow rates of the instrument are checked automatically and in case of a failure the program recommends the next steps to solve the problem. The instrument status is added to each analysis record. Also a scheduled run of a check standard with defined tolerances is part of the diagnostic system.
- Plausibility check of results.
After each run of a sample the results must satisfy several criteria. At first all concentrations or coating weights of the analytes are compared with defined operating ranges. The finger print of the sample has to meet the specific method definition. This avoids mix-up of samples as well as drift standards or the usage of a wrong analysis method. In addition statistical parameters like standard deviation and relative standard deviation are checked.
- Documentation and transmission of results
The whole data of the analysis of a sample is saved into an archive file. Also important parameters and status information of the instrument are logged in a special system file. Each method is able to transmit the results of a sample to its own target process control system via local area network. The operator can perform a printout of each sample-datasheet, if one is needed.

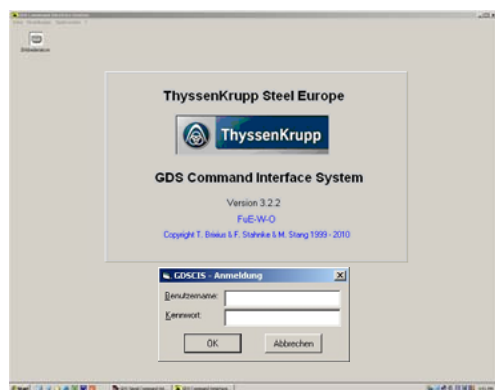


Figure 1: Logon

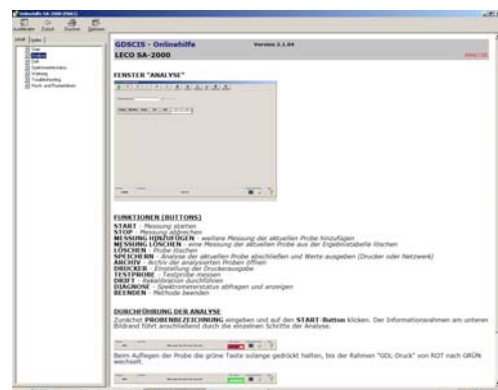


Figure 2: Online help system

This software concept enables us to adapt technically requirements of production lines as well as analytical requirements of products. Last but not least we implemented a multilingual desktop with three selectable languages (German, English, Spanish) to offer an user friendly, easy to use instrument for strip coating lines.

One of the main applications at a hot dip galvanizing line is the bulk analysis of the metal bath. First long term tests were performed to find the optimum source conditions which fulfil the requirements like short analysis time, low detection limits, good repeatability and long maintenance intervals. At the very beginning we used a plasma power of 24 W for zinc as a recommendation of the manufacturer, but one effect of this source condition was a lot of zinc particles in and around the anode which reduced the lifetime of the source. Nowadays we use a plasma power of 14 W without any loss of precision for the given analytes (e.g. Al, Fe) resulting in longer maintenance intervals. As an example the comparison of the variation of the plasma power for a RF-source with a 4 mm anode is shown in table 1 below.

Table 1: Comparison of RF-source conditions for zinc

Sample	Plasma power (4mm anode)	Aluminium		Iron	
		average (n=10) wt %	s	average (n=10) wt %	s
Zn-Check-Std 1 ^{III}	14 W (700 V RMS)	0,207	0,0041	0,047	0,0019
Zn-Check-Std 1 ^{III}	18 W (600 V RMS)	0,205	0,0040	0,049	0,0019

In addition to the bulk analysis of charge materials the depth profile analysis of coatings is a relevant application for hot-dip galvanizing lines. Pre-treatments, post-treatments and coatings of paint become more and more complex. This wide spreading of products cannot be analysed with one method. To adapt each product a special extension of the calibration is needed. Graduated standards of the original product over the full operation range are necessary, which are analysed under the same conditions as the sample. With these results the calibration is extended and a new adapted method for the given product is created. This procedure is resulting in a good correlation between specifications and results of the depth profile analysis as well as wet chemical analysis results.

As an example results of a passivation, a pre-treatment and an anti-fingerprint are shown in table 2 and the quantitative depth profiles in figure 3, 4 and 5 as follows.

Table 2: Comparison of wet chemical results and GDOS results

Treatment	Results wet chemical analysis	Results GDOS
Passivation	28,7 mg Cr / m ²	28,5 mg Cr / m ²
Pre-treatment	9,5 mg Ti / m ²	9,6 mg Ti / m ²
Anti-fingerprint	12,4 mg Ti / m ²	12,1 mg Ti / m ²

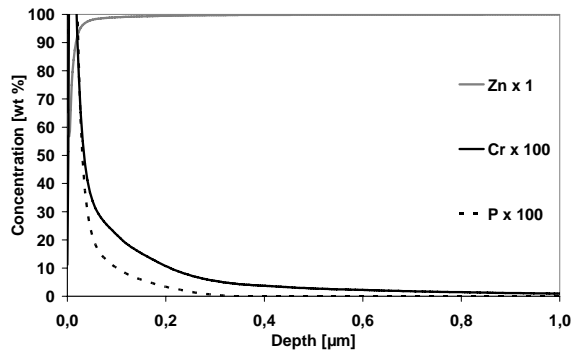


Figure 3: Passivation

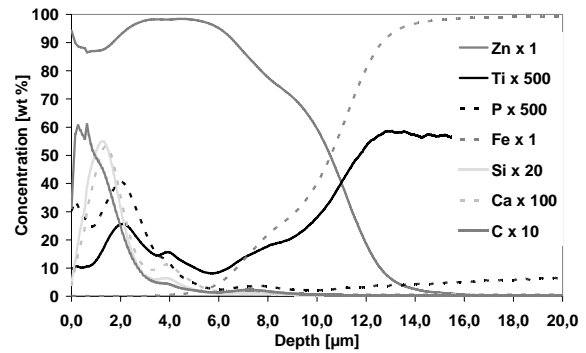


Figure 4: Pre-treatment with primer

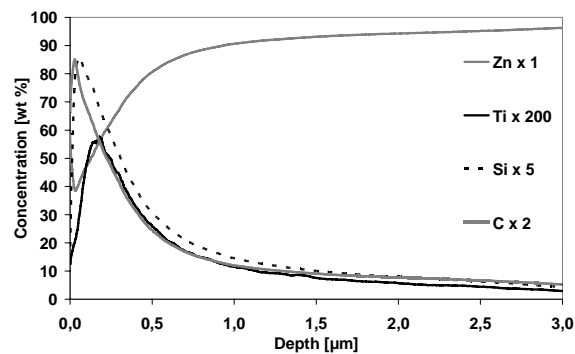


Figure 5: Anti-fingerprint coating

Usually commercial instruments are designed for lab use. The operating conditions at production lines are mostly different to those at labs. Ambient temperatures, floor vibrations and dust are not the only ones that can vary in a wide range. In addition a higher sample output and increased handling of the instrument are typically for at-line use. A look at the manufacturer specification for ambient conditions is helpful, but how robust an instrument is and how the analytical performance is, must be verified by a long term test.

For the first two years we were satisfied with all topics, but after that time the hinges of the door of the glow discharge lamp compartment got an unacceptable clearance. We installed new heavy duty hinges to solve this problem (Figure 6 and 7) and replaced the door switch unit to improve the door closed indication.

A second problem was the cabling of the RF-source. After each run the sample drops down and hits the cable underneath the RF-source. After a time the isolation of the cable became thinner and thinner and we had to replace the cable. To solve this problem we remount the RF-source with a 90° turn so that the sample cannot hit the cable anymore.



Figure 6: Original door hinges



Figure 7: New door hinges

These adaptations made the instrument more robust and we get an availability >99% by a maintenance interval of 3 month. With the long term experience we setup new replacement intervals for spare parts controlled by the number of sample burns, which are resulting in lower operation costs.

The positive experience with the first instrument was resulting in the installation of additional instruments. Today we run a total number of eight instruments at our facilities in Germany, Spain, USA and China which are listed below in table 3 and shown in figure 8.

Table 3: Glow discharge spectrometers at ThyssenKrupp Steel facilities

Country	City	Number of instruments	Type of instrument
Germany	Duisburg	3	Leco SA-2000 / Leco GDS-850A
	Finnentrop	1	Leco SA-2000
	Kreuztal-Eichen	1	Leco SA-2000
Spain	Puerto Sagunto	1	Leco SA-2000
USA	Calvert	1	Leco GDS-850A
China	Dalian	1	Leco SA-2000



Figure 8: Glow discharge spectrometers at ThyssenKrupp Steel facilities

Conclusion

The glow discharge technique with its layer by layer sputtering is a good approach to meet the complex analytical requirements of coated steel products as well as bulk materials. An easy sample preparation and the robust design of a glow discharge spectrometer make it serviceable for the at-line use at strip coating lines. The development of a user friendly desktop software package with built-in plausibility checks, an online help system and instrument diagnostics assists the operator to get accurate results and a high availability. This combination of an applicable hardware with adapted software is resulting in a powerful tool for at-line analysis at hot dip galvanizing lines.

Notes:

- I) Serial Command Software
Leco Corporation, St. Joseph MI, USA
- II) Glow Discharge Spectrometer Command Interface System
ThyssenKrupp Steel Europe AG, Duisburg, Germany
- III) Setting up sample by SUS, Ulrich Nell, Oberhausen, Germany

References:

- 1) Boumans, P. W. J. M., Introduction to Atomic Emission Spectrometry. In Inductively Coupled Plasma Emission Spectroscopy - Part I; Boumans P.W.J.M. Ed.; Wiley: New York, 1987; Vol. 90; pp 1-34.
- 2) Wachtendonk, H. J., Das neue automatisierte Stahlwerkslabor Ruhrort, Stahl und Eisen, 116, S.55-59, (1996)
- 3) K. Marshall, Glow Discharge Optical Emission Spectrometry 137 (1997)
- 4) W. Grimm, Naturwissenschaften 54, 586 (1967)

ESTABLISHMENT AND APPLICATION OF ANALYSIS MODEL FOR AL INCLUSION SIZE ON THE BASIS OF ABNORMAL SPARK FREQUENCY DISTRIBUTION

Meiling Li, Dawei Cheng, Dongling Li, Hongbin Gao, Yunhai Jia, Haizhou Wang

Central Iron & Steel Research Institute, Beijing 100081, China

Abstract:

Two middle-low alloy samples, produced under the similar technology conditions were investigated by OPA (Original Position Statistic Distribution Analysis) technique. It was firstly demonstrated by SEM technique that great difference existed between the two samples. For instance, the inclusion ratios in 0-3 μ m region were 40.2% and 55.2% respectively for sample 1[#] and 2[#], and the ratios changed into 49.3% and 27.9% in next region of 3-5 μ m. Then by using OPA technique, it was found that the two samples exhibited completely different OPA net intensity frequency distribution of abnormal signals compared to each other. Accumulative frequency distribution of OPA was further analyzed and the precise responding OPA intensity corresponding to each inclusion size was eventually determined. By proper mathematics simplification treatment, the fitting equation of $Y=3E-13X^3 - 2E-08X^2 + 0.0006X + 2.1749$ which can calculate the inclusion size Y in terms of the net intensity X, was established. The model was applied to several actual samples for Al inclusion size analysis and satisfactory results were acquired.

Key words: OPA technique; abnormal spark; middle and low alloy; inclusion aluminium; size distribution

Non-metal inclusions with great size will inevitably damage the properties of iron and steel due to its destructive effect to the continuity of materials^[1]. Granular size distribution is thus considered to be one of the important factors when the influence of inclusion on the properties of materials is investigated. Conventional methods such as SEM technique is usually adopted to perform some statistic analysis of inclusions. However, the operation will be labour and time-consuming for large area because massive micro-visual-fields need to be observed to fully understand the distribution of inclusions with various sizes.

Original position statistic distribution analysis (OPA) technique can get much information closely concerning the inclusion size. We have been dedicating to the investigation about the relation between OPA abnormal signal and inclusion size for a very long time and got lots of important results^[2-8]. Generally, the inclusion with bigger size generates stronger signal and some certain relation has been proved to be existing between the two parameters. However, the exact relationship is still difficult to be established due to the great span of net abnormal signal intensity from zero to ten thousands generated from the inclusions with extensive sizes and thus the usual data-treatment approach can not be suitably utilized for the fitting within the entire intensity range. In the present paper, with the aid of SEM technique, two middle-low alloy samples, produced under the similar technology conditions but with apparently different Al inclusion average size, were experimented on using OPA technique to check the intensity frequency changes rule and then the precise relation of intensity with the inclusion size was ascertained. The inclusion analysis model has eventually been established by means of simplification mathematics treatment. After applying the model to several real samples, it is demonstrated that the method established in the present paper is suitable for Al inclusion size analysis with satisfactory results.

1 Experimental

1.2 Samples

Two samples 1[#] and 2[#] used for the establishment of model coming from the same factory are middle-low alloy billets with the cross section area of 150mm×150mm. The area for OPA scanning is 80mm×80mm. The two samples are elementarily proved in advance to contain similar Al inclusion composition with high purity but with obviously different size distribution and average diameter. Other seven samples are all real samples coming from different factories or certified spectrum samples.

All the samples were observed by JSM-6400 SEM and the statistic analysis of the ratio for particular inclusion size region was carried out according to the method described in our previous work^[7]. Inclusion size regions were suggested to be 0-3 μ m , 3-5 μ m , 5-7 μ m , 7-10 μ m , 10-15 μ m , above 15 μ m and so on respectively. The area used for SEM statistic analysis was the same as that used for OPA for all samples.

1.3 OPA instrument

OPA-100, metal original position analyzer, made by Beijing NCS Analytical Instruments Co. Ltd., the instrument parameters are as follows:

Excitation frequency: 480 Hz; Purity of Argon: 99.999%; Flux of Argon: 80 ml/sec; Collecting speed of signals: 200 kHz/channel; Monitoring wavelengths: Al : 396.1nm.

Continuous exciting along X axis direction, step-by-step in the distance of 2mm along Y axis direction were adopted for the scan of the entire area.

2 Results and discussion

2.1 Inclusion size statistic results of SEM

After checking samples 1[#] and 2[#] for the distribution analysis of inclusion size by SEM method, it has been confirmed that Al inclusion distribution including both position and size is stable. Moreover, the two samples present their own particular inclusion size distribution characteristics compared to each other. That is, the ratios of Al inclusion in one common region for this two samples is fairly different. For instance, the ratio of inclusions within the region of 0-3 μ m to the inclusions in all sizes for sample 1[#] is about 40.2%, while it is 55.2% for 2[#] and the difference gets up to 15%; within the next region of 3-5 μ m, the ratio for sample 1[#] is statistically about 49.3%, exceeding that of sample 2[#] about 20%, which is only 27.9%. Such gradient difference existing between the two samples is beneficial to the establishment of the exact relationship between OPA net intensity and inclusion size. In addition, it can be seen from the Table 1 that for the region of 7-25 μ m, the ratio of sample 2[#] is evidently greater than that of sample 1[#].

Table 1 SEM statistica results of samples 1[#] and 2[#]

Inclusion size region / μm	Samples 1 [#]	Sample 2 [#]
	Inclusions ratio / %	Inclusions ratio / %
0-3	40.2	55.2
3-5	49.3	27.9
5-7	9.0	10.1
7-10	0.5	3.5
10-15	0.5	1.9
15-25	0.5	1.4

2.2 Ascertainment of the relation between the intensity frequency of OPA and the inclusion size

Threshold values of sample 1[#] and 2[#], 6750 and 6250, which can discern the abnormal spark from normal one, are firstly obtained by using the method defined in our previous study^[8] (the high threshold value is got for sample 1[#] mainly due to its Al content of 0.040%, which is higher compared to that of sample 2[#], 0.025%). Then the frequency statistic of abnormal spark net intensity is done with the software of Origin in proper intensity step of 500 and partial statistic results are listed in Table 2.

In order to establish the relation between the intensity frequency of OPA and the inclusion size, the following analysis work is carried out with those obtained frequency distributions. Taking SEM result of sample 1[#], 40.2% within the region of 0-3 μm as the reference, carefully checking the accumulative frequency of OPA and it is noticed that in the OPA intensity range of 0-1500, the accumulative frequency, 42.94%, is just near to 40.2% of SEM. In the ascertained intensity range of 0-1500, the accumulative frequency of sample 2[#], 55.19%, is also the exact statistic result of SEM, namely 55.2%. Accordingly, the net intensity value of 1500 is suggested to be related to the size of 3 μm for both samples.

Continuing referring to the ratio in the region of 3-5 μm from SEM to ascertain OPA intensity range, it is ensured that in the intensity range of 1500 to 5500, the accumulative frequency of sample 1[#] reaches 47.91% and is close to that from SEM, namely, 49.3%. In the ascertained range of 1500 to 5500, the accumulative frequency of sample 2[#], found to be 29.03%, is also just near to that from SEM, namely, 27.9%. Therefore, it is reasonable to consider that the newly ascertained value of 5500 corresponds to the size of 5 μm for the region of 3-5 μm . Similarly, the up edge values of 7 μm , 10 μm , 15 μm , 25 μm for the size regions of 5-7 μm , 7-10 μm , 10-15 μm and 15-25 μm is suggested to be related with those OPA intensities of 13500, 24500, 45500, 58500 and so on, as listed in the Table 3.

Table 2 Partial net intensity frequency and added frequency in certain intensity range of samples 1[#] and 2[#]

1 [#]				2 [#]				Inclusion size/ μm
Intensity	Net intensity	Frequency/%	Accumulative frequency/%	Intensity	Net intensity	Frequency/%	Accumulative frequency/%	
6750	0	5.75		6250	0	12.48		
7250	500	15.56		6750	500	19.61		
7750	1000	11.36		7250	1000	13.48		
8250	1500	10.27	42.94	7750	1500	9.62	55.19	3
8750	2000	8.50		8250	2000	7.05		
9250	2500	7.62		8750	2500	5.50		
9750	3000	7.20		9250	3000	4.38		
10250	3500	6.86		9750	3500	3.16		
10750	4000	5.76		10250	4000	2.87		
11250	4500	4.59		10750	4500	2.56		
11750	5000	3.95		11250	5000	1.79		
12250	5500	3.44	47.92	11750	5500	1.72	29.03	5

Table3 Established relation between net intensity and inclusion size

Net intensity	Size/ μm
1500	3
5500	5
13500	7
24500	10
45500	15
58500	25

The data listed in the Table 3 are fitted, taking the net intensity as X-axis and inclusion size as Y-axis. Because of the wide intensity variation range, it is difficult to make well fitting of all the data including 0 to almost 60000 to get one well curve. Accordingly, in order to get the fitting curve which has good relativity and thus can be applied feasibly, under the condition of no-setting of Y-intercept, polynomial fitting is made according to the tendency of these data. It is found that the fitting curve has good linearity with the relative coefficient of 0.9984 (See Figure 1). Even though the curve does not include the theoretical dot of (0, 0), the simplified working curve can be effectively applied without significant influence on the analytical result. The reason is that the statistic frequency value within the inclusion size region of 0-3 μm , which is the real important one in case of inclusion size distribution analysis, will not change even the dot of (0, 0) is not included in fitting. The number of 2.1749 in the formula is the intercept on Y-coordinate and does not represent the real detection limit of inclusion size. Our previous study showed that the actual detection limit of Al inclusion size is lower to about 0.68 μm for OPA technique^[5].

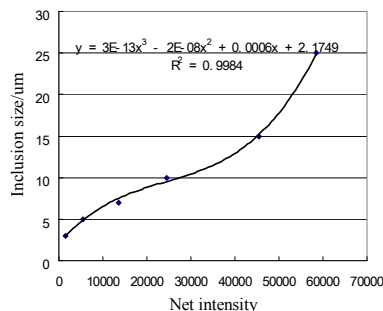


Fig 1. Fitting curve as well as calculating equation of inclusion size in terms of OPA net intensity

2.3 Analysis of real samples by OPA technique

Apply the formula in section 2.2 to Al inclusion analysis of seven different middle-low alloy steel samples and list all the results in Table 5, 6 and 7, respectively.

Among these samples, 11[#], 15[#] and 16[#] are circular column with Al content of 0.061%, 0.018% and 0.019%. The average inclusion size of 15[#] is the greatest one and 16[#] the smallest one. It can be seen that the results from OPA technique are well agreement with those from SEM. In particular, the consistency of OPA result and SEM result is perfect for sample 11[#]. After examining the composition and the shape of Al inclusion existing in all these samples, it is found that the Al inclusion in 11[#] is very pure and the shape is closest to sphere. This is possibly the major reason of the high degree consistency of OPA and SEM for this sample.

For the sample SG[#], its total content of Al is about 0.045%, with many tiny inclusions and for the region of 0-3 μ m the ratio is high up to 54%. It is also found by OPA technique that in this sample, the amount of the big inclusion is greater than that observed by SEM. Through further investigation, it is found that the difference is probably caused by uncompletely the same for the analysis area of OPA as the observation area of SEM. Being slab, large amounts of great inclusion locate near up or bottom surface, and OPA technique might cover the area and thus find the great inclusions. For the sample 3L[#] with Al content of 0.036%, the result from OPA shows that most of inclusions belong to the region of 0-3 μ m with high frequency of 73.29%, which is supported by SEM method.

82[#] and 70[#] are a pair of samples coming from the same factory, with very close Al content of 0.008% and 0.010%. It is confirmed by OPA that the two samples present almost the same distribution of Al inclusion size, which is also supported by SEM technique.

Table 4 Comparison of results from OPA and SEM for samples of 11[#], 15[#] and 16[#]

Size region/ μ m	Inclusion ratio of 11 [#]		Inclusion ratio of 15 [#]		Inclusion ratio of 16 [#]	
	OPA /%	SEM /%	OPA /%	SEM /%	OPA /%	SEM /%
0-3	28.99	28.7	26.29	21.0	39.23	44.6
3-5	33.51	33.0	29.86	32.7	34.17	33.1
5-7	16.89	21.9	21.33	20.6	18.78	13.1
7-10	13.78	11.2	13.29	17.6	5.43	7.7
10-15	3.38	4.2	6.65	5.1	1.57	1.1
Above 15	3.45	1.0	2.58	3.0	0.82	0.4

Table 5 Comparison of results from OPA and SEM for samples of SG[#]、3L[#]

Size region/ μm	Inclusion ratio of SG [#]		Inclusion ratio of 3L [#]	
	OPA /%	SEM /%	OPA /%	SEM /%
0-3	54.52	55.5	73.29	69.7
3-5	26.41	31.7	19.47	24.2
5-7	9.33	8.3	4.70	6.1
7-10	5.79	3.5	1.94	0
10-15	2.08	0.7	0.42	0
Above 15	1.87	0.3	0.18	0

Table 6 Comparison of results from OPA and SEM for samples of SG[#]、3L[#]

Inclusion region/ μm	Inclusion ratio of 82 [#]		Inclusion ratio of 70 [#]	
	OPA /%	SEM /%	OPA /%	SEM /%
0-3	53.39	53.0	53.77	56.7
3-5	31.61	33.0	32.96	32.5
5-7	9.17	10.5	8.60	10.1
7-10	4.72	2.9	3.91	0.5
10-15	0.73	0.5	0.38	0.2
Above 15	0.38	0.1	0.38	0

It is clear that when adopting the fitting formula in the present study to perform the analysis of actual samples the results indeed embody the size distribution characteristics of Al inclusions. The results from OPA and SEM correspond to each other, illustrating that OPA method can realize the accurate analysis of Al inclusion distribution for different types of middle-low steels.

Massive previous experiments have already proved that the performance of abnormal sparks is closely related to the type of steel, that is, the same size distribution existing in different matrix possibly presents different spark signal behaviour state. In the present study, due to all the samples being low-middle alloy, the slight distinction among the steel types has not been taken into account. However, for actual inclusion content and size distribution analysis, adopting the matching type steel or even the standard steel sample under the same technology, the error should dramatically be decreased.

During the actual analysis process, for standard sample used for inclusion size analysis (namely, the sample with stable inclusion position and size, its development method has already applied for the patent), the percent of particles to all inclusions obtained by SEM, as being the unique characteristic parameter, will keep the same value and will not change. Its corresponding abnormal spark signal intensity distribution can be gotten timely by OPA method. After re-assuring the critical edge intensity values and fitting again, the working curve is thus calibrated, that is, the working curve can be calibrated at any time with the application of standard sample used for inclusion size analysis.

3 Conclusion

On the basis of comparison of abnormal signal frequency difference and analysis of the varying patterns of two samples with obviously distinction of inclusion size distribution, the relationship between the inclusion size and the net intensity has been ensured and the working curve which can be applied into practical analysis has been established. The accurate analysis of seven real samples indicates that the mathematics model basically reflects the response rules of spectrum signal of inclusion size. With the help of standard sample inclusion size in the future, the timely calibration of the model can be realized and therefore the fast, accurate statistic analysis of inclusion size for actual samples is possible.

References

- [1] A. Ghazanchyan Chappuis, C. L. Davis. Sulphur segregation and precipitation in HAZ of boiler steel thick section welds. *Materials Science and Technology*. Vol 22 (8), P937-943.
- [2] Wenjun Qu. Preparation of the references materials of non-metallic inclusions of Al_2O_3 with different size of distributions and study on the spectrum characterization. Doctoral Dissertation of Central Iron & Steel Research Institute.
- [3] Lei Zhao, Yunhai Jia, etc. Determination of inclusion manganese content in iron & steel with signal discharge analysis. *Metallurgical Analysis*. 2006, 26 (1): 1-5.
- [4] Zhijun Yang, Haizhou Wang. Research on segregation and inclusion of continuous casting slab by original position analysis. *Iron & Steel*. 2003, 38 (3): 61-63.
- [5] Xiuxin Zhang, Yunhai Jia, ect. Size determination of aluminium inclusions in steel by original position statistic distribution analysis technique. *Metallurgical Analysis*. 2009, 29 (4): 1-6.
- [6] Hongbin Gao, Haizhou Wang. Investigation on behavior of inclusion discharge in original position statistic distribution analysis. *Metallurgical Analysis*. 2008, 28 (Suppl): 867-873.
- [7] Hongbin Gao, Behavior analysis of abnormal discharge for inclusion in steel and the model research of inclusion grain size distribution analysis using Original Position Statistic Distribution Analysis technique. Doctoral Dissertation of Central Iron & Steel Research Institute.
- [8] Hui Wang, Yunhai Jia. Original position statistic distribution analysis of aluminum inclusion in middle- low alloy steel. *Metallurgical Analysis*. 2007, 27 (8): 1-4.

APPLICATION OF EXTRACTION METHODS FOR INVESTIGATION OF NON-METALLIC INCLUSIONS AND CLUSTERS IN ALLOYS

Diana Vasiljevic¹⁾, Ryo Inoue²⁾, Andrey Karasev¹⁾ and Pär Jönsson¹⁾

¹⁾ Division of Applied Process Metallurgy, Royal Institute of Technology (KTH), SE-100 44 Stockholm, Sweden.

²⁾ Institute of Multidisciplinary Research for Advanced Materials (IMRAM), Tohoku University, Sendai 980-8577, Japan.

Abstract

The characterization of non-metallic inclusions is of importance for the production of clean steel in order to improve the mechanical properties. In this respect, a three-dimensional (3D) investigation is of particular importance for an accurate estimation of inclusion characteristics. Thus, the main purpose of this study was to examine and discuss the application of various extraction methods, 3D investigations of non-metallic inclusions part of clusters, and clusters in high-alloyed steels.

Characteristics such as size, number, composition and morphology of inclusions and clusters were investigated in an Fe-10mass%Ni alloy (laboratory experiments, 250-350 g) and in stainless steel (steel grade 18/8, 350 kg pilot plant trial) samples deoxidized with Al (addition of 0.02-0.2% Al). The following two methods were applied for the extraction of inclusions and clusters: i) potentiostatic or galvanostatic electrolytic extraction by using a 10%AA solution as an electrolyte, and ii) chemical extraction and etching by a halogen-alcohol solution (5-10v/v% Br-CH₃OH). Results from the present study were compared with results from other studies in which also I₂-methanol, and the electrolytes 4% MS and 2%TEA were used.

The possibility of dissolution of Al₂O₃ particles during extraction was evaluated in a previous study by using standard fine Al₂O₃ powders with a known particle size distributions in the size range from 0.06 to 3 μm. It was found that the size and number of Al₂O₃ particles practically did not change during electrolytic extraction for 11 hours or halogen-alcohol extraction for up to 2 hours.

A comparison of dissolution ratio between different extraction solutions showed that the halogen-methanol solutions had the highest ratio; however, they were also somewhat unstable. Furthermore, it was shown that the real size distribution could be estimated by the extraction methods, which also showed to give an insignificant effect from the metal matrix during chemical composition analysis of inclusions. The etching method was advantageous for a quick assessment of inclusions characteristics such as morphology and composition. Finally, for an estimation of largest cluster in a sample, a 2D investigation has shown to be required prior to extraction.

Keywords: Al-deoxidation, non-metallic inclusions, clusters, extraction.

1. Introduction

The characterization of non-metallic inclusions is of importance for the improvement of mechanical properties as well as the production of clean steel. Some characteristics such as number, size and composition of inclusions are particularly important for understanding of the formation and growth mechanism of inclusions [1]. Previous studies [2, 3] have shown that three-dimensional (3D) studies are more reliable regarding number and size of inclusions compared to a cross sectional study (2D). In this respect, a 3D investigation is significant for an accurate estimation of inclusion characteristics in steel. Available 3D methods which have been used extensively for these

purposes are so-called extraction methods. These include electrolytic extraction as well as chemical extraction using halogen-alcohols and acids.

The purpose of this study is to compare some available extraction methods applied for 3D investigations of inclusions and clusters in steel samples taken during the deoxidation process. The application of various extraction methods and results obtained in the present and from a previous study [4] are compared, and advantages as well as some limitations are discussed.

2. Experimental

2.1 Dissolution of Al_2O_3 powder in solution

In a study performed by Inoue et al. [4], the possibility of dissolution of Al_2O_3 particles in acids ($\text{HCl-HNO}_3\text{-H}_2\text{O}$ or $\text{H}_2\text{SO}_4\text{-HNO}_3\text{-H}_2\text{O}$), halogen-methanol (5v/v% bromine-methanol and 14w/v% iodine-methanol), 4%MS (4v/v% methylsalicylate-1w/v% tetramethylammoniumchloride-methanol) or 10%AA (10 v/v% acetylacetone– 1 w/v% tetramethylammonium chloride - methanol) mixture was evaluated using standard fine Al_2O_3 powders. More specifically, the powders had a known size distribution with an average size ranging from 0.06 to 1 μm . Stirring of the halogen-methanol mixtures using an ultrasonic vibration bath during dissolution was included in the experiments. After suction and filtering of 5 ml of solution, the contents of the eluted Al_2O_3 in the solution were measured.

2.2 Etching and extraction of alumina inclusions and clusters from a stainless steel alloy

A stainless steel (350 kg of Fe-18mass%Cr-8mass%Ni) was melted in an induction furnace (600 Hz, 600 W) in an Al_2O_3 -crucible during a pilot plant trial [5]. Dual thickness lollipop samples were taken from the melt (1600 °C) at different holding times after an addition of 0.1 mass% Al. One of the sides of the thicker parts (12 mm) were ground and polished, followed by etching using a 5-10v/v% bromine-methanol mixture during 30-180 s for partial 3D observations of alumina inclusions and clusters on the metal surface. Longer etching times (5-10 minutes) were used for extraction of alumina inclusions and clusters for full 3D observations on a film filter. The solution was filtered using two polycarbonate (PC) film filters with open pore sizes of 3 μm and 1 μm . Inclusion and cluster characteristics such as size, number, morphology and composition were evaluated using a SEM equipped with an EPMA.

2.3 Etching and extraction of alumina inclusions and clusters from an Fe-10%Ni alloy

An Fe-10mass% Ni alloy (250-350 g) was melted in a high induction furnace (100kHz, 20kW) in a high purity Al_2O_3 -crucible under Ar atmosphere using a graphite susceptor. Quartz tube samplers were used for sampling of the melt (1600 °C) at different holding times after additions of varied amounts of Al (0.04, 0.08, 0.12 or 0.2 mass%). After sampling, the ingot was cooled in the furnace to 1400 °C (cooling rate ~ 0.65 °C/s), followed by rapid water quenching. Specimens from the ingot were cut, ground and polished, followed by etching with a Br_2 -methanol mixture for 15 s. Then, the surfaces of these specimens were observed using a SEM. Specimens from the ingot and quartz tube samples were also dissolved in a 10%AA solution using the potentiostatic electrolytic extraction method with a current of 45-60 mA, voltage of 150mV and a charge of 800 or 1200 coulombs. During these electrolytic extractions, the ingot specimens were dissolved on all sides, while the quartz tube specimens were dissolved on only one side. The solution which contained inclusions was filtered using a PC film filter with an open pore size of 0.05 μm . Inclusion and cluster characteristics such as size, number, morphology and composition were evaluated using a SEM.

3. Results and Discussion

3.1 Dissolution of alumina powder in solution

The possibility of dissolution of Al_2O_3 particles has been evaluated in various mixtures in a previous study [4]. Figure 1 presents the dissolution ratio of Al_2O_3 particles with an average size of $0.1\ \mu\text{m}$ as a function of time in acid (a), and in Br_2 -methanol, I_2 -methanol, or 10% AA solutions (b). It is obvious from these figures that the acid is the strongest solution of the tested mixtures. In this solution around 20% of Al_2O_3 powder has dissolved after about 5 hours. The dissolution ratio in Br_2 -methanol and I_2 -methanol is much lower after 10 hours, i.e. about 0.5% and 0.3%, respectively. Since the halogen-methanol experiments included stirring in an ultrasonic vibration bath, an even lower dissolution ratio could probably be expected without stirring. Finally, the lowest values of the dissolution ratio are seen for the 10% AA solution, in which approximately 0.1% is dissolved after just over 11 hours.

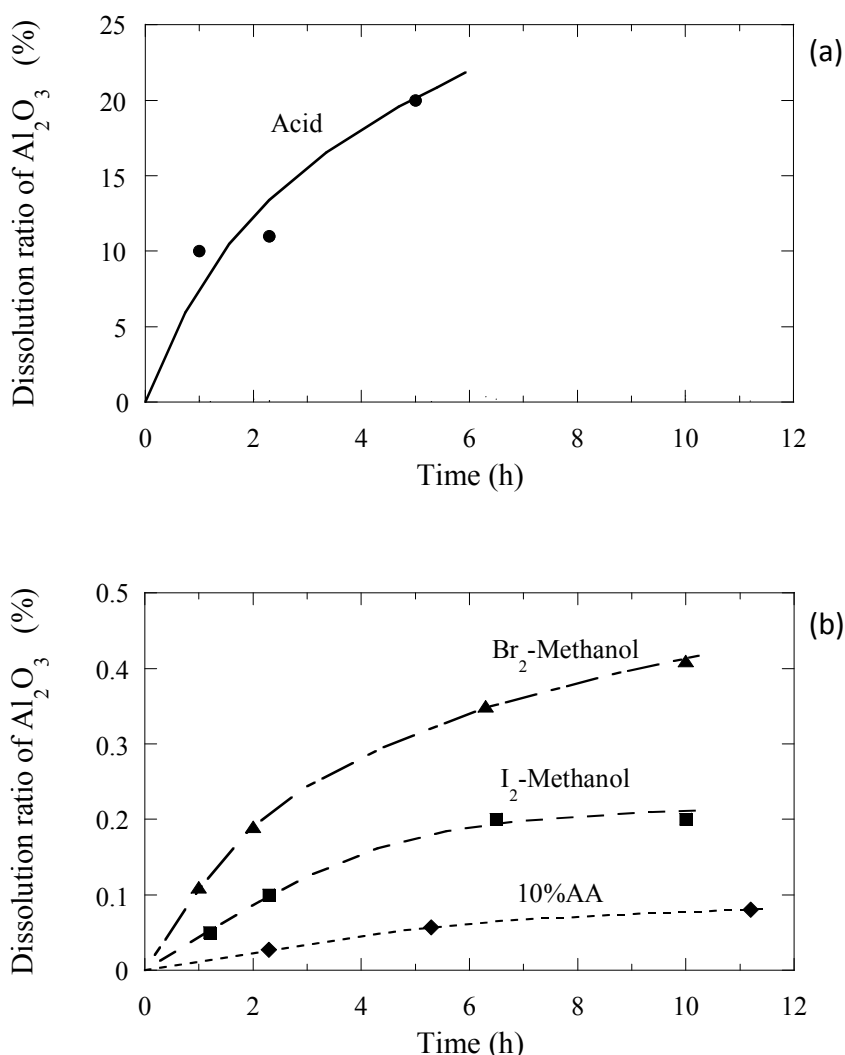


Figure 1: Dissolution ratio of Al_2O_3 powders as a function of time in (a) acid and (b) Br_2 -methanol, I_2 -methanol and 10% AA.

Figure 2 shows a comparison of the dissolution ratio of Al_2O_3 with time using powders with average sizes of $0.06\ \mu\text{m}$ and $1\ \mu\text{m}$ in Br_2 -methanol and I_2 -methanol solutions. According to this figure, the eluted ratio is higher for the finer powder for both halogen-methanol solutions. Further, the Br_2 -methanol is showing to be the stronger solution in both powder cases when compared to the ratio values when using the I_2 -methanol solution.

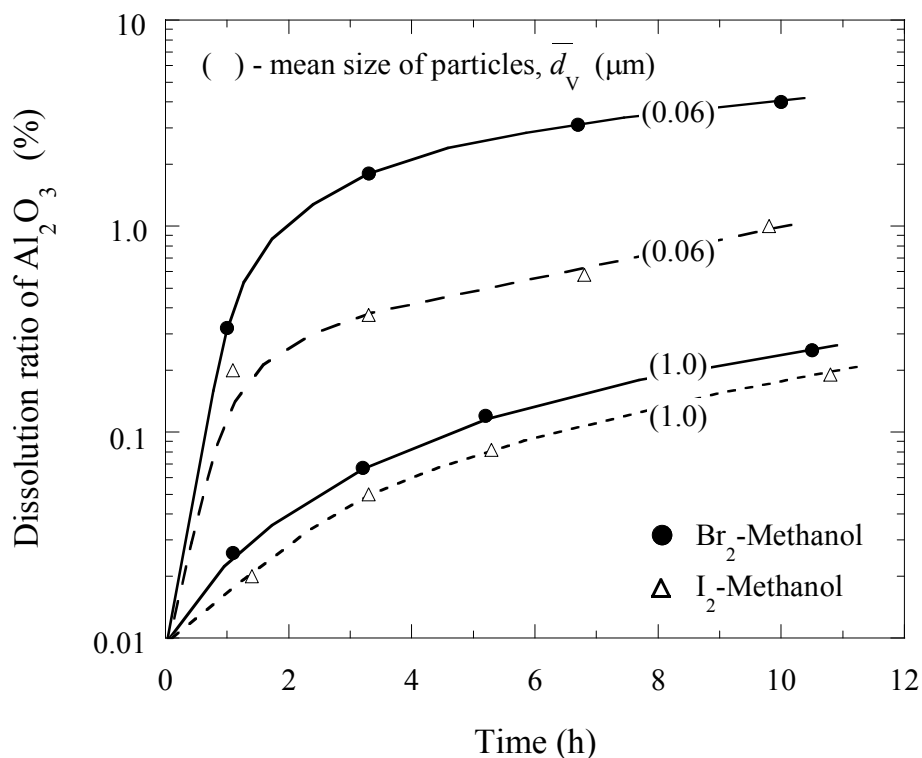


Figure 2: Dissolution ratio of Al_2O_3 powders with average size 0.6 and 1 μm Br_2 -methanol and I_2 -methanol.

These results indicate that if an acid or halogen-methanol solution during extraction contains small size particles ($<0.1 \mu\text{m}$), it could run the risk of giving false results regarding e.g. particle size distribution for small size particles. Thus, a recommendation would be to only use these mixtures, and especially acids, for short time dissolution experiments of large size Al_2O_3 particles. For the study of small size Al_2O_3 particles, electrolytic extraction is recommended. Moreover, other inclusions such as CaO and MgO have shown to dissolve easily by acids and halogen-alcohols [4]. Therefore, the electrolytic extraction method is again recommended for inclusions containing these compounds.

3.2 Comparison of dissolution parameters between various extraction methods

Based on the etching and extraction experiments on stainless steel and Fe-10mass% Ni samples described in sections 2.2 and 2.3, parameters such as dissolution rate and dissolved depth of metal samples were compared between different extraction methods. Figure 3(a) presents dissolution rates of metal samples for the halogen-alcohols Br_2 -methanol and I_2 -methanol, and for the electrolytes 10% AA, 4% MS or 2% TEA. It is clear from this figure that the Br_2 -methanol solution has a much higher dissolution rate (0.006-0.015 g/min) compared to the other solutions. These results indicate that the Br_2 -methanol is a stronger solution. However, it should be mentioned that the rates obtained by using Br_2 -methanol are more scattered even though the values are obtained from the same set of stainless steel samples for which the same mixed solution was used. Clearly, a more stable dissolution rate is preferred in order to give a more reliable prediction of the aimed dissolved weight of the sample. Therefore, in this case, the electrolytic extraction methods can be recommended. However, the Br_2 -methanol solution is still recommended for short time dissolutions.

Figure 3(b) presents a comparison of the dissolved layer thickness as a function of time for different extraction solutions. It can be observed that the Br_2 -methanol solution has the highest dissolution rate as also mentioned previously. Data representing the dissolved layer depth when one side of the sample is exposed to the electrolyte as well as all sides are also presented for 10% AA. Here, obtaining a certain depth can be achieved faster using

the one-side dissolution case compared to the two-side case. Overall, it takes longer time to dissolve a certain layer thickness if using a 10% AA solution compared to a Br₂-methanol solution. These figures may be useful to some extent for future experiments if it is required to estimate the time to dissolve a certain layer depth.

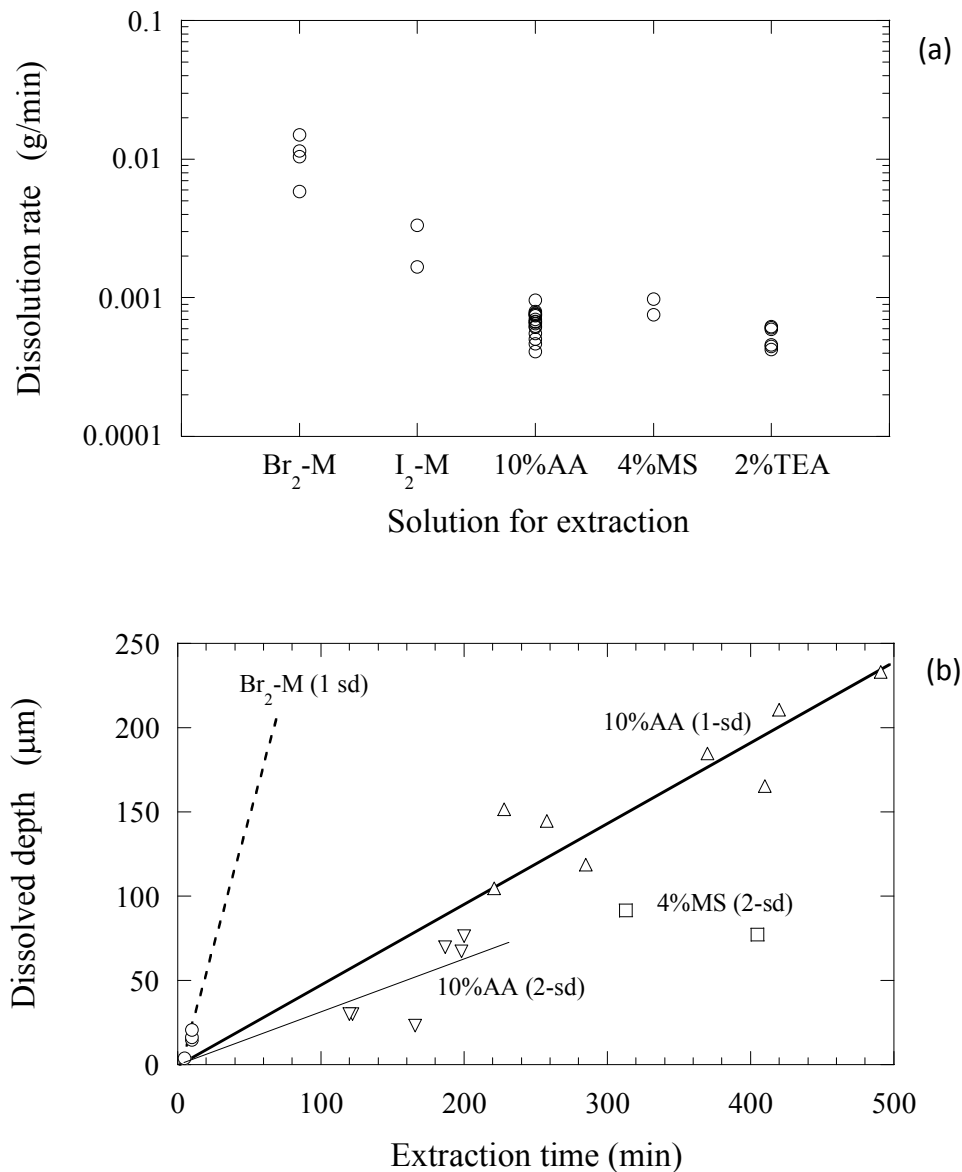


Figure 3: Comparison of (a) dissolution rate and (b) dissolved layer of metal samples when using halogen-methanol and 10% AA mixtures.

3.3 Application of various 3D methods on investigations of alumina inclusions and clusters

This section presents some applications and limits of etching and extraction methods on the evaluation of alumina inclusions and clusters characteristics in a stainless steel grade and an Fe-10mass%Ni alloy. The extraction methods give a full 3D observation view of inclusions and clusters on the film filter, while observing an etched metal surface is considered to give a partial 3D view. As mentioned, for the study of inclusion formation and growth mechanism, it is necessary to determine the inclusion size distribution in a metal sample. If using the extraction methods, the number of inclusions per unit volume as well as real inclusion size can be estimated, and thus the size distribution.

Figure 4 shows an example of estimated size distributions for inclusions in clusters in stainless steel samples taken from the melt at different holding times after Al-deoxidation. The approach for this study was etching and extraction using Br_2 -methanol, as described in section 2.2. From this figure, valuable information can be obtained by studying the peaks. As can be seen, the peaks are shifting towards larger inclusion sizes as the holding time after Al-addition increases. This indicates that inclusion growth is occurring during this process. The peaks are also becoming wider with the holding time which indicates that the variation of inclusion sizes is increased during the process.

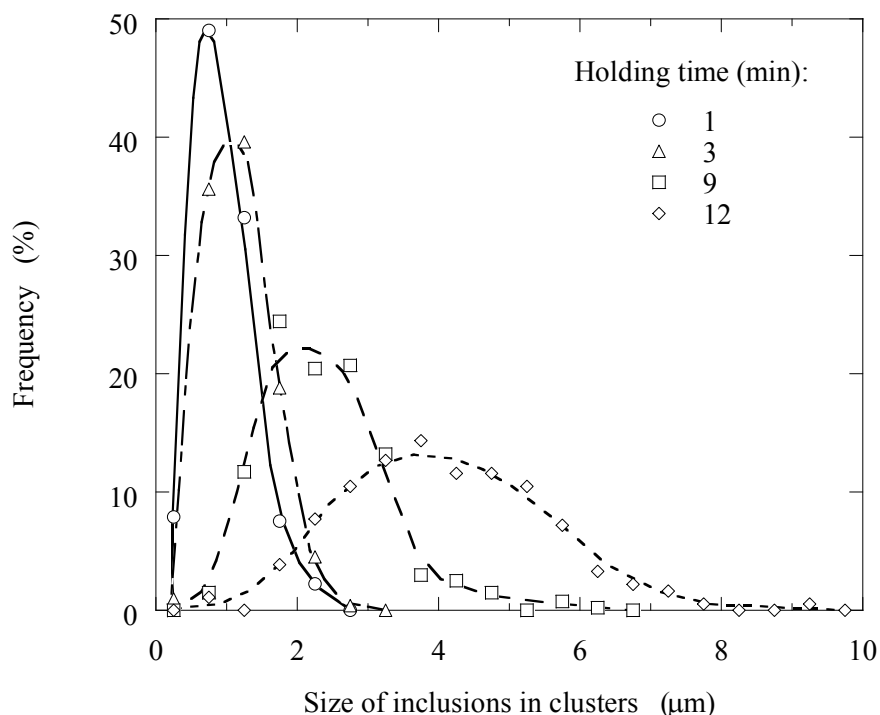


Figure 4: Particle size distribution measured for inclusions in clusters in stainless steel samples taken at different holding times.

The real size of e.g. clusters would be hard to estimate through observation of an etched surface since one part of the cluster is exposed while the other is still fixed in the metal matrix. Therefore, for determination of the real size distribution of clusters, the extraction method followed by observation on a film filter is the preferred method.

Another advantage with the extraction methods is shown in Figure 5. It shows to what extent the metal matrix affects the results from the analysis of inclusions using SEM in terms of measured Fe and Ni contents. The electrolytic extraction method, cross section and etching, and the cross section method are compared. It is clear from this figure that the effect of the matrix is highest for the cross sectional method and the lowest effect is obtained after electrolytic extraction.

Even though the etching method gives higher matrix contents compared to extraction methods, it is still used because it is a faster method for assessment of some inclusion characteristics in clusters. E.g. morphology, composition, location, and to some level also size of inclusions can be evaluated.

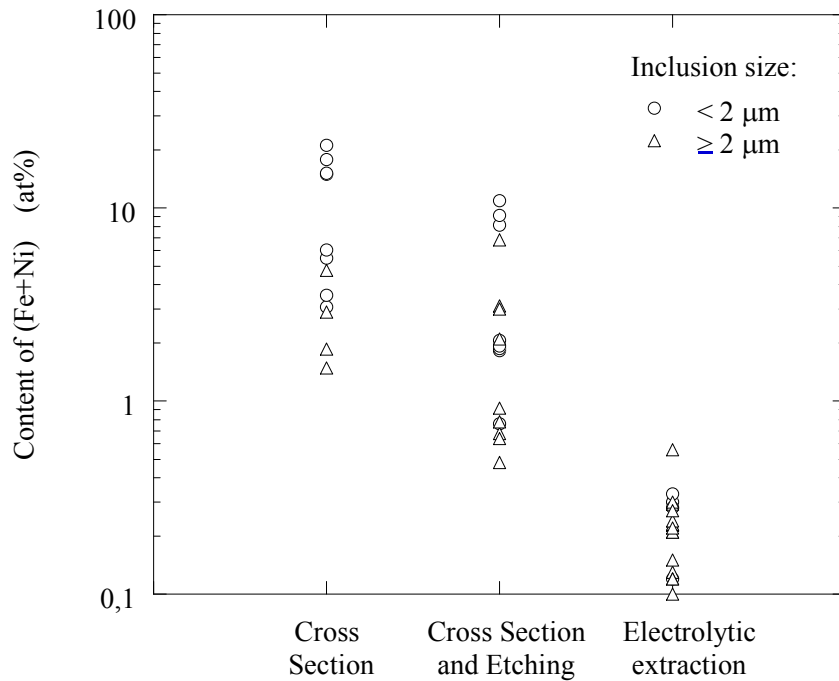


Figure 5: Effect of the metal matrix (Fe+Ni content) on analysis of alumina inclusions in Fe-10mass%Ni for different evaluation methods.

Figure 6 is showing the measured equivalent cluster size as a function of holding time after Al-addition estimated by the cross sectional method and after Br₂-methanol extraction in the same set of steel samples. The dissolved layer after extraction is calculated and also presented in the figure.

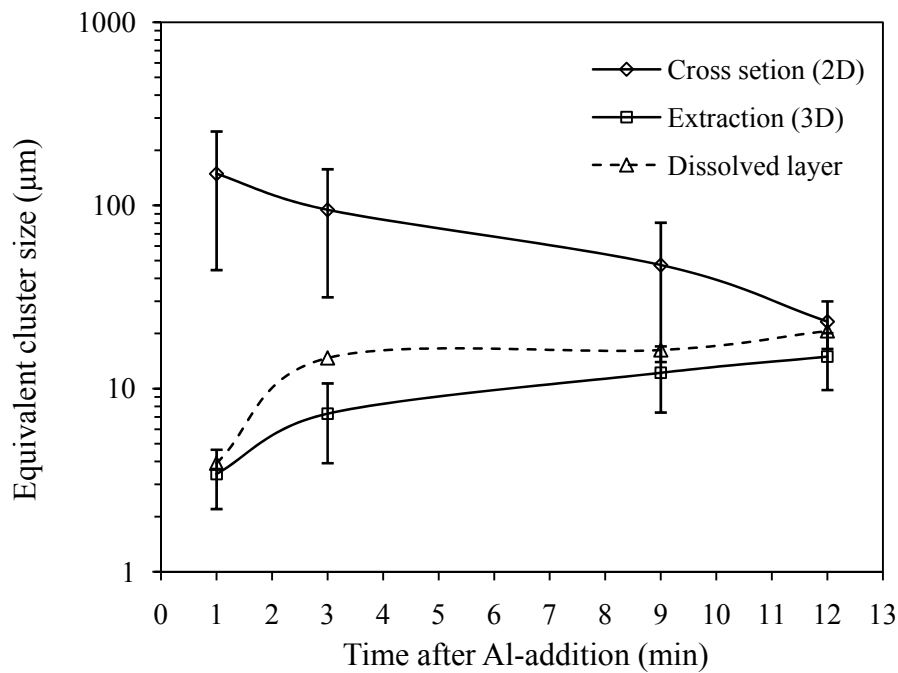


Figure 6: Cluster size measured using the 2D and 3D method as a function of holding time. The calculated dissolved layer for extraction experiments is also shown for different samples.

The cross sectional method is showing a decrease of cluster size with holding time, while the extraction method is showing an increase. Also, the 2D method shows a larger cluster size compared to the 3D method. Usually, the trend that the 2D method is showing is the expected one, i.e. a decrease in cluster size as a consequence of cluster separation. The increase in cluster size as well as the smaller size obtained by the 3D method can be explained by studying the dissolved layer. Since the dissolved layer is not larger than the cluster sizes measured by the 2D method, it cannot be expected to obtain the same cluster sizes with the 3D method. This example shows clearly that for an investigation of the cluster size in a sample, a quick evaluation of the largest cluster with the 2D method using e.g. a LOM is required before the starting of extraction. After the quick 2D evaluation, the proper dissolved depth can be chosen.

4. Conclusions

For a quick assessment of large size Al_2O_3 inclusions short time etching using acids or halogen methanol solutions can be applied. For investigation of small size Al_2O_3 inclusions, electrolytic extraction is recommended.

Br_2 -methanol has shown to have approximately a 10 times higher dissolution rate compared to the electrolytic extraction solutions. However, it has shown to be more unstable which in turn can make the estimation of time to dissolve a certain layer depth more difficult.

From the present experiments, it is shown that by using extraction methods the real size of inclusions can be estimated and a low effect from the matrix during composition analysis is obtained. However, the etching method can contribute to a faster assessment of characteristics such as morphology, composition and location of inclusions. For estimation of largest clusters a 2D investigation is usually required prior to extraction.

5. Acknowledgements

The Swedish Governmental Agency for Innovation Systems (VINNOVA), Jernkontoret – The Swedish Steel Producers' Association and technical area TO45, Sweden-Japan Foundation and foundations of "Axel Hultgrens fond", "Skandinaviska Malmö Metallforsknings- och utvecklingsfond", and "Överingenjörens Gustaf Janssons Jernkontorsfond" are acknowledged for financial support.

References:

- 1) Hiroki OHTA and Hideaki SUIITO, Characteristics of Particle Size Distribution of deoxidation Products with Mg, Zr, Al, Ca, Si/Mn and Mg/Al in Fe-10mass%Ni Alloy, ISIJ International, Vol. 46 (2006), No. 1, pp. 14-21.
- 2) A. Karasev and H. Suito, Analysis of Size Distribution of Primary Oxide Inclusions in Fe-10mass%Ni-M (M=Si, Ti, Al, Zr and Ce) Alloy, Met. and Mater. Trans. B, 30B (1999), pp. 259-270.
- 3) Y. Kanbe, A. Karasev, H. Todoroki and P.G. Jönsson, Application of Extreme Value Analysis for Two- and Three-Dimensional Determinations of the Largest Inclusions in Metal Samples, ISIJ Int., 51 (2011), No.4.
- 4) Ryo INOUE, Tatsuro ARIYAMA, and Hideaki SUIITO: "Extraction and Evaluation of Inclusion Particles in Steel", Asia Steel International Conference 2009, S11-16, pp 1-9, May 24-27, 2009, The Korean Institute of Metals and Materials.
- 5) N. Kojola, S. Ekerot, and P. Jönsson, A pilot-plant study of clogging rates in low-carbon and stainless steel grades, Ironmaking and Steelmaking, Vol. 38, Issue 2, Feb (2011), pp. 81-89.



AUTHORS LIST

AIGNER	S.	OC13	CIAPARRA	D.	<u>OC22</u>
AKIYOSHI	T.	OC78	COLLA	V.	OC74
ANDERSON	D.	OC20	DABALÀ	M.	OC48
ANDREA	G.	<u>OC49</u>	DAL-MOLIN	F.	<u>OC20</u>
ARGELIA FABIOLA	M. P.	OC51	DAVIDE	M.	<u>OC49</u>
ARIES	E.	OC20	DE VYT	A.	OC79
ARIYAMA	T.	OC17	DEL FRARI	D.	OC31
ARNE	B.	<u>OC29</u>	DEMIRANDA	U.	OC08
ARNOULT	C.	OC31	DENG	X.	OC56
AUBRIET	H.	OC80	DHONT	A.	OC07
BALLAND	P.	OC43	DIDRIKSSON	R.	OC18
BARDON	J.	<u>OC31</u>	DIEGUEZ	A. C.	OC01
BARDON	J.	OC80	DONGLING	L.	<u>OC67</u>
BASSIN	M.	<u>OC40</u>	DORIER	J.-L.	OC15
BEHRENS	K.	<u>OC76</u>	DUCHACZEK	H.	<u>OC34</u>
BELLAVIA	L.	OC61	EGGER	M.	<u>OC13</u>
BENGTSON	A.	OC08	EILERS	D.	OC08
BENGTSON	A.	OC16	ENGKVIST	T.	OC16, <u>OC18</u>
BERGERS	K.	<u>OC35</u>	ERICSSON	O.	<u>OC45</u>
BÉRUBÉ	L.	<u>OC39</u>	EVARD	S.	OC43
BILSTEIN	W.	<u>OC63</u>	FAGUNDES	L.	<u>OC01</u>
BLECK	W.	OC24, OC71	FALK	H.	<u>OC24</u>
BOMFIM	J. A. S.	<u>OC80</u>	FALK	M.	OC24
BORDIGNON	L.	OC33	FARINHA	A. I.	<u>OC21</u>
BOUCHARD	M.	OC39	FERDINAND	H.	OC50
BOUR	J.	OC31	FISHER	R.	OC20
BRITTA	L.	OC53	FLOCK	. J.	OC35
BRIXIUS	T.	<u>OC81</u>	FRANCESCO	M.	<u>OC49</u>
BRUNELLI	K.	OC48	FRANCISCONO	A.	OC02
BÖHLEN	J.-M.	OC15, OC58	FRICKE-BEGEMANN	C.	<u>OC19</u>
CABALÍN	L. M.	OC65	FUJIMOTO	K.	OC78
CALLIARI	I.	<u>OC48</u>	GAO	Y.	<u>OC56</u>
CARLO	M.	<u>OC49</u>	GERALD	K.	OC50
CARMELE	D.	<u>OC71</u>	GIAMPIETRO	T.	OC51
CHANG WOO	R.	OC14	GIAN LUCA	G.	OC57
CHEN	J.-W.	OC59	GONZÁLEZ	A.	OC65
CHEN	J.	<u>OC27</u>	GOSENS	M.	OC81
CHEN	S.	OC46	GUOHUA	X.	<u>OC67</u>
CHEN	W.	OC56	HAIZHO	W.	OC26
CHEN	Y.-Y.	OC59	HAIZHOU	W.	OC25, <u>OC67</u>
CHEN	Y.	OC27	HALÁSZ	E.	OC15, <u>OC58</u>
CHIARA	S.	OC57	HAN	P.-C.	OC59
CHIAROTTI	U.	OC08	HAN	P.	OC27



AUTHORS LIST

HEEMSKERK	R.	<u>OC38</u>	MADANI	M.	<u>OC32</u>
HEINRICH	K.	OC53	MAGRINI	M.	OC48
HENNINGSSON	P.	<u>OC44</u>	MAKOWE	J.	OC08
HENRICH	A.	<u>OC05</u>	MARION	H.	OC53
HERRMANN	K.	OC71	MATHY	C.	<u>OC60</u>
HIRAIDE	M.	<u>OC10</u>	MATILHA	A.	OC01
HOLBRECHT	W.	OC60	MATSUMIYA	H.	OC10
HONGQUAN	M.	OC25, OC26	MATTIA	M.	<u>OC57</u>
HU	J.	<u>OC59</u>	MENDES	M.	OC01
HU	X.	OC54	MEYER	S.	OC71
HUBER	F.	OC24	MIHAELA	A.	<u>OC50</u>
INOUE	R.	<u>OC17</u>	MONFORT	G.	<u>OC61</u>
INOUE	R.	OC73	MOREAS	G.	OC63
INOUE	R.	OC83	MOREAS	G.	<u>OC64</u>
IRENE	C.	<u>OC51</u>	MOROLI	V.	OC08
ISHIDA	T.	<u>OC78</u>	MÜLLER	G.	OC65
ISTVAN	M.	OC51	MÜLLER	J.	OC81
JACQUES	S.	<u>OC77</u>	NASTASI	G.	<u>OC74</u>
JANSSEN	S.	OC28	NIEDERSTRAßER	J.	<u>OC41</u>
JIE	S.	OC30	NOLL	R.	OC08, OC19 OC74
JOHANSSON	L.	OC44	NORDEN	M.	OC24
JOHNSTON	S.	OC20	OVERKAMP	B.	OC41
JOOSTEN	H.-G.	OC52	PAPPERT	E.	<u>OC04</u>
JUNXIANG	W.	OC30	PENG	W.	<u>OC25, OC26</u>
JÖNSSON	P.	OC45, OC83	PETER	M.	OC50
JÖNSSON	P. G.	OC73	PETERSEN	J.	OC80
JÖRG	F.	OC04	PIERO LUCA	L.	<u>OC49</u>
KARASEV	A.	OC45, OC83	PIERRET	J.-C.	OC60
KARASEV	A. V.	<u>OC73</u>	PIETRO	S.	<u>OC49</u>
KINOSHIRO	S.	OC78	PISSENBERGER	A.	OC13
KIYOKAWA	K.	OC17	POERSCHKE	D.	<u>OC28</u>
KLEMRADT	U.	OC71	PORTA	D.	OC76
LAACHACHI	A.	OC80	QU	H.	OC27
LAMANDE	A.	OC77	QU	H.	OC59
LARS	H.	OC29	RAMPIN	I.	OC48
LASERNA	J.	OC65	RECKNAGEL	S.	<u>OC53</u>
LE	Y.	<u>OC68</u>	REYNA	V.	OC57
LEDE	M.	<u>OC69</u>	RIEGER	T.	<u>OC71</u>
LEGROS	P.	OC23	RIVARD	S.	OC39
LEI	L.	<u>OC30</u>	ROLLET	S.	<u>OC02</u>
LI	K.	OC15	RUBY-MEYER	F.	<u>OC43</u>
LI	M.	<u>OC82</u>	RUCH	D.	OC31
LIPPMANN	T.	OC71			



AUTHORS LIST

LUMEN	W.	OC60	XHOFFER	C.	<u>OC07</u> , OC79
RUCH	D.	OC80	XU	J.	<u>OC54</u>
RUIZ	J.	<u>OC65</u>	XUE	N.	OC54
RUNNSJÖ	G.	<u>OC16</u> , OC18	XUEJING	S.	OC25, <u>OC26</u>
SAKASHITA	A.	OC78	YAO	N.-J.	OC59
SCHWERDT	C.	OC65	YAO	N.	OC27
SEDLAK	M. O.	OC16	YI	Z.	OC69
SHAO	M.	OC46	YONG TAE	S.	<u>OC14</u>
SHAO	X.	<u>OC47</u>	YUAN	L.-J.	OC59
SHAOCHENG	H.	OC25, OC26	YUAN	L.	OC27
SHEYING	Z.	OC30	YUNHAI	J.	<u>OC67</u>
SIMONNET	M.	OC77	ZANFORLIN	M.	OC08
SPERANDIO	C.	OC80	ZANI	M.	OC08
STANG	M.	OC81	ZHAO	L.	<u>OC27</u>
STARK	A.	OC71	ZHAO	L.	<u>OC59</u>
STAS	F.	OC60	ZHIGANG	Y.	OC25, OC26
STRAUß	N.	OC19	ZHU	Y.	OC46
STURM	V.	<u>OC08</u>	ZWETTLER		F.
THOMAS	I.	OC35			
TOMODA	K.	OC17			
TUSSET	V.	OC61			
UEDA	S.	OC17			
VALENTINA	M.	OC57			
VAN CASTEREN	H.	OC38			
VAN DRIEL	R.	OC52			
VAN LIERDE	V.	<u>OC23</u>			
VAN					
STUIJVENBERG	B.	OC52			
VANDEN EYNDE	X.	OC21, <u>OC33</u>			
VANDERHEYDEN	B.	OC60			
VANDERHEYDEN	B.	OC61			
VASILJEVIC	D.	<u>OC83</u>			
VERGAUWENS	M.	OC43			
VESTIN	F.	OC08			
VOLPONI	V.	OC08			
WANG	H.-Z.	OC59			
WANG	H.	OC27			
WEIHER	N.	OC81			
WEN	X.	<u>OC46</u>			
WERHEIT	P.	OC08			
WESTER	R.	<u>OC74</u>			
WILLEMS	A.	OC07			
WIZENTY	N.	OC77			